

Transactions of the ASME®

HEAT TRANSFER DIVISION
Chairman, J. R. WELTY
Secretary, O. A. PLUMB
Technical Editor, R. VISKANTA
Associate Technical Editors,
R. O. BUCKIUS (1993)
W. A. FIVELAND (1992)
L. S. FLETCHER (1992)
F. P. INCROPERA (1993)
H. R. JACOBS (1992)
J. H. KIM (1993)
J. R. LLOYD (1992)
D. M. McELIGOT (1992)
R. J. SIMONEAU (1993)
W. A. SIRIGNANO (1992)
L. C. WITTE (1992)

BOARD ON COMMUNICATIONS
Chairman and Vice President
M. E. FRANKE

Members-at-Large
W. BEGELL
T. F. CONRY
T. DEAR
R. L. KASTOR
J. KITTO
R. MATES
W. MORGAN
E. M. PATTON
R. E. REDER
A. VAN DER SLUYS
F. M. WHITE
B. ZIELS

President, N. H. HURT, JR.
Executive Director,
D. L. BELDEN
Treasurer,
ROBERT A. BENNETT

PUBLISHING STAFF
Mng. Dir., Publ.,
CHARLES W. BEARDSLEY
Managing Editor,
CORNELIA MONAHAN
Sr. Production Editor,
VALERIE WINTERS
Production Assistant,
MARISOL ANDINO

Transactions of the ASME, Journal of Heat Transfer (ISSN 0022-1481) is published quarterly (Feb., May, Aug., Nov.) for \$160.00 per year by The American Society of Mechanical Engineers, 345 East 47th Street, New York, NY 10017. Second class postage paid at New York, NY and additional mailing offices. POSTMASTER: Send address changes to Transactions of the ASME, Journal of Heat Transfer, c/o THE AMERICAN SOCIETY OF MECHANICAL ENGINEERS, 22 Law Drive, Box 2300, Fairfield, NJ 07007-2300.

CHANGES OF ADDRESS must be received at Society headquarters seven weeks before they are to be effective. Please send old label and new address. PRICES: To members, \$36.00, annually; to nonmembers, \$160.00. Add \$15.00 for postage to countries outside the United States and Canada.

STATEMENT from By-Laws. The Society shall not be responsible for statements or opinions advanced in papers or ... printed in its publications (B7.1, para. 3).

COPYRIGHT © 1992 by The American Society of Mechanical Engineers. Reprints from this publication may be made on condition that full credit be given the TRANSACTIONS OF THE ASME, JOURNAL OF HEAT TRANSFER, and the author, and date of publication be stated.

INDEXED by Applied Mechanics Reviews and Engineering Information, Inc. Canadian Goods & Services Tax Registration #126148048

Journal of Heat Transfer

Published Quarterly by The American Society of Mechanical Engineers

VOLUME 114 • NUMBER 1 • FEBRUARY 1992

ANNOUNCEMENTS

- 2 Journal of Heat Transfer Referees—1991
- 29 Change of address form for subscribers
- 293 Announcement and Call for Papers: Third World Conference on Experimental Heat Transfer, Fluid Mechanics, and Thermodynamics
- 294 Information for authors

TECHNICAL PAPERS

- 5 An Adaptive Inverse Heat Conduction Method With Automatic Control
G. P. Flach and M. N. Özışik
- 14 Comparative Studies on Nonlinear Hyperbolic and Parabolic Heat Conduction for Various Boundary Conditions: Analytic and Numerical Solutions
A. Kar, C. L. Chan, and J. Mazumder
- 21 Thermal Contact Conductance of Metallic Coated BiCaSrCuO Superconductor/Copper Interfaces at Cryogenic Temperatures
J. M. Ochterbeck, G. P. Peterson, and L. S. Fletcher
- 30 Solidification of an Aqueous Salt Solution in a Circular Cylinder
A. S. Burns, L. A. Stickler, and W. E. Stewart, Jr.
- 34 Melting Heat Transfer From a Horizontal Ice Cylinder Immersed in Quiescent Saline Water
S. Fukusako, M. Tago, M. Yamada, K. Kitayama, and C. Watanabe
- 41 Differential Methods for the Performance Prediction of Multistream Plate-Fin Heat Exchangers
B. S. V. Prasad and S. M. K. A. Gurukul
- 50 Temperature Distribution Near a Heat Exchanger Wall Immersed in High-Temperature Packed and Fluidized Beds
G. Flamant, N. Fatah, G. Olalde, and D. Hernandez
- 56 Turbulent Heat Transfer Augmentation and Friction in Periodic Fully Developed Channel Flows
T.-M. Liou and J.-J. Hwang
- 65 Influence of Jet-Grid Turbulence on Flat Plate Turbulent Boundary Layer Flow and Heat Transfer
C. D. Young, J. C. Han, Y. Huang, and R. B. Rivir
- 73 Evaluation of the Stagnation Point Region Overshoot
H. H. Sogin
- 79 Measurements of the Free Surface Flow Structure Under an Impinging, Free Liquid Jet
J. Stevens and B. W. Webb
- 85 Transient Convective Heat Transfer in Planar Stagnation Flows With Time-Varying Surface Heat Flux and Temperature
D. A. Zumbrunnen
- 94 Experimental Study of Laminar Natural Convection in Cells With Various Convex and Concave Bottoms
W. M. Lewandowski and M. J. Khubeiz
- 99 Free Two-Dimensional Convective Bifurcation in a Horizontal Annulus
A. Cheddadi, J. P. Caltagirone, A. Mojtabi, and K. Vafai
- 107 Experimental Heat Transfer Rates of Natural Convection of Molten Gallium Suppressed Under an External Magnetic Field in Either the X, Y, or Z Direction
K. Okada and H. Ozoe
- 115 Three-Dimensional Natural Convection From Vertical Heated Plates With Adjoining Cool Surfaces
B. W. Webb and T. L. Bergman
- 121 Natural Convection Heat Transfer From a Plate in a Semicircular Enclosure
G. A. Moore and K. G. T. Hollands
- 127 Turbulent Free Convection Heat Transfer to Drag-Reducing Fluids From Arbitrary Geometric Configurations
A. Nakayama and A. V. Shenoy
- 135 Measurements of Velocity and Turbulence in Vertical Axisymmetric Isothermal and Buoyant Jets
J. Peterson and Y. Bayazitoglu
- 143 Mixed Convection Through Vertical Porous Annuli Locally Heated From the Inner Cylinder
C. Y. Choi and F. A. Kulacki

(Contents continued)

- 152 Convective Nucleate Boiling on a Heated Surface Cooled by a Impinging, Planar Jet of Water
D. T. Vader, F. P. Incropera, and R. Viskanta
- 161 An Experimental Study of Subcooled Film Boiling on a Vertical Surface—Hydrodynamic Aspects
R. Vijaykumar and V. K. Dhir
- 169 An Experimental Study of Subcooled Film Boiling on a Vertical Surface—Thermal Aspects
R. Vijaykumar and V. K. Dhir
- 179 Critical Heat Flux in Horizontal Tube Bundles in Vertical Crossflow of R113
K. M. Leroux and M. K. Jensen
- 185 Considerations in Predicting Burnout of Cylinders in Flow Boiling
P. Sadasivan and J. H. Lienhard
- 194 Droplet Condensation in Rapidly Decaying Pressure Fields
P. F. Peterson, R. Y. Bai, V. E. Schrock, and K. Hijikata
- 201 Condensation of a Nonazeotropic Refrigerant Mixture R114/R113 in Horizontal Annuli With an Enhanced Inner Tube
Sh. Nozu, K. Ozaki, H. Inaba, and H. Honda
- 211 Surface Roughness and Its Effects on the Heat Transfer Mechanism in Spray Cooling
M. R. Pais, L. C. Chow, and E. T. Mahefkey
- 220 Thermal Analysis of Droplet Spray Evaporation From a Heated Solid Surface
K.-K. Tio and S. S. Sadhal
- 227 Thickness-Dependent Radiative Properties of Y-Ba-Cu-O Thin Films
P. E. Phelan, G. Chen, and C. L. Tien
- 234 Transient Radiation Properties of a Subgrid Scale Eddy
J. P. Gore and J. H. Jang
- 243 Generalized State-Property Relations of Nonluminous Flame Absorption Coefficients
W. L. Grosshandler and E. M. Thurlow
- 250 Radiation, Conduction, and Convection From a Sphere in an Absorbing, Emitting, Gray Medium
P. D. Jones and Y. Bayazitoglu
- 255 Thermal Analysis and Control for Sputtering Deposition of High- T_c Superconducting Films
M. I. Flik, B. I. Choi, A. C. Anderson, and A. C. Westerheim
- 264 Thermal Analysis of Electron-Beam Absorption in Low-Temperature Superconducting Films
M. I. Flik and K. E. Goodson
- 271 Moving Front Fixing in Thin Film Laser Annealing
C. P. Grigoropoulos and W. E. Dutcher, Jr.

TECHNICAL NOTES

- 278 A Solution for the Parallel-Flow Regenerator
F. E. Romie
- 280 Vortex Generator Induced Heat Transfer Augmentation Past a Rib in a Heated Duct Air Flow
T. A. Myrum, A. Acharya, S. Inamdar, and A. Mehrotra
- 284 Heat Transfer From a Square Source to an Impinging Liquid Jet Confined by an Annular Wall
D. L. Besserman, F. P. Incropera, and S. Ramadhyani
- 287 Surface Factors Influencing Burnout on Flat Heaters
J. M. Ramilison, P. Sadasivan, and J. H. Lienhard
- 290 On the Pulse Boiling Frequency in Thermosyphons
J. F. Liu and J. C. Y. Wang

An Adaptive Inverse Heat Conduction Method With Automatic Control

G. P. Flach

M. N. Özişik

Department of Mechanical and Aerospace
Engineering,
North Carolina State University,
Raleigh, NC 27695-7910

An adaptive sequential method is presented for solving the one-dimensional inverse heat conduction problem. The step size, order of parameterization, and amount of the step retained are variable and chosen automatically for each sequence such that optimal, stable results are obtained. A statistical analysis accounting for the stochastic error contributions from both the measured and initial temperatures is derived. Results from the statistical analysis are used to predict stability or instability for a given selection of parameters controlling the inverse method. Simulated experimental applications using inexact data illustrate the practicality of the approach and the effectiveness of the automatic control criteria.

Introduction

The most effective inverse heat conduction methods have parameters that can be adjusted to suit the particular characteristics of a set of measured data. Examples are the number of future temperatures in Beck's method (Beck et al., 1985), the number of measurement times in the digital filter in the approach taken by Hills and Hensel (1986), and the regularization parameter of Tikhonov and Arsenin (1977). The effects of such parameters on the deterministic and stochastic errors in the inverse solution have been quantified for several methods. However, quantitative criteria for automatically selecting optimal values of parameters without guesswork, expert user input, or prior knowledge are needed for practical application of inverse methods. Beck et al. (1985) summarize much of the work to date related to optimal parameter selection.

In this paper, the optimization of a very adaptive sequential inverse heat conduction method for estimating time-dependent surface conditions of a one-dimensional region with temperature-dependent properties is investigated. The step size, order of parameterization, and step retention in the method are all variable from sequence to sequence. Three criteria are developed for achieving optimal, stable results on a local basis. A statistical analysis is developed for the purpose of defining confidence bounds on the computed inverse results and predicting the stability or instability of the sequential procedure for a given selection of the control parameters. The sequential inverse heat conduction method considered is conceptually most similar to Beck's sequential function-specification method (Beck et al., 1985), but is a generalization designed to allow much more flexibility so that more optimal results can be obtained. Primary emphasis is placed on achieving optimal results so computational efficiency is generally sacrificed with the present method. Results are given in two stages. First, the stability of the sequential procedure is investigated using results from the statistical analysis. Then, the effectiveness of the three automatic control criteria is demonstrated using simulated measured temperature data.

Formulation and Inverse Solution Overview

The inverse heat conduction problem considered involves determining the surface temperatures and heat fluxes at both boundaries of a one-dimensional slab with temperature-dependent thermal properties. The governing equations are

$$\frac{\partial}{\partial x} \left[k(T) \frac{\partial T}{\partial x} \right] = \rho c_p(T) \frac{\partial T}{\partial t} \quad 0 < x < L, \quad t > 0 \quad (1a)$$

$$T = f_1(t); \quad -k \frac{\partial T}{\partial x} = q_1(t) \quad x = 0 \quad (1b, c)$$

$$T = f_2(t); \quad k \frac{\partial T}{\partial x} = q_2(t) \quad x = L \quad (1d, e)$$

$$T = T_0(x) \quad t = 0 \quad (1f)$$

The boundary conditions $f_i(t)$ and $q_i(t)$, $i = 1$ or 2 , are not to be interpreted as independent quantities; rather, given a surface temperature $f_i(t)$ there also exists a corresponding heat flux $q_i(t)$, and vice versa. The temperature-dependent thermal properties and initial temperature distribution are considered known while the surface conditions are unknown and to be estimated from interior temperature readings. Temperature sensors are assumed to be located at multiple spatial positions x_k ; $k = 1, 2, \dots, NX$. For each sequence of the calculations in the time domain, readings from these sensors are considered available at times t_j ; $j = 1, 2, \dots, NT$ for a total of $N = NX \times NT$ temperature measurements. The measured temperature data for a given sequence are denoted as

$$\begin{aligned} \bar{T}_i &\equiv \bar{T}(x_k, t_j); \quad i = 1, 2, \dots, N; k \\ &= 1, 2, \dots, NX; j = 1, 2, \dots, NT \quad (2) \end{aligned}$$

where explicit reference to the particular sequence is omitted. Later, the procedure for specifying the input data for a sequence is described. Since sequences overlap, some of the measured data used in the current sequence are reused in the next sequence. The accuracy of the temperature sensors is assumed to be known in the form of a standard deviation value, σ_i ; $i = 1, 2, \dots, N$, associated with each temperature reading. The measurement errors are also assumed to be additive, independent, and have zero means. Correlated errors can also be handled as outlined in the Appendix.

The following deterministic analysis presents the basic mechanism for estimating the unknown surface conditions from the measured interior temperature data. A subsequent statistical analysis estimates the effects of measurement error on the estimated results. Finally, criteria for automatically selecting the parameters controlling the sequential procedure are developed.

Deterministic Analysis

Inverse heat conduction problems are mathematically ill-posed in their initial formulations in the sense that existence, uniqueness, and stability of the inverse solution are not all

Contributed by the Heat Transfer Division for publication in the JOURNAL OF HEAT TRANSFER. Manuscript received by the Heat Transfer Division September 12, 1989; revision received August 31, 1990. Keywords: Conduction, Transient and Unsteady Heat Transfer.

ensured. A successful solution of an inverse problem generally involves reformulation of the problem, resulting in an approximate solution, which is well posed. Therefore, solution steps addressing the existence, uniqueness, and stability of the inverse solution are necessary to guarantee a well-posed solution. Keeping these points in mind, the present sequential inverse heat conduction solution is constructed in the following steps:

1) Direct Solution: The solution to the equivalent direct heat conduction problem is obtained by using a finite difference scheme.

2) Parameterization: A pair of the unknown surface conditions ($f_1(t)$ or $q_1(t)$ and $f_2(t)$ or $q_2(t)$) are parameterized by modeling these functions with linear B -splines.

3) Parameter Estimation: Parameter values that minimize a weighted least-squares norm are selected. The nonlinear algebraic set of equations is solved using the Levenberg-Marquardt algorithm.

4) Uniqueness Conditions: Conditions on the number of spatial and temporal temperature measurements are established that ensure uniqueness of the inverse solution.

5) Stabilization: Smoothing or stability for the inverse solution is provided through the use of overspecified data.

6) Sequential Procedure: The above steps are implemented in a sequential manner in the time domain.

Function specification in step (2) is needed on a practical basis in order to reduce the problem to finite-dimensional parameter estimation. Existence of the inverse solution is guaranteed by step (3); requiring the inverse solution to minimize a norm between the measured and estimated data, rather than make it necessarily zero, ensures a solution will exist. Uniqueness of the inverse solution is ensured in step (4) by determining discrete uniqueness conditions for the algebraic least-squares equations. Stability is obtained in step (5) by using overspecified data, i.e., fewer parameters than independent data.

In the detailed inverse analysis that follows, estimation of the surface conditions for a single sequence of the calculations is initially considered and steps 1-5 are discussed in this context. Then, the integration of these steps into a sequential procedure is described. Therefore, the measured temperature data, \bar{T}_i , and initial temperature distribution for a particular sequence

are initially considered known quantities and specification of these quantities is discussed later.

Direct Solution. The equivalent direct heat conduction problem is the same as equations (1) but with the boundary conditions considered known instead of unknown and the initial temperature $T_0(x)$ is replaced with $\hat{T}_0(x)$. Since temperature-dependent thermal properties make the problem nonlinear, a finite control volume formulation was selected for solving the direct problem. The thermal property values are lagged one time level and an adjustable weight θ is given to successive time levels when approximating the time derivative. The numerical examples in the Results and Discussion section involve estimating surface temperature and for this case the following scheme results:

$$\theta \left[\left(\frac{k_{i-1}^n + k_i^n}{2\Delta x} \right) T_{i-1}^{n+1} - \left(\frac{k_{i-1}^n + 2k_i^n + k_{i+1}^n}{2\Delta x} \right) T_i^{n+1} + \left(\frac{k_i^n + k_{i+1}^n}{2\Delta x} \right) T_{i+1}^{n+1} \right] + (1-\theta) \left[\left(\frac{k_{i-1}^n + k_i^n}{2\Delta x} \right) T_{i-1}^n - \left(\frac{k_{i-1}^n + 2k_i^n + k_{i+1}^n}{2\Delta x} \right) T_i^n + \left(\frac{k_i^n + k_{i+1}^n}{2\Delta x} \right) T_{i+1}^n \right] = (\rho c_p)_i^n \frac{\Delta x}{\Delta t} (T_i^{n+1} - T_i^n) \quad (3a)$$

$$T_{x=0}^{n+1} = f_1(t^{n+1}) \quad (3b)$$

$$T_{x=L}^{n+1} = f_2(t^{n+1}) \quad (3c)$$

The weight θ is chosen as 2/3 since this selection tends to give accurate results.

Parameterization. Parameterization is accomplished by representing a chosen pair of the estimated surface conditions, i.e., $\hat{f}_1(t)$ or $\hat{q}_1(t)$ and $\hat{f}_2(t)$ or $\hat{q}_2(t)$, with piecewise linear segments. Linear B -splines are chosen to construct the connected line segments conveniently. Letting $\hat{b}(t)$ denote any one of $\hat{f}_1(t)$, $\hat{q}_1(t)$, $\hat{f}_2(t)$, or $\hat{q}_2(t)$, the B -spline representation for l segments or spline intervals is

$$\hat{b}(t) = \hat{b}_0 B_1(t) + \sum_{j=1}^l \hat{b}_j B_{j+1}(t) \quad (4)$$

Nomenclature

b = surface condition (i.e., f_1 , f_2 , q_1 , or q_2)		$\bar{\alpha}$ = thermal diffusivity
$B_j(t)$ = B -spline functions	peratures in common to successive sequences	δ = distance from surface to temperature sensor
C = covariance matrix defined by equation (A.2b)	NT = number of temporal measurements for a given sequence	ϵ = additive measurement error
c_p = specific heat	NX = number of spatial measurement locations	θ = finite difference formulation weighting factor
cov = covariance	$\hat{\mathbf{p}}$ = composite surface condition parameter vector	μ_k = Levenberg-Marquardt parameter
D^2 = sum squared deterministic error in the estimated interior temperatures	q = surface heat flux	ρ = mass density
$E(\bullet)$ = statistical expected value operator	r = autoregressive error model parameter	σ = standard deviation
f = surface temperature	S = weighted least-squares norm	τ = nondimensional time
$\hat{\mathbf{g}}$ = general function of $\hat{\mathbf{p}}$ and $\hat{\mathbf{T}}_0$	t = time	
k = thermal conductivity	T = temperature	Subscripts
l = number of spline intervals	var = variance	0 = initial temperature distribution
L = slab thickness	x = spatial variable	max = maximum
n = total number of surface condition parameters	\mathbf{w} = weighting factor matrix defined by equation (6b)	opt = optimal
N = total number of temperature measurements for a sequence	Δt_{TOTAL} = sequence step size	Superscripts
N_c = number of measured temperatures	Δt_{RETAIN} = portion of sequence retained	\sim = measured
		$\hat{\sim}$ = estimated
		old = current sequence
		new = next sequence

where the parameters \hat{b}_j are the values of $\hat{b}(t)$ at the spline knot positions. Since \hat{b}_0 is the initial value of $\hat{b}(t)$, it is already known from the initial temperature distribution $\hat{T}_0(x)$. The parameters $\hat{b}_j, j = 1, 2, \dots, l$ are to be determined. The B -spline functions $B_j(t)$ can be easily evaluated through an efficient, stable recursion formula (de Boor, 1978, p. 131). If the surface temperatures $\hat{f}_1(t)$ and $\hat{f}_2(t)$ are parameterized through equation (4), for instance, then the composite parameter vector to be estimated is constructed by collecting both sets of spline coefficients as

$$\hat{\mathbf{p}} \equiv \{\hat{p}_1, \hat{p}_2, \dots, \hat{p}_n\}^T \\ \equiv \{\hat{f}_{11}, \hat{f}_{12}, \dots, \hat{f}_{1l}, \hat{f}_{21}, \hat{f}_{22}, \dots, \hat{f}_{2l}\}^T \quad (5)$$

where $n \equiv 2l$. The surface heat fluxes $\hat{q}_1(t)$ and $\hat{q}_2(t)$ are obtained as auxiliary quantities from the direct solution. Alternatively, $\hat{q}_1(t)$ and $\hat{q}_2(t)$ could be modeled with B -splines and $\hat{f}_1(t)$ and $\hat{f}_2(t)$ obtained as auxiliary quantities, for instance.

Parameter Estimation. A natural approach for selecting the estimated surface condition parameters, $\hat{\mathbf{p}}$, is to require the computed interior temperatures to match the measured temperatures as closely as possible for a given number of spline intervals. The weighted sum of squares norm, S , is formed as

$$S(\hat{\mathbf{p}}) \equiv (\tilde{\mathbf{T}} - \hat{\mathbf{T}}(\hat{\mathbf{p}}))^T \mathbf{w}^T \mathbf{w} (\tilde{\mathbf{T}} - \hat{\mathbf{T}}(\hat{\mathbf{p}})) \quad (6a)$$

where

$$\mathbf{w} \equiv \begin{bmatrix} \sigma_1^{-1} & 0 & \dots & 0 \\ 0 & \sigma_2^{-1} & & \vdots \\ \vdots & & \ddots & \\ 0 & \dots & & \sigma_N^{-1} \end{bmatrix} \quad (6b)$$

The weighting factor matrix was chosen to minimize statistical uncertainty. Parameters minimizing equation (6a) satisfy the following system of nonlinear algebraic equations:

$$\left[\frac{\partial \hat{\mathbf{T}}^T}{\partial \hat{\mathbf{p}}} \right] \mathbf{w}^T \mathbf{w} [\tilde{\mathbf{T}} - \hat{\mathbf{T}}] = 0 \quad (7)$$

To solve equations (7), we choose the Levenberg-Marquardt iterative algorithm

$$\hat{\mathbf{p}}^{k+1} = \hat{\mathbf{p}}^k + \left(\frac{\partial \hat{\mathbf{T}}^T}{\partial \hat{\mathbf{p}}} \mathbf{w}^T \mathbf{w} \frac{\partial \hat{\mathbf{T}}}{\partial \hat{\mathbf{p}}^T} + \mu_k \mathbf{I} \right)^{-1} \frac{\partial \hat{\mathbf{T}}^T}{\partial \hat{\mathbf{p}}} \mathbf{w}^T \mathbf{w} (\tilde{\mathbf{T}} - \hat{\mathbf{T}}) \quad (8)$$

where μ_k is a positive parameter. The derivatives are approximated by a forward finite difference formula using the direct solution.

We have not extensively investigated convergence issues either analytically or numerically. For most practical problems, the temperature dependence of the thermal properties introduces only a mild nonlinearity and, since the inverse method is applied in a sequential manner, a very good starting guess is available from the previous sequence. As a result, we have not observed difficulties with convergence. In fact, the thermal properties can be evaluated based on the initial temperature distribution of a sequence and assumed to be constant with time over that sequence to a good approximation and then the estimation is linear.

Uniqueness Conditions. Implicit in the previous discussion of the least-squares equations is that the given measured temperature data are sufficient to define the estimated parameters uniquely. One obvious requirement is that the total number of temperature measurements should meet or exceed the total number of parameters:

$$N = NX \times NT \geq n = 2l \quad (9)$$

Since the boundary conditions at both surfaces are considered unknown, at least two measurement spatial locations are also required (Beck et al., 1985, Chap. 7):

$$NX \geq 2 \quad (10)$$

The number of readings required in the time domain is determined simultaneously from equations (9) and (10). For example, with two temperature sensors the minimum number of temporal readings is $NT = 2l/2 = l$.

Stabilization. Several techniques can be chosen to stabilize or smooth the inverse solution including the use of overspecified data, regularization, and digital filtering, among others (Beck et al., 1985). Overspecified data stabilization is chosen presently. That is, the number of parameters to be estimated is reduced to a number less than the maximum allowable number when smoothing is desired, i.e., $n \ll N$. Later the automatic selection of the number of parameters is discussed.

Sequential Procedure. The above analysis is implemented in a sequential manner in the time domain. The global surface conditions are estimated in steps over comparatively small intervals. Only a subset of the global measured temperature data is used in a given sequence. Only the beginning portion of the sequence results are retained. The next sequence starts at the end of the last retained point. Therefore, successive sequences overlap and some measured data are common to both sequences. The cutoff time between retained and rejected results in a particular sequence is restrained to occur at one of the data point times. The spatial temperature distributions are saved at all the measurement times during the sequence calculations since one of these distributions (to be defined later) will become the initial temperature distribution, $\hat{T}_0(x)$, for the next sequence. Criteria for controlling the sequential procedure are developed after the following statistical analysis.

Statistical Analysis

Both the initial temperature distribution and the measured interior temperature data explicitly used in a given sequence contribute to the statistical uncertainty in the computed inverse results. The computed initial temperature distribution, $\hat{T}_0(x)$, has stochastic error since it is computed from the previous sequence. In this section the combined effect of these two sources of error on the estimated surface temperatures and heat fluxes is derived from a linearized statistical analysis. First, the covariance matrix for an arbitrary function of the parameter vector, $\hat{\mathbf{p}}$, and the initial temperature distribution, $\hat{T}_0(x)$, is derived. From this expression the variances of $\hat{f}_1(t)$, $\hat{q}_1(t)$, $\hat{f}_2(t)$, and $\hat{q}_2(t)$ are obtained as special cases. In order to evaluate these expressions, covariance matrices of the initial and measured temperatures are required; these matrices are derived last.

General Covariance Matrices. In order to avoid working with a continuous function, we first generate an equivalent discrete parameter vector, which describes the estimated initial temperature distribution function, $\hat{T}_0(x)$. In particular, a B -spline series similar to equation (4) but in the x variable was created by interpolating the continuous function $\hat{T}_0(x)$. Let the resulting parameter vector containing discrete values of the continuous initial temperature distribution be denoted by $\hat{\mathbf{T}}_0$.

The surface temperatures and heat fluxes depend on the parameter values, $\hat{\mathbf{p}}$, and the initial temperature distribution, $\hat{\mathbf{T}}_0$. Let $\hat{\mathbf{g}}$ denote a function of $\hat{\mathbf{p}}$ and $\hat{\mathbf{T}}_0$. Since the parameter vector itself, $\hat{\mathbf{p}}$, is computed from $\tilde{\mathbf{T}}$ and $\hat{\mathbf{T}}_0$ we have

$$\hat{\mathbf{g}} = \hat{\mathbf{g}}(\hat{\mathbf{p}}, \hat{\mathbf{T}}_0) = \hat{\mathbf{g}}(\hat{\mathbf{p}}(\tilde{\mathbf{T}}, \hat{\mathbf{T}}_0), \hat{\mathbf{T}}_0) \quad (11)$$

Alternatively, $\hat{\mathbf{g}}$ could be viewed as a function of all the measured temperature data up to and including the present sequence (in practice, the contribution of sufficiently early data is negligible so only a finite portion of the previous data need be considered). This is the approach taken by Beck et al. (1985) and Hills et al. (1986), for example. Hills et al. (1986) also accounted for errors in the temperature distribution at time zero. We preferred the former approach since the uncertainty

in the initial temperature distribution being passed from the previous sequence to the current sequence is explicitly calculated. Also, the latter viewpoint requires retracing through the inverse algorithm used in each of the previous sequences in some fashion in order to generate sensitivity coefficients with respect to the prior data. Since the present inverse method will subsequently be applied in a variable manner, keeping track of the specific algorithm used in each of the preceding sequences adds an inconvenience, which can be avoided by consolidating the uncertainty in the previous sequences into the uncertainty in the initial temperature.

Since $\hat{\mathbf{g}}$ is generally a nonlinear function of the parameters involved, we linearize the analysis by writing a truncated Taylor series for $\hat{\mathbf{g}}$. The resulting approximate covariance matrix for $\hat{\mathbf{g}}$ becomes

$$\begin{aligned} \text{cov}(\hat{\mathbf{g}}, \hat{\mathbf{g}}^T) &= \frac{\partial \hat{\mathbf{g}}}{\partial \hat{\mathbf{p}}^T} \text{cov}(\hat{\mathbf{p}}, \hat{\mathbf{p}}^T) \frac{\partial \hat{\mathbf{g}}^T}{\partial \hat{\mathbf{p}}} + \frac{\partial \hat{\mathbf{g}}}{\partial \hat{\mathbf{p}}^T} \text{cov}(\hat{\mathbf{p}}, \hat{\mathbf{T}}_0^T) \frac{\partial \hat{\mathbf{g}}^T}{\partial \hat{\mathbf{T}}_0} \\ &+ \frac{\partial \hat{\mathbf{g}}}{\partial \hat{\mathbf{T}}_0^T} \text{cov}(\hat{\mathbf{T}}_0, \hat{\mathbf{p}}^T) \frac{\partial \hat{\mathbf{g}}^T}{\partial \hat{\mathbf{p}}} + \frac{\partial \hat{\mathbf{g}}}{\partial \hat{\mathbf{T}}_0^T} \text{cov}(\hat{\mathbf{T}}_0, \hat{\mathbf{T}}_0^T) \frac{\partial \hat{\mathbf{g}}^T}{\partial \hat{\mathbf{T}}_0} \end{aligned} \quad (12)$$

Similarly, a truncated Taylor series is written for $\hat{\mathbf{p}}$ and its covariance matrix becomes

$$\begin{aligned} \text{cov}(\hat{\mathbf{p}}, \hat{\mathbf{p}}^T) &= \frac{\partial \hat{\mathbf{p}}}{\partial \hat{\mathbf{T}}^T} \text{cov}(\hat{\mathbf{T}}, \hat{\mathbf{T}}^T) \frac{\partial \hat{\mathbf{p}}^T}{\partial \hat{\mathbf{T}}} + \frac{\partial \hat{\mathbf{p}}}{\partial \hat{\mathbf{T}}^T} \text{cov}(\hat{\mathbf{T}}, \hat{\mathbf{T}}_0^T) \frac{\partial \hat{\mathbf{p}}^T}{\partial \hat{\mathbf{T}}_0} \\ &+ \frac{\partial \hat{\mathbf{p}}}{\partial \hat{\mathbf{T}}_0^T} \text{cov}(\hat{\mathbf{T}}_0, \hat{\mathbf{T}}^T) \frac{\partial \hat{\mathbf{p}}^T}{\partial \hat{\mathbf{T}}} + \frac{\partial \hat{\mathbf{p}}}{\partial \hat{\mathbf{T}}_0^T} \text{cov}(\hat{\mathbf{T}}_0, \hat{\mathbf{T}}_0^T) \frac{\partial \hat{\mathbf{p}}^T}{\partial \hat{\mathbf{T}}_0} \end{aligned} \quad (13)$$

Furthermore,

$$\text{cov}(\hat{\mathbf{p}}, \hat{\mathbf{T}}_0^T) = \frac{\partial \hat{\mathbf{p}}}{\partial \hat{\mathbf{T}}^T} \text{cov}(\hat{\mathbf{T}}, \hat{\mathbf{T}}_0^T) + \frac{\partial \hat{\mathbf{p}}}{\partial \hat{\mathbf{T}}_0^T} \text{cov}(\hat{\mathbf{T}}_0, \hat{\mathbf{T}}_0^T) \quad (14)$$

and

$$\text{cov}(\hat{\mathbf{T}}_0, \hat{\mathbf{p}}^T) = \{\text{cov}(\hat{\mathbf{p}}, \hat{\mathbf{T}}_0^T)\}^T \quad (15)$$

Substituting equations (13)–(15) into equation (12) produces

$$\begin{aligned} \text{cov}(\hat{\mathbf{g}}, \hat{\mathbf{g}}^T) &= \frac{\partial \hat{\mathbf{g}}}{\partial \hat{\mathbf{p}}^T} \left\{ \frac{\partial \hat{\mathbf{p}}}{\partial \hat{\mathbf{T}}^T} \text{cov}(\hat{\mathbf{T}}, \hat{\mathbf{T}}^T) \frac{\partial \hat{\mathbf{p}}^T}{\partial \hat{\mathbf{T}}} + \frac{\partial \hat{\mathbf{p}}}{\partial \hat{\mathbf{T}}^T} \text{cov}(\hat{\mathbf{T}}, \hat{\mathbf{T}}_0^T) \frac{\partial \hat{\mathbf{p}}^T}{\partial \hat{\mathbf{T}}_0} \right. \\ &+ \left. \frac{\partial \hat{\mathbf{p}}}{\partial \hat{\mathbf{T}}_0^T} \text{cov}(\hat{\mathbf{T}}_0, \hat{\mathbf{T}}^T) \frac{\partial \hat{\mathbf{p}}^T}{\partial \hat{\mathbf{T}}} + \frac{\partial \hat{\mathbf{p}}}{\partial \hat{\mathbf{T}}_0^T} \text{cov}(\hat{\mathbf{T}}_0, \hat{\mathbf{T}}_0^T) \frac{\partial \hat{\mathbf{p}}^T}{\partial \hat{\mathbf{T}}_0} \right\} \frac{\partial \hat{\mathbf{g}}^T}{\partial \hat{\mathbf{p}}} \\ &+ \frac{\partial \hat{\mathbf{g}}}{\partial \hat{\mathbf{p}}^T} \left\{ \frac{\partial \hat{\mathbf{p}}}{\partial \hat{\mathbf{T}}^T} \text{cov}(\hat{\mathbf{T}}, \hat{\mathbf{T}}_0^T) + \frac{\partial \hat{\mathbf{p}}}{\partial \hat{\mathbf{T}}_0^T} \text{cov}(\hat{\mathbf{T}}_0, \hat{\mathbf{T}}_0^T) \right\} \frac{\partial \hat{\mathbf{g}}^T}{\partial \hat{\mathbf{T}}_0} \\ &+ \frac{\partial \hat{\mathbf{g}}}{\partial \hat{\mathbf{T}}_0^T} \left\{ \text{cov}(\hat{\mathbf{T}}_0, \hat{\mathbf{T}}^T) \frac{\partial \hat{\mathbf{p}}^T}{\partial \hat{\mathbf{T}}} + \text{cov}(\hat{\mathbf{T}}_0, \hat{\mathbf{T}}_0^T) \frac{\partial \hat{\mathbf{p}}^T}{\partial \hat{\mathbf{T}}_0} \right\} \frac{\partial \hat{\mathbf{g}}^T}{\partial \hat{\mathbf{p}}} \\ &+ \frac{\partial \hat{\mathbf{g}}}{\partial \hat{\mathbf{T}}_0^T} \{\text{cov}(\hat{\mathbf{T}}_0, \hat{\mathbf{T}}_0^T)\} \frac{\partial \hat{\mathbf{g}}^T}{\partial \hat{\mathbf{T}}_0} \end{aligned} \quad (16)$$

Consider each of the components of equation (16). The derivatives $\partial \hat{\mathbf{g}}/\partial \hat{\mathbf{p}}^T$ and $\partial \hat{\mathbf{g}}/\partial \hat{\mathbf{T}}_0^T$ are available from the direct solution by using a forward finite difference approximation. The covariance matrices involving the initial temperature distribution, namely $\text{cov}(\hat{\mathbf{T}}_0, \hat{\mathbf{T}}_0^T)$, $\text{cov}(\hat{\mathbf{T}}_0, \hat{\mathbf{T}}^T)$, and $\text{cov}(\hat{\mathbf{T}}, \hat{\mathbf{T}}_0^T)$, should be provided by calculations performed in the previous sequence. These quantities are considered known for the moment and later expressions are derived to evaluate these covariances. However, the following expression, derived similarly to equation (16), is needed to do so:

$$\begin{aligned} \text{cov}(\hat{\mathbf{g}}, \hat{\mathbf{T}}^T) &= \frac{\partial \hat{\mathbf{g}}}{\partial \hat{\mathbf{p}}^T} \left\{ \frac{\partial \hat{\mathbf{p}}}{\partial \hat{\mathbf{T}}^T} \text{cov}(\hat{\mathbf{T}}, \hat{\mathbf{T}}^T) + \frac{\partial \hat{\mathbf{p}}}{\partial \hat{\mathbf{T}}_0^T} \text{cov}(\hat{\mathbf{T}}_0, \hat{\mathbf{T}}^T) \right\} \\ &+ \frac{\partial \hat{\mathbf{g}}}{\partial \hat{\mathbf{T}}_0^T} \{\text{cov}(\hat{\mathbf{T}}_0, \hat{\mathbf{T}}^T)\} \end{aligned} \quad (17)$$

Continuing, the covariance matrix of the measured interior temperatures, $\text{cov}(\hat{\mathbf{T}}, \hat{\mathbf{T}}^T)$, is known from the earlier assumptions of additive, independent errors to be

$$\text{cov}(\hat{\mathbf{T}}, \hat{\mathbf{T}}^T) = \begin{bmatrix} \sigma_1^2 & 0 & \dots & 0 \\ 0 & \sigma_2^2 & & \vdots \\ \vdots & & \ddots & \\ 0 & \dots & & \sigma_N^2 \end{bmatrix} \quad (18)$$

Finally, expressions are needed for computing the derivatives $\partial \hat{\mathbf{p}}/\partial \hat{\mathbf{T}}^T$ and $\partial \hat{\mathbf{p}}/\partial \hat{\mathbf{T}}_0^T$ appearing in equation (16). Implicit differentiation of the nonlinear least-squares equations, given by equations (7), and neglecting higher order terms, yields

$$\frac{\partial \hat{\mathbf{p}}}{\partial \hat{\mathbf{T}}^T} = \left[\frac{\partial \hat{\mathbf{T}}^T}{\partial \hat{\mathbf{p}}} \mathbf{w}^T \mathbf{w} \frac{\partial \hat{\mathbf{T}}}{\partial \hat{\mathbf{p}}} \right]^{-1} \frac{\partial \hat{\mathbf{T}}^T}{\partial \hat{\mathbf{p}}} \mathbf{w}^T \mathbf{w} \quad (19)$$

and

$$\frac{\partial \hat{\mathbf{p}}}{\partial \hat{\mathbf{T}}_0^T} = - \frac{\partial \hat{\mathbf{p}}}{\partial \hat{\mathbf{T}}^T} \frac{\partial \hat{\mathbf{T}}}{\partial \hat{\mathbf{T}}_0^T} \quad (20)$$

Much of the information needed to compute the above statistical quantities can be gotten from the solution of the least-squares problem. Namely, $\partial \hat{\mathbf{p}}/\partial \hat{\mathbf{T}}^T$ and all derivatives with respect to $\hat{\mathbf{p}}$ are available based on the next to last iterate $\hat{\mathbf{p}}^k$. The only additional quantities needed are the derivatives with respect to the initial temperature distribution $\hat{\mathbf{T}}_0$. No attempt has been made to derive a more computationally efficient version of this statistical analysis for specific situations such as a linear problem. Substantial savings have been achieved for other inverse methods through reformulations of the original methods (Beck et al., 1985; Hills et al., 1986).

Surface Condition Variances. The variances of the estimated surface conditions are obtained as special cases of equation (16). Typically the variances of the surface conditions are desired at several points in a sequence so that confidence bounds may be plotted. Let \hat{b} denote any of the surface quantities \hat{f}_1 , \hat{f}_2 , \hat{q}_1 , or \hat{q}_2 and \mathbf{b} denote the desired vector of $\hat{b}(t)$ values. The covariance matrix of \mathbf{b} is a special case of equation (16) obtained by replacing $\hat{\mathbf{g}}$ with \mathbf{b} . Since only the diagonal elements are of interest we obtain

$$\text{var}(\hat{b}) = \sigma_b^2 = \text{diag}[\text{cov}(\mathbf{b}, \mathbf{b}^T)]. \quad (21)$$

Approximate confidence bounds on the mean response can then be constructed in the form

$$\text{Prob}\{\hat{\mathbf{b}} - 2.576\sigma_b < E(\hat{\mathbf{b}}) < \hat{\mathbf{b}} + 2.576\sigma_b\} \cong 99 \text{ percent} \quad (22)$$

by assuming the distributions involved are approximately nor-

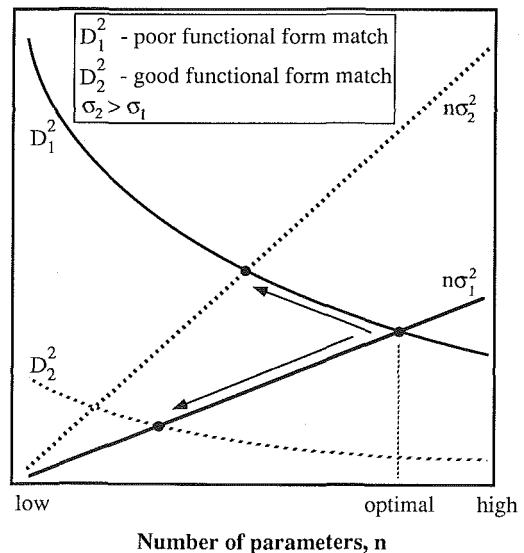


Fig. 1 Schematic diagram illustrating the behavior of equation (32) in selecting an optimal number of parameters for variations in the data uncertainty and the sum squared deterministic error in the estimated interior temperatures

mal and recalling the earlier assumption that the standard deviations of the measured data are known.

Initial and Measured Temperature Covariance Matrices. Still unresolved are the covariance matrices, $\text{cov}(\hat{\mathbf{T}}_0, \hat{\mathbf{T}}_0^T)$, $\text{cov}(\hat{\mathbf{T}}_0, \hat{\mathbf{T}}^T)$ and $\text{cov}(\hat{\mathbf{T}}, \hat{\mathbf{T}}_0^T)$, which are needed by the next sequence in order to evaluate equation (16). Since $\text{cov}(\hat{\mathbf{T}}, \hat{\mathbf{T}}_0^T)$ is the transpose of $\text{cov}(\hat{\mathbf{T}}_0, \hat{\mathbf{T}}^T)$, discussion is limited to the evaluation of $\text{cov}(\hat{\mathbf{T}}_0, \hat{\mathbf{T}}_0^T)$ and $\text{cov}(\hat{\mathbf{T}}_0, \hat{\mathbf{T}}^T)$. First, we need to begin explicitly differentiating between the initial and measured temperature vectors for the current sequence and those for the next sequence. Letting "old" and "new" denote the current and next sequences, respectively, the desired covariance matrices are $\text{cov}(\hat{\mathbf{T}}_0^{\text{new}}, \hat{\mathbf{T}}_0^{\text{new}T})$ and $\text{cov}(\hat{\mathbf{T}}_0^{\text{new}}, \hat{\mathbf{T}}^{\text{new}T})$, $\hat{\mathbf{T}}_0$ and $\hat{\mathbf{T}}$ appearing in equations (16) and (17) are $\hat{\mathbf{T}}_0^{\text{old}}$ and $\hat{\mathbf{T}}^{\text{old}}$, respectively. Therefore,

$$\begin{aligned} &\text{cov}(\hat{\mathbf{T}}_0^{\text{new}}, \hat{\mathbf{T}}_0^{\text{new}T}) \\ &= \text{right-hand side of equation (16) with } \hat{\mathbf{g}} \text{ replaced with } \hat{\mathbf{T}}_0^{\text{new}} \end{aligned} \quad (23)$$

and

$$\begin{aligned} &\text{cov}(\hat{\mathbf{T}}_0^{\text{new}}, \hat{\mathbf{T}}_0^{\text{old}T}) \\ &= \text{right-hand side of equation (17) with } \hat{\mathbf{g}} \text{ replaced with } \hat{\mathbf{T}}_0^{\text{new}}. \end{aligned} \quad (24)$$

Equation (23) completes the determination of $\text{cov}(\hat{\mathbf{T}}_0^{\text{new}}, \hat{\mathbf{T}}_0^{\text{new}T})$, but equation (24) does not provide $\text{cov}(\hat{\mathbf{T}}_0^{\text{new}}, \hat{\mathbf{T}}^{\text{new}T})$ as desired.

Since successive sequences generally overlap, some of the old measured interior temperature data contained in $\hat{\mathbf{T}}^{\text{old}}$ are reused in the next sequence. Therefore, if the last k elements of $\hat{\mathbf{T}}^{\text{old}}$ form the first k elements of $\hat{\mathbf{T}}^{\text{new}}$ then the last k columns of $\text{cov}(\hat{\mathbf{T}}_0^{\text{old}}, \hat{\mathbf{T}}^{\text{old}T})$ become the first k columns of $\text{cov}(\hat{\mathbf{T}}_0^{\text{new}}, \hat{\mathbf{T}}^{\text{new}T})$. Let this number of columns in common to successive sequences be denoted N_c . The remaining columns of $\text{cov}(\hat{\mathbf{T}}_0^{\text{new}}, \hat{\mathbf{T}}^{\text{new}T})$ contain all zero elements since the new additional temperature readings were not involved in the calculation of $\hat{\mathbf{T}}_0^{\text{new}}$. This means there can be no statistical correlation between these quantities and their covariances must be zero. More explicitly,

$$\begin{aligned} \text{cov}(\hat{\mathbf{T}}_0^{\text{new}}, \hat{\mathbf{T}}^{\text{new}T}) = &\{ \text{cov}(\hat{\mathbf{T}}_0^{\text{new}}, \hat{\mathbf{T}}_{N-N_c+1}^{\text{old}}, \text{cov}(\hat{\mathbf{T}}_0^{\text{new}}, \hat{\mathbf{T}}_{N-N_c+2}^{\text{old}}, \\ &\dots, \text{cov}(\hat{\mathbf{T}}_0^{\text{new}}, \hat{\mathbf{T}}_N^{\text{old}}, 0, \dots, 0 \} \end{aligned} \quad (25)$$

where N_c is the number of measured temperatures in common to $\hat{\mathbf{T}}^{\text{old}}$ and $\hat{\mathbf{T}}^{\text{new}}$ and N is the total number of readings in the current sequence.

Automatic Control Criteria

Three parameters must be selected for each sequence of the calculation:

- 1 $\Delta t_{\text{TOTAL}} \equiv$ sequence step size.
- 2 $l =$ number of spline intervals in which to divide Δt_{TOTAL} .
- 3 $\Delta t_{\text{RETAIN}} \equiv$ amount of the sequence step size to retain.

The control parameter Δt_{TOTAL} defines the amount of future temperature data to use in a given sequence. The order of parameterization, l , sets the amount of smoothing being introduced.

Step Size. Because the interior temperature is a damped and lagged response to the surface conditions, "future" interior temperature data are necessary to estimate the current surface conditions, as is well known (Beck et al., 1985). The time it takes for the surface condition to affect the interior temperature significantly at a given temperature sensor position depends on the thermal diffusivity and distance from the surface. The nondimensional time is defined as

$$\tau \equiv \frac{\bar{\alpha} t}{\delta^2} \quad (26)$$

where δ is the distance from the surface to the sensor and $\bar{\alpha}$ is a space-averaged thermal diffusivity. The longer the nondimensional time, τ , the more complete is the information about the surface condition received at the sensor. Therefore the accuracy of the computed surface condition improves with increasing τ . However, the computational effort increases also since more data and parameters must be processed. As a compromise, $\tau = 1$ was selected. Setting $\tau = 1$ in equation (26) produces the sequence step size as

$$\Delta t_{\text{TOTAL}} = \frac{\delta^2}{\bar{\alpha}} \quad (27)$$

For constant thermal properties and measurement sampling rate, the step size is constant, which means each sequence obtains the same amount of measured data regardless of the number of spline intervals or the proportion of the sequence results retained. Note that Δt_{TOTAL} approaches zero as δ goes to zero or $\bar{\alpha}$ becomes very large according to equation (27). In practice however, we are constrained by a finite data sampling rate so Δt_{TOTAL} must be at least as large as the time increment between data points.

Order of Parameterization. In general, the computed inverse solution is not exact. Error is introduced in two ways. First, the true or exact inverse quantity cannot generally be resolved exactly when only a discrete amount of input data is given, even when such data are exact. This error is due to incomplete input information and is deterministic in nature. The deterministic error is defined to be the error when exact input data are used. A second source of error is introduced when the input data are inexact due to random measurement errors. The stochastic error augments the deterministic error to form the total error when inexact input data are used. In particular, the mean squared total error is the sum of the variance and the square of the deterministic error (Beck et al., 1985). Our objective is to select the order of parameterization such that the mean squared total error is minimized. Two basic approaches have been proposed for this purpose.

The first method discussed is treated in detail by Beck et al. (1985). Applied to the present inverse formulation, the variance component of the mean squared total error is computed from expressions in the previous section. The deterministic component is estimated from test cases by generating exact simulated temperature data, processing the data through the inverse method, and computing the squared deterministic error from its definition. After various nondimensionalizations and normalizations, general plots of the mean squared total error as a function of the order of parameterization for various levels of uncertainty in the measured data are constructed. The optimal order of parameterization for a specified level of uncertainty in the data is the value that gives the minimum mean squared total error. Such optimization charts typically indicate that the optimal order of parameterization is in between the lowest and highest allowable values, reflecting a compromise between minimum variance and minimum squared deterministic error. Also, the optimal order decreases with an increasing level of uncertainty in the data. A weakness of this first method is that it is only as good as the assumed test cases used to estimate the deterministic error. Consider the following (reasonable) specific example. Suppose the surface condition is actually constant with time. For this case, the deterministic error is zero regardless of the order of parameterization and the mean squared total error is minimized by minimizing the variance. This is done by selecting the lowest order of parameterization. In contrast, a generic optimization plot would typically choose a larger value.

A second basic approach for optimizing the order of parameterization was proposed by Tikhonov and Arsenin (1977). The expected value of the weighted sum of squares norm for the measurement errors is

$$E[(\hat{\mathbf{T}} - \mathbf{T})^T \mathbf{w}^T \mathbf{w} (\hat{\mathbf{T}} - \mathbf{T})] = N \quad (28)$$

A reasonable requirement to impose is that the weighted sum of squares norm for the estimated errors should exhibit the same behavior:

$$S(I_{\text{opt}}) = (\hat{\mathbf{T}} - \hat{\mathbf{T}})^T \mathbf{w}^T \mathbf{w} (\hat{\mathbf{T}} - \hat{\mathbf{T}}) \approx N \quad (29)$$

The optimal order of parameterization is chosen as the value best satisfying equation (29). Murio (1985) and Flach and Özisik (1988) report good success using this criterion. Insight into the characteristics of this criterion can be gained by examining the expected value of S :

$$E(S) = N + E[(\hat{\mathbf{T}} - E(\hat{\mathbf{T}}))^T \mathbf{w}^T \mathbf{w} (\hat{\mathbf{T}} - E(\hat{\mathbf{T}}))] - 2E[(\hat{\mathbf{T}} - E(\hat{\mathbf{T}}))^T \mathbf{w}^T \mathbf{w} \epsilon] + (E(\hat{\mathbf{T}}) - \mathbf{T})^T \mathbf{w}^T \mathbf{w} (E(\hat{\mathbf{T}}) - \mathbf{T}) \quad (30)$$

The criterion given by equation (29) on average implies

$$(E(\hat{\mathbf{T}}) - \mathbf{T})^T \mathbf{w}^T \mathbf{w} (E(\hat{\mathbf{T}}) - \mathbf{T}) = 2E[(\hat{\mathbf{T}} - E(\hat{\mathbf{T}}))^T \mathbf{w}^T \mathbf{w} \epsilon] - E[(\hat{\mathbf{T}} - E(\hat{\mathbf{T}}))^T \mathbf{w}^T \mathbf{w} (\hat{\mathbf{T}} - E(\hat{\mathbf{T}}))] \quad (31)$$

The properties of equation (31) are most easily illustrated by considering the special case of no uncertainty in the initial temperature distribution $\hat{\mathbf{T}}_0$ and constant variance errors. For this case equation (31) reduces to

$$D^2(n_{\text{opt}}) \equiv (E(\hat{\mathbf{T}}) - \mathbf{T})^T (E(\hat{\mathbf{T}}) - \mathbf{T}) = n_{\text{opt}} \sigma^2 \quad (32)$$

where D^2 is defined as the left-hand side of equation (31) multiplied by σ^2 and $n_{\text{opt}} = 2I_{\text{opt}}$. The left-hand side of equation (32) is the sum squared deterministic error in the estimated interior temperatures and depends on the order of parameterization. The right-hand side depends on the order and on the uncertainty level of the measured data in the current sequence and the estimated initial temperature. For exact input data the right hand side is zero. Figure 1 schematically illustrates the behavior of equation (32). The solid lines indicate a base case for which the optimal order is the midrange as defined by the intersection of the solid lines. Note that as the uncertainty level in the data increases from σ_1 to σ_2 , equation (32) dictates a lower order of parameterization, just as a generic optimization plot would. Also, note that as the deterministic error decreases from D_1^2 to D_2^2 , the order decreases to compensate. Returning to the example of a constant surface condition for which the deterministic error is zero, observe that equation (32) dictates the optimal order to be the lowest allowable value (the desired result). Hence equation (32) takes into account the actual deterministic error rather than relying on a reference value as a generic optimization chart would. These observations pertain to setting the average value of S equal to N . A weakness of this second approach is that criterion (29) requires each particular value of S to equal N . If S deviates significantly from its average, then the optimal order may not be achieved.

In summary, both methods seek to minimize the mean squared error. Both methods correctly dictate a lower order of parameterization as the uncertainty level in the data increases. Both methods may fail to give optimal results. The first approach may fail if the actual deterministic error deviates significantly from the reference deterministic error. The second approach accounts for the actual deterministic error but may fail if the actual S deviates significantly from its average value. Fortunately for both methods, the mean squared error has a fairly flat minimum so there is a range of orders that gives acceptable results. The first method requires up-front computational costs in constructing the general optimization plot but is applied without need for iteration subsequently. The second method does not require up-front computations, but an iterative procedure is needed to satisfy criterion (29). More work is certainly needed toward refining both of these criteria and comparing their relative merits.

Lacking a definitive choice between these methods, we selected the second approach since it appears to handle variations

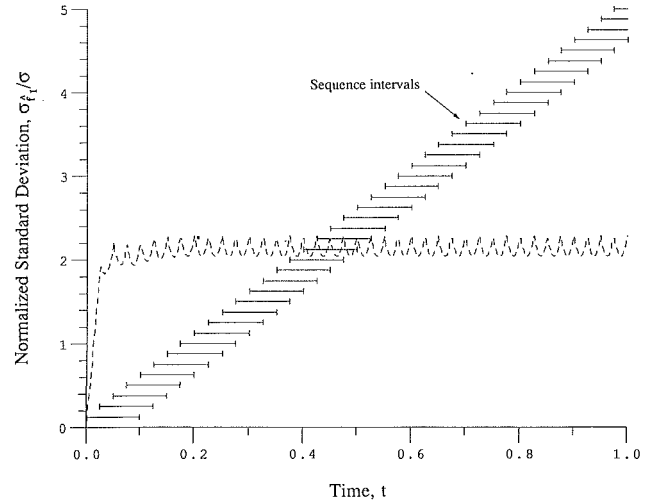


Fig. 2(a) Normalized standard deviation of the surface temperature \hat{f}_1 for zero temperature input data at increments of $\Delta t = 0.025$, 4 measurement times per sequence, 1 spline segment per sequence, and 1 measurement time retained per sequence

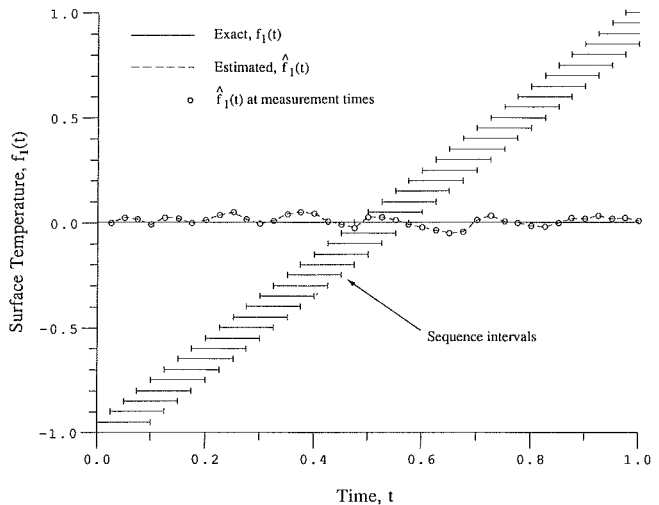


Fig. 2(b) Estimated surface temperature \hat{f}_1 for zero temperature input data at increments of $\Delta t = 0.025$, 4 measurement times per sequence, 1 spline segment per sequence, and 1 measurement time retained per sequence

in the deterministic error component better and is easy to apply. With this choice, the procedure is to start with the maximum number of spline intervals allowed by the uniqueness conditions given by equations (9) and (10). Typically, $S(I_{\text{max}}) < N$ so the number of intervals is reduced by one. The number of intervals is decreased by one until equation (29) is approximately satisfied.

Step Retention. The statistical uncertainty tends to increase with increasing time in a given sequence since fewer and fewer future data are available. Therefore, some portion of the computed results must be rejected and successive sequences therefore overlap. One criterion for determining the amount of surface results to retain is based on monitoring the standard deviation of the surface condition of interest. The idea is to reject computed results that have a standard deviation exceeding some desired, prescribed maximum value. The practical implementation of this idea follows. For simplicity, we apply this criterion to only one of the surface conditions denoted by \hat{b} .

First, we will monitor conditions only at a discrete number

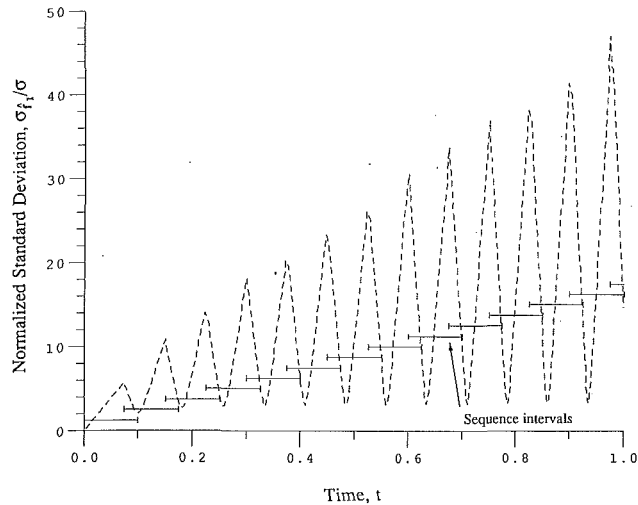


Fig. 3(a) Normalized standard deviation of the surface temperature \hat{f}_1 for zero temperature input data at increments of $\Delta t = 0.025$, 4 measurement times per sequence, 1 spline segment per sequence, and 3 measurement times retained per sequence

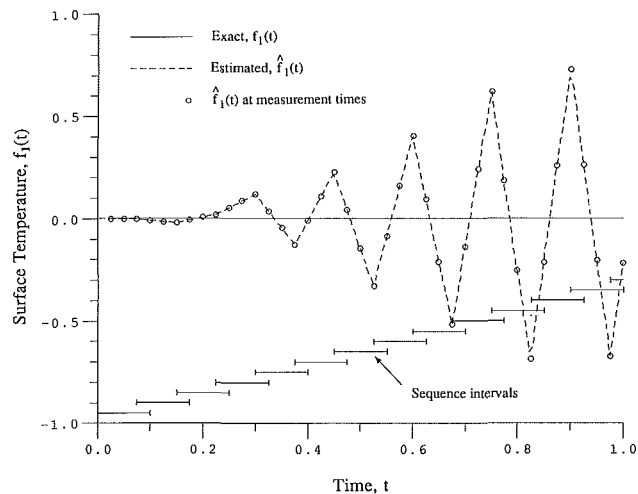


Fig. 3(b) Estimated surface temperature \hat{f}_1 for zero temperature input data at increments of $\Delta t = 0.025$, 4 measurement times per sequence, 1 spline segment per square, and 3 measurement times retained per sequence

of points in a sequence, namely, at the measurement times. The measurement times for a given sequence are numbered consecutively from $j = 1$ to NT . Starting with $j = 1$ and advancing to NT , we in general retain up to the computed surface condition, \hat{b}_j , until the standard deviation exceeds the prescribed maximum value, $\sigma_{b,\max}$. Sometimes even the first standard deviation exceeds $\sigma_{b,\max}$. In this case, if the next standard deviation is still larger, only $j = 1$ is retained. If the next standard deviation is lower, then an additional portion of the surface condition is retained until the standard deviation increases. More specifically, we advance the retention cutoff point to the next measurement time in a sequence until one of the following stopping conditions is met or the end of the sequence is reached.

For $j = 1$:

$$\text{If } \sigma_{b_j} > \sigma_{b,\max} \text{ and } \sigma_{b_{j+1}} > \sigma_{b_j} \text{ then retain through } j=1 \quad (33a)$$

For $1 < j < NT$:

$$\text{If } \sigma_{b_j} > \sigma_{b,\max} \text{ and } \sigma_{b_{j-1}} > \sigma_{b_j} \text{ and } \sigma_{b_{j+1}} > \sigma_{b_j} \\ \text{then retain through } j \quad (33b)$$

$$\text{If } \sigma_{b_j} > \sigma_{b,\max} \text{ and } \sigma_{b_{j-1}} < \sigma_{b_j} \text{ then retain through } j-1 \quad (33c)$$

For $j = NT$:

$$\text{If } \sigma_{b_j} > \sigma_{b,\max} \text{ and } \sigma_{b_{j-1}} > \sigma_{b_j} \text{ then retain through } j \quad (33d)$$

$$\text{If } \sigma_{b_j} > \sigma_{b,\max} \text{ and } \sigma_{b_{j-1}} < \sigma_{b_j} \text{ then retain through } j-1 \quad (33e)$$

Note that at least one point in each sequence is always retained. There are two advantages to using the criterion specified by equations (33). First, only results having a statistical uncertainty below a desired level are accepted (if possible) and no such results are prematurely rejected either. Second, by monitoring the statistical uncertainty, unstable conditions are never allowed to persist for long; that is, conditions (33) ensure the stability of the sequential procedure.

Results and Discussion

First the stability of the sequential inverse heat conduction method is investigated using results from the statistical analysis. Then two representative test cases, one with exact simulated measurements and one using inexact measurements, are presented to illustrate the effectiveness of the automatic control criteria. In all cases, numerical results are given for the following (nondimensional) conditions. We consider a slab with thickness, thermal conductivity, and heat capacity all equal to 1.0. Two temperature sensors ($NX = 2$) are assumed to be located at $x = 0.5$ and $x = 1.0$. The sensor $x = 1.0$ measures the surface temperature at that boundary while the surface temperature and heat flux at $x = 0$ are to be estimated.

Stability Considerations. Instability in sequential inverse methods has been observed during numerical experimentation; see Beck et al. (1985, pp. 179–181) for instance. The standard deviation of a computed surface condition is a measure of the sensitivity of the estimate to random errors in the input data. If the standard deviation is bounded, then the actual stochastic error in the computed surface condition will be effectively bounded. Therefore, the statistical analysis derived earlier is expected to provide insight into the stability of the inverse solution.

For example, we considered temperature readings taken at increments of $\Delta t = 0.025$ and $NT = 4$ measurement times per sequence, which corresponds to a step size of $\Delta t_{\text{TOTAL}} = 0.1$. Exact simulated data and one linear spline segment ($l = 1$) were chosen for each sequence. Here manual, as opposed to automatic, control of the parameter is being used so that the parameters can be set to predetermined, fixed values. The initial temperature distribution and all measured temperatures are taken to be exactly zero. Although no measurement errors have been introduced, insight into the inherent error propagation characteristics of the sequential procedure can be gained by computing the standard deviation of the surface temperature normalized with respect to the standard deviation of the measured data.

Figure 2(a) illustrates the normalized standard deviation in the estimated surface temperature at $x = 0$ when computed results up to the first measurement time in each sequence are retained ($\Delta t_{\text{RETAIN}} = 0.025$). The covariance matrix of the initial temperature at $t = 0$ was assumed to be zero so the normalized standard deviation starts off zero in the first sequence. The normalized standard deviation increases from zero for $t > 0$, reflecting a propagation of random errors (if present) in the measured interior temperatures for the first sequence. The initial temperature distribution for the second sequence is computed from calculations in the first sequence; therefore, it propagates any random errors present in the first sequence. As a consequence, the normalized standard deviation of the surface temperature at $x = 0$ is not zero at the start of the second sequence. Effectively, stochastic error from the previous sequence augments stochastic error already being intro-

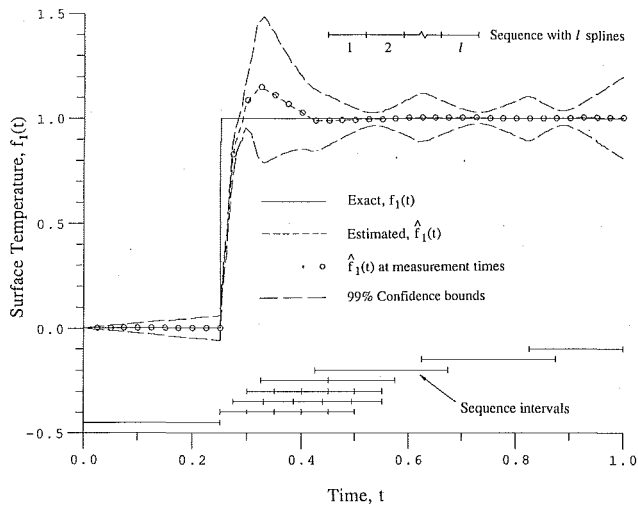


Fig. 4 Estimated surface temperature \hat{f}_1 for a step input exact surface temperature, exact measurements taken at increments of $\Delta t = 0.025$, and automatic control of the sequential procedure.

duced from the measured data in the current sequence if inexact data are used. Eventually however, the average normalized standard deviation levels off at a stable value. This indicates the stochastic error is bounded and a stable inverse solution is expected when inexact data are used. To test this hypothesis we added normally distributed, zero mean, constant variance errors with $\sigma = 0.01$ to the above input data. The resulting computed surface temperature, $\hat{f}_1(t)$, is shown in Fig. 2(b). The computed results contain error due to random errors in the input data, but the important observation is that these errors are bounded and the estimation procedure is stable. The sample standard deviation of \hat{f}_1 for $0.2 \leq t \leq 1.0$ is 0.026, while the expected value from Fig. 2(a) is about $0.01 \times 2.2 = 0.022$. The sample value is consistent with the expected value at a 95 percent confidence level.

In contrast, consider Figs. 3(a) and 3(b), which are for the identical conditions as Figs. 2(a) and 2(b) except that results up to the third measurement time in each sequence are retained ($\Delta t_{\text{RETAIN}} = 0.075$). The standard deviation in Fig. 3(a) grows unbounded, as does the actual computed surface temperature shown in Fig. 3(b). Obviously, this selection of the parameters controlling the inverse procedure results in an unstable inverse solution. From results such as those shown in Figs. 2 and 3, we conclude that the statistical confidence bounds can be used to predict the stability or instability of the sequential procedure.

Representative Applications. Now examples are presented primarily for the purpose of illustrating the effectiveness of the three automatic control criteria. An exact surface temperature at $x = 0$ in the form of a step input is chosen as shown in Fig. 4. The exact surface temperature at $x = 1.0$ is chosen as zero. Overall stabilization is added by setting $\sigma_i = 0.01$ in the evaluation of S in equation (29). The maximum allowable standard deviation value is chosen as $\sigma_{f_1, \text{max}} = 0.05$. Computed results using exact simulated temperature data are illustrated in Fig. 4. Since exact data were used the discrepancy between the exact and estimated curves is the deterministic error. Stochastic confidence bounds based on $\sigma_i = 0.01$ are also illustrated in Fig. 4 only to indicate the amount of sensitivity present in the computed results; there is no actual stochastic error since exact measurements were used. Also shown schematically in Fig. 4 are the sizes of the sequences and the number of spline intervals in each sequence. Figure 4 represents the best single example for illustrating the average behavior of the control criteria we could conceive.

The important observation from Fig. 4 is how the sequential procedure is automatically adjusted from sequence to sequence

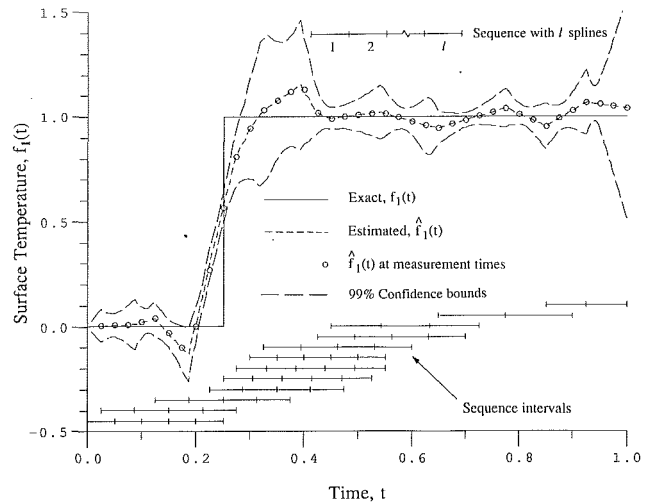


Fig. 5 Estimated surface temperature \hat{f}_1 for a step input exact surface temperature, inexact measurements with $\sigma = 0.01$ taken at increments of $\Delta t = 0.025$, and automatic control of the sequential procedure

to give optimal local results. First, the sequence step length is kept nominally constant so that the same, sufficient amount of information is received by each sequence regardless of the number of spline intervals, the amount of calculations retained, etc. Second, note that the number of spline intervals or order of parameterization is low where there is low curvature in the exact surface temperature and vice versa. Effectively, a large amount of smoothing is being used to reduce the stochastic error whenever the deterministic error would not be unduly increased. Third, observe that a larger proportion of each sequence is retained when the order of parameterization is low since the sensitivity is lower due to fewer parameters. That is, the maximum amount of accurate results is retained but no inaccurate results are retained, if possible. Also, we point out that the stability of the inverse solution is guaranteed since the criteria given by equations (33) will not let the standard deviation grow unbounded as is the case for instability.

A second case was prepared under identical conditions as in Fig. 4 except that simulated normally distributed, zero mean, constant variance measurement errors with $\sigma_i = 0.01$ were added to the exact temperature distribution. The results are shown in Fig. 5 and are similar to those in Fig. 4. The stochastic error augmenting the deterministic error is evident. The particular set of simulated errors selected for this example is interesting in that it clearly illustrates a situation for which criterion (29) fails to give an optimal result. For the first sequence, the deterministic error is zero as can be seen from Fig. 4. Ideally, one spline interval would be chosen since one interval is sufficient to model the true surface temperature exactly and would give the minimum variance. Instead, criterion (29) selected five spline intervals because the value of $S(l)$ for the first sequence happens to be much larger than the average due to the particular set of measurement errors involved. The deterministic error is again zero towards the end of the transient. Here criterion (29) performs better by selecting a low order of parameterization. The confidence bounds shown in Fig. 5 account for stochastic error but neglect deterministic error; therefore, the confidence bounds are not accurate relative to the exact solution around $t = 0.25$. Also note that the confidence bounds are large near the end of the simulation since "future" temperature data were not available for $t > 1.0$.

The inverse solutions shown in Figs. 4 and 5 required 982 and 1725 cumulative evaluations of the direct solution, respectively. Several aspects of the inverse methodology contributed to the total number of function evaluations. The Levenberg-Marquardt method was set up for solving a general nonlinear problem (μ_1 nonzero) so iterations were required even

though the example problems are linear. Criterion (29) required an iterative procedure for selecting the optimal number of spline intervals for each sequence. The statistical analysis required additional function evaluations over those required for the parameter estimation in order to evaluate derivatives with respect to $\hat{\mathbf{T}}_0$.

Conclusions

A new variable-order, variable-step sequential method has been presented for solving the nonlinear one-dimensional inverse heat conduction problem. The control criteria developed to optimize the method automatically and ensure stability give promising results. More work is needed in developing a more computationally efficient version of the approach and in refining the optimization criteria.

Acknowledgments

This work is supported in part through National Science Foundation Grant NSM-88-16107. One of the authors (GPF) acknowledges the support of a National Science Foundation Graduate Fellowship.

References

- Beck, J. V., Blackwell, B., and St. Clair, C. R., Jr., 1985, *Inverse Heat Conduction*, Wiley, New York.
- de Boor, C., 1978, *A Practical Guide to Splines*, Springer-Verlag, New York.
- Flach, G. P., and Ozisik, M. N., 1988, "Inverse Heat Conduction Problem of Periodically Contacting Surfaces," *ASME JOURNAL OF HEAT TRANSFER*, Vol. 110, pp. 821-829.
- Hills, R. G., and Hensel, E. C., Jr., 1986, "One-Dimensional Nonlinear Inverse Heat Conduction Technique," *Numerical Heat Transfer*, Vol. 10, pp. 369-393.
- Hills, R., Raynaud, M., and Hensel, E., 1986, "Surface Variance Estimates Using an Adjoint Formulation for a One-Dimensional Nonlinear Inverse Heat Conduction Technique," *Numerical Heat Transfer*, Vol. 10, pp. 441-461.
- Murio, D. A., 1985, "On the Characterization of the Solution of the Inverse Heat Conduction Problem," *ASME Paper No. 85-WA/HT-41*.
- Tikhonov, A. N., and Arsenin, V. Y., 1977, *Solutions of Ill-Posed Problems*, Winston and Sons, Washington, DC.

APPENDIX

Two modifications are needed to the statistical analysis developed for independent errors to treat the case of correlated errors. Specifically, $\text{cov}(\tilde{\mathbf{T}}, \tilde{\mathbf{T}}^T)$ given by equation (18) and $\text{cov}(\hat{\mathbf{T}}_0^{\text{new}}, \hat{\mathbf{T}}_0^{\text{new}T})$ given by equation (25) need to be generalized. Rather than trying to present a completely general analysis designed to cover any conceivable correlation model, we prefer to consider an illustrative specific example. Suppose we have two sensor locations with the measurement errors correlated in time according to the steady-state, first-order, autoregressive error model defined by

$$\epsilon_i = r\epsilon_{i-1} + u_i; \quad \epsilon_0 = 0; \quad r^2 < 1 \quad (\text{A.1a, b, c})$$

$$E(u_i) = 0 \quad (\text{A.1d})$$

$$E(u_i u_j) = \begin{cases} 0 & i \neq j \\ \sigma_u^2 & i = j = 1 \\ \sigma_u^2 & i = j \neq 1 \end{cases} \quad (\text{A.1e})$$

If the temperatures are grouped by location and ordered sequentially in time when constructing $\tilde{\mathbf{T}}$, the first covariance matrix becomes

$$\text{cov}(\tilde{\mathbf{T}}, \tilde{\mathbf{T}}^T) = \sigma^2 \begin{bmatrix} \mathbf{C} & \mathbf{0} \\ \mathbf{0} & \mathbf{C} \end{bmatrix}; \quad \mathbf{C} \equiv \begin{bmatrix} 1 & r & r^2 & \dots \\ r & 1 & r & \\ r^2 & r & 1 & \\ \vdots & & & \ddots \end{bmatrix} \quad (\text{A.2a, b})$$

where $\sigma^2 \equiv \sigma_u^2 / (1 - r^2)$. The first N_c columns of the second covariance matrix remain the same as given by equation (25). The remaining columns are obtained by recursively applying the formula

$$\text{cov}(\hat{\mathbf{T}}_0^{\text{new}}, \tilde{\mathbf{T}}_{j+1}) = r \text{cov}(\hat{\mathbf{T}}_0^{\text{new}}, \tilde{\mathbf{T}}_j) \quad (\text{A.3})$$

at each sensor location where $\tilde{\mathbf{T}}_{j+1}$ and $\tilde{\mathbf{T}}_j$ are successive temperature readings at the same location. The calculation starts with $\tilde{\mathbf{T}}_j$ equal to the last temperature in $\tilde{\mathbf{T}}^{\text{old}}$ at the sensor location of interest.

A. Kar
C. L. Chan¹
J. Mazumder

Laser Aided Materials Processing
Laboratory,
Department of Mechanical and Industrial
Engineering,
University of Illinois at Urbana-Champaign,
Urbana, IL 61801

Comparative Studies on Nonlinear Hyperbolic and Parabolic Heat Conduction for Various Boundary Conditions: Analytic and Numerical Solutions

With the advent of lasers with very short pulse durations and their use in materials processing, the effect of thermal wave propagation velocity becomes important. Also, localized heating in laser-aided materials processing causes significant variations in the material properties. To account for these two effects, hyperbolic heat conduction is studied in this paper by considering all the thermophysical properties, except the thermal diffusivity, to be temperature dependent. The resulting nonlinear hyperbolic equations are linearized by using Kirchhoff transformation. Both analytical and numerical solutions are obtained for finite domains. Results are presented and compared with parabolic conduction results.

Introduction

Thermal analysis is indispensable in materials processing. Processes such as annealing, cladding, cutting, and drilling involve heat transfer, which may set up thermal stress in the materials or alter its microstructure. When the heat flux or the temperature involved in the heat transfer process is not very high, or the phenomena occurring at a time scale smaller than the thermal relaxation time of the material are not of interest, the conventional parabolic heat conduction equation can be used. In conventional materials processing, the parabolic heat conduction equation is adequate to model heat transfer in the material because the temperature gradient involved in such processes is moderate. Recent developments in laser technology have drawn a lot of interest in using lasers for materials processing such as cladding, drilling, and cutting. In these types of process, laser energy is deposited on a small area of the material over a short duration and thus the material is subject to a very high temperature gradient. Under this condition, the finite speed of heat propagation becomes important. Also, the thermalization time during laser annealing of some of the semiconductor materials such as silicon is about one picosecond (Lietoila and Gibbons, 1982). For such processes, the hyperbolic heat conduction equation can shed light on the transient heating phenomena over a few nanoseconds for better understanding of localized material modifications.

At very low temperatures near absolute zero, thermal waves have been observed (Peshkov, 1944; Bertman and Sandiford, 1970) to propagate at finite speeds. In 1940, Tisza predicted small heat-propagation rates in liquid helium II (Atkins, 1959). Peshkov (1944) determined these values experimentally. He referred to the phenomenon of propagation of thermal waves as "second sound" because of the similarity between the acoustic waves and the thermal waves. Since these findings, there have been a lot of theoretical studies to accommodate the finite propagation speed of thermal waves.

Many investigators (e.g., Boley, 1964) have pointed out that the parabolic formulation of heat conduction implies infinite propagation velocity of thermal disturbances. To account for the finite propagation velocity of thermal waves, Morse and

Feshbach (1953) argued heuristically and postulated that the damped hyperbolic equation should be the correct heat conduction equation. From kinetic considerations, Maxwell (1867) and later Vernotte (1958) and Chester (1963) proposed a modified Fourier law of heat conduction. According to this modified law, the heat flux equilibrates to the imposed temperature gradient via a relaxation phenomenon. Because of the qualitative nature of the arguments used by these investigators, Weyman (1967) and Taitel (1972) obtained an expression for the modified Fourier law via random walk model. Simons (1972) used the Boltzmann equation to obtain the modified Fourier law. He also pointed out that the actual heat conduction in a medium is governed by a set of equations of increasing complexity.

Using the modified Fourier law of heat conduction, the conservation of energy equation is transformed into a hyperbolic partial differential equation. This hyperbolic equation becomes the governing equation for heat conduction when the propagation velocity of thermal waves is finite. It can be found in the literature that this hyperbolic heat equation has been solved for various physical situations. Baumeister and Hamill (1969) solved it for a semi-infinite medium using the Laplace transform. Taitel (1972) used the Laplace transform to solve it for a finite medium. Vick and Ozisik (1983) studied the growth and decay of a thermal pulse in an infinite medium using the integral transform technique. Using this technique together with the Green's function, Ozisik and Vick (1984) also examined the propagation and reflection of thermal waves in a finite medium. The hyperbolic heat conduction has also been formulated in terms of the heat flux by Frankel et al. (1985). They solved the governing hyperbolic heat flux equation using the Green's function. A solution for the hyperbolic conduction with surface radiation was obtained by Wu (1988, 1989). He used the Laplace transform to obtain an analytical solution for the case of specified surface temperature. Subsequently, a nonlinear Volterra integral equation of the second kind is derived to satisfy the radiation condition. The method of successive approximations is used to solve the nonlinear integral equation. Glass et al. (1985) used MacCormack's method to solve the hyperbolic heat conduction problem. Also, Glass et al. (1986) solved numerically the hyperbolic heat conduction problem with temperature-dependent thermal conductivity for a semi-infinite slab. Tamma and Raikar (1988)

¹Present address: Department of Aerospace and Mechanical Engineering, University of Arizona, Tucson, AZ 85721.

Contributed by the Heat Transfer Division for publication in the JOURNAL OF HEAT TRANSFER. Manuscript received by the Heat Transfer Division November 16, 1990; revision received June 7, 1991. Keywords: Conduction.

applied the transfinite element method to solve a class of one-dimensional hyperbolic heat conduction problems. The essential idea combines transform methods and Galerkin schemes with specially tailored elements to track the discontinuity accurately.

With regard to the application of hyperbolic heat conduction equation to problems of practical interest Chan et al. (1971) examined the effect of finite propagation velocity of heat on the temperature rise of crystallites in exothermic catalytic reactions. They have presented interesting results that cannot be predicted by the parabolic heat conduction equation. Maurer and Thompson (1973) studied non-Fourier effects at high heat flux. They concluded that for heat fluxes of the order of 10^7 W/cm² or greater, the effect of hyperbolic heat conduction is significant. In laser processing (such as cutting, welding, or drilling) of materials, high heat flux is often encountered. A laser beam of diameter 0.2 mm and power 10 kW will give rise to high heat flux of the above order. Under such conditions, as pointed out by Maurer and Thompson (1973), any design of structural integrity based on the classical parabolic heat conduction model may fail due to thermal shock. Also, it should be noted that the heat flux is not proportional to the temperature gradient in the hyperbolic case when the speed of the thermal wave is finite in contrast to the infinite speed assumed in the parabolic case. This has been a source of confusion in using hyperbolic heat conduction with specified heat flux boundary condition. As pointed out by Maurer and Thompson (1973), and later by Frankel et al. (1985), Brazel and Nolan (1966) formulated the problem with heat flux boundary conditions incorrectly for finite speed of heat propagation.

This paper presents analytic and numerical solutions for the hyperbolic heat conduction equations with temperature-dependent thermal conductivity, heat capacity, and density while the thermal diffusivity is considered to be constant. The nonlinear equations are linearized by using the Kirchhoff transformation and analytic solutions are obtained by using separation of variables and Laplace transform techniques. Numerical solutions are determined by using the method of characteristics. A generalized boundary condition is formulated so

that all three types of boundary condition (temperature, heat flux, and convective conditions) can be handled. Results are obtained with linear temperature dependence of the thermal conductivity.

Mathematical Analysis. The hyperbolic heat conduction equation becomes nonlinear when the material properties, such as density, specific heat, and thermal conductivity, are considered to be temperature dependent. However, the thermal diffusivity varies with temperature slower than the thermal conductivity for most materials. In this study, we assume that the thermal diffusivity is independent of temperature. Because of this assumption, the nonlinear hyperbolic heat conduction equation can be linearized by using the Kirchhoff transformation (Carslaw and Jaeger, 1986; Ozisik, 1980):

$$T_1^* = \int_{T_r^*}^T k(\bar{T}) d\bar{T} \quad (1)$$

Before applying this transformation to the governing equations, let us define the following dimensionless variables:

$$x = x^*/a, \quad (2a)$$

$$t = t^*/\tau_c, \quad (2b)$$

$$T_1 = T_1^*/T_r^*, \quad (2c)$$

$$q = q^*a/k_r T_r^*, \quad (2d)$$

$$\delta^2 = \alpha/(ac) \quad (2e)$$

Here τ_c is the characteristic time for the diffusion of heat, which is defined as a^2/α . The dimensionless variable δ^2 is called the Veron number (Luikov, 1980). It is a ratio of the thermal diffusion speed to the speed of thermal wave in the medium. With these dimensionless quantities and the transformation (Eq. (1)), the energy conservation and the constitutive law can be, respectively, rewritten as

$$\frac{\partial T_1}{\partial t} = -\frac{\partial q}{\partial x} \quad (3)$$

and

Nomenclature

a = width of the medium
 $b_{1,2}$ = parameters for the generalized boundary conditions; see Eq. (11)
 $Bi_{1,2}$ = Biot number; see Eqs. (11) and (12)
 c = thermal wave propagation speed in the medium
 $C_p(T^*)$ = temperature-dependent specific heat
 $d_{1,2}$ = parameters for the generalized boundary conditions; see Eq. (12)
 $k(T^*)$ = temperature-dependent thermal conductivity
 k_r = thermal conductivity at the reference temperature
 q^* = heat flux
 q = dimensionless heat flux = $q^*a/(k_r T_r^*)$
 q_0 = dimensionless heat flux at $x = 0$
 q_a = dimensionless heat flux at $x = 1$
 t^* = time variable

t = dimensionless time variable = t^*/τ_c
 T^* = temperature
 T = dimensionless temperature = T^*/T_r^*
 T_1^* = transformed temperature
 T_1 = dimensionless transformed temperature = T_1^*/T_r^*
 T_r^* = reference temperature
 T_o^* = temperature at $x^* = 0$
 T_o = dimensionless transformed temperature at $x = 0$
 T_a = dimensionless transformed temperature at $x = 1$
 x^* = space variable
 x = dimensionless space variable = x^*/a
 α = thermal diffusivity
 δ^2 = Veron number = $\alpha/(ac)$
 $\gamma_{+,-}$ = parameterization variables
 ϵ^* = temperature coefficient of thermal conductivity
 ϵ = dimensionless temperature

coefficient of thermal conductivity = $\epsilon^* T_r^*$
 $\zeta_{+,-}$ = characteristics directions
 $\rho(T^*)$ = temperature-dependent density
 τ = thermal relaxation = α/c^2
 τ_c = characteristic thermal diffusion time = a^2/α

Subscripts

A = location of node for right-hand side boundary calculation; see Fig. 1
 B = location of node for left-hand side boundary calculation; see Fig. 1
 P = intersection of the two characteristics at the next time step; see Fig. 1
 P_+ = intersection of ζ_+ characteristic at the current time step; see Fig. 1
 P_- = intersection of ζ_- characteristic at the current time step; see Fig. 1

$$q + \delta^2 \frac{\partial q}{\partial t} = -\frac{\partial T_1}{\partial x} \quad (4)$$

Temperature Dependence of Thermal Conductivity. Although the Kirchhoff transformation is applicable for any $k(T^*)$, one has to introduce a particular expression for $k(T^*)$ in order to determine the temperature from the transformed variable, T_1 . In this paper, we assume that $k(T^*)$ varies linearly around some reference temperature T_r^* . This implies that the product $\rho(T^*)C_p(T^*)$ also varies linearly with T^* . Then one can write

$$k(T^*) = k_r^* \{1 + \epsilon^*(T^* - T_r^*)\} \quad (5)$$

By using Eq. (1), the transformed temperature T_1^* can be written as

$$T_1^* = (T^* - T_r^*) + \frac{1}{2} \epsilon^* (T^* - T_r^*)^2$$

Here ϵ^* is the temperature coefficient of thermal conductivity. Defining a dimensionless ϵ by

$$\epsilon = \epsilon^* T_r^*$$

and using the dimensionless variables defined in Eq. (2c), the transformed temperature can be written as

$$T_1 = (T - 1) + \frac{1}{2} \epsilon (T - 1)^2, \quad (6)$$

and the inverse of this transformed temperature is given by

$$T = 1 + \frac{-1 + (1 + 2\epsilon T_1)^{1/2}}{\epsilon} \quad (7)$$

It should be pointed out that the above transformation (Eq. (6)) is applicable over the ranges $T > 0$ for $\epsilon > 0$ and $0 < T < 1 - 1/\epsilon$ for $\epsilon < 0$.

Analytic Solutions. Analytic expressions for the temperature distributions due to hyperbolic heat conduction are obtained for three cases by considering the initial and the boundary conditions constant.

Case 1—Temperatures Specified at Both Ends. The boundary and initial conditions in dimensionless form are:

$$T_1(0, t) = T_0, \quad T_1(1, t) = T_a, \quad T_1(x, 0) = 0, \quad \frac{\partial T_1}{\partial t}(x, 0) = 0$$

Under these conditions, the hyperbolic heat conduction equation is solved by using the separation of variables technique and the solution is found to be

$$T_1(x, t) = T_0 + (T_a - T_0)x + \sum_{n=1}^{\infty} e^{-t/2\delta^2} [F_n f_n(t) + g_n(t)] D_n \sin(\lambda_n x) \quad (8)$$

where

$$\left. \begin{aligned} f_n(t) &= \sin\left(\frac{(4\delta^2\lambda_n^2 - 1)^{1/2}}{2\delta^2} t\right) \\ g_n(t) &= \cos\left(\frac{(4\delta^2\lambda_n^2 - 1)^{1/2}}{2\delta^2} t\right) \end{aligned} \right\} \text{for } \delta\lambda_n > 1/2$$

$$\left. \begin{aligned} f_n(t) &= \exp\left(\frac{(1 - 4\delta^2\lambda_n^2)^{1/2}}{2\delta^2} t\right) \\ g_n(t) &= \exp\left(-\frac{(1 - 4\delta^2\lambda_n^2)^{1/2}}{2\delta^2} t\right) \end{aligned} \right\} \text{for } \delta\lambda_n < 1/2$$

$$\left. \begin{aligned} f_n(t) &= 1 \\ g_n(t) &= t \end{aligned} \right\} \text{for } \delta\lambda_n = 1/2$$

$$\lambda_n = n\pi, \quad n = 1, 2, \dots, \infty$$

$$F_n = -\frac{2\delta^2 g_n'(0) - g_n(0)}{2\delta^2 f_n'(0) - f_n(0)}$$

$$D_n = \frac{2}{n\pi} \frac{(-1)^n T_a - T_0}{F_n f_n(0) + g_n(0)}$$

Case 2—Fluxes Specified at Both Ends. The boundary and initial conditions in dimensionless form are:

$$q(0, t) = q_0, \quad q(1, t) = q_a, \quad T_1(x, 0) = 0, \quad \frac{\partial T_1}{\partial t}(x, 0) = 0.$$

Under these conditions, the hyperbolic heat conduction equation is solved by the separation of variables technique, and then $T_1(x, t)$ is determined to be

$$T_1(x, t) = -(q_a - q_0)t - \sum_{n=1}^{\infty} D_n \lambda_n \cos(\lambda_n x) [F_n G_n(t) + H_n(t)] \quad (9)$$

Here

$$G_n(t) = \int_0^t e^{-t'/2\delta^2} f_n(t') dt',$$

$$H_n(t) = \int_0^t e^{-t'/2\delta^2} g_n(t') dt',$$

and $F_n, f_n(t), g_n(t)$, and λ_n are the same as those defined in the context of Eq. (8).

Case 3—Temperature Specified at $x = 0$ and Flux Specified at $x = 1$. The boundary and initial conditions in dimensionless form are:

$$T_1(0, t) = T_0, \quad q(1, t) = q_a, \quad T_1(x, 0) = 0, \quad \frac{\partial T_1}{\partial t}(x, 0) = 0.$$

For this case, the method of Laplace transform is used by considering Eqs. (3) and (4) as two coupled first-order linear partial differential equations and $T_1(x, t)$ is found to be

$$T_1(x, t) = T_0 \sum_{n=1}^{\infty} (-1)^{n-1} \sum_{i=1}^2 \theta_{in}(x, t) + q_a \sum_{n=1}^{\infty} (-1)^{n-1} \sum_{i=3}^4 \theta_{in}(x, t). \quad (10)$$

For $i = 1, 2$, we have

$$\theta_{in}(x, t) = u(t - \eta_{in}(x)) \left\{ e^{-\eta_{in}(x)/2\delta^2} + \frac{\eta_{in}(x)}{8\delta^4} \int_{\eta_{in}(x)}^t dt' e^{-t'/2\delta^2} [I_0(\beta_i) - I_2(\beta_i)] \right\}$$

$$\eta_{in}(x) = 2\delta(n - 2 + i) - (-1)^i \delta x,$$

$$\beta_i = \frac{(t'^2 - \eta_{in}^2(x))^{1/2}}{2\delta^2}$$

Here $u(t - \eta_{in}(x))$ is the unit step function, and $I_0(\beta_i), I_2(\beta_i)$ are the modified Bessel functions of the first kind of order 0 and 2, respectively.

For $i = 3, 4$, we have

$$\theta_{in}(x, t) = u(t - \eta_{in}(x)) \left[e^{-\eta_{in}(x)/2\delta^2} \left\{ \eta_{in}'(x) + (t - \eta_{in}(x)) \right\} \frac{\eta_{in}'(x)}{2\delta^2} \left(1 + \frac{\eta_{in}(x)}{4\delta^2} \right) - \int_{\eta_{in}(x)}^t dt' (t - t') \frac{e^{-t'/2\delta^2}}{8\delta^4} \eta_{in}'(x) \right. \\ \left. \{ I_0(\beta_i) - I_2(\beta_i) \} - \frac{\eta_{in}^2(x)}{16\delta^4} \left\{ I_0(\beta_i) - \frac{4}{3} I_2(\beta_i) + \frac{1}{3} I_4(\beta_i) \right\} \right]$$

$$\eta_{in}(x) = \delta(2n - 1) - (-1)^i \delta x$$

$$\eta_{in}'(x) = -(-1)^i \delta \frac{(t'^2 - \eta_{in}^2(x))^{1/2}}{2\delta^2},$$

and $I_4(\beta_i)$ is the modified Bessel function of the first kind of order 4.

It should be pointed out that Eqs. (8), (9), and (10) are the solution for the transformed temperature. The original dimensionless temperature (T) can be obtained by using Eq. (7).

Numerical Solution. The method of characteristics (Wiggert, 1977) is used to solve the governing Eqs. (3) and (4). A generalized boundary condition is used.

We write the boundary conditions as

at $x = 0$

$$b_1 q = \text{Bi}_1 (b_2 T - T_0^*/T_r^*), \quad (11)$$

at $x = 1$

$$d_1 q = -\text{Bi}_2 (d_2 T - T_0^*/T_r^*) \quad (12)$$

It can be seen from Eqs. (11) and (12) that all three types of boundary conditions are specified by assigning different values to b_1 , Bi_1 , b_2 , T_0^*/T_r^* , d_1 , d_2 , and Bi_2 . For instance, the temperature condition at $x = 0$ can be obtained by setting $b_1 = 0$, $\text{Bi}_1 = 1$, $b_2 = 1$, and T_0^*/T_r^* to the specified temperature. These values for various boundary conditions are tabulated in Table 1. The variable T appearing in Eqs. (11) and (12) is the dimensionless temperature and is a nonlinear function of the dimensionless transformed temperature T_1 . For the case of $k(T^*)$ varying linearly with temperature, T can be expressed as a function of T_1 as given by Eq. (7).

According to Eqs. (1), (2c), (2d), and (3), the initial conditions may be expressed as

$$T_1 = 0 \quad (13)$$

and

$$q = 0 \quad (14)$$

Method of Characteristics. A schematic diagram of the computational grid is given in Fig. 1. This grid is chosen according to the characteristic directions so that the Courant stability conditions (Wiggert, 1977) are satisfied.

Following Wiggert (1977), the compatibility condition may be written in finite difference form as

$$\delta(q_p - q_{p+}) + (T_{1p} - T_{p+}) + \frac{1}{2}(q_p + q_{p+})\Delta x = 0 \quad (15)$$

Table 1 Numerical values of parameters for various boundary conditions

at $x = 0$				
Condition Type	b_1	b_2	Bi_1	T_0^*/T_r^*
Temperature	0	1	1	T_{01}^*/T_r^*
Flux	1	0	q_0	1
Convective	1	1	Bi_1	T_0^*/T_r^*
at $x = 1$				
Condition Type	d_1	d_2	Bi_2	T_0^*/T_r^*
Temperature	0	1	1	T_{01}^*/T_r^*
Flux	1	0	q_0	1
Convective	1	1	Bi_2	T_0^*/T_r^*

$$\delta(q_p - q_{p-}) - (T_{1p} - T_{p-}) + \frac{1}{2}(q_p + q_{p-})\Delta x = 0 \quad (16)$$

The simultaneous solutions of Eqs. (15) and (16) provide the expressions for the interior temperatures and fluxes,

$$T_{1p} = \frac{1}{2} \left[(q_{p+} - q_{p-}) \left(\delta - \frac{\Delta x}{2} \right) + T_{p+} + T_{p-} \right] \quad (17)$$

$$q_p = \frac{(q_{p+} - q_{p-}) \left(\delta - \frac{\Delta x}{2} \right) + T_{p+} - T_{p-}}{(2\delta + \Delta x)} \quad (18)$$

Depending on the types of boundary condition, Eqs. (11) and (12) will in general involve both T and q . An additional equation from the compatibility condition along ζ_- or ζ_+ characteristics for the $x = 0$ or $x = 1$ boundary, respectively, is required to satisfy the boundary conditions.

At $x = 0$, the compatibility condition along ζ_- , Eq. (16), can be combined with the boundary condition, Eq. (11), by eliminating q .

A nonlinear algebraic equation for T_1 is obtained:

$$b_1 T_1 + \left(-\delta - \frac{x_B}{2} \right) \text{Bi}_1 \left(b_2 T - \frac{T_0^*}{T_r^*} \right) = \left(T_{1B} + \left(-\delta + \frac{x_B}{2} \right) q_B \right) b_1 \quad (19)$$

Similarly, at $x = 1$, we can obtain a nonlinear algebraic equation for T_1 ,

$$d_1 T_1 - \left(\delta + \frac{1-x_A}{2} \right) \text{Bi}_2 \left(d_2 T - \frac{T_0^*}{T_r^*} \right) = \left(T_{1A} + \left(\delta - \frac{1-x_A}{2} \right) q_A \right) d_1 \quad (20)$$

A Newton-Raphson iteration is employed to solve for T_1 . q is then given by

$$q = \frac{T_{1B} - T_1 + \left(-\delta + \frac{x_B}{2} \right) q_B}{-\delta - \frac{x_B}{2}} \quad \text{at } x = 0 \quad (21)$$

and

$$q = \frac{T_{1A} - T_1 + \left(\delta - \frac{1-x_A}{2} \right) q_A}{\delta + \frac{1-x_A}{2}} \quad \text{at } x = 1 \quad (22)$$

It should be pointed out that for a given type of boundary condition, the initial temperature and/or heat flux at the boundaries can be calculated by using Eqs. (19)–(22) in the limit of x_A and x_B going to one and zero, respectively.

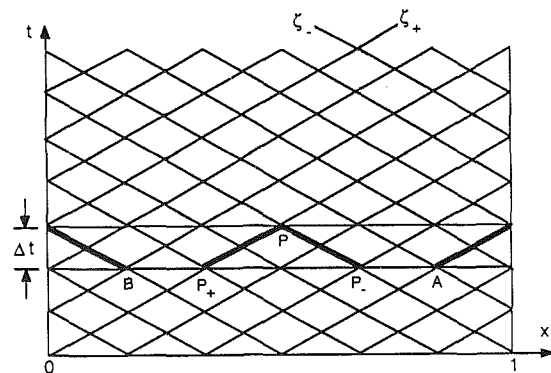


Fig. 1 Schematic diagram of the computational grid for the method of characteristics

Table 2 Temperature field for Case 3 at $t = 0.05$ for $T_o = 9$, $q_o = -7$, $\delta = 0.2$, and $\epsilon = 0.2$

x	T from equations (10) and (7)	T from numerical solution
0.00	9.0	9.0
0.06	8.5253	8.5252
0.12	8.0237	8.0237
0.18	7.4944	7.4944
0.24	6.9358	6.9358
0.30	1.0	1.0
0.36	1.0	1.0
0.42	1.0	1.0
0.48	1.0	1.0
0.54	1.0	1.0
0.60	1.0	1.0
0.66	1.0	1.0
0.72	1.0	1.0
0.78	1.2515	1.2515
0.84	1.2973	1.2973
0.90	1.3426	1.3427
0.96	1.3877	1.3877
1.0	1.4177	1.4177

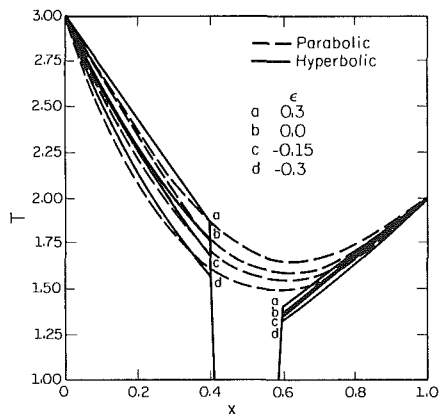


Fig. 2 Temperature distributions for various ϵ and $\delta = 0.2$ at $t = 0.08$ for temperature conditions

Results and Discussion

In the present study, the closed-form solutions expressed in Eqs. (8), (9), and (10) are evaluated using 300, 600, and 4000 terms, respectively, and the series were considered to converge when the difference between the absolute values of the successive terms of the series is less than or equal to 10^{-4} . In the numerical solution, the grid size Δx is 0.01 and the time step Δt is $\delta \Delta x$. The convergence of the numerical solution is examined by grid refinement. Improvement of the numerical solution beyond the grid size 0.01 is found to be insignificant. For comparison purposes, results from the closed-form solutions are tabulated along with the numerical solution obtained by the method of characteristics in Table 2. It can be observed that the results agree with each other very well, and for this reason, only the numerical solution results are used in all the graphs. To compare the analytic solution with the numerical solution for all three cases, we computed the temperature fields by changing x in steps of $\Delta x = 0.01$. For Fig. 2, T has a very large value at $x = 0.4$ and then T drops sharply, eventually to assume values very close to unity, which continues until we reach the neighborhood of the point $x = 0.6$. The closeness of these values to unity can be perceived from Table 2 where results for Case 3 are presented. The seemingly vertical lines in Fig. 2 near the points $x = 0.4$ and $x = 0.6$ are really not vertical as can be seen from the figure, which shows that

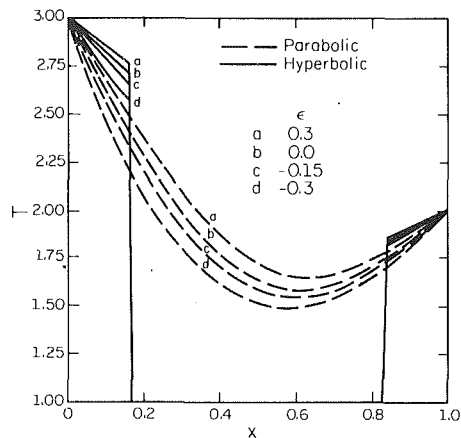


Fig. 3 Temperature distributions for various ϵ and $\delta = 0.5$ at $t = 0.08$ for temperature conditions

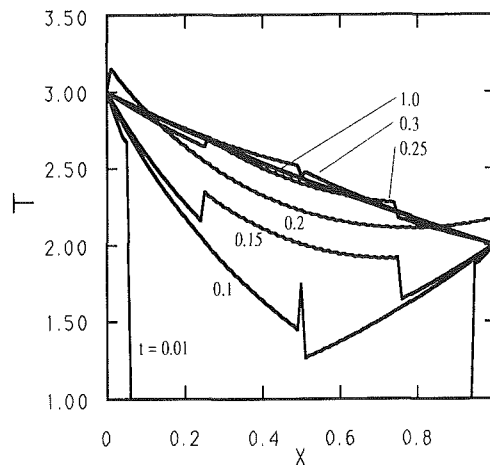


Fig. 4 Temperature distributions at various time steps for $\epsilon = -0.3$, $\delta = 0.2$, and temperature conditions

the series solution is essentially a curve-fit for the discontinuity of temperature at the thermal wave propagation front. The analytic results obtained for other cases are also found to compare well with the numerical solution, but due to brevity, they are not tabulated in this study. The results of the conventional parabolic heat conduction equation solved by separation of variables are also presented so that a direct comparison can be made.

The results of Case 1 (temperatures specified at both ends) are presented in Figs. 2-4. In all cases, the left-hand boundary ($x = 0$) is kept at $T^*/T_o^* = 3.0$ and the right-hand boundary ($x = 1.0$) is kept at $T^*/T_o^* = 2.0$. The temperature distributions within the medium for various ϵ , and $\delta = 0.2$ at $t = 0.08$ are plotted in Fig. 2. The discontinuities predicted by the hyperbolic conduction equation are due to the finite propagation speed. The thermal wave, generated by a sudden change in boundary temperature, propagates in the material with finite speed so that in the region $0.4 < x < 0.6$ the material is not yet affected. The effects of ϵ on the temperature fields can also be examined from Fig. 2. In the cases of negative ϵ , the thermal conductivity is smaller than its value at the reference temperature because the temperature is higher than the reference temperature everywhere. It can be observed that the temperature field for $\epsilon < 0$ is lower than the case $\epsilon = 0$. When ϵ is positive, the temperature field becomes higher than the $\epsilon = 0$ case.

The temperature distributions within the medium for various ϵ , and $\delta = 0.5$ at $t = 0.08$ are plotted in Fig. 3. The value of δ is increased to 0.5 from 0.2 in the previous case. Conse-

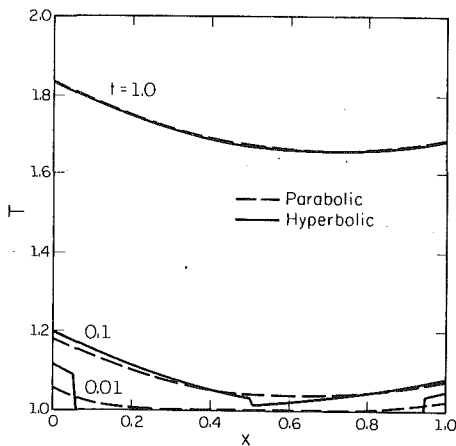


Fig. 5 Temperature distributions at various time steps for $\epsilon = 0$, $\delta = 0.2$, and flux conditions

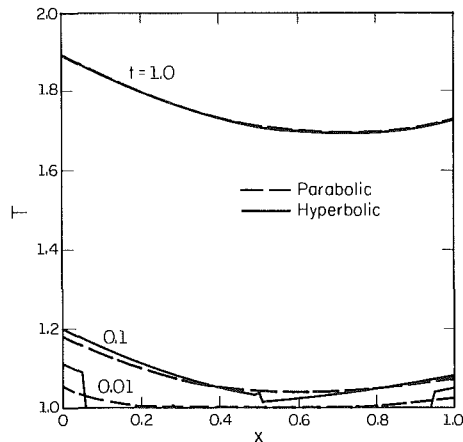


Fig. 6 Temperature distributions at various time steps for $\epsilon = -0.15$, $\delta = 0.2$, and flux conditions

quently, the dimensionless speed of the thermal wave becomes smaller in this case compared to the previous one. This can be observed by comparing Fig. 3 with Fig. 2. The discontinuities in the present case do not travel as far into the material as in the previous case. The effects of the temperature-dependent thermal conductivity presented in Fig. 2 can also be observed in Fig. 3.

The transient behavior of the temperature distribution is examined next. The temperature distribution predicted by the hyperbolic heat conduction at various time steps for $\epsilon = -0.3$ and $\delta = 0.2$ are plotted in Fig. 4. For the sake of clarity, the results predicted by the parabolic heat conduction equation are not plotted in this figure. The hyperbolic equation predicts propagation of two thermal waves, one from the left and the other from the right. At $t = 0.1$, the two thermal waves meet and are superimposed. As time progresses, the thermal waves propagate back and forth within the slab. At $t = 1.0$, the temperature field is at steady state. It can be observed that steady state is attained due to the thermal waves traveling back and forth within the material. Because of the fact that ϵ is nonzero, the steady-state solution is no longer a straight line temperature profile.

We will now present the results for Case 2 (specified heat flux on both ends). In all the cases presented below, the flux is specified to be 0.3 on the left-hand boundary and -0.2 on the right. According to the convention used in the constitutive law (Eq. (2)), this corresponds to heating from both boundaries. The temperature distributions for various time steps and $\delta = 0.2$ are plotted in Figs. 5 and 6 for $\epsilon = 0$ and -0.15 , respectively. At $t = 0.01$ and 0.1 , the effects of finite prop-

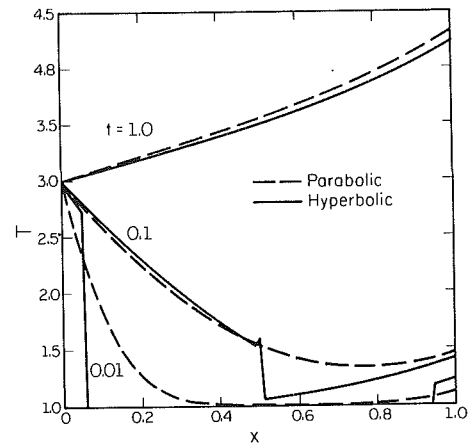


Fig. 7 Temperature distributions at various time steps for $\epsilon = -0.15$, $\delta = 0.2$, and mixed conditions

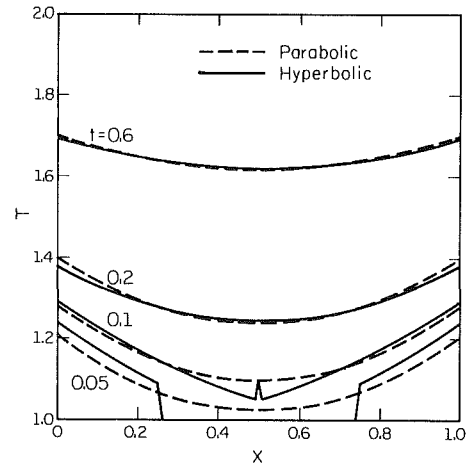


Fig. 8 Temperature distributions at various time steps for $\epsilon = -0.15$, $\delta = 0.2$, and convective boundary conditions

agation speed of heat can be observed. It can be seen that the thermal waves are traveling back and forth. At a later time, $t = 1.0$, the parabolic and the hyperbolic predictions are identical. It should be pointed out that the case of $\epsilon = -0.15$ has a higher temperature than the case of $\epsilon = 0$. The reason is as follows. In the case of negative ϵ , the thermal conductivity decreases as the temperature increases. As a result, ρC_p decreases as the temperature increases because the thermal diffusivity is considered constant in this study. Since the heating from both boundaries is kept constant, the temperature field has to rise in the negative ϵ case in order to compensate for the decrease in ρC_p so that the energy can be conserved.

For Case 3, the temperature is kept at $T^*/T_r^* = 3.0$ at $x = 0$ and the flux is kept at -1.0 at $x = 1$ in this study. The temperature distributions for various time steps, $\delta = 0.2$, and $\epsilon = -0.15$ are plotted in Fig. 7. Behavior similar to the flux condition results can be observed. Heat is transferred within the medium via diffusion in parabolic conduction and thermal wave propagation in hyperbolic conduction.

The effects of convective boundary conditions, which correspond to the case where the material is either cooled or heated by convection in ambient fluid, are examined in this study by the method of characteristics only. All the cases presented below are characterized by Biot number equal to 1 and the ambient temperature is kept at $T^*/T_r^* = 2.0$ on both sides. Physically, this corresponds to convective heating by the hotter ambient fluid. The temperature distributions for various time steps, $\delta = 0.2$, and $\epsilon = -0.15$, are plotted in Fig. 8. The propagation of thermal waves in hyperbolic conduction is once

again observed. However, as time progresses, the results of the hyperbolic and parabolic conduction become identical. This is because the relaxation term becomes unimportant for large time.

Summary

Hyperbolic conduction equations with variable thermo-physical properties, such as thermal conductivity, heat capacity, and density, but constant thermal diffusivity, are considered. The nonlinear equations are transformed to linear equations by using Kirchhoff transformation. Analytic solutions are obtained for (i) temperatures specified at both ends, (ii) heat fluxes specified at both ends, and (iii) temperature specified at $x = 0$ and heat flux specified at $x = 1$. Numerical solutions are obtained using the method of characteristics. In the numerical solutions, a generalized boundary condition is formulated to account for the above three as well as the convective boundary conditions. For the convective boundary condition, the transformed condition becomes nonlinear, and is handled using a Newton-Raphson iterative scheme. Results for temperature, heat flux, and convective boundary conditions are presented and discussed. Parabolic conduction results are also presented and compared with the hyperbolic cases via numerical examples. The hyperbolic equation predicts a discontinuous evolution of the temperature field in which the thermal waves travel back and forth at finite propagation speed. The effects of temperature-dependent thermal conductivity, heat capacity, and density but constant thermal diffusivity are found to be significant.

Acknowledgment

A part of this work was made possible by a grant (N00014-89-J-1473) from the U.S. Office of Naval Research. Dr. George Yoder is the program manager.

References

Atkins, K. R., 1959, *Liquid Helium*, Cambridge University, United Kingdom.
 Baumeister, K. J., and Hamill, T. D., 1969, "Hyperbolic Heat-Conduction Equation—A Solution for the Semi-infinite Body Problem," *ASME JOURNAL OF HEAT TRANSFER*, Vol. 91, pp. 543-548.
 Bertman, B., and Sandiford, D. J., 1970, "Second Sound in Solid Helium," *Scient. Am.*, Vol. 222, pp. 92-101.
 Boley, B. A., 1964, "The Analysis of Problems of Heat Conduction and Melting," in: *High Temperature Structures and Materials*, Pergamon Press, New York, pp. 260-315.
 Brazel, J. P., and Nolan, E. J., 1966, "Non-Fourier Effects in Transmission

of Heat," *6th Conf. on Thermal Conductivity*, U.S. Air Force Materials Lab., Dayton, OH, pp. 238-243.

Carlslaw, H. S., and Jaeger, J. C., 1986, *Conduction of Heat in Solids*, 2nd ed., Clarendon Press, Oxford, pp. 10-11, 18.

Chan, S. H., Low, M. J. D., and Mueller, W. K., 1971, "Hyperbolic Heat Conduction in Catalytic Supported Crystallites," *AIChE J.*, Vol. 17, pp. 1499-1501.

Chester, M., 1963, "Second Sound in Solids," *Phys. Rev.*, Vol. 131, pp. 2013-2015.

Frankel, J. I., Vick, B., and Ozisik, M. N., 1985, "Flux Formulation of Hyperbolic Heat Conduction," *J. Appl. Phys.*, Vol. 58, pp. 3340-3345.

Glass, D. E., Ozisik, M. N., McRae, D. S., and Vick, B., 1985, "On the Numerical Solution of Hyperbolic Heat Conduction," *Numerical Heat Transfer*, Vol. 8, pp. 497-504.

Glass, D. E., Ozisik, M. N., McRae, D. S., and Vick, B., 1986, "Hyperbolic Heat Conduction With Temperature-Dependent Thermal Conductivity," *Journal of Applied Physics*, Vol. 59, pp. 1861-1865.

Lietoila, A., and Gibbons, J. F., 1982, "Calculation of Carrier and Lattice Temperatures Induced in Si and GaAs by Picosecond Laser Pulses," in: *Laser and Electron-Beam Interactions With Solids*, B. R. Appleton and G. K. Celler, eds., Elsevier Science, New York, pp. 163-168.

Luikov, A. V., 1980, *Heat and Mass Transfer*, translated from the Russian by T. Kortneva, Mir, Moscow, pp. 116-123.

Maurer, M. J., and Thompson, H. A., 1973, "Non-Fourier Effects at High Heat Flux," *ASME JOURNAL OF HEAT TRANSFER*, Vol. 95, pp. 284-286.

Maxwell, J. C., 1867, "On the Dynamical Theory of Gases," *Phil. Trans. R. Soc.*, Vol. 157, pp. 49-88.

Morse, P. M., and Feshbach, H., 1953, *Methods of Theoretical Physics, Part I*, McGraw-Hill, New York, pp. 865-869.

Ozisik, M. N., 1980, *Heat Conduction*, Wiley, New York, pp. 440-441.

Ozisik, M. N., and Vick, B., 1984, "Propagation and Reflection of Thermal Waves in a Finite Medium," *Int. J. Heat Mass Transfer*, Vol. 27, pp. 1845-1854.

Peshkov, V., 1944, "Second Sound in Helium II," *J. Phys. USSR*, Vol. VIII, p. 381.

Simons, S., 1972, "On the Differential Equation for Heat Conduction," *Trans. Theory Stat. Phys.*, Vol. 2, pp. 117-128.

Taitel, Y., 1972, "On the Parabolic, Hyperbolic, and Discrete Formulation of the Heat Conduction Equation," *Int. J. Heat Mass Transfer*, Vol. 15, pp. 269-371.

Tamma, K. K., and Railkar, S. B., 1988, "Specially Tailored Transfinite Element Formulations for Hyperbolic Heat Conduction Involving Non-Fourier Effects," *Collected Papers in Heat Transfer*, Vol. 1, pp. 13-20.

Vernotte, M. P., 1958, "Les Paradoxes de la Theorie Continue de l'Equation de la Chaleur," *Comptes Rendus*, Vol. 246, pp. 3154-3155.

Vick, B., and Ozisik, M. N., 1983, "Growth and Decay of a Thermal Pulse Predicted by the Hyperbolic Heat Conduction Equation," *ASME JOURNAL OF HEAT TRANSFER*, Vol. 105, pp. 902-907.

Weyman, H. D., 1967, "Finite Speed of Propagation in Heat Conduction, Diffusion, and Viscous Shear Motion," *Am. J. Phys.*, Vol. 36, pp. 488-496.

Wiggert, D. C., 1977, "Analysis of Early-Time Transient Heat Conduction by Method of Characteristics," *ASME JOURNAL OF HEAT TRANSFER*, Vol. 99, pp. 35-40.

Wu, C. Y., 1988, "Integral Equation Solution for Hyperbolic Heat Conduction With Surface Radiation," *Int. Comm. Heat Mass Transfer*, Vol. 15, pp. 365-374.

Wu, C. Y., 1989, "Hyperbolic Heat Conduction With Surface Radiation and Reflection," *Int. J. Heat Mass Transfer*, Vol. 32, pp. 1585-1587.

Thermal Contact Conductance of Metallic Coated BiCaSrCuO Superconductor/Copper Interfaces at Cryogenic Temperatures

J. M. Ochterbeck
Graduate Research Assistant.

G. P. Peterson
Professor.
Mem. ASME

L. S. Fletcher
Professor.
Fellow ASME

Department of Mechanical Engineering,
Texas A&M University,
College Station, TX 77843

The effects of vapor deposited coatings on the thermal contact conductance of cold pressed, normal state BiCaSrCuO superconductor/oxygen-free copper interfaces were experimentally investigated over a pressure range of 200 to 2000 kPa. Using traditional vapor deposition processes, thin coatings of indium or lead were applied to the superconductor material to determine the effect on the heat transfer occurring at the interface. The test data indicate that the contact conductance can be enhanced using these coatings, with indium providing the greater enhancement. The experimental program revealed the need for a better understanding and control of the vapor deposition process when using soft metallic coatings. Also, the temperature-dependent microhardness of copper was experimentally determined and found to increase by approximately 35 percent as the temperature decreased from 300 to 85 K. An empirical model was developed to predict the effect of soft coatings on the thermal contact conductance of the superconductor/copper interfaces. When applied, the model agreed well with the data obtained in this investigation at low coating thicknesses but overpredicted the data as the thickness increased. In addition, the model agreed very well with data obtained in a previous investigation for silver-coated nickel substrates at all coating thicknesses.

Introduction

The advent of copper-oxide superconductors with transition temperatures above the temperature of liquid nitrogen has greatly expanded the research fields and possible applications of superconducting materials. Prior to the discovery of high transition temperature (high- T_c) superconductors, superconductivity was limited to the research laboratory or applications where cost was not an issue, due to the required cooling with expensive liquid helium. However, high- T_c superconductors potentially may be cooled by liquid nitrogen, which is at least twenty times less expensive (in both equipment and substance costs) and has a latent heat of vaporization of eight times greater than liquid helium (Scalapino et al., 1988).

Present applications for both high- T_c and low- T_c superconducting materials include nuclear magnetic-resonance imaging and spectroscopy in medical diagnostics, radio-frequency devices, research and development magnets, magnetic shielding, colliders, and infrared sensors (National Academy of Sciences, 1987; Foner and Orlando, 1988). Potential applications currently being investigated, but not yet economical, include energy storage and electrical transmission for power utilities and high-speed trains using magnetic levitation (Douglas, 1987; Foner and Orlando, 1988; Wolsky et al., 1989). Computers of the future might be designed with semiconducting-superconducting hybrids (Van Duzer, 1988), which would combine the superior qualities of both materials.

Two important parameters govern the potential application of superconductors: the critical current density and the upper critical magnetic field density. The critical current and magnetic field densities for a superconductor generally reach a peak value near $T < 0.5 T_c$ and rapidly decrease as the temperature increases. A general rule for application is that the superconductor material must be operated below $T < 0.75 T_c$

to allow for usable critical density levels (National Academy of Sciences, 1987).

Comprehensively, the stability of superconductors can be described as being directly dependent upon the temperature of the superconductor, the current density, and the magnetic field strength generated by the current (Foner and Orlando, 1988). A corresponding change in any one condition could cause the superconductor to return to the normal state. This would require that the current carried by the superconductor be effectively dissipated. To handle this requirement, most superconductor devices could be designed such that a substrate or carrier material, possibly copper or aluminum, would operate in parallel with the superconductor and serve as a dissipating medium. The substrate could also be used to transfer the heat away from the superconductor during cooling or in the event of a normal state occurrence, which would generate heat resulting from the current and the normal state electrical resistance. This, combined with the general temperature requirements of the superconductors, illustrates that for these devices to operate effectively and economically it is necessary to understand the thermal behavior of these materials better.

Many parameters govern the heat transfer characteristics in superconducting devices. One significant parameter is the thermal contact conductance between the superconductor and the substrate or carrier material. The thermal contact conductance is defined as the heat flux through the interface divided by the temperature discontinuity at the interface, or

$$h_c = \frac{Q/A}{\Delta T} \quad (1)$$

Of the various methods previously utilized to enhance the thermal contact conductance of interfaces, the use of vapor-deposited metallic coatings has been demonstrated by Antonetti (1983) and Kang et al. (1990) to provide the greatest potential. However, the use of metallic coatings has not been studied for interfaces containing a ceramic material or for interfaces with metallic coatings at cryogenic temperatures.

Contributed by the Heat Transfer Division and presented at the 3rd ASME/JSME Thermal Engineering Joint Conference, Reno, Nevada, March 17-22, 1991. Manuscript received by the Heat Transfer Division October 16, 1990; revision received July 1, 1991. Keywords: Conduction, Cryogenics, Measurement Techniques.

Literature Review

Since the YBaCuO superconducting compound initially yielded transition temperatures above liquid nitrogen, most of the available literature focuses on this material. The thermal conductivity of YBaCuO has been experimentally measured by several investigators, including Jezowski et al. (1987), Uher and Kaiser (1987), Gottwick et al. (1987), Morelli et al. (1987), Bayot et al. (1987), Kirk et al. (1989), and Fletcher et al. (1991). Fletcher et al. (1991) also provided a review of several other YBaCuO properties.

Although the trends of the thermal conductivity have been consistent, the magnitude has varied significantly. Differences in the thermal conductivity, as noted by Fletcher et al. (1991), may occur from differences in sample density that result from different sample fabrication methods (cold or hot pressed) or from slight variations in the oxygen content of the samples. Also, Pandey et al. (1988) indicate that, in general, cold-pressed samples result in a much lower density (usually 50–60 percent theoretical) than hot-pressed samples. Kirk et al. (1989) noted that the thermal conductivity of the YBaCuO compound is anisotropic with respect to the pressing direction for hot pressed samples.

Recently, attention has been directed toward the BiCaSrCuO and lead-doped BiPbCaSrCuO compounds. These compounds have shown more promise for applications due to higher transition temperatures (110 K) and higher critical current densities. However, little information on the thermal properties of these compounds is presently available. Kirk (1990) presented the thermal conductivity measurements for the lead-doped BiPbCaSrCuO compound below room temperature. The sample tested was cold pressed and comprised of 25 percent 105 K phase and 75 percent 70 K phase. The thermal conductivity exhibited an almost linear decrease from approximately 1.8 W/mK at 200 K to 1.0 W/mK at 50 K.

Thermal Contact Conductance of Bare Interface. The major obstacle in the study of thermal contact conductance is to find theoretical correlations that will accurately predict the thermal contact conductance between two contacting surfaces. In the past, experimental work and empirical correlations have been widely used.

An analytical investigation conducted by Yovanovich (1982) resulted in an expression to predict the thermal contact conductance between two metal surfaces. The dimensionless contact conductance equation was expressed as

$$\frac{h_c \sigma}{mk_m} = 1.25 \left(\frac{P}{H} \right)^{0.95} \quad (2)$$

This expression was found to be reasonably accurate by Yovanovich et al. (1983), Antonetti (1983), and Hegazy (1985). It has also been demonstrated to be applicable not only to similar and dissimilar metallic contacts but to nonmetallic contacts. This was done by Eid and Antonetti (1986), using an aluminum–silicon interface, and by Peterson and Fletcher (1988), using a substrate/spreader material-mold compound interface found in microelectronic components.

Madhusudana and Fletcher (1983) noted the difficulty in measuring the mean profile slope and that it was seldom reported in previous investigations. Therefore, the mean profile slope was deleted and a dimensionless power law correlation for Zircaloy-2/Uranium Oxide interfaces commonly found in nuclear reactors was developed. The general form of the correlation was given as

$$\frac{h_c \sigma}{k_m} = c \left(\frac{P}{M} \right)^n \quad (3)$$

The constants, c and n , were empirically determined to provide a best-fit curve using data from several previous investigations.

Thermal Contact Conductance of Coated Interface. The use of vapor-deposited metallic coatings has been previously investigated by Mal'kov and Dobashin (1969), Antonetti (1983), and Kang et al. (1990). Mal'kov and Dobashin (1969) presented one of the first works concerning the use of soft-metal coatings. However, this study was limited to constant coating thickness. Also, no theoretical or empirical correlations were presented.

Antonetti (1983) presented the only theoretical model to predict the thermal contact conductance of a coated surface. This model assumed the enhancement was due to mechanical effects (increased surface contact area) and to thermal effects (a high thermal conductivity coating that allows heat to be dissipated more easily). The derived equation approximated the thermal contact conductance of a coated junction as a bare junction multiplied by mechanical and thermal correction factors. Antonetti (1983) also developed a modified form of the correlation developed by Yovanovich (1982). This modification substituted an effective thermal conductivity, k' , and an effective microhardness, H' , for the thermal conductivity and microhardness, respectively. Both models were found to be in good agreement with experimental data for silver coatings on nickel substrates.

Kang et al. (1990) performed the most extensive experimental work in this area. Different thicknesses of indium, lead, and tin coatings on aluminum substrates were studied and an optimum thickness was determined for each coating. The thermal contact conductance was shown to be enhanced by as much

Nomenclature

A = area	conductivity (layer/substrate)	ΔT = temperature discontinuity
b = empirical pressure factor	$k_{m,s}$ = harmonic mean thermal conductivity (substrate/substrate)	t = coating thickness
c = empirical constant	K = harmonic mean thermal conductivity ratio	$\beta(t, P)$ = empirical thermal constriction parameter
d = Vickers indentation depth	m = mean profile slope	Γ_1 = empirical thermal constriction parameter
f = exponential function of t , σ , and b	M = mean effective flow pressure	Γ_2 = empirical thermal constriction parameter
FD = flatness deviation	n = empirical constant	Γ_3 = empirical constriction parameter
h, h_c = thermal contact conductance	P = apparent pressure	σ = surface roughness
H = Vickers microhardness	Q = heat flow rate	Subscripts
H_l = coating layer microhardness	R = thermal resistance or electrical resistance	c = contact
H_s = substrate microhardness	T = temperature	Superscripts
k = thermal conductivity	T_c = transition temperature	' = indicates layer present
k_m = harmonic mean thermal conductivity		
$k_{m,l}$ = harmonic mean thermal conductivity (layer/substrate)		

as 700, 400, and 50 percent for indium, lead, and tin, respectively. As a result of this work, it was concluded that for the coatings tested, the coating hardness was more significant than the coating thermal conductivity.

The investigations of Kang et al. (1990) and Antonetti (1983) both demonstrated that the thermal contact conductance can be enhanced through the use of a soft metallic coating and that the enhancement was primarily a function of the microhardness. As predicted, the experimental results of Antonetti (1983) showed an initial rapid increase followed by an asymptotic approach to a maximum value. The analytical model, however, did not contain any mechanism by which enhancement would decrease when a softer coating was applied to a harder substrate having a thermal conductivity on the order of or greater than the thermal conductivity of the substrate. Kang et al. (1990) showed the same initial rapid increase up to a maximum peak value, but as the thickness was increased further, the enhancement decreased.

Microhardness. The complexity between the hardness of a given surface and the indentation depth increases considerably when a thin coating has been applied to the surface. Antonetti (1983) developed an analysis, referred to as the effective microhardness, for nickel substrates with silver coatings. The effective microhardness was divided into three linear regions based upon the ratio of the thickness of the coating and depth of the indenter. In the first region, $t/d < 1.00$, the indenter penetrates the relatively thin coating and the substrate. In the next region, $1.00 < t/d < 4.90$, the indenter penetrates only the coating but the microhardness is still influenced by the properties of the underlying substrate. The final region, $t/d > 4.90$, is simply the microhardness of the coating with no effect by the substrate. Kang et al. (1990) measured the effective microhardness of aluminum substrates with lead, tin, and indium coatings. Trends similar to that of Antonetti (1983) were reported. The slope of the data for the region $t/d < 1.00$ was greatest for indium, followed by lead and tin, respectively. This corresponds to the order of microhardness for the coatings from softest to hardest.

In a discussion on the low-temperature properties of structural materials, Scott (1988) reported a direct correlation between the crystal lattice structure and the behavior of a material in terms of ductile-brittle transition. Unlike body-centered cubic metals, face-centered cubic metals, e.g., copper, do not become brittle at liquid nitrogen temperatures. Even though copper remains ductile, a 30 to 40 percent increase in the tensile strength of copper as the temperature decreases from 300 to 80 K has been reported by Scott (1988). Teed (1950) reported an increase of 62 percent in the ultimate tensile strength from 300 to 93 K. Since the hardness of a material is often used to predict the tensile strength, intuitively, this would indicate that the hardness should also increase.

Experimental Program

The experimental apparatus used in this investigation has been fully discussed by Ochterbeck (1990) and is similar to the apparatus described by Kang et al. (1990). The primary part of the apparatus was the vertical test column; see Fig. 1. This column was composed of three 2.54-cm-dia specimens: (1) a 304 stainless steel bar in contact with copper coils, (2) an oxygen-free high conductivity (OFHC) copper bar in contact with a cooling bath, and (3) a 0.1-cm-thick, cold-pressed BiCaSrCuO superconductor sample inserted between the stainless steel and copper bars. The coils and cooling bath were supplied by -40°C constant temperature circulating fluid and by liquid nitrogen, respectively. To insure that the cooling bath was constantly filled with liquid nitrogen, a liquid/gas differentiating cryogenic control valve was used to vent the boiled-off gas while restraining the liquid within the lines and the cooling bath.

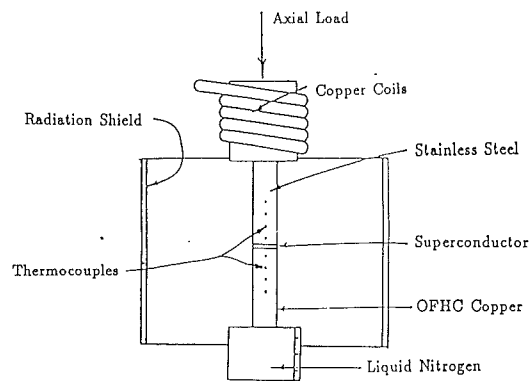


Fig. 1 Experimental test apparatus

To minimize convective heat losses, the system was operated within a vacuum chamber capable of maintaining a vacuum quality of greater than 1.0×10^{-6} Torr. In addition to the vacuum chamber, a radiation shield was utilized to minimize any radiation heat losses. Loading of the column was provided by pressurized nitrogen gas supplied to a load bellows and monitored by a 0–8000 N load cell.

Test Sample Preparation. The stainless steel 304 and oxygen-free high-conductivity copper samples were both cut from standard bar stock and turned to the appropriate diameter. The contacting surfaces were first machined flat using a turning process and then ground smooth using a diamond grinding wheel.

The superconductor samples used in this investigation were cold pressed and manufactured from a copper oxide compound based on the nominal formula $\text{BiCaSrCu}_2\text{O}_x$ (2224). In the processing of this formula, several possible phases have been found. These include a 110 K T_c phase $\text{Bi}_2\text{Ca}_2\text{Sr}_2\text{Cu}_3\text{O}_x$ (2223), an 80 K T_c phase $\text{Bi}_2\text{CaSr}_2\text{Cu}_2\text{O}_x$ (2122), and a 20 K T_c phase $\text{Bi}_2\text{Sr}_2\text{CuO}_x$ (2021). In this investigation it was desirable for the samples to contain as much as possible of the 110 K phase (2223) with the remainder being the 80 K phase (2122). A process, similar to the one described in Pandey et al. (1988) and developed in the Electrical Engineering Materials Lab at Texas A&M University, demonstrated the elimination of the 20 K (2021) phase and a resulting high amount of the 110 K phase (2223). Therefore, this process was used to manufacture the samples.

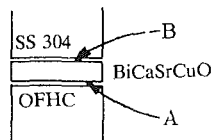
Two different sample sets were manufactured with each set resulting in three to four 2.54-cm-dia, approximately 1.0-cm-long pellets. One pellet from each lot was selected and tested using a standard DC four-probe resistance measurement technique to determine the electrical resistance as a function of the temperature. The results of the resistance measurements for both sets exhibited almost equivalent transition temperatures of 110 K (onset) and 72 K (zero).

Each pellet was sliced into four or five disks using a diamond wheel saw with *n*-propyl alcohol as a cutting lubricant. It should be noted that the samples were never allowed to come in contact with water, since this would damage the lattice structure. The thickness of the rough-cut disks varied between 1.2 and 1.5 mm. The rough-cut disks were then lapped to a smooth finish and a final thickness of 1.00 ± 0.01 mm. The average surface roughness, maximum peak-to-valley height, and flatness deviation of each sample were then measured using a Taylor-Hobson Surtronic 3P surface profilometer. The results are presented in Table 1.

Experimental Procedure. Since each sample was to be tested twice (uncoated and coated), the samples were aligned as pre-

Table 1 Surface characteristics of test samples

Set No. I				Set No. II			
SURFACE	σ_a (μm)	σ_l (μm)	FD (mm)	SURFACE	σ_a (μm)	σ_l (μm)	FD (mm)
1A	1.02	7.52	0.034	11A	1.58	12.10	0.010
1B	1.03	6.91	0.034	11B	1.51	14.23	0.010
2A	1.13	8.53	0.034	12A	1.34	10.45	0.015
2B	1.02	8.49	0.034	12B	1.60	11.65	0.015
3A	1.15	9.63	0.051	13A	1.59	11.56	0.015
3B	1.15	9.59	0.051	13B	1.72	11.87	0.015
4A	1.19	9.61	0.051	14A	1.86	12.40	0.015
4B	1.17	7.87	0.051	14B	1.66	11.10	0.015
5A	0.98	8.74	0.051	15A	1.44	12.93	0.020
5B	1.07	8.23	0.051	15B	1.35	10.87	0.020
6A	1.10	8.01	0.051	16A	1.84	14.21	0.025
6B	1.16	9.43	0.051	16B	2.01	14.76	0.025
7A	1.02	7.61	0.102	17A	1.64	13.13	0.025
7B	1.15	7.61	0.102	17B	1.59	11.72	0.025
8A	1.14	9.34	0.127	18A	1.43	11.07	0.030
8B	0.98	7.84	0.127	18B	1.63	11.98	0.030
9A	1.05	8.21	0.051	19A	1.22	9.02	0.033
9B	1.02	8.65	0.051	19B	1.32	10.16	0.033
				20A	1.51	10.31	0.033
				20B	1.36	9.82	0.033
OFHC Cu I	0.11	1.04	-	OFHC Cu II	0.10	1.22	-
SS 304	0.051	0.512	-				



viously described and prestressed with a load of approximately 2500 kPa. The samples were then separated and realigned, a load of approximately 200 kPa was applied, and the system was evacuated. Once the prescribed vacuum level was obtained, the fluid and the liquid nitrogen were supplied to the heat source and heat sink, respectively. The system was allowed to stabilize for approximately 4 hours.

The heat flux through the system was calculated by Fourier's Law using the thermal conductivity and temperature gradient of the stainless steel. Prior to testing, the stainless steel sample was calibrated using a National Institute of Standards and Technology (NIST) electrolytic iron reference sample of known conductivity. To determine the temperature discontinuity across the superconductor, the temperature distributions were extrapolated to the upper and lower surfaces of the two metal samples using a least-squares technique. The joint conductance was then calculated from the heat flux and the temperature discontinuity. This joint conductance was comprised of three separate resistances: (1) the contact resistance between the superconductor and the stainless steel, (2) the bulk resistance of the superconductor, and (3) the contact resistance between the superconductor and the OFHC copper. Because of the test procedure utilized, it was not possible to measure these three resistances independently, hence preliminary tests were conducted to determine the thermal resistance resulting from the stainless steel/superconductor interface and the thermal conductivity of the superconductor material. These resistances were subtracted from the overall conductance to obtain the resistance of the copper/coated superconductor interface. Additional testing confirmed that this process would yield consistent results and that after the second loading cycle, the resistance of the stainless steel/superconductor interface did not vary with respect to the number of loading cycles.

The heat flux through the OFHC copper sample was not calculated due to a slight oscillation in the sample temperatures. This oscillation was caused by the liquid/gas differentiating valve. When gas was released by the valve, a slight pressure drop (along with a corresponding temperature decrease) oc-

curred in the lines and cooling bath, and therefore, reduced the accuracy of the temperature measurements. However, due to the very high thermal conductivity of copper at cryogenic temperatures (508 W/mK at 90 K) the sample was essentially isothermal in comparison with the entire system. Therefore, the extrapolated surface temperature was not significantly affected. The experimental data showed only a 0.4 K fluctuation at the copper surface. This corresponded to a worst case (lowest temperature discontinuity) of 0.47 percent (0.4 K fluctuation for an 86 K temperature discontinuity) variation in the calculated temperature discontinuity. The temperatures in the stainless steel sample were never observed to fluctuate.

Following the acquisition of each data set, the pressure on the interface was increased in increments of approximately 180 kPa and allowed to stabilize for two hours before again measuring the contact conductance. Throughout testing, the mean junction temperature remained within the range 140 ± 7 K with no external adjustment of the cooling conditions. The test fixtures were then separated and the superconductor sample was removed. The surface of the superconductor that was in contact with the OFHC copper was coated with a vapor deposited metallic coating of a predetermined thickness. The entire experimental process was then repeated to determine the level of enhancement due to the coatings.

Microhardness Testing. The ambient and temperature-dependent microhardness measurements in this experiment were obtained using a Buehler Micromet II digital microhardness tester with a Vickers diamond indenter. As stated earlier, it was expected that the microhardness of the copper would increase as the temperature decreased. To verify this, experimentally, an aluminum test fixture was manufactured for testing of the OFHC copper. To monitor the temperature of the OFHC copper sample, a large bead K-type thermocouple was press fit into a small surface hole.

One of the obstacles encountered in cryogenic temperature testing was the resulting condensation and corresponding freezing of the water vapor from the atmosphere on the surface of the sample as it was cryogenically cooled. To alleviate this phenomenon, the microhardness test stand and the test fixture were enclosed and sealed in clear plastic. Dry nitrogen was then supplied to the chamber to purge the water vapor from the system. This system was adequate for testing down to 120 K.

To measure the microhardness of the copper sample at liquid nitrogen temperatures, the sample was immersed in a small shallow container filled with liquid nitrogen to a level of approximately 1.0 mm below the surface of the sample. The formation of ice on the surface of the sample was hindered by the evaporation of the liquid nitrogen.

Ideally, the temperature-dependent microhardness of the superconductor should also be determined; however, two factors prevented this. To measure the microhardness accurately, the indentation must be clearly visible. Due to the formation of small amounts of liquid nitrogen on the surface of the sample at liquid nitrogen temperatures and the deep black color of the sample, the indentation clarity was too poor for the microhardness to be accurately determined. Secondly, no effective means of attaching a thermocouple to the surface was found. Although the tests clearly indicated that the superconductor material was softer than the copper, due to the uncertainty associated with these measurements, no quantitative data are presented here.

Results and Discussion

To obtain a generalized correlation for predicting the uncoated thermal contact conductance, the dimensionless empirical correlation of Madhusudana and Fletcher (1983), given by

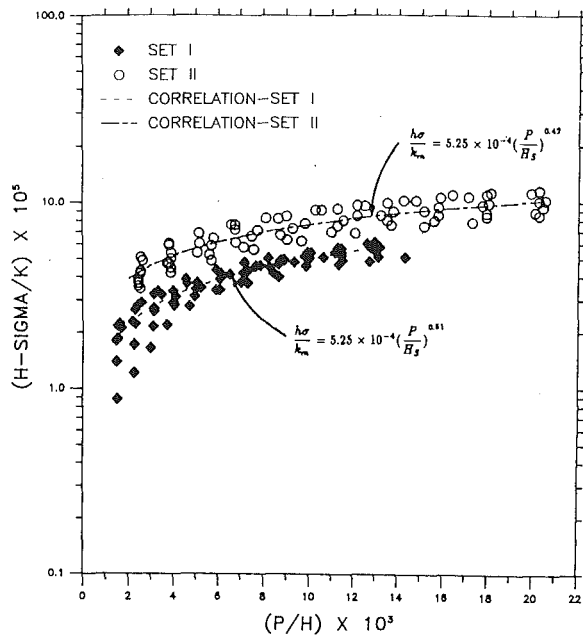


Fig. 2 Comparison of dimensionless uncoated test data with empirical correlation

$$\frac{h_c \sigma}{k_m} = c \left(\frac{P}{M} \right)^n \quad (4)$$

was used. The constants c and n were determined using a root-sum-square method to find the minimum variation between the data and the empirical correlation. The resulting constants were $c = 5.25 \times 10^{-4}$ for both sets, $n = 0.51$ for Set I, and $n = 0.42$ for Set II. Examination of the values resulting from this expression along with examination of the experimental data indicate that the difference between the values of n for the two sets was due to the variation in the average flatness deviations for the two sets.

The nondimensionalized data along with the resulting empirical correlations are presented in Fig. 2. As shown, the correlations accurately predict both the values and trends for the uncoated contact conductance. The most noticeable variation between the experimental data and the correlation is for Set I at low values of P/H . When analyzed further, it was determined that the test values of a single sample corresponded to the nondimensional values that deviated from the correlation and the other test values. This may be due to a misalignment of the test sample and column. The full effect of this variation will be discussed later.

Incorporating the effects of the coating layer would require a considerably more complicated model; therefore, an empirical correlation was again used. As previously discussed, the general form of the effective microhardness for a single point contact can be divided into three linear regions. However, for a system consisting of multiple contacts, one would expect the behavior to exhibit smooth transitions between regions. Therefore, for a constant indentation depth, the effective microhardness was expressed as an exponentially decreasing quantity with increasing coating thickness. This resulted in an equation of the form

$$H' = H_s(1-f) + H_L f \quad (5)$$

where

$$f = e^{-b\sigma/t} \quad (6)$$

and the parameter b is a function of the applied pressure and must be determined experimentally.

The limits of this expression must be consistent with the actual system in order for the correlation to be valid. As the

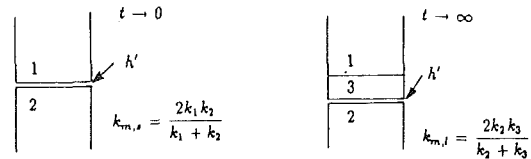


Fig. 3 Limits of h' and harmonic thermal conductivity with respect to coating thickness

layer thickness approaches zero, the function f approaches zero and the effective microhardness is equal to the substrate microhardness. As the layer thickness approaches infinity, f approaches one and the effective microhardness is equal to that of the layer material.

If the limits for the contact conductance of a coated interface are examined, the same results should be apparent. As t approaches zero, the joint conductance should approach that of an uncoated interface, or

$$h' = c \frac{k_{m,s}}{\sigma} \left(\frac{P}{H_s} \right)^n \quad (7)$$

As t approaches infinity, the joint conductance should approach that of a solid layer material interface, or

$$h' = c \frac{k_{m,l}}{\sigma} \left(\frac{P}{H_l} \right)^n \quad (8)$$

where Fig. 3 shows a graphic representation of the above limits. Since the rate at which the interface contact conductance changes as a function of coating thickness has been demonstrated to be primarily dependent on the effective microhardness, the coated contact conductance should vary between the two limits in proportion to the effective microhardness. The behavior of the experimental data indicates that the contact conductance also exhibits an exponential behavior and can be expressed empirically in the same general form as that of the effective microhardness, or

$$h' = c \frac{k_{m,s}}{\sigma} \left(\frac{P}{H_s} \right)^n (1-f) + c \frac{k_{m,l}}{\sigma} \left(\frac{P}{H_l} \right)^n f \quad (9)$$

where f is as defined before. This can be nondimensionalized by dividing both sides by $k_{m,s}$ and multiplying by σ , with the result being

$$\frac{h' \sigma}{k_{m,s}} = c \left(\frac{P}{H_s} \right)^n (1-f) + c \frac{k_{m,l}}{k_{m,s}} \left(\frac{P}{H_l} \right)^n f \quad (10)$$

Although the microhardness has been shown to be the most significant factor in the enhancement of the thermal contact conductance using metallic coatings, the thermal conductivity of the coating material does have an effect on the amount of enhancement. For the present correlation this is demonstrated by the presence of the ratio $k_{m,l}/k_{m,s}$. However, the effect of the thermal conductivity ratio is not simply a constant.

An effective thermal conductivity that is a function of substrate conductivities and a constriction parameter was used in the theoretical model of Antonetti (1983). The constriction parameter in turn is primarily a function of the substrate/layer thermal conductivity ratio, the layer thickness, the contact spot radius (which is a function of surface parameters and interface pressure), and the relative contact spot radius (also a function of pressure). Therefore, a constriction-effects term, $\beta(t, P)$, has been included in the above correlation to account for this thermal constriction phenomenon, resulting in the final expression

$$\frac{h' \sigma}{k_{m,s}} = c \left(\frac{P}{H_s} \right)^n (1-f) + c \beta(t, P) \frac{k_{m,l}}{k_{m,s}} \left(\frac{P}{H_l} \right)^n f \quad (11)$$

where $\beta(t, P)$ must also be determined empirically. It is important to note that in this model the hardness penetration is

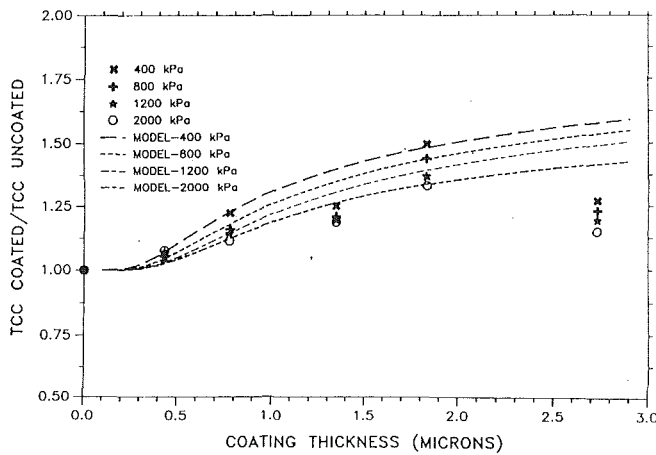


Fig. 4 Lead-coated contact conductance results and model comparison

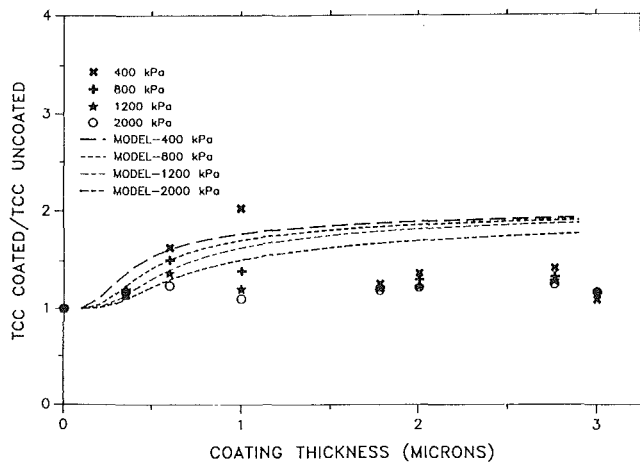


Fig. 5 Indium-coated contact conductance results and model comparison

assumed to be adequately described by the parameter f , and that because the effect of flatness deviation nullifies the more detailed approach of Antonetti, which assumes that the behavior of a single asperity can be approximated by the behavior of the Vickers indenter, this aspect has not been included.

Using a third-order polynomial curve fit for each sample, an enhancement factor, defined as the contact conductance coated divided by the contact conductance uncoated, was calculated for four different pressures at each coating thickness. This enhancement factor is illustrated in Fig. 4 for lead coatings and Fig. 5 for indium coatings as a function of layer thickness. Also, the results of the empirical correlation derived in this investigation are presented along with the test data.

The empirical correlation modeled the lead and indium coated test data with reasonable accuracy at low coating thickness values. However, the data and the model disagree at greater values of coating thickness. As this correlation was empirical, the exact values of the model are controlled by two empirically determined parameters, which can be altered to trace the data at different locations. The lower values of coating thickness were primarily used as governing factors of the empirical parameters. Also, the model was not allowed to underestimate any of the test data, since any deviation from the theoretical would be in the form of lower results. One exception to this was for the indium coated sample corresponding to a coating thickness of $1.0 \mu\text{m}$. The uncoated contact conductance test data for this sample deviated from the rest of Set I at low pressures, due to the possible misalignment previously dis-

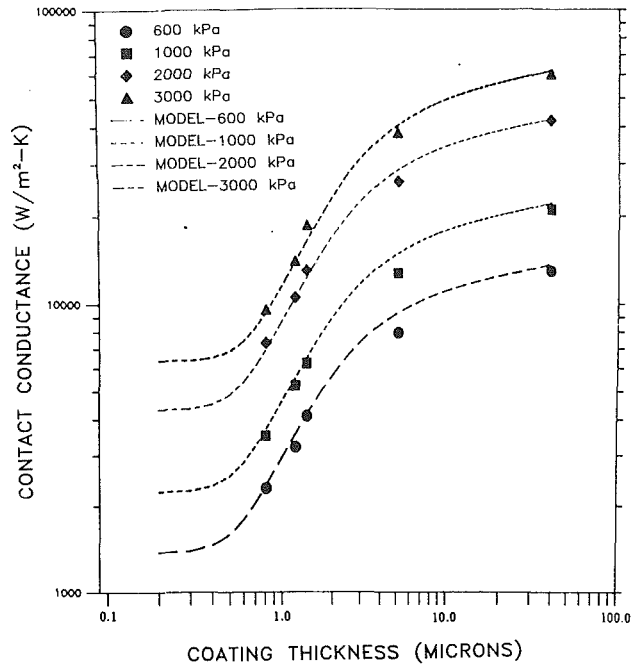


Fig. 6 Comparison of present correlation with data of Antonetti (1983)

cussed. These lower uncoated test values exaggerated the enhancement factor (TCC coated/TCC uncoated).

The results of Antonetti (1983) indicated that the coated contact conductance increased asymptotically as the coating thickness increased; hence, the experimental data of Antonetti (1983) for silver coatings on nickel substrates were compared with the present model. If the previous method is applied to the uncoated correlation used by Antonetti (1983), a resulting equation for the coated contact conductance is given by

$$\frac{h' \sigma}{mk_{m,s}} = 1.25 \left(\frac{P}{H_s} \right)^{0.95} (1-f) + 1.25 \beta(t, P) \frac{k_{m,l}}{k_{m,s}} \left(\frac{P}{H} \right)^{0.95} f \quad (12)$$

Figure 6 presents the results of this equation along with the test data for a silver coated nickel substrate with a surface roughness of $4.27 \mu\text{m}$ and a mean profile slope of 0.234.

As can be seen, the model accurately predicts the test data with only a slight overestimation at a coating thickness of $5.1 \mu\text{m}$. The theoretical model of Antonetti (1983) also accurately predicted the experimental data except that a "knee" appeared in the curve at a layer thickness of approximately one-half to three-fourths of the surface roughness. However, this "knee" does not appear in the present correlation. Antonetti (1983) attributed this to the abrupt change in the slope of the effective microhardness curve at $t/d < 1.0$. Therefore, since the effective microhardness in this investigation was assumed to be of a smooth curve type, the "knee" is absent from the present model. This is believed to be a more realistic representation of the effective microhardness since, intuitively, a sudden abrupt change should not occur.

Finally, the present model contained two parameters that were determined empirically. These were the exponential constant, b , and the thermal constriction factor, $\beta(t, P)$. Figure 7 shows the parameter b as a function of the interface pressure divided by the substrate microhardness. As can be seen, b is dependent upon the ratio P/H with the empirically determined data being consistent among three different systems (Set I, Set II, and Antonetti).

The thermal constriction-effects term, $\beta(t, P)$ was found to follow the expression of the form

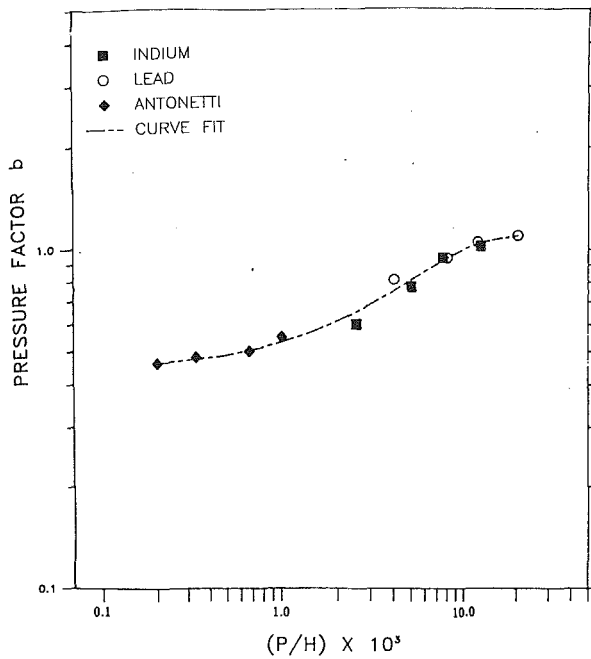


Fig. 7 Variation of parameter b with respect to dimensionless interface pressure

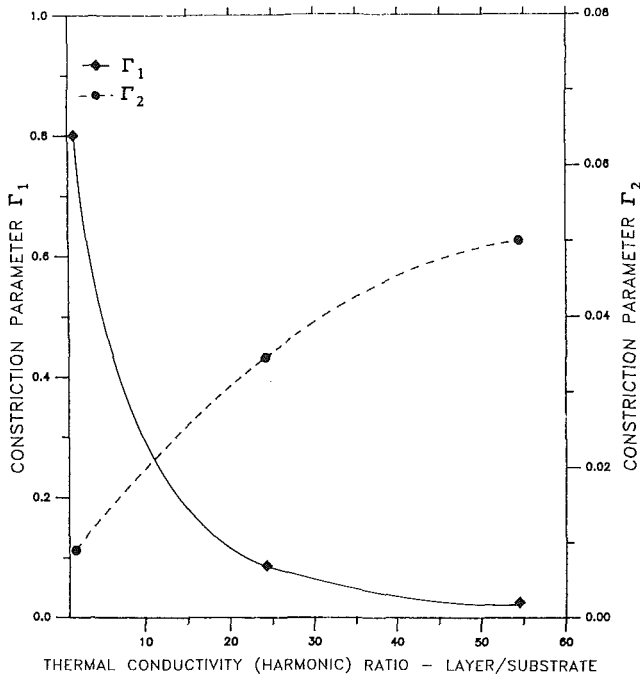


Fig. 8 Variation of thermal constriction parameters Γ_1 and Γ_2 with respect to harmonic thermal conductivity ratio

$$\beta(t, P) = \Gamma_1 + \alpha \left(\frac{t}{\sigma} \right) \quad (13)$$

where

$$\alpha = \Gamma_2 - \Gamma_3 \left(\frac{P}{H_s} \right) \quad (14)$$

for load values between 400 and 2000 kPa. The values Γ_1 and Γ_2 are given in Fig. 8 as functions of the harmonic thermal conductivity ratio, K , defined as

$$K = \frac{k_{m,s}}{k_{m,l}} \quad (15)$$

The parameter Γ_3 followed the linear expression

$$\Gamma_3 = 0.06K - 0.06 \quad (16)$$

As the ratio K approaches one, the thermal constriction-effects term $\beta(t, P)$ also approaches one, as should be the case where the layer and substrate thermal conductivities are equivalent. Also, the values of α and $\beta(t, P)$ (for constant P/H) have only been demonstrated to be linear for the scope of this investigation. The model must be compared extensively with further data in order to refine and understand the exact trends of the parameters, $\beta(t, P)$ and b , for variations in the harmonic conductivity ratio and the relative pressure ratio.

The behavior of the enhancement factor data in this investigation followed the trends of Kang et al. (1990) in that as the layer thickness increased, the enhancement increased to a maximum peak followed by a decreasing slope for further increases in layer thickness. This phenomenon did not occur in the work of Antonetti (1983) where an asymptotically increasing enhancement was observed. Kang et al. (1990) explained the resulting decrease in the enhancement on the increased bulk thermal resistance of the layer material once the maximum peak was reached.

To verify this explanation, the test data for the indium coated interfaces of Kang et al. (1990) were examined. The data for test pairs No. 6 (indium-2.5 μm) and No. 8 (indium-3.7 μm) at approximately 270 kPa corresponded to thermal contact resistances of 0.170 K/W and 0.403 K/W, respectively. The bulk thermal resistance of a 1.2 μm coating of indium corresponds to 2.6×10^{-5} K/W, which is several orders of magnitude less than the difference in the contact resistances. Therefore, the decrease in the enhancement for the data of Kang et al. (1990) and this investigation must be the result of some other phenomenon.

One possible explanation for this results from the coating process and equipment used, which was identical to that used by Kang et al. (1990). For coating thicknesses in excess of 0.7 μm , it became necessary to vent the vacuum chamber and replenish the depleted coating material source. When the chamber was vented, the sample and coating were exposed to the atmosphere such that a very thin oxide layer may have formed. This oxide layer then may have hindered the adhesion of the subsequent coating layer as well as increasing the overall microhardness of the coating. Also, the venting and evacuating of the chamber may have resulted in thermal cycling and corresponding thermal stresses resulting from the different coefficients of thermal expansion for the substrate and coating materials. If the stresses became too great, poor adhesion of the coating to the substrate might result. Another possible phenomenon may have resulted from the deposition equipment and procedure. The source temperature, which was controlled by optical sighting of the source, determines the vapor pressure of the coating material and resulting evaporation rate. Holland (1958) discussed that for slow rates of deposition it was noted that larger amounts of film granulation occurred and hindered the development of a fully connected homogeneous structure. This would imply that the contact conductance might be lower than the theoretical value due to microscopic resistances.

It also should be noted that the theoretical model of Antonetti (1983) contains no mechanism by which the enhancement would decrease for increasing layer thickness, assuming a softer coating is applied to a harder substrate and the thermal conductivity of the coating is not significantly lower than that of the substrate. The model followed the trends of the experimental data obtained by Antonetti (1983), an asymptotically approaching maximum. This was also a basic assumption in the development of the empirical correlation used in this investigation, which also does not contain any mechanism for a decreasing enhancement.

The ambient microhardness testing resulted in values (at all indenter loads) of 125 kg/mm² for the OFHC copper sample, 16 kg/mm² for Set I superconductor samples and 10 kg/mm²

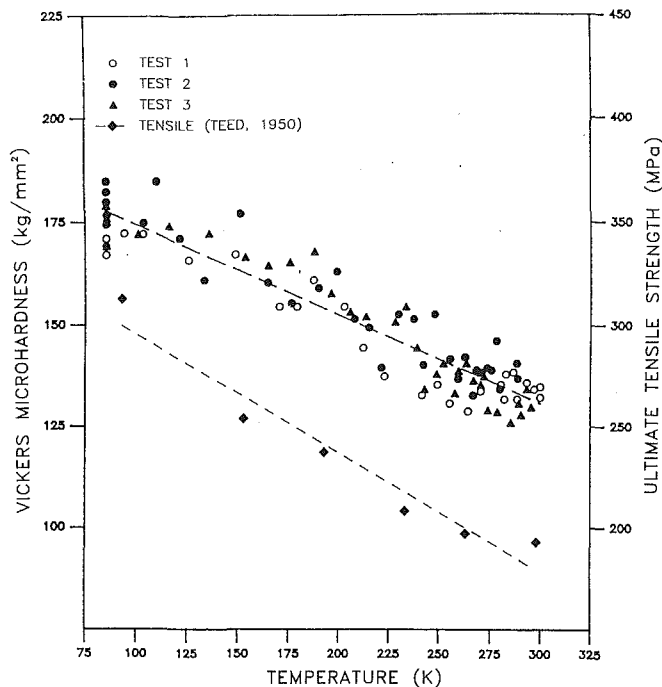


Fig. 9 Temperature-dependent Vickers microhardness for OFHC copper sample

for Set II samples. The temperature-dependent results for the OFHC copper sample are presented in Fig. 9 for three different tests along with the tensile strength as reported by Teed (1950). An overall increase in the microhardness of approximately 35 percent is seen as the temperature decreased from ambient to 85 K. As the microhardness is used extensively in modeling the thermal contact conductance of contacting surfaces, this illustrates that the temperature at which the microhardness is tested must reflect the surface temperature in experimental testing or in applications.

Conclusions and Recommendations

Experimentally, it has been demonstrated that the thermal contact conductance between interface pressures of 200 and 2000 kPa of a normal state BiCaSrCuO superconductor/copper interface at cryogenic temperatures can be enhanced by vapor-deposited lead and indium coatings, with the overall magnitude of enhancement being greater for the indium coatings. An empirical correlation for predicting the thermal contact conductance of a coated interface was developed that compared favorably with test data from Antonetti (1983) and somewhat favorably at thin layer thickness values with test data obtained in this investigation. This correlation offers several advantages over previously developed theoretical models, primarily in the relative ease with which the model may be applied. The model is a modification of an existing uncoated correlation and requires only a knowledge of easily obtainable parameters: the surface roughnesses, thermal conductivities, and microhardness values.

The effect of temperature on the microhardness of OFHC copper was also experimentally determined and found to increase by approximately 35 percent as the temperature was decreased from 300 to 85 K. This demonstrates the importance of the microhardness measurements reflecting the actual system conditions in experimental testing or in applications where a correlation containing the microhardness is to be used to model the system.

Further work must be performed to verify and refine the empirical parameters used in this investigation. A more fundamental understanding of the thermal constriction effects parameter used herein would be beneficial to any further work

utilizing this method. Presently, the model has only been compared with lapped and bead blasted surfaces, and as a result, further data will be required to determine whether the assumptions are valid for other types of surface finishes and load ranges.

Additionally, understanding the effect of temperature on the microhardness of the coating materials would be beneficial in determining the range of applications for these coatings. This also implies that the effects of the temperature at initial loading and at increases in the interface load are of interest since the contact conductance of surfaces initially brought together at room temperature would be different from that of surfaces at cryogenic temperatures.

Several possible problems and unexplained phenomena have been uncovered during the course of this investigation. These have been almost exclusively directed toward the method used to vapor deposit the metallic coatings. An experimental program may be necessary to determine the entire range of effects upon the thermal contact conductance resulting from the vacuum chamber venting and evacuating cycle for thicker coatings. Specifically, the possible formation of oxide layers during the venting/evacuation cycle and the adhesion capability of layers applied to this oxide layer need to be addressed. Also, the effect of variations in the source and substrate temperatures should be investigated to determine its effect on the layer formation structure and the corresponding microhardness characteristics of the layer.

Acknowledgments

The authors would like to acknowledge the support of The Texas Advanced Technology Program.

References

- Antonetti, V. W., 1983, "On the Use of Metallic Coatings to Enhance Thermal Contact Conductance," Ph.D. Thesis, Mechanical Engineering Department, University of Waterloo, Waterloo, Ontario, Canada.
- Bayot, V., Delannay, F., Dewitte, C., Erauw, J.-P., Gonze, X., Issi, J.-P., Jonas, A., Kinany-Alaoui, M., Lambricht, M., Michenaud, J.-P., Minet, J.-P., and Piroux, L., 1987, "Strong Electron-Phonon Coupling From Thermal Conductivity Measurements in a YBaCuO Type Superconducting Compound," *Solid State Communications*, Vol. 63, No. 11, pp. 983-986.
- Douglas, J., 1987, "Pursuing the Promise of Superconductivity," *EPRI Journal*, Sept., pp. 4-15.
- Eid, J. C., and Antonetti, V. W., 1986, "Small Scale Thermal Contact Resistance of Aluminum Against Silicon," *Proceedings of the 8th International Heat Transfer Conference*, pp. 659-664.
- Fletcher, L. S., Peterson, G. P., and Schaup, R., 1991, "Thermal Conductivity of Selected Superconducting Materials," *ASME JOURNAL OF HEAT TRANSFER*, Vol. 113, pp. 274-276.
- Foner, S., and Orlando, T. P., 1988, "Superconductors: The Long Road Ahead," *Technology Review*, Feb./Mar., pp. 36-47.
- Gottwick, U., Held, R., Sparr, G., Steglich, F., Rietschel, H., Ewert, D., Renker, B., Bauhofer, W., Von Molnar, S., Wilhelm, M., and Hoenig, H. E., 1987, "Transport Properties of YBaCuO: Resistivity, Thermal Conductivity, Thermopower, and Hall Effect," *Europhysics Letters*, Vol. 4, pp. 1183-1188.
- Hegazy, A. A., 1985, "Thermal Joint Conductance of Conforming Rough Surfaces: Effects of Surface Microhardness Variations," Ph.D. Thesis, Mechanical Engineering Department, University of Waterloo, Waterloo, Ontario, Canada.
- Holland, L., 1958, *Vacuum Deposition of Thin Films*, Wiley, New York, New York.
- Jezowski, A., Mucha, J., Rogacki, K., Horyn, R., Bukowski, Z., Horobiowski, M., Rafalowicz, J., Stepień-Damm, J., Sulkowski, C., Trojnar, E., Zaleski, A. J., and Klamut, J., 1987, "Thermal Conductivity and Electrical Resistivity of the High- T_c Superconductor YBaCuO," *Physics Letters A*, Vol. 122, pp. 431-433.
- Kang, T. K., Peterson, G. P., and Fletcher, L. S., 1990, "Enhancing the Thermal Contact Conductance Through the Use of Thin Metallic Coatings," *ASME JOURNAL OF HEAT TRANSFER*, Vol. 112, pp. 864-871.
- Kirk, W. P., Kobiela, P. S., Tsumura, R. N., and Pandey, R. K., 1989, "Thermal Conductivity of Hot-Pressed 123 YBCO Superconducting Oxides: Anisotropic Behavior at High and Very Low Temperatures," *Ferroelectrics*, Vol. 92, pp. 151-157.
- Kirk, W. P., 1990, Physics Department, Texas A&M University, unpublished data.
- Madhusudana, C. V., and Fletcher, L. S., 1983, "Solid Spot Thermal Conductance of Zircaloy-2/Uranium Dioxide Interfaces," *Nuclear Science and Engineering*, Vol. 83, pp. 327-332.

Mal'kov, V. A., and Dobashin, P. A., 1969, "The Effect of Soft-Metal Coatings and Linings on Contact Thermal Resistance," *Inzhenerno-Fizicheskii Zhurnal*, Vol. 17, pp. 871-879.

Morelli, D. T., Heremans, J., and Swets, D. E., 1987, "Thermal Conductivity of Superconductive Y-Ba-Cu-O," *Physics Review B*, Vol. 36, pp. 3917-3919.

National Academy of Sciences, National Academy of Engineering, Institute of Medicine, 1987, "Research Briefing on High-Temperature Superconductivity," National Academy Press, Washington, DC.

Ochterbeck, J. M., 1990, "Thermal Contact Conductance of Metallic Coated Superconductor/Copper Interfaces at Cryogenic Temperatures," M. S. Thesis, Mechanical Engineering Department, Texas A&M University, College Station, TX.

Pandey, R. K., Gilbert, G. R., Kirk, W. P., Kobiela, P. S., Clearfield, A., and Squattrito, P. J., 1988, "Processing of Single-Phase Ceramic 123 YBaCu-Oxide Superconductor by Hot Pressing," *Journal of Superconductivity*, Vol. 1, pp. 45-52.

Peterson, G. P., and Fletcher, L. S., 1988, "Evaluation of the Thermal Contact Conductance Between Substrate and Mold Compound Materials," *ASME JOURNAL OF HEAT TRANSFER*, Vol. 110, pp. 996-999.

Scalapino, D. J., Clarke, D. R., Clarke, J., Schwall, R. E., Clark, A. F., and Finnemore, D. K., 1988, "New Research Opportunities in Superconductivity," *Cryogenics*, Vol. 28, pp. 711-723.

Scott, R. B., 1988, *Cryogenic Engineering*, 1963 ed., reprinted by Met-Chem Research Inc., Boulder, CO.

Teed, P. L., 1950, *The Properties of Metallic Materials at Low Temperature*, Wiley, New York.

Uher, C., and Kaiser, A. B., 1987, "Thermal Transport Properties of YBaCuO Superconductors," *Physics Review B*, Vol. 36, pp. 5680-5683.

Van Duzer, T., 1988, "Superconductor-Semiconductor Hybrid Devices, Circuits and Systems," *Cryogenics*, Vol. 28, pp. 527-531.

Wolsky, A. M., Giese, R. F., and Daniels, E. J., 1989, "The New Superconductors: Prospects for Applications," *Scientific American*, Feb., pp. 61-67.

Yovanovich, M. M., 1982, "Thermal Contact Correlations," in: T. E. Horton, ed., *Progress in Aeronautics and Astronautics: Spacecraft Radiative Transfer and Temperature Control*, Vol. 83, MIT Press, Cambridge, MA, pp. 83-95.

Yovanovich, M. M., Hegazy, A., and Antonetti, V. M., 1983, "Experimental Verification of Contact Conductance Models Based Upon Distributed Surface Microhardness," AIAA Paper No. 83-0532.

Solidification of an Aqueous Salt Solution in a Circular Cylinder

A. S. Burns

L. A. Stickler

W. E. Stewart, Jr.

Energy Research Laboratory,
Truman Campus,
University of Missouri—Kansas City,
Independence, MO 64050

The situation of one-dimensional, transient inward solidification of a binary solution in a circular cylinder is studied numerically. The solution is assumed to be of a hypoeutectic initial concentration and to be initially at a superheated temperature above its initial melting point temperature. The boundary temperature of the cylinder is below that of its heterogeneous nucleation temperature and no supercooling occurs. The boundary temperatures and final solution concentrations are assumed to be above and below, respectively, the eutectic point of the solution. The finite difference numerical model predicts the time for the radial formation of the mush type of ice to reach the center of the cylinder and the time for the entire cylinder to reach the cylinder boundary temperature, based upon the assumptions of negligible diffusion and convection of solute during solidification. The results reveal that closure times are significantly increased for the solutions compared to pure water due to decreased conductivity of the mush compared to ice.

Introduction

The solidification of aqueous electrolyte solutions is a process that has important applications in many fields of interest, including antifreeze materials, biological purification, ice mechanics, oceanography, and heat exchanger design. At solute concentrations below the eutectic point (hypoeutectic) the solvent begins to solidify as the temperature is decreased, resulting in a mixture of liquid solution and solid solvent in the partially solidified region, called mush.

The coexistence of liquid and solid in a mush form represents a porous medium and, in the case of forced or gravity-driven flows, the flow characteristics of the porous medium must be incorporated as part of a detailed numerical model (Neilson et al., 1990). Even though detailed numerical energy models attempt to model flow in the porous matrix, ice frequently has anomalous crystallization and growth characteristics, which may foil attempts to compare numerical results with experimental results (Szekely and Jassel, 1978; Neilson et al., 1990; Christenson et al., 1989).

The presence of any solute decreases the freezing (melting) point temperature of the solvent, such as water, according to its phase diagram. Such is the case for a binary, eutectic forming, solution of sodium chloride and water whose eutectic point is approximately 23.3 percent by weight of sodium chloride at -21.1°C . The decrease in freezing point temperature along with the lower thermal conductivity of liquid water than that of solid ice decreases the solidification rate from that of pure water to ice. In the inward solidification of a solution in a circular cylinder, for example, the closure of the cylinder with porous mush is accomplished when the liquid at the centerline of the cylinder reaches the freezing point of the liquid at its original concentration, if it is assumed that the mush region does not reject solute ahead of the phase change boundary as the solvent partially solidifies.

Under certain physical arrangements, when a concentrating solute in the mush region has an increasing density, the solute may not be rejected from the mush region across the phase change boundary, as is the case for upward, vertical solidification for some salt solutions (Braga and Viskanta, 1990), though buoyancy-driven mass transfer may occur with the mush. If the thermal diffusivity of the solution is greater than the mass diffusivity of the solute in the solvent, then the solute should not be rejected ahead of the mush boundary. If the

density of the solution increases as the solute concentration increases in the mush region, a buoyancy-driven flow can occur and be of a much greater magnitude than diffusive mass transfer. In the case of a water solution, the decreased density of the ice crystals formed may also reject part of the solute at a greater rate than from diffusion alone. For a density changing solute in the mush region where the mush boundary is vertical or downward, the rejection of the greater density solution can be significant (e.g., Fang et al., 1984), although the buoyancy-driven rejection of solute rich solution from the mush region to the liquid region is affected by the solidification rate.

Under the assumptions of an invariant density and one-dimensional, radially inward solidification in a cylinder, a numerical model is presented to compare the relative solidification rates of sodium chloride and water solutions to that of water at two initial solution temperatures and two boundary temperatures.

Numerical Model

The numerical model is based upon conservation of energy in the cylinder in one dimension, the radial direction. It is assumed that the solute is rejected from the freezing solid crystals only locally, and the mass-averaged concentration of solute in the cylinder remains constant for both the liquid and two-phase (mush) regions. This presumes that the solute is not rejected ahead of or along with the solidification (phase change) boundary by either diffusion or gravitational forces, as is the more probable situation at low solidification rates as in purification types of solidification processes. The thermal diffusivity of salt water solutions is nearly one hundred times that of the mass diffusivities (Braga and Viskanta, 1990) and, as such, the solidification process should be conduction dominated. The assumption that solute will not be rejected out of the solidifying two-phase region is not absolutely correct, for it ignores density change effects in the solute when the solvent solidifies and concentrates the remaining solute. The assumption is made, though, that the densities of the solid, liquid, and two-phase (solid solvent and concentrated solute) region are equal and constant. It is further assumed that the energy (heat of solution) required to segregate the solvent from the solution to enable the formation of the solid solvent is negligible. It is also assumed that any energy associated with forcing the solute from the mush region during crystallization is negligible. The model simplifies to the extent that heat and mass transfer by convection are nonexistent.

The thermophysical data used in the model are those of a

Contributed by the Heat Transfer Division for publication in the JOURNAL OF HEAT TRANSFER. Manuscript received by the Heat Transfer Division September 12, 1990; revision received January 28, 1991. Keywords: Double Diffusion Systems, Numerical Methods, Phase-Change Phenomena.

sodium chloride and water solution. The hypoeutectic liquidus curve for a sodium chloride and water solution was used to define the initial freezing point temperature of the solution. All boundary temperatures of the cylinder are above the eutectic temperature (-21.1°C) and initial salt concentrations modeled are below the eutectic concentration. The ice crystals formed are assumed not to incorporate ions into the crystals and, hence, the fraction of ice formed is only a function of concentration at a given temperature and the initial solution concentration as

$$f = \frac{C(T) - C_o}{C(T)} \quad (1)$$

where $C(T)$ is the concentration as a function of freezing point temperature from the liquidus curve, where the relationship is approximated as a quadratic function of temperature as

$$C(T) = a_0 + a_1T + a_2T^2 \quad (2)$$

The thermophysical properties of the mush region are simply modeled as a linear function of the mass fraction of ice, f , and concentrated solution in the mush region, except for density, which is assumed invariant in all phases and at all locations. With these assumptions and definitions the normalized energy balance in the mush region and the liquid region can be written, respectively, as

$$\left\{ (c_i^* - 1) \left[(\theta + \theta_f) \frac{\partial f}{\partial \theta} + f \right] + 1 - \frac{1}{\text{Ste}} \frac{\partial f}{\partial t} \right\} \frac{\partial \theta}{\partial t} = (k_i^* - 1) \frac{\partial f}{\partial t} \left(\frac{\partial \theta}{\partial r} \right)^2 + \{ f(k_i^* - 1) + 1 \} \frac{1}{r} \frac{\partial \theta}{\partial r} + \{ f(k_i^* - 1) + 1 \} \frac{\partial^2 \theta}{\partial r^2} \quad (3)$$

and

$$\frac{\partial \theta}{\partial t} = \frac{1}{r} \frac{\partial}{\partial r} \left(r \frac{\partial \theta}{\partial r} \right) \quad (4)$$

The dimensionless boundary conditions for the cylinder are

$$\theta(r_w, t) = -1 \quad (5a)$$

$$\theta(r_f, t) = 0 \quad (5b)$$

$$\frac{\partial \theta}{\partial r}(0, t) = 0 \quad (5c)$$

$$k_i \frac{\partial \theta}{\partial r}(r_f, t) = k_s \frac{\partial \theta}{\partial r}(r_f, t) \quad (5d)$$

and the initial conditions are

$$\theta(r, 0) = \theta_0 \quad (6a)$$

$$r_i = 0 \quad (6b)$$

The governing equations used for the pure water solidifi-

Table 1 Inlet and boundary conditions

Simulation No.	C_o (% wt)	T_o ($^{\circ}\text{C}$)	T_w ($^{\circ}\text{C}$)	T_f ($^{\circ}\text{C}$)	Ste	θ_o
S1	0	0.0	-10.5	0	0.126	0
S2			-20.0		0.240	0
S3		23.0	-10.5		0.126	2.19
S4			-20.0		0.240	1.15
S5	3.4	0.0	-10.5	-2.04	0.101	0.24
S6			-20.0		0.215	0.11
S7		23.0	-10.5		0.101	2.96
S8			-20.0		0.215	1.39
S9	5.0	0.0	-10.5	-3.05	0.089	0.41
S10			-20.0		0.203	0.18
S11		23.0	-10.5		0.089	3.50
S12			-20.0		0.203	1.54

cation cases are similar. For the solid region the dimensionless energy equation becomes

$$\frac{\partial \theta}{\partial t} = \frac{\alpha_i}{\alpha_f} \frac{\partial}{\partial r} \left(r \frac{\partial \theta}{\partial r} \right) \quad (7)$$

The governing equation for the liquid region is identical to Eq. (4), except that the properties for the liquid are those of pure water. The boundary condition, at the phase change boundary, in dimensionless form is

$$\frac{\partial \theta}{\partial r} = \frac{1}{k_i^*} \frac{\partial \theta}{\partial r} + \frac{\alpha_f \rho_i h_{if}}{(T_f - T_w) k_i} \frac{\partial r}{\partial t} \quad (8)$$

For the case of solidification in the sodium chloride-water system Eqs. (3) and (4) are solved using an explicit finite difference method, solving for θ in the liquid region and θ and f in the mush region, using the functional form of f in terms of θ as

$$f = a_0 + a_1 \{ T_f + (T_f - T_w)\theta \} + a_2 \{ T_f^2 + 2T_f(T_f - T_w)\theta + (T_f - T_w)^2 \theta^2 \} \quad (9)$$

The computational region was evenly divided into a finite number of elements, or rings. As the temperature of each element decreased to the freezing point of the particular solution, the element was considered to be either frozen for the pure water cases, or mush for the case of a salt water solution, for which the mass fraction of solid in the element was then calculated and recalculated at each time step from Eq. (9), according to the temperature of the element. For the case of pure water solidification the same finite difference scheme is used to determine θ in the solid and liquid regions from Eqs. (7) and (4). Equation (8) was used to calculate the solidification rate, $\partial r / \partial t$.

Nomenclature

a = constant, Eq. (2)
 c = specific heat
 C = solution concentration
 f = mass fraction of solid in two-phase (mush) region
 F = integrated value of f , Eq. (10)
 Fo = Fourier number = $\alpha_f t / r_w^2$, identical to t
 h_{if} = heat of fusion of solvent
 k = thermal conductivity
 Q = heat removed from solution
 r = radial coordinate, dimensionless coordinate = \tilde{r} / r_w
 Ste = Stefan number = $c_i(T_f - T_w) / h_{if}$

T = temperature
 t = time
 α = thermal diffusivity
 θ = dimensionless temperature = $(T - T_f) / (T_f - T_w)$
 θ_o = dimensionless initial temperature = $(T_o - T_f) / (T_f - T_w)$
 θ_f = dimensionless solidification (liquidus) temperature = $T_f / (T_f - T_w)$

Subscripts

c = closure with ice or mush

f = freezing, solidification, the liquidus condition
 i = solid (ice)
 l = liquid
 o = initial condition
 s = mush
 t = total value
 w = boundary (wall) condition

Superscripts

$*$ = dimensionless quantity, normalized by the liquid property
 \sim = dimensional quantity

Table 2 Ice mass fractions, dimensional closure times, and solidification rates

Simulation Number	F_c (%)	\bar{t}_c (mins)	$\Sigma Q/t_c$ (kW)	$\Sigma Q/\bar{t}_c$ (kW)
S1	100.0	17.53	2.43	1.47
S2	100.0	12.07	4.00	3.16
S3	100.0	31.58	1.76	1.17
S4	100.0	21.85	2.80	2.31
S5	43.4	22.73	0.81	0.17
S6	54.5	20.80	1.49	0.19
S7	47.6	41.82	0.75	0.19
S8	58.0	34.85	1.26	0.20
S9	38.2	25.88	0.68	0.15
S10	49.5	23.00	1.21	0.18
S11	42.0	43.73	0.59	0.17
S12	52.0	36.20	1.23	0.19

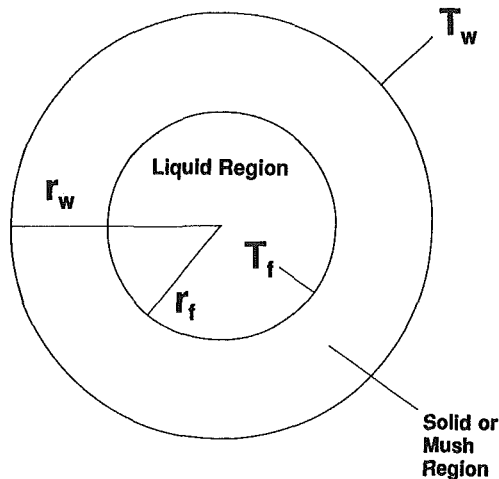


Fig. 1 Schematic of cylinder

Results

The numerical model was used to simulate the one-dimensional radially inward solidification of pure water and 3.4 and 5 percent by weight sodium chloride-water solutions. Both initial concentrations are below the eutectic concentration and both cylinder wall temperatures are greater than the eutectic temperature. Two different initial temperatures of 0°C and 23°C were modeled, which represents superheated temperature conditions for the salt solutions. A summary of the initial conditions for the simulations performed is shown in Table 1.

The singularity of a below freezing point temperature at the cylinder wall at time zero was accommodated by assuming that a small mass of ice (solid) existed at the boundary at zero time. Since the boundary temperatures were assumed to be below typical heterogeneous nucleation temperatures of both the pure water and the NaCl water solutions, the effect of assuming that ice exists at the boundary at time zero should represent little, if any, error.

As shown in Table 2, in terms of dimensional time, \bar{t}_c , the effect of the salt in the solution is to increase the closure time of the mush region over that of the growth of pure ice in pure water by 50-90 percent for T_o of 0°C, though the difference in closure times for the 3.4 and 5 percent NaCl solutions is only about 10 percent. The increase in closure time for the salt solutions relative to pure water for T_o of 23°C is approximately 30-70 percent. The increase in closure times for the salt so-

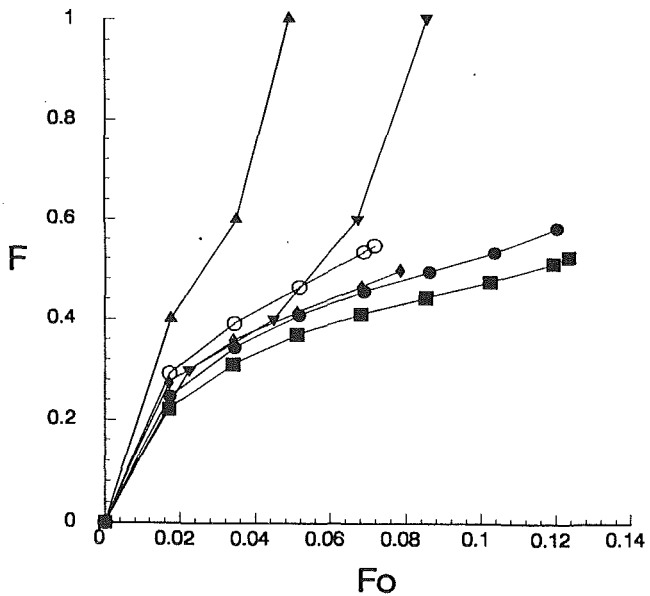


Fig. 2 Mass fraction of ice formed until closure for T_w of -10.5°C

- ▲ $C_i = 0.0$ percent, $T_o = 0^\circ\text{C}$
- ▼ $C_i = 0.0$ percent, $T_o = 23^\circ\text{C}$
- $C_i = 3.4$ percent, $T_o = 0^\circ\text{C}$
- $C_i = 3.4$ percent, $T_o = 23^\circ\text{C}$
- ◆ $C_i = 5.0$ percent, $T_o = 0^\circ\text{C}$
- $C_i = 5.0$ percent, $T_o = 23^\circ\text{C}$

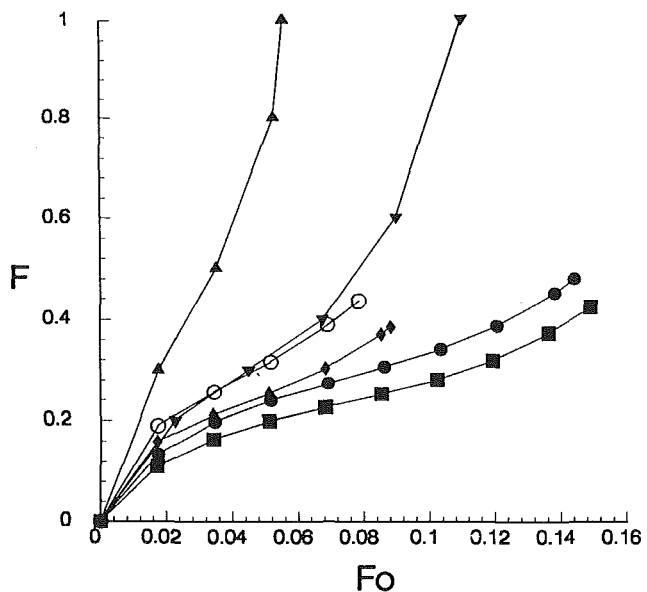


Fig. 3 Mass fraction of ice formed until closure for T_w of -20.0°C

- ▲ $C_i = 0.0$ percent, $T_o = 0^\circ\text{C}$
- ▼ $C_i = 0.0$ percent, $T_o = 23^\circ\text{C}$
- $C_i = 3.4$ percent, $T_o = 0^\circ\text{C}$
- $C_i = 3.4$ percent, $T_o = 23^\circ\text{C}$
- ◆ $C_i = 5.0$ percent, $T_o = 0^\circ\text{C}$
- $C_i = 5.0$ percent, $T_o = 23^\circ\text{C}$

lutions is due to the depressed freezing point temperature of the solution and the decreased thermal conductivity of the mush relative to ice, which decreases the ice growth rate. The decrease in heat of fusion removal required for the center of the cylinder to reach the freezing point temperature for the mush system is not sufficient to offset the higher thermal conductivity and the higher total heat of fusion removal of the pure water system, even for the superheated temperature initial conditions. These opposing effects of decreased ice mass and decreased conductivity on closure time for the mush ice

simulations and the opposing effects of increased ice mass (total heat of fusion removed) and increased thermal conductivity in the pure water/ice system are seen to be dominated by the increased ice thermal conductivity in the pure water/ice system, since the phase-change boundary grows at a greater rate for the pure water/ice system.

The effect of decreased cylinder wall temperature in decreasing closure times is most significant for the pure water/ice simulations. The decrease in closure times for the 3.4 percent NaCl solution from T_o of 23°C to T_o of 0°C is approximately 85 percent for T_w of -10.5°C and 67 percent for the case of T_w of -20.0°C.

Shown in Figs. 2 and 3 are the total percent fraction of ice mass formed, F , until closure, when the value of F becomes F_c . The value of F_c for the pure water simulations ($C_i = 0.0$ percent) is, of course, 100 percent when the phase-change boundary reaches the center of the cylinder. The ice mass in the salt solution is, however, composed of concentrated solute in the liquid and ice crystals. As in the definition of ice mass fraction, f , in Eq. (1), the mass of ice is only a function of mush region temperature and initial concentration. The total mass of mush ice in the cylinder at any time is found by integrating f over the radius of the cylinder as

$$F = \int_0^{r_w} f dr. \quad (10)$$

The value of F_c at closure for the greatest initial salt concentration will be the smallest, for the same values of T_o and T_w . An interesting result shown in Figs. 2 and 3 is that the fraction of ice at closure, F_c , is greater for the higher value of T_o for both concentrations of salt, though the closure times are greater. The greater closure times for the higher value of T_o allow a greater amount of heat to be removed, resulting in a less steep temperature profile and hence a greater amount of ice mass to be formed. Ice mass fractions at closure are shown in Table 2.

The effect of the higher salt concentration, 5.0 percent, in the solution is to further decrease the growth rate of the phase-change boundary over that of the 3.4 percent salt solution at the same initial temperature, shown in Fig. 2 for T_w of -10.5°C. The dimensionless time is approximately 13 percent greater for T_o of 0°C for the 5.0 percent solution than for the 3.4 percent solution. The increase, though, is only 3.5 percent for T_o of 23°C. The increase in Fo_c for T_w of -20.0°C and

T_o of 0°C is 9.3 percent, as shown in Fig. 3, and 2.8 percent for T_o of 23°C. The effect of increasing T_o from 0°C to 23°C is approximately to double the value of Fo_c . The effect of adding salt has a nonlinear increase in Fo_c where it appears to have an asymptotic effect of decreasing change in Fo_c with increasing C_o .

Shown in Table 2 are the values of the total heat removed from the cylinder at closure, ΣQ_c , and at the point when the temperature of the center of the cylinder reaches the wall temperature, ΣQ_t . The ratios, $\Sigma Q_c / \bar{t}_c \Sigma Q_c / \bar{t}_t$, are used to represent time-averaged solidification rates. As discussed previously, the relatively large value of the thermal conductivity of ice compared to that of mush results in greater solidification rates for the pure water simulations than for the solution simulations.

Concluding Remarks

Numerical simulations of one-dimensional inward solidification of pure water and salt solutions in a cylinder were performed at different cylinder wall temperatures and initial liquid temperatures. The four times greater thermal conductivity of ice compared to that of water and the solutions results in a time-averaged solidification rate to closure of the cylinder approximately three times greater for pure water than for the solutions. The effect of the greater thermal conductivity of ice results in an order of magnitude greater solidification rate during the time required for the center of the cylinder to reach the cylinder wall temperature.

References

- Braga, S. L., and Viskanta, R., 1990, "Solidification of a Binary Solution on a Cold Isothermal Surface," *Int. J. Heat Mass Transfer*, Vol. 33, No. 4, pp. 745-754.
- Christenson, M. S., Bennon, W. D., and Incropera, F. P., 1989, "Solidification of an Aqueous Ammonium Chloride Solution in a Rectangular Cavity—II. Comparison of Predicted and Measured Results," *Int. J. Heat Mass Transfer*, Vol. 32, No. 1, pp. 69-79.
- Fang, L. J., Cheung, F. B., Linehan, J. H., and Pedersen, D. R., 1984, "Selective Freezing of a Dilute Salt Solution on a Cold Ice Surface," *ASME JOURNAL OF HEAT TRANSFER*, Vol. 106, pp. 385-393.
- Neilson, D. G., Incropera, F. P., and Bennon, W. D., 1990, "Numerical Simulation of Solidification in a Horizontal Cylindrical Annulus Charged With an Aqueous Salt Solution," *Int. J. Heat Mass Transfer*, Vol. 33, No. 2, pp. 367-380.
- Szekely, J., and Jassal, X. X., 1978, "An Experimental and Analytical Study of the Solidification of a Binary Dendritic System," *Metall. Trans. B*, Vol. 9B, pp. 389-398.

S. Fukusako
Professor.

M. Tago
Research Associate.

M. Yamada
Lecturer.

K. Kitayama
Graduate Student.

C. Watanabe
Graduate Student.

Department of Mechanical Engineering,
Hokkaido University,
Sapporo 060, Japan

Melting Heat Transfer From a Horizontal Ice Cylinder Immersed in Quiescent Saline Water

The melting characteristics of a horizontal circular ice cylinder immersed in quiescent saline water were determined experimentally. The experiments were carried out in 3.5 wt% saline water for ambient liquid temperatures ranging from 2.8 to 20.3°C. It was observed that the flow consisted of a laminar bidirectional flow at the lower portion of the melting ice cylinder, and an upward turbulent flow at the upper portion of the cylinder, and that the melting ice surface was characterized variously by secondary flow caused by instabilities based on buoyancy forces in the boundary layer flow. It was also found that the melting heat transfer behavior was markedly affected by the character of the flow in the boundary layer.

Introduction

When an ice slab melts in saline water, complicated transport phenomena arise in the buoyancy-induced flow adjacent to the ice, due to the coupled effects of thermal and saline diffusion on the motion-causing buoyancy force, resulting in considerable added complexity. Neshyba (1977) suggested that the upwelling produced by melting icebergs could strongly influence the supply of nutrients to Antarctic surface water. Free convection melting of a vertical ice surface immersed in saline water was analytically investigated by Marschall (1977), who obtained similarity solutions of the boundary-layer equations governing momentum, heat, and mass transfer by using a coordinate system fixed to the ice-saline water interface and then deriving an expression for the blowing velocity at the ice surface due to the melting. Huppert and Turner (1978) studied experimentally the effect of ambient stratification on the flow and transport adjacent to a vertical ice surface melting in sea water. Johnson (1978) determined some of the melting characteristics of a flat vertical ice slab immersed in saline water at a salinity level of 3.5 wt% for ambient temperatures ranging from -1.08 to 24.4°C . He used a Schlieren system with differential thermocouples to determine flow direction. He reported that the flow was upward and laminar at low ambient temperatures, while at higher ambient temperatures, transition to turbulence took place.

An extensive observation of the flow adjacent to a melting vertical ice surface in saline water was conducted by Josberger and Martin (1981). By illuminating suspended particles in the saline water and injecting dye to visualize the flow, they observed the flow characteristics near the ice surface for ambient temperatures ranging from -1.15 to 26°C . They found that for T_i less than about 18°C the flow near the ice surface was laminar and bidirectional near the bottom, while near the top of the vertical ice the flow was fully upward and turbulent. They also conducted some experiments at lower salinities of 1.42 and 0.8 wt% for low ambient temperatures ranging from

0.05 to 1.8°C and reported that fully laminar upward flow was observed at both salinity levels.

Carey and Gebhart (1982a) reported some numerical calculations for laminar buoyancy flows driven by thermal and saline transport arising near a vertical ice surface melting in saline water. They found that solutions were possible only to salinity level of 3.1 wt% at low temperatures and only at very low salinities at high temperatures. Carey and Gebhart (1982b) also reported results of a visualization experiment at $S_\infty = 1.0$ wt%, in which time exposure photographs were utilized to visualize the fine details of the flow generated adjacent to a vertically melting ice surface. In addition, similar problems were studied extensively by Sammakia and Gebhart (1983), Johnson and Mollendorf (1984), and Qureshi and Gebhart (1986). Recently, Fukusako et al. (1990) presented experimental results on steady-state heat transfer around a horizontal ice cylinder immersed in saline water at a salinity of 3.5 wt%.

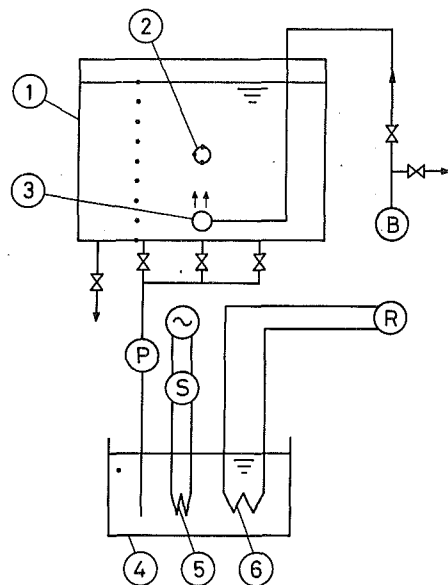
The purpose of this paper is to report some of the melting characteristics of a horizontal ice cylinder immersed in quiescent saline water at a salinity level of 3.5 wt% for ambient temperatures ranging from 2.8 to 20.3°C . Flow visualization photographs for free convection flow adjacent to the melting ice surface obtained by illuminating suspended particles in saline water are presented. Local and average heat transfer coefficients at the ice-saline water interface were extensively determined using ice profiles measured from photographs of the ice layer. The experimental results for the average Nusselt numbers are compared with the experimental data from a normal circular cylinder without melting.

Experimental Apparatus and Procedures

Experimental Apparatus. A schematic of the experimental apparatus is depicted in Fig. 1. The apparatus consists essentially of a test section, heat exchangers, coolant-circulating system, and associated instrumentation. The rectangular test vessel measures 200 mm wide, 770 mm high, and 1000 mm long, and is made of transparent acrylic plate 10 mm in thickness, except for double glazing in the front.

The copper concentric cylinder (28.6 mm o.d., wall thickness

Contributed by the Heat Transfer Division and presented at the ASME Winter Annual Meeting, Dallas, Texas, November 25-30, 1990. Manuscript received by the Heat Transfer Division December 12, 1990; revision received April 29, 1991. Keywords: Moving Boundaries, Natural Convection, Phase-Change Phenomena.



- ① TEST SECTION ② MAIN COOLER ③ AIR NOZZLE ④ SEA WATER TANK ⑤ HEATER ⑥ AUX. COOLER
- ⑦ BLOWER ⑧ REFRIGERATOR ⑨ PUMP ⑩ SLIDAC • THERMOCOUPLES

Fig. 1 Schematic diagram of experimental apparatus

1.5 mm, and length 200 mm), which was utilized to make a bubble-free ice cylinder, was placed horizontally at the center of the test section. As shown in Fig. 2, a coiled spring was inserted in the annular space in order to promote turbulence of the coolant (a mixture of ethylene glycol and water) circulating in the cylinder for high heat transfer rates. In addition, the temperature-controlled coolant was intensively spouted from many holes (3 mm dia) drilled through the inner cylinder wall. The coolant was circulated at a high velocity between the cylinder and a temperature-controlled bath with a prescribed temperature. The quite uniform surface temperature of the cylinder was confirmed as the inlet and outlet temperatures of the coolant at the cylinder were within about 0.1°C of each other.

The surface temperature of the cylinder was measured at 90-deg intervals from the top of the cylinder using twelve $\phi 0.1$ mm chromel-alumel thermocouples. Ambient saline-water temperature was also measured at 50-mm intervals from the

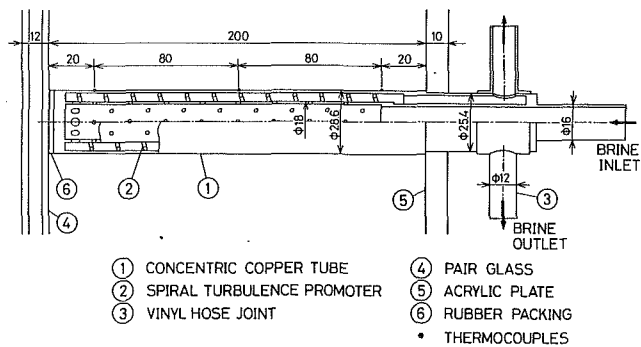


Fig. 2 Detail of cooled cylinder

bottom of the saline-water bath using nine $\phi 0.3$ mm chromel-alumel thermocouples. The salinity of the water was estimated by use of a salinity meter (Yokogawa SC8221-J).

The coolant-circulation system consisted of a refrigerator (3.5 kW), coolant bath (400 liter), an agitator, and two centrifugal pumps. A mixture of ethylene glycol and water was adopted as a coolant.

The flow pattern for free convection flow around the ice cylinder was visualized by mixing an aluminum powder of about 5 μm size into the saline water. A He-Ne laser (NEC-GLG5800, 50 mW) was utilized as the light source, which was expanded to two-dimensional light beam by use of a lens. The length of the exposures for the streak photographs was between 30 and 40 seconds.

Experimental Procedures. Saline water of 3.5 wt% salinity level was utilized as a testing liquid. The ambient saline-water temperature was varied between 2.8 and 20.3°C. Saline water was a mixture of pure water and pure NaCl.

First, a bubble-free ice cylinder was made in the bath filled with pure water by injecting air bubbles against the cooled tube from the air nozzles set at the bottom of the bath. In this process, thermocouples (0.1-mm-dia chromel-alumel) were successively embedded in the ice layer formed around the cooled tube at 5-mm intervals. After reaching a prescribed diameter of ice cylinder (60 to 70 mm dia), temperature-controlled saline water was introduced into the bath instead of the pure water. Special care was taken in introducing the saline water. The saline water was quite slowly introduced through three pipes ($\phi 20$ mm in diameter), which were connected to the bottom of the test section and whose nozzles were arranged horizontally along the bottom surface to minimize the effect of the fluid-spouting. When the fluid level arrives just below the bottom of the horizontal ice cylinder, the fluid supply was once stopped for few minutes. Then the fluid supply again started so that the fluid would arrive at the prescribed level

Nomenclature

a = thermal diffusivity, m^2/s
 A_ϕ = local heat transfer surface, m^2
 b = distance perpendicular to ice surface, m
 D_{in} = initial diameter of ice cylinder, m
 g = gravitational acceleration, m/s^2
 h_ϕ = local heat transfer coefficient defined in Eq. (2), $\text{W}/\text{m}^2\text{K}$
 h_m = average heat transfer coefficient defined in Eq. (3), $\text{W}/\text{m}^2\text{K}$
 L = latent heat of fusion per unit mass, J/kg

Nu_m = average Nusselt number defined in Eq. (4)
 Nu_m^* = modified average Nusselt number defined in Eq. (5)
 S = concentration of salt, wt%
 t = time, s or min
 T = temperature, °C
 T_{fp} = fusion temperature, °C
 T_{so} = freezing temperature of solvent in solution, °C
 ΔT = temperature difference = $T_\infty - T_o$, °C
 \dot{X} = average melting velocity defined in Eq. (6), m/s

β = coefficient of thermal expansion, $1/\text{K}$
 λ = thermal conductivity, W/mK
 ν = kinematic viscosity, m^2/s
 ρ = density, kg/m^3
 ϕ = angle measured from top of cylinder, deg

Subscripts

in = initial
 l = liquid
 m = average
 max = maximum value
 o = ice surface
 ∞ = ambient

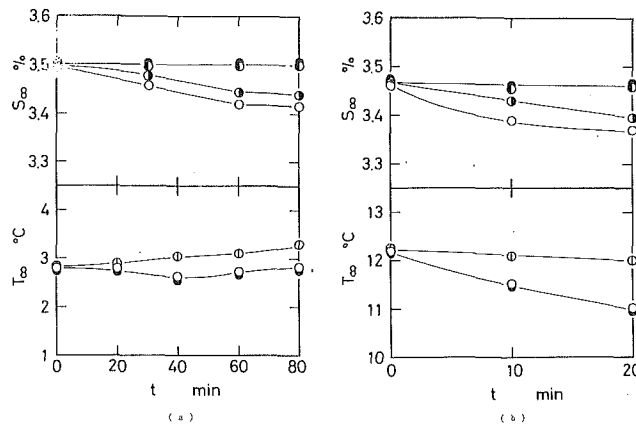


Fig. 3 Variations of temperature and salinity in saline-water bath: (a) $T_m = 2.8^\circ\text{C}$; (b) $T_m = 12.2^\circ\text{C}$; temperature: 90 mm (\bullet), 350 mm (\odot), 610 mm (\circ); salinity: 90 mm (\bullet), 300 mm (\ominus), 400 mm (\oplus), 610 mm (\circ) (length is distance from bottom of bath)

above the ice cylinder. Then, the ice cylinder started to melt. The ice contour, flow pattern, and ice-surface feature were recorded successively via photography.

Data Reduction

Ambient Temperature and Salinity. The model investigated in the present experiment is melting heat transfer around an ice cylinder immersed in a quiescent liquid with uniform temperature and uniform salinity. To maintain uniform far-field conditions, the mass of the saline-water tank was made quite large. Any artificial heating of liquid and controlling of salinity during the melting process were not carried out to prevent additional undesirable effects that would be introduced due to such handling. Figure 3 shows vertically local temperature and salinity distributions against the melting time at a horizontal distance of 250 mm from the center of the ice cylinder. It seems in the figure that the liquid temperature may be highest at the level of the ice cylinder. This is because the cooled saline water tends to flow downward and the melt liquid (mixture of melt water and saline water) tends to flow upward, as described in detail later. As the ice melts, salinity at the upper levels of the ice cylinder decreases, while salinity at the lower levels of the ice cylinder is invariant. This is due to the fact that the melt liquid flows upward (see Fig. 9):

Through the present experiments it was observed that the maximum variation (relative ratio of variation to initial value) for ambient temperature was about 5 percent, while that for ambient salinity was about 3 percent during the melting process, as shown in Fig. 3. The temperature at 350 mm (\odot) and the salinity at 300 (\ominus) were adopted as the reference temperature (T_∞) and the reference salinity (S_∞), respectively.

Determination of Heat Transfer Coefficient. A local thermal energy balance at the melting surface of the ice cylinder, which is at the fusion temperature, can be written as

$$\rho_i L (db/dt)_\phi = h_\phi (T_\infty - T_o) \quad (1)$$

At any angular position ϕ , the local heat transfer coefficient h_ϕ can be determined from

$$h_\phi = [\rho_i L / (T_\infty - T_o)] \cdot (db/dt)_\phi \quad (2)$$

Consequently, the average heat transfer coefficient h_m can be written as

$$h_m = \frac{\sum h_\phi A_\phi}{\sum A_\phi} \quad (3)$$

The local melting velocity $(db/dt)_\phi$ was evaluated by the ice contours, which were recorded successively through photography at designated time intervals.

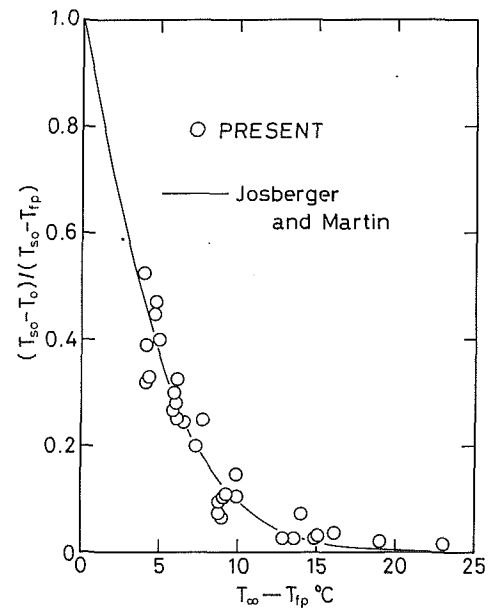


Fig. 4 Temperature of melting ice surface

Relationship Between Ice-Liquid Interface Temperature and Ambient Temperature. Josberger and Martin (1981) observed the liquid-solid interface temperature as a vertical ice plate melts within the saline water and found that the temperature was not constant, as for melting in pure water, but was a function of the ambient saline-water temperature. A similar phenomenon was obtained as a horizontal ice cylinder melts within quiescent saline water. The interface temperature measurements are presented in Fig. 4. The ordinate variable is the nondimensional interface temperature $(T_{so} - T_o) / (T_{so} - T_{fp})$, where T_{so} denotes the freezing temperature of solvent in the solution. The abscissa variable is the temperature difference between the ambient temperature T_∞ and freezing point T_{fp} . In the figure, the previous data (Josberger and Martin, 1981) for turbulent boundary layer flow are adopted for comparison. Figure 4 shows that $(T_{so} - T_o) / (T_{so} - T_{fp})$ decreases monotonically from near unity when the ice is close to equilibrium with the ambient conditions to near zero for $T_\infty - T_{fp} > 15^\circ\text{C}$. This can be explained by considering that the melt water causes a decrease in salinity of saline water just adjacent to the ice surface, which corresponds to an increase in freezing point.

Results and Discussion

Melting Phenomena of Ice Cylinder and Flow Patterns. Figures 5-8 show the variations of the ice-cylinder profiles and of flow patterns with time elapsed from the start of the experiment. The far-field temperatures are 2.8, 6.0, 12.2, and 18.0°C , respectively. The deviation of the ice-liquid interface from the circular shape results from strong free convection effects. A representative ice profile through melting in all the experiments is that as the melting advances, a step (see Fig. 9) forms at the upper portion of the ice cylinder, and the flat area near the top of the ice cylinder tends to increase in size with an increase in far-field temperature T_∞ . It was observed in the range of the parameters covered that the location of the onset of the step might be between 40 and 75 deg (angle from the top of the ice cylinder) and that the step location tended to move downward with increasing far-field temperature T_∞ as well as increasing initial ice-cylinder diameter D_{in} . Based on the above, the step probably results from the transition of laminar to turbulent flow.

As shown in Figs. 5-8, the flow patterns around the melting ice cylinder do not basically change as time elapses. Figure 9

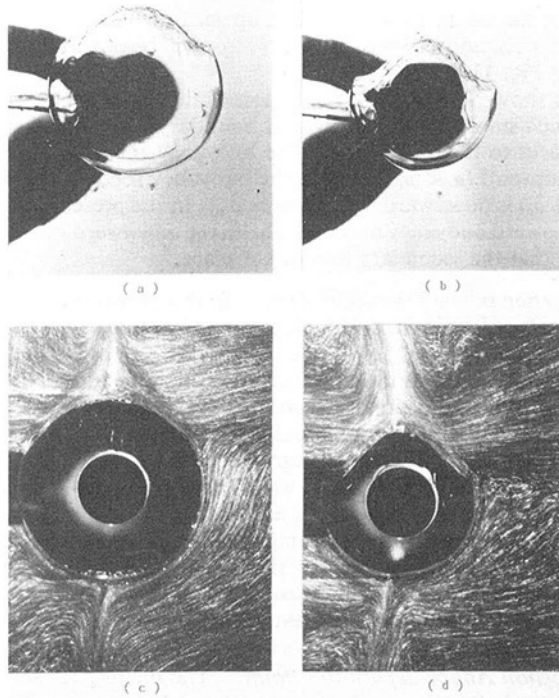


Fig. 5 Melting ice profile and flow pattern ($T_{\infty} = 2.8^{\circ}\text{C}$): (a) 40 min elapsed; (b) 80 min elapsed; (c) 15 min elapsed; (d) 60 min elapsed

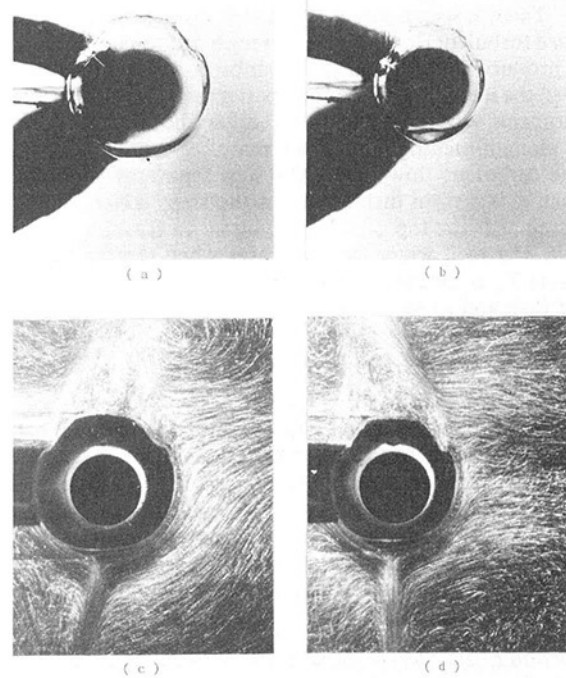


Fig. 7 Melting ice profile and flow pattern ($T_{\infty} = 12.2^{\circ}\text{C}$): (a) 4 min elapsed; (b) 8 min elapsed; (c) 2 min elapsed; (d) 8 min elapsed

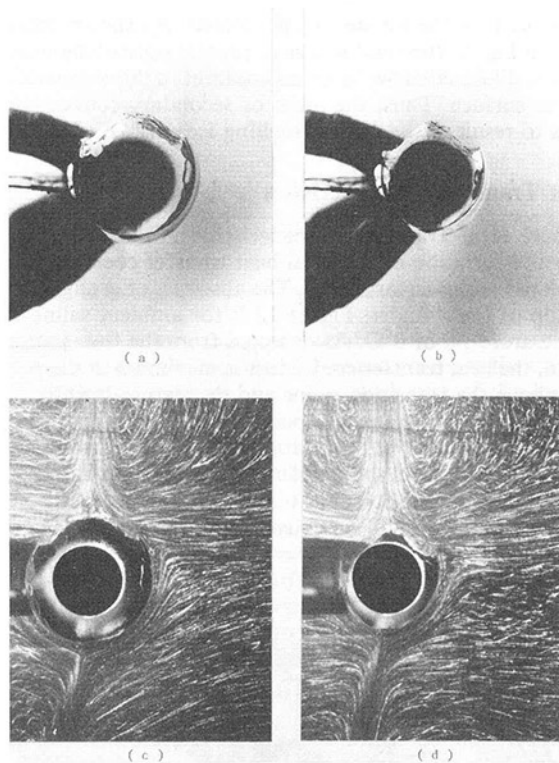


Fig. 6 Melting ice profile and flow pattern ($T_{\infty} = 6.0^{\circ}\text{C}$): (a) 20 min elapsed; (b) 30 min elapsed; (c) 15 min elapsed; (d) 30 min elapsed

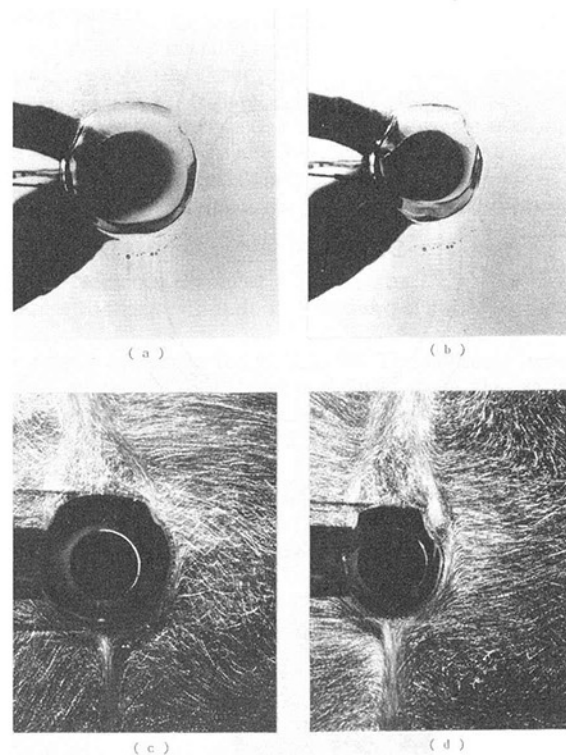


Fig. 8 Melting ice profile and flow pattern ($T_{\infty} = 18.0^{\circ}\text{C}$): (a) 4 min elapsed; (b) 8 min elapsed; (c) 2 min elapsed; (d) 8 min elapsed

shows schematically the representative flow pattern. Along the lower portion of the ice cylinder, the laminar velocity field is bidirectional, consisting of a quite narrow upward inner flow adjacent to the ice cylinder inside of a wider downward outer flow. Along the upper portion of the ice cylinder, the velocity

field is unidirectional and upward turbulent flow above the step, which probably results from the abrupt increase in heat transfer coefficient at the transition point. At the level of transition to turbulence, it appears that the turbulent diffusion may transport both dilute saline water and upward momentum away from the ice over a horizontal distance comparable to

the thermal boundary layer thickness. This upward buoyancy and momentum may overcome the downward buoyancy such that the net result is an upward-flowing turbulent boundary layer. Then, it seems that the resultant divergence between the upward turbulent flow and the downward laminar thermal flow may produce a horizontal jet of ambient saline water flowing toward the ice cylinder (see flow patterns in Figs. 5–8). Similar phenomena were observed by Josberger and Martin (1981) for flow along a melting vertical ice plate.

The turbulent flow above the step separates from the ice surface at a certain distance from the step, which causes the flat area near the top of the ice cylinder to form, as shown in Fig. 9. The melt water rate increases when the far-field temperature T_∞ is increased, which leads to stronger upward dilute water flow and to earlier separation. Then, the higher ambient temperature results in a wider flat area near the top of the ice cylinder.

Characteristics of Melting Ice Surface. There exists a concentration (salinity) boundary layer as well as a thermal boundary layer adjacent to the ice cylinder. As a result, secondary flows may occur and a variety of ice-surface characteristics are observed, as shown in Fig. 10, in which the experimental condition for Fig. 10(a) nearly corresponds to that for Fig. 6, while the condition for Figs. 10(b) and 10(c) corresponds to that for Fig. 8. In addition, the photograph of Fig. 10(b) is taken from obliquely below.

Portion From Step to Separation Point. As shown in Fig. 10(a), the ice surface develops longitudinal grooves with regular amplitude. The depth of the grooves increases with time;

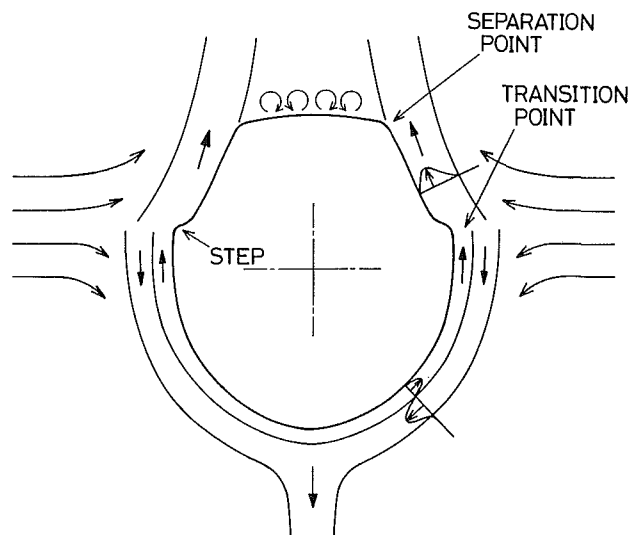


Fig. 9 Flow model around melting ice cylinder

the neighboring grooves tend to interfere with each other and finally they combine, resulting in grooves with irregular amplitude and depth. The grooves probably result from the onset of the secondary flow within the upward turbulent flow. The onset mechanism of the secondary flow will be now considered using Fig. 11(a).

As shown in Fig. 11(a), a concentration boundary layer δ_c is much smaller than the thermal boundary layer δ_t and exists adjacent to the ice cylinder. The buoyancy force in the layer δ_c is upward ($\rho < \rho_{\max}$), while the buoyancy force in the layer $(\delta_t - \delta_c)$ is downward ($\rho_{\max} > \rho > \rho_\infty$). In the present portion the upward buoyancy may overwhelm the downward buoyancy such that the secondary flow takes place.

Portion Below Transition Point. In this portion the melting ice surface is smooth for the lower ambient temperatures. As T_∞ increases, some amplitude waves with smooth crests are observed, as shown in Fig. 10(b). This may be interpreted in terms of the bidirectional structure of the boundary layer flow. Figure 11(b) shows schematically the onset mechanism of the secondary flow. The flow is upward in the layer δ_c , which is potentially stable ($\rho < \rho_{\max}$), while there exists the maximum density in the layer between δ_c and δ_t ($\rho_{\max} > \rho > \rho_\infty$), which destabilizes the downward laminar flow. Therefore, the bidirectional flow is stable for the lower T_∞ , while the flow becomes unstable with increasing T_∞ and the onset of the secondary flow takes place, thus resulting in the uneven ice surface.

Portion Above Separation Point. The melting ice surface is quite similar to a surface scooped out by a spoon. Figure 10(a) shows the somewhat circular depressions on the narrow flat area at the top of the ice cylinder. In Fig. 10(c), it is observed that a wider flat area with a number of depressions distributed on the ice surface is formed. As shown schematically in Fig. 9, the fluid in this portion is potentially unstable because dilute saline water exists adjacent to the comparatively flat ice surface. Thus, the onset of secondary convection appears to result in the uneven melting ice surface.

Heat Transfer Characteristics

Local Heat-Transfer Characteristics. Figures 12 and 13 show the variation of the local heat transfer coefficient using the elapsed time as parameter. The abscissa is the angle ϕ from the top of the cylinder. Figure 12 is for ambient saline-water temperature T_∞ of 6°C. As expected from the flow pattern in Fig. 6, the heat transfer coefficient is maximum at the portion just above the transition point and decreases abruptly at the portion below the transition point. Smaller values of the heat transfer coefficient at the portion below the transition point probably result from the smaller upward velocity based on the small melt rate due to small temperature difference between the ice surface and the ambient fluid. As the melting time

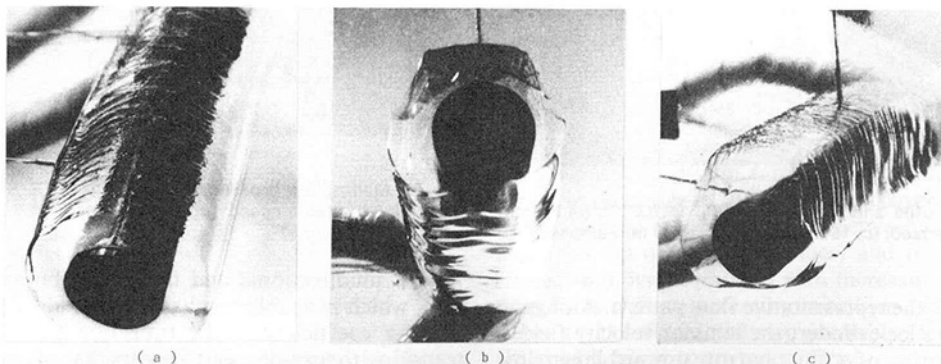


Fig. 10 Characteristics of melting ice surface: (a) $T_\infty = 6.0^\circ\text{C}$, 15 min elapsed; (b) $T_\infty = 17.0^\circ\text{C}$, 20 min elapsed; (c) $T_\infty = 17.0^\circ\text{C}$, 15 min elapsed

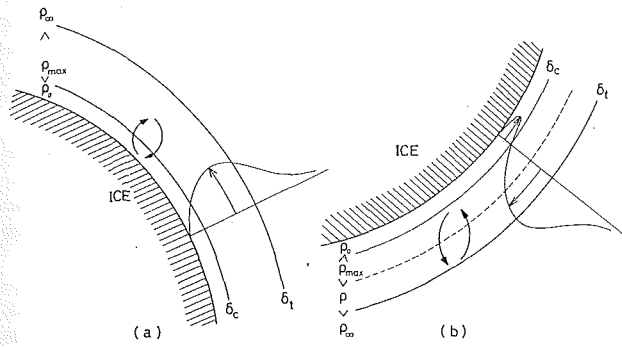


Fig. 11 Instability of flow adjacent to ice cylinder

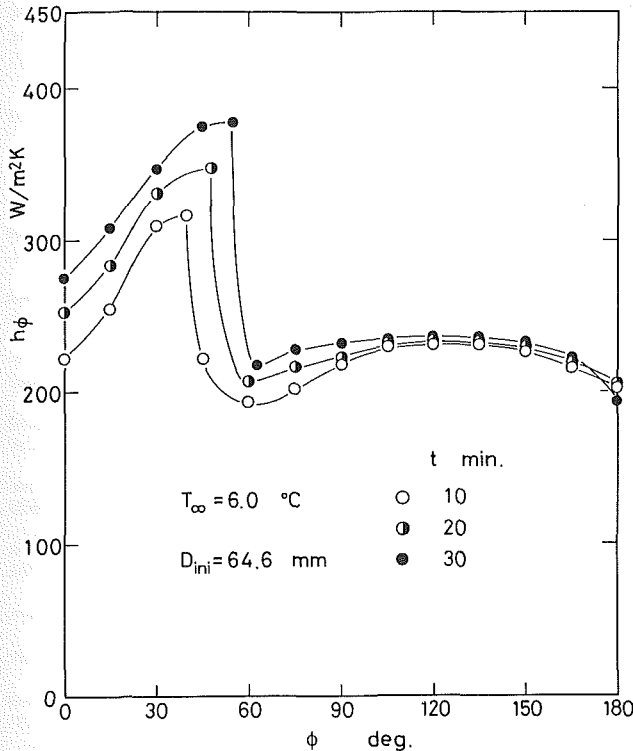


Fig. 12 Local heat transfer coefficient distribution

elapses, the step (transition point) tends to move downward. This is attributed to the fact that the heat transfer at the upper portion of the ice cylinder is greater than that at the lower portion of the ice cylinder.

Figure 13 is for the higher ambient saline-water temperature T_∞ of 18°C . As estimated from the ice profile (see Fig. 8), the heat transfer coefficient is small at the portion above the separation point, attains a maximum between the separation point and the transition point, and decreases monotonically downward. Furthermore, the values of the heat transfer coefficient at the portion above the transition point are greater than those at the portion below the transition point. This is explained by considering that the large temperature difference between the ice surface and the ambient fluid results in the large melt rate, which causes higher velocity of the dilute saline water. As the melting time elapses, the position at which the heat transfer coefficient becomes maximum tends to move upward, which corresponds to movement of the separation point.

Average Heat Transfer Characteristics. By adopting the initial ice cylinder diameter D_{in} as the reference length, one defines an average Nusselt number as follows:

$$\text{Nu}_m = h_m D_{in} / \lambda_l \quad (4)$$

where the thermal conductivity λ_l is the arithmetic mean value $(\lambda_o + \lambda_\infty)/2$ of the interface and the ambient. In the present

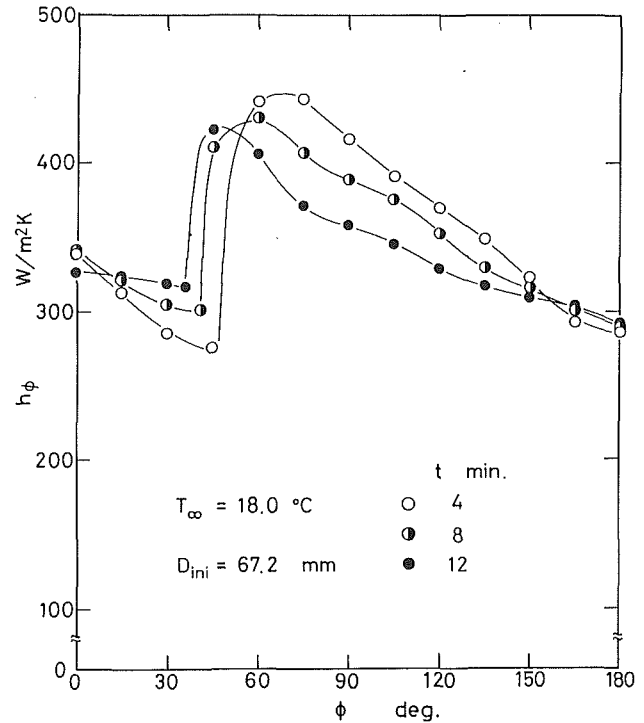


Fig. 13 Local heat transfer coefficient distribution

experiments, the ambient saline-water temperature T_∞ ranged from 2.8 to 20.3°C and the initial ice-cylinder diameter was in general between 60 and 70 mm. Then, a modification is necessary since the initial ice-cylinder diameter is not always the same through the experiments. The Nusselt number was divided by $(D_{in}/D_o)^{3/4}$ (Cheng et al., 1981, 1988; Saitoh, 1976), since the Nusselt number as defined by Eq. (4) is proportional to the reference length to the $3/4$ power in the range where the boundary-layer approximation is valid. One defines the modified average Nusselt number by the following expression

$$\text{Nu}_m^* = \text{Nu}_m / (D_{in}/D_o)^{3/4} \quad (5)$$

where the reference diameter was taken as $D_o = 100$ mm to compare with the previous data (Fukusako et al., 1990; Saitoh, 1976).

The results are presented in Fig. 14. The ordinate denotes modified average Nusselt number Nu_m^* , while the abscissa denotes temperature difference between the ambient and ice-cylinder surface $\Delta T (= T_\infty - T_o)$. In the figure, the experimental results both for steady-state heat transfer around the ice cylinder (solid line) (Fukusako et al., 1990) and for melting heat transfer of the ice cylinder in pure water (dotted line) (Saitoh, 1976) are also shown for comparison. Examination of the figure reveals that for $\Delta T < 13^\circ\text{C}$ the Nu_m^* increases monotonically with increasing ΔT , while for $\Delta T > 13^\circ\text{C}$ Nu_m^* tends to approach a constant value. This probably results from the increased flat area near the top of the melting ice cylinder. It is of interest that for $\Delta T < 13^\circ\text{C}$ the present Nu_m^* is in good agreement with that for steady state without melting.

Melt Rate Characteristics. The melting velocity is generally adopted as a measure of the melt rate. Utilizing the local melting velocity $(db/dt)_\phi$, the average melting velocity \dot{X} is defined as

$$\dot{X} = \frac{\sum_\phi (db/dt)_\phi A_\phi}{\sum_\phi A_\phi} \quad (6)$$

Figure 15 shows the average melting velocity \dot{X} versus the temperature difference $\Delta T (= T_\infty - T_o)$. In the figure, the data for the vertical melting ice plate (Josberger and Martin,

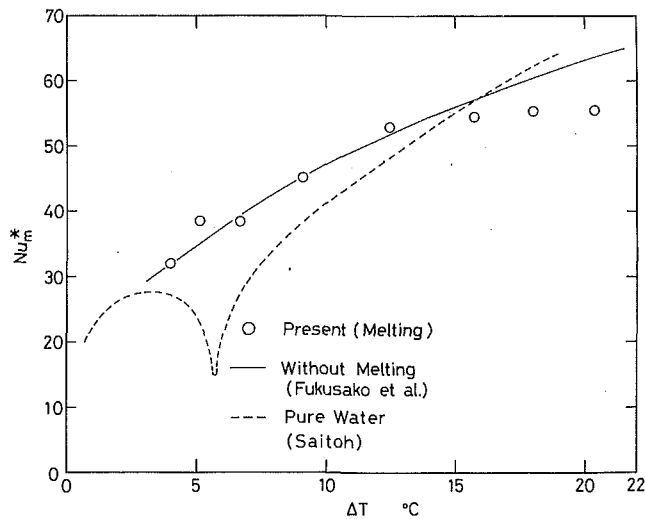


Fig. 14 Relationship between modified average Nusselt number Nu_m^* and temperature difference ΔT

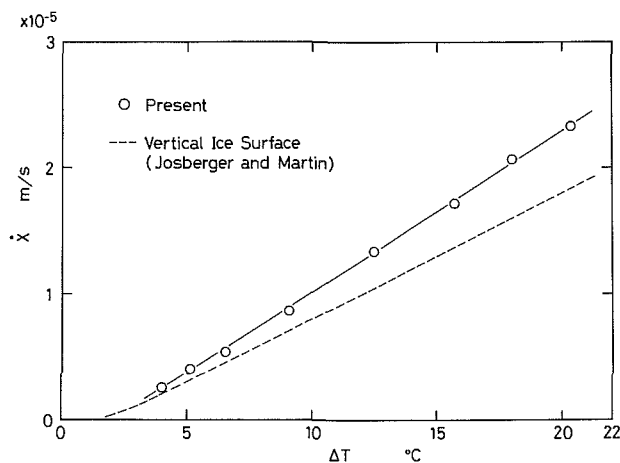


Fig. 15 Relationship between melting velocity \dot{X} and temperature difference ΔT

1981) are also presented for comparison. From the figure, it is clearly seen that the melting velocity \dot{X} increases linearly with an increase in ΔT . The present data are somewhat greater than those for the vertical ice plate. One of the reasons for this fact is that at least for the horizontal ice cylinder there occurs a flat portion near the top of the cylinder where the heat transfer increases unexpectedly due to the onset of the secondary flow (see Figs. 7, 8, and 10).

Conclusions

The melting heat transfer characteristics of a horizontal circular ice cylinder immersed in quiescent saline water were determined. The following conclusions may be drawn within the parameters covered:

1 The flow pattern around the melting ice cylinder is quite complicated. At the lower portion of the ice cylinder the laminar velocity field is bidirectional, consisting of a narrow upward inner flow adjacent to the ice cylinder inside of a wider downward outer flow.

2 The laminar upward inner flow becomes turbulent downstream. Above the level of transition to turbulence, the turbulent velocity field is unidirectional and soon separates from the ice surface. Increasing ambient temperature lowers the location of transition to turbulence.

3 At the transition point a step is formed and at the separation point a profile with somewhat sharp corner is observed. Above the separation point a flat surface is formed and its area increases with increasing ambient temperature.

4 A variety of ice-surface features are observed, depending on the flow characteristics adjacent to the ice surface. At the upper portion of the ice cylinder, longitudinal grooves with regular amplitude are formed by the secondary flow.

5 The melting velocity increases linearly with an increase in ambient fluid temperature.

References

- Carey, V. P., and Gebhart, B., 1982a, "Transport Near a Vertical Ice Surface Melting in Saline Water: Some Numerical Calculations," *J. Fluid Mech.*, Vol. 117, pp. 379-402.
- Carey, V. P., and Gebhart, B., 1982b, "Transport Near a Vertical Ice Surface Melting in Saline Water: Experiments at Low Salinities," *J. Fluid Mech.*, Vol. 117, pp. 403-423.
- Cheng, K. C., Inaba, H., and Gilpin, R. R., 1981, "An Experimental Investigation of Ice Formation Around an Isothermally Cooled Cylinder in Cross-flow," *ASME JOURNAL OF HEAT TRANSFER*, Vol. 103, pp. 733-738.
- Cheng, K. C., Inaba, H., and Gilpin, R. R., 1988, "Effects of Natural Convection on Ice Formation Around an Isothermally Cooled Horizontal Cylinder," *ASME JOURNAL OF HEAT TRANSFER*, Vol. 110, pp. 931-937.
- Fukusako, S., Tago, M., Yamada, M., and Kitayama, K., 1990, "Free Convection Heat Transfer Around a Horizontal Ice Cylinder Formed Through Melting in Saline Water," *ASME HTD-Vol. 139*, pp. 35-41.
- Gebhart, B., and Mollendorf, J., 1978, "Buoyancy-Induced Flows in Water Under Conditions in Which Density Extreme May Arise," *J. Fluid Mech.*, Vol. 89, pp. 673-707.
- Huppert, H. E., and Turner, J. S., 1978, "On Melting Icebergs," *Nature*, Vol. 271, pp. 46-48.
- Johnson, R. S., 1978, "Transport From a Melting Vertical Ice Slab in Saline Water," M. S. thesis, State University of New York at Buffalo.
- Johnson, R. S., and Mollendorf, J. C., 1984, "Transport From a Vertical Ice Surface Melting in Saline Water," *Int. J. Heat Mass Transfer*, Vol. 27, pp. 1928-1932.
- Josberger, E. G., and Martin, S., 1981, "A Laboratory and Theoretical Study of the Boundary Layer Adjacent to a Vertical Melting Ice Wall in Salt Water," *J. Fluid Mech.*, Vol. 111, pp. 439-473.
- Marschall, E., 1977, "Free Convection Melting on Glacial Ice in Saline Water," *Let. Heat Mass Transfer*, Vol. 4, pp. 381-384.
- McAdams, W. H., 1954, *Heat Transmission*, McGraw-Hill, New York, pp. 258-261.
- Mollendorf, J. C., Johnson, R. S., and Gebhart, B., 1981, "Several Plume Flows in Pure and Saline Water at Its Density Extremum," *J. Fluid Mech.*, Vol. 113, pp. 269-282.
- Neshyba, S., 1977, "Upwelling by Iceberg," *Nature*, Vol. 267, pp. 507-508.
- Qureshi, Z. H., and Gebhart, B., 1986, "The Stability of Vertical Thermal Buoyancy Induced Flows in Cold Pure and Saline Water," *Int. J. Heat Mass Transfer*, Vol. 29, pp. 1383-1392.
- Saitoh, T., 1976, "Natural Convection Heat Transfer From a Horizontal Ice Cylinder," *Appl. Sci. Res.*, Vol. 32, pp. 429-451.
- Sammakia, B., and Gebhart, B., 1983, "Transport Near a Vertical Ice Surface Melting in Water of Various Salinity Levels," *Int. J. Heat Mass Transfer*, Vol. 26, pp. 1439-1452.

Differential Methods for the Performance Prediction of Multistream Plate-Fin Heat Exchangers

B. S. V. Prasad

S. M. K. A. Gurukul

Research & Development Division,
Bharat Heavy Plate & Vessels Ltd.,
Visakhapatnam—530 023, India

Use of traditional methods of rating can prove inaccurate or inadequate for many plate-fin heat exchanger applications. The superiority in practical situations of differential methods, based on dividing the heat exchanger into several sections and a step-wise integration of the heat transfer and pressure loss functions, is discussed. Differential methods are developed for counterflow, crossflow, and cross-counterflow heat exchangers. The methods developed also avoid iterations at the section level calculations. Design of computer algorithms based on these methods is outlined. Two computer programs developed using the methods are presented and the results for a few typical cases are discussed.

1 Introduction

Plate-fin heat exchangers are widely used in cryogenic and aero-space applications where their traditional advantages, viz., compactness, low weight, high efficiency, and ability to handle multiple streams, remain unmatched by any other type of exchanger. Feed gas precoolers used in cryogenic process industry are often designed for $Ntu = 50$, and provide excellent cold recovery from the outgoing streams. The high performance delivered by and expected from these exchangers puts an equally high premium on the performance prediction methods used in their design. For example, the feed air precooler in a cryogenic air separation unit underperforming by only about 3% would have vast consequences for the entire plant. Thus the usage of accurate and reliable performance calculation methods is the key to successful design. The following sections describe some methods developed and used by the authors and the development of algorithms for performance prediction using them.

Considerable literature already exists on the design and performance prediction of plate-fin heat exchangers. Excellent introductions, dealing with all aspects of design and construction, are available, such as those of Lenfestey (1961) and Shah (1983a); aspects of design such as surface selection, optimization, sizing, and rating have been dealt with thoroughly by Shah (1983b), London (1983), and Kern and Kraus (1972). However, as also pointed out by Haseler (1983), there are not many publications dealing with practical situations where: there are more than one hot and one cold stream; variation in thermohydraulic properties of streams may be pronounced; accommodation of multiple streams results in a different flow length for each stream, etc. The authors could find only a few earlier attempts, viz., Denton and Ward (1960), Prasad and Gurukul (1980, 1987), and Weimer and Hartzog (1977). Spalding (1983) lists a few others, though in a different context. All the above factors have a considerable impact on the overall performance of the exchanger, and methods that do not take them into consideration may not provide a reliable performance prediction.

2 Qualities Desirable in Performance Prediction Methods

The following qualities would be highly desirable in any performance prediction method:

(i) **Accuracy and Reliability.** The method should be accurate, i.e., the temperature and pressure loss figures predicted by it should not differ significantly from those of the exchanger after it is built. This makes the method reliable for refining and optimizing the design. Reliability also means that the algorithm using the method should never fail, i.e., it should not “crash”; if failure is inevitable under certain situations, the user should at least be warned beforehand.

(ii) **Detail and Versatility.** Detail is a very important characteristic. The method should be capable of providing the user with a detailed picture of the variation of important process parameters such as temperatures, pressures, Reynolds numbers, heat transfer coefficients, etc., throughout the exchanger. This is invaluable in optimization of design through stratagems such as (1) changing fin surface at an intermediate point; (2) varying flow cross sections; (3) varying entry/exit locations, etc. In addition, versatility involves ability to account for such secondary effects as (1) longitudinal conduction; (2) flow maldistribution; (3) stacking patterns, etc. This in turn makes the method more accurate.

(iii) **Modularity.** The method should be modular, i.e., it should consist of a series of logical steps ending in the performance prediction. Modular methods can be programmed easily and quickly, and the resulting program is often very structured and flexible, allowing easy enhancements in the future.

(iv) **Compactness and Speed.** Compact programs have greater portability and can be implemented on small personal computers with limited resources. Compact programs usually run faster as there is less code to be executed. Carefully designed algorithms for fast convergence of iterations further improve speed. Both compactness and speed have a positive impact on design cycle time and cost.

3 Differential Versus Integral Methods

The authors define an “integral” method as one in which the heat exchanger is treated as an integral whole and thermohydraulic properties of process streams (specific heat, density, viscosity, thermal conductivity, heat transfer coefficient, and friction factor) are considered essentially invariant at their “mean” values. The mean values are usually made to correspond to a mean temperature between entry and exit temperature. Most methods appearing in the literature belong to this category.

Contributed by the Heat Transfer Division for publication in the JOURNAL OF HEAT TRANSFER. Manuscript received by the Heat Transfer Division March 26, 1990; revision received April 23, 1991. Keywords: Finned Surfaces, Heat Exchangers, Numerical Methods.

As opposed to this, in a "differential" method, the heat transfer and pressure loss functions are integrated from one end to the other in a stepwise manner, incorporating the variation in thermohydraulic properties and the influence of secondary effects at each step. Hence in addition to being more accurate and realistic, the differential method provides the designer with a very detailed insight into the status of various process parameters throughout the exchanger.

It can be seen that the differential method scores over the integral method in reliability, accuracy, detail, and versatility. The integral method may be more compact and faster, mainly because it involves far fewer calculations, but this is more than offset by disadvantages in other qualities. The "blackbox" nature of integral methods is a major disadvantage, since the designer gets no information on process conditions between entry and exit. While integral methods are excellent platforms for studying heat exchanger design theory, they often fall short of providing reliable and satisfactory solutions in practical situations.

The following equations form the basis of relations to be developed in subsequent sections:

$$h = jC_p G(\text{Pr})^{-2/3} \quad (1)$$

$$q = C(T_{in} - T_{out}) = hA \left[\frac{T_{in} + T_{out}}{2} - T_s \right] \quad (2)$$

$$Q = \sum_{i=1}^{nh} h_i A_i \left[\frac{T_{in,i} + T_{out,i}}{2} - T_s \right] = \sum_{i=1}^{nc} h_i A_i \left[T_s - \frac{T_{in,i} + T_{out,i}}{2} \right] \quad (3)$$

$$\Delta P \approx \frac{G^2 L f}{2g_c \rho r_h} \quad (4)$$

4 Performance Prediction of Counterflow Heat Exchangers

Feed gas precoolers in the cryogenic process industry typify

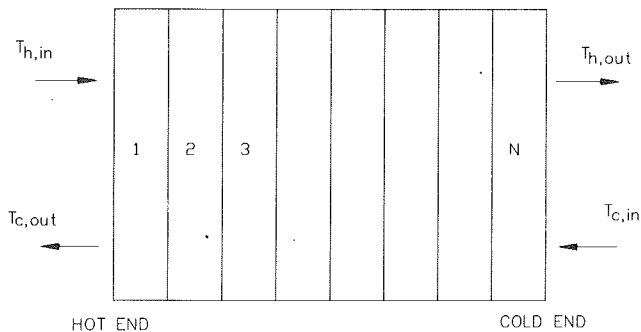


Fig. 1 Counterflow heat exchanger divided into N sections

the usual counterflow exchanger design problem. These are essentially balanced counterflow exchangers with a hot feed stream exchanging heat with several return product streams. The feed stream cools to almost its dew point at the cold end. Flow regimes may change from laminar at the hot end to turbulent at the cold end; temperature ranges are a few hundred degrees Celsius; very low pressure loss is permitted and very close temperature approaches ($\leq 4^\circ\text{C}$) are demanded between hot and cold streams to achieve maximum cold conservation. Accuracy, reliability, detail, and versatility are needed to achieve a competitive design.

Figure 1 shows an ideal two-stream counterflow exchanger divided into a large number of sections along its length. Thermohydraulic properties of streams are considered invariant in the exchanger. The temperature ranges in the 1st section are

$$\Delta t_{h,1} = \frac{(UA)\Delta T_1}{NC_h} \quad (5)$$

$$\Delta t_{c,1} = \frac{(UA)\Delta T_1}{NC_c} \quad (6)$$

The temperature difference between hot and cold streams at the end of the first section and the beginning of the second section is

Nomenclature

A = net effective surface area of stream = $A_p + \eta A_s$, m^2	nh = number of hot streams in exchanger	
A_C = free flow area of stream, m^2	nc = number of cold streams in exchanger	Δt = temperature range of stream in section, K
A_p = primary surface area of stream, m^2	N = number of sections in exchanger	(UA) = overall heat transfer rate in section, kJ/Ks
A_s = secondary surface area of stream, m^2	ΔP = pressure loss of stream, Pa	ϵ = exchanger effectiveness
C = capacity rate of stream = $\dot{m} c_p$, kJ/Ks	Pr = Prandtl number	η = fin efficiency
C_{\min} = lesser of the two net capacity rates C_h and C_c , kJ/Ks	q = quantity of heat transferred from stream, kJ	ρ = density, kg/m^3
c_p = specific heat, kJ/kgK	Q = net quantity of heat transferred, kJ	Subscripts
f = Fanning friction factor	ΔQ = quantity of heat transferred in section, kJ	c = cold streams
g = gravitational constant, m/s^2	ΔQ_{\max} = maximum heat transfer possible between hot and cold stream, kJ	ce = cold end
G = mass velocity of stream = \dot{m}/A_c , $\text{kg}/\text{m}^2\text{s}$	r_h = hydraulic radius of surface, m	cur = current value
h = heat transfer coefficient of stream, $\text{kJ}/\text{s m}^2\text{K}$	Re = Reynolds number	f = far end
j = Colburn j factor = $\text{St} \cdot \text{Pr}^{-2/3}$	St = Stanton number	h = hot streams
L = effective flow length of stream, m	T = temperature, K	he = hot end
\dot{m} = mass flow rate of stream, kg/s	ΔT = net temperature differential between warm and cold streams at near end of section, K	i = section number and stream number
n = number of streams in exchanger		in = entry value
		m = mean value
		n = near end
		out = exit value
		ov = overall
		prev = previous value
		s = surface

$$\Delta T_2 = \Delta T_1 \left[1 - \frac{UA}{N} (1/C_h - 1/C_c) \right] \quad (7)$$

and temperature ranges in the second section will be

$$\Delta t_{h,2} = \frac{UA\Delta T_1}{NC_h} \left[1 - \frac{UA}{N} (1/C_h - 1/C_c) \right] \quad (8)$$

$$\Delta t_{c,2} = \frac{UA\Delta T_1}{NC_c} \left[1 - \frac{UA}{N} (1/C_h - 1/C_c) \right] \quad (9)$$

for the N th section

$$\Delta t_{h,N} = \frac{UA\Delta T_1}{NC_h} \left[1 - \frac{UA}{N} (1/C_h - 1/C_c) \right]^{N-1} \quad (10)$$

$$\Delta t_{c,N} = \frac{UA\Delta T_1}{NC_c} \left[1 - \frac{UA}{N} (1/C_h - 1/C_c) \right]^{N-1} \quad (11)$$

$$\Delta T_{N+1} = \Delta T_{ce} = \Delta T_1 \left[1 - \frac{UA}{N} (1/C_h - 1/C_c) \right]^N \quad (12)$$

Each set of temperature ranges constitutes a geometric series; summing the series, and allowing N to increase to infinity,

$$(T_{h,in} - T_{h,out}) = \frac{C_c \Delta T_{he}}{(C_c - C_h)} [1 - e^{UA(1/C_c - 1/C_h)}] \quad (13)$$

$$(T_{c,out} - T_{h,in}) = \frac{C_c \Delta T_{he}}{(C_c - C_h)} [1 - e^{UA(1/C_c - 1/C_h)}] \quad (14)$$

$$\Delta T_{ce} = \Delta T_{he} e^{UA(1/C_c - 1/C_h)} \quad (15)$$

When the calculation starts from the cold end, the above equations take the form

$$(T_{h,in} - T_{h,out}) = \frac{C_c \Delta T_{ce}}{(C_h - C_c)} [1 - e^{UA(1/C_h - 1/C_c)}] \quad (16)$$

$$(T_{c,out} - T_{c,in}) = \frac{C_h \Delta T_{ce}}{(C_h - C_c)} [1 - e^{UA(1/C_h - 1/C_c)}] \quad (17)$$

$$\Delta T_{he} = \Delta T_{ce} e^{UA(1/C_h - 1/C_c)} \quad (18)$$

Equations (13)–(18) have not been previously derived in this form and fashion. While Kays and London (1964) use a geometric method to derive the effectiveness expression for counterflow, the present series summation approach effectively brings out the simplicity of relation between the variables involved; further, the effectiveness expression itself can be derived from Eqs. (13)–(18). The main advantage of these equations lies in the facility with which they can be used in a differential method, as will be brought out in the following sections.

4.1 Application of Eqs (13)–(18) to Performance Prediction. Consider Fig. 1 again, now as a “real” heat exchanger. Since temperature ranges in individual sections would be quite small, the thermohydraulic properties can be considered constant in each section with negligible error; Eqs. (13)–(18) can now be applied to each section starting from either the hot or cold end, based on suitably estimated temperatures for streams exiting at that end. The calculation proceeds in a stepwise manner to the other end. A comparison is made between predicted and actual entry temperatures for the relevant streams and the calculation is repeated with corrected exit temperatures till a satisfactory match is obtained. The use of Eqs. (13)–(18) obviates the necessity for an iteration at the section level, and thus considerably speeds up the calculation as only one level of iteration has to be performed for the entire exchanger.

4.2 Extension of Eqs. (13)–(18) to Multistream Exchangers. The validity of Eqs. (13)–(18) can be extended to the case of multiple streams on either side if we can prove that they satisfactorily represent the behavior of hot and cold sides in a multistream exchanger.

Ideally, a multipassage exchanger has to be analyzed in terms of the total number of passages rather than the total number of streams, as pointed out by Haseler (1983) also. In a multipassage plate-fin heat exchanger, in addition to transfer by convection to streams, heat is also transferred by conduction through the fins in the transverse direction. Since the transverse conductance is finite, surface temperature cannot be uniform through the depth of the exchanger core, and various models to determine this surface temperature profile have been developed and applied by Chato et al. (1971), Haseler (1983), and Prasad (1990). However, a multipassage analysis usually leads to a large set of simultaneous equations, which must be solved to obtain the temperatures of streams and surfaces in each passage. When the numbers of sections and the number of passages in the exchanger are both large, such an approach is computationally daunting, and cannot be entertained except where very detailed performance is desired, or performance is expected to be strongly dependent on the stacking pattern. The effect of stacking pattern on performance of an exchanger is discussed in detail by Prasad (1990).

One assumption that can be made at this point is that of constant surface temperature at any given cross section of the exchanger through the depth of the stack. The usage of this assumption eliminates the complications in the calculation, as the number of unknowns reduces to the respective stream temperatures and the surface temperature; it is tantamount to assuming an infinite heat conductance through the fins in the transverse direction. It has been shown illustratively by Wejmer and Hartzog (1977), and Prasad (1990), that with a good stacking pattern a performance close to that predicted by the above assumption can be obtained. A simple and effective method for achieving a good stacking pattern at the sizing stage itself is given by Suessman and Mansour (1979). In addition, the constant surface temperature criterion can be reasonably applied to multistream exchangers in which streams on each side (*i*) do not have widely divergent entry temperatures; (*ii*) display comparable thermohydraulic properties, (*iii*) the net temperature differential between hot and cold sides is small; (*iv*) the fin efficiencies are high; and (*v*) the number of passages in the exchanger is large (see Weimer and Hartzog, 1977). Since these conditions apply in most multistream plate-fin exchangers in counterflow, further discussion here will be limited to the constant surface temperature model, for which the following equations can be derived:

$$T_s = \frac{\sum_{i=1}^{i=nh} h_i A_i T_i + \sum_{i=1}^{i=nc} h_i A_i T_i}{\left(\sum_{i=1}^{i=nh} h_i A_i + \sum_{i=1}^{i=nc} h_i A_i \right)} \quad (19)$$

$$\Delta T_{he} = (T_{h,in,m} - T_{c,out,m}) = \frac{\sum_{i=1}^{i=nh} h_i A_i T_{in,i} - \sum_{i=1}^{i=nc} h_i A_i T_{out,i}}{\sum_{i=1}^{i=nh} h_i A_i - \sum_{i=1}^{i=nc} h_i A_i} \quad (20a)$$

$$\Delta T_{ce} = (T_{h,out,m} - T_{c,in,m}) = \frac{\sum_{i=1}^{i=nh} h_i A_i T_{out,i} - \sum_{i=1}^{i=nc} h_i A_i T_{in,i}}{\sum_{i=1}^{i=nh} h_i A_i - \sum_{i=1}^{i=nc} h_i A_i} \quad (20b)$$

Equations (19) and (20) allow us to extend the utility of Eqs. (13)–(18) to multistream exchangers. In the general case of an exchanger with multiple hot and cold streams, the weighted mean entry temperature of streams (defined in Eq. (20)) entering at the far end is used for checking the iteration. Once

this is matched, Eq. (19) is used to predict the surface temperature for each section, and Eq. (2) for predicting the individual stream temperatures using the above surface temperature.

5 Design of a Computer Program for the Performance of Counterflow Heat Exchangers

A possible scheme for the development of a computer program, based on the derivations in Section 4, is given below. The graphic postprocessor indicated in step 6 is optional, but the additional programming effort involved in providing such graphic user interfaces is more than offset by the facility they afford the user in reviewing results.

Step 1. Read in entry and estimated exit temperatures, pressure and flow rate; read in density, specific heat, enthalpy, viscosity, and thermal conductivity versus temperature data; prepare thermophysical property arrays for interpolation—for each stream in the exchanger.

Step 2. Read in fin data and “*j*” and “*f*” versus Reynolds number arrays; prepare arrays for interpolation; calculate primary and secondary areas and free flow area—for each fin surface used in the exchanger.

Step 3. Start at the first section at one end; obtain thermohydraulic variables by interpolation; calculate temperature range and pressure loss; calculate entry conditions for next section; repeat until the other end is reached.

Step 4. Compare predicted temperatures of streams entering at this end with actual entry temperatures; correct estimated exit temperatures for them and iterate step (3) till a reasonable match is obtained.

Step 5. Print a streamwise output report with section number, entry and exit temperatures, Reynolds number, stepwise and net heat transferred, sectionwise and cumulative pressure loss, heat exchanger coefficient, fin efficiency, etc., with a succinct summary at the end.

Step 6. On request, output graphs of above process variables versus length on terminal and generate hardcopy on plotter.

It is obvious that step (4) is the most critical in the calculation. The use of analytical iterative methods, such as the Newton-Raphson, provides higher order convergence, but these cannot be conveniently applied in our case where the objective function (the difference between the calculated and actual entry temperature of the streams entering at the far end), cannot be derived in terms of the independent variable (the near end temperature) for the whole exchanger, because of the interim variation of thermohydraulic properties. Other slope-dependent methods such as the regula-falsi can also fail in particular cases, such as unbalanced exchangers, or when there is a pure stream condensing or vaporizing on one side. For these reasons, a numerical search method such as the Fibonacci or Golden section, which is not dependent on the slope of the control function, has to be employed.

Even though the calculation can start from either the hot or the cold end, it is preferable to start from the end where the temperature differential between hot and cold sides is expected to be greater. This sometimes becomes obligatory, as in the case of an unbalanced exchanger with a lower cold capacity rate, which will have practically identical cold and hot stream temperatures at the hot end (see Fig. 4); the calculation must be started from the cold end in this case, as the hot end temperature differential would be vanishingly small.

The following are some additional features for the counterflow rating program. Additional refinements can include modules for the following, incorporated appropriately in the program:

(i) *Longitudinal Heat Conduction Through the Matrix of the Exchanger:* In plate-fin exchangers, conduction is mainly through exchanger core between hot and cold ends. The surface temperature difference between hot and cold ends is the driving force, and it has the effect of flattening the temperature curves.

(ii) *Flow Maldistribution:* The effects of flow maldistribution in given streams can be simulated by considering each section as consisting of several subsections in parallel, with variable flow rates across them. The predicted exit conditions for all subsections are then averaged to yield the exit conditions of the section. The variation in flow rates of the target streams can be tied to the expected maldistribution derived from header and distribution geometry and the fin geometry; for example, when interrupted fins such as serrated fins are employed, a passage-to-passage maldistribution model is usually sufficiently faithful, but in the case of others such as plain or herringbone fins, which form individual channels, a two-dimensional maldistribution model similar to those described by Chiou (1980) needs to be developed.

(iii) *Intermediate Entry and Exit of Streams:* This is done by initially calculating between which sections the stream is present; then the stream calculations are appropriately “switched on” in the active sections, possibly through the use of a boolean variable.

(iv) *Intermediate Change of Fin Type:* This is similar to (iii) above, and can be incorporated by maintaining a status list of current fin type for all streams and switching the fin at the appropriate location. This involves additional pressure change calculations at the location of change, which must be incorporated into the pressure loss calculation at that section.

(v) *Pressure Loss in Distributors, Headers, Fittings, and Internal Distributors:* This can be attempted only after all exchanger design variables are frozen, i.e., number of individual cores in parallel, number of passages per stream, entry and exit locations and flow length of each stream, distributor fin orientations at entry and exit for each stream, fitting and header sizes, etc., are all fixed. Thus these modules can be incorporated in the program and “switched on” only in the final rating runs. Pressure losses in the distribution network have to be kept small in relation to core pressure loss to avoid serious maldistribution.

(vi) *Exchanger Volume and Weight:* This assumes additional importance in aerospace applications where often both need to be minimized. Hence a routine that provides details such as space envelope, orientational footprints, and detailed weight breakdown of each component in each stream needs to be developed. The can be switched on and off depending on need.

6 Performance Prediction of Crossflow and Cross-Counterflow Heat Exchangers

The crossflow pattern is invariably used where a high heat transfer effectiveness is not necessary. Construction of crossflow exchangers is simple as headers can be located on all sides and internal distribution is minimal. Cross-counterflow exchangers, with multiple passes on one side, offer higher performance, at the cost of relatively higher pressure losses on the multipass side. The simplicity of construction and attendant volume and weight savings makes crossflow and cross-counterflow design particularly attractive for aerospace applications.

Aircraft engine bleed air coolers are typical of this type of exchanger. Temperatures may range over several hundred degrees Celsius on the hot side where high pressure losses are tolerated. Flow regimes are often turbulent. There are usually only two streams in the exchanger; both crossflow and cross-

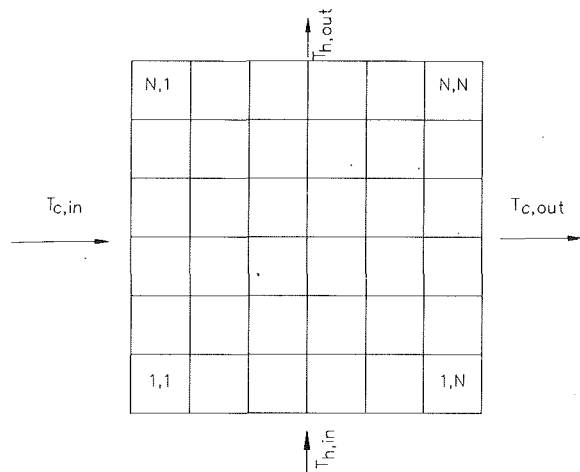


Fig. 2 Crossflow heat exchanger divided into $N \times N$ sections

counterflow patterns are employed in design. Low volume and weight are mandated.

As process variables change along both length and breadth in these exchangers, their graphs are surfaces rather than curves. Figure 2 shows a crossflow exchanger divided into a grid of $N \times N$ sections. It is clear that the sectionwise calculation should be performed in two loops of N steps each, one over the other. Calculation proceeds from section (1, 1) to section (N , N) either along length or along breadth. Ultimately N exit temperatures and N cumulative pressure losses result for each stream; these are averaged to obtain representative figures for the whole exchanger.

A sectionwise calculation is in order. It is obvious that Eqs. (13) and (14) cannot be used here as they are derived for a counterflow section. In fact, each section in Fig. 1 can be considered a counterflow exchanger with near end conditions known, whereas each section in Fig. 2 can be considered a crossflow exchanger with entry conditions known. The overall heat balance in a section may be expressed as:

$$\Delta Q = \frac{C_h \Delta t_h}{N} = \frac{C_c \Delta t_c}{N} \quad (21)$$

from which

$$\Delta t_h = \frac{N \Delta Q}{C_h} \quad (22)$$

and

$$\Delta t_c = \frac{N \Delta Q}{C_c} \quad (23)$$

since

$$\Delta Q = \frac{h_h A_h}{N} \left[\frac{T_{h,in} + T_{h,out}}{2} - T_s \right] = \frac{h_c A_c}{N} \left[T_s - \frac{T_{c,in} + T_{c,out}}{2} \right] \quad (24)$$

employing the values of Δt_h and Δt_c in Eq. (24),

$$T_c = T_{h,in} = \frac{N \Delta Q}{2 C_h} - \frac{N \Delta Q}{h_h A_h} = T_{c,in} + \frac{N \Delta Q}{2 C_c} + \frac{N \Delta Q}{h_c A_c} \quad (25)$$

from which

$$\Delta Q = [T_{h,in} - T_{c,in}] / N \left[\frac{1}{2 C_h} + \frac{1}{2 C_c} + \frac{1}{h_h A_h} + \frac{1}{h_c A_c} \right] \quad (26)$$

Since all the values on the righthand side are known, the respective exit temperatures can be determined by first obtaining the value of ΔQ from Eq. (26) and using the same in Eqs. (21) and (24). The procedure is then repeated for the next section. It may be noted that unlike in the case of the coun-

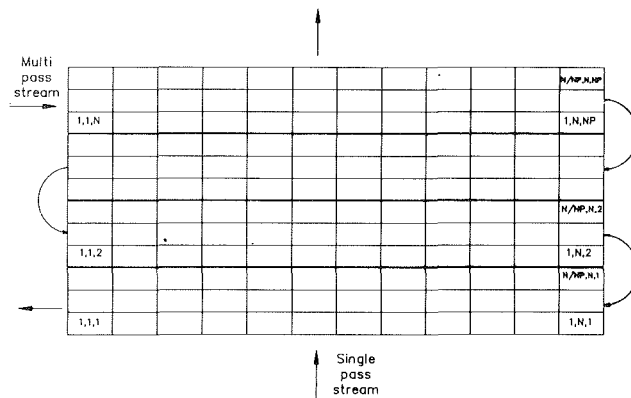


Fig. 3 Multipass cross-counterflow heat exchanger divided into $N \times N$ sections, with NP passes on the multipass side

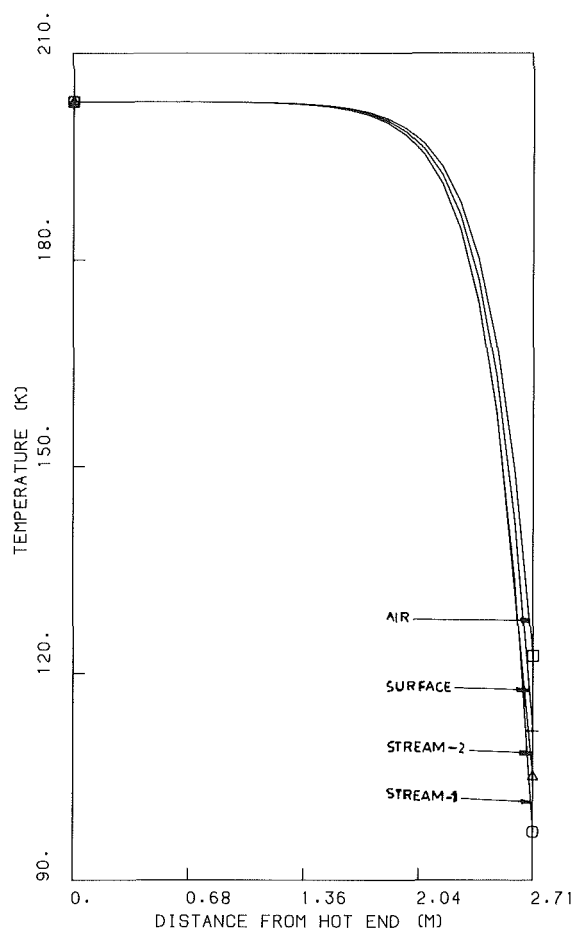


Fig. 4 Variation of stream temperatures in unbalanced three-stream heat exchanger

terflow exchanger no iteration over all sections is involved; the calculation for a crossflow exchanger is accordingly rapid.

7 Performance Prediction of Multipass Cross-Counterflow Exchangers

Figure 3 shows a multipass cross-counterflow exchanger divided into $N \times N$ sections, with NP passes on the multipass side. Multipass cross-counterflow exchangers can be considered as several crossflow exchangers in series, with the exit temperatures of each section in one pass matching the entry temperatures of the corresponding section in the next. To achieve this matching, an overall iteration between passes be-

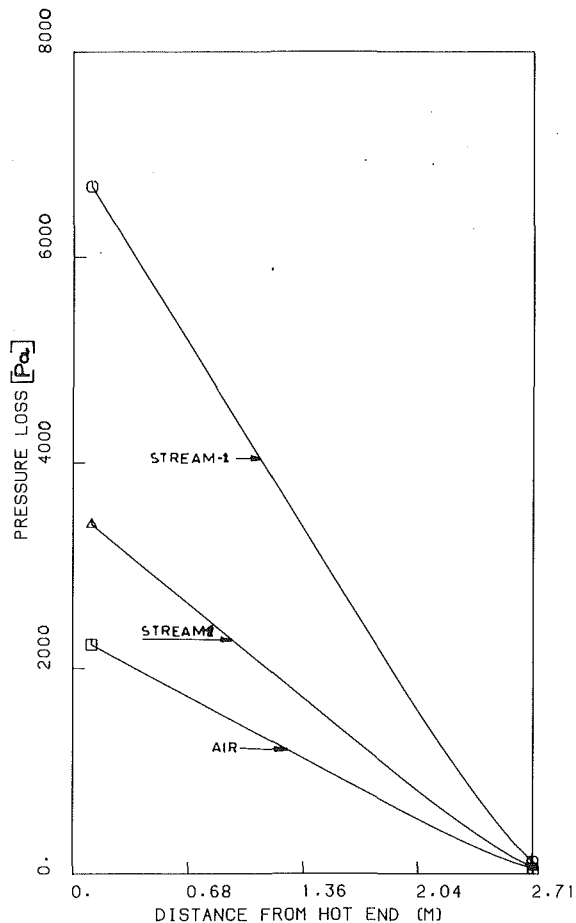


Fig. 5 Variation of pressure losses in unbalanced three-stream heat exchanger

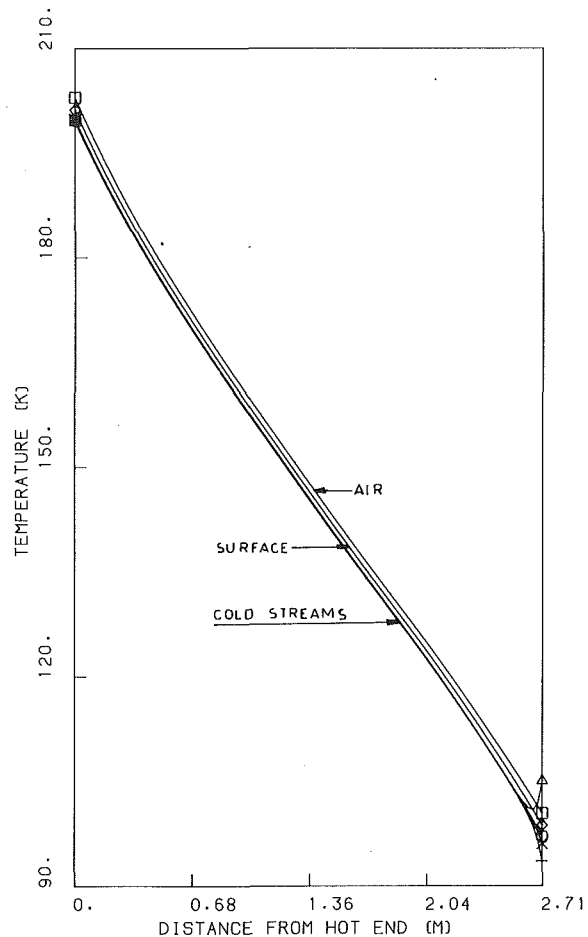


Fig. 6 Variation of stream temperatures in balanced multistream heat exchanger

comes necessary. To start this iteration, reasonably estimated interpass temperatures must be used. They are then corrected over subsequent iterations until a satisfactory match is obtained. The calculation involves the following steps:

Step 1. Estimate interpass temperatures for the single-pass streams using Eqs. (27) and (28) (ΔQ here refers to one pass).

$$\Delta Q \approx Q/_{NP} \quad (27)$$

$$\epsilon = \frac{\Delta Q}{\Delta Q_{\max}} = \frac{C_h[T_{h,\text{in}} - T_{h,\text{out}}]}{C_{\min}[T_{h,\text{in}} - T_{c,\text{in}}]} = \frac{C_c[T_{c,\text{out}} - T_{c,\text{in}}]}{C_{\min}[T_{h,\text{in}} - T_{c,\text{in}}]} \quad (28)$$

Step 2. Iteration starts. Calculate performance and exit temperatures for all passes using the procedure of Section 6.

Step 3. With the new exit temperatures, calculate the error function ($T_{\text{cur}} - T_{\text{prev}}$) for each interpass section. Calculate a weighted average value ($T_{\text{cur}} - T_{\text{prev}}$)_{ov} for each interpass.

Step 4. Iterate steps (2)–(3) until the interpass error functions ($T_{\text{cur}} - T_{\text{prev}}$)_{ov} fall below the tolerance value.

The following observations can be made on this procedure:

(i) The exit temperature matching need be done for only one side; matching on one side automatically leads to matching on the other.

(ii) On the multipass side the temperature matching is needed for only $N/_{NP}$ sections, making the iteration faster; besides, multipass streams are frequently assumed to mix in the return headers, so that exit temperatures of previous pass must be averaged and taken as entry temperatures for the current pass. This mixing can be conveniently incorporated

into the algorithm if temperature matching is done for the multipass streams.

(iii) The procedure outlined above is similar to that used by Weimer and Hartzog (1977) for counterflow exchangers, in which the calculation is started with an assumed temperature profile, which is corrected progressively, each iteration using the profile obtained in the previous iteration. At the end of each iteration the profile obtained is compared with the previous one, and the process is continued until the difference between subsequent profiles is insignificant, at which point the true profile is deemed to have been found. The calculation is inherently stable, but convergence is a slow first-order process, particularly when the number of sections is large and the exchanger is unbalanced. However, since the calculation is relatively insensitive to initial estimates of the exit temperatures (to establish the assumed profile), it is particularly suited for the cross-counterflow exchanger, for which linearly interpolated interpass temperatures can be used to start the calculation. The method is also more rapid for a cross-counterflow exchanger as the number of passes (which are equivalent in this case to the sections of the counterflow exchanger) is usually small.

8 The Computer Programs "PERF" and "CROSFLO"

Based on the methods discussed in the previous sections, the authors developed a program called PERF for counterflow plate-fin heat exchangers. This program is written in FORTRAN 77, and can be implemented on a personal computer. It incorporates a graphic postprocessor that can display variation of important process parameters along exchanger length

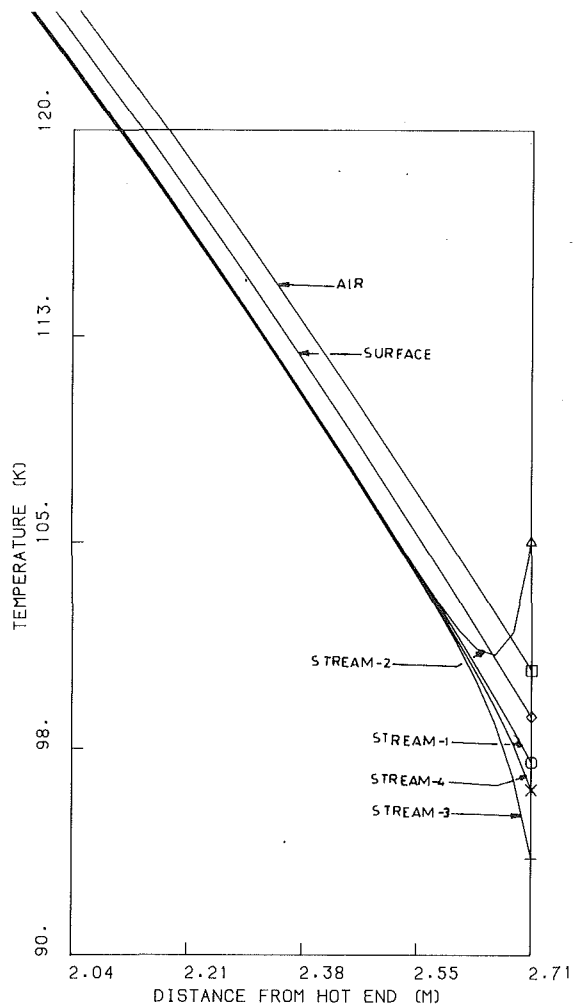


Fig. 7 Detail of temperature cross in multistream heat exchanger

and optionally generate a hard copy on a plotter. Figures 4–10 show sample plots obtained during actual rating runs. Structured programming practices have been employed in the design of the program, with independent modules doing specific tasks, and each module having its own diagnostic and debugging facilities. For example, the geometry module calculates the surface area and free flow area for each surface specified; a separate “j” and “f” interpolator uses the “j” and “f” versus Reynolds number data supplied for each surface to generate relevant values for each stream, at each section, based on the calculated Reynolds number. Similarly, temperature-dependent stream properties are interpolated by another module. The interpolator routines normally use cubic splines for their task. The program has independent modules for accounting for longitudinal heat conduction through core, and passage-to-passage flow maldistribution in a given target stream. These, and other modules for calculating header and distributor pressure losses, etc., can be switched on and off through the use of a setup file, which tailors the working environment of the program, such as debug modes, postprocessing modes, output modes, tolerance on the temperature matching iteration, etc. This program was originally written several years ago and improved over the years, by incorporating most of the features mentioned in Section 5, and has been used in the design of several exchangers.

A step decimation search method based on Golden section search is employed for the temperature matching iteration mentioned in Section 5. The time taken for calculation is dependent on the number of sections into which the exchanger

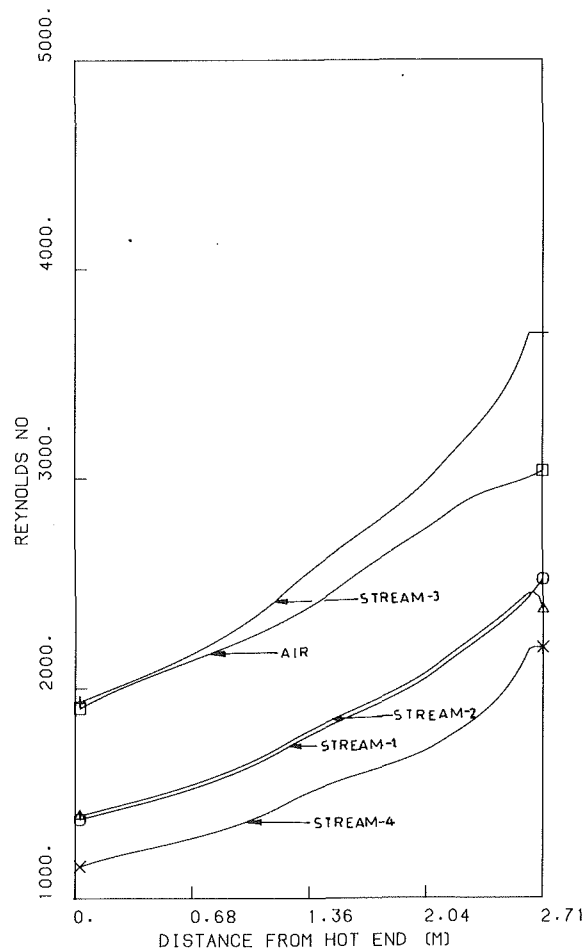


Fig. 8 Variation of Reynolds numbers in multistream heat exchanger

is divided and the initial estimates of exit temperatures given to the program. More than 50 sections are rarely needed and a rating run typically takes less than 5 seconds on a multi-user DEC MicroVAX II computer; this includes the time taken for all explicit disk I/O operations also.

CROSFLO has been written relatively recently and shares the same structured design philosophy. The program can rate both crossflow and cross-counterflow exchangers. Routines for fin geometry calculation, fin and stream data interpolation, etc., are common to PERF and CROSFLO. Since the input data format is also common to both, the designer can quickly compare crossflow and counterflow designs for a given problem, using the same input data set. Standard options provided include mixing of cross-counterflow streams in return headers, a detailed unit weight breakdown report and an effectiveness-NTU calculation module, incorporating the formulae of Kays and London (1964). The last mentioned is particularly useful during initial sizing trials. Operating modes and output are controlled through initial setup and results can be postprocessed into a three-dimensional graph (Fig. 11).

9 Discussion of Results

Figures 4–10, obtained from rating runs using the above programs, are typical of the sort of detailed performance obtainable from the use of differential methods. Figures 4 and 5 show the thermal and pressure loss performance of the feed air precooler in an air separation plant, with one hot and two cold streams. The net cold capacity rate is about 85 percent that of the hot side; yet, note that nearly 50 percent of the

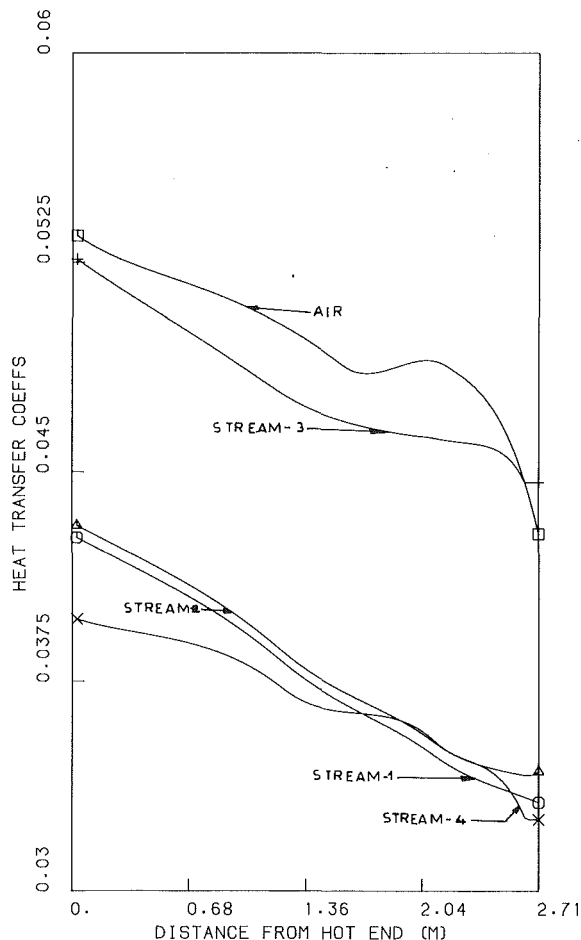


Fig. 9 Variation of heat transfer coefficients in multistream heat exchanger

surface near the hot end is wasted, since there is no significant change in temperature; this wasted area causes nearly half the pressure loss in all streams. Figures 4 and 5 illustrate the massive penalty that has to be tolerated for even moderate unbalance in capacity rates in high effectiveness counterflow plate-fin exchangers. Figure 6 shows the same exchanger, after the addition of two more cold streams, accommodated in about 10 percent more passages (i.e., with an overall increase of about 10 percent surface and free-flow areas of the exchanger). The exchanger is now balanced; note that the hot stream now exits at a temperature lower than that of Stream 2, resulting in a temperature cross at the cold end (Fig. 7). Such temperature crosses can often occur in multistream plate-fin exchangers because of disparity in entry temperature of the cold streams. Since in such cases the cold stream must first be cooled and then heated, temperature crosses can, in some cases, quite severely reduce the efficiency of exchangers; this is because (i) surface area is wasted in gainless heat transfer and (ii) a local unbalance in capacity rates is caused in the exchanger. Use of rating packages based on differential methods can help in deciding the correct entry location for such streams, so that temperature crosses can be avoided.

Figure 8 shows the variation in Reynolds numbers in various streams of the above exchanger between the hot and cold ends. Note that the hot and cold end values differ by nearly a factor of two for all streams. This variation in Reynolds numbers is caused by rapid fall in viscosities of all gaseous streams toward the cold end. The nonlinearity in the variation of heat transfer coefficients is even more marked (Fig. 9), even though overall variation is less than in the case of Reynolds numbers; this variability reflects the combined effect of variation in heat

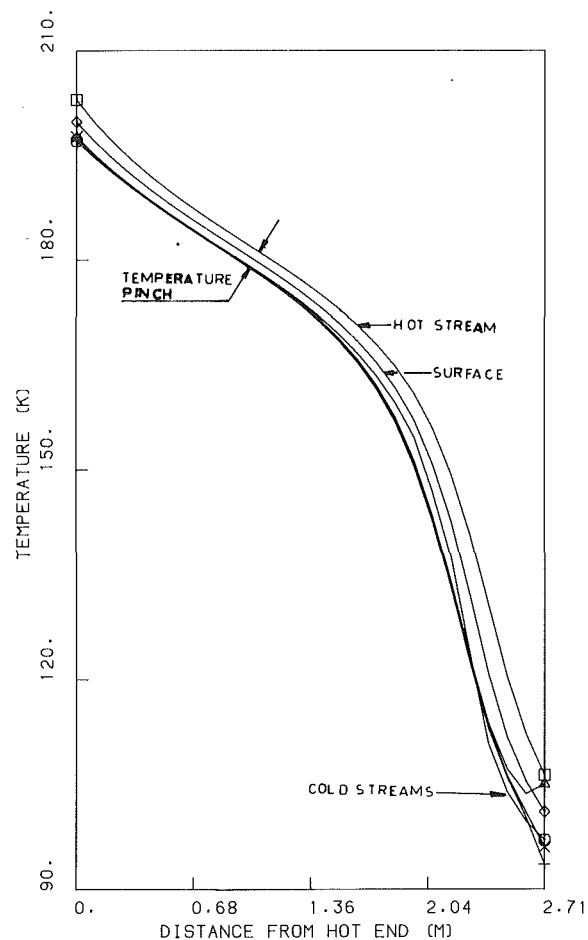


Fig. 10 Temperature pinch in a multistream heat exchanger

capacity and Reynolds numbers. Figures 8 and 9 demonstrate that integral methods, which assume "mean" values of thermohydraulic properties to hold for the entire exchanger, can be considerably in error in rating even gas-to-gas exchangers.

A temperature pinch is another effect sometimes observed in balanced multistream plate-fin exchangers (Fig. 10). Temperature pinches are caused by local excess of capacity rate on the hot or cold side, usually because of anomalous variations of heat capacity in streams consisting of mixtures of gases; multiple pinches in a single exchanger are also not unknown. Because of a local depression of the temperature differential between hot and cold sides, a temperature pinch can seriously affect the performance of an exchanger. This loss in performance is rarely apparent at the sizing and rating stages, unless differential methods have been used in both stages. Severe temperature pinches are sometimes evened out by incorporating an additional stream in the pinch region to achieve balance in the capacity rates.

Figure 11 shows the performance of a crossflow exchanger in which hot moist air exchanges heat with cold air. Both streams are considered "unmixed" (see Kays and London, 1964). Note the dual curvature in the temperature surfaces. In this case, the designer is required to provide an arrangement to collect water condensing on the hot side, and hence needs to know where in the exchanger the hot stream temperatures fall below 100°C. This information is easily obtained from Fig. 10, as is shown by the dotted lines. Note that obtaining information such as this is possible only when a detailed thermal performance of the streams inside the exchanger can be predicted.

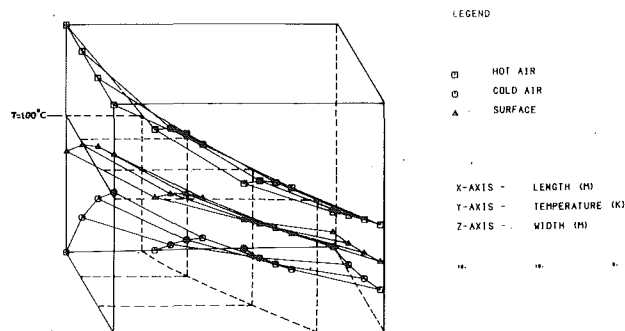


Fig. 11 Variation of stream temperatures in crossflow heat exchanger

10 Conclusions

Differential methods that allow for variation in process parameters and integrate the heat transfer and pressure loss functions in a stepwise manner provide a general and accurate prediction of the performance of multistream plate-fin heat exchangers. Usage of the methods described provides the designer with powerful, versatile, and accurate tools to solve practical real world problems in a competitive manner. It is hoped that in the future better and more elegant methods will appear in the literature.

Acknowledgments

The authors acknowledge their gratitude to the management of M/S Bharat Heavy Plate & Vessels Ltd., Visakhapatnam, India, for allowing them to publish this paper.

References

Chato, J. C., Laverman, R. J., and Shah, J. M., 1971, "Analysis of Parallel Flow Multistream Heat Exchangers," *International Journal of Heat and Mass Transfer*, Vol. 14, pp. 1691-1705.

Chiou, J. P., 1980, "The Advancement of Compact Heat Exchanger Theory Considering the Effects of Longitudinal Conduction and Flow Nonuniformity," in: *Compact Heat Exchangers—History, Technological Advancement, and Mechanical Design Problems*, R. K. Shah et al., eds., ASME, pp. 101-121.

Denton, W., and Ward, D. E., 1960, "Applications and Design of Plate-Fin Heat Exchangers," *Br. Chem. Engg.*, Jan.

Haseler, L. E., 1983, "Performance Calculation Methods for Multistream Plate-Fin Heat Exchangers," in: *Heat Exchangers, Theory and Practice*, J. Taborek et al., eds., Hemisphere Publishing, Washington, DC, pp. 495-506.

Kays, M. W., and London, A. L., 1964, *Compact Heat Exchangers*, 2nd ed., McGraw-Hill, New York.

Kern, D. Q., and Kraus, A. D., 1972, *Extended Surface Heat Transfer*, McGraw-Hill, New York, pp. 593-641.

Lenfestey, A. G., 1961, "Low Temperature Heat Exchangers," in: *Advances in Cryogenics*, K. Mendelssohn, ed., Heywood & Co., London, pp. 23-48.

London, A. L., 1983, "Compact Heat Exchangers—Design Methodology," in: *Low Reynolds Number Flow Heat Exchangers*, S. Kakac et al., eds., Hemisphere Publishing, Washington, DC, pp. 815-844.

Prasad, B. S. V., and Gurukul, S. M. K. A., 1980, "An Approach to Design and Performance of Compact Heat Exchangers in Low Temperature Plants," presented at the V National Symposium on Cryogenics, Lucknow, India, 1980; *Ind. J. Cryogenics*, Vol. 8(2), 1983, pp. 74-80.

Prasad, B. S. V., and Gurukul, S. M. K. A., 1987, "Differential Method for Sizing Multistream Plate-Fin Heat Exchangers," *Cryogenics*, Vol. 27, pp. 257-262.

Prasad, B. S. V., 1990, "The Performance Prediction of Multi-stream Plate-Fin Heat Exchangers Based on Stacking Pattern," *Heat Transfer Engineering*, accepted for publication.

Shah, R. K., 1983a, "Compact and Enhanced Heat Exchangers," in: *Heat Exchangers, Theory and Practice*, J. Taborek et al., eds., Hemisphere Publishing, Washington, DC, pp. 425-468.

Shah, R. K., 1983b, "Compact Heat Exchanger Surface Selection, Optimization and Computer Aided Thermal Design," in: *Low Reynolds Number Flow Heat Exchangers*, S. Kakac et al., eds., Hemisphere Publishing, Washington, DC, pp. 845-874.

Shah, R. K., 1983c, "Heat Exchanger Basic Design Methods," in: *Low Reynolds Number Flow Heat Exchangers*, S. Kakac et al., eds., Hemisphere Publishing, Washington, DC, pp. 21-72.

Spalding, D. B., 1983, "The Calculation of Heat-Exchanger Performance," in: *Low Reynolds Number Flow Heat Exchangers*, S. Kakac et al., eds., Hemisphere Publishing, Washington, DC, pp. 677-691.

Suessman, W., and Mansour, A., 1979, "Passage Arrangement in Plate-Fin Exchangers," *Proceedings of XV International Congress of Refrigeration*, Vol. 1, pp. 421-429.

Weimer, R. F., and Hartzog, D. G., 1977, "Effect of Maldistribution on the Performance of Multistream Multipassage Heat Exchangers," *Adv. Cryo. Engg.*, Vol. 18, pp. 52-64.

Temperature Distribution Near a Heat Exchanger Wall Immersed in High-Temperature Packed and Fluidized Beds

G. Flamant

N. Fatah

G. Olalde

D. Hernandez

Institut de Science et de Génie des
Matériaux et Procédés,
Centre National de la Recherche
Scientifique,
Odeillo—66120—Font-Romeu, France

Experimental results dealing with both particle and gas temperature distribution in the vicinity of a water-cooled wall immersed in fixed and fluidized beds are presented. The measurement of particle temperature is based on the use of a mobile optical fiber connected to a two-color radiometer. The gas temperature is obtained on the basis of the indications of a bare thermocouple. Particle and gas temperature fields are compared in fixed and fluidized beds for alumina and silicon carbide particles. In the fixed bed, temperature differences as large as 300°C between the gas and the solid are measured. In the fluidized bed, temperature decreases of both solid and gas phase are shown for large particle at incipient fluidization. The temperature variation reaches more than 100°C for corundum particles and 200°C in the gas. The temperature distribution in the solid phase is shown to be dependent on the thermophysical properties of the particles (thermal conductivity and emissivity).

1 Introduction

Previous studies have demonstrated the complexity of combined heat transfer in high-temperature fixed and fluidized beds and the effects of heat transfer on chemical reactor performances (Smith, 1973). A review of literature data about thermal radiation exchanges in such systems was provided by Tien (1988). Concerning the flow structure near the wall, the problem is difficult because of the bed properties variation (Govindarao and Froment, 1986). Vafai et al. (1985) and Tien and Hunt (1987) studied the non-Darcian flow effects on heat transfer in packed beds. They showed that nonhomogeneous effects cause a large local velocity variation close to the wall that increases the transport rate, but their analysis neglects the heat exchange between the fluid and the solid phase; moreover, the main velocity and temperature variations near the wall are limited to about one particle diameter. In addition, the experimental results reported by Ziolkowska et al. (1989) prove that the inhomogeneity of the radial velocity profile in a packed bed is larger than that of the porosity distribution.

When conduction, convection, and radiation may occur, the determination of the main heat transfer mode needs accurate measurements of both gas and particle temperatures. Bead-inserted thermocouples have been used by Farber and Kohne (1987), but this method does not provide a precise local solid temperature and it cannot be used in a fluidized bed.

Combined conduction and radiation heat transfer was studied by Flamant and Menigault (1987) in fluidized beds of group B particles, using the diffusion approximation. Gas convection becomes significant for either $Ar > 2.17 \times 10^4$ (Saxena and Ganzha, 1984) or $Ar > 1.4 \times 10^4$ (Flamant et al., 1990). In this case the main questions to be solved are: Are the particles near the wall isothermal? What are the gas velocity and temperature profiles? In a bidimensional boundary layer model, Adams and Welty (1979) assumed there is no temperature variation near the wall and heat transfer occurs in the fluid through stagnant gas near the contact point between particle and wall and by turbulent convection in the rest. On the contrary, Mazza and Barreto (1988) developed a heat transfer model based on the existence of significant gas and solid temperature variations close to the wall.

Contributed by the Heat Transfer Division for publication in the JOURNAL OF HEAT TRANSFER. Manuscript received by the Heat Transfer Division November 1, 1990; revision received July 1, 1991. Keywords: High-Temperature Phenomena, Measurement Techniques, Packed and Fluidized Beds.

This analysis points out the lack of experimental data on real temperature profile near heat exchangers in both fixed and fluidized bed, and the importance of these data on heat transfer. This paper gives some new information in this field of interest.

2 Experimental

Experimental Setup. A schematic of the system is shown in Fig. 1. It is composed of: a preheater (1), a high-temperature heat exchanger (3), and a test section (5). The high-temperature heat exchanger is a fixed-fluidized bed located inside a 40 kW electric furnace made of nine silicone carbide electric resistances. The column is 1.05 m long and 105 mm in diameter. Thermal radiation emitted by the furnace is absorbed by the wall and then exchanged from the wall to the gas (air) through corundum particles (1.4 mm i.d.) fluidized inside the interstices of large corundum beads of 20 mm i.d. The maximum outlet air temperature reaches 850°C.

The test section is a refractory steel tube, 200 mm long and 105 mm in diameter, connected to a disengaging zone. The gas distributor is a perforated plate composed of 500 holes of 1.5 mm i.d. (voidage fraction 11.2 percent).

The heat exchanger is a flat, vertical, cooper disk 42 mm in diameter, cooled by water. A centered orifice, located 75 mm above the distributor, is used for inserting the temperature probe.

The mean bed temperature is controlled by three thermocouples (chromel-alumel type). Pressure taps are located on the wall of the test section in order to measure the pressure drop across the porous media.

Temperature Probe. The probe is also shown in Fig. 1. The setup was designed to provide measurements of both thermal radiation and bed temperature. It is composed of two probes inserted inside an alumina tube: a chromel-alumel bare thermocouple and a silica optical fiber (core diameter 400 μm) connected with a radiometer. The alumina tube is fixed on a micrometer screw in order to change the radial position of the probe. The radiation intensity is filtered at 1.3 μm and 1.5 μm in the radiometer and then quantified by germanium detectors for the color temperature calculation (Hernandez et al., 1988).

Two different thermocouples were used: a classical bare thermocouple and a protected one. The latter was protected

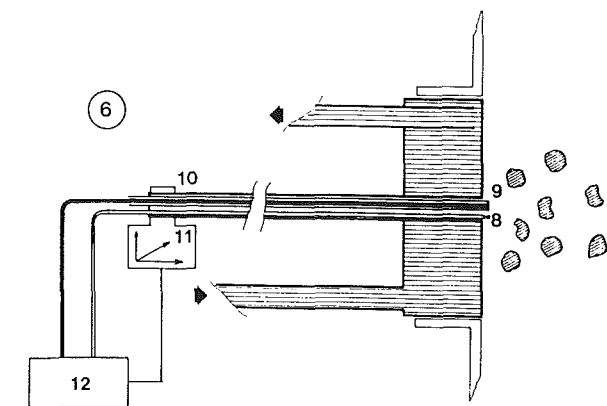
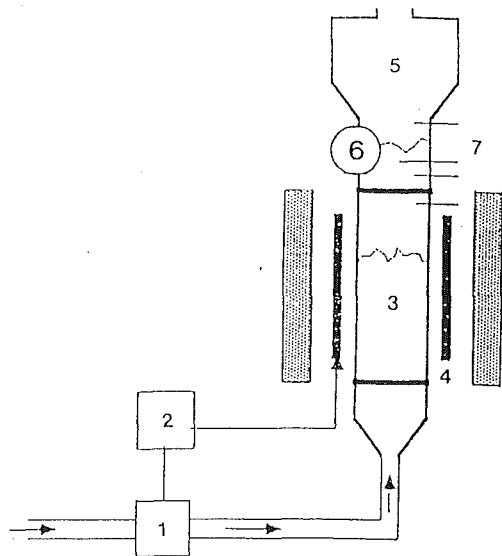


Fig. 1 Experimental setup: (1) preheater; (2) electric regulation; (3) fixed-fluidized bed superheated; (4) electric furnace; (5) test section; (6) water-cooled dish; (7) thermocouples; (8) optical fiber; (9) thin thermocouple; (10) alumina tube; (11) micrometer screw; (12) signal treatment and acquisition

against contact with the particle by using a perforated stainless steel tube covered with a grid. The first system will be called in the text Probe 1, the second one Probe 2.

Thermal Intensity and Temperature Measurement Procedures. The optical fiber immersed in the porous medium collects the thermal radiation emitted by the particles and it transmits the energy from the bed to the detectors. The detected

signal (transmitted intensity) is a function of the local intensity $I(T)$ and of intrinsic disruptions and external disturbances; it may be expressed as:

$$D_\lambda = K_\lambda \cdot \tau_\lambda \cdot S_\lambda \cdot (1 - L_\lambda) I_\lambda(T) \quad (1)$$

where K is a geometric constant; τ is the transmittance of the filter; S is the spectral detectivity of the detector; L represents the spectral loss of the whole device including bending, connection, surface heterogeneity.

Equation (1) indicates a strong dependence of the output signal on measurement device assembly and operating conditions. In order to obtain a more accurate technique, a bi-chromatic procedure was used. In this case the detected signal is proportional to the ratio of both monochromatic intensities:

$$D_{\lambda_2, \lambda_1} = \frac{K_{\lambda_2} \tau_{\lambda_2} S_{\lambda_2} (1 - L_{\lambda_2}) I_{\lambda_2}(T)}{K_{\lambda_1} \tau_{\lambda_1} S_{\lambda_1} (1 - L_{\lambda_1}) I_{\lambda_1}(T)} \quad (2)$$

Assuming that the device characteristics vary identically for both channels, the measured signal is proportional to the ratio of the intensities:

$$D_{\lambda_2, \lambda_1} = K \frac{I_{\lambda_2}(T)}{I_{\lambda_1}(T)} \quad (3)$$

Since $I_\lambda(T)$ is given by Planck's radiation law, we have

$$\ln D_{\lambda_1, \lambda_2} = a/T_c + b \quad (4)$$

where T_c is the color temperature.

Assuming the medium is gray in the range $\lambda_1 - \lambda_2$, the color temperature T_c is equal to the local particle temperature T_p .

In order to reduce the effect of the fiber inlet surface abrasion on the detected signal, the radiometer was calibrated using a black body after each experiment.

Finally, the probes deliver two signals: the thermocouple indication, which is related to the gas temperature, and the fiber optic pyrometer indication, giving the thermal emission of the particles. Concerning Probe 2, the thermocouple signal is proportional to gas temperature in both cases: fixed and fluidized beds. On the contrary, for Probe 1 (unprotected bare thermocouple) the thermocouple signal cannot be easily related to the gas temperature in the fluidized bed, because of the direct contact between the probe and the particle.

3 Results

Experiments were run using 2.36 mm, 2.97 mm, 3.57 mm i.d. corundum particles and 2.36 mm silicon carbide particles. Most of the experiments were carried out at a mean bed temperature of 750°C.

The properties of the particles are listed in Table 1. The main thermophysical properties of corundum and silicon carbide particles are quite different. The thermal conductivity (λ_p) of silicon carbide is three times larger than that of corundum.

Nomenclature

d_p = particle diameter
 C_p = specific heat mean
 D = detected signal
 h_g = convective heat transfer coefficient
 I = spectral intensity
 K = constant
 L = spectral loss
 S = spectral detectivity of the detector
 T = temperature
 T_c = color temperature, indication of the radiometer

T_g = real gas temperature after correction of T_{th}
 T_p = particle temperature
 T_{th} = indication of the thermocouple
 U = velocity
 χ = distance from the wall
 $z = x/d_p$
 ϵ = emissivity
 λ = thermal conductivity
 ξ = porosity
 Φ = sphericity

ρ = density
 σ = Stefan-Boltzmann constant
 τ = spectral transmissivity

Subscripts

C = color
 g = gas
 m_F = minimum fluidization condition
 p = particle
 λ = spectral quantity

Table 1 Properties of the particles

Material	Corundum	Silicon carbide
d_p (10^{-3} m)	2.36, 2.97, 3.57	2.36
Φ_s	0.61, 0.51, 0.48	0.6
U_{mf} (700°C) ($\text{m}\cdot\text{s}^{-1}$)	2.52, 3.44, 4.38	1.93
ξ_{mf} (700°C)	0.54, 0.6, 0.63	—
λ_p 300 K < T < 1273 K ($\text{W}\cdot\text{m}^{-1}\text{K}^{-1}$)	$2.8\text{--}3.5 \times 10^{-3}$ ($T-1273$)	$11.6\text{--}6.5 \times 10^{-3}$ ($T-1273$)
ρ_p ($\text{kg}\cdot\text{m}^{-3}$)	3950	3200
C_p ($\text{kJ}\cdot\text{kg}^{-1}\text{K}^{-1}$)	1.2	0.78
ϵ_p (700°C) (total)	~ 0.5	~ 0.9

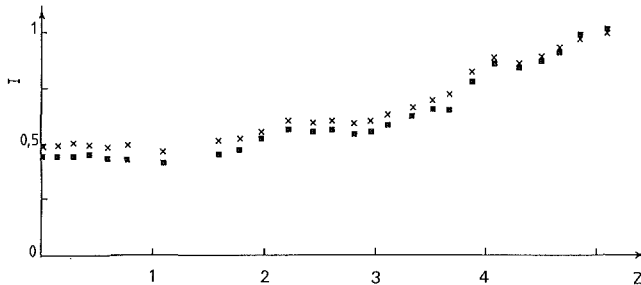


Fig. 2 Relative intensities given by the detectors for the wavelengths λ_1 and λ_2 ; Al_2O_3 , $d_p = 3.57$ mm, $U_g = 2$ m·pds $^{-1}$, $T_b = 750^\circ\text{C}$

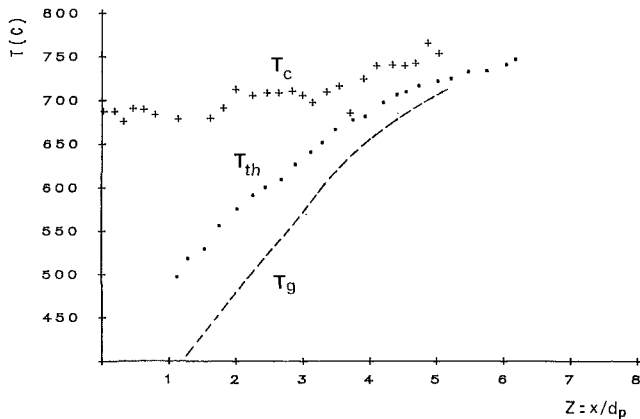


Fig. 3 Temperature profiles as a function of the distance from the water-cooled wall (Probe 1); fixed bed; Al_2O_3 , $d_p = 3.57$ mm, $U_g = 2$ m·s $^{-1}$, $T_b = 750^\circ\text{C}$, +: color temperature, o: thermocouple temperature, ... corrected gas temperature

The volumetric heat capacity ($\rho_p C_p$) of corundum is about twice the heat capacity of siC and the particle total emissivities are very different: about 0.5 for Al_2O_3 and 0.9 for SiC (estimated values from Touloukian).

Packed Bed. The spectral relative intensity profiles are plotted in Fig. 2(a) for 3.57-mm corundum particles at a mean bed temperature of about 750°C . The transition zone between the particle layers can be observed. No significant variation is measured up to $\chi = 2 d_p$, then a small intensity increase is detected for $2 d_p < \chi < 3 d_p$ and finally a more regular rise of I is obtained for $\chi > 3 d_p$ and up to $5 d_p$. For depths larger than d_p no significant intensity variation is detected.

The corresponding temperature profiles measured by Probe 1 are shown in Fig. 3 for both thermocouple and radiometer sensors. The solid phase temperature exhibits a very smooth variation in the range $z = \chi/d_p = 0$ to $z = 5$ and the total temperature decrease near the wall is about 60°C . The comparison between the thermocouple and the radiometer indications at $z=5$ shows a good agreement between both measurement techniques. In the bed core the solid temperature

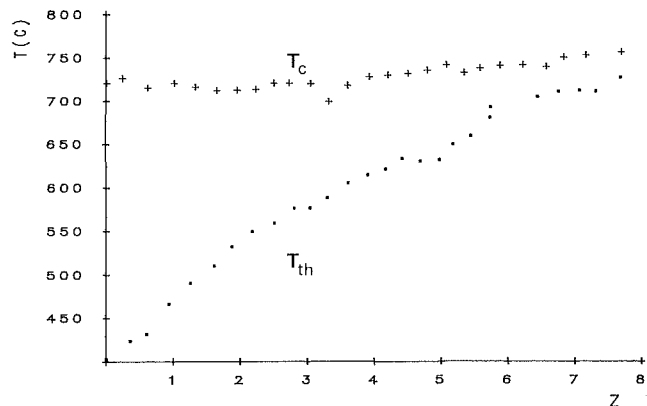


Fig. 4 Temperature profiles versus distance from the wall (Probe 1); fixed bed; Al_2O_3 , $d_p = 2.36$ mm, $U_g = 2$ m·s $^{-1}$, $T_b = 750^\circ\text{C}$ (uncorrected temperature)

(color temperature) is roughly equal to the gas temperature; differences of about 30°C are measured. The analysis of this phenomenon is proposed in the next section.

On the contrary, the profile given by the thermocouple near the wall indicates a large variation of the gas temperature. Since the conduction points between the thermocouple and the particles are very poor, the thermocouple is more influenced by the air than by the particles. Nevertheless, the measured values are overestimated because of the thermal radiation of the surrounding solid. The real gas temperature (T_g) may be estimated by the following steady-state heat balance equation:

$$T_g = T_{th} + \frac{\epsilon_{th}}{h_g} \sigma (T_{th}^4 - T_p^4) \quad (5)$$

where T_{th} and ϵ_{th} are the thermocouple temperature and emissivity, respectively, and h_g is the convective heat exchange coefficient between the gas and the thermocouple.

Assuming $h_g = 160\text{--}180$ $\text{W}\cdot\text{m}^{-2}\text{K}^{-1}$ ($U_g = 2$ m s $^{-1}$) and $\epsilon_{th} = 0.8$ the decrease of the gas temperature, by comparison with the thermocouple indication, ranges from 30°C at $z = 5$ to 130°C at $z = 1.5$ (dotted line on Fig. 3). As a result for $z = 1$, the solid temperature is 680°C and the gas temperature is about 400°C , thus the temperature difference is about 300°C .

The same result is observed for 2.36 mm i.d. corundum particles as plotted in Fig. 4, the temperature decrease of the particles is not significant (less than 30°C) while a large variation of the gas temperature is measured for $z < 5$.

The effect of the solid thermophysical properties may be illustrated by a comparison between Figs. 4 and 5. A significant variation of the solid temperature is shown in Fig. 5 related to 2.36 mm i.d. silicon carbide particles. No significant variation of the solid temperature is observed for $z > 4$, but the decrease occurs in two steps, first between $z = 4$ and $z = 2$ and then for $z \leq 2$. At the wall, the solid temperature is about 630°C , while at the bed core the mean temperature is 750°C .

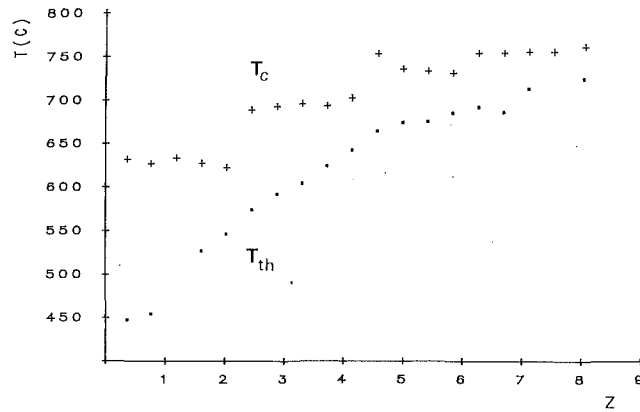


Fig. 5 Temperature profile versus distance from the wall (Probe 1); fixed bed, SiC, $d_p = 2.36$ mm, $U_g = 2$ m·s⁻¹, $T_b = 750^\circ\text{C}$ (uncorrected temperature)

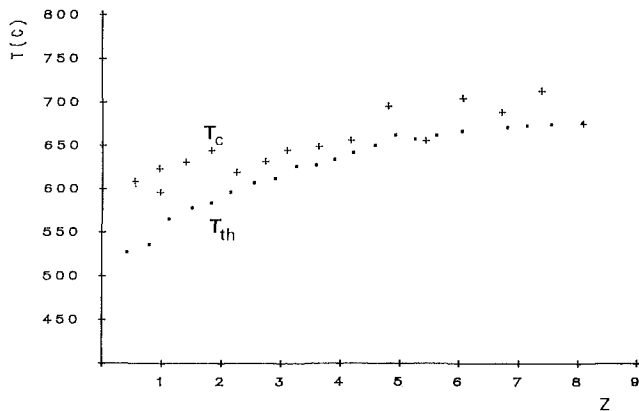


Fig. 6 Temperature profiles versus distance from the wall; fluidized bed (Probe 1), Al_2O_3 , $d_p = 2.36$ mm, $U_g = 2.8$ m·s⁻¹, $T_b = 700^\circ\text{C}$ (uncorrected temperature)

The "step shape" of the curve is certainly due to the rearrangement of the particles around the probe when it moves.

The comparison of Figs. 4 and 5 shows a similar gas temperature decreasing trend (indications of the thermocouple without correction); on the contrary, a clear difference appears when looking at the solid temperature distribution. For silicon carbide the temperature decrease is larger than 100°C through a depth of about four particle diameters, while for corundum the temperature variation is not significant.

Fluidized Bed. The results obtained with fluidized beds are plotted on Figs. 6 and 7 for beds of corundum and silicon carbide, respectively ($d_p = 2.36$ mm). The fluid velocity is closed to incipient fluidization condition ($U/U_{mf} \approx 1.2$). The radiometer indicates a small, but significant, variation of the solid temperature in both cases through a depth of about four particle diameters: about 100°C for Al_2O_3 and more than 150°C for SiC (for $1 \leq Z \leq 4$). The thermocouple indication is far from the gas temperature because of the direct heat transfer between the probe and the moving particles. Nevertheless, an obvious temperature decrease is measured. In order to detect a more realistic gas temperature, the protected thermocouple was used (Probe 2). Results are shown in Fig. 8 for a bubbling bed regime (without correction of color and thermocouple temperature). The variation of both solid and gas temperatures is confirmed: there exists a temperature variation of both fluid and solid phase near the water-cooled wall and a large temperature difference between the gas and the particles through a depth of about four particle diameters.

The temperature distributions near the cold heat exchange surface in 2.36 mm i.d. corundum and silicon carbide fluidized beds are compared in Figs. 7 and 8. Temperature decreases of

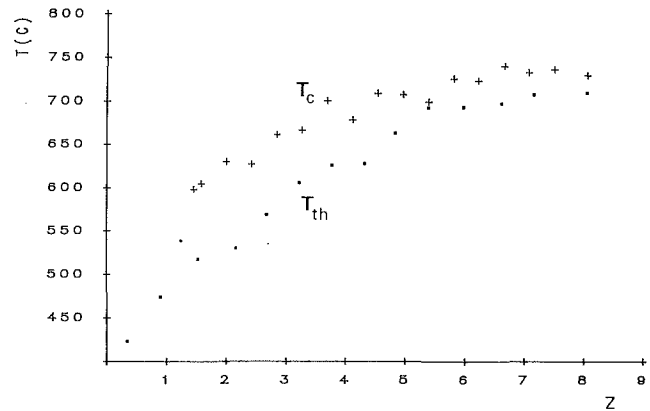


Fig. 7 Temperature profiles versus distance from the wall; fluidized bed (Probe 1); SiC, $d_p = 2.36$ mm, $U_g = 2.5$ m·s⁻¹, $T_b = 750^\circ\text{C}$ (uncorrected temperature)

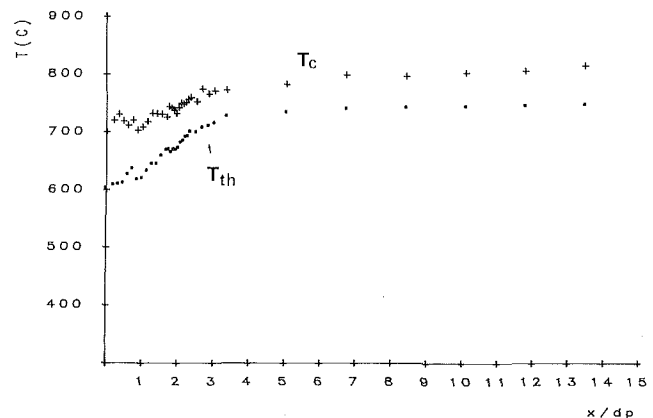


Fig. 8 Solid and gas temperature profile versus distance from the wall; fluidized bed (Probe 2); Al_2O_3 , $d_p = 2.97$ mm, $U_g = 3.6$ m·s⁻¹, $T_b = 746^\circ\text{C}$ (uncorrected temperature)

about 100 and 150°C are measured for corundum and silicon carbide, respectively.

4 Discussion

In order to make conclusions about the measurement validity, a discussion about the accuracy of the measurement method and about the effect of the probe on the result (intrusive method) has to be proposed.

Accuracy of the Radiometer Measurement. Looking at the temperature profiles, a significant temperature difference between the fluid and the particle is shown in the bed core. In order to explain this observation the main assumption of the radiometer signal treatment method must be discussed.

Equation (4) is verified if the particle emissivity at the two wavelengths $\lambda_1 = 1.3$ μm and $\lambda_2 = 1.5$ μm (ϵ_1 and ϵ_2 , respectively) are equal. Literature data about ϵ_1 and ϵ_2 for corundum range in a large domain; for example Touloukian and DeWitt's (1972) data range from 0.1 to 0.9 for ϵ_2 , with most of the results between 0.2 and 0.5 (at $\lambda_2 = 1.5$ μm). However, in spite of this discrepancy, these data indicate clearly that the emissivities at λ_1 and λ_2 could be different: variations as large as 20 percent are reported between $\lambda_1 = 1.3$ μm and $\lambda_2 = 1.5$ μm . The influence of this nongray effect on the temperature measurement is analyzed here after.

Using Wien's approximation, the color temperature variation due to the difference between ϵ_1 and ϵ_2 may be written as (Hernandez et al., 1991):

$$\frac{1}{T_c} = \frac{1}{T} - \ln \left[\frac{2 + \Delta\epsilon/\epsilon}{2 - \Delta\epsilon/\epsilon} \right] C_2 \left[\left\{ \frac{1}{\lambda_1} - \frac{1}{\lambda_2} \right\} \right]^{-1} \quad (6)$$

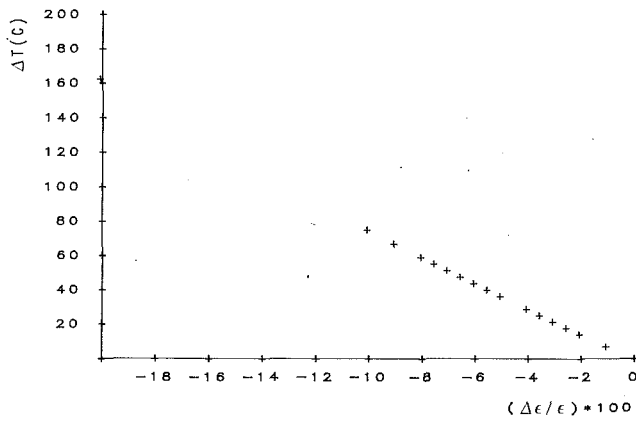


Fig. 9 Difference between the real particle temperature and the color temperature as a function of the relative emissivity difference $\Delta\epsilon/\epsilon$

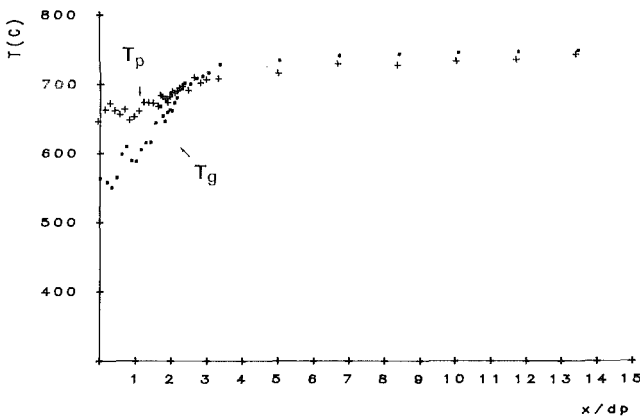


Fig. 10 Corrected gas and solid temperature profiles; fluidized bed, Al_2O_3 , $d_p = 2.97$ mm (see Fig. 8)

where: $\Delta\epsilon = \epsilon_2 - \epsilon_1$; $\epsilon = (\epsilon_1 + \epsilon_2)/2$; $C_2 = 1.4388 \cdot 10^{-2} \text{ m} \cdot \text{K}$; and where T is the real temperature of the particle and T_c the indication of the radiometer.

In order to illustrate the order of magnitude of the error as a function of the "nongray" behavior of the bed, the variation of $T_c - T$ as a function of $\Delta\epsilon/\epsilon$ is shown in Fig. 9 for $T_b = 750^\circ\text{C}$. For example, the temperature difference reaches 75°C for a variation of ratio of 10 percent.

Looking at the temperature profile in a fluidized bed far from the wall where gas and particle temperatures are equal, differences between the thermocouple and the radiometer indications range from 30°C to 45°C , corresponding to the ratio $\Delta\epsilon/\epsilon$ ranging from 4 to 6 percent. This calculation is coherent with the variation of the emissivity ϵ_1 and ϵ_2 between λ_1 and λ_2 given in the literature. As a consequence the radiometer indication can be corrected in order to account for this derivation from the basic hypothesis (gray medium).

Finally, the corrected profiles for gas (Eq. (5)) and solid (Eq. (6)) are given in Fig. 10 for the experimental conditions of Fig. 8. The particle temperature is corrected for a ratio $\Delta\epsilon/\epsilon$ equal to 0.04 identified by comparison of T_c , T_g , and T_b in the bed core. T_b is measured by a bare thermocouple, T_g by the protected thermocouple, and T_c by the radiometer (probe 2). The temperature fields may be characterized as follows:

- The gas and particle temperature are equal from the bed core to a depth of two particle diameters, accounting for the uncertainty of the particle temperature measurement: $\pm 15^\circ\text{C}$ (for $Z > 3$ the gas temperature is slightly larger than the solid temperature but this small difference is due to the measurement uncertainty). Nevertheless, a significant decrease of both T_p and T_g is observed at $Z = 3$.

- The total temperature variation of the particle phase is

about 100°C ; for the gas phase this decrease reaches 200°C . This observation is in agreement with the results shown in Fig. 6 for 2.36 mm i.d. corindon particle.

- There exists a thin zone of about $2 d_p$ in depth near the wall where the temperatures of the solid and the fluid are different, i.e., heat exchange between the phases is significant. For example at $Z = 1$, the solid and gas temperatures are the following: $T_p = 653^\circ\text{C}$ and $T_g = 586^\circ\text{C}$.

Influence of the Probe on the Results. The probe is intrusive; as a consequence, the medium thermal behavior may be modified by it. The diameter of the whole probe is larger than one particle diameter (but less than two) and during the tests, the alumina tube behaves like an insulator; therefore the solid cooling very near the wall cannot be detected because of the probe. We think that the depth of the disturbed region is equal to about one particle diameter ($z = 1$). Finally, the probe indicates the real solid temperature for distances from the wall larger than $z = 1$. For $Z < 1$, the radiometer indicates a particle temperature larger than the real temperature of the first row of particles adjacent to the wall because of the probe disturbance. This phenomenon can be observed, for example, in Fig. 10. A small increase of the particle temperature is measured for $Z < 1$ while an extra-polation of the particle gradient observed for $Z > 1$ gives a solid cooling 50°C larger than the measured one (i.e., a total temperature decrease of about 150°C instead of 100°C). Concerning the variation of the radiation view factor between the thermocouple and the surroundings, when the probe moves from the core to wall, a comment is necessary. When the probe reaches the first row of particles, the cooled wall may influence the thermocouple. The wall temperature was not measured but a rough heat balance in this zone indicates that the copper wall surface temperature is less than 100°C (the water temperature is about 30°C). In this case the thermocouple may be cooled by radiant loss. This effect was neglected because the view factor between the thermocouple and the wall is small due to the alumina tube (see Fig. 1) and the screening effect of the particles.

Effect of the Particles Thermophysical Properties on the Temperature Fields. Remember the main experimental results: for a fixed bed, a large gas temperature decrease is observed for both corundum and silicon carbide particles, but a significant variation of the solid temperature is measured only for SiC. For fluidized bed a significant gas and solid temperature decrease is observed near the wall but the variation is larger for the gas phase. Concerning the solid phase, the difference between the bulk temperature and the particle temperature near the wall is larger for SiC than for Al_2O_3 (see Figs. 6 and 7).

In our opinion this behavior is due to the thermal properties of silicon carbide. In such systems, radiation is an important heat transfer mode—33 percent of the total heat transfer at 1100 K, after Adams and Wely (1979)—and consequently the temperature field is influenced by the particle emissivity. It reaches 0.90 for silicon carbide, but the mean total emissivity of alumina is about 0.5 (large variations are reported by Touloukian and Dewitt (1972)); the silicon carbide losses by thermal emission toward the heat exchange wall are twice those of corundum. On the other hand, the thermal conductivities of both particles are different. The thermal conductivity of alumina porous system is about $0.75 \text{ W} \cdot \text{m}^{-1} \text{ K}^{-1}$ at 750°C (Luikov et al., 1968) whereas the conductivity of silicon carbide packed bed is $1 \text{ W} \cdot \text{m}^{-2} \text{ K}^{-1}$. Both emissivity and thermal conductivity increase the heat transfer efficiency between the wall and the SiC particles by comparison with corundum. The influence of the thermal properties cannot be separated from these experiments, and specific work must be done on this field of interest.

Temperature Distribution Inside the Particle. The last

question about the experimental results is related to the temperature distribution inside the particle: are the surface and the core of the particle at the same temperature? The Biot number gives an indication about this problem:

$$\text{Bi} = \frac{h_{gp}d_p}{\lambda_p} \quad (7)$$

For a heat transfer coefficient between the gas and the particle (h_{gp}) equal to $200 \text{ W}\cdot\text{m}^{-2}\text{K}^{-1}$, the Biot number ranges from 0.126 to 0.158 for Al_2O_3 and it is equal to 0.035 for SiC. These values indicate that the temperature may be considered as constant inside the particle in a first approximation, although a small difference may exist for corundum particles.

Conclusion

Gas and particle temperature fields are measured near a water-cooled surface in packed and fluidized beds (at incipient condition) using probes equipped with a fiber optic radiometer and a thermocouple. The main results are the following:

For a fixed bed, very large temperature variations are measured through a distance of about five particle diameters from the wall between $Z = 5$ and Z and 1. Temperature decreases as large as 400°C are shown. The profiles do not exhibit any significant difference with particle diameter variations (3.57 mm and 2.36 mm). Concerning the solid phase, the results depend on the particle thermal properties: No temperature variation is shown for corundum but a significant decrease of the solid temperature is measured for silicon carbide.

For fluidized beds, temperature gradients near the wall are shown for both gas and solid phases, but the total temperature decrease is smaller than for fixed beds. The temperature variations is observed through a depth of about three or four particle diameters, but the fluid and the solid temperatures become different only very near the wall, at about $Z = 1.5$. The temperature decrease in the solid phase is about 100°C and 150°C for Al_2O_3 and SiC respectively, but the real particle temperature cannot be measured for depths smaller than one particle diameter. The total gas temperature decrease reaches about 200°C .

These results are related to incipient fluidization conditions, and measurements versus gas velocity are needed in order to confirm these preliminary data and to study the temperature field as a function of fluidization regimes.

More experimental data are needed, but this paper indicates that several assumptions of classical models, based on negligible temperature variation near the heat exchange surface in large particle fluidized beds must be revised (Decker and Glicksman, 1981). In particular, it is shown that conduction (particle convection) cannot be neglected during wall-to-bed heat transfer, even in large particle fluidized beds, and that

solid-gas exchange is significant near the wall. In addition, the depth involved in the thermal perturbation seems to be larger than one particle diameter, where the variation of the bed voidage is very strong. Unfortunately, literature experimental or theoretical data about this type of temperature distribution are not available. A theoretical investigation of this problem is now in progress.

References

- Adams, R. L., and Welty, J. R., 1979, "A Gas Convection Model of Heat Transfer in Large Particle Fluidized Beds," *AIChE Journal*, Vol. 5, pp. 395-404.
- Decker, N. A., and Glicksman, C. R., 1981, "Conduction Heat Transfer at the Surface of Bodies Immersed in Gas-Fluidized Bed of Spherical Particles," *AIChE Symp. Series No. 208*, Vol. 77, pp. 341-349.
- Farber, P., and Kohne, H., 1987, "Zum Wärmetransport in eine durchströmten Kugelschüttung bei Temperaturen bis 1100°C ," *Wärme Gas Int.*, Vol. 36, pp. 453-459.
- Flamant, G., and Menigault, T., 1987, "Combined Wall-to-Fluidized Bed Heat Transfer, Bubbles and Emulsion Contribution at High Temperature," *Int. J. Heat Mass Transfer*, Vol. 30, pp. 1803-1812.
- Flamant, G., Flitris, Y., and Gauthier, D., 1990, "Heat Transfer to Walls in a High Temperature Fluidized Bed of Group II Particles," *Chem. Eng. Processes*, Vol. 27, pp. 175-184.
- Govindarao, V. M. H., and Froment, G. F., 1986, "Voidage Profiles in Packed Beds of Spheres," *Chemical Engineering Science*, Vol. 41, Vol. 3, pp. 533-539.
- Hernandez, D., Olalde, G., and Py, J., 1988, "Dispositif de mesure de rayonnement notamment pour la mesure de température," French Patent No. 8814757, Nov.
- Hernandez, D., Ciaurritz, C., and Olalde, G., 1991, "Détermination de l'émissivité à haute température à l'aide de systèmes photoniques équipés d'hémisphères réflecteurs," *J. Phys. III France*, Vol. 1, pp. 1575-1586.
- Korelev, V. N., and Syromyatnikov, N. I., 1971, "Structure of a Fixed and a Fluidized Bed of Granular Material Near an Immersed Surface," *J. Engng. Phys.*, Vol. 21, pp. 1475-1478.
- Luikov, A. V., Shashkov, A. G., Vasiliev, L. L., and Fraiman, Yu. E., 1968, "Thermal Conductivity of Porous Systems," *Int. J. Heat Mass Transfer*, Vol. 11, pp. 117-140.
- Mazza, G., and Barreto, G., 1988, "The Gas Contribution to Heat Transfer Between Fluidized Beds of Large Particles and Immersed Surfaces," *Int. J. Heat Mass Transfer*, Vol. 31, pp. 603-614.
- Saxena, S. C., and Ganzha, V. L., 1984, "Heat Transfer to Immersed Surfaces in Gas-Fluidized Beds of Large Particles and Powder Characterization," *Powder Technology*, Vol. 39, pp. 199-208.
- Smith, J. M., 1973, "Heat Transfer in Fixed Bed," *The Chemical Engineering Journal*, Vol. 5, pp. 109-116.
- Tien, C. L., 1988, "Thermal Radiation in Packed and Fluidized Beds," *ASME JOURNAL OF HEAT TRANSFER*, Vol. 110, pp. 1230-1240.
- Tien, C. L., and Hunt, M. L., 1987, "Boundary-Layer Flow and Heat Transfer in Porous Beds," *Chem. Eng. Process ZI*, pp. 53-63.
- Touloukian, Y. S., and Dewitt, D. P., 1972, "Thermal Radiative Properties, Nonmetallic Solids," *Thermophysical Properties of Matter*, Vol. 8, Ed. IFI-Plenum.
- Vafai, K., Alkire, R. L., and Tien, C. L., 1985, "An Experimental Investigation of Heat Transfer in Variable Porosity Media," *ASME JOURNAL OF HEAT TRANSFER*, Vol. 107, pp. 642-647.
- Ziolowska, I., Ziolowski, D., and Flejter, B., 1989, "Effects of Organized Structures of Beds Packed Within Tubular Flow Apparatus on the Homogeneity of the Radial Distribution of Fluid Velocity," *Chem. Eng. Process*, Vol. 25, pp. 141-151.

Turbulent Heat Transfer Augmentation and Friction in Periodic Fully Developed Channel Flows

T.-M. Liou
Professor.

J.-J. Hwang
Graduate Student.

Power Mechanical Engineering Department,
National Tsing Hua University,
Taiwan

Measurements are presented of the distribution of average friction factors (f) as well as local and average (Nu) heat transfer coefficients for fully developed channel flows with two rib-roughened opposite walls. The temperature measurements were made by using both a laser holographic interferometer and thermocouples. In addition, the reattachment length was determined by flow visualization. The Reynolds number (Re) was varied from 5.0×10^3 to 5.4×10^4 ; the rib pitch-to-height ratios (Pi/H) were 10, 15, and 20; and the rib height-to-hydraulic diameter ratios (H/De) were 0.063, 0.081, and 0.106. The detailed results allowed the peaks of heat transfer augmentation and the regions susceptible to hot spots to be located and allowed the relative contribution of the rib surface and the channel wall to the heat transfer augmentation to be determined. Moreover, relative to a smooth duct, the enhancement of both Nu and f at various Re , Pi/H , and H/De was documented in detail. Furthermore, compact correlations in terms of Re , Pi/H , and H/De were developed for both Nu and f .

Introduction

Pipes or channels containing ribs are often used for heat transfer augmentation (Webb et al., 1971; Arvizu and Moffat, 1981; Han et al., 1985; Metzger et al., 1990). In gas turbine blade cooling design, repeated rib-turbulators are cast on two opposite walls of the internal cooling passages of the nearly rectangular cross sections in order to enhance the removal of heat from the blade external surfaces that are directly exposed to the flow of hot gases. Moreover, to improve thermal efficiency and power density, the trend in modern aeroengine design is toward high gas outlet temperature from the combustor; heat transfer augmentation of turbine cooling channels becomes, therefore, more and more critical. Information relevant to the local as well as average heat transfer and fluid flow characteristics is highly desired. The present paper focuses on turbulent heat transfer augmentation and friction in rectangular channels with repeated rib pairs.

For the sake of brevity, only the most relevant work will be cited below. Burggraf (1970) reported the results of turbulent air flow in a square duct with two opposite ribbed walls. The wall temperature distribution was measured by using thermocouples. Similar trends were obtained for three channel entrance geometries. The augmentation of the average Nusselt number and friction factor was approximately 2.38 times and 8.6 times that of fully developed smooth duct flows, respectively. However, only one particular rib geometry (i.e., $Pi/H = 10$, $H/De = 0.055$, and $\alpha = 90$ deg) was tested. Moreover, the friction factor was not reported in all tests. Han (1984) systematically investigated the effects of the rib pitch-to-height ratio ($Pi/H = 10, 20$, and 40) and the rib height-to-equivalent diameter ratio ($H/De = 0.021, 0.042$, and 0.063) on the heat transfer coefficient and the friction factor of fully developed turbulent air flow in a square duct that had two opposite ribbed walls. The rib angle-of-attack was kept at $\alpha = 90$ deg. The temperature distribution was also measured by thermocouples. The results showed that the Stanton number and the average

friction factor of the ribbed duct are about 1.5 to 2.2 times and 2.1 to 6.0 times, respectively, those of the smooth duct for the range of the test data. Later, Han et al. (1985) further investigated the effect of α on the average heat transfer coefficients and pressure drop in the same duct flow. Rowley and Patankar (1984) performed a numerical study for the periodic fully developed laminar flow and heat transfer in tubes with repeated internal circumferential fins ($\alpha = 90$ deg). An important finding made by them was that, in laminar flow, the presence of the fins often decreases the heat transfer coefficient rather than augmenting it. The studies of Sparrow and Tao (1984) were based on the local mass transfer measurements in rectangular channels with high aspect ratios (6.4 and 12.8) by using the naphthalene sublimation technique. The rib turbulators are of circular cross section ($\alpha = 90$ deg). It was found that, relative to a rib-free duct, the presence of periodic circular ribs at both principal walls yielded up to a threefold increase in the Sherwood Number (Sh) at $Re = 1.0 \times 10^4$ and up to 2.4-fold increase at $Re = 4.1 \times 10^4$. The same measurement technique was adopted by Molki and Mostoufizadeh (1989) for study of turbulent heat transfer in rectangular ducts with staggered baffle blockages ($\alpha = 90$ deg). However, the surface of the baffles was not covered with naphthalene, that is, the contribution of additional surface area due to the presence of the baffles to the heat transfer enhancement was not considered in their study.

In view of the foregoing discussion, it is evident that a systematic experimental study of turbulent heat transfer in a rectangular duct with two opposite ribbed walls using laser holographic interferometry, in contrast to the aforementioned thermocouple and naphthalene sublimation techniques, would be worthwhile. The noninvasive holographic interferometry is mostly used in studying thermal diffusion and free convection phenomena. In this paper it was applied to a forced convection study. Furthermore, to resolve time variations of the temperature distribution and scales of eddy motion, which have not been achieved previously in the rib pair-roughened channel, the holographic interferometry was operated in real-time mode. Additionally, the emphasis was placed on the effects of Re , Pi/H , and H/De on the heat transfer coefficients and friction

Contributed by the Heat Transfer Division for publication in the JOURNAL OF HEAT TRANSFER. Manuscript received by the Heat Transfer Division July 16, 1990; revision received April 1, 1991. Keywords: Augmentation and Enhancement, Finned Surfaces, Turbines.

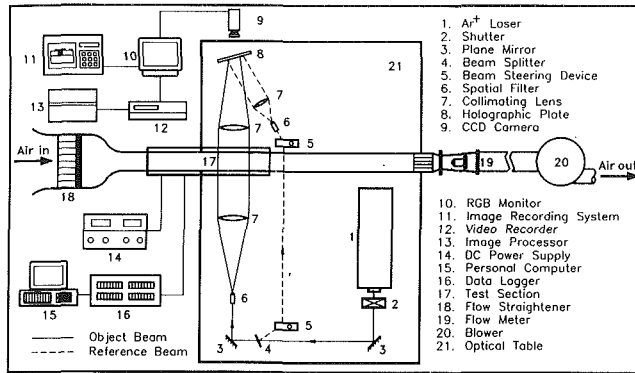


Fig. 1 Schematic drawing of overall experimental system

factors in the periodic fully developed flow region. In particular, larger rib heights $H/De = 0.063, 0.081, \text{ and } 0.106$ were selected so that the results obtained in this study and those reported in previous work (Han, 1984) ($H/De = 0.021, 0.042, \text{ and } 0.063$) may complement each other. Other objectives of the present study were (1) to locate the peaks of heat transfer enhancement and the region susceptible to the hot spots, since the latter has not been previously reported; (2) to determine the relative contribution of the rib surface and the channel wall to the heat transfer augmentation, since it has been previously done for laminar flow only and since previous studies of the turbulent flow fields in a rectangular duct with one rib pair (Liou and Kao, 1988) and two rib pairs in tandem (Liou et al., 1990) reveal the presence of turbulent-kinetic-energy peaks near the rib top surface and near the reattachment point, and (3) to develop compact correlations in terms of rib and flow parameters for both the average heat transfer coefficient and friction factor.

Experimental Apparatus and Conditions

Experimental Apparatus. The flow system and laser holographic interferometry setup are shown in schematic form in Fig. 1. Air at room temperature was drawn into the test section

through a flow straightener and four screens in the settling chamber and a 10:1 contraction by a 3 hp blower at the downstream end. The air then flowed through the repeated rib pairs, a flow straightener, a rotameter, and a bellows, and was exhausted by the blower.

Two techniques, thermocouple probing and laser holographic interferometry, were used to measure the local temperature of the air in the test section. T-type thermocouples, made of 0.25-mm-dia wires, were used for temperature traverses across the test section and for wall temperature measurements. The positioning accuracy of the thermocouple bead was ± 0.1 mm. In the case of laser holographic interferometry, the temperature measurements were nonintrusive. After passing through a shutter, the beam of a 3W argon-ion laser (514.5-nm wavelength) was split and expanded into two beams of 150-mm diameter with plane wave fronts. The object beam passed through the test section, and the reference beam bypassed it. The two expanded beams then interfered on a hologram plate. The phase hologram represented a diffraction grating in which the comparison beam was stored. The comparison beam described the state in which the ribbed walls were not heated. As the ribbed walls were heated, the expanded object beam would be distorted as a result of the refractive index field generated by local temperature variation in the test section. The distorted object beam passed through the hologram, and interfered behind it continuously with the comparison beam reconstructed by the reference beam. Thus an instantaneous interference field, at infinite-fringe setting, formed behind the hologram plate and indicated approximately the instantaneous temperature field of the enhanced internal cooling passage of the simulated turbine blade. The entire test section was mounted on a modified milling machine with four vibration-isolation mounts to allow successive scanning of the expanded object beam.

A combination of the holographic film plate holder and liquid gate was used to provide in-place development of film plate as required for real time holographic interferometry. The photographic emulsion 8E56, made by Agfa-Gevaert Limited, was found to be a suitable material for the present work. Through a CCD camera, the instantaneous interference field was monitored on a multisync monitor and recorded on a VHS

Nomenclature

A_t = total heat transfer area in one pitch	Q_{rib} = rib heat transfer in one pitch	X = axial coordinate ($X = 0$ at inlet reference, Fig. 2)
A_{rib} = rib heat transfer area in one pitch	Q_t = total heat transfer in one pitch	X_N = axial coordinate ($X_N = 0$ at rib real edge, Fig. 2)
B = half height of channel	q'' = heat flux supplied by thermocouple foil	X_h = axial coordinate for heated test section (Fig. 2)
C = Gladstone Dale constant	Re = Reynolds number = $U \cdot De / \nu$	Y = transverse coordinate, Fig. 2
c_p = specific heat at constant pressure	S = fringe order	Y^+ = dimensionless transverse displacement = $Y \cdot \sqrt{(\tau_w / \rho)} / \nu$
De = hydraulic diameter	Sh = Sherwood number	Z = spanwise coordinate, Fig. 2
f = average friction factor	T_b = local bulk mean temperature of air	α = rib angle of attack
G = mass flux = ρU	\bar{T}_b = average bulk mean temperature of air	ρ = air density
g = gravitational acceleration	T_w = local wall temperature	λ = wave length of laser light
H = rib height	\bar{T}_w = average wall temperature	ν = kinetic viscosity of air
k = turbulent kinetic energy	T^+ = dimensionless temperature = $(T_w - T) \rho c_p u^* / Q''$	τ_w = apparent wall shear stress = $(\Delta P / \Delta L) De / 4$
L_h = wetted length in one pitch	t = time	
ΔL = channel length for fully developed pressure drop	U = mean velocity	
Nu = local Nusselt number, Eq. (3)	u^* = friction velocity = $\sqrt{(\tau_w / \rho)}$	
\bar{Nu} = average Nusselt number, Eq. (4)	W = half-width of channel	
Pi = rib pitch	w = rib width	
ΔP = pressure drop across the fully developed test section	W = quantity of heat given to air from entrance to the considered cross section of the duct	
Q'' = heat transfer rate per unit area		

Subscripts

i = fringe order index
N = rib index
r = reference
w = wall

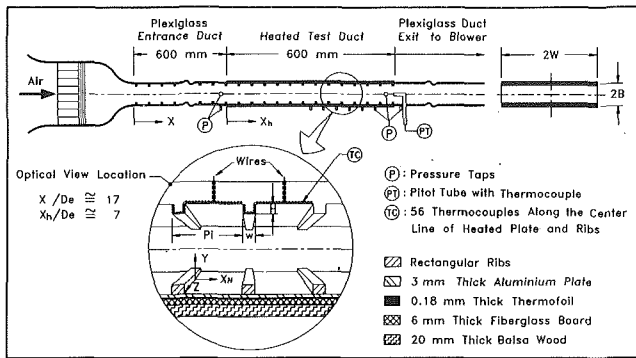


Fig. 2 Sketch of configuration, coordinate system, and dimensions of the test section

videocassette recorder for storage and further image processing.

Additionally, a microdifferential transducer (Kyowa PDL-40B, ± 0.1 percent) was used for pressure loss measurements across the test duct (Fig. 2). To measure static pressure, the transducer was connected to each pressure tap on the duct wall. The measured pressure signal was subsequently amplified by a Kyowa WGA-200A amplifier and read from a digital readout.

Test Model. The configuration, coordinate system, and dimensions of the test section are sketched in Fig. 2. The test channel was 1200 mm long and had a rectangular cross section 160×40 mm² (X - Y plane), i.e., an aspect ratio of 4:1. The top and bottom walls of this channel, consisting of heated aluminum plates, were 600 mm long and covered by square ribs of size 5.2×5.2 mm² and 52 mm apart for the baseline case. The two ribbed walls were made by gluing square brass ribs to the 3-mm-thick aluminum plates, as shown in Fig. 2. Thermofoils of thickness 0.18 mm were adhered uniformly between the aluminum plate and a 6-mm-thick fiberglass board to insure good contact. Each thermofoil could be independently controlled by the 60-W d-c power supply. Additionally, a 20-mm-thick sheet of balsa wood was glued to the above fiberglass board to insure good insulation. The thermal resistance associated with the glue, 0.13 mm thick or less, found at each of the above mentioned interfaces is negligible (Han, 1984).

The side walls of the entire heated test duct were made of plexiglass plates to provide optical access for laser holographic interferometry measurements. The unheated entrance duct was also made of plexiglass plates and was ribbed over its 600-mm length (Fig. 2). This entrance duct served to establish hydrodynamically fully developed flow at the entrance to the heated duct, since the previous work of Liou and Lin (1988) reported that both mean-velocity and turbulent intensity profiles attained hydrodynamic fully developed condition after 480 mm in the rib-roughened section.

Experimental Conditions. The room temperature was kept at $24 \pm 1.0^\circ\text{C}$. The local wall temperature read from thermocouple output was rather uniform, with a scatter of $\pm 1.5^\circ\text{C}$ about the mean. Generally speaking, the heat input into the fluid is highly localized, due to the presence of ribs, and the idealized circumstance of perfectly isothermal or isoflux over the heated wall, with uniform heat flux over the thermofoil, clearly does not arise in the experiments. A similar observation was also made by Kang et al. (1990) for heat transfer from an isolated heat module on a horizontal plate. The majority of temperature measurements were done for the region between the 9th and 10th heated ribs ($X_h/De \cong 7$, Fig. 2) where the air flow was thermally fully developed, as reported by the previous

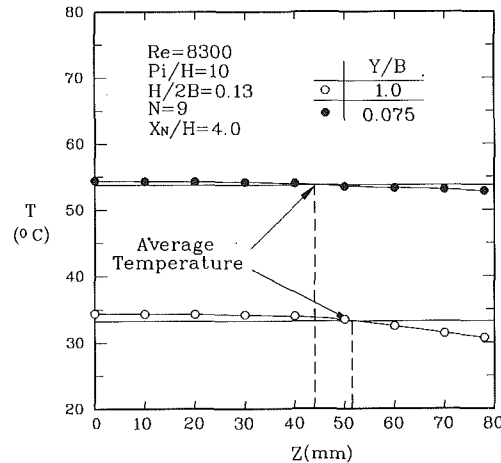


Fig. 3 Temperature distribution along the laser-beam path

work (Han, 1985) in which the flow was in the thermally fully developed region after $X_h/De \geq 5$. The thermal periodicity will be further verified using the present data. The region of optical view was instrumented with 56 thermocouples distributed along the centerline ($Z = 0$) of the heated plate and ribs for wall temperature measurements, as shown in Fig. 2, and was also instrumented with thermocouple probes through the side wall to allow temperature measurements of the air flow at 216 locations. For the purpose of comparing with holographic interferometry data and checking on the two dimensionality of spanwise temperature profiles of the air flow shown in Fig. 3, the temperature mapping by using thermocouple probes was made along a longitudinal plane ($Z/B = 2.5$) located 30 mm from the side wall and the scatter in the spanwise direction was less than 6 percent of the channel spanwise average temperature. Note that the drop in the temperature near the side wall (Fig. 3) was due to the end effects. By using the interferometry error analysis suggested by Goldstein (1976), it was found that the resulting error in the fringe (or temperature) shift due to the end effects was about 8 percent.

In the test duct, eight pressure taps along the bottom ribbed wall and two along the smooth side wall, as shown in Fig. 2, were used for the static pressure drop measurements. Pressure taps were located at $X_N/H = 7.0$ of each pitch (i.e., $2H$ upstream of the rib and $2.9H$ downstream of the reattachment point). Further, to study the effects of various parameters on the fluid flow and heat transfer characteristics of ribbed channels, the Reynolds number (Re) in this study, based on the channel hydraulic diameter and bulk mean velocity, extended from 5.5×10^3 to 5.4×10^4 ; the ratios of rib pitch to height (Pi/H) were 10, 15, and 20; the rib-to-channel-height ratios ($H/2B$) were 0.10, 0.13, and 0.17; and the ratios of the rib height to channel hydraulic diameter (H/De) were 0.063, 0.081, and 0.106.

Data Reduction

The friction factor in fully developed channel flow can be determined by measuring the pressure drop across the flow channel and the mass flow rate of the air. The average friction factor can then be calculated from

$$f = \frac{\Delta P}{G^2/2\rho g} \cdot \frac{De}{4\Delta L} \quad (1)$$

In the present investigation, the average friction factor was obtained under the adiabatic conditions. The maximum uncertainty in f was estimated to be less than 7.1 percent for Reynolds number greater than 5500 by using the uncertainty estimation method proposed by Kline and McClintock (1953).

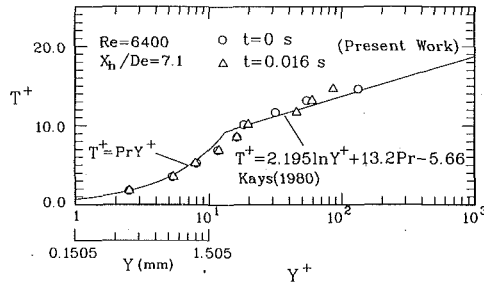


Fig. 4 Universal temperature profiles in the near wall region of a smooth duct

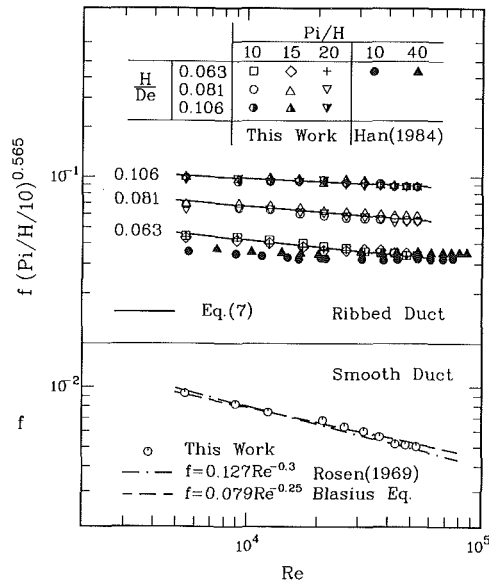


Fig. 5 Fully developed friction factors versus Reynolds number

To determine the temperature field described by the interferogram, the equation of interferometry for a two-dimensional incompressible flow is as follows (Hauf and Grigull, 1970):

$$S_i - S_{i-1} = \frac{2T_r \rho_r C W}{\lambda} \left(\frac{1}{T_{S_i}} - \frac{1}{T_{S_{i-1}}} \right) \quad (2)$$

where $S_i - S_{i-1}$ is the fringe shift, S_i the fringe order, C the Gladstone Dale constant, and ρ_r the air density evaluated at reference temperature T_r . By setting $S_i - S_{i-1} = 1$, the temperature differences $T_{S_i} - T_{S_{i-1}}$ associated with each fringe are determined. Knowledge of at least one temperature and the temperature difference in the region of interest will provide the approximate heat transfer feature from wall to air.

By assuming that a thin layer of air is stationary next to the wall, and hence that the heat transfer in this region is by conduction only, the local Nusselt number can be determined from the expression:

$$\text{Nu} = \frac{De}{(T_w - T_b)} \cdot \left(\frac{dT}{dy} \right)_w \quad (3)$$

where T_w , the local wall temperature of the heated plate and ribs, was read from the output of the thermocouples. The local bulk mean air temperature, T_b , was calculated from an energy balance and is defined as $T_b = T_{in} + \dot{W}/(Gc_p)$. It was also checked by measuring the bulk mean air temperatures entering and leaving the heated test section and assuming a linear air temperature rise along the flow duct. The difference between the two measurements was estimated to be less than 6 percent.

The local wall-temperature gradient $(dT/dy)_w$ was determined by curve fitting, based on the least-square method, through the near wall values for temperature and fringe shift. The Nu thus obtained was estimated to have an uncertainty less than 6.5 percent. Figure 4 is a comparison between present interferometric data and the well-known universal profile in the near-wall flow region of a smooth duct. Reasonable agreement between the interferometric profiles and the time-averaged theoretical profile, in particular the nearly identical results for $Y^+ < 10$, is demonstrated and supports the present experiment and extrapolation procedures. The apparent wall shear stress τ_w in the definition of $Y^+ = Y \cdot \sqrt{\tau_w / \rho} / \nu$ in Fig. 4 was obtained from the measured pressure drop through the force balance $\tau_w = (\Delta P / \Delta L) De / 4$. Note that ΔP is the average value. In fact, during the experiments the magnitude of pressure drop was nearly the same on the side and bottom walls. Further, the average Nusselt number was defined as (Rowley and Pantankar, 1984)

$$\bar{\text{Nu}} = \frac{\bar{h} De}{k_f} = \frac{De}{L_h (\bar{T}_w - \bar{T}_b)} \int_0^{L_h} \left(\frac{dT}{dy} \right)_w dx \quad (4)$$

In Eq. (4) the average heat transfer coefficient \bar{h} was evaluated from

$$\bar{h} = \frac{q''_{\text{conv}}}{\bar{T}_w - \bar{T}_b} = \frac{\int_0^{L_h} \left[k_f \left(\frac{dT}{dY} \right)_w \right] dX}{L_h (\bar{T}_w - \bar{T}_b)} \quad (5)$$

where L_h was the wetted length of heated surface and roughness, \bar{T}_w was the average wall temperature in one pitch, and average bulk mean air temperature, \bar{T}_b , was evaluated as $\left(\int_0^{L_h} T_b dx \right) / L_h$. The maximum uncertainty of $\bar{\text{Nu}}$ was estimated to be less than ± 9.6 percent. It is worthwhile to note that the validity of the definition of $\bar{\text{Nu}}$ in Eq. (4) was not confined to constant temperature surfaces. The average Nusselt number can be checked by the energy balance. That is

$$\bar{\text{Nu}} = \frac{q''_{\text{conv}} De}{(\bar{T}_w - \bar{T}_b) k_f} = \frac{(q'' - q''_{\text{loss}}) De}{(\bar{T}_w - \bar{T}_b) \cdot k_f} \quad (6)$$

Here, q'' was the wall heat flux supplied by the electrical input. The convective heat flux, q''_{conv} , was estimated by subtracting the heat loss (q''_{loss}) from the supplied electrical input (q''). Thermal conductive loss along the flow direction near the start and the end of heating and from the insulation material (fiberglass board and balsa wood) of the top and bottom heated plates was estimated by measuring the wall temperatures and assuming one-dimensional heat flow, and was found to be 0.5 and 12.8 percent, respectively. Heat loss from the side walls (plexiglass) of the flow passage material was also calculated by applying the natural convection between them and atmosphere, and was about 4 percent. The values of mean Nusselt number obtained by these two methods were found to agree closely with each other.

Results and Discussion

Average Friction Factor. The Reynolds number dependence of average friction factor for fully developed duct flows with different rib heights and pitches is depicted in Fig. 5, where the results in the same duct with smooth walls are also included for comparison. All the curves show a decrease of f with increasing Re. For the smooth duct, the distribution of f measured in this study coincides well with the theoretical expressions correlated by Blasius (Rohsenow and Choi, 1969). The maximum deviations of the measured data from the former and the latter correlations are 3 and 4 percent, respectively. Moreover, a comparison of f distributions between the smooth

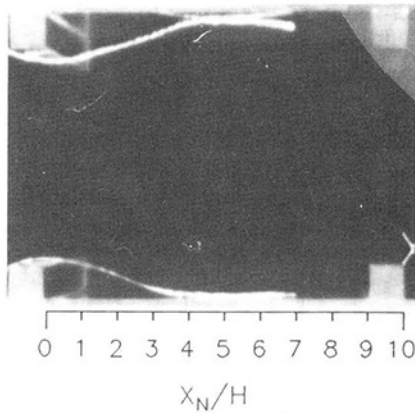


Fig. 6 Photograph of separating bubble and reattachment length

Table 1 Coefficients C_1 , C'_1 , m , and n in Eq. (7)

H/De	C_1	C'_1	m	n	Deviation, percent
0.063	0.5603	0.1526	0.1402	0.5655	2.2
0.081	0.7139	0.1943	0.1129	0.5642	1.4
0.106	0.9069	0.2469	0.0953	0.5661	2.8

duct flow and the ribbed duct flow clearly reveals the large friction loss caused by the existence of the ribs; the extent of increased toll in friction increases with rib height and is approximately factors of 4–6, 6–10, and 10–17, for $H/De = 0.063, 0.081,$ and $0.106,$ respectively, for the range of Re tested. This trend is physically reasonable and is due to the increased blockage of the flow passage with increasing rib height.

The effects of Reynolds number ($5.5 \times 10^3 \leq Re \leq 5.4 \times 10^4$) and rib pitch ($Pi/H \geq 10$) on the average friction factor can be correlated by the following expression:

$$f = C_1 \cdot Re^{-m} \cdot (Pi/H)^{-n} = C_1 \cdot Re^{-m} \cdot (Pi/H)^{-0.565} \quad (7a)$$

or

$$f = C'_1 \cdot Re^{-m} \cdot (Pi/H/10)^{-0.565} \quad (7b)$$

where $C_1, C'_1, m,$ and n are constants for a given rib height and are listed in Table 1 for various H/De . Equation (7) is plotted as straight lines of $f(Pi/H/10)^{0.565}$ versus Re in Fig. 5 for different rib heights. The average deviations in Eq. (7) from the measured data are $\pm 2.2, \pm 1.4,$ and ± 2.8 percent, respectively, for $H/De = 0.063, 0.081,$ and 0.106 . It is worth mentioning that an inclusion of the H/De effect in Eq. (7) based on two rib heights would lead to a correlation having a form of $f = C_1 Re^{-m} (Pi/H/10)^{-n} (H/De/0.063)^q$ with ± 13 percent maximum deviation from the measured data; however, a deviation as high as ± 32 percent resulted from a correlation based on three rib heights. It is for this reason that the parameter H/De was not included in Eq. (7). Sparrow and Tao (1984) in a similar study ($1 \times 10^4 \leq Re \leq 4.5 \times 10^4$) did not include H/De in their correlation, either. They gave a correlation $f = C_1 Re^{-m}$ where C_1 and m vary with H/De and Pi/H .

From Fig. 5 and Table 1, it is seen that the slope m of the $f(Pi/H/10)^{0.565}$ versus Re curve becomes flatter with increasing rib height. This is also physically reasonable since the cross-sectional blockage increases with rib height and, therefore, the inertial loss relative to friction loss is more significant as H/De increases; the result illustrates a flatter curve for the higher H/De . As for the effect of rib pitch, Eq. (7) indicates that f decreases with increasing Pi for a given rib height H . This trend can be explained as follows. Since the sizes of the recirculating zones immediately downstream and upstream of the rib vary slightly as $Pi/H \geq 10$, approximately $(4.1 \pm 0.2)H$

for the former case as shown by flow visualization using a light thread (Fig. 6), the pressure loss generated by the sudden expansion and sudden contraction due to the presence of the two opposite ribs for $Pi/H = 10$ is approximately the same as for $Pi/H = 15$ and $Pi/H = 20$. Moreover, the increased flow-redevelopment distance for larger Pi/H has only minor contribution to the pressure loss. The value of f is, therefore, dominated by the value of L_h , which increases with increasing Pi and appears in the denominator of Eq. (1). The above discussion explains why the average friction factor decreases with increasing rib pitch, as revealed by Eq. (7).

At the dimensionless rib height of $H/De = 0.063$, a comparison of the present data with Han's data (1984) is also made in Fig. 5. The aspect ratios of the present channel and Han's channel are 4:1 and 2:1, respectively. Although the different aspect ratios result in different slopes m between the two works, the qualitative trend is in agreement, that is, the average friction factor first decreases and subsequently approaches an approximately constant value as the Reynolds number increases. For the present data, the curve tends to approach horizontal approximately as $Re \geq 4.5 \times 10^4$. This result is also consistent with the Moody chart, which shows a transition of friction curve to a horizontal line approximately as $Re \geq 4.5 \times 10^4$ for $H/De = 0.05$.

Temperature Distributions. Some examples of holographic interferograms of periodic fully developed channel flows are displayed in Fig. 7. The typical temperature differences associated with each fringe shift derived from the cutout region ($X_N/H = 0.5$) in Fig. 7(a) are listed in Table 2. It is seen from Figs. 7(a) and 7(b) that the interference fringes in the near rib region are thin and the fringe spacings are narrow, indicating that the turbulence eddies are small in the flow region close to the rib and that the heat flux is large due to steep temperature gradients, whereas the fringes far away from the rib are thick and the spacings are wide, indicating that the turbulence eddies are large in the core flow region and the temperature gradients are small. A comparison of Fig. 7(a) with Fig. 7(b) further reveals the effect of Reynolds number on the temperature distribution near the rib. As the Reynolds number is increased from 6.4×10^3 to 1.02×10^4 , the acceleration of the flow through the passage between the two opposite ribs is increased and in turn the forced convection is enhanced, as shown by the thinner thermal boundary layer on the rib top at higher Reynolds numbers. The secondary thermal boundary layer thickness at the trailing edge of the top surface of the rib is estimated as $Y^+ = 20$, which is calculated from the apparent shear stress of ribbed duct (Webb et al., 1971) by measured average pressure drop through the force balance as previously made in the smooth duct (Fig. 4). It should be pointed out that the value of ΔP is almost the same when measured from the pressure taps, either on the ribbed wall or on the smooth side wall. Figures 7(c) and 7(d) are examples of full-field interferograms taken at different instants and exhibit the time dependence feature of measured line integrals of temperature in the core flow region where the turbulence length scale is of the same order as the optical path length across the test section. However, in the flow regions close to the ribs and channel walls the flow patterns (i.e., line integral measurements) vary little with time since turbulence eddies closed to the ribs and walls are small compared with the total disturbed optical path.

The temperature profiles at $X_N/H = 1$ and $X_N/H = 7$, which are two axial stations across the separation bubble immediately downstream of the rib and across the redeveloping flow region, respectively, are also interesting and, therefore, are plotted in Fig. 8. The different open symbols represent temperature distributions at different instants calculated from the corresponding interferograms. In the redeveloping flow region, the profiles at $X_N/H = 7$ have very steep gradients near the channel wall, indicating the existence of a thermal

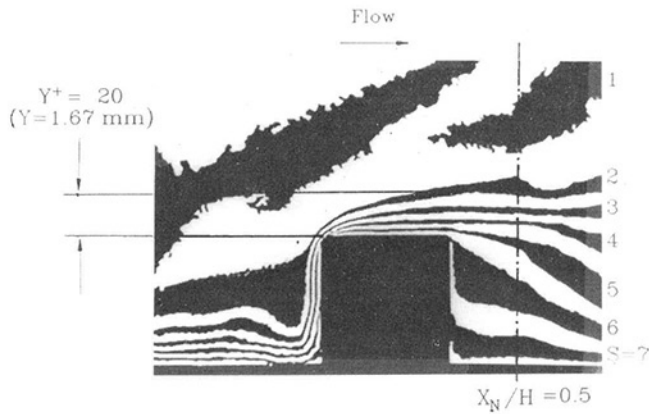


Fig. 7(a) $Re = 6400$, $Pi/H = 10$, $H/De = 0.081$ ($\times 6$ magnification of near rib region)

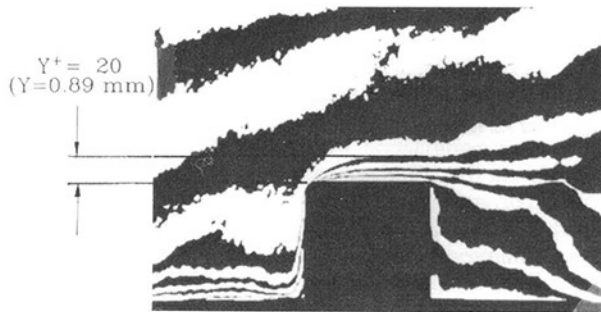


Fig. 7(b) $Re = 10200$, $Pi/H = 10$, $H/De = 0.081$ ($\times 6$ magnification of near rib region)



Fig. 7(c) $Re = 8300$, $Pi/H = 10$, $H/De = 0.081$, 0 s ($\times 1$ full field)

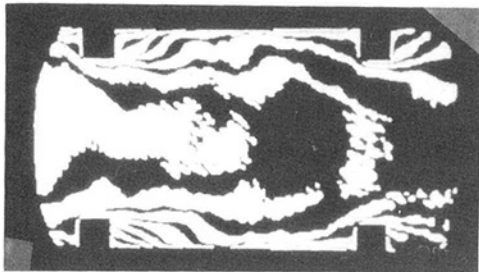


Fig. 7(d) $Re = 8300$, $Pi/H = 10$, $H/De = 0.081$, 0.033 s ($\times 1$ full field)

Fig. 7 Examples of holographic interferograms of periodically fully developed channel flows

boundary layer (also see Fig. 7), whereas the profiles at $X_N/H = 1$ do not exhibit a thermal boundary layer due to the presence of recirculating flow. It is worthwhile to note that all the profiles within the separation bubble (approximately $Y/H < 1$) and within the thermal boundary layer tend to collapse into one curve, indicating again the feature of time independence of the line average due to the small-scale turbulent motion

Table 2 Temperature differences associated with each fringe shift derived from cutout region in Fig. 7(a)

ΔS (fringe shift)	Y (mm)	ΔT ($^{\circ}\text{C}$)	T ($^{\circ}\text{C}$)
7	0.743	4.43	61.60
6	2.715	4.31	57.17
5	4.828	4.21	52.86
4	5.664	4.09	48.65
3	6.277	3.99	44.56
2	7.057	3.90	40.57
1	10.029		36.67

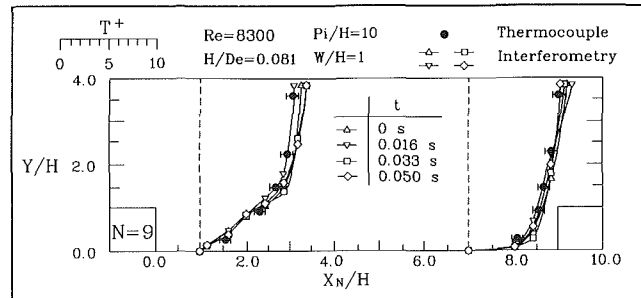


Fig. 8 Temperature profiles measured by interferometry and thermocouple probing

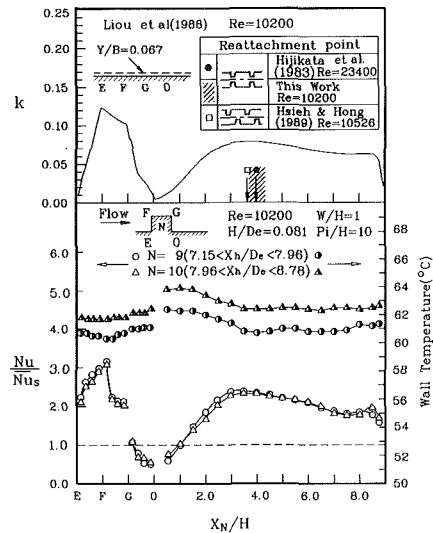


Fig. 9 Streamwise distributions of local Nusselt number, turbulent kinetic energy, and wall temperature

in these regions. Outside the separation bubble and thermal boundary layer, however, Fig. 8 shows that the instantaneous temperature profiles are quite time dependent with a maximum variance of about 10 percent of the temperature difference between the wall and channel centerline, and that the turbulent motions are large scale, as addressed in the previous section.

The solid circle in Fig. 8 represents the time-averaged mean temperature distribution probed by using thermocouples. A comparison of this thermocouple measured temperature distribution with the instantaneous temperature distribution measured by holographic interferometry reveals that a fluctuation can be as high as 28 percent of the mean value. A comparison between the mean temperature profile measured by thermocouples and that calculated from 50 instantaneous interferograms is also worthwhile, and reasonable agreement, with a relative difference of 4 percent, is found.

Local Heat Transfer Coefficient. The local Nusselt number ratio, calculated from the interferograms taken at conditions

of $Pi/H = 10$, $Re = 1.02 \times 10^4$, and $X_h/De > 7.15$, is plotted as a function of position along the surface for two consecutive pitches, $N = 9$ to 10 and $N = 10$ to 11 , in Fig. 9. The nearly identical Nu/Nu_s distributions between these two consecutive pitches suggest that the flow region downstream of the rib pair $N = 10$ has already achieved fully developed thermal periodicity. The periodic thermally fully developed region is also characterized by the almost constant increase (about 2.5°C) of wall temperature from a pitch of $N = 9$ to a pitch of $N = 10$, as shown in Fig. 9, and by the parallel relation between the wall temperature and the bulk mean air temperature at consecutive pitches.

It is known that turbulence can enhance the heat transfer. Figure 9 further illustrates the close correlation between the local Nusselt number and turbulent kinetic energy distributions. The latter was calculated by Liou et al. (1988) using the $k-\epsilon$ turbulence model. Both Nu/Nu_s and k distributions exhibit two major peaks. The first peak is located slightly downstream of the rib's leading edge (F) where both the temperature gradient (thin thermal boundary layer, Fig. 7) and velocity gradient are steep due to enhanced forced convection of the flow's acceleration and turbulent transport by sudden contraction. The second peak appears approximately 0.5 to 1.0 rib heights upstream of the reattachment point measured in this study (Fig. 6) and previous works (Hijikata et al., 1983; Hsieh and Hong, 1989) and is therefore in the separation bubble. It is worthwhile to note that this result is consistent with the fact that in most cases axial turbulence intensity reaches a peak value approximately one step height upstream of reattachment, as concluded by Eaton and Johnson (1981) in a review of research on subsonic turbulent flow reattachment in sudden expansion pipe or channel flows, and further verified by Vogel and Eaton (1985) in measuring heat transfer and fluid dynamic downstream of a backward-facing step. In addition, there exists the third peak, although not so obvious as the aforementioned two major peaks, located at a small distance upstream of the rib's leading edge ($X_N/H = 9.0$) due to the high turbulence intensity generated by the mean velocity gradient associated with part of the fluid that has to turn from the duct wall into the rib contraction.

The dashed line ($Nu/Nu_s = 1$) in Fig. 9 represents the Nu distribution for the smooth-wall duct; hence, the part of heat transfer enhancement due to the presence of rib pairs is displayed in terms of $Nu/Nu_s > 1$. It is also seen that the net contribution to heat transfer enhancement for the region of $G \leq X_N/H \leq 3.0$, i.e., for most of the separation bubble, is approximately zero. The reason is that the recirculating fluids near the surface ($G0$) and concave corner (0) of the rib are nearly stagnant so that the heat transfer rate of this part of the ribbed duct is even less than that of the corresponding smooth duct, which underwent forced convection at the same duct Reynolds number. Consequently, if a hot gas flows outside a ribbed channel that is cooled from the inside, as investigated in the present work, the rear surface of the rib ($X_N/H = 0$) and the duct wall of $0 < X_N/H < 1.0$ are susceptible to hot spots.

It is interesting that the very high temperature gradients on the upstream vertical and top surfaces of the ribs observed in Fig. 7 tend to suggest that the extended surface effects may dominate over enhanced transport due to increased turbulence by the rib turbulators. However, a comparison of the average Nusselt number for the extended surface ($EF G0$ in Fig. 9), $Nu_{EF G0} = 1.96 Nu_s$, with that for the duct wall (OE in Fig. 9), $Nu_{OE} = 1.94 Nu_s$, reveals that heat transfer augmentation due to increased turbulence by the rib turbulators is comparable to, although slightly lower than, that due to the extended surface effects. In addition, the order of magnitude of $Nu_{OE} = 1.94 Nu_s$ is comparable to the mass transfer coefficient enhancement, $Sh_{OE} = 1.90 Sh_s$, measured by Molki and Moustoufizadeh (1989) in turbulent heat transfer in a rectangular

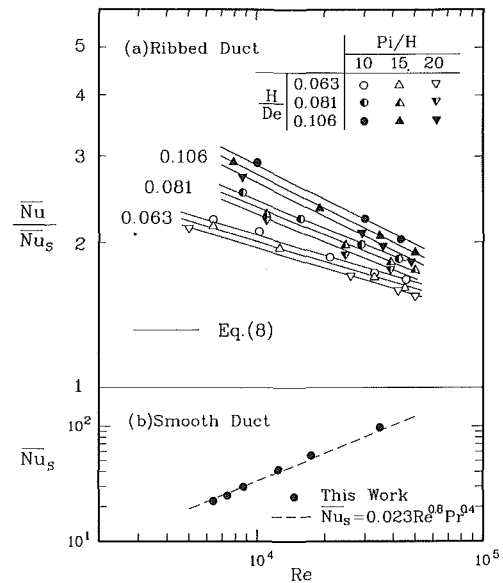


Fig. 10 (a) Nu/Nu_s versus Re at various H/De and Pi/H for ribbed duct; (b) Nu_s versus Re for smooth duct

duct with repeated-baffle blockages using naphthalene sublimation techniques. Note that the surface of the baffles was not covered with naphthalene in their work and hence the mass (heat) transfer enhancement is only due to improved turbulence.

Average Heat Transfer Coefficient. The dependence of the average Nusselt number on the rib height, rib pitch, and Reynolds number can be well correlated by an equation of the form

$$\bar{Nu} = C_2 \cdot Re^r \cdot (Pi/H)^{-S} = C_2 \cdot Re^r \cdot (Pi/H)^{-0.122} \quad (8a)$$

or

$$\bar{Nu} = C_2' \cdot Re^r \cdot (Pi/H/10)^{-0.122} \quad (8b)$$

where the constants C_2 , C_2' , and r vary with the rib height. They are listed in Table 3. The average Nusselt number ratio (\bar{Nu}/Nu_s) is also presented as a function of Reynolds number (Re) for various dimensionless pitches (Pi/H) and rib heights (H/De) in Fig. 10. The solid lines passing through the data points of Fig. 10 are the least-squares fits. Moreover, the dependence of the average Nusselt number (Nu_s) for the corresponding smooth-walled duct is included in Fig. 10 for comparison. For the smooth duct good agreement is found between Nu_s , determined by the present interferometric method, and those calculated by the empirical relationship (Rohsenow and Choi, 1969)

$$Nu_s = 0.023 \cdot Re^{0.8} \cdot Pr^{0.4} \quad (9)$$

over the tested range $6.4 \times 10^3 \leq Re \leq 3.5 \times 10^4$. Both smooth (Nu_s , Fig. 10) and ribbed ducts (\bar{Nu} , Table 3) display an increase of average Nusselt number with increasing Reynolds number; however, the rate of increase is slower for the ribbed duct ($\sim Re^{0.6}$) than for the smooth one ($\sim Re^{0.8}$) and hence the \bar{Nu}/Nu_s shown in Fig. 10 all decrease with increasing Reynolds number. The reason for the shift of $Re^{0.8}$ dependence in the smooth-walled case to $Re^{0.6}$ in the rib-walled case is that in the latter case part of mean-flow energy used for convection heat transfer has been transferred into turbulent kinetic energy, which subsequently enhances the heat transfer rate through enhanced turbulent transport.

Table 3 further shows that, due to the larger increase of the constant C_2 , \bar{Nu} increases with increasing rib height for ranges of Re and Pi/H tested, although the constant r decreases

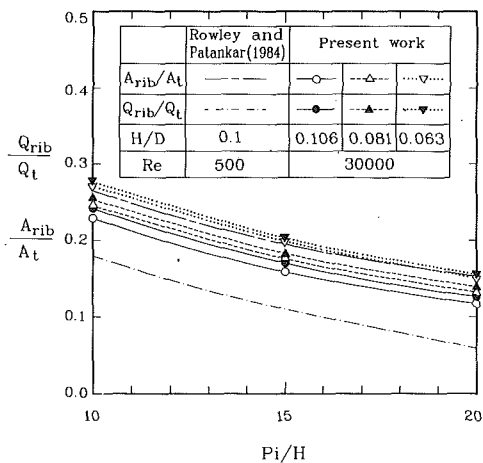


Fig. 11 Q_{rib}/Q_t and A_{rib}/A_t versus Pi/H at various H/De for ribbed ducts

slightly. The slight decrease of r with increasing rib height was also found by Sparrow and Tao (1984) for Sherwood number. Physically, the increase of Nu with rib height is due to the increased surface area and flow acceleration caused by rib contraction. As for the effect of pitch, Fig. 10 shows that $\overline{Nu}/\overline{Nu}_s$ decreases with increasing Pi/H for a given rib height. The reason is that for $Pi/H > 10$ the length of the separation bubble alters slightly, as addressed previously, whereas the distance between the reattachment point and the successive rib increases with Pi/H . In other words, within one pitch range the major contribution to the heat transfer enhancement resulting from regions upstream of reattachment alters slightly with Pi/H ; however, downstream of the reattachment point the local Nusselt number shown in Fig. 9 has a larger distance for continuous decay, and hence the Nusselt number is decreased after averaging over one pitch distance as Pi/H increases beyond 10. It is interesting to note that, in a previous study of fully developed turbulent air flow of a rib-walled square duct for $Pi/H = 10$ and $Pi/H = 20$ using the energy balance method by thermocouple technique, Han et al. (1985) also showed that the average heat transfer enhancement for $Pi/H = 20$ is smaller than for $Pi/H = 10$. Additionally, the level of heat transfer augmentation of the ribbed duct over the smooth one is approximately 1.5–2.2, 1.7–2.5, and 1.8–2.9 times \overline{Nu}_s for $H/De = 0.063, 0.081, \text{ and } 0.106$, respectively, for the test ranges of Pi/H and Re , as depicted in Fig. 10.

Rib Heat Transfer. It is instructive to investigate the separate contributions of the rib pair to the total heat transfer (Q_t) and area (A_t) per pitch. Figure 11 displays the ratios of Q_{rib}/Q_t (solid symbols) and A_{rib}/A_t (open symbols) as functions of Pi/H for $Re = 3 \times 10^4$ and various H/De . The quantity Q_{rib} is the heat transferred by one rib pair per pitch and A_{rib} is the wetted area of one rib pair. It is seen that at a given H/De the Q_{rib}/Q_t curve lies above the A_{rib}/A_t curve for the present turbulent flow, that is, the rib pair can be considered to transfer more heat than the duct wall on a unit area basis. In contrast, a completely opposite trend (Fig. 11) due to the lack of heat transfer enhancement by turbulent transport is found for the laminar-flow case studied computationally by Rowley and Patankar (1984) under approximately the same H/De . Figure 11 further shows that the difference between curve Q_{rib}/Q_t and curve A_{rib}/A_t increases with increasing H/De due to enhanced convection and turbulent transport with increasing H/De , a trend consistent with that of $\overline{Nu}/\overline{Nu}_s$ versus H/De depicted in Fig. 10. In addition, similar to the behavior of $\overline{Nu}/\overline{Nu}_s$ versus Pi/H shown in Fig. 10, both Q_{rib}/Q_t and A_{rib}/A_t decrease with increasing Pi/H , whether the flow is laminar or turbulent, as shown in Fig. 11.

Table 3 Coefficients C_2, C_2', r , and s in Eq. (8)

H/De	C_2	C_2'	r	s	Deviation, percent
0.063	0.2466	0.1862	0.6556	0.1211	1.8
0.081	0.3552	0.2682	0.6294	0.1223	4.2
0.106	0.5809	0.4286	0.5931	0.1216	2.1

Summary and Conclusions

This study has presented experimental results for turbulent heat transfer and friction in a rectangular duct with and without repeated rib pairs. The duct has hot gas flowing outside and is cooled from the inside. For the ribbed duct flow, the time-averaged temperature profiles measured by using holographic interferometry are found to be in good agreement with those measured by using thermocouples. In addition, the measured average friction factor distribution is consistent with that of previous work and with the Moody chart. For the smooth duct flow, both the measured average Nusselt number and friction factor coincide well with available theoretical correlations. Moreover, the present interferometric data are in reasonable agreement with the well-known universal temperature profile in the near-wall flow region. The main findings are:

1 For the ribbed duct flow, the distribution of local Nusselt number parallels that of the turbulent kinetic energy and reveals two major enhancement peaks, one located slightly downstream of the rib's leading edge and the other 0.5 to 1.0 rib heights upstream of the reattachment point.

2 The rib's rear surface and the duct wall of $0 < X_N/H < 1.0$ are found to be susceptible to hot spots.

3 Relative to a smooth duct, the presence of periodic ribs at two opposite walls yields up to 2.2-fold and 6-fold, 2.5-fold and 10-fold, and 2.9-fold and 17-fold increases in the fully developed average Nusselt number and friction factor for $H/De = 0.063, 0.081, \text{ and } 0.106$, respectively, for the ranges of Reynolds number and dimensionless rib pitch investigated in this study.

4 For the range of dimensionless pitch studied, the rib pair transfers more heat than the duct wall does on a unit area basis. This finding is contrary to that of the previously reported laminar-flow case and serves to emphasize the importance of including mass transfer from the ribs as one adopts the naphthalene sublimation technique mentioned in the Introduction.

5 Correlations in terms of Reynolds number and dimensionless rib pitch and height are obtained for both the periodic fully developed average friction factor and Nusselt number.

Acknowledgments

Support for this work was provided by the National Science Council of the Republic of China under contract No. NSC 79-04101-E007.

References

- Arvizu, D. E., and Moffat, R. J., 1981, "Experimental Heat Transfer From an Array of Heated Cubical Elements on an Adiabatic Channel Wall," Report No. HMT-33, Department of Mechanical Engineering, Stanford University, Stanford, CA, pp. 82–83.
- Burggraf, F., 1970, "Experimental Heat Transfer and Pressure Drop With Two-Dimensional Discrete Turbulence Promoters Applied to Two Opposite Walls of a Square Tube," *Augmentation of Convective Heat and Mass Transfer*, E. E. Bergles and R. L. Webb, eds., ASME, New York, pp. 70–79.
- Eaton, J. K., and Johnston, J. P., 1981, "A Review of Research on Subsonic Turbulent Flow Reattachment," *AIJA Journal*, Vol. 19, No. 9, pp. 1093–1100.
- Goldstein, R. J., 1976, "Optical Measurement of Temperature," *Measurements in Heat Transfer*, 2d ed., E. R. G. Eckert and R. J. Goldstein, eds., Hemisphere, Washington, DC, pp. 241–294.
- Han, J. C., 1984, Heat Transfer and Friction in Channels With Two Opposite Rib-Roughened Walls," *ASME JOURNAL OF HEAT TRANSFER*, Vol. 106, pp. 774–782.

- Han, J. C., Park, J. S., and Lei, C. K., 1985, "Heat Transfer Enhancement in Channels With Turbulence Promoters," *ASME Journal of Engineering for Gas Turbines and Power*, Vol. 107, pp. 628-635.
- Hauf, W., and Grigull, U., 1970, "Optical Method in Heat Transfer," *Advances in Heat Transfer*, Vol. 6, J. P. Hartnett and T. F. Irvine, Jr., eds., Academic, New York, pp. 133-136.
- Hijkata, K., Ishiguro, H., and Mori, Y., 1983, "Heat Transfer Augmentation in a Pipe Flow With Smooth Cascade Turbulence Promoters and Its Application to Energy Conversion," *Proc. ASME-JSME Thermal Engineering Joint Conf.*, Vol. 4, pp. 368-379.
- Hsieh, S. S., and Hong, Y. J., 1989, "Separating Flow Over Repeated Surface-Mounted Ribs in a Square Duct," *AIAA Journal*, Vol. 27, No. 6, pp. 770-776.
- Kang, B. H., Jaluria, Y., and Tewari, S. S., 1990, "Mixed Convection Transport From an Isolated Heat Module on a Horizontal Plate," *ASME JOURNAL OF HEAT TRANSFER*, Vol. 112, pp. 653-661.
- Kay, W. M., and Crawford, M. E., 1980, *Convective Heat and Mass Transfer*, McGraw-Hill, New York.
- Kline, S. J., and McClintock, F. A., 1953, "Describing Uncertainties on Single-Sample Experiments," *Mechanical Engineering*, Vol. 57, pp. 3-8.
- Liou, T. M., Hwang, D. G., and Kao, C. F., 1988, "Computations of Turbulent Flow and Heat Transfer Enhancement in Channel With a Pair of Turbulence Promoters," *3rd International Symposium on Transport Phenomena in Thermal Control*, Taipei, Taiwan.
- Liou, T. M., and Kao, C. F., 1988, "Symmetric and Asymmetric Flow in a Rectangular Duct With a Pair of Ribs," *ASME Journal of Fluids Engineering*, Vol. 110, pp. 373-379.
- Liou, T. M., and Lin, J., 1988, "Measurements of Turbulent Flow in a Duct With Repeated Ribs Applied to Two Opposite Walls," *Journal of the Chinese Institute of Engineers*, Vol. 11, No. 4, pp. 319-326.
- Liou, T. M., Hwang, D. W., and Chang, Y., 1990, "Experimental and Computational Study of Turbulent Flows in a Channel With Two Pairs of Turbulence Promoters in Tandem," *ASME Journal of Fluids Engineering*, Vol. 112, pp. 302-310.
- Metzger, D. E., Fan, C. S., and Yu, Y., 1990, "Effects of Rib Angle and Orientation on Local Heat Transfer in Square Channels With Angled Roughness Ribs," *Compact Heat Exchangers*, A Festschrift for A. L. London, Hemisphere, Washington, DC.
- Molki, M., and Mostoufizadeh, A. R., 1989, "Turbulent Heat Transfer in Rectangular Ducts With Repeated-Baffle Blockages," *Int. J. Heat Mass Transfer*, Vol. 32, No. 8, pp. 1491-1499.
- Rohsenow, W. M., and Choi, H. Y., 1969, *Heat, Mass and Momentum Transfer*, Prentice-Hall, Englewood Cliffs, NJ.
- Rowley, G. J., and Patankar, S. V., 1984, "Analysis of Laminar Flow and Heat Transfer in Tubes With Internal Circumferential Fins," *Int. J. Heat Mass Transfer*, Vol. 27, No. 4, pp. 553-560.
- Sparrow, E. M., and Tao, W. Q., 1984, "Symmetric Versus Asymmetric Periodic Disturbances at the Walls of a Heated Flow Passage," *Int. J. Heat Mass Transfer*, Vol. 27, pp. 2133-2144.
- Vogel, J. C., and Eaton, J. K., 1985, "Combined Heat Transfer and Fluid Dynamic Measurements Downstream of a Backward-Facing Step," *ASME JOURNAL OF HEAT TRANSFER*, Vol. 107, pp. 922-929.
- Webb, R. L., Eckert, E. R. G., and Goldstein, R. J., 1971, "Heat Transfer and Friction in Tubes With Repeated-Rib Roughness," *Int. J. Heat Mass Transfer*, Vol. 14, pp. 601-617.

C. D. Young¹
Research Assistant.

J. C. Han
Professor.
Fellow ASME

Y. Huang
Research Associate.

Turbine Heat Transfer Laboratory,
Department of Mechanical Engineering,
Texas A&M University,
College Station, TX 77843

R. B. Rivir
Research Scientist,
AFWAL/POTX,
Wright-Patterson Air Force Base, OH 45433
Mem. ASME

Influence of Jet-Grid Turbulence on Flat Plate Turbulent Boundary Layer Flow and Heat Transfer

The influence of high mainstream turbulence on turbulent boundary layer flow and heat transfer is experimentally investigated for length Reynolds numbers between 4×10^4 and 1.5×10^6 . The high mainstream turbulence is produced by a round tube grid with uniform jet injection. Injected air is blown in either an upwind or downwind direction at a controllable flow rate. A flat plate test section instrumented with foil thermocouples is located downstream from the jet grid. The turbulence intensity decay and length scale growth along the test plate, the mean velocity and temperature profiles across the boundary layer, and surface heat transfer distribution are measured. The results show that the grid with downwind injection produces a slightly higher turbulence intensity and a smaller length scale than the grid with upwind injection. A higher turbulence intensity and a smaller length scale further enhance the surface heat transfer coefficient. The jet-induced high turbulence does not alter the downstream velocity and temperature profiles in their logarithmic regions, but the wake regions are lower than the zero turbulence profiles. The Reynolds analogy factor, the augmented friction factor, and the augmented Stanton number are higher than those from existing correlations when the jet grid turbulence intensity is greater than 6 percent.

Introduction

The influence of high mainstream turbulence on turbulent boundary layer flow and heat transfer is a critical problem in gas turbine airfoil design. In a wind tunnel with grid-generated turbulence intensity of up to 6 percent and length scale to boundary layer thickness ratio of up to 5, Simonich and Bradshaw (1978) and Hancock and Bradshaw (1983) found that the Stanton number increases with increasing turbulence intensity and with decreasing turbulence length scale ratio. Blair (1983a, 1983b) conducted extensive experiments to determine the influence of mainstream turbulence on flat plate, turbulent boundary layer heat transfer and mean profile development with wind tunnel, grid-generated turbulence intensity ranging from 0.25 to 6 percent. Blair's data support Simonich, Hancock, and Bradshaw's conclusions. He reported that the Stanton number with a 6 percent intensity was 18 percent higher than the zero-turbulence case. Blair also found that the logarithmic region of the mean velocity and temperature profiles is not altered by mainstream turbulence intensity of up to 6 percent. Correlations for increased heat transfer and friction factor were obtained to account for the combined effects of turbulence intensity, length scale, and momentum thickness Reynolds number. In all the above studies, the effect of mainstream turbulence on turbulent boundary layer flow and heat transfer was examined in a wind tunnel, with a nominal grid-generated turbulence intensity of up to 6 percent; the turbulence intensity over the test flat plate was nearly homogeneous and nearly isotropic. However, it is common for turbulence intensity in a gas turbine mainstream to be as high as 15 to 20 percent. Here we investigate whether the previous results can be extended to very high turbulence conditions, and whether the Stanton number continuously increases with further turbulence intensity or remains constant above a particular level of intensity. It is difficult, however, to obtain very high main-

stream turbulence with the simulated length scale in engine conditions in standard grid-generated, turbulence experiments in a wind tunnel.

One technique for producing high turbulence is by use of a wind tunnel grid with uniform jet injection (jet grid) (Gad-El-Hak and Corrsin, 1974; Tassa and Kamotani, 1975). Compressed air flowing inside the hollowed grids was injected (through small injection holes uniformly distributed on the grid surface) in the upwind or downwind direction at a controllable flow rate. A turbulence intensity as high as 15 percent, with isotropy and homogeneity, was attainable. The turbulent boundary layer heat transfer and mean profile development were not investigated in these studies. O'Brien and VanFossen (1985) applied the technique to study the influence of jet grid turbulence on heat transfer from the stagnation region of a cylinder in a cross flow. With the injection ratio adjusted to an optimal value for flow uniformity, the turbulence intensity at 16 grid diameters downstream from the jet grid was 12 percent for downwind injection and the heat transfer was 37 to 53 percent higher than that for zero turbulence. Mean velocity and temperature profiles across the boundary layers were not measured.

In the present investigation, the round tube grid with uniform jet injection (jet grid) was employed to stimulate the effect of high mainstream turbulence on turbulent boundary layer flow and heat transfer. The temperature of the injected air (from air compressor) was about 1°C lower than the mainstream (ambient air). A turbulence level as high as 12 percent for upwind injection and as high as 25 percent for downwind injection was attainable at 20 grid diameters downstream from the jet grid device. A flat plate test section, instrumented with foil thermocouples, was placed 9.25 grid diameters downstream from the jet grid. The following quantities were measured, with and without injection: turbulence intensity decay along the test plate; mean velocity and temperature profiles across the boundary layers; and distributions of the test plate surface temperature. The integral length scale growth along the test plate, the logarithmic velocity and temperature profiles across the boundary layers, the Reynolds analogy factors, and the local Stanton number distributions on the test plate were

¹Current address: General Electric Company, Aircraft Engine Group, Cincinnati, OH.

Contributed by the Heat Transfer Division for publication in the JOURNAL OF HEAT TRANSFER. Manuscript received by the Heat Transfer Division November 1990; revision received July 31, 1991. Keywords: Forced Convection, Turbines, Turbulence.

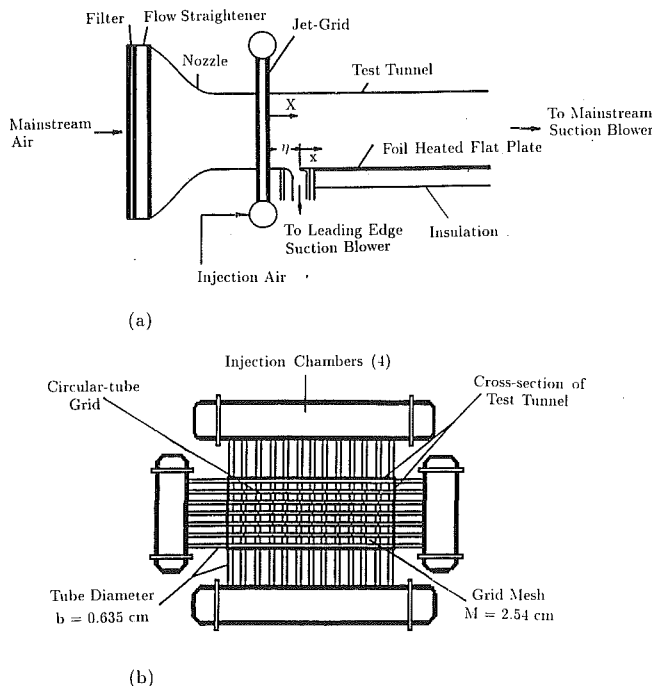


Fig. 1 (a) Schematic of the test rig; (b) schematic of the jet grid device

calculated. The combined effects of turbulence intensity, length scale, and momentum thickness Reynolds number on the augmented Stanton number and the augmented friction factor are determined under jet grid-generated high turbulence environments.

This study focuses on four objectives: (1) to create high turbulence by varying the jet grid injection direction; (2) to obtain augmented heat transfer distributions under the selected high turbulence conditions; (3) to extend the existing augmented heat transfer and friction factor correlation that ac-

count for the combined effects of high turbulence intensity, length scale, and Reynolds number; and (4) to extend an existing Reynolds analogy factor correlation from 6 percent turbulence intensity to much higher intensity levels. Han and Young (1988), Young (1989), and Mehendale et al. (1991) furnish further details.

Experimental Apparatus

Wind Tunnel and Jet Grid System. Figure 1(a) is a schematic of the low-speed wind tunnel with a jet grid system. The wind tunnel has an inlet cross section of 60.96 cm \times 30.48 cm. A 5 μ m cotton filter and a packed plastic straw flow straightener box are installed in front of the nozzle inlet. The contraction ratio of the nozzle is 4:1. The cross section of the test tunnel is 30.48 cm \times 15.24 cm. The wind tunnel operates in the suction mode with a 5.6 kW axial blower. The turbulence intensity of the wind tunnel without a jet grid device at a mainstream velocity of 9.75 m/s is measured to be 0.75 percent. A weak suction blower eliminates the boundary layer developed inside the nozzle. The suction flow rate is about 1.66 percent of the main stream.

The jet grid is inserted between the nozzle and the test tunnel. The grid is biplanar and square-mesh, with 13 \times 7 oriented aluminum tubes. There are thirteen tubes in the vertical direction and seven tubes in the horizontal direction. The grid has a solidity of 44 percent (tube diameter = 0.635 cm and tube center line spacing = 2.54 cm), as shown in Fig. 1(b). The grid is joined to four steel chambers that are 10 cm in diameter and individually connected to the orifice-metered, compressed air supply. A Sullair air compressor of 20 m³/min capacity delivers 690 kPa of demineralized compressed air to two consecutive air filters for further particle (3 μ m) and oil fume removal. The upstream pressure of the orifice meter is measured by a 1379 kPa face scale pressure gage. The pressure drop across the orifice is measured by a 30.5 cm mercury manometer. A motorized valve and a 1724 kPa pressure transducer control the proper opening of injection air for repeatable operation.

Nomenclature

b = grid diameter
 C_f = local friction factor
 $= 2\tau_w/(\rho U^2)$
 C_{f0} = local friction factor for zero turbulence
 ΔC_f = augmented friction factor
 $= C_f - C_{f0}$
 C_p = specific heat at constant pressure
 h = heat transfer coefficient
 J = injection ratio; injection mass flow rate/(injection mass flow rate + mainstream flow rate)
 L_e^u = streamwise dissipation length scale
 M = grid mesh length
 Pr = molecular Prandtl number
 q'' = heat transfer rate per unit surface area
 Re_x = length Reynolds number
 $= Ux/\nu$
 Re_θ = momentum thickness Reynolds number
 $= U\theta/\nu$
 St = local Stanton number
 $= h/(\rho UC_p)$
 St_0 = local Stanton number for zero turbulence

ΔSt = augmented Stanton number
 $= St - St_0$
 T = local profile temperature
 T_w = flat plate surface temperature
 T_{aw} = adiabatic wall temperature
 Tu = streamwise turbulence intensity measured by a single hot-film sensor
 Tu_x = streamwise turbulence intensity measured by a crossed hot-film sensor
 $= (\bar{u}'^2)^{1/2}/U$
 Tu_y = normal turbulence intensity measured by a crossed hot film sensor
 $= (\bar{v}'^2)^{1/2}/U$
 T^+ = dimensionless local temperature
 $= (T_w - T)/(q''/(\rho u^* C_p))$
 U = mainstream (core) streamwise velocity
 u = local streamwise profile velocity
 u^+ = dimensionless local streamwise velocity
 $= u/u^*$
 u' = local streamwise fluctuating velocity
 v' = local normal fluctuating velocity

u^* = local friction velocity
 $= (\tau_w/\rho)^{1/2}$
 x = axial distance from flat plate leading edge
 X = axial distance from jet grid device
 y = distance from the flat plate surface
 y^+ = dimensionless distance from the flat plate surface
 $= (yu^*)/\nu$
 α = length scale parameter
 $= L_e^u/\delta + 2$
 β = momentum Reynolds number parameter
 $= 3 \cdot \exp(-Re_\theta/400) + 1$
 δ = boundary layer thickness
 η = distance between the jet grid and the flat plate leading edge
 θ = momentum thickness
 Λ_f = streamwise integral length scale
 ν = kinematic viscosity of air
 ξ = unheated starting length from the flat plate leading edge
 ρ = mainstream air density
 τ = time delay in the autocorrelation
 τ_w = local wall shear stress
 $= \rho u^{*2}$

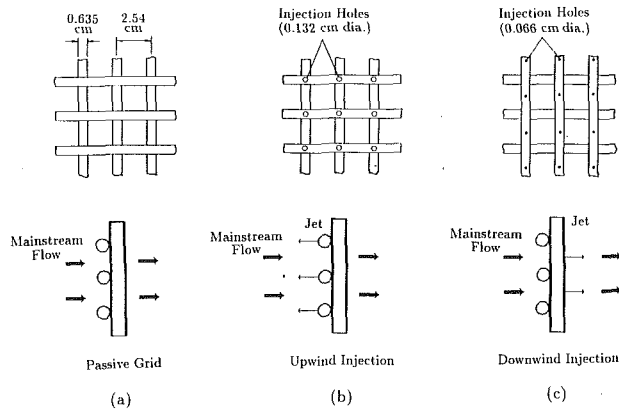


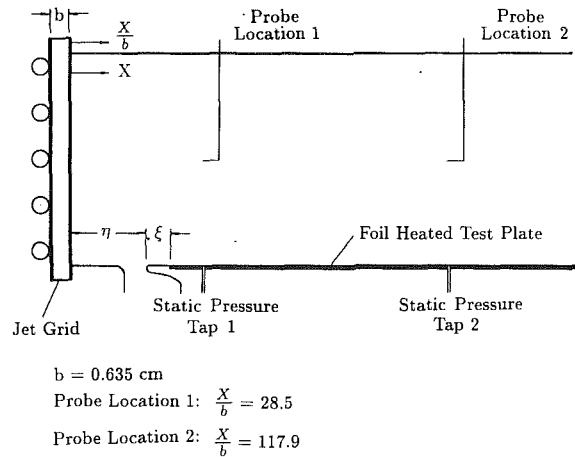
Fig. 2 Conceptual view of high turbulence grids: (a) passive grid; (b) jet grid with upwind injection; (c) jet grid with downwind injection

Figure 2 shows the conceptual view of three high-turbulence grids: (a) passive grid with no injection; (b) jet grid with upwind injection; 55 injection holes (hole diameter = 0.132 cm and hole spacing = 2.54 cm) uniformly distributed on the five horizontal tubes in the upstream direction; (c) jet grid with downwind injection; 66 injection holes (hole diameter = 0.066 cm and hole spacing = 2.54 cm) uniformly distributed on the eleven vertical tubes in the downstream direction.

Test Section and Instrumentation. The test plate is 5.08 cm ($X/b = 9.25$) downstream from the jet grid device. As seen in Fig. 3(a), the test plate is constructed with the leading edge having a 0.32-cm-thick, 3.81-cm-long ellipse and a 1.27 cm suction slot in front of the plate to lead the flow direction. The locations between the surface sensors (thermocouples, pressure tap) and the space probes (hot-wire probe, total pressure probe, and temperature probe) are shown in Fig. 3(b). Twenty-seven pieces of stainless steel foil, each 0.00254 cm thick, 5.08 cm wide, and 33 cm long, are cemented directly on a 7.62-cm-thick, flat insulation material (33 cm wide and 152.4 cm long, glass fiber, reinforced polyisocyanurate foam). The foils are connected in series by copper bus bars and powered by an a-c variac to supply a nearly uniform surface heat flux. Since the foil temperatures were between 35 and 50°C over the entire test plate, the foils were not rippled. The current is read from a digital multimeter. Fifty-five 36 gage, copper-constantan thermocouples are soldered underneath the foils at strategic locations to measure surface temperature distributions. The temperature drop from the back of the foil is expected to be relatively small, but is estimated and taken into account for heat transfer calculation. All thermocouples are wired to a Fluke 2285B data logger and interfaced with an IBM XT personal computer for data acquisitions. Four readings are taken at each thermocouple location and averaged to eliminate minor temperature fluctuations on the surface.

A computer-controlled traversing device on the top of the test tunnel holds the probe (hot-film probe, total pressure probe, or temperature probe) for data acquisition. It is driven by a Superior Electric stepping motor (3.957 kg-cm, 200 steps/revolution). A ball screw (1.905 cm diameter and 0.508 cm pitch) and an anti-backlash supernut assembly yield 0.00254 cm/step in either direction with no backlash.

A four-channel TSI IFA 100 Constant Temperature Anemometer (CTA) with a four-channel TSI IFA 200 high-speed digitizer is connected to an IBM XT personal computer through a TSI DMA connector for hot-film data recording. The hot film is calibrated in the air jet from a third-order polynomial nozzle. The local streamwise root mean square (rms) calculations of velocity fluctuations were based on 1032 readings from the hot-wire anemometer. The local streamwise turbulence intensity was then based on the average of five sets of

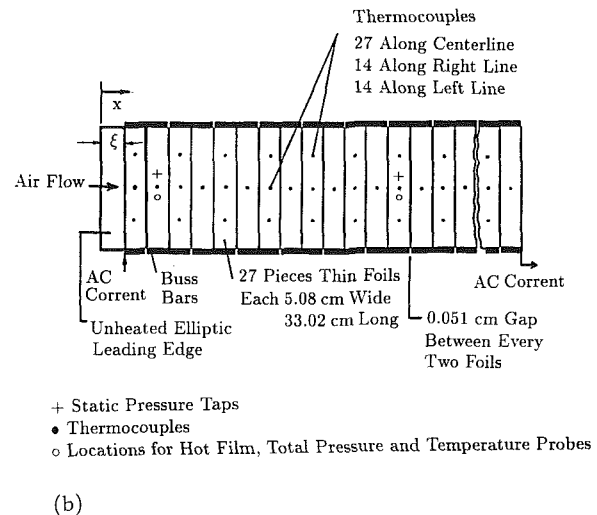


$$b = 0.635 \text{ cm}$$

$$\text{Probe Location 1: } \frac{X}{b} = 28.5$$

$$\text{Probe Location 2: } \frac{X}{b} = 117.9$$

(a)



+ Static Pressure Taps

• Thermocouples

o Locations for Hot Film, Total Pressure and Temperature Probes

(b)

Fig. 3 (a) Relative locations of the test plate and probes; (b) distributions of the thin foils and thermocouples

rms values (5160 readings) normalized by the local streamwise velocity. Note that the total digitizing time for gathering the 5160 readings was about 0.1–0.5 s.

Surface static pressure taps are installed at $X/b = 28.5$ and $X/b = 117.9$. These taps are incorporated with the total pressure probe for boundary layer velocity profile measurements. A total pressure probe (United Sensor) with a flattened tip size of 0.0508 cm \times 0.1016 cm measures the boundary layer velocity profiles. This probe is moved manually to touch the wall while viewing through a 3 \times magnifying lens. The calculated y^+ value of this setup is around 10. A special miniature thermocouple probe (United Sensor) made of 36 gage copper-constantan thermocouple wire measures boundary layer temperature profiles. The bead size is measured as 0.0508 cm o.d. Two sheathed leads threaded through two separate 0.05588 cm i.d., U-shaped hypodermic stainless steel tubing minimize the flow disturbance and give better support.

Experimental Procedures and Data Analysis

Experiments are performed for downwind, upwind, and zero injections with two mainstream velocities of 9.75 m/s and 19.5 m/s. An optimal injection ratio that produces high turbulence intensity and maintains flow uniformity is employed to study the effect on the flat plate turbulent boundary layer heat transfer. Four selected test runs are listed in Table 1. The streamwise decay of turbulence intensity (Tu_x) is measured along the test channel centerline. The corresponding streamwise growth of

Table 1 Experimental conditions of current study

Experimental Setups			
Case	Mainstream Velocity	Grid Type	Injection Ratio
1	9.75 m/s	clear wind tunnel with no grid	-
2	9.75 m/s	passive grid with no injection	0%
3	9.75 m/s	jet grid with downwind injection	2.2%
4	9.75 m/s	jet grid with upwind injection	2%

integral length scale (Λ_f) is determined along the test channel centerline. In each case, the local Stanton number (St) versus length Reynolds number (Re_x) is determined. The local Stanton number is converted from the local heat transfer coefficient. The local heat transfer coefficient is calculated as

$$h = (q'' - q''_{loss}) / (T_w - T_{aw}) \quad (1)$$

where q'' is the uniform surface heat flux determined by the electric current and the foil resistance (I^2R), and by the electric current and voltage drop across the foil (IV). The q''_{loss} is the heat loss by conduction from the foil to the insulation material, and by radiation from the foil to the channel walls. The T_w is the local foil surface temperature (about 35 to 50°C) read from thermocouples and T_{aw} is the corresponding local adiabatic wall temperature (about 25°C) measured before each run so as to compensate for drift in ambient conditions. The heat losses from conduction and radiation are about 7 and 8 percent, respectively, for the high and low mainstream velocities. The radiation loss was calculated based on the stainless steel foil emissivity of 0.2. The emissivity of stainless steel foil was experimentally determined by an Omega Optical pyrometer. Since the foil temperatures were between 35 and 50°C over the entire test plate, the test surface was approximately considered as a uniform heat flux boundary condition. The flat plate laminar and turbulent heat transfer correlations with zero turbulence intensity are employed for comparison and are shown in Eqs. (2) and (3), respectively.

$$St_0 = 0.453 Pr^{-2/3} Re_x^{-1/2} (1 - (\xi/x)^{3/4})^{-1/3} \quad (2)$$

$$St_0 = 0.0307 Pr^{-0.4} Re_x^{-0.2} (T_w/T_{aw})^{-0.4} \quad (3)$$

The mean velocity and temperature profiles across the boundary layers are measured at two selected locations: the upstream location of $X/b = 28.5$ and the downstream location of $X/b = 117.9$. According to Kays and Crawford (1980), the turbulent boundary layer profiles can be divided into two regions:

1 Sublayer region ($y^+ < 10$):

$$u^+ = y^+ \quad (4)$$

$$T^+ = Pr \cdot y^+ \quad (5)$$

2 Logarithmic-law region ($y^+ > 10$):

$$u^+ = \frac{1}{0.41} \cdot \ln y^+ + 5 \quad (6)$$

$$T^+ = 2.195 \cdot \ln y^+ + 13.2 Pr - 5.66 \quad (7)$$

Several iterations are necessary to determine the region of the logarithmic velocity profiles. The friction velocity (u^*) is curve fitted from Eq. (6) with the measured u and y values in the logarithmic region. The same friction velocity u^* is used to determine the region of the logarithmic temperature profiles by Eq. (7). Note that a turbulent Prandtl number of 0.9 is assumed in Eq. (7) for both low and high mainstream turbulence. Further study is needed to determine the turbulent Prandtl number under highly turbulent flow. The air properties are determined by using the average of wall and local temperatures. The calculated frictional factors from the curve-fitted u^* in Eq. (6) are compared with the following empirical correlation for zero turbulence intensity (Schlichting, 1968):

$$C_{f0}/2 = 0.0296 \cdot Re_x^{-0.2} \quad (8)$$

Blair (1983b) found that the Reynolds analogy factor increases with increasing turbulence intensity for Tu up to 6 percent as shown in the following equation:

$$St/(C_f/2) = 1.18 + 1.3 \cdot Tu \quad (9)$$

The St , C_f , and Tu are based on values calculated between $X/b = 28.5$ and 117.9. In this study, it is of interest whether Eq. (9) holds for even higher turbulence levels.

Hancock and Bradshaw (1983) indicated that the surface heat transfer and friction factor are affected by the mainstream turbulence intensity (Tu), the length scale to boundary layer thickness ratio (L_e^u/δ), and momentum thickness Reynolds number (Re_θ). They used grid-generated turbulence for extensive experiments and provided correlations between $\Delta C_f/C_{f0}$ (or $\Delta St/St_0$) and $(Tu \cdot 100)/(\alpha \cdot \beta)$, where $\alpha = L_e^u/\delta + 2$, and $\beta = 3 \cdot \exp(-Re_\theta/400) + 1$. Blair (1983b) modified Hancock and Bradshaw's correlations to match his experimental data for Tu up to 6 percent. In this study, we will investigate whether the correlations can be extended to higher turbulence levels.

Hancock and Bradshaw (1983) defined the streamwise turbulence dissipation length scale as

$$L_e^u = -(\bar{u}'^2)^{3/2} / (U \cdot (d\bar{u}'^2/dx)) \quad (10)$$

Blair and Werle (1980) defined the streamwise integral length scale as

$$\Lambda_f = U \cdot \int_{\tau=0}^{\tau=\infty} R \cdot d\tau \quad (11)$$

where

$$R = \overline{u'(t) \cdot u'(t+\tau)} / \bar{u}'^2 \quad (12)$$

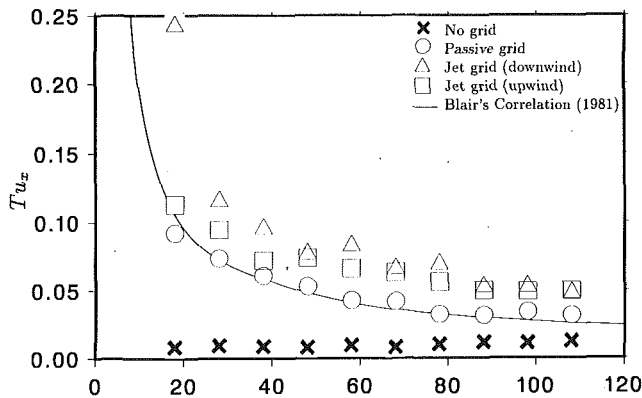
Blair (1983b) indicated that $L_e^u \cong 1.5 \Lambda_f$ for grid-generated turbulence. In this study, the streamwise dissipation length scale (L_e^u) and the integral length scale (Λ_f) were calculated by solving Eq. (10) and Eqs. (11) and (12), respectively. The real time turbulent fluctuations (u') were measured by a single hot-film sensor.

Kline and McClintock (1953) outlined a method to propagate the uncertainties of the data. The uncertainties of the basic measurement variables are: wall temperature = 1.1 percent of the measured value, current = 2 percent, voltage drop = 3.1 percent, length measurements = 5 percent, pressure drop = 3.3 percent. The uncertainties of the typical derived variables, based on a 90 percent confidence interval, are: injection ratio = 5.1 percent, $u' = 7$ percent, $Re_x = 5.2$ percent, $Tu_x = 7$ percent of the measured value, $St = 6.5$ percent, $u^* = 5.1$ percent, $y^+ = 7.2$ percent, $u^+ = 7.2$ percent, $T^+ = 7.2$ percent, $\Lambda_f = 8.6$ percent, $C_f = 6.5$ percent.

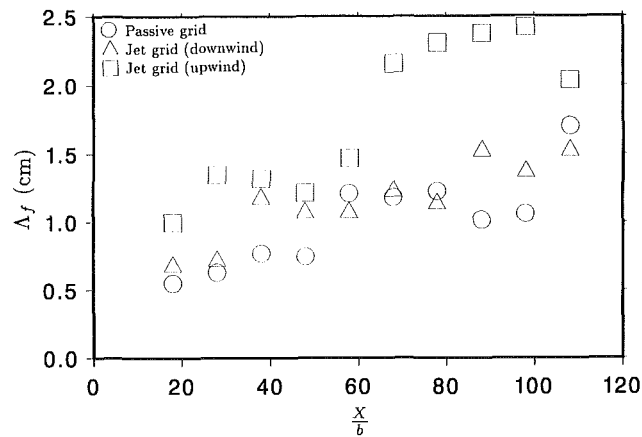
Experimental Results and Discussion

Uniform Periodic Flow at the Leading Edge. The periodic uniform flow at the leading edge of the flat plate is checked first. Periodic flow is caused by the grid. The uniformity of the periodic flow in the Y - Z plane is controlled by a boundary layer bleed at the plate leading edge as shown in Fig. 1(a). With proper leading edge suction, the test plate leading edge encounters an oncoming uniform periodic mainstream with respect to the Y - Z plane. This was done by moving the pitot tube probe across the Y - Z plane at the test plate leading edge for both high and low mainstream velocities. The optimum suction rate of leading edge to the mainstream is calculated as 1.66 percent (Young, 1989).

Mainstream Turbulence Intensity Decay. The mainstream turbulence intensity decay was measured by a single hot-film and crossed hot-film probe, respectively. It was found that the streamwise turbulence intensity measured by the single hot film (Tu) was slightly higher than that measured by the crossed hot



(a)



(b)

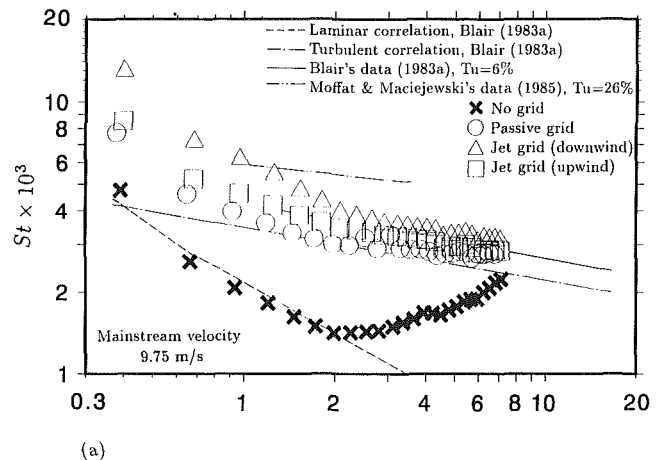
Fig. 4 (a) Streamwise turbulence intensity decay; (b) streamwise integral length scale growth

film in the streamwise direction (Tu_x). The streamwise turbulence intensity (Tu_x) was about 10–20 percent higher than the normal turbulence intensity (Tu_y). The variation of streamwise turbulence intensity at the upstream region could be as high as 10 percent, but the variation at the downstream region was relatively small (Young, 1989). Figure 4(a) shows that, as expected, streamwise turbulence intensity (Tu_x) decreases with increasing distance from the jet grid device. The jet grid turbulence intensity (upwind or downwind injection) is higher than the passive grid (without injection) at the same axial location. The turbulence intensity with downwind injection is higher than the upwind injection at the upstream developing region and they approach each other at the downstream developed region. The intensity has a larger decay rate immediately downstream from the jet grid, and the decay rate becomes equivalent to the other cases at X/b greater than 40. The turbulence intensity in a clear tunnel (no grid) is the lowest with a constant value of 0.75 percent. The intensity decay for the passive grid agrees with that obtained by Blair et al. (1981): $Tu = 0.78 (X/b)^{-5/7}$, but is lower than that proposed by Baines and Peterson (1951) for the square bar grid: $Tu = 1.12 (X/b)^{-5/7}$. This may be caused by the round-tube grid in the present investigation.

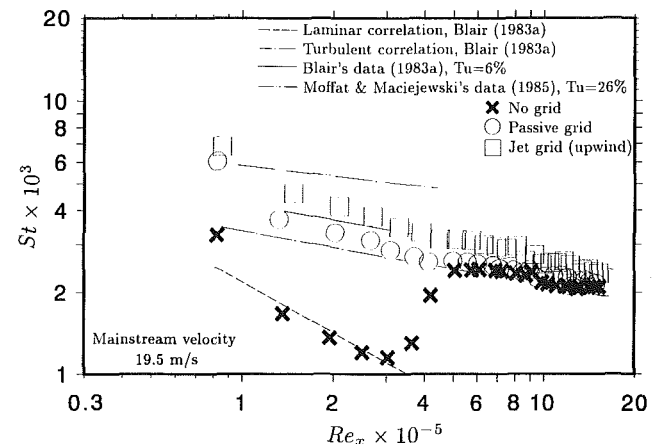
Mainstream Integral Length Scale Growth. The streamwise integral length scale (Λ_f) growth rate along the test tunnel is shown in Fig. 4(b). For the passive grid, the eddy size at the grid location is about the same as the grid diameter and expands downstream from the grid location. The length scale for the grid with injection is slightly larger than that without injection at the same downstream location. The upwind injection, where the jet has additional traveling distance from upstream to

Table 2 Turbulence intensity decay and length scale growth

Turbulence Intensity and Length Scale		
CASES	Tu_x ($X/b = 18$ to 110)	Λ_f , cm ($X/b = 18$ to 110)
Case 2	9.2% - 3.2%	0.55 - 1.7
Case 3	24.4% - 5.0%	0.7 - 1.55
Case 4	11.3% - 5.0%	1.0 - 2.0



(a)

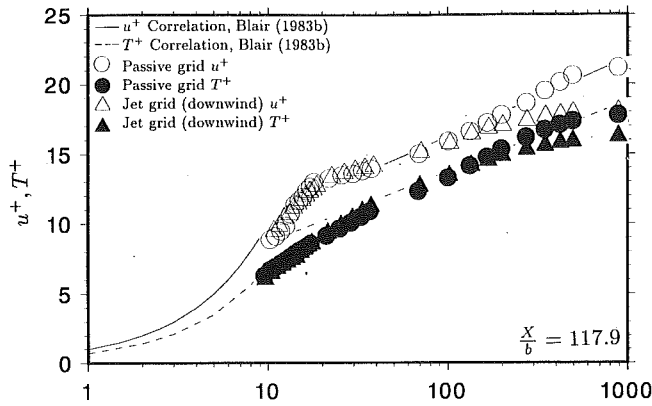


(b)

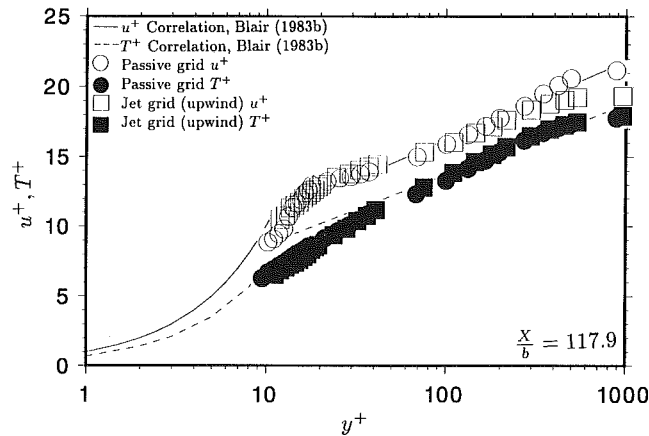
Fig. 5 Stanton number versus Reynolds number: (a) effect of grid injection for mainstream velocity of 9.75 m/s; (b) effect of grid injection for mainstream velocity of 19.5 m/s

downstream of the grid, produces a larger scale than the downwind injection. In the present investigation, the downwind injection produces a slightly higher turbulence intensity but much smaller length scale compared to that with upwind injection. The comparison between the turbulence intensity decay and the corresponding length scale growth from $X/b = 18$ to 110 are listed in Table 2.

Heat Transfer Measurements. Figure 5(a) shows a comparison of the local heat transfer distributions for cases 1, 2, 3, and 4. This compares the effect of different turbulence on the surface heat transfer coefficients in a 9.75 m/s mainstream velocity. To check the uniformity in the spanwise direction, the Stanton numbers along three axial lines of the foil-heated test section are measured at a 9.75 m/s mainstream velocity. The results show the spanwise Stanton numbers are uniform within 5–10 percent (Young, 1989). For the case of clear wind tunnel with no grid low turbulence, the Stanton number decreases monotonically from the leading edge because of the growth of a laminar boundary layer. The laminar boundary layer is transitioned to the turbulent boundary layer at Reyn-



(a)



(b)

Fig. 6 Universal velocity and temperature profiles across the boundary layer at $X/b = 117.9$: (a) effect of downwind injection; (b) effect of upwind injection

olds numbers between 2×10^5 and 7×10^5 . For the cases of grid and jet grid high turbulence, the Stanton numbers are much higher than the zero-turbulence correlation. This means that the grid and jet grid artificially create turbulent flow over the flat plate. As expected, the heat transfer coefficients are higher for the grid with downwind injection than that with upwind injection, and subsequently higher than that with no injection (passive grid). The grid with downwind injection has a higher turbulence intensity and a smaller length scale compared to that with upwind injection; therefore, the heat transfer is higher. At $Re_x = 10^5$, the Stanton numbers for the grid with downwind injection are 75 percent higher than the zero turbulence correlation. Heat transfer results from Blair (1983a) with a 6 percent grid-generated turbulence and from Moffat and Maciejewski (1985) with a 26 percent free jet turbulence are included for comparison. Note that the slope of St versus Re_x is deeper than those of Blair and Moffat and Maciejewski at the upstream region ($Re_x < 2 \times 10^5$). However, they are parallel to each other at the downstream region ($Re_x > 2 \times 10^5$). Figure 5(b) shows the effect of the upwind injection in a higher mainstream flow (19.5 m/s). The results show that the laminar boundary layer is transitioned to the turbulent boundary layer at Reynolds numbers between 3×10^5 and 5×10^5 for the no grid low turbulence case. The grid and jet grid high turbulence produce turbulent flow over the entire flat plate as evidenced by higher heat transfer than the zero turbulence correlation. The Stanton numbers with the upwind injection are higher than with the passive grid (no injection) because the turbulence intensity is higher.

Based on these experimental observations, one may conclude that with the same level of mainstream turbulence intensity

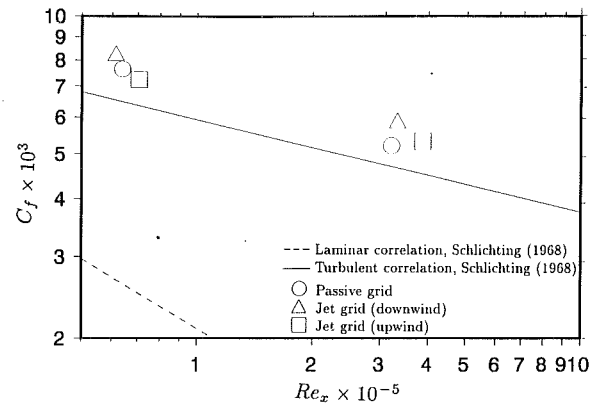


Fig. 7 Friction factor versus Reynolds number

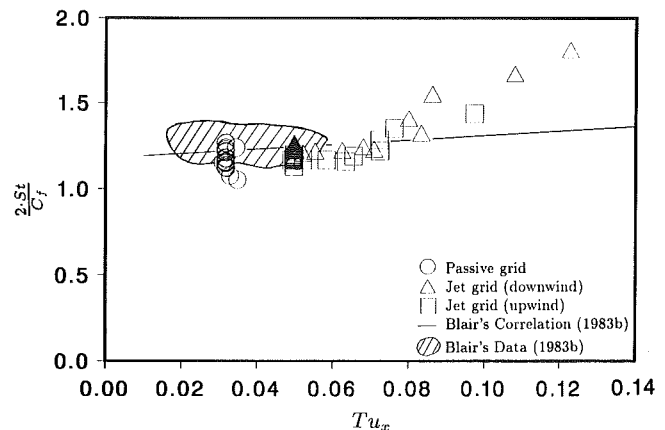


Fig. 8 Reynolds analogy factor versus streamwise turbulence intensity

the small-scale eddy seems to have more capability to penetrate into the boundary layer than the large-scale eddy. This implies that the small-scale eddy with high intensity (i.e., the downwind injection grid) may approach the surface and enhance the surface heat transfer. The large-scale eddy with high intensity (i.e., upwind injection grid) may not effectively penetrate into the boundary layer. Therefore, the augmented heat transfer for large-scale eddy is reduced. The mainstream turbulence should have a high level of intensity and a small-scale size to produce high heat transfer augmentation.

Universal Velocity and Temperature Profiles. Figure 6 shows the universal velocity and temperature profiles at $X/b = 117.9$. The u^+ and T^+ versus y^+ correlations for the zero turbulence flow are included for reference. At the downstream location ($X/b = 117.9$), the u^+ and T^+ profiles for the passive grid with no injection are about the same as the zero turbulence correlations. The u^+ and T^+ profiles for the upwind and downwind injections are about the same as the zero turbulence correlations except they are lower in the wake region. The wake region for the case of downwind injection is slightly lower than that of the upwind injection.

Influence of Mainstream Turbulence on Skin Friction. Figure 7 shows the friction factor versus length Reynolds number. The friction factor decreases with increasing length Reynolds number. The friction factor for the downwind injection grid is higher than the upwind injection and the passive grid with no injection. The present C_f versus Re_x curves are approximately parallel to that of the zero turbulence correlation over the entire range of the test section. Note in Fig. 5 that the St versus Re_x curves are parallel to the correlation at the downstream region ($Re_x > 2 \times 10^5$), but the slopes of St versus Re_x are higher at the upstream region ($Re_x < 2 \times 10^5$).

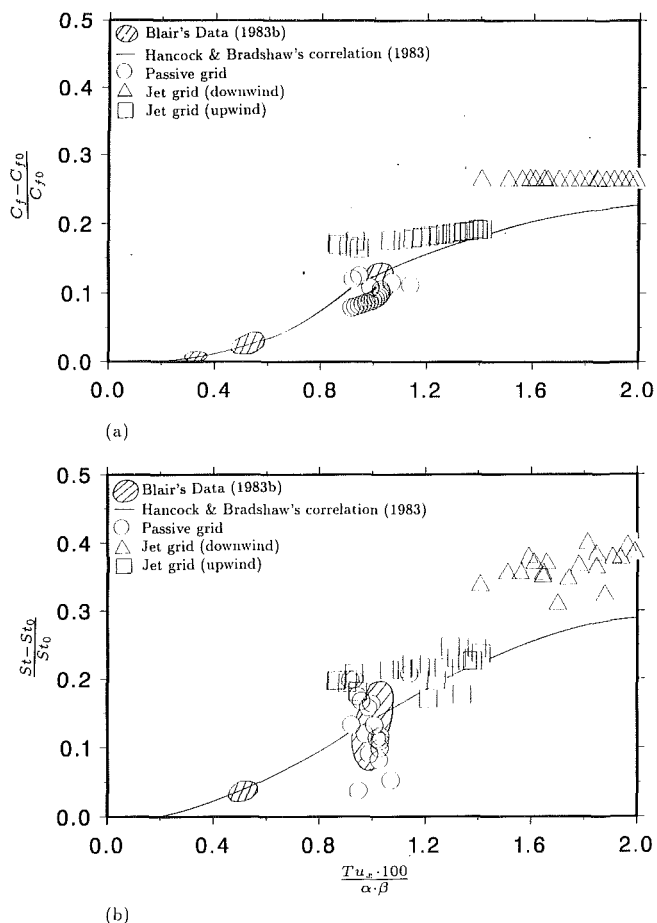


Fig. 9 (a) Augmented friction factor correlation; (b) augmented Stanton number correlation

The Reynolds Analogy Factor. The Reynolds analogy factor measures the response of the heat transfer coefficient and friction factor to the high mainstream turbulence. Figure 8 shows the Reynolds analogy factor ($2St/C_f$) versus streamwise turbulence intensity. The Stanton numbers and friction factors are taken from Figs. 5 and 7, respectively. Blair's correlation (Eq. (9)), which was based on experimental data for turbulence intensity up to 6 percent, is included for comparison. The Reynolds analogy factors increase with increasing mainstream turbulence intensity. The present data support the trend of the correlation for turbulence intensity up to 8 percent. The present data are much higher than the correlation for even higher values of turbulence intensity. The mainstream turbulence has more effect on the Stanton number augmentation than the friction factor; therefore, the Reynolds analogy factors are higher in the high mainstream turbulence flow.

Influence of Turbulence Intensity, Length Scale, and Reynolds Number. Hancock and Bradshaw (1983) found that the augmented friction factor $\Delta C_f/C_{f0}$ increases with increasing turbulence intensity (Tu) and momentum thickness Reynolds number (Re_θ), but with decreasing ratio of length scale to boundary layer thickness (L_e^u/δ). Figure 9(a) shows the correlation between $\Delta C_f/C_{f0}$ and $(Tu \cdot 100)/(\alpha \cdot \beta)$. The present passive grid data supports the correlation for $(Tu \cdot 100)/(\alpha \cdot \beta)$ up to 1.0, but the downwind and upwind injection grid produce much higher values of $\Delta C_f/C_{f0}$ for $(Tu \cdot 100)/(\alpha \cdot \beta)$ up to 2.

Blair (1983b) modified the Hancock and Bradshaw friction correlation to match his experimental heat transfer data. He found that the augmented friction factor $\Delta C_f/C_{f0}$ can be used to correlate the augmented Stanton number $\Delta St/St_0$ by mul-

tiplying a scale factor of 1.3 (this is the slope of Reynolds analogy factor equation); i.e., $\Delta St/St_0 = 1.3 \cdot \Delta C_f/C_{f0}$. Figure 9(b) shows the correlation between $\Delta St/St_0$ and $(Tu \cdot 100)/(\alpha \cdot \beta)$. Note that for flow with a given turbulence intensity (Tu), the smaller L_e^u/δ ratio (smaller α), and the larger Re_θ (smaller β) imply the larger $(Tu \cdot 100)/(\alpha \cdot \beta)$ value. The $\Delta St/St_0$ shifts to a higher value (shifts to the right-hand side of the curve). The reverse is also true. Consequently, the higher turbulence flow with the higher turbulence intensity, smaller scale eddy, and larger momentum thickness Reynolds number produces the higher heat transfer (and friction) augmentation. The present passive grid data support the correlation for $(Tu \cdot 100)/(\alpha \cdot \beta)$ up to 1.0. Figure 9(b) shows that the present $\Delta St/St_0$ values for the downwind and upwind injection grid are much higher than those predicted from the existing correlation for $(Tu \cdot 100)/(\alpha \cdot \beta)$ up to 2. The data presented in Figs. 9(a) and 9(b) are based on the assumption that the dissipation length scale equals the integral length scale, $L_e^u = \Lambda_f$, for jet grid-generated turbulence. This is different from Blair (1983b) who found that $L_e^u \cong 1.5 \Lambda_f$ for grid-generated turbulence.

Based on these observations, Hancock and Bradshaw's correlations for the augmented friction factor and augmented Stanton number are acceptable for $(Tu \cdot 100)/(\alpha \cdot \beta)$ up to 1.0 for grid turbulence. However, they are not applicable for $(Tu \cdot 100)/(\alpha \cdot \beta)$ up to 2.0 for jet grid turbulence. This implies that there are some fundamental differences of turbulent structure between grid and jet grid turbulence.

MacMullin et al. (1989) investigated the circular-wall-jet high turbulence on the flat plate heat transfer augmentation. They also found that the augmented Stanton numbers are much higher than Hancock and Bradshaw's correlations. This denies the wide applicability of the predictive correlations for arbitrary high free-stream turbulence.

Concluding Remarks

1 Controllable free-stream turbulence can be obtained by the wind tunnel jet grid system. The turbulence intensity for the downwind injection grid can be as high as 25 percent at 20 grid diameters downstream from the jet grid. The downwind injection can produce a higher turbulence intensity with a smaller length scale than the upwind injection. For the upwind injection, an additional traveling distance from upstream to downstream of the grid makes the length scale larger than the downwind injection.

2 The universal velocity and temperature profiles at the downstream developed region are not affected by the jet grid-generated turbulence intensity. The universal velocity and temperature profiles in the wake region are slightly lower than the zero turbulence correlation.

3 The surface heat transfer coefficients and friction factors increase with increasing mainstream turbulence intensity but the heat transfer coefficients increase faster. At the upstream developing region ($Tu_x > 6$ percent), the slopes of the St versus Re_x curves are higher than that of the zero turbulence correlation. At the downstream developed region ($Tu_x < 6$ percent), the slopes are parallel to each other.

4 The present Reynolds analogy factors agree with Blair's correlation for turbulence intensity up to 8 percent, but the present data are much higher than the correlation when the turbulence intensity is greater than 8 percent.

5 The combined effects of turbulence intensity, length scale, and momentum thickness Reynolds number in the augmented friction factor are determined by the Hancock and Bradshaw correlation. The augmented friction factors agree with the correlation for $(Tu \cdot 100)/(\alpha \cdot \beta)$ up to 1.0, but the present augmented friction factors $\Delta C_f/C_{f0}$ are much higher than those predicted from the correlation for $(Tu \cdot 100)/(\alpha \cdot \beta)$ up to 2.0.

6 The augmented Stanton numbers agree with the corre-

lation for $(Tu \cdot 100)/(\alpha \cdot \beta)$ up to 1.0. However, the present augmented Stanton numbers $\Delta St/St_0$ are much higher than those predicted from the correlation for $(Tu \cdot 100)/(\alpha \cdot \beta)$ up to 2.0. In general, the correlation can predict the augmented friction factor and augmented Stanton number for grid turbulence but it underpredicts those for jet grid turbulence.

Acknowledgments

This project was sponsored by the U.S. Air Force Wright-Patterson Air Force Base under contract No. F33615-86-C-2723.

References

- Baines, W. D., and Peterson, E. G., 1951, "An Investigation of Flow Through Screens," *Transactions of ASME*, Vol. 73, pp. 467-480.
- Blair, M. F., and Werle, M. J., 1980, "The Influence of Free-Stream Turbulence on the Zero Pressure Gradient Fully Turbulent Boundary Layer," UTRC Contract Report R80-914388-12, pp. 17-18.
- Blair, M. F., Bailey, D. A., and Schlinker, R. H., 1981, "Development of a Large Scale Wind Tunnel for the Simulation of Turbomachinery Airfoil Boundary Layers," *ASME Journal of Engineering for Power*, Vol. 103, pp. 678-687.
- Blair, M. F., 1983a, "Influence of Free-Stream Turbulence on Turbulent Boundary Layer Heat Transfer and Mean Profile Development, Part I—Experimental Data," *ASME JOURNAL OF HEAT TRANSFER*, Vol. 105, pp. 33-40.
- Blair, M. F., 1983b, "Influence of Free-Stream Turbulence on Turbulent Boundary Layer Heat Transfer and Mean Profile Development, Part II—Analysis of Results," *ASME JOURNAL OF HEAT TRANSFER*, Vol. 105, pp. 41-47.
- Gad-El-Hak, M., and Corrsin, S., 1974, "Measurements of the Nearly Isotropic Turbulence Behind a Uniform Jet Grid," *Journal of Fluid Mechanics*, Vol. 62, Part 1, pp. 115-143.
- Han, J. C., and Young, C. D., 1988, "The Influence of Jet-Grid Turbulence on Turbulent Boundary Layer Flow and Heat Transfer," *Transport Phenomena in Turbulent Flow*, M. Hirata and N. Kasagi, eds., Hemisphere Publishing Corporation, New York, pp. 501-514.
- Hancock, P. E., and Bradshaw, P., 1983, "The Effect of Free-Stream Turbulence on Turbulent Boundary Layers," *ASME Journal of Fluids Engineering*, Vol. 105, pp. 284-289.
- Kays, W. M., and Crawford, M. E., 1980, *Convective Heat and Mass Transfer*, McGraw-Hill, New York.
- Kline, X. X., and McClintock, Y. Y., 1953, "Experimental Uncertainty," *Mechanical Engineering*, Vol. 75, pp. 3-8.
- MacMullin, R., Elrod, W., and Rivir, R., 1989, "Free-Stream Turbulence From a Circular Wall Jet on a Flat Plate Heat Transfer and Boundary Layer Flow," *ASME Journal of Turbomachinery*, Vol. 111, pp. 78-86.
- Mehendale, A. B., Han, J. C., and Ou, S., 1991, "Influence of High Mainstream Turbulence on Leading Edge Heat Transfer," *ASME JOURNAL OF HEAT TRANSFER*, Vol. 113, pp. 843-850.
- Moffat, R., and Maciejewski, P. K., 1985, "Heat Transfer With Very High Free-Stream Turbulence," *Proceedings of the 1985 Turbine Engine Hot Section Technology Conference*, NASA Conference Publication 2405, pp. 203-215.
- O'Brien, J. E., and VanFossen, G. J., 1985, "The Influence of Jet-Grid Turbulence on Heat Transfer From the Stagnation Region of a Cylinder in Crossflow," *ASME Paper No. 85-HT-58*.
- Schlichting, H., 1968, *Boundary Layer Theory*, 6th ed., McGraw-Hill, New York.
- Simonich, J. C., and Bradshaw, P., 1978, "Effect of Free-Stream Turbulence on Heat Transfer Through a Turbulent Boundary Layer," *ASME JOURNAL OF HEAT TRANSFER*, Vol. 100, pp. 671-677.
- Tassa, Y., and Kamotani, Y., 1975, "Experiments on Turbulence Behind a Grid With Jet Injection in Downstream and Upstream Direction," *Physics of Fluids*, Vol. 18, No. 4, pp. 411-414.
- Young, C. D., 1989, "The Influence of Jet-Grid Turbulence on Turbulent Boundary Layer Flow and Heat Transfer," Ph.D. Dissertation, Texas A&M University.

Evaluation of the Stagnation Point Region Overshoot

H. H. Sogin

Emeritus Professor
of Mechanical Engineering,
Tulane University,
New Orleans, LA 70118

Stagnation point region overshoot is the augmentation of total heat transfer owing to the presence of insulation at the stagnation point region of an otherwise isothermal body. Evidence summarized by the present work indicates that this paradoxical event can be made to occur. The overshoot is due to the singularly high temperature gradient that is impressed upon the boundary layer just as it arrives at the leading edge of the heated surface after passing over the insulated central portion. The evidence comprises experimental results based on the mass-heat analog using sublimation of naphthalene and on theoretical boundary layer calculations using a method of local similarity. In the experiments, the insulated surfaces were simulated with inert wax, and isothermal regions with active naphthalene. The surfaces were circular disks facing uniform airstreams. The finding was that the total rate of mass transfer would be as much as 10 percent greater than that of a fully active disk if the radius of the central inert region were half the radius of the disk. Put another way, if only the 30-percent annulus at the outer edge of the disk were active, it would transfer mass at the same rate as the completely active disk under the same circumstances of flow. Corresponding results are expected from analogically heated disks operating with Prandtl number near unity and disk Reynolds number ranging from 5000 to 250,000.

Introduction

Stagnation point region overshoot is the augmentation of total heat transfer owing to the presence of insulation at the stagnation point region of an otherwise isothermal body. Evidence summarized by the present work indicates that this paradoxical event can be made to occur.

This topic is related to the analytical treatment of heat transfer to boundary layers from nonisothermal surfaces (e.g., Klein and Tribus, 1953; Kays and Crawford, 1980), or to the influence of a hydrodynamic starting length, which is usually associated with flat plates and internal flow through tubes (Kays and Crawford, 1980; Lau and Sparrow, 1980; Sogin, 1961).

The heat-mass analog using sublimation of naphthalene to airstreams afforded the opportunity to study the influence of an adiabatic starting surface at the stagnation point region of circular disks (Sogin and Oskay, 1960). The central region was made inert (analogous to the insulated starting surface) by replacing the naphthalene in this area with a wax and leaving the naphthalene on the contiguous, concentric surface active (analogous to the isothermally heated surface). The mass transfer recession was measured by means of a machinist's dial indicator gage contacting the surface of a disk indexed to a graduated turntable; profiling the surface was performed before and after the disk was exposed to an airstream during a metered time interval. The least count of the dial indicator gage was 0.0025 mm (0.0001 in.), and the turntable adapted to the method of measurement was in all aspects of comparable machinist's precision.

The purpose of this paper is to summarize the experimental evidence for the overshoot, to evaluate it analytically, and to determine the optimum radius of the inert central region.

We begin with homogeneous naphthalene disks facing uniform airstreams: Their surfaces normal to the flow are entirely active. Experimental results are compared with an analytical distribution calculated by a method based on simple (first-order) local similarity. The procedure is repeated for nonhomogeneous disks, that is, for disks having inert centers at the region of the stagnation point. We shall see that the experi-

mental results confirm the method of the calculations. Finally, the optimum overshoot is evaluated.

Summary of Apparatus and Scope of Data in the Experimentation by Sogin and Oskay

Description of the recent work by Sparrow and Geiger (1985) on local mass transfer from homogeneous naphthalene disks is readily available. However, the work by Sogin and Oskay (1960), which includes experimentation on both homogeneous and nonhomogeneous disks, has until now not appeared in the open literature. Therefore, before the results of these studies are presented and analyzed, some aspects of the earlier work are briefly reviewed with respect to its principal apparatus and scope of the data.

The wind tunnel had an induced draft and an open circuit. Its test section was 81 cm wide by 56 cm high (32 by 22 in.), and the contraction ratio was approximately 7:1. The turbulence intensity ranged from about 0.8 to 1.4 percent, depending upon air speed and location. Air speeds were held steady during every run, and they ranged from 21.0 to 39.4 m/s.

All of the disks used by Sogin and Oskay were 10.2 cm (4 in.) in diameter. They were mounted on a fine sting held in place by means of guy wires. The forward end of the sting was designed so that the disks could be engaged quickly on male-female ground tapered fittings. The appropriate orientation of the sting was checked by simultaneously balancing multiple pressures at taps located at a uniform distance from the central axis, near the edge of a dummy substitute disk.

The temporal average air temperatures of the runs reported here ranged from 25.6 to 32.3°C (78.1 to 90.1°F), with the exception of one run at 35.1°C (95.1°F). Each temporal average temperature was itself the average of a set of four calibrated thermocouples deployed to various locations in the airstream. In reducing the data for each run, the temporal average temperature was first corrected for the cooling due to the latent heat of sublimation. The corrected value was used to determine the equilibrium vapor pressure at the air-naphthalene interface. The temperature corrections were about 0.15 K on the average and never more than 0.33 K.

Reagent grade naphthalene was used throughout the investigation. The integrated mean depth of recession of the

Contributed by the Heat Transfer Division for publication in the JOURNAL OF HEAT TRANSFER. Manuscript received by the Heat Transfer Division October 18, 1990; revision received July 1, 1991. Keywords: Analog Techniques, Forced Convection, Mass Transfer.

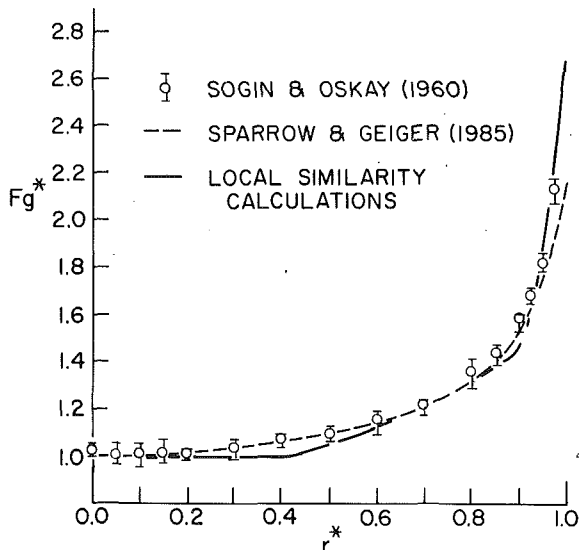


Fig. 1 Radial distribution of the local Frössling number ratio on homogeneous disks: $5000 < Re < 250,000$

naphthalene for all runs reported here ranged from 0.05 to 0.26 mm (0.0021 to 0.0102 in.). Times of exposure to the airstream ranged from 0.5 to 2.0 hours.

Experiments on Homogeneous Disks

The experiments by Sparrow and Geiger (1985) on homogeneous disks established that the distribution of the local mass transfer coefficient $K(r)$ is everywhere proportional to the square root of the disk Reynolds number $Re = UD/\nu$ in the range from 5000 to 50,000. This suggests correlating results independently of Re , in terms of the local mass transfer Frössling number

$$Fg(r) = \frac{K(r)}{U} \sqrt{Re} \quad (1)$$

The radial distribution of the ratio $Fg^* \equiv Fg(r^*)/Fg(0)$ for results taken from Sogin and Oskay (1960) and from Sparrow and Geiger (1985) is plotted in Fig. 1. The value of $Fg(0)$ is arbitrarily set at 0.414 throughout the present work. The result of a "real flow" solution of the boundary layer equations (Sogin, 1991), the value 0.414 is 3–6 percent less than comparable experimental findings. The differences may be ascribed to effects of turbulence, to questionable porosity of the solid and the resulting questionable value of specific gravity used in reducing data from local measurements, to difference of model geometry and size, or to any combination of these. However, it will be seen that these uncertainties cannot profoundly affect the analytical results of the present work. The points in Fig. 1 indicate averages of the results at corresponding locations in the five runs of the Series B experiments, in which Re ranged from 138,000 to 251,000. Each point of every run

represents the average of six determinations, the recession of the naphthalene having been measured every 60 deg on a circular pattern. The vertical bars are subtended by the local extremes of the data spread. The dashed graph in Fig. 1 represents the correlating curves drawn by Sparrow and Geiger (1985, Figs. 3 and 4); these are averages obtained on unshrouded disks of 3.493-cm diameter. Thus Fig. 1 establishes a correlation of the ratio $Fg^*(r^*)$ in the range of Re from 5000 to 250,000. The uncertainty of the data is about ± 4 percent on the average. The greatest difference between the two sets of experimental averages—10 percent near the edge, at $r^* = 0.975$ —may be owing to the geometric dissimilarities of the two experimental models, particularly their dissimilar wakes. The solid graph in Fig. 1 is the result of the calculations explained in the next section.

Local Similarity Calculations for Homogeneous Disks

Basic assumptions underlying all of the calculations in this paper are that the oncoming airstream is steady, incompressible, and irrotational while the boundary layer on the forward surface of the disk is steady, incompressible, nondissipative, and laminar. Further, the naphthalene vapor, a trace component, does not affect the thermophysical properties of the air; and the concentration of the naphthalene vapor at the disk wall is uniform along the active surface while the concentration of the vapor in the oncoming air is zero.

In order to employ a method of local similarity for the purpose of calculating the mass transfer, we now suppose that corresponding to each point on the disk there exists a point on an equivalent wedge (Evans, 1968) such that the local Frössling number on the wedge equals the local Frössling number on the disk. Neither hydrodynamic nor concentration information feeds upstream, and every particle in the boundary layer reacts to its local environment without memory of its recent history. Thus in order to calculate the mass transfer coefficient at a point on the disk, we have first to determine the equivalent wedge flow at that point and second to calculate the Frössling number at the corresponding point on that wedge. Calculations repeated at successive points will yield the radial distribution of the ratio $Fg^*(r^*)$.

From the boundary layer solutions for isothermal wedges (Evans, 1968), the expression for the Frössling number is given by

$$Fg(r^*) = \left[\frac{6f(r^*)}{(2-\beta)r^*} \right]^{1/2} \frac{\theta'(0)}{Sc} \quad (2)$$

where $f(r^*) = v(r^*)/U$, $v(r^*)$ being the radial velocity at the outer edge of the boundary layer on the disk; β is the wedge-angle ($\beta\pi$) parameter of the equivalent wedge; $\theta'(0)$, a similarity solution of the boundary layer equations, represents the concentration gradient at the surface of the wedge—the analog of the temperature gradient; and Sc is the Schmidt number (the analog of the Prandtl number), 2.55 for naphthalene vapor in air. Values of $\theta'(0)$ have been tabulated by Evans (1968) as a function of β and Sc . To pursue the evaluation of $Fg(r^*)$,

Nomenclature

B = beta function	m = wedge flow exponent for disk	x = radius of inert center
c = an exponent in Eq. (6)	Pr = Prandtl number	β = wedge-angle boundary layer parameter
D = diameter of disk	Re = Reynolds number = UD/ν	$\theta'(0)$ = parameter in boundary layer mass (heat) transfer solution
$Fg(\)$ = local Frössling number for mass transfer	r = radial coordinate	ν = kinematic viscosity
$f(r)$ = velocity ratio = $v(r)/U$	Sc = Schmidt number	
I_z = incomplete beta function	U = velocity of uniform oncoming flow	Superscript
$K(r)$ = local mass transfer coefficient	$v(r)$ = radial velocity at outer edge of boundary layer	* = dimensionless ratio, or normalized quantities
$M(\)$ = total rate of mass transfer		

Table 1 Local similarity calculations of the Frössling number distribution for the entirely active disk surface

r^*	m	β	$\theta'(0)$	F_g	F_g^*
0.000	1.000	0.5000	0.7618	0.414	1.000
0.100	1.000	0.5000	0.7618	0.414	1.000
0.200	1.000	0.5000	0.7618	0.414	1.000
0.300	1.000	0.5000	0.7618	0.414	1.000
0.400	1.000	0.5000	0.7618	0.414	1.000
0.500	1.195	0.5697	0.7708	0.431	1.041
0.600	1.434	0.6468	0.7801	0.462	1.116
0.700	1.673	0.7160	0.7879	0.500	1.208
0.800	1.912	0.7785	0.7943	0.544	1.314
0.850	2.032	0.8075	0.7973	0.570	1.377
0.900	2.151	0.8352	0.7998	0.596	1.440
0.925	3.220	1.0354	0.8042	0.673	1.626
0.950	5.845	1.3217	0.7295	0.762	1.841
0.975	8.976	1.4990	0.6926	0.915	2.210
1.000	11.508	1.5864	0.6771	1.108	2.676

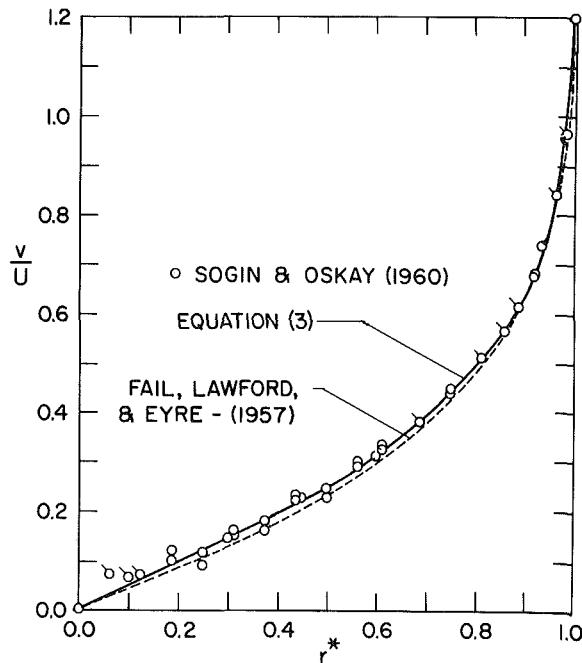


Fig. 2 Velocity ratio $v(r^*)/U$ at the outer edge of the boundary layer on a disk

therefore, we need to know the quantities $f(r^*)$ and β , which are intimately related (as we shall see), and which we need also for the first part of the calculations, namely, for determining the equivalent wedge flows.

The velocity ratio function $f(r^*)$ was determined (Sogin and Oskay, 1960) by measuring the pressure distribution on two different 10.2-cm-dia disk models (at different times) mounted on a 19-mm-dia sting fixed to the wind tunnel walls by guy wires. Both models were uniformly 12.5 mm in thickness. Bernoulli's theorem was used to calculate $v(r^*)/U$. One of the disks was instrumented with multiple manometers, and the other with a single movable eccentric tap and a micromanometer. Since there was no significant difference in the results, the summary of data in Fig. 2 treats the two models alike; the

flags indicate coinciding data points. The base (rear surface) pressure coefficient was -0.44 , and, consequently, the separation velocity ratio at the disk edge was 1.20. The dashed graph in Fig. 2, representing measurements by Fail et al. (1957), reinforce the data of Sogin and Oskay (1960). The solid curve is the graph of the following patchwork of expressions, which the authors joined so that the data are represented continuously and smoothly.

$$f(r^*) = \begin{cases} 0.480r^*, & 0 \leq r^* \leq 0.418 \\ 0.0735 \exp(2.39r^*), & 0.418 \leq r^* \leq 0.9 \\ 1.200 - 13.81z + 120.9z^2 - 396z^3, & 0.9 \leq r^* \leq 1.0 \end{cases} \quad (3)$$

where $z = 1 - r^*$. We are now prepared to establish the wedge-angle parameter β .

A power function $C \cdot r^m$, where C and m are constants, is said to be the velocity of a wedge flow whether or not the shape of the surface in question is in fact a wedge. This includes the velocity at the outer edge of the boundary layer on a disk, either on the whole or at a local position; in the latter case C and m are regarded as local constants. Using a prime to represent differentiation, $v'(r) = C \cdot m \cdot r^{m-1} = m \cdot v(r)/r$, whence

$$m = \frac{r^* f'(r^*)}{f(r^*)} \quad (4)$$

By virtue of the Mangler transformation (Evans, 1968) the wedge-angle parameter

$$\beta = \frac{2m}{m+3} \quad (5)$$

Thus the quantity m , which is a local property of the axially symmetric flow, is related to the quantity β , a property of a locally equivalent plane flow.

We now have all that is needed in order to calculate a local Frössling number on the disk. Table 1 provides details of the calculations; the solid graph in Fig. 1 represents the radial distribution of the ratio $F_g^*(r^*)$, as already mentioned.

Comparing the experimental and calculated results in the range of r^* from zero to 0.925, we see that without exception the calculated results are either equal to or less than the average values in both sets of experiments. In this range, most notably

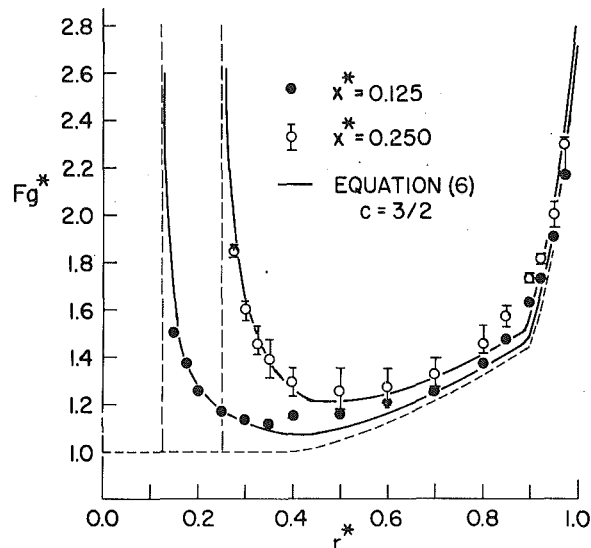


Fig. 3 Radial distribution of the local Frössling number ratio on non-homogeneous disks: $Re = 200,000$

in the neighborhoods of the two patches in Eq. (3), the maximum differences are less than 8 percent. At about $r^* = 0.95$, a crossover occurs. At the extreme edge, the calculated result exceeds the finding in the more recent experiments by 24 percent. However, the calculated results follow the trend of the data points taken from the earlier work, as far as they go. (The disks were traversed until $r^* = 0.975$, clearing 1.3 mm from the edge of the naphthalene for the staging of the mechanical stylus.) This agreement is consistent with the fact that the measurements of pressure distribution, upon which the calculations are based, were made on models congruent with the naphthalene disks. The mean value of the calculated Frössling number integrated on the surface area of the disk is 0.544 as compared with 0.577, the result that Sparrow and Geiger (1985) found experimentally by weighing.

The broad agreement between the results from the two sets of experiments and the calculations satisfactorily confirms the validity of the local similarity approximation, and it promises a reasonable estimate of the overshoot.

Experiments on Nonhomogeneous Disks (Inert Centers)

The inert centers were made by machining away the central naphthalene and replacing it with molten wax of a low melting temperature range. The final working surfaces were machined flush. Local rates of recession were measured as before. All of these test runs were carried out at Re approximately 200,000.

The radial distributions of the test results are shown in Fig. 3, where $Fg^*(x^*, r^*) \equiv Fg(x^*, r^*)/Fg(0, 0)$; x^* denotes the dimensionless radius $2x/D$ of the inert center and is, of course, a constant for any particular disk. Again, $Fg(0, 0) = 0.414$, independently of the presence of an active stagnation point. The closed circles depict the distribution measured during a singular run for $x^* = 0.125$. The open circles are the averages of four runs for $x^* = 0.250$. The ends of the bars show the extreme data spread; the maximum deviation of an extreme from the average is about 8 percent of the average; and the average of the absolute discrete deviations is about 4 percent. Part of the scatter may be ascribed to unstable, transient separation and reattachment, which undoubtedly occurs as the boundary layer fills the very slight cavity that forms behind the surface discontinuity (at the edge of the wax) as the naphthalene recedes. The dashed graph in Fig. 3 represents the homogeneous disks, corresponding to $x^* = 0$. The solid graphs are the results of the calculations in the next section.

Local Similarity Calculations for Nonhomogeneous Disks

Following the summary work of Klein and Tribus (1953, Table II), the Frössling number that accounts for the hydrodynamic starting length of the boundary layer at the stagnation point region is now presumed to be of the form

$$Fg^*(x^*, r^*) = \begin{cases} 0, & r^* < x^* \\ Fg^*(0, r^*) \cdot [1 - (x^*/r^*)^c]^{-1/3}, & r^* > x^* \end{cases} \quad (6)$$

where $Fg^*(0, r^*)$ is identically $Fg^*(r^*)$ in Table 1, and exponent c is here taken to be an empirical constant suitable to the data. The two solid curves in Fig. 3 are graphs of Eq. (6) with $c = 3/2$. The fit of the graphs to the experimental results, the one at $x^* = 0.125$ and the other for the averages at $x^* = 0.250$, appears to be very satisfactory albeit on the basis of an approximative theory and an empirical constant.

Again, the degree of agreement between the experimental and calculated results is considered satisfactory for the present purpose. Equation (6) with $c = 3/2$ accounts for the influence of hydrodynamic starting lengths up to $x^* = 0.250$. Its local, stepwise application to the rest of the disk provides reasonable agreement with the experimental results. Since the calculations almost universally underestimate the average experimental values, they also will underestimate the overshoot.

Clearly, the effect of the inert center is to introduce a very steep concentration gradient at the leading edge of the active surface. The resulting high flux contributes so very much to the total rate of mass transfer that, indeed, it may exceed the total rate from the corresponding homogeneous disk in the same flow situation.

Calculation of the Total Mass Transfer and Its Optimization

The total rate of mass transfer from the disk would be calculated according to

$$M(x^*) = \frac{D^2}{4} \cdot \int_{x^*}^1 2\pi r^* \cdot K(x^*, r^*) \cdot c_w dr^* \quad (7)$$

where c_w is the uniform concentration of the vapor at the active wall. Our interest, however, lies in the ratio of the mass transfer from a disk having an inert center of radius x to the mass transfer from a disk having an entirely active surface: $M^*(x^*, r^*) \equiv M(x^*, r^*)/M(0, r^*)$. Hence

$$M^*(x^*) = \frac{\int_{x^*}^1 Fg^*(x^*, r^*) \cdot r^* dr^*}{\int_0^1 Fg^*(0, r^*) \cdot r^* dr^*} \quad (8)$$

The base integral, the denominator, is essentially the mean Frössling number of the homogeneous disk; the value is 0.544. The convolution integral in the numerator is improper for $x^* > 0$. That it converges for $c = 3/2$ is fortuitous.

The integral can be evaluated in two parts: the first analytically from x^* to r_1^* , the interval where $Fg^*(r^*) = 1.00$; and the second part numerically in the interval from r_1^* to 1.0. The development of the analytical part is summarized in the appendix. The result is

$$M(x^*, r_1^*) = 2\pi r_1^{*2} \left[g(X) \cdot (1-X)^{2/3} - \left(\frac{2\pi}{9} \right)^{1/2} \Gamma^{-3} \left(\frac{4}{3} \right) \cdot J_{(1-X)} \left(\frac{5}{3}, \frac{5}{3} \right) \right] \quad (9)$$

$$g(X) = \frac{1}{2} + X + \frac{1}{2} X^2 - X^3$$

$$X = \left(\frac{x^*}{r_1^*} \right)^{3/2}$$

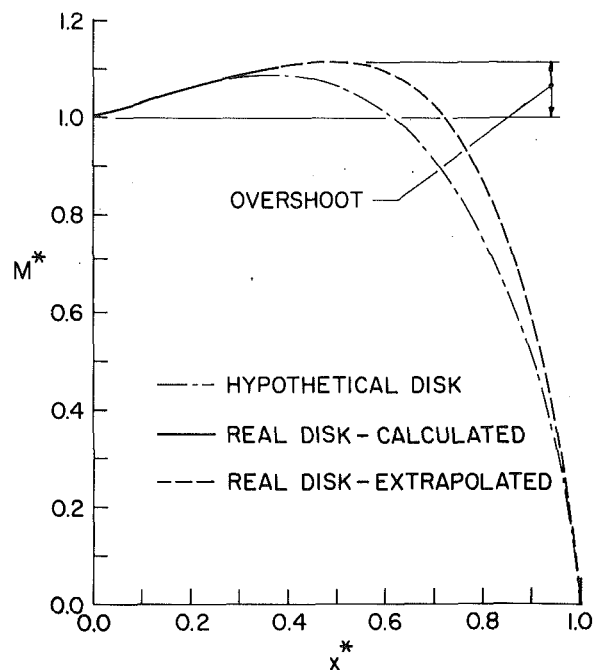


Fig. 4 Mass transfer ratio as a function of radius of the inert central region, showing the overshoot

where $I_{(z)}$ ($5/3, 5/3$) is an incomplete beta function, briefly tabulated in the appendix.

Postponing further consideration of the real disk, let us now consider a hypothetical disk surface on which the velocity at the outer edge of the boundary layer would increase in direct proportion to the radius all the way to the edge of the disk, so that the coefficient of mass transfer from the homogeneous disk would be uniform on the entire surface. Then Eq. (9) with $r_1^* = 1.0$ yields the mass transfer ratio $M^*(x^*)$ as represented by the dashed-dotted curve in Fig. 4. The maximum total rate of mass transfer occurs at $x^* = 0.37$, and the overshoot is 8.8 percent of the mass transfer from the corresponding hypothetical homogeneous disk, whose mean Frössling number would be 0.414. Another way of looking at the overshoot is to consider the hardware. Only the 40-percent annulus at the edge of the disk has to be made active in order to achieve as much mass transfer as would obtain if the entire surface were active.

On the real disk, the velocity at the outer edge of the boundary layer ultimately accelerates very rapidly at radii $r^* > 0.4$, the range where extrapolation by means of Eq. (6) or of an alternative is as yet unsubstantiated. For this reason Eq. (9) is used with $r_1^* = 0.4$, cutting the analytical calculations short at $x^* = 0.4$. Then, as x^* ranges from 0.0 to 0.4, calculations of the ratio $M^*(x^*)$ are completed for r^* in the range from 0.4 to 1.0 by numerical integration. The results of these calculations for $M^*(x^*)$ are shown by the solid portion of the upper curve in Fig. 4. The dashed continuation is an extrapolation freely sketched, allowing for the obvious trend suggested by the graph for the hypothetical disk and satisfying the constraints at the ends of the closed interval of x^* from 0.4 to 1.0. Thus it is estimated that the maximum occurs at $x^* \approx 0.5$ on the real disk and that the overshoot is about 10 percent of the mass transfer from the corresponding homogeneous disk, whose mean Frössling number is 0.544. In terms of hardware, it would be sufficient to activate only the outer 30-percent annulus to achieve the same mass transfer as with the disk of fully active surface.

What has been found for mass transfer applies as well to heat transfer at Prandtl number near unity. The heat transfer Frössling number is the product of a Stanton number and the square root of the disk Reynolds number; thus

$$Fg_{\text{heat}} = \frac{h(r)}{\rho c_p U} \sqrt{\text{Re}} \quad (10)$$

where $h(r)$ is the local coefficient of heat transfer, and ρ and c_p are the density and specific heat of the fluid. In applying the mass-heat analog, the following equation will interpolate from the mass transfer results to corresponding heat transfer predictions:

$$\frac{Fg_{\text{heat}}}{Fg} = \left(\frac{\text{Sc}}{\text{Pr}} \right)^{0.64} \quad (11)$$

This relationship is equivalent to that of Eq. (15) by Sparrow and Geiger (1985) recast in terms of Frössling numbers.

A configuration much more practical than the disk, of course, is the tube in crossflow. Chun and Boehm (1990) provide some numerical results for the circular tube in the Reynolds number range from 200 to 3480. They consider several cases, including adiabatic stagnation regions followed by contiguous isothermal surfaces. Their choice of parameterization and the limited breadth of numerical coverage preclude evaluation of any overshoot. However, their results qualitatively corroborate the trend of the results in the present work.

As for mass experiments that include inert stagnation point regions in the two-dimensional case, I have seen no reports in this area.

Conclusions

Experiments on homogeneous and nonhomogeneous disks confirm that local similarity calculations satisfactorily predict the local mass transfer rates through the accelerating laminar boundary layer flow on the forward surface of a disk up to disk Reynolds number of 250,000.

Table 1 correlates local mass transfer on homogeneous disks in the Reynolds number range from 5000 to 250,000, underestimating the experimental values about 4 percent.

The step function appearing in Eq. (6) with $c = 3/2$ empirically correlates data on nonhomogeneous disks (whose centers are inert) and allows calculation of the total mass transfer by supporting convergence of the integral in the numerator of Eq. (8).

It has been estimated that when the radius of the inert center of a nonhomogeneous disk is about half of the disk radius, the overshoot reaches a maximum, which is about 10 percent of the total rate of mass transfer from the front surface of the corresponding homogeneous disk. From another viewpoint, it would be sufficient to activate the 30-percent annulus adjacent to the edge of the disk for the rate of mass transfer to equal that from the homogeneous counterpart.

Additional experiments ought to be performed for inert centers of radii greater than a quarter of the disk radius, particularly out toward the region of highly accelerated flows ($\beta > 1$). The purpose would be to extend the use of the step function in Eq. (6) or to find an appropriate substitute.

Experiments also should be performed to establish a calculation scheme for the plane nonhomogeneous stagnation region in practical ranges of Reynolds number.

References

- Chun, W., and Boehm, R. F., 1990, "Forced Convection From a Nonisothermal Cylinder in Crossflow," *ASME JOURNAL OF HEAT TRANSFER*, Vol. 112, pp. 781-784.
- Evans, H. L., 1968, *Laminar Boundary-Layer Theory*, Addison-Wesley Publishing Co., Reading, MA, Chaps. 7, 8, and 9.
- Fail, R., Lawford, J. A., and Eyre, R. C. W., 1957, "Low Speed Experiments on the Wake Characteristics of Flat Plates Normal to an Airstream," RAE Technical Note Aero 2516.
- Kays, W. M., and Crawford, M. E., 1980, *Convective Heat and Mass Transfer*, 2d ed., McGraw-Hill, New York, Chaps. 8 and 9.
- Klein, J., and Tribus, M., 1953, *Heat Transfer Symposium*, Engineering Research Institute, University of Michigan, Ann Arbor, pp. 211-235.
- Lau, S. C., and Sparrow, E. M., 1980, "Average Heat Transfer Coefficients

for Forced Convection on a Flat Plate With An Adiabatic Starting Length," ASME JOURNAL OF HEAT TRANSFER, Vol. 102, pp. 364-366.

Sogin, H. H., and Oskay, V., 1960, "Heat Transfer From Surfaces of Non-uniform Temperature Distribution. Final Report Part II: Local Sublimation From Disks in Axisymmetric Flow," AFOSR TR-60-78, Air Force Office of Scientific Research, Contract No. AF49(638)-46, Project No. 17500.

Sogin, H. H., 1961, "Laminar Transfer From Isothermal Spanwise Strips on a Flat Plate," ASME JOURNAL OF HEAT TRANSFER, Vol. 82, pp. 53-63.

Sogin, H. H., 1991, "An Improved Correlation of Stagnation Point Mass Transfer From Naphthalene Circular Disks Facing Uniform Airstreams," ASME JOURNAL OF HEAT TRANSFER, Vol. 113, pp. 772-773.

Soper, H. E., 1921, *Numerical Evaluation of the Incomplete Beta Function*, Cambridge University Press, United Kingdom.

Sparrow, E. M., and Geiger, G. T., 1985, "Local and Average Heat Transfer Characteristics for a Disk Situated Perpendicular to a Uniform Flow," ASME JOURNAL OF HEAT TRANSFER, Vol. 107, pp. 321-326.

APPENDIX

Analytical Evaluation of the Integral in Eq. (7) From x^* to r_1^* for the Case $Fg^*(0, r^*) = 1.0$

The asterisks are omitted for convenience. We seek a closed form for the integral

$$A = 2\pi \int_x^{r_1} [1 - (x/r)^{3/2}]^{-1/3} r dr \quad (A1)$$

Substitute

$$\lambda = (x/r)^{3/2}; \quad X = (x/r_1)^{3/2} \quad (A2)$$

Then

$$A = \frac{4\pi}{3} r_1^2 \int_X^1 \lambda^{-7/3} (1-\lambda)^{-1/3} d\lambda \quad (A3)$$

The integral can now be closed in terms of standard beta functions:

$$A = \frac{4\pi}{3} r_1^2 \cdot B\left(-\frac{4}{3}, \frac{2}{3}\right) \cdot \left[1 - I_X\left(-\frac{4}{3}, \frac{2}{3}\right)\right] \quad (A4)$$

A tabulation of the incomplete beta function $I_X(p, q)$ with $p = -4/3$ and $q = 2/3$ is unlikely to be either found or successfully evaluated by numerical integration. Upon applying Soper's (1921) recursion formula "by raising p ,"

$$I_X\left(-\frac{4}{3}, \frac{2}{3}\right) = \frac{X^{-4/3}(1-X)^{2/3}}{-\frac{2}{3}B\left(-\frac{1}{3}, \frac{2}{3}\right)} + I_X\left(-\frac{1}{3}, \frac{2}{3}\right) \quad (A5)$$

(The coefficient of the beta function B is $p+q$.) After applying the recursion formula two more times, the identity $I_Z(q, p) = 1 - I_{(1-Z)}(p, q)$, and the recursion formula once again, and after some algebraic simplification, we come to Eq. (9) of the main text.

Evaluation of $I_Z(5/3, 5/3)$ is amenable to numerical integration. Following is a brief tabulation of

$$I_Z\left(\frac{5}{3}, \frac{5}{3}\right) = \frac{1}{B\left(\frac{5}{3}, \frac{5}{3}\right)} \cdot \int_0^Z \lambda^{2/3} (1-\lambda)^{2/3} d\lambda \quad (A6)$$

Z	0.0	.1	.2	.3	.4	.5	.6	.7	.8	.9	1.0
I_Z	0.0000	.0422	.1279	.2392	.3659	.5000	.6341	.7608	.8721	.9578	1.000

$B(5/3, 5/3) = 0.293337$ Linear interpolation is inadequate.

Measurements of the Free Surface Flow Structure Under an Impinging, Free Liquid Jet

J. Stevens

B. W. Webb

Heat Transfer Laboratory,
Brigham Young University,
Provo, UT 84602

The objective of this research was to characterize the flow structure under an impinging liquid jet striking a flat, normally oriented surface. The approach was the measurement of the free surface velocities of the jet prior to impingement and the surface velocities of the radially spreading liquid layer. A novel laser-Doppler velocimetry technique was used. The LDV system was configured such that the measurement volume would span the time-dependent fluctuations of the free surface, with the surface velocity being measured. The mean and fluctuating components of a single direction of the velocity vector were measured. It was found that the radial liquid layer data collapsed well over the range of jet Reynolds numbers $16,000 < Re < 47,000$ if plotted in dimensionless coordinates, where the measured velocity was normalized by the average jet exit velocity and the radial coordinate was normalized by the nozzle diameter. Mean liquid layer depths were inferred from the velocity measurements by assuming a velocity profile across the layer, and were reported. Pre-impingement jet measurements suggest that the flow development is nearly complete two diameters from the nozzle exit.

Introduction

Heat transfer studies of free liquid impinging jets have demonstrated the relatively high transfer coefficients that are found in such configurations (Stevens and Webb, 1991a; Vader et al., 1990; Chaudhry, 1964; Ma and Bergles, 1983; Inada et al., 1981). These high heat transfer rates have recently stirred interest in using impinging liquid jets to dissipate the anticipated high heat fluxes of next-generation VLSI circuits (Kiper, 1984; Yamamoto et al., 1987). As in all convective heat transfer situations, the flow field of an impinging liquid jet controls the heat transfer characteristics. In an attempt to understand the flow field and heat transfer under axisymmetric free liquid impinging jets, this study was undertaken to measure liquid velocities at the free surface of such jets, both prior to and following impingement against a flat, normally oriented surface. The measurements prior to impingement were made on the cylindrical stream free surface formed by the axisymmetric jet, while those following impingement were conducted on the free surface of the radially spreading liquid layer. An LDV system was used to measure the mean and fluctuating free surface velocities in a single direction by positioning the LDV measurement volume so that it spanned the spatial fluctuations of the free surface.

While the flow structure for submerged jets, in general, and for air jets in particular, has been studied extensively in the literature for the cases of both impinging and a nonimpinging jets, free liquid jets have received comparatively little attention. Theoretical flow solutions for laminar axisymmetric and plane liquid jets were discussed by Adachi (1987). Nakoryakov et al. (1978) have discussed the flow field of an impinging liquid jet in an experimental and theoretical study on the mass transfer and friction factor under such a jet. Thomas et al. (1990) studied experimentally the radial flow originating from a pressurized container on a rotating and stationary disk. For the stationary configuration, before the hydraulic jump, it was found that the film thickness either increased monotonically (lower flow rates) or decreased slightly, then increased (higher

flow rates). These effects are a combined result of the tendency for the layer to thin as it spreads out over the plate, and for it to thicken as it slows due to friction, with the second effect overtaking the first at large radius. Numerical calculations were carried out for this case by Rahman et al. (1990) using boundary conditions determined by the measurements of Thomas et al. (1990). Results agreed well with measurements for both liquid layer thickness and radial location of the hydraulic jump. Well upstream from the hydraulic jump, the liquid layer was characterized by a parabolic velocity profile.

Watson (1964) analytically examined the laminar and turbulent radial spread of a liquid jet over a flat impingement surface out to, and including, the hydraulic jump using boundary layer theory. A similarity solution for laminar flow was developed of the form $u = U(r)f(\eta)$ where $\eta = z/h(r)$. Turbulent flow was also considered using an eddy viscosity model and proceeding analogously to the development for laminar flow. The flow of a planar liquid jet was discussed as well.

Carper (1989) examined two approximate solutions to the laminar momentum equations for a free liquid impinging jet as part of a larger study of the heat transfer in such a configuration. One of the approximate solutions was that of Watson, discussed above. The author also modified the solution from Hung (1982) by using an improved initial condition, and found that it agreed well with the results of Watson.

Olsson and Turkdogan (1966) examined experimentally the radial flow field of an impinging liquid jet. Dimensionless nozzle-to-plate spacings (z/d) of 26 and 64 were used, and experiments included a variety of liquids with varying viscosities. A vernier height gage was used to measure the local liquid layer depth. Surface velocities were measured by using tracer particles and high speed photography. It was found that the surface velocity of the liquid layer was constant out to the hydraulic jump, and significantly less than the mean velocity of the falling stream.

Azuma and Hoshino (1983) reported LDV measurements inside the radial liquid layer formed by placing an axisymmetric nozzle very close to a flat plate (results were reported for dimensionless nozzle-to-plate spacings of 0.07, 0.08, and 0.3). It was found that the radial film flow begins with a laminar boundary layer, which eventually reaches the free surface, absorbing the entire flow. For sufficiently large Re , the laminar

Contributed by the Heat Transfer Division and presented at the 3rd ASME/JSME Thermal Engineering Joint Conference, Reno, Nevada, March 17-22, 1991. Manuscript received by the Heat Transfer Division February 19, 1991; revision received June 30, 1991. Keywords: Forced Convection, Jets, Thin Film Flow.

flow later changes to a turbulent flow so that the entire flow is a turbulent boundary layer. They found that a fourth-order polynomial assumption for the velocity profile represented the measured velocities better in the region of the laminar boundary layer, while Watson's profile fit the flow better in the region where the laminar boundary layer engulfed the entire flow.

The literature review presented in the foregoing reveals little experimental work aimed at the characterization of the flow structure under free liquid jets. The objective of this study was to examine the flow structure of such a system. The approach was to measure liquid velocities at the free surface of several liquid jets prior to and after normal impingement against a flat plate. The surface velocities measured prior to impingement were used to characterize the axial development of the jet after leaving the nozzle and before impingement. The measurements on the radially spreading liquid layer were used to infer the depth of the layer, and to make general observations about the flow field.

Experimental Apparatus and Methods

The impinging jet was formed in a closed-loop system containing a centrifugal pump, flow meters, jet nozzle, and apparatus for collecting spent liquid and directing it back to the pump. Nozzles of inside diameter 2.1, 4.6, and 9.3 mm were used. All nozzles were long enough to insure fully developed turbulent flow at the nozzle exit. A schematic of the system is shown in Fig. 1. The pump was a Teel Model 2PO19 with maximum capacity of 53 lpm at 0.069 MPa and 7.6 lpm at 1.1 MPa. A bypass flow circuit was included in order to allow the pump to operate at optimal conditions while maintaining the jet at the desired flow rate. The flow meters had a combined measurement range of 0.38 to 45.6 lpm (0.1 to 12 gpm) with uncertainty of 0.038 lpm for flow rates less than 3.8 lpm and uncertainty of 0.38 lpm for flow rates greater than 3.8 lpm. The average jet exit velocity was calculated from the flow meter readings and the known nozzle diameter. A heat exchanger included in the flow circuit maintained the circulating water near a constant temperature of 14°C. Fluid properties were evaluated at this temperature.

Velocity measurements were made with a TSI laser-Doppler velocimeter using a Spectra-Physics 5 Watt argon-ion laser. The optics were configured for backscatter operation. Only one component of the velocity was measured in this study, using the 488 nm (blue) line of the laser. A 250 mm focal distance lens was employed at the end of the optics train. Beam expansion was omitted in order to increase the length of the measurement volume. A field stop system was employed with an aperture of 0.20 mm to optically filter extraneous light. This configuration resulted in the ellipsoidal measurement volume having dimensions of approximately 0.118 mm and 2.78 mm on the minor and major axes, respectively, and a beam intersection half-angle of 2.43 deg. The measurement volume

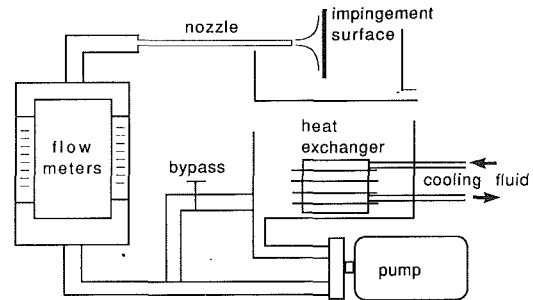


Fig. 1 Schematic of liquid jet and flow loop

contained approximately 21 fringes. The optics were deliberately configured to yield a long, thin measurement volume that would span the full range of estimated spatial fluctuations of the free surface flow in the jet and the radial layer. In order to insure that this would occur, the measurement volume was positioned so that the diagnostic volume was approximately centered on the mean location of the spatially fluctuating free surface.

Photodetector output was processed by a TSI model 1980B signal processor operating in continuous data collection mode. The signal processor was normally set to accept data at 32 cycles/burst and 1 percent comparison (5/8 comparison ratio over 20 cycles). Frequency shifting was employed, at either 1 or 2 MHz, in order to gather data at sufficiently high data rate despite turbulent fluctuations in the liquid layer thickness. Five thousand data points were gathered to determine each reported mean velocity and fluctuating velocity measurement. The measurement volume was moved relative to the stationary experimental setup by moving the entire LDV system on a three-axis traversing table with ± 0.1 mm resolution in each direction. The table positioning was accomplished using software on the same microcomputer used for the data acquisition.

The flow was opacified for LDV surface velocity measurements by diluting the water with 5 percent whole milk. This dilution provided a reflective, free surface for the LDV measurements without significantly altering the viscosity of the water. Viscometer measurements revealed that the addition of 5 percent whole milk changed the measured viscosity of the liquid by less than 3 percent. The long measurement volume designed to span the free surface fluctuations had the disadvantage that it was capable of penetrating far below the free surface, and for most measurements on the spreading liquid layer, could span the entire depth of the flow. Hence, an opaque flow was desired in order to insure that velocity measurements would come only from the free surface. While it seems likely that the velocity measurements included data from some small, finite depth below the surface rather than just from the liquid-air interface, the velocity distributions showed that opacifying the water as described restricted the penetration

Nomenclature

δ = thickness of boundary layer growing from stagnation point	Re = jet Reynolds number = $V_j d / \nu$	v = local mean velocity in the axial direction
η = dimensionless coordinate normal to plate in spreading layer	r, z = coordinate directions, defined in Fig. 2	V = measured surface velocity of free liquid jet prior to impingement
ν = kinematic viscosity	u = local mean velocity in the radial direction	V' = local rms variation of the free surface velocity in the pre-impingement jet
d = jet exit diameter	U = measured mean surface velocity of the radially spreading liquid jet	V_j = mean jet exit velocity = $4Q / \pi d^2$
f = local velocity profile in the spreading layer, Eq. (5)	U' = local rms variation of the surface velocity in the radially spreading liquid layer	$V_{j,g}$ = jet exit velocity corrected for the effect of gravity
h = local depth of liquid layer	\bar{u} = average radial velocity across the liquid layer at a given radial location	z' = distance from the nozzle exit, measured along the jet axis
K = constant representing \bar{u}/U for a single assumed velocity profile		
Q = jet volume flow rate		

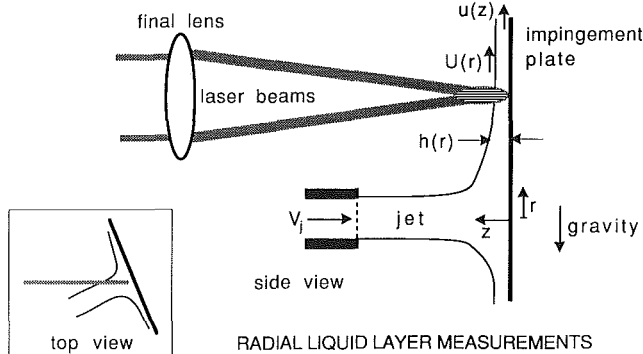
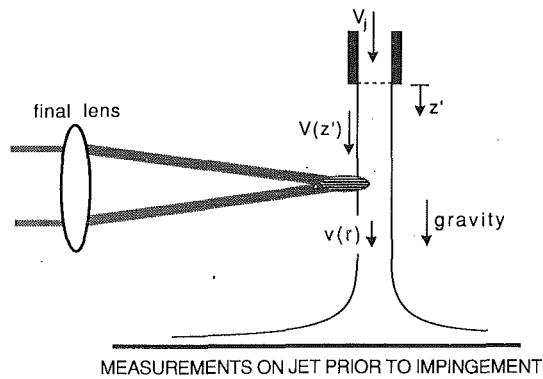


Fig. 2 Surface velocity measurement configurations and nomenclature

of the optical probe volume to a very small depth. Velocity measurements from well below the free surface would have caused the velocity histogram to be skewed, particularly toward the zero-velocity signal from the stationary impingement surface. However, no such conditions were observed as the data was taken.

For velocity measurements on the jet surface prior to impingement, the LDV system and jet were oriented as shown in the upper panel of Fig. 2. In this portion of the study, the jet flow was vertical with respect to gravity. The measurement volume was positioned as close as possible (where a useful signal could still be distinguished) to the nozzle exit, and measurements were made at discrete locations as the positioning table was moved downward. Observations using a strobe light showed that the free liquid jet surface began to destabilize, developing a wavy structure approximately 3–4 diameters from the nozzle exit. The LDV data rate decreased rapidly in that region as well, so fewer measurements were taken beyond $z'/d = 3$.

For measurements on the surface of the spreading layer, the system was oriented as shown in the lower panel of Fig. 2. In this case the jet flow was horizontal, and struck a vertical flat plate positioned normally to the axis of the jet. The plane of the laser beams was approximately 20 deg from normal with respect to the impingement plate, while still oriented to measure the radial component of the surface velocity. Since the impingement plane was oriented vertically with respect to gravity, and since the radially spreading flow decelerates with radial distance, gravitational effects became important at some radial location regardless of the initial flow rate. In order to quantify the effect of gravity on the measurements for each flow rate and nozzle size, free surface velocities were measured along a vertical diametral line intersecting the stagnation point. Measurements were made along this line on both sides of the jet from a position near the jet boundary (as close to $r/d = 0.5$ as possible) out to $r/d \approx 10$. One scan was made by traversing the table upward, and the other by traversing the table downward with respect to the gravity vector. Axially symmetric flow

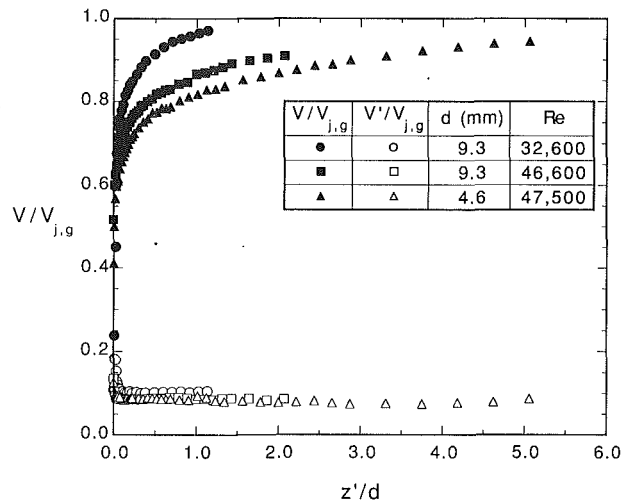


Fig. 3 Typical mean and rms surface velocities for pre-impinging free liquid jet

caused the scans to be identical except for the influence of gravity. Thus, the effect of gravity on the flow structure can be clearly seen as any difference in the two scans. Since the hydraulic jump occurred only on the upward scan, the downward traverse was usually terminated at the same radial distance that was reached in the upward scan. Reynolds numbers were chosen so that the effect of gravity would be small near the impingement point. This will be assessed and quantified later.

Maximum uncertainty in the average jet velocity (measured with the flow meters) was estimated to be 7 percent. Uncertainty in the local surface velocity measurements (measured with the LDV) was estimated to be less than 2 percent.

Results and Discussion

Experiments were performed with nozzle diameters of $d = 2.1, 4.6,$ and 9.3 mm and Reynolds numbers ranging from 8500 to 47,500. Surface velocity measurements were made on the liquid jet prior to impingement in order to assess the axial development of the jet velocity as it changed from the fully developed pipe flow at the nozzle exit to the eventual flat velocity profile dictated by the boundary conditions. Figure 3 illustrates this development for three jet configurations. The measured surface and rms velocities are normalized by the average jet exit velocity corrected for the effect of gravity (since the jet was oriented vertically) according to the mechanical energy equation

$$V_{j,g} = (2gz' + V_j^2)^{1/2} \quad (1)$$

This gravity correction was typically very slight, amounting to less than 2 percent in the worst case. It can be seen that for the large nozzle at the lower Reynolds number, the flow development is very rapid, with the measured velocity within 5 percent of the mean jet exit velocity at one nozzle diameter from the exit. For the large nozzle at higher Re , and the smaller nozzle, the flow development was slower, requiring approximately two and three nozzle diameters, respectively, to reach $V/V_{j,g} = 0.9$. This is also clear from the rms surface velocity fluctuation profiles, which decrease sharply in the region $0 \leq z'/d \leq 0.25$, with much more gradual change thereafter. The mean and rms surface velocity results give some indication as to the relative flow development in the free liquid jet prior to impingement. The jet was observed to destabilize for spacings beyond $z'/d \approx 4$, rendering surface velocity measurements very difficult. Most of the free surface velocity measurements that follow, except where noted, were taken with nozzle-to-plate spacing $z'/d = 1.0$. For the configurations demonstrated in Fig. 3, as well as other measurements not shown, this corre-

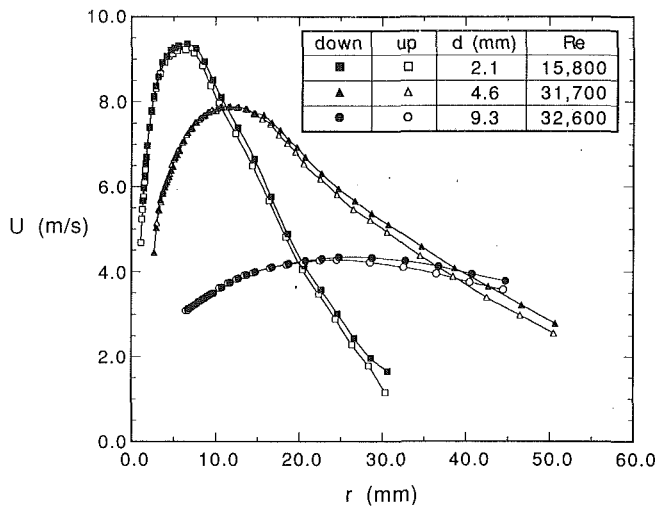


Fig. 4 Measured surface velocities in spreading liquid layer

sponded to a dimensionless development, $V/V_{j,g}$, of at least 0.8. If a cubic polynomial in r is assumed for the axial velocity profile, $v(r)$, in the pre-impingement liquid jet, and the shear at the free surface is assumed negligible, $V/V_{j,g} = 0.8$ corresponds to a centerline velocity of $1.47 V_j$, while a ratio of 0.95 yields a centerline velocity of $1.12 V_j$. Thus, at a nozzle-to-plate spacing of $z/d = 1$, the pre-impingement jet velocity profile is distinctly different from the fully developed pipe flow profile, but has not, in most cases, approached a flat velocity profile, $v(r) = V_j$.

Turning now to the measurements from the free surface of the radially spreading liquid layer, Fig. 4 demonstrates sample measured surface velocity profiles for each of the three nozzles used in this study. Each of the profiles exhibits a pronounced maximum. The radial position where gravity begins to affect the flow can be clearly seen as the upward traversing profile separates from the downward profile. This separation point could not be generally correlated at a radial position for the data taken in this study, although it appeared to occur at or after the maximum. Data from the upward and downward traverses were not taken at exact matching radial locations; however, the shape of the profiles can still be seen clearly in Fig. 4. The gravity effect was found to be less than 8 percent for all r/d measured and less than 3 percent for $r/d \leq 3$. While each profile in Fig. 4 contains a maximum, the profiles are otherwise dissimilar for each of the different nozzles. However, when the measurements are plotted in dimensionless coordinates as in Fig. 5, nearly all of the data collapse around a single band. To reduce confusion in the plot, only the data for upward scans are shown in Fig. 5. The one data set that falls well away from the rest corresponds to a Reynolds number of 8500, while the next lowest Re is 15,800. The difference in Re may explain the difference in shape. Although not entirely consistent, the data appear to follow a general trend of higher U/V_j for lower Re at a given radial position. A correlation of all measured data is also shown in Fig. 5. The correlation divides the radially spreading jet into two regions, and represents the data as a parabola matched (in both magnitude and slope) with a straight line:

$$0.5 \leq r/d \leq 2.86 \quad U/V_j = -0.125(r/d)^2 + 0.625(r/d) + 0.303 \quad (2a)$$

$$2.86 \leq r/d \leq 14 \quad U/V_j = -0.0936(r/d) + 1.33 \quad (2b)$$

Equation (2) fits 97 percent of the data within ± 20 percent and 80 percent of the data within ± 10 percent. This evaluation (as well as the correlation itself) is based on both upward and downward scans, as well as several repeated tests.

Plotted in dimensionless coordinates, all of the U/V_j profiles of Fig. 5 have a maximum at $r/d \approx 2.5$. This maximum exhibits

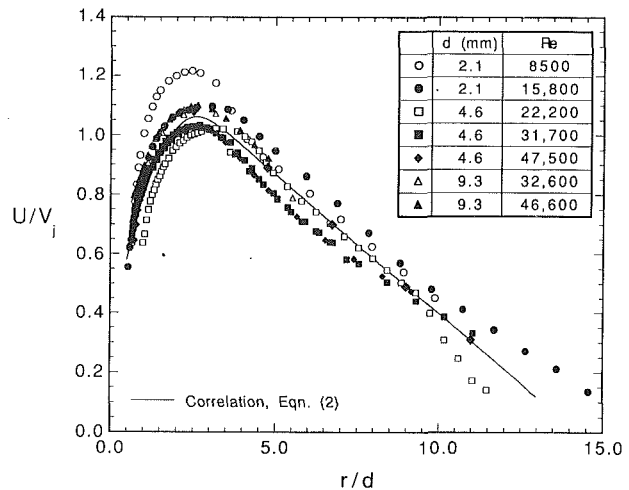


Fig. 5 Dimensionless surface velocity profiles versus normalized radial position

two unexpected features. First, its magnitude is generally greater than unity ($U > V_j$). Indeed, the data for the $d = 2.1$ mm nozzle at $Re = 8500$ exhibit a maximum surface velocity 25 percent higher than the average jet exit velocity, V_j . This contradicts Watson's assumption that the free surface velocity is equal to the average jet exit velocity until the boundary layer reaches the free surface. The second unexpected observation is that the radial location of the maximum at $r/d \approx 2.5$ is well beyond any observable curvature in the free surface, which, using crude measurements, was estimated to be confined to $r/d < 0.7$. Since only the radial component of the velocity was measured, low velocities would be expected very near $r/d = 0.5$ where significant curvature exists on the free surface and the total velocity vector contains a significant axial component. However, by $r/d = 1.0$, geometric calculations show that the radial surface velocity component constitutes greater than 95 percent of the free surface velocity vector. The location of the local maximum might be explained as an effect of the acceleration in the radially redirected jet flow. Outside the boundary layer, the flow accelerates in the radial direction starting from zero at the jet axis, while satisfying continuity across the liquid layer. The maximum occurs when the accelerating radial flow is overtaken by the retarding effect of wall shear (as the boundary layer reaches the free surface). This would explain why no such maximum was observed by Azuma and Hoshino (1983). The jet in that study was essentially a radial wall jet due to the proximity between the plate and nozzle, and would exit the annular space between the plate and nozzle at a maximum velocity. Thus, only constant velocity and decelerating flows would be measured at the free surface.

The effect of nozzle-to-plate spacing on the flow of the radially spreading liquid layer was evaluated by repeating measurements of a single nozzle size and flow rate at spacings of $z/d = 1, 2, 3$, and 4 (Stevens and Webb, 1991b). Over this range, the effect was negligible, with all measured data clustered in bands of average width of 2 and 8 percent for the mean and rms velocities, respectively. In the bands, no consistent dependence of the velocity on the nozzle-to-plate spacing was apparent. While spacing would undoubtedly begin to affect the flow at some z/d , no measurements were conducted at $z/d > 4$ in this study due to jet destabilization and the attendant sampling difficulties.

Predictions of the free surface velocity from Watson's analysis are compared with the data of this study in Fig. 6 for several measurement configurations. As discussed previously, Watson's analysis assumes that $U/V_j = 1.0$ for $r < r_o$. All curves with Watson's analysis begin at $r/d = 1.5$, because an additional assumption of the theoretical development is that $r/d \gg 0.5$, since a term of order $(d/2)^3/r^3$ is neglected. For

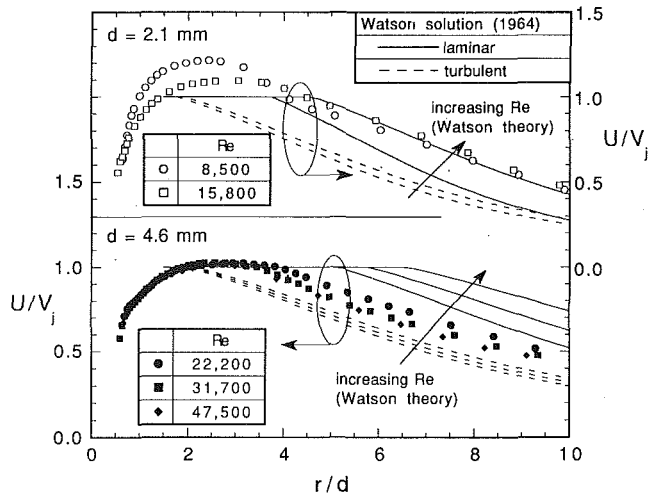


Fig. 6 Comparison of measured free surface velocity data with Watson's analysis (1964)

the smallest nozzle only the laminar theory predicts closely the experimental data, while for the 4.6-mm-diam nozzle the data fall between the laminar and turbulent predictions, the turbulent flow theory being slightly better. In all cases the analysis fails to predict the local maximum near $r/d \approx 2.5$ with corresponding $U/V_j > 1.0$.

Figure 7 shows the calculated dimensionless layer depth using an assumed parabolic velocity profile, $u(z)$, across the liquid layer. To reduce confusion, only data from the upward scans are shown. The mean liquid layer depth was calculated from considerations of global continuity at a given radial position, r :

$$\pi d^2 V_j / 4 = 2\pi r h \bar{u} \quad (3)$$

which upon rearranging yields

$$(h/d) = \left(\frac{1}{8}\right) \left(\frac{1}{r/d}\right) \left(\frac{1}{\bar{u}/V_j}\right) \quad (4)$$

If the substitutions $\eta = z/h$ and $f(\eta) = u/U$ are made, then

$$\bar{u} = U \int_0^1 f(\eta) d\eta = KU \quad (5)$$

where K is a constant determined for each assumed velocity profile, $f(\eta)$. Equation (4) then takes the form

$$(h/d) = \left(\frac{1}{8K}\right) \left(\frac{1}{r/d}\right) \left(\frac{1}{U/V_j}\right) \quad (6)$$

The assumption of a different profile for the liquid layer would simply shift the curves in Fig. 7 up or down by the ratio of the profile constants, K . Table 1 shows the value of the constant K for a variety of velocity profiles which might be used. The parabolic profile (based on no slip at the wall and no shear at the free surface) is supported by the numerical study of Rahman et al. (1990). The cubic profile was proposed by Hung (1982), while the quartic was suggested by Azuma and Hoshino (1983). All profiles feature the maximum velocity in the liquid layer at the free surface. Measurements of radial velocity profiles inside the liquid layer reveal that this is perhaps true only for $r/d \geq 2.5$ (Stevens, 1991). As can be seen from Table 1, most laminar profiles yield values of the integration constant, K , that are very close. Hence, little error is made in the calculation of the local mean layer depth regardless of the assumed velocity profile beyond $r/d > 2.5$. The quadratic profile, for which $K = 0.667$, was used in the calculation of layer depths at all radial locations.

Also shown in Fig. 7 is the dimensionless depth calculated

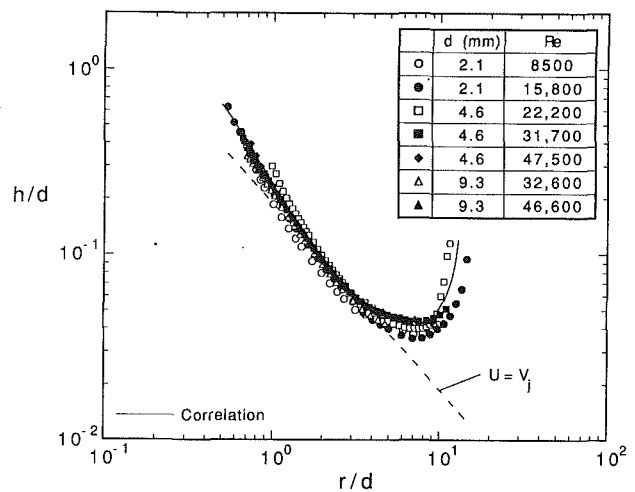


Fig. 7 Local mean layer depth calculated according to Eq. (6) with an assumed parabolic profile of the radial velocity component

as though U/V_j were always unity. The assumption of constant surface velocity equal to V_j is in error by approximately 50 percent close to the stagnation region. By $r/d > 7$, the slowing of the liquid layer (due to the effect of viscous shear) has become so pronounced that the calculated depth visibly deviates from the $U = V_j$ curve. At larger r/d , the reduced velocities become sufficiently small that the dimensionless depth begins to increase. This depth increase was also predicted by Watson (1964), as discussed below, and seen by Thomas et al. (1990). While the latter reference used a radial wall jet rather than an impinging jet, and thus had a different shape for the depth profiles, the cause and effect of the decreasing, then increasing, layer depth were identical to this study. The experimental depth data of Olsson and Turkdogan (1966), though inconclusive, appear to exhibit a similar trend. Figure 7 also includes the dimensionless depth predicted by the velocity correlation, Eq. (2), in conjunction with Eq. (6).

Figure 8 compares the calculated local mean layer depth from the three upward scan profiles of Fig. 4 with the predictions from Watson's laminar and turbulent flow analyses for those configurations. The data for water reported by Olsson and Turkdogan (1966) are also included. As with the surface velocity, it can be seen that the Watson flow predictions agree moderately well with the experimental data. The use of an assumed turbulent mean velocity profile across the layer depth would do little to improve the general agreement between analysis and experimental data, given the relative magnitudes of the integration factor, K , for the turbulent flow velocity profiles given in Table 1. Figure 8 does show, however, that the analysis predicts qualitatively the measured increase in depth for $r/d > 9$ for the two smallest nozzles. If the velocity profile across the layer, $u(z)$, is assumed accurate, the uncertainty in h/d is estimated to be approximately 8 percent. However, as indicated previously, the assumed parabolic profile may suffer some inaccuracy for $r/d < 2.5$ (Stevens, 1991).

Figure 9 shows the fluctuating component of the radial velocity corresponding to the data of Figs. 5 and 7. With the fluctuating component normalized by the local mean velocity, and plotted as a function of dimensionless distance, r/d , the curves show some similarity for $r/d < 3$. A minimum is reached in the collapsed curve near $r/d = 2$, very near where U/V_j was observed to be a maximum. By $r/d = 4$, the curves have begun to separate. The distinct minimum in the turbulent fluctuations near $r/d = 2.0$, along with the peak in the dimensionless velocity profiles of Fig. 5 at approximately $r/d = 2.5$, suggest that a boundary layer may be reaching the free surface in that region. This is supported by velocity measurements made inside the liquid layer (Stevens, 1991).

Table 1 Constants from the integration of different velocity profiles, Eq. (5)

Assumed Velocity Profile, $f(\eta)$:		K
parabolic	$2\eta - \eta^2$	0.667
cubic	$1.5\eta - 0.5\eta^3$	0.625
quartic	$\eta^4 - 2\eta^3 + 2\eta$	0.700
Watson's laminar	—	0.615
Watson's turbulent	—	0.919
1/7th power law	$\eta^{1/7}$	0.875

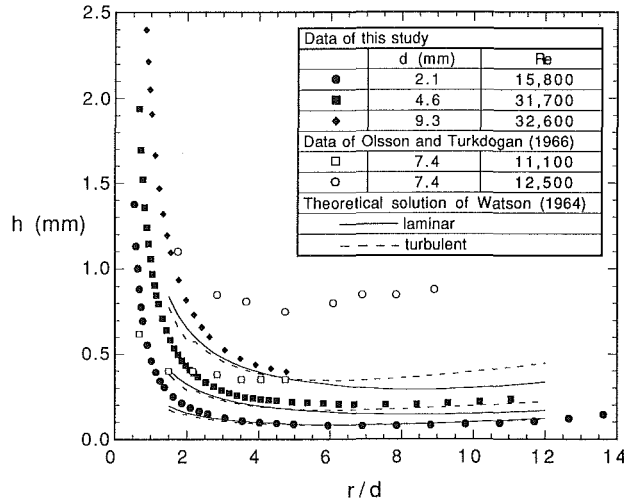


Fig. 8 Comparison of local liquid layer depth with predictions from Watson's analysis (1964)

Conclusions

Laser-Doppler velocimetry was used to measure the mean and fluctuating parts of a single component of the free surface velocity of an impinging liquid jet striking a flat surface. Some measurements were carried out on the jet flow prior to impingement in order to characterize the development of the velocity profile in the pre-impingement jet. It was found that the measured free surface velocity profiles of the spreading liquid layer collapsed to a band if they were plotted in dimensionless coordinates. The dimensionless coordinates were formulated by normalizing the measured surface velocity by the average jet exit velocity, and the radial coordinate by the nozzle exit diameter. The depth of the spreading liquid layer was calculated by assuming a parabolic radial velocity profile across the layer and negligible shear at the free surface. Other possible profiles were discussed. Comparisons were made for both surface velocity and layer depth, and the theoretical predictions of Watson (1964) were found to agree moderately well with the experimental data.

Acknowledgments

Financial support of this work under U.S. National Science Foundation Grant No. CBT-8552493 is gratefully acknowledged.

References

Adachi, K., 1987, "Laminar Jets of a Plane Liquid Sheet Falling Vertically in the Atmosphere," *Journal of Non-Newtonian Fluid Mechanics*, Vol. 24, pp. 11-30.

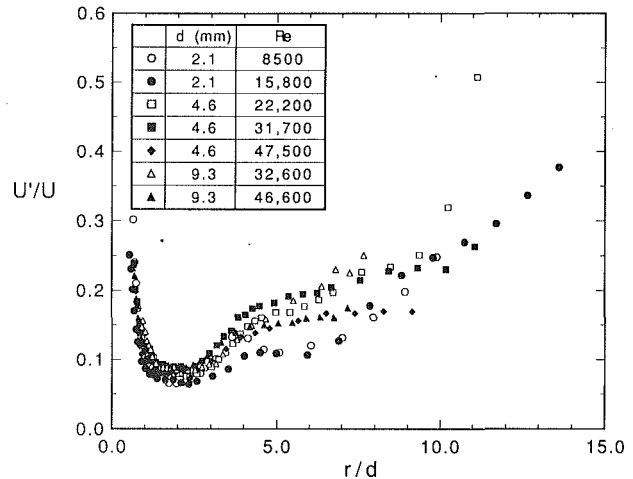


Fig. 9 The rms turbulent fluctuations of free surface velocity as a function of radial position

Azuma, T., and Hoshino, T., 1983, "LDV Measurement in Radial Flow of Thin Liquid Film," *Proceedings of the Osaka Symposium on Flow Measuring Techniques: The Application of LDV*, Association for the Study of Flow Measurements, Osaka, Japan, pp. 1-15.

Carper, H. J., 1989, "Impingement Cooling by Liquid Jet," *Porous Media, Mixtures and Multiphase Heat Transfer*, ASME HTD-Vol. 117, K. Vafai et al., eds., pp. 23-30.

Chaudhry, Z. H., 1964, "Heat Transfer in a Radial Liquid Jet," *Journal of Fluid Mechanics*, Vol. 20, pp. 501-511.

Hung, Y. T., 1982, "A Numerical Analysis of Jet Impingement Cooling of a Rotating Disk," M.S. Thesis, Texas Tech University, Lubbock, TX.

Inada, S., Miyasaka, Y., and Izumi, R., 1981, "A Study on the Laminar-Flow Heat Transfer Between a Two-Dimensional Water Jet and a Flat Surface," *Bulletin of the JSME*, Vol. 24, pp. 1803-1810.

Kiper, A. M., 1984, "Impinging Water Jet Cooling of VLSI Circuits," *International Communications in Heat and Mass Transfer*, Vol. 11, pp. 517-526.

Ma, C. F., and Bergles, A. E., 1983, "Boiling Jet Impingement Cooling of Simulated Microelectronic Chips," *Heat Transfer in Electronic Equipment*, S. Oktay and A. Bar-Cohen, eds., ASME, New York, pp. 5-12.

Modarress, D., Tan, H., and Elghobashi, S., 1984, "Two-Component LDA Measurement in a Two-Phase Turbulent Jet," *AIAA Journal*, Vol. 22, pp. 624-630.

Nakoryakov, V. E., Pokusaev, B. G., and Troyan, E. N., 1978, "Impingement of an Axisymmetric Liquid Jet on a Barrier," *International Journal of Heat and Mass Transfer*, Vol. 21, pp. 1175-1184.

Olsson, R. G., and Turkdogan, E. T., 1966, "Radial Spread of a Liquid Stream on a Horizontal Plate," *Nature*, Vol. 211, pp. 813-816.

Rahman, M. M., Faghri, A., and Hankey, W. L., 1990, "The Flow of a Thin Liquid Film on a Stationary and Rotating Disk—Part II: Theoretical Prediction," *Heat Transfer in Space Systems*, ASME HTD-Vol. 135, pp. 135-142.

Schlichting, H., 1979, *Boundary-Layer Theory*, 7th ed., McGraw-Hill, New York.

Stevens, J., 1991, "Measurements of Local Fluid Velocities in an Axisymmetric, Free Liquid Jet Impinging on a Flat Plate," Ph.D. Dissertation, Brigham Young University, Provo, UT.

Stevens, J., and Webb, B. W., 1991a, "Local Heat Transfer Coefficients Under an Axisymmetric, Single-Phase Liquid Jet," *ASME JOURNAL OF HEAT TRANSFER*, Vol. 113, pp. 71-78.

Stevens, J., and Webb, B. W., 1991b, "Measurements of the Free Surface Flow Structure Under an Impinging, Free Liquid Jet," *Proceedings 3rd ASME/JSME Thermal Engineering Joint Conference*, J. R. Lloyd and Y. Kurosaki, eds., Vol. 3, ASME, New York, pp. 135-142.

Thomas, S., Faghri, A., and Hankey, W. L., 1990, "The Flow of a Thin Liquid Film on a Stationary and Rotating Disk—Part I: Experimental Analysis and Flow Visualization," *Heat Transfer in Space Systems*, ASME HTD-Vol. 135, pp. 125-133.

Vader, D. T., Incropera, F. P., and Viskanta, R., 1991, "Local Convective Heat Transfer From a Heated Surface to an Impinging Planar Jet of Water," *International Journal of Heat and Mass Transfer*, Vol. 34, pp. 611-623.

Watson, E. J., 1964, "The Radial Spread of a Liquid Jet Over a Horizontal Plane," *Journal of Fluid Mechanics*, Vol. 20, part 3, pp. 481-499.

Yamamoto, H., Udagawa, Y., and Suzuki, M., 1987, "Cooling System for FACOM M-780 Large-Scale Computer," *Proceedings of the International Symposium on Cooling Technology for Electronic Equipment*, W. Aung and P. Cheng, eds., Pacific Institute for Thermal Engineering, pp. 96-109.

Transient Convective Heat Transfer in Planar Stagnation Flows With Time-Varying Surface Heat Flux and Temperature

D. A. Zumbrunnen

Thermal/Fluids Laboratory,
Department of Mechanical Engineering,
Clemson University,
Clemson, SC 29634-0921

Impinging flows are used in a variety of applications where effective and localized heat transfer is mandated by short residence times or by space constraints, as in cooling materials moving along a conveyor or removing heat dissipated within microelectronic circuitry. A wide selection of heat transfer correlations is available for steady-state conditions. However, instantaneous heat transfer coefficients can differ significantly from steady-state values when temporal variations occur in the surface heat flux or surface temperature. Under these conditions, the temperatures of fluid layers near the surface are affected preferentially due to their proximity to the temporal variation. A theoretical model is formulated to assess the importance of a time-varying surface heat flux or temperature on convective heat transfer in a steady, planar stagnation flow. A governing equation for the transient heat transfer response is formulated analytically from the boundary layer equations for momentum and energy conservation in the fluid. Numerical solutions to the governing equation are determined for ramp and sinusoidal changes in the surface heat flux or temperature. Results indicate that the time response is chiefly governed by the velocity gradient in the free stream and to a lesser extent by the Prandtl number. Departures from steady-state Nusselt numbers are larger for more rapid transients and smaller or comparable in size to the magnitude of the imposed variation at the surface.

Introduction

High convective heat transfer coefficients have led to the wide use of impinging flows in many manufacturing processes and have attracted much interest as a means to cool microelectronic circuitry (Incropera, 1988; Zumbrunnen et al., 1989). However, little attention has been given to the influence of a time-varying surface heat flux or surface temperature on convective heat transfer in impinging flows. Convection correlations are uniformly developed in the laboratory under steady-state conditions, and consequently, guidance is unavailable with regard to the applicability of a correlation to transient conditions. Moreover, parameters governing the time response of the thermal boundary layer in a steady impinging flow have not been identified. Convective heat transfer is directly affected by temporal variations in the surface heating condition, since corresponding temporal variations are also induced in the fluid temperature distribution near the surface. Time-varying temperatures on a cooled surface can arise, for example, when heat generation is due to electrical dissipative losses in an alternating current, when transients are induced as a surface heat flux changes from one steady value to another, or when a surface is subjected to periodic radiative heating from a pulsed laser. An understanding of how temporal variations affect convective heat transfer may be of special significance to the design of sensors or systems subjected to transient operation.

Transient convective heat transfer in impinging flows has been considered in several studies where the transients are induced by a periodic or impulsive motion in the free-stream velocity or in a constant temperature impingement surface. An early work was reported by Lighthill (1954), in which heat transfer for two-dimensional, laminar boundary layer flow

about the front stagnation region of a cylindrical body was determined using approximate analytical techniques. Small sinusoidal fluctuations in the oncoming free-stream velocity about a fixed mean flow velocity were specified. Heat transfer variations were found to lag behind those in the free-stream velocity due to thermal inertia in the boundary layer. The boundary layer equations for the same configuration as Lighthill's can be solved exactly with similarity methods if the free-stream velocity is inversely proportional to a linear function of time (Yang, 1958). Nusselt numbers in the stagnation region were found to deviate significantly in this case from steady-state values. The formulation of the velocity and thermal boundary layers when a constant temperature flat plate is suddenly exposed to a steady, parallel flow was investigated approximately using local similarity by Nagendra (1973). Results indicated that transient heat transfer rates greatly exceed steady values and thermal boundary layer growth is faster for lower Prandtl number fluids.

The response of the velocity boundary layer in impinging flows to oscillations of the velocity of the impingement surface in the plane of the impingement surface has received attention (Glauert, 1956; Watson, 1959) due to its relationship to airfoil flutter. Rott (1956) qualitatively demonstrated that, in such cases, convective heat transfer is only affected when the surface temperature varies spatially. Flow and heat transfer in the stagnation region of a periodic axisymmetric boundary layer flow about a cylinder have been studied approximately by perturbation analyses (Gorla et al., 1988a, 1988b). Results are applicable to small amplitudes in the oscillating velocity. Variations in friction coefficients occurred with a leading phase angle and became larger at higher frequencies in the free-stream fluctuations. The amplitude of fluctuations in the heat transfer coefficient monotonically decreased with increasing frequency and lagged fluctuations in the free stream due to thermal inertia in the boundary layer, as in the results reported earlier by Lighthill (1954).

Contributed by the Heat Transfer Division for publication in the JOURNAL OF HEAT TRANSFER. Manuscript received by the Heat Transfer Division October 11, 1990; revision received July 1, 1991. Keywords: Forced Convection, Jets, Transient and Unsteady Heat Transfer.

In the aforementioned studies, transients were induced by varying the velocities of the free stream or the impingement surface. The purpose of this study by contrast is to ascertain the importance of a temporally varying surface temperature or surface heat flux to convective heat transfer in impinging flows. Fluid flow is considered to be steady and the impingement surface at rest. Attention is given to impinging flows due to the widespread and increasing use of jets in a variety of technologies. Physically correct ramp and sinusoidal variations in surface heat flux and temperature are specified. Heat transfer coefficients are found to deviate significantly from steady-state values for transients with periods similar to or smaller than the period for the unforced response of the thermal boundary layer.

The stagnation region considered is depicted in Fig. 1 and corresponds to planar stagnation flow (Schlichting, 1979; Zumbrennen et al., 1991). Such flows arise beneath impinging planar or "slot" jets, on a cylinder in a crossflow, or in the front stagnation region of any bluff body where the frontal surface can be effectively represented by a tangent plane. The incident flow is steady and the vertical flow velocity components decrease near the surface. The flow bifurcates symmetrically along a stagnation line ($x = 0$) subtending the surface ($y = 0$) in the spanwise direction. Near the surface and the stagnation line but beyond the velocity boundary layer, the flow velocity is given by (Schlichting, 1979)

$$u_{\infty}(x) = Cx \quad (1a)$$

$$v_{\infty}(y) = -Cy \quad (1b)$$

The heat transfer condition at the impingement surface is specified by the functions $q_s(t)$ or $T_s(t)$ while the temperature T_{∞}

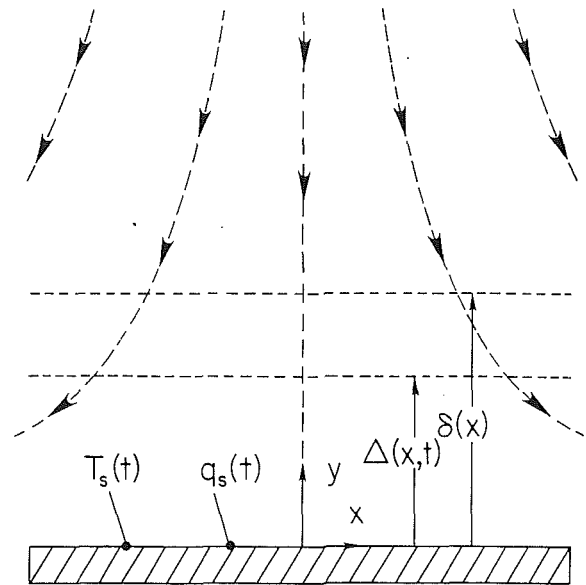


Fig. 1 Steady planar stagnation flow on a surface with time-varying heat flux or temperature

of the fluid is constant. The free-stream velocity gradient C can be calculated from potential flow theory or from experimental static pressure measurements along the impingement surface (Zumbrennen et al., 1991). In the analysis that follows, it is found to influence the transient response significantly.

Nomenclature

c_p = specific heat at constant pressure	t = time	Γ^* = ratio of instantaneous value of Γ to value at steady state (Table 2 of Appendix)
C = free-stream velocity gradient [Eq. (1) and Table 1 of Appendix]	T = fluid temperature	δ = velocity boundary layer thickness
\bar{C} = dimensionless velocity gradient = LC/V (Table 1 of Appendix)	T_s = temperature of impingement surface	Δ = thermal boundary layer thickness
d = cylinder diameter	T_{∞} = fluid free-stream temperature	ϵ_1 = ratio of values for θ_s before and after specified ramp change [Eq. (21)]
f = frequency for sinusoidal surface heat flux	T_{s0} = initial surface temperature = $T_s(t = 0)$	ϵ_2 = ratio of surface heat fluxes before and after specified ramp change [Eq. (26)]
\tilde{f} = dimensionless frequency = f/C	u = x component of fluid velocity	ϵ_3 = magnitude of dimensionless fluctuation in specified oscillatory surface heat flux [Eq. (27)]
h = convective heat transfer coefficient	u_{∞} = x component of free-stream velocity near surface [Eq. (1a)]	η = dimensionless position y/δ
k = thermal conductivity	\tilde{u} = dimensionless fluid velocity = u/u_{∞}	θ = dimensionless fluid temperature = $(T - T_{\infty})/(T_{s0} - T_{\infty})$
L = characteristic length for stagnation flow (Table 1 of Appendix)	v = y component of fluid velocity	θ_s = dimensionless surface temperature = $(T_s - T_{\infty})/(T_{s0} - T_{\infty})$
Nu_x = Nusselt number = hx/k	v_{∞} = y component of free-stream velocity near surface [Eq. (1b)]	Λ = variable related to velocity boundary layer = $C\delta^2/\nu$
Nu_* = ratio of instantaneous Nusselt number to Nusselt number at steady state	V = free-stream velocity far from surface or nozzle discharge velocity at centerline	ν = kinematic viscosity
Pr = Prandtl number = ν/α	w = planar jet width	ρ = mass density
q_s = heat flux at impingement surface	x = distance along impingement surface from stagnation line (Fig. 1)	τ = dimensionless time = Ct
\tilde{q}_s = instantaneous dimensionless heat flux [Eqs. (26) and (27)]	y = distance along stagnation line from impingement surface (Fig. 1)	ϕ = parameter governing rapidity of ramp change in θ_s or \tilde{q}_s [Eqs. (21a) and (26a)]
\tilde{q}_{s0} = initial steady-state dimensionless surface heat flux [Eq. (25)]	α = thermal diffusivity = $k/\rho c_p$	ω = $(\Gamma Pr d\theta_s/d\tau)/2$
Re_x = Reynolds number = $u_{\infty}x/\nu$	β = dimensionless position = y/Δ	
	γ = boundary layer thickness ratio = Δ/δ	
	Γ = variable related to thermal boundary layer = $C\Delta^2/\nu$	

Values are therefore provided for some common stagnation flows in Table 1 of the Appendix.

Theoretical and experimental studies have shown that the local heat transfer coefficient is spatially uniform to within 1 percent over a distance equal to about one-half jet width from the stagnation line of a laminar planar jet with a constant fluid discharge velocity across the nozzle width (Inada et al., 1981). This uniformity is attributable to the symmetry of the impinging flow (Fig. 1) and extends the validity of the theoretical model, which is formulated with Eq. (1), to regions away from the stagnation line. Since heat transfer is highest in the stagnation region and impinging jets are normally configured to impinge directly on an object, the stagnation region is of greatest interest and attention to it is considered to be appropriate. Laminar flow is assumed in order to provide physical insight into the nature of transient effects. Laminar solutions also are of utility when the characteristic dimension of a cylinder or nozzle, and thereby the associated Reynolds number, is small. Miniature jets can be used to cool microelectronic components and fine diameter wires are often employed in various fluid flow sensors. Predictions with laminar convective heat transfer models also have been shown to be in good agreement with experimental results for impinging jet flows at Reynolds numbers based on jet width up to 25,000 (Aziz, 1991). Agreement was attributed to the use of a convergent nozzle geometry, which abates turbulence in the jet flow, and to more effective damping of smaller eddies associated with high impingement velocities (Tran and Taulbee, 1989).

Analysis

Description of Analytical Method and Assumptions. Consideration of transient effects in convection often precludes an exact analytical approach, such as the use of similarity methods, since transient terms that are routinely omitted in many convection studies must be retained. Where transient effects can be incorporated into a similarity approach, restrictions are often necessary regarding functional relationships between variables (Yang, 1958; Hansen, 1964). A numerical approach can be adopted, but only at the expense of reduced physical insight. Moreover, transient two-dimensional problems of the type treated here are computationally time consuming. The unambiguous relationship among governing parameters, if derivable, would greatly illuminate physical processes and dynamic behavior. A method related to the von Karman-Pohlhausen technique (Schlichting, 1979) is therefore utilized and governing equations for the transient response of the thermal boundary layer are presented. The von Karman-Pohlhausen technique utilizes the integrated momentum conservation equation together with a detailed polynomial representation for flow velocity in the velocity boundary layer. The technique has been widely used in studies of boundary layers on airfoils where, as in the flow considered here, the boundary layer flow is significantly influenced by a pressure gradient. In the related technique used in this study, the integrated momentum and energy equations are employed. Predicted Nusselt numbers are shown to agree to within about 1 to 2 percent of values predicted by the well-known Falkner-Skan solutions for stagnation flow (Evans, 1962).

The specific assumptions of the analysis are: (i) steady, incompressible laminar flow, (ii) constant thermophysical properties, (iii) negligible viscous heating, (iv) negligible body forces in comparison to viscous forces, and (v) $\Delta \leq \delta$. The last assumption restricts the model to fluids with Prandtl numbers greater than about unity; but as will be demonstrated, results remain accurate to within 2 percent for $Pr \geq 0.7$.

Conservation Equations and Boundary Conditions. Equations for the conservation of momentum in differential and integral forms, which correspond to the

mentioned assumptions and boundary layer flow in Fig. 1, are given by

$$u \frac{\partial u}{\partial x} + v \frac{\partial u}{\partial y} = u_{\infty} \frac{du_{\infty}}{dx} + \nu \frac{\partial^2 u}{\partial y^2} \quad (2)$$

$$\frac{d}{dx} \int_0^{\delta} u(u - u_{\infty}) dy + \frac{du_{\infty}}{dx} \int_0^{\delta} u dy = \frac{\delta}{2} \frac{d(u_{\infty}^2)}{dx} - \nu \frac{\partial u}{\partial y} \Big|_{y=0} \quad (3)$$

Time-dependent differential and integral energy conservation equations for the constant property, boundary layer flow are given by

$$\rho c_p \left(\frac{\partial T}{\partial t} + u \frac{\partial T}{\partial x} + v \frac{\partial T}{\partial y} \right) = k \frac{\partial^2 T}{\partial y^2} \quad (4)$$

$$\frac{\partial}{\partial t} \int_0^{\Delta} T dy - T_{\infty} \frac{\partial \Delta}{\partial t} + \frac{\partial}{\partial x} \int_0^{\Delta} u(T - T_{\infty}) dy = \frac{-k}{\rho c_p} \frac{\partial T}{\partial y} \Big|_{y=0} \quad (5)$$

An ordinary nonlinear differential equation for the velocity boundary layer $\delta(x)$ in the steady impinging flow can be obtained from Eq. (3) by employing a suitable expression for the flow velocity $u(x, y)$. Since the fluid is subject to a time-varying heating condition (Fig. 1), the fluid temperature T in Eqs. (4) and (5) depends on the time t in addition to the spatial variables x and y . Thus, when combined with Eq. (5), a suitable expression for $T(x, y, t)$ in the thermal boundary layer yields a partial differential equation for Δ , with x and t as independent variables. The differential forms of the momentum and energy conservation equations [Eqs. (2) and (4)] and physically appropriate matching conditions that must be satisfied by the expressions for $u(x, y)$ and $T(x, y, t)$ give the following:

Surface ($y = 0, v = 0$):

$$u = 0, \quad (6a)$$

$$\nu \frac{\partial^2 u}{\partial y^2} = -u_{\infty} \frac{du_{\infty}}{dx} \quad (6b)$$

$$T = T_s, \quad (7a)$$

$$\frac{\partial^2 T}{\partial y^2} = \frac{Pr}{\nu} \frac{dT_s}{dt} \quad (7b)$$

Edge of velocity boundary layer ($y = \delta$):

$$u = u_{\infty}(x), \quad (8a)$$

$$\frac{\partial u}{\partial y} = 0, \quad (8b)$$

$$\frac{\partial^2 u}{\partial y^2} = 0 \quad (8c)$$

Edge of thermal boundary layer ($y = \Delta$):

$$T = T_{\infty}, \quad (9a)$$

$$\frac{\partial T}{\partial y} = 0 \quad (9b)$$

$$\frac{\partial^2 T}{\partial y^2} = 0 \quad (9c)$$

Model Formulation. As is common in the Karman-Pohlhausen technique, fourth-order profiles are specified for velocity and temperature in the boundary layers. A steady profile is used for velocity, and transient effects are incorporated in the temperature profile through the energy balance in the fluid at the impingement surface given by Eq. (7b). When subject to Eqs. (6)–(9) and expressed in terms of dimensionless variables defined in the Nomenclature section, the polynomials are readily found to be given by Eqs. (10) and (11).

$$\bar{u} = \left(2 + \frac{\Lambda}{6}\right)\eta - \frac{\Lambda}{2}\eta^2 + \left(\frac{\Lambda}{2} - 2\right)\eta^3 + \left(1 - \frac{\Lambda}{6}\right)\eta^4 \quad (10)$$

$$\theta = \theta_s - \beta \left(\frac{\omega}{3} + 2\theta_s\right) + \omega\beta^2 + (2\theta_s - \omega)\beta^3 + \left(\frac{\omega}{3} - \theta_s\right)\beta^4 \quad (11)$$

The ordinary differential equation for the velocity boundary layer thickness in terms of the variable Λ , with Eqs. (1a), (3), and (10), is given by

$$-\frac{u_\infty(x)}{2C} \left[\frac{5}{9072} \Lambda^2 + \frac{1}{315} (\Lambda - 37) \right] \frac{d\Lambda}{dx} = \frac{\Lambda^3}{4536} + \frac{79\Lambda^2}{7560} - \frac{116}{315} \Lambda + 2 \quad (12)$$

A well-known characteristic of impinging flows is the constancy of the velocity boundary layer thickness δ , or equivalently Λ , within the stagnation region. This characteristic arises due to the symmetry in the dividing flow about the stagnation streamline and suggests that a single stagnation value for Λ can be found from Eq. (12) with $d\Lambda/dx = 0$. Symmetry also pertains to the thermal boundary layer gradient $\partial\Delta/\partial x$, as supported by the related aforementioned uniformity in experimental and theoretical heat transfer distributions near the stagnation line (Inada et al., 1981; Zumbrennen et al., 1991). With the condition $\partial\Delta/\partial x = 0$, Eqs. (1a), (5), and (11) yield the ordinary differential equation below for the time-dependent, thermal boundary layer in terms of the Prandtl number Pr and the dimensionless variables $\Gamma (= C\Delta^2/\nu)$, $\gamma (= \Delta/\delta)$, and $\tau (= Ct)$.

$$\sqrt{\Lambda\Gamma} \left(3 - \frac{\Gamma Pr}{4\theta_s} \frac{d\theta_s}{d\tau} \right) \frac{d\Gamma}{d\tau} = 20\Gamma \left(\frac{2}{Pr\gamma} - \psi_1\Gamma + \psi_2\Gamma^2 - \psi_3\Gamma^3 \right) \quad (13)$$

where

$$\psi_1 = \frac{1}{15} \left[2 + \frac{\Lambda}{6} + \frac{2}{\gamma\theta_s} \frac{d\theta_s}{d\tau} \right], \quad (14)$$

$$\psi_2 = \frac{1}{12} \left\{ \frac{1}{7\gamma} + \frac{Pr}{10\theta_s} \left[\frac{1}{3} \left(2 + \frac{\Lambda}{6} \right) \frac{d\theta_s}{d\tau} + \frac{1}{\gamma} \frac{d^2\theta_s}{d\tau^2} \right] \right\}, \quad (15)$$

and

$$\psi_3 = \frac{Pr}{1680\gamma\theta_s} \frac{d\theta_s}{d\tau}. \quad (16)$$

It was noted during the course of the laborious analysis leading to Eqs. (13)–(16) that the term $\partial\Delta/\partial x$ appeared as a product with terms including explicitly the independent spatial variable x . Invoking the symmetry condition $\partial\Delta/\partial x = 0$ thereby conveniently transformed a partial differential equation with independent variables x and t to an ordinary differential equation [Eq. (13)] with time as the independent variable. Several features of Eq. (13) are noteworthy. The dimensionless time $\tau (= Ct)$ resulted as a consequence of the functional relationship for the free-stream velocity u_∞ [Eq. (1a)]. The transient response of the thermal boundary layer to time-varying heating conditions at the surface is thereby closely related to the free-stream velocity gradient C . The thermal boundary layer response in terms of $d\Gamma/d\tau$ depends on the Prandtl number Pr and on the time rates of change in the dimensionless surface temperature θ_s . However, in forced convection of a constant property fluid, the heat transfer coefficient and corresponding thermal boundary layer thickness under steady-state conditions are known to be independent of the dimensionless surface temperature θ_s . Equations (13)–(16) satisfy this property when $d^2\theta_s/d\tau^2 = d\theta_s/d\tau = 0$, since θ_s^{-1} appears as a product with these terms. The steady-state value for Γ can therefore be determined for a specified Prandtl number with all time derivative terms set to zero.

The convective heat transfer coefficient h is found from an energy balance at the impingement surface.

$$h = \frac{-k \frac{\partial T}{\partial y}|_{y=0}}{T_s - T_\infty} = \frac{-k \frac{\partial \theta}{\partial \beta}|_{\beta=0}}{\theta_s \Delta} \quad (17)$$

With a Reynolds number $Re_x = u_\infty x/\nu$ and $\partial\theta/\partial\beta|_{\beta=0}$ determined from Eq. (11), the Nusselt number referenced to the distance x (Fig. 1) is then given by

$$Nu_x Re_x^{-1/2} = \Gamma^{-1/2} \left(2 + \frac{\Gamma Pr}{6\theta_s} \frac{d\theta_s}{d\tau} \right) \quad (18)$$

The product $Nu_x Re_x^{-1/2}$ is spatially constant and thereby independent of the distance x , as expected in the stagnation region, since Γ and θ_s depend only on the dimensionless time τ .

Forcing Functions for Surface Temperature and Heat Flux. Physically plausible forcing functions are specified for surface temperature and surface heat flux in order to ascertain the influence of temporal variations on the Nusselt number Nu_x . The terms $d\theta_s/d\tau$ and $d^2\theta_s/d\tau^2$ in Eqs. (13)–(16) and (18) are determined from these functions.

Transients in which the surface temperature or heat flux change from one steady value to another (i.e., ramp changes) are representative of changes in the operating conditions of engineering systems. Thermal capacitance in these systems leads to ramp changes having continuous first and second derivatives. A fifth-order polynomial is used for the dimensionless ramp temperature change and is thereby subject to the following conditions:

$$\tau = 0: \quad \theta_s = 1, \quad (19a)$$

$$\frac{d\theta_s}{d\tau} = 0, \quad (19b)$$

$$\frac{d^2\theta_s}{d\tau^2} = 0 \quad (19c)$$

$$\tau = \phi^{-1}: \quad \theta_s = \epsilon_1, \quad (20a)$$

$$\frac{d\theta_s}{d\tau} = 0, \quad (20b)$$

$$\frac{d^2\theta_s}{d\tau^2} = 0 \quad (20c)$$

In the conditions above, $\theta_s(0) = 1$ and $\theta_s = \epsilon_1$ ($\epsilon_1 > 0$) correspond to the *steady* values that prevail prior to and after the ramp change in θ_s , which is completed when $\tau = \phi^{-1}$. Higher values of ϕ thereby correspond to more rapid transients. The resulting expressions for the ramp change in θ_s are then:

$$0 \leq \tau \leq \phi^{-1}: \quad \theta_s(\tau) = 1 + (\epsilon_1 - 1)(\phi\tau)^3 [10 - 15\phi\tau + 6(\phi\tau)^2] \quad (21a)$$

$$\tau > \phi^{-1}: \quad \theta_s(\tau) = \epsilon_1 \quad (21b)$$

When the heat flux $q_s(t)$ is specified, θ_s is found from an energy balance at the impingement surface.

$$q_s = -k \frac{\partial T}{\partial y}|_{y=0} = -\frac{k}{\Delta} (T_s - T_\infty) \frac{\partial \theta}{\partial \beta}|_{\beta=0} \quad (22)$$

The dimensionless temperature gradient $\partial\theta/\partial\beta|_{\beta=0}$ can be determined from Eq. (11) and, upon insertion and rearrangement in Eq. (22), yields

$$\frac{d\theta_s}{d\tau} = \frac{6}{Pr\Gamma} [\tilde{q}_s \Gamma^{-1/2} - 2\theta_s] \quad (23)$$

where \tilde{q}_s is the dimensionless heat flux given by

$$\tilde{q}_s = \frac{q_s}{k \sqrt{\frac{C}{\nu}} (T_s - T_\infty)|_{\tau=0}} \quad (24)$$

The dimensionless surface temperature for a specified surface heat flux can then be determined by integrating Eq. (23).

All transients in the surface heat flux will be considered to begin from steady-state conditions. The initial dimensionless heat flux \tilde{q}_{s0} can therefore be determined from Eq. (23) with $d\theta_s/d\tau = 0$ and $\theta_s(\tau = 0) = 1$.

$$\tilde{q}_{s0} = 2\Gamma^{-1/2}|_{\tau=0} \quad (25)$$

An expression for the ramp change in the surface heat flux, which is analogous to Eq. (21), is given by

$$0 \leq \tau \leq \phi^{-1}$$

$$\tilde{q}_s(\tau) = \tilde{q}_{s0} \{ 1 + (\epsilon_2 - 1)(\phi\tau)^3 [10 - 15\phi\tau + 6(\phi\tau)^2] \} \quad (26a)$$

$$\tau > \phi^{-1}$$

$$\tilde{q}_s(\tau) = \epsilon_2 \tilde{q}_{s0} \quad (26b)$$

where $\epsilon_2 > 0$.

Oscillatory heat fluxes can arise in systems that are subject to periodic heating conditions. In terms of the dimensionless frequency \tilde{f} ($= f/C$) and a parameter ϵ_3 ($0 \leq \epsilon_3 < 1$), the specified oscillatory variation about the initial steady-state dimensionless surface heat flux [Eq. (25)] is given by

$$\tilde{q}_s(\tau) = \tilde{q}_{s0} [1 + \epsilon_3 \sin(2\pi\tilde{f}\tau)] \quad (27)$$

Solution Methodology and Model Verification

Equation (12) and the symmetry condition $d\Lambda/dx = 0$ were used with the secant method (Gerald, 1978) to determine the value of Λ in the stagnation region of the steady, impinging flow. A convergence criterion of 10^{-5} percent was specified and a calculated value of 7.052324 was found. Steady-state values for Γ were similarly evaluated for specified Prandtl numbers from Eqs. (13)–(16), with $d\Gamma/d\tau = d\theta_s/d\tau = d^2\theta_s/d\tau^2 = 0$. The fourth-order Runge–Kutta method (Gerald, 1978) was employed to evaluate $\Gamma(\tau)$ from Eqs. (13)–(16) with $\theta_s(\tau)$, $d\theta_s/d\tau$, and $d^2\theta_s/d\tau^2$ determined from Eq. (21) or (23). When Eq. (23) was used, it was necessary also to employ the fourth-order Runge–Kutta method to determine $\theta_s(\tau)$ since it is not given explicitly when the surface heat flux is specified. Step sizes of $0.001 \tilde{f}^{-1}$ or $0.001 \phi^{-1}$ were selected and determined to provide accurate plotted results.

Heat transfer coefficients in the stagnation region are given under steady-state conditions by the similarity solution for flow past a wedge (Evans, 1962). A comparison between model predictions and the similarity solution is presented in Table 2 of the Appendix, wherein agreement is from 1.0 to 2.3 percent. Although the model was formulated for $\Delta \leq \delta$ [$\text{Pr} \geq 1$, see assumption (v)], accurate results are obtained for $\text{Pr} = 0.7$, which is representative of the Prandtl number for air. The model performance continues to be adequate when $\text{Pr} = 0.7$, since $\Delta \approx \delta$ and the velocity profile in the thermal boundary layer is given effectively by Eq. (10). These accuracies are only slightly greater than those reported in many finite difference solutions and attest to the adequacy of the detailed semi-analytical approach implemented here.

Results and Discussion

The transient response of the thermal boundary layer in terms of the variables Γ ($= C\Delta^2/\nu$) and τ ($= Ct$) is governed by Eqs. (13)–(16). These equations and expressions for $\theta_s(\tau)$ and $q_s(\tau)$ constitute a complex nonlinear system. The transient

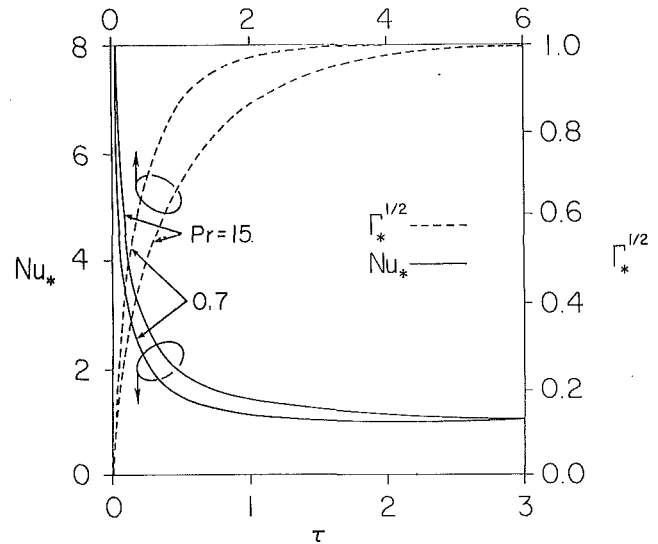


Fig. 2 Forced transient response of the thermal boundary layer and Nusselt number with $\Gamma_*(\tau = 0) = 0$ and $\theta_s = 1$

response is dependent on the Prandtl number Pr as well as on the instantaneous values of θ_s , $d\theta_s/d\tau$, and $d^2\theta_s/d\tau^2$. The transient response is strongly influenced in dimensional terms by the free-stream velocity gradient C of Eq. (1). Free-stream velocity gradients are smaller for larger characteristic dimensions of stagnation flows since larger dimensions give rise to a more uniform pressure distribution. Thus, the thermal boundary layer response is slower for impinging planar jets with larger widths or for cylinders in a crossflow with larger diameters. Values of dimensionless free-stream velocity gradients are given in Table 1 of the Appendix for some common planar stagnation flows.

Careful inspection of Eqs. (13)–(16) will show only dependence on the Prandtl number for steady-state conditions ($d\theta_s/d\tau = 0$ and $d^2\theta_s/d\tau^2 = 0$), in accordance with similarity solutions for constant property, impinging flows (Evans, 1962). A comparison at steady-state conditions between model-predicted Nusselt numbers from Eq. (18) and those from a similarity analysis is presented for $0.7 \leq \text{Pr} \leq 15$ in Table 2 of the Appendix, wherein agreement is from 1 to 2.3 percent. These small differences are due to the approximate nature of the semi-analytical technique. Model-predicted values of the variable Γ at steady state are also presented. In the results that follow, the transient response is given relative to steady-state values in terms of \tilde{q}_s , Nu_* and Γ_* (see Nomenclature). Tabulated steady-state results in the Appendix can be used to find the related, actual transient values.

Before proceeding with results for the transient heat transfer due to imposed surface heating conditions, it is of interest to consider first the *unforced* response of Eqs. (13)–(16). For the unforced response, a constant surface temperature ($\theta_s = 1$) is specified and the thermal boundary layer thickness is initially taken to be zero. The unforced response reveals the boundary layer behavior with no external stimulus or forcing when it initially deviates from its steady-state value. Although not representative of physical systems, the unforced response is useful in understanding the forced response, which in this study, corresponds to time-varying heating conditions at the impingement surface beneath a steady, impinging flow. The unforced response of the thermal boundary layer in terms of the variable $\Gamma_*^{1/2}$ with $\Gamma_*(\tau = 0) = 0$ is given in Fig. 2, wherein development is more rapid at the lower Prandtl number ($\text{Pr} = \nu/\alpha$). The thermal boundary layer thickness is within 1 percent of its steady-state value at dimensionless times of $\tau \approx 4$ and $\tau \approx 6$ for Prandtl numbers of 0.7 and 15, respectively. Thus, as in the work by Nagendra (1973) described earlier for flow past

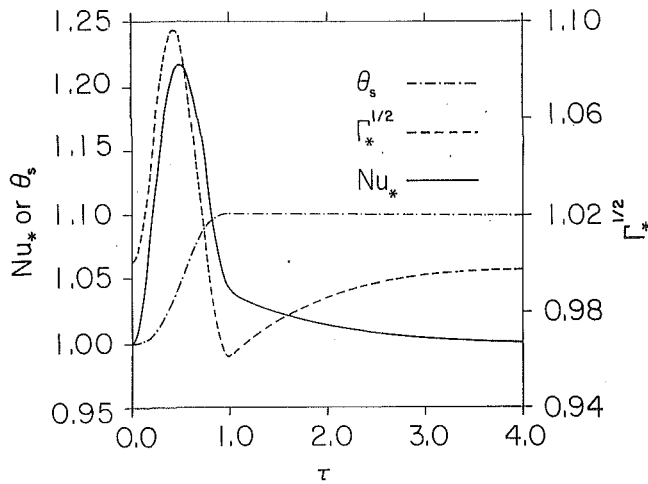


Fig. 3 Transient response of thermal boundary layer and Nusselt number to a ramp increase in the surface temperature with $Pr = 6$, $\epsilon_1 = 1.1$, and $\phi = 1.0$

a flat plate, the thermal boundary layer develops more quickly in fluids with lower Prandtl numbers. This result is intuitively correct, since heat is transferred more readily in fluids with higher thermal diffusivities ($\alpha = k/\rho c_p$) in accordance with Eq. (4).

The ratio of the instantaneous Nusselt number to the steady-state Nusselt number, Nu_* , is also presented in Fig. 2. Small thermal boundary layer thicknesses that prevail early in the transient correspond to large Nusselt numbers given by Eq. (18). Steady-state Nusselt numbers ($Nu_* = 1$) are approached as the dimensionless time τ increases, as expected. Although the Prandtl numbers differ significantly, it is interesting to note that differences in the responses are not great. Values of the free-stream velocity gradient C from Table 1 of the Appendix can be employed to place the rapidity of the transient in perspective. For example, $C = 0.7854 V/w$ for an impinging planar jet with velocity V and width w . With $w = 0.01$ m and $V = 1$ m/s, $\tau = Ct = 1$ corresponds to $t = 0.0127$ s, whereas for $w = 0.001$ m and the same jet velocity, $t = 0.00127$ s. Similar calculations can be performed for a cylinder of diameter d in a crossflow where $C = 4V/d$.

The transient responses of the thermal boundary layer and Nusselt number to the ramp change in surface temperature given by Eq. (21) are shown in Fig. 3 beginning from steady state for $Pr = 6$. Over the dimensionless time period $0 < \tau < 1$, θ_s increases by a factor given by $\epsilon_1 (= 1.1)$. Thermal energy initially accumulates in the fluid layers near the surface and heat transport is facilitated to points farther into the flow. The thermal boundary layer thickness in terms of $\Gamma_*^{1/2}$ consequently becomes larger. Interestingly, this increase is accompanied by an increase in the Nusselt number ratio Nu_* , in accordance with Eq. (18) for $d\theta_s/d\tau > 0$. Physically, the higher Nusselt number arises since the fluid temperature gradient $d\theta/d\beta$ near the surface [Eq. (17)] becomes greater due to the increasing surface temperature. Eventually, the initial behavior is retarded and then reversed due to the growing influence of the term ψ_1 in Eq. (13). For $\tau > 1$, the change in surface temperature is complete and the thermal boundary layer decreases below its steady value since it responds too slowly to changes in θ_s . The Nusselt number decreases monotonically to its initial value despite the overshoot and convective heat transfer is therefore more effective throughout the transient.

Transient responses due to a 10 percent ramp increase ($\epsilon_2 = 1.1$) in the surface heat flux [Eq. (26)] are depicted in Fig. 4 for different values of the parameter ϕ . Results are presented with $\phi\tau$ as the independent variable to permit representation of the surface heat flux by a single curve in Fig. 4(a). Di-

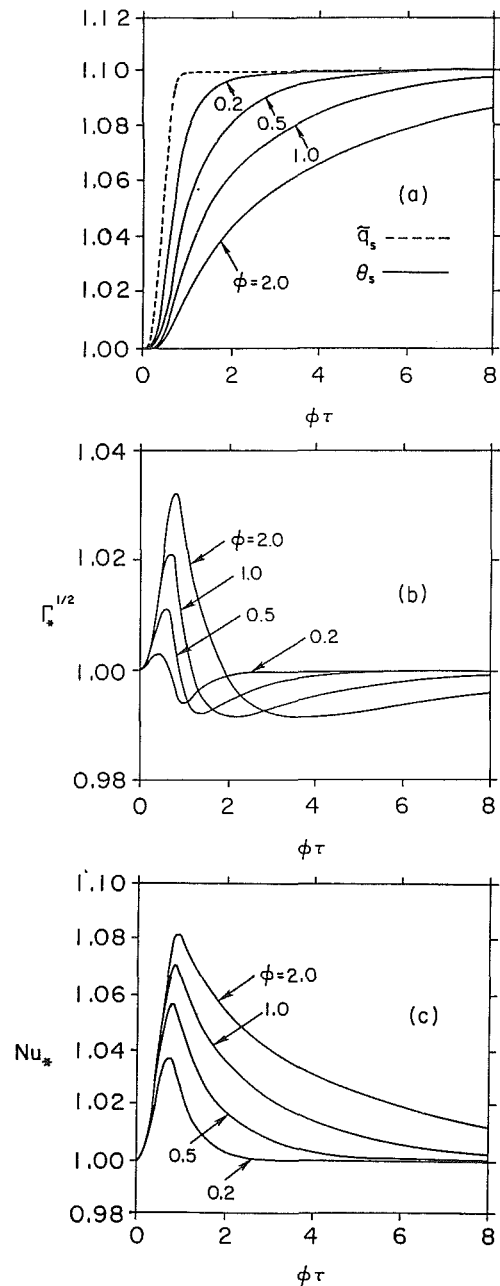


Fig. 4 Transient response due to a ramp increase in the surface heat flux with $Pr = 6$ and $\epsilon_2 = 1.1$: (a) surface temperature, (b) thermal boundary layer, and (c) Nusselt number

mensionless surface temperatures θ_s , calculated with Eq. (23), follow the increase in surface heat flux more closely at lower values of ϕ , since lower values correspond to slower changes in the surface heat flux. Responses with $\phi = 1.0$ for the thermal boundary layer in Fig. 4(b) and the instantaneous Nusselt number in Fig. 4(c) are similar to the responses shown in Fig. 3 for the imposed ramp change in surface temperature. However, excursions from steady-state values in Fig. 4 for the same value of ϕ are smaller. Variations in the surface heat flux lead to smaller excursions since time must transpire to yield changes in the temperature of the fluid layers near the surface, in contrast with an imposed surface temperature variation. Deviations from steady-state values are greater for larger values of ϕ and prevail for longer times after the imposed change in surface heat flux is completed. This characteristic arises due to the nonlinearity associated with the terms in Eqs. (13)–(16)

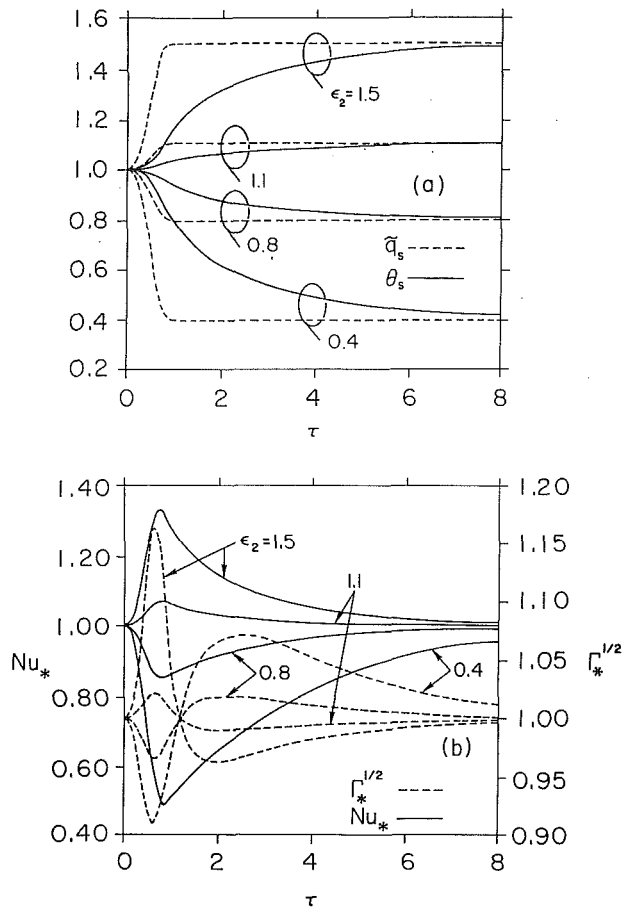


Fig. 5 Effect of the magnitude of the surface heat flux ramp change for $Pr = 6$ and $\phi = 1.0$: (a) surface temperature, (b) thermal boundary layer and Nusselt number

containing $d\theta_s/d\tau$ and $d^2\theta_s/d\tau^2$. In all cases, enhanced convection heat transfer, in terms of Nu_* , prevails during the periods of increasing surface heat flux. As the instantaneous Nusselt number and thermal boundary layer thickness approach their respective steady-state values, the dimensionless surface temperature θ_s [$= (T_s - T_\infty)/(T_{s0} - T_\infty)$] approaches the factor ϵ_2 ($= 1.1$) in accordance with Newton's law of cooling. An opportunity for heat transfer enhancement is suggested by the results, wherein nonlinearities in the response are exploited by generating a pulsed heat flux at the surface with a profile which increases the time-averaged Nusselt number.

In Figs. 5(a) and 5(b), responses to surface heat flux ramp changes of different sizes are compared for $\phi = 1.0$. The behavior for $\epsilon_2 > 1$ pertains to increasing heat fluxes and is thereby similar to the conditions of Fig. 4. It is evident from Fig. 5(b) that the deviations from steady-state thermal boundary layer thicknesses and Nusselt numbers are greater for larger changes in the surface heat flux. For example, a 50 percent increase in surface heat flux ($\epsilon_2 = 1.5$) leads to a maximum Nusselt number deviation of about 17 percent ($Nu_* \approx 1.17$), whereas the deviation is about 10 percent ($Nu_* \approx 1.10$) for a 10 percent increase ($\epsilon_2 = 1.1$). In contrast to cases where the surface heat flux or surface temperature becomes higher, decreases in the surface heat flux ($\epsilon_2 < 1$) lead to smaller transient Nusselt numbers. The thermal boundary layer thickness decreases initially as less heat is available from the surface to maintain the temperature of the fluid at points far into the flow. As in Fig. 3, the response of the boundary layer to the changing surface heat flux is too slow and an overshoot of the steady-state condition ($\Gamma_*^{1/2} = 1$) occurs. In all cases, the same

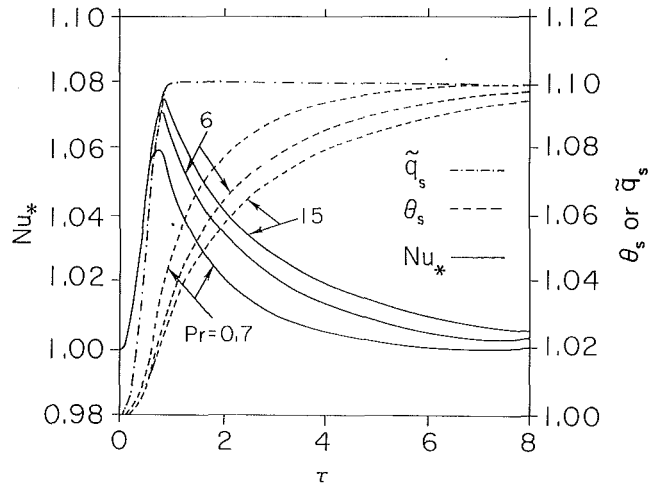


Fig. 6 The influence of Prandtl number on the transient response to a ramp increase in the surface heat flux with $\epsilon_2 = 1.1$ and $\phi = 1.0$

time period is required to re-establish steady-state conditions. Thus, the length of time in which deviations from steady-state values occur is not dependent on the magnitude of the change in surface heat flux, but is instead strongly dependent on the rapidity of the induced variation as demonstrated in Fig. 4.

The effect of the Prandtl number on the transient response to a ramp change in the surface heat flux is given in Fig. 6. Lower thermal diffusivities give rise to larger fluid temperature gradients near the surface since an increasing surface temperature results in an accumulation of thermal energy near the surface that is not readily transported to more distant fluid layers. Deviations from steady-state Nusselt numbers are therefore greater in Fig. 6 at higher Prandtl numbers. However, as in the unforced response shown in Fig. 2, transients occur over similar time periods and do not differ greatly.

Responses for the case where a 10 percent sinusoidal surface heat flux variation [$\epsilon_3 = 0.1$, Eq. (27)] is suddenly superimposed at $\tau = 0$ on a previously steady surface heat flux is given in Fig. 7 for different dimensionless frequencies \bar{f} ($= f/C$). In order to present results succinctly, the product $\bar{f}\tau$, which appears in Eq. (27), is employed for the independent variable. The dimensionless sinusoidal heat flux \tilde{q}_s and calculated dimensionless surface temperatures θ_s are shown in Fig. 7(a). Thermal boundary layer thickness and Nusselt number responses are given in Figs. 7(b) and 7(c), respectively. An initial transient is evident in the boundary layer and Nusselt number responses but is largely abated for $\bar{f}\tau > 1$, after which responses are periodic. Surface temperatures lag further behind the heat flux variation at higher values of \bar{f} , since the rapidity of the changing heat flux leads to more pronounced transients in the thermal boundary layer (Fig. 7b). However, larger deviations from steady-state boundary layer thicknesses and more effective convective heat transfer associated with significant increases in the Nusselt number in Fig. 7(c) lead to smaller amplitudes of the surface temperature variations at the higher frequencies. Larger amplitudes in the induced surface temperature variation at the lower frequencies are more directly in response to the imposed varying surface heat flux, since the thermal boundary layer and Nusselt number remain closer to their steady-state values. Calculations performed with $\bar{f} > 1$ were found to be in close agreement with the response for $\bar{f} = 1.0$ shown in Fig. 7. Thus, convection heat transfer continues to be affected at higher frequencies, but fluctuation amplitudes in the Nusselt number approach maximum values with amplitudes dependent on the magnitude of the imposed heat flux variation.

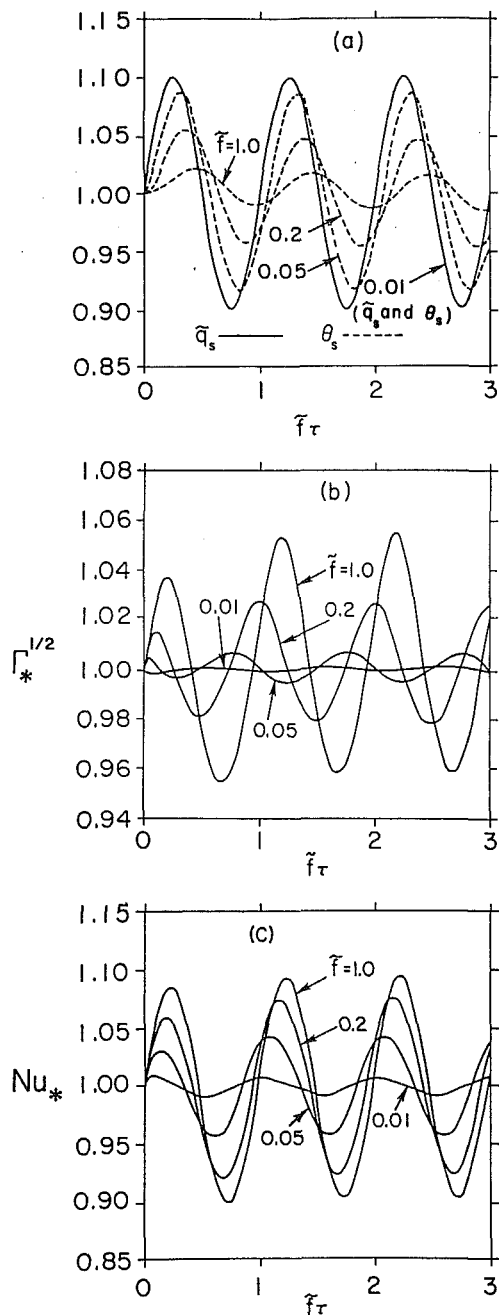


Fig. 7 Transient response due to oscillatory variations in the surface heat flux with $Pr = 6$ and $\epsilon_3 = 0.1$: (a) surface temperature, (b) thermal boundary layer thickness, (c) Nusselt number

Conclusions

Temporal variations in the surface heat flux or surface temperature can significantly affect convective heat transfer in planar stagnation flows. Heat transfer correlations developed under steady-state conditions, such as those for impinging jets or for cylinders in a crossflow, may thereby yield inaccurate estimates of heat transfer rates when transients occur. The transient response is more rapid at lower Prandtl numbers but is chiefly governed by the free-stream velocity gradient C . Thermal boundary layers in impinging flows with higher free-stream velocity gradients respond more quickly to changing conditions at the surface and deviations from steady-state heat transfer coefficients are thereby smaller. Fluid temperature

gradients adjacent to a cooled surface become greater during periods of increasing surface temperature or surface heat flux due to an accumulation of thermal energy in fluid layers near the surface. When the surface temperature or heat flux decrease, fluid temperature gradients become smaller as thermal energy is transported to fluid layers farther from the cooled surface. Consequently, convective heat transfer is more effective when surface temperature or surface heat flux increases but is less effective when surface temperature or surface heat flux decreases. Departures from steady-state heat transfer coefficients are greater for larger and more rapid transients. Enhancement to convective heat transfer may be possible by exploiting nonlinearities in the thermal boundary layer response. For a sinusoidal fluctuation of a specific amplitude, departures approach a limiting value as the fluctuation frequency increases. The results can be used to estimate departures from steady-state heat transfer coefficients for a particular stagnation flow.

Acknowledgment

Support for this work was provided by the National Science Foundation of the United States under Grant No. CTS-8918154.

References

- Aziz, M., 1991, "The Effect of Intermittent Flow on Convective Heat Transfer to a Planar Impinging Water Jet," MS Thesis, Clemson University, Clemson, SC.
- Evans, H. L., 1962, "Mass Transfer Through Laminar Boundary Layers. 7. Further Similar Solutions to the B -Equation for the Case $B = 0$," *International Journal of Heat and Mass Transfer*, Vol. 5, pp. 35-57.
- Gerald, C. F., 1978, *Applied Numerical Analysis*, Addison Wesley, New York, pp. 11-13, 257-260.
- Glauert, M. B., 1955, "The Laminar Boundary Layer on Oscillating Plates and Cylinders," *Journal of Fluid Mechanics*, Vol. 1, pp. 97-110.
- Gorla, R. S. R., Jankowski, F., and Textor, D., 1988a, "Periodic Boundary Layer Near an Axisymmetric Stagnation Point on a Circular Cylinder," *International Journal of Heat and Fluid Flow*, Vol. 9, pp. 421-426.
- Gorla, R. S. R., Jankowski, F., and Textor, D., 1988b, "Thermal Response of a Periodic Boundary Layer Near an Axisymmetric Stagnation Point on a Circular Cylinder," *International Journal of Heat and Fluid Flow*, Vol. 9, pp. 427-430.
- Hansen, A. G., 1964, *Similarity Analyses of Boundary Value Problems*, Prentice-Hall, Englewood Cliffs, NJ.
- Inada, S., Miyasaka, Y., and Izumi, R., 1981, "A Study of the Laminar Flow Heat Transfer Between a Two-Dimensional Water Jet and a Flat Surface With Constant Heat Flux," *Bulletin of the JSME*, Vol. 24, pp. 1803-1810.
- Incropera, F. P., 1988, "Convection Heat Transfer in Electronic Equipment Cooling," *ASME JOURNAL OF HEAT TRANSFER*, Vol. 110, pp. 1097-1111.
- Kuethe, A. M., and Schetzler, J. D., 1959, *Foundation of Aerodynamics*, Wiley, New York.
- Lighthill, M. J., 1954, "The Response of Laminar Skin Friction and Heat Transfer to Fluctuations in the Stream Velocity," *Proceedings of the Royal Society of London*, Vol. 224, pp. 1-23.
- Nagendra, H. R., 1973, "Transient Forced Convection Heat Transfer From an Isothermal Flat Plate," *AIAA Journal*, Vol. 11, pp. 876-878.
- Rott, N., 1956, "Unsteady Viscous Flow in the Vicinity of a Stagnation Point," *Quarterly of Applied Mathematics*, Vol. 13, pp. 444-451.
- Schlichting, H., 1979, *Boundary-Layer Theory*, 7th ed., McGraw-Hill, New York, pp. 95-99, 206-217.
- Tran, L. T., and Taulbee, D. B., 1989, "Prediction of Stagnation Point Heat Transfer With Free Stream Turbulence," in: *Proceedings of the National Heat Transfer Conference*, ASME HTD-Vol. 107, pp. 27-34.
- Watson, J., 1959, "The Two-Dimensional Laminar Flow Near the Stagnation Point of a Cylinder Which Has an Arbitrary Transverse Motion," *Quarterly Journal of Mechanics and Applied Mathematics*, Vol. 12, pp. 175-190.
- Yang, K. T., 1958, "Unsteady Laminar Boundary Layers in an Incompressible Stagnation Flow," *ASME Journal of Applied Mechanics*, Vol. 25, pp. 421-427.
- Zumbrunnen, D. A., Incropera, F. P., and Viskanta, R., 1989, "Convective Heat Transfer Distributions on a Plate Cooled by Planar Water Jets," *ASME JOURNAL OF HEAT TRANSFER*, Vol. 111, pp. 889-896.
- Zumbrunnen, D. A., Incropera, F. P., and Viskanta, R., 1991, "A Laminar Boundary Layer Model of Heat Transfer Due to a Nonuniform Planar Jet Impinging on a Moving Plate," *Wärme- und Stoffübertragung* (in press).

APPENDIX

Table 1 Free-stream velocity gradients in common stagnation flows

¹Free surface jet with uniform discharge velocity across nozzle width.
²Free surface jet with parabolic velocity profile across nozzle width and flow unaffected by gravitational acceleration.

	$\bar{C} = LC/V$	L	References
Cylinder (cross-flow)	4.0	d	Kuethe and Schetzer (1959)
Uniform Jet ¹	0.785	w	Inada et al. (1981)
Nonuniform Jet ²	1.73	w	Zumbrunnen et al. (1991)

Table 2 Steady-state values ($d\theta_s/d\tau = d^2\theta_s/d\tau^2 = 0$) of Nu_x , $Re_x^{-1/2}$ and Γ predicted by model with $\Lambda = 7.052324$ and comparison with an exact solution

Pr	Similarity Solution (Evans, 1962)	Model	
	$Nu_x Re_x^{-1/2}$	$Nu_x Re_x^{-1/2}$	Γ
0.7	0.496	0.501	15.951
0.8	0.523	0.528	14.327
1.0	0.570	0.577	11.995
2.0	0.744	0.756	7.003
4.0	0.962	0.980	4.161
6.0	1.115	1.138	3.090
10.0	1.339	1.369	2.135
15.0	1.546	1.582	1.600

Experimental Study of Laminar Natural Convection in Cells With Various Convex and Concave Bottoms

W. M. Lewandowski

M. J. Khubeiz

Department of Chemical Engineering,
Technical University of Gdańsk,
Gdańsk, Poland

Heat transfer and free convective motion in limited space from the bottoms of different hemispherical convex or concave shapes have been studied experimentally. The ratio of the diameter of the hemisphere (d) to the diameter of the bottom (D) ($0 < d/D < 1$) has been tested for a range of Rayleigh numbers ($10^5 < Ra < 10^7$). In comparison with a flat bottom ($d/D = 0$), about 40 percent inhibition or about 50 percent intensification depending on the bottom configuration (d/D) have been observed. The mechanism of the phenomenon based on dead space, local overheating, and shape influence effects has been proposed.

1 Introduction

Free convection from curved, especially spherical, surfaces presently constitutes a classical subject of heat transfer investigations together with vertical, horizontal, and inclined plates (Bromhan and Mayhew, 1962; Fendel, 1968; Amato and Tien, 1972, 1976; Ceoola and Cornish, 1981; Singh and Hassan, 1983; and also studies of other authors described in detail by Cieśliński and Pudlik, 1988, and Jaluria, 1980).

Heat transfer from the hemisphere studied by Merk and Prins (1953) and Jaluria and Gebhart (1975) or from spherical sections by Cieśliński and Pudlik (1988) are the next steps of spherical surface investigations.

All the abovementioned problems refer to heat exchange in unlimited space. Although we have found some works dealing with natural convection in closed space, as, for example, hemispherical slots (Shiina et al., 1988) or concentric spherical slots (Bishop et al., 1966; Riahi, 1984), but the results presented in these papers are not complete and cannot be used for practical applications.

Therefore the subject of this work is connected with experimental explanation of influence of bottom shape on free convective heat transfer in cylindrical closed space.

II Experimental Apparatus

Experimental investigations of natural convection were carried out on a cylindrical cell with nine forms of bottom configuration (Fig. 1). The internal diameter of the bottom was constant ($D = 0.047$ m) but the diameters of the convex or concave hemispheres (d) were different as was the height of the fluid (H) above the bottom.

Difficulties in heating such complicated bottom shapes were overcome by using steam heating instead of electrical. In Fig. 2 a diagram of the experimental equipment is presented. The condensate tank (3) of the capacity between marks ($V = 3.5 \cdot 10^{-6}$ m³) is the main measuring device. After filling with condensate it automatically empties through an overflow pipe. The time of filling of the tank (τ) and heat of condensation (i'') of the fluid inside the vapor generator (glass tank) (2) were a measure of the heat flux transferred through the bottom of the cell (1) to the tested fluid. The height of the layer of fluid above the heated bottom (H) was changed with a movable cooler (6) with a flat copper plate (5). Owing to the reflux

condenser (7) it has been possible also to use volatile organic solvents of low boiling points (ethanol, carbinol, acetone, and so on) as the heating agents. As a matter of fact, this was the only way of changing the temperature of the bottom (T_W). A change of the cooler plate (5) temperature (T_F) is achieved by means of the ultra thermostat (8) set at temperature T_U . The sealings (10) were made of a material resistant to boiling and organic solvents. The electric heater (4) with an auto transformer (9) rendered possible the regulation of the boiling intensity of the fluid inside the tank (2). Apart from the spiral part immersed in the boiling fluid, the heater (4) also consists of vertical heating elements slightly superheating vapor.

The temperatures T_W and T_F were measured with copper-constantan thermocouples. In order to visualize the convective fluid motions, the walls of the cell (1) and the vapor generator (2) were made of glass.

Heat losses from the lateral surface of the cell (1) were limited by heat insulation, removed only during the visualization experiments. We know from our previous calculations that for the parameters of the cell used in this work the conduction heat flux transferred through the wall is about 150 times smaller than convective heat flux from the bottom. Therefore heat loss flux and conduction flux were neglected in our calculations. On the other hand, the magnitude of these fluxes did

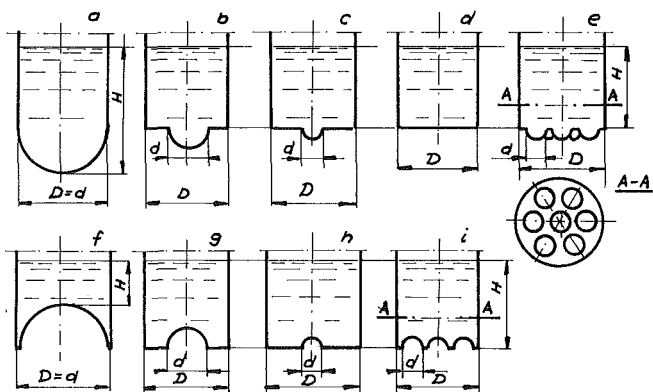


Fig. 1 Types of tested bottoms of the model of the honeycomb cell: convex: $d/D = 1$ (hemispherical), $A_n = 3.47 \times 10^{-3}$ m² (a); $d/D = 0.5$, $A_n = 2.17 \times 10^{-3}$ m² (b); $d/D = 0.25$, $A_n = 1.84 \times 10^{-3}$ m² (c); multiconvex $7 * d/D = 0.25$, $A_n = 2.49 \times 10^{-3}$ m² (d); concave: $d/D = 1$ (hemispherical), $A_n = 3.47 \times 10^{-3}$ m² (e); $d/D = 0.5$, $A_n = 2.17 \times 10^{-3}$ m² (f); $d/D = 0.25$, $A_n = 1.84 \times 10^{-3}$ m² (g); multiconcave $7 * d/D = 0.25$, $A_n = 2.49 \times 10^{-3}$ m² (h) and flat bottom $d/D = 0$, $A_n = 1.73 \times 10^{-3}$ m² (i)

Contributed by the Heat Transfer Division for publication in the JOURNAL OF HEAT TRANSFER. Manuscript received by the Heat Transfer Division June 13, 1990; revision received March 18, 1991. Keywords: Enclosure Flows, Natural Convection, Solar Energy.

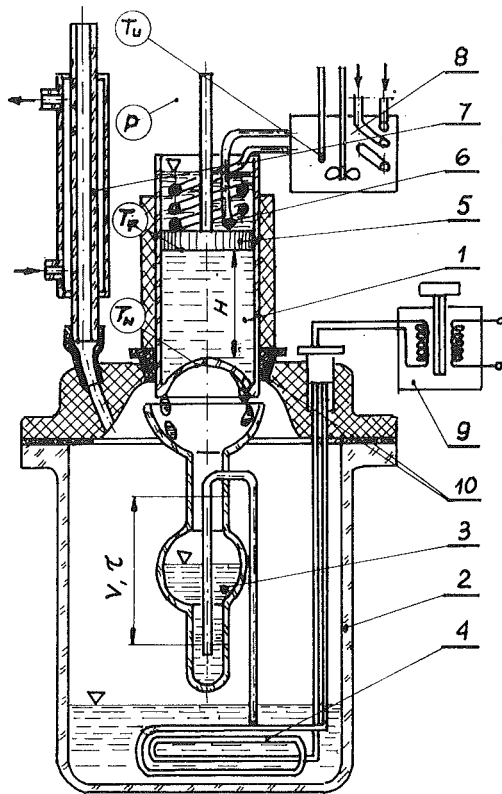


Fig. 2 Diagram of the experimental equipment: (1) model of honeycomb cell, (2) tank of boiling medium, (3) measurement tank of condensate volume, (4) electric heater, (5) cooler plate, (6) cooler, (7) reflux condenser, (8) ultra thermostat, (9) auto transformer, and (10) sealings

not affect the final conclusions, since these fluxes did not depend directly on the bottom configuration but on the lateral cylindrical wall of the cell.

Experiments were carried out in a blackened and isothermal room and the tested fluid (glycerine) with aluminum dust dispersed inside it was illuminated with a "knife light" and then photographed at different exposure times. Based on the illumination time and on traces of powder particles, it was possible to determine the velocity and streamlines of the cold fluid flowing down onto the bottom as well as the warm fluid leaving it. Without this method of visualization, the explanation of the convective heat transfer as a result of different bottom configurations would be more difficult.

Nomenclature

a = thermal diffusivity, m^2/s	H = height of fluid layer above the bottom, m	λ = thermal conductivity, $W/m \cdot ^\circ C$
A_n = area of the internal surface of the bottom of a cylindrical cell, m^2	i'' = heat of condensation, J/kg	μ = dynamic viscosity, $N \cdot s/m^2$
C = constant defined by Eq. (9)	n = superscript in Eq. (9)	ν = kinematic viscosity, m^2/s
C_p = specific heat at constant pressure of the fluid, $J/(kg \cdot K)$	Nu = Nusselt number; Eq. (7)	ρ = density, kg/m^3
d = internal diameter of hemispherical convexity or concavity, m	Q = heat flux, W	τ = time, s
D = internal diameter of the bottom, m	Ra = Rayleigh number; Eq. (8)	
g = acceleration due to gravity, m/s^2	T = temperature, $^\circ C$	
	$\Delta T = T_w - T_F$ = temperature difference, $^\circ C$	
	V = volume of the condensate tank, m^3	
	α = heat transfer coefficient, $W/m^2 \cdot ^\circ C$	
	β = coefficient of volumetric expansion, $^\circ C^{-1}$	
		Subscripts
		ch = refers to characteristic
		$EtOH$ = refers to ethanol
		F = refers to ambient temperature of the fluid
		w = refers to temperature of the bottom

III Experimental Investigations

Experimental investigations were carried out in anhydrous glycerine dehydrated with a molecular sieve. Tests of glycerine's physical properties were made at various temperatures ($10 < T_{ch} < 80^\circ C$). Approximations of experimental points led to the following relations for the dynamic viscosity coefficient μ , density ρ , thermal conductivity λ , and specific heat C_p :

$$\mu = -4.329E^{-6} \cdot T_{ch}^3 + 6.947E^{-4} \cdot T_{ch}^2 - 3.740E^{-2} \cdot T_{ch} + 0.7059 \quad [Pa \cdot s] \quad (1)$$

$$\rho = 0.006 \cdot T_{ch}^2 - 0.850 \cdot T_{ch} + 1275.5 \quad [kg/m^3] \quad (2)$$

$$\lambda = 0.0001 \cdot T_{ch} + 0.283 \quad [W/m^2 \cdot K] \quad (3)$$

$$C_p = 0.005 \cdot T_{ch} + 2.280 \quad [kJ/kg \cdot K] \quad (4)$$

In the above relationships T_{ch} is a characteristic temperature, being an arithmetic mean of the bottom and cooler temperatures ($T_{ch} = (T_w + T_f)/2$).

Absolute ethanol ($EtOH$) with a boiling point $T_w = 78.3^\circ C$, density $\rho_{EtOH} = 735 \text{ kg/m}^3$, and heat of condensation $i''_{EtOH} = 879.228 \text{ kJ/kg}$ was used as the heating medium. Ethanol overheated vapors condensed on the bottom and gave up heat. The magnitude of this heat flux Q was determined from the relation:

$$Q = V \cdot \rho_{EtOH} \cdot i''_{EtOH} / \tau \quad [W] \quad (5)$$

where V is the volume of the condensate set up on the investigated bottom during the time τ .

Since the measuring tank (3) was situated inside the vessel (2), the temperature of the condensate during the determination of its volume remained constant and equal to T_w . Thus, the loss of heat flux from the bottom through the condensate does not exist and measurement of the condensate temperature was unnecessary. It is a modification in comparison with the experimental equipment described by Lewandowski and Kubski (1984) where the measurement of the condensate volume was performed outside the apparatus. In the installation used in the present work, the boiling ethanol was condensing not only on the bottom of the tested cells (1) but also on the walls of the tank (2), the measurement tank (3) with overflow pipe, and inside the reflux condenser (7), so the temperature of all these elements was the same (T_w). In this situation there is no heat flux lost from the bottom onto the sides and all the heat flux of condensation (Q) was transferred into the tested fluid (glycerine).

Based on the heat flux Q , the magnitude of the bottom surface of each cell A_n and the temperature difference $\Delta T (= T_w - T_F)$, the heat transfer coefficient α and subse-

Shape of bottoms	Experimental correlations C and n fitted	Experimental correlations C fitted, n = constant
Fig. 1a)	$Nu_H = 0.00327 \cdot Ra_H^{0.384} \pm 3.2\%$	$Nu_H = 0.00402 \cdot Ra_H^{0.4} \pm 3.8\%$
Fig. 1b)	$Nu_H = 0.00594 \cdot Ra_H^{0.382} \pm 5.3\%$	$Nu_H = 0.00498 \cdot Ra_H^{0.4} \pm 5.1\%$
Fig. 1c)	$Nu_H = 0.00929 \cdot Ra_H^{0.307} \pm 7.2\%$	$Nu_H = 0.00495 \cdot Ra_H^{0.4} \pm 6.8\%$
Fig. 1d)	$Nu_H = 0.00184 \cdot Ra_H^{0.453} \pm 5.8\%$	$Nu_H = 0.00477 \cdot Ra_H^{0.4} \pm 6.9\%$
Fig. 1e)	$Nu_H = 0.00141 \cdot Ra_H^{0.407} \pm 2.6\%$	$Nu_H = 0.00448 \cdot Ra_H^{0.4} \pm 10.5\%$
Fig. 1f)	$Nu_H = 0.00145 \cdot Ra_H^{0.442} \pm 2.6\%$	$Nu_H = 0.00311 \cdot Ra_H^{0.4} \pm 4.8\%$
Fig. 1g)	$Nu_H = 0.00267 \cdot Ra_H^{0.425} \pm 4.2\%$	$Nu_H = 0.00459 \cdot Ra_H^{0.4} \pm 5.1\%$
Fig. 1h)	$Nu_H = 0.00443 \cdot Ra_H^{0.408} \pm 7.5\%$	$Nu_H = 0.00506 \cdot Ra_H^{0.4} \pm 7.6\%$
Fig. 1i)	$Nu_H = 0.00374 \cdot Ra_H^{0.415} \pm 3.7\%$	$Nu_H = 0.00485 \cdot Ra_H^{0.4} \pm 10.0\%$

quently the Nusselt number are calculated from the following equations:

$$\alpha = Q / (A_n \cdot \Delta T) \quad [W/m^2 \cdot K] \quad (6)$$

$$Nu = \alpha \cdot H / \lambda \quad (7)$$

Next, the Rayleigh number is defined by the equation:

$$Ra = g \cdot \beta \cdot \Delta T \cdot H^3 / (\nu \cdot a) \quad (8)$$

where g is gravitational acceleration, β is the coefficient of volumetric expansion, H is the height of the fluid layer, ν ($=\mu/\rho$) is the kinematic viscosity, and a ($=\lambda/C_p\rho$) is the thermal diffusivity.

The first measurement series has been carried out for one heat flux at $T_w = 78.3^\circ C = \text{const}$ and $T_f = 50^\circ C = \text{const}$ and for several values of fluid layer height (H) above the tested bottoms expressed with ratios $H/D = 0.25, 0.5, 0.75$, and 1.5 . Subsequent tests were carried out for heat fluxes (Q) corresponding to $T_w = 78.3^\circ C = \text{const}$. and $T_f = 20, 30, 40, 55$, and $60^\circ C$ and for $H/D = 0.5, 1.0$, and 2.0 .

The investigations were carried out under steady-state conditions. Thermal equilibrium was attained after about 2.5 h for all the values of heat flux and about 1.5 h after the cooler change position H . Under such conditions the time of filling of the measurement tank τ , the temperature of the bottom T_w , the temperature of the cooler T_f , and atmospheric pressure p (to determine the boiling point of ethanol) were measured. These measurements were repeated until the time of filling up of the tank with condensate differed from the previously obtained result by about $\Delta\tau = 2-3$ s. Then the heat flux Q , height of fluid layer above the bottom H , or shape of the bottom were changed and the entire procedure had to be repeated.

In addition to the balance quantitative measurements, the qualitative (visualization) investigations were also done by photographing the convection movements and sketching the fluid flow directions, which could neither be recorded nor shown merely on photographs.

IV Results of Experimental Investigations

The obtained experimental results are presented in the form of relations of Nusselt (Nu_H) and Rayleigh (Ra_H) numbers.

$$Nu_H = C \cdot (Ra_H)^n \quad (9)$$

Correlations of experimental points presented in Table 1 were calculated using least-square regression analysis in the range $1 \times 10^6 < Ra < 3 \times 10^9$. A comparison of the dimensionless equations listed in Table 1 with that obtained by Romanow (1956):

$$Nu_H = 0.0192 \cdot (Ra_H)^{0.4}, \quad (10)$$

proves that the exponents are similar ($n \approx 0.4$), while the coefficients C differ to a certain extent. Romanow (1956) also investigated the convective heat transfer inside a cylinder closed with a flat bottom. However, his interpretation of H was not

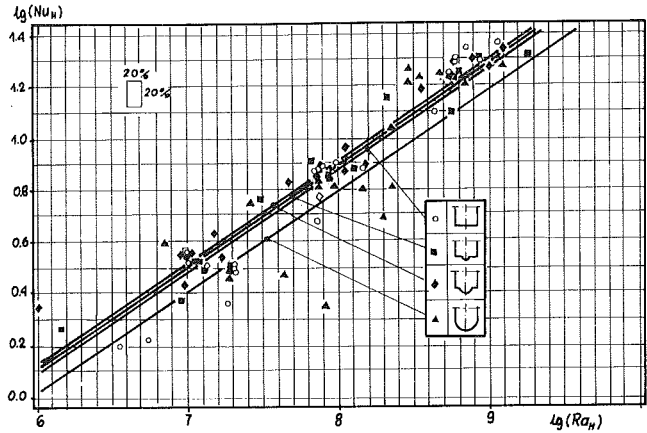


Fig. 3 Experimental correlations of Nusselt (Nu_H) and Rayleigh (Ra_H) numbers obtained for convex: ($d/D = 1, 0.5$, and 0.25) and flat ($d/D = 0$) bottoms

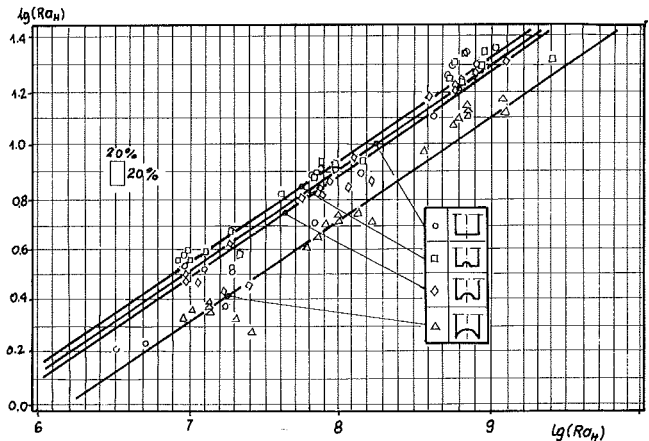


Fig. 4 Experimental correlations of Nusselt (Nu_H) and Rayleigh (Ra_H) numbers obtained for concave: ($d/D = 1, 0.5$, and 0.25) and flat ($d/D = 0$) bottoms

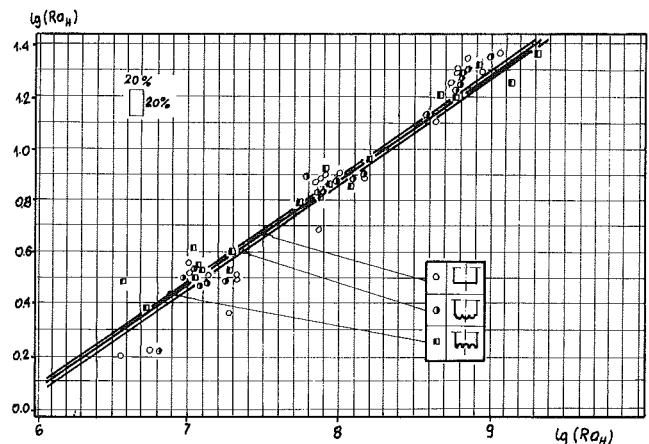


Fig. 5 Experimental correlations of Nusselt (Nu_H) and Rayleigh (Ra_H) numbers obtained for multiconvex: ($7 \cdot d/D = 0.25$), multiconcave ($7 \cdot d/D = 0.25$), and flat ($d/D = 0$) bottoms

the same as above: It was the height of the heated cylindrical wall measured from the bottom.

Comparison between the experimental correlations and the result obtained by Shiina (1956) has demonstrated a greater discrepancy:

$$Nu_R = 0.2356 \cdot (Ra_R)^{0.242}, \quad (11)$$

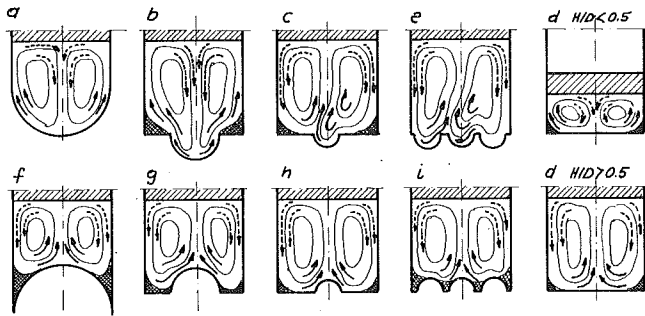


Fig. 6 Influence of the bottom shape on convection flow of the fluid presented in graphic form obtained by visual methods. The thin lines are streamlines, the thick continuous lines show the directions of warm fluid flow, and the thick dashed ones the directions of cold fluid flow.

but correlation (11) was obtained for convective heat transfer inside a hemisphere of a radius R with heating horizontal flat bottom and cooling bowl surface. The comparison with other correlations quoted by Shiina et al. (1988) and the results of other authors (Bishop et al., 1966; Riahi, 1984) indicates also some considerable discrepancies. It seems most likely that it is the result of different configuration of the close spaces. In typical cases of natural convective heat transfer in closed spaces the ratio $H/D \ll 1$, whereas in the present study $H/D > 1$.

The differences of the exponents of equations presented in Table 1 make a direct comparison of the influence of the shape bottom configuration on heat transfer rates more difficult. So in this situation we decided to recalculate our experimental data but with fixed exponent ($n=0.4$). The results of these recalculations are shown in Figs. 3, 4, and 5 and in the second column of Table 1.

For the sake of clarity of the presented data the results obtained for bottoms of similar (convex or concave) configurations together with the results obtained for flat bottoms were grouped in the same pictures.

Figure 3 presents the results obtained for the bottoms of various convexities, defined by the ratio ($d/D=0.0, 0.25, 0.5$, and 1.0). The first of these values corresponds to the extreme case of a flat bottom, while the last corresponds to a hemispherical bottom.

Figure 4 illustrates in a similar manner the results obtained for the bottoms of various concavities ($d/D=0$ (flat bottom), $0.25, 0.5$, and 1.0 (concave hemisphere)).

The results obtained for the bottoms having seven concavities or convexities of the ratio of single concavity or convexity to the diameter of the bottom equal to $d/D=0.25$ are compared with those obtained for a flat bottom in Fig. 5.

V Analysis of Experimental Results

Investigations presented in this study tend toward the determination of the influence of the configuration of a cell bottom on convective heat transfer. This influence may be estimated by a comparison of the results obtained for the particular shapes of the bottom with the result for a flat-bottomed cell.

Analysis of the results listed in a second column in Table 1 indicates that the convective heat transfer coefficient is reduced to the highest extent (by 34.8 percent in relation to the flat bottom) in the cell with a concave hemispherical bottom ($d/D=1$) (Fig. 6f).

These observations may be of some practical use in, for instance, construction of solar collectors. The replacement of the flat surface of cell bottoms of a honeycomb panel with a concave bottom (as in Fig. 6f) increases the solar energy absorbing surface of the collector by a factor of 2 while the convective heat loss flux from the bottom increases by a factor of 1.26 only. Thus the thermal efficiency and profitability

gained due to application of hemispherical concave bottom in honeycomb panels instead of a flat bottom would increase.

On the other hand, the greatest intensification of the heat exchange (by 6 percent) was observed in the cell with the concave bottom of ratio $d/D=0.25$ (Fig. 6h).

An explanation of the factors that bring about a decrease or an increase of the convective fluid motions with regard to the shape of the cell bottom is more complex and requires further investigations.

VI Mechanism of the Phenomenon

Analysis of the experimental data including visualization and observation of the investigated phenomenon leads to a general statement that three fundamental effects depending on the configuration of the bottom can be distinguished in the mechanism of the convective heat transfer. They are: (a) dead space effect, (b) effect of local overheating, and (c) shape effect. These three effects counteract one another and their contributions change in relation to the bottom configuration.

The illustration of these effects is Fig. 6, in which their summary actions due to the configuration of the bottom are presented in graphic form. In the pictures the streamlines are marked with thin lines, whereas the thick continuous lines are the directions of the heated fluid flow, and the thick dashed ones are the directions of cold fluid flow.

(a) **Dead Space Effect.** The action of the dead space effect is most visible in the case of the concave hemispherical bottom of ratio $d/D=1$ (Fig. 6f). The configuration of this bottom inhibits fluid flow and the motionless, shape-bounded fluid layer (hatched region in Fig. 6) insulates the heated surface. Through this layer, instead of convection, the heat is transferred by conduction. The movement of the fluid in the boundary layer and in the plume is insufficiently intensive to move the shape-bounded fluid in the neighborhood of the heating bottom.

(b) **Effect of Local Overheating.** The effect of local overheating is inversely proportional to the diameter of the concavity in the bottom (d). The smaller the concavity, easier the fluid contained in it is heated. This local overheating of fluid generates a free convective flux (plume), which sets in motion the whole fluid in a closed space and intensifies the convective heat transfer. This effect is most visible for convex bottom of ratio $d/D=0.25$ (Fig. 6c) and $d/D=0.5$ (Fig. 6b).

(c) **Effect of Bottom Shape.** The effect of the bottom shape results from the fact that the continuity of the boundary layer is broken on the convexity of the bottom. As a result this layer parts from the bottom and transforms into a plume flowing upward and mixes the entire volume of the fluid, thus intensifying the heat exchange.

However, in the case of closed spaces, this effect occurs only if $d/D \leq 0.25$ (Fig. 6h). An increase in d is accompanied by the inhibiting dead space effect. For $d/D=0.5$ (Fig. 6g), these effects neutralize each other and the heat exchange is the same as for the flat bottom. In the case of a concave bottom of $d/D=1$ (Fig. 6f) the dead space effect predominates over the intensifying effect of the shape.

The heat transfer is additionally intensified with an increase of the number of curvatures in the bottom, especially for small values of H . In these cases several plumes spring up instead of one, and form a convective cell flow similar to the Bénard structure. For greater values of the fluid layer height H (Fig. 6i and 6e) only one convective cell exists because vertically flowing fluxes merge into one plume. As a consequence, the fluid flowing horizontally moves concentrically to the center of the bottom and undergoes fluctuations and turbulences on the curvatures of the bottom, which intensifies the heat transfer.

The above-proposed mechanism of the phenomenon concerns only the cases where the effect of the bottom shape predominates over the influence of the height of the fluid layer, i.e., $H/D \leq 1$. Within this range the changes in the flow direction of the fluid were observed only for flat bottom. For $H < D/2$ the hot fluid moves from the center of the bottom to the walls as in the case of the hemispherical convex bottom (Fig. 6a). At $H > D/2$ the hot fluid moves concentrically from the walls to the center of the bottom as in the case of a hemispherical concave bottom (Fig. 6f).

When $H/D > 1$ the greatest changes in the structure of flow were observed for the hemispherical convex bottom (Fig. 6a). Probably this was the reason for this bottom at different values of the ratio $H/D = 0.5, 0.75, 1.0, 1.5$ and 2.0 .

However, due to the character of the paper and to the fact that it would be difficult to compare directly the mechanism of the convective motions over hemispherical concave and convex bottoms, some detailed considerations on this topic should be carried out separately.

VII Conclusions

The concave hemispherical bottom (Figs. 1f and 6f) has the most inhibitory influence on convective heat transfer. If this effect, shown for a single cell, could be proved for a honeycomb panel, this shape of the bottom seems to be the best configuration for honeycomb cells in solar collectors or insulating cellular materials for building engineering. It would be an effective way to limit the heat losses from collectors and buildings.

The intensifying influence of some configurations of the bottom should also be used in installations and devices that utilize solar energy because these effects act particularly at small values of heat flux. This problem occurs in the case of intensifying the heat recovery from low-temperature heating media, such as fluid circulating in solar collectors or in solar ponds.

References

- Amato, W. S., and Chi Tien, 1972, "Free Convection Heat Transfer From Isothermal Spheres in Water," *International Journal of Heat and Mass Transfer*, Vol. 15, pp. 327-339.
- Amato, W. S., and Chi Tien, 1976, "Free Convection Heat Transfer From Isothermal Spheres in Polymer Solutions," *International Journal of Heat and Mass Transfer*, Vol. 19, pp. 1257-1266.
- Bishop, E. H., Mack, L. R., and Scanlon, J. A., 1966, "Heat Transfer by Natural Convection Between Concentric Spheres," *International Journal of Heat and Mass Transfer*, Vol. 9, pp. 649-662.
- Bromhan, R., and Mayhew Y., 1962, "Free Convection From a Sphere in Air," *International Journal of Heat and Mass Transfer*, Vol. 5, pp. 83-84.
- Cane, R. L. D., et al., 1977, "Free Convection Heat Transfer Across Inclined Honeycomb Panels," *ASME JOURNAL OF HEAT TRANSFER*, Vol. 99, No. 1, pp. 86-91.
- Ceola, F., and Cornish, A., 1981, "Numerical Solution of Steady State Free Convective Heat Transfer From a Solid Sphere," *International Journal of Heat and Mass Transfer*, Vol. 24, pp. 1369-1379.
- Cieśliński, J., and Pudlik, W., 1988, "Laminar Free-Convection From Spherical Segments," *International Journal of Heat and Fluid Flow*, Vol. 9, No. 4, pp. 405-409.
- Fendel, F. E., 1968, "Laminar Natural Convection About an Isothermally Heated Sphere at Small Grashof Numbers," *J. Fluid Mech.*, Vol. 34, Part 1, pp. 163-176.
- Jaluria, Y., and Gebhart, B., 1975, "On the Buoyancy Induced Flow Arising From a Heated Hemisphere," *International Journal of Heat and Mass Transfer*, Vol. 18, pp. 415-431.
- Jaluria, Y., 1980, *Natural Convection Heat and Mass Transfer*, Pergamon Press, New York.
- Lewandowski, W. M., and Kubski, P., 1984, "Effect of the Use of the Balance and Gradient Methods as a Result of Experimental Investigations of Natural Convection Action With Regard to the Conception and Construction of Measuring Apparatus," *Wärme- und Stoffübertragung*, Vol. 18, pp. 247-256.
- Merk, H. J., and Prins, J. A., 1953, "Thermal Convection in Laminary Boundary Layers," *Journal Applied Scientific Research*, Vol. A4, pp. 11-24.
- Riahi, N., 1984, "Nonlinear Convection in a Spherical Shell," *Journal Physical Society of Japan*, Vol. 53, No. 8, pp. 2506-2512.
- Romanow, A. G., 1956, "Issledovanie tieploobmienna w głuchym kanale w usłowjach jestestwiennej konwekcji," *Izw. AN SSSR, O.T.N.*, No. 6, p. 63.
- Shiina, Y., et al., 1988, "Natural Convection Heat Transfer in a Hemisphere," *Journal of Nuclear Science and Technology*, Vol. 25, pp. 254-262.
- Singh, S. N., and Hassan, M., 1983, "Free Convection About a Sphere at Small Grashof Number," *International Journal of Heat and Mass Transfer*, Vol. 26, pp. 781-783.

A. Cheddadi

Ecole Mohammadia d'Ingénieurs,
Université Mohamed V,
Rabat-Agdal, Morocco

J. P. Caltagirone

Modélisation Avancée des Systèmes
Thermiques et des Écoulements Réels,
ENSCP,
Université de Bordeaux 1,
33400 Talence, France

A. Mojtabi

Laboratoire de Mécanique et Institut de
Mécanique des Fluides,
Université Paul Sabatier,
31062 Toulouse, France

K. Vafai

Department of Mechanical Engineering,
The Ohio State University,
Columbus, OH 43210

Free Two-Dimensional Convective Bifurcation in a Horizontal Annulus

Natural convection is investigated numerically and experimentally in a cylindrical annulus. The governing equations based on primitive variables are solved using Chorin's method. In addition to the unicellular flows reported in the literature, depending on initial conditions, bicellular flows are observed for high Rayleigh numbers. The bifurcation point is determined numerically. The velocity field for unicellular flows is measured by laser-Doppler anemometry in an air-filled annulus. A perturbation solution is also presented. The experimental results are in good agreement with numerical predictions and the perturbation solution.

1 Introduction

The horizontal concentric cylinder geometry has been widely studied theoretically and experimentally. An extensive description of different flow regimes depending on Rayleigh number Ra and radial aspect ratio R has been given by Powe et al. (1969, 1971). The flow is observed to be stationary and two dimensional as long as the Rayleigh number does not exceed a critical value, Ra_c . Exceeding this value leads to multicellular, spiral or oscillatory regimes depending on the aspect ratio R . Grigull and Hauf (1966) described three-dimensional structures corresponding to moderate aspect ratios and large Rayleigh numbers. The stability of two-dimensional flows occurring for small Rayleigh numbers was investigated by Mojtabi and Caltagirone (1979), and the existence of a critical line in the (R, Ra) plane was demonstrated. Since Crawford and Lemlich (1962) gave the first numerical solution for the problem, several numerical investigations have been published. In most of these investigations, the stream function-vorticity formulation is utilized for two-dimensional analysis (for example, Kuehn and Goldstein, 1976). Takata et al. (1984) utilized the potential vector-vorticity formulation for the three-dimensional analysis.

Although several numerical studies have been performed in recent years on steady two-dimensional natural convection in a cylindrical fluid annulus, all of them were restricted to a unicellular flow pattern, except for the work of Rao et al. (1985). They observed that for a narrow annulus, the unicellular flow pattern (at low Ra numbers) becomes multicellular for higher values of Rayleigh number. For the case of the cylindrical, porous annulus Rao et al. (1987) demonstrated the existence of multicellular flow structures, and Himasekhar and Bau (1988) developed a linear stability analysis to determine the stability of various solution branches. Multicellular flows were also observed numerically in both fluid and porous, spherical annuli (Fauveau et al., 1978; Caltagirone et al., 1980).

The purpose of this paper is to study unicellular and bicellular flows computed for high Rayleigh numbers. Several initial

conditions, including pure conduction temperature field with and without perturbations, are adopted and their effects on determining final solutions are discussed. The influence of the bicellular flow on the local and overall heat transfer is examined, and a bifurcation point as characterized by a critical Rayleigh number is determined, over which both families of solutions exist. In this work, previous experimental studies in this area have been expanded upon. Flow visualizations were done using cigar smoke or suspended aluminum powder as tracer material (Bishop and Carley, 1966) and local heat transfer rates were determined by the measurement of the temperature field using thermocouples (Kuehn and Goldstein, 1976). In our experiments, which were conducted in conjunction with the numerical analysis, the tangential velocity field was measured by laser-Doppler anemometry in an air-filled annulus with an aspect ratio of 1.6 and for Rayleigh numbers less than the critical value. Very good agreement was found between experimental and numerical results. Comparison with computed values leads to the conclusion that the flow is two-dimensional, and has a unicellular configuration for the range of the Rayleigh numbers investigated.

2 Problem Formulation

2.1 Configuration and Set of Equations. Consider a fluid annular space bounded by horizontal concentric cylinders of radii r_i and r_o . As shown in Fig. 1, the surfaces of the cylinders are maintained at constant uniform temperatures T_i and T_o , where $T_i > T_o$. Assuming that the Boussinesq approximation is valid, the dimensionless equations governing the two-dimensional fluid motion may be reduced to:

$$\text{div } \mathbf{V} = 0 \quad (1)$$

$$\frac{\partial}{\partial t} U + (\mathbf{V} \cdot \text{grad})U = -\frac{\partial}{\partial r} p + Ra \text{Pr} T \cos \theta + \text{Pr} \Delta_r \mathbf{V} \quad (2)$$

$$\frac{\partial}{\partial t} V + (\mathbf{V} \cdot \text{grad})V = -\frac{\partial}{r \partial \theta} p - Ra \text{Pr} T \sin \theta + \text{Pr} \Delta_\theta \mathbf{V} \quad (3)$$

$$\frac{\partial}{\partial t} T + (\mathbf{V} \cdot \text{grad})T = \Delta T \quad (4)$$

Contributed by the Heat Transfer Division for publication in the JOURNAL OF HEAT TRANSFER. Manuscript received by the Heat Transfer Division August 7, 1990; revision received March 15, 1991. Keywords: Flow Instability, Natural Convection.

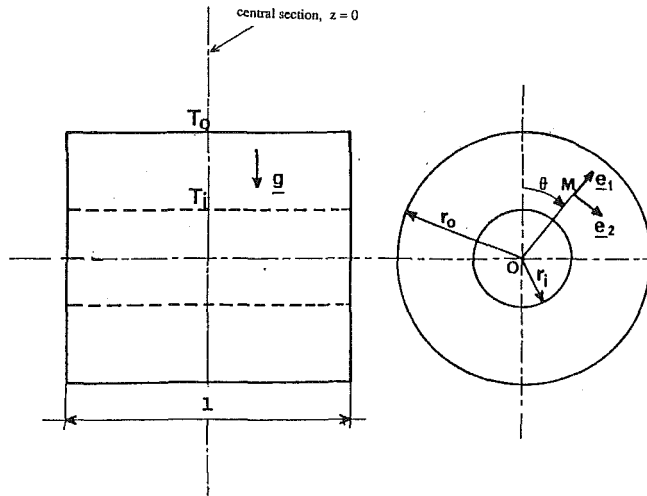


Fig. 1 Schematic of the problem under investigation

where \mathbf{V} is the velocity vector having dimensionless velocity components (U , V) normalized with r_i and the diffusion time r_i^2/a as the length and time scales, respectively. The dimensionless temperature, T , is defined by $(T' - T_o)/(T_i - T_o)$, where T' is the dimensional temperature and p and t are the dimensionless pressure and time variables, respectively, Δ is the symbol for Laplacian and $\Delta_r \mathbf{V}$ and $\Delta_\theta \mathbf{V}$ are the radial and angular components of $\Delta \mathbf{V}$. The boundary conditions can be expressed as:

$$r = 1, R \quad U = V = 0 \quad (5)$$

$$r = 1 \quad T = 1 \quad (6)$$

$$r = R \quad T = 0 \quad (7)$$

In the above equations Ra is the Rayleigh number given by $g\beta r_i^3(T_i - T_o)/\nu a$, Pr the Prandtl number given by ν/a , and R is the radii ratio given by r_o/r_i . A Rayleigh number based on the gap width ($r_o - r_i$), given by $Ra_L = (R - 1)^3 Ra$, is also considered in this work.

2.2 Numerical Method. The adopted numerical method is based on direct computation of the pressure p and the radial and tangential velocities U and V . The resolution of the pressure field is determined by the "Artificial Compressibility Method" (Chorin, 1967). To avoid the computational difficulties due to the incompressibility constraint, Eq. (1), a time-evolving equation for the pressure is introduced:

$$\epsilon \frac{\partial}{\partial t} p + \text{div } \mathbf{V} = 0 \quad (8)$$

with ϵ being a positive number. Clearly, the case of incom-

pressible fluids, studied in this paper, corresponds to very small values of ϵ . Keeping the time-dependent term allows acquisition of the steady solution without being concerned with nonstationary behavior. It should be noted that no transient information could be obtained from Eq. (8). Following Temam (1979), Eqs. (2), (3), and (4) are "perturbed" as follows:

$$\epsilon \frac{\partial}{\partial t} p + \text{div } \mathbf{V} = 0 \quad (9)$$

$$\frac{\partial}{\partial t} U + (\mathbf{V} \cdot \text{grad})U + \frac{\partial}{\partial r} p - Pr \Delta_r \mathbf{V} + \frac{1}{2} (\text{div } \mathbf{V})U = Ra Pr T \cos \theta \quad (10)$$

$$\frac{\partial}{\partial t} V + (\mathbf{V} \cdot \text{grad})V + \frac{\partial}{r \partial \theta} p - Pr \Delta_\theta \mathbf{V} + \frac{1}{2} (\text{div } \mathbf{V})V = -Ra Pr T \sin \theta \quad (11)$$

$$\frac{\partial}{\partial t} T + (\mathbf{V} \cdot \text{grad})T + \frac{1}{2} (\text{div } \mathbf{V})T - \Delta T = 0 \quad (12)$$

When ϵ goes to zero, the solution of this system of equations becomes identical with the solution of Eqs. (1)–(4). Admitting that the flow is symmetric about a vertical plane containing the axis of the cylinders, the angular interval of interest is $\theta \in [0, \pi]$. Thus, in addition to the boundary conditions specified by Eqs. (5)–(7), we need to specify the following symmetry boundary condition:

$$\theta = 0, \pi \quad \frac{\partial}{\partial \theta} T = 0, \quad \frac{\partial}{\partial \theta} U = 0, \quad V = 0 \quad (13)$$

It should be noted that our results were also obtained for the entire annulus ($0 \leq \theta \leq 2\pi$). However, no differences were observed between any of the results obtained for half and those obtained for the entire annulus. No boundary conditions were needed for the pressure since they are implicitly included in the modified continuity Eq. (9). The heat transfer is evaluated by a local Nusselt number defined as follows:

$$Nu(r, \theta) = \left(UT - \frac{\partial}{\partial r} T \right) r \log R \quad (14)$$

For a given value of r , integration of $Nu(r, \theta)$ leads to a per-line Nusselt number:

$$Nu_l(r) = \frac{1}{\pi} \int_0^\pi Nu(r, \theta) d\theta \quad (15)$$

and lastly the average Nusselt number is defined as:

$$\overline{Nu} = \frac{1}{R-1} \int_1^R Nu_l(r) dr \quad (16)$$

The differential equations are discretized in space and time by central differencing scheme with second-order accuracy. The energy and momentum equations are solved by an alter-

Nomenclature

a = thermal diffusivity
 g = gravitational acceleration
 l = axial length of the test cell
 N_i = number of iterations
 Nu = local Nusselt number
 \overline{Nu} = average Nusselt number
 p = pressure
 Pr = Prandtl number = ν/a
 r = radial coordinate
 r_i = inner-cylinder radius
 r_o = outer-cylinder radius
 R = radii ratio = r_o/r_i

Ra = Rayleigh number based on the inner radius = $g\beta r_i^3(T_i - T_o)/\nu a$
 Ra_L = Rayleigh number based on the gap width = $(R - 1)^3 Ra$
 t = time
 T = temperature
 T_i = temperature at inner cylinder
 T_o = temperature at outer cylinder
 U, V = velocity components in r and θ directions, respectively
 \mathbf{V} = velocity vector

z = axial coordinate
 β = thermal expansion coefficient
 Δ = Laplacian symbol
 ϵ = penalty parameter
 θ = angular coordinate
 ν = kinematic viscosity
 ψ = stream function

Subscripts

c = critical
 i = inner
 L = gap width = $r_o - r_i$
 o = outer

Table 1 A grid sensitivity analysis for $R = 1.6$, $Ra_L = 3 \times 10^3$

Grid	\overline{Nu}	Ψ_{max}
17 x 17	1.249	6.929
17 x 33	1.224	6.935
33 x 33	1.213	7.043
49 x 49	1.199	7.080

nating direction implicit scheme. The pressure is obtained by the explicit scheme:

$$p^{n+1} = p^n - \frac{\Delta t}{\epsilon} (\text{div } \mathbf{V})^{n+1} \quad (17)$$

where n refers to the number of iterations. The convergence of the pressure field leads to minimizing the $\text{div } \mathbf{V}$ term.

Several different size grids were used in this work as part of grid independence investigation: 17×17 , 17×33 , 33×33 , and 49×49 . For all our numerical runs we had ascertained that our results and specifically the resulting flow fields are independent of the grid size. Based on our grid independence study it can be stated that the location of the bifurcation point should not depend on a 49×49 (or more refined) grid structure. Steady-state conditions are assumed to have been reached when $\text{div } \mathbf{V}$ becomes less than 10^{-4} at every grid point, and when the average Nusselt number remains unchanged up to four digits. In this work, three types of initial conditions are used:

(i) temperature field corresponding to pure conduction:

$$T(r) = 1 - \log r / \log R \quad (18a)$$

with velocity and pressure fields set equal to zero. It is worth noting that using a hydrostatic pressure field would have been more efficient. However, no such solution exists for our geometry.

(ii) temperature and velocity fields obtained analytically through a perturbation solution described in the appendix. In fact, the perturbation solution, up to second order, was used as an initial condition for the temperature field to obtain a unicellular two-dimensional flow. (18b)

(iii) temperature field including a downward velocity in the upper zone of the annulus ($\theta = 0$). This case is presented later in Eq. (21). (18c)

To compare our results with previous numerical investigations, the stream function ψ is determined at each node (after satisfying the convergence criteria) by solving the Poisson equation given by

$$\Delta \psi + f = 0 \quad (19)$$

where f depends on r , U , V , and their derivatives. Although it is possible to compute ψ using U and V fields by a straightforward line integral, in this work we have opted for obtaining U and V fields by solving the Poisson equation given by Eq. (19). For numerical convenience, Eq. (19) is transformed as

$$\frac{\partial}{\partial t^*} \psi + \Delta \psi + f = 0 \quad (20)$$

where t^* is a relaxation parameter, and solved in the same way as Eqs. (10)–(12). All results in this paper are for air ($Pr = 0.7$). The calculations were performed on an IBM 3090-VF.

2.3 Preliminary Study of the Scheme. To the best of our knowledge the use of Chorin's method for this type of problem is new. A further check on the accuracy was done by obtaining our results by ADI using a stream-function vorticity formu-

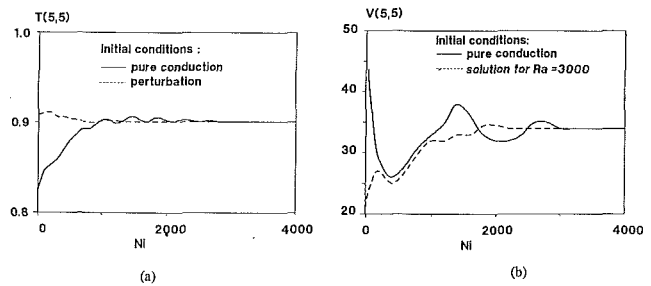


Fig. 2 Convergence characteristics for node (5, 5) for $R = 1.6$: (a) temperature, for $Ra_L = 3 \times 10^3$; (b) tangential velocity, for $Ra_L = 10^4$

lation. Other authors have used SOR methods. The results obtained by all methods (Chorin's, ADI, and SOR methods) were found to be in good agreement. To make the numerical scheme most efficient, the following observations are made:

In practice, ϵ , called the penalty parameter, should be small but not arbitrary. Cuvelier (1976) carried out a mathematical study of the stability and convergence conditions for the case of Cartesian coordinates. Here, we have found an optimized value of ϵ by trial and error. This value of ϵ accelerates the convergence toward a stationary solution. However, it should be noted that all "possible" values of ϵ we considered led exactly to the same average Nusselt numbers.

The proper grid resolution depends on parameters such as R and Ra_L . The results of a grid dependence investigation for $R = 1.6$ and $Ra_L = 3 \times 10^3$ are given in Table 1. A mesh of 17×17 nodal points leads to a value of the average Nusselt number 4 percent larger than that given by a mesh of 49×49 . To keep the convergence time to a minimum without losing accuracy, a grid of 33×33 nodes has been used for values of R less than 2. For radii ratios above 2 and for $R = 2$ with $Ra_L \geq 10^4$, a 49×49 grid distribution is used for a comparable accuracy.

3 Results and Discussion

Figure 2 illustrates the evolution of temperature and tangential velocity for a point close to the hot cylinder, using initial conditions (18a) and (18b). The dashed line curve corresponds to the perturbation solution. The solid line curve corresponds to the pure conduction solution. As it can be seen, the two types of initial condition mentioned above lead to the same steady-state results in all cases investigated in this work, even though using a perturbation solution is more efficient than the pure conduction solution. In Fig. 2(b) the results for $Ra_L = 10,000$ were presented for two initial conditions. These were:

- initial conditions were based on the pure conduction solution.
- initial conditions were based on the solutions for $Ra_L = 3000$.

For high Rayleigh numbers, intermediate solutions for lower values were used as initial conditions to conserve CPU.

3.1 Unicellular Flows. For $Pr = 0.7$, small and moderate radii ratios were investigated. In Table 2, average Nusselt numbers for different Ra_L numbers and maximum values of the stream function are shown. In the same table, results from a classical stream function-vorticity formulation obtained by Mojtabi (1979) are also shown. The present numerical results are in good agreement with those obtained by Mojtabi (1979).

Unicellular flows have been described earlier by several authors (such as Grigull and Hauf (1966) and Kuehn and Goldstein (1976)). As the Rayleigh number increases, the convective effects become more pronounced and subsequently, boundary layers develop on both boundaries. The isotherms deform, especially at the top of the annular space, and a stagnant zone appears in the lower part of the layer. Figure 3 shows the flow pattern in this case, for $R = 2$ and $Ra_L = 10^4$. Figure 4 shows

Table 2 Representative values of the average Nusselt number and the maximum value of the stream function. The number in parentheses is from Mojtabi (1979).

R	Ra_L	\overline{Nu}	Ψ_{max}
1.2	2500	1.037 (1.001)	6.388 (6.469)
	4000	1.080	10.057
	7000	1.186 (1.145)	16.896 (16.343)
$\sqrt{2}$	2500	1.104 (1.080)	6.178 (6.075)
	4000	1.208	9.478
	7000	1.412	15.275
1.6	3000	1.213	7.043
	7000	1.557	14.028
2	1000	1.063 (1.054)	2.435 (2.486)
	1700	1.151 (1.129)	4.014 (4.090)
	2500	1.264 (1.185)	5.649 (5.645)
	10^4	1.925 (1.843)	15.076 (15.113)

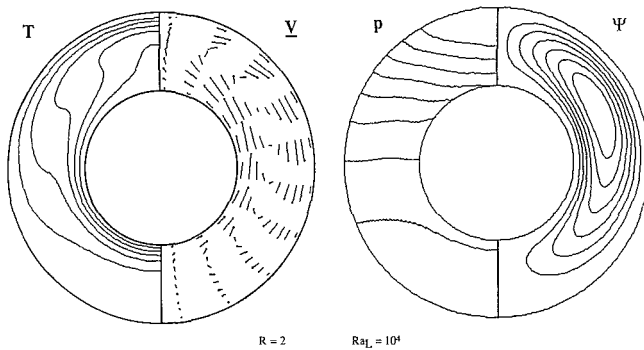


Fig. 3 Flow pattern and the temperature field for $R=2$ and $Ra_L=10^4$

local Nusselt numbers on both cylinder surfaces for $R=2$, $Ra_L=1700$ and 10^4 . In Fig. 5, dimensionless radial temperatures are compared with experimental measurements of Kuehn and Goldstein (1976) for $R=2.6$ and $Ra_L=4.7 \times 10^4$. As can be seen, a good agreement exists between the present results and those of Kuehn and Goldstein (1976).

3.2 Bicellular Flows. In this subsection, we investigate the effect of the initial conditions on the final solution. In natural convection problems, two or more types of flow may be obtained for the same value of the Rayleigh number, as has been pointed out by Fauveau et al. (1978) and Caltagirone et al. (1980) for the spherical gap, and Rao et al. (1987) for the porous annular geometry. The multiplicity of solutions occurs at high Rayleigh numbers and is related to bifurcation phenomena.

The initial conditions play a determining role in problems involving instability. The unicellular flows previously discussed are obtained by using essentially a pure conduction temperature field as initial condition. The instabilities that are expected to occur in this problem are mainly due to a temperature gradient reversal at the top of the annulus. In nature and experiments, small perturbations play an important role in affecting such metastable situations as the existence of a temperature gradient reversal. To simulate such situations, a perturbed temperature field such as:

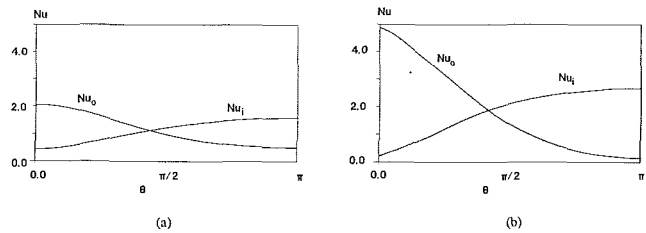


Fig. 4 Local Nusselt number distribution for unicellular flows: (a) $R=2$, $Ra_L=1700$; (b) $R=2$, $Ra_L=10^4$

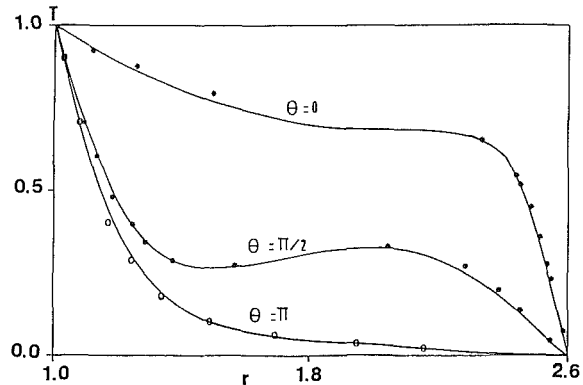


Fig. 5 Comparison of dimensionless radial temperature profiles between the present study (solid line) and the experimental results of Kuehn and Goldstein (1976) for $R=2.6$ and $Ra_L=4.7 \times 10^4$

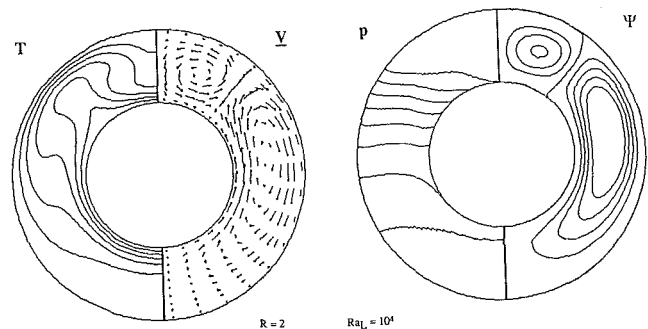


Fig. 6 Flow, temperature, and pressure fields for a bicellular flow ($R=2$, $Ra_L=10^4$)

$$T(r, \theta) = 1 - \log r / \log R + \alpha \sin(\pi \log r / \log R) \cos(\eta \theta) \quad (21)$$

where α is an amplification coefficient and η a wavenumber (integer or not) is used as an initial condition. The temperature field given by Eq. (21) was used with appropriate values of the amplification coefficient α . A systematic study to determine the optimal value of α to obtain the two-dimensional bicellular flow was not done since there was really no need to do this in our investigation. This type of perturbation makes it possible to introduce either a symmetric or a nonsymmetric temperature field with respect to the vertical axis. When Ra is more than 4000, the nonsymmetric field induces a downward velocity along the vertical axis in the upper part of the annulus (however, we consider only the half-annulus). This initial condition then leads to bicellular flows characterized by a counterrotating secondary flow appearing at the top of the annulus. That is for Ra greater than the critical Rayleigh number, Ra_c , and $\sqrt{2} \leq R \leq 2$, using the perturbation solution (given in the appendix) as the initial condition induces unicellular flows, and using the initial condition given by Eq. (21) leads to bicellular flows. A typical flow pattern is shown in Fig. 6 for $R=2$, $Ra_L=10^4$. These flows are always associated with overall heat

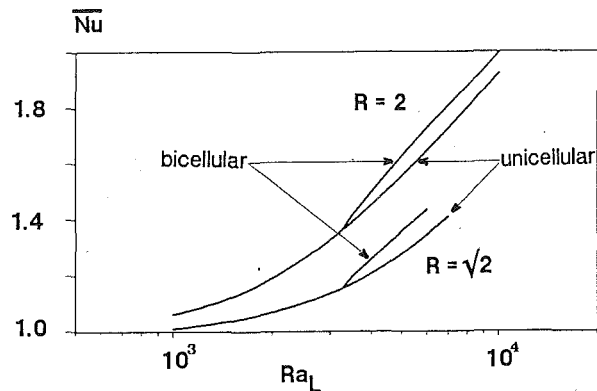


Fig. 7 Average Nusselt numbers for unicellular and bicellular flows

transfer rates higher than those of unicellular flows. This fact is best illustrated in Fig. 7. As can be seen in Fig. 8 (when compared with Fig. 4b), fundamental differences appear in local Nusselt number profiles for the same value of (R, Ra_L). In this figure, these profiles are plotted for the outer cylinder for $R=2$ and $Ra_L=10^4$. It is worth noting that a bicellular flow exhibits a new peak for the outer cylinder at the boundary between the counterrotating eddies. This peak corresponds to the augmentation of the isotherms that can be observed in Fig. 6 near $\theta=40$ deg. Thus, in this region the heat is transported almost directly from the inner to the outer cylinder. It should be noted that at any relevant Rayleigh number, we obtained the same two-dimensional bicellular flow using a numerical scheme, which was based on the ADI (stream function-vorticity) scheme.

3.3 Bifurcation Phenomenon. There exist two domains for the Rayleigh numbers based on whether the flow structure is independent or dependent on the initial conditions. It is necessary to delineate these domains carefully. As seen in Fig. 7, a critical value of Ra_L exists at which both unicellular and bicellular flows have the same overall heat transfer rate. This point where the two $\overline{Nu}(Ra_L)$ curves separate is determined using the method described by Rao et al. (1987). Converged bicellular solutions obtained by using initial condition (21) are manipulated by progressively decreasing Ra_L so that, at every step, the converged steady-state solution can be used as a new initial condition for the next step, as shown in Fig. 9.

As the Rayleigh number is decreased, the zone at the top of the annulus where the secondary flow appears becomes more and more narrow, and we finally obtain a unicellular flow identical to the one given by the initial condition (18a). The Rayleigh number at which this occurs is the critical value corresponding to the bifurcation point. In our investigation the critical Ra number was computed for three different values of the radius ratio R . These were: $2^{1/2}$, 1.6, and 2. For $R=2$ (Fig. 9), this critical Rayleigh number is near 3250 (based on a 49×49 grid system). Note that this value is slightly greater than the critical value associated with the development of periodic perturbations along the axis of the cylinders given by a linear theory of stability (Mojtabi and Caltagirone, 1979). The latter characterizes the transition from the two-dimensional unicellular flow to a three-dimensional flow. Detailed information on the physics and flow structure for the three-dimensional natural convection in a horizontal annulus can be found in the work of Vafai and Etefagh (1991). The study of Mojtabi and Caltagirone (1979) shows that in the presence of axial perturbations, the unicellular flow does not occur for $Ra > Ra_c$. However, their study does not make any predictions about the plane orthogonal to the z -axis, i.e., the $r-\theta$ plane with which we are dealing in the present investigation. The flow may or may not

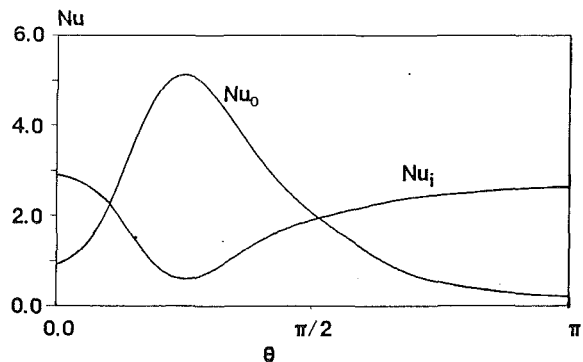


Fig. 8 Local Nusselt numbers for a bicellular flow for $R=2$ and $Ra_L=10^4$

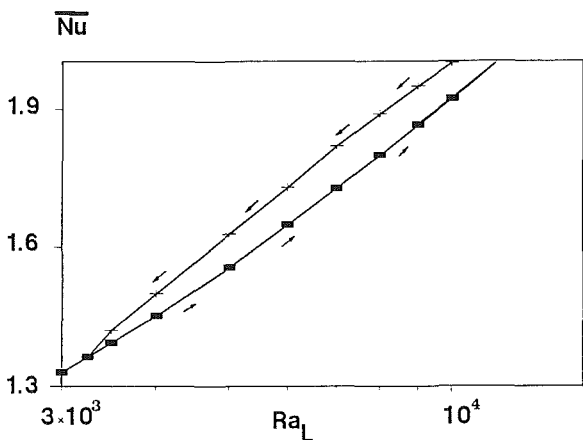


Fig. 9 Determination of the bifurcation point ($R=2$)

Table 3 A grid sensitivity analysis for the location of the bifurcation point, for $R=1.6$

Grid ($r \times \theta$)	17x17	17x33	33x33	33x49	33x65	49x49	33x81	49x65
Ra_{Lc}	---	3200	3200	2850	2750	2800	2750	2800

be three dimensional for $Ra > Ra_c$ as can be seen in the map of Powe et al. (1969). In fact, Powe et al. (1971) have experimentally detected small counterrotating cells in the upper part of the annulus for $1.2 < R < 1.7$ and a Rayleigh number that is just above the critical Rayleigh number.

As pointed out by Himasekhar and Bau (1988), it is important to investigate the effect of the truncation error, or the choice of grid points. For $R=1.6$, our calculations were repeated for the following grid systems: 17×17 , 17×33 , 33×33 , 33×49 , 33×65 , 49×49 , 49×65 , and 33×81 . Table 3 shows the computed values of the critical Rayleigh numbers. For the 17×17 grid, no multicellular flow could be obtained. The fact that a bicellular flow could be observed for a 17×33 grid shows that the number of points in the θ direction is of great importance. We note that the magnitude of Ra_c depends on the grid size. It turns out, however, that using a 49×49 or even a 33×49 grid is satisfactory and gives a good compromise between precision and CPU time. We note in passing that the computational time for determining Ra_c becomes prohibitive for refined grids. This is because when $Ra \rightarrow Ra_c^+$, the solution converges very slowly. This fact is also reported by Rao et al. (1987) and Himasekhar and Bau (1988).

Rao et al. (1985) had found that using different initial conditions such as pure conduction solution or a steady-state solution have no effect on either the unicellular or the multicellular flow patterns. For narrow annuli ($R \leq 1.2$), the unicellular and bicellular flows were obtained for two distinct intervals of Rayleigh numbers separated by a critical value. However, our

computations have clearly shown that, regardless of the initial conditions, for $\sqrt{2} \leq R \leq 2$ (which is the range of radii ratio where the bifurcation phenomenon has been studied in our work), two solutions are obtained for the same values of Ra and R , in a range of Rayleigh numbers corresponding to $Ra > Ra_c$. These two solutions persist up to a specific Rayleigh number. For example, for $R=2$, our two solutions persist up to $Ra_L = 10^4$, however, the solutions may lose their stability via Hopf bifurcation at higher Ra numbers. It should be noted that no hysteresis effects have been observed in our study. In the range of radii ratios considered ($\sqrt{2} \leq R \leq 2$), the critical Ra number, Ra_c , increases slightly with an increase in R .

4 Experimental Study

4.1 Experimental Apparatus and Procedure. The apparatus consists of an outer aluminum AU4G tube of 80 mm i.d., and an inner coaxial aluminum tube of 50 mm diameter. Therefore, the radii ratio for the experimental setup is $R=1.6$. Both tubes are 160 mm long, as that the longitudinal aspect ratio $1/r_i$ equals 6.4. Experimental observations are made through an annular plexiglass window.

The outer cylinder is cooled by an internal water circulation in the form of a helix. Cooling water is maintained isothermal by a constant temperature water bath. The inner cylinder is internally heated by an electrical resistance, which is controlled through a regulated power supply. To insure a uniform temperature distribution, this resistance is embedded in Freon. Inner and outer temperatures measured by chromel-alumel thermocouples are recorded continuously with a multichannel recorder and may also be displayed on a digital voltmeter, so that any nonuniformity in temperature on either cylinder could be depicted. Laser-Doppler anemometry is used to determine the tangential velocity field within the test cell. A SPECTRA 2000 argon laser connected to a counter processor constitutes the essential part of the setup. Data acquisition was done with a PDP-11 computer. The uncertainty in the experimental measurements was determined to be approximately 2 percent.

Steady-state conditions were usually achieved six hours after cooling water circulation and power supply are switched on. Before taking a set of measurements, incense smoke would be injected into the test section to achieve flow visualization. The data acquisition system was entirely automated so that the Doppler frequency and the velocity in mm/s were continually displayed. Further details of the experimental apparatus and procedure are available from Cheddadi (1986).

4.2 Experimental Results. Tangential velocity fields were measured in the central section of the annulus ($z=0$, Fig. 1) for three values of Ra_L number: 518, 691, and 994. Figure 10 displays the measured velocity vectors. The measured flow field

was found to be symmetric about the vertical $\theta=0$ or π plane. In fact, a variety of comparisons were performed for different angular coordinates θ and $-\theta$, which are shown in Fig. 10. These comparisons made it amply clear that the flow is indeed symmetric (Cheddadi, 1986; Cheddadi et al., 1987). Comparison with the numerical results is shown in Fig. 11 for $Ra_L = 994$. As can be seen, there is good agreement between numerical and experimental results. For this comparison, the experimental velocity at any point (r, θ) has been calculated as the average of velocities at points (r, θ) and $(r, -\theta)$. Comparison with the perturbation solution (18b) is given in Fig. A2 of the Appendix.

For completeness, other sections around $z=0$ were also investigated for an angular position of $\theta=10$ deg. In Fig. 12, in addition to the comparisons between numerical and experimental results; comparisons between experimental measurements for the same radial coordinate and different axial locations z are also presented for $r=1.12$ and $z=1.5$ cm. As can be seen in Fig. 12, no noticeable effect along the axial coordinate could be observed, except for one value, which seems to be due to experimental inaccuracies. Based on these comparisons it can be concluded that the flow for the range of Rayleigh numbers investigated in this work is two dimensional, stationary, unicellular, and can be described using the adopted numerical method. As it was not possible to determine experimental velocity fields corresponding to bicellular flows, further experiments are in order.

Our experimental investigation was limited to relatively low Ra numbers for which only unicellular flow was detected. Despite many trials, we were not able to obtain reliable data at higher Rayleigh numbers due to difficulties in maintaining uniform surface temperatures on the inner and outer cylinders at higher Rayleigh numbers. The use of laser-Doppler anemometry needs very precise experimental boundary conditions, i.e., the existence of true isothermal conditions. We have obtained flow visualizations of the stream lines at moderate and high Ra numbers. For $R=1.6$, we have found that the unicellular two-dimensional flow undergoes a Hopf bifurcation leading to a three-dimensional oscillatory motion for Ra_L of about 3500 up to 8000. At higher Rayleigh numbers ($Ra_L > 8000$) the flow obtains a three-dimensional spiral structure (Cheddadi et al., 1987). These results are reported in the map (however, in the present investigation R is used as abscissa instead of the relative gap width in the original map) of Powe et al. (1969) where the appearance of the three-dimensional oscillatory motion was not mentioned (Fig. 13). We did not obtain the two-dimensional bicellular flow, even at Rayleigh numbers that were larger than the Rayleigh number for which the bifurcation point was numerically detected. Furthermore,

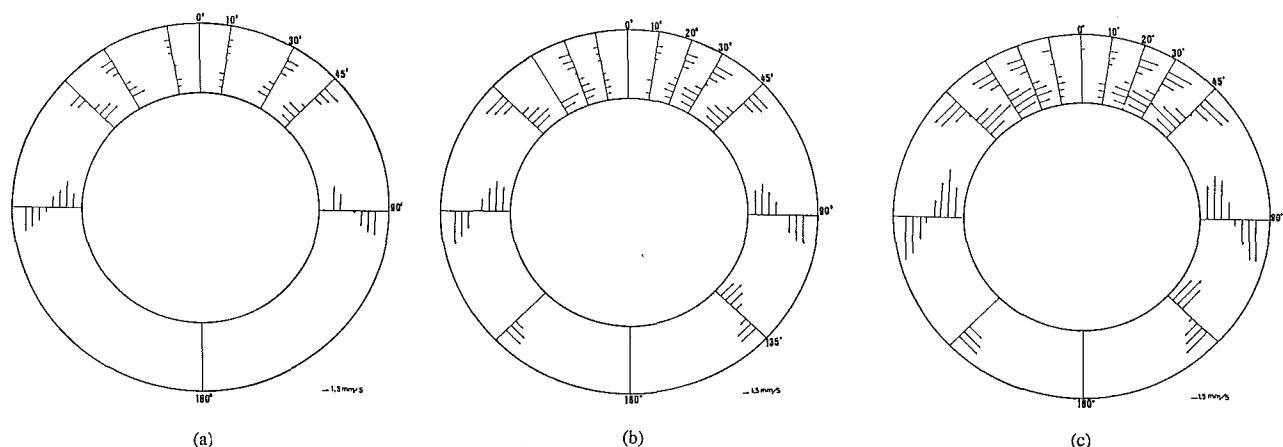


Fig. 10 Experimental tangential velocities ($R=1.6$): (a) $Ra_L = 518$; (b) $Ra_L = 691$; (c) $Ra_L = 994$

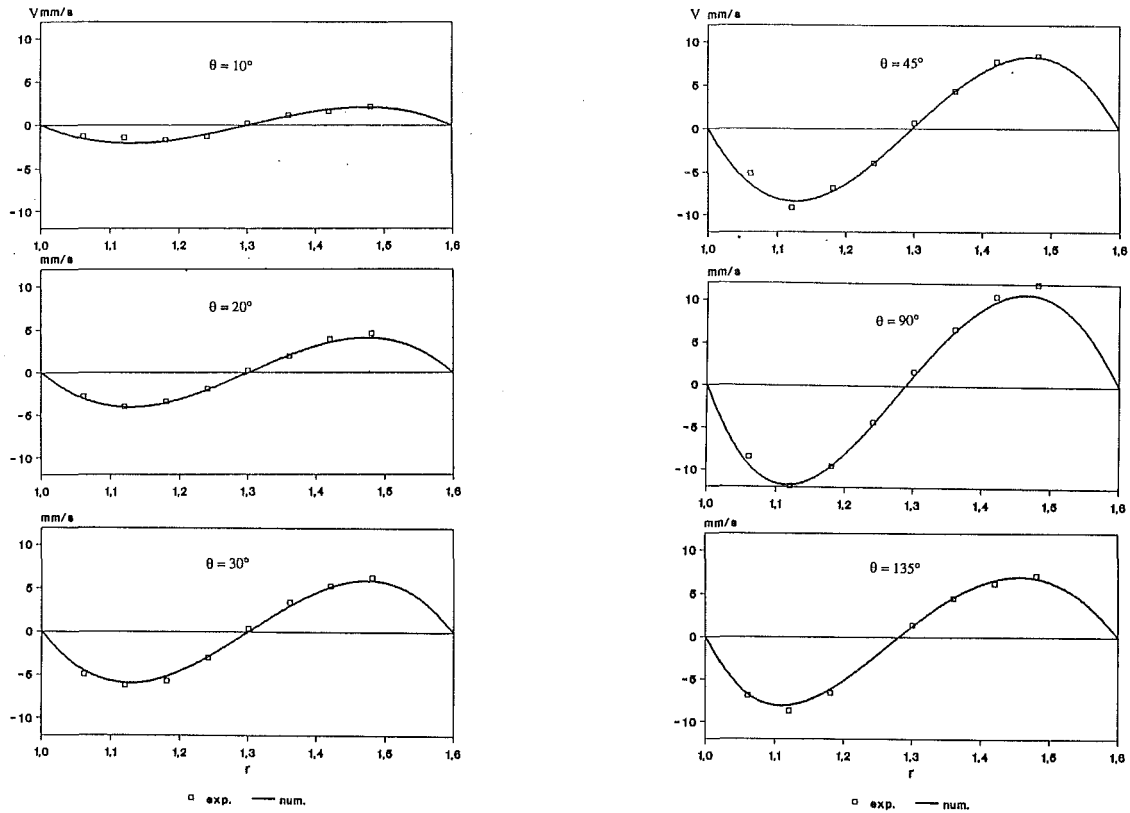


Fig. 11 Comparison of experimental and numerical tangential velocities for $R=1.6$ and $Ra_L=994$

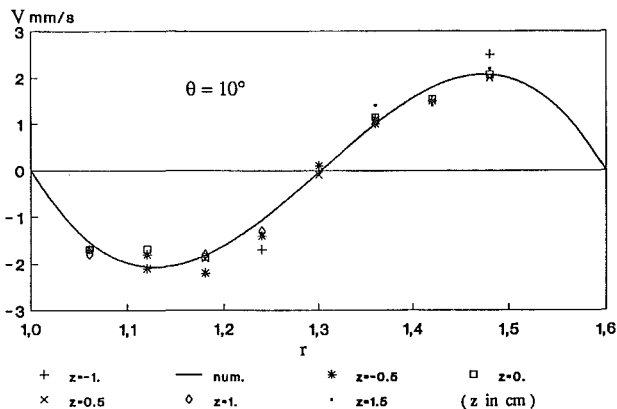


Fig. 12 Experimental tangential velocities at different axial locations corresponding to $\theta=10$ deg

in our experimental runs we had used many different initial conditions. Yet, we were unable to generate the two-dimensional bicellular flow. This is the reason for not presenting a comparison between our experimental and two-dimensional bicellular numerical results. We consistently obtained the numerical behavior that was discussed earlier (by different numerical schemes and after thorough accuracy tests); however, we were not able to generate them experimentally.

Nevertheless, an experimental investigation by Powe (1968) using air as the working fluid has revealed that a stable secondary cell forms at the top of the inner cylinder for $R=1.6$ as the Rayleigh number is increased beyond 13,000. That is, for $R=1.6$, the experimental critical Ra for the onset of the secondary cells is found to be 13,000, or in terms of the Rayleigh number based on the gap width, $Ra_L=(R-1)^3 Ra$, it translates to $Ra_L=2808$ compared to 2800 obtained from our

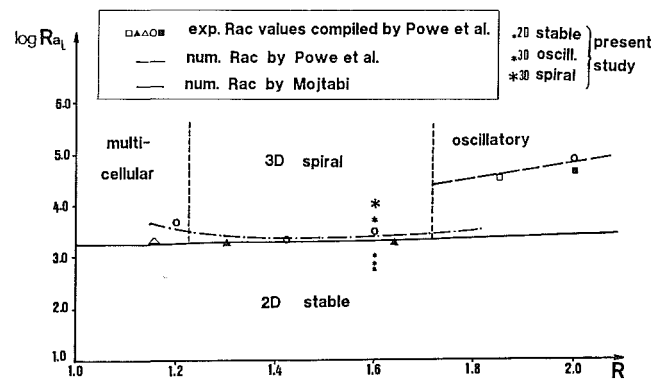


Fig. 13 Flow pattern map with respect to the results presented by Powe et al. (1969)

numerical results. This shows a very good agreement between these experiments and our numerical results.

5 Conclusions

Unicellular and bicellular free convection flows in a horizontal annulus are analyzed in this work. The bifurcation phenomena for this type of geometry are discussed and analyzed. Good agreement is observed between the numerical, experimental, and perturbation results obtained in this investigation. The numerical scheme is based on the Artificial Compressibility Method. For unicellular flows, the numerical results are in good agreement with the results obtained by the stream function-vorticity formulation.

It is demonstrated that at high Rayleigh numbers, the steady-state solution is not unique and is dependent on the proper initial conditions. Finally, the existence of a critical Ra number

related to the bifurcation phenomenon, at which both unicellular and bicellular flows have the same average Nusselt number for a fixed value of radii ratio R is established.

Acknowledgments

A grant from the CNUSC (National Computing Center of Montpellier) is gratefully acknowledged. The experimental part of this work was performed at the laboratory LEPT of the University of Bordeaux 1. The authors and in particular K. Vafai would like to express their appreciation to Professor M. Combarous.

References

- Bishop, E. H., and Carley, C. T., 1966, "Photographic Studies of Natural Convection Between Concentric Cylinders," *Heat Transfer Fluid Mech. Inst.*, pp. 63-78.
- Caltagirone, J. P., Combarous, M., and Mojtabi, A., 1980, "Natural Convection Between Concentric Spheres: Transition Towards a Multicellular Flow," *Num. Heat Transfer*, Vol. 3, pp. 107-114.
- Cheddadi, A., 1986, "Contribution à l'étude de la convection naturelle dans un espace annulaire horizontal," Thèse de Docteur-Ingénieur, E.M.I., Rabat, Morocco.
- Cheddadi, A., Caltagirone, J. P., Meyer, G., and Mojtabi, A., 1987, "Etude théorique et expérimentale de la convection naturelle dans un espace annulaire horizontal," *Comptes rendus des 3èmes Journées Internationales de Thermique*, Vol. 1, pp. 57-66, Lyon, France.
- Chorin, A. J., 1967, "A Numerical Method for Solving Incompressible Viscous Flow Problems," *J. Comp. Phys.*, Vol. 2, pp. 12-26.
- Crawford, L., and Lemlich, R., 1962, "Natural Convection in Horizontal Concentric Cylindrical Annuli," *Indus. Eng. Chem. Fundamentals*, Vol. 1, pp. 260-264.
- Cuvelier, C., 1976, "Perturbation, approximation et contrôle optimal d'un système d'équations gouverné par les équations de Navier-Stokes et celle de la chaleur," Thèse, Univ. Technique de Delft, Netherlands.
- Fauveau, J., Caltagirone, J. P., and Combarous, M., 1978, "Apparition d'écoulements thermoconvectifs multicellulaires dans une couche poreuse sphérique," *Comptes Rendus de l'Académie de Sciences*, Paris, B, Vol. 287, pp. 285-288.
- Grigull, U., and Hauf, W., 1966, "Natural Convection in Horizontal Cylindrical Annuli," *Proc. of the 3rd Int. Heat Transfer Conference*, Paper No. 60, pp. 182-195.
- Himasekhar, K., and Bau, H. H., 1988, "Two-Dimensional Bifurcation Phenomena in Thermal Convection in Horizontal, Concentric Annuli Containing Saturated Porous Media," *J. Fluid Mech.*, Vol. 187, pp. 267-300.
- Kuehn, T. H., and Goldstein, R. J., 1976, "An Experimental and Theoretical Study of Natural Convection in the Annulus Between Horizontal Concentric Cylinders," *J. Fluid Mech.*, Vol. 74, pp. 695-719.
- Mojtabi, A., 1979, "Instabilités thermoconvectives dans des espaces confinés et semi-confinés," Thèse d'Etat, Univ. Paris VI, France.
- Mojtabi, A., and Caltagirone, J. P., 1979, "Etude de la stabilité d'un écoulement de convection naturelle dans un espace annulaire horizontal," *J. de Mécanique*, Vol. 18, pp. 225-241.
- Powe, R. E., 1968, "Natural Convective Flows in Horizontal Cylindrical Annuli," M.S. Thesis, Mississippi State University.
- Powe, R. E., Carley, C. T., and Bishop, E. H., 1969, "Free Convective Flow Pattern in Cylindrical Annuli," *ASME JOURNAL OF HEAT TRANSFER*, Vol. 91, pp. 310-314.
- Powe, R. E., Carley, C. T., and Carruth, S. L., 1971, "A Numerical Solution for Natural Convection in Cylindrical Annuli," *ASME JOURNAL OF HEAT TRANSFER*, Vol. 93, pp. 210-220.
- Rao, Y. F., Miki, Y., Fukuda, K., Takata, Y., and Hasegawa, S., 1985, "Flow Patterns of Natural Convection in Horizontal Cylindrical Annuli," *Int. J. Heat Mass Transfer*, Vol. 28, pp. 705-714.
- Rao, Y. F., Fukuda, K., and Hasegawa, S., 1987, "Steady and Transient Analyses of Natural Convection in a Horizontal Porous Annulus With the Galerkin Method," *ASME JOURNAL OF HEAT TRANSFER*, Vol. 109, pp. 919-927.
- Takata, Y., Iwashige, K., Fukuda, K., and Hasegawa, S., 1984, "Three-Dimensional Natural Convection in an Inclined Cylindrical Annulus," *Int. J. Heat Mass Transfer*, Vol. 27, pp. 747-754.
- Temam, R., 1979, *Navier-Stokes Equations*, North Holland.
- Vafai, K., and Etefagh, J., 1991, "An Investigation of Transient Three Dimensional Natural Convection in a Closed Horizontal Annulus," *Int. J. Heat Mass Transfer*, Vol. 34, pp. 2555-2570.

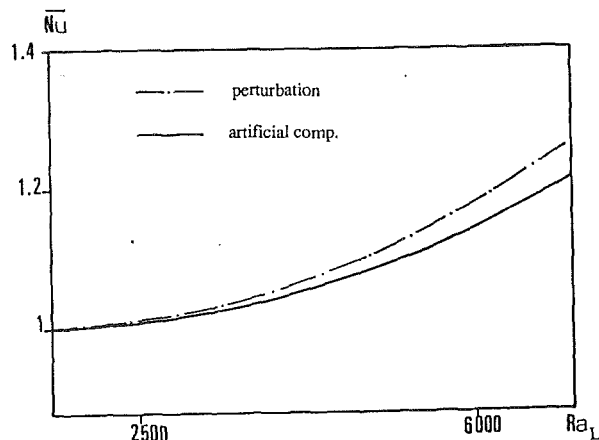


Fig. A1 Average Nusselt numbers obtained by the perturbation expansion and by the numerical scheme ($\zeta = 0.2$)

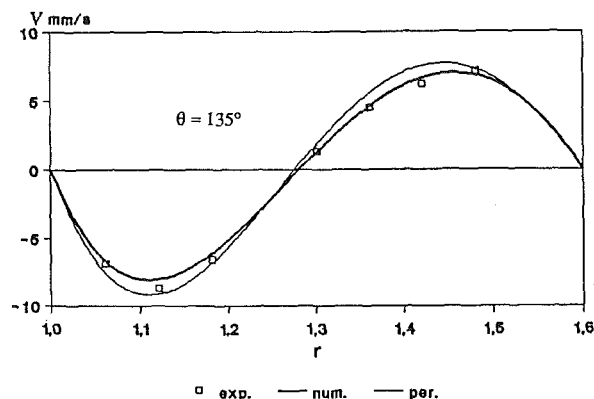


Fig. A2 Comparison among numerical, experimental, and perturbation results for the tangential velocity for $\zeta = 0.6$ and $Ra_L = 994$

APPENDIX

Here, an analytical solution is constructed by applying a regular perturbation expansion for small annular spaces. The perturbation parameter is picked as $\zeta = (r_o - r_i)/r_i$ and the radial coordinate is scaled by $(r_o - r_i)$. Expanding T and ψ in terms of ζ yields

$$T(x, \theta) = \sum_{i=0}^{\infty} \zeta^i T_i(x, \theta) \text{ and } \psi(x, \theta) = \sum_{i=0}^{\infty} \zeta^i \Psi_i(x, \theta)$$

where $x = (r - 1)/\zeta$. Introducing these expansions into the governing equations adopting the stream function-vorticity formulation, and equating coefficients of like powers in ζ , we obtain a set of linear partial differential equations.

The analytical solution of the above-found differential equations up to the second order leads to the following mathematical expression for the average Nusselt number:

$$\bar{Nu} = 1 + a Ra_L \zeta^2 + O(\zeta^3)$$

where $a = 1.37 \times 10^{-7}$. As can be seen in Fig. A1, this expression compares favorably with the numerical results. A comparison among numerical, experimental, and perturbation results for the tangential velocity is shown in Fig. A2. Again, a good agreement is observed among all three methods.

Experimental Heat Transfer Rates of Natural Convection of Molten Gallium Suppressed Under an External Magnetic Field in Either the X, Y, or Z Direction

K. Okada

H. Ozoe

Institute of Advanced Material Study,
Kyushu University,
Kasuga 816, Japan

The heat transfer rates of natural convection of molten gallium were measured under various strengths of heating rates and three coordinate directional magnetic fields. Molten gallium ($Pr = 0.024$) was filled in a cubic enclosure of $30 \text{ mm} \times 30 \text{ mm} \times 30 \text{ mm}$ whose one vertical wall was uniformly heated and an opposing wall was isothermally cooled, with otherwise insulated walls. An external magnetic field was impressed either perpendicular and horizontal to the heated wall (x direction) or in parallel and horizontal to the heated wall (y direction) of the enclosure or in a vertical direction (z direction). For the modified Grashof number, based on the heat flux, less than 4.24×10^5 and the Hartmann number less than 461, the average Nusselt numbers were measured. These results proved that our previous three-dimensional numerical analyses for an isothermal hot wall boundary were in good qualitative agreement. A much higher suppression effect is given in the x - and z -directional magnetic fields than that in the y -directional one. The measured heat transfer rates were correlated as follows:

$$\frac{Nu_B - 1}{Nu_0 - 1} = 1 - [1 + (aGr^{1/3}/Ha)^b]^{-1/n}$$

Magnetic field	a	b	n
x -directional	0.57	3.19	1.76
y -directional	4.19	2.07	1.45
z -directional	0.52	2.72	1.44

1 Introduction

Ozoe and Okada [1] carried out three-dimensional numerical analyses of natural convection of liquid metal in a cubic enclosure heated from one vertical wall and cooled from an opposing wall with otherwise thermally insulated walls. They studied the effect of the direction of the external magnetic field. The direction of the external magnetic field was in either the x , y , or z direction, as shown in Fig. 1. They reported that the natural convection and then the rate of heat transfer was strongly suppressed by the x - and z -directional external magnetic fields but was weakly suppressed by the y -directional magnetic field. They expected that the y -directional magnetic field would be the most effective to suppress the convection, since the y -directional magnetic field was perpendicular to both the vertical boundary layer flow and the horizontal flow along the upper and lower boundaries. However, this was not the case. They computed the following Lorentz force term F in the momentum equation:

$$F = J \times B \quad (1)$$

$$J = \sigma_e(E + u \times B) = \sigma_e(-\nabla\psi_e + u \times B) \quad (2)$$

$$F = \sigma_e(-\nabla\psi_e + u \times B) \times B = F_e + F_u \quad (3)$$

where J is an electric current, E an electric field intensity, B magnetic induction, σ_e electric conductivity of fluid, and ψ_e

scalar potential for an electric field, respectively. The equation of continuity for electric current allowed them to compute ψ_e . They computed each term in the Lorentz force and found that the Lorentz term in the z -directional momentum equation is large in the x -directional magnetic field but becomes very small in the y -directional magnetic field because of the cancellation of the components F_e and F_u with different signs. They found this is the reason that the y -directional magnetic suppression is very weak in comparison to that in the x - and z -directional ones. Their findings, however, need to be examined by experimental measurements. This is the primary purpose of this paper. The experimental rates of heat transfer of natural convection in an external magnetic field are also correlated in empirical equations. Some of the related previous works are discussed below.

Mori [2] studied laminar free convection in an electrically conducting fluid on a vertical plate in a transverse magnetic field and gave a series expansion solution. Sparrow and Cess [3], dealing with a similar problem, gave a series solution for Prandtl numbers 10, 0.72, and 0.02 and pointed out the significant suppression effect of a magnetic field for the free convection of liquid metals. Lykoudis [4] treated a similar problem and gave a similarity solution. He derived a parameter, known as the Lykoudis number, $Ly = 2Ha^2/Gr^{1/2}$, for an isothermal vertical wall. His computation covered from $Pr = 0.73$ to 0.01 for $Ly = 0$ to 5 .

After these pioneering works, Lykoudis and Yu [5], Michiyoshi et al. [6], Seki et al. [7], Takahashi et al. [8], and

Contributed by the Heat Transfer Division for publication in the JOURNAL OF HEAT TRANSFER. Manuscript received by the Heat Transfer Division August 28, 1990; revision received March 13, 1991. Keywords: Enclosure Flows, Liquid Metals, Natural Convection.

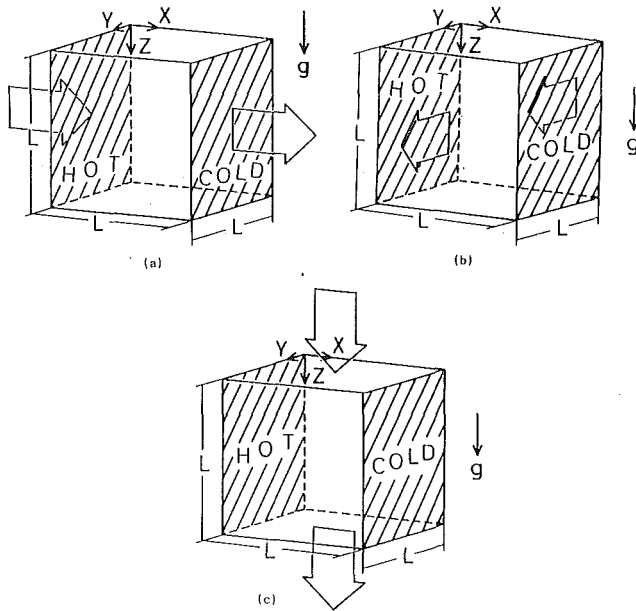


Fig. 1 Schematic of the system with the external magnetic field either in the x , y , or z directions in (a), (b), and (c), respectively

others reported on the combined effect of gravitational and magnetic fields on the natural convection of liquid metals. Extensive research efforts have been made also in the field of forced convection magnetohydrodynamics, as seen in the review by Lielausis [9] and cosmic magnetic fields as reviewed by Proctor and Weiss [10]. This subject is also closely related to various industrial processes such as semiconducting material manufacturing and continuous steel casting processes. Recent

work on the magnetic Czochralski convection for crystal growth was reviewed by Langlois [11].

On the effect of the direction of a magnetic field, Maekawa and Tanasawa [12] carried out theoretical analyses for the two-dimensional natural convection of a horizontal electrically conducting fluid layer heated from below for an arbitrary angle of the direction of the magnetic field and reported the maximum suppression for the vertical magnetic field. Their work, however, was apparently limited to a two-dimensional system heated from below.

In the present paper, the authors carried out an experimental measurement of the rate of heat transfer of natural convection of molten gallium in a cubic enclosure both without and with the external magnetic field in either the x , y , or z direction.

2 Experimental Apparatus

The experimental schematic is shown in Fig. 2. Experimental fluid was poured into a cubic enclosure (3), which was placed between two polar faces of an electromagnet (2). One vertical wall was heated uniformly through a constant power regulator and a watt meter. An opposing vertical wall of the enclosure was cooled by water from a constant temperature bath. Temperature differences between the hot and cold walls were measured by thermocouples and a strip-chart recorder (1). An electromagnet was placed in a small room of $900 \times 800 \times 1235 \text{ mm}^3$ maintained at a constant temperature approximately equal to an average of the hot and cold wall temperatures. A thermocouple hole was drilled through a side wall of the cooled copper plate up to a geometric center in which one $0.32 \text{ mm} \phi$ and three $0.05 \text{ mm} \phi$ copper-constantan thermocouples were inserted. Other junctions of thermocouples were fixed on the liquid side surface of the heated copper plate with instant glue (Aron Alpher) at the center, at 10 mm up and at 10 mm below midheight. The copper plate was coated with Teflon spray coating to avoid direct contact with molten gallium. If this

Nomenclature

A = heat transfer area, m^2	Ly = Lykoudis number = $2Ha^2/Gr^{1/2}$	Z = dimensionless coordinate = z/x_0
a_i = empirical coefficients	Nu = $Q_{net}D/(Ak\Delta\theta)$ = average Nusselt number	z = coordinate of the experimental enclosure, m
B = magnetic induction, Tesla = $V \cdot s \cdot m^{-2}$ = Weber $\cdot m^{-2}$	Nu_B = average Nusselt number in a magnetic field	$D/D\tau$ = $\partial/\partial\tau + U\partial/\partial X + V\partial/\partial Y + W\partial/\partial Z$
B_0 = uniform magnetic induction, Tesla	Nu_0 = average Nusselt number in a nonmagnetic field	∇ = $(\partial/\partial x, \partial/\partial y, \partial/\partial z)$
b_i = empirical coefficients	n = Churchill-Usagi correlation parameter	α = thermal diffusivity, m^2/s
C = specific heat of gallium, $J/(kg \cdot K)$	Pr = Prandtl number = ν/α	β = volumetric coefficient of expansion, K^{-1}
c_i = empirical coefficients	Q = heat transfer rate, W	η = coordinate of the electromagnet or dummy variable
D = distance between a cold and a hot wall, m	Q_{net} = net rate of heat transfer, W	θ = temperature, K
d_i = empirical coefficients	Ra^* = modified Rayleigh number = $g\beta D^4 Q_{net}/(A\alpha\nu k)$	θ_h = average hot wall temperature, K
E = electric field intensity, $V \cdot m^{-1}$	Ra = Rayleigh number = $g\beta(\theta_h - \theta_c)D^3/(\alpha\nu)$	θ_c = average cold wall temperature, K
e = a unit vector for an external magnetic field	T = dimensionless temperature = $0.5(2\theta - \theta_h - \theta_c)/(\theta_h - \theta_c)$	$\Delta\theta$ = $\theta_h - \theta_c$, K
e_i = empirical coefficients	U = dimensionless velocity vector	μ = viscosity, $kg/(m \cdot s)$
F = Lorentz force, N/m^3	u = velocity vector, m/s	μ_m = magnetic permeability, $H/m = m \cdot kg/(s \cdot A)^2$
f_i = empirical coefficients	X = dimensionless coordinate = x/x_0	ν = kinematic viscosity, m^2/s
Gr = Grashof number = $g\beta(\theta_h - \theta_c)D^3/\nu^2$	x = coordinate of the experimental enclosure, m	ξ = coordinate of the electromagnet or dummy variable
Gr^* = modified Grashof number = $g\beta D^4 Q_{net}/(A\nu^2 k)$	x_0 = reference coordinate = $DRa^{-1/3}$, m	ρ = density, kg/m^3
g = acceleration coefficient due to gravity, m/s^2	Y = dimensionless coordinate = y/x_0	σ_e = electric conductivity, $1/(\Omega \cdot m)$
Ha = Hartmann number = $\sqrt{\sigma_e/\mu} B_0 D$	y = coordinate of the experimental enclosure, m	τ = dimensionless time
J = electric current, $A \cdot m^{-2}$		$\Psi_e = \psi_e/(\alpha B_0)$
k = thermal conductivity, $W/(m \cdot K)$		ψ_e = scalar potential for an electric field, Weber $\cdot s^{-1} = V$
		Ω = dimensionless vorticity

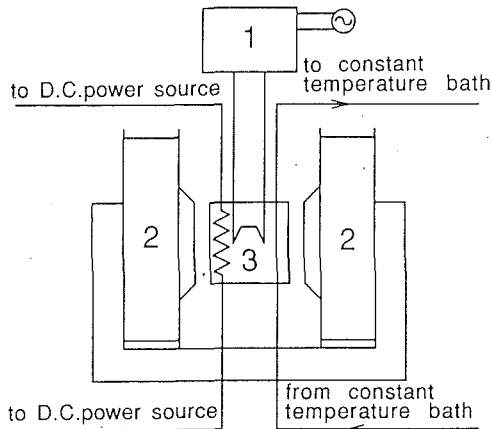


Fig. 2 Schematics of the experimental setup: (1) strip-chart recorder, (2) electromagnet, (3) convection chamber

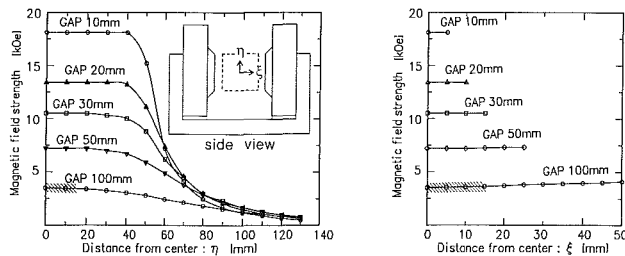


Fig. 3 (a) Uniformity of magnetic strength in η direction; (b) uniformity of magnetic strength in ξ direction; shaded area corresponds to the fluid regime

was not done, Ga extensively dissolved the copper plate whose surface became rough. The copper walls are therefore electrically adiabatic.

Heated and cooled walls were clamped firmly with bolts. This experimental enclosure was clamped into another plexiglass chamber that was fixed between the electromagnets. This enabled the experimental enclosure to be placed perpendicular or parallel to the pole faces of the electromagnet. A small laboratory jack was employed to position the enclosure centrally between the magnetic pole faces. Inside this chamber, fiberglass thermal insulation was firmly packed to minimize the influence of the variation in the room temperature where the experiment was conducted. The uniformity of the magnetic field in an experimental space could be ascertained by the reports supplied by the manufacturer of the electromagnet, as shown in Figs. 3(a) and 3(b). The actual internal length of the enclosure is 15 mm from the center and uniform strength of the magnetic field can be expected for a gap of 100 mm between the two polar end planes employed in this experiment.

Thermocouple outputs were measured with a strip-chart recorder (Yokogawa 3056-31). Other temperatures were monitored and recorded on a data logger (Takeda TR2731). These outputs were calibrated to temperature via a curve prepared before the experiment. The electromagnet was made by Electromagnet Inc. (CMD-10). Its one end pole can be moved between 0 to 100 mm from the other end plate. The strength of the magnetic field can be varied up to 0.4 Tesla for pole faces 100 mm apart. The strength of a magnetic field was monitored with a gauss meter whose sensor was attached to the pole face during the experiment.

3 Experimental Fluid

Liquid gallium was selected as the experimental fluid because its melting temperature is 302.93 K and it is easy to handle. Mercury is more common but is documented to be toxic in both liquid and vapor form. Although Ga is not known to

have such negative effects, it was handled carefully. The physical properties of Ga are summarized in the appendix.

4 Experimental Procedures

4.1 Filling the Enclosure With Ga. Molten Ga was found to be oxidized easily and quickly when it is exposed to air. Then its free surface is covered by a thin but rather viscous film layer. To avoid the oxygenation, the experimental convection enclosure was air sealed; oxygen-free air was introduced inside and then Ga was injected with a needle-less plastic syringe. Extra gas was evacuated carefully through a 1 mm ϕ hole at a corner of the convection chamber, which was then sealed.

4.2 Estimation of Heat Loss From a Convection Enclosure. The experimental room was thermally controlled to an average temperature between a hot and a cold wall of the convection enclosure to minimize the thermal loss. However, we can still not deem the heat loss as negligible. An accurate estimate of the heat loss is the most difficult part of the experiment in natural convection because the total heating amount is very small. The estimate procedure followed was originally invented by Ozoe and Churchill [13].

At the beginning, an experiment was carried out with air (known thermal conductivity) heated from above and cooled from below. The temperature differences between the hot and cold plates were measured for various rates of electrical heating Q_{total} . In the working graph, the computed rate of heat transfer by pure conduction in air and the measured heat input are both plotted versus the temperature on the hot wall. The difference between them is considered to be the heat loss, Q_{loss} , as follows:

$$Q_{loss} = Q_{total} - Ak_{air}(\theta_h - \theta_c)/D \quad (4)$$

This heat loss was approximated by a linear equation through a least-square method as follows:

$$Q_{loss} = -8.685 + 0.02831\theta_h \quad (5)$$

This heat loss to the surroundings is expected to be the same even when convection occurs inside the experimental enclosure. Net heat input to the experimental fluid is given as follows:

$$Q_{net} = Q_{total} - Q_{loss} \quad (6)$$

4.3 Determination Procedure for an Average Nusselt Number. The net heat flux can be estimated by the above method for the electrically heated system. The rate of heat transfer has been presented in a dimensionless Nusselt number, which is defined as a ratio: the total heat flux divided by the conduction heat flux. The system heated from a side wall by an electric resistance dissipates a uniform heat flux and the vertical heated wall has a temperature distribution. The opposing cold wall is kept at a uniform temperature for this system. One method of computing the reference conduction heat transfer rate is to employ the midheight temperature difference between two opposing walls. However, this scheme does not represent a real conduction rate of heat transfer. Another method is to employ an average temperature difference with an assumption that heat conduction is almost one dimensional due to the large thermal conductivity of liquid gallium. The temperature differences between a hot and a cold wall were measured at three points for the 30 mm high hot wall as described in section 2. The reference conduction heat flux can be given as follows under such temperature differences. The hot wall temperature distribution was approximated by a second-order equation of location z as follows:

$$\theta_h = az^2 + bz + c \quad (7)$$

The coefficients a , b , and c are given by the temperatures at three locations. An average conductive heat flux is given as follows:

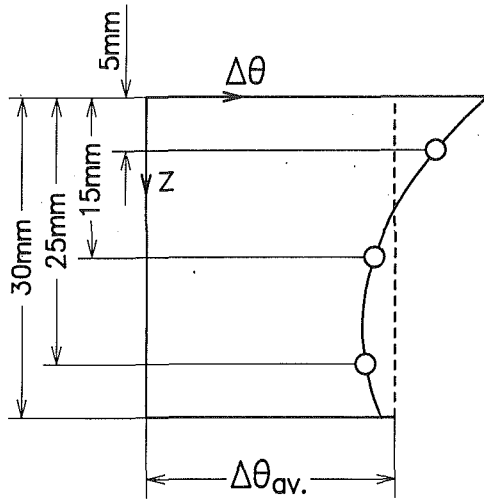


Fig. 4 Temperature differences between the hot and cooled walls at three points measured. Integrated average temperature difference $\Delta\theta_{av}$ was employed as a reference conductive rate to get an average Nusselt number.

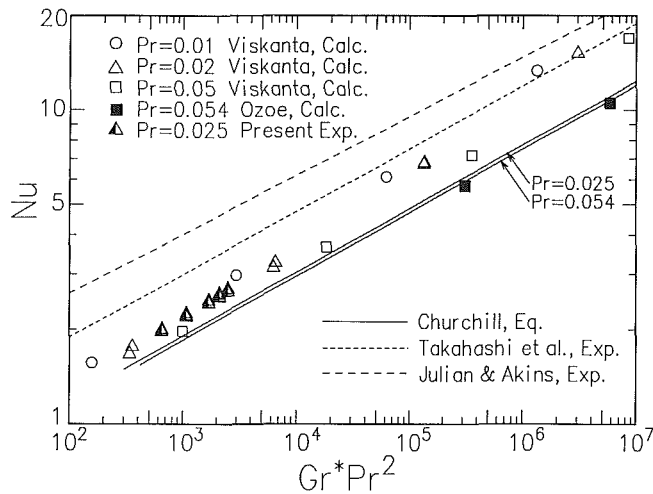


Fig. 5 Comparison of the average Nusselt number for liquid metal without a magnetic field; Viskanta is from [14]; Churchill is from [15]; Takahashi et al. is from [8]; Julian and Akins is from [16]; Ozoe and Okada is from [1]

$$Q_{cond} = k \cdot A \cdot D^{-1} \int_0^D \frac{\theta_h - \theta_c}{D} dz = kD \left(\frac{a}{3} D^2 + \frac{b}{2} D + c - \theta_c \right) \quad (8)$$

The average Nusselt numbers under various heating rates and magnetic forces were computed from the net heat flux divided by this equivalent conduction heat flux. The average temperature difference can be given as shown in Fig. 4 and the average Nusselt number is given as follows:

$$Nu = Q_{net} / Q_{cond} \quad (9)$$

The following Nusselt numbers were all computed by this empirical procedure. The following boundary conditions were in effect. The cubic enclosure was heated uniformly from one vertical wall and cooled isothermally from an opposing wall. The other four walls were thermally insulated. All boundaries were electrically insulated.

5 Experimental Results

5.1 Heat Transfer Rate of Liquid Gallium Without a Magnetic Field. The natural convection heat transfer rates were

Mag. direction	x-Mag.	y-Mag.
z= 5mm	○	●
z= 15mm	△	▲
z= 25mm	□	■
Q [W]	2.99	7.96

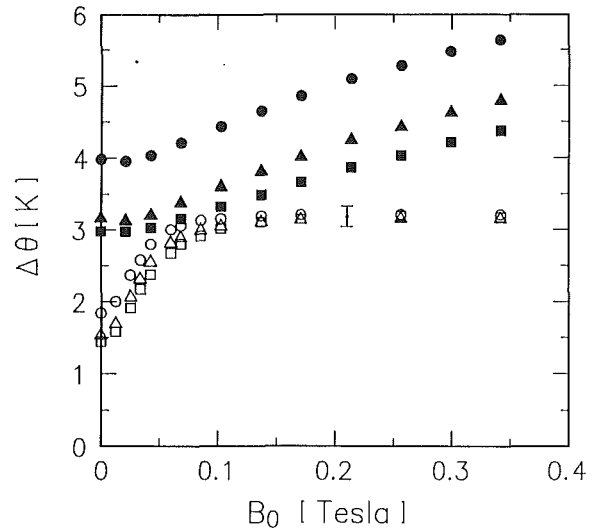


Fig. 6 Measured temperature differences between a hot wall and a cold wall center for the case when the total heat input is 2.99 W with the x-directional magnetic field (open symbols) and for the case when the total heat input is 7.96 W with the y-directional magnetic field (black symbols); the range of uncertainty is indicated at 0.2 Tesla

measured without a magnetic field prior to the magnetic experiment. The average Nusselt numbers are plotted versus $Gr \cdot Pr^2$ in Fig. 5. This abscissa has been employed for the liquid metal heat transfer. In the same graph, three-dimensional numerical analyses reported by Viskanta et al. [14] for three different Prandtl numbers and that by Ozoe and Okada [1] are also plotted for comparison. The correlation equation derived by Churchill [15] for a rectangular enclosure is indicated by a rigid line for comparison. The other experimental results for free convection found by Takahashi et al. [8] for $Pr = 0.016$ to 0.022 and by Julian and Akins [16] for $Pr = 0.022$ are also plotted, although they are for a boundary layer type flow along a single plate with a uniform heat flux. The average Nusselt numbers computed by Viskanta et al. are in excellent agreement with the present experimental rate of natural convection heat transfer in a cube for the almost same Prandtl number in a range $Gr \cdot Pr^2 = 10^2$ to 10^4 . For a much higher range of the abscissa, the data from various sources are in less agreement for the modified Grashof number 10^7 to 10^{10} . The dotted and hatched lines are for boundary layer type flow and give higher average Nusselt numbers.

5.2 The Effect of the Magnetic Field on the Rate of Heat Transfer. Prior to the experiment, the experimental room was set at about 35°C and the cooling bath temperature was controlled at $32.6^\circ\text{C} \pm 0.1^\circ\text{C}$. It took about 2 hours to satisfy these conditions. A hot wall heater was then started and the temperature difference between the hot and cold walls was measured. After two hours, the temperature difference became less than $1 \mu\text{V}$ (about 0.024°C) and an electromagnet was started by setting stepwise at specific strength.

Temperature differences between three points on a hot wall and a midheight junction in the cold wall became less than 0.1°C in about 10 to 15 min. The strength of the magnetic field was raised step by step up to 0.4 Tesla and then decreased down to zero so that hysteresis, if any, could be checked. No hysteresis was observed. Similar experiments were carried out for three directions of the magnetic field as shown in Fig. 1.

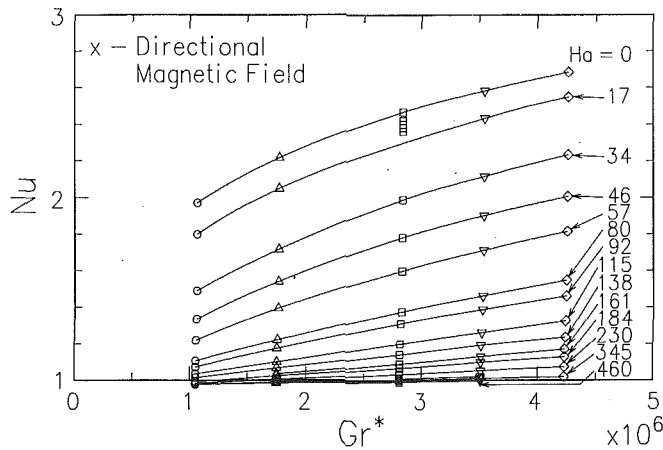


Fig. 7 The effect of the modified Grashof number and the Hartmann number on an average Nusselt number for the system in the x direction of a magnetic field

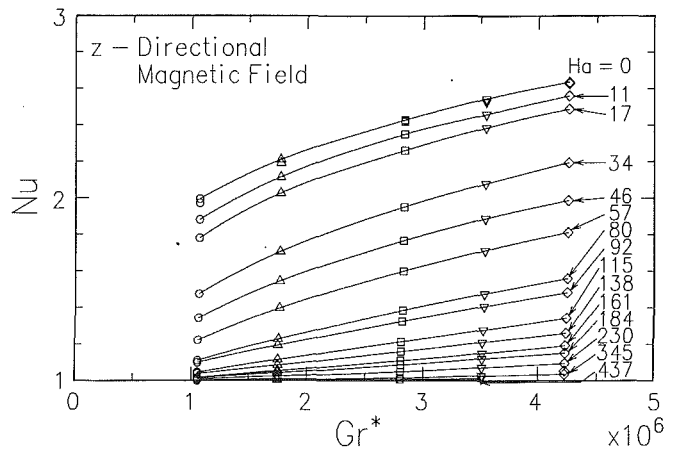


Fig. 9 The effect of the modified Grashof number and the Hartmann number on an average Nusselt number for the system in the z direction of a magnetic field

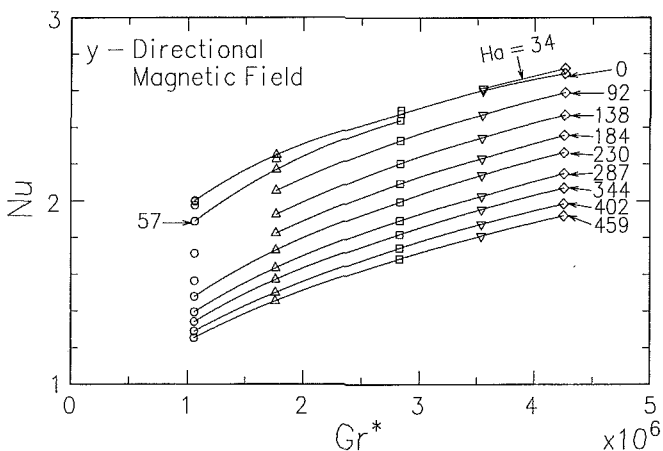


Fig. 8 The effect of the modified Grashof number and the Hartmann number on an average Nusselt number for the system in the y direction of a magnetic field

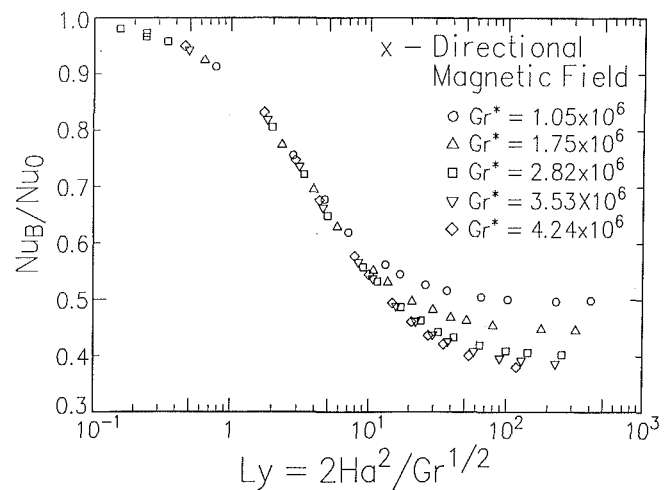


Fig. 10 Traditional plot for the rate of heat transfer of natural convection under a magnetic field

For each direction of the magnetic field, either the heating rate or the magnetic strengths were changed. Figure 6 shows steady-state temperature differences $\Delta\theta$ [K] at three thermocouple locations (at $z = 5, 15,$ and 25 mm) as a function of the strength of a magnetic induction B [Tesla] when the total heat input was 2.99 W with the x -directional magnetic field. The temperature at $z = 5$ mm on the hot wall was higher than those at $z = 15$ and 25 mm when the magnetic field was zero or weak. This is because of the convection under the uniform heat flux heating. However, the difference became less than 0.1°C when the magnetic field became 0.3 to 0.4 Tesla to indicate the conduction. Similar graphs were obtained for higher heat inputs. Under different heat inputs, the temperature differences converged nicely to the conduction data as the strength of a magnetic field attained 0.3 to 0.4 Tesla, where the conduction data were the ones obtained by heating from above in separate experiments.

When the magnetic field is in the y direction (horizontal and parallel to the heated wall), the temperature differences between the hot and cold walls are also included in Fig. 6 for total heat input of 7.96 W with black symbols. Even at 0.4 Tesla, the temperature differences between the hot and cold walls are increasing, which indicate that convection becomes weak (but not zero) due to the magnetic force. When the magnetic field was in the z direction, the general characteristics were quite similar to those seen in Fig. 6 for the x -directional magnetic field and are not shown.

These results were translated into dimensionless values of the Gr^* , Nu , and Ha numbers. They are plotted as Nu versus

Gr^* with the Hartmann number as a parameter in Fig. 7 for the x -directional magnetic field, in Fig. 8 for the y -directional magnetic field, and in Fig. 9 for the z -directional magnetic field. It was found out the suppression effect was dramatically strong in the x and z directions in comparison with the one in the y direction. For example, at $Gr^* = 4.25 \times 10^6$, $Nu = 2$ at $Ha = 46$ for the x direction of a magnetic field. On the other hand at $Gr^* = 4.25 \times 10^6$, $Nu = 2$ was attained at $Ha = 402$ for the y -directional magnetic field. This means that one order of magnitude larger magnetic induction in the y direction is required to have the same effect of suppression in comparison to that in the x or z direction.

5.3 Preparation of the Graphic Presentation of the Heat Transfer Rate in an External Magnetic Field. The Lykoudis number Ly has been traditionally employed to correlate the heat transfer rate of free convection of liquid metal in an external magnetic field. The effect of the magnetic field on the rate of heat transfer has been represented as the Nusselt number in a magnetic field, Nu_B , divided by that in a non-magnetic field, Nu_0 , and the data of the measured ratio Nu_B/Nu_0 are plotted versus Lykoudis number Ly in Fig. 10. The parameter is a modified Grashof number. As the Lykoudis number decreases, the effect of the magnetic force is also decreased and the ratio of the Nusselt numbers converges to unity. On the other hand, as the Lykoudis number is increased, the ratio of the Nusselt numbers approaches $1/Nu_0$ as a function of the modified Grashof number. This type of plotting is

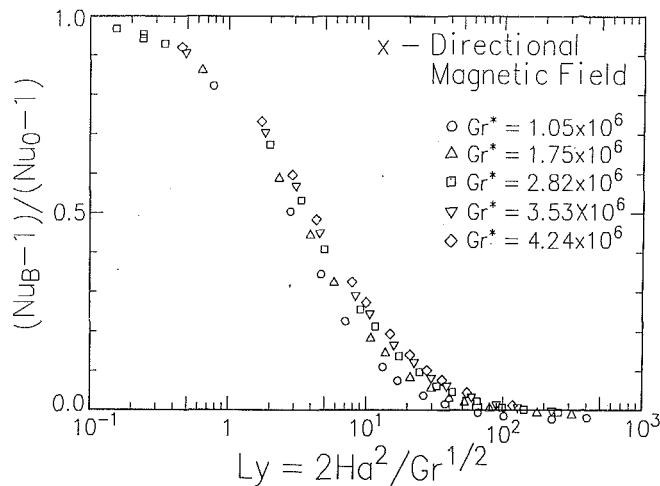


Fig. 11 Newly normalized ordinate for the rate of heat transfer versus the traditional Lykoudis number

a traditional method and similar graphs can be found from Takahashi et al. [8].

On the other hand, Ozoe and Maruo [17] previously carried out two-dimensional computations for magnetic and gravitational natural convection of liquid metal in a square enclosure heated from one vertical wall and cooled from an opposing vertical wall. They plotted the computed results in a graph $(Nu_B - 1)/(Nu_0 - 1)$ versus $Ha/Ra^{1/3}$. This provided a single correlation curve for different values in the Rayleigh numbers. Concerning the ordinate, the ratio $(Nu_B - 1)/(Nu_0 - 1)$ was employed in place of the traditional ratio Nu_B/Nu_0 because of the above reason. In the extreme case of zero Hartmann (or Lykoudis) number, $(Nu_B - 1)/(Nu_0 - 1)$ converges to unity because $Nu_B = Nu_0$. At another extreme of the infinite Hartmann number, Nu_B converges to unity and then $(Nu_B - 1)/(Nu_0 - 1)$ to zero irrespective of the Rayleigh (or Grashof) number. This ratio $(Nu_B - 1)/(Nu_0 - 1)$ apparently provides much better characteristics than the traditional Nu_B/Nu_0 .

The experimental data are plotted for $(Nu_B - 1)/(Nu_0 - 1)$ versus the Lykoudis number Ly as shown in Fig. 11. This graph provides almost a single data group for different values in the modified Grashof number. However, there is still some scatter for the Lykoudis number from 1 to 100. The original Lykoudis number was found to provide a similarity solution for the free convection along a vertical heated wall with a horizontal magnetic field, which varies with the location in a vertical direction. The Lykoudis number has been employed to correlate the heat transfer rate for boundary layer type free convection of liquid metal in a magnetic field. However, it may not be the only parameter to correlate the heat transfer rate for natural convection of liquid metal in an enclosure that produces two- and three-dimensional flow modes.

Ozoe and Maruo [17] derived $Ha/Ra^{1/3}$ in the de-dimensionalization process of the vorticity equation including a Lorentz term, and Ozoe and Okada [1] again employed it for the three-dimensional magnetic natural convection in a cubic enclosure as follows:

$$\frac{D\Omega}{Dt} = (\Omega \cdot \nabla)U + Pr \nabla^2 \Omega + Pr(-\partial T/\partial Y, \partial T/\partial X, 0)^T + Ha^2 Ra^{-2/3} Pr \{ -\nabla \times (\nabla \Psi_e \times e) + \nabla \times [(U \times e) \times e] \} \quad (10)$$

where e is a unit vector for an external magnetic field in either the x -, y -, or z -directional coordinate. The Lorentz term has a coefficient $Ha^2 Pr Ra^{-2/3} = (Ha/Gr^{1/3})^2 Pr^{1/3}$. Following their correlation, we replotted the same data for $Ha/Gr^{1/3}$ with the translation $Gr^* = Gr \cdot Nu$ as shown in Fig. 12. It gives a much better correlation than Fig. 11.

Lykoudis [4] derived the Lykoudis number $2Ha^2/Gr^{1/2}$ and

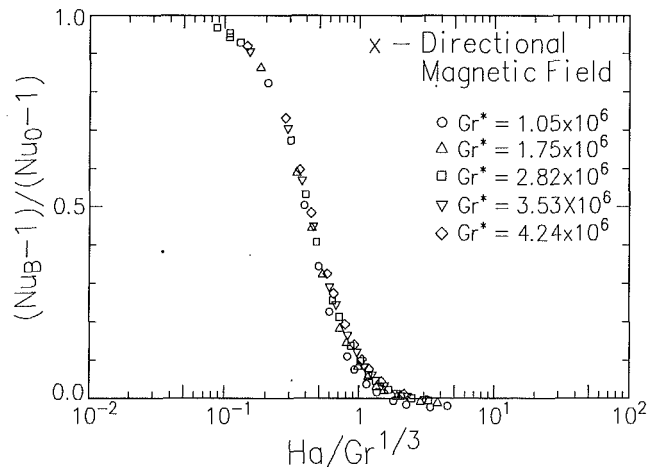


Fig. 12 More consistent data correlation ordinate and abscissa for the magnetic natural convection

Mag. Direction	x-Mag.	y-Mag.	z-Mag.
Present Exp.	omitted	△	□
3D Calc.	●	▲	■
Correlation Eq.	—	—	---

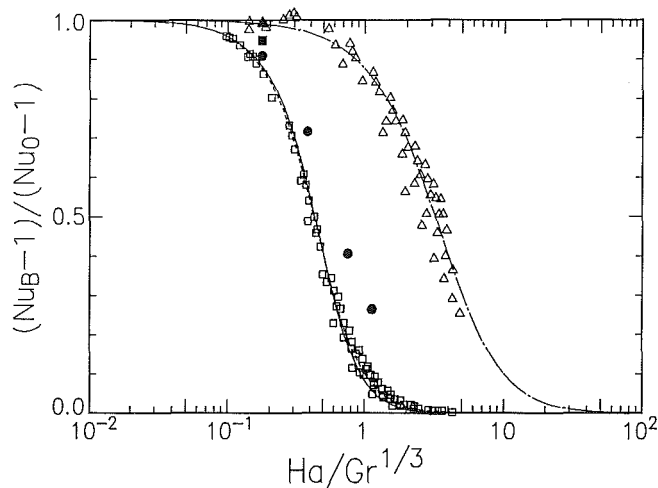


Fig. 13 Comparison of the present experimental results with the theoretical results by Ozoe and Okada [1]; lines are those correlated by Churchill and Usagi plot [18]

mentioned that it represents the ratio of the ponderomotive force over the viscous force. In the following, we employed $Ha/Gr^{1/3}$ since it is simpler than $Ha^2/Gr^{2/3}$, although Ha^2 has a physical meaning as mentioned by Lykoudis.

5.4 Derivation of Correlation Equations for the Rate of Heat Transfer in Both a Gravitational and a Magnetic Field.

The heat transfer rates in the y - or z -directional magnetic field at various modified Grashof numbers are plotted in Fig. 13. The data group for the x -directional magnetic field almost coincides with that for the z -directional one and therefore is omitted. The black circles show the rates computed by Ozoe and Okada [1] in the three-dimensional numerical analyses and they agreed well with the experimental result. Especially the least magnetic suppression of the y -directional field was proved by much larger rates represented by white triangles. The black triangles show the rates obtained by three-dimensional computations and also agreed well with the experimental ones.

Churchill and Usagi [18] proposed to derive a compact empirical equation for such data as seen herein, using two limiting

cases and selecting a single parameter n to fit the data. Let $(Nu_B - 1)/(Nu_0 - 1)$ be represented by ξ and $Ha/Gr^{1/3}$ by η . The present system does have the limiting characteristics seen in Fig. 13 as follows:

$$\begin{aligned} \text{as } \eta \rightarrow 0, \quad \xi &\rightarrow 1 \\ \text{as } \eta \rightarrow \infty, \quad \xi &\rightarrow 0. \end{aligned}$$

We presume the following form to satisfy these conditions:

$$\left(\frac{1}{1-\xi}\right)^n = 1^n + \left\{ \left(\frac{\eta_A}{\eta}\right)^\gamma \right\}^n \quad (11)$$

When $(Nu_0 - Nu_B)/(Nu_0 - 1) = 1 - \xi$ is plotted versus $Ha/Gr^{1/3} = \eta$ on a logarithmic graph, the gradient gives an unknown index γ and any data point gives the cross-sectional point η_A . Another exponent n is determined to fit the data well on the next equation on the graph.

$$\frac{1}{1-\xi} = \left[1 + \left\{ \left(\frac{\eta_A}{\eta}\right)^\gamma \right\}^n \right]^{1/n} \quad (12)$$

This type of equation includes two extreme cases of variables of η at 0 and infinity as well as the intermediate range in such a simple form. In this way, the unknown parameters were determined for the x -directional data group and the following equation was obtained. It is indicated by a rigid line in the graph to fit the data group excellently.

$$\frac{Nu_B - 1}{Nu_0 - 1} = 1 - \left[1 + \left(\frac{0.57 Gr^{1/3}}{Ha} \right)^{3.19} \right]^{-1/1.76} \quad (13)$$

The same method gives the one for the y -directional magnetic field.

$$\frac{Nu_B - 1}{Nu_0 - 1} = 1 - \left[1 + \left(\frac{4.19 Gr^{1/3}}{Ha} \right)^{2.07} \right]^{-1/1.45} \quad (14)$$

For the z -directional magnetic field,

$$\frac{Nu_B - 1}{Nu_0 - 1} = 1 - \left[1 + \left(\frac{0.52 Gr^{1/3}}{Ha} \right)^{2.72} \right]^{-1/1.44} \quad (15)$$

6 Conclusions

The effect of the external magnetic field was studied for the natural convection of liquid Ga in a cubic box heated from one vertical wall and cooled from an opposing wall. The rate of heat transfer was measured and correlated as a function of $Ha/Gr^{1/3}$ for the direction of a magnetic field either perpendicular to the vertical hot wall (x direction) or parallel and horizontal to the hot wall (y direction) or vertical (z direction). The x - or z -directional magnetic field was almost 10 times as effective in suppressing the rate of heat transfer as that in the y direction. The strong suppression effects in the x - and z -directional magnetic fields proved the previous prediction in three-dimensional numerical analyses by Ozoe and Okada. The rates of heat transfer were correlated with the Churchill and Usagi correlation.

Acknowledgments

The authors gratefully acknowledge the advice provided by the reviewers in preparing the revised version of this manuscript.

References

- Ozoe, H., and Okada, K., "The Effect of the Direction of the External Magnetic Field on the Three-Dimensional Natural Convection in a Cubical Enclosure," *Int. J. Heat Mass Transfer*, Vol. 32, No. 10, 1989, pp. 1939-1954.
- Mori, Y., "On a Laminar Free Convection Flow and Heat Transfer of Electrically Conducting Fluid on a Vertical Plate in the Presence of a Transverse Magnetic Field," *Trans. Japan Soc. Aero. Space Science*, Vol. 2, 1959, pp. 22-26.
- Sparrow, E. M., and Cess, R. D., "The Effect of a Magnetic Field on Free Convection Heat Transfer," *Int. J. Heat Mass Transfer*, Vol. 3, 1961, pp. 267-274.

4 Lykoudis, P. S., "Natural Convection of an Electrically Conducting Fluid in the Presence of a Magnetic Field," *Int. J. Heat Mass Transfer*, Vol. 5, 1962, pp. 23-34.

5 Lykoudis, P. S., and Yu, C. P., "The Influence of Electrostrictive Forces in Natural Thermal Convection," *Int. J. Heat Mass Transfer*, Vol. 6, 1963, pp. 853-862.

6 Michiyoshi, I., Takahashi, O., and Serizawa, A., "Natural Convection Heat Transfer From a Horizontal Cylinder to Mercury Under Magnetic Field," *Int. J. Heat Mass Transfer*, Vol. 19, 1976, pp. 1021-1029.

7 Seki, M., Kawamura, H., and Sanokawa, K., "Natural Convection of Mercury in a Magnetic Field Parallel to the Gravity," *ASME JOURNAL OF HEAT TRANSFER*, Vol. 101, 1979, pp. 227-232.

8 Takahashi, O., Nagase, N., Michiyoshi, I., and Takenaka, N., "Natural Convection Heat Transfer From a Vertical Cylindrical Heater to Liquid Metals Under Horizontal Magnetic Field," *8th Int. Heat Transfer Conference*, San Francisco, CA, Vol. 3, 1986, pp. 1317-1322.

9 Lielausis, O., "Liquid-Metal Magnetohydrodynamics," *Atomic Energy Review*, Vol. 13, No. 3, 1975, pp. 527-581.

10 Proctor, M. R. E., and Weiss, N. O., "Magnetocovection," *Rep. Prog. Phys.*, Vol. 45, 1982, pp. 1317-1379.

11 Langlois, W. E., "Computer Simulation of Czochralski Melt Convection in a Magnetic Field," *J. Cryst. Growth*, Vol. 70, 1984, pp. 73-77.

12 Maekawa, T., and Tanasawa, I., *22nd Nat. Heat Transf. Symp. (Japan)*, c303, 1985, pp. 410-412.

13 Ozoe, H., and Churchill, S. W., "Hydrodynamic Stability and Natural Convection in Newtonian and Non-Newtonian Fluids Heated From Below," *AICHE Symp. Series, Heat Transfer*, Vol. 69, No. 131, 1973, pp. 126-133.

14 Viskanta, R., Kim, D. M., and Gau, C., "Three-Dimensional Natural Convection Heat Transfer of Liquid Metal in a Cavity," *Int. J. Heat Mass Transfer*, Vol. 29, No. 3, 1986, pp. 475-485.

15 Churchill, S. W., *Heat Exchanger Design Handbook*, X. X. Schlunder, ed., sec. 2.5.8, Hemisphere, 1983.

16 Julian, D. V., and Akins, R. G., "Experimental Investigation of Natural Convection Heat Transfer to Mercury," *Ind. & Eng. Chem. Fundamentals*, Vol. 8, No. 4, 1969, pp. 641-646.

17 Ozoe, H., and Maruo, E., "Magnetic and Gravitational Natural Convection of Melted Silicon: Two-Dimensional Numerical Computation for the Rate of Heat Transfer," *JSME International Journal*, Vol. 30, No. 263, 1987, pp. 774-784.

18 Churchill, S. W., and Usagi, R., "A General Expression for the Correlation of Rates of Transfer and Other Phenomena," *AICHE J.*, Vol. 18, No. 6, 1972, pp. 1121-1128.

19 Spells, K. E., "The Determination of the Viscosity of Liquid Gallium Over an Extended Range of Temperature," *Proc. Phys. Soc.*, Vol. 48, 1936, pp. 299-311.

20 Cubbery, W. H., *Metals Handbook II*, 9th ed., ASM, 1979, pp. 735-737.

21 Moffat, R. J., "Using Uncertainty Analysis in the Planning of an Experiment," *ASME Journal of Fluids Engineering*, Vol. 107, 1985, pp. 173-178.

APPENDIX A

Physical Properties of Ga

(a) **Density.** K. E. Spells [19] reported measured values, which were correlated by a least-square approximation as follows:

$$\begin{aligned} \rho &= a_0 + a_1\theta \quad [\text{kg/m}^3] \\ a_0 &= 6330 \quad [\text{kg/m}^3] \\ a_1 &= -0.7717 \quad [\text{kg}/(\text{m}^3\text{K})] \end{aligned} \quad (A1)$$

for $303.65 \text{ K} \leq \theta \leq 375.15 \text{ K}$.

(b) **Viscosity.** Measured values by K. E. Spells [19] are correlated by a least-square approximation as follows:

$$\begin{aligned} \mu &= b_0 + b_1\theta + b_2\theta^2 \quad [\text{kg}/(\text{m}\cdot\text{s})] \\ b_0 &= 1.207 \times 10^{-2} \quad [\text{kg}/(\text{m}\cdot\text{s})] \\ b_1 &= -5.754 \times 10^{-5} \quad [\text{kg}/(\text{m}\cdot\text{s}\cdot\text{K})] \\ b_2 &= 7.981 \times 10^{-8} \quad [\text{kg}/(\text{m}\cdot\text{s}\cdot\text{K}^2)] \end{aligned} \quad (A2)$$

for $303.65 \text{ K} \leq \theta \leq 323.15 \text{ K}$.

(c) **Specific Heat.** According to the *Metals Handbook II* [20],

$$C = 397.6 \quad [\text{J}/(\text{kg}\cdot\text{K})] \quad (A3)$$

from 285.65 K to 473.15 K .

(d) **Thermal Conductivity.** According to the *Metals Handbook II* [20],

$$k = 28.68, \quad [\text{W}/(\text{m}\cdot\text{K})]$$

$$34.04,$$

$$\text{or } 38.31 \quad (\text{A4})$$

at 350.15 K. Since these values differ substantially from one another, the thermal conductivity of Ga was measured directly in our convection enclosure. The measurement of thermal conductivity should be carried out for a shallow fluid layer. However, the thermal conductivity of liquid Ga is about 1300 times larger than that of air and 42 times that of plexiglass, and we presumed the heat flux could be measured accurately by the method described in section 4.2. The thermal conductivity of Ga can be described as follows:

$$k_{\text{Ga}} = -7.448 + 0.1256\theta \quad [\text{W}/(\text{m}\cdot\text{K})] \quad (\text{A5})$$

for $306.15 \text{ K} \leq \theta \leq 312.15 \text{ K}$.

(e) **Volumetric Coefficient of Thermal Expansion.** The previous correlation equation for density was inserted into the following definition for a volumetric coefficient of thermal expansion:

$$\beta = -\frac{\partial \rho / \partial \theta}{\rho} = -\frac{a_1}{(a_0 + a_1 \theta)} \quad (\text{A6})$$

Since experimental data are mostly between 303.15 and 326.15 K, this equation can be employed for this temperature range.

(f) **Electric Conductivity.** According to the *Metals Handbook II* [20], the conductivity is

$$\sigma = 3.85 \times 10^6 \text{ [1}/(\Omega\cdot\text{m})]$$

$$\text{at } \theta = 313.15 \text{ K.} \quad (\text{A7})$$

(g) **Magnetic Permeability.** The permeability is almost equivalent to that in a vacuum and

$$\mu_m = 4\pi \times 10^{-7} \text{ [H/m]} = [\text{m}\cdot\text{kg}/(\text{s}\cdot\text{A})^2]. \quad (\text{A8})$$

(h) **Melting Point.** Melting point is 302.93 K [20].

APPENDIX B

Uncertainty Analysis

There are extensive numbers of parameters in the present experiments. Following is the list of estimated error range for various parameters. Then, following Moffat [21], the uncertainty analysis was applied for the dimensionless parameters such as the Grashof, Prandtl, Hartmann, and Nusselt numbers. These numbers are expressed as a product of terms and the relative uncertainty can be given as follows. If experimental result is

$$R = x_1^a x_2^b x_3^c \cdots x_N^N, \quad (\text{B1})$$

then

$$\frac{\delta R}{R} = \left\{ \left(a \frac{\delta x_1}{x_1} \right)^2 + \left(b \frac{\delta x_2}{x_2} \right)^2 + \cdots + \left(N \frac{\delta x_N}{x_N} \right)^2 \right\}^{1/2}. \quad (\text{B2})$$

The following are the possible error ranges for both measured values and the correlated physical properties as listed in Appendix A.

1 Temperature was measured with Cu-constantan thermocouples connected to a data logger. Estimated accuracies are as follows:

(a) Accuracy = \pm [0.03 percent of temperature readings + 0.3] $^\circ\text{C}$.

(b) Temperature coefficient for accuracy = \pm [0.0015 percent of temperature reading + 0.0010] $^\circ\text{C}/^\circ\text{C}$.

(c) Accuracy for internal compensation for the standard point = $\pm 0.5^\circ\text{C}$.

Table B1 Relative errors (percent) at $Q = 11.95 \text{ W}$

Exp. No.	Nu	Ha	Gr*	Ha/Gr ^{1/3}
1	5.70	—	12.23	—
2	5.49	18.7	12.18	19.25
3	5.11	10.7	12.10	11.57
4	4.86	8.75	12.06	9.77
5	4.50	7.60	11.98	8.72
6	4.07	6.33	11.89	7.59
7	3.97	5.95	11.88	7.27
8	3.72	5.42	11.83	6.82
9	3.57	9.40	11.81	10.26
10	3.47	8.48	11.80	9.42
11	3.41	7.80	11.79	8.81
12	3.36	6.86	11.80	7.99
13	3.34	5.66	11.80	6.98

(d) Temperature coefficient for internal compensation = $\pm 0.004^\circ\text{C}/^\circ\text{C}$.

Experimental room temperature was controlled so that the maximum deviation is less than 2°C . The temperature was read from 33.5 to 39.4 $^\circ\text{C}$. Then the temperature uncertainty is $\delta\theta = \pm(0.033 \text{ percent of temperature reading} + 0.81) = \pm 0.82^\circ\text{C}$.

2 Temperature difference between a hot wall and a cold wall, $\Delta\theta$. Possible errors are from

(a) Strip-chart recorder itself as described in section 1, and reading error from a recorder-chart paper = $\pm(0.05 \text{ percent of temperature reading} + 0.048)^\circ\text{C}$.

(b) Empirical equation for thermocouple output = $\pm 0.077^\circ\text{C}$.

(c) Reference temperature inaccuracy employed for a recorder output = $\pm 0.018^\circ\text{C}$. In total, $\delta\Delta\theta = \pm(0.05 \text{ percent of temperature difference reading} + 0.143)^\circ\text{C} = \pm 0.149^\circ\text{C}$.

3 Length of a cubic enclosure, $\delta D = \pm 2.5 \times 10^{-4} \text{ m}$.

4 Heat flux measurement suffers from the following errors:

(a) Watt-meter output = $\pm 0.048 \text{ W}$.

(b) Reading error = $\pm 0.02 \text{ W}$.

(c) Heat loss correlation = $\pm 0.023 \text{ W}$.

(d) Fluctuation error in the heat loss equation = $\pm 0.005 \text{ W}$. In total, $\delta Q = \pm 0.096 \text{ W}$.

5 Magnetic induction B [Tesla]. The inaccuracy is ± 2 percent of the full-scale range and reading error and the nonuniformity of the magnetic field causes the following errors. $\delta B = [(-2.1 \text{ percent to } 4.3 \text{ percent}) \text{ of readings } \pm (21-210) \times 10^{-4}] \text{ [Tesla]}$.

6 Density, $\delta\rho = \pm 2.61 \text{ kg/m}^3$.

7 Viscosity, $\delta\mu = \pm 1.07 \times 10^{-4} \text{ kg}/(\text{m}\cdot\text{s})$.

8 Thermal conductivity of gallium.

This was measured and correlated as described in Appendix A. The inaccuracies increase for the lower temperature difference and they are as follows:

$\theta_{av} \text{ K}$	$\delta k, \text{ W}/(\text{m}\cdot\text{K})$
307.67	± 2.57
308.80	± 1.46
310.39	± 1.11
311.41	± 0.97
312.08	± 0.91

9 Volumetric coefficient of expansion.

$$\delta\beta = \pm 5.4 \times 10^{-8} \text{ 1/K}$$

The above inaccuracies are reflected in the dimensionless values as follows. The relative errors (percent) of the selected dimensionless numbers for each data are listed in Table B1, for example, at the total heat input $Q = 11.95 \text{ W}$. Similar errors were also computed for other heat inputs but not listed because of the space limitation.

Three-Dimensional Natural Convection From Vertical Heated Plates With Adjoining Cool Surfaces

B. W. Webb

Associate Professor,
Department of Mechanical Engineering,
Brigham Young University,
Provo, UT 84602
Assoc. Mem. ASME

T. L. Bergman

Associate Professor,
Department of Mechanical Engineering,
The University of Texas at Austin,
Austin, TX 78712
Assoc. Mem. ASME

Natural convection in an enclosure with a uniform heat flux on two vertical surfaces and constant temperature at the adjoining walls has been investigated both experimentally and theoretically. The thermal boundary conditions and enclosure geometry render the buoyancy-induced flow and heat transfer inherently three dimensional. The experimental measurements include temperature distributions of the isoflux walls obtained using an infrared thermal imaging technique, while the three-dimensional equations governing conservation of mass, momentum, and energy were solved using a control volume-based finite difference scheme. Measurements and predictions are in good agreement and the model predictions reveal strongly three-dimensional flow in the enclosure, as well as high local heat transfer rates at the edges of the isoflux wall. Predicted average heat transfer rates were correlated over a range of the relevant dimensionless parameters.

Introduction

Although most of the information concerning buoyancy-induced transport in enclosures is related to two-dimensional plane and axisymmetric flows (Gebhart et al., 1988), these systems only approximate the three-dimensional motions that occur in reality. A review of investigations that deal with three-dimensional natural convection in enclosures (for example, Ozoe et al., 1976; Mallinson and de Vahl Davis, 1977; Yang et al., 1986; Kirchartz and Oertel, 1988; de Vahl Davis et al., 1989; Lock and Han, 1989; Hamady et al., 1989) reveals that little consideration has been given to systems other than those possessing at least some insulating or perfectly conducting boundaries. From the practical perspective, it may be expected that heat dissipation from warm surfaces would be enhanced if insulated boundaries were replaced with cool, isothermal surfaces proving beneficial, for example, in electronics cooling applications.

A typical electronics package consists of a series of vertically stacked circuit cards, between which flows a fan- or buoyancy-driven coolant. As packaging density increases, the area available for throughflow decreases and, in the limiting case, the openings that surround the card can be completely blocked with connections and wiring. Blockage also occurs in applications where isolation from a hostile environment is necessary. In either situation, the configuration may be similar to that shown in Fig. 1 for which thermal energy is transferred from vertical heated surfaces, through the coolant to front, back, top, and bottom enclosure walls, which are maintained at relatively cool temperatures.

Due to the thermal boundary conditions imposed upon the enclosure, it is clear that three-dimensional effects will exist, since the front and back surfaces participate actively in the heat transfer process. The degree of heat transfer augmentation that may be attributed to three-dimensionality cannot be anticipated, however, since the enhancement associated with cooling at the front and back surfaces may be offset by the competing role of the hydrodynamic end effects in reducing

coolant circulation (Mallinson and de Vahl Davis, 1977). The coolant convection is expected to be complex, with thermal stratification near the enclosure bottom, thermal destabilization in the upper portions adjacent to the heated wall, and downflow at the front and back enclosure surfaces. Because the convective heat transfer rates cannot be anticipated, the objectives of this study are (i) to develop a numerical model to predict local and average convective heat transfer rates across the enclosure, (ii) validate the model by comparing its predictions with experimental measurements, and (iii) develop a heat transfer correlation for the system of interest.

Mathematical Model

The enclosure whose coordinate system and geometric parameters are illustrated in Fig. 1 is considered here. An identical, spatially uniform heat flux is imposed on the two large, parallel faces of a three-dimensional cavity of width B , depth D , and height H . The four isothermal enclosure faces adjoining the isoflux surfaces (front, back, top, and bottom) are maintained at T_0 , leading to advection within the coolant (air). To determine the convection resistance between the heated surfaces and the cool walls, the flow and heat transfer are assumed to be steady and laminar, and the Boussinesq approximations are presumed to be valid. Radiative transfer across the cavity

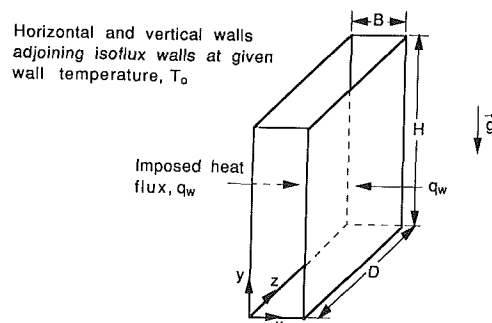


Fig. 1 Schematic of the physical system with imposed thermal boundary conditions and definition of coordinate system and geometric parameters

Contributed by the Heat Transfer Division for publication in the JOURNAL OF HEAT TRANSFER. Manuscript received by the Heat Transfer Division February 19, 1991; revision received May 23, 1991. Keywords: Electronic Equipment, Natural Convection.

is assumed negligible, although this mode may be important in many applications. It is noted that symmetry planes exist within the enclosure at $x = B/2$ and $z = D/2$. Nondimensionalization of the governing equations reveals that the relevant dimensionless parameters are Gr^* , Pr , and two enclosure geometric aspect ratios, H/B and D/B . Note that the isoflux plate separation, B , has been used as the characteristic length in Gr^* . The two geometric parameters define the dimensionless height and depth of the system; a large value of H/B indicates a slender enclosure vertically, while a large D/B is associated with the limiting case of two-dimensional flow.

The coupled partial differential equations governing transport of mass, momentum, and energy for laminar, three-dimensional natural convection of a Boussinesq fluid are:

Continuity:

$$\frac{\partial U}{\partial X} + \frac{\partial V}{\partial Y} + \frac{\partial W}{\partial Z} = 0 \quad (1)$$

X-Momentum:

$$\frac{\partial^2 U}{\partial X^2} + \frac{\partial^2 U}{\partial Y^2} + \frac{\partial^2 U}{\partial Z^2} = -\frac{\partial P}{\partial X} + \frac{\partial^2 U}{\partial X^2} + \frac{\partial^2 U}{\partial Y^2} + \frac{\partial^2 U}{\partial Z^2} \quad (2)$$

Y-Momentum:

$$\frac{\partial^2 V}{\partial X^2} + \frac{\partial^2 V}{\partial Y^2} + \frac{\partial^2 V}{\partial Z^2} = -\frac{\partial P}{\partial Y} + \frac{\partial^2 V}{\partial X^2} + \frac{\partial^2 V}{\partial Y^2} + \frac{\partial^2 V}{\partial Z^2} + Gr^* \theta \quad (3)$$

Z-Momentum:

$$\frac{\partial^2 W}{\partial X^2} + \frac{\partial^2 W}{\partial Y^2} + \frac{\partial^2 W}{\partial Z^2} = -\frac{\partial P}{\partial Z} + \frac{\partial^2 W}{\partial X^2} + \frac{\partial^2 W}{\partial Y^2} + \frac{\partial^2 W}{\partial Z^2} \quad (4)$$

Energy:

$$\frac{\partial^2 \theta}{\partial X^2} + \frac{\partial^2 \theta}{\partial Y^2} + \frac{\partial^2 \theta}{\partial Z^2} = \frac{1}{Pr} \left(\frac{\partial^2 \theta}{\partial X^2} + \frac{\partial^2 \theta}{\partial Y^2} + \frac{\partial^2 \theta}{\partial Z^2} \right) \quad (5)$$

Two sets of boundary conditions were applied to Eqs. (1)–(5). Exploiting the system symmetry about the planes $x = B/2$ and $z = D/2$, and for the idealized conditions of Fig. 1, the boundary conditions are stated as:

$$X=0 \quad U=V=W=0, \quad \partial\theta/\partial X = -1 \quad (6a)$$

$$X=1/2: \quad U=\partial V/\partial W=\partial W/\partial X=\partial\theta/\partial X=0 \quad (6b)$$

$$Y=0, H/B: \quad U=V=W=\theta=0 \quad (6c)$$

$$Z=0: \quad U=V=W=\theta=0 \quad (6d)$$

$$Z=(D/2B): \quad \partial U/\partial Z=\partial V/\partial Z=W=\partial\theta/\partial Z=0 \quad (6e)$$

A second and different thermal boundary condition, which accounted for the conjugate nature of the transport along the

isoflux wall, will be described in a later section dealing with model validation. In any case, it is noted that the flow and heat transfer were solved only for one quadrant of the enclosure bounded in part by the appropriate symmetry planes.

The average Nusselt number may be expressed in terms of the temperature field using the appropriate relation for uniform heat flux surfaces, $\bar{Nu} = 1/\bar{\theta}_w$, where the average wall temperature is determined by

$$\bar{\theta}_w = \frac{1}{(D/2B)(H/B)} \int_0^{D/2B} \int_0^{H/B} \theta(Y, Z) dY dZ \quad (7)$$

The governing equations and corresponding boundary conditions were solved with a control volume-based finite difference scheme. The coupling between pressure and continuity was handled using the SIMPLER algorithm (Patankar, 1980). A nonuniform grid was used in all simulations. Lines forming x - and z -direction control surfaces were deployed according to $x_i = (B/2)[(i-1)/i_{\max}]^n$ and $z_k = (D/2)(k-1)/k_{\max}$ for $(i, k) = 1, 2, \dots, (i_{\max}, k_{\max})$. Y -direction control surfaces were generated over half the vertical height of the cavity with the relation $y_j = (H/2)[(j-1)/j_{1/2}]^n$ for $j = 1, 2, \dots, j_{1/2}$ where $2j_{1/2} - 1$ is the total number of control surfaces in the y direction. The remaining half of the cavity height was discretized such that the grid distribution was symmetric about $y = H/2$. In all simulations $n = 1.5$. Simulations were performed on a Convex C220 vectorizing supercomputer, and required approximately 800 iterations to achieve a converged solution. In general, lower Gr^* predictions were used as input in the higher Gr^* simulations.

A preliminary study was performed to determine an adequate grid size to ensure grid-independent prediction of global quantities. Simulations were performed for $Gr^* = 10^6$, $H/B = 1.0$, and $D/B = 1.5$ using $12 \times 12 \times 12$, $22 \times 22 \times 22$, and $32 \times 32 \times 32$ grids. The predicted \bar{Nu} for these grids were 8.105, 8.387, and 8.447, respectively. Since (i) the difference in \bar{Nu} between successive grid refinements is 3.5 and 0.7 percent, respectively and (ii) the $32 \times 32 \times 32$ simulations were significantly more costly than those associated with the intermediate grid, the $22 \times 22 \times 22$ mesh was used in all simulations reported here. It is estimated that the predicted \bar{Nu} are accurate to within 5 percent; however, no claims are made with regard to the grid independence of predicted local quantities.

Experimental Apparatus

Due to the anticipated complexity of flow and heat transfer in the three-dimensional system, it was deemed necessary to perform experiments to validate the theoretical model outlined

Nomenclature

B = width of enclosure, Fig. 1	P = dimensionless pressure = $p/\rho(\nu/B)^2$	α = thermal diffusivity
D = depth of enclosure, Fig. 1	Pr = Prandtl number = ν/α	β = volumetric coefficient of thermal expansion
Gr^* = modified Grashof number = $g\beta q_w B^4/k\nu^2$	q_w = convective heat flux imposed along heated surfaces	θ = dimensionless temperature = $(T - T_o)/(q_w B/k)$
H = height of enclosure, Fig. 1	T_o = temperature of cooled top, bottom, and front and back walls	ν = kinematic viscosity
k = thermal conductivity	T_w = local heated wall temperature	ρ = fluid density
n = grid deployment exponent	(U, V, W) = dimensionless velocities = $(u, v, w)B/\nu$	Subscripts
Nu = local Nusselt number along heated wall = $q_w B/k(T_w - T_o)$	(X, Y, Z) = dimensionless coordinates = $(x, y, z)/B$	i, j, k = indices for $x, y,$ and z directions, respectively
\bar{Nu} = average Nusselt number = $q_w B/k(\bar{T}_w - \bar{T}_o)$		\max = maximum

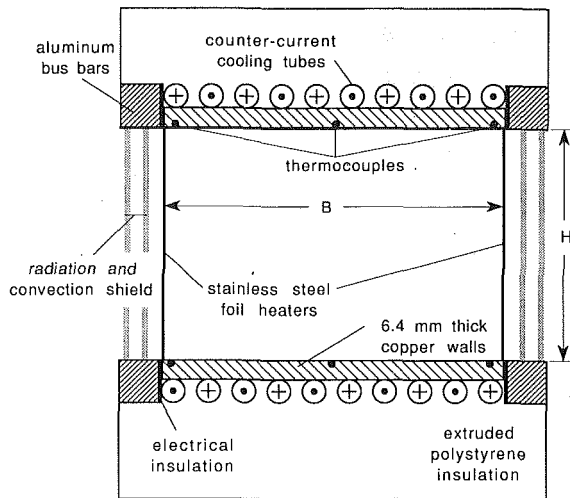


Fig. 2 Schematic of experimental test cell

in the foregoing. Two enclosures, whose construction is illustrated in Fig. 2, were fabricated to permit experimental study of the heat transfer over a range of H/B and Gr^* .

The top, bottom, and front and back (isothermal) walls of the enclosures were constructed of 6.4-mm-thick copper plates, which were silver-soldered at the corner joints and polished to reduce the radiative heat transfer across the enclosure. The height and depth dimensions of the two enclosures were identical at $H = 88.9$ mm and $D = 140$ mm while the widths of the enclosures were $B = 12.7$ and 102 mm, respectively. Thus, the aspect ratios of the two cavities were $H/B = 7.0$ and 0.87 with corresponding D/B of 11.0 and 1.37.

Thermally regulated water from a constant temperature bath was circulated through copper tubing, which was soldered to the exterior surface of the isothermal walls. The tubing was arranged with two independent, counterflow circuits to ensure wall isothermality. Wall temperatures were monitored with multiple thermocouples embedded in small holes near the interior surface of the copper walls and measurements revealed that the temperature of the cool surfaces was uniform to 0.1°C . It should be noted that the coolant temperature was adjusted so that the average of the mean heated wall and cooled wall temperatures was near ambient, thereby minimizing heat transfer with the environment during data acquisition. The maximum difference between the local heated wall and cooled wall temperature never exceeded 10°C , justifying use of the Boussinesq assumption (Gray and Giorgini, 1976; Hamady et al., 1989).

The heated vertical walls were constructed of identical sheets of 0.051-mm-thick stainless steel shim stock. The sheet was cut slightly larger than the interior $H \times D$ dimensions of the enclosure to ensure air-tight conditions, and was clamped to the edges of the top and bottom copper walls using 12.7-mm-square, 152.4-mm-long aluminum bus bars. The interior surfaces of the shim stock were also polished to a high luster to minimize radiative transfer, while the contact between each bus bar and the shim stock was made with nickel-impregnated paint to insure good electrical contact. The shim stock was electrically insulated from the copper walls with Teflon tape.

Electrical power was supplied to both foil heaters by connecting them in series to a d-c power supply stable to 0.1 percent. The current was read from the digital display on the power supply, while the voltage drop across each foil was determined by probing with a voltmeter. Measurement of the voltage drop revealed that the heat flux on the two vertical sides was identical to within 6 percent. A preliminary estimate based on a simplified zonal analysis of the enclosure showed

that the radiative contribution of the heat transfer was approximately 7 and 12 percent of the Ohmic heat flux for the $B = 12.7$ and 102 mm test cells, respectively.

Because of the test cell construction, optical access to the interior of the enclosure is impossible. To visualize system behavior, therefore, an infrared thermal imaging camera (Inframetrics 600) was used to measure the temperature distribution to within a spatial resolution of 0.3 mm on the back side of the isoflux walls, which, due to the small wall thickness, is presumed to be identical to the corresponding interior temperature distribution. The back sides of the shim stock were painted flat black to maximize the signal of the emitted energy. The emissivity of the test surface was measured with the thermal camera to be 0.95 within the spectral range of the imaging system ($8 \mu\text{m} \leq \lambda \leq 12 \mu\text{m}$). To minimize heat transfer with the surroundings, the isoflux walls were insulated with a composite, double sheet of aluminum foil with an intermediate stagnant air space. Heat transfer with the surroundings was estimated to be less than 10 percent of the imposed Ohmic heat flux.

The experiment was allowed to come to steady state (4–6 h) before data were taken. To acquire data, the insulation was quickly removed from the test surface and approximately 5 s of radiometric data were collected using 1/30 s scans. Although prolonged exposure of the test surface to the laboratory surroundings induced significant temperature modification, observation of the acquired infrared images showed that only minor changes in the wall temperatures occurred over the data capture interval. The thermal data were recorded on standard videocassette tape and were analyzed using a personal computer-based frame grabber board and commercial digital image processing software. Image averaging over 16 frames was employed to minimize the effects of random noise.

The experiments included investigations of the $B = 12.7$ mm test cell under imposed heat fluxes from 10.7 to 150.7 W/m^2 , corresponding to $1.23 \times 10^3 \leq Gr^* \leq 2.02 \times 10^4$. Imposed heat fluxes of 21.8 and 198.3 W/m^2 for the $B = 102$ mm test apparatus yielded $1.11 \times 10^7 \leq Gr^* \leq 1.01 \times 10^8$. The Gr^* range spanned conduction- to buoyancy-dominated transport. There was no experimental indication of oscillatory flow, turbulence, or asymmetry about $z = D/2$.

Results and Discussion

Model Verification. The model was validated in a qualitative sense by comparing its predictions with experimental measurements. Despite using 0.051-mm-thick stainless steel shim stock as the heater material, however, significant conjugate effects were present in the experiments. The influence of wall conduction was to smear the temperature gradients of the heated wall established solely by convection. Hence, the boundary conditions and solution procedure were modified slightly to include conjugate effects in this portion of the study.

Attempts to account for conjugate effects through direct incorporation of the heat diffusion equation in the algorithm (by re-assigning thermophysical properties and neglecting advective terms in Eq. (5)) failed because of the drastically different thermal conductivities ($k_{\text{wall}}/k_{\text{air}} > 500$). The modified solution procedure that proved successful was the following. The two-dimensional temperature distribution of the heated wall was initially estimated by solving the heat diffusion equation with T_0 imposed at all four boundaries, using a uniform volumetric energy generation corresponding to the Ohmic heating in the foil (less the estimated radiative losses). The resulting temperature distribution was subsequently imposed in the three-dimensional convection simulation in lieu of the thermal condition of Eq. (6a). Upon solution of the convective heat transfer, the predicted local convective heat flux was subtracted from the guessed heat flux (energy generation) used in the conduction solution, and the heat diffusion equation was re-

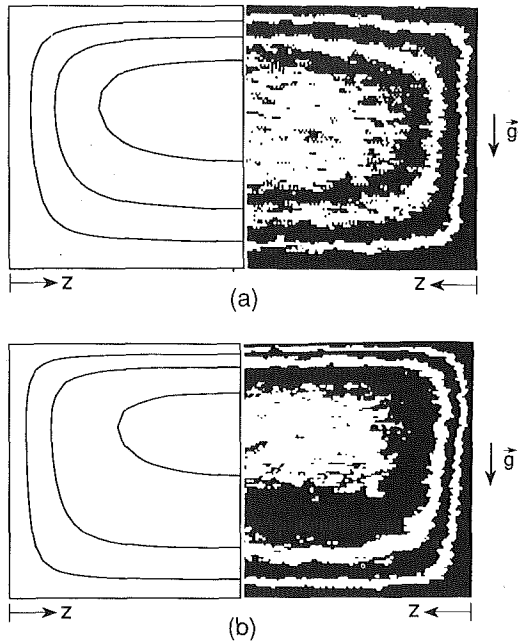


Fig. 3 Comparison of predicted and experimentally measured wall temperature distribution for (a) $H/B = 7.0$, $D/B = 11.0$, and $Gr^* = 1.23 \times 10^3$, contour values $(T_w - T_o)/(T_{max} - T_o) = 0.32, 0.59$, and 0.85 , and (b) $H/B = 0.87$, $D/B = 1.37$, and $Gr^* = 1.11 \times 10^7$, $(T_w - T_o)/(T_{max} - T_o) = 0.32, 0.63$, and 0.93 . Predictions and experimental data are joined at the cavity depthwise centerplane, $z = D/2$.

solved. The global solution procedure thus consisted of iteration between (i) the two-dimensional conduction solution for the heated plate and (ii) the three-dimensional natural convection simulation for the enclosure. Upon convergence, therefore, the Ohmic heat flux (less estimated radiative loss) was balanced by a conjugate redistribution of energy in the metallic foil and natural convection heat flux to or from the air inside the cavity. It is noted that this procedure conserves energy at both the local and global levels.

Figure 3 shows a comparison between the measured and predicted wall temperature distribution for $H/B = 7.0$, $D/B = 11.0$, and $Gr^* = 1.23 \times 10^3$, as well as $H/B = 0.87$, $D/B = 1.37$, $Gr^* = 1.11 \times 10^7$. Since thermal symmetry about $z = D/2$ was observed experimentally and imposed in the theoretical predictions, the figure illustrates contours of predicted and experimentally measured wall temperature for only half of the heated surface. For both experiments, the predicted average wall temperatures are within 9 percent of the measurements; for the small Gr^* case, the predicted and measured dimensionless average wall temperatures are $\bar{\theta}_w = 0.75$ and 0.69 ($T_w - T_o = 3.6$ and 3.3°C), respectively, while the analogous $\bar{\theta}_w$ values for the large Gr^* experiment are 0.045 and 0.043 ($T_w - T_o = 3.9$ and 3.7°C). It is noted, however, that significant differences exist between predicted and measured local wall temperatures. The predicted and measured maximum wall temperature differences, $T_{max} - T_o$, for the $Gr^* = 1.23 \times 10^3$ case, were 6.5 and 5.0 , respectively. Corresponding predicted and experimental values of $T_{max} - T_o$ for the $Gr^* = 1.11 \times 10^7$ experiment were 6.6 and 4.4 . In all cases the maximum wall temperature was overpredicted by the theoretical model. This is attributed to (i) simplified treatment of the radiative transport, (ii) contact resistance between the heated foil and the cooled walls, (iii) lateral conduction in the insulating aluminum foil, and (iv) possibly grid-dependent predicted local quantities. As such, the experimental and predicted isotherms presented in Fig. 3 are of different value. Specifically, the predicted and experimental contour values are plotted for identical values of $(T_w - T_o)/(T_{max} - T_o)$ indicated in the figure caption.

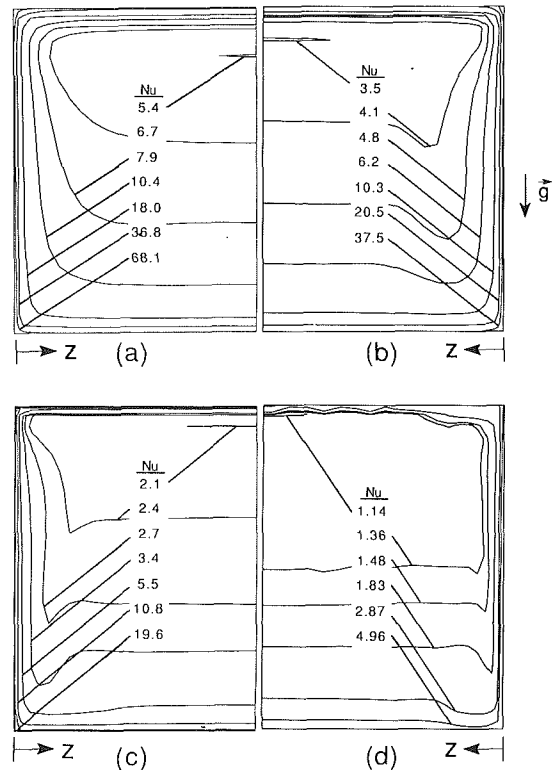


Fig. 4 Variation of predicted local Nusselt number for $Gr^* = 10^6$, $H/D = 2/3$: (a) $H/B = 1$, (b) $H/B = 2$, (c) $H/B = 4$, and (d) $H/B = 8$

Despite the model's failure to predict local temperatures quantitatively, the qualitative comparison between measurement and local prediction is considered to be good, as is the quantitative agreement in average wall temperatures presented previously. It is noted that the ratio of wall convective heat transfer to total Ohmic dissipation, Q_{conv}/Q_{Ohm} , gives an indication of the magnitude of the conjugate heat transfer in the heated wall. The Q_{conv}/Q_{Ohm} ratios for the small and large Gr^* experiments were predicted to be 0.083 and 0.25 , respectively, indicating that lateral conduction in the metallic foil was dominant in the experimental study.

As evident in Figs. 3(a) and 3(b), maximum temperatures exist near the center of the heated wall, with cooler temperatures confined to regions near the isothermal surfaces. Note that even for this relatively small Gr^* , the influence of buoyancy-induced flow and heat transfer is evident with an upward displacement of the maximum temperature from the center of the domain. A comparison of Figs. 3(a) and 3(b) shows that, as expected, the location of the maximum wall temperature is shifted upward as Gr^* increases.

Parametric Numerical Study. Simulations were performed to investigate the flow and heat transfer over a range of the governing dimensionless parameters in order to discern changes in and correlate the system thermal response. Since the objective is to correlate the system's thermal behavior, conjugate effects and radiative transport were neglected here. Predictions were made in ranges $10^2 \leq Gr^* \leq 10^7$, $1.0 \leq H/B \leq 8.0$, and $1.5 \leq D/B \leq 12.0$ for a $Pr = 0.71$ fluid. Additionally, asymptotic results, for $Gr^* \rightarrow 0$ and $H/D \rightarrow \infty$ were generated by solving the pure conduction problem and the two-dimensional natural convection problem, respectively. The range of dimensionless parameters selected for study was motivated by applications of engineering relevance (typical circuit board array dimensions).

Figure 4 shows the predicted Nu distributions for $Gr^* = 10^6$, $H/D = 2/3$, and $H/B = 1, 2, 4$, and 8 . Strong variations

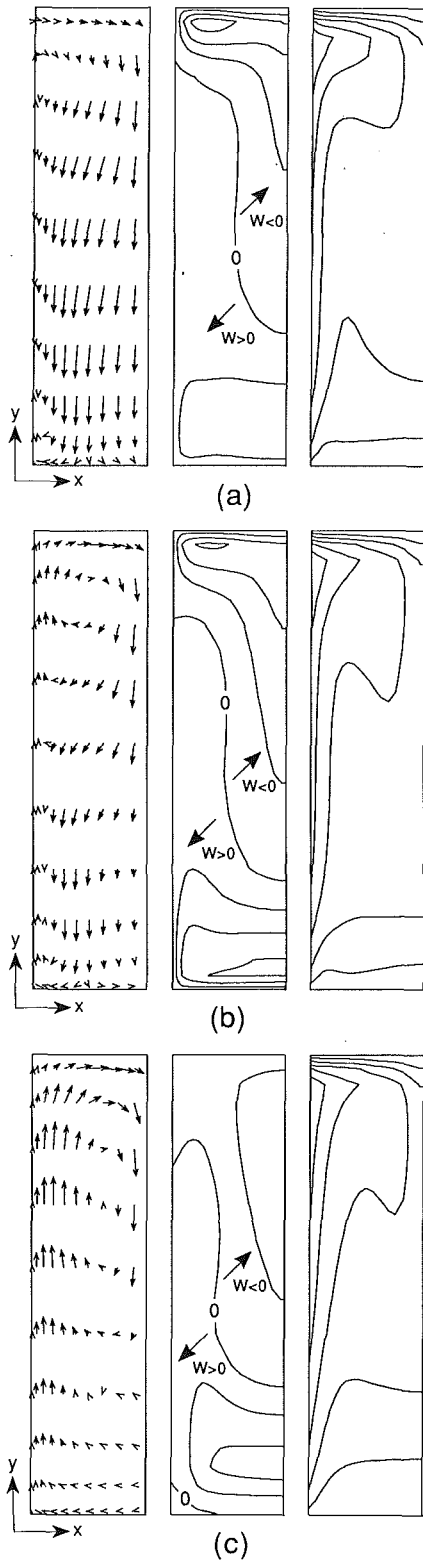


Fig. 5 Predicted U - V velocity vectors (left), W velocity contours (middle), and isotherms (right) for $H/B = 2$, $D/B = 3$, and $Gr^* = 10^6$: (a) $z/(D/2) = 0.058$, (b) $z/(D/2) = 0.125$, and (c) $z/(D/2) = 0.585$

in Nu are most evident near $Z = 0$, while the local heat transfer over the central depthwise two-thirds of the heated wall is nearly independent of Z . As was evident in Fig. 3, the lowest temperatures (highest Nu) are confined to a narrow region near the cooled walls. The highest temperatures (minimum Nu) are displaced upward from the center of the heated wall due

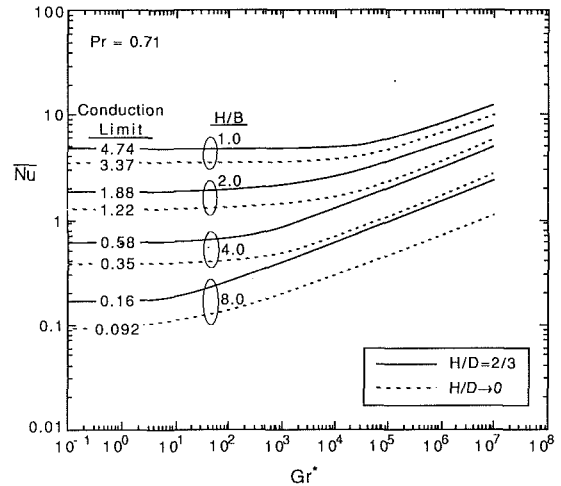


Fig. 6 Predicted variation of \bar{Nu} with Gr^* and H/B for $H/D = 2/3$ and $Pr = 0.71$

to the buoyancy-induced fluid motion, and the location of the minimum Nu rises with increasing H/B . Note that the relatively coarse grid used is unable to accurately resolve the wall temperature gradients for the $H/B = 8$ case (Fig. 4d).

The predicted flow and thermal structure for the $Gr^* = 10^6$, $H/B = 2$, $D/B = 3$ case (Fig. 4b) is illustrated in Fig. 5. The flow patterns at three depthwise X - Y planes are presented in the two leftmost panels as U - V velocity vectors and contours of the W -velocity component, respectively. The magnitudes of the maximum U - V velocity vectors of Figs. 5(a), 5(b), and 5(c) are, respectively, 218, 178, and 195. The W -velocity contours are referenced to the $W = 0$ value; each contour is at an increment of $\Delta W = 20, 30$, and 25 at $z/(D/2) = 0.058, 0.125$, and 0.585 , respectively. The isotherms of the rightmost panel are equally spaced between T_0 and the predicted maximum temperature in each plane. The maximum temperatures are $\theta_{max} = 0.221, 0.266$, and 0.285 for the three planes shown.

As implied by inspection of the U - V velocity vectors, the flow is seen generally to rise along the heated wall and fall near the cooled front surface due to buoyancy and along the cavity midplane as required by conservation of mass. Near the vertical corner formed by the cooled and heated wall at $X = 0$, the rising fluid near the heated wall and the falling fluid near the cooled wall experience a complex shear interaction with resulting mixing. Thermal stratification is evident near $Y = 0$ while thermal destabilization exists near $Y = H/B$. The W -velocity contours illustrate the complexity and importance of the three-dimensional flow in the cavity as the maximum W -velocity is nearly half that of the maximum U - V vector magnitude. A strong horizontal flow component is observed moving toward the vertical isothermal wall at $Z = 0$ in the upper part of the enclosure, while the lateral flow in the lower part is directed toward the enclosure depthwise centerline, $z/(D/2) = 1$. It is clear that three-dimensional motion exerts significant influence on the transport in the enclosure.

The variation of \bar{Nu} with Gr^* and H/B for $H/D = 2/3$ is illustrated in Fig. 6. Also shown is the corresponding two-dimensional system behavior ($H/D = 0$) generated using a model similar to the three-dimensional model described here. The data show clearly the influence of the three-dimensional flow on the transport since the actual \bar{Nu} are significantly higher than the corresponding two-dimensional predictions, differing by a factor of two at low H/B . In addition, the predictions asymptote to a constant \bar{Nu} for $Gr^* \rightarrow 0$. These asymptotic conduction solution Nusselt numbers, predicted for the buoyancy-free system, are noted in the figure for both two-dimensional and three-dimensional simulations. Interestingly, the destabilizing influence of buoyancy occurs at smaller Gr^* for

the larger H/B enclosures. The most slender enclosure investigated, $H/B = 8.0$, is clearly influenced by buoyancy-driven fluid motion even at $Gr^* = 10$, whereas \overline{Nu} for the $H/B = 1.0$ configuration deviates from the pure conduction results by only 1 percent at $Gr^* = 10^4$.

The \overline{Nu} predictions were correlated using a least-squares regression for $H/D = 2/3$ yielding

$$\overline{Nu} = 0.87 (Gr^*)^{0.17} (H/B)^{-0.85} \quad (8)$$

Equation (8) reflects all predicted results with an average and maximum error of 5.0 and 15.0 percent, respectively over the range $10^4 \leq Gr^* \leq 10^7$ and $1.0 \leq H/B \leq 8.0$. The relatively high errors are attributed to the multiplicity of length scales in the system. As expected, the 0.17 exponent on Gr^* is not significantly different from the $\overline{Nu} \sim (Gr^*)^{0.2}$ relationship found for natural convection from a vertical plate with isoflux wall heating (Sparrow and Gregg, 1956).

Conclusions

Natural convection in an enclosure with imposed uniform heat flux on two vertical walls and constant temperature along the adjoining four walls has been investigated both experimentally and theoretically. Experimental results were used to validate a numerical model based on the solution of the full three-dimensional equations of motion and energy. The model predictions reveal strong three-dimensional flow, with the highest local heat transfer coefficient occurring at the edges of the isoflux wall, and nearly constant local Nusselt number over the central portion of the heated walls. Average heat transfer results were correlated for use in engineering design situations.

Acknowledgments

One of the authors (B.W.W.) acknowledges financial sup-

port of this work under U. S. National Science Foundation Grant No. CBT-8552493. Computational facilities were made available by the Brigham Young University Computer-Aided Engineering, Design, and Manufacturing Network.

References

- de Vahl Davis, G., Leonardi, E., and Van Schie, M. P., 1989, "Three-Dimensional Natural Convection in a Cavity With Localized Heating and Cooling," in: *Transport Phenomena in Thermal Control*, G.-J. Hwang, ed., Hemisphere Publishing Corp., New York, pp. 615-630.
- Gebhart, B., Jaluria, Y., Mahajan, R. L., and Sammakia, B., 1988, *Buoyancy-Induced Flows and Transport*, Hemisphere Publishing Co., New York.
- Gray, D. D., and Giorgini, A., 1976, "The Validity of the Boussinesq Approximation for Liquids and Gases," *International Journal of Heat and Mass Transfer*, Vol. 19, pp. 545-551.
- Hamady, F. J., Lloyd, J. R., Yang, H. Q., and Yang, K. T., 1989, "Study of Local Natural Convection Heat Transfer in an Inclined Enclosure," *International Journal of Heat and Mass Transfer*, Vol. 32, pp. 1697-1708.
- Kirchartz, K. R., and Oertel, H., 1988, "Three-Dimensional Thermal Cellular Convection in Rectangular Boxes," *Journal of Fluid Mechanics*, Vol. 192, pp. 249-286.
- Lock, G. S. H., and Han, J.-C., 1989, "Flow and Heat Transfer in a Long Horizontal Rectangular Cavity With Differentially-Heated Ends," in: *Transport Phenomena in Thermal Control*, G.-J. Hwang, ed., Hemisphere Publishing Corp., New York, pp. 687-699.
- Mallinson, G. D., and de Vahl Davis, G., 1977, "Three-Dimensional Natural Convection in a Box: A Numerical Study," *Journal of Fluid Mechanics*, Vol. 83, pp. 1-31.
- Ozoe, H., Yamamoto, K., Churchill, S. W., and Sayama, H., 1976, "Three-Dimensional Numerical Analysis of Laminar Natural Convection in a Confined Fluid Heated From Below," *ASME JOURNAL OF HEAT TRANSFER*, Vol. 98, pp. 202-207.
- Patankar, S. V., 1980, *Numerical Heat Transfer and Fluid Flow*, Hemisphere Publishing Corp., Washington, DC.
- Sparrow, E. M., and Gregg, J. L., 1956, "Laminar Free Convection From a Vertical Plate With Uniform Surface Heat Flux," *ASME JOURNAL OF HEAT TRANSFER*, Vol. 78, pp. 435-440.
- Yang, H. Q., Yang, K. T., and Lloyd, J. R., 1986, "Flow Transition in Laminar Buoyant Flow in a Three-Dimensional Tilted Rectangular Enclosure," *Proc. 8th Int. Heat Transfer Conf.*, San Francisco, CA, Hemisphere Publ. Co., Washington, DC, Vol. 4, pp. 1495-1500.

Natural Convection Heat Transfer From a Plate in a Semicircular Enclosure

G. A. Moore¹

K. G. T. Hollands

Centre for Solar Thermal Engineering,
Department of Mechanical Engineering,
University of Waterloo,
Waterloo, Canada

In the subject geometry, a long thin plate at uniform temperature is contained coaxially and symmetrically in a long semicircular trough closed at the top and having a uniform but different temperature. Heat flows across the air-filled region between the two by both natural convection and gaseous conduction. The problem of characterizing the free convective component of this heat transfer—that is, the component caused by bulk fluid motion—is treated experimentally by using a heat balance technique, with the measurements being repeated at different pressures, in order to cover a wide Rayleigh number range, from $Ra \approx 10$ to $Ra \approx 10^8$. Nusselt number versus Rayleigh number plots are presented for each of several combinations of plate-to-trough spacing and tilt angle, and the plots are correlated by equations. The problem of characterizing the conductive component is treated by numerically solving the steady diffusion equation in the air-filled region, and the results are correlated as a function of the spacing and the plate thickness.

Introduction

Natural convection heat transfer across a two-dimensional region between two isothermal bodies, one of which envelops the other and each at a different temperature, arises in many situations of practical interest and has been the subject of several past investigations. An important special case, namely convection in the region between two concentric or eccentric cylinders, was studied extensively in the past (Kuehn and Goldstein, 1976a, 1976b, for example, have summarized much of this work). Only a very few studies, however, have reported on body shapes other than circular. Among these has been the work of Singh and Liburdy (1986), who studied the convective heat transfer from a flat plate in a circular enclosure.

The present paper is about characterizing the two-dimensional convective transfer across the air-filled region between a flat plate and a semicircular cylindrical enclosure, as shown in Fig. 1. This particular problem has arisen in the design of a concentrating solar collector of the low concentration ratio, nonimaging, nonevacuated kind (Rabl, 1985; Hollands et al., 1989). In this application, the inner plate represents the solar absorber, the curved surface of the enclosure represents the reflector, and the flat part of the enclosure represents the glazing across the aperture. Natural convection is the dominant mechanism for heat loss from the absorber plate to the enclosure. For modeling purposes, plate and enclosure are both treated as uniform in temperature.

Dimensional analysis can be used (Moore, 1989) to show that the Nusselt number, Nu , i.e., the dimensionless heat transfer by conduction and convection (see Nomenclature), is a function of four dimensionless groups, as follows:

$$Nu = Nu(Ra, Pr, \theta, \sigma, \tau) \quad (1)$$

where the Rayleigh number, Ra , is based on the length, H , of the plate (see Nomenclature), Pr is the Prandtl number of the fluid, $\sigma = S/H$ is the nondimensionalized spacing between the plate and the semicircle (assumed the same at each end of the plate), θ is the angle of inclination of the plate from the vertical, and $\tau = t/H$ is the dimensionless plate thickness. This paper

presents an experimental determination of the convective component of this relationship for $Pr \approx 0.7$ (its value for air) and for $\tau = 0.037$, covering the following range of the other relevant parameters: $10 \leq Ra \leq 10^8$, $0.042 \leq \sigma \leq 0.091$, and $0 \leq \theta \leq \pi/2$. The conductive component, that is, the limit of Nu as $Ra \rightarrow 0$, was determined by numerically solving the steady diffusion equation. The details of the latter analysis are contained in the appendix.

Experiment

An experimental model of the subject geometry, sketched in exploded view in Fig. 2, was constructed in copper and instrumented for temperature and heat flow measurements. To make the results of the measurements on the model applicable over a wide Rayleigh number range and to permit the radiative transfer to be more readily separated out, the measurements were conducted with the model inside a vessel of

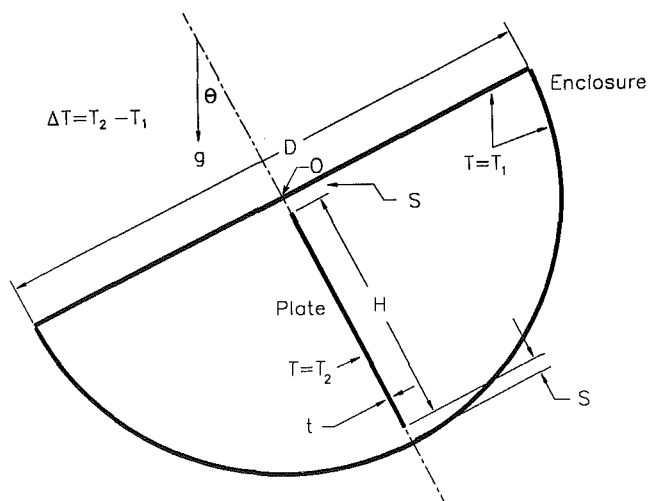


Fig. 1 Cross-sectional sketch defining the geometry of the problem under consideration; a long thin plate is located centrally in a long semicircular trough closed at the top

¹Current address: Electrical Research Department, Ontario Hydro, Toronto, Ontario M8Z 5S4, Canada.

Contributed by the Heat Transfer Division for publication in the JOURNAL OF HEAT TRANSFER. Manuscript received by the Heat Transfer Division February 12, 1991; revision received August 19, 1991. Keywords: Conduction, Natural Convection, Solar Energy.

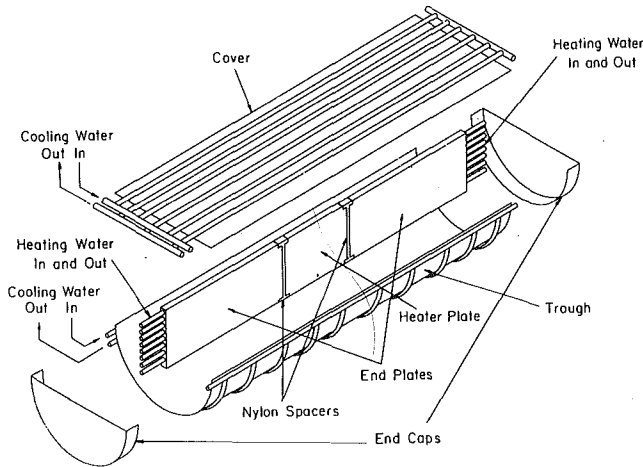


Fig. 2 Exploded view of the apparatus

variable pressure (Hollands, 1988). The Rayleigh number could then be varied by repeating the experiment at various pressure settings.

The model's semicircular enclosure was 1.13 m long by 248 mm in diameter and made up in two parts: a "trough" and a flat cover. Both had tubes soldered to their outside surfaces, so that by circulating water from a constant temperature bath (set at about 25°C), through the tubes at a sufficient rate, one could maintain both at the same uniform temperature. The plate, located centrally inside this enclosure, consisted of three parts: two identical end plates and a central "heater" plate. The end plates contained integral passages so that when water from another constant-temperature bath (set at about 35°C) was passed through these passages, the two end plates would together take up the same uniform temperature, different from the enclosure temperature. The heater plate had an electrical heater embedded in it. By varying the power supplied to the heater, the temperature difference between the heater plate

and the end plates could be adjusted to be very nearly zero, creating a situation in which there is almost no heat transfer between the heater plate and the two end plates. Under this condition virtually all the (measured) electrical power into the heater plate passes as heat from the heater plate to the semicircular enclosure. After subtracting away the radiative component of this heat rate and dividing by the heater plate length, one obtains the plate heat transfer per unit length, for substitution into the Nusselt number.

The various copper bodies were each designed to take up a uniform temperature during the experiment. Both the semicircular trough and its flat cover were made from 1.22-mm-thick copper sheet with 3.18 mm o.d. copper tubes soldered to the outside surfaces at a 65 mm center-to-center spacing. Fin-type and energy balance calculations showed that, at the design flow rate of water circulation, the overall variation in the enclosure temperature should not exceed 1 percent of the overall design temperature difference between plate and enclosure. Semicircular 1.22-mm-thick copper caps were placed at each end of the enclosure to close the cavity.

The end plates on each side of the heater plate had channels, 3.2 mm wide, milled into them to accommodate the 3.18 mm o.d. copper tubes, which were then pressed into the channels to form the plate's integral passages. The rest of the channel space was filled with soft solder, so that, after being machined to its final 4.2 mm thickness, each end plate presented a smooth flat surface to the outside world. The channels and tubes ran straight, at 14 mm centers, except for U-bends at one end of the plate (the end that abuts the heater plate). At the opposite end of the plate the tubes were connected to common headers.

The heater plate measured 114 mm wide, 152 mm long, and 4.2 mm thick. It had a 1028-mm-long nichrome wire (the electrical heater) embedded into it, the wire running in a serpentine fashion with a spacing between turns of 19 mm. The wire ran in a groove that had been machined into the plate, high-conductivity epoxy resin being used to fill the rest of the groove. Following this, the plate was polished to a smooth finish.

A nylon spacer, 5 mm wide and of the same thickness and height as the heater plate, was inserted between the heater plate

Nomenclature

b = parameter used in fitting $Nu_{c,N}$ as a function of N , according to Eq. (A-1)
 C_e = calibration constant for thermopile, $W/\mu V$
 D = diameter of semicircle (Fig. 1), m
 e = thermopile emf μV
 g = acceleration of gravity, m/s^2
 h_{lp} = heat transfer coefficient, per unit length, between plate and enclosure at low-pressure condition, $W/m K$
 H = height of plate (Fig. 1), m
 I = heater plate current, A
 k = thermal conductivity of fluid, $W/m K$
 K_i, K_t = fitting parameters in Eq. (2)
 L = length of heater plate in horizontal (or axial) direction, m

m, n = fitting parameters in Eq. (2)
 N = number of control volumes used in numerically solving for Nu_c
 Nu = Nusselt number = $q/k\Delta T$
 Nu_c = conduction Nusselt number, i.e., Nu when fluid is stationary
 $Nu_{c,0}^N$ = $Nu_{c,0}$ as calculated in a numerical solution of the steady diffusion equation, using N control volumes
 $Nu_{c,0}$ = Nu_c when $\tau = 0$
 p = parameter used in fitting $Nu_{c,N}$ as a function of N , according to Eq. (A-1)
 P = gas pressure, Pa
 Pr = Prandtl number = ν/α
 q = convective/conductive heat transfer from the plate per unit length in the horizontal (axial) direction = Q/L , W/m

Q = convective/conductive heat transfer from plate over length L , W
 Ra = Rayleigh number = $g\beta\Delta TH^3/\nu\alpha$
 S = width of spacing between ends of plate and the semicircular enclosure (Fig. 1), m
 t = thickness of plate (Fig. 1), m
 T_1, T_2 = temperatures of plate and semicircle, respectively, K
 $T_m = (T_1 + T_2)/2$, K
 $\Delta T = T_1 - T_2$, K
 v = heater plate voltage, V
 α = thermal diffusivity of fluid, m^2/s
 β = volumetric thermal expansion coefficient of the fluid, K^{-1}
 θ = angle of tilt of plate from vertical (Fig. 1), rad
 ν = kinematic viscosity of fluid, m^2/s
 $\sigma = S/H$
 $\tau = t/H$

and each end plate, keeping these plates separated by a constant spacing. The purpose of the spacers was to provide some insulation between the heater plates and the end plates; since it is never possible to make these plates exactly equal in temperature, there will always be some heat flow between them. To measure this residual heat flow, four thermocouple junctions were attached to each spacer's face adjacent to the heater plate, and another four were attached to the face adjacent to the end plate. The thermocouples were connected in thermopile to give a sensitive measure of the temperature difference across the spacer, which was proportional to the heat flow through the spacer. A second thermopile was similarly connected around the other spacer, and the two piles were connected in series, so that their combined emf measured the heat transfer through both spacers, i.e., the heat flow between the heater plate and the end plates. The coefficient of proportionality C_e between the combined emf and this heat flow was determined in a calibration procedure, in which the heater plate temperature was kept equal to the enclosure temperature, so that all of the electrical power had to go through the spacers as heat flow. Thus by varying the end plate temperature, one can obtain a graph of spacer heat flow (i.e., electrical power) versus emf, and from such a graph, the proportionality constant was inferred. In subsequent measurements of the heat flow, the electrical power was corrected for the heat flow through the spacer—determined from the proportionality constant and the thermopile emf—to obtain the heat flow at the outer face of the heater. This correction never exceeded 2 percent of the measured power.

To determine the radiative heat transfer from the heater plate, the plate heat transfer was measured with the vessel pressure low enough that the Rayleigh number is sufficiently low for convection to be unimportant. This measured heat transfer was therefore known to be by conduction and radiation only. Its value was then divided by the overall temperature difference ΔT between the plate and the enclosure to obtain a "low-pressure" heat transfer coefficient h_{lp} across the cavity. The conductive component of h_{lp} was calculated using the results of a numerical solution of the steady diffusion equation, which had determined the conduction Nusselt number (see the appendix), and assuming the air's thermal conductivity is equal to its value at atmospheric pressure (see later). Subtracting this calculated conductive component from h_{lp} yielded the radiative heat transfer coefficient. This coefficient, being independent of the pressure, was then used to calculate the radiative transfer at higher values of the Rayleigh number. For this radiative correction technique to work, it is essential that there be no convection at the low-pressure condition, and also that the pressure there is not so low that the air's thermal conductivity departs significantly from its atmospheric value. That these conditions had been achieved was assured by finding a pressure range (or "window") over which the heat transfer is insensitive to pressure (either convection or rarefied conduction would change with pressure), and then locating the "low-pressure condition" inside that window. A suitable window was found for every setup, its typical range being from 200 to 3000 Pa. This range roughly corresponds to a Rayleigh number range of 100 to 1300, and a Knudson number² range of 0.003 to 0.001. This observed pressure window range is roughly what one would expect: based on experience in other free convection problems, one would expect convection to commence when the Rayleigh number is greater than about 1000, and rarefied

conduction effects normally begin when the Knudson number is greater than about 0.003 (Kaganer, 1969).

The overall temperature difference ΔT between the plate and the enclosure was measured by means of a thermopile containing five copper-constantan junctions embedded in the heater plate and five in the enclosure (three junctions on the trough, and two on the cover). The mean T_m of the plate and enclosure temperatures (required for converting this thermopile emf into a temperature difference and for evaluating the properties of air) was measured by averaging the readings of mercury-in-glass thermometers immersed in the constant temperature baths. (Heat losses from the insulated piping connecting baths to the model had been shown to be small.) The vessel pressure, which varied from 100 Pa to 1 MPa, was measured using a variable capacitance diaphragm transducer.

A series of measurements at each of five values of the angle θ , namely, 0, 30, 45, 60, and 90 deg, was performed at each of three values of the spacing S , namely, 4.78, 7.95 and 10.35 mm. (The different values of S were achieved by changing the diameter of the trough; the same plate was used for all tests.) Each series of measurements started with the low-pressure measurements at which the radiative heat transfer coefficient was evaluated for that geometry. These tests generally fell in the pressure range of from 1 to 3 kPa. Following this, the pressure was increased in steps of about 40 percent of the current pressure, heat transfer and temperature measurements being repeated at each pressure setting, until the maximum allowable tank pressure of 1 MPa was reached. All the required steps were performed automatically by a microcomputer. To measure the heat transfer, the power required to make the heater plate and the end plate temperatures essentially equal and steady had to be found. This was done by microcomputer, which was programmed to change the supply voltage to the heater, from an upper to a lower bound, whenever the emf from the nylon spacer thermopile changed sign. The upper and lower bounds of the voltage supply variation were gradually altered until the required power was found, the decision for altering the voltage bounds being based on the ratio of times spent at each voltage setting. Once the correct power had been found, a 20 min. "test period" was entered into during which the microcomputer measured I , v , ΔT , e , T_m , and p at repeated intervals, and then averaged the results.

The 95 percent uncertainties in the Nusselt number and the Rayleigh number were calculated by the method described by Moffat (1988), using Eqs. (20), (21), and (25)–(27) of his paper. Details are given by Morrison (1990). The measured quantities $X_1 \dots X_{10}$ entering into Nu and for Ra are listed in Table 1, together with the bias limit B_i of each measurement. The quantities represented by the first six entries in the table (i.e., X_i , $i = 1-6$) were measured about 250 times over the 20 min test period used, and averaged to produce one experimental Nu, Ra point. Then the precision index S_i of the mean of each was calculated, using Eqs. (20) and (21) of Moffat (1988). Since the precision index varied somewhat, it is not possible to give a single value for each X_i ; Table 1 presents maximum observed value of S_i or, more precisely, its ratio to B_i . Generally $S_i^2 \ll B_i^2$, so that the precision index of these measurements did not contribute appreciably to the uncertainty U in Nu or Ra. The remaining four measured quantities (X_i , $i = 7-10$) were presumed to have no precision index, as they were fixed for the experiment, the random error in their measurement having been "fossilized." The bias error in h_{lp} was assumed to be equal to the uncertainty U in this quantity, this U having been calculated in the same way that the uncertainty in Nu or Ra was calculated; that is in the manner described in this paragraph. The same is true of C_e . Note that the measured quantities entering into the calculation of h_{lp} and C_e are common to those used in determining Nu, so their values of B_i and S_i are already included in Table 1. The computer program used to calculate Nu and Ra also printed out the 95 percent uncer-

²In this Knudson number ($Kn = \Omega/L$, where Ω is the mean free path), the length dimension L was taken equal to spacing S , because rarefied effects would first occur at the smallest spacing. The equation (Kaganer, 1969) $k = k_0/(1 + 3.7 Kn)$ can be used to calculate the effect of pressure on thermal conductivity k ; here k_0 is the atmospheric pressure value and k is the value at the pressure in question. (This equation assumes an accommodation coefficient of 0.95.)

Table 1 Errors in measured quantities, x_i

Index i	Quantity X_i	Unit	Normal Value of X_i , or Experimental Range of X_i	Bias Limit B_i	Precision Index + Bias Limit, S_i/B_i
1	l	A	$0.2 \leq l < 1.0$	$0.0017l$	$< 10^{-2}$
2	v	V	$1 \leq v \leq 6$	$0.00015v + .0001$	$< 10^{-2}$
3	ΔT	K	$7 \leq \Delta T \leq 15$	0.1	< 0.006
4	e	μV	$1 \leq e \leq 10$	4	< 0.025
5	T_m	K	$295 \leq T_m \leq 315$	0.1	< 0.06
6	P	Pa	$P \leq 10^4$	$\sqrt{(5 \times 10^{-4} P)^2 + 1.04^2}$	< 0.003
			$10^4 < P < 10^5$	$\sqrt{(5 \times 10^{-4} P)^2 + 8^2}$	$< .05$
			$P \geq 10^5$	$\sqrt{(5 \times 10^{-4} P)^2 + 80^2}$	< 0.16
7	L	m	0.152	2.5×10^{-4}	---
8	H	m	0.114	2.5×10^{-4}	---
9	C_z	$W/\mu V$	3.5×10^{-4}	1×10^{-5}	---
10	h_p	W/mK	$0.3 \leq h_p < 0.4$	0.005	---

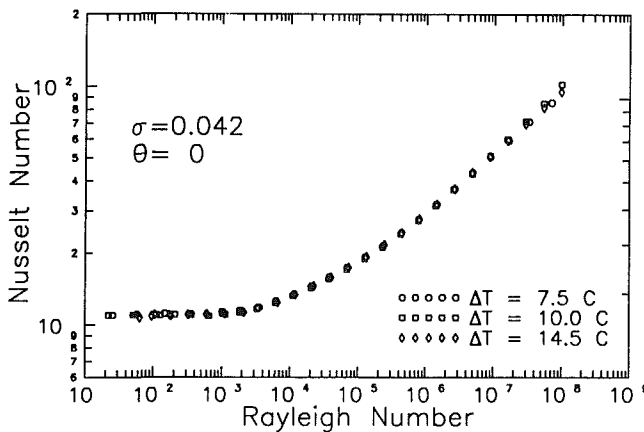


Fig. 3 Nusselt number versus Rayleigh number plate for $\sigma = 0.042$ and $\theta = 0$, using three different settings for the temperature difference ΔT . That the data for different values of ΔT overlap verifies the dimensional analysis and checks the soundness of the experimental method.

tainties U in each of the measurements. The uncertainty in Nu , so calculated, varied from 2.5 percent at the conduction limit, to 1.7 percent at the highest Rayleigh number. The uncertainty in Ra was approximately 2.3 percent for all Ra .

Results

To validate the apparatus, a series of measurements were conducted with fixed values of angle θ and spacing S , but with different values for the temperature difference ΔT . To allow a true comparison, care was taken to ensure that the Rayleigh numbers for the different ΔT values lay very close to one another. The results are shown in Fig. 3, which plots Nusselt number versus Rayleigh number for $\sigma = 0.042$, $\theta = 0$, and three values for ΔT , 7.5°C, 10°C, and 14.5°C. If the dimensional analysis is correct and if the experimental method is sound, the results should lie on top of each other, which indeed they do, within experimental error.

The complete set of results is given in Fig. 4, which shows Nu versus Ra plots for all combinations of σ and θ . For fixed values of the other variables, the heat transfer almost everywhere decreases with increasing θ , the most pronounced effect of θ being observed at high Rayleigh number and at values of

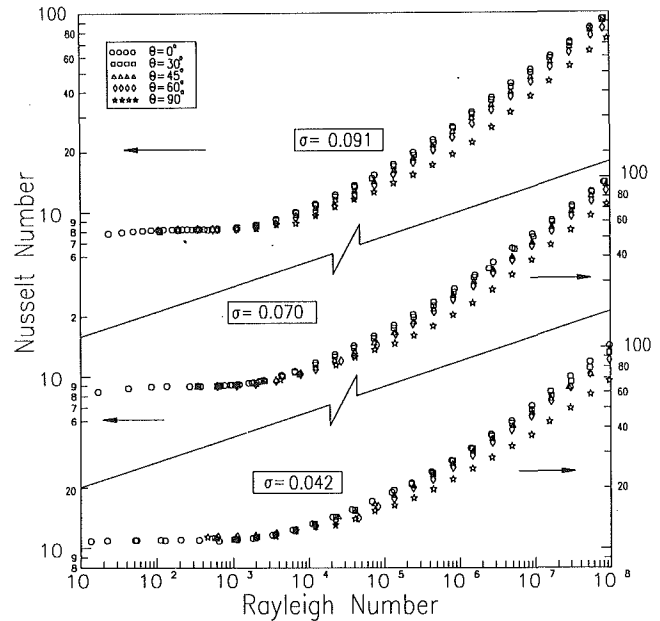


Fig. 4 Full set of results plotted in the form of Nusselt number versus Rayleigh number

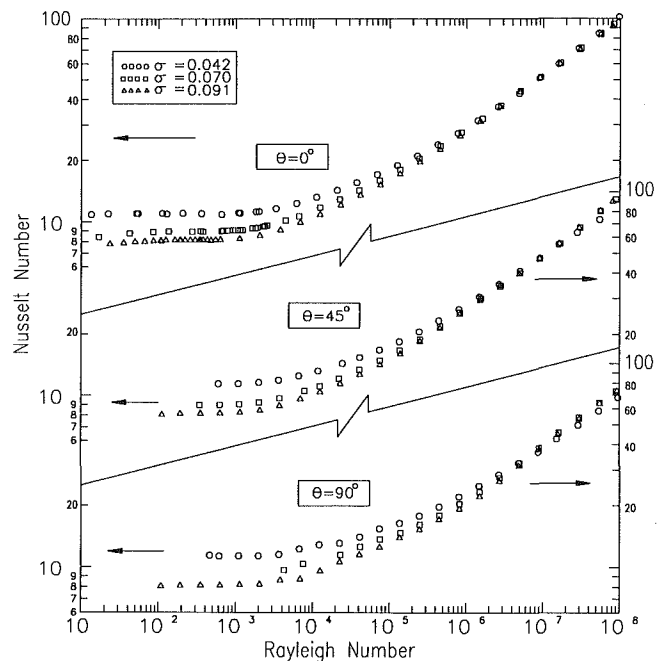


Fig. 5 A replot of Fig. 4, better showing the effect of spacing parameter, $\sigma = S/H$

θ from 60 to 90 deg. To show better the effect of spacing, some of the data are replotted in Fig. 5 in a different format. Spacing is seen to have a pronounced effect at low Rayleigh number, where the heat transfer is dominated by conduction, but it has essentially no effect at high Rayleigh number, where convection dominates.

Correlation of Results

Examination of the slopes of the logarithmic plots shown in the figures reveals a nearly 1/4 power law dependence of Nu on Ra , at Ra around 10^6 , and that for large values of Ra , the slope increases, approaching 1/3. Also, the heat transfer is obviously controlled by conduction at low Rayleigh numbers.

Guided by these observations and by the form of correlation equation found useful by Hassani and Hollands (1989), we decided to attempt to fit the data by the equation form:

$$Nu = \{Nu_c^n + [(K_l Ra^{1/4})^m + (K_r Ra^{1/3})^{n/m}]^{1/n}\} \quad (2)$$

where Nu_c is the conduction Nusselt number, and m , n , K_l and K_r are parameters that will depend on σ and θ . The equation uses a Churchill–Usagi relation to interpolate between the various regimes. The parameters were found by an heuristic process. First, by fitting power law curves to the high Rayleigh number data over two appropriate ranges, values were found for K_l and K_r . Fortunately, the Nu_c term does not contribute appreciably in Eq. (2) when the Rayleigh number is high, thus m could be found by fitting the data at high Rayleigh number to Eq. (2) with $Nu_c = 0$. Finally, n was determined by fitting all the data to Eq. (2). This process was repeated at each combination of σ and θ , and the resulting parameter values are given in Table 2, which also shows the rms average and maximum deviations for the data from Eq. (2) with the parameter values as given in the table. The next step was to relate the parameters to σ and θ by means of equations. This was done by simply plotting the functions and from observing the form of the dependence, guessing an appropriate functional form, with appropriate constants. The constants were then determined from least-squares fits. This process resulted in the following equations:

$$K_l = 0.24 \cos \theta - 0.60 \sigma + 0.71 \quad (3)$$

$$K_r = 0.06 \cos \theta + 0.16 \quad (4)$$

$$m = 6.0 + 0.044\sigma^{-1.8} \quad (5)$$

and finally,

$$n = 2.1 + 18.4\sigma \quad (6)$$

Equations (2)–(6) fit the data with an rms deviation of 2.5 percent and a maximum difference of 4.1 percent.

Conclusions

Equations (2)–(6) are recommended for determining the natural convection heat transfer across the subject cavity for the range of variables: $Ra \leq 10^8$, $0 \leq \theta \leq \pi$, and $0.042 \leq \sigma \leq 0.091$. While these equations were derived with a fixed value for dimensionless plate thickness $\tau = 0.037$, it is felt that the effect of τ on the natural convection component of the heat transfer should be small, and hence that the equation should be valid for $0 \leq \tau \leq 0.037$, although no supporting evidence is provided here. The conductive heat transfer, characterized by the conductance Nusselt number Nu_c in Eq. (2), should be given closely by Eq. (A-2) and (A-3). Nu_c will definitely be a function of τ , and this dependence should be closely modeled by Eq. (A-3).

Acknowledgments

The authors would like to thank the Department of Energy, Mines and Resources Canada, and the Natural Science and Engineering Research Council of Canada for financial support for this work. They would also like to thank Bert Habicher for his invaluable technical assistance, and Professor Alfred Brunger for his useful ideas and comments.

References

- Hassani, A. V., and Hollands, K. G. T., 1989, "On Natural Convection Heat Transfer From Three-Dimensional Bodies of Arbitrary Shape," *ASME JOURNAL OF HEAT TRANSFER*, Vol. 111, pp. 363–371.
- Hollands, K. G. T., 1988, "Direct Measurement of Gaseous Natural Convective Heat Fluxes," in: *Experimental Heat Transfer, Fluid Mechanics and Thermodynamics*, R. K. Shaw, E. N. Ganic, and K. T. Yang, eds., Elsevier, New York.
- Hollands, K. G. T., Brunger, A. P., and Mikkelsen, J. V., 1989, "Unit Concentration Ratio, Nonimaging, Long-Ground-Based Solar Collector: Recent

Table 2 Best values for parameters K_l , K_r , m , and n , and differences between each experimental data point and those calculated by Eq. (2) with these best values used for the parameters

σ	θ	K_l	K_r	m	n	RMS % Diff.	Max % Diff.
0.042	0	0.910	0.219	13.3	2.9	1.87	3.62
	30	0.888	0.200	16.3	2.7	1.59	3.41
	45	0.853	0.201	20.9	2.6	0.85	1.85
	60	0.832	0.1902	26.9	2.9	1.64	4.11
	90	0.661	0.143	21.3	2.3	1.52	3.95
0.070	0	0.908	0.210	11.4	3.8	2.02	5.04
	30	0.874	0.210	11.1	3.3	1.76	3.86
	45	0.840	0.205	14.1	3.5	1.54	2.98
	60	0.805	0.191	14.1	3.6	1.36	2.73
	90	0.669	0.161	9.5	2.6	2.35	4.27
0.091	0	0.882	0.214	9.3	3.7	1.93	4.70
	30	0.856	0.208	8.5	3.4	1.71	3.12
	45	0.828	0.206	9.9	3.6	1.24	2.31
	60	0.788	0.188	10.2	3.9	1.03	1.94
	90	0.640	0.162	8.3	2.8	2.61	4.58

Table 3 Values for conduction Nusselt number $Nu_{c,0}$ as calculated for differing values of σ

σ	$Nu_{c,0}$
0.0200	10.88
0.0418	9.22
0.0696	7.98
0.0906	7.38
1.2000	6.75
2.000	5.71
0.3500	4.70
0.5000	4.13

Developments," *Proceedings of North Sun '88, Solar Energy at High Latitudes*, Aug. 29–31, 1988, Borlänge, Sweden, L. Broman and M. Ronnelid, eds., Swedish Council of Building Research, Stockholm, Sweden, pp. 345–350.

Kaganer, M. G., 1969, *Thermal Insulation in Cryogenic Engineering*, Israel Program for Scientific Translations Press, Jerusalem, [translation from Russian], pp. 5–7.

Kuehn, T. H., and Goldstein, R. J., 1976a, "An Experimental and Theoretical Study of Natural Convection in the Annulus Between Horizontal Concentric Cylinders," *J. Fluid Mech.*, Vol. 74, pp. 695–719.

Kuehn, T. H., and Goldstein, R. J., 1976b, "Correlating Equations for Natural Convection Heat Transfer Between Horizontal Circular Cylinders," *Int. J. Heat Mass Transfer*, Vol. 19, pp. 1127–1134.

Moffat, R. J., 1988, "Describing the Uncertainties in Experimental Results," *Experimental Thermal and Fluid Science*, Elsevier Science Publishing, New York, pp. 3–17.

Moore, G. A., 1989, "Natural Convection From an Isothermal Plate Suspended in a Semi-cylindrical Enclosure," Masters Thesis, Department of Mechanical Engineering, University of Waterloo, Waterloo, Ontario, Canada.

Morrison, I. D., 1990, "Thermal Improvements of Low-Concentration Ratio Non-imaging Solar Collectors," Master's Thesis, Department of Mechanical Engineering, University of Waterloo, Waterloo, Ontario, Canada.

Patankar, S. V., 1980, *Numerical Heat Transfer and Fluid Flow*, Hemisphere Publishing Corp., New York, pp. 71–73.

Rabl, A., 1985, *Active Solar Collectors and Their Applications*, Oxford University Press, New York, pp. 156–157.

APPENDIX

The conduction Nusselt number $Nu_{c,0}$ for a zero thickness plate ($t = 0$ in Fig. 1) was first determined by numerically solving the two-dimensional diffusion equation in the planar region shown in Fig. 1, with the appropriate boundary conditions. Because the region is symmetric about a plane running down the center plane of the plate, only one half of the region needed to be subjected to analysis, the plane of symmetry being made adiabatic in the region between the plate and the semicircle. Following a polar coordinate system, the region was discretized into N control volumes; that is, the control volumes were bounded by lines of constant values for the radial coordinate r and by lines of constant values of the angular coordinate θ , of a polar coordinate system centered at the intersection of the plane of symmetry and the flat part of the semicircle (i.e., at the point marked 0 in Fig. 1). The number N_r of divisions for the radial coordinate was made nearly equal to the number N_θ of divisions for the angular coordinate, the total number of control volumes then being $N = N_\theta \times N_r$. The discretized form of the diffusion equation in polar coordinates (see Patankar, 1980) was solved, using a diagonal matrix solver, for the temperatures at the nodal points of the control volumes. The heat transfer from the one side of the plane was then calculated from a discretized form of Fourier's law, numerically integrated along the length of the plate, and the result was converted into a conduction Nusselt number $Nu_{c,0}^N$ as estimated by the current value of N . The values of $Nu_{c,0}^N$ so

calculated were then plotted against the number N of control volumes, covering a range of N values typically running from 500 to 7000. The resultant plot was found to be closely fitted by the equation

$$Nu_{c,0}^N = Nu_{c,0} + bN^{-p} \quad (\text{A-1})$$

where $Nu_{c,0}$, b , and p were constants chosen to fit the plot most closely, being those that minimized the sum of the squares of the differences between the left and right sides of Eq. (A-1). Once the value of p had been so obtained, a standard linear regression analysis was entered into to refine the estimate for $Nu_{c,0}$ and to determine the limit of error of this estimate, at the 95 percent confidence level.

The process was repeated for various values of σ , and the results are tabulated in Table 3. At each setting for σ , the uncertainty in Nu was found to be essentially the same, and closely equal to 0.1. The equation

$$Nu_{c,0} = 3.48 \sigma^{-0.3} \quad (\text{A-2})$$

was found to fit the tabulated data to within 2.5 percent when $0.04 \leq \sigma \leq 0.35$.

A lower-bound estimate for the heat transfer over the finite area of thickness t at the two ends of the plate can be obtained by assuming one-dimensional heat transfer across the region between the ends and the semicircle, giving an additional Nusselt number equal to $2t/S$, which must be added to the $Nu_{c,0}$ calculated as above for $t = 0$, so that the total conduction Nusselt number Nu_c is estimated as

$$Nu_c = Nu_{c,0} + \tau/\sigma \quad (\text{A-3})$$

Turbulent Free Convection Heat Transfer to Drag-Reducing Fluids From Arbitrary Geometric Configurations

A. Nakayama

A. V. Shenoy

Department of Energy and Mechanical Engineering,
Shizuoka University,
3-5-1 Johoku, Hamamatsu, 432 Japan

The problem of turbulent free convection heat transfer from curved surfaces to drag-reducing fluids has been investigated using the Nakayama-Koyama solution methodology. The surface wall temperature is allowed to vary in the streamwise direction in an arbitrary fashion and calculations are carried out for the turbulent free convection about the horizontal circular cylinder and the sphere for the sake of illustration.

Introduction

A number of research workers, such as Colburn and Hougen (1930), Eckert and Jackson (1950), Bayley (1955), Fujii (1959), Kato et al. (1968), Cheesewright (1968), Kutateladze et al. (1972), Mason and Seban (1974), Papailiou and Lykoudis (1974), Cebeci and Kahatab (1975), Noto and Matsumoto (1975), Plumb and Kennedy (1977), Lin and Churchill (1978), George and Capp (1979), Thomas and Wood (1979), Ruckenstein and Felske (1980), Kawase and Ulbrecht (1984), and Nakayama and Koyama (1985) have made attempts to analyze the turbulent free convection heat transfer problem in Newtonian fluids. However, the same is not the case for non-Newtonian fluids as mentioned in the review articles by Shenoy (1986a, 1988) and Irvine and Karni (1987). In turbulent fluid flow, the importance of the drag reduction phenomenon resulting from the addition of minute quantities (in parts per million of certain additives) need not be emphasized here, as it has been the subject of a number of comprehensive reviews (Lumley, 1969, 1973; Patterson et al., 1969; Gadd, 1971; Darby, 1972; Hoyt, 1972; Landahl, 1973; Virk, 1975; Sellin et al., 1982a; Shenoy, 1984; Berman, 1986; Wilson, 1988; Singh, 1990). Despite the tremendous interest in the field of drag reduction, the only theoretical works on the effect of buoyancy on heat transfer during turbulent flow of drag reducing fluids are those of Ghosh et al. (1985) and Shenoy (1987). Ghosh et al. (1985) have provided an expression for predicting the heat transfer rate from a vertical flat plate but only under maximum drag reducing conditions while Shenoy (1987) has dealt with the flow inside vertical pipes. Thus, there is no analysis covering the external flow situation for different geometric shapes for mildly elastic drag-reducing fluids not necessarily flowing under maximum drag-reducing conditions.

In the present paper, we extend the Nakayama and Koyama (1985) solution method for Newtonian fluids so as to be able to provide a general analysis of the turbulent free convection problem from bodies of arbitrary geometric configurations to mildly elastic drag-reducing fluids.

Analysis

It is assumed that the geometric configuration has an arbitrary shape and the coordinate system is as shown in Fig. 1. The body may be planar or axisymmetric, and its wall geometry is defined by the function $r(x)$. The wall surface is heated to $T_w(x)$ above the ambient temperature T_e , which is assumed to be constant (although the analysis can be easily extended

to the variable T_e case, as done by Nakayama et al. (1983) for laminar free convection). The flow is induced against the gravitational force g under the influence of the buoyancy force component parallel to the wall surface. The appearance of turbulence in the flow begins at the top of the surface and gradually extends to cover more and more of the surface as the Grashof number increases. Turbulence occurs when the surface in question is big or the temperature difference is large.

A usual control volume analysis within the boundary layer of thickness δ leads to the following integral forms of the momentum and energy equations under the Boussinesq approximation on the buoyancy force:

$$\frac{d}{dx} \int_0^\delta r^* \rho u^2 dy = r^* \rho \beta_0 g_x \int_0^\delta (T - T_e) dy - r^* \tau_w \quad (1a)$$

$$\frac{d}{dx} \int_0^\delta r^* \rho u C_p (T - T_e) dy = r^* q_w \quad (1b)$$

where

$$r^* = \begin{cases} 1: & \text{planar flow} \\ r(x): & \text{axisymmetric flow} \end{cases} \quad (1c)$$

and

$$g_x = g \cos \phi = g \left\{ 1 - \left(\frac{dr}{dx} \right)^2 \right\}^{1/2} \quad (1d)$$

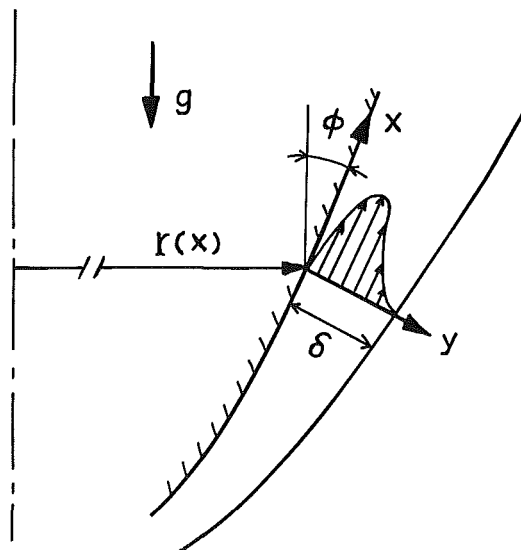


Fig. 1 Physical model and its coordinate system

Contributed by the Heat Transfer Division for publication in the JOURNAL OF HEAT TRANSFER. Manuscript received by the Heat Transfer Division December 12, 1990; revision received July 21, 1991. Keywords: Natural Convection, Non-Newtonian Flows and Systems, Turbulence.

In the above equations τ_w and q_w are the local wall shear and heat flux, while ρ , C_p , and β_0 are the density, specific heat, and thermal expansion coefficient, respectively. The tangential component of the acceleration due to gravity is indicated by g_x , which is related to the local surface orientation ϕ through the Eq. (1d). Moreover, the streamwise velocity and the local wall temperature are denoted by u and T with the subscripts e and w specifically pertaining to the boundary layer edge and the wall surface, respectively.

Theoretical analysis of free convection is normally more difficult than forced convection due to the coupling of the momentum and energy equation in the former case. When dealing with non-Newtonian fluids, this task becomes even more formidable. Hence, certain simplifications are sought in order to facilitate a solution without much sacrifice of accuracy.

The first step is to see how the equations would scale if the flow was purely forced convection. When dealing with turbulent non-Newtonian boundary layer flow, it is known that there exists a viscous sublayer that is very thin and close to the wall where the flow would be akin to a laminar forced convection flow. Also at the wall it is obvious that the local shear stress and the local heat flux assume their maximum value. Thus, an order of magnitude analysis of the kind used by Bejan (1984) for Newtonian fluids can be used for the present case:

$$\tau_w \sim \rho u_c^2 (\rho u_c l_c / \mu)^{-1/2} \quad (2a)$$

$$\frac{q_w}{(T_w - T_e)} \sim \frac{k}{l_c} \text{Pr}^{1/3} (\rho u_c l_c / \mu)^{1/2} \quad (2b)$$

where u_c is the characteristic velocity and Pr is the Prandtl number for drag reducing fluids defined in the conventional manner as given below:

$$\text{Pr} = C_p \mu / k \quad (2c)$$

Combing Eqs. (2a) and (2b) gives the following:

$$\frac{q_w}{\rho C_p (T_w - T_e) u_c} \sim \frac{\tau_w}{\rho u_c^2} \text{Pr}^{-2/3} \quad (2d)$$

It is now assumed that the above equation would hold even for the free convection flow if the characteristic velocity is related to the buoyancy rather than the free-stream velocity as in the forced convection case.

The dimensionless functions F and θ for the velocity and temperature profiles may be introduced as follows:

$$F(\eta) = u/u_c \quad (3a)$$

and

$$\theta(\eta) = (T - T_e) / \Delta T \quad (3b)$$

where

$$\Delta T = T_w - T_e \quad (3c)$$

and

$$\eta = y/\delta \quad (3d)$$

The characteristic velocity u_c and the temperature difference ΔT are assumed to be functions of x . Further, defining the parameter ξ , the ratio of the buoyancy force to the shear force, as

$$\xi = \rho \beta_0 g_x \int_0^\delta (T - T_e) dy / \tau_w \quad (4)$$

Nomenclature

a = exponent of Grashof number defined by Eq. (31a)
 A = function of β defined by Eq. (15a)
 b = exponent of Prandtl number defined by Eq. (31b)
 B = function of β defined by Eq. (15b)
 C_1, C_2 = coefficients defined by Eqs. (31c) and (31d)
 C_3 = coefficient defined in Eq. (30b)
 C_p = specific heat per unit mass
 d = diameter of cylinder or sphere
 D = function of β as defined by Eq. (15c)
 De = Deborah number defined by Eq. (7)
 f = friction factor defined in Eq. (8b)
 F = function for velocity profile given by Eq. (13a)
 g = acceleration due to gravity
 g_x = tangential component of gravity defined by Eq. (1d)
 Gr_x = local Grashof number based on g_x and x and defined in Eq. (19a)
 Gr_d = Grashof number based on g and d
 h = local heat transfer coefficient in Eq. (20)

h_{av} = average heat transfer coefficient in Eq. (32)
 i = integer associated with the coordinate system in Eq. (24a)
 I, I_1 = functions associated with deviation from unity and defined in Eqs. (19b) and (19c)
 j = integer associated with the body shape given in Eq. (24b)
 k = thermal conductivity
 L = characteristic length of geometric shape as used in Eq. (32)
 m_t = exponent associated with the wall temperature distribution as given by Eq. (26)
 Nu_d = average Nusselt number based on diameter
 Nu_x = local Nusselt number defined by Eq. (20)
 $Nu_{L,av}$ = average Nusselt number based on characteristic length and defined by Eq. (32)
 Pr = Prandtl number = $\mu C_p / k$
 q = function of β as defined by Eq. (14)
 q_w = heat flux at the wall
 r^* = function representing geo-

metric configuration in Eq. (1c)
 T = temperature
 ΔT = temperature difference defined by Eq. (3c)
 T_e = ambient temperature
 T_w = temperature of the body surface
 u = streamwise velocity component
 u_c = characteristic velocity in Eq. (3a)
 x, y = boundary layer coordinates
 α, β = dimensionless functions of De appearing in Eq. (8b)
 β_0 = expansion coefficient of the fluid
 δ = boundary layer thickness
 η = dimensionless variable defined by Eq. (3d)
 θ = dimensionless temperature profile defined by Eq. (3b)
 μ = viscosity
 ν = kinematic viscosity
 ξ = acceleration parameter defined by Eq. (4)
 ρ = density of the fluid
 τ_w = local surface shear stress
 ϕ = local surface orientation in Eq. (1d)
 Ω = coefficient defined in Eq. (10)

one can rewrite the governing Eqs. (1a, b) using Eq. (2d) as

$$A \frac{d}{dx} r^* u_c^2 \delta = (\xi - 1) Br^* g_x \beta_0 \Delta T \delta / \xi \quad (5a)$$

$$D \frac{d}{dx} r^* u_c \Delta T \delta = r^* \tau_w \Delta T Pr_c^{-2/3} / \rho u_c \quad (5b)$$

where

$$A = \int_0^1 F^2 d\eta \quad (6a)$$

$$B = \int_0^1 \theta d\eta \quad (6b)$$

$$D = \int_0^1 F \theta d\eta \quad (6c)$$

Based on the right-hand side of Eq. (5a), it is evident that the parameter ξ directly governs the flow acceleration and that the condition $\xi(x) \geq 1$ must be satisfied everywhere for the flow to be thermally stable.

Before solving the above equations, it is necessary to get an expression for τ_w for the free convection turbulent flow under consideration. Drag-reducing fluids are known to be Newtonian in viscosity but exhibit mild elasticity characterized by a relaxation time θ_{fl} . Detailed discussions on the determination of relaxation times for drag-reducing fluids are available from Argumedo et al. (1978) and Cho and Hartnett (1982). For such fluids, one assumes the friction factor f to be a function of the Reynolds number Re and the Deborah number De (which is the ratio of the fluid relaxation time θ_{fl} and the characteristic process time ν/u^*).

Thus,

$$De = \theta_{fl} u^* / \nu \quad (7)$$

where u^* is the friction velocity and ν is the kinematic viscosity. The choice of characteristic time scales for defining De has been discussed by Astarita (1965), Seyer and Metzner (1969a), and Virk (1975). Reported experimental studies on the determination of fluid relaxation times published by Seyer and Metzner (1969a) show that θ_{fl} varies as γ^{-m} where m lies between 0.5 and 1.0. The general practice is to assume that m is equal to 1 so that the Deborah number can be taken as a constant independent of shear rate knowing that u^{*2}/ν is directly proportional to wall shear rate. This assumption, though not truly accurate, renders itself useful for the derivation of an approximate expression for the wall shear stress in turbulently flowing drag reducing fluids.

Assuming Deborah number to be independent of shear rate, Seyer and Metzner (1969b) wrote an expression for friction factor for turbulent flow of drag reducing fluids as follows:

$$(2/f)^{1/2} = A_1(1 - \xi_1)^2 \ln Re f^{1/2} + (1 - \xi_1)^2 [B_1 - A_1 \ln 2(2)^{1/2}] - 3.0 \quad (8a)$$

where the values of A_1 , B_1 , and ξ_1 are given by Seyer and Metzner (1969b). A straightforward manipulation of the above equation can be done to obtain an explicit Blasius-type friction factor-Reynolds number relationship as given below:

$$f = \frac{\alpha}{Re^\beta} \quad \begin{array}{l} 5 \times 10^3 \leq Re \leq 10^5 \\ 0 \leq De \leq 10 \end{array} \quad (8b)$$

where α and β are functions of De for the case of drag-reducing fluids, and their values for varying De are presented in Table 1. It has been suggested by Virk et al. (1967) that the maximum drag reduction that can be achieved in practice can be described by a unique asymptote given by $\alpha = 0.42$ and $\beta = 0.55$ in the above equation. In Table 1, these values correspond to the limit $De \geq 20$, which has been used to denote the maximum drag reduction asymptote. As can be seen, the value of α is almost constant for $1 \leq De \leq 10$ but jumps by about 600

Table 1 Values of α , β , C_1 and C_2

De	α	β	a	b	C_1	C_2
0	0.0790	0.250	0.400	0.200	0.0402	2.02
1	0.0782	0.262	0.396	0.208	0.0404	1.91
2	0.0767	0.271	0.393	0.213	0.0401	1.82
3	0.0741	0.278	0.391	0.218	0.0393	1.76
4	0.0726	0.285	0.389	0.222	0.0390	1.71
5	0.0689	0.289	0.388	0.224	0.0375	1.67
6	0.0655	0.292	0.387	0.226	0.0362	1.65
7	0.0662	0.301	0.384	0.231	0.0368	1.59
8	0.0687	0.312	0.381	0.238	0.0383	1.51
9	0.0732	0.324	0.378	0.245	0.0406	1.43
10	0.0762	0.334	0.375	0.250	0.0422	1.38
≥ 20	0.420	0.550	0.323	0.355	0.141	0.623

percent for a change of De from 10 to 20. Actually, this is due to the fact that around $De = 20$ and beyond it, the f versus Re curve has a sudden change of slope and hence it is not only the value of α but also the value of β that undergoes a sudden change. Detailed explanation of the maximum drag reduction asymptote and its uniqueness are available in the exhaustive article of Virk (1975), which can be referred to for more details. Equation (8b) has been used when analyzing turbulent flow in horizontal pipes by Shenoy and Mashelkar (1983), in curved tubes by Shenoy et al. (1980), in rotating straight tubes by Shenoy (1986b), in annular ducts by Shenoy and Shintre (1986) and in vertical tubes by Shenoy (1987).

Following the procedure of Skelland (1967), a suitable expression for the local surface shear stress can be obtained from Eq. (8b) as follows:

$$\tau_w / \rho u_c^2 = \Omega (\mu / \rho u_c \delta)^\beta \quad (9)$$

where

$$\Omega = \alpha (0.817)^{2-\beta} / 2^{\beta+1} \quad (10)$$

Note that for the Newtonian case

$$\beta = 0.25, \quad \Omega = 0.02332 \quad (11)$$

$$\tau_{wN} / \rho u_c^2 = 0.02332 (\mu / \rho u_c \delta)^{1/4} \quad (12)$$

Substitution of Eq. (9) into Eqs. (5a, b) gives the final simplified forms of the governing equations that are now to be solved. This requires expressions for the dimensionless velocity and temperature profiles. These are sought by following the arguments set forth by Eckert and Jackson (1950). They noted that in turbulent forced convection equations of the form $F(\eta) = \eta^{1/7}$ and $\theta(\eta) = 1 - \eta^{1/7}$ hold rather well. For turbulent free convection, they found that experimental data could be fitted well with the same equation for temperature profile while the velocity profile needed to be modified to $F(\eta) = \eta^{1/7} (1 - \eta)^4$. For drag-reducing fluids, the velocity profile for turbulent forced convection flow can be taken as $F(\eta) = \eta^q$ where $q = \beta / (2 - \beta)$ as given by Skelland (1967). In the present free convection case, the velocity and temperature profiles will be assumed by analogous arguments to those of Eckert and Jackson (1950), making use of the forced convection expression for drag-reducing fluids as stated above. Thus, the dimensionless velocity and temperature profiles that are assumed to fit the turbulent free convection flow of drag reducing fluids are

$$F(\eta) = \eta^q (1 - \eta)^4 \quad (13a)$$

$$\theta(\eta) = 1 - \eta^q \quad (13b)$$

where

$$q = \beta / (2 - \beta) \quad (14)$$

Using Eqs. (13a, b), the expressions for A , B , and D as defined in Eqs. (6a, b, c) can be easily obtained as

$$A = \frac{1}{2q+1} - \frac{4}{q+1} + \frac{28}{2q+3} - \frac{28}{q+2} + \frac{70}{2q+5} - \frac{28}{q+3} + \frac{28}{2q+7} - \frac{4}{q+4} + \frac{1}{2q+9} \quad (15a)$$

$$B = q/(q+1) \quad (15b)$$

$$D = \frac{3}{q+1} - \frac{2}{q+2} + \frac{6}{q+3} - \frac{4}{q+4} + \frac{1}{q+5} - \frac{1}{2q+1} - \frac{6}{2q+3} - \frac{1}{2q+5} \quad (15c)$$

Note that for Newtonian fluids when q takes the value of $1/7$, we have $A = 0.0523$, $B = 1/8$, and $D = 0.0366$, which are all identical to the values obtained by Nakayama and Koyama (1985).

Upon combining Eqs. (4) and (9), one obtains the following expression for u_c :

$$u_c = (B g_x \beta_0 \Delta T / \Omega \nu^\beta \xi)^{1/2} \delta^{1+\beta} \delta^{2-\beta} \quad (16)$$

where ν is the kinematic viscosity. This equation along with Eq. (9) can now be substituted into the governing Eqs. (5a, b) to eliminate u_c and τ_w and thus results in the following equations after mathematical rearrangement of the terms:

$$\frac{d}{dx} \delta^{2(1+\beta)} + \delta^{2(1+\beta)} \frac{d}{dx} \ln \{ r^* \Delta T (g_x \Delta T / \xi)^{2-\beta} \}^{4+\beta} = \frac{2(1+\beta) B}{4+\beta} \frac{\Omega}{A} \left(\frac{\Omega}{B} \right)^{2-\beta} (\xi-1) (\xi \nu^2 / g_x \beta_0 \Delta T)^{\beta/2} \quad (17a)$$

$$\frac{d}{dx} \delta^{2(1+\beta)} + \delta^{2(1+\beta)} \frac{d}{dx} \ln \{ r^* \Delta T (g_x \Delta T / \xi)^{2-\beta} \}^3 = \frac{2(1+\beta) \Omega}{3 D} \left(\frac{\Omega}{B} \right)^{2-\beta} \text{Pr}^{-2/3} (\xi \nu^2 / g_x \beta_0 \Delta T)^{\beta/2} \quad (17b)$$

Integration of the above set of equations yields two distinct expressions as follows:

$$\left(\frac{\delta}{x} \right)^{2(1+\beta)} \text{Gr}_x^{2-\beta} = \frac{2(1+\beta) B}{4+\beta} \frac{\Omega}{A} \left(\frac{\Omega}{B} \right)^{2-\beta} (\xi-1) \xi^{2-\beta} I \quad (18a)$$

and

$$\left(\frac{\delta}{x} \right)^{2(1+\beta)} \text{Gr}_x^{2-\beta} = \frac{2(1+\beta) \Omega}{3 D} \left(\frac{\Omega}{B} \right)^{2-\beta} \text{Pr}^{-2/3} \xi^{2-\beta} I_t \quad (18b)$$

where

$$\text{Gr}_x = g_x \beta_0 \Delta T x^3 / \nu^2 \quad (19a)$$

is the local Grashof number and

$$I = \frac{\int_0^x (\xi-1) \{ r^* \Delta T (g_x \Delta T / \xi)^{2+\beta} \}^{1/(4+\beta)} dx}{x (\xi-1) \{ r^* \Delta T (g_x \Delta T / \xi)^{2+\beta} \}^{1/(4+\beta)}} \quad (19b)$$

$$I_t = \frac{\int_0^x (r^* \Delta T)^{2(1+\beta)/3} (g_x \Delta T / \xi)^{1/3} dx}{x (r^* \Delta T)^{2(1+\beta)/3} (g_x \Delta T / \xi)^{1/3}} \quad (19c)$$

The foregoing functions I and I_t account for the total combined effects of arbitrary geometries and wall temperature distributions.

The local Nusselt number Nu_x , which is of primary interest, is related to u_c and δ via the Colburn analogy as

$$\text{Nu}_x = \frac{hx}{k} = \text{Pr}^{1/3} \left(\frac{u_c x}{\nu} \right) \left(\frac{\tau_w}{\rho u_c^2} \right) = \text{Pr}^{1/3} \Omega \left(\frac{u_c x}{\nu} \right)^{1-\beta} \left(\frac{x}{\delta} \right)^\beta \quad (20)$$

where h and k are the local heat transfer coefficient and thermal conductivity. u_c in the above equation may be eliminated in favor of δ , using Eq. (16). Then, Eq. (18b) may be substituted into the equation. After some manipulation, one obtains the Nu_x expression as follows:

$$\text{Nu}_x = \left\{ \frac{2(1+\beta) I_t}{3D} \right\}^{1-2\beta} (\Omega B^{1/2})^{1+\beta} \text{Pr}^{1+\beta} (\text{Gr}_x / \xi)^{1/(2(1+\beta))} \quad (21)$$

Having established all the necessary relations, the solution of the problem is now reduced to the determination of the unknown acceleration parameter $\xi(x)$. For this purpose, the two distinct expressions for δ , namely, Eqs. (18a) and (18b), are equated to give the following characteristic equation:

$$\xi = 1 + \frac{A(4+\beta) I_t}{3DI} \text{Pr}^{-2/3} \quad (22)$$

Since Eqs. (19b) and (19c) for I and I_t also involve the unknown $\xi(x)$, the foregoing characteristic equation is implicit in ξ . Thus, the determination of $\xi(x)$ in general requires an iterative procedure at each integration step. A simple way to find $\xi(x)$ may be to guess ξ at the end of each integration step, and evaluate Eqs. (19b) and (19c), using this guessed value and the value determined during the preceding integration step (corresponding to the value at the beginning of the current integration step). The integration results are to be substituted back into the characteristic Eq. (22) to check if the estimated ξ at the end of the integration step satisfies the relation. This sequence has to be repeated to determine ξ within a desired accuracy before marching one step further. The boundary value $\xi(0)$ needed for initiation of such integrations, however, must be provided prior to the downstream marching in consideration of the similarity solutions presented in the following section.

Results and Discussion

It is of great interest to investigate certain cases for which the functions I and I_t remain constant so that similarity solutions are possible. Any geometry near the stagnation point may be specified as

$$r = \left(\frac{dr}{dx} \Big|_{x=0} \right) x, \text{ hence,}$$

$$\cos \phi = \left\{ 1 - \left(\frac{dr}{dx} \Big|_{x=0} \right)^2 \right\}^{1/2} = \text{const: pointed body} \quad (23a)$$

and

$$r = r_0 \sin(x/r_0), \text{ hence, } \cos \phi = \sin(x/r_0): \text{ blunt body} \quad (23b)$$

where r_0 is the local radius at $x = 0$. The foregoing consideration reveals the following proportional relationship:

$$r^* \propto x^i \text{ where } i = \begin{cases} 0 & \text{plane body} \\ 1 & \text{axisymmetric body} \end{cases} \quad (24a)$$

$$g_x \propto x^j \text{ where } j = \begin{cases} 0 & \text{pointed body} \\ 1 & \text{blunt body} \end{cases} \quad (24b)$$

For example, the integers (i, j) should be set to $(0, 0)$ for a flat plate, $(1, 0)$ for a vertical cone pointing downward, $(0, 1)$ for the stagnation region on a horizontal circular cylinder, and $(1, 1)$ for the stagnation region of a sphere. Equations (19b) and (19c) under the conditions described by the foregoing proportional relationships yield

$$I = \left\{ 1 + \frac{2(1+\beta)i + (2+\beta)(j+m_t)}{4+\beta} \right\}^{-1} \quad (25a)$$

$$I_t = \left\{ 1 + \frac{2(1+\beta)i}{3} + \frac{j}{3} + \frac{(3+2\beta)m_t}{3} \right\}^{-1} \quad (25b)$$

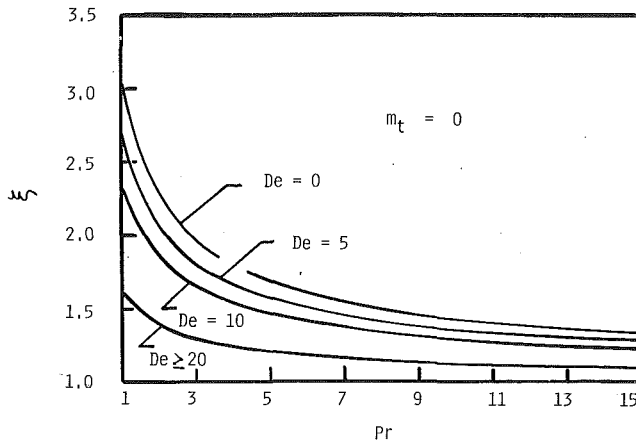


Fig. 2 Effects of Pr and De on ξ for the isothermal vertical flat plate

where m_t is associated with the wall temperature distribution around the stagnation point, which is assumed to follow

$$\Delta T \propto x^{m_t} \quad (26)$$

The wall temperature distribution reflects on the functions I and I_t in such a manner that both I and I_t diminish as ΔT_w increases downstream (i.e., $m_t > 0$). Substitution of Eqs. (25a) and (25b) into the characteristic Eq. (22) gives an explicit equation for ξ :

$$\xi = 1 + \frac{A(4+\beta)}{3D} \frac{1 + \frac{2(1+\beta)i + (2+\beta)(j+m_t)}{4+\beta}}{\left\{ 1 + \frac{2(1+\beta)i}{3} + \frac{j}{3} + \frac{(3+2\beta)m_t}{3} \right\} Pr^{2/3}} \quad (27)$$

Thus, ξ stays constant around $x = 0$, and a similarity solution exists around the stagnation point. For the vertical isothermal flat plate exposed to the Newtonian fluids (i.e., $\beta = 1/4$ and $i = j = m_t = 0$), both I and I_t become unity, and

$$\xi = 1 + 2.023 Pr^{-2/3} \quad (28)$$

When the above equation is substituted into Eq. (21), it reduces to the form derived by Eckert and Jackson (1950) for an vertical isothermal flat plate, namely,

$$Nu_x = \frac{0.0402 Pr^{1/5}}{(1 + 2.023 Pr^{-2/3})^{2/5}} Gr_x^{2/5} \quad (29)$$

For the drag-reducing fluids in general, the expressions for the acceleration parameter ξ and the local Nusselt number Nu_x may be given as

$$\xi = 1 + C_2 (I_t/I) Pr^{-2/3} \quad (30a)$$

and

$$Nu_x = \frac{C_1 I_t^{a-b} Pr^b}{\{1 + C_2 (I_t/I) Pr^{-2/3}\}^a} Gr_x^a = C_3(De, Pr) Gr_x^a \quad (30b)$$

where

$$a = 1/2(1+\beta) \quad (31a)$$

$$b = \beta/(1+\beta) \quad (31b)$$

$$C_1(De) = \left\{ \frac{2(1+\beta)}{3D} \right\}^{\frac{1-2\beta}{2(1+\beta)}} (\Omega B^{1/2})^{\frac{1}{1+\beta}} \quad (31c)$$

$$C_2(De) = \frac{A(4+\beta)}{3D} \quad (31d)$$

For the similarity solutions, I and I_t in the above expressions should be provided according to Eqs. (25a) and (25b). The numerical values for a , b , C_1 and C_2 are furnished in Table 1, as function of De. The effects of De and Pr on the acceleration

Table 2 Coefficient C_3 for isothermal bodies ($Pr = 7$)

De	flat plate (0, 0)	cone (1, 0)	cylinder (0, 1)	sphere (1, 1)
0	0.0498	0.0450	0.0460	0.0428
1	0.0512	0.0465	0.0476	0.0444
2	0.0518	0.0472	0.0483	0.0452
3	0.0515	0.0471	0.0481	0.0451
4	0.0517	0.0474	0.0484	0.0455
5	0.0502	0.0461	0.0470	0.0443
6	0.0487	0.0448	0.0456	0.0430
7	0.0503	0.0465	0.0473	0.0447
8	0.0533	0.0495	0.0503	0.0478
9	0.0577	0.0539	0.0547	0.0521
10	0.0810	0.0572	0.0579	0.0554
20	0.267	0.275	0.267	0.275

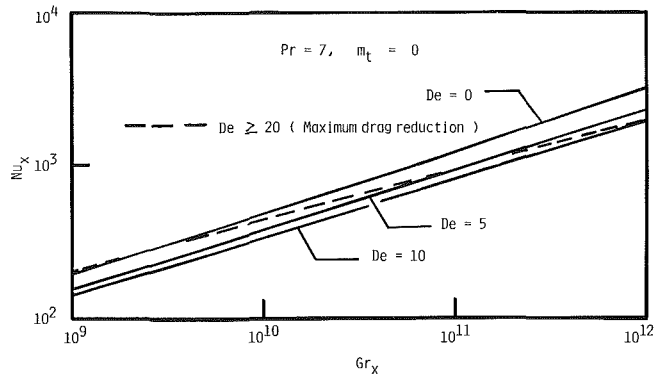
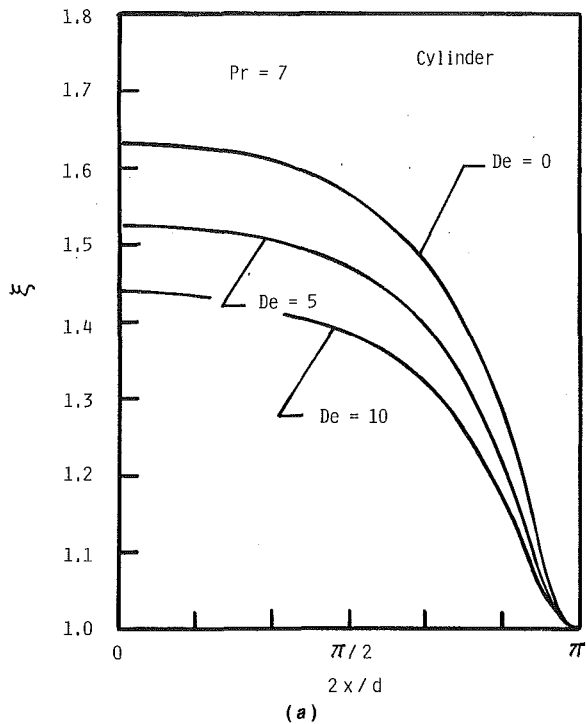
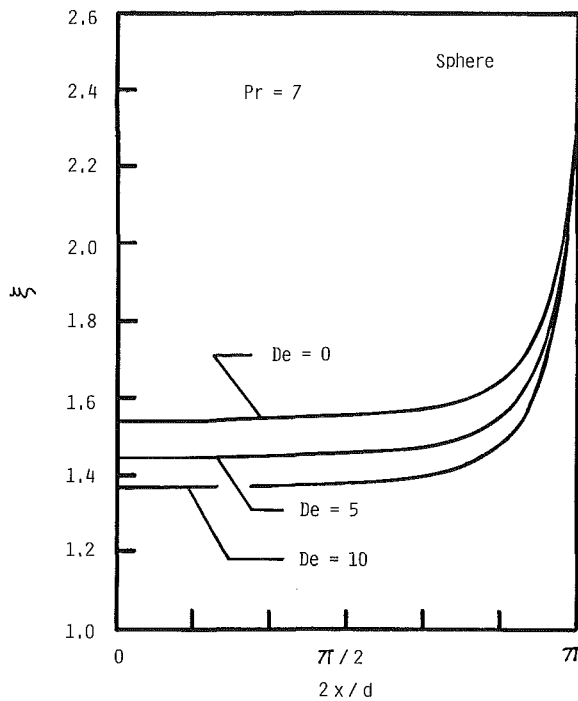


Fig. 3 Heat transfer results for the isothermal vertical flat plate ($Pr = 7$)

parameter are illustrated in Fig. 2, for the case of the isothermal flat plate. As may easily be expected from Eq. (30a), increase in either De or Pr results in decrease in ξ . It should be noted that ξ decreases down to unity as Pr goes to infinity, and the inertia effects vanish totally. The values for the multiplicative constant C_3 (as a function of both De and Pr) were calculated assuming $Pr = 7$, and listed in Table 2 for the isothermal flat plate and cone as well as the stagnation regions of isothermal cylinder and sphere. The table shows that C_3 is nearly constant for $De \leq 7$, and thereafter increases jumping to a high level at $De = 20$. Within the range of $De \leq 7$, the C_3 value goes up slightly and then comes down slightly. This "up-and-down" variation in C_3 should not be considered to be serious, since it is not the slight change in the C_3 value, but the exponent a ($= 1/2(1+\beta)$) that virtually determines the level of Nu_x when Gr_x is large as in the present case of turbulent natural convection. It is to be noted that each set of a and C_3 for $De \leq 10$ follows the expected trend that increase in De results in decrease in Nu_x , as shown in Fig. 3, for the case of isothermal flat plate. The figure clearly shows that the addition of small amounts of a drag-reducing polymer results in reduction in heat transfer as well. This fact, though well known for turbulent forced convection heat transfer to drag-reducing fluids, is being shown for the first time to hold for turbulent free convection as well by the present analysis. In Fig. 3, the asymptote corresponding to maximum drag reduction is indicated by the dashed line. It is interesting to note that, within the Gr_x range considered herein, the heat transfer rate for $De = 10$ is found to be even lower than the rate for the case of the maximum drag reduction. This is not an anomaly because it is known that there is a delay in the onset of drag reduction with increasing drag reducing efficiency. This delay is not pronounced at lower De and hence is not noticeable for $De \leq 10$ within the considered Gr_x range. However, for the maximum drag reduction asymptote, the onset of drag reduction is delayed to a predominant extent and hence the heat transfer rate



(a)

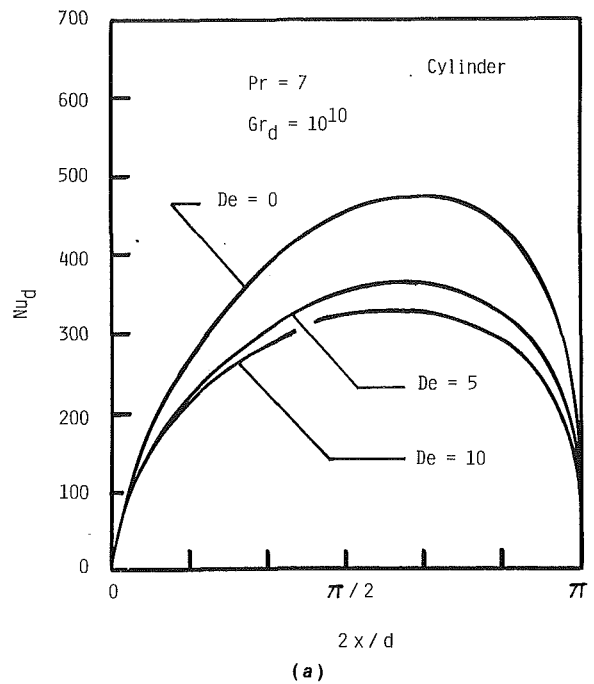


(b)

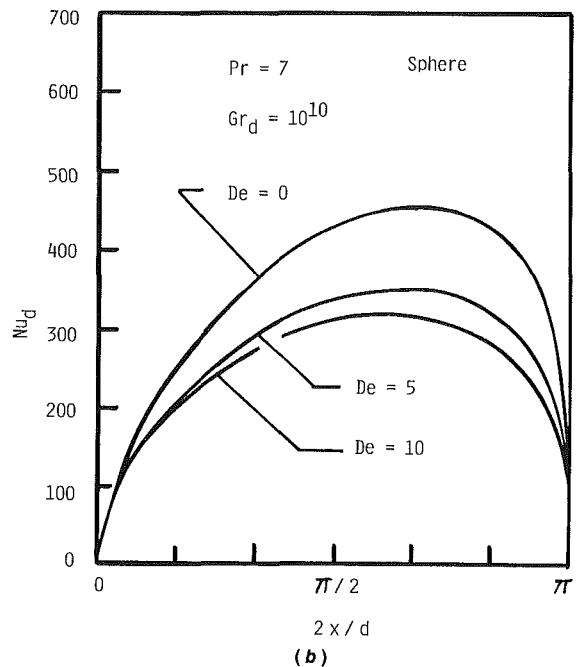
Fig. 4 Peripheral variation of acceleration parameter ($Pr = 7$): (a) isothermal horizontal circular cylinder; (b) isothermal sphere

departure from the Newtonian case would also be delayed to a great extent. It is worth noting that the maximum drag reduction asymptote will, undoubtedly, result in the maximum reduction in the heat transfer rate, but this will occur at much higher Gr_x beyond what is covered in Fig. 3.

There is evidence in the literature (see, for example, Astarita, 1967; Mizushima and Usui, 1977; Ng et al., 1980; Cho and Hartnett, 1982) that the heat transfer reduction is comparatively larger than the drag reduction during turbulent flow through smooth circular pipes. This is likely to hold good even for external flow situations. However, it must be borne in



(a)



(b)

Fig. 5 Peripheral variation of local heat transfer coefficient ($Pr = 7$): (a) isothermal horizontal circular cylinder; (b) isothermal sphere

mind that the present analysis was initiated through a scaling of the terms of the governing equations resulting in Eq. (2d), which implied that the heat and momentum transfer are of the same order. Hence, the results of the present analysis may underpredict the heat transfer reductions to a certain extent.

The averaged Nusselt number $Nu_{L,av}$, which is often more convenient to use for heat transfer estimation, can easily be derived by taking an integrated average over a length L .

$$Nu_{L,av} = \frac{h_{av}L}{k} = \frac{L \int_0^L (Nu_x/x) r^* dx}{\int_0^L r^* dx} = \frac{1+i}{i + \frac{3+j+m_t}{2(1+\beta)}} Nu_x|_{x=L} \quad (32)$$

For illustration of the generality acquired in the present integral method, the aforementioned stepwise iterative calculations were carried out for an isothermal horizontal circular cylinder and also for an isothermal sphere, assuming $Pr = 7$. As already inferred, the boundary values $\xi(0)$ needed for the initiation of integrations were provided by substituting into Eq. (27), $(i, j, m_i) = (1, 0, 0)$ for the cylinder and $(i, j, m_i) = (1, 1, 0)$ for the sphere. The peripheral variations of the acceleration parameter ξ are plotted in Figs. 4(a) and 4(b), for the cylinder and sphere, respectively. The uniform distribution of ξ observed around the front stagnation point is consistent with the argument that has led to the explicit expression for ξ , namely, Eq. (27). The acceleration parameter ξ decreases downstream for the cylinder, while it increases toward the rear stagnation point for the case of sphere. This contrast between the two geometries may be appreciated in consideration of the axisymmetric nature of the spherical body where the boundary layer grows rapidly over the upper half of the spherical surface. Since $\xi \propto g_x(\delta/\tau_w)$, whether ξ decreases or increases toward the rear stagnation point, depends on how drastically (δ/τ_w) increases downstream. The growth rate of the thermal boundary layer thickness is only moderate for the case of the cylinder, while that for the sphere, is so high that ξ increases toward the rear stagnation point, even when g_x vanishes there. The figures also show that the increase in De leads to a decrease in ξ , as in the case of the flat surface. The corresponding variations of the local heat transfer coefficient for the Grashof number based on the diameter $Gr_d = 10^{10}$ are plotted in Figs. 5(a) and 5(b), for the isothermal cylinder and sphere, respectively. The ordinate variable in the figure is chosen to be $Nu_d = h d/k$ (where d is the diameter). On account of the assumption that the turbulent boundary layer starts right from the stagnation point, the local heat transfer coefficient h there is predicted to be zero, despite the fact that it should remain finite since the laminar boundary layer covers the stagnation point. The errors due to this assumption, however, are expected to diminish downstream, by virtue of the parabolic nature of the boundary layer. The local heat transfer rate increases downstream and attains its maximum value somewhere at the upper half of the cylinder, and then decreases abruptly to zero towards the rear stagnation point where the boundary layer grows infinitely. The heat transfer rate increase observed in the lower half of the cylinder is obviously due to the flow acceleration resulting from the increase in the streamwise component of the gravitational force, namely, $g_x = g \sin \alpha$. Very much similar peripheral variations are observed in the case of an isothermal sphere.

Conclusions

In the present effort, the Nakayama–Koyama solution methodology for turbulent free convection from curved surfaces to Newtonian fluids has been successfully extended to the case of drag-reducing fluids. The integrated momentum and energy equations were combined to form an implicit equation, which provides the local variation of the acceleration parameter, namely, the ratio of the buoyancy force to the wall shear force. Possible similarity solutions, in which the parameter remains constant, have been presented in a general form.

Illustrative calculations have been carried out for a flat plate, a cone pointing downward, a horizontal circular cylinder, and a sphere. Numerical values have been furnished for speedy estimation of local and average heat transfer rates. The results thus obtained using the Colburn analogy suggest that the addition of a drag-reducing polymer results in a substantial reduction of turbulent free convective heat transfer. For the nonsimilar flow cases of the isothermal circular cylinder and sphere, integration-stepwise iterative calculations have been carried out, assuming $Pr = 7$ and $Gr_d = 10^{10}$. The results reveal that the acceleration parameter remains very much con-

stant near the front stagnation point, and then either decreases (for the cylinder) or increases (for the sphere) abruptly toward the rear stagnation point. The local heat transfer rate increases from the stagnation point, and attains its maximum somewhere at the upper half of the body, and then decreases down to zero toward the rear stagnation point. The peripheral variations of local heat transfer coefficient are found to be very much similar between the cylinder and sphere.

References

- Argumedo, A., Tung, T. T., and Chang, K. I., 1978, "Rheological Property Measurements of Drag Reducing Polyacrylamide Solutions," *Trans. Soc. Rheol.*, Vol. 22, p. 449.
- Astarita, G., 1965, "Possible Interpretation of the Mechanism of Drag Reduction in Viscoelastic Liquids," *Ind. Eng. Chem. Fundam.*, Vol. 4, pp. 354–356.
- Astarita, G., 1967, "Turbulent Heat Transfer in Viscoelastic Liquids," *Ind. Eng. Chem. Fundam.*, Vol. 6, p. 470.
- Bayley, F. J., 1955, "An Analysis of Turbulent Free Convection Heat Transfer," *Proc. IMechE*, Vol. 169, p. 361.
- Bejan, A., 1984, *Convective Heat Transfer*, Wiley, New York, p. 254.
- Berman, N. S., 1986, "Molecular Interactions in Drag Reduction in Pipe Flows," *Encyclopedia Fluid Mechanics*, Gulf Publishing Co., Vol. 1, Ch. 32, pp. 1060–1082.
- Cebeci, T., and Kahttab, A., 1975, "Prediction of Turbulent Free Convective Heat Transfer From a Vertical Flat Plate," *ASME JOURNAL OF HEAT TRANSFER*, Vol. 97, pp. 469–471.
- Cheeswright, R., 1968, "Turbulent Natural Convection From a Vertical Plane Surface," *ASME JOURNAL OF HEAT TRANSFER*, Vol. 90, pp. 1–8.
- Cho, Y. I., and Hartnett, J. P., 1982, "Non-Newtonian Fluids in Circular Pipe Flow," *Advances in Heat Transfer*, Vol. 15, pp. 59–141.
- Colburn, A. P., and Hougou, O. A., 1930, "Studies in Heat Transfer Particularly as Applied to Tubular Gas Condensers," *Bull. Univ. Wisc. Eng. Ser.* No. 70.
- Darby, R., 1972, "A Review and Evaluation of Drag Reduction Theories," Naval Research Laboratory, NRL Memo Report 2446.
- Eckert, E. R. G., and Jackson, T., 1950, "Analysis of Turbulent Free Convection Boundary Layer on Flat Plate," *Nat. Advisory Comm. Aeronaut. Note* 2207.
- Fisher, M. C., and Ash, R. L., 1974, "A General Review of the Concepts for Reducing Skin Friction, Including Recommendations for Future Studies," *NASA TMX-2894*.
- Fujii, T., 1959, "An Analysis of Turbulent Free Convection Heat Transfer From a Vertical Surface," *Bull. JSME*, Vol. 2, p. 559.
- Gadd, G. F., 1971, "Friction Reduction," *Encyclopedia of Polymer Science and Technology*, New York, Vol. 15.
- George, W. K., and Capp, S. P., 1979, "A Theory for Natural Convection Turbulent Boundary Layers Next to Heated Vertical Surfaces," *Int. J. Heat Mass Transfer*, Vol. 22, pp. 813–826.
- Ghosh, A. K., Kawase, Y., and Ulbrecht, J. J., 1985, "Turbulent Natural Convection Heat Transfer From a Vertical Plate to the Power-Law Fluid at High Prandtl Numbers," *Int. Comm. Heat Mass Transfer*, Vol. 12, pp. 687–696.
- Hoyt, J. W., 1972, "The Effect of Additives on Fluid Friction," *ASME Journal of Basic Engineering*, Vol. 94, pp. 258–285.
- Irvine, T. F., Jr., and Karni, J., 1987, "Non-Newtonian Fluid Flow and Heat Transfer," *Handbook of Single-Phase Convective Heat Transfer*, Wiley, Ch. 20, pp. 20.1–20.57.
- Kato, H., Nishiwaki, N., and Hirata, M., 1968, "On the Turbulent Heat Transfer by Free Convection From a Vertical Plate," *Int. J. Heat Mass Transfer*, Vol. 11, pp. 1117–1125.
- Kawase, Y., and Ulbrecht, J. J., 1984, "Approximate Solution to the Natural Convection Heat Transfer From a Vertical Plate," *Int. Comm. Heat Mass Transfer*, Vol. 11, pp. 143–155.
- Kutateladze, S. S., Kiriyashkin, A. G., and Ivakin, V. P., 1972, "Turbulent Natural Convection on a Vertical Plate and in a Vertical Layer," *Int. J. Heat Mass Transfer*, Vol. 15, pp. 193–202.
- Landahl, M. T., 1973, "Drag Reduction by Polymer Addition," *Proc. 18th Intern. Theor. and Appl. Mechanics*, Moscow, E. Booker and C. K. Mikhailov, eds., p. 177.
- Lin, S. J., and Churchill, S. W., 1978, "Turbulent Free Convection From a Vertical Isothermal Plate," *Numerical Heat Transfer*, Vol. 1, pp. 129–145.
- Lumley, J. L., 1969, "Drag Reduction by Additives," in: W. R. Sears, ed., *Annual Review of Fluid Mechanics*, Annual Reviews Inc., Palo Alto, CA, Vol. 1, pp. 367–384.
- Lumley, J. L., 1973, "Drag Reduction in Turbulent Flow by Polymer Additives," *J. Polymer Sci., Macromolecular Reviews*, Vol. 7, pp. 263–290.
- Mason, H. B., and Seban, R. A., 1974, "Numerical Predictions for Turbulent Free Convection From Vertical Surfaces," *Int. J. Heat Mass Transfer*, Vol. 17, pp. 1329–1336.
- Mizushima, T., and Usui, H., 1977, "Reduction of Eddy Diffusion for Momentum and Heat in Viscoelastic Fluid Flow in a Circular Tube," *Phys. Fluids*, Vol. 20, p. S100.
- Nakayama, A., and Koyama, H., 1985, "An Analysis of Turbulent Free

Convection About Bodies of Arbitrary Geometrical Configurations," *Wärme- und Stoffübertragung*, Vol. 19, pp. 263-268.

Nakayama, A., Koyama, H., and Ohsawa, S., 1983, "An Approximate Solution Procedure for Laminar Free and Forced Convection Heat Transfer Problems," *Int. J. Heat Mass Transfer*, Vol. 26, pp. 1721-1726.

Ng, K. S., Cho, Y. I., and Hartnett, J. P., 1980, "Heat Transfer Performance of Concentrated Polyethylene Oxide and Polyacrylamide Solutions," *AICHE Symp. Series No. 199*, Vol. 76, pp. 250-256.

Noto, K., and Matsumoto, R., 1975, "Turbulent Heat Transfer by Natural Convection Along an Isothermal Vertical Flat Surface," *ASME JOURNAL OF HEAT TRANSFER*, Vol. 97, pp. 621-624.

Papailiou, D. D., and Lykoudis, P. S., 1974, "Turbulent Free Convection Flow," *Int. J. Heat Mass Transfer*, Vol. 17, pp. 161-172.

Patterson, G. K., Zakin, J. L., and Rodrigues, J. M., 1969, "Drag Reduction in Polymer Solutions, Soap Solutions and Solid Particle Suspensions in Pipe Flow," *Ind. Engg. Chem.*, Vol. 61, pp. 22-30.

Plumb, O. A., and Kennedy, L. A., 1977, "Application of a $K-\epsilon$ Turbulence Model to Natural Convection From a Vertical Isothermal Surface," *ASME JOURNAL OF HEAT TRANSFER*, Vol. 99, pp. 79-85.

Ruckenstein, E., and Felske, J. D., 1980, "Turbulent Natural Convection at High Prandtl Numbers," *ASME JOURNAL OF HEAT TRANSFER*, Vol. 102, pp. 773-775.

Sellin, R. H. J., Hoyt, J. W., and Scrivener, O., 1982a, "The Effect of Drag Reducing Additives on Fluid Flows and Their Industrial Applications, Part 1: Basic Concepts," *J. Hydraulic Res.*, Vol. 20, pp. 29-68.

Sellin, R. H. J., Hoyt, J. W., Pollert, J., and Scrivener, O., 1982b, "The Effect of Drag Reducing Additives on Fluid Flows and Their Industrial Applications, Part 2: Present Applications and Future Proposals," *J. Hydraulic Res.*, Vol. 20, pp. 235-292.

Seyer, F. A., and Metzner, A. B., 1969a, "Drag Reduction in Large Tubes and the Behaviour of Annular Films of Drag Reducing Fluids," *Can. J. Chem. Engg.*, Vol. 47, pp. 525-529.

Seyer, F. A., and Metzner, A. B., 1969b, "Turbulence Phenomena in Drag Reducing Systems," *AICHE J.*, Vol. 15, pp. 426-434.

Shenoy, A. V., and Mashelkar, R. A., 1978, "Turbulent Free Convection Heat Transfer From a Flat Vertical Plate to Power-Law Fluid," *AICHE J.*, Vol. 24, pp. 344-347.

Shenoy, A. V., Ranade, V. R., and Ulbrecht, J. J., 1980, "Turbulent Flow of Mildly Viscoelastic Liquids in Curved Tubes," *Chem. Eng. Commun.*, Vol. 5, pp. 268-286.

Shenoy, A. V., and Mashelkar, R. A., 1983, "Engineering Estimate of Hydrodynamic Entrance Lengths in Non-Newtonian Turbulent Flow," *Ind. Eng. Chem. Process Des. Dev.*, Vol. 22, pp. 165-168.

Shenoy, A. V., 1984, "A Review of Drag Reduction With Special Reference to Micellar Systems," *Colloid and Polymer Sci.*, Vol. 262, pp. 319-337.

Shenoy, A. V., 1986a, "Natural Convection Heat Transfer to Power-Law Fluids," *Handbook Heat Mass Transfer*, Gulf Publishing Co., Vol. 1, Ch. 5, pp. 183-210.

Shenoy, A. V., 1986b, "Turbulent Flow of Mildly Elastic Fluids Through Rotating Straight Circular Tubes," *Appl. Sci. Research*, Vol. 43, pp. 39-54.

Shenoy, A. V., and Shintre, S. N., 1986, "Developing and Fully Developed Turbulent Flow of Drag Reducing Fluids in an Annular Duct," *Can. J. Chem. Engg.*, Vol. 64, pp. 190-195.

Shenoy, A. V., 1987, "Effect of Buoyancy on Heat Transfer During Turbulent Flow of Drag Reducing Fluids in Vertical Pipes," *Wärme- und Stoffübertragung*, Vol. 21, pp. 15-18.

Shenoy, A. V., 1988, "Natural Convection Heat Transfer to Viscoelastic Fluids," *Encyclopedia Fluid Mechanics*, Gulf Publishing Co., Vol. 7, Ch. 10, pp. 287-304.

Singh, R. P., 1990, "Drag Reduction and Shear Stability Mechanisms," *Encyclopedia of Fluid Mechanics*, Gulf Publishing Co., Vol. 9, pp. 425-480.

Skelland, A. H. P., 1967, *Non-Newtonian Flow and Heat Transfer*, Wiley, New York, pp. 291 and 415.

Thomas, L. C., and Wood, M. L., 1979, "A New Approach to the Analysis of Turbulent Free Convection Heat Transfer," *Int. J. Heat Fluid Flow*, Vol. 1, pp. 93-96.

Virk, P. S., Merrill, E. W., Mickley, H. S., Smith, K. A., and Mollo-Christiansen, E. L., 1967, "The Toms Phenomenon: Turbulent Pipe Flow of Dilute Polymer Solutions," *J. Fluid Mech.*, Vol. 30, pp. 305-328.

Virk, P. S., 1975, "Drag Reduction Fundamentals, Journal Review," *AICHE J.*, Vol. 21, pp. 625-656.

Wilson, K. C., 1988, "Mechanisms of Drag Reduction in Turbulent Non-Newtonian Pipe Flow," *Encyclopedia Fluid Mechanics*, Gulf Publishing Co., Vol. 7, Ch. 17, pp. 505-523.

Measurements of Velocity and Turbulence in Vertical Axisymmetric Isothermal and Buoyant Jets

J. Peterson¹

Y. Bayazitoglu

Mechanical Engineering & Materials Science
Department,
Rice University,
Houston, TX 77005

The current study examines the transition region of axisymmetric isothermal and buoyant jets of low Reynolds number, directed vertically upward into a stagnant, unstratified ambient. The region in which measurements were obtained allows examination of two types of transition occurring in the jet: from nozzle exit dominated to fully developed, and from momentum to buoyancy-dominated flow. Isothermal velocity data were acquired using a two-channel laser-Doppler anemometer for Reynolds numbers ranging from 850 to 7405. The buoyant cases studied had Froude numbers ranging from 12 to 6425 and Reynolds numbers from 525 to 6500. In each case data were taken from 5 to 44 nozzle diameters downstream. Curve fit approximations of the data were developed by assuming polynomial similarity profiles for the measured quantities. Each profile was individually curve fit because in the transition region under consideration the flow field is not necessarily similar. Profile constants were then curve fit to determine profile variation as a function of nozzle exit parameters and downstream location. These allow prediction of the downstream velocity flow field and turbulent flow field as a function of the Reynolds number, Froude number, and density ratio at the nozzle exit. Profile width and entrainment increased at low Reynolds number. Axial and radial velocity fluctuations were found to increase at low Reynolds number. The buoyant cases studied were found to have lower velocity fluctuations and significantly lower Reynolds stresses than isothermal cases of similar Reynolds number.

Introduction

The study detailed here is of an axisymmetric jet of low Reynolds number exhausting vertically into a stagnant ambient. Both isothermal and buoyant cases were considered. In the present work, the term "isothermal" indicates a jet exiting the nozzle at ambient temperature, driven solely by momentum, while "plume" indicates a natural convective flow above a point heat source, generated solely by buoyancy. Buoyant jets exist between these two limiting cases, as they are driven at the nozzle exit by both momentum and buoyancy. The buoyant jet behaves as if it were driven solely by momentum in an initial, nonbuoyant region. As it moves downstream, the flow undergoes a transition and becomes buoyancy dominated, ultimately exhibiting characteristics of a plume. The specific objective of this study was to examine and quantify parameters that affect entrainment, mixing capacity, and turbulent velocities in the transition region of isothermal and buoyant jet flows. Such flows possessing free shear boundaries are commonly found in the environment. Examples include buoyant jets caused by effluents from principal industrial sources, agricultural or industrial discharges into large bodies of water, and other free shear turbulent mixing and dilution processes. Experimental information is needed to verify predictions of pollutant spread into a stagnant ambient. Jet and plume transition profile width data can be used as a source term in larger numerical models predicting pollutant spread of plumes and jets exhausting into a crossflows. Experimental data on mean flow velocities are also required to assess entrainment modeling

and numerical results, while empirical turbulence data are required for assessment of numerical turbulence models.

Integral type methods are commonly used to predict profile widths and entrainment of jet and plume flows. Rouse et al. (1952), Seban and Behnia (1976), George et al. (1977), Capp (1983), and Papanicolaou and List (1988) have all addressed the entrainment issue for a variety of jet exit conditions. Chen and Rodi (1980) surveyed existing experimental data for vertical buoyant jets. They found that few data were available on axisymmetric jet centerline velocity decay and spread rate for varying buoyancy. Lack of information on the influence of buoyancy and density ratio is also noted. Beuther et al. (1979) and Shabbir (1987) present data on mean as well as turbulent fluxes for the axisymmetric plume. Ramaprian and Chandrasekhara (1989) present mean flow and turbulence measurements for the vertical plane turbulent plume. It was concluded that in the plane plume, buoyancy caused an increase in turbulent intensities and turbulent fluxes. The dimensionless asymptotic peak shear stresses were approximately 50 percent higher in the buoyant case. In the chapter by List (Rodi, 1982) a thorough review is given of flow regions of isothermal and buoyant jets and plumes, and the various approaches commonly used for analysis of the flow characteristics. List notes a lack of experimental information detailing the changes in a jet or buoyant jet through the different regions of flow development. Profile widths are summarized and averaged for a variety of experimental conditions. Insufficient information is available in the literature to detail individually the effects of such nozzle exit conditions as Reynolds number, Froude number, and density ratio on the spread rate and mean flow quantities.

The present study focuses on the transition region of the turbulent isothermal and buoyant axisymmetric jet. It is an examination of the effect of variation of downstream distance,

¹Current address; Department of Mechanical Engineering, University of Florida, Gainesville, FL.

Contributed by the Heat Transfer Division and presented at the ASME Winter Annual Meeting, Dallas, Texas, November 25-30, 1990. Manuscript received by the Heat Transfer Division August 13, 1990; revision received July 1, 1991. Keywords: Jets, Mixed Convection, Plumes.

Reynolds number, Froude number, and density ratio on both the mean flow quantities and turbulent quantities. In order to accomplish this, an extensive database was developed. Data were taken at 11 downstream locations for 4 isothermal and 8 heated cases. Approximately 20 points spanning the jet profile were taken at each axial level. The measurement locations were selected such that two types of transition could be examined: from momentum to buoyancy-dominated flow, and from nozzle-dominated to fully developed similar flow. Reynolds numbers were selected such that, within experimental equipment limitation, buoyancy and momentum at the nozzle exit could be in the same order of magnitude. A two-component laser-Doppler anemometer (LDA) system was used to measure orthogonal velocity components instantaneously. The study extends the range of downstream locations and nozzle exit conditions considered previously (Bayazitoglu and Peterson, 1990). The effect of varying Reynolds number and buoyancy on turbulent fluxes is now also considered.

Experimental Method

The experimental equipment consisted of a flow generator, which exhausted a low-velocity jet of isothermal or heated air into a large stagnant ambient. The experimental apparatus, instrumentation, and procedure are the same as that described by Bayazitoglu and Peterson (1990). The nozzle was conical converging (Fig. 1) of 2 cm diameter. The nozzle exit velocity profile was approximately a "top hat shape." The velocity profile across the "top" portion was slightly depressed in the center due to the conical nozzle. Maximum nozzle exit velocity was encountered at a radius of 0.9 cm, where the time-averaged velocity ranged from 0 to 4 percent above the centerline value. From the radius of 0.9 cm to the edge of the nozzle, the velocity decreased to zero in an approximately linear manner. Nozzle exit turbulence was 1 to 3 percent in the isothermal cases, and 3 percent in the heated cases. Air mass flow rate was controlled

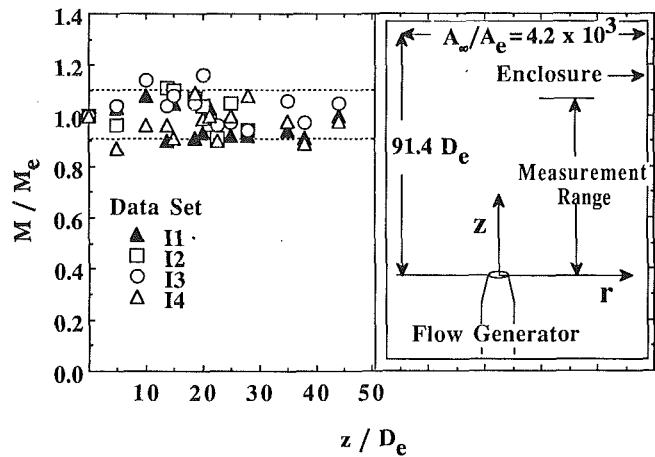


Fig. 1 Total axial momentum

by a rotameter, and the flow was seeded with droplets of corn oil to allow LDA measurement. The nozzle exit temperature was measured with thermocouples. A control point at the nozzle exit was checked prior to and after each set of measurements, and nozzle and exit temperature monitored to insure consistency of nozzle exit conditions. To prevent interference of room drafts and to contain LDA seeding material, the jet exhausted into an enclosure of area to nozzle exit area ratio 4.2×10^3 . The chamber height to nozzle diameter ratio was 91.4. The enclosure had symmetrically spaced vents at the top and bottom. Venting allowed free entrainment of ambient fluid and avoided flow recirculation due to the enclosure. This open system allowed simulation of an infinite stagnant ambient with minimum enclosure interference.

The two-component LDA used for all velocity measurements had a control volume of approximately 5 mm in length and

Nomenclature

a, b, c, d, e = empirically determined curve fit constants (Table 2, and Eqs. (14) and (15))
 A_u = isothermal velocity decay constant (Eq. (5))
 A_∞/A_e = ratio of enclosure area to nozzle exit area (Fig. 1)
 b_u = mean axial velocity profile width (Eq. 9)
 $b_{u'}$ = fluctuating axial velocity profile width (Eq. (10))
 $b_{v'}$ = fluctuating radial velocity profile width (Eq. (11))
 B_u = plume velocity decay constant (Eq. (6))
 C_1 = axial centerline turbulence intensity (Eq. (10))
 C_2 = radial centerline turbulence intensity (Eq. (11))
 C_3 = Reynolds stress constant (Eq. (13))
 D_e = nozzle exit diameter, m

Fr = Froude number (Eq. (1))
 g = gravitational constant, m^2/s^2
 M = momentum flux, m^4/s^2
 M_e = momentum flux at nozzle exit, m^4/s^2
 $Parameter_i$ = profile parameter for curve fitting ($C_1, C_2, C_3, b_u, b_{u'}$, or $b_{v'}$)
 Q = volumetric flow rate, m^3/s
 Re = Reynolds number based on nozzle exit diameter
 S = stratification parameter (Eq. (16))
 r = radial coordinate, m
 T_e = nozzle exit temperature, $^\circ C$
 T_∞ = ambient temperature, $^\circ C$
 u = time mean axial velocity, m/s
 u_i = measured velocity at radial location i , m/s
 $u_{calc\ i}$ = calculated velocity at radial location i , m/s

u' = fluctuating axial velocity, time averaged, m/s
 $u'v'$ = Reynolds stresses, time averaged, m^2/s^2
 U_{cl} = time mean centerline velocity, m/s
 U_e = time mean nozzle exit velocity, m/s
 U = dimensionless time mean axial velocity (Eq. (4))
 v' = fluctuating radial velocity, time averaged, m/s
 w' = fluctuating azimuthal velocity, time averaged, m/s
 z = axial coordinate, m
 Z = dimensionless axial coordinate (Eq. (3))
 β = coefficient of thermal expansion, $^\circ C^{-1}$
 ρ = fluid density, kg/m^3
 ρ_e = nozzle exit fluid density, kg/m^3
 ρ_∞ = ambient density, kg/m^3

Table 1 Experimental conditions

Data Set	U_e (m/s)	T_e (° C)	Reynolds Number	Froude Number	Density Ratio
----------	----------------	----------------	--------------------	------------------	------------------

Isothermal

I1	1.5	21	1960	∞	1.0
I2	0.66	21	850	∞	1.0
I3	2.9	21	3700	∞	1.0
I4	5.7	21	7405	∞	1.0

Heated

H1	3.15	163	2100	150	0.678
H2	1.07	185	625	15	0.644
H3	1.03	227	525	12	0.590
H4	5.09	176	3200	390	0.659
H5	1.78	174	1135	50	0.662
H6	5.35	30	6500	6425	0.977
H7	2.67	33	3325	1150	0.967
H8	3.28	53	3650	650	0.916

0.17 mm in diameter. Uncertainty of mass flow rate was calculated using the method of Moffat (1985), and estimated at 5.3 percent for the isothermal cases considered and 5.4 percent for the buoyant studies.

Use of the LDA was determined to be essential to obtain accurate data. Prior experimentalists have used hot-wire anemometers. However, this instrument is accurate only in the center of the jet as it is incapable of distinguishing flow reversals that occur at the jet edges. Previous measurements in axisymmetric jets have been thought reliable to a radial location of $r/z = 0.15$ (Beuther et al., 1979). In the present work, use of frequency shift with the LDA system allowed accurate measurement of both positive and negative velocities. Probability histograms of velocity readings indicated that significant flow reversals and negative velocities were encountered at the $r/z = 0.1$ radial location, leading to the conclusion that previous hot-wire measurements at this radial location and beyond may be inaccurate. In the current study, velocity readings were taken across the entire jet profile, to a value of $r/z = 0.3$ or 0.4 . Radial symmetry of the flow field was verified by traversing in two different directions. Measurements were taken for four cases of isothermal jet flows and eight cases of heated jet flows. Downstream locations ranged from 5 to 44 nozzle exit diameters. The experimental initial conditions are summarized in Table 1, where the densimetric Froude number is defined:

$$Fr = \frac{U_e^2}{g\beta D_e(T_e - T_\infty)} \quad (1)$$

Initial conditions were selected for the heated sets such that the entire range of transition from momentum to buoyancy-dominated flow could be examined.

The governing conservation equations are the main tool available for assessment of the quality of experimental data. The total momentum at any axial location in the isothermal jet can be written:

$$M = \int_0^\infty \left[u^2 + (u')^2 - \frac{(v')^2 + (w')^2}{2} \right] r dr \quad (2)$$

Demonstration that the isothermal measurements conserve momentum validates that the experimental system is accurately producing the desired flow field: free shear axisymmetric flow into an infinite stagnant ambient. Failure to satisfy the conservation equations would indicate such difficulties as inaccurate and inconsistent control of initial nozzle exit conditions, asymmetry of the flow, or interference of the enclosure with the flow field. The total axial momentum at each downstream location was determined by numerical integration of velocity measurements, and is given in Fig. 1. As uncertainty of nozzle exit mass flow rate was determined to be 5.3 percent for the isothermal cases, it is expected that the total momentum at any axial location will be conserved within 10.6 percent. It can be seen in Fig. 1 that the majority of data sets do conserve momentum within the uncertainty of the experiment. Only data sets that conserved momentum within 10 percent were used for further data reduction.

Theoretical Framework

Chen and Rodi (1980) review existing experimental data for buoyant jets. General scaling laws are developed from a dimensional analysis of the three influential parameters: the weight deficit, initial momentum flux, and the ambient density. As detailed in Appendix A, the general scaling laws developed for buoyant jets in a uniform environment are:

Length:

$$Z = \frac{z}{D_e} Fr^{-1/2} \left(\frac{\rho_e}{\rho_\infty} \right)^{-1/4} \quad (3)$$

Centerline Velocity:

$$U = \frac{U_{cl}}{U_e} Fr^{1/2} \left(\frac{\rho_e}{\rho_\infty} \right)^{-1/4} \quad (4)$$

Here Z and U are dimensionless length and velocity. By introducing empirical decay laws into the scales above, it is demonstrated that the decay laws are valid in both the initial momentum-dominated region and the buoyancy-dominated region far downstream:

Nonbuoyant region:

$$U = A_u Z^{-1} \quad (5)$$

Plume region:

$$U = B_u Z^{-1/3} \quad (6)$$

In the nonbuoyant region, the nondimensional velocity decays in proportion to Z^{-1} , while in the plume region the decay is proportional to $Z^{-1/3}$. This is as expected from standard similarity analysis. The values of the decay constants, A_u and B_u , are determined from experimental data. Between these two asymptotic conditions the transition region will occur. Chen et al. conclude that the scaling laws presented above are appropriate for interpretation of heated jet and plume data. The relationships in physical variables are:

Nonbuoyant region:

$$\frac{U_{cl}}{U_e} = A_u \left(\frac{\rho_e}{\rho_\infty} \right)^{1/2} \left(\frac{z}{D_e} \right)^{-1} \quad (7)$$

Plume region:

$$\frac{U_{cl}}{U_e} = B_u Fr^{-1/3} \left(\frac{\rho_e}{\rho_\infty} \right)^{1/3} \left(\frac{z}{D_e} \right)^{-1/3} \quad (8)$$

The value of A_u has been commonly found to be 6.2 (Chen and Rodi, 1980; Rodi, 1982), and 5.8 (Capp, 1983; Ogino et al., 1980). The plume value of B_u has been stated to be between 3.4 and 3.6 (Beuther et al., 1979; George et al., 1977; Ogino, 1980), while Chen and Rodi determined a plume decay constant of 4.7 (1980).

Data Reduction

Velocity data at each nozzle exit condition and axial location were measured at approximately 20 radial locations spanning the jet. Similarity profiles were assumed for each measurement variable to approximate its variation across the jet profile. For the mean axial velocity, a polynomial profile suggested by the analytic solution (Schlichting, 1979) was used:

$$u(r, z) = \frac{U_{cl}}{\left(1 + \frac{r^2}{b_u^2}\right)^2} \quad (9)$$

Here U_{cl} is the centerline velocity, while b_u is the length used for nondimensionalization of the radial position. It can be seen that b_u is the radial location where the velocity falls to one fourth of its centerline value.

The approximate profiles assumed for the turbulent terms, u' and v' , are written:

$$u'(r, z) = \frac{U_{cl} \left(C_1^2 + \frac{r^2}{b_u^2}\right)^{1/2}}{\left(1 + \frac{r^2}{b_u^2}\right)^2} \quad (10)$$

and

$$v'(r, z) = \frac{U_{cl} \left(C_2^2 + \frac{r^2}{b_v^2}\right)^{1/2}}{\left(1 + \frac{r^2}{b_u^2}\right)^2} \quad (11)$$

It can be seen that C_1 in Eq. (10) is the value of the centerline turbulence intensity in the axial direction. b_u indicates the spread of axial turbulence. Similarly, C_2 in Eq. (11) indicates the value of the centerline turbulence intensity in the radial direction, while b_v measures the width of the radial fluctuating profile. The radial location where $r = b_u$, or $r = b_v$, is the radius at which the square of the local turbulence intensity, (u'^2/u^2 or v'^2/v^2), has increased to 100 percent over the centerline value (u'^2/U_{cl}^2). The final physical variable measured by the LDA is the Reynolds cross stresses, $u'v'$. An approximate profile for this quantity can be found by use of the eddy viscosity assumption:

$$u'v' \propto \frac{\partial u(r, z)}{\partial r} \quad (12)$$

Taking the derivative of the assumed profile for mean axial velocity (Eq. (9)), the approximate profile for the Reynolds stress terms is written:

$$u'v' = \frac{C_3 U_{cl} r}{b_u^2 \left(1 + \frac{r^2}{b_u^2}\right)^3} \quad (13)$$

In the present work, this equation is used as an assumed similarity profile in the same manner as profiles assumed above for u , u' , and v' . The parameter C_3 is assumed to be a constant for each profile. A value of C_3 is determined that minimizes the true error: the average difference between calculated and experimental values. This amounts to determination of an average eddy viscosity across the jet width. In a true eddy viscosity approximation, C_3 would not be constant across the jet but would be a function of radial position. The eddy viscosity model is used here only to obtain an appropriately shaped similarity profile.

Equations (9), (10), (11), and (13) define the similarity profiles for the physical variables measured with the LDA. Prior experimentalists have assumed these profiles to be independent of Reynolds number, Froude number, density ratio, and down-

Table 2 Curve approximation coefficients

	$\frac{b_u}{D_e}$	C_1	$\frac{b_{u'}}{D_e}$	C_2	$\frac{b_{v'}}{D_e}$	$\frac{C_3}{U_e D_e}$
--	-------------------	-------	----------------------	-------	----------------------	-----------------------

Isothermal

a	0.233	0.243	0.549	0.312	0.360	0.337
b	1.010	0.100	0.729	0.147	0.610	0.199
c	-0.059	-0.029	0.009	-0.105	0.119	-0.305
% uncertainty	9.8	9.8	18.9	7.2	12.0	23.8

Heated

a	0.582	0.622	0.521	0.252	1.619	28.7
b	0.882	0.076	0.725	0.040	0.585	0.480
c	-0.176	-0.218	0.012	-0.112	-0.114	-1.145
d	0.057	0.086	0.012	0.071	0.071	0.232
e	-0.179	-0.181	-0.024	-0.254	-0.649	0.148
% uncertainty	9.8	7.5	12.7	8.2	16.9	28.6

stream distance. This indeed has been demonstrated to be the case in the fully developed isothermal or plume flow. Previously no experimental database has been available to perform a detailed examination of the independent effect of each parameter. The objective here is to examine the development and transition of mean flow and turbulent quantities. Therefore for each profile data were reduced separately using a least-squares analysis to determine the values of the coefficients in the equation assumed for that profile: U_{cl} , b_u , C_1 , $b_{u'}$, C_2 , $b_{v'}$, and C_3 . The data reduction procedure is detailed in Appendix B. Reducing each profile separately allowed consideration of each parameter as functions of downstream distance, Reynolds number, Froude number, and density ratio. The profile parameters were then all curve fit using a weighted multiple regression procedure similar the least-squares analysis noted above. Because the data taken are in a region where several complex transitions occur (i.e., laminar to turbulent, momentum to buoyancy dominated, and nozzle exit geometry dominated to similar), the only assumption was a general exponential form:

$$\text{Parameter}_i = a \left(\frac{z}{D_e}\right)^b \text{Re}^c \quad (14)$$

in the isothermal cases, and:

$$\text{Parameter}_i = a \left(\frac{z}{D_e}\right)^b \text{Re}^c \text{Fr}^d \left(\frac{\rho_e}{\rho_\infty}\right)^e \quad (15)$$

in the heated cases, where Parameter_i indicates b_u , C_1 , $b_{u'}$, C_2 , $b_{v'}$, or C_3 . Data reduction in this manner allowed independent assessment of the significance of each parameter in transitional flow without a priori assumptions that would define the exponents. Uncertainty estimates were obtained from an error propagation analysis in some cases and from the standard deviation of the data in others. Error bars on the graphs indicate profile variation when curve approximation coefficients are varied by the percent uncertainty indicated in Table 2.

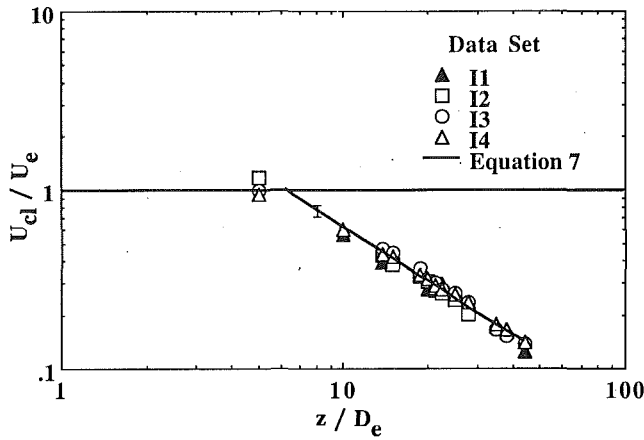


Fig. 2(a) Isothermal centerline velocity

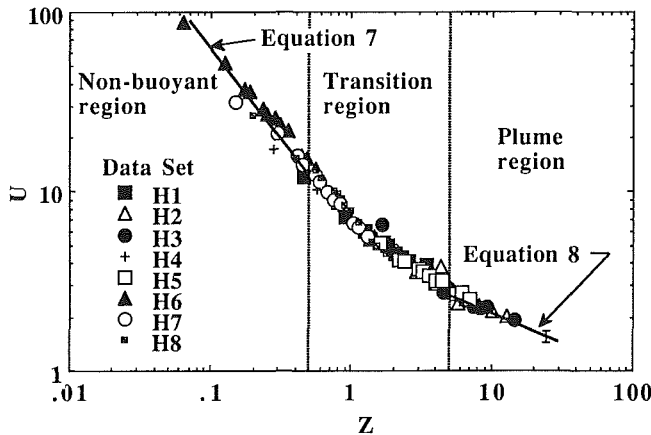


Fig. 2(b) Heated centerline velocity

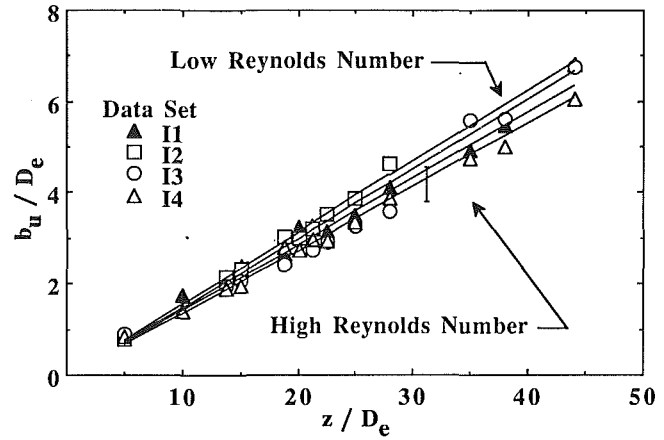


Fig. 3(a) Isothermal mean axial velocity profile width

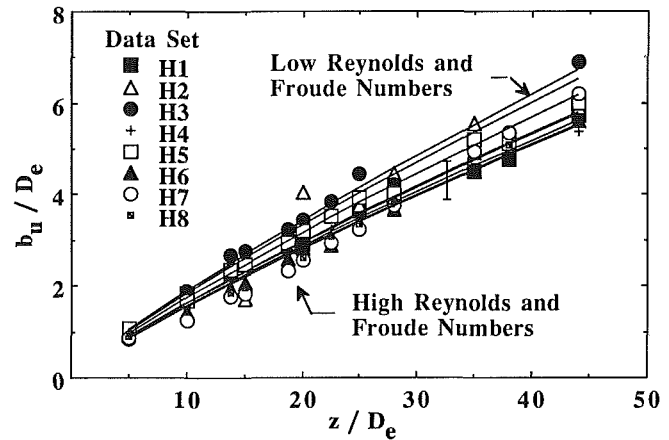


Fig. 3(b) Heated mean axial velocity profile width

Results and Discussion

The initial result considered is that of the centerline mean axial velocity predicted from the curve fit results of Eq. (9). Figure 2(a) shows the centerline velocity decay as calculated for the four isothermal cases considered. It can be seen to be in agreement with Eq. (5) presented by Rodi (1982) and Chen and Rodi (1980) for isothermal and the nonbuoyant region of heated jets, with a proportionality constant $A_u = 6.2$.

Figure 2(b) presents the centerline mean axial velocity decay of a heated jet for the eight cases considered. It can be seen that the scaling laws developed by Chen et al. (Eqs. (3) and (4)) successfully collapse the centerline mean velocity data. The data also support the arbitrary definition by Chen and Rodi of a transition region from $Z = 0.5$ to $Z = 5.0$. Clearly, for $Z < 0.5$, the centerline velocities decay in proportion to Z^{-1} and follow the nonbuoyant decay law of Eq. (5) above. In the plume region, it is seen that velocity decays in proportion to $Z^{-1/3}$, indicating that the mean flow characteristics in this region are indeed dominated by buoyancy. The centerline velocity in the plume region was determined to follow the decay law of Eq. (8), with a proportionality constant, B_u , of 4.7. The value of B_u is 30 percent higher than the value of 3.5 reported as noted above, but corresponds to the 4.7 value determined by Chen and Rodi as reported by Ogino et al. (1980). A parameter for assessing ambient stratification (assuming laminar nozzle exit flow) can be derived from the energy conservation equation (Shabbir, 1987):

$$S = \frac{Q_z}{Q_e} \frac{z}{(T_e - T_\infty)} \frac{dT_\infty}{dz} \quad (16)$$

where Q_z and Q_e indicate the volumetric flow rate at axial

location z ratioed to that at the nozzle exit. This parameter was valued 0.3 and 0.003 by Beuther and by Shabbir (both cited by Shabbir) and 0.15 in the present work. The corresponding B_u values were 3.8, 3.2, and 4.7, respectively. Therefore it appears that the discrepancy in proportionality constant seen in the literature may not be attributed solely to stratification. In the present work, heated data in the plume region exactly follow the $-1/3$ decay law as required by similarity, and collapse consistently in all cases. Data in the transition region can be seen to gradually turn from the Z^{-1} to $Z^{-1/3}$ slope. Transition appears to have been essentially completed by a value of $Z = 2.0$. In the transition region, the recommended relationship that connects nonbuoyant to plume is written:

$$U = 7.88 Z^{-0.654} \quad (17)$$

The mean axial profile widths, b_u , for the isothermal cases are presented in Fig. 3(a). The data for b_u were curve fit to Eq. (14) for determination of constants a , b , and c . The resultant constants are presented in Table 2. It can be seen that the increase in b_u is linear with downstream distance (in Table 2, $b = 1.010$), and weakly dependent on Reynolds number ($c = -0.059$). It can be seen in Fig. 3(a) that the isothermal profile width, and thus entrainment, are increased at low Reynolds number. Indication of increased entrainment at Reynolds numbers below 10,000 has been noted previously by Ricou and Spalding (1961), and current data confirm and quantify this observation. It can be seen that by a distance of 44 nozzle diameters downstream, b_u/D_e increases by approximately 17 percent from the lowest to highest Reynolds number considered. Data and the corresponding curve fit approximations are

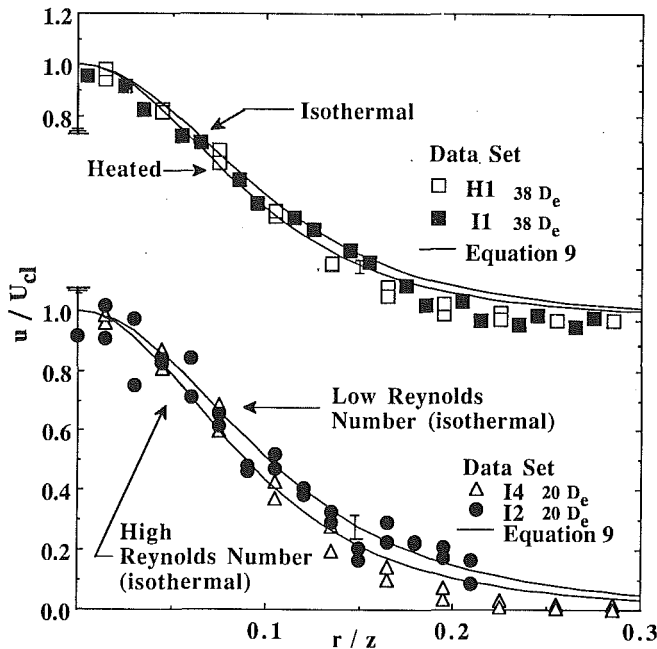


Fig. 4 Effect of buoyancy and Reynolds number on the time mean axial velocity distribution across the jet

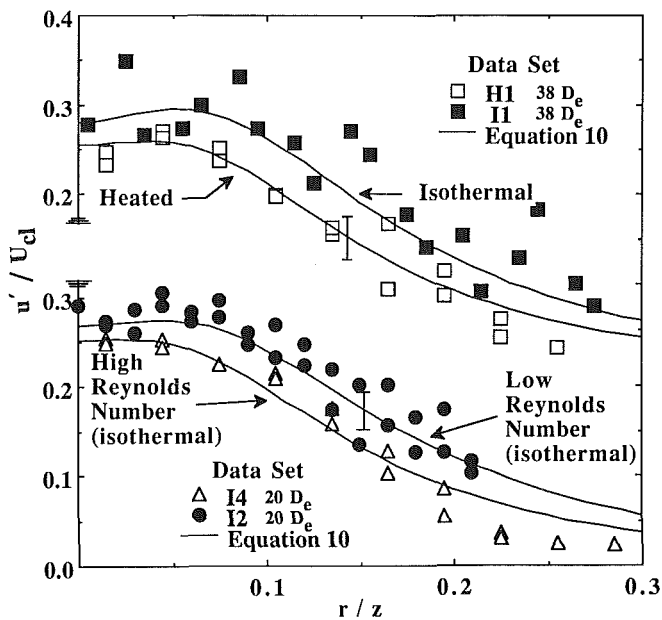


Fig. 5 Effect of buoyancy and Reynolds number on the time-averaged fluctuating axial velocity distribution across the jet

seen in the lower profiles of Fig. 4 for isothermal mean axial velocity at two Reynolds numbers. The increased profile width at lower Reynolds number is visible. Also seen in Fig. 4 is the velocity profile predicted by Eq. (9). The width parameter b_u was calculated from Eq. (14) using the values of a , b , and c , in Table 2. Buoyant mean axial profile widths are seen in Fig. 3(b) to be similar to the isothermal case. Now b_u is a function of downstream distance, Reynolds number, Froude number, and nozzle exit density ratio. The values were curve fit to the form of Eq. (15) to determine the exponents a , b , c , d , and e . Again, the constants for the curve fit approximation are presented in Table 2. It is seen that b_u increases with downstream distance in a nonlinear manner ($b = 0.8820$). Reynolds

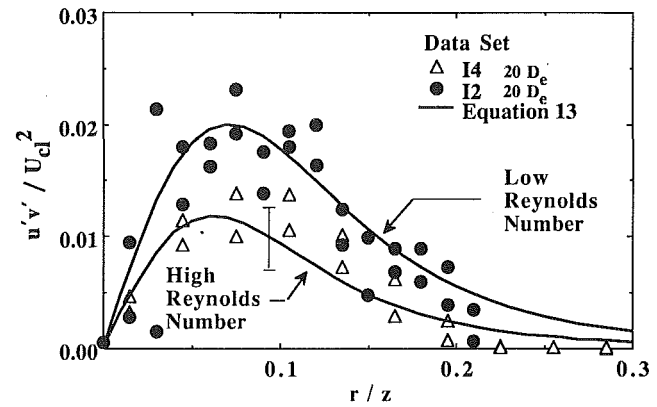


Fig. 6(a) Effect of Reynolds number on the time-averaged Reynolds stress distribution across the isothermal jet

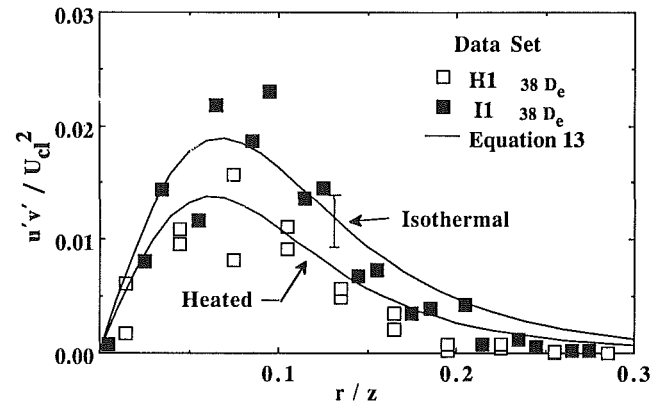


Fig. 6(b) Effect of buoyancy on the time-averaged Reynolds stress distribution across the jet

number and density ratio significantly affect results (exponents $c = -0.176$ and $e = -0.179$), while the effect of Froude number is seen to be less ($d = 0.057$). The smaller effect of Froude number reflects the fact that most of the data considered are in the nonbuoyant and transition region (Fig. 2b). The upper portion of Fig. 4 shows time mean axial velocity for two jets of similar Reynolds number at 44 nozzle diameters downstream. It can be seen that the buoyant jet entrainment at this level is not significantly different from the isothermal.

Now the turbulent flow quantities are considered. Curve fit approximations were developed for the region 10 to 44 nozzle exit diameters downstream. The data from 5 diameters were at substantially lower turbulence, and therefore in the near nozzle region, not the transition region. Figure 5 presents the axial fluctuating velocity for two isothermal cases of different Reynolds number (lower curves) and for an isothermal and buoyant case of similar Reynolds number (upper curves). Considerable scatter can be seen in the data. This is expected since transition from laminar to turbulent flow is unpredictable. The curve fit approximations of the data reflect axial centerline turbulence intensity (C_t) approaching 29 percent. This compares well with the value of 28 to 29 percent observed in the fully developed flow region in previous works (Rodi, 1982). It is also seen that the higher Reynolds number jet exhibits a longer development length to reach the 29 percent asymptotic centerline value. Centerline turbulence intensity of the low Reynolds number jet rises to the fully developed value in a shorter distance. The velocity fluctuations in the low Reynolds number jet measurements and predicted profile are consistently higher than the high Reynolds number jet. The upper curves of Fig. 5 show the axial fluctuating velocity for the heated jet.

The values of the component constants in Table 2 show all four parameters—downstream location, Reynolds number, Froude number, and density ratio—to be significant. The centerline value of 30 percent turbulence intensity attained at the farthest distances downstream compares favorably again with the 28 percent figure reported by Chen et al. Figure 5 shows that axial turbulence was 10 to 15 percent lower in the buoyant jet than in the isothermal jet of similar Reynolds number. The radial fluctuating velocity data and curve fit approximations also indicated that velocity fluctuations increased at lower Reynolds number, and decreased in the heated cases examined. These results are consistent as the higher Reynolds number jet and the buoyant jet both have more momentum driving them than the low Reynolds number isothermal jet. The asymptotic value of C_2 , centerline turbulence intensity in the radial direction, appears to be approximately 0.25 in the isothermal case, a good comparison to the survey results found by Rodi: 0.23 to 0.25. The radial centerline turbulence intensity in the heated case is found to be approximately constant at 20 percent. This apparently low value indicates that the heated flows had not reached similarity in the turbulent terms by a distance of 44 nozzle diameters downstream of the nozzle.

Figures 6(a) and 6(b) show data for Reynolds stresses and the curve approximations. It can be seen in Fig. 6(a) that the isothermal jets of low Reynolds number had Reynolds stresses that were substantially higher than the high Reynolds number cases. This indicates that the turbulence flow field of the high Reynolds number flow is still developing at 20 nozzle diameters downstream. Figure 6(b) shows that the heated jet exhibited significantly lower Reynolds stresses than the isothermal jet. In the current work, the data and curve fit predictions consistently show that high Reynolds number and highly buoyant jets exhibit lower axial and radial fluctuations and lower Reynolds stresses. The magnitude of the variation as seen in Figs. 6(a) and 6(b) indicates that failure to consider Reynolds stress variation would result in large errors in turbulence modeling. The correlation equation presented can be viewed as a specific turbulence model applicable to the axisymmetric buoyant or isothermal jet in the ranges examined. The ability of a general turbulence model to predict the turbulent terms correctly for an isothermal or buoyant axisymmetric jet can be assessed by comparison to the equations developed in the present work.

Conclusions

Isothermal and buoyant jets have been extensively measured to examine the effect of Reynolds number, buoyancy, density ratio, and downstream distance on the mean and turbulent velocity flow field. Correlation equations developed from the database allow prediction of mean axial velocity, fluctuating axial and radial velocities, and Reynolds stresses as a function of downstream distance and nozzle exit conditions. Centerline velocity decay was found to compare favorably with previously accepted values in the isothermal and nonbuoyant cases. A higher centerline velocity was found in the plume region than had been previously measured by some experimentalists, but the decay rate in this region was found to be proportional to $z^{-1/3}$ as expected. Entrainment was found to be increased at low Reynolds numbers in both isothermal and buoyant jets. Examination of the turbulent terms revealed that turbulence consistently increased in low Reynolds number jets over high Reynolds number jets. It was found in the transition region considered here, that buoyancy decreased turbulence in jets of similar Reynolds number. The largest changes were seen in the Reynolds stress terms. Failure to consider the effect of buoyancy, Reynolds number, and density ratio on the turbulent flow field would result in large errors in turbulence modeling. The correlation equations presented here can assist in accurate turbulence modeling and testing.

Acknowledgments

This research was supported in part by the National Science Foundation under grant No. CBT 84-192-3:

References

- Bayazitoglu, Y., and Peterson, J., 1990, "Modified Similarity Prediction of Jet and Buoyant Jet Entrainment in the Transition Region," *Experimental Thermal and Fluid Science*, Vol. 3, pp. 174-183.
- Beuther, P. D., Capp, S. P., and George, W. K., 1979, "Momentum and Temperature Balance Measurements in an Axisymmetric Turbulent Plume," ASME Paper No. 79-HT-42.
- Capp, S. P., 1983, "Experimental Investigation of the Turbulent Axisymmetric Jet," Ph.D. Dissertation, State University of New York at Buffalo, Buffalo, NY.
- Chen, C. J., and Rodi, W., 1980, *Vertical Turbulent Buoyant Jets*, Pergamon Press, New York.
- George, W. K., Alpert, R. L., and Tamanini, F., 1977, "Turbulence Measurements in an Axisymmetric Buoyant Plume," *International Journal of Heat and Mass Transfer*, Vol. 20, pp. 1145-1154.
- Moffat, R. J., 1985, "Using Uncertainty Analysis in the Planning of an Experiment," *ASME Journal of Fluids Engineering*, Vol. 107, pp. 173-178.
- Ogino, F., Takeuchi, H., Kudo, I., and Mizushima, T., 1980, "Heated Jet Discharged Vertically Into Ambients of Uniform and Linear Temperature Profiles," *International Journal of Heat and Mass Transfer*, Vol. 23, pp. 1581-1588.
- Papanicolaou, P. N., and List, E. J., 1988, "Investigations of Round Vertical Turbulent Buoyant Jets," *Journal of Fluid Mechanics*, Vol. 195, pp. 341-391.
- Ramaprian, B. R., and Chandrasekhara, M. S., 1989, "Measurements in Vertical Plane Turbulent Plumes," *ASME Journal of Fluids Engineering*, Vol. 111, pp. 69-77.
- Ricou, F. P., and Spalding, D. B., 1961, "Measurements of Entrainment by Axisymmetric Turbulent Jets," *Journal of Fluid Mechanics*, Vol. 11, pp. 21-32.
- Rodi, W., ed., 1982, *Turbulent Buoyant Jets and Plumes*, Pergamon Press, New York.
- Rouse, H., Yih, C. S., and Humphreys, H. W., 1952, "Gravitational Convection From a Boundary Source," *Tellus* 4, pp. 201-210.
- Schlichting, H., 1979, *Boundary Layer Theory*, McGraw-Hill, New York.
- Seban, R. A., and Behnia, M. M., 1976, "Turbulent Buoyant Jets in Unstratified Surroundings," *International Journal of Heat and Mass Transfer*, Vol. 19, pp. 1197-1204.
- Shabbir, A., 1987, "An Experimental Study of an Axisymmetric Turbulent Buoyant Plume and Investigation of Closure Hypothesis," Ph.D. Dissertation, State University of New York at Buffalo.
- Taylor, J. R., 1982, *An Introduction to Error Analysis*, University Science Books, Mill Valley, CA.

APPENDIX A

General Scaling Laws

The dimensionless length and velocity scales for axisymmetric jets driven by both momentum and buoyancy at the nozzle exit are stated in Eqs. (3) and (4). These are derived by recognizing that in this buoyant flow there are three parameters of importance: initial momentum flux ($\rho_e U_e^2 D_e^2$), weight deficit or buoyancy ($g(\rho_e - \rho_\infty) U_e D_e$), and ambient density (ρ_∞). Forcing these three parameters to combine yielding dimensions of length gives:

$$z = D_e Fr^{1/2} \left[\frac{\rho_e}{\rho_\infty} \right]^{1/4} Z, \quad (A1)$$

where Z is the dimensionless length scale. Similarly, combining the initial momentum, buoyancy fluxes, and ambient density to produce units of velocity:

$$u = U_e Fr^{-1/2} \left[\frac{\rho_e}{\rho_\infty} \right]^{1/4} U. \quad (A2)$$

The centerline velocity of an isothermal round jet is known from similarity analysis to decay inversely with downstream distance. Equations (A1) and (A2) are combined using this relationship with an empirically determined proportionality constant, and recognizing that the quantities U and Z should be independent of density ratio (Chen and Rodi, 1980). The resulting relationship between dimensionless velocity and dimensionless downstream distance for the nonbuoyant region of a buoyant jet is seen in Eq. (5). Similarly, it is known that centerline velocity of an axisymmetric plume decays in pro-

portion to $z^{-1/3}$. Combining this knowledge with an empirical proportionality constant (B_u) and again Eq. (A2) yields Eq. (6): centerline velocity decay in the plume region of a buoyant jet. Equations (5) and (6) are then transformed back into physical variables to determine a centerline velocity relationship (Eqs. (7) and (8)) predicted by this combination of dimensional analysis, similarity solution, and empirical knowledge.

APPENDIX B

Data Reduction Procedure

For the application here, two modifications to the standard least-squares method were made in reducing the data to the form of Eqs. (9), (10), (11), and (13). The first is due to the nonlinear transformations necessary to express the above similarity equations in a form that is linear in the unknown coefficients. While the uncertainty of each velocity measurement is essentially equal, the uncertainty in the transformed (line-

arized) equations is not. Therefore a weighted least-squares method was used (Taylor, 1982), in which each data point was weighted to compensate for the nonlinear transformation. A second modification was made due to the fact that the assumed polynomial profiles are only an approximation of the true physical system. For example, the polynomial approximation of mean axial velocity asymptotically approaches zero, while the jet will reach zero velocity in a finite distance. Therefore, subsets of points were considered for each curve fit, starting with the central points. Successively more points were added until the calculated curve was found to have minimized the true error between all calculated and measured values. For the mean axial velocity the true error to be minimized was defined:

$$\text{True Err} = \sum_{i=1}^N (u_i - u_{\text{CALC } i})^2. \quad (\text{B1})$$

The true error was similarly minimized in curve fit approximations for the other experimental variables: u' , v' , and $u'v'$.

Mixed Convection Through Vertical Porous Annuli Locally Heated From the Inner Cylinder

C. Y. Choi

Department of Aerospace and Mechanical Engineering,
University of Arizona,
Tucson, AZ 85721

F. A. Kulacki

Department of Mechanical Engineering,
Colorado State University,
Fort Collins, CO 80523
Fellow ASME

Mixed convection in a vertical annulus filled with a saturated porous medium is numerically and experimentally investigated. Calculations are carried out under the traditional Darcy assumptions and cover the ranges $10 \leq Ra \leq 200$ and $0.01 \leq Pe \leq 200$. Both numerical and experimental results show that the Nusselt number increases with either Ra or Pe when the imposed flow is in the same direction as the buoyancy-induced flow. When the imposed flow opposes buoyancy-induced flow, the Nusselt number first decreases with an increase of the Peclet number and reaches a minimum before increasing again. Under certain circumstances, the Nusselt number for a lower Rayleigh number may exceed that for larger value. Nusselt numbers are correlated by the parameter groups $Nu/Pe^{1/2}$ and $Ra/Pe^{3/2}$. Good agreement exists between measured and predicted Nusselt numbers, and the occurrence of a minimum Nusselt number in mean flow that opposes buoyancy is verified experimentally.

Introduction

An understanding of the convective heat transfer in porous annuli is essential for its numerous applications in geophysics and energy-related problems, such as insulation of buildings and pipes, design of regenerative heat exchangers, and thermal energy storage systems. Recently, it has received considerable attention for its application in the deep geological disposal of high level nuclear waste. In a proposed repository, a waste canister surrounded by crushed rock (the "engineered" barrier to radionuclide release) can be adequately modeled as a porous annulus. If the repository is flooded by groundwater, mixed convection at low Peclet number is the probable heat transfer mechanism.

Unlike the literature on natural convection in vertical annuli and channels, the literature on the present problem is scant by comparison. Parang and Keyhani (1987) have obtained closed-form solutions for the special case where the inner and outer walls are heated by uniform but unequal heat fluxes. Fully developed flow under the Darcy-Brinkman formulation was considered, and wall effects were parameterized by the group $\epsilon/\gamma^2 Da$. Their solutions indicated that, for certain values of γ and heat flux ratio, the heat transfer coefficient on one of the walls may diminish.

Clarksean et al. (1988) conducted an experimental and numerical study of mixed convection for a large gap ($\gamma = 11$) annulus for which the inner cylinder is adiabatic and the temperature of the outer cylinder is constant. The study was motivated by the development of geothermal energy extraction techniques. For $0.05 < Ra/Pe < 0.5$, Nusselt numbers were proportional to $(Ra/Pe)^{-0.5}$, which indicated that forced convection dominated the heat transfer mechanism. Reda (1988) also investigated mixed convection for large radius ratio ($\gamma = 23.7$). Using the total disappearance of buoyancy-induced up-flow as a criterion and results of both experimental and numerical analyses, he concluded that the transition from mixed to forced convection in opposing flow occurs when $Ra/Pe = 0.5$, regardless of the heated length or power input. However, the results for aiding flows and the heat transfer coefficients were not presented. Recently, Choi and Kulacki (1992) numerically investigated inertial and viscous effects for the same geometry. They observed an increase of the Nusselt number

due to the viscous and inertial effects in a limited range of the Peclet number for opposing flows.

Muralidhar (1989) has numerically examined the effects of a superimposed mean flow in the direction of buoyancy-induced flow ("aiding" flow) in an annulus with constant temperature inner and outer walls ($T_i > T_o$). He considered the Darcy flow model for $0 < Ra < 500$ and $0 < Pe < 10$ for height gap = 10 and $\gamma = 1$ ($r_o/r_i = 2$). Generally, Nusselt numbers occurred for $0 < Pe < 1$. Muralidhar's results indicate that the region of mixed convection is defined by $Ra > 100$ and $0 < Pe < 10$.

The purpose of the present study is to examine the influence of both aiding and opposing external flows on the buoyancy-induced natural convection in vertical porous annuli. The effects of radius ratio are taken into account in a numerical study. Measurements of heat transfer coefficients in aiding and opposing flows cover the free to forced convective heat transfer regimes.

Formulation and Numerical Method

The geometry considered is a vertical porous annulus in which a constant-flux heat source of finite length is located on the inner cylinder, while the outer cylinder is cooled at a constant temperature. The porous medium is assumed to be fully saturated and to possess homogeneous and isotropic properties. A pressure-driven external flow, either with or opposite to buoyancy force, is maintained through the porous channel. The physical and mathematical models are sketched in Fig. 1. In the present study, the heater length equals the annular gap.

Based on the Darcy law and Boussinesq approximation, the dimensionless governing equations are

$$\frac{\partial}{\partial R} \left(\frac{1}{\gamma R + 1} \frac{\partial \psi}{\partial R} \right) + \frac{\partial}{\partial Z} \left(\frac{1}{\gamma R + 1} \frac{\partial \psi}{\partial Z} \right) = - \frac{Ra}{Pe} \frac{\partial \theta}{\partial R}, \quad (1)$$

$$\frac{\partial}{\partial R} \left(\theta \frac{\partial \psi}{\partial Z} \right) - \frac{\partial}{\partial Z} \left(\theta \frac{\partial \psi}{\partial R} \right) = \frac{1}{Pe} \left[\frac{\partial}{\partial R} \left\{ (1 + \gamma R) \frac{\partial \theta}{\partial R} \right\} + \frac{\partial}{\partial Z} \left\{ (1 + \gamma R) \frac{\partial \theta}{\partial Z} \right\} \right], \quad (2)$$

where Ra , Pe , and coordinate variables are based on D .

Boundary conditions are

Contributed by the Heat Transfer Division for publication in the JOURNAL OF HEAT TRANSFER. Manuscript received by the Heat Transfer Division February 12, 1991; revision received June 22, 1991. Keywords: Geophysical Heat Transfer, Mixed Convection, Porous Media.

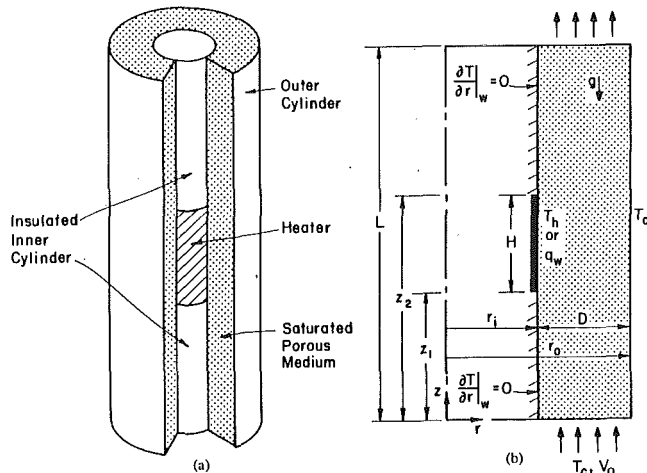


Fig. 1 A vertical porous annulus with a finite heat source of a length $H = D$: (a) Schematic figure, (b) Two-dimensional model with aiding external flow.

$$R = 0 \left[\begin{array}{l} Z_1 \leq Z \leq Z_2: \psi = 0, \frac{\partial}{\partial R} = -1 \\ \left\{ \begin{array}{l} 0 \leq Z \leq Z_1 \\ Z_2 \leq Z \leq L/D \end{array} \right\}: \psi = 0, \frac{\partial \theta}{\partial R} = 0 \end{array} \right], \quad (3a)$$

$R = 1, 0 \leq Z \leq L/D$:

$$\theta = 0, \left\{ \begin{array}{l} \psi = -\left(1 + \frac{\gamma}{2}\right) \text{ for aiding flows} \\ \psi = 1 + \frac{\gamma}{2} \text{ for opposing flows} \end{array} \right\}, \quad (3b)$$

$$0 \leq R \leq 1: \left[\begin{array}{l} \left\{ \begin{array}{l} Z = 0: \psi = -\left(R + \frac{\gamma R^2}{2}\right), \theta = 0 \\ Z = L/D: \frac{\partial \psi}{\partial Z} = 0, \frac{\partial \theta}{\partial Z} = 0 \end{array} \right\} \text{ for aiding flows} \\ \left\{ \begin{array}{l} Z = 0: \frac{\partial \psi}{\partial Z} = 0, \frac{\partial \theta}{\partial Z} = 0 \\ Z = L/D: \psi = \left(R + \frac{\gamma R^2}{2}\right), \theta = 0 \end{array} \right\} \text{ for opposing flows} \end{array} \right] \quad (3c)$$

Nomenclature

A_h = area of the heat source, m^2
 A_{cs} = cross-sectional area of the porous annulus, m^2
 d = dimensionless average particle diameter
 D = gap width = $r_o - r_i$, m
 Da = Darcy number = K/D^2
 h = heat transfer coefficient, W/m^2K
 H = heater length, m
 k = thermal conductivity, W/mK
 K = permeability of porous medium = $\epsilon^3 d^2 / 180 (1 - \epsilon)^2$, m^2
 Nu = Nusselt number = hD/k_m
 P = pressure, Pa
 P_{net} = net power, W
 Pe = Peclet number = $V_o D / \alpha$
 q = uniform heat flux, W/m^2
 Q = flow rate, m^3/s
 r = cylindrical coordinate, m
 R = dimensionless distances on r axis = $(r - r_i)/D$

Ra = Rayleigh number for porous medium, $g\beta k D^2 q / \alpha \nu k_m$
 T = temperature, $^\circ C$
 u, v = r and z direction dimensional velocity, m/s^2
 U = R -direction dimensionless velocity = $\{1/(1 + \gamma R)\} (\partial \psi / \partial Z)$
 V_o = Z -direction dimensionless velocity = $\{-1/(1 + \gamma R)\} (\partial \psi / \partial R)$
 V_0 = inlet velocity m/s
 z = vertical coordinate, m
 z_1 = bottom of the heater, m
 z_2 = top of the heater, m
 Z = dimensionless distance on z axis = z/D
 α = thermal diffusivity of porous medium = $k_m / \rho C$, m^2/s
 β = coefficient of thermal expansion, $^\circ C^{-1}$
 γ = radius ratio parameter = D/r_i

ϵ = porosity
 ζ = convergence criterion
 θ = dimensionless temperature = $(T - T_o) / (qD/k_m)$
 μ = dynamic viscosity, $kg/m \cdot s$
 ν = kinematic viscosity = μ/ρ , m^2/s
 ρ = density of fluid, kg/m^3
 ψ = stream function

Subscripts

c = cold outer wall
 f = fluid
 h = heat source
 i = inner cylinder
 m = porous medium
 o = outer cylinder
 s = solid

Superscripts

$\bar{\quad}$ = average
 N = number of iteration

where the downstream boundary conditions are based on the fact that the flow becomes parallel again after releasing a large portion of energy to the outer wall far downstream of the heat source, i.e., axial conduction is negligible for downstream (Roache, 1975).

In computation, the upper and lower boundaries should be located far enough from the heat source to satisfy the above boundary conditions. A series of numerical experiments indicate that the improvement in the Nusselt number is less than 2 percent when the distances from the upper and lower ends of the heat source to the upper and lower boundaries are greater than seven and four times the heater length, respectively. For the present numerical study, distances of fifteen and five times the heater length are allowed for the upper and lower boundaries. With these choices, the boundary conditions are well satisfied at reasonable computational cost without sacrificing accuracy. However, the minimum distances have been chosen for the experimental apparatus, which will be described later, in order to reduce the cost of materials. It should be noted that Ettfagh and Vafai (1988) and Vafai and Ettfagh (1990) numerically tested the boundary conditions in open-ended cavities. The latter, in particular, investigated the effect of a spatial domain extension by increasing the size of the open-ended region. Through their extensive numerical experiments, they found that the heat transfer results were independent of the computational domain beyond a certain extension.

A finite difference method has been employed to solve the governing equations given above. The dimensionless equations are discretized using the control volume approach (Patankar, 1980). The convergence criterion, ζ , has been determined from a series of numerical calculations, i.e.,

$$|X^N - X^{N+1}|_{\max} < \zeta, \quad (4)$$

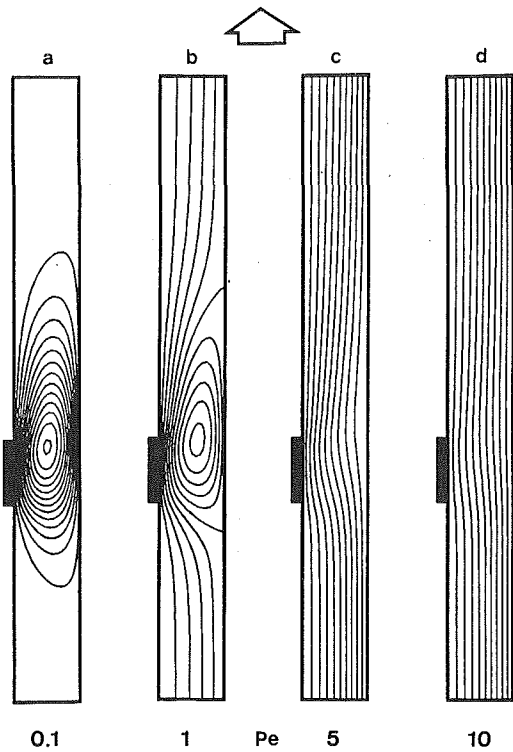


Fig. 4 Streamlines for aiding flow. $Ra = 50$, $\gamma = 1$. (a) $\Delta\psi = 2$, (b) $\Delta\psi = 0.3$, (c) $\Delta\psi = 0.15$, (d) $\Delta\psi = 0.15$.

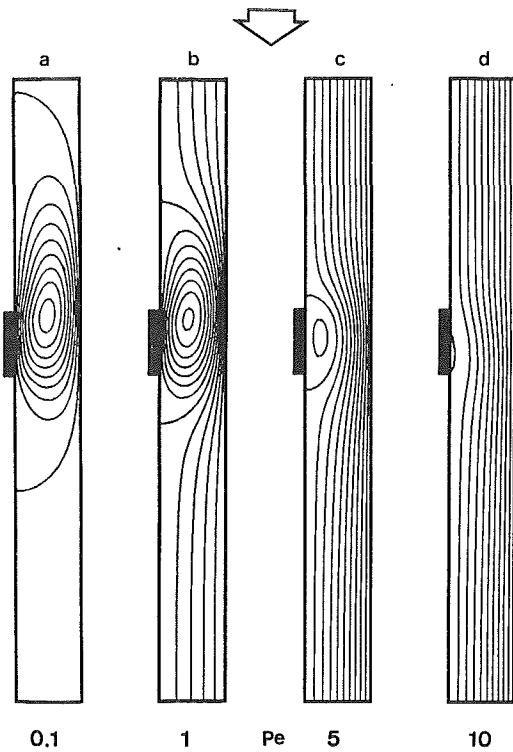


Fig. 6 Streamlines for opposing flow. $Ra = 50$, $\gamma = 1$. (a) $\Delta\psi = 2$, (b) $\Delta\psi = 0.3$, (c) $\Delta\psi = 0.15$, (d) $\Delta\psi = 0.15$.

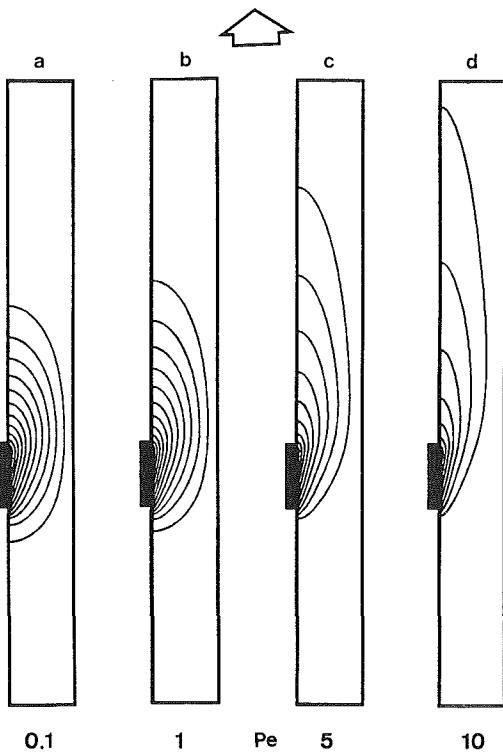


Fig. 5 Isotherms for aiding flow. $Ra = 50$, $\gamma = 1$. (a)-(d) $\Delta\theta = 0.03$.

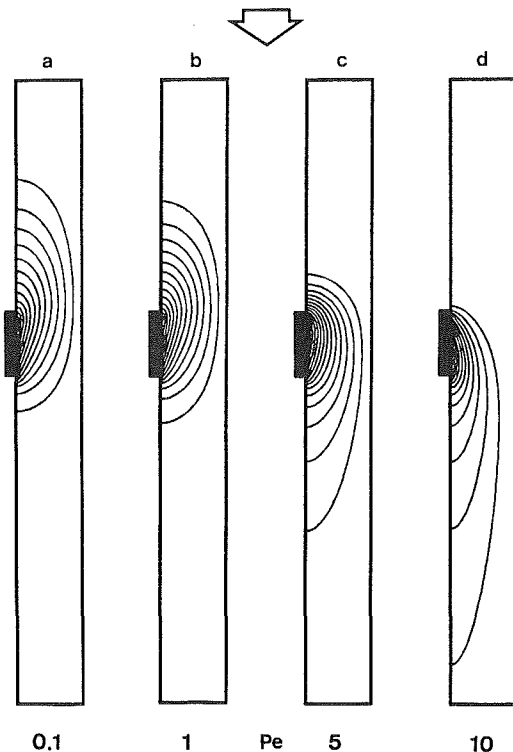


Fig. 7 Isotherms for opposing flow. $Ra = 50$, $\gamma = 1$. (a)-(d) $\Delta\theta = 0.03$.

temperature variations, the outer cylinders are wrapped with insulation. A 1270 mm \times 152.4 mm o.d. \times 6.35 mm thick Plexiglas tube has been used as a main inner cylinder. It is supported by a 181.2 mm \times 152.4 mm o.d. brass cylinder. Six strip heaters, each 482.6 mm \times 25.4 mm, are mounted on the grooved surface of the main inner cylinder to serve as heat sources. Each is designed to provide a uniform heat flux and

is individually controlled. For the present study, the heaters numbered 3, 4, and 5 in Fig. 2 are used. To avoid radial and axial heat conduction, a layer of polystyrene insulation has been installed between the heaters and grooved surface.

Duplex insulated copper-constantan (type T) thermocouples have been used for all temperature measurements, and Fig. 3 illustrates their arrangement in the apparatus. Since the cal-

ulation of Nusselt numbers requires the knowledge of average surface temperature of the heater, seven thermocouples are placed on the surface of each heater. To minimize the interference to the flow field, fine gage thermocouple wires (36 Ga, 0.1270 mm dia) have been used. Five arrays of eight thermocouples are used to measure the temperature of the outer cylinder, and relatively thick thermocouple wires (20 Ga) are used.

Thermocouple junctions are attached to the surface of the heater and the main outer cylinder by applying high-temperature, high-thermal-conductivity epoxy adhesive. Additional details of the experimental apparatus, its operation, and related instrumentation and data processing are provided by Choi (1990).

Experiments have been performed using randomly oriented 3-mm-dia glass beads and water to comprise the porous medium. A series of tests indicates that the accuracy of each temperature reading is within $\pm 0.2^\circ\text{C}$, and the fluctuation of each thermocouple reading is less than 0.05°C . The permeability used in the calculation of Ra is based on the Kozeny-Carman equation, and the thermal conductivity is based on the mean thermal conductivity, k_m based on the mixture rule

$$k_m = \epsilon k_f + (1 - \epsilon)k_s \quad (5)$$

It has been reported that this model, although simple in form, gives very responsible values of the stagnant thermal conductivity as long as there is no significant difference between k_f and k_s . In the present experiments, $0.63 < k_f/k_s < 0.65$.

Values of temperature used to determine dimensionless groups are averages of three readings over a five minute period. In the calculation of the Nusselt, Rayleigh, and Peclet numbers, the values of fluid properties are determined at the average fluid temperature $(T_c + T_h)/2$. The net power to the heaters, P_{net} , is used in calculating the Rayleigh and Nusselt numbers. Thus,

$$\text{Ra} = \frac{g\beta P_{\text{net}} D^2 K}{\nu \alpha k_m A_h} \quad \text{and} \quad \text{Nu} = \frac{P_{\text{net}} D}{A_h (\bar{T}_h - T_c) k_m}$$

The Peclet number is determined from

$$\text{Pe} = \frac{QD}{A_{cs}\alpha} \quad (7)$$

where Q and A_{cs} denote the flow rate of forced flow and the cross-sectional area of the annulus, respectively.

After the preparation of the test section is completed, power to the heaters and variable speed micropump are turned on. Voltages supplied to the heaters are carefully controlled to obtain a desired Rayleigh number, while the micropump is adjusted to achieve a desired flow rate through the annulus. To achieve the constant temperature, T_c , along the outer cylinder, the flow rate of cooling water is controlled carefully, and deviations from the average temperature along the outer cylinder are generally within $\pm 0.3^\circ\text{C}$ at steady state. Sufficient time, typically three to twelve hours, has been allowed in order to let the system reach a steady state. The Nusselt and Rayleigh numbers are considered to have reached constant values when fluctuations of T_h and T_c are negligible.

Based on the law of summation of fractional errors, estimated experimental uncertainties are 4 percent and 3.9 percent for the Rayleigh and Peclet numbers, respectively, while the uncertainty for the Nusselt number ranges from 5 to 13.6 percent. The uncertainty in the Nusselt number is a maximum when the temperature difference between the heat source and the outer cylinder is minimum; thus, the higher uncertainties are generally expected at either the low Rayleigh numbers or the high Peclet numbers.

Results and Discussion

The effects of aiding and opposing imposed flows on buoyancy-induced convection can be well visualized in Figs. 3–6 at

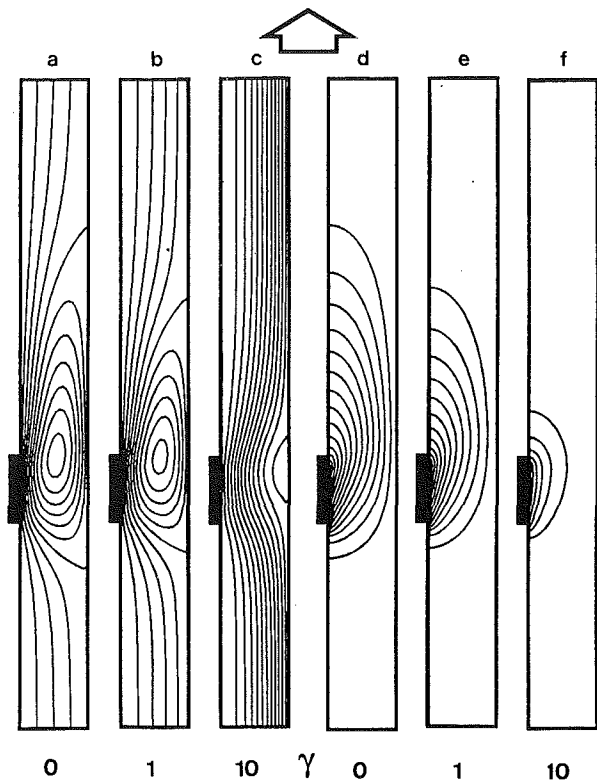


Fig. 8 Curvature effects on velocity and temperature fields for aiding flow. Ra = 50. (a), (b) $\Delta\psi = 0.25$, (c) $\Delta\psi = 0.5$, (d)–(f) $\Delta\theta = 0.03$.

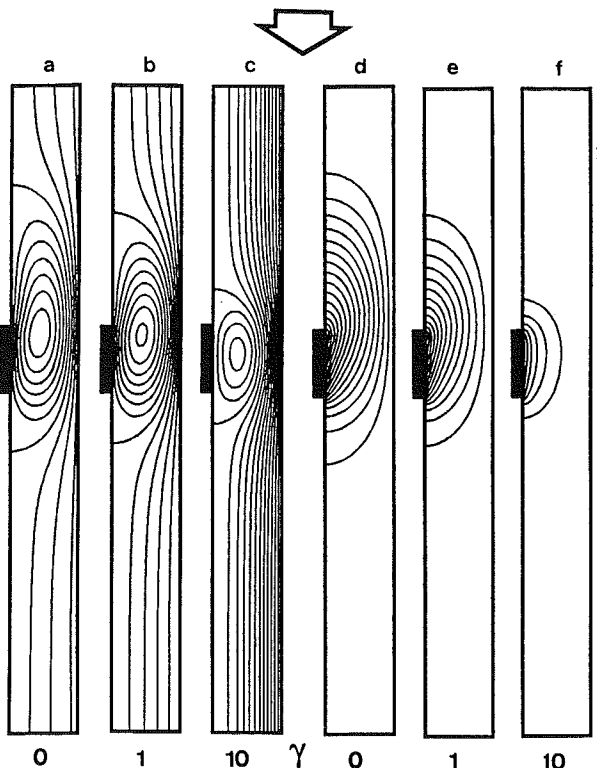


Fig. 9 Curvature effects on velocity and temperature fields for opposing flow. Ra = 50. (a), (b) $\Delta\psi = 0.3$, (c) $\Delta\psi = 0.5$, (d)–(f) $\Delta\theta = 0.03$.

Ra = 50. When the Peclet number is small, flow and temperature fields retain the major characteristics of natural convection. With the heat source located on the left side, i.e., the inner cylinder, the rotational direction of the recirculation cell is clockwise. As the Peclet number increases, an influence of

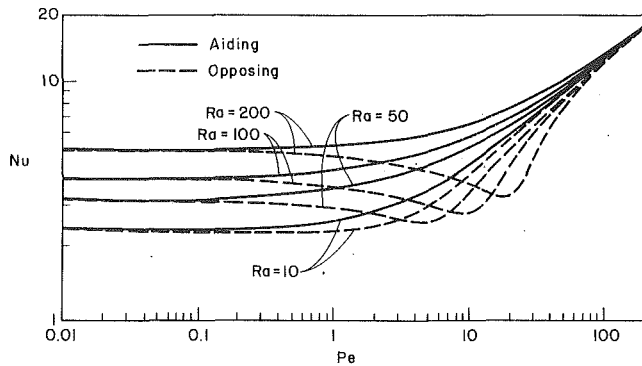


Fig. 10 Nusselt numbers for $\gamma = 1$

the flow direction on the location of the recirculating cell is observed; i.e., for aiding flows, the cell is pushed toward the outer wall (Fig. 4b) as the upflow is swept toward the heat source by the clockwise circulation cell. Thus, the cold flow directly contacts the surface of the heat source, and the convective heat transfer coefficient is expected to be enhanced as Pe increases.

For opposing flows, the downward throughflow again follows the clockwise natural convection cell and is swept toward the outer cylinder surface. Consequently, the natural convection cell is pushed toward the heat source (Fig. 6(b)). The "trapped" recirculating cell near the heat source raises the average temperature of the heat source, and thus the heat transfer coefficient is reduced. Reda (1988) also reported similar development in streamline patterns as the rate of the downflow increases. As the Peclet number increases further, the strength of the recirculating cell becomes weaker for both aiding and opposing flows (Figs. 4c and 6c). At $Pe = 10$, the natural convection cell finally vanishes (Figs. 5d and 7d); this indicates the weakening buoyant forces as the momentum of the external flow becomes large. As shown in Figs. 5 and 7, wall plumes move downstream from the region next to heat source as Pe increases.

Curvature effects on flow and temperature fields are also significant, as shown in Figs. 8 and 9. As the radius ratio parameter increases, the strength of the convective cell decreases considerably for both aiding and opposing flows. Based on this observation, it is expected that the convective cell will eventually vanish when the radius ratio parameter approaches infinity; i.e., the influence of the cold outer wall diminishes. Thus, the convective heat transfer coefficient is expected to approach an asymptotic value as the radius ratio parameter approaches infinity.

Nusselt number as a function of the Peclet number is shown in Fig. 10. The Nusselt number is primarily a function of the Rayleigh number in the natural convection regime ($Pe < 0.1$, approximately), while it is a function of the Peclet number in the forced convection regime ($Pe > 50$, approximately).

For aiding flows, as mentioned earlier, the cold external flow always contacts the surface of the heat source; therefore, an increase in either the Rayleigh or the Peclet number enhances the heat transfer coefficient. For opposing flows, the external flow always acts against buoyancy, and buoyancy-induced circulation is suppressed and the natural convection cell is trapped near the heat source. Such an interaction leads to a reduction in the Nusselt number until the cold opposing flow starts to contact the surface of the heat source. For $Ra = 50$, as an example, Fig. 10 shows that the Nusselt number reaches a minimum point when the Peclet number reaches approximately six and seven, or Figs. 6(c, d), imply that the direct contact of opposing flow to the heat source starts to occur in the same range of Peclet numbers. After this point, the Nusselt number increases, since the cold external flow transfers heat away from

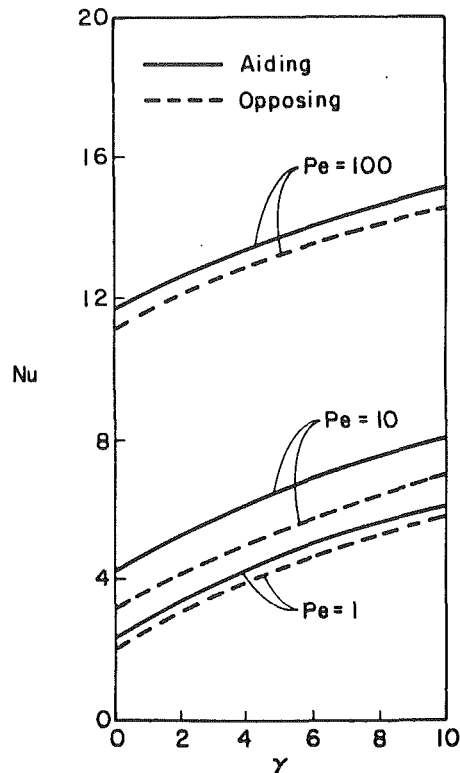


Fig. 11 Effects of radius ratio on the Nusselt number. $Ra = 50$.

the heat source and forced convection eventually dominates the flow and the temperature fields.

Figure 10 further indicates that the deviation of the Nusselt number from the natural and forced convection asymptotes occurs at the higher Peclet numbers as Ra increases for both aiding and opposing flows. It is obvious that stronger forced flow is needed in order to influence, or wipe out, the vigorous natural convection cell at the high Rayleigh number. It is also apparent that the start of mixed or forced convection in aiding flow occurs at higher Peclet numbers than those for opposing flow. Later the "5 percent deviation rule" by Sparrow et al. (1959) will be applied to determine the mixed convection region and confirm these observations.

The effects of curvature on the heat transfer results are shown in Fig. 11. It is observed that the enhancement of the Nusselt number occurs with an increase in the radius ratio parameter. Nusselt numbers increase as $\gamma \rightarrow 10$ and eventually approach asymptotic values when $\gamma > 10$, which corresponds to the case that the inner cylinder is located in an infinite porous medium. Minkowicz and Cheng (1976) reported a similar result with a different boundary condition, i.e., the surface temperature of the cylinder varying as the function of a vertical coordinate.

The full range of convective heat transport, from natural to forced convection, is covered by the present experiments, i.e., $0.1 \leq Pe \leq 150$ and $Ra = 50, 100, 150$, and 200 . The temperature distribution on the heater surface is important in obtaining the heat transfer results not only because the Nusselt number is inversely proportional to the average dimensionless temperature on the heater, but also because the Rayleigh and Peclet numbers are functions of temperature-dependent fluid properties. In general, the temperature distribution on the heater surface is greatly influenced by the power input and the velocity of the forced flow. Figures 12(a) and 12(b) demonstrate the temperature distribution on the heater surface for selected cases. The experimental data are in good agreement with the numerical results at the low Peclet number ($Pe = 1$ and 10), and the deviations between these two results are generally within

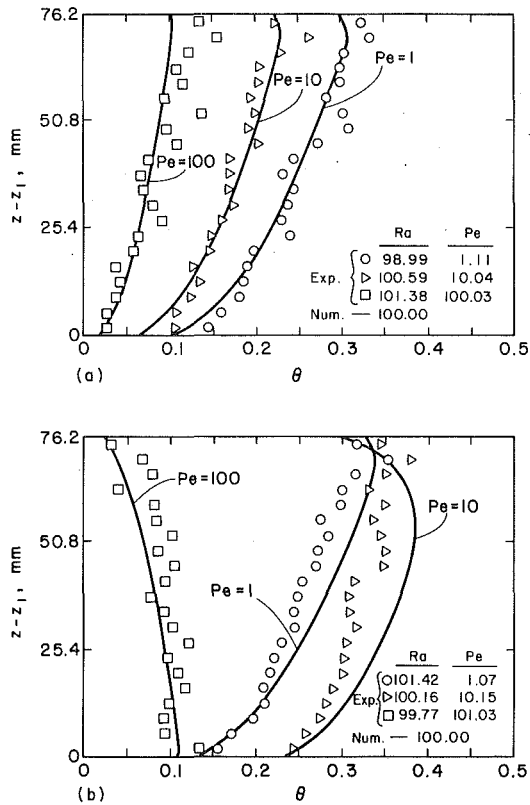


Fig. 12 Temperature variation on the heated surface. Ra = 100. (a) Aiding Flow (b) Opposing Flow.

10 percent. Dimensionless temperatures decrease as the Peclet number increases for aiding flow, but for opposing flow, they increase along the heater surface toward the minimum value of the Nusselt number (i.e., at $Pe = 10$). With an increase in Pe to 100, the percentage differences in numerically and experimentally obtained Nusselt numbers are pronounced for each case. Clearly, Figs. 12(a) and 12(b) indicate that the experimental measurements of dimensionless temperature at $Pe = 100$ are larger than the numerical predictions; i.e., the measured Nusselt numbers are expected to be lower than those obtained numerically, which will be discussed later. For opposing flows, the maximum temperature on the heated surface moves down the heater surface as the Peclet number increases. Since forced convection is fully dominant at $Pe = 100$, the maximum and minimum dimensionless temperature points for aiding and opposing flows are at opposite points on the heater surface.

For selected cases ($Ra = 100$ and 200), heat transfer results in terms of the Nusselt number on the heated surface as a function of the Peclet number are presented in Figs. 13(a, b). The experimental data agree quite well with the numerical results at the lower Peclet numbers ($Pe < 50$). The maximum difference between the numerical predictions and experimental measurements is 15 percent, but mostly they are within 10 percent. For opposing flow, predictions agree well with the measurements near the minimum Nusselt numbers. When $Pe \geq 50$, the experimental data are 5 to 20 percent less than the numerical results. One of the possible reasons for the deviation of the data is non-Darcy effects, since the Nusselt number generally decreases in this Peclet number range due to the viscous and inertial effects, and the difference between the numerical results based on Darcy's model and experimental data should increase as either Ra or Pe increases if non-Darcy effects are the main reason (Choi and Kulacki, 1992). In general, the Darcy model is considered to be valid as long as the Reynolds number based on the square root of permeability

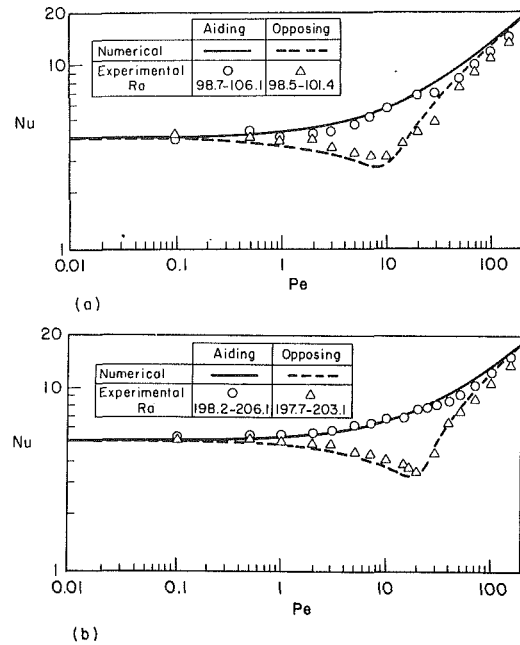


Fig. 13 Comparison of predicted and measured Nusselt numbers. (a) Ra = 100 (b) Ra = 200.

does not exceed unity (Cheng, 1985; Bejan, 1987). For the present study, the maximum Reynolds number is less than 10^{-2} ; therefore, viscous and inertial effects are not the primary reason for the deviation from the numerical results.

In the present experiments, $(T_h - T_c)$ generally decreases as the Peclet number increases, and it is observed that the experimental data are widely scattered and lower than the numerical results when $(T_h - T_c) < 30^\circ\text{C}$ as mentioned earlier. Therefore, the measurement error in temperature readings due to the decrease of $(T_h - T_c)$ may be a major reason for the increase of the deviation at higher Peclet numbers. It should be noted that relatively cold cooling water ($5^\circ\text{C} < T_c < 8^\circ\text{C}$) has been used for the high Peclet number range in order to increase the temperature difference and improve the accuracy of experimental results.

Another possible cause of the deviation is due to the stagnant thermal conductivity (k_m) at the high Peclet numbers. Prasad et al. (1985) proposed a model to obtain the effective thermal conductivity in order to explain the deviation of the experimental data at the very high Rayleigh numbers range for natural convection in a vertical porous annulus. Such a model can be valid if other possible errors of the experimental data are fully explained and corrected. However, the model has not been adopted here since part of the error may be due to the small difference between T_h and T_c .

The numerical heat transfer results can be reduced to correlations between Nusselt, Rayleigh, and Peclet numbers for $\gamma = 1$, $0 < Pe < 200$, and $50 < Ra < 200$. Correlations are sought in the form

$$\frac{Nu}{Pe^a} = \left[C_1 + C_2 \left(\frac{Ra}{Pe^b} \right) \right]^{C_3} \quad (8)$$

The constant a can be obtained from $\{\partial \ln Nu\} / \{\partial \ln Pe\}$ in the forced convection region where $\ln(Nu)$ depends linearly on $\ln(Pe)$; therefore, $a = 1/2$ from Fig. 10. Through a regression analysis of the numerical results based on Darcy's law, the constant $b = 3/2$. In the limit of natural convection ($Pe \rightarrow 0$), the above correlation shows that the Nusselt number depends approximately on $Ra^{1/3}$, while the influence of the Peclet number is negligible. In the mixed convection regime, the proposed form gives an excellent regression line for aiding flows. However, for the opposing flows, the regression line does not

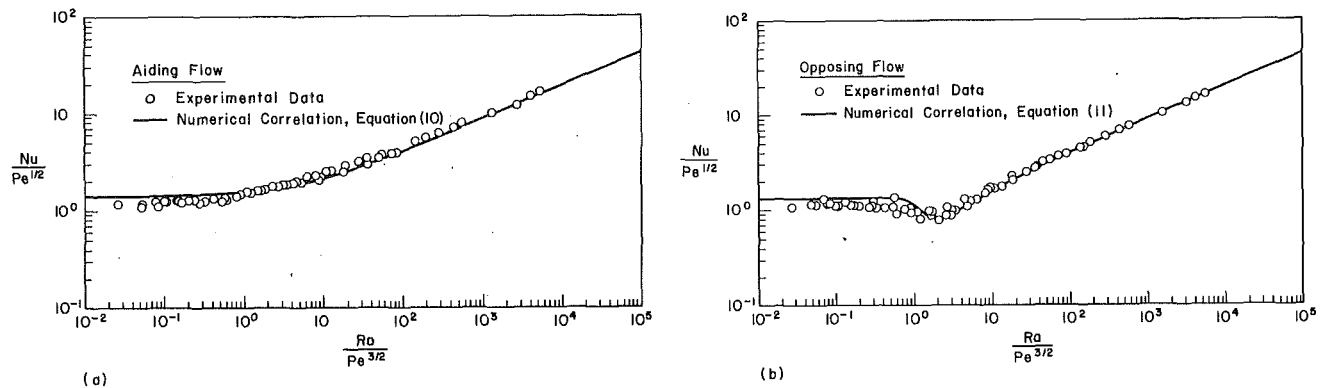


Fig. 14 Comparison of numerical correlation and experimental data. (a) Aiding Flow (b) Opposing Flow.

fit the numerical data for $0.1 < Ra/Pe^{3/2} < 10$, although the correlation gives good agreement between experimental data and numerical predictions in the natural and forced convection limits. This is primarily due to the decrease of $Nu/Pe^{1/2}$ in the mixed convection region. After a series of trials of possible correlation equations, it is found that the results can best correlated in the following form:

$$\frac{Nu}{Pe^a} = \left[C_1 + C_2 \left(\frac{Ra}{Pe^b} \right) \right]^{C_3} + \left[C_4 \left(\frac{Ra}{Pe^b} \right)^2 + C_5 \left(\frac{Ra}{Pe^b} \right) + C_6 \right] \exp \left[- \left| \frac{\left(\frac{Ra}{Pe^b} \right)}{1.3} \right| \right] \quad (9)$$

Here, the second-order function corrects the discrepancy, and an exponential function restricts the influence of the second-order function in $0.1 < Ra/Pe^{3/2} < 10$. Therefore, the additional term on the right-hand side of Eq. (9) is negligible in the natural and forced convection limits. For aiding flow,

regression lines are nearly the same as expected. Both figures indicate that the experimental data in the form of $Nu/Pe^{1/2}$ are in good agreement with the regression lines in the mixed and natural convection regime, i.e., $1 < Ra/Pe^{3/2} < 10^5$, while the experimental data are consistently lower than the numerical predictions as the flow approaches the forced convection regime ($Ra/Pe^{3/2} \rightarrow 0$). This is primarily due to the difference between the numerical predictions and measurements at high Peclet numbers (Fig. 13).

The dependence of the mixed convection regime on the Rayleigh number and the forced flow direction was discussed earlier. In order to verify this, the "5 percent deviation rule" has been applied to the present results. Originally, Sparrow et al. (1959) established the rule as a criterion for pure, mixed, and forced convection in fluids. This rule states that a flow for which the heat transfer results differ by more than 5 percent from that for forced or natural convection is considered a mixed flow. Based on the numerical correlations in Fig. 14, the following criteria have been obtained:

	Aiding flow	Opposing flow
Natural convection regime:	$Ra/Pe^{3/2} > 9800$	$Ra/Pe^{3/2} > 17100$
Mixed convection regime:	$0.2 < Ra/Pe^{3/2} < 9800$	$0.6 < Ra/Pe^{3/2} < 17100$
Forced convection regime:	$< Ra/Pe^{3/2} < 0.2$	$Ra/Pe^{3/2} < 0.6$

The corresponding mixed convection regimes at $Ra = 50$, 100, 150, and 200 are:

	Aiding flow	Opposing flow
$Ra = 50$:	$0.030 < Pe < 39.69$	$0.024 < Pe < 19.08$
$Ra = 100$:	$0.047 < Pe < 63.00$	$0.033 < Pe < 30.29$
$Ra = 150$:	$0.062 < Pe < 82.56$	$0.043 < Pe < 39.69$
$Ra = 200$:	$0.075 < Pe < 100.00$	$0.052 < Pe < 48.09$

$$\frac{Nu}{Pe^{1/2}} = \left[2.924 + 0.669 \left(\frac{Ra}{Pe^{3/2}} \right) \right]^{0.333}, \quad (10)$$

where the standard deviation of the correlation is 0.195. For opposing flow,

$$\frac{Nu}{Pe^{1/2}} = \left[2.084 + 1.886 \left(\frac{Ra}{Pe^{3/2}} \right) \right]^{0.300} + \left[0.312 - 0.814 \left(\frac{Ra}{Pe^{3/2}} \right) + 1.895 \times 10^{-5} \left(\frac{Ra}{Pe^{3/2}} \right)^2 \right] \exp \left[- \left| \frac{\left(\frac{Ra}{Pe^{3/2}} \right)}{1.3} \right| \right], \quad (11)$$

where the standard deviation of the correlation is 0.101.

Figure 14 compares the regression lines and experimental data for aiding and opposing flows. In the limit of natural or forced convection ($Ra/Pe^{3/2} \rightarrow 10^5$ or $Ra/Pe^{3/2} \rightarrow 10^{-2}$), both

The above results confirm that the Nusselt number deviates from the natural and forced convection asymptotes at higher Peclet numbers as Ra increases, and that the mixed and forced convection regimes begin at lower Peclet numbers for opposing flows. It should be further noted that the transition from the mixed to forced convection in opposing flow occurs at $Ra/Pe^{3/2} = 0.6$, which is different from the results of Reda (1988), i.e., $Ra/Pe = 0.5$. This discrepancy is apparently due to differences in the radius ratio parameter, inlet and exit boundary conditions, criterion for the transition point, and ranges of the Peclet and Rayleigh numbers.

Conclusion

Mixed convection in a vertical annulus filled with saturated porous media has been numerically and experimentally investigated. Overall, the experimental data are in good agreement

with the numerical results for mixed convection in aiding and opposing flows. Particularly important for opposing flows, the decrease of the Nusselt number in a limited range of the Peclet numbers has been experimentally identified. Based on numerical results, correlations through nonlinear regression analysis have been obtained. For $50 \leq Ra \leq 200$ and $0.01 \leq Pe \leq 200$, the results are best correlated by $Nu/Pe^{1/2}$ and $Ra/Pe^{3/2}$. The results have been compared with the experimental data, and the comparison shows good agreement when $Ra/Pe^{3/2} > 1$, i.e., in mixed and natural convection regime.

Acknowledgments

Support of this work by the U.S. Nuclear Regulatory Commission and the Computer Center at the Colorado State University is greatly appreciated.

References

- Bejan, A., 1987, "Convective Heat Transfer in Porous Media," in: *Handbook of Single-Phase Convective Heat Transfer*, S. Kakac, R. K. Shah, and W. Aung, eds., Wiley, New York, pp. 16.1–16.34.
- Cheng, P., 1985, "Geothermal Heat Transfer," *Handbook of Heat Transfer Applications*, McGraw-Hill, New York.
- Choi, C. Y., 1990, "Mixed Convection in Vertical Porous Annuli," Ph.D. Dissertation, Colorado State University, Fort Collins, CO.
- Choi, C. Y., and Kulacki, F. A., 1992, "Non-Darcy Effects on the Mixed Convection in Vertical Porous Annuli," ASME JOURNAL OF HEAT TRANSFER, submitted.
- Clarksean, R., Kwendakwema, N., and Boehm, R., 1988, "A Study of Mixed Convection in a Porous Annulus Between Vertical Concentric Cylinders," *Proceedings, 1988 ASME/AIChE National Heat Transfer Conference*, ASME, New York, Vol. 2, pp. 339–344.
- Ettefagh, J., and Vafai, K., 1988, "Natural Convection in Open-Ended Cavities With a Porous Obstructing Medium," *International Journal of Heat and Mass Transfer*, Vol. 31, pp. 673–693.
- Gosman, A. D., Pun, W. M., Runchal, A. K., Spalding, D. B., and Wolfshtein, M., 1969, *Heat and Mass Transfer in Recirculating Flows*, Academic Press, New York.
- Minkowicz, W. J., and Cheng, P., 1976, "Free Convection About a Vertical Cylinder Imbedded in a Porous Medium," *International Journal of Heat and Mass Transfer*, Vol. 19, p. 805.
- Muralidhar, K., 1989, "Mixed Convection Flow in a Saturated Porous Annulus," *International Journal of Heat and Mass Transfer*, Vol. 32, pp. 881–888.
- Parang, M., and Keyhani, M., 1987, "Boundary Effects in Laminar Mixed Convection Flow Through Annular Porous Medium," ASME JOURNAL OF HEAT TRANSFER, Vol. 109, pp. 688–696.
- Patankar, S. V., 1980, *Numerical Heat Transfer and Fluid Flow*, Hemisphere/McGraw-Hill, New York.
- Prasad, V., Kulacki, F. A., and Keyhani, M., 1985, "Natural Convection in Porous Media," *Journal of Fluid Mechanics*, Vol. 150, pp. 89–119.
- Reda, D. C., 1988, "Mixed Convection in a Liquid-Saturated Porous Medium," ASME JOURNAL OF HEAT TRANSFER, Vol. 110, pp. 147–154.
- Roache, P. J., 1976, *Computational Fluid Dynamics*, Hermosa Publishers.
- Sparrow, E. M., Eichhorn, R., and Gregg, J. L., 1959, "Combined Forced and Free Convection in a Boundary Layer," *Physics of Fluids*, Vol. 2, pp. 319–329.
- Vafai, K., and Effefagh, J., 1990, "Thermal Fluid Flow Instabilities in Buoyancy-Driven Flows in Open-Ended Cavities," *International Journal of Heat and Mass Transfer*, Vol. 33, pp. 2329–2344.
- Vanover, D. E., and Kulacki, F. A., 1987, "Experimental Study of Mixed Convection in a Horizontal Porous Annulus," ASME HTD-Vol. 84, pp. 61–66.

Convective Nucleate Boiling on a Heated Surface Cooled by an Impinging, Planar Jet of Water

D. T. Vader¹
Research Assistant.

F. P. Incropera
Professor.

R. Viskanta
Professor.

Heat Transfer Laboratory,
School of Mechanical Engineering,
Purdue University,
West Lafayette, IN 47907

Convective nucleate boiling has been studied on a flat, upward facing, constant heat flux surface cooled by a planar, impinging water jet. Surface temperature distributions are presented for jet velocities between 1.8 and 4.5 m/s, fluid temperatures of 30, 40, and 50°C, and heat fluxes between 0.25 and 2.5 MW/m². Although the critical Reynolds number, $Re_{x^,c}$ is independent of heat flux for $q'' < q''_{ONB}$, boiling incipience strongly affects the transition to a turbulent boundary layer. As the heat flux increases, vapor bubbles of 1 mm diameter first appear at the point of maximum surface temperature, which also marks the onset of boundary layer turbulence. The leading edge of these bubbles moves toward the stagnation line and $Re_{x^*,c}$ decreases with further increases in heat flux. Acceleration in the stagnation region stabilizes the flow, however, so that boundary layer turbulence is restricted to $x/w_j \geq 1.6$. With increasing heat flux, vigorous nucleate boiling covers more of the heater and surface temperature variations decrease.*

1 Introduction

Forced convection increases the critical heat flux (CHF) in nucleate boiling, thereby extending the maximum possible heat flux for many applications. The desired fluid motion can be induced by an impinging jet, applications of which include the cooling of hot sheet materials and arrays of coplanar computer chips.

Ruch and Holman (1975) measured average convection coefficients for a circular R-113 jet in convective nucleate and film boiling (Table 1). The authors reported that the jet velocity and diameter affect the radius of nucleate-to-film boiling transition, but do not affect the nucleate boiling convection coefficient. Ma and Bergles (1983, 1986) measured stagnation point heat transfer to a R-113 jet. They found that the convection coefficient depends on the jet velocity and temperature in single-phase convection but is independent of velocity and shows limited sensitivity to free-stream temperature in fully developed nucleate boiling.

Since heat fluxes ranging from 10^6 to 10^7 W/m² are needed to support flow boiling in an impinging water jet, related studies have been limited to small test areas. Ishigai et al. (1978) measured partial and fully developed nucleate boiling, as well as film boiling, heat transfer at the stagnation line of a planar water jet. Steady and transient experiments were performed. Although the partial boiling results and CHF were sensitive to fluid temperature and jet velocity, these parameters had little effect on the developed portion of the boiling curve. Similar results were reported by Miyasaka and Inada (1980) and Miyasaka et al. (1980), who showed that partial boiling could be estimated as the sum of independent contributions of single-phase convection and fully developed nucleate pool boiling.

Hatta et al. (1983, 1984) and Kokado et al. (1984) have studied the quenching of a steel plate from 900°C with a circular water jet. The authors measured local temperatures and solved the transient conduction equation in the plate to obtain the heat flux at the cooled surface. They suggest the existence of a single-phase convection region directly beneath the jet, followed by nucleate and film boiling with increasing radial distance from the stagnation point. The maximum radius for single-phase convection increased with time.

¹Current address: IBM Corporation, Advanced Thermal Laboratory, Poughkeepsie, NY 12603.

Contributed by the Heat Transfer Division for publication in the JOURNAL OF HEAT TRANSFER. Manuscript received by the Heat Transfer Division January 7, 1991; revision received June 30, 1991. Keywords: Boiling, Materials Processing and Manufacturing Processes, Measurement Techniques.

This study examines boiling heat transfer from a uniform heat flux surface to a planar free-surface jet. The results are unique in that local measurements have been made in the stagnation ($x/w_j = 0$), impingement ($0 < x/w_j \leq 3$), and parallel ($x/w_j \geq 3$) flow regions. It is therefore possible to evaluate combined forced convection and nucleate boiling processes in the transition from laminar to turbulent boundary layer flow.

2 Experimental Method

Since a detailed description of the experimental procedures has been published (Vader et al., 1990a), this discussion is limited to essential features of the apparatus and measurement method. Heat transfer to the jet was computed from measured heater temperatures and power. To facilitate these measurements, thin plate heaters were made from 304 stainless steel and Haynes alloy number 230 (Fig. 1G). Each plate was 260 mm long and 35.7 mm wide and of thickness equal to 0.381

Table 1 Experimental studies of impingement cooling with convective nucleate boiling

Authors	Fluid	Jet	Heat Source
Ruch and Holman (1975)	R-113 $\Delta T_{sub} = 47.6^\circ\text{C}$	Circular, free-surface $1.23 \leq V_n \leq 6.87$ m/s $0.21 \leq d \leq 0.43$ mm $H/d = 22.6$	Facing down Indirect heating $D = 12.9$ mm $7 \times 10^4 \leq q'' \leq 7 \times 10^5$ W/m ²
Ma and Bergles (1983, 1986)	R-113 $0 \leq \Delta T_{sub} \leq 29.5^\circ\text{C}$	Circular, submerged $1.08 \leq V_n \leq 10.05$ m/s $d = 1.07$ mm, 1.81 mm, $H/d = 2$	Vertical Indirect heating 5x5, 3x3 mm $10^3 \leq q'' \leq 7 \times 10^6$ W/m ²
Ishigai et al. (1978)	Water $5 \leq \Delta T_{sub} \leq 75^\circ\text{C}$	Planar, free-surface $0.6 \leq V_n \leq 4$ m/s $w_n = 6.2$ mm $H/w_n = 2.4$	Facing up Direct heating 12x20 mm $3 \times 10^3 \leq q'' \leq 2 \times 10^7$ W/m ²
Miyasaka and Inada (1980)	Water $\Delta T_{sub} = 85^\circ\text{C}$	Planar, free-surface $V_n \leq 16$ m/s $w_n = 10$ mm $H/w_n = 1.5$	Facing up Direct heating 4 x 8 mm $10^3 \leq q'' \leq 5 \times 10^7$ W/m ²
Miyasaka, Inada and Owase (1980)	Water $\Delta T_{sub} = 85^\circ\text{C}$	Planar, free-surface $V_n \leq 16$ m/s $w_n = 10$ mm $H/w_n = 1.5$	Facing down Indirect heating $1.5 \leq D \leq 2$ mm $10^6 \leq q'' \leq 5 \times 10^7$ W/m ²
Hatta et al. (1983, 1984) Kokado et al. (1984)	Water $12 \leq \Delta T_{sub} \leq 80^\circ\text{C}$	Circular, free-surface $V_n \leq 1.5$ m/s $d = 10$ mm $5 \leq H/d \leq 60$	Facing up Quench ($T_1 = 900^\circ\text{C}$) 200 x 200 x 10 mm

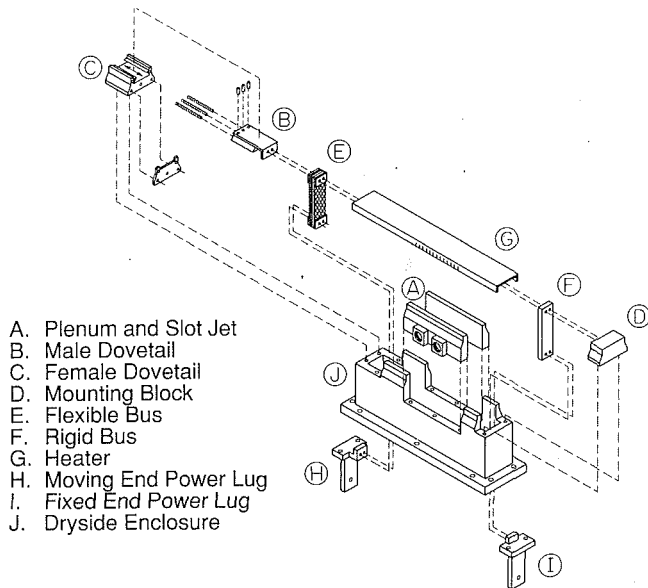


Fig. 1 Assembly drawing of the heater module

mm for the stainless steel and 0.635 mm for the Haynes 230. A 119-mm-long portion of the plate was heated by an electric current, and when installed in the heater module, the plate was placed in tension by a spring-loaded dovetail assembly to inhibit buckling (Fig. 1B, C). Air jets (Fig. 1A) prevented water from passing through the sliding contact between the heater (Fig. 1G) and the enclosure on which it rested (Fig. 1J). The surface of each heater was treated by vapor blasting, using a 325 mesh, silica rock based abrasive in a Liquid Honing Model 2820 blaster. This treatment insured a consistent boiling surface for each test.

A cartridge-like measurement module (Fig. 2) was designed for insertion into the cavity below the heater plate (Fig. 1). Temperatures were measured by spring-loaded thermocouples at the dry face of the heater. The thermocouples were positioned at 5.08-mm intervals along the longitudinal midline (Fig. 3). A metal-filled paste reduced thermal contact resistance between the thermocouple junction and the heater. The paste also electrically isolated the thermocouple circuits from the heater. Substrates A and B (Fig. 2), which were pressed against the heater by springs, insulated the dry face of the heater so that the corresponding surface heat flux was small compared to the heat flux at the wetted face. The temperature and heat flux at the wetted face were found by solving the steady heat

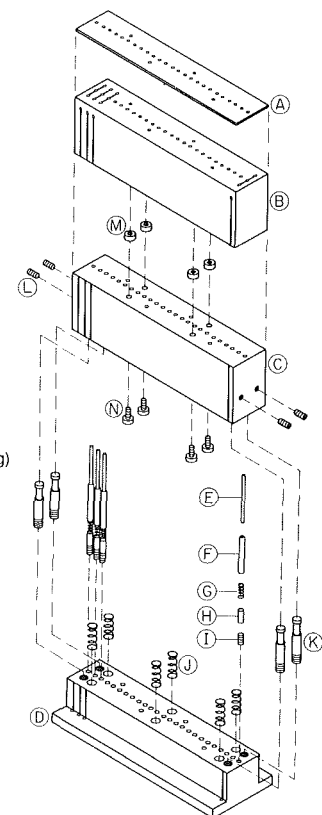


Fig. 2 Assembly drawing of the measurement module

equation for the plate. Boundary conditions were assigned from a least-squares cubic spline fit of the measured temperatures (Vader et al., 1990a).

Heat dissipation in the plate was controlled with a d-c power supply whose peak output was 15 kW (1500 A and 10 V). The Joulean heat generation term in the energy equation for the plate was computed from the voltage drop across the heated section and the electrical resistivity of the heater material. The voltage drop was measured by a differential probe positioned along the heater midline.

Characterizing heat transfer to the impinging jet requires knowledge of the jet's temperature, velocity, width, and thermophysical properties. The jet temperature, which was controlled by a heater and cooling coil in a water reservoir, was

Nomenclature

D = diameter of a circular heated area
 d = diameter of a circular jet
 H = nozzle discharge-to-heater spacing
 h = heat transfer coefficient; specific enthalpy
 k = thermal conductivity
 n'' = area number density of active nucleation sites
 q'' = heat flux
 Re_j = jet Reynolds number = $V_j w_j / \nu$
 Re_{x*} = plate Reynolds number = $u_\delta x / \nu$
 r_c = minimum cavity radius for bubble growth

T = temperature
 ΔT_{sat} = wall superheat = $T_w - T_{\text{sat}}$
 ΔT_{sub} = liquid subcooling = $T_{\text{sat}} - T_j$
 u = x component of velocity
 V = jet velocity
 v = specific volume
 w = jet width
 x = streamwise position measured from the stagnation line
 y = vertical position measured from the plate surface
 δ = velocity boundary layer thickness
 ν = kinematic viscosity
 ρ = density
 σ = surface tension

Subscripts

c = critical value associated with onset of boundary layer turbulence
 f = property of the liquid
 fg = difference in a property for saturated vapor and saturated liquid
 g = property of the vapor
 i = initial
 j = value for the impinging jet
 n = value at the nozzle discharge
ONB = onset of nucleate boiling
OVB = onset of visible boiling
sat = saturated condition
sub = subcooled condition
 w = value at the heated surface
 δ = value at distance δ from the heated surface

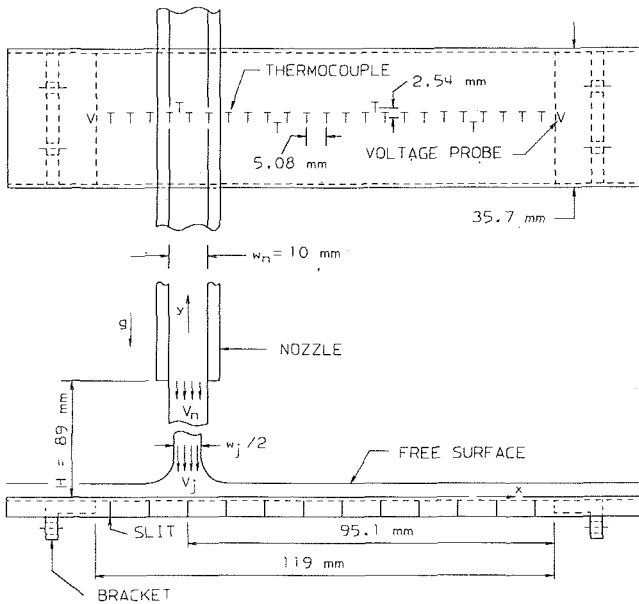


Fig. 3 Schematic drawing of the experiment

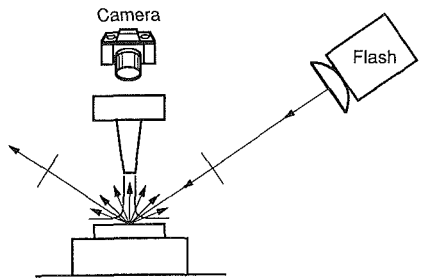


Fig. 4 Arrangement of the flash and camera used in the photographic study

measured in a plenum directly above the nozzle entrance. The flow system could deliver between 1 and 7 l/s at temperatures between 20 and 60°C through a 10.2 mm by 105 mm rectangular nozzle discharge (Fig. 3). A convergent nozzle, with a honeycomb straightener at the entrance, was used to minimize turbulence in the flow. Jet velocity and width were corrected for the effects of gravitational acceleration between the nozzle discharge and the impingement surface (Table 2).

Stop action photographic studies of vapor in the flow were made using a 0.5 μ s flash. Key to the flash-camera arrangement of Fig. 4 is the propagation of light from the flash at a right angle to the viewing direction of the camera. When the surface of the heater was polished, vapor bubbles appeared white against a black background, since the heater reflected the flash specularly and only light scattered by the bubbles entered the camera's field of view. Roughening the heater surface, however, increased diffuse reflection, which reduced the contrast between the bubbles and the heater.

The standard procedure for computing experimental uncertainty in single sample experiments (Moffat, 1988) was applied, and uncertainties were estimated as follows: temperature, $\delta(T_w - T_f)/(T_w - T_f) \approx \pm 10$ percent; convection coefficient, $\delta h/h \approx \pm 12$ percent; jet velocity, $\delta V_j/V_j \approx \pm 3$ percent; jet width, $\delta w_j/w_j \approx \pm 3$ percent; Reynolds number, $\delta Re_j/Re_j \approx \pm 5$ percent and $\delta Re_{x*}/Re_{x*} \approx \pm 5$ percent. These uncertainties are based on 20:1 odds and do not account for variations caused by system specific parameters.

Repeatability measurements were made on several different heaters. Nonboiling heat transfer data were repeatable to within ± 5 percent. However, due to the effect of noncondensibles

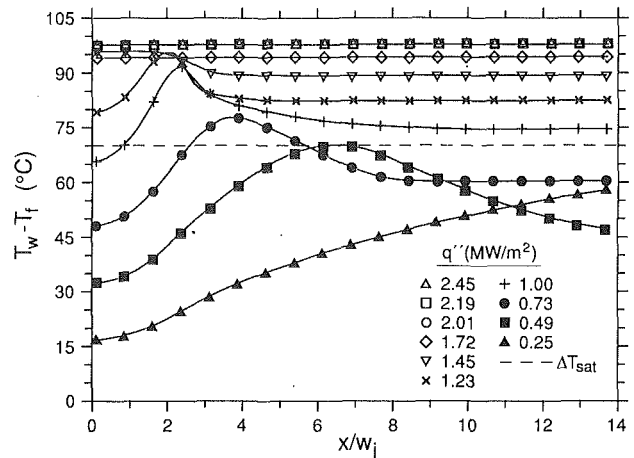


Fig. 5 Effect of heat flux on local surface temperature when $V_j = 1.8$ m/s and $T_f = 30^\circ\text{C}$

Table 2 Jet velocity and width for various flow rates when $w_n = 10.2$ mm and $H = 89.7$ mm

$G(\text{l s}^{-1})$	$V_n(\text{m s}^{-1})$	$V_j(\text{m s}^{-1})$	$w_j(\text{mm})$
1.26	1.23	1.8	6.9
1.74	1.69	2.1	8.0
2.21	2.13	2.5	8.6
3.15	3.05	3.3	9.3
3.79	3.66	3.9	9.6
4.42	4.28	4.5	9.7

on boiling incipience, results downstream of incipience showed deviations of up to ± 20 percent. Sensitivity to variations in the concentration of noncondensibles diminished, however, as boiling approached fully developed conditions. The repeatability at higher heat fluxes was within the experimental uncertainty.

3 Results and Discussion

Interactions between convective and boiling heat transfer were examined using quantitative and photographic data. The heat flux was varied in approximately 0.25 MW/m^2 increments (Fig. 5), and each experiment for which the heat flux exceeded approximately 0.75 MW/m^2 was photographed to identify regions of boiling on the heater surface (Fig. 6).

As shown in Fig. 5, at the lowest heat flux, 0.25 MW/m^2 , heat is dissipated by single-phase convection. The thermal boundary layer thickness increases in the streamwise direction, thereby increasing the resistance to heat transfer and the surface temperature. Although not shown in the figure, a local maximum in temperature would eventually be reached downstream of the stagnation line, near the onset of transition to turbulence in the boundary layer. Turbulent mixing would reduce the resistance to heat transfer, causing a reduction in the surface temperature. With incipient boiling, however, boundary layer transition is accelerated, thereby advancing the location at which the surface temperature begins to decrease.

Incipient Boiling. A vapor bubble immersed in a liquid will grow when its thermal pressure, which depends on the wall superheat, is sufficient to overcome surface tension forces, which are inversely proportional to the bubble radius. For uniform surface heat flux, Hsu (1962) established the following expression between the superheat and the incipience heat flux:

$$(\Delta T_{\text{sat}})_{\text{ONB}} = \left[\frac{8\sigma q''_{\text{ONB}} T_{\text{sat}}}{h_{fg} k_f \rho_g} \right]^{1/2} \quad (1)$$

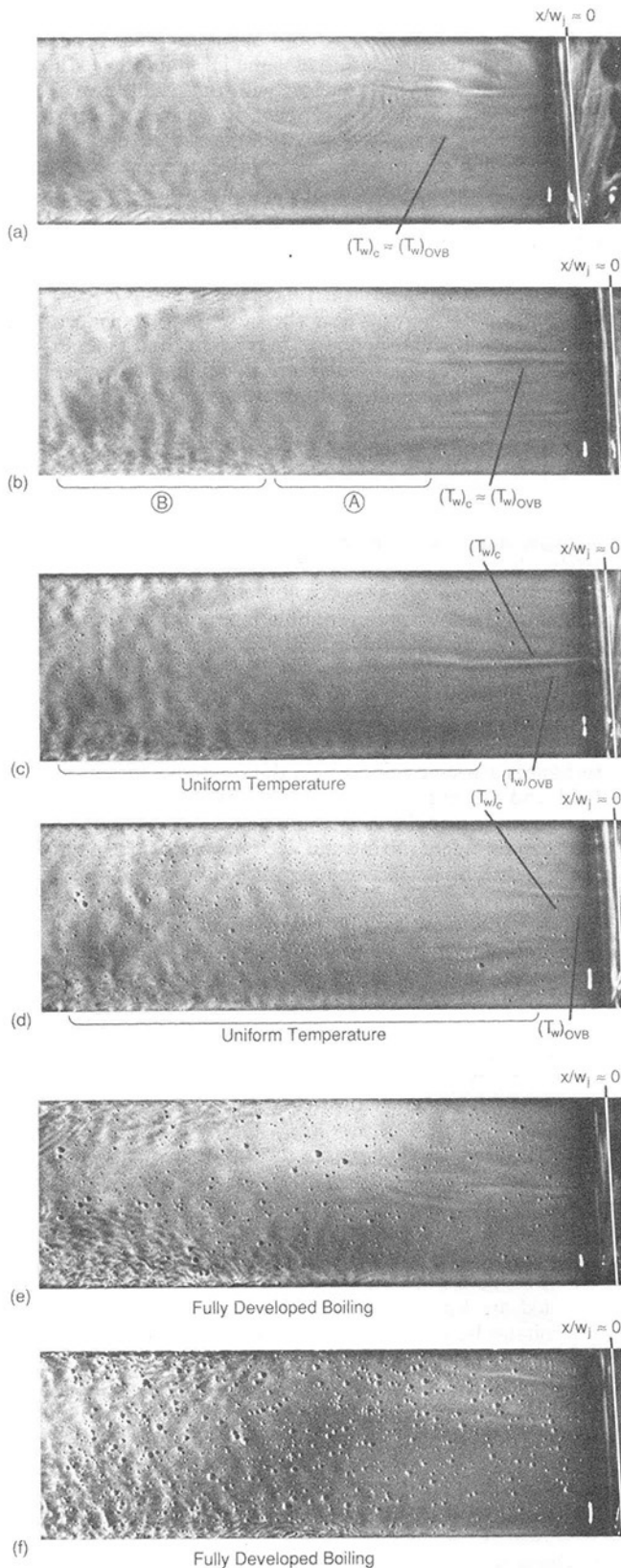


Fig. 6 Convective nucleate boiling when $V_j = 1.8$ m/s, $T_f = 30^\circ\text{C}$: (a) 0.73 MW/m 2 , (b) 1.00 MW/m 2 (A—reduced bubble diameter and number, B—increased bubble diameter and number), (c) 1.23 MW/m 2 , (d) 1.45 MW/m 2 , (e) 1.72 MW/m 2 , (f) 2.45 MW/m 2

which, if satisfied, would activate nuclei of radius

$$r_c = -\frac{\sigma}{p_f} + \left[\left(\frac{\sigma}{p_f} \right)^2 + \left(\frac{Bk_f}{q''} \right)^2 \right]^{1/2} \quad (2a)$$

Table 3 Parameters marking transition to a turbulent boundary layer and boiling incipience

$\frac{q''}{10^6}$ ($\frac{\text{W}}{\text{m}^2}$)	$\frac{Re_{x,c}}{10^5}$	$(T_w)_c$ ($^\circ\text{C}$)	$(T_w)_{\text{OVB}}$ ($^\circ\text{C}$)	$(T_w)_{\text{ONB}}$ ($^\circ\text{C}$) Eq. (1)	r_c (μm) Eq. (2)
$T_f = 30^\circ\text{C}, V_j = 2.5$ m/s					
0.25	3.98	74	-	107	8.9
0.49	3.62	102	-	109	6.2
0.50	3.86	106	-	110	6.1
0.50	3.34	102	-	110	6.1
0.50	3.20	101	-	110	6.1
0.50	3.43	104	-	110	6.1
0.50	3.58	105	-	110	6.1
0.73	2.07	105	104	111	5.0
0.74	2.42	116	116	111	5.0
1.00	1.65	115	114	113	4.2
1.00	1.64	120	120	113	4.2
1.00	2.01	126	121	113	4.2
1.00	1.56	116	116	113	4.2
1.23	1.06	123	123	114	3.7
1.50	1.13	130	127	116	3.3
1.72	0.97	136	-	117	3.0
$T_f = 30^\circ\text{C}, V_j = 2.5$ m/s					
0.24	3.47	86	-	107	9.1
0.48	2.87	110	-	109	6.3
0.72	1.99	117	117	111	5.0
0.97	1.24	121	120	113	4.2
1.23	1.12	131	125	114	3.7
$T_f = 30^\circ\text{C}, V_j = 1.8$ m/s					
0.49	1.83	100	-	109	6.2
0.73	1.09	107	107	111	5.0
1.00	0.736	122	121	113	4.2
1.23	0.637	126	119	114	3.7

where

$$B = \frac{2\sigma T_{\text{sat}} \nu_{fg}}{h_{fg}} \quad (2b)$$

Additional wall superheat will activate nucleation sites of smaller and larger radii. If no cavity of size r_c contains a vapor embryo, additional wall superheat or heat flux will be required to initiate boiling.

Conditions for boiling incipience were estimated from Eqs. (1) and (2) and were also determined photographically by identifying the position of the first observed vapor bubble downstream of the stagnation line. The results are summarized in Table 3. Boiling point suppression due to stagnation pressure rise was estimated to be approximately 1.5 percent for the lower velocities and 4.5 percent for the higher velocities. This effect was neglected since the magnitude is well within the uncertainty of both computed and observed incipience conditions. Very close to the wall ($y \sim 10$ μm), where heterogeneous nucleation occurs, the temperature gradient normal to the wall is governed by Fourier's law, and is determined completely by the heat flux and fluid properties. According to Hsu's model, heat transfer affects incipience only through this temperature gradient. Consequently, although forced convection and subcooling can influence incipience, they do not affect the relationship between q''_{ONB} and $(\Delta T_{\text{sat}})_{\text{ONB}}$, but may determine whether the needed superheat is achieved.

Equation (1) is expected to overestimate the wall superheat needed for incipience, since the presence of noncondensable gases, which reduce the superheat required for activation of nucleation sites, is neglected. The photographic data are also expected to overestimate $(T_w)_{\text{ONB}}$, since bubbles at the actual location of incipience may be too small to be resolved, especially when free-stream subcooling is high. Jiji and Clark (1962) photographically studied incipient boiling with forced convection of degassed water and concluded that the heat flux needed to permit visual detection of bubbles exceeds that which causes heat transfer enhancement.

The relationship between $(T_w)_{\text{ONB}}$, as prescribed by Eq. (1), and the surface temperature required for the onset of visible boiling $(T_w)_{\text{OVB}}$, is less certain. At low heat fluxes, a few values of $(T_w)_{\text{OVB}}$ were less than $(T_w)_{\text{ONB}}$ (Table 3), which indicates a substantial reduction in the incipient boiling wall superheat

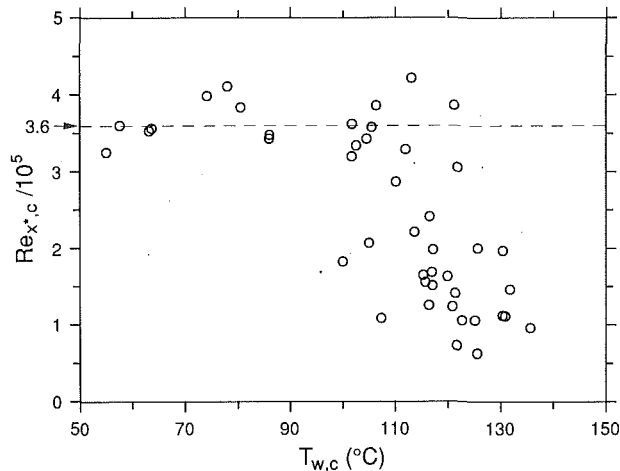


Fig. 7 Effect of boiling on transition to a turbulent boundary layer

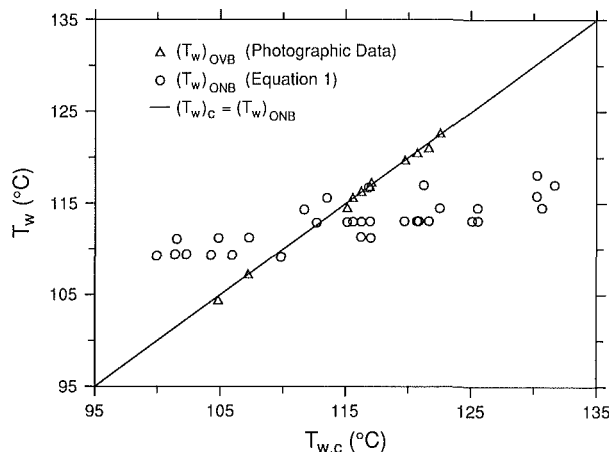


Fig. 8 Relationship between the temperature of boiling incipience and maximum surface temperature

due to the presence of noncondensibles. Most of the data, however, showed $(T_w)_{OVB}$ to be greater than $(T_w)_{ONB}$, with the difference between these values increasing with increasing surface temperature. With increasing heat flux and $(T_w)_{OVB}$, noncondensibles are more likely to come out of solution upstream of the OVB region. Gas that was trapped when the surface was first flooded with liquid is driven out of downstream nucleation sites, and the presence of noncondensibles and their effect on bubble growth in the OVB region is diminished.

If $(T_w)_{OVB}$ were assumed to indicate the true condition for incipience, and the effects of subcooling on OVB were neglected, the observation that $(T_w)_{OVB} > (T_w)_{ONB}$ (Table 3) might suggest that only nucleation sites of dimensions less than r_c exist. This hypothesis is difficult to support, however, since the sensitivity of incipience to surface finish is known to decline with increasing forced convection and subcooling. Furthermore, computed values of r_c are consistently less than $r_{max} \approx 10 \mu\text{m}$ (Brown, 1967), which has been suggested as an upper limit on the size of active nucleation sites for most surfaces (Table 3). Anderson (1988) tested a copper surface that had been prepared by the vapor blast process used in this study and found a sharp (36 percent) peak in the pore size distribution near $15 \mu\text{m}$.

Because the activation of nucleation sites depends on the wall superheat, boiling heat transfer is coupled to convection through the surface temperature. A heat flux of approximately 0.5 MW/m^2 caused $(T_w)_c$, the maximum surface temperature, to approach the saturation temperature (Fig. 5). With increas-

ing q'' above this value, surface temperatures exceeded T_{sat} over a portion of the heater, both upstream and downstream of x_c/w_j . This result suggests that the minimum heat flux for incipient boiling, q''_{ONB} , coincides with the condition $(T_w)_{ONB} = (T_w)_c$ and that boiling propagates upstream and downstream of x_c/w_j as the heat flux is increased beyond q''_{ONB} .

In a developing laminar boundary layer, the number of active nucleation sites increases to a maximum when $T_w = (T_w)_c$. However, the onset of turbulent mixing in the boundary layer will subsequently reduce boiling activity, as the surface temperature and the number of active nucleation sites decrease. Hence, for a prescribed heat flux, boiling should occur only on a portion of the wall near the onset of turbulence in the boundary layer. This phenomenon is revealed in Fig. 6(a) ($q'' = 0.73 \text{ MW/m}^2$), for which there is boiling near $x/w_j \approx 4$, but no boiling upstream or downstream of this region.

Transition to Turbulence. For both boiling-induced and turbulent mixing, length and time scales can vary temporally and spatially. Turbulent mixing, however, is self-sustained and virtually independent of heat transfer, while boiling-induced mixing is continually driven by the growth and collapse of vapor bubble discrete sites distributed over the heated surface, as well as by downstream bubble interactions. Since acceleration is known to stabilize and laminarize fluid flow (Patel and Head, 1968; Narashima, 1977), laminar boundary layer conditions will exist in a finite region about the stagnation line of the jet, where the velocity is zero and the adjoining flow is rapidly accelerated. In this region, boiling related flow disturbances are superimposed on the surrounding laminar flow field and are eventually dissipated by viscous forces. Since transition to turbulence is characterized by a streamwise increase in turbulent mixing and declining surface temperatures, the increase of surface temperature downstream of boiling incipience for $q'' = 0.73 \text{ MW/m}^2$, Figs. 5 and 6(a), is evidence of a laminar flow boiling regime. Farther downstream, as acceleration of the flow decreases and the free-stream velocity approaches the jet velocity, the flow becomes less stable and boiling related disturbances are more likely to initiate a transition to turbulence. In the absence of boiling a critical Reynolds number, $Re_{x^*,c} \approx 3.6 \times 10^5$, was found to characterize conditions over a broad range of values for q'' , V_j , and T_f (Vader et al., 1990b). However, Fig. 7, which is plotted from the data of Table 3, shows $Re_{x^*,c}$ falling as low as 6.4×10^4 as $(T_w)_c$ is increased above the saturation temperature. Figure 8, which is also plotted from the data of Table 3, shows that the onset of visible boiling correlates well with transition, since $(T_w)_c \approx (T_w)_{OVB}$. Although incipience in a highly subcooled flow is expected upstream of the first visible vapor bubble, Fig. 8 suggests that the first bubbles to be photographically detected are large enough to create a flow disturbance that precipitates boundary layer turbulence. The predicted boundary layer thickness and observed bubble diameter corresponding to OVB are both on the order of 1 mm.

Because $Re_{x^*,c} = u_\delta x_c / \nu$ is a constant when $q'' \leq q''_{ONB}$, x_c/w_j must increase if V_j decreases and viscosity (T_f) is held constant. In this case, it is the maximum wall temperature at x_c/w_j that ultimately determines the onset of nucleate boiling and therefore the value of $(x/w_j)_{ONB}$. Conversely, if the heat flux exceeds q''_{ONB} , vapor-induced disturbances initiate boundary layer turbulence [Fig. 6(a)], and it is the onset of nucleate boiling at $(x/w_j)_{ONB}$ that determines x_c/w_j and the maximum wall temperature. In this case, as V_j decreases, boiling is enhanced and $(x/w_j)_{ONB} = x_c/w_j$ also decreases (Fig. 9). As shown in Fig. 10, however, there is a limit to upstream propagation of the transition point. The limit corresponds to $x_c/w_j \approx 1.6$ and is attributed to fluid acceleration in the impingement flow region ($x_c/w_j \leq 1.6$), which is sufficient to stabilize the flow to boiling-induced disturbances. Under conditions for

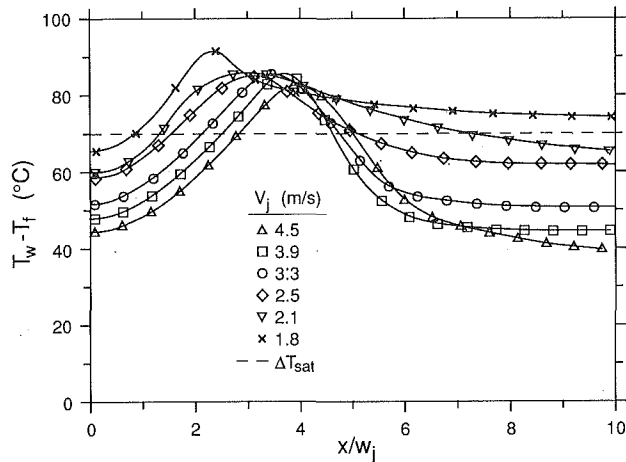


Fig. 9 Effect of jet velocity on local surface temperature when $q'' = 1.00 \text{ MW/m}^2$ and $T_f = 30^\circ\text{C}$

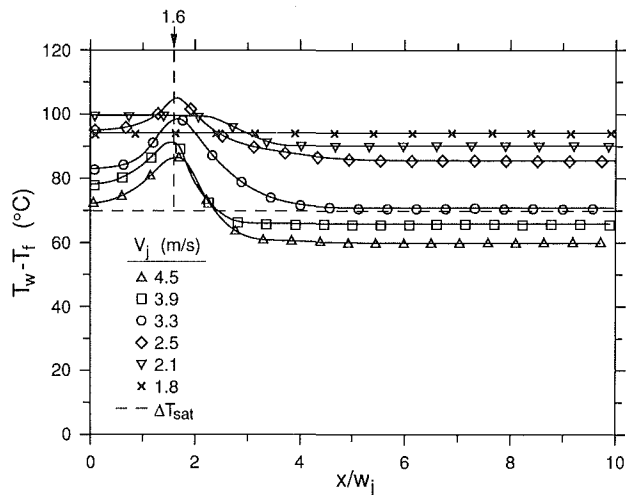


Fig. 10 Effect of jet velocity on local surface temperature when $q'' = 1.72 \text{ MW/m}^2$ and $T_f = 30^\circ\text{C}$

which boiling occurs over the entire surface, there is no further decrease in x_c/w_j , irrespective of jet velocity or temperature.

Partial Boiling. Heat transfer in partial boiling is due to the combined effects of forced convection and nucleate boiling. For example, visual observations indicated that nucleate boiling did not extend uniformly downstream of incipience near x_c/w_j to cover the entire surface. For certain operating conditions vapor bubbles were detected near x_c/w_j and in a separate region further downstream. In Fig. 6(b), for example, lower temperatures downstream of boiling incipience caused a decrease in the size and number density of bubbles (region A). Farther downstream, however, boiling activity increased (region B) with no increase in T_w . This phenomenon is also shown in Fig. 11. For a constant heat flux, as the surface temperature decreases, the number of active nucleation sites can increase only if the temperature gradient normal to the wall also decreases. Since the temperature gradient varies only with the heat flux (see the section on incipience), boiling is expected in Figs. 6(b) and 11 throughout the turbulence region corresponding to $x > x_c$. The photographs do not preclude such a condition. Vapor bubbles must grow much larger than r_c to be detected photographically, while bubble growth can be inhibited by subcooled fluid (Collier, 1981; Jiji and Clark, 1962), such as that mixed into the boundary layer by developing turbulence. If the fluid next to the heated surface is highly subcooled, any vapor entering the flow may quickly condense yielding no net vapor generation. Bubbles that originate from

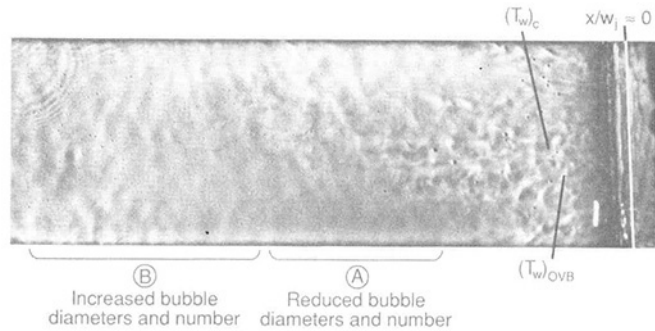


Fig. 11 Convective nucleate boiling when $V_j = 2.5 \text{ m/s}$, $T_f = 50^\circ\text{C}$, and $q'' = 1.23 \text{ MW/m}^2$

active nucleation sites in region B of Figs. 6(b) and 11 could be larger than those originating from sites in region A because the thickness of the heated fluid layer adjacent to the wall increases with x/w_j . Furthermore, if vapor bubbles cannot grow large enough for buoyancy and drag forces to overcome surface tension forces, they remain attached to the wall and can grow and collapse while sliding along the wall (Collier, 1981). Warmer fluid near the wall would also permit larger bubbles to form, as smaller bubbles that slide along the wall coalesce.

In partial boiling, surface temperatures downstream of the onset of boundary layer turbulence approach a constant value (Fig. 5). This trend is inconsistent with heat transfer by single-phase convection, for which the surface temperature decreases in the streamwise direction as turbulence develops and reaches a local minimum, but not a constant value, once the flow is fully turbulent. Boiling, however, is known to diminish streamwise surface temperature variations associated with single-phase convection. The tendency for temperature to approach a constant value as boiling increases is commonly attributed to a decrease in the sensitivity of heat transfer to parameters that are important in single-phase convection, such as free-stream velocity and temperature. Convective nucleate boiling studies have consistently shown that for a given heat flux, the surface temperature becomes invariant when vigorous, boiling-induced mixing becomes the dominant mechanism for heat transfer (Kutateladze, 1961).

Unexpectedly, the data for $q'' = 0.73 \text{ MW/m}^2$ (Fig. 5) also show a region of nearly uniform surface temperature downstream of x_c/w_j , where $T_w \approx 90^\circ\text{C}$ for $x/w_j > 9$. The minimum heat flux required to achieve a uniform downstream temperature appears to correspond to the condition $(T_w)_{\text{ONB}} \approx (T_w)_c$, leading to speculation that vapor bubbles entering the flow near x_c/w_j influence mixing in the downstream boundary layer. Bubbles of noncondensable gases, which leave solution when the fluid is heated, could also effect mixing near the wall.

Heat transfer by partial convective boiling has been modeled as the weighted sum of contributions by single phase convection and pool boiling (Kutateladze, 1961; Bergles and Rohsenow, 1964). These models are consistent with the premise that the effects of fluid velocity and temperature on heat transfer decrease as boiling increases. In the limit of fully developed boiling, the heat flux attributed to single-phase convection is assumed to be zero and T_w is independent of free-stream velocity or subcooling. Data from this study could not be fit by any of these models, since they require knowledge of the contributions of local convection and boiling to heat transfer. Typically, the two cooling mechanisms are assumed to act independently, allowing separate evaluation from single-phase convection and pool boiling data. Although this approach has been moderately successful for laminar and fully turbulent boundary layers, most of the partial boiling data of this study pertain to conditions for which there is transition to turbulence, and a satisfactory correlation of nonboiling transition data

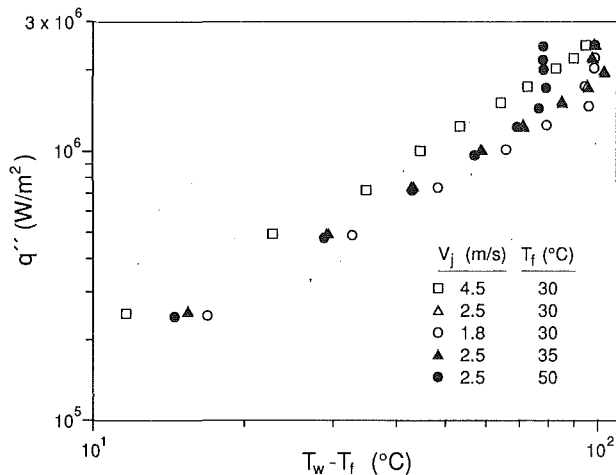


Fig. 12 Stagnation line boiling curves

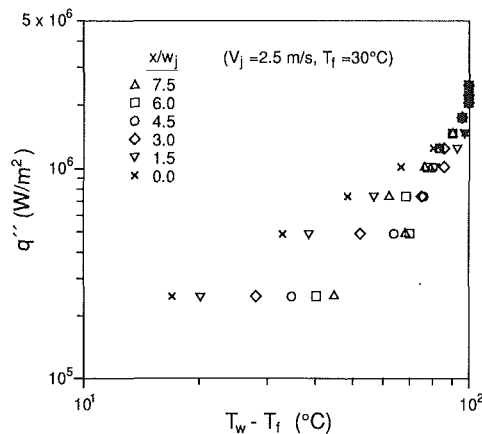


Fig. 13 Boiling curves at different streamwise positions

could not be obtained. Furthermore, the coupling that exists between boiling induced flow disturbances, flow acceleration in the impingement region, and the transition to turbulence casts doubt on the validity of assuming independent boiling and nonboiling heat transfer mechanisms.

Fully Developed Boiling. Fully developed boiling is a condition for which boiling-induced mixing controls fluid motion near the wall. In such cases, local wall temperature variations become less pronounced and conditions become less sensitive to the free-stream velocity and temperature. Furthermore, $q'' \sim \Delta T_{\text{sat}}^n$, where n is unity for single-phase convection and is typically between 2 and 4 for fully developed boiling. The data of Fig. 5 show, for $q'' \geq 2 \text{ MW/m}^2$, a negligible increase in surface temperature with increasing heat flux. With increasing heat flux, fully developed boiling is first approached near x_c/w_j , where $(T_w)_c$ continues to be the maximum surface temperature in partial boiling. For $V_j = 1.8 \text{ m/s}$ and $T_f = 30^\circ\text{C}$ (Fig. 5), the value of $(T_w)_c$ shows little change when the heat flux is increased above 1.23 MW/m^2 .

The stagnation surface temperature for single-phase convection is lower than the wall temperatures corresponding to $x/w_j > x_c/w_j$. Figures 5, 6(b), and 6(c) show that partial boiling is first established in the region downstream of x_c/w_j , thereby reducing, relative to the nonboiling data, the sensitivity of wall temperatures to increasing heat flux. Consequently, as the heat flux increases and boiling propagates into the stagnation region, the value of T_w for $x/w_j < x_c/w_j$ increases more rapidly than that corresponding to $x/w_j > x_c/w_j$. As revealed by the 1.45 MW/m^2 data of Fig. 5 and by much of the data of Fig.

10, the stagnation temperature can exceed values of T_w for portions of the region $x/w_j > x_c/w_j$. The temperature peak associated with the onset of turbulent mixing becomes less pronounced as boiling increases upstream and downstream of x_c/w_j .

Boiling Curve. Partial and developed boiling data are commonly plotted on a log scale as q'' versus $(T_w - T_{\text{ref}})$, where use of T_{sat} as the reference temperature is appropriate for fully developed boiling. However, if the free-stream temperature is constant and there is no transition from laminar to turbulent boundary layer flow, T_f can be used as the reference temperature without loss of clarity in the graphical presentation of results. As suggested by the open symbols of Fig. 12, for which the difference between T_f and T_{sat} is equivalent for each data set, the fully developed boiling data collapse to a single curve. The single-phase convection data lie on parallel lines that merge into the fully developed portion of the boiling curve at heat fluxes that increase with increasing velocity. If the free-stream temperature is not constant, its use as a reference temperature causes fully developed boiling curves for different values of T_f to be separated by amounts that are approximately equal to the differences in subcooling (shaded symbols of Fig. 12). The fully developed boiling data collapse to a single curve if T_{sat} is used as the reference temperature, but linearity of the single-phase data is lost.

The transition from single-phase convection to developed boiling is typically identified, and transition processes, such as temperature overshoot, can be detected by observing slope changes in the standard q'' versus ΔT boiling curve. This becomes difficult, however, downstream of the stagnation region where the slope of the single-phase convection data increases with transition to turbulence (Fig. 13). Moreover, the heat flux and temperature difference corresponding to transition vary with the jet velocity and fluid temperature. Data for different values of x/w_j do not, therefore, collapse on a q'' versus ΔT plot, and both developing turbulence and developing boiling affect changes in the slope of these curves.

Figure 13 appears to show temperature overshoot at all locations downstream of the stagnation line. Clearly, however, traditional pool boiling explanations of this phenomenon do not apply, since incipience and turbulence transition are coupled. Hysteresis, due to the activation and deactivation of nucleation sites, could occur near the stagnation line, where the velocity is low and the flow is laminar. Downstream, however, a sudden reduction in $T_w(x/w_j)$ with increasing heat flux could also be the result of a shift from a laminar to turbulent boundary layer, precipitated by incipient boiling. A more complete evaluation of hysteresis in the stagnation and wall jet regions will require regulation of dissolved gases and systematic measurements for rising and falling heat flux.

Data from this study do not extend to sufficiently high heat fluxes to permit derivation of a fully developed boiling correlation. However, Figs. 12 and 13 suggest an S-shaped boiling curve (Orell, 1967), for which an incipience-related decrease in surface temperature is followed by steady or falling T_w with increasing heat flux. Since $q'' \sim (n'')^m \Delta T_{\text{sat}}^n$, an increase in heat flux can be supported by constant or falling surface temperatures if there is a sufficient increase in the area number density of active nucleation sites. Eventually, the usual condition of $q'' \sim \Delta T_{\text{sat}}^n$ is observed as (n'') approaches a constant value.

Heat Transfer Coefficients. Representative heat transfer coefficient data are shown in Fig. 14. Except for $T_f = 30^\circ\text{C}$, results from experiments for which fully developed boiling covered the entire surface have been excluded from the figure, since the heat transfer coefficient did not vary with position. Convection coefficients for single-phase heat transfer increased much less in response to changes in heat flux, Fig. 14(a), than

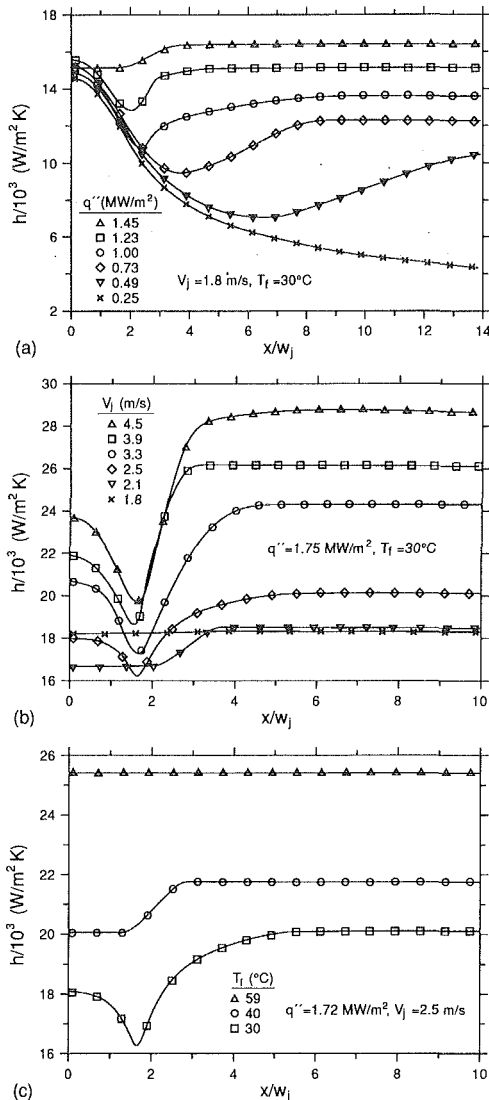


Fig. 14 Heat transfer coefficient distributions for different (a) heat fluxes, (b) jet velocities, and (c) jet temperatures

in response to changes in jet velocity, Fig. 14(b). However, since nucleate boiling is enhanced with increasing jet temperature or heat flux, partial boiling convection coefficients increase substantially with increasing q'' and T_j , as well as with increasing V_j . The convection coefficient becomes increasingly more sensitive to changes in heat flux as fully developed boiling is approached, while sensitivity to the jet velocity and subcooling decreases. Ruch and Holman (1975) and Miyasaka and Inada (1980) report $q'' \propto \Delta T_{\text{sat}}^3$ for fully developed boiling in the stagnation region in an impinging jet. It follows that $h = q'' / \Delta T_{\text{sat}} \propto \Delta T_{\text{sat}}^2$.

4 Conclusions

Key trends associated with the influence of surface heat flux are summarized by the surface temperature distributions shown schematically in Fig. 15. In the absence of boiling, surface temperature increases in the streamwise direction to a local maximum near the onset of boundary layer turbulence, Fig. 15(A). As the uniform heat flux is increased, incipient boiling coincides with x_c/w_j , which is the point of maximum surface temperature, Fig. 15(B). With an additional increase in heat flux, there is partial boiling in a region upstream, as well as downstream, of x_c/w_j , Fig. 15(C). Without boiling, the critical

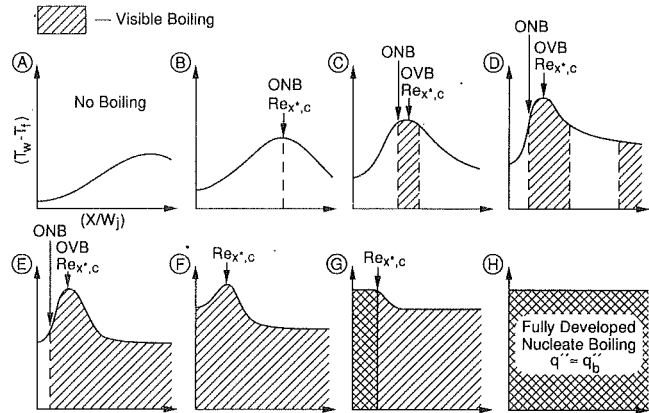


Fig. 15 Schematic of typical surface temperature distributions for forced convection boiling (Effect of increasing heat flux: A—single-phase convection; B—incipient boiling, $(T_w)_c = (T_w)_{\text{ONB}}$; C, D, E—single-phase convection and partial nucleate boiling; F, G—partial nucleate boiling; H—fully developed nucleate boiling)

Reynolds number is nearly constant ($Re_{x^*,c} \approx 3.6 \times 10^5$). When the heat flux for boiling incipience is exceeded, however, turbulence in the velocity boundary layer is closely coupled to incipience. Photographs show that x_c/w_j corresponds to the position in the flow stagnation line at which vapor bubbles are visually detected. The bubbles that can be photographically resolved also seem to be large enough to trip the boundary layer, Fig. 15(C). Although boiling covers the entire heated surface when sufficient heat flux is supplied, fluid acceleration stabilizes flow in the stagnation region, and transition is limited to the region $x_c/w_j \approx 1.6$.

The spread of visible boiling on the heated surface with increasing heat flux is not confined to a continuous area. The number and size of vapor bubbles sometimes diminishes in part of the region over which transition to turbulence occurs, while increasing farther downstream, Fig. 15(D). The surface temperature and heat flux are sufficient to support boiling in both regions, while turbulent mixing of free-stream fluid with heated liquid near the wall may suppress bubble growth until there is sufficient development of the turbulent thermal boundary layer.

Sensitivity to fluid velocity and temperature diminishes as boiling-induced mixing becomes more vigorous. Local variations in surface temperature are suppressed first in the region farthest from the stagnation line, Fig. 15(E), and the surface temperature response to increasing heat flux diminishes in regions of vigorous boiling. Consequently, surface temperatures in the stagnation region, where boiling is suppressed at lower heat fluxes, increase more quickly in response to additional heat flux once boiling is established at downstream locations, Fig. 15(E, F). Fully developed boiling is first established in the impingement region, Fig. 15(G), and spreads over the entire surface with increasing heat flux, Fig. 15(H).

The trends of Fig. 15 were observed with increasing heat flux for fixed V_j and T_j . With increasing jet velocity, regimes were shifted to higher heat fluxes, although the trends were qualitatively unchanged. Similarly, increasing the fluid temperature caused a shift to lower heat fluxes for each regime.

Acknowledgments

This study was supported by the National Science Foundation under Grants Nos. CPE-8414613 and CTS-8912831.

References

- Anderson, T. M., 1988, "Enhancement of Pool Boiling From a Simulated

Microelectronic Heat Source," MSME Thesis, Purdue University, W. Lafayette, IN.

Bergles, A. E., and Rohsenow, W. M., 1964, "The Determination of Forced-Convection Surface-Boiling Heat Transfer," *ASME JOURNAL OF HEAT TRANSFER*, Vol. 86, pp. 365-372.

Brown, W. T., 1967, "A Study of Flow Surface Boiling," Ph.D. Thesis, MIT, Cambridge, MA.

Collier, J. G., 1981, *Convective Boiling and Condensation*, McGraw-Hill, New York, pp. 109-205.

Hatta, N., Kokado, J., and Hanasaki, K., 1983, "Numerical Analysis of Cooling Characteristics for Water Bar," *Transactions of the Iron and Steel Institute of Japan*, Vol. 23, pp. 555-564.

Hatta, N., Kokado, J., Takuda, H., Harada, J., and Hiraku, K., 1984, "Predictable Modelling for Cooling Process of a Hot Steel Plate by a Laminar Water Bar," *Archiv. für Eisenhüttenwesen*, Vol. 55, pp. 143-148.

Hsu, Y. Y., 1962, "On the Size Range of Active Nucleation Cavities on a Heating Surface," *ASME JOURNAL OF HEAT TRANSFER*, Vol. 84, p. 207.

Ishigai, S., Nakanishi, S., and Ochi, T., 1978, "Boiling Heat Transfer for a Plane Water Jet Impinging on a Hot Surface," *Proceedings of the 6th International Heat Transfer Conference*, Vol. 1, pp. 445-450.

Jiji, L. M., and Clark, J. A., 1962, "Incipient Boiling in Forced Convection Channel Flow," presented at the ASME Winter Annual Meeting, Paper No. 62-WA-202.

Kokado, J., Hatta, N., Takuda, H., Harada, J., and Yasuhira, N., 1984, "An Analysis of Film Boiling Phenomena of Subcooled Water Spreading Radially on a Hot Steel Plate," *Archiv. für Eisenhüttenwesen*, Vol. 55, pp. 113-118.

Kutateladze, S. S., 1961, "Boiling Heat Transfer," *International Journal of Heat and Mass Transfer*, Vol. 4, pp. 31-45.

Ma, C. F., and Bergles, A. E., 1983, "Boiling Jet Impingement Cooling of

Simulated Microelectronic Chips," *Heat Transfer in Electronic Equipment*, ASME HTD-Vol. 28, pp. 5-12.

Ma, C. F., and Bergles, A. E., 1986, "Jet Impingement Nucleate Boiling," *International Journal of Heat and Mass Transfer*, Vol. 29, pp. 1095-1101.

Miyasaka, Y., and Inada, S., 1980, "The Effect of Pure Forced Convection on the Boiling Heat Transfer Between a Two-Dimensional Subcooled Water Jet and a Heated Surface," *Journal of Chemical Engineering of Japan*, Vol. 13, pp. 22-28.

Miyasaka, Y., Inada, S., and Owase, Y., 1980, "Critical Heat Flux and Subcooled Nucleate Boiling in Transient Region Between a Two-Dimensional Water Jet and a Heated Surface," *Journal of Chemical Engineering of Japan*, Vol. 13, pp. 29-35.

Moffat, R. J., 1988, "Describing the Uncertainties in Experimental Results," *Experimental Thermal and Fluid Science*, Vol. 1, pp. 3-17.

Narasimha, R., 1977, "The Three Archetypes of Relaminarization," *Proceedings of the Sixth Canadian Congress of Applied Mechanics (CANCAM 77)*, pp. 503-527.

Orell, A., 1967, "On S-Shaped Boiling Curves," *International Journal of Heat and Mass Transfer*, Vol. 10, pp. 967-971.

Patel, V. C., and Head, M. R., 1968, "Revision of Turbulent to Laminar Flow," *Journal of Fluid Mechanics*, Vol. 34, pp. 371-392.

Ruch, M. A., and Holman, J. P., 1975, "Boiling Heat Transfer to a Freon-113 Jet Impinging Upward Onto a Flat Heated Surface," *International Journal of Heat and Mass Transfer*, Vol. 18, pp. 51-59.

Vader, D. T., Incropera, F. P., and Viskanta, R., 1990a, "A Method for Measuring Steady, Local Heat Transfer to an Impinging Liquid Jet," *Experimental Thermal and Fluid Science*, Vol. 4, pp. 1-11.

Vader, D. T., Incropera, F. P., and Viskanta, R., 1990b, "Local Convective Heat Transfer From a Heated Surface to an Impinging, Planar Jet of Water," *International Journal of Heat and Mass Transfer*, Vol. 34, pp. 611-623.

An Experimental Study of Subcooled Film Boiling on a Vertical Surface—Hydrodynamic Aspects

R. Vijaykumar

V. K. Dhir

Mechanical, Aerospace, and Nuclear
Engineering Department,
School of Engineering and Applied Science,
University of California, Los Angeles,
Los Angeles, CA 90024

Interface and liquid velocities near the leading edge of a vertical wall 6.3 cm wide and 10.3 cm high were measured during subcooled film boiling of water at 1 atm pressure. The interface and liquid velocities in the boundary layer adjacent to the interface were measured using the hydrogen bubble flow visualization method. Photographs taken from the front and side showed the existence of a finite vapor layer at the leading edge and the existence of ripples and large-amplitude waves (bulges) on the interface. The bulges and ripples did not slide on the interface but moved in unison with the interface. The wave amplitude and wavelength were also measured. For a given subcooling and wall superheat, the amplitude, the interfacial velocity, and the wavelength were found to attain an equilibrium value several millimeters downstream of the leading edge. The waves were highly nonlinear and the interface velocities, which are found to be governed by the wave amplitude, were much larger than those predicted from the smooth interface, laminar flow theory. Streamlines in the liquid were found to expand into the wave valleys. At the wave peaks the streamlines appeared to be clustered together and the measured interface velocity gradients were high. The overall picture is one of expansion in the wave valleys and contraction (of flow) at the wave peaks. The flow field in turn is found to affect the liquid side heat transfer in subcooled film boiling significantly.

Introduction

Subcooled film boiling has been studied extensively in the past because of its application to quenching of an overheated nuclear reactor core after a loss of coolant accident, cooldown of superconducting magnets, and heat treatment of metals. Researchers have either obtained simplified analytical models (for example, Sparrow and Cess, 1962; Nishikawa and Ito, 1966), which do not take into account the actual conditions that prevail at the interface, or have obtained experimental correlations (for instance, Sakurai et al., 1986) with little emphasis placed on the interfacial behavior. Subcooled pool film boiling on spheres has been studied by Dhir and Purohit (1978). Their work involved both experiments and analysis of the film boiling heat transfer. They found that the observed film boiling heat transfer coefficients were 50–60 percent higher than those predicted by the laminar plane interface theory. It was proposed that the higher heat fluxes were caused by the vapor film oscillation and by the increase in interfacial area due to the presence of ripples on the interface. However, no mechanistic model was developed for the enhancement of subcooled film boiling heat transfer coefficient. The purpose of the present work is experimentally to investigate interfacial wave action during subcooled film boiling.

Few studies can be found in the literature in which the role of interfacial waves in altering the liquid flow pattern has been investigated. Moalem maron and Brauner (1987) have quantified the role of waves in increasing drag and friction factors in a falling film flow. A detailed study of the structure of waves on falling liquid films has been reported by Chu and Dukler (1977). Two kinds of wave were identified on the film interface. The large waves were lumps of liquid that traveled

much faster than the liquid substrate. The small waves rode on the large waves. A literature review of interfacial turbulence in gas-liquid flows can be found from Sideman (1974). The lack of investigations of the flow fields adjacent to interfacial waves is puzzling since there exists a large body of literature that describes the mechanism of production of turbulence adjacent to smooth and rough surfaces. Rashidi and Bannerjee (1989) used the oxygen bubble technique to study the flow field in a water layer adjacent to the interface between air and water and showed that burst formation led to the production of turbulence adjacent to the free surface. But in their study precaution was taken to avoid the formation of interfacial waves; thus their work is not directly relevant to the present work.

The effect of interfacial waves on heat transfer during saturated film boiling was studied mechanistically by Bui and Dhir (1985). Experiments were performed by Toda and Mori (1982) to obtain interfacial parameters for subcooled film boiling on a horizontal wire and on a sphere. The wire diameter was 0.3 mm and the sphere was 12.7 mm in diameter. Vapor film thickness, heat transfer rates, and minimum film boiling temperatures were measured. The vapor film thickness was found to vary with time. The magnitude and frequency of oscillations was found to decrease with increased subcooling. Unfortunately they neither correlated their data nor compared it with results from existing analyses. As yet no study of subcooled film boiling exists in the literature in which an attempt is made to develop a physical understanding of the effect of the interfacial waves on hydrodynamics and heat transfer. The aim of the present study is:

- 1 To determine the physical characteristics of the interfacial waves for different wall superheats and liquid subcoolings.
- 2 To determine the velocity field adjacent to the interface at different locations along the interface.

Contributed by the Heat Transfer Division for publication in the JOURNAL OF HEAT TRANSFER. Manuscript received by the Heat Transfer Division January 1991; revision received August 1991. Keywords: Boiling, Multiphase Flows, Phase-Change Phenomena.

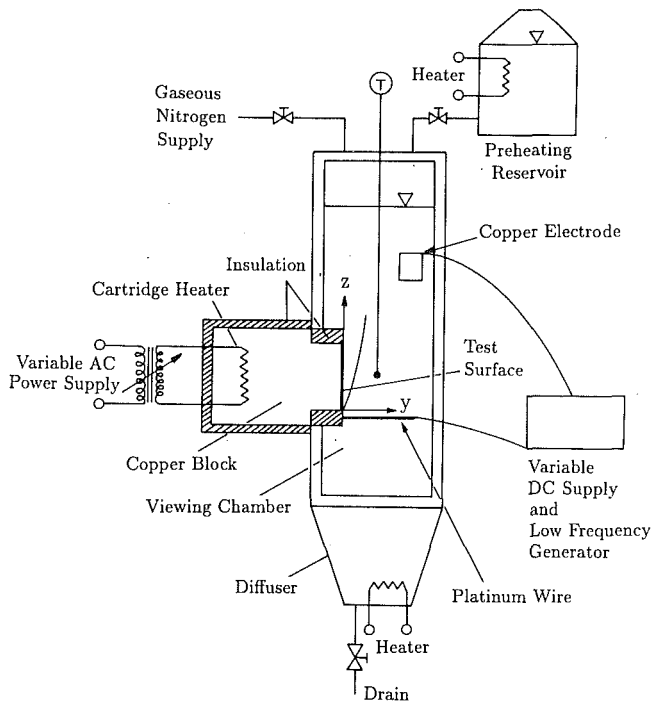


Fig. 1 Schematic diagram of experimental apparatus

3 To provide a semi-quantitative picture of the flow field resulting from the presence of the waves.

The hydrogen bubble technique is used to obtain velocity profiles in the liquid. Combined with the use of a video photographic system, it is possible to obtain the magnitude and the direction of liquid velocities. A detailed description of the hydrogen bubble technique is found from Shraub et al. (1965).

2.1 Experimental Apparatus. Figure 1 shows the apparatus. It includes the test section and a viewing chamber. The test section is mounted on one side of the viewing chamber and glass windows are placed on the other three sides for viewing the boiling process. The heater surface is rectangular, with a width of 6.3 cm and a height of 10.3 cm. It is formed by machining one end of a copper cylinder. The other end of the cylinder is drilled to insert several cartridge heaters. Temperature is measured with thermocouples embedded in the test block. The test liquid is confined to the viewing chamber and is boiled on the copper surface. The apparatus is mounted on a holographic table. Complete details of the apparatus are given by Bui (1984).

The primary aim of this experimental program was to obtain

interface and liquid velocities in subcooled film boiling of water on a vertical plate. A platinum wire was placed normal to the copper plate at various distances downstream and upstream of the leading edge. The platinum wire was 0.05 mm in diameter. A potential difference was established between this wire and a copper plate electrode immersed in the liquid. The voltage was applied by a variable d-c source and the supply was pulsed using a relay circuit in conjunction with a low-frequency generator. The frequency of the pulse and the voltage difference were varied until a well-defined succession of bubble rows was observed. Strong side lighting along the wire showed, by scattered light, the hydrogen bubbles against a dark background. These bubbles were photographed on videotape using a camera.

In the experiments, rows of the hydrogen bubbles were released at fixed predetermined intervals of time. The applied voltage was maintained between 80–100 v. The current was pulsed at either 40, 80, or 175 c/s. The wire was placed at two positions either 1.2 cm ahead of the leading edge or 0.8 cm downstream of the leading edge. The bubble sizes were estimated to be about half of the wire diameter or about 0.02 mm. These bubbles have very low rise velocities (0.7 mm/s). About 15–20 bubbles were released at each pulse during velocity measurements and since the volume occupied by the bubbles and their rise velocities are small, bubble induced mixing can be neglected. The hydrogen bubble experiments were performed in subcooled film boiling with liquid subcooling ranging from 1.4 K to 7.0 K. In these experiments the wall superheat was either 200 K or 300 K.

Simultaneous measurements of the interface wave amplitude, the vapor substrate thickness, and the wavelength of the dominant waves were made. All of the measurements were made from the video pictures. The framing rate was either 30 or 60 frames/s. A few time exposure still photographs were also taken. These photographs provide streaklines in the liquid. Streamlines in the liquid could be captured by still photographs when a large number of hydrogen bubbles were introduced into the flow field.

2.2 Experimental Procedure. Startup of a typical experiment began with deaeration of the test liquid by vigorous boiling in a separate reservoir and with preheating of the test section. The chamber was purged with nitrogen gas during the preheating period to avoid oxidation of the test surface. The block was heated to 673 K and the test section was filled with water from the reservoir. The wall superheat was set by adjusting the voltage applied to the cartridge heaters. When steady state was reached, thermocouple output was recorded on a Fluke data-logger. Tests were considered to be at steady state when the temperature of the test block changed less than ± 1

Nomenclature

c_f = interfacial friction factor defined as $2\mu_i \partial u / \partial y / \rho_l \mu_i^2$	u = liquid velocity in the z direction	λ = wavelength
\bar{c}_f = average interfacial friction factor over one wavelength	v = liquid velocity in the y direction	μ = molecular viscosity
d = diameter of the hydrogen bubble	y = distance normal to the heater wall	ρ = density
f = framing rate of the video camera	z = distance along the heater from the leading edge	ψ = stream function
g = gravitational acceleration	ΔT_w = wall superheat defined as $T_w - T_{sat}$	Subscripts
Re_η = Reynolds number based on wave amplitude, defined as $\rho \mu \eta_{max} / \mu_l$	ΔT_{sub} = liquid subcooling defined as $T_{sat} - T_l$	b = bubble
S = magnification of the video picture	Δz = displacement of the hydrogen bubble	i = interface
T = temperature	η = amplitude of the dominant wave	l = liquid
		max = maximum
		sat = saturated
		sub = subcooled
		t = terminal
		w = wall
		Superscripts
		$\bar{\quad}$ = average

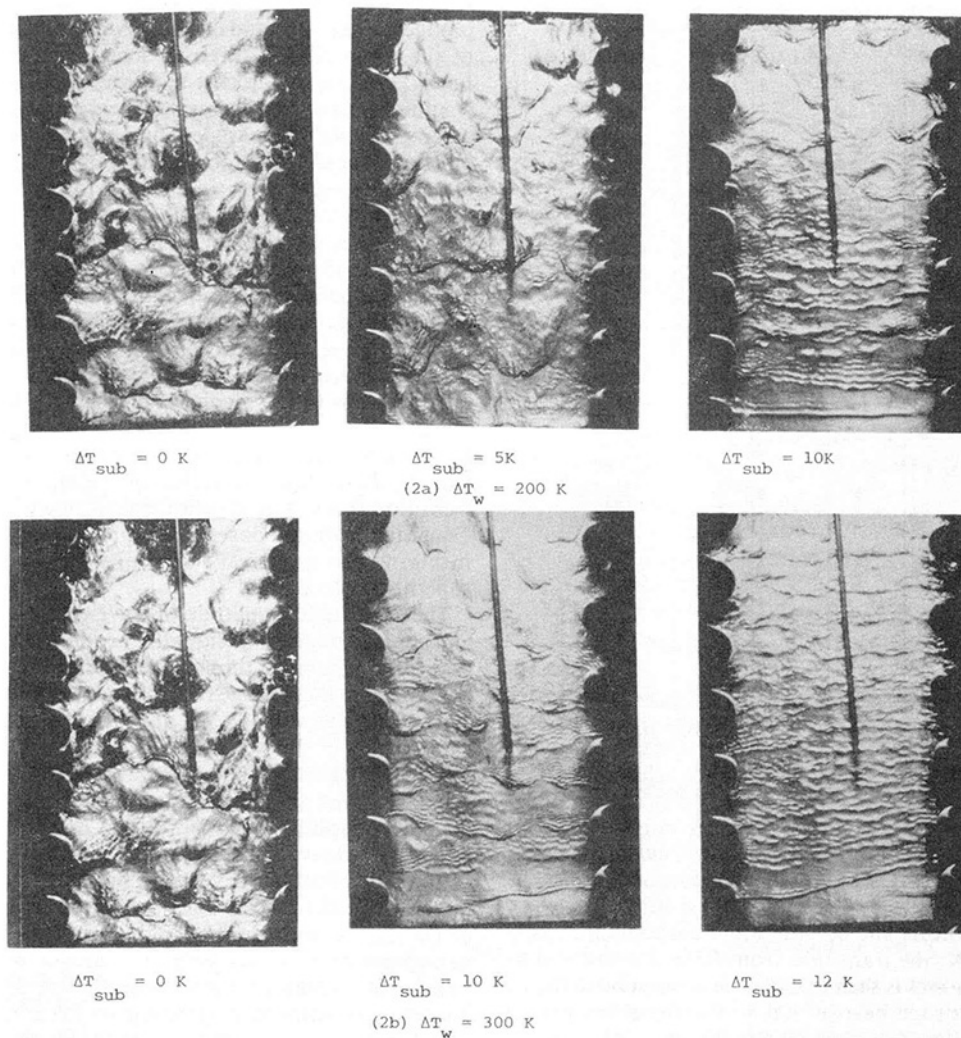


Fig. 2 Frontal view of the interface in subcooled film boiling

K in 5 min. The liquid temperature changes were less than ± 0.2 K in 1 min up to a liquid subcooling of 10 K. Care was taken to avoid thermal stratification. The liquid thermal stratification was found to be less than 0.7 K over a height of 10 cm. Once steady-state conditions were established, the wire was pulsed to generate hydrogen bubbles and the bubble paths were photographed.

2.3 Data Reduction. Liquid velocity was measured from the bubble markers in two ways. In the pathline method, the displacement of a specific bubble in the bubble row was measured between two consecutive video frames to obtain the velocity as

$$u = \frac{\delta z}{S} f \quad (1)$$

where f is the framing rate of the video camera and S is the magnification factor of the camera. The magnification factor had a value of 6. The calculated value of the velocity is assigned to the halfway point between the initial and final locations of the bubble.

Alternatively, the relative displacement between two bubbles that were generated at the same spot on the wire at different but known times was measured. This method is termed the single frame method. The velocity u is measured by the same expression as noted above except that, now, f is the bubble wire pulsing rate and δz is the relative displacement. It should be pointed out that the measured velocity is an average velocity

and is not the random or fluctuating velocity due to turbulence in the liquid.

The interface velocities were measured from the video pictures either by noting the movement of any position of the interface between two frames or by noting the displacement of a hydrogen bubble which straddles the interface. The streak lines were obtained from time exposure photographs in which the exposure time was 1/15 second. As shown in the appendix, the overall uncertainties in the measurement of bubble displacement and velocity are calculated to be ± 11 and ± 12 percent, respectively.

3 Results and Discussion

Visual observations of film boiling on the vertical surface indicated that in saturated film boiling the interface was covered by two types of waves: large waves, which evolve into vapor domes, and small waves, which are here referred to as ripples. The large waves were three dimensional whereas the ripples appeared to be two dimensional. With increase in subcooling, the amplitude and wavelength of the large waves shrank until no distinction could be made between the two types of wave and all the waves appeared to be two dimensional. Also, in saturated film boiling, a thick vapor layer was observed to exist at the leading edge. The waves tended to form a few millimeters downstream of the leading edge. With increases in subcooling, the leading edge vapor layer thinned and the distance to form the waves became longer. At a wall superheat

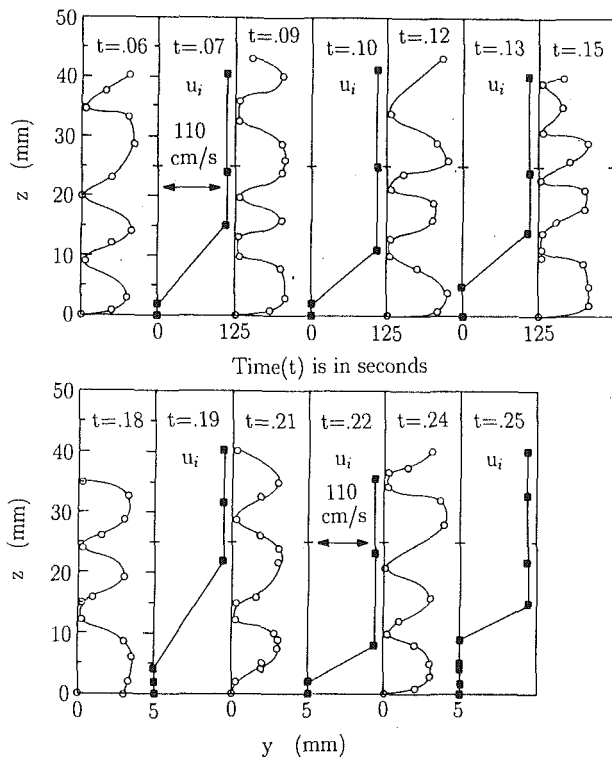


Fig. 3 Side view of the interface subcooled film boiling ($\Delta T_w = 200$ K, $\Delta T_{sub} = 1.5$ K)

of 200 K and a liquid subcooling of 10 K, the waves were seen to form at about 20 mm from the leading edge. Photographs in Figs. 2(a) and 2(b) show the frontal view of the interface for two wall superheats and several liquid subcoolings. For a superheat of 200 K, the transition from three-dimensional to two-dimensional waves is seen to occur between subcooling of 5 and 10 K. For a superheat of 300 K, the transition occurs at a higher subcooling (between 10 and 20 K).

Figure 3 shows the side view of the interface as obtained from the video pictures taken at a wall superheat of 200 K and a liquid subcooling of 1.5 K. The interface velocity obtained by measuring the displacement of any location of the interface between two successive frames of the video is plotted between each pair of figures showing the contour of the interface at the time when they were videotaped. In Fig. 3 the measured interface velocity is assigned a time that is the average of the times corresponding to the two locations of the interface. It is seen that the leading edge vapor layer is stationary and probably acts as a vapor reservoir. Vapor shoots out of this reservoir and quickly attains its terminal velocity. This behavior is very similar to that of a falling film originating from a liquid container. The size of the leading edge vapor layer is observed to increase with time and the vapor mass eventually (time period between $t = 1/5$ and $7/30$ s) leaves as a part of the moving interface. This process repeats in a cyclic fashion. The large wave amplitude and the wavelength appear to be nearly independent of the distance from the leading edge. For the experimental conditions corresponding to Fig. 3, the interface velocity downstream of the leading edge vapor layer is found to remain constant at about 110 cm/s.

It should be noted here that no distinction could be made between the wave and the interface velocity. The interface contoured in the shape of large bulges and ripples simply slipped through the liquid. This behavior is different from that observed in falling liquid films where large waves in the form of lumps of liquid move much faster than the liquid substrate.

The wavelength, the wave amplitude, and the interfacial velocity data obtained from figures such as Fig. 3 and from similar data for other subcoolings and wall superheats are

plotted in Figs. 4, 5, and 6. The wave amplitude is the thickness of the vapor film at different locations along the interface. From Fig. 4, it is seen that both the amplitude and the wavelength decrease with increasing liquid subcooling. At low subcoolings the wave amplitude shows a much stronger dependence on the liquid subcooling as compared to the wavelength. The effect of increased wall superheat is to push the curves faired through the data slightly up and to the right. From the data two distinct regimes can be identified: a low subcooling regime and a high subcooling regime. In the low subcooling regime a gradual reduction of wavelength and amplitude is observed. In the second or high subcooling regime, the limited data show that the wavelength and the amplitude become nearly independent of subcooling. For the two superheats, the transition from the first to the second regime occurs in a narrow range of subcoolings. In the transition region a rapid drop in wavelength and wave amplitude is observed. Photographic observations show that this transition regime coincides with the transition from three-dimensional to two-dimensional waves. Consistent with the observations made from the photographs in Fig. 2, the transition shifts to higher subcoolings as wall superheat is increased.

The maximum amplitude-to-wavelength ratio is plotted in Fig. 5 as a function of liquid subcooling. The height of the peak of the bulge is termed the maximum amplitude and is not related to the average film thickness. At subcoolings higher than 10 K, the ratio $\bar{\eta}_{max}/\lambda$ appears to approach a constant value of about 0.16. It suggests that for all subcoolings the interfacial waves are nonlinear in nature ($\bar{\eta}_{max}/\lambda \gg 0.01$). It was also noted that for studied subcoolings and superheats, the wave amplitude was more than one order of magnitude larger than the vapor substrate thickness. Interfacial velocity as measured with the hydrogen bubble technique as well as directly from the video pictures is plotted in Fig. 6 as a function of the wave amplitude. For both superheats, the data appear to collapse on a single curve. The unique dependence of the interfacial velocity on the wave amplitude is indicative of the important role played by vapor bulges (large waves). The vapor bulges protruding into the liquid provide an additional buoyancy force, which causes the wavy interface to move much faster than a plane interface. As an example, for saturated film boiling, the velocities calculated from the plane interface analysis in which vapor and liquid velocities and shear stresses are matched at the interface are about 80 times smaller than those observed in the experiments. Bui and Dhir (1985), by balancing the buoyancy force with the drag force on a spherical bulge, showed that for saturated film boiling the interfacial velocity should vary as¹:

$$u_i \sim \bar{\eta}_{max} \left[\frac{(\rho_l - \rho_v) g}{\rho_l \sqrt{\nu_l}} \right]^{2/3} \quad (2)$$

In Fig. 6 Eq. (2) is plotted as a dotted line. The observed velocity of about 3 m/s for $\bar{\eta}_{max} = 10.4$ mm (saturated film boiling) is about the same as that predicted by Bui and Dhir. However, as the amplitude becomes small, the interfacial velocity decreases more strongly with the amplitude. For a two-dimensional wave ($\bar{\eta}_{max} = 0.5$ mm), the interface velocity is seen to vary approximately as $\bar{\eta}_{max}^{-2.5}$. In the asymptotic limit ($\bar{\eta}_{max}/\lambda \sim 0.16$), the interfacial velocity is about one order of magnitude higher than that given by the plane interface analysis (see Vijaykumar, 1990).

The interfacial velocity introduced by the vapor bulges alters the velocity profile in the vapor film and the flow field in the liquid adjacent to the wall. These in turn affect the heat transfer from the interface and from the wall. The dominant wavelength and wave amplitude are affected by the velocity profile in the

¹Here it is assumed that maximum amplitude of the bulge is equal to the base diameter of the bulge.

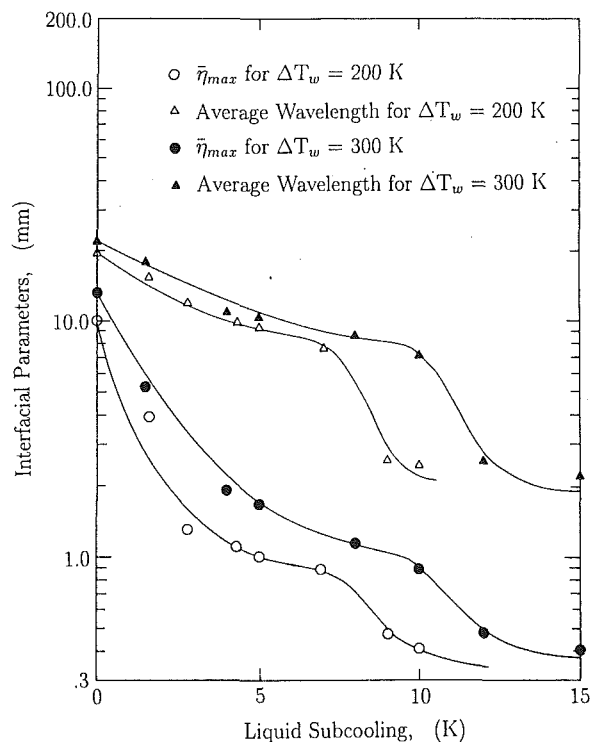


Fig. 4 Interfacial parameters as a function of subcooling

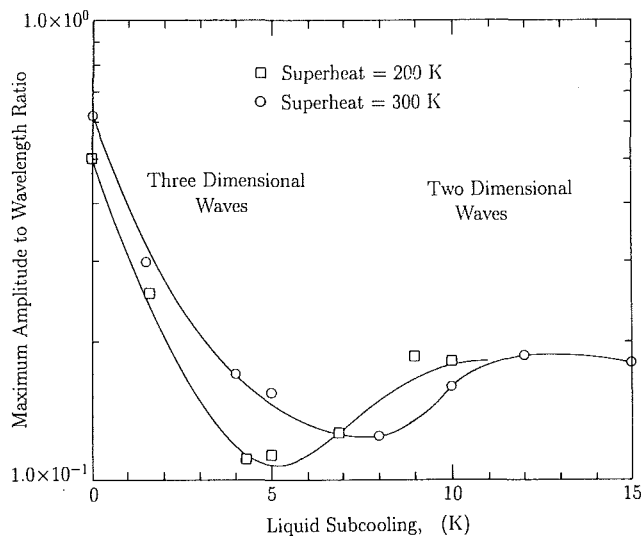


Fig. 5 Ratio of amplitude to wavelength as a function of subcooling

vapor film as well as the rate of heat transfer. Thus the wave amplitude, interfacial velocity, and the rate of heat transfer are all coupled quantities that provide feedback to one another. Earlier film boiling studies employing the plane interface analysis have shown that the heat transfer rates predicted with the slip condition at the interface generally fair better with the data. However, the reason as to why the results from the analysis in which interfacial velocity and shear stress were matched compared poorly with the data was not entirely clear. The present work shows that the additional buoyancy force provided by the vapor bulges protruding into the liquid results in larger interfacial velocities. The increased interfacial velocity leads to enhancement in heat transfer from the heater surface.

Velocities at different locations in the liquid adjacent to the interface were obtained from video pictures. Complete flow field information was developed from a composite of velocity distribution from several frames of video pictures. It should be noted that the path line method requires bubble positions

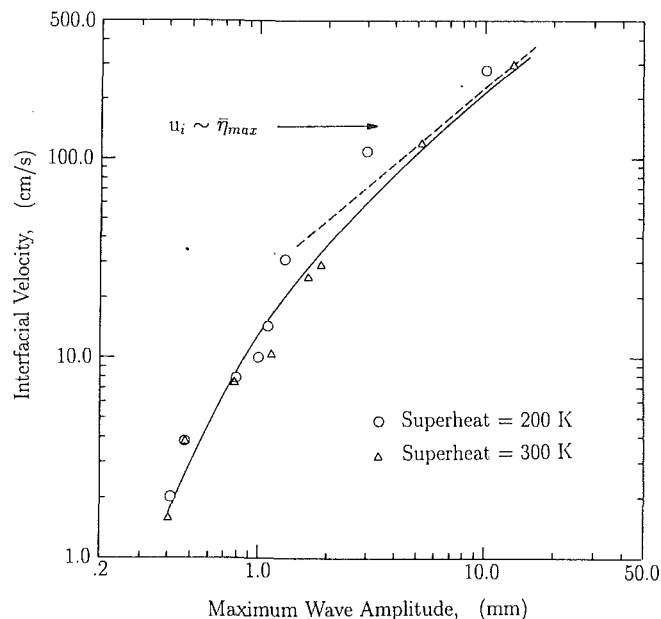


Fig. 6 Interface velocity as a function of wave amplitude

from two successive frames to be averaged and that the interface moves relative to a stationary observer. Hence it is clear that instantaneous local velocity profiles cannot be obtained for a particular shape and location of the interface. The path-line method was used to measure liquid velocities outside of the wavy region. For the wave valleys, all of the liquid velocities were obtained by the single frame method. Knowing the velocity components parallel to and normal to the plate, the streamlines can be determined from the equation

$$d\psi = udy + vdz. \quad (3)$$

Figure 7 shows the approximate streamline pattern, while Figs. 8 and 9 show the profiles of the velocity components u and v , respectively. The velocities were obtained by both the single frame method and the pathline method. The velocities obtained from single frame method are plotted alongside the interface contour obtained at the same instant. However, the velocities obtained by the pathline method are plotted alongside the contour of the interface obtained at a time corresponding to the initial location of the bubbles. (A more detailed discussion of this procedure is given by Vijaykumar, 1990.) For the data plotted in Figs. 7-9, the wall superheat was 203 K and the liquid subcooling was 1.8 K. From Fig. 7 it is seen that the temperature difference between the stationary vapor-liquid interface of the leading edge vapor layer and the liquid introduces a weak upward flow. The rapid acceleration of the interface downstream of the leading edge vapor layer causes the liquid from the pool to be drawn into the valley downstream of the stationary leading edge vapor layer. The liquid drawn into the valley turns around and is ejected out near the peak. At the peak, fluid stream exiting the valley and the fluid stream in the liquid layer outside the wavy region merge. As a result the streamlines are compressed there. Downstream of the peak, the flow divides, leading to the expansion of the streamlines. The expansion is followed by a contraction at the peak of the second wave. Thus a cyclic expansion of the streamlines in the valleys and contraction at the peaks occur.

In Fig. 8, the profiles for liquid velocities parallel to the plate are plotted for several locations at the interface. At locations a and b on the stationary interface of the leading edge vapor layer, the velocity profiles are of the natural convection boundary layer type with maximum velocity occurring away from the interface. The measured thickness of the boundary layer at points a and b is relatively large. This is probably a result of the flow induced by the moving interface downstream

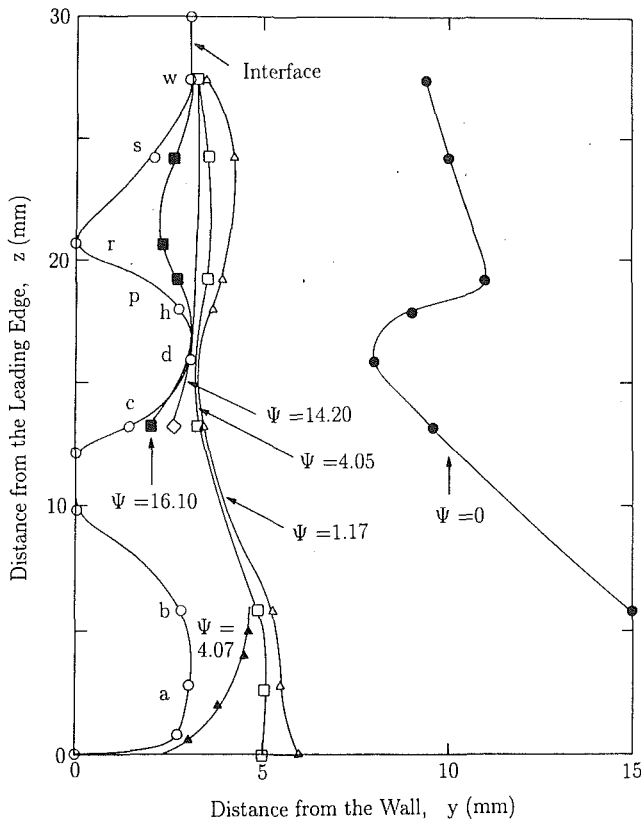


Fig. 7 Streamlines adjacent to the interface ($\Delta T_w = 203$ K, $\Delta T_{sub} = 1.8$ K)

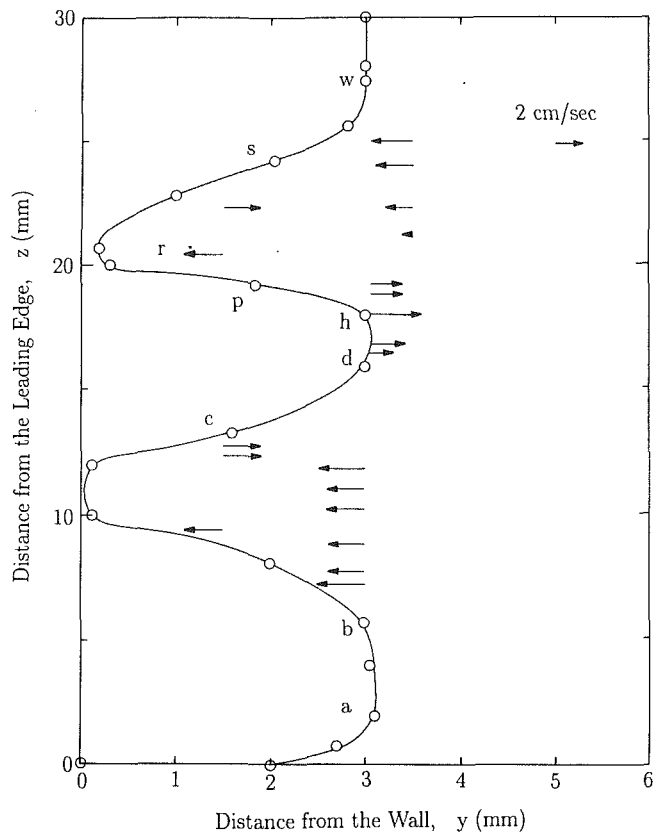


Fig. 9 Velocity profiles of the v component of the velocity ($\Delta T_w = 203$ K, $\Delta T_{sub} = 1.8$ K)

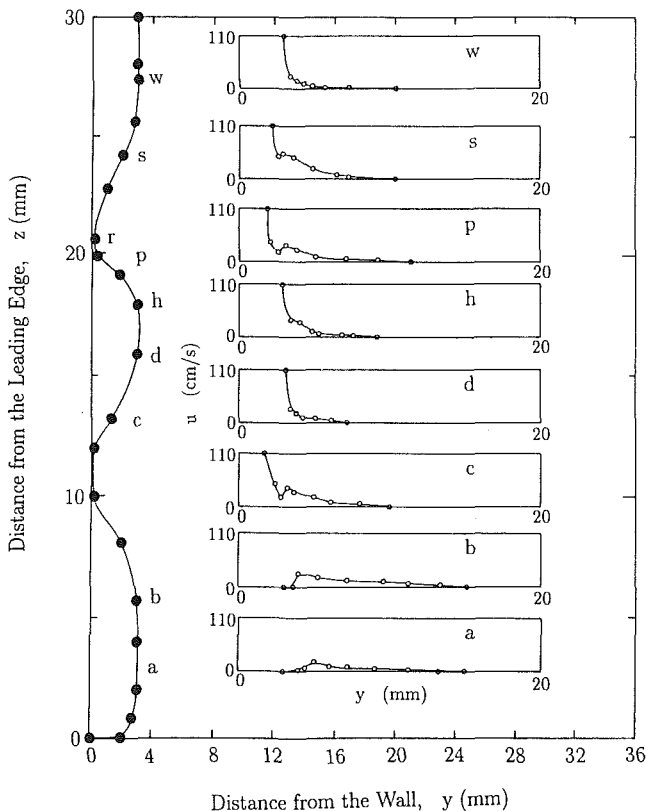


Fig. 8 Velocity profiles of the u component of the velocity ($\Delta T_w = 203$ K, $\Delta T_{sub} = 1.8$ K)

of the leading edge stationary vapor layer. The magnitude of the velocity increases in the direction of the flow. Beyond location b , the boundary layer thins. The thinning of the

boundary layer is the result of the turning of the flow toward the first valley of the wave. At point c on the front side of the first wave peak, the u component of velocity decreases in magnitude from a maximum at the interface to a minimum at about 1.2 mm from the interface. Thereafter the velocity attains another maximum value before asymptotically decreasing to zero. At the first peak of the wave (location d), the liquid velocity has a maximum at the interface and declines rapidly to near zero at the edge of the boundary layer. The boundary layer at location d is much thinner than that at location c . The observed steep velocity gradient corresponds to a high shear stress at the interface.

At location h downstream of point d but still on the top portion of the peak of the wave, the velocity profile is similar to that at d except that the boundary layer is thicker with a smaller velocity gradient at the interface. At point p on the back side of the first peak and at point s on the front side of the second peak, the velocity profiles are similar to those observed at c in that they have a hump. The hump at location c is indicative of the merger of the liquid stream exiting the wave valley and the liquid stream resulting from the flow induced in the pool. At location p the flow splits into two streams, one flowing into the valley and the other flowing out of the valley. The two streams merge again near s . The boundary layer thicknesses at points c , p , and s are much larger than those at points d and h . At point w on the second peak, the velocity profile is similar to that observed at point d .

The v velocity vectors plotted in Fig. 9 show flow into and out of the valleys and away from the peaks of the waves. The observed velocities normal to the plate are at least one order of magnitude smaller than those observed parallel to the plate. The flow into the valleys occurs at the back of the peaks, whereas the flow out of the valley occurs in front of the peaks. Or, in other words, the flow splits into two parts just behind the peaks. One of the streams travels outside the wave valleys

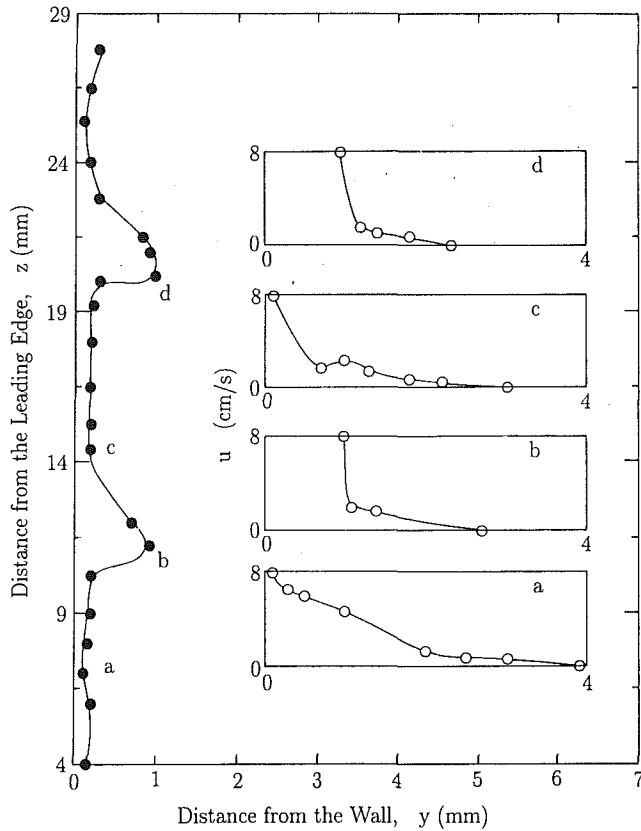
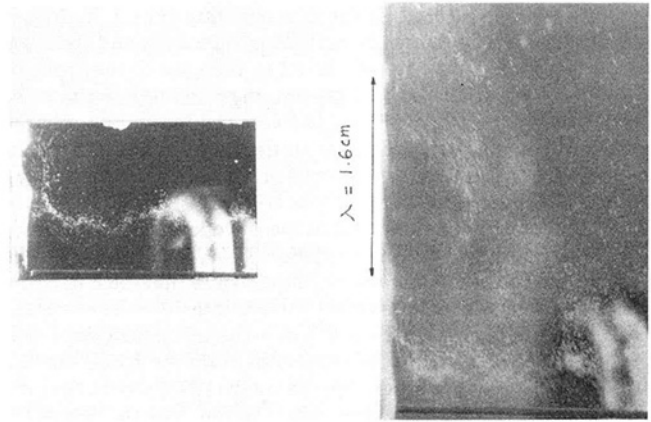


Fig. 10 Velocity profiles of the u component of the velocity ($\Delta T_w = 207$ K, $\Delta T_{sub} = 6.7$ K)

whereas the other travels in the wave valleys. The two streams merge into each other at the wave peaks. The process is reflective of the expansion of the flow in the wave valleys and contraction at the front of the peaks.

Figure 10 shows the interface shape and u velocity profiles for a wall superheat of 207 K and for a liquid subcooling of 6.7 K. For this case the vapor film thickness and the amplitude of wave bulges are much smaller than those for a subcooling of 1.8 K. The interface velocity of 8 cm/s is about one order of magnitude smaller than that observed at a subcooling of 1.8 K. At point a just downstream of the location where the interface velocity accelerates to the terminal velocity, the u velocities show a gradual drop from the velocity at the interface to a near zero velocity in the pool. At locations b and d on the first and the second peaks, a rapid drop in liquid velocity from a maximum at the interface is observed and this leads to a steep velocity gradient at the interface. At point c located on the back of the first peak, a hump in the velocity profiles is noted. These observations are similar to those made earlier for a subcooling of 1.8 K. Thus it appears that the phenomenon of expansion and contraction of the flow fields in the valleys and at the peaks respectively continues to persist at higher subcoolings. Similar results for intermediate subcoolings are given by Vijaykumar (1990). The essential features of flow in the liquid layer are illustrated in the photographs displayed in Fig. 11. In Fig. 11, photograph (i) shows the flow field outside of the waves. This photograph supports the result shown in Fig. 7, that the bulk of the flow adjacent to the wavy interface occurs outside the wave valleys. Photograph (ii) shows the streamlines in the liquid flow. The streamlines are split just behind the wave peak. The flow in the wave valleys shown by the very faint streamlines is very small. The flow ejected outside the wave valleys tends to return to the interface and seems to collide on the wave peak. Although some three-dimensional effects tend to obscure the picture, the essential features can still be seen.



(i) Figure Showing Flow Field Outside the Waves. $\Delta T_w = 200$ K; $\Delta T_{sub} = 2.0$ K.
(ii) Figure Showing Splitting of Streamlines at the Wavepeak $\Delta T_w = 202$ K; $\Delta T_{sub} = 1.8$ K.

Fig. 11 Photographs of flow in subcooled film boiling

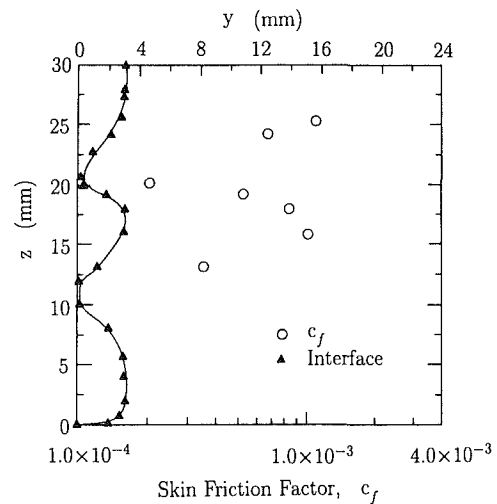


Fig. 12 Skin friction factor plotted as a function of z ($\Delta T_w = 203$ K, $\Delta T_{sub} = 1.8$ K)

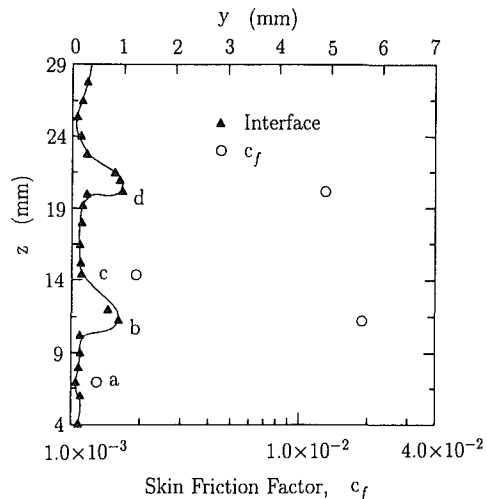


Fig. 13 Skin friction factor plotted as a function of z ($\Delta T_w = 207$ K, $\Delta T_{sub} = 6.7$ K)

In Figs. 12 and 13 the local interfacial skin friction coefficient is plotted adjacent to the contour of the interface for the two cases of liquid subcooling discussed earlier. The velocity used in the computation of the skin friction is the interface velocity. Since the leading edge vapor layer is stationary, the skin friction

factors plotted in Fig. 12 for a subcooling of 1.8 K do not include the results for the skin friction factor around the leading edge. In Fig. 12, c_f is observed to increase in the front of the first peak and reaches a maximum at the top of the wave peak. Behind the wave peak, c_f decreases to a minimum in the wave valley and increases again in the front of the next peak. The skin friction factor is plotted in Fig. 13 for a subcooling of 6.7 K. These results are similar to those seen in Fig. 12, in that c_f increases to a maximum at the wavepeaks, and decreases to a minimum in the wave valleys. Thus, it is seen that the waves alter the shear stress in the liquid such that local maxima and minima of shear stress occur on the interface. The average skin friction factor over each wave for all subcoolings was found to be a function of Reynolds number based on the maximum wave amplitude. Vijaykumar (1990) shows that the relation between the average skin friction and the Reynolds number was of the form $\bar{c}_f = 0.55\text{Re}_\eta^{-0.65}$. These results have important implications for heat transfer, but that discussion is reserved for the companion paper.

Summary and Conclusions

1 The vapor-liquid interface in subcooled film boiling is composed of a vapor substrate on which there exist two types of waves, termed the ripples and large waves. These waves are preceded by a leading edge vapor layer. The leading edge vapor layer is quasi-stationary but the interface downstream moves at nearly a constant velocity.

2 The amplitude of the dominant wave controls the interface velocity. The maximum amplitude of the waves is much larger than the vapor substrate thickness and bears a relation to the wavelength. Based on the amplitude-to-wavelength ratio, the interface in subcooled film boiling can be divided into two regimes of behavior.

3 In the low subcooling regime (three dimensional waves), adjacent to the thick leading edge vapor layer, the flow due to the developing liquid boundary layer and that due to the acceleration of the interface downstream merge. The flow so formed is then entrained by the moving interface. At the top of the first peak, the velocity profiles show a steep gradient at the interface. In the valley behind the first wave, flow expands and the velocities decrease in the boundary layer. A local minimum and a maximum in velocity could be noted in the boundary layer. Flow was found to contract and expand at the succeeding wave peak and valley, respectively.

4 At higher subcoolings (two dimensional waves), the liquid boundary layer thins but the phenomenon of expansion and contraction of the flow in the valleys and at the peaks, respectively, is similar to that for low subcoolings.

Acknowledgments

This work received support from the NSF under grant No. CBT-88-17684.

References

- Bui, T. D., 1984, "Film and Transition Boiling on a Vertical Surface," Ph.D. Dissertation, University of California, Los Angeles.
- Bui, T. D., and Dhir, V. K., 1985, "Film Boiling Heat Transfer on an Isothermal Vertical Surface," *ASME JOURNAL OF HEAT TRANSFER*, Vol. 107, pp. 764-771.
- Chu, K. M., and Dukler, A. E., 1977, "Flow in a Falling Wavy Liquid Film," *Chem. Eng. Science*, Vol. 9, pp. 108-119.
- Dhir, V. K., and Purohit, G. P., 1978, "Subcooled Film Boiling Heat Transfer From Spheres," *Nuclear Engineering and Design*, Vol. 47, pp. 49-66.
- Moalem maron, D., and Brauner, N., 1987, "Characterization of Interfacial Velocity in Wavy Thin Film Flow," *International Communications in Heat and Mass Transfer*, Vol. 14, p. 293-302.
- Nishikawa, K., and Ito, T., 1966, "Two Phase Boundary Layer Treatment of Film Boiling," *Int. J. Heat Mass Transfer*, Vol. 9, pp. 103-115.
- Rashidi, M., and Banerjee, S., 1989, "Turbulence Structure in a Free Surface Channel Flow," *Physics of Fluids*, Vol. 31, pp. 2491-2503.
- Sakurai, A., Shiotsu, S., and Hata, K., 1986, "Effects of Subcooling of Film Boiling Heat Transfer From a Horizontal Cylinder in a Pool of Water," *Heat Transfer*, 1986, Vol. 4, Hemisphere Publishing Co., Washington, DC, pp. 2043-2048.
- Schlichting, H., 1979; *Boundary-Layer Theory*, McGraw-Hill, New York, pp. 426-427.
- Shraub, F. A., Kline, S. J., Henry, J., Runstadler, P. W., and Littel, A., 1965, "Use of Hydrogen Bubbles for Qualitative Determination of Time-Dependent Velocity Fields in Low Speed Water Flows," *ASME Journal of Basic Engineering*, Vol. 87, pp. 429-444.
- Sideman, S., 1974, "Interfacial Turbulence," *Advances in Transport Phenomena*, Vol. 4, pp. 153-213.
- Sparrow, E. M., and Cess, R. O., 1962, "The Effects of Subcooled Liquid on Laminar Film Boiling," *ASME JOURNAL OF HEAT TRANSFER*, Vol. 84, pp. 139-152.
- Toda, S., and Mori, M., 1982, "Subcooled Film Boiling and Behavior of Vapor Film on a Horizontal Wire and a Sphere," *Proc. 7th Int. Heat Transfer Conf.*, Vol. 4, Munich, pp. 173-178.
- Vijaykumar, R., and Dhir, V. K., 1989, "A Holographic Study of Subcooled Film Boiling Heat on a Vertical Surface," *Multiphase Flow, Heat, and Mass Transfer*, ASME HTD-Vol. 109, pp. 125-132.
- Vijaykumar, R., 1990, "Hydrodynamics and Heat Transfer Aspects of Subcooled Film Boiling on a Vertical Surface," Ph.D. Dissertation, University of California, Los Angeles.

APPENDIX

Error Analysis

The uncertainty in determining the velocity from Eq. (1) is

$$\frac{\Delta u}{u} = \sqrt{\left(\frac{\Delta f}{f}\right)^2 + \left(\frac{\Delta S}{S}\right)^2 + \left(\frac{\Delta(\delta z)}{\delta z}\right)^2} \quad (\text{A.1})$$

The estimated error in frequency determination is ± 1.5 percent. The error in magnification factor as determined from a photograph of a reference ruler is ± 0.4 percent. However, the uncertainty in measuring the displacement arises from a variety of sources as enumerated below:

1 Measurement of δz on the video monitor. The error is estimated to be ± 10.3 percent.

2 Averaging effects due to a changing velocity field. This error results from the prediction of the exact fluid velocity from time-averaged velocity of the bubble over a small time interval. This error is estimated to be ± 4.1 percent.

3 Bubble rise velocity. The terminal velocity of a bubble is calculated as

$$u_t = \frac{1}{18} \frac{\rho_l - \rho_b}{\mu_l} g d^2 \quad (\text{A.2})$$

and equals 0.7 mm/s for the 0.02-mm-dia bubble. The error due to terminal velocity of the bubble is assumed to be low except at the edge of the boundary layer.

4 Response uncertainties due to finite size of the bubbles. According to Shraub et al. (1965), the response time of the 0.02 mm bubbles is 10^{-7} s. Thus error in the displacement measurement due to response time uncertainty can be neglected.

5 The displacement of the bubble from the z - y plane. Although the bubbles were seen to move out of the plane of release, the displacement error due to this effect is meaningful only at very low velocities.

The net error in displacement measurement is calculated to be ± 11 percent, whereas the net error in determination of velocity is ± 12 percent.

R. Vijaykumar

V. K. Dhir

Mechanical, Aerospace, and Nuclear
Engineering Department,
School of Engineering and Applied Science,
University of California, Los Angeles,
Los Angeles, CA 90024

An Experimental Study of Subcooled Film Boiling on a Vertical Surface—Thermal Aspects

Wall and liquid side heat fluxes near the leading edge of a vertical wall 6.3 cm wide and 10.3 cm high were measured during subcooled film boiling of water at 1 atm pressure. The heat flux from the interface into the liquid and temperature profiles in the liquid thermal layer were measured using real time holographic interferometry. The wall heat flux was measured with thermocouples embedded in a copper block, one face of which served as the heated wall. The role of the leading edge vapor layer, ripples, and large bulges in modifying the liquid side heat transfer is quantified.

1 Introduction

Since Bromley's (1950) study of film boiling, numerous studies of saturated and subcooled film boiling on heaters of various geometries have appeared in the literature. Subcooled film boiling from a vertical wall was studied theoretically by Sparrow and Cess (1962). Employing a boundary layer type analysis and assuming a rigid wall condition at the vapor-liquid interface, they showed that the heat transfer coefficient depended on five dimensionless parameters based on fluid properties, wall superheat, and liquid subcooling.

Frederking and Hoppenfeld (1964) used an integral method to study subcooled film boiling on a vertical wall and obtained heat transfer coefficients for the extreme cases of low and high subcoolings. For moderate subcoolings a weighted average of the two extreme cases was used. No experimental verification was provided.

A theoretical study of subcooled film boiling on horizontal cylinders and a vertical plate was performed by Nishikawa and Ito (1966), who solved the boundary layer type equations for the two phases. Nishikawa and Ito matched velocity and shear stress at the interface and showed that the heat transfer coefficient was dependent on six parameters instead of five, as suggested earlier by Sparrow and Cess (1962).

The results of analytical work of the above type, in which a stable laminar vapor film with a smooth vapor-liquid interface is assumed, appear to agree with experimental data for boiling only up to a few millimeters from the leading edge. For longer surfaces, these analyses tend to underpredict the average heat transfer coefficient and inaccurately predict the dependence of the heat transfer coefficient on the distance from the leading edge. Two kinds of modification of the laminar film approach have been attempted in the past for saturated film boiling. The first type of modification involves the assumption of turbulent flow in the vapor film. A model for turbulent saturated film boiling heat transfer has been proposed by Suryanarayana and Merte (1972) and a model for turbulent forced convection subcooled film boiling from a horizontal plate was proposed by Wang and Shi (1985).

Coury and Dukler (1970) proposed a model for turbulent film boiling while taking into consideration the heat transfer enhancement by interfacial waves. They assumed that the amplitude of the waves was of the order of the vapor film thickness and that the interface experienced low-frequency oscillations due to the waves. Experimental measurements of instantaneous and time-averaged rates of heat transfer showed good agreement with their turbulence-based model.

The second type of modification is based on the assumption that as the vapor flow path becomes longer with increasing surface size, the liquid-vapor interface becomes unstable, and interfacial waves are formed. The peaks of the waves appear like bulges. By dividing the vapor film into cells supporting a single bulge, the film boiling heat transfer coefficients are evaluated over each cell. Such a model has been proposed by Bui and Dhir (1985) for saturated film boiling on a vertical plate. Their model was found to compare well with their experimental results for saturated film boiling heat transfer from a vertical plate.

A number of experimental studies on subcooled film boiling have been reported in the literature that show that waves exist on the interface and that these waves enhance the film boiling heat transfer. Subcooled pool film boiling on spheres was studied by Dhir and Purohit (1978) and involved both experiments and analysis of the film boiling heat transfer. They found that the observed film boiling heat transfer coefficients were 50–60 percent higher than those predicted by the smooth interface theory. It was proposed that the higher heat fluxes were caused by the vapor film oscillations and by the increase in interfacial area caused by the ripples on the interface. However, no mechanistic model was developed for the enhancement of subcooled film boiling heat transfer coefficient.

Experiments were performed by Toda and Mori (1982) for subcooled film boiling on a horizontal wire and on a sphere. The wire diameter was 0.3 mm and the sphere was 12.7 mm in diameter. Vapor film thickness, heat transfer rates, and minimum film boiling temperatures were measured. The vapor film thickness was found to vary with time. The magnitude and frequency of oscillations were found to decrease with increased subcooling. Unfortunately, they neither correlated their experiments nor compared them with results from existing analyses.

Subcooled pool boiling heat transfer from cylinders was studied by Sakurai et al. (1986). Their cylinders were 2 to 4 mm in diameter. For the cylinder of diameter 2 mm, they found that experimental results of heat transfer compared well with prediction from a two-phase boundary layer model similar to the one proposed by Nishikawa and Ito (1966). For the larger cylinders, the lack of agreement between the experimental and the analytical results using the two-phase boundary layer model is probably due to the neglect of the effect of waves upon the heat transfer. Mention must also be made of the studies of forced flow subcooled film boiling heat transfer from spheres reported by Orozco and Witte (1986) and the theoretical model proposed by Witte and Orozco (1984). However, the influence of interfacial waves was not included in their work. An attempt to evaluate liquid side heat transfer from interface including the effect of the waves was made by

Contributed by the Heat Transfer Division for publication in the JOURNAL OF HEAT TRANSFER. Manuscript received by the Heat Transfer Division January 1991, revision received August 1991. Keywords: Boiling, Multiphase Flows, Phase-Change Phenomena.

Ayazi and Dhir (1987) during a study of the minimum heat flux in subcooled pool boiling from cylinders. The liquid side heat transfer coefficients on the wave peak or bubble were obtained using natural convection correlations. However, the liquid side heat transfer in the wave valleys was obtained by using the two-phase boundary layer model. Although excellent agreement was obtained for minimum heat flux, no comparison between theoretical and experimental results was made beyond the minimum heat flux.

All of the available evidence suggests that for surfaces with large characteristic length, the two-layer model proposed by Nishikawa and Ito (1966) is unable to predict the observed heat transfer coefficients. To understand the mechanics of interfacial heat transfer, in this work, wall and liquid side heat fluxes are measured for various liquid subcoolings and wall superheats. In the preceding paper, the structure of the interfacial waves was described. It was shown that a quasi-stationary vapor layer existed at the leading edge. This layer was followed by a moving vapor-liquid interface composed of a vapor substrate on which there exist ripples and large waves or bulges. The amplitude of the waves controls the interface velocity. The measured interface velocity was much larger than that predicted from the smooth interface theory. The flow in the liquid adjacent to the interface was found to expand in the wave valleys and contract at the wave peaks. Here the flow field results are used in conjunction with the results for liquid side heat transfer, temperature profiles, and isotherms in the liquid layer to provide a description of the mechanism of heat transfer enhancement by the interfacial waves.

2.1 Experimental Apparatus. The experimental apparatus was the same as described in the preceding paper. The liquid side heat fluxes and temperature profiles were measured by holographic interferometry. The optical layout is shown in Fig. 1. The beam from a N.E.C. 880A, 50 MW He-Ne laser

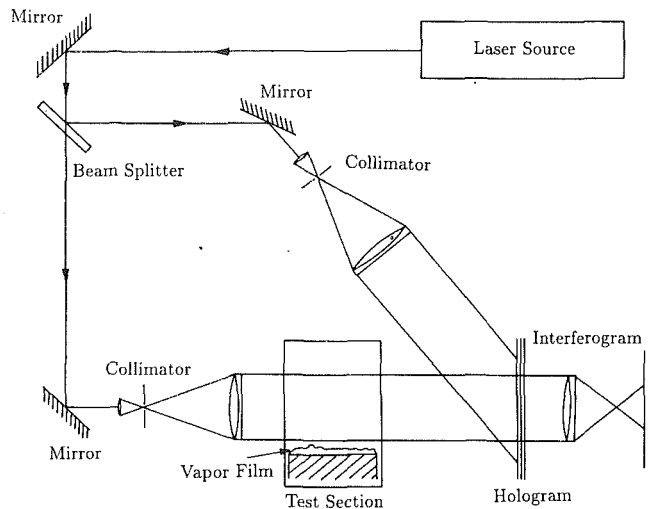


Fig. 1 Details of the optical layout

split into two parts with a beam splitter. The object beam is enlarged with a collimator and it traverses the test section tangential to the heating surface and is finally incident upon the holographic plate. The reference beam traverses a similar path but without passing through the test section and is incident upon the holographic plate at an angle of 37 deg. The hologram is placed in a plate holder. The virtual image is photographed in real time with a Canon AE-1, 35 mm camera fitted with a zoom lens located behind the plate holder.

2.2 Experimental Procedure. Startup of a typical experiment began with deaeration of the test liquid by vigorous

Nomenclature

c = function defined as $4\omega\alpha/v^2$	r_l = distance from the wall to the edge of the thermal layer adjacent to the bubble	z_0 = distance from the leading edge to the location where the leading edge vapor layer joins the moving interface downstream
c_f = interfacial friction factor defined as $\tau_i/0.5\rho u_i^2$	R = nondimensional ratio, defined as $2 \cdot \text{Nu}_l / [\text{Re}_l c_f \text{Pr}_l]$	α = thermal diffusivity of the liquid
c_p = specific heat	Re = Reynolds number, defined as $\rho \mu_i x / \mu_l$	λ = dominant wavelength or the spacing between consecutive bulges in the interface
f = function obtained by integrating refractive index over the thermal layer	S = constant	Λ = wavelength of the laser beam
g = gravitational acceleration	St = Stanton number, defined as $\text{Nu} / \text{Re} \cdot \text{Pr}$	ξ = function defined as $(1 + \sqrt{1 + c^2}) / \sqrt{2(1 + c^2)^{0.25}}$
h = heat transfer coefficient	$\langle \text{St} \rangle$ = time-averaged Stanton number	ρ = density
h_{fg} = latent heat of vaporization	T = temperature	τ = shear stress, defined as $\mu \partial u_l / \partial y$
h_w = wall heat transfer coefficient defined as $q_w / [T_w - T_{\text{sat}}]$	ΔT = temperature difference	ω = wave frequency, defined as $\pi u_l / \lambda$
j = a number corresponding to the fringe shift	ΔT_w = superheat, defined as $T_w - T_{\text{sat}}$	
k = thermal conductivity	ΔT_{sub} = subcooling, defined as $T_{\text{sat}} - T_l$	
L = width of the test surface	\bar{T} = nondimensional liquid temperature, defined as $(T - T_l) / (T_{\text{sat}} - T_l)$	
n = refractive index	u = velocity in the z direction	Subscripts
Nu = Nusselt number, defined as $h_l z / k_l$	v = velocity in the y direction	e = experimental
Pr = Prandtl number	y = distance normal to the heater	f = film
q = heat flux	z = distance along the heater from the leading edge	i = interface
\bar{q} = heat flux averaged over distance	\bar{z} = dimensionless distance along the heater defined as $(z - z_0) / \lambda$	l = liquid
$\langle q \rangle$ = time-averaged heat flux		sat = saturated
q_{wf} = wall heat flux calculated from film thickness		sub = subcooled
r_b = thickness of the vapor film at different locations on the bubble		t = theoretical
		v = vapor
		w = wall

boiling in a separate reservoir and with preheating of the test section. The chamber was purged with nitrogen gas during the preheating period to avoid oxidation of the test surface. The test block was heated to 673 K and the test section was filled with water from the reservoir. The desired wall superheat was obtained by adjusting the voltage applied to the cartridge heaters. After a steady-state condition had been reached, thermocouple output was recorded on a Fluke data-logger. Tests were considered to be at steady state when the temperature of the test block changed by less than 1 K in 5 min. The liquid temperature changes were less than 0.2 K in 1 min up to a liquid subcooling of 10 K. Care was taken to avoid thermal stratification. The liquid thermal stratification was found to be less than 0.7 K over a height of 10 cm.

Holographic interferometry has been well described in the literature and only its salient features will be described here. The base hologram was recorded on an Agfa 88HD-1 photographic plate with a reference beam to object beam intensity ratio of 3:1. The liquid in the test section was maintained at room temperature when the base hologram was made. Thereafter the hologram was developed and the experiments in film boiling were commenced. Upon the commencement of subcooled film boiling, the reference beam to object beam intensity ratio was set at infinity. The object beam was then slightly inclined to cause small differences in the path length between the object and the reference beams. This caused the fringe field to be of the finite fringe type. Real time pictures were taken with the camera. The processed negatives were enlarged by a factor of 25. From the photographs, liquid temperature profiles and interfacial heat fluxes were obtained.

2.3 Data Reduction. The wall heat fluxes were obtained from the temperature distribution in the copper block. The temperature distribution in the copper block was found to be linear away from the top and bottom ends of the plate. As such, away from the ends, the heat conduction in the block could be assumed to be one dimensional. The liquid temperature distribution was obtained by extending the horizontal fringes representing the thermal condition in the undisturbed pool to the interface and noting the temperature corresponding to each location where the line extrapolating the horizontal fringes intersects the adjacent inclined fringe. The temperature at two locations is related as

$$T_j = T_{j-1} + \frac{j\Lambda}{L \frac{dn}{dT}} \quad |j = 1, 2, \dots \quad (1)$$

The interfacial heat flux could be obtained by extrapolating the temperature profiles to the interface and noting the slope (of the temperature profiles) there. But the above procedure of data reduction holds only if the heat flux is constant in the x direction. For low subcoolings, the vapor film thickness and the interfacial heat flux vary across the width of the heater. For this case, the data reduction was carried out by following the procedure outlined by Beer (1972). The temperature distribution in the liquid was determined in the same way as described above but the interfacial heat flux was obtained as

$$q \sim \frac{\partial T}{\partial y} = \frac{j\Lambda}{2 \left(\frac{\partial n}{\partial T} \right) f (r_b - r_i)} \quad (2)$$

The fringe shift around the bubble is approximated by a quadratic profile, and the parameter, f is obtained by the integration of the assumed refractive index profile (i.e., temperature profile) in the thermal layer over one bubble radius. The derivation of parameter f is given by Beer (1972) and the numerical evaluation is outlined by Vijaykumar (1990).

Prior to the use of holographic interferometry in subcooled film boiling, the method was used in natural convection of water at about 368 K and the heater at 372 K. The natural

convection data showed that wall heat flux obtained using interferometry was 7 percent less than that given by the thermocouples embedded in the copper block. It was about 4.3 percent less than the results obtained by using the correlation given in Eckert and Drake (1972). The overall uncertainty in the liquid temperature is determined to be 7.3 percent. The total error in determination of the liquid side heat flux is 15.4 percent. An error analysis is made in Appendix A. The maximum error in the determination of wall heat flux was calculated by Bui (1984) to be 11 percent.

3 Results and Discussion

Wall Heat Transfer Results. In Fig. 2 measured wall heat transfer coefficients are plotted as a function of distance from the leading edge for several liquid temperatures and a constant wall superheat. In this figure liquid heat transfer coefficients predicted from a two-phase boundary layer analysis similar to that of Nishikawa and Ito (1966) are also plotted. Complete details are given by Vijaykumar (1990). It is seen that the laminar smooth interface analysis underpredicts the experimental wall heat transfer results. Also it can be seen that experimentally obtained wall heat transfer coefficient shows a very weak dependence, if at all, on the distance from the leading edge. The boundary layer analysis, however, suggests that the heat transfer coefficient should vary as $z^{-0.25}$.

Figure 3 shows the variation of heat transfer coefficients with liquid subcooling for wall superheats ranging from 150 to 300 K. The data indicate a linear dependence of heat transfer coefficients on liquid subcooling for a fixed wall superheat. This is consistent with the prediction of Dhir and Purohit (1978) for subcooled film boiling on a sphere. The plotted data were obtained at the middle section of the heated wall.

Liquid side heat transfer from the interface is described next for the liquid subcooling ranging from 1.6 to 6.7 K and the wall superheat varying from 160 K to 207 K.

Liquid Side Heat Transfer When the Wave Structure Is Three Dimensional.

Liquid side heat fluxes were measured near the leading edge for low subcoolings for which the wave structure was found to be three dimensional. All of the liquid side heat flux data reported in this section were obtained within 35 mm of the leading edge. Thus these data are for distances that span the first one to two wavelengths.

Figure 4 shows an interferogram of the leading edge region

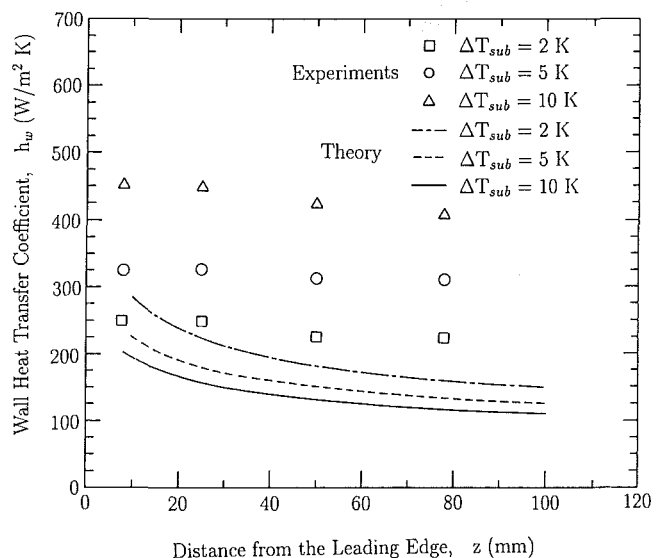


Fig. 2 Wall heat transfer coefficient as a function of distance from the leading edge

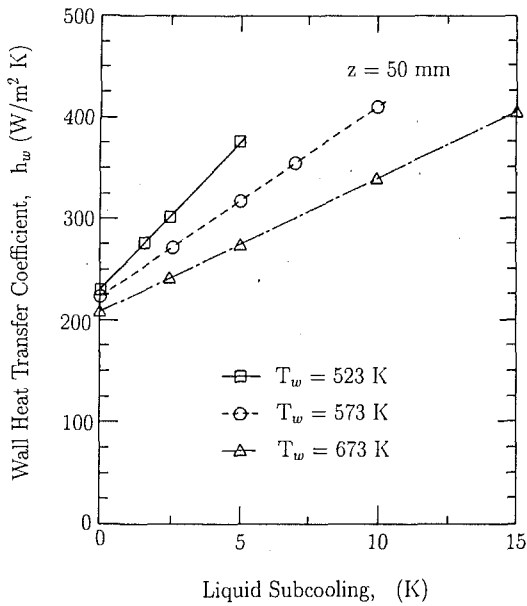


Fig. 3 Wall heat transfer coefficient as a function of subcooling

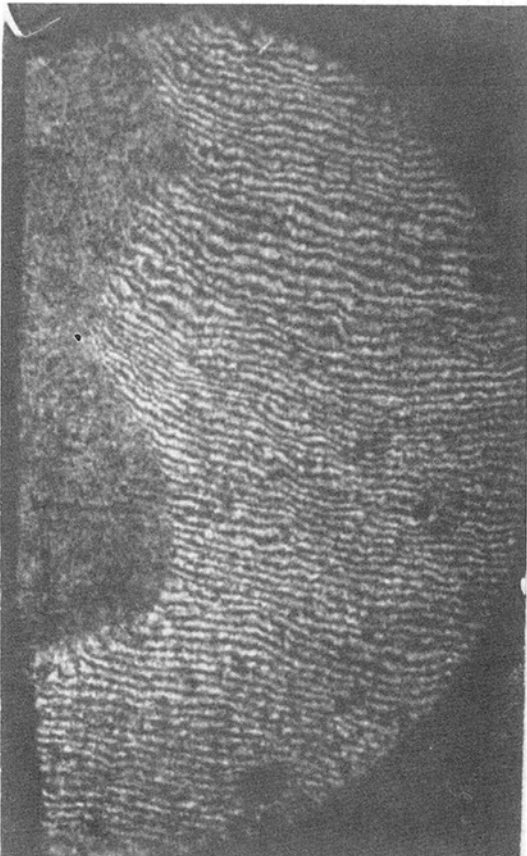


Fig. 4 Hologram for the case of $\Delta T_w = 160$ K, $\Delta T_{sub} = 1.6$ K

for a liquid subcooling of 1.6 K. A large vapor mass is present at the leading edge. However, it should be noted that the vapor film looks much thicker than it actually is because of refraction in the liquid. The vapor film thickness after it is corrected for refraction error and the liquid side heat fluxes deduced from the interferogram are plotted in Fig. 5. It is seen that a relatively high heat flux exists at the frontal region of the leading edge layer (location *a*). The rate of heat transfer decreases to a minimum value at the peak (location *f*). Thereafter the heat

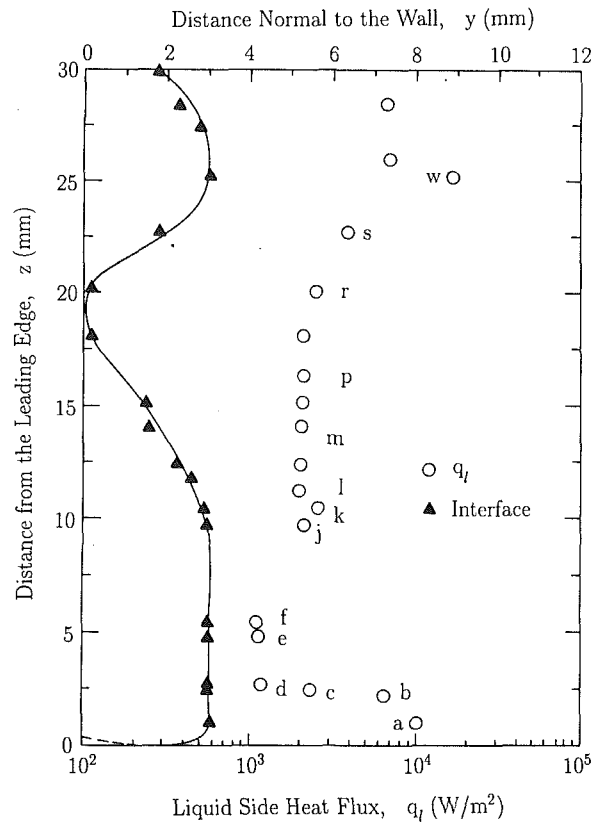


Fig. 5 Liquid side heat transfer as a function of *z* for $\Delta T_w = 160$ K, $\Delta T_{sub} = 1.6$ K

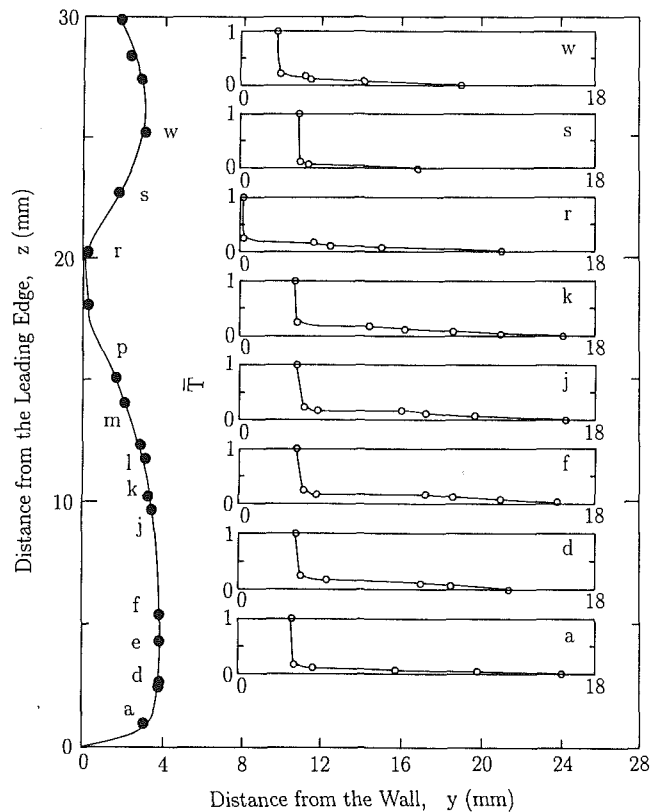


Fig. 6 Temperature profiles in the liquid layer for $\Delta T_w = 160$ K, $\Delta T_{sub} = 1.6$ K

flux increases again and remains constant at the upper back region of the vapor mass until the frontal part of the large

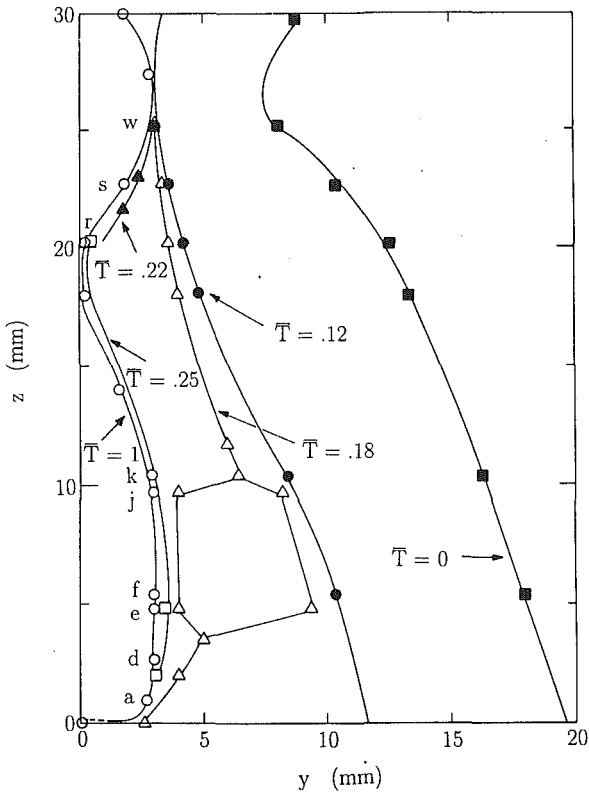


Fig. 7 Isotherms in the liquid layer for $\Delta T_w = 160$ K, $\Delta T_{sub} = 1.6$ K

wave is encountered. At the frontal region of the first peak, the heat flux is seen to increase gradually. The heat flux reaches a maximum at the top of the first peak before decreasing again.

Temperature profiles in the liquid region adjacent to the interface are plotted in Fig. 6. In each case the dimensionless temperature \bar{T} , varies from 0 ($T = T_l$) to 1 ($T = T_{sat}$). The horizontal axis represents the distance normal to the wall and the vertical axis represents the temperature. Using the temperature data of Fig. 6, isotherms corresponding to dimensionless temperature of 0.25, 0.22, 0.18, 0.12, and approximately 0 are plotted in Fig. 7. The interface represents an isotherm of $\bar{T} = 1$. To facilitate the discussion, the thermal layer bounded by the isotherms of 0.18 and 0 is called the outer layer. The middle layer spans the isotherms of 0.18 and 0.25. Most of the temperature drop occurs in the inner layer, which lies between 1 and 0.25. In the companion paper, streamlines and velocity profiles were obtained for about the same subcooling.

From Figs. 5, 6, and 7 and from Fig. 7 of the companion paper, the following observations are made:

1 The insulation ahead of the leading edge is not adiabatic. Heat transfer by natural convection from the insulation induces fluid motion toward the vapor dome at the leading edge. The leading edge vapor dome was noted to be stationary. Hence a stagnation point is formed coincident with high heat transfer. At the stagnation point, *a*, the 0.18 isotherm falls very close to the interface. Thereafter the thermal layer grows thicker and the rate of liquid side heat transfer drops. The rate of liquid side heat transfer is much larger than the heat flux calculated by assuming conduction across the vapor dome. This suggests that the vapor dome acts like a large bubble with evaporation occurring at the base of the bubble. The high rate at which energy is deposited into the liquid in the frontal region can only be supported by condensation of the vapor.

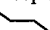
2 Between points *d* and *e*, the isotherm corresponding to 0.18 splits, leading to the formation of step () shaped

Table 1 Average wall and liquid side heat fluxes obtained from experiments and plane interface analysis

ΔT_w K	ΔT_{sub} K	z mm	Theoretical heat flux		Experimental heat flux		
			q_w w/m^2	q_l w/m^2	q_w w/m^2	q_{wf} w/m^2	q_l w/m^2
160	1.6	29	30800	5650	42300	30000	8790
188	2.8	22	40900	8450	51225	40680	13850
207	4.3	35	46550	12680	61700	49920	21994
203	6.6	22.5	59250	17850	78450	61035	67235

profiles at points *f* and *j*. The temperature drop between the interface and the pool occurs in two distinct regions: once in the region near the interface (inner and middle layers) and once in the region far away from the interface (outer layer). From the velocity profiles, it is seen that the isothermal region is formed as a result of the flow induced by the motion of the interface downstream. Immediately adjacent to the interface, the velocities are very low and the heat transfer is by natural convection only. Hence the rate of heat transfer is low at the wave peak between locations *d* and *j*. Also, it must be pointed out that in the velocity profiles shown in Fig. 8 of the companion paper, the velocity profile due to natural convection (immediately adjacent to the interface at locations *d* and *j*) is not shown since the hydrogen bubble method has an accuracy of about 1 mm/s.

3 At about point *j*, the inner layer starts to shrink because of the high velocity of the liquid that is sucked into the valley preceding the accelerating interface. This signals an increase in heat transfer. The isotherms obtained from the temperature profiles at *j* and *k* show that the middle and outer layers merge near location *k* and the isothermal region completely disappears. The inner layer thickness remains nearly constant from *k* until point *r* and corresponds to a nearly constant heat flux condition.

4 From point *r*, the thermal layer (chosen to be the region between $\bar{T} = 0$ and $\bar{T} = 0.25$ isotherms) does not follow the interface and thins in front of the large wave, thus causing an increase in heat transfer there. At point *s* (which corresponds approximately to point *c* in the *u* velocity profiles, shown in Fig. 7 of the companion paper), the velocity gradient at the interface is comparatively high. The higher velocity gradient accompanied by the thinning of the thermal layer at location *s* results in a high-temperature gradient at the interface and a high heat flux. At location *w* at the top of the first peak, both the 0.18 isotherm and the 0.12 isotherm seem to collapse on the interface. This corresponds to a very high rate of heat transfer. At location *w*, the isotherms are extremely closely spaced (a behavior shown by the streamlines at point *d* in Fig. 7 of the companion paper).

The liquid heat flux averaged over a distance of 29 mm from the leading edge is found to be 30 percent higher than that obtained from the boundary layer type analysis (see Vijaykumar, 1990). As given in Table 1, the wall heat flux calculated by assuming conduction across the film is only about 65 percent of that obtained from the thermocouples. The difference is probably due to the uncertainty in the measurement of film thickness, neglect of inertia in the film, and heat loss to the insulation ahead of the leading edge vapor layer.

For a liquid subcooling of 2.8 K and a wall superheat of 188 K, the vapor film thickness and the experimental liquid side heat fluxes are plotted in Fig. 8. The experimental wall heat flux and the liquid heat flux from laminar theory are also plotted in the same figure. A relatively high heat flux can be seen near the leading edge (points *a* and *b*). The heat flux decreases downstream of the leading edge until it reaches a minimum value at about 11 mm from the leading edge at point *f*. The drop in heat transfer is solely due to the thickening of the liquid boundary layer or thinning of the vapor layer behind the quasi-stationary leading edge layer. A ripple can be seen between 9 and 19 mm from the leading edge. The rate of heat

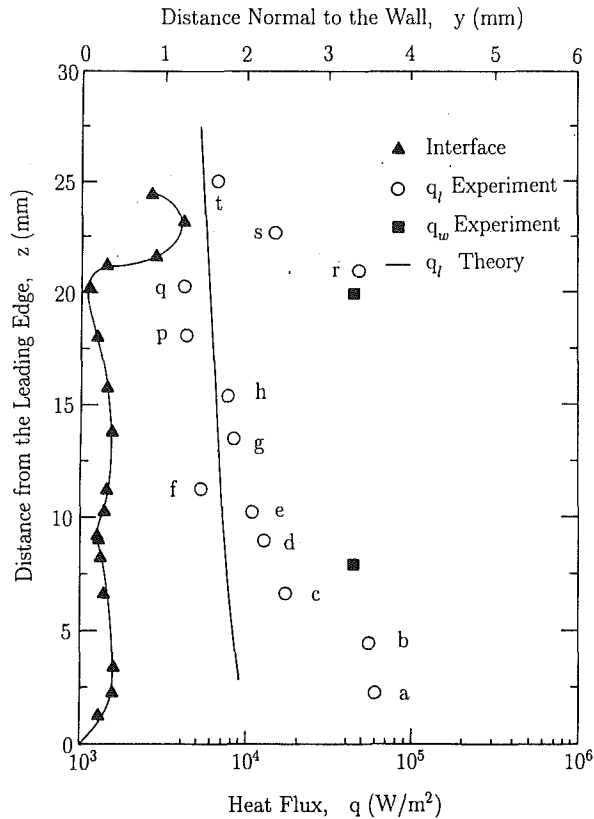


Fig. 8 Liquid side heat transfer as a function of z for $\Delta T_w = 188$ K, $\Delta T_{sub} = 2.8$ K

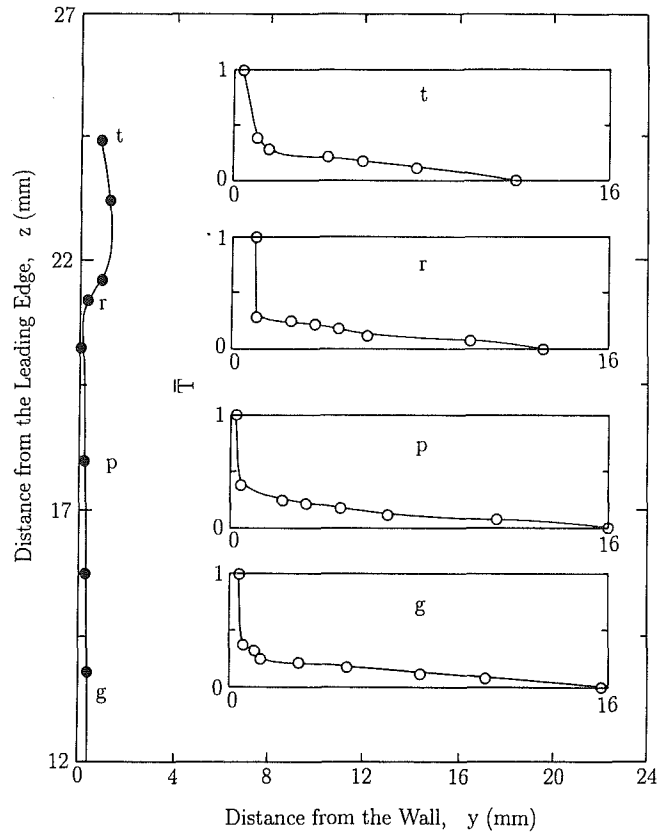


Fig. 9 Temperature profiles in the liquid layer. ($\Delta T_w = 188$ K, $\Delta T_{sub} = 2.8$ K)

transfer increases slightly near the peak of the ripple. Thereafter the heat flux decreases at the back of the ripple and attains the lowest value at the location where the vapor film is the thinnest. The heat transfer shows a sharp rise at location r in the frontal region of the bubble. It should be noted that a poor comparison exists between the experimental liquid heat fluxes and those predicted from the laminar theory. The laminar theory here and in subsequent figures refers to the results of two phase boundary analysis such as that performed by Nishikawa and Ito (1966) and repeated by Vijaykumar (1990). Near locations a , b , and r , the liquid side heat flux is observed to be equal to or higher than the wall heat flux.

In Fig. 9, the nondimensional liquid side temperature profiles are plotted for locations g , p , r , and t . The locations chosen are beyond 11 mm from the leading edge, since we are primarily concerned about the temperature profiles in the liquid adjacent to the interfacial waves. The temperature profile at location g is similar to a boundary layer profile. However the temperature profiles at locations at p and r show three separate zones of temperature drop. Isotherms of $\bar{T} = 1, 0.38, 0.32, 0.28, 0.22$, and 0 deduced from the temperature profiles are plotted in Fig. 10. Most of the temperature drop occurs in the inner layer between $\bar{T} = 1$ and $\bar{T} = 0.38$.

It is also noted from Fig. 9 and 10 that the inner layer thins substantially at point r on the front side of the bulge. As a result a large increase in heat flux is observed. The corresponding streamlines and liquid velocities are reported by Vijaykumar (1990) and it was noted that the streamlines in the fluid in the vicinity of the interface at r do not follow the interface and simply run into the protruding interface. At location r , the interface acts like a large protrusion and the flow from the middle layer seems to impinge on the interface. It is seen that the isotherm, $\bar{T} = 0.38$ is almost forced into the front portion of the bulge. The heat flux at the location where the thermal layer is the thinnest is about 8.1 times the

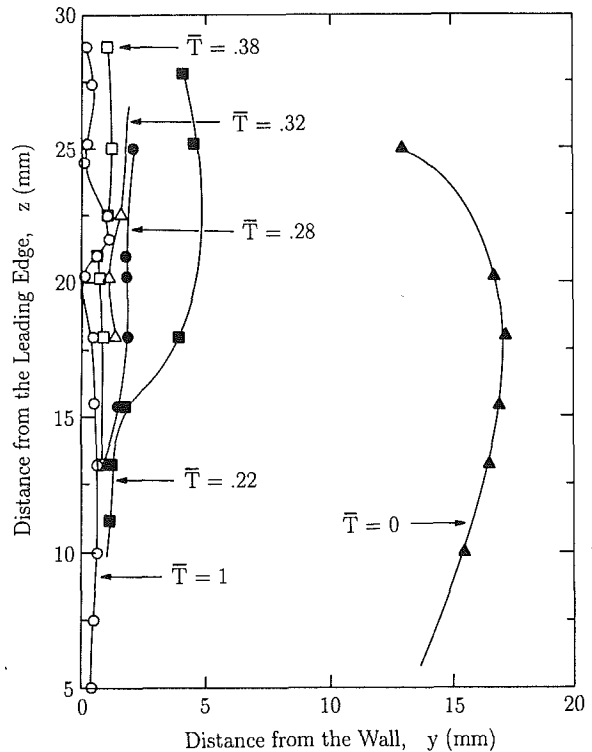


Fig. 10 Isotherms in liquid layer ($\Delta T_w = 188$ K, $\Delta T_{sub} = 2.8$ K)

wall heat flux calculated from conduction under the bubble. Since the instantaneous liquid heat flux from the interface is found to be much larger than the calculated conduction heat flux, condensation of the vapor must occur to support the high

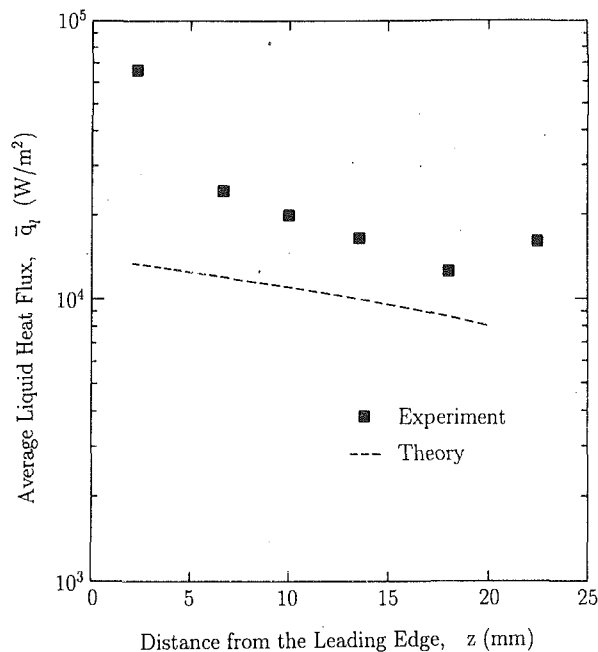


Fig. 11 Average liquid side heat transfer as a function of z for $\Delta T_w = 188$ K, $\Delta T_{sub} = 4.3$ K



Fig. 12 Hologram for the case of $\Delta T_w = 207$ K, $\Delta T_{sub} = 4.3$ K

heat flux. The condensation of the vapor in the front portion of the bubbles may be responsible for the little growth seen in the substrate thickness and the bulge height downstream.

Downstream of the first bubble, the isotherms and streamlines expand into the valley and the heat transfer is seen to reduce at the back of the bulge and the wave valley. The instantaneous liquid side heat fluxes in the leading edge region, the ripple, and the bubble regions were calculated. The area correction was found to be a function of the liquid subcooling and varied from 4 to 28 percent near the leading edge, from 9 to 15 percent near the ripple, and was as much as 63 percent over the bubble or large bulge. Wall heat fluxes were obtained both from thermocouples embedded in the copper block and from refraction corrected film thicknesses assuming conduction across the film. Theoretical wall and liquid heat fluxes were calculated from a plane interface analysis. In Fig. 11, the experimentally obtained average liquid side heat flux averaged over a given distance from the leading edge is compared with that from the plane interface analysis. It is seen that the observed

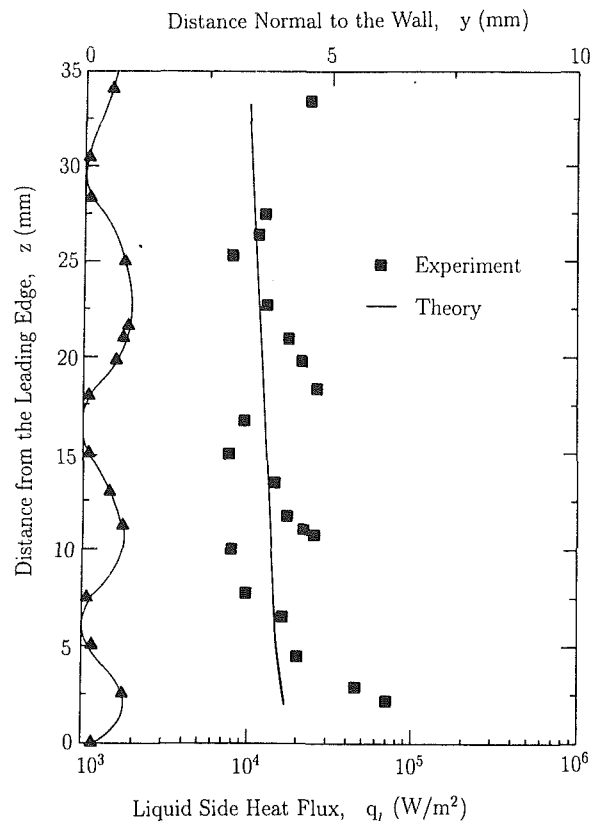


Fig. 13 Liquid side heat transfer as a function of z for $\Delta T_w = 207$ K, $\Delta T_{sub} = 4.3$ K

liquid side heat flux shows a much stronger dependence on the distance from the leading edge and is consistently higher than that obtained from the analysis. At a distance of 22 mm from the leading edge, the average liquid side heat flux is about 60 percent higher than that obtained from theory. The underprediction of wall heat transfer results can be substantially attributed to the underprediction of liquid side heat transfer. Table 1 gives the comparative magnitude of the various heat fluxes.

Local liquid side heat flux for water subcooling of 4.3 K (interferogram shown in Fig. 12) is plotted in Fig. 13 as a function of the distance from the leading edge. The wall superheat was 207 K. The liquid heat flux is plotted over two wavelengths and the leading edge vapor layer. The liquid side heat flux decreases rapidly behind the leading edge vapor layer and then shows an oscillatory behavior over each wavelength thereafter. The oscillations in the magnitude of the heat fluxes appear to be caused by the expansion of the flow field behind the peak and the subsequent contraction in the front of the next peak. This type of flow behavior results in stagnation conditions at the front of the peak and subsequent high heat flux there. In the back of each peak, the liquid boundary layer thickens owing to the expansion of the flow in the valleys and the heat transfer decreases behind the wave peaks and in the valleys. Figure 14 shows the average liquid side heat fluxes plotted as a function of the distance from the leading edge. The experimentally obtained average liquid heat flux is observed to be about twice that predicted by the analysis. From Table 1 it can be inferred that most of the increase in wall heat flux beyond that predicted from the analysis can be attributed to the enhancement of the liquid heat flux by the wavy interface.

Liquid Side Heat Transfer When the Wave Structure Is Two Dimensional. Liquid side heat fluxes were obtained for a higher subcooling of 6.7 K for which the wave structure was

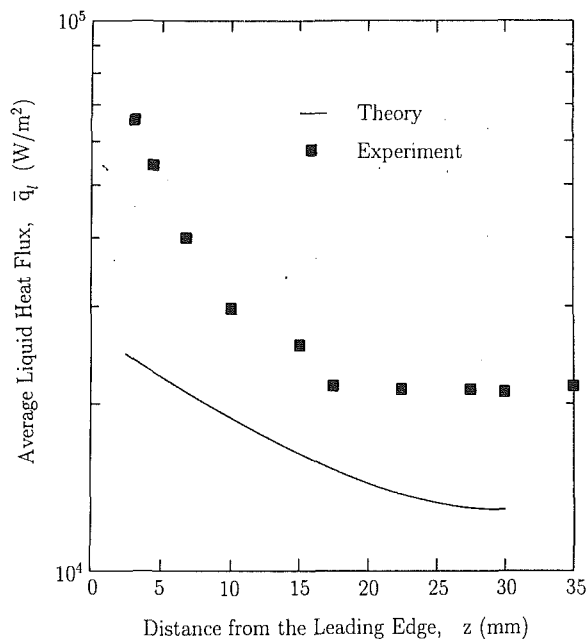


Fig. 14 Average liquid side heat transfer as a function of z for $\Delta T_w = 207$ K, $\Delta T_{sub} = 4.3$ K

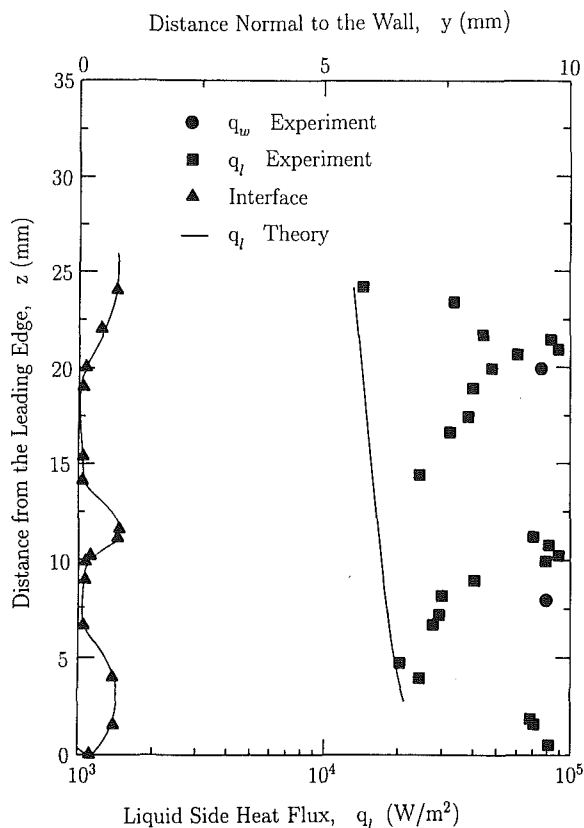


Fig. 15 Average liquid side heat transfer as a function of z for $\Delta T_w = 203$ K, $\Delta T_{sub} = 6.6$ K

two dimensional (described in detail by Vijaykumar, 1990). Only a brief summary of those results is presented here. Figure 15 shows the results of the liquid heat flux plotted as a function of the distance from the leading edge. The results are similar to those for the low subcooling cases. Figure 16 shows a comparison between the measured contour of the interface and the contour of the interface as obtained from the plane interface analysis. It was found that the leading edge vapor layer was

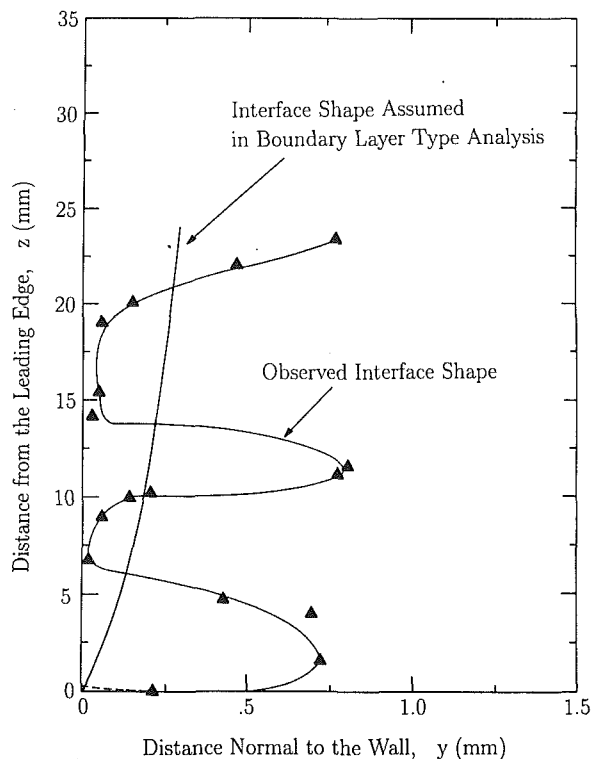


Fig. 16 A comparison of predicted and measured interface shape for $\Delta T_w = 203$ K, $\Delta T_{sub} = 6.6$ K

quasi-stationary with liquid evaporating at its base. Liquid side heat fluxes at the peak of the leading edge vapor layer were found to be larger than those given by simple conduction across the vapor layer. This suggests that some condensation must occur at the wave peak. The net vapor generated in the leading edge vapor layer left like a wall jet of high velocity. The change in velocity from zero to a finite velocity downstream caused the vapor film to thin in the valley downstream of the leading edge vapor layer. The thickness of the vapor film in the valley is smaller than that given by the plane interface analysis. In the valley as well as at the subsequent peak, the liquid side heat fluxes are observed to be higher than those obtained from the analysis. An inference with respect to the possibility of condensation at the subsequent peak can be made in a manner similar to that made for the stationary wave. The average liquid side heat flux over a distance of 21.5 mm (shown in Table 1) is about 88 percent of the wall heat flux. Thus it is seen that at higher liquid subcooling, most of the wall heat flux is transferred to the liquid either directly through convection at the wave valleys or by condensation at the wave peaks.

The essential features of liquid side heat transfer as seen in the above examples can be summed up as follows: Liquid side heat transfer has a cyclic behavior around each wave with maximum heat transfer at the peaks and minimum at the valleys; average liquid side heat transfer is enhanced and in the range of liquid subcoolings studied, the enhancement is found to increase with increasing liquid subcooling. The implication of this behavior of liquid side heat transfer on the wall heat transfer can be described as follows: The calculated liquid side heat flux at the peak is much larger than the wall heat flux determined by using thickness of the vapor film at the peak. The situation reverses in the valley where the liquid side heat flux is much smaller than the conductive heat flux across the vapor film. This suggests that most of the evaporation occurs in the valley with some of the vapor being condensed at the wave peaks. As a result the peaks attain an equilibrium height, which changes very little along the direction of vapor flow.

Because of the finite velocity of the interface, a given location on the heater surface experiences alternate periods of high and low heat fluxes. The frequency of these periods is dependent on the wall superheat and on the liquid subcooling. The thermocouples embedded in the copper block give a time-averaged value of the wall temperature. The time-averaged heat fluxes deduced from the thermocouple data show little dependence on the distance from the leading edge and are substantially higher than those predicted by laminar plane interface analysis. Large interface velocities, high liquid side heat transfer rates at the wave peaks, high wall heat transfer rates at the wave valleys, and reduced vapor flow pathlengths contribute to the overall enhancement of the time-averaged rate of heat transfer from the wall.

Assessment of Applicability of Classical Reynolds Analogy to Subcooled Film Boiling. The result of application of Reynolds' analogy in its most general form to forced convection is written as

$$Nu_l = \frac{1}{2} \cdot c_f \cdot Re_l \cdot Pr^n \cdot F(z/l) \quad (4)$$

The exponent n generally has a value of 1/3. The function $F(z/l)$ shows the dependence of the Nusselt number on the entry length of the flow for the case in which the hydrodynamic and thermal layers start at different locations. The ratio $2 \cdot Nu_l / (Re_l \cdot c_f \cdot Pr_l)$ is chosen to assess the validity of the results obtained in this study. This ratio R is simply $St_l / c_f / 2$. Noting that the ratio R involves u_i , the Reynolds analogy is employed only for the moving interface downstream of the stationary vapor layer. To compare the skin friction and heat transfer coefficient at corresponding locations, the distance \bar{z} has been chosen as the distance from the location where the quasi-static leading edge vapor layer joins the substrate. The distance is normalized by the wavelength. The ratio R is plotted as a function of the normalized distance \bar{z} in Fig. 17. It is seen that the ratio is approximately constant at about 3 for all subcoolings and is weakly dependent on \bar{z} . For most of the experimental conditions considered here, the Prandtl number is approximately constant at about 1.8. From the classical boundary layer theory, the constant Pr^{n-1} is expected to be less than 1. The observed threefold increase in the ratio R is indicative of the net enhancement of the liquid side heat transfer due to wave action.

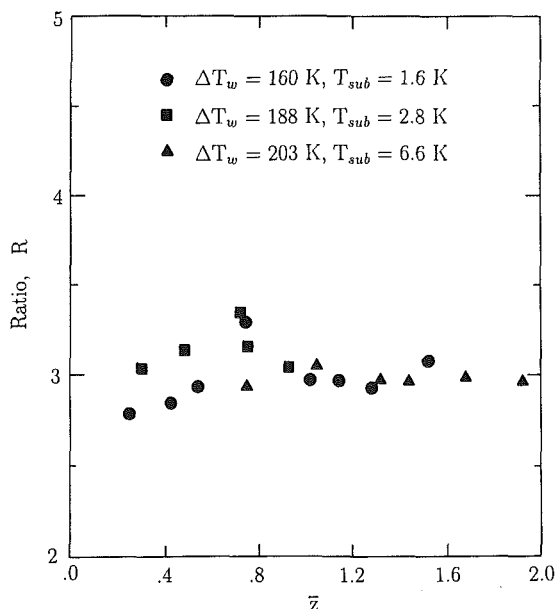


Fig. 17 Nondimensional number R plotted as a function of \bar{z}

Assessment of Liquid Side Heat Transfer. The liquid side heat transfer is simulated by using transient conduction into a slab of liquid. Two types of situation are considered.

In the first case, heat transfer to the liquid over one wavelength is modeled as heat transfer to a semi-infinite slab of liquid initially at a constant temperature T_l with the temperature of the face of the slab of liquid being assumed to vary sinusoidally with time during the period the wave travels a distance of one wavelength.

For the one-dimensional transient heat conduction equation,

$$\frac{\partial^2 \bar{T}}{\partial y^2} = \frac{1}{\alpha} \frac{\partial \bar{T}}{\partial t} \quad (4)$$

The initial and boundary conditions are written as

$$\text{At } t=0, \bar{T}=0, \text{ for all } y \quad (4a)$$

$$\text{At } y=\infty, \bar{T}=0, \text{ for all } t \quad (4b)$$

$$\text{At } y=0, \bar{T}=\Delta T_{\text{sub}} \cos(\omega t) \text{ for all } y \quad (4c)$$

The solution of Eq. (4) is given by Carslaw and Jaeger (1962). The surface heat flux averaged over one time period is

$$\langle q_l \rangle = 0.586 \frac{k_l \Delta T_{\text{sub}}}{\pi} \sqrt{\frac{\omega}{\alpha}} \quad (5)$$

or in terms of the heat transfer coefficient,

$$\langle St_l \rangle = \frac{Nu}{Re \cdot Pr} = 1.04 \sqrt{\frac{\alpha}{\lambda u_i}} \quad (6)$$

In Table 2, the results from Eq. (6) are compared with the experimentally determined values. The predictions from this simple model are found to be in agreement with the data for low subcoolings only. The lack of agreement between theory and experiments as the subcooling increases is probably due to neglect of flow in the liquid layer. At low subcoolings, the interface velocity is sufficiently high so that the liquid can be assumed to be stationary. But at higher subcoolings, the interface velocity is low and the liquid velocity normal to the interface cannot be neglected. Thus in the second case, the transient conduction equation is modified to include this velocity. Assuming that the velocity v is independent of time and distance, the governing energy equation for this case is written as

$$\frac{\partial^2 \bar{T}}{\partial y^2} = \frac{\rho c_p}{k} \frac{\partial \bar{T}}{\partial t} + v \frac{\partial \bar{T}}{\partial y} \quad (7)$$

The initial and boundary conditions are the same as those in Eqs. (4a)-(4c). Assuming a solution of the form

$$\bar{T} = F_1(y) e^{i\omega t} \quad (8)$$

and by separating the variables, the expression for the temperature profile in the liquid is obtained as

$$\bar{T} = \Delta T_{\text{sub}} e^{-\frac{v}{2\alpha} y [1 + \xi]} \cos\left(\omega t - \frac{v}{2\alpha} \xi y\right) \quad (9)$$

where $\xi = (1 + \sqrt{1 + c^2}) / [\sqrt{2}(1 + c^2)^{0.25}]$ and $c = 4\omega\alpha/v^2$

In the limit $v \rightarrow 0$, $v(1 + \xi)/2\alpha$ becomes $\sqrt{\omega/2\alpha}$. Hence in the limit $v \rightarrow 0$, Eq. (9) becomes

Table 2 Average Stanton number over a wavelength/waveperiod obtained from experiments and from transient conduction analysis

ΔT_w K	ΔT_{sub} K	$\langle St_l \rangle$ Theory	St_l Expt.
160	1.6	2.0×10^{-3}	1.8×10^{-3}
188	2.8	4.2×10^{-3}	$4. \times 10^{-3}$
207	4.3	5.8×10^{-3}	6.6×10^{-3}
203	6.6	9.9×10^{-3}	3.0×10^{-2}

Table 3 Average Stanton number obtained from the experiments and from modified transient conduction analysis

$\frac{\Delta T_w}{K}$	$\frac{\Delta T_{sub}}{K}$	v m/sec	$\langle St_t \rangle$ Theory	\overline{St}_t Expt.
160	1.6	0.02	2.3×10^{-3}	1.8×10^{-3}
188	2.8	0.0099	4.8×10^{-3}	4.0×10^{-3}
207	4.3	0.0089	7.2×10^{-3}	6.6×10^{-3}
203	6.6	0.008	2.4×10^{-2}	3.0×10^{-2}

$$\bar{T} = \Delta T_{sub} e^{-\left(\frac{\omega}{2\alpha}\right)^{1/2} y} \cos \left[\omega t - \left(\frac{\omega}{2\alpha}\right)^{1/2} y \right] \quad (10)$$

This expression is the same as that obtained by solving Eq. (5).

The instantaneous heat flux at the face of the slab is determined to be

$$q_t = k_l \Delta T_{sub} \sqrt{2} \frac{v}{2\alpha} (1 + \xi) \cos \left(\omega t - \frac{v}{2\alpha} \xi y + \frac{\pi}{4} \right) \quad (11)$$

The heat flux can then be integrated and averaged over one cycle. The corresponding heat transfer coefficient or Stanton number for this case is

$$\langle St_t \rangle = \frac{v(1 + \xi)}{u \sqrt{2}} \quad (12)$$

Using the experimentally determined average values of v and u_i , Eq. (12) was evaluated. Table 3 compares the prediction from Eq. (12) with the data. It can be seen that for all subcoolings, the predicted $\langle St_t \rangle$ are within about 20 percent of the data. It suggests that for high subcooling, as the interface velocity becomes small, the crossflow contribution can be important.

Summary and Conclusions

1 By using holographic interferometry, it has been shown that in subcooled film boiling, liquid side heat flux is affected by the presence of a finite vapor layer at the leading edge and ripples and large waves on the interface.

2 At low subcoolings, the presence of the stationary vapor layer at the leading edge and a moving interface downstream leads to very high fluxes in the front of the layer.

3 The liquid side heat transfer over each wavelength shows a cyclic behavior with the maximum heat flux occurring at the peaks and the minimum heat transfer occurring in the wave valleys. High local liquid heat flux at the peaks suggests the possibility of local condensation. Evaporation at the valleys and condensation at the peaks results in little increase in the substrate film thickness in the vapor flow direction.

4 The liquid side heat transfer is enhanced both by the cyclic behavior and by area correction. To a great extent, the underprediction of the wall heat transfer can be approximately

attributed to the underprediction of liquid side heat flux on a wavy interface.

5 The liquid side heat fluxes averaged over each wavelength can be modeled by a simple transient heat conduction model for very low and low subcoolings. For higher subcoolings, the results for liquid side heat transfer are better predicted by analytical results from a transient conduction model that includes the effect of the velocity normal to the interface.

Acknowledgments

This work received support from the NSF under grant No. CBT-84-17684.

References

- Ayazi, F., and Dhir, V. K., 1987, "Minimum Heat Flux and Wall Superheat During Subcooled Film Boiling on Horizontal Cylinders," Paper No. AIAA 87-1335.
- Beer, H., 1972, "Interferometry and Holography," *Boiling Phenomena*, Vol. 2, Hemisphere Publishing Corporation, New York, pp. 824-843.
- Bromley, L. A., 1950, "Heat Transfer in Stable Film Boiling," *Chemical Engineering Progress*, Vol. 46, No. 5, pp. 221-227.
- Bui, T. D., and Dhir, V. K., 1985, "Film Boiling Heat Transfer on a Vertical Plate," *ASME JOURNAL OF HEAT TRANSFER*, Vol. 107, pp. 756-763.
- Carslaw, H. S., and Jaeger, J. C., 1962, *Conduction of Heat in Solids*, Oxford University Press, Oxford, United Kingdom, pp. 65-67.
- Coury, G. E., and Dukler, A. E., 1970, "Turbulent Film Boiling on Vertical Surfaces," *Proceedings of International Heat Transfer Conference*, Paper No. B 3.6, pp. 38-45.
- Dhir, V. K., and Purohit, G. P., 1978, "Subcooled Film Boiling Heat Transfer From Spheres," *Nuclear Engineering and Design*, Vol. 47, pp. 49-66.
- Eckert, E. R. G., and Drake, R. M., 1972, *Analysis of Heat and Mass Transfer*, McGraw-Hill, New York, pp. 528-529.
- Frederking, T. H. K., and Hoppenfeld, J., 1964, "Laminar Two Phase Boundary Layers in Natural Convection Film Boiling of Subcooled Liquids," *J. Appl. Math Phys.*, Vol. 15, pp. 475-481.
- Hauf, R. T., and Grigull, W. V., 1970, "Optical Methods in Heat Transfer," *Adv. in Heat Transfer*, Vol. 6, Academic Press, New York, pp. 137-366.
- Mayinger, F., and Panknin, W., 1978, "Holography in Heat and Mass Transfer," *Proc. 5th Int'l Heat Transfer Conf.*, Vol. 7, pp. 212-217, Tokyo.
- Nishikawa, K., and Ito, T., 1966, "Two Phase Boundary Layer Treatment of Film Boiling," *Int'l. J. Heat Mass Transfer*, Vol. 9, pp. 103-115.
- Orozco, J. A., and Witte, L. C., 1986, "Flow Film Boiling From a Sphere to Subcooled Freon-11," *ASME JOURNAL OF HEAT TRANSFER*, Vol. 108, pp. 934-938.
- Sakurai, A., Shiotsu, S., and Hata, K., 1986, "Effects of Subcooling on Film Boiling Heat Transfer From a Horizontal Cylinder in a Pool of Water," *Heat Transfer*, 1986, Vol. 4, Hemisphere, Washington, DC, pp. 1043-1048.
- Sparrow, E. M., and Cess, R. O., 1962, "The Effects of Subcooled Liquid on Laminar Film Boiling," *ASME JOURNAL OF HEAT TRANSFER*, Vol. 84, pp. 139-152.
- Suryanarayana, N. V., and Merte, H., 1972, "Film Boiling on a Vertical Surface," *ASME JOURNAL OF HEAT TRANSFER*, Vol. 94, pp. 377-384.
- Toda, S., and Mori, M., 1982, "Subcooled Film Boiling and Behavior of Vapor Film on a Horizontal Wire and a Sphere," *Proc. 7th Int'l Heat Transfer Conf.*, Vol. 4, pp. 173-178, Munich.
- Vijaykumar, R., 1990, "Hydrodynamics and Heat Transfer Aspects of Subcooled Film Boiling on a Vertical Surface," Ph.D. dissertation, Univ. of California, Los Angeles.
- Wang, B. X., and Shi, D. H., 1985, "A Semi-empirical Theory for Forced Flow Turbulent Film Boiling of Subcooled Liquid Along a Horizontal Plate," *Int'l J. Heat Mass Transfer*, Vol. 28, No. 8, pp. 1499-1504.
- Witte, L. C., and Orozco, J. A., 1984, "The Effect of Vapor Velocity Profiles Shape on Flow Film Boiling From Submerged Bodies," *ASME JOURNAL OF HEAT TRANSFER*, Vol. 106, pp. 191-197.

Critical Heat Flux in Horizontal Tube Bundles in Vertical Crossflow of R113

K. M. Leroux

M. K. Jensen

Department of Mechanical Engineering,
Aeronautical Engineering, and Mechanics,
Rensselaer Polytechnic Institute,
Troy, NY 12180-3590

The critical heat flux (CHF) on a single tube in a horizontal bundle subject to an upward crossflow of R113 has been studied in three bundle geometries. Effects of local quality, mass flux, pressure, and bundle geometry on the CHF were investigated. The shapes of the CHF-quality curves display three distinct patterns, which progress from one to another as mass flux increases. At low mass fluxes, the CHF data monotonically decreased with increasing quality. At intermediate mass fluxes with increasing quality, the CHF data initially decreased to a relative minimum, then increased to a relative maximum, and finally began to decrease again as the higher qualities were reached. At high mass fluxes, as quality increased, the CHF rose gradually from the zero quality value to a maximum and then began to decrease. For all mass fluxes, the zero-quality CHF points clustered around an average value, which varied slightly with test section geometry. Mechanisms for the CHF condition are suggested.

Introduction

Shellside boiling on horizontal bundles is common in the power, process, and refrigeration industries. However, not enough is known about the fluid dynamics and heat transfer of boiling in bundles or of the critical heat flux (CHF) condition to prevent overdesign. As a result, design methods must be conservative. Recommended design calculations rely on pool boiling CHF information for single tubes (e.g., Palen and Small, 1964), but, as a result of cautious calculations, some heat exchangers may be as much as 300 percent overdesigned (Niels, 1979). Hence, accurate predictions of bundle maximum heat flux could reap savings in materials and energy by eliminating the large uncertainty in design.

A survey of the literature reveals that the number of crossflow CHF studies is small; specific information about effects of mass flux, quality, pressure, and geometry on the CHF on a single tube in a channel by itself or in a bundle is scarce. Jensen and Pourdashti (1986) investigated the CHF on a single tube in subcooled and low-quality R113 upflows. The CHF decreased linearly with quality from the subcooled region up to about 10 percent quality and then leveled out. Yao and Hwang (1989) found a similar trend for the CHF on a single heated tube in a channel and noted that the CHF decreased with an increasing ratio of tube diameter to channel width; the CHF on a tube in an unheated bundle increased with increasing mass flux for a given subcooling.

Hasan et al. (1982) found that an unheated in-line cylinder within four diameters upstream of the heated test cylinder could reduce the saturated liquid CHF of the heater by as much as 90 percent. Upstream staggered cylinders caused only a slight decrease in the CHF below that of a single tube. The effect of upstream tubes became noticeable above a very low liquid velocity. Downstream cylinders had little effect.

Schuller and Cornwell (1984) studied a slice of a kettle boiler with electrically heated tubes, as well as a smaller in-line array in a channel with forced flow; each had a P/D of 1.33. Dryout heat fluxes for tubes in the bundle were lower than those for a single tube in an infinite flow field and decreased as local quality increased. The authors also remarked

that a significant change in tube temperature did not distinguish the onset of the dryout condition.

Cumo et al. (1980) studied the CHF condition on a single heated tube in a 3×3 rotated square bundle ($P/D = 1.25$) subject to a known two-phase upward crossflow of R12 at 7.85 bar. Qualities ranged from 0 to 30 percent and mass fluxes (based on the minimum flow area) ranged from about 40 to 140 $\text{kg/m}^2\text{s}$. Under all flow conditions the CHF increased with increasing quality and leveled out at higher qualities. Experimental results showed that the saturated liquid CHF depended very weakly on mass flux.

From this review (for more details see Leroux, 1990), it is clear that few investigations for the CHF in tube bundles under two-phase flow conditions have been performed. Studies that involve two-phase flow in bundles, with the exception of that of Cumo et al., do not include specific information about local quality and mass flux at a tube undergoing CHF. Likewise, the ranges of flow conditions studied have been limited. Hence, this investigation seeks to establish the effects of variations of fluid flow conditions and geometry on the CHF condition on a tube in an unheated bundle. To this end, an experimental investigation has been performed in which mass flux, pressure, local quality, and test section geometry were controlled and varied over a wide range of conditions. The experiments performed for this study involved heating only one tube in the tube bundle. R113 was used as the working fluid because it is a good modeling fluid for the CHF condition, requires lower pressures and power than water, and is safer than hydrocarbons.

Apparatus and Procedure

In this investigation, CHF studies on a heated tube in an unheated bundle were carried out on two test section geometries. These results and those obtained by Dykas and Jensen (1990) on a third bundle geometry form the basis of this paper.

The flow loop used in this experiment is described by Dykas and Jensen (1990) and consisted of a positive displacement pump, electric preheaters, condenser/aftercooler, storage/surge tank, and the test section assembly (Fig. 1). Degassed R113 was the working fluid. Each test section chamber enclosed a tube bundle consisting of 7.94 mm o.d., 7.62 mm i.d., 82.6-mm-long stainless steel tubes; the heated length of the tube

Contributed by the Heat Transfer Division and presented at the National Heat Transfer Conference and Exposition, Minneapolis, Minnesota, July 28–31, 1991. Manuscript received by the Heat Transfer Division January 31, 1991; revision received May 23, 1991. Keywords: Boiling, Heat Exchangers, Multiphase Flows.

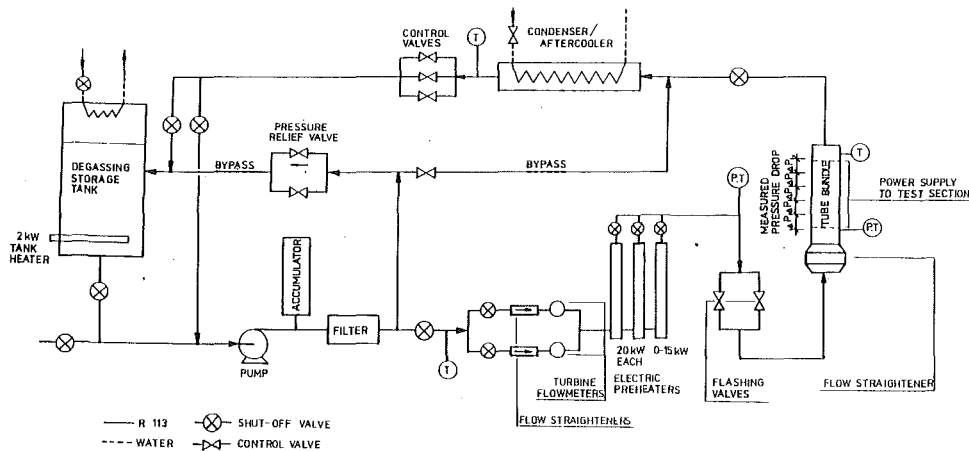


Fig. 1 Schematic of flow loop

was 82.6 mm. A 5 column by 27 row equilateral triangular array with $P/D = 1.30$ and a 5×27 square, in-line array with $P/D = 1.70$ were tested for this project. Dykas and Jensen tested a 5×27 square, in-line array with $P/D = 1.30$. In each bundle, half of each tube in the outside columns was imbedded in the chamber walls. The tube on which the CHF condition was obtained (Fig. 2) in all cases was the center tube of the 25th row from the bottom. This tube was situated far from the chamber inlet to avoid entrance effects. The tube had brass ends to which power leads were attached and was electrically isolated from the chamber walls (Fig. 3).

The test section inlet pressure was measured with a Bourdon-tube gage. Five inverted U-tube manometers measured the pressure differential between six pressure taps distributed along the tube bundle. Copper-constantan thermocouples at the inlet and the exit of the test section, and elsewhere in the loop, were placed in the center of the flow channels. The mass flow rate was measured upstream of the preheaters by means of a turbine flow meter. The CHF tube was heated by joulean heating, and the direct current to the tube was found by measuring the voltage across a shunt in the voltage lead to the tube. Thermocouple voltages, flow meter frequencies, and CHF tube voltage drops were measured using a computer-controlled data acquisition system, while pressure readings were manually entered into the computer.

After the flow and pressure levels were established, the electric preheaters were set to raise the R113 temperature to that necessary to attain the desired quality at the heated tube in the bundle. One variable 15 kW and two 20 kW preheaters were used. The 5 kW gap in the preheater power prevented obtaining all inlet qualities at all mass fluxes, thus resulting in gaps in the CHF- x curves. A high pressure was maintained in the preheaters; as the high-pressure liquid passed through the flashing valves (Fig. 1), the liquid flashed and the two-phase mixture flowed vertically upward through the test section. (The large pressure drop across the flashing valves also prevented thermal-hydraulic instabilities from occurring in the loop.) Quality at the CHF tube was determined by an equilibrium energy balance across the flashing valves. CHF data points were taken once conditions in the loop had reached steady state. The power to the CHF tube was increased in small increments until an increase in wall temperature, as reflected by the tube resistance, indicated that the CHF condition had occurred. The power was then shut off. The CHF tube was

periodically removed from the bundle and inspected. If there was discoloration due to the high temperatures attained or evidence of scaly buildup due to decomposed refrigerant (usually small), the tube was replaced.

As the electric current was incremented slowly, the tube resistance remained essentially constant between power increments, but upon the attainment of the CHF power level, the tube resistance would begin to rise steadily due to a temperature rise of the tube. Such a temperature rise indicated the CHF condition on the tube. The current would then begin to fall while the resistance rose until power was shut off. A current drop of at least 1 A was accompanied by a 2 percent rise in resistance at CHF. The average current value (and its corresponding voltage) since the last increment and prior to current dropoff was chosen as the CHF value and manually entered into the computer.

The CHF point did not always distinguish itself by a steadily declining current and rising tube resistance. At high mass fluxes (300 kg/m^2 or greater) and qualities greater than 30 percent, the current displayed a phenomenon best described as "ratcheting." Upon reaching a value set by the operator, the current would decrease by 1-2 A and level out for several seconds; it then might rise again to the originally set value. When the current was manually increased the same behavior was repeated. Resistance began to increase steadily at the same time the current first dropped. The ratcheting would continue until the power was shut off to prevent tube damage.

As a result of ratcheting, identification of the initiation of the CHF condition was difficult at higher mass fluxes because, apparently, only small patches on the tube would overheat while the remainder of the tube would stay wetted and cooled. Because there were no visual observations of conditions on the tube, a decision had to be made regarding which point to interpret as the CHF condition. One test section was instrumented with four thermocouples equally spaced around the inside circumference of the tube at the tube midline. While the CHF condition did not always initiate immediately around these locations, during one test run it did. The temperature indicated by the thermocouple at the rear stagnation point rose sharply (from 85°C to 178°C), an adjoining one also experienced elevated temperatures, and the remaining two showed small temperature increases. This temperature rise was accompanied by an increase in the tube resistance of 1-2 percent and a corresponding drop in current. Based on the tube temperature

Nomenclature

D = tube diameter, m
 G = mass flux, $\text{kg/m}^2\text{s}$
 P = pitch, m

p = pressure, kPa
 q_{cr}'' = critical heat flux, kW/m^2
 x = quality

Subscripts

loc = local conditions at CHF tube

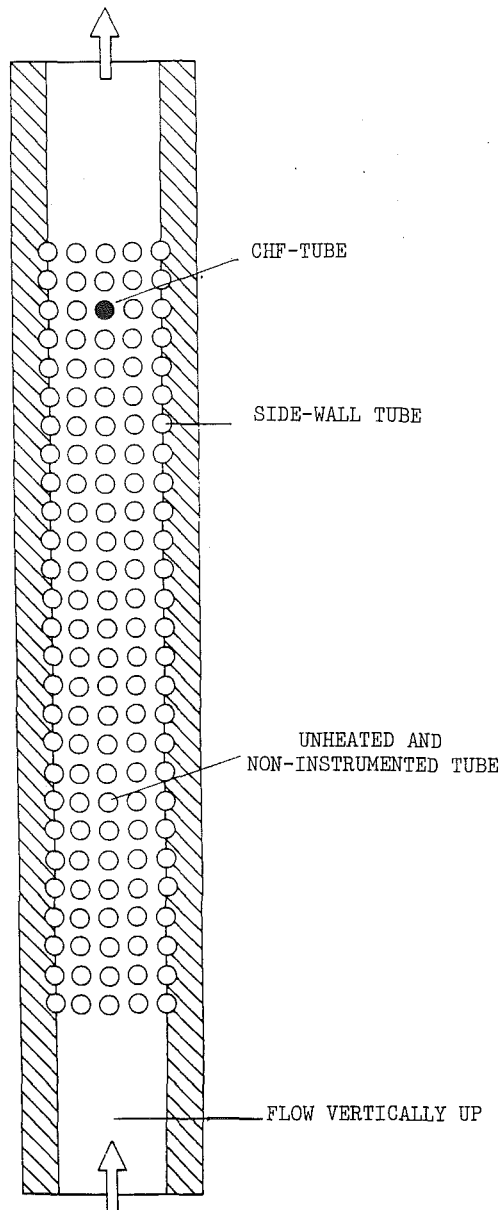


Fig. 2 Typical in-line tube bundle test section

observations during the specially instrumented CHF run and on a model of tube resistance under patchwise dryout (see Leroux, 1990), it was concluded that the first increase in tube resistance and fall in current would be accepted as indicating the initiation of the CHF condition.

After data at several mass fluxes had been taken, there was often a thin patch of black, scaly deposit on the downstream side of the tube at midlength. No such deposit appeared on the upstream side of the tube. This evidence, along with the temperature measurements taken during a CHF run, suggests that the CHF condition initiated on the downstream side of the tube.

Mass fluxes from 50 to 500 kg/m²s, pressures of 1.5 and 5.0 bar, and qualities from 0 to 70 percent were tested. Maximum preheater capacity restricted the range of quality at higher mass fluxes and pressures, especially in the 1.70 in-line test section. Mass flux was calculated through the minimum flow area within the tube array. Local pressure at the CHF tube was calculated by linear interpolation between pressure taps. The saturation temperature at the CHF tube was then derived from the local pressure. Quality at the CHF tube was then

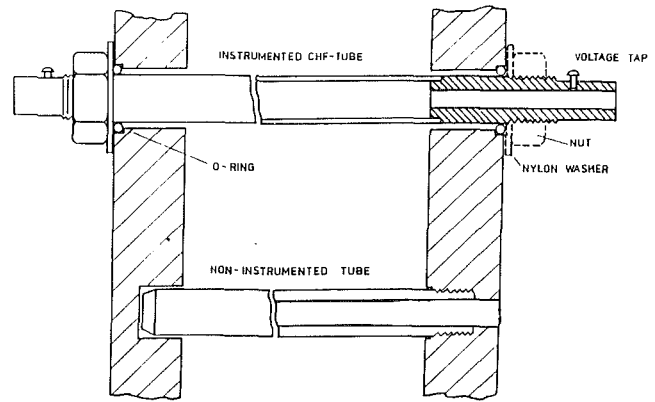


Fig. 3 Cross section of CHF and uninstrumented tubes

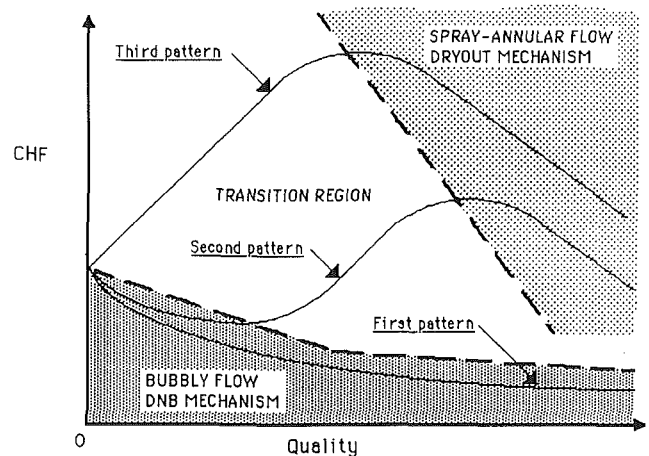


Fig. 4 Basic curve patterns observed in the data and postulated flow regimes and CHF mechanisms mapped out of typical CHF curves

found from an energy balance. The CHF was calculated from the electric power supplied to the tube and the tube surface area. Uncertainties in the experimentally measured quantities were estimated through a propagation of uncertainty analysis as: G , ± 3.0 percent; p_{loc} , ± 0.5 percent; x_{loc} , ± 0.5 percent; q''_s , ± 5.0 percent. Tabulated data can be obtained upon request or from Leroux (1990).

Results and Discussion

Three different CHF-condition curve patterns exist in the CHF data obtained in this study, and the patterns are a function of mass flux and quality for a given test section and pressure. These will be briefly described now so that examination of the data can be made with reference to these trends. The first pattern (Fig. 4) generally occurs with low mass fluxes. In this pattern, the CHF monotonically decreases from the zero-quality value to one as much as 50 percent lower as quality increases from zero to the highest value tested.

The second pattern appears at low and intermediate mass fluxes. This pattern's shape resembles an inverted sine wave. The second pattern behaves similar to the first at low qualities. At higher mass fluxes and qualities, the CHF begins to increase rather than continuing the monotonic decrease in CHF, thus departing from the first pattern. Eventually, for a given mass flux, a maximum CHF is reached and the CHF-quality curve again decreases monotonically with increasing quality. As mass flux increases, the local minimum CHF shifts to the left and approaches the zero-quality CHF value; the local maximum CHF also shifts left, and becomes higher.

The third pattern appears at high mass fluxes. The zero-

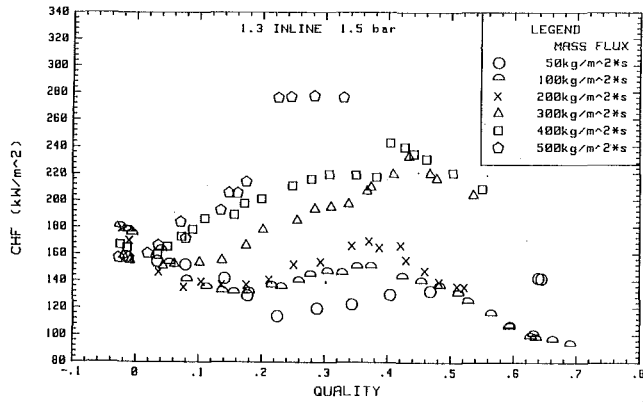


Fig. 5 Variation of CHF with quality: 1.3 in-line bundle at 1.5 bar (Dykas and Jensen, 1990)

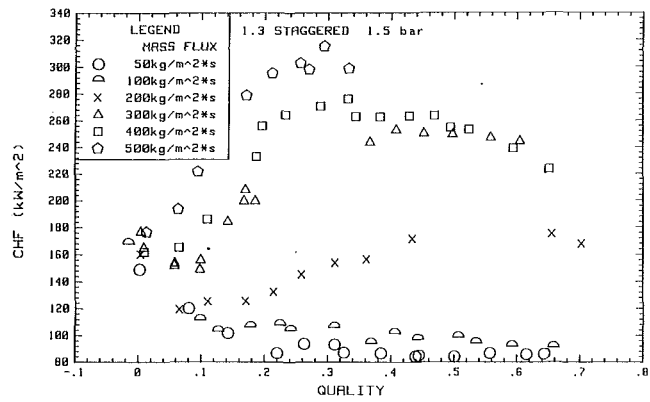


Fig. 7 Variation of CHF with quality: 1.3 staggered bundle at 1.5 bar

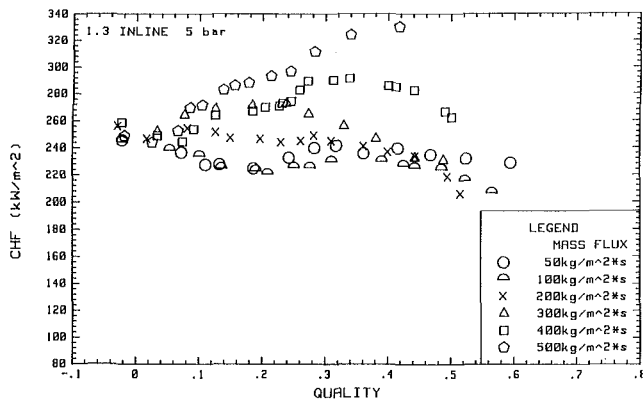


Fig. 6 Variation of CHF with quality: 1.3 in-line bundle at 5.0 bar (Dykas and Jensen, 1990)

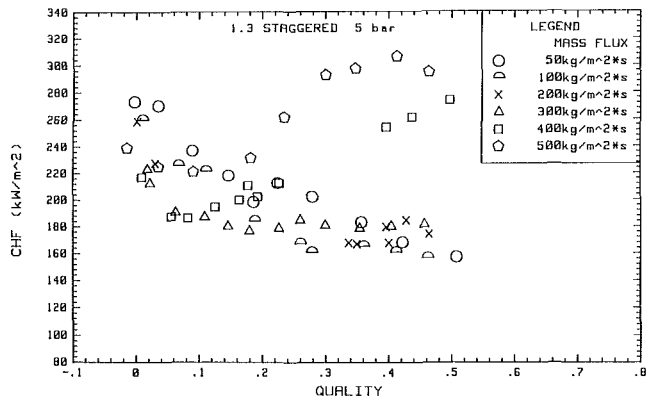


Fig. 8 Variation of CHF with quality: 1.3 staggered bundle at 5.0 bar

quality CHF value remains roughly the same as in the second and first patterns. Unlike the other patterns, the third CHF-quality pattern shows an immediate increase in CHF with increasing quality; apparently no local minimum CHF exists. As quality increases, the CHF reaches a maximum and then begins a monotonic decrease.

Two-Phase CHF Data. For the 1.30 in-line test section (all data from Dykas and Jensen, 1990) at 1.5 bar (Fig. 5), the shape of the second pattern characterizes the data at all but the highest mass fluxes. The low-pressure data for mass fluxes of 400 and 500 kg/m²s experience step changes in the CHF upon reaching qualities of about 40 and 20 percent, respectively. The reason for these jumps is unknown; they do not recur under any other conditions, and repeated data runs confirmed these points. At 5.0 bar (Fig. 6) the peaks of the 400 and 500 kg/m²s curves occur at successively higher qualities than that of the 300 kg/m²s curve. Observation of the trends in the other test sections indicates that this right shift of the peaks is anomalous. We can speculate that these two unusual trends are attributable to the uncertainty of the CHF point when the ratcheting phenomenon (discussed previously) begins at high mass fluxes. The low-pressure data for the 1.30 staggered bundle offer the clearest example of the evolution of the three curve shapes with mass flux and quality (Fig. 7); at high pressure (Fig. 8), all the CHF curves for mass fluxes less than 400 kg/m²s have the negative slope of the first curve pattern.

In the 1.70 in-line test section at low pressure, the CHF reaches the maximum value at a mass flux of 200 kg/m²s (Fig. 9). The maximum CHF values for higher mass fluxes all fall below this maximum. This is the most prominent phenomenon that distinguishes this larger pitch in-line bundle from the 1.30

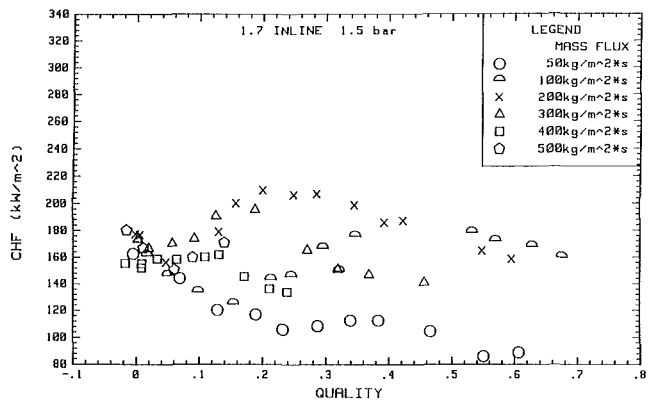


Fig. 9 Variation of CHF with quality: 1.7 in-line bundle at 1.5 bar

in-line bundle. At the highest mass flux, data were not obtained after about $x = 0.14$ because of equipment limitations. At the high pressure (Fig. 10), data also are limited due to equipment limitations, but the data appear to follow the patterns noted with the other test sections.

Zero-Quality CHF. The CHF-quality curves at all mass fluxes in all three test sections pass through a narrow range of values at zero quality. At 1.5 bar the range centers around approximately 165 kW/m². Most of the zero-quality CHF data fell within ± 10 percent of this value. At 5.0 bar, the zero-quality values centered around approximately 245 kW/m², and the scatter is comparable. Note that the saturated liquid pool boiling CHF values calculated with Sun and Lienhard's (1970) correlation (as modified by Lienhard and Dhir, 1973) are 203 kW/m² at 1.5 bar, and 276 kW/m² at 5.0 bar. Hence, at least

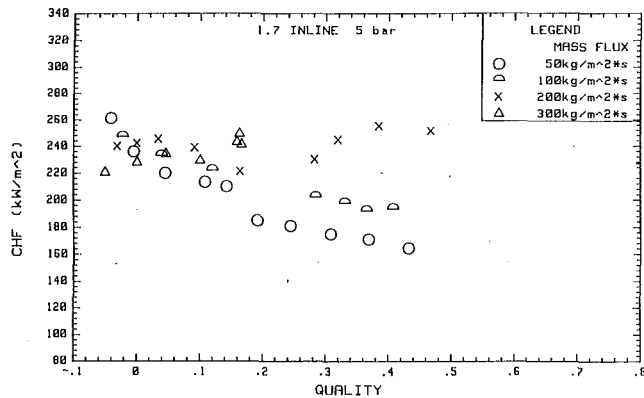


Fig. 10 Variation of CHF with quality: 1.7 in-line bundle at 5.0 bar

for the flow conditions and geometries tested, variations in bundle geometry cause only small variations in the saturated liquid CHF. At the same time, the CHF of a single tube in a bundle subject to crossflow is greatly reduced compared to that of a single isolated tube in pool boiling. Other researchers have noticed little variation in CHF on single tubes and in tube bundles in low-velocity saturated liquid flows (e.g., Cumo et al., 1980; Katto and Haramura, 1983). The similarity between low-velocity saturated flows and pool boiling conditions has been noted by Lienhard and Eichhorn (1976) and may account for the small variation of CHF with liquid velocity in low-velocity saturated flows.

Subcooled CHF. Few data were taken in subcooled flows. The maximum inlet subcooling was 8°C. In most cases, the subcooled trend extends slightly into the low-quality region, as found by Dykas and Jensen (1990) and by Jensen and Pourdashti (1986). In some cases, however, the data trend in the subcooled region is opposite to that in the low-quality region. For example, the 1.5 bar data for 400 kg/m²s in the 1.30 in-line bundle decrease as subcooling increases, but begin to rise at low positive qualities. Hence, these data follow the second curve pattern, with the local minimum occurring at or near zero quality. This suggests that the curve patterns described in the two-phase region extend into the subcooled region.

Effect of Pressure. In general, the CHF values for a given test section cover a narrower range at 5.0 bar than they do at 1.5 bar, as can be seen by comparing the high and low-pressure data for each test section. The ascending portions of the high-pressure data curves have smaller slopes than do their low-pressure counterparts, especially at low mass fluxes. Besides affecting the relative slopes of the mass flux curves, increased pressure also affects the development of the CHF-quality curves with increasing mass flux. In a particular test section at 5.0 bar, the same pattern may first appear at a lower mass flux than it does at 1.5 bar. For example, in the 1.30 in-line test section, the high-pressure curves develop the third curve pattern at 200 kg/m²s, while the low-pressure data do not develop it until 400 kg/m²s.

Effect of Bundle Geometry. The effects of tube layout may be assessed by comparing the data of the 1.30 staggered and 1.30 in-line test sections. In the staggered bundle, as mass flux increased, there was a more pronounced difference between the slopes of the CHF-quality curves for different mass fluxes than there was in any other test section. Consequently, at a given pressure, the range of CHF values covered by the three curve shapes displayed by the data of the staggered bundle is wider than the range in either of the in-line test sections. At the low pressure, the data of the staggered bundle for mass fluxes less than 300 kg/m²s fall below their in-line counterparts, while the higher mass flux data in the staggered bundle are

greater than in the in-line bundle. At the high pressure, the staggered bundle CHF generally fall below those of the in-line bundle at every mass flux.

The differences in the data between the 1.30 and the 1.70 in-line test sections demonstrate the large influence of pitch-to-diameter ratio on the CHF condition. At low pressure, the 1.70, low-mass-flux data are lower than those from the 1.30 test section. With increasing mass flux, the 1.70 data become equal to or greater than their 1.30 counterparts. At high pressure, the low-mass-flux data from the 1.70 test section are lower than those from the 1.30 test section, but, again, as mass flux increases, the CHF values from the two test sections become similar.

Comparison With Other Data. Although few studies of the critical heat flux on a tube in a bundle in two-phase upward crossflow have been reported in the literature, favorable comparisons may be made between the data trends of the present experiment and the trends in those few studies that have similar geometries and conditions. The present data agree well with the data of Schuller and Cornwell (1984). In their "tube column rig," they observed that the CHF generally decreased with increasing quality. In the present data, the low-quality data trends of the first and second curve patterns agree with this downward trend. Their liquid velocities fall near the middle of the present experiment's range of 0.034 to 0.37 m/s.

Another study in which the CHF tube is subject to the influence of parallel neighbors is that of Hasan et al. (1982). For a fixed P/D , the saturated liquid CHF decreased with liquid velocity until, at a certain velocity, the CHF began to increase. This pattern is similar to that of the second curve pattern. Because increasing quality at a given mass flux results in an increase in flow velocity, the decrease and subsequent increase of the present data with quality in the second curve pattern are similar to the trends in Hasan's data.

The investigation of Cumo et al. (1980) concerning the critical heat flux in a bundle is most similar to the present one. However, the CHF-quality curves of Cumo's investigation do not agree with the present investigation's data for similar mass fluxes, and there are ambiguities in the interpretation of Cumo's data. For qualities up to 30 percent and mass fluxes less than 140 kg/m²s, the Cumo CHF-quality curves were similar to the curves for mass fluxes of 300 kg/m²s and above in the present investigation. Attempts to reconcile Cumo's data with those of the present experiment were made by comparing nondimensional mass fluxes through such groups as a liquid and two-phase Reynolds number, the Weber number, the Froude number, etc.; however, the nondimensional mass flux values were different by a factor of at least three.

Speculation on CHF Mechanisms. The three CHF-quality curve patterns are composed of three trends. These are a downward trend at low quality and at low mass flux, an upward trend that may occur at low to intermediate qualities at moderate to high mass fluxes, and another downward trend that appears at intermediate to high qualities. Mechanisms governing the CHF phenomena for each trend in the data can be suggested, along with accompanying flow patterns. A speculative CHF mechanism and flow pattern map is presented in Fig. 4, where the different mechanisms and flow patterns are superimposed on typical CHF curves.

A departure from the nucleate boiling (DNB) phenomenon similar to that which occurs in pool boiling may bring on the CHF condition at low mass fluxes and low qualities where the CHF decreases monotonically with quality. Lienhard and Eichhorn (1976) noticed the same vapor jet escape pattern in both pool boiling and low-velocity saturated flow boiling. Furthermore, Lienhard (1988) remarked that the same CHF mechanism applies in both subcooled and saturated pool boiling. One may conclude that for low-velocity subcooled and satu-

rated flows, the CHF mechanism is the same as in pool boiling. Extending Jensen and Pourdashti's (1986) reasoning to tube bundles, the pool boiling CHF mechanism may apply for a specific trend whether the local flow is subcooled or low quality. The accompanying flow pattern may be described as bubbly, a pattern often witnessed in low-velocity, low-quality flows.

It is believed that the high-quality CHF behavior is the result of a dryout process. The downward CHF trend at high quality may result from an evaporating thin liquid film on the tube in a spray-annular flow pattern. Quality, void fraction, and vapor velocity are high in this regime, and entrainment and evaporation compete with droplet deposition on the tube to determine the CHF in a process similar to that which occurs in in-tube flows.

At intermediate qualities, the upward slope of the CHF trend may reflect a transition from the low-quality to the high-quality mechanism. The flow pattern in this region of the curves also may be transitional. In this region, one may speculate that the intermediate quality flow results in increased liquid convection and faster bubble removal due to increased vapor shear, but this only results in enhancement of the heat transfer process and is not large enough for the vapor shear to detrimentally thin the liquid film on the surface. Hence, this raises the CHF as quality increases until the transition to a vapor-dominated flow occurs at the peak of the curve.

Where the same data trends are observed in the different tube bundle geometries at different qualities, mass fluxes, and pressures, certain flow conditions must be common. The occurrence of a given trend within a given bundle's data is probably determined by particular combinations of mass flux, quality (or void fraction), and pressure, which results in a specific flow pattern. Because no general flow pattern map for crossflow in multitube bundles is available, it is not presently possible to confirm this speculation. However, it is reasonable to assume that the flow pattern is a key parameter needed to describe the CHF-quality behavior. Pressure drop versus quality curves for various mass fluxes were plotted in an attempt to identify flow pattern changes (which then could be compared to the CHF- x curves) through changes in the pressure drop trends. This work was inconclusive.

Conclusions

This investigation sought to establish the effects of tube bundle geometry, pressure, mass flux, and quality upon the CHF on a single tube in a bundle subject to upward vertical crossflow. The data gathered over the range of conditions studied displayed complex yet orderly behavior. From this study the following conclusions can be drawn:

1 The CHF data exhibited three different curve patterns as mass flux and quality increased. As mass flux increased, the curve patterns evolved into one another. At low qualities and low mass fluxes, the CHF decreased with increasing quality. At intermediate qualities and mass fluxes, the CHF increased with increasing quality, and at high qualities, the CHF decreased with increasing quality.

2 At zero quality the CHF values for all mass fluxes are concentrated in a narrow range of values, which varied little

with test section geometry, but were consistently lower than the saturated liquid pool boiling CHF.

3 Three separate regions of the CHF-quality curves were defined by changes in the CHF mechanism and flow pattern. It can be speculated that for all the CHF-quality curves at different mass fluxes, only two different mechanisms for the CHF condition occur, a DNB-type at lower mass fluxes and qualities and a dryout-type at higher qualities; flow patterns probably dictate the mechanism.

4 In general, less convective enhancement of the CHF takes place in the 1.30 staggered and 1.70 in-line bundles compared to the 1.30 in-line bundle. The larger P/D has a detrimental effect on the CHF. The increased distance to the nearest upstream tube has a similar detrimental effect on the CHF in the 1.30 staggered bundle except at the highest mass fluxes and low pressure.

Acknowledgments

This study was sponsored by the National Science Foundation under Grant No. CBT-8704693. The NSF support is gratefully acknowledged. Sincere thanks are extended to Dave Edwards and Stan Dykas for their work on the experimental apparatus and for their collaboration in gathering data.

References

- Cumo, M., Farello, G. E., Gasiorowski, J., Iovino, G., and Naviglio, A., 1980, "Quality Influence on the Departure From Nucleate Boiling in Cross Flows Through Bundles," *Nuclear Technology*, Vol. 49, pp. 337-346.
- Dykas, S., and Jensen, M. K., 1991, "Critical Heat Flux on a Tube in a Horizontal Tube Bundle," *Experimental Thermal and Fluid Science*, in press.
- Hasan, M. M., Eichhorn, R., and Lienhard, J. H., 1982, "Burnout During Flow Across a Small Cylinder Influenced by Parallel Cylinders," *Seventh International Heat Transfer Conference*, Munich, Vol. 4, pp. 285-290.
- Jensen, M. K., and Pourdashti, M., 1986, "Critical Heat Flux on a Horizontal Cylinder in an Upward Subcooled and Low-Quality Two-Phase Crossflow," *ASME JOURNAL OF HEAT TRANSFER*, Vol. 108, pp. 441-447.
- Katto, Y., and Haramura, Y., 1983, "Critical Heat Flux on a Uniformly Heated Horizontal Cylinder in an Upward Cross Flow of Saturated Liquid," *International Journal of Heat and Mass Transfer*, Vol. 26, pp. 1199-1205.
- Kern, D. Q., 1950, *Process Heat Transfer*, McGraw-Hill, New York.
- Leroux, K. M., 1990, "Critical Heat Flux in Shellside Boiling on Horizontal Tube Bundles in Vertical Crossflow," M.S. Thesis, Mechanical Engineering Department, Rensselaer Polytechnic Institute, Troy, NY.
- Lienhard, J. H., and Dhir, V. K., 1973, "Hydrodynamic Prediction of Peak Pool-Boiling Heat Fluxes From Finite Bodies," *ASME JOURNAL OF HEAT TRANSFER*, Vol. 95, pp. 152-158.
- Lienhard, J. H., and Eichhorn, R., 1976, "Peak Boiling Heat Flux on Cylinders in a Cross Flow," *International Journal of Heat and Mass Transfer*, Vol. 19, pp. 1135-1141.
- Lienhard, J. H., 1988, "Burnout on Cylinders," *ASME JOURNAL OF HEAT TRANSFER*, Vol. 110, pp. 1271-1286.
- Niels, G. H., 1979, "Some Boiling Aspects in Kettle Evaporators," *Boiling Phenomena: Physicochemical and Engineering Fundamentals and Applications*, Vol. 2, Ch. 29, Hemisphere Publishing Co., pp. 937-938.
- Palen, J. W., and Small, W. M., 1964, "A New Way to Design Kettle and Internal Reboilers," *Hydrocarbon Processing*, Vol. 43, pp. 199-208.
- Schuller, R. B., and Cornwell, K., 1984, "Dryout on the Shell-Side of Tube Bundles," *First U.K. National Conference on Heat Transfer*, Inst. Chem. Engineering Symposium Series No. 86, Vol. 2, pp. 795-805.
- Sun, K. H., and Lienhard, J. H., 1970, "The Peak Pool Boiling Heat Flux on Horizontal Cylinders," *International Journal of Heat and Mass Transfer*, Vol. 13, pp. 1425-1439.
- Yao, S. C., and Hwang, T. H., 1989, "Critical Heat Flux on Horizontal Tubes in an Upward Crossflow of Freon-113," *International Journal of Heat and Mass Transfer*, Vol. 32, No. 1, pp. 95-103.

Considerations in Predicting Burnout of Cylinders in Flow Boiling

P. Sadasivan
Research Associate.

J. H. Lienhard
Professor.
Fellow ASME

Heat Transfer/Phase Change Laboratory,
Mechanical Engineering Department,
University of Houston,
Houston, TX 77204-4792

Previous investigations of the critical heat flux in flow boiling have resulted in widely different hydrodynamic mechanisms for the occurrence of burnout. Results of the present study indicate that existing models are not completely realistic representations of the process. The present study sorts out the influences of the far-wake bubble breakoff and vapor sheet characteristics, gravity, surface wettability, and heater surface temperature distribution on the peak heat flux in flow boiling on cylindrical heaters. The results indicate that burnout is dictated by near-surface effects. The controlling factor appears to be the vapor escape pattern close to the heater surface. It is also shown that a deficiency of liquid at the downstream end of the heater surface is not the cause of burnout.

Introduction

The peak heat flux (burnout), q_{\max} , on a horizontal cylinder in a liquid crossflow has been investigated since the 1950s. In this geometry and flow configuration, the vapor removal pattern takes the form of a two-dimensional vapor sheet in the wake region. This is shown in Fig. 1. Cylindrical bubbles break away from the sheet in a periodic manner. Early studies of burnout by Vliet and Leppert (1964) and Cochran and Andracchio (1974) led to restrictive empirical predictions for the peak heat flux.

The first mechanistic prediction of burnout was proposed by Lienhard and Eichhorn (1976). They based their predictions for the peak heat flux, on the hypothesis that burnout occurs when the two-dimensional vapor sheet becomes unstable. They developed a criterion for the instability of the vapor sheet, based on a mechanical energy inventory in the wake. In its original form, their so-called Mechanical Energy Stability Criterion (MESC) stated that the vapor wake becomes unstable, and therefore burnout occurs, when the rate of kinetic energy of the vapor entering the wake ($\rho_g u_g^3 \alpha D/2$) exceeds the rate at which surface energy is consumed in the wake ($2\sigma u_\infty$). The parameter α is the ratio of the vapor sheet thickness to the heater diameter; this had to be evaluated empirically.

Several subsequent studies led to the refinement and correction of the original version of the MESC. Hasan et al. (1981) defined the region where gravity influences the peak heat flux. Based on experimental data they obtained in the upflow and downflow configuration, they proposed that gravity does not affect the peak heat flux, when a "gravity influence parameter," defined as

$$G = \frac{u_\infty}{\sqrt[4]{g\sigma/\rho_f}} \quad (1)$$

is greater than 10.0. Many of the existing data were found to be in the region where gravity influences burnout. Using data obtained in the gravity-uninfluenced region, they derived revised correlations for the parameter α .

Kheyrandish and Lienhard (1985) observed in their water experiments that the frequency with which cylindrical bubbles broke away from the vapor sheet was exactly 120 Hz when a-c (60 Hz) heating was employed. With d-c heating, the bubble breakoff frequency was much lower. They divided existing data

into a-c-influenced and a-c-uninfluenced sets, and obtained correlations for the peak heat flux in each case.

Haramura and Katto (1983) proposed an alternative mechanism for flow boiling burnout. Unlike the theory of Lienhard and Eichhorn (1976), which focused on the far wake vapor sheet, their theory suggested that burnout is dictated by a thin liquid sublayer immediately adjacent to the heater surface. Small vapor jets perforate this liquid sublayer.

Haramura and Katto originally applied their theory to flow boiling on a vertical flat plate. This configuration is shown in Fig. 2. For this case, they assumed that the liquid enters the sublayer only at the forward stagnation point and moves at the same velocity as the bulk liquid flow. The sublayer thickness decreases progressively in the downstream direction, due to evaporation. They proposed that burnout occurs when conditions are such that the liquid sublayer evaporates completely when it just reaches the downstream stagnation point. They extended the theory to the case of a horizontal cylinder, by substituting the half circumference of the cylinder for the heater length. In doing so, they implicitly neglected the curvature of the cylindrical heater.

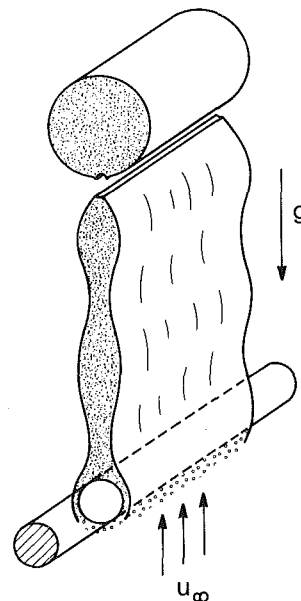


Fig. 1 Vapor removal pattern during flow boiling on a horizontal cylinder

Contributed by the Heat Transfer Division for publication in the JOURNAL OF HEAT TRANSFER. Manuscript received by the Heat Transfer Division February 21, 1991; revision received June 30, 1991. Keywords: Boiling, Phase-Change Phenomena.

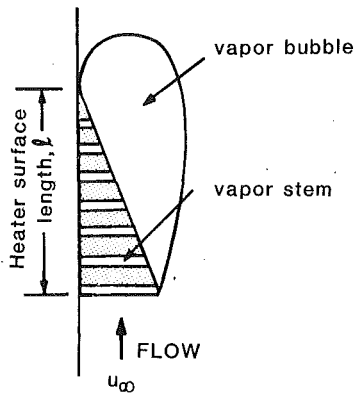


Fig. 2 Near-surface vapor removal pattern assumed by Haramura and Katto (1983)

Haramura and Katto (1983) assumed that the thickness of the sublayer at the upstream stagnation point is a fourth of the Helmholtz unstable wavelength, λ_H . That is less than the critical wavelength and too short an interface to suffer hydrodynamic collapse. Despite this and other shortcomings of their model, their notion that burnout could be dictated by near-surface effects reawakened interest in behavior near the heater surface.

Open Issues

The far-wake model for burnout is the only one that focuses on experimentally observable aspects of the flow—the far-wake vapor escape pattern. However, the results of several recent studies have pointed to the possibility of inadequacies in this representation. These issues have been discussed by Lienhard (1988).

The flow boiling experiments of Ungar (1987) on acetone yielded unusually high values of the peak heat flux. While predicted values are higher for isopropanol, experimental data show the reverse trend. The reason for this behavior has not been understood. In fact, a similar behavior can be noted if acetone pool boiling data are compared with the established predictions of q_{\max} in this geometry (Sun and Lienhard, 1970). This behavior is inconsistent with dimensional analysis based on purely hydrodynamic burnout.

Some recent studies such as those by Chowdhury and Winterton (1985) on pool boiling on horizontal cylinders and by Liaw and Dhir (1989) on pool boiling of water on a vertical plate revealed a strong influence of the liquid–solid contact angle on nucleate boiling as well as on the peak heat flux. It is possible that the anomalous behavior of acetone is a man-

ifestation of similar effects in flow boiling burnout. No systematic study of surface wettability effects on flow boiling burnout has yet been reported. Any surface wettability effects will necessitate considerable modification of the basic dimensionless functional equation for the peak heat flux¹

$$\phi = \phi(r, We_f, Fr) \quad (2)$$

to include the contact angle as an additional variable.

While the a-c influence on the *vapor wake* has been established in earlier studies, the quantitative effect of the heating mode on the *peak heat flux* is not known. Actual comparison of a-c and d-c heated data, for cases when the wake is a-c influenced, will shed light on the role of the vapor wake and bubble breakoff pattern in burnout. An examination of the influence of heater surface temperature and heat flux distributions would also be useful to ascertain the relative importance of the far-wake and near-surface in burnout.

The sublayer-controlled mechanism of Haramura and Katto does not account for possible gravity influences on burnout. This can be seen by recognizing that the model evaluates the initial thickness of the sublayer using stability considerations on a liquid–vapor interface that is *parallel* to the direction of gravity forces. From this point, isolating the role of gravity would help to verify the validity of the surface-controlled model.

The objectives of the present study are therefore:

- to examine the role of the far wake (vapor sheet) on the peak heat flux.
- to isolate the role of gravity on burnout.
- to investigate surface wettability effects on burnout.
- to examine issues relating to the heater surface temperature distribution.
- to develop new predictions for q_{\max} based on what we have learned in the items above.

Experimental Results

Two flow loops were employed in the present study. Experiments carried out under normal gravity conditions made use of the flow loop (L1) shown in Fig. 3. Variable gravity experiments were conducted using the flow loop (L2) shown in Fig. 4. This loop was mounted on a centrifuge; thus different gravity levels could be simulated at the heater by varying the speed of rotation of the centrifuge. Detailed descriptions of loops L1 and L2 are provided by Ungar (1987) and Sadasivan (1990), respectively. In both flow loops, flow velocity is cal-

¹If we assume that burnout is of hydrodynamic origin, the dimensional functional equation yields eight variables— q_{\max} , ρ_g , ρ_f , h_{fg} , u_∞ , g , D , and σ —in four dimensions—J, s, m, kg. Then dimensional analysis yields four pi-groups— ϕ , Fr , We_f , and r .

Nomenclature

D = diameter of cylindrical heater	r = density ratio = ρ_f/ρ_g	
Fr = Froude number = u_∞/\sqrt{gD}	T = temperature	
g = gravitational acceleration	T_r = reduced temperature	α_h = heater thermal diffusivity
G = gravity influence parameter, defined in Eq. (1)	$T_{r,(h,n)}$ = reduced homogeneous nucleation temperature	α_{liq} = liquid thermal diffusivity
h = heat transfer coefficient	T_{sat} = saturation temperature	β_r = receding contact angle
h_{fg} = latent heat of vaporization	u_∞ = liquid flow velocity	λ_H = Helmholtz unstable wavelength
k = thermal conductivity	u_g = velocity of vapor in the vapor sheet relative to the liquid	ρ_f = liquid density
MESC = Mechanical Energy Stability Criterion	We_f, We_g = Weber number = $\rho_f u_\infty^2 D/\sigma; \rho_g u_\infty^2 D/\sigma$	ρ_g = vapor density
q_{\max} = peak heat flux	α = ratio of vapor sheet thickness to heater diameter	σ = surface tension
		ϕ = dimensionless peak heat flux = $\pi q_{\max}/\rho_g h_{fg} u_\infty$
		ψ = half-angle of liquid contact

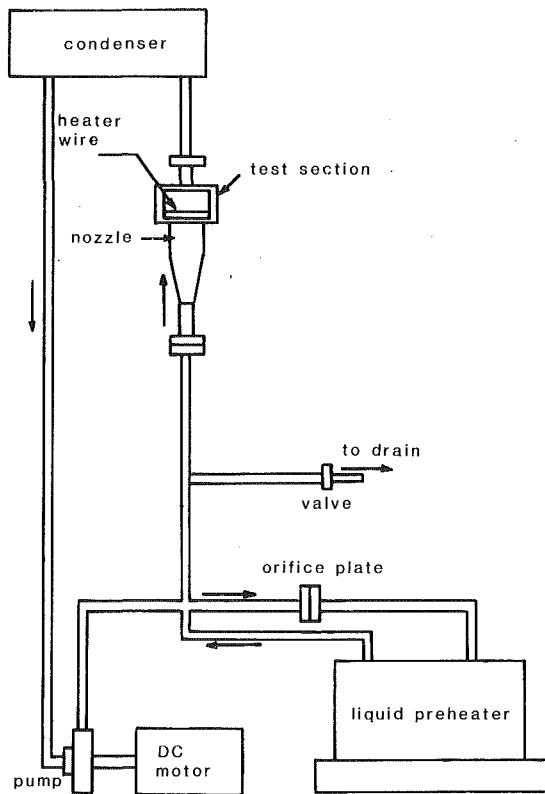


Fig. 3 Sketch of flow loop L1

culated based on the exit area of the nozzle. The nozzles were designed to provide a flat velocity profile at the heater.

We used loop L1 to obtain peak heat flux data in acetone, isopropanol, methanol, and water. Heater diameters ranged from 0.030 cm to 0.241 cm. The heaters were 8 cm in length. Flow velocities ranged from 0.3 m/s to about 3.0 m/s. The uncertainty in the determination of the peak heat flux was 3.0 percent, and that in the measurement of velocity was 2.6 percent.

Flow loop L2 was used to obtain peak heat flux data in isopropanol and methanol. Heater diameters ranged from 0.03 cm to 0.10 cm. Flow velocities ranged from 0.1 m/s to nearly 0.8 m/s. Data could not be obtained for velocities higher than 0.8 m/s due to experimental constraints. The uncertainty in the determination of the peak heat flux was 3.0 percent, and that in the measurement of flow velocity was 5.9 percent.

The departure from saturation conditions was within 1°C for organic liquids and 2°C for water, for experiments in L1. In loop L2, the experiments were done at subcooling from 2° to 5°C. For these cases, CHF values were measured for three subcoolings and the saturation value was obtained by extrapolation. CHF values at subcoolings up to 2°C were found to be within the experimental error range of the corresponding saturation values.

Visual Observations. The observations described below were made during experiments in Loop L1. It was not possible to make detailed observations of the vapor escape pattern during experiments in loop L2. However, strobe light illumination revealed that the overall nature of the pattern was similar to that seen in L1.

In all cases, nucleation initiates at points on the downstream surface of the heater. A steady stream of bubbles leaves each active site. To the naked eye, this has the appearance of tiny vapor jets leaving each point. Figure 5(a) is a photograph of the heater surface and vapor escape pattern for $q = 0.15 q_{max}$. Larger bubbles are visible at a short distance from the heater surface. These are the result of the merger of individual bubbles

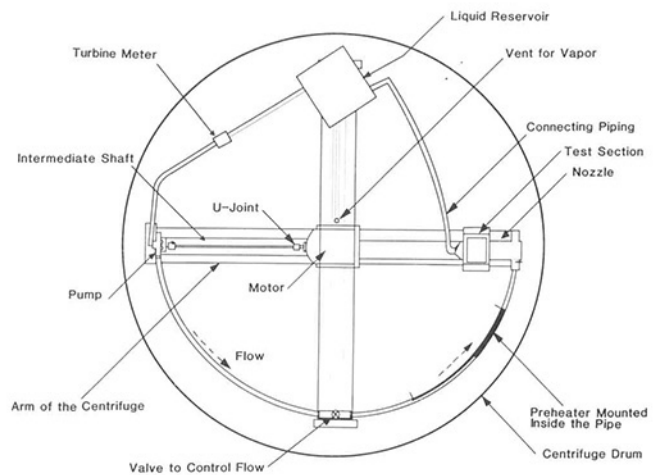
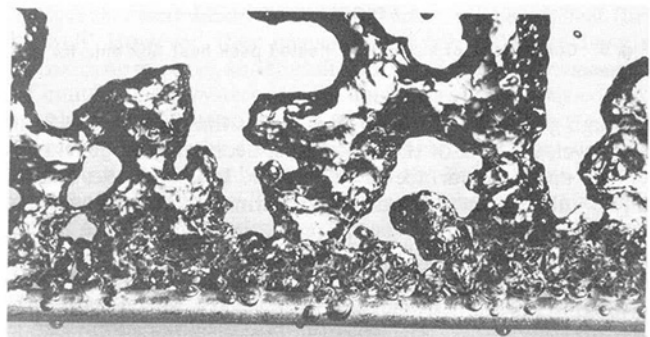


Fig. 4 Sketch of flow loop L2



(a)



(b)

Fig. 5 Photographs of heater surface and near-surface vapor escape pattern at (a) 0.15 q_{max} and (b) 0.60 q_{max} ; liquid: water; velocity: 0.80 m/s

released from each active nucleation site. A continuous vapor cavity is still not clearly established in the wake. Only a broken cavity exists, and liquid still extends down to the heater at several points on the rear surface of the heater.

As the heat flux is increased, nucleation progressively spreads to the upstream surface as well, and a vapor sheet is established in the wake. At low heat fluxes, the bubbles formed on the upstream surface slide downstream around the heater surface, in a manner similar to that observed by Cornwell and Schuller (1982) on tube bundles. Figure 5(b) was taken at a heat flux that is about 60 percent of q_{max} . At this stage, the entire front surface of the heater appears to be covered with bubbles. These bubbles travel downstream, merge with bubbles formed at neighboring sites, and move around the heater surface in the form of a continuous curved vapor conduit. These conduits merge with the vapor cavity close to the 90 deg point. Near the 90 deg position, the vapor channels are so closely packed that it becomes difficult for any liquid to enter the vapor wake

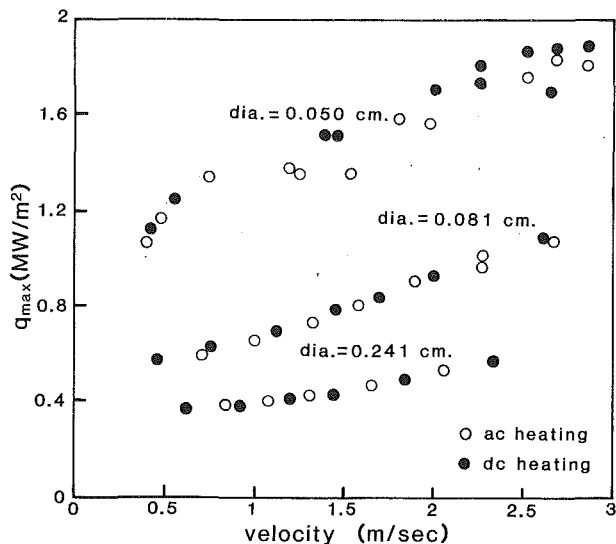


Fig. 6 Comparison of a-c and d-c heated peak heat flux data for isopropanol

through gaps between them. This means that beyond this heat flux level, the bulk of the vapor must necessarily be generated on the upstream surface of the heater. It also implies that a liquid sublayer cannot exist in a continuous manner, on the downstream surface of the heater as presumed by the Haramura and Katto model. The curvature of the heater surface will prevent any significant quantity of liquid from being swept around to the rear surface. Any liquid that is able to reach the downstream surface can enter the vapor cavity only through gaps between bubbles close to the separation line on the heater or by entrainment at the walls of the cavity. Chang and Witte (1990) determined from their experiments with tube heaters that sporadic liquid-solid contact does occur on the rear surface of the heater during flow film boiling. Evidence of such contact has not yet been reported in the upper portion of the nucleate boiling curve. Even allowing for the possibility of such contacts in the present experiments, it is unlikely that such intermittent contact can result in a continuous liquid layer all the way around the heater surface.

As the bubbles from various sites on the front surface of the heater move downstream over the heater surface, small areas of the surface are periodically exposed briefly to oncoming liquid. Thus further nucleation is initiated. Careful observation of the bubble pattern on the heater surface showed that the thickness of the vapor covering at any point on the surface changes over time. Presumably this is because of the cyclic formation and sliding upward of the bubbles formed at that point. When a bubble formed at a point on the surface just begins to slide upward along the heater surfaces, there is a short time interval over which liquid contacts that point. Then another bubble begins to form there. This pattern exists up to the peak heat flux point.

At low velocities, cylindrical bubbles break away from the vapor sheet. At higher velocities, bubble breakoff becomes random, except in the case of water, which sustains the cylindrical breakoff pattern in the entire range of velocities.

The Role of the Vapor Wake. The frequency of bubble breakoff from the vapor sheet is an important aspect of the far-wake theory of flow boiling burnout on cylinders. In the present study, we measured peak heat flux data using a-c and d-c heating alternately on the same heater. In choosing experimental conditions for the purpose of establishing the effect of a-c heating on the peak heat flux, we chose those for which Ungar (1987) observed clear a-c influences on the wake and on bubble breakoff. Figure 6 depicts typical results from these

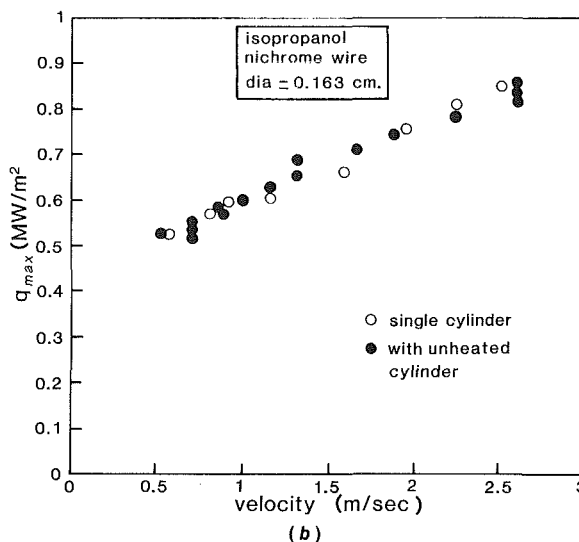
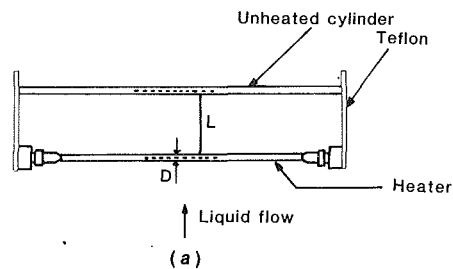
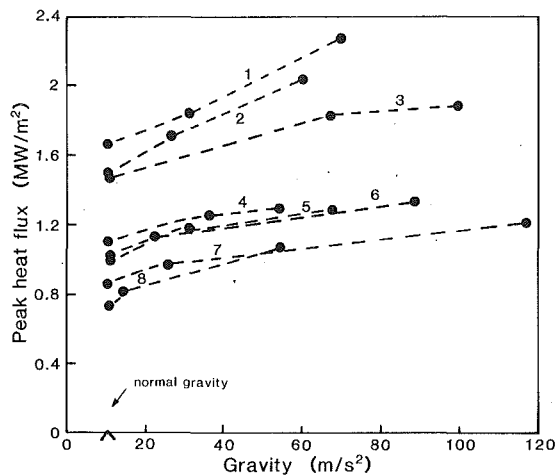


Fig. 7 Influence of an unheated cylinder in the heater wake: (a) configuration; (b) data

experiments. For the Nichrome heater of diameter 0.050 cm and the stainless steel tubes of diameter 0.241 cm, with a-c heating, we measured a clear 120 Hz frequency of bubble breakoff, when cylindrical bubbles were seen. With d-c heating, the frequency of breakoff was much lower—typically between 20 and 40 Hz. For the Nichrome heater of diameter 0.081 cm, the frequency of bubble breakoff with a-c heating was the same as for d-c heating. However, there was a distinct 120 Hz wave in the vapor wake. It is clear from the figure that the mode of heating, while it may affect bubble breakoff and vapor sheet characteristics, has little effect on the values of the peak heat flux.

The above observations indicate that the far-wake vapor sheet and bubble breakoff play only a minimal role, if any, in determining the peak heat flux. To test further the role of the far wake, we carried out a series of experiments in which we altered the vapor escape pattern by using a tube bundle configuration; an unheated cylinder was placed in the wake region. This arrangement is shown in Fig. 7(a). The presence of this second cylinder caused the normal vapor removal mode to be altered significantly. However, as shown in Fig. 7(b), the disruption of the normal mode of vapor escape and bubble breakoff does not cause any systematic change in the peak heat flux. Similar results were obtained in experiments in which a thin square plate was located at various distances downstream of the heater.

The foregoing results imply that burnout is dictated by near-surface effects, and not by the characteristics of the far wake as Lienhard and Eichhorn's (1976) model envisions. We must next verify whether the existing surface-controlled model is an accurate representation of the process. The existence of a liquid sublayer all the way around the heater surface has not yet been demonstrated experimentally. Indeed, our observations suggest that at heat fluxes close to burnout, very little liquid-solid contact occurs on the rear surface of the heater. Then there is little likelihood that the sublayer can exist as presumed by the surface-controlled model.



Line no.	Liquid	Diameter (cm.)	Velocity (m/sec)
1	Methanol	0.05	0.62
2	Methanol	0.05	0.42
3	Methanol	0.08	0.67
4	Isopropanol	0.05	0.66
5	Isopropanol	0.04	0.30
6	Isopropanol	0.04	0.24
7	Isopropanol	0.08	0.58
8	Isopropanol	0.08	0.33

Fig. 8 Influence of gravity on q_{max}

We also offer the following argument to suggest that the curvature of the heater prevents any considerable quantity of liquid from accessing the downstream surface of the heater: As the liquid-vapor mixture flows downstream around the equatorial plane of the heater, the mixture will be subjected to a centripetal force that separates the liquid and vapor; the vapor then moves into the wake region, and the liquid is thrown tangentially away from the wake region. There is still the possibility that some liquid can penetrate through to the wake region; however this would not sustain a continuous liquid sublayer on the downstream surface of the heater.

Gravity Influences on Burnout. During experiments in the centrifuge-mounted flow loop L2, it was not possible to maintain the fluid velocity constant with changes in the speed of rotation of the centrifuge. Figure 8 represents results obtained for various heater diameters for isopropanol and methanol. The corresponding normal gravity q_{max} data are also shown in the figure. In these figures, data points for each fixed velocity and heater diameter have been connected by straight lines only for ease of illustration.

Data shown in these figures clearly indicate that an increase in the gravity level leads to a corresponding increase in the peak heat flux, in the range of velocities tested. Since a sublayer-controlled mechanism does not have provisions to account for gravity influences, we can conclude that the controlling mechanism of burnout is not primarily related to a liquid sublayer on the heater surface. The next issue that will be examined is that of wettability influences on burnout.

Investigation of Surface Wettability Effects. It is generally accepted that the liquid-solid contact angle is the suitable indicator of surface wettability. Some investigations of surface wettability effects on nucleate pool boiling have been reported

Table 1 Measured values of receding contact angles for various liquid-solid combinations

Liquid	Heater surface	Receding contact angle, β_r (degrees)	Range of variation (degrees)
Isopropanol	Nichrome	27°	± 3°
Acetone	Nichrome	15°	± 3°
Methanol	Nichrome	20°	± 2°
Acetone	Stainless Steel	15°	± 3°
Water	Nichrome	36°	± 3°
Water	Stainless Steel	34°	± 3°

Altered contact angles

Water	Teflon-coated Nichrome	62°	± 2°
Surfactant solutions in water ^a	Nichrome	24° to 33°	± 2°

^a The contact angles were found to vary depending upon the concentration of the surfactant. The concentrations ranged from 100 ppm to 300 ppm.

in the literature. The previously mentioned study of Liaw and Dhir (1989) examined wettability effects on the peak heat flux as well. However, they measured the contact angle using a sessile drop method, and thus did not consider the phenomenon of contact angle hysteresis. The contact angle is often considerably different depending on whether the liquid is advancing or receding over the solid surface.² Burnout is characterized by drying out of the heater surface; the liquid front recedes over the heater surface. Therefore, we used the receding contact angle, β_r , in our considerations. Ideally, the dynamic receding contact angle is the relevant parameter that must be used; however, lacking means for measuring this parameter in situ, we measured the receding angle using a separate apparatus.

We used a conventional tilting plate method to measure β_r . However, to replicate actual experimental conditions as closely as possible, we used the cylindrical heaters from our experiments in place of the plate generally used in the tilting plate method. Typically contact angle measurements were made when the liquid temperature was within 20°C of saturation. Previous studies (Zisman, 1964, for example) suggest that the contact angle is only an extremely weak function of temperature; hence precise control of temperature in the measurements was not attempted. Our measured values of the receding contact angles for various liquid-solid combinations are listed in Table 1.

We used two strategies to alter the contact angle:

- Microcoating the Nichrome surface with Teflon; this reduces the wettability (increases contact angle).
- Adding small concentrations of surfactant to the water; this improves wettability.

The thickness of the Teflon coating varied slightly from wire to wire; in no case did the thickness exceed 0.0005 cm. Details of the coating method and surface preparation are provided by Sadasivan (1990).

Typical peak heat flux results obtained on Teflon-coated wires ($\beta_r = 62$ deg) are compared with data on bare Nichrome wires ($\beta_r = 36$ deg) in Fig. 9. Clearly the peak heat flux values are considerably lower on the Teflon-coated heaters. Since the coating thicknesses are sufficiently small, the heater thermal characteristics are not altered. It is possible that the cavity size distribution on the heater surface is changed by the Teflon coating. We do not have quantitative data on the changes in roughness and cavity size distribution as a result of the Teflon coating. Several previous studies (Berenson, 1960, for example) have shown that surface roughness has only a minor influence on CHF. We have recently completed a study of flat-plate pool boiling CHF (Ramilison et al., 1992), and it has also revealed that surface chemistry is far more important than surface roughness in CHF. In view of the above considerations, we

²While hysteresis would be negligible in the case of "ideal" surfaces, the more typical surfaces they used would exhibit considerable hysteresis.

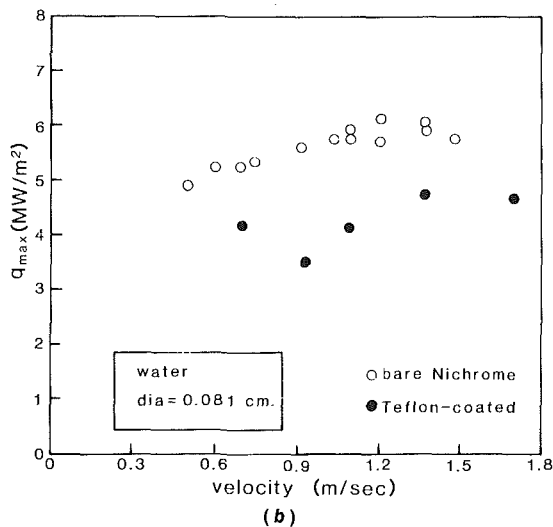
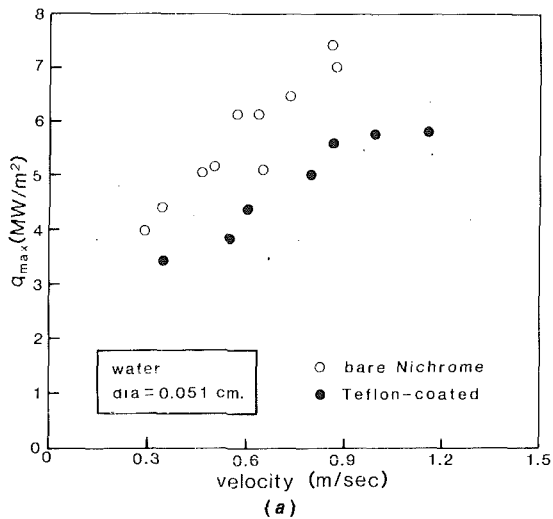


Fig. 9 Effect of teflon coating on q_{\max} : (a) dia = 0.05 cm, (b) dia = 0.08 cm

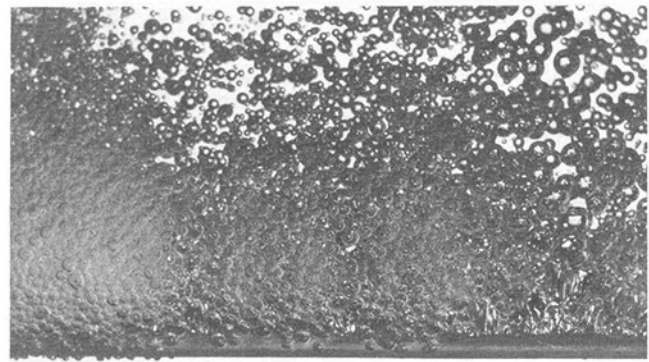
have neglected roughness effects and have attributed the reduction in the peak heat flux entirely to reduced wettability.

In the second set of experiments, we added small quantities of sodium dodecyl sulfate (SDS) to the water. The concentration of surfactant in the solution ranged from 100 to about 300 ppm.³ For the range of concentrations employed, the only relevant physical property that is altered by the presence of the surfactant is the liquid surface tension (and the resultant change in the contact angle). Other properties such as density and the latent heat of vaporization are not affected. Therefore, we can rule out any mass diffusion effects, etc., on the boiling process, as are observed in the case of mixtures.

The surface tension of the surfactant solution was measured after each experimental run. A DuNuoy tensiometer was used for this purpose. Measurements could not be made under saturated liquid conditions, since bubbles disturbed the liquid surface. To overcome this problem, we measured the surface tension at various points between 40°C and 80°C, and obtained the saturation value by linear extrapolation.⁴ The uncertainty of the measurement of surface tension was 3.6 percent. Details of the measurement procedure are provided by Sadasivan (1990).

³Since the surface tension and the contact angle were measured individually for each test sample, the concentration itself was not a critical variable.

⁴Although the surface tension of most liquids is not an exact linear function of temperature, it is very nearly so at temperatures well below the critical temperature for most organic liquids.



(a)



(b)

Fig. 10 Photographs of heater surface and near-surface vapor escape pattern at (a) 0.15 q_{\max} and (b) 0.60 q_{\max} ; liquid: surfactant solution in water; velocity: 0.80 m/s

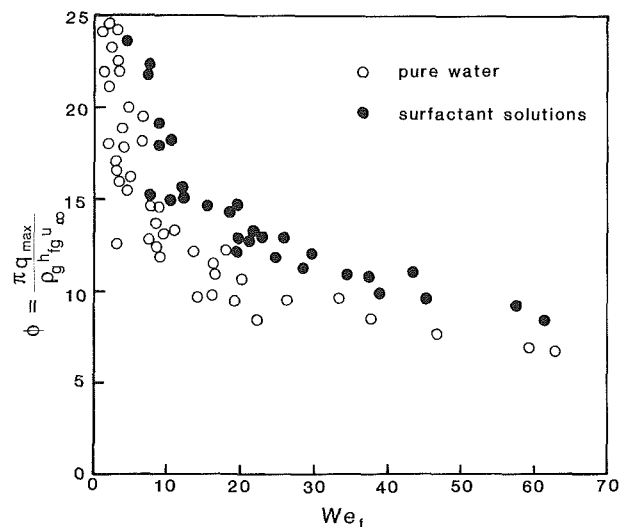


Fig. 11 Effect of reduced contact angle on q_{\max} (dimensionless coordinates)

The contact angles for the surfactant solutions ranged from 23 to 33 deg. The saturation values of surface tension ranged from 0.022 N/m to 0.030 N/m. The appearance of the boiling process in the wake region is considerably different for the case of the surfactant solution, as compared with pure water. Figures 10(a, b) are photographs taken during flow boiling of a surfactant solution at various heat flux levels. The size of the bubbles leaving the heater surface is much smaller, and the number of bubbles is much greater. This is in agreement with the observations of Tzan and Yang (1990) for pool boiling. The dimensionless peak heat flux values obtained with the surfactant solutions are compared with the corresponding val-

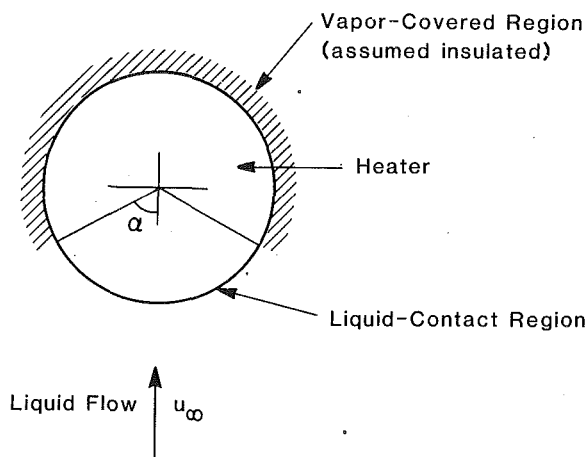


Fig. 12 Idealized heat removal configuration on the heater surface

ues for pure water for two heater diameters, in Fig. 11. It is clear that the improved wettability leads to an increase in the peak heat flux.

We emphasize here that the influence of wettability has not been, by itself, used to verify the validity of either of the models we have discussed earlier. Our results so far clearly suggest that burnout in this geometry is determined by near-surface effects. The causal mechanism could be either a breakdown in the vapor escape pattern close to the heater surface, or a deficiency of liquid at the downstream stagnation point on the heater. In order to clarify this further it would be useful to look at the temperature distribution on the heater surface at heat fluxes close to burnout.

Temperature Distribution on the Heater Surface. Solid cylindrical heaters were used in the present study. Therefore, it is extremely difficult to make direct measurements of the surface temperature. We attempted to learn the essential features of the temperature distribution by means of a theoretical calculation.

We can describe the burnout process by visualizing a heat removal configuration as shown in Fig. 12. In this configuration, we assume that the region of the heater downstream of the separation line is insulated. As we have already pointed out, any heat that is transferred over the downstream surface is the result of sporadic liquid-solid contact. On the upstream surface, liquid impinges the heater almost directly. This is necessarily a far more efficient heat removal mechanism as compared to that on the downstream surface. Under these circumstances, it is reasonable to neglect the heat transfer on the downstream surface. So, we idealize the entire boiling process as being concentrated in an arc of about 2ψ deg as shown in the figure. On this part, we assume a uniform heat transfer coefficient. Despite the fact that these are somewhat restrictive assumptions, we will see subsequently that this nevertheless enables us to obtain extremely useful qualitative information about the mechanism of burnout.

Assuming uniform electrical heat generation within the heater as well as the absence of axial variation in temperature (infinite heater length assumption), we can solve the two-dimensional heat conduction equation to determine the azimuthal temperature distribution on the heater surface. The governing equation is then

$$\frac{\partial^2 T}{\partial r^2} + \frac{1}{r} \frac{\partial T}{\partial r} + \frac{1}{r^2} \frac{\partial^2 T}{\partial \theta^2} + \frac{q'''}{k} = 0 \quad (3)$$

The following conditions can be imposed:

$$T(r, \theta) = T(r, \theta + 2\pi), \quad (4)$$

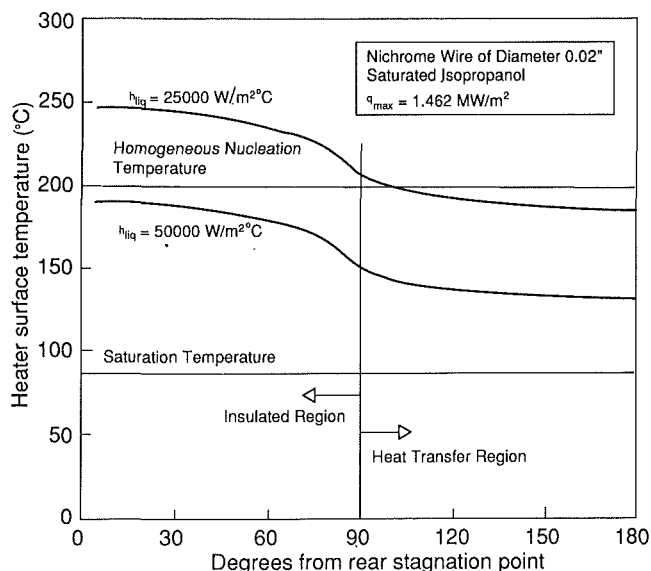


Fig. 13 Temperature distribution on the heater surface

and

$$-k \frac{\partial T}{\partial r} (r=R, \theta) = \begin{cases} h(T - T_\infty \text{ adjacent to liquid}; & -\psi < \theta < +\psi \\ 0 & \text{elsewhere} \end{cases} \quad (5)$$

We solved this system of equations using finite differences. In solving this system, the values of q''' , R , k , h , and ψ must be supplied. The first three of these variables are known quantities for each data point. From our visual and photographic observations, the half-angle of direct liquid contact is close to 90 deg. However, there are no means to determine the heat transfer coefficient. The above problem was solved for various assumed values of the heat transfer coefficient. The lowest values of h used in each case corresponded to typical values encountered in *pool* boiling situations. In flow boiling situations, we can be certain that actual values of h are considerably higher than these pool boiling values.

Figure 13 shows the solution for a typical data point obtained in the present study. This is for the case of isopropanol flowing at 1.5 m/s past a Nichrome heater of diameter 0.051 cm. For this case the peak heat flux obtained was 1.46 MW/m²; this corresponds to a volumetric heat generation rate of 1.5×10^{10} W/m³. It is clear from the figure that the surface temperature varies considerably along the periphery of the heater.

The heater surface temperature that will cause homogeneous nucleation in the liquid upon contact has also been indicated in the figure. The homogeneous nucleation temperature for each liquid was calculated using the following equation of Lienhard et al. (1986):

$$\Delta T_r = T_{r,(h.n.)} - T_{r,sat} = 0.923 - T_{r,sat} + 0.077 T_{r,sat}^9 \quad (6)$$

For isopropanol, Eq. (6) yields a homogeneous nucleation temperature of 198°C. Liquid can contact the heater surface only if the interface temperature that results after contact, is less than this value. The interface temperature at the instant of liquid contact on the heater surface can be calculated by treating the heater and liquid as semi-infinite bodies. It is given by

$$\frac{T_{\text{interface}} - T_{\text{liq}}}{T_h - T_{\text{liq}}} = \frac{k_h / \sqrt{\alpha_h}}{k_h / \sqrt{\alpha_h} + k_{\text{liq}} / \sqrt{\alpha_{\text{liq}}}} \quad (7)$$

For the interface temperature not to exceed 198°C, Eq. (7) gives a limiting heater surface temperature of 206°C. This value is marked in Fig. 13. Even for the lowest value of heat transfer

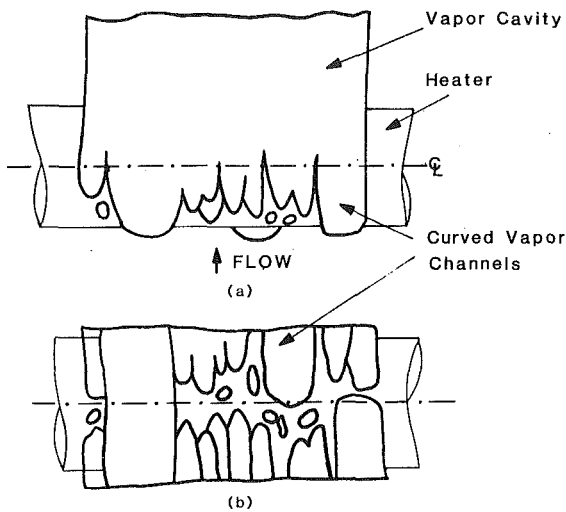


Fig. 14 Sketch of vapor removal pattern on the heater surface: (a) side view; (b) view from bottom (conceptualized)

coefficient, the heater surface temperature on the upstream surface of the heater is less than the homogeneous nucleation temperature. In other words, even this "worst-case" analysis (with the entire rear half-surface of the heater assumed insulated) yields a surface temperature distribution that is perfectly viable.⁵ Although the calculation is rather straightforward, it nevertheless sheds considerable light on the causal mechanism of burnout in this configuration—that burnout is not the immediate consequence of a deficiency of liquid at the downstream end of the heater, as has been assumed in the surface-controlled model of Haramura and Katto (1983). Similar results were obtained for calculations based on other data obtained in the present study. Also, it appears that for the range of conditions for which data are currently available, the mechanism of burnout is not related to the homogeneous nucleation limit of temperature.

Discussion

We found from the first set of experiments that the frequencies of bubble breakoff and the wave in the wake do not affect the peak heat flux to any significant degree. Also complete disruption of the far-wake vapor escape pattern did not affect the peak heat flux either. It is clear therefore that the far-wake is not the primary factor that determines burnout.

The experiments with Teflon-coated wires and surfactant solutions clearly show that surface wettability effects are important in determining the peak heat flux in flow boiling. We can note in Table 1, that acetone has a contact angle of 15 deg on Nichrome, while isopropanol has a value of 26 deg. In view of our findings, we can conclude that the high values of the peak heat flux for acetone, as compared to isopropanol, is the result of the better wettability exhibited by acetone on Nichrome.

We have already noted that thermodynamic effects such as the homogeneous nucleation temperature are not responsible for the occurrence of burnout and that burnout is not the result of a deficiency of liquid at the rear surface of the heater. Under these circumstances, we can conclude that burnout must be the result of a breakdown in the vapor removal pattern close to the upstream surface of the heater. Figure 14 is a sketch of the vapor removal pattern close to the heater surface as best discerned from visual and photographic observations. We can

⁵The temperatures on the insulated portion of the heater surface can exceed the value dictated by the homogeneous nucleation limit, since we assume there is no liquid contact there.

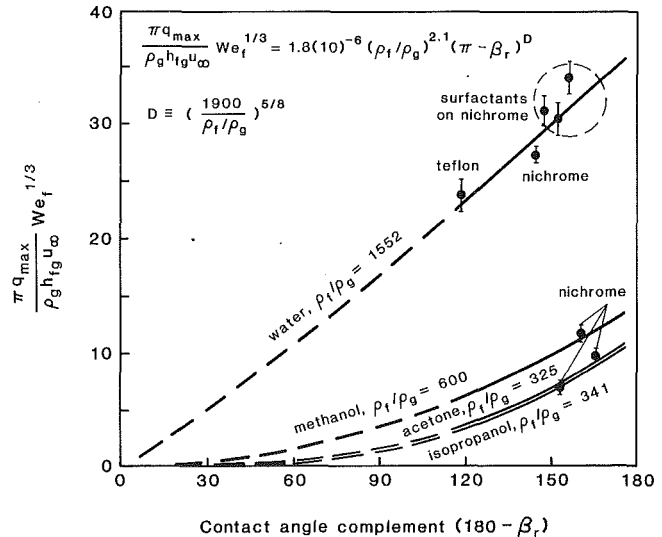


Fig. 15 Comparison of data with Eq. (10)

note the existence of curved vapor channels along the heater surface. We speculate that the breakdown in vapor removal occurs as a result of the collapse of these channels due to instabilities on their walls. Further study is needed to establish this fact definitively.

Contact angle influences the heat removal in the region of liquid contact by altering the manner in which the vapor channels adhere to the heater surface as they move around the heater surface in the downstream direction. Contact angle also influences the characteristics of bubble departure on the heater surface, and, in turn, the liquid impingement process on the front surface. If burnout is the result of a hydrodynamic collapse of the vapor channels, with the additional influence of the liquid-solid contact angle, the dimensionless functional equation for q_{\max} takes the following form:

$$\phi = \phi(r, We_f, Fr, \beta_r) \quad (8)$$

For the gravity-uninfluenced region—in the region of high velocities—the Froude number is no longer a variable and we can write

$$\phi = \phi(r, We_f, \beta_r) \quad (10)$$

We have correlated all our data in the high-velocity region (gravity-uninfluenced region) for the following cases:

- acetone on Nichrome
- isopropanol on Nichrome
- methanol on Nichrome
- water on Nichrome
- water on Teflon
- surfactant solution of water on Nichrome

The correlation takes the following form:

$$\phi = 1.8 \times 10^{-6} r^{2.1} We_f^{-1/3} (\pi - \beta_r)^C \quad (10)$$

where C , the exponent of β_r , is given by $(1900/r)^{0.625}$.

The choice of the particular form of Eq. (10) is somewhat arbitrary. The only physical constraint we have imposed is that the peak heat flux must be zero for the case of a perfectly nonwetting liquid, that is, for β_r equal to 180 deg. In this case, the heater will be blanketed with vapor almost immediately after the first vapor bubble is generated. The one-third power dependence of ϕ on the Weber number was an outcome of the correlation procedure. This agrees with similar results that have been observed in practically all existing correlations of burnout on various configurations. The physical reason for this dependence is not clear.

Equation (10) fits all the data within an rms error of 13.3 percent. Figure 15 shows a plot of the parameter $\phi/We_f^{1/3}$ as a function of the contact angle complement, $\pi - \beta_r$, for the

various cases listed earlier. Each data point in this figure represents the average of the $\phi/We_f^{-1/3}$ values for all the data for that particular case. While obtaining Eq. (5), only those data obtained on solid cylindrical heaters were used; data on tubes were omitted, since the heater surface boundary condition is different in the case of tubular heaters.⁶ The lines represent predicted values based on Eq. (5) above. Dotted lines are used to represent the predictive equations in the range of the contact angle complement between 0 and 118 deg, since we have no experimental data for this region. Equation (5), and perhaps the form of the correlating equation itself, should be adjusted as additional data are obtained in the range of $(\pi - \beta_c)$ between 0 and 118 deg.

In closing, we reemphasize that this study has focused on the configuration of a horizontal cylinder only. Whether a sublayer model or a far-wake type model can explain burnout in other configurations remains an open issue.

Summary and Conclusions

The main conclusions of this study are listed below:

1 Existing mechanistic explanations of flow boiling burnout on cylinders are not sufficiently realistic. The far-wake bubble breakoff and vapor sheet characteristics do not play any significant role in burnout. Burnout is dictated by near-surface effects; however, a deficiency of liquid at the downstream stagnation point does not automatically lead to burnout.

2 Surface wettability effects upon burnout are considerable. The receding contact angle appears to be the relevant parameter that must be considered in peak heat flux studies. The lower contact angle on Nichrome exhibited by acetone as compared to isopropanol accounts for the higher peak heat flux values that have previously been measured with acetone on Nichrome.

3 Based on observations and information from items above, we speculate that burnout is the result of a hydrodynamic collapse of the vapor removal pattern close to the heater surface. The vapor removal mechanism on the upstream surface of the heater is in the form of curved vapor channels around the heater surface.

4 A tentative correlation is presented for the peak heat flux during gravity-uninfluenced flow boiling on horizontal cylinders. It represents existing data (totally 280 data points) within an rms error of ± 13.3 percent.

⁶For electrically heated tubular heaters, the heater surface boundary condition is approximately a uniform heat flux condition. For solid heaters the surface heat flux is not uniform. Typically CHF values are up to 20 percent less on tubular heaters than on corresponding solid heaters.

Acknowledgments

This work was supported in part by grant No. 2040-ATP under the Texas Advanced Technology Research Program. We are grateful for their assistance.

References

- Berenson, P. J., 1960, "Transition Boiling From a Horizontal Surface," MIT Heat Transfer Lab. Tech. Rept. No. 17.
- Chang, K. H., and Witte, L. C., 1990, "Liquid-Solid Contact During Flow Film Boiling of Subcooled Freon-II," *ASME JOURNAL OF HEAT TRANSFER*, Vol. 112, pp. 465-471.
- Chowdhury, S. K. R., and Winterton, R. H. S., 1985, "Surface Effects in Pool Boiling," *Int. J. Heat Mass Transfer*, Vol. 28, pp. 1881-1889.
- Cochran, T. N., and Andracchio, C. R., 1974, "Forced Convection Peak Heat Flux on Cylindrical Heaters in Water and Refrigerant 113," NASA TN D-7553.
- Cornwell, K., and Schuller, R. B., 1982, "A Study of Boiling Outside a Tube Bundle Using High Speed Photography," *Int. J. Heat Mass Transfer*, Vol. 25, pp. 683-690.
- Dhir, V. K., and Liaw, S. P., 1989, "Framework for a Unified Model for Nucleate and Transition Pool Boiling," *ASME JOURNAL OF HEAT TRANSFER*, Vol. 111, pp. 739-746.
- Haramura, Y., and Katto, Y., 1983, "A New Hydrodynamic Model of Critical Heat Flux, Applicable Widely to Both Pool and Forced Convection Boiling on Submerged Bodies on Saturated Liquids," *Int. J. Heat Mass Transfer*, Vol. 26, No. 3, pp. 389-399.
- Hasan, M. Z., Hasan, M. M., Eichhorn, R., and Lienhard, J. H., 1981, "Boiling Burnout During Crossflow Over Cylinders, Beyond the Influence of Gravity," *ASME JOURNAL OF HEAT TRANSFER*, Vol. 103, pp. 478-484.
- Kheyrandish, K., and Lienhard, J. H., 1985, "Mechanisms of Burnout in Saturated Flow Boiling Over a Horizontal Cylinder," AICHE/ASME Heat Transfer Conference, Denver, CO.
- Liaw, S. P., and Dhir, V. K., 1989, "Void Fraction Measurements During Pool Boiling of Water on Partially Wetted Surfaces," *ASME JOURNAL OF HEAT TRANSFER*, Vol. 111, pp. 731-738.
- Lienhard, J. H., and Eichhorn, R., 1976, "Peak Boiling Heat Flux on Cylinders in a Cross-flow," *Int. J. Heat Mass Transfer*, Vol. 19, pp. 1135-1142.
- Lienhard, J. H., Shamsundar, N., and Biney, P. O., 1986, "Spinodal Lines and Equations of State," *Nucl. Eng. and Design*, Vol. 95, pp. 297-314.
- Lienhard, J. H., 1988, "Burnout on Cylinders," *ASME JOURNAL OF HEAT TRANSFER*, Vol. 110, pp. 1271-1286.
- Ramilison, J. M., Sadasivan, P., and Lienhard, J. H., 1992, "Surface Factors Influencing Burnout on Flat Heaters," *ASME JOURNAL OF HEAT TRANSFER*, Vol. 114, this issue.
- Sadasivan, P., 1990, "Factors Influencing Flow Boiling Burnout on Cylindrical Heaters," Doctoral Dissertation, Department of Mechanical Engineering, University of Houston, TX.
- Sun, K. H., and Lienhard, J. H., 1970, "The Peak Pool Boiling Heat Flux on Horizontal Cylinders," *Int. J. Heat Mass Transfer*, Vol. 13, pp. 1425-1439.
- Tzan, Y. L., and Yang, Y. M., 1990, "Experimental Study of Surfactant Effects on Pool Boiling Heat Transfer," *ASME JOURNAL OF HEAT TRANSFER*, Vol. 112, pp. 207-212.
- Ungar, E. K., 1987, "Saturated Pool and Flow Boiling From Heated Cylinders," Doctoral Dissertation, Department of Mechanical Engineering, University of Houston, TX.
- Vliet, G. C. and Leppert, G., 1964, "Critical Heat Flux for Nearly Saturated Water Flowing Normal to a Cylinder," *ASME JOURNAL OF HEAT TRANSFER*, Vol. 86, pp. 68-74.
- Zisman, W. A., 1964, "Relation of Equilibrium Contact Angle to Liquid and Solid Constitution," in: *Contact Angle, Wettability and Adhesion*, Advances in Chemistry Series, Vol. 43.

P. F. Peterson
Mem. ASME

R. Y. Bai

V. E. Schrock
Life Fellow ASME

Department of Nuclear Engineering,
University of California, Berkeley,
Berkeley, CA 94720

K. Hijikata

Department of Mechanical
Engineering Science,
Tokyo Institute of Technology,
Tokyo, Japan

Droplet Condensation in Rapidly Decaying Pressure Fields

Certain promising schemes for cooling inertial confinement fusion reactors call for highly transient condensation in a rapidly decaying pressure field. After an initial period of condensation on a subcooled droplet, undesirable evaporation begins to occur. Recirculation within the droplet strongly impacts the character of this condensation–evaporation cycle, particularly when the recirculation time constant is of the order of the pressure decay time constant. Recirculation can augment the heat transfer, delay the onset of evaporation, and increase the maximum superheat inside the drop by as much as an order of magnitude. This numerical investigation identifies the most important parameters and physics characterizing transient, high heat flux droplet condensation. The results can be applied to conceptual designs of inertial confinement fusion reactors, where initial temperature differences on the order of 1500 K decay to zero over time spans the order of tens of milliseconds.

Introduction

Due to its importance in a wide variety of applications, condensation on subcooled liquid droplets has received extensive attention (Hijikata et al., 1984; Sundararajan and Ayyaswamy, 1984, 1985; Huang and Ayyaswamy, 1987). Droplet condensation possesses many similarities with the more extensively studied droplet mass transport problem (Clift et al., 1978). During the earliest stages of the condensation transient, thermal boundary layers form on the surface of the droplet liquid, and a similarity solution for this boundary layer is possible (Chao, 1969). However these early stages, at dimensionless times less than 10^{-3} , have received scant attention because typical drop residence times are many orders of magnitude greater. The long residence time makes resolution of the earliest period both complicated and unnecessary.

The most promising means for cooling of inertial-confinement (ICF) fusion reactors, using liquid curtains to protect the reactor wall from the blast and intense neutron radiation, require ultrahigh condensation rates. In such systems, droplets will be subjected to initial temperature differences on the order of 1500 K. This very high initial temperature permits significant heat transfer during the earliest phases of the droplet condensation transient, when condensation rates can be very large. As the reactor pressure decays due to condensation, the driving temperature difference drops to zero over time spans the order of tens of milliseconds. In strong contrast to steady boundary conditions studied previously, with decaying surface temperature, at some point condensation on the droplets ceases and undesirable evaporation begins. Furthermore, temperatures within the drop end up higher than the surface temperature, due to the rapidly decaying pressure field, resulting in superheating inside the droplet interior. Droplet recirculation not only augments condensation, but can also delay the subsequent evaporation, simultaneously increasing the maximum interior superheat levels by as much as an order of magnitude.

This work provides the first numerical study of condensation on liquid droplets under highly transient pressure conditions, considering the detailed effects of liquid recirculation. The work identifies the most important parameters and physics of recirculation under decaying pressure. The issues of numerical diffusion due to spatial and temporal averaging are addressed carefully, due to the very large impact during the earlier phases

of transient condensation. As noted by Polyanin (1984), at early times standard numerical formulations result in considerable numerical diffusion except for very close grid spacing. He further notes that many previous investigators have not reported the effects of grid spacing on the accuracy of solutions, consequently producing results with potentially significant error. In particular, cross-stream numerical diffusion is large near the pole regions for spherical axisymmetric grids. The streamline-fitted coordinate system employed here eliminates this diffusion source, providing accurate solutions based on the Hill's vortex velocity distribution. These solutions provide parametric information on recirculation effects, and more importantly a numerical-diffusion-free benchmark for more ambitious efforts to model the earliest stages of the velocity distribution development.

To help motivate this study, first a brief summary of the application to cooling of ICF reactors, particularly the HYLIFE-II conceptual design, is presented. Formulation of the numerical problem is then presented, with particular attention to the use of streamline-fitted grids and temporal averaging for convection. Numerical results show that effects of recirculation in rapidly decaying pressure fields, relative to stagnant drops, are relatively independent of the fluid properties and depend primarily on the parameter Ut_d/R , based on the recirculation velocity, surface temperature decay time constant, and droplet radius.

Inertial Confinement Fusion

After a thermonuclear microexplosion in an ICF reactor, typically 32 percent of the energy is carried by X-rays and energetic debris and the remainder by neutrons. The energy radiates in every direction inside the cavity. To provide blast attenuation and to protect the inside wall from radiation damage, curtains of liquid lithium have been investigated in the HYLIFE ICF concept (Monsler and Meier, 1981). More recently the HYLIFE-II design has proposed curtains of Flibe (a molten LiF-BeF₂ salt mixture) jets for neutron absorption and blast attenuation, coupled with cool Flibe liquid spray for condensation of vaporized Flibe (Bai and Schrock, 1991). On the jets around the inside of the curtain, a thin surface layer is irradiated by target debris and soft X-rays. This results in sudden evaporation, dissociation, and ionization of a considerable amount of Flibe liquid. Most of the plasma is very energetic and implodes violently into the site of the microexplosion. A small fraction of the mass evaporated within the

Contribution by the Heat Transfer Division and presented at the 3rd ASME/JSME Thermal Engineering Joint Conference, Reno, Nevada, March 17–22, 1991. Manuscript received by the Heat Transfer Division October 29, 1990; revision received June 22, 1991. Keywords: Condensation, Sprays/Droplets, Transient and Unsteady Heat Transfer.

chamber is less energetic and disperses within the chamber volume, raising the pressure significantly.

The imploded gaseous material has an average internal energy far in excess of the saturated vapor stage, but can be expected to release this energy rapidly via radiation and direct contact heat transfer, evaporating more Flibe. After the explosion of a fuel pellet, a vapor pressure of hundreds of MPa builds up at the center of the cavity. The subsequent vapor flow is highly transient and complicated, with shock waves propagating through the jet columns during the earliest portion of the transient. After the shock waves propagate through the jet curtain to the region with droplets, additional vaporization has occurred from the jets and the vapor pressure and temperature are substantially reduced. To create a beam path for the next laser beam or ion beam bombardment, the pressure must be further lowered to 10 Pa or 0.1 Pa, respectively, by condensation on the Flibe droplets. Accurate prediction of the condensation rate is required to insure that the condensation occurs rapidly enough to achieve the desired repetition frequency of several Hertz. It is an interesting progression in history that this proposed method for cooling ICF reactors has much in common with the first Newcomen steam engines, where cold water was sprayed into a cylinder to condense steam, so the resulting vacuum could drive a piston.

For rapid condensation on a droplet with zero circulation, subject to an exponentially decaying surface-temperature forcing function, an analytical series solution for the drop temperature has been obtained by Bai and Schrock (1991). They have initiated the study of transient condensation on drops with time-dependent boundary conditions by using a pure-conduction analysis based on the Duhamel superposition integral, augmented by a "convection factor" deduced from the work of Hijikata et al. (1984). The present work provides the first numerical study of transient convection with the time-dependent boundary condition and further identifies the key parameters and physics for the problem. This type of solution provides a convenient basis for detailed modeling of the large number of droplets in a reactor, which all experience different life cycles depending on their introduction time. Of interest here is examination of the change of the condensation rate from the base one-dimensional solution, due to recirculation. Also of interest is the maximum superheat level inside the droplet.

Theory

This investigation is concerned primarily with transport inside recirculating droplets, so simplifying assumptions are in-

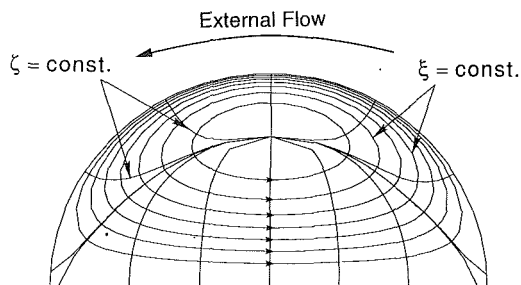


Fig. 1 Droplet schematic showing the Hill vortex streamlines, corresponding to selected points on the numerical grid

troduced that permit qualitative and quantitative assessment of the heat transfer rate:

1) The droplet is initially at uniform temperature T_o . This is true of droplets away from the inside edge of the curtain.

2) At time $t=0$ the surface temperature jumps from T_o to T_{so} , and then decays exponentially. This approximates vapor pressure history that would result from a full-system model. With saturated vapor, assumed here, radiation heat transport is negligible. For highly superheated vapor radiation provides an additional heat flux to the surface, an effect addressed by Bai and Schrock (1990).

3) The thermal resistance of the condensate and change in the droplet size are neglected. This assumption is valid for small values of the Jakob number, $Ja = c_p(T_{so} - T_o)/h_{fg}$. For the highest temperature differences expected in this reactor ($Ja = 0.3$) this assumption provides qualitative approximation of the heat transfer behavior.

4) The external effects of vapor mass transport and non-condensables are neglected.

5) Surface tension is assumed large, such that the droplet shape is approximately spherical. In reality droplet oscillation may result in heat transport augmentation (Hijikata et al., 1984).

6) The flow distribution inside the droplet is assumed to be constant and that of the Hill vortex, as shown in Fig. 1. Because the vapor dynamics are quite complex and are different for individual droplets, the resulting recirculation strength is left as an adjustable parameter. Scaling arguments for the recirculation strength are provided in a following section. The Hill vortex solution permits use of a streamline fitted grid, which eliminates the strong effects of cross-stream numerical diffusion, providing benchmark solutions for more detailed modeling of the vapor/droplet coupling.

With these assumptions, energy transport inside the droplet

Nomenclature

a = finite-difference influence coefficient	T = nondimensional temperature = $(\tilde{T} - \tilde{T}_o)/(\tilde{T}_{so} - \tilde{T}_o)$	ρ = mass density, kg/m^3
ΔA = control-volume face area	U = characteristic velocity in droplet, m/s	τ = nondimensional time = $t\alpha/R^2$
C = Courant number = $u\Delta A_w(n_o - G)\Delta\tau/\Delta V$	U_∞ = droplet velocity, m/s	Subscripts
G = interpolation parameter	v = velocity, m/s	1 = one-dimensional pure-conduction solution
Ja = Jakob number = $c_p(T_{so} - T_o)/h_{fg}$	V = nondimensional velocity = v/U	d = temperature decay constant
L = total path length	ΔV = volume of control volume	e = east node
n = time step level	x = distance	g = vapor phase
n_o = number of previous time steps	α = thermal diffusivity, m^2/s	l = liquid phase
Pe = Peclet number = $2RU/\alpha$	ζ = nondimensional orthogonal coordinate	max = maximum
r = radial coordinate, m	η = nondimensional radius = r/R	n = north node
R = drop radius, m	θ = angular coordinate	o = initial condition
Re = Reynolds number = $2\rho RU_\infty/\mu_g$	μ = dynamic viscosity, $\text{kg}/(\text{m s})$	p = center node
t = time, s	ξ = nondimensional orthogonal coordinate	r = radial direction
\tilde{T} = absolute temperature, K		s = surface, south node
		t = total residence time
		w = west node
		θ = angular direction

is governed by the energy equation, which can be written in spherical axisymmetric coordinates,

$$\frac{\partial \bar{T}}{\partial t} + v_r \frac{\partial \bar{T}}{\partial r} + \frac{v_\theta}{r} \frac{\partial \bar{T}}{\partial \theta} = \alpha \left(\frac{1}{r^2} \frac{\partial}{\partial r} r^2 \frac{\partial \bar{T}}{\partial r} + \frac{1}{r^2} \frac{1}{\sin \theta} \frac{\partial}{\partial \theta} \sin \theta \frac{\partial \bar{T}}{\partial \theta} \right) \quad (1)$$

where v_r and v_θ are the radial and angular velocity components, \bar{T} the temperature, α the thermal diffusivity, t time, r the radial coordinate, and θ the angular coordinate. The boundary conditions are an exponentially decaying surface-temperature forcing function, and symmetry along the centerline axis,

$$\text{at } r=R \quad \bar{T} = \bar{T}_o + (\bar{T}_{so} - \bar{T}_o) \exp(-t/t_d) \quad (2)$$

$$\text{at } \theta=0, 180 \quad \partial \bar{T} / \partial \theta = 0 \quad (3)$$

where R is the drop radius, \bar{T}_o the initial droplet temperature, \bar{T}_{so} the initially applied surface temperature, and t_d the time constant for the temperature decay. This exponential function approximates the anticipated surface temperature history, where pressure decay will be governed by the rate of mass removal in the system. The initial condition is

$$\text{at } t=0 \quad \bar{T} = \bar{T}_o \quad (4)$$

It is convenient to nondimensionalize the governing equation, boundary condition, and initial condition

$$\frac{\partial T}{\partial \tau} + \frac{Pe}{2} V_\eta \frac{\partial T}{\partial \eta} + \frac{Pe}{2} \frac{V_\theta}{\eta} \frac{\partial T}{\partial \theta} = \frac{1}{\eta^2} \frac{\partial}{\partial \eta} \eta^2 \frac{\partial T}{\partial \eta} + \frac{1}{\eta^2} \frac{1}{\sin \theta} \frac{\partial}{\partial \theta} \sin \theta \frac{\partial T}{\partial \theta} \quad (5)$$

$$\text{at } \eta=1 \quad T = \exp(-\tau/\tau_d) \quad (6)$$

$$\text{at } \theta=0, 180 \quad \partial T / \partial \theta = 0 \quad (7)$$

$$\text{at } \tau=0 \quad T=0 \quad (8)$$

where the following nondimensional parameters have been introduced:

$$Pe = 2RU/\alpha \quad \tau = t\alpha/R^2$$

$$T = \frac{\bar{T} - \bar{T}_o}{\bar{T}_{so} - \bar{T}_o} \quad V = v/U \quad \eta = r/R \quad (9)$$

where Pe is the Peclet number and U the maximum velocity inside the drop. Here the velocity distribution is approximated by that of the Hill vortex,

$$V_r = (1 - \eta^2) \cos \theta \quad (10)$$

$$V_\theta = -(1 - 2\eta^2) \sin \theta \quad (11)$$

For shorter time periods, boundary-layer-type analytic solutions are available for the droplet heat transfer. Chao (1969) showed that thermal boundary layers form on the droplet surface, and that a similarity solution for the temperature distribution in the liquid phase is possible. He identified the parameter,

$$Pe \tau/2 = Ut/R \quad (12)$$

which is independent of the flow properties. A value $Ut/R = 2$ corresponds approximately to the time required for a fluid particle to travel from one side of the droplet to the other. For $Ut/R < 0.1$, he showed that the boundary layer solution reduced to the simple conduction problem. For larger values the boundary layers grow, and reach steady state by $Ut/R = 1.0$. Soon afterward the solution becomes invalid as warm fluid wells from the center of the drop. As Chao noted, due to the linearity of the problem, this analytic solution can be generalized to the case of time-dependent surface temperature by application of Duhamel's theorem. However, this generalization requires numerical integration, provides no information on the effects of convection on the temperature distribution near the center of the droplet, and can only be applied for shorter time spans. Thus for this investigation numerical finite-difference methods were applied.

Numerical Technique

In the case of transient droplet condensation, cross-stream and streamwise numerical diffusion both become important. Raithby (1976a) provides a critical review of both sources. Cross-stream diffusion occurs under upwind differencing, when the flow direction is oblique to the grid lines and a gradient in the temperature exists normal to the flow direction. For an axisymmetric spherical grid, cross-stream diffusion will be particularly large near the pole regions during the early phases of a transient, due to the very high gradients normal to the flow. For these regions, skew-upwind differencing can reduce cross-stream diffusion (Raithby, 1976b; Hassan et al., 1983; Schneider and Raw, 1986). Here, however, because the velocity field is given, cross-stream diffusion is eliminated completely by an orthogonal coordinate transformation to lines of constant ξ and ζ ,

$$\xi = 4(\eta^2 - \eta^4) \sin^2 \theta \quad (13)$$

$$\zeta = \eta^4 \cos^4 \theta / (2\eta^2 - 1) \quad (14)$$

where constant ξ lines coincide with the streamlines of the Hill vortex and constant ζ lines are perpendicular to ξ constant lines, as seen in Fig. 1. Thus the solutions presented here provide a benchmark for solutions based on spherical axisymmetric grids.

Unfortunately, numerical diffusion due to streamwise numerical diffusion also becomes important for transient droplet condensation, due to the transport of a steep streamwise temperature gradient (thermal "shock front") through the droplet center. A variety of convective differencing schemes is available, including implicit and explicit upwind, Crank-Nicolson, QUICK, predictor-corrector, hybrid, leapfrog, Lax-Wendroff, box, Fromms, and other schemes, all of which possess various difficulties due to numerical diffusion and instability. Roe (1983) provides a useful summary of several of these schemes as applied to solutions of the Euler equation, discussing both dissipation (amplitude) and dispersion (phase) effects.

In general, first-order schemes can be expected to create rather large streamwise numerical diffusion, while higher order schemes tend to be unstable and produce spurious oscillations and nonphysical values in the solution. The use of artificial damping to reduce oscillations reintroduces, to some extent, numerical diffusion. Here a rather novel technique is applied for tracking the steep convected gradients of highly transient droplet convection, based on the method of characteristics. Under such Lagrangian approaches, the problem of convection reduces to accurately interpolating to find the temperature of a fluid particle at some previous time and location, typically interpolating in space at the previous time step, where Huffenus and Khaletsky (1981) provide a good example and formulation. A similar interpolation method is introduced here, but interpolation is performed in time at the upstream node location, using values from several previous time steps. This gives a discretization equation implicit in the diffusive terms and explicit in convection,

$$\frac{\Delta V}{(n_o - G)\Delta \tau} (T_p^n - T_p^{n-n_o+G}) = -u \Delta A_w (T_p^{n-n_o+G} - T_w^{n-n_o+G}) + a_e T_e^n + a_w T_w^n + a_n T_n^n + a_s T_s^n + a_p T_p^n \quad (15)$$

where ΔV is the volume, ΔA the face area of the control volume, and convective information comes only from the upwind node w due to the streamline fitted coordinate system. Here $a_p = a_e + a_w + a_n + a_s$, where for example, $a_e = (\Delta A_e / \Delta x)$. Defining the Courant number C as

$$C = \frac{u \Delta A_w (n_o - G) \Delta \tau}{\Delta V} \quad (16)$$

the discretization Eq. (15) can be rewritten

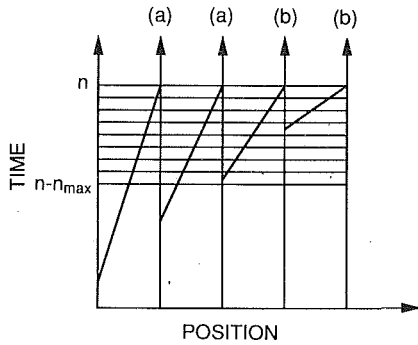


Fig. 2 Particle characteristic trajectories along streamlines in space-time, with discretized time steps

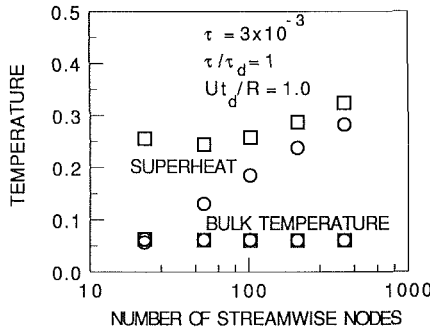


Fig. 3 Effect of streamwise grid spacing on predicted interior superheat and bulk temperature, for standard (circles) and modified (squares) finite-difference schemes

$$T_p^n = \frac{(1-C)T_p^{n-n_o+G} + CT_w^{n-n_o+G} + \frac{(n_o-G)\Delta\tau}{\Delta V} \Sigma T}{\left(1 + \frac{(n_o-G)\Delta\tau}{\Delta V} a_p\right)} \quad (17)$$

where

$$\Sigma T = (a_e T_e^n + a_w T_w^n + a_n T_n^n + a_s T_s^n)$$

and $T_w^{n-n_o+G} = GT_w^{n-n_o+1} + (1-G)T_w^{n-n_o}$, linearly interpolated from stored values at previous time steps, as is shown in Fig. 2, case (b). For the case where $C=1$, then the first term on the right side become zero and Eq. (17) depends only on the upstream temperature at the previous time step $n-n_o+G$, making the formulation similar to the method of characteristics. Indeed, with this formulation convective information cannot propagate faster than the physical velocity, a reasonable constraint.

Due to the very short time scales of interest here ($\tau = 10^{-5}$ to 10^{-2}), exponential grid spacing was applied in the ξ direction to concentrate grid points at the drop surface and provide sufficient resolution of the initial transients. A grid with 25 cross-stream nodes was employed, with a cross-stream grid spacing factor of 1.08. In the ξ direction, equal numbers of grid points were spaced at uniform values of θ along the drop surface and uniform values of η along the centerline axis, as shown in Fig. 1. With this nonuniform grid distribution the difference between the maximum stagnant bulk droplet temperature and exact solutions for the one-dimensional problem (Bai and Schrock, 1991) was under 2 percent, and at later times the bulk temperature solutions converged to within less than 1 percent. Convergence was assumed at each time step when the maximum change of nondimensional temperature at any node was under 10^{-5} .

With the modified method, the upwind temperature value from the n_o-G previous time step was used, in contrast to standard techniques. Figure 2 illustrates the scheme. For case

(b) in regions where the convective velocity is relatively high, $\Delta V/u\Delta A_w\Delta\tau < n_{\max}$,

$$C=1, \quad n_o-G = \Delta V/u\Delta A_w\Delta\tau \quad (18)$$

is used, where n_o is an integer and $0 < G < 1$. Since the grid was fit to the streamlines, $u\Delta A_w$ was constant. For case (a) in regions where the convective velocity is relatively low, $\Delta V/(u\Delta A_w\Delta\tau) > n_{\max}$,

$$C = n_{\max}u\Delta A_w\Delta\tau/\Delta V, \quad G=0 \quad n_o = n_{\max} \quad (19)$$

For the results presented here, the grid spacing and time step were adjusted so that most nodes were described by Eq. (18). For early times $n < n_{\max}$, the maximum number of time steps was reset so that $n_{\max} = n$. For each time step the boundary condition was evaluated at the average time $\tau = (n-0.5(n_o-G))\Delta\tau$.

For convection the accuracy of Eq. (17) is of order $\Delta\tau$, but for diffusion the accuracy is of order $(n_o-G)\Delta\tau$. The larger truncation error for diffusion requires closer streamwise grid spacing at lower (nonzero) convective velocities, to obtain sufficient accuracy and permit use of Eq. (18) at most nodes. Thus calculations were not performed in the range $0 < Ut_d/R < 1$, to keep the number of nodes and the calculation expense reasonable while preserving good accuracy. For the calculations presented here, $n_{\max} = 20$ and, for the center node, $n_o = 10$ were used. For sufficient accuracy for diffusion, the streamwise grid spacing was set to give $(n_o-G)\Delta\tau = 0.05\tau_d$. These constraints gave from 22 to 402 streamwise grid points, for the range of higher and lower values of Ut_d/R investigated.

Because information from previous time steps is used in this modified formulation, the potential exists for some time-step decoupling as is observed with leap-frog methods (Roe, 1983). However, such decoupling was not observed here, perhaps due to the variation of n_o over the computational domain, such that information from several previous time steps was used for the iteration at any given time step. Some oscillation was observed for the coarsest grids investigated, due to passing of the peak of the temperature front between grid points. These oscillations disappeared for the finer grids.

Because the finite-difference formulation used here is not standard, the solutions were verified by solutions using the standard implicit hybrid formulation (Patankar, 1980). Figure 3 gives an example of the effects of node spacing in the streamwise direction. The surface temperature decay constant is $\tau_d = 10^{-3}$, $Ut_d/R = 3$, and the time $\tau = 1.0 \times 10^{-3}$. Both methods accurately predict the volume-averaged bulk temperature, even for coarse grids. But with lower numerical diffusion, the modified method performs much better in predicting the local temperature distribution, as seen by the prediction of the droplet superheat (the difference between the surface and maximum interior temperatures). The computational effort was approximately equal for the first-order upwind and modified methods, for the same grid spacing and time step size. However, the modified method permits coarser grids, decreasing computational effort.

Scaling

Although more detailed numerical treatments are possible for the fluid mechanics of single droplets experiencing transient condensation, droplet sprays are considerably more complex. The extremely transient conditions present in an ICF reactor make the spray fluid mechanics even more difficult to treat. However, it is still possible to provide some qualitative assessment of the condensation heat transfer that can be expected, relative to that on a stagnant drop. In this section scaling arguments are given based on vapor shear effects, and neglecting initial condition and surface tension effects. This scaling provides some quantification of the range of parameters that can be expected for the droplet sprays in rapidly decaying pressure fields, particularly in ICF reactors.

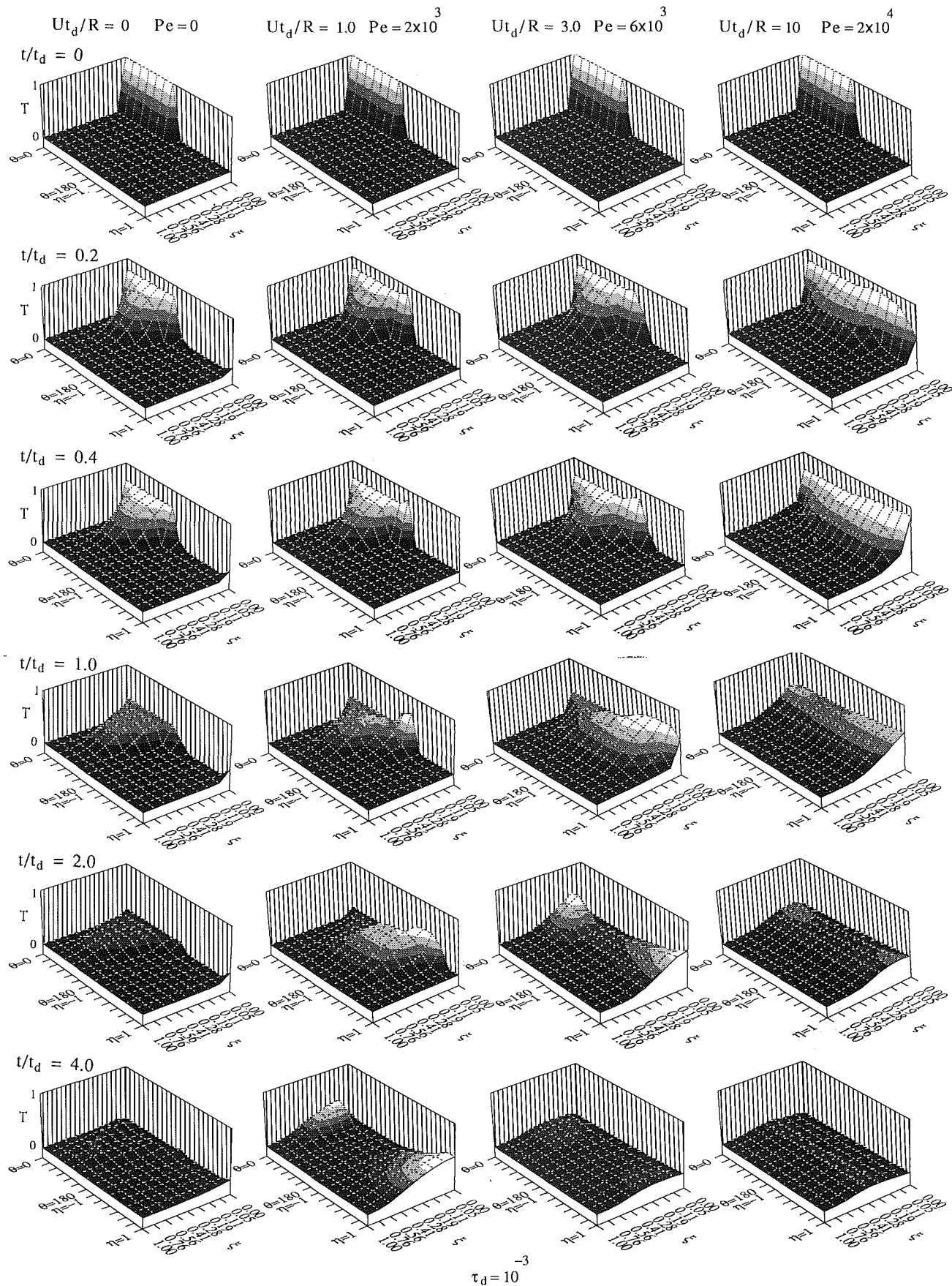


Fig. 4 Droplet temperature distribution in ξ - η coordinates, $\tau_d = 10^{-3}$ (this is an unwrapped version of Fig. 1; $\theta = 180$ and $\eta = -1$ are the same point)

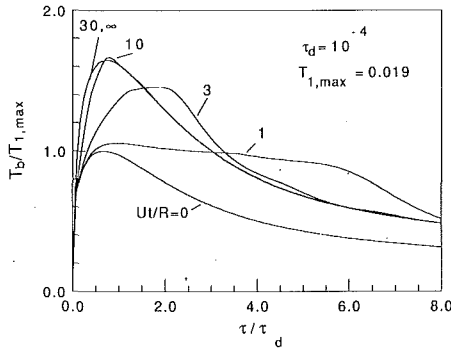


Fig. 5 Comparison of droplet bulk temperature at various recirculation rates with one-dimensional solution, $\tau_d = 10^{-4}$

In an ICF reactor the desire is to reduce the chamber pressure, and thus the saturation temperature, by some large factor over as short a time as possible, to maximize the microexplosion repetition rate. To minimize evaporation, it can be expected that the residence time of individual droplets τ_i will be of the order of one to five times the temperature decay time constant τ_d ,

$$\tau_i = N_i \tau_d \quad (20)$$

Furthermore, the total path length L the droplets will traverse will be on the order of 500 to 10,000 times the drop radius,

$$L = N_p R \quad (21)$$

For a Reynolds number of order 100 the drop circulation velocity will be of the order (Law et al., 1977)

$$U/U_\infty = N_v = O[(\rho_g \mu_g / \rho_l \mu_l)^{1/3}] \quad (22)$$

where N_v is an effective slip ratio. This expression, based on vaporizing droplets, will conservatively underpredict the slip ratio for condensation, where the surface shear stress increases significantly (Sundararajan and Ayyaswamy, 1984). Thus the product of the Peclet number and the nondimensional decay time can be scaled as

$$Pe \tau_d / 2 = Ut_d / R = N_v N_p / N_i = O\left[\frac{t_d}{t_i} \frac{L}{R} \left(\frac{\rho_g \mu_g}{\rho_l \mu_l}\right)^{1/3}\right] \quad (23)$$

In practice vapor entrainment in the center region of the curtains will decrease the slip ratio somewhat. As will be shown later, the value of Ut_d/R characterizes the effect of recirculation, relative to pure conduction, under rapidly decaying pressure fields. Furthermore it is the most important parameter determining the maximum droplet superheat and the potential for homogeneous nucleation and droplet fragmentation. The effective slip ratio N_v is fixed by the total pressure in the system and the fluid properties. The ratio of the pressure decay constant to total residence time N_i is limited by the desire to prevent excessive reevaporation. Thus the primary variable that can be adjusted to change the effect of recirculation is the ratio of total path length to droplet radius N_p . For the HYLIFE reactor, this scaling gives values of Ut_d/R ranging from 0.3 to 2.6.

Results

The temperature distribution inside a droplet in a decaying pressure field can be studied in Fig. 4. A matrix of surface plots is provided, for different times and recirculation values. Because the thermal boundary layers are very thin, selected node values of T are plotted in ζ - ξ coordinates, an unwrapped version of Fig. 1. The mapping between Fig. 4 and the spherical droplet geometry of Fig. 1 is most easily seen by examining the initial condition. As seen in Fig. 4 at the initial time $t/\tau_d = 0$ the temperature along streamline $\xi = 0$ is unity along the drop surface from $\theta = 0$ to 180 and zero along the centerline from radius $\eta = -1$ to 1, and the temperature is zero for all interior points, $\xi > 0$. At short times all cases are similar, with

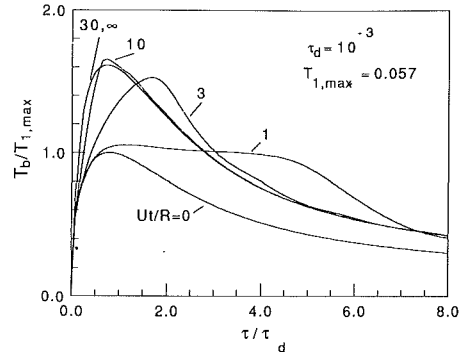


Fig. 6 Comparison of droplet bulk temperature at various recirculation rates with one-dimensional solution, $\tau_d = 10^{-3}$

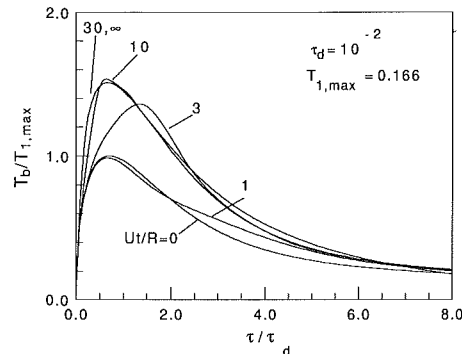


Fig. 7 Comparison of droplet bulk temperature at various recirculation rates with one-dimensional solution, $\tau_d = 10^{-2}$

diffusion most significant around $\theta = 90$, where the streamlines are closest together. The effects of circulation become rapidly apparent at later times, as the surface temperature decays and the temperature shock front is convected across the droplet interior. It is important to note that the numerical method employed here was able to capture the front, while first-order upwind methods showed very large streamwise diffusion except at the closest grid spacings. Of greatest interest is the longer-term behavior of the case of $Ut_d/R = 1$, where substantial superheat remains in the droplet interior due to convection.

Figures 5-7 compare the bulk-temperature history for different values of τ_d with the reference one-dimensional, pure-conduction solution ($Ut_d/R = 0$). The horizontal axis is scaled by the decay time and the vertical axis by the maximum bulk temperature from the one-dimensional solution, $T_{1,max}$, to aid the comparison. When $Ut_d/R > 10$, the solutions approach those of Kronig and Brink, where the stream lines are also isotherms. In these high recirculation cases the heat transfer can be approximated by multiplying the one-dimensional pure-conduction solution by a factor of approximately 1.85. For $t_d \leq 10^{-3}$ the bulk temperature histories become similar, that is, the behavior scaled to the one-dimensional solution is a function of Ut_d/R only. For $t_d \leq 10^{-3}$ the most interesting behavior occurs when $Ut_d/R = 1$, such that the time required for a fluid particle to traverse from one side of the droplet to the other side is approximately twice the time constant for the pressure decay. Then the drop bulk temperature is seen to climb rapidly to a value slightly higher than the pure-conduction case, and then remain approximately constant. This stabilization of the bulk temperature for $Ut_d/R = 1$ occurs because the liquid from the drop surface is pulled into the drop center, and fresh cold liquid wells up from the other side of the drop, offsetting the effect of the pressure decay. The convection of hot surface fluid to the droplet center can be seen clearly in Fig. 4. Eventually the hot liquid must emerge from the other side, and at that point the drop temperature begins to decay.

Figures 8-10 show the superheat levels that can occur in the

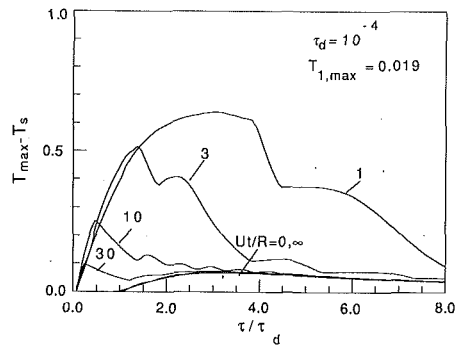


Fig. 8 Maximum in droplet superheat as function of time, $\tau_d = 10^{-4}$

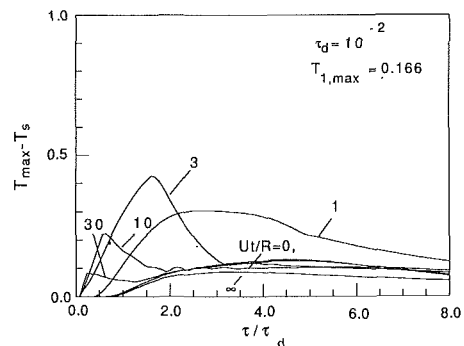


Fig. 9 Maximum in droplet superheat as function of time, $\tau_d = 10^{-3}$

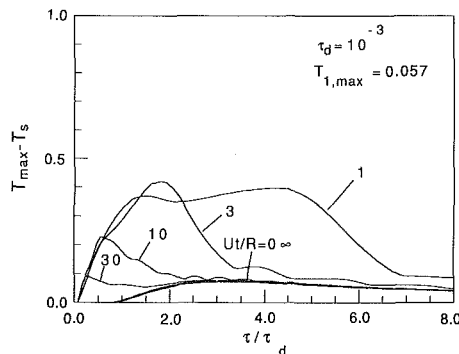


Fig. 10 Maximum in droplet superheat as function of time, $\tau_d = 10^{-2}$

droplets as the pressure decays. The figures show the difference between the maximum temperature inside the droplet and the surface temperature, in nondimensional form. These superheat values are several times higher than the maximum bulk temperature that occurs inside the drop, due to the highly non-uniform temperature distribution, particularly when the surface temperature decay time constant is short. Particularly high superheat values are encountered for the case of $Ut_d/R = 1.0$, because under this condition hot fluid from the surface is convected through the interior of the drop during a period over which the pressure drops greatly. The spike of superheated fluid at the droplet centerline can be seen most clearly in Fig. 4 for $Ut_d/R = 1.0$ and $t/t_d = 1.0$. Interestingly, for the limits of large and small Ut_d/R the superheat solutions become approximately equal.

Conclusions

Convection has important effects on heat transport inside droplets experiencing condensation and subsequent evaporation in rapidly decaying pressure fields. For $t_d \leq 10^{-3}$ the change in the heat transfer rate, relative to one-dimensional conduction, is a function primarily of the parameter Ut_d/R and depends only weakly on the fluid properties. Moderate convection can significantly increase the superheat level inside the droplet. The modified numerical formulation used here helped to assess these superheat levels accurately, where a standard formulation would result in excessive numerical diffusion. Results from the streamline fitted grid and modified convective formulation presented here provide benchmarks for future studies. Furthermore the modified formulation improves assessment of the local surface conditions. Accurate assessment of the local surface temperature, concentration, and heat flux are important for analysis of condensation in the presence of binary vapor mixtures or noncondensable gases, particularly when surface tension effects are considered. Other effects are important in the droplet condensation, including the potential for augmentation due to surface oscillation, which has been shown to be important over longer time frames (Hijikata et al., 1984).

Acknowledgments

This work was performed, in part, under the auspices of the U.S. Department of Energy by the Lawrence Livermore National Laboratory under Contract No. W-7405-Eng-48. Additional support for PFP by the Japan Society for the Promotion of Science Fellowship Program is deeply appreciated.

References

- Bai, R. Y., and Schrock, V. E., 1990, "A Note on Condensation Criterion for Jets in HYLIFE-II," Univ. of California, Berkeley Report UCB-NE-4175, July.
- Bai, R. Y., and Schrock, V. E., 1991, "An Approximate Method for Estimating Condensation in HYLIFE-II," *Fusion Technology*, Vol. 19, pp. 732-739.
- Chao, B. T., 1969, "Transient Heat and Mass Transfer to a Translating Droplet," *ASME JOURNAL OF HEAT TRANSFER*, Vol. 91, pp. 273-281.
- Clift, R., Grace, J. R., and Weber, M. E., 1978, *Bubbles, Drops, and Particles*, Academic Press, New York.
- Hassan, Y. A., Rice, J. G., and Kim, J. H., 1983, "A Stable Mass-Flow-Weighted Two-Dimensional Skew Upwind Scheme," *Numerical Heat Transfer*, Vol. 6, pp. 395-408.
- Hijikata, K., Mori, Y., and Kawaguchi, S., 1984, "Direct Contact Condensation of Vapor to Falling Cooled Droplets," *International Journal of Heat and Mass Transfer*, Vol. 27, No. 9, pp. 1631-1634.
- Huang, L. J., and Ayyaswamy, P. S., 1987, "Heat Transfer of a Nuclear Reactor Containment Spray Drop," *Nuclear Engineering and Design*, Vol. 101, pp. 137-148.
- Huffenus, J. P., and Khaletzky, D., 1981, "The Lagrangian Approach of Advective Term Treatment and Its Application to the Solution of Navier-Stokes Equations," *Int. J. for Numerical Methods in Fluids*, Vol. 1, pp. 365-387.
- Lane, J. A., MacPherson, H. G., and Maslan, F., 1958, *Fluid Fuel Reactors*, Addison-Wesley, Reading, MA.
- Law, C. K., Prakash, S., and Sirignano, W. A., 1977, "Theory of Convective, Transient, Multicomponent Droplet Vaporization," *Proceedings of the 16th Symposium (International) on Combustion*, The Combustion Institute, pp. 605-617.
- Monsler, M. J., and Meier, W. R., 1981, "A Conceptual Design Strategy for Liquid-Metal-Wall Inertial Fusion Reactors," *Nuclear Engineering and Design*, Vol. 63, pp. 289-313.
- Patankar, S. V., 1980, *Numerical Heat Transfer and Fluid Flow*, Hemisphere, New York.
- Polyanin, A. D., 1984, "Unsteady-State Extraction From a Falling Droplet With Nonlinear Dependence of Distribution Coefficient on Concentration," *Int. J. Heat Mass Transfer*, Vol. 27, pp. 1261-1276.
- Raithby, G. D., 1976a, "A Critical Evaluation of Upstream Differencing Applied to Problems Involving Fluid Flow," *Computer Methods in Applied Mechanics and Engineering*, Vol. 9, pp. 75-103.
- Raithby, G. D., 1976b, "Skew Upwind Differencing Schemes for Problems Involving Fluid Flow," *Computer Methods in Applied Mechanics and Engineering*, Vol. 9, pp. 153-164.
- Roe, P. L., 1983, "An Introduction to Numerical Methods Suitable for the Euler Equations," von Karman Institute for Fluid Dynamics Lecture Series 1983-01, Jan. 24-28.
- Schneider, G. E., Raw, M. J., 1986, "A Skewed, Positive Influence Coefficient Upwinding Procedure for Control-Volume-Based Finite-Element Convection-Diffusion Computation," *Numerical Heat Transfer*, Vol. 9, pp. 1-26.
- Sundararajan, T., and Ayyaswamy, P. S., 1984, "Hydrodynamics and Heat Transfer Associated With Condensation on a Moving Drop: Solutions for Intermediate Reynolds Numbers," *Journal of Fluid Mechanics*, Vol. 149, pp. 33-58.
- Sundararajan, T., and Ayyaswamy, P. S., 1985, "Heat and Mass Transfer Associated With Condensation on a Moving Drop: Solutions for Intermediate Reynolds Numbers by a Boundary Layer Formulation," *ASME JOURNAL OF HEAT TRANSFER*, Vol. 107, pp. 409-416.

Condensation of a Nonazeotropic Refrigerant Mixture R114/R113 in Horizontal Annuli With an Enhanced Inner Tube

Sh. Nozu

K. Ozaki

H. Inaba

Department of Mechanical Engineering,
Okayama University,
3-1 Tsushima, Okayama 700, Japan

H. Honda

Institute of Advanced Material Study,
Kyushu University,
Kasuga, Fukuoka 816, Japan

Local heat transfer and pressure drop measurements are made during condensation of a nonazeotropic refrigerant mixture R114/R113 in the annuli of horizontal double-tube condensers. The inner tube is a 19.1-mm-o.d. corrugated tube with copper wire fins soldered on the outer surface. The outer tubes are smooth tubes with different i.d. of 29.9 and 25.0 mm. The heat transfer coefficient based on the bulk-vapor to wall temperature difference is considerably smaller for R114/R113 mixtures than for pure R113. An empirical equation for the vapor phase mass transfer coefficient is derived, in which the dimensionless parameters are introduced on the basis of the previous results for turbulent single phase flow in smooth and rough tubes with and without surface suction. The measured condensation heat transfer coefficients for R114/R113 mixtures are correlated by the present model to a mean absolute deviation of 14.3 percent.

Introduction

Use of a nonazeotropic binary mixture in vapor compression heat pump and refrigeration systems has been considered to be an effective means for raising the thermal performance of the system. Comprehensive reviews on the condensation and vaporization of mixtures and some suggestions for design practice have been given in the literature (e.g., Bell, 1988; Breber, 1988). In condensers using a nonazeotropic mixture, buildup of the vapor diffusion layer near the condensate surface impairs the thermal performance of the condenser. While three types of method for predicting the heat and mass transfer processes during condensation of mixtures have been developed, these methods are only available for simple geometric configurations and for simple mixtures (Breber, 1988).

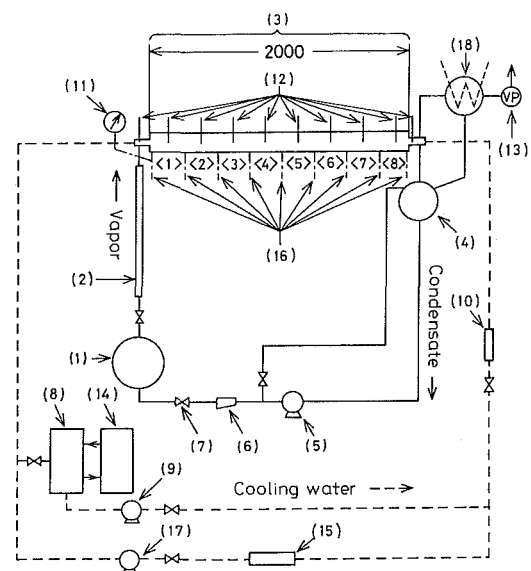
Condensation in tubes and annuli is pertinent to condensers for refrigeration and air-conditioning applications. For in-tube condensation of nonazeotropic binary mixtures, a number of experimental studies have been reported in recent years. Mochizuki et al. conducted experiments in vertical (1984) and horizontal (1988) tubes using R114/R11 and R11/R113 mixtures as the test fluids, respectively. Their findings showed little difference in the heat transfer characteristics between the mixtures and their components. Hijikata et al. (1989) derived a boundary-layer theory-based equation for the vapor phase mass transfer coefficient. However, they made no comparison of the local mass transfer coefficient between the prediction and their R114/R113 data. Shizuya et al. (1990) conducted experiments in horizontal smooth and grooved tubes using several kinds of vapor mixture. They connected the measured heat transfer data with the estimated flow patterns. Koyama et al. (1990) carried out experiments in a horizontal microfin tube using R22/R114 mixtures. They proposed an empirical equation for the average heat transfer coefficient based on the vapor-to-wall temperature difference, in which an empirical term of the inlet mole fraction of R22 is introduced to account for the mass transfer effects.

The foregoing review of the recent studies reveals that one of the major problems to be clarified is the characteristics of

the vapor phase mass transfer. Furthermore, no available data exist for the condensation of a nonazeotropic binary mixture in an annulus. The present study was undertaken to provide a carefully measured set of data on the vapor phase mass transfer during the condensation of a nonazeotropic binary mixture R114/R113 in horizontal annuli with an enhanced inner tube.

Experimental Apparatus and Procedure

The experimental apparatus, shown schematically in Fig. 1, consists of forced circulation loops of test fluid and cooling



- | | |
|-----------------------|---|
| 1 Boiler | 11 Pressure gage |
| 2 Superheater | 12 Sheath thermocouples and sampling probes |
| 3 Test tube | 13 Vacuum pump |
| 4 Condensate receiver | 14 Chiller |
| 5 Circulation pump | 15 Heater |
| 6 Strainer | 16 Pressure taps |
| 7 Needle valve | 17 Cooling water pump |
| 8 Cooling water tank | 18 Auxiliary condenser |
| 9 Cooling water pump | |
| 10 Rotameter | |

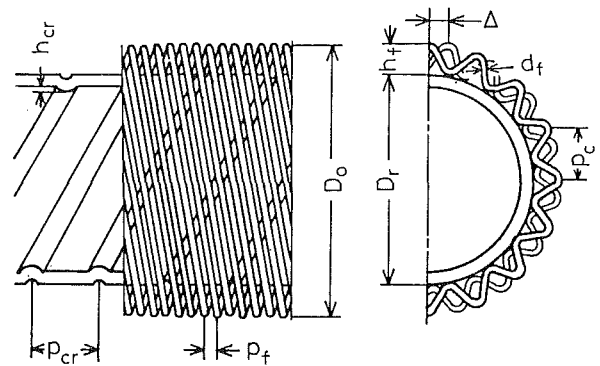
Fig. 1 Schematic diagram of experimental apparatus

Contributed by the Heat Transfer Division and presented at the 3rd ASME/JMSE Thermal Engineering Joint Conference, Reno, Nevada, March 17-22, 1991. Manuscript received by the Heat Transfer Division November 26, 1990; revision received May 23, 1991. Keywords: Condensation, Finned Surfaces, Mass Transfer.

water. It is basically the same as that used in the previous test for pure refrigerants R11 and R113 with the exception of the inner tube, and is described in detail by Honda et al. (1989).

The test section is a horizontal double-tube condenser with the test fluid flowing in the annulus and the cooling water flowing countercurrently in the inner tube. The vapor condenses almost completely in the test section. Two test sections with the same inner tube and the outer tubes with different inside diameters are used to study the geometric effects of the annular gap. As shown in Fig. 2, the inner tube is a corrugated tube with copper wire fins soldered on the outer surface (wire-finned tube). The fin geometry and fin dimensions of the inner tube are the same as those used in the previous study (Honda et al., 1989), except that the crest distance between adjacent fins Δ is 1.72 times as large as that used in the previous study. The outer surface area is 3.04 times that of an equivalent smooth tube. The outer tubes are smooth tubes with inside diameters D_i of 29.9 and 25.0 mm, respectively. The 2-m-long test section is subdivided into eight 250-mm-long subsections, which are called the 1st, 2nd, ..., and 8th subsections from the vapor inlet. The test section with $D_i = 25.0$ mm is provided with three sight glasses having the same inner diameter as the outer tube at the 2nd, 5th, and 8th subsections. Concentricity of the inner and outer tubes was ensured by inserting teflon spacers into the annuli at three subsections.

Nine type-T thermocouples for measuring the cooling water temperature T_c at the inlet and exit of each subsection are inserted in the inner tube. The inner tube is electrically insulated from the outer tube to measure the average wall temperature of each subsection by the resistance thermometry. The inner tube and a standard resistor of 1 m Ω are connected in series by a lead wire to a d-c power supply, and a constant current of 40 A is passed through the circuit. Nine voltage taps are



Diameter at fin tip	D_o	20.6 mm
Diameter at fin root	D_r	19.1 mm
Crest pitch	P_c	1.8 mm
Fin height	h_f	0.8 mm
Wire diameter	d_f	0.3 mm
Fin pitch	P_f	0.48 mm
Tube thickness		0.95 mm
Corrugation pitch	P_{cr}	7.0 mm
Internal ridge height	h_{cr}	0.3 mm
Crest distance between adjacent fins	Δ	0.77 mm

Fig. 2 Details of inner tube

soldered to the outer surface of the inner tube at the same longitudinal positions as the cooling water thermocouples. Nine pressure taps with 1-mm-dia holes are drilled at the bottom of the outer tube at 250-mm intervals from the vapor inlet. The adjoining pressure taps are connected to inverse U-tube manometers, reading to 1 mm, to measure the difference in condensate level. Static pressure at the vapor inlet is measured by

Nomenclature

a, b, c = constants in Eq. (19)
 c_f = friction factor = $2D(-dP/dz)/\rho u^2$ or $2(D_i - D_r)(-dP/dz)/\rho u^2$
 D = inner diameter
 D_i = inner diameter of outer tube
 D_o = diameter at fin tip
 D_r = diameter at fin root
 \mathcal{D} = diffusion coefficient
 G = test fluid mass velocity
 g = gravitational acceleration
 i = specific enthalpy
 i_{fg} = specific enthalpy of evaporation
 m = mass flux through interface
 m_n = condensation mass flux based on nominal surface area
 P = pressure
 q_n = local heat flux based on nominal surface area
 Re = Reynolds number = uD/ν or $u(D_i - D_r)/\nu$
 Sc = Schmidt number
 Sh = Sherwood number = $\beta D/\mathcal{D}$ or $\beta_n(D_i - D_r)/\mathcal{D}$
 T_c = cooling water temperature
 T_{eq} = equilibrium temperature
 T_f = average fin surface temperature
 T_i = condensate surface temperature
 T_{vb} = bulk-vapor temperature

T_w = fin root tube surface temperature
 u = axial velocity
 v_i = suction velocity
 X = vapor mass quality
 X_{it} = Lockhart and Martinelli parameter, Eq. (15)
 x_j = mass fraction of component j in liquid phase
 y_j = mass fraction of component j in vapor phase
 z = distance measured from vapor inlet
 α = heat transfer coefficient
 α_{f0} = heat transfer coefficient of condensate film on fin surface, Eq. (32)
 α_n = heat transfer coefficient based on nominal surface area, Eq. (6)
 α_{n0} = heat transfer coefficient of condensate film based on nominal surface area, Eq. (8b)
 α_{r0} = heat transfer coefficient of condensate film on fin root tube surface, Eq. (33)
 β = mass transfer coefficient
 β_n = vapor phase mass transfer coefficient based on nominal surface area, Eq. (7)
 γ = suction parameter, Eq. (20)
 η = fin efficiency

λ = thermal conductivity
 μ = dynamic viscosity
 ν = kinematic viscosity
 ρ = density
 σ = surface tension
 ϕ_v = Lockhart and Martinelli parameter, Eq. (14)
 ω = dimensionless quantity = $(y_{1b} - x_{1i})/(y_{1i} - x_{1i})$

Subscripts

b = bulk
 f = fin
 g = gravity-controlled condensation regime
 i = condensate surface on inner tube
 in = vapor inlet
 l = liquid
 n = based on nominal surface area (surface area of a smooth tube with D_r)
 r = fin root tube surface
 s = surface tension controlled condensation regime
 v = vapor; also vapor shear controlled condensation regime
 0 = without suction; also condensate film
 1 = volatile component (R114)
 2 = less volatile component (R113)

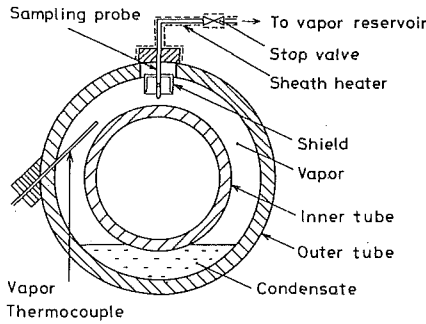


Fig. 3 Arrangement of vapor thermocouple and vapor sampling probe in a subsection

a precision Bourdon tube gauge, reading to 10^3 Pa, and a Fortin barometer. Cooling water flow rate is measured by a calibrated rotameter.

The vapor temperatures at the inlet and exit of the test section and also the condensate temperature in the strainer are measured by 1-mm-dia type-K sheathed thermocouples. The local vapor temperature at the midpoint of each subsection, T_{vb} (except the 2nd, 5th, and 8th subsections for $D_i = 25.0$ mm), is also measured by the same type of thermocouple. The local vapor composition is determined at the same longitudinal position as the vapor temperature using a gas chromatograph. Arrangement of the vapor thermocouple and vapor sampling probe installed in a subsection is shown in Fig. 3. The thermocouple is inserted obliquely upward in the upper part of the annulus and its hot junction is located at the midpoint of the annular gap. A stainless-steel sampling probe of 0.4 mm o.d. is inserted through the top of the outer tube. In order to avoid sampling droplets entrained in vapor flow, the tip of the probe is covered with a cuplike shield made of polyvinyl chloride. The probe is connected, via a stop valve, to an evacuated vessel kept about 340 K.

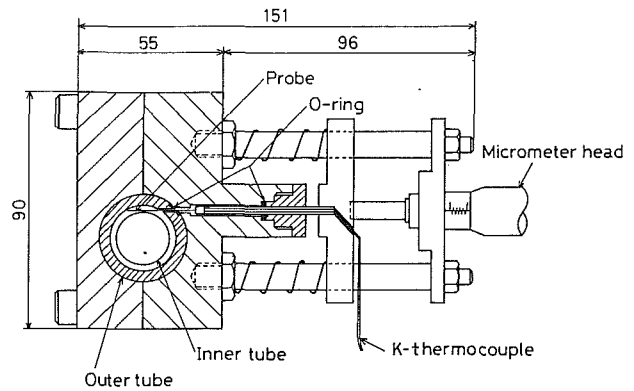
For the test section with $D_i = 25.0$ mm, the vapor temperature distribution in a transverse cross section is measured at the 8th subsection. As shown in Fig. 4, the probe is a 50- μ m-dia enamel-coated type-K thermocouple. It is traversed horizontally by a micrometer head and is zeroed by detecting the electric contact of the hot junction with the inner surface of the outer tube. The temperature signal is recorded by a pen recorder with pen speed of 1 m/s. The radial distance ξ measured from the fin tip is obtained from the geometric arrangement of the probe as $\xi = \{(l_2/2 - \zeta)^2 + l_1\}^{1/2} - D_o/2$.

After steady state is reached, the thermocouple outputs and the voltage drops of the inner tube and the standard resistor are read to $1 \mu V$ using a data acquisition system. Samples of the vapor mixture are led to the evacuated vessels and analyzed successively using a calibrated gas chromatograph. Mass velocity of the test fluid G is obtained from the heat balance of the electrically heated boiler by application of steady flow energy balance for the test fluid.

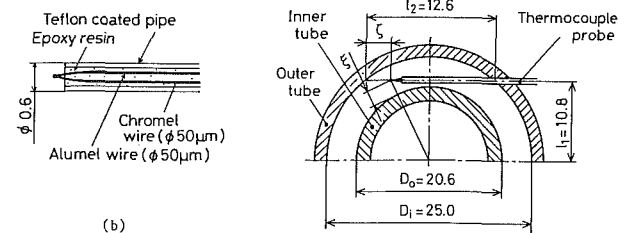
Experiments were performed at a constant inlet vapor temperature of 325 K. Two kinds of R114/R113 mixtures with different inlet R114 mass fractions, y_{1in} , of 0.23 and 0.36 were used as the test fluids. For comparison, the condensing data for pure R113 were also obtained. The G value ranged from 80 to 270 kg/m²s. In order to study the effects of condensation mass flux on the vapor phase mass transfer characteristics, the vapor mass quality at the tube exit was changed in three steps for a few prescribed values of G .

Data Reduction

In order to obtain the axial distributions of relevant quantities, a steady-state energy balance is applied to each sub-



(a)



(b)

(c)

Fig. 4 Details of traversing device: (a) cross-sectional view perpendicular to tube axis; (b) temperature probe; (c) geometric arrangement of probe

section. An energy balance in the j th subsection is expressed as

$$Q_j = W[\{X i_v + (1 - X) i_l\}_{jin} - \{X i_v + (1 - X) i_l\}_{jout}] \quad (1)$$

where Q_j is the heat transfer rate of the j th subsection, W is the test fluid flow rate, X is the vapor mass quality, i_v and i_l are the enthalpies of the vapor and liquid, respectively. Subscripts jin and $jout$ denote the inlet and exit of the j th subsection, respectively.

The vapor and liquid phases of R114/R113 are assumed to be an ideal mixture. Thus, i_v in Eq. (1) is given by

$$i_v = y_{1b} i_{v1} + (1 - y_{1b}) i_{v2} \quad (2)$$

where y_{1b} is the mass fraction of R114 in the bulk vapor. If the bulk vapor is assumed to be dry saturated, y_{1b} can be calculated using the measured values of the static pressure P and the bulk-vapor temperature T_{vb} as

$$y_{1b} = A / \{M_2 / M_1 + A(1 - M_2 / M_1)\} \quad (3)$$

where $A = P_{s1}(P - P_{s2}) / \{P(P_{s1} - P_{s2})\}$, M is the molecular weight, P_s is the vapor pressure of pure component.

The i_l in Eq. (1) is evaluated on the basis of the simplifying assumptions as follows: (i) No variations of the temperature and composition exist across the condensate film on the inner tube and these values are equal to that at the condensate surface. (ii) The enthalpy change of the condensate flowing through the lower part of the annulus is negligible. On the basis of these assumptions, i_l and the enthalpy change of the condensate in the j th subsection are respectively given by

$$i_l = x_{1i} i_{l1} + (1 - x_{1i}) i_{l2} \quad (4)$$

$$\{(1 - X) i_l\}_{jin} - \{(1 - X) i_l\}_{jout} = (X_{jout} - X_{jin}) (i_l)_j \quad (5)$$

where x_{1i} is the liquid mass fraction of R114 at the condensate surface on the inner tube.

Axial variation of X is obtained by executing the following procedures:

- (i) Assume $X = 1$ at the vapor inlet.

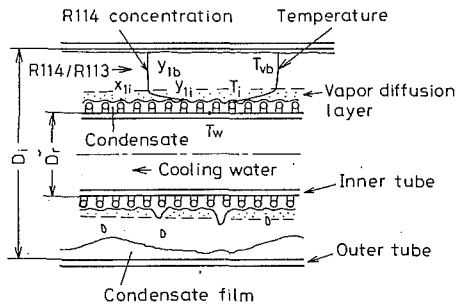


Fig. 5 Typical two-phase flow pattern observed for R114/R113 mixture and profiles of temperature and concentration in vapor phase

(ii) Calculate y_{1b} from Eq. (3), calculate the condensate surface temperature T_i and x_{1i} from Eqs. (8) ~ (10) (described later), then obtain i_v and i_l at the midpoint of each subsection from Eqs. (2) and (4), respectively.

(iii) Interpolate i_v and i_l at the inlet and exit of each subsection using the results obtained in (ii).

(iv) Calculate X_{jout} successively from the vapor inlet using Eq. (5).

It is recognized that condensation is not an equilibrium process. But in most cases the vapor and liquid phases are assumed to be in equilibrium with each other at any cross section of the conduit (e.g., Breber, 1988). In this paper, the equilibrium temperature T_{eq} is also calculated for comparison.

The local heat transfer coefficient α_n and the local vapor phase mass transfer coefficient β_n are defined respectively on the basis of the nominal surface area (i.e., surface area of a smooth tube with diameter D_i) as

$$\alpha_n = q_n / (T_{vb} - T_w) \quad (6)$$

$$\beta_n = m_n / \rho_v (1 - \omega) \quad (7)$$

where q_n and m_n are the local heat flux and the local condensation mass flux based on the nominal surface area, respectively, T_w is the wall temperature at the tube surface, $\omega = (y_{1b} - x_{1i}) / (y_{1i} - x_{1i})$ and y_{1i} is the vapor mass fraction of R114 at the condensate surface on the inner tube. The T_w value is obtained from the measured local wall temperature, making a small correction for radial conduction.

In order to discuss the R114/R113 data, it is necessary to determine the T_i value. Neglecting the effect of convective heat flux, q_n is respectively related to m_n and the heat transfer coefficient of the condensate film, α_{n0} , as

$$q_n = m_n \{ x_{1i} (i_{fg})_1 + (1 - x_{1i}) (i_{fg})_2 \} \quad (8a)$$

$$q_n = \alpha_{n0} (T_i - T_w) \quad (8b)$$

According to Honda et al. (1989), α_{n0} is composed of the heat transfer coefficient of the condensate film on the fin surface, α_{f0} , and that on the fin root tube surface, α_{r0} , as

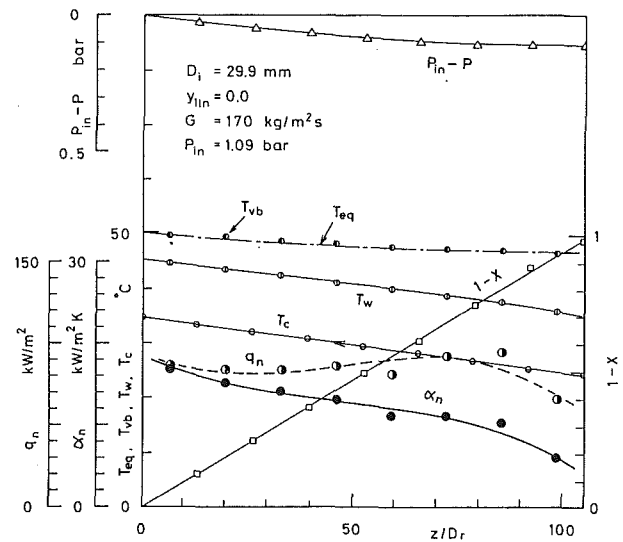
$$\alpha_{n0} = 1 / \{ p_c p_f (1 / \pi d_f \eta \alpha_{f0} + R_s) \} + \alpha_{r0} (1 - A_f) \quad (9)$$

where p_c is the fin crest pitch, p_f is the fin pitch, d_f is the wire fin diameter, $\eta = \tanh(\lambda_f \sqrt{\alpha_{f0} / \lambda_f d_f} / (\lambda_f \sqrt{\alpha_{f0} / \lambda_f d_f}))$ is the fin efficiency, λ_f is the fin length per fin pitch, R_s is the thermal resistance of the solder layer at the fin base, and A_f is the ratio of fin base area to tube surface area. The expressions for α_{f0} and α_{r0} are given by Eqs. (35) and (34), respectively. The T_i value can be calculated iteratively from Eq. (8b) using the measured values of q_n , T_w , and Eq. (9). Then, x_{1i} and y_{1i} are respectively obtained from

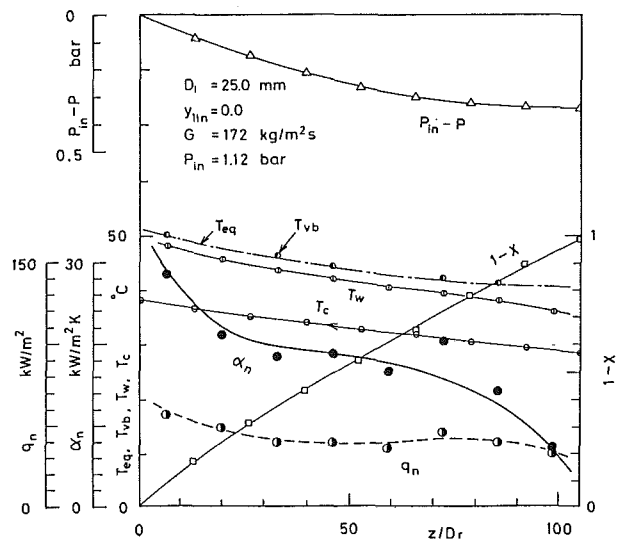
$$P = \{ (P_{s1} / M_1) x_{1i} + (P_{s2} / M_2) (1 - x_{1i}) \} / \{ x_{1i} / M_1 + (1 - x_{1i}) / M_2 \} \quad (10)$$

and

$$y_{1i} = (P_{s1} / x_{1i}) / \{ P_{s1} x_{1i} + P_{s2} (1 - x_{1i}) \} \quad (11)$$



(a)



(b)

Fig. 6 Distribution of measured quantities along test tube, $y_{1in} = 0.0$: (a) $D_i = 29.9$ mm; (b) $D_i = 25.0$ mm

In the data reduction the properties of the condensate and vapor are respectively evaluated at the reference temperatures of $T_w + 0.3(T_i - T_w)$ and $(T_{vb} + T_i)/2$, except for the specific enthalpy of evaporation i_{fg} and the surface tension σ , which are evaluated at T_i . The mixture properties are obtained from the pure component data (JSME, 1982) using mixing rules as follows: Densities and enthalpies of both phases are evaluated assuming ideal mixtures. Liquid viscosity and surface tension are evaluated by the methods of Reid et al. (1977). Vapor viscosity is evaluated by the method of Wilke (1950). Thermal conductivity of condensate is evaluated by the method of Chen et al. (1987). The diffusion coefficient of vapor is obtained from the equation proposed by Fuller et al. (1966).

The uncertainty in the measured α_n value is estimated to be within ± 13 percent. At low X regime, the lower part of the inner tube was submerged in the condensate pool, which resulted in a lower accuracy of m_n in Eq. (7). Taking this into account, the data analysis for the vapor phase mass transfer is performed at $X_{1i} \leq 0.2$, where the effect of the submergence can be negligible (Honda et al., 1989). The uncertainty in the measured β_n value is estimated to be within 32 percent.

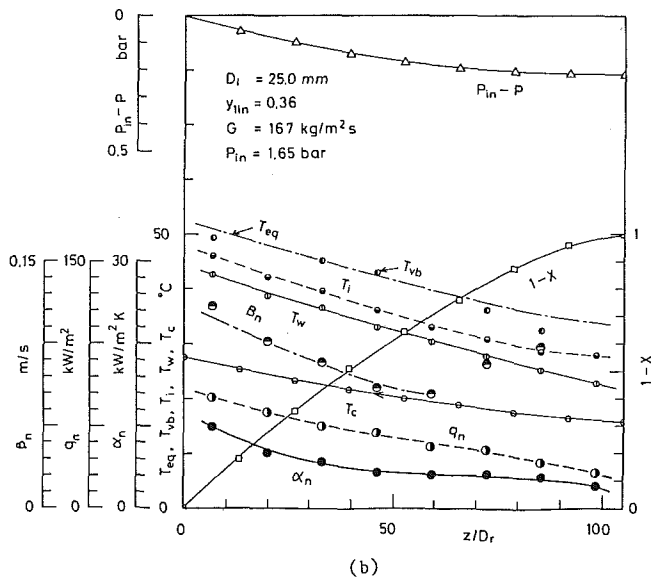
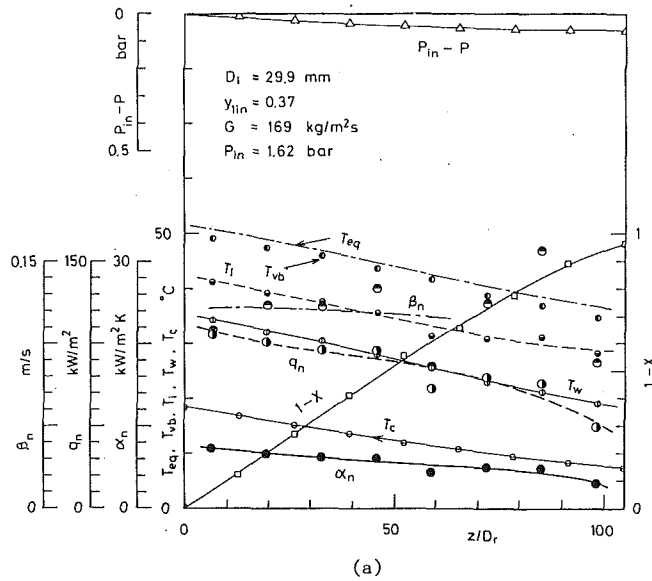


Fig. 7 Distribution of measured quantities along test tube, $y_{in} \approx 0.36$: (a) $D_i = 29.9$ mm; (b) $D_i = 25.0$ mm

Experimental Results and Discussion

Flow Observation. Figure 5 illustrates a typical flow pattern observed for R114/R113 condensing flow. The behavior of the condensate is similar to the results for pure refrigerants R11 and R113 (Honda et al., 1989). At high X , the condensate is retained between some of the wire fins and the inner tube surface. At low X , on the other hand, the space between the wire fins and the inner tube surface is completely filled with the condensate. Most of the condensate on the inner tube falls off the tube bottom. At high G and X , some of the condensate is entrained in the flowing vapor. The condensate film thickness on the lower part of the outer tube increases as condensation proceeds.

Axial Distributions of Measured Quantities. Figure 6 shows the axial distributions of α_n , q_n , T_{eq} , T_{vb} , T_w , T_c , the wetness fraction $(1 - X)$, and the static pressure drop from the vapor inlet $(P_{in} - P)$ for pure R113 at $G \approx 170$ kg/m²s. Comparison of Figs. 6(a) and 6(b) for different D_i reveals that the values of q_n and the condensation temperature difference $(T_{vb} - T_w)$ are larger for $D_i = 29.9$ mm, whereas the values of α_n and

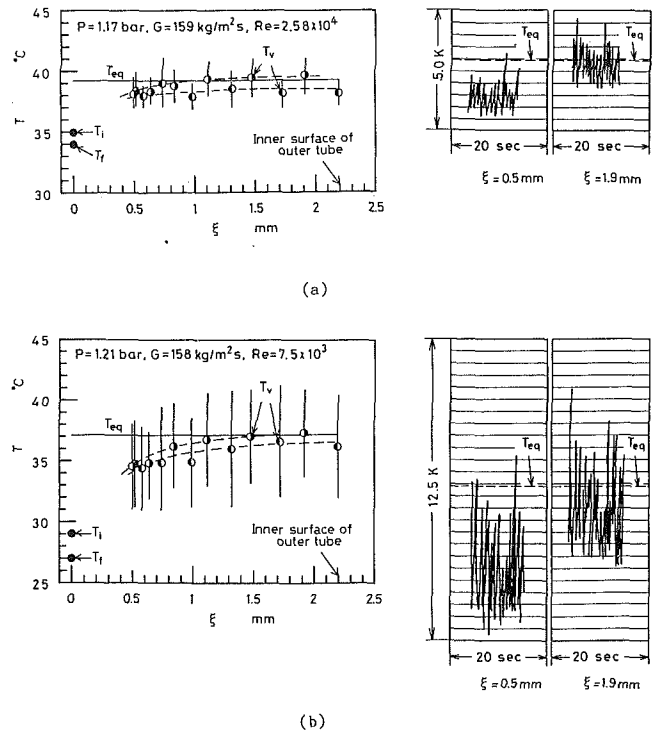


Fig. 8 Distribution of vapor temperature plotted on T versus ξ coordinates, $G = 159$ kg/m²s and $y_{in} = 0.23$: (a) $X = 0.30$; (b) $X = 0.09$

$(P_{in} - P)$ and the axial variation of T_{vb} are smaller for $D_i = 29.9$ mm. In both tubes, the T_{vb} agrees fairly well with the T_{eq} .

Figure 7 shows similar results for R114/R113 mixtures at $G \approx 170$ kg/m²s. Also shown in Fig. 7 are the distributions of T_i and β_n . A significant decrease in α_n is observed for R114/R113 mixtures as compared to the pure R113 results in Fig. 6. This indicates the presence of the mass transfer resistance in the vapor phase. Comparison of Figs. 7(a) and 7(b) reveals that the ratio of temperature drop in the vapor phase to vapor-to-wall value, $(T_{vb} - T_i)/(T_{vb} - T_w)$, is larger for $D_i = 25.0$ mm, whereas the β_n value is larger for $D_i = 29.9$ mm. It is also seen that the T_{vb} is in close agreement with T_{eq} except downstream subsections for $D_i = 25.0$ mm, where the T_{vb} deviates toward a lower value as condensation proceeds.

Variation of Vapor States. Figure 8 shows the distribution of vapor temperature for R114/R113 mixtures at $G \approx 159$ kg/m²s and $y_{in} \approx 0.23$ plotted on the coordinates of T versus the radial distance ξ measured from the fin tip (Fig. 4c). In Fig. 8, the maximum and minimum vapor temperatures recorded at each position are connected by a vertical line, and their arithmetic average value T_v is plotted by symbols \bullet and \circ for the left ($0 \leq \xi \leq 6.3$ mm) and right ($6.3 \leq \xi \leq 12.6$ mm) halves of the annulus, respectively. Comparison of Figs. 8(a) and 8(b) for different X reveals that the temperature fluctuation is larger for $X = 0.09$ than for $X = 0.30$. Also shown in Fig. 8 are the values of T_{eq} , T_i , the average fin surface temperature T_f and the temperature traces at $\xi = 0.5$ and 1.9 mm. The T_i and T_f are plotted at $\xi = 0$ mm for convenience. The T_f value is obtained from the definition of η as

$$T_f = T_i - \eta(T_i - T_{wf}) \quad (12)$$

where T_{wf} is the fin root temperature given by

$$T_{wf} = T_w + q_{nf} \rho_c \mu R_s \quad (13)$$

and q_{nf} is the heat flux on the fin surface (nominal surface area basis).

In Fig. 8, dashed lines show approximate distribution of T_v . Comparison of Figs. 8(a) and 8(b) reveals that the temperature

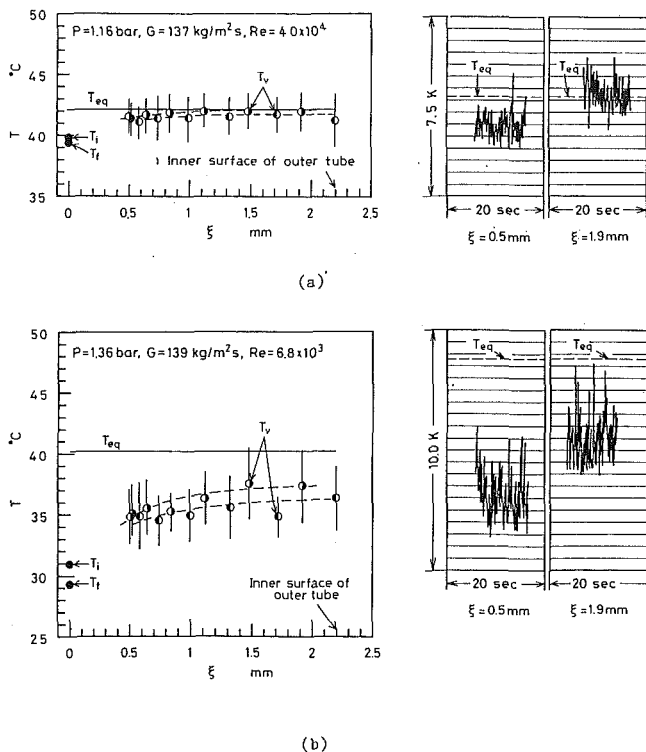


Fig. 9 Distribution of vapor temperature plotted on T versus ξ coordinates, $G \approx 139 \text{ kg/m}^2\text{s}$ and $y_{1in} \approx 0.23$: (a) $X = 0.54$; (b) $X = 0.09$

profile is flatter for larger X . This indicates that the vapor diffusion layer develops axially along the outer surface of the inner tube as shown in Fig. 5. The T_v almost agrees with T_{eq} value at larger ξ . It is also seen that the T_v value in the left half of the annulus is about 1 K lower than that in the right half except in the vicinity of $\xi = 0.5 \text{ mm}$. This discrepancy may be ascribed to the swirl flow of the vapor induced by the corrugation on the inner tube.

Figure 9 shows similar results at $G \approx 139 \text{ kg/m}^2\text{s}$ and $y_{1in} \approx 0.23$. The distribution of T_v is similar in trend to the case of Fig. 8 except that the T_v value for $X = 0.09$ (Fig. 9b) is considerably lower than T_{eq} in the whole range of ξ . The result as shown in Fig. 9(b) was observed at low Re regime, with the difference becoming more marked for lower Re.

Figure 10 shows the measured values of y_{1b} and T_{vb} for R114/R113 mixtures at $G \approx 76 \text{ kg/m}^2\text{s}$ plotted on the temperature-composition diagram, where, as recommended by Butterworth (1983), the lowest pressure observed in the tube is adopted for the calculation of the dew and bubble lines. The measured T_{vb} value decreases with the increase of y_{1b} . In Fig. 10(a) for $D_i = 29.9 \text{ mm}$, the T_{vb} agrees fairly well with the dewpoint temperature at the 1st to 5th subsections; thereafter, the former deviates toward a lower value as condensation proceeds. In Fig. 10(b) for $D_i = 25.0 \text{ mm}$, on the other hand, the T_{vb} agrees closely with the dewpoint temperature except near the tube exit.

A major factor leading to the "near-equilibrium condensation" between bulk phases is considered to be the well-mixed phase distribution. Applying the flow regime transition criteria for two-phase gas-liquid flow in a horizontal tube (Taitel and Dukler, 1976) to the conditions corresponding to Figs. 10(a) and 10(b), the transition between the annular-dispersed liquid and stratified wavy regimes is considered to take place at the 5th and 7th subsections for $D_i = 29.9$ and 25.0 mm , respectively. This is in accord with the results shown in Fig. 10 where the tube with smaller D_i tends to provide the "near-equilibrium condensation" process. Similar results are found in the previous data for R114/R152a mixtures in vertical shellside con-

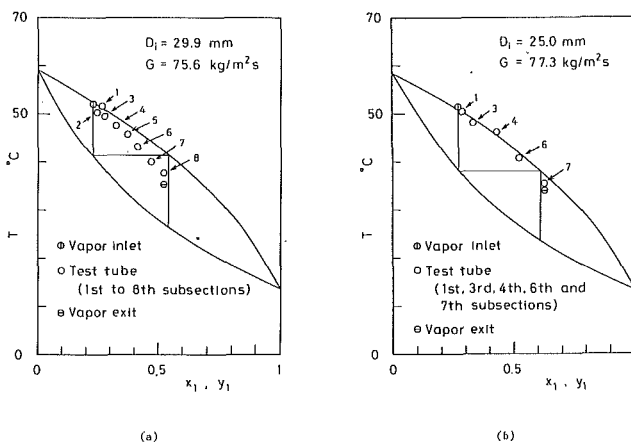


Fig. 10 Measured local vapor states plotted on temperature-composition diagram: (a) $D_i = 29.9 \text{ mm}$; (b) $D_i = 25.0 \text{ mm}$

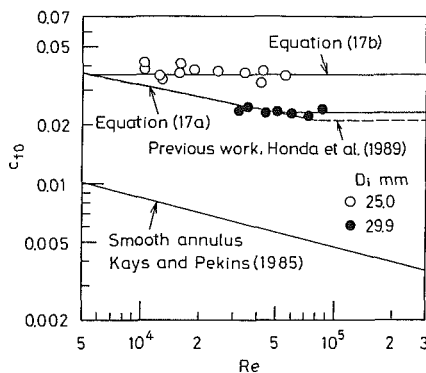


Fig. 11 Variation of friction factor with Reynolds number, superheated R113 vapor

densers with different tube pitch-to-diameter ratio (Kawano, 1990). It is also seen from Fig. 10 that the vapor mass fraction at the tube exit is close to that predicted from the assumption of integral condensation mode.

In the range $G \geq 100 \text{ kg/m}^2\text{s}$, the measured distribution of y_{1b} became more irregular with increasing G . This is probably due to the fact that the entrained droplets were sampled along with the vapor mixture.

Pressure Drop. The frictional pressure gradient $(-dP/dz)_F$ for R114/R113 mixtures is compared with the previous results for pure refrigerants R11 and R13 (Honda et al., 1989) in terms of the Lockhart and Martinelli parameters (1949)

$$\phi_v = \{(-dP/dz)_F / (-dP/dz)_v\}^{0.5} \quad (14)$$

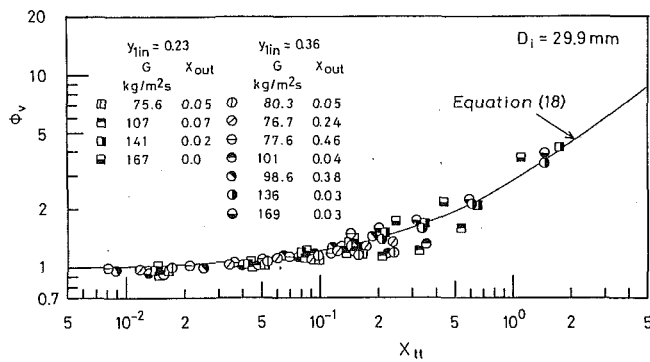
and

$$X_H = \{(-dP/dz)_l / (-dP/dz)_v\}^{0.5} \quad (15)$$

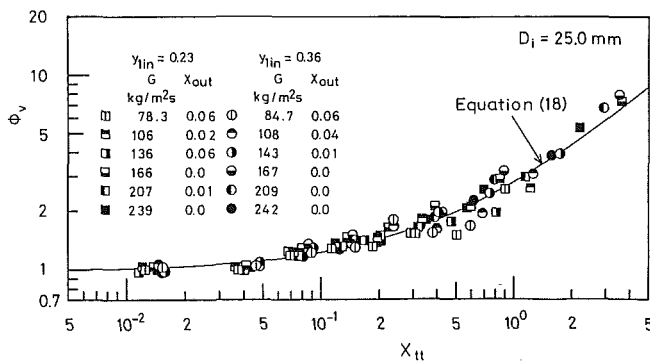
The single-phase pressure gradients $(-dP/dz)_l$ and $(-dP/dz)_v$ are obtained from

$$(-dP/dz)_{l,v} = (2c_{f0}\rho u^2)_{l,v} / (D_i - D_o) \quad (16)$$

where c_{f0} is the friction factor without suction and u is the axial velocity. The c_{f0} value is obtained experimentally using a superheated R113 vapor. The results are shown in Fig. 11 on the coordinates of c_{f0} versus the Reynolds number $Re = u(D_i - D_o)/\nu$, along with the correlation for a smooth annulus (Kays and Perkins, 1985) and the previous correlation (Honda et al., 1989). The present data exhibit a clear dependence on D_i , i.e., the c_{f0} values for smaller D_i are higher than those for larger D_i . The results are in line with the trends of turbulent



(a)



(b)

Fig. 12 Comparison of frictional pressure gradient data for R114/R113 with the prediction of Eq. (18): (a) $D_i = 29.9$ mm; (b) $D_i = 25.0$ mm

single-phase flow in rough tubes, and are correlated by the following expressions:

For the tube with $D_i = 29.9$ mm

$$\begin{aligned} c_{f0} &= 0.2\text{Re}^{-0.2} & \text{for } \text{Re} < 5.2 \times 10^4 \\ c_{f0} &= 0.023 & \text{for } \text{Re} \geq 5.2 \times 10^4 \end{aligned} \quad (17a)$$

For the tube with $D_i = 25.0$ mm

$$\begin{aligned} c_{f0} &= 0.2\text{Re}^{-0.2} & \text{for } \text{Re} < 5.2 \times 10^3 \\ c_{f0} &= 0.036 & \text{for } \text{Re} \geq 5.2 \times 10^3 \end{aligned} \quad (17b)$$

Figure 12 compares the frictional pressure gradient data for R114/R113 condensing flow with the previous correlation (Honda et al., 1989).

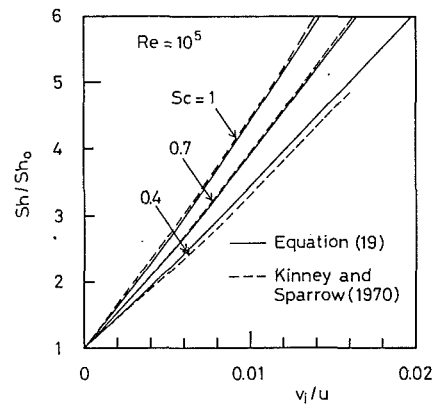
$$\phi_v = 1 + 1.8X_{tt}^{0.9} \quad (18)$$

The R114/R113 data are correlated by Eq. (18) to a mean absolute deviation of 9.5 percent, although the present inner tube has a larger fin crest distance than the previous tube.

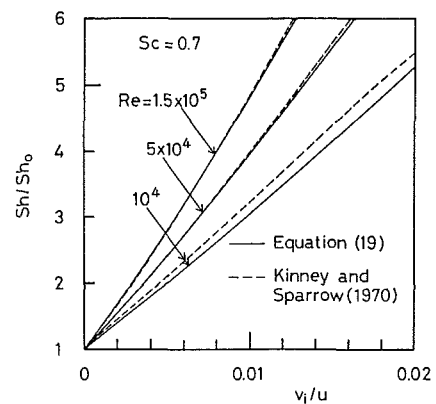
Vapor Phase Mass Transfer. On the basis of the previous results for turbulent single-phase flow in a tube with and without surface suction, we develop an approximate expression for turbulent mass transfer and extend it to the case of condensation of nonazeotropic binary vapor mixture in an annulus. The functional form of the expression is assumed as

$$\frac{\text{Sh}}{\text{Sh}_0} = \frac{1}{1 + a\gamma^b \text{Sc}^c} + \frac{v_i \text{ReSc}}{u \text{Sh}_0} \quad (19)$$

where $\text{Sh} = \beta_n D / \mathcal{D}$ and Sh_0 are the Sherwood numbers with and without suction, respectively, $v_i = m/\rho$ is the suction velocity, $\text{Re} = uD/\nu$, D is the tube inner diameter, Sc is the Schmidt number, γ is the suction parameter, a , b , and c are positive constants to be determined. The parameter γ is as-



(a)



(b)

Fig. 13 Comparison of Sh/Sh_0 ratio between prediction of Eq. (19) and numerical result obtained by Kinney and Sparrow (1970): (a) $\text{Re} = 10^5$; (b) $\text{Sc} = 0.7$

summed with reference to the Reynolds flux model (Wallis, 1968) as

$$\gamma = v_i / (uc_{f0}) \quad (20)$$

Excepting the definition of γ , Eq. (19) is identical in form to the expression for the laminar forced convection condensation on a flat plate obtained by Rose (1980).

The values of a , b , and c are determined on the basis of the numerical results for turbulent single phase flow in a smooth tube with suction obtained by Kinney and Sparrow (1970). Since the numerical solutions of Sh_0 and c_{f0} are not shown in their paper, these values are respectively calculated from the following expressions for fully developed turbulent flow in a smooth tube:

$$\text{Sh}_0 = \frac{(c_{f0}/2)(\text{Re} - 1000)\text{Sc}}{1 + 12.7\sqrt{c_{f0}/2}(\text{Sc}^{2/3} - 1)} \quad (21)$$

$$c_{f0} = 1 / (3.64 \log_{10} \text{Re} - 3.28)^2 \quad (22)$$

Equation (21) is derived using the analogy between heat and mass transfer from the heat transfer correlation proposed by Gnielinski (1976). Equation (22) was proposed by Petukhov (1970).

Figure 13 shows the comparison of the numerical results with the prediction of Eq. (19), where the values of a , b , and c have been obtained after some trials as 0.5, 1.0, and 1.0, respectively. An agreement of within ± 4 percent is found between the numerical results and the prediction, except in the region $v_i/u \geq 0.005$ at $\text{Re} = 10^4$.

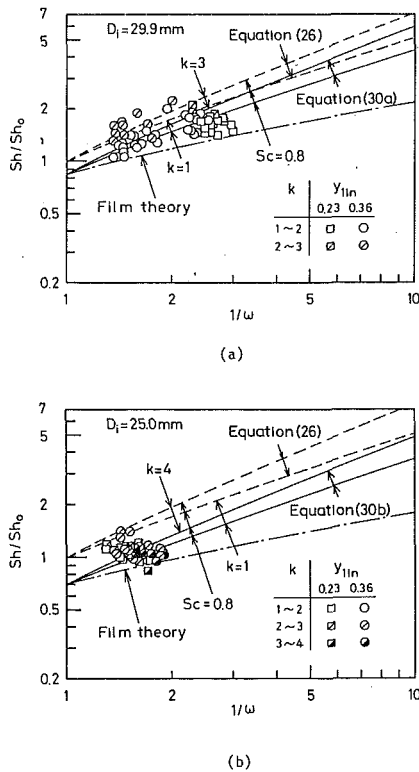


Fig. 14 Plot of vapor phase mass transfer data on the coordinates of Sh/Sh_0 versus $1/\omega$: (a) $D_i = 29.9$ mm; (b) $D_i = 25.0$ mm

Turning now to the condensation problem, the condition of mass conservation at the condensate surface gives

$$\frac{v_i}{u_w} = \frac{(1-\omega)Sh}{ReSc} \quad (23)$$

Substituting Eqs. (20), (23), and the values of a , b , c into Eq. (19) yields

$$Sh = \frac{Rec_{f0} \{ [1 + 2Sh_0(1/\omega - 1)/(Rec_{f0})]^{0.5} - 1 \}}{(1-\omega)} \quad (24)$$

In order to compare the prediction of Eq. (24) with the present data, the c_{f0} value and an expression for Sh_0 are required. As illustrated in Figs. 2 and 5, the wire fins are wound onto the inner tube and the condensate is formed both on the fins and on the inner tube surface. In addition, the characteristics of single-phase flow are similar in trend to that in a rough tube as shown in Fig. 11. Therefore, it is sufficiently accurate to assume that the vapor phase mass transfer characteristics in the annuli are similar to those in a rough tube with equivalent diameter $(D_i - D_r)$. The following expression is adopted for the expression of Sh_0 , since no available data exist for the present annuli:

$$Sh_0 = (c_{f0}/2)ReSc/k \quad (25)$$

where $k = 1 + \psi \sqrt{c_{f0}/2}$, $\psi = 5.19 \{ Re \sqrt{c_{f0}/2} \epsilon_s / (D_i - D_r) \}^{0.22} Sc^{0.44} - 8.48$, $\epsilon_s / (D_i - D_r) = \exp \{ [3.0 - 1/\sqrt{c_{f0}/2}] / 2.5 \}$. Equation (25) is derived using the analogy between heat and mass transfer from the empirical equation of turbulent heat transfer in rough tubes obtained by Dipprey and Sabersky (1963). Combining Eqs. (24) and (25) yields

$$\frac{Sh}{Sh_0} = \frac{2k \{ [1 + Sc(1/\omega - 1)/k]^{0.5} - 1 \}}{(1-\omega)Sc} \quad (26)$$

According to Wallis (1970), the suction effect on the c_f value is expressed satisfactorily by

$$c_f = c_{f0} + (v_i/u_w) \quad (27)$$

The c_f value for the condensing flow is obtained by substituting the measured $(-dP/dz)_F$ into the defining equation

$$(-dP/dz)_F = 2c_{f0} \rho_v u_w^2 / (D_i - D_r) \quad (28)$$

Then, the c_{f0} is obtained from Eq. (27).

Figure 14 shows the vapor phase mass transfer data plotted on the coordinates of Sh/Sh_0 versus $1/\omega$, where Sh is defined as

$$Sh = \beta_n (D_i - D_r) / \mathcal{D} \quad (29)$$

It is seen from Fig. 14(a) that the Sh/Sh_0 ratio for the same range of k increases with the increase of $1/\omega$, and the Sh/Sh_0 ratio at the same value of $1/\omega$ is larger for larger k . As is evident from the definition of the parameter k , the larger k value corresponds to the larger values of u and c_{f0} . Dashed lines given by Eq. (26) for the extreme experimental values of k are also shown in Fig. 14. The data show a good agreement with Eq. (26) in trend, but show a dependence on $(D_i - D_r)$ not predicted by Eq. (26). In addition, the data take lower values than the prediction of Eq. (26) by about 15 and 30 percent for $D_i = 29.9$ mm and 25.0 mm, respectively. A possible source of these discrepancies includes the difference in the property of surface roughness between the condensate film formed both on the fins and on the inner tube and the granular close-packed roughness used by Dipprey and Sabersky (1963). With reference to the functional form of Eq. (26), the present data are correlated by the following expressions to a mean absolute deviation of 13.5 percent.

For the tube with $D_i = 29.9$ mm

$$\frac{Sh}{Sh_0} = \frac{1.7k \{ [1 + Sc(1/\omega - 1)/k]^{0.5} - 1 \}}{(1-\omega)Sc} \quad (30a)$$

For the tube with $D_i = 25.0$ mm

$$\frac{Sh}{Sh_0} = \frac{1.4k \{ [1 + Sc(1/\omega - 1)/k]^{0.5} - 1 \}}{(1-\omega)Sc} \quad (30b)$$

For comparison, chain lines given by the well-known film theory (Bird et al., 1960) are shown so as to agree with the prediction of Eq. (30) at $1/\omega = 1$. As seen from Fig. 14, the film theory gives lower Sh/Sh_0 values than both the measurement and the prediction of Eq. (30), with the differences increasing with $1/\omega$.

Heat Transfer. In the previous paper (Honda et al., 1989), q_n is divided into two parts as

$$q_n = q_{nf} + q_{nr} \quad (31)$$

where q_{nf} and q_{nr} are the components of the heat flux on the fin surface and on the fin root tube surface, respectively. The q_{nf} is related to the heat transfer coefficient of the condensate film on the fin surface, α_{f0} , as

$$q_{nf} = (T_i - T_w) / \{ p_f p_c (1/\pi d_f l_f \alpha_{f0} + R_s) \} \quad (32)$$

The q_{nr} is related to the heat transfer coefficient of the condensate film on the fin root tube surface, α_{r0} , as

$$q_{nr} = \alpha_{r0} (T_i - T_w) (1 - A_f) \quad (33)$$

Equation (9) for α_{r0} is obtained by substituting Eqs. (32) and (33) into Eq. (31). The empirical expression for α_{r0} (Honda et al., 1989) was obtained by combining the expressions for the two extreme condensation regimes, i.e., the surface tension controlled condensation and vapor shear controlled condensation regimes. The α_{r0} was, on the other hand, estimated by

$$\alpha_{r0} = (\alpha_{r0}^4 + \alpha_{r0}^4)^{0.25} \quad (34)$$

where α_{r0} and α_{r0} are the heat transfer coefficients in the gravity controlled and vapor shear controlled regimes, respectively. The Nusselt (1916) and the Cavallini et al. (1982) equations were adopted for the expressions of α_{r0} and α_{r0} , respectively.

For the present work, Eq. (34) is adopted for the expression of α_{r0} , since a data reduction as described by Honda et al. (1989) showed that the relation $q_{nf} \gg q_{nr}$ also holds. The measured α_{r0} values for pure R113 were higher than the previous prediction by about 7 and 20 percent for the surface tension and vapor shear controlled regimes, respectively. Therefore, the previous expression for α_{r0} is modified to obtain a more reliable estimate of T_i for R114/R113 mixtures. This modification may be justified because the present and previous inner tubes have different values of Δ . The new expression for α_{r0} obtained from the present pure R113 data is written as

$$\text{Nu}_f = \alpha_{r0} d_f / \lambda_i$$

$$= [(\text{Nu}_{fs}^4 + \text{Nu}_{fv}^4) / \{1 + 55(2D_r/D_i - 1)X_{it}^2\}]^{0.25} \quad (35)$$

where

$$\text{Nu}_{fs} = 0.6 S_d^{0.25} \quad (36a)$$

$$\text{Nu}_{fv} = 0.12(1+B)^{1/3} (u_v d_f / \nu_i)^{0.5}$$

$$\times \{1 + 6.5 \times 10^{-5} (1 + 4 \times 10^5 \bar{h}_f^6 / C^3)\}^{0.25} \quad (36b)$$

$S_d = \sigma i_{fg} d_f / \lambda_i \nu_i (T_i - T_j)$, $B = \mu_i i_{fg} (\rho_v \mu_v / \rho_i \mu_i)^{0.5} / \lambda_i (T_i - T_j)$, $C = (\rho_i / \rho_v)^{0.5} \text{Re}_f^{1/6} (g \nu_i)^{1/3} / u_v$, $\bar{h}_f = h_f / (D_i - D_r)$, $\text{Re}_f = G D_r (1 - X) \{ (D_i / D_r)^2 - 1 \} / \mu_i$, and g is the gravitational acceleration. The Nu_{fs} and Nu_{fv} in Eq. (35) represent the effects of surface tension and vapor shear acting on the condensate film on the fin surface, respectively. The denominator of the right-hand side of Eq. (35) accounts for the effect of submergence of the inner tube in the condensate pool. The measured α_{r0} for the pure R113 condensing flow are correlated by Eq. (9) to a mean absolute deviation of 7.8 percent.

For given conditions of vapor mixture and tube wall, the values of T_i and q_n are obtained by executing the following procedures:

(i) Assume T_i , calculate x_{1i} and y_{1i} at T_i using the temperature-composition diagram, then calculate ω .

(ii) Calculate α_{n0} from Eq. (9) by using Eqs. (34) and (35), then calculate q_n from Eq. (8b).

(iii) Calculate c_f from Eqs. (14) ~ (18) and (28), then obtain c_{r0} from Eq. (27).

(iv) Substitute Eq. (25) and the values of ω and c_{r0} into Eq. (30) to obtain Sh , then calculate β_n and m_n using Eqs. (29) and (7), respectively.

(v) Calculate q_n from Eq. (8a).

(vi) Repeat procedures (i) ~ (v) until the q_n values obtained in (ii) and (v) agree with each other to within 0.01 percent.

The α_n value, if necessary, is calculated from Eq. (6) after the converged solution is obtained. In applying the expressions for α_{r0} and α_{r0} to R114/R113 mixtures, i_{fg} involved in Eqs. (34) and (35) should be replaced with $x_{1i}(i_{fg})_1 + (1 - x_{1i})(i_{fg})_2$.

Results are shown in Fig. 15 on the coordinates of $(\alpha_n)_{\text{mea}}$ and $(\alpha_n)_{\text{pre}}$, where the former and the latter show the measured and predicted α_n values, respectively. As may be seen from Fig. 15, the present model gives satisfactory prediction, although the present model underpredicts the α_n value at low X regimes for $D_i = 25.0$ mm. All the data plotted in Fig. 15 are correlated to a mean absolute deviation of 14.3 percent.

Conclusions

Experiments have been performed during condensation of R114/R113 mixtures in horizontal annuli with an enhanced inner tube. A consideration has been given for the mass transfer resistance in the vapor phase both experimentally and theoretically. Methods for predicting the condensation heat transfer and frictional pressure gradient have also been proposed. The conclusions are as follows:

1 The frictional pressure gradient data for R114/R113 mixtures have been correlated fairly well by using the Lockhart and Martinelli parameters. The measured data have been correlated by Eq. (18) to a mean absolute deviation of 9.5 percent.

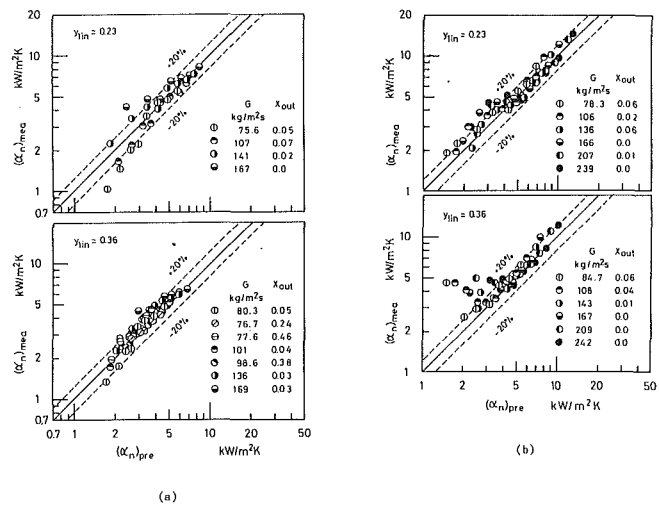


Fig. 15 Comparison of measured and predicted heat transfer coefficients: (a) $D_i = 29.9$ mm; (b) $D_i = 25.0$ mm

2 An expression for the heat transfer coefficient of the condensate film on the fin surface has been obtained. The present data for pure R113 have been correlated by Eq. (9) to a mean absolute deviation of 7.8 percent.

3 An expression for the vapor phase mass transfer coefficient has been derived on the basis of the previous results for turbulent single-phase flow in tubes with and without suction. The present data have been correlated by Eq. (30) to a mean absolute deviation of 13.5 percent.

4 For given conditions of the vapor mixture and tube wall, the condensation heat transfer rate is obtained by simultaneously solving Eqs. (8a) and (8b). The measured heat transfer coefficients for R114/R113 mixtures have been correlated to a mean absolute deviation of 14.3 percent.

Acknowledgments

Financial support for the present work from the Japanese Association of Refrigeration, through a Grant-in-Aid for research and survey of heat pump technology, is gratefully acknowledged. We appreciate very much the constructive suggestions that were made by the reviewers of the original manuscript. We acknowledge Mr. Nakata of Daikin Industries Ltd. for providing the refrigerants and the inner tube, and also Messrs. T. Imai, Y. Akashi, and K. Okabe of Okayama University for fabrication of the experimental apparatus and the measurements.

References

- Bell, K. J., 1988, "Two-Phase Flow Regime Considerations in Condenser and Vaporizer Design," *Int. Comm. Heat Mass Transfer*, Vol. 15, pp. 429-448.
- Bird, R. B., Stewart, W. E., and Lightfoot, E. N., 1960, *Transport Phenomena*, Wiley, New York, pp. 658-668.
- Breber, G., 1988, "Intube Condensation," in: *Heat Transfer Equipment Design*, R. K. Shah, E. C. Subbarao, and R. A. Mashelkar, eds., Hemisphere Publishing Corp., Washington, DC, pp. 451-473.
- Butterworth, D., 1983, "Condensation of Vapor Mixtures," in: *Heat Exchanger Design Handbook*, E. U. Schlunder, editor-in-chief, Hemisphere Publishing Corp., Vol. 2, Section 6.
- Cavallini, A., Frizzarin, S., and Rossetto, L., 1982, "Condensation of Refrigerants Inside Annuli," *Proc. 7th Int. Heat Transfer Conf.*, Vol. 5, pp. 45-51.
- Chen, Z.-S., Fujii, T., Fujii, M., and Ge, X.-S., 1987, "An Equation for Predicting Thermal Conductivity of Binary Liquid Mixtures," *Reports of Research Institute of Industrial Science*, Kyushu University, No. 82, pp. 159-171.
- Dipprey, D. F., and Sabersky, R. H., 1963, "Heat and Momentum Transfer in Smooth and Rough Tubes at Various Prandtl Numbers," *Int. J. Heat Mass Transfer*, Vol. 6, pp. 329-353.
- Fuller, E. N., Schettler, P. D., and Giddings, J. C., 1966, "A New Method for Predicting of Binary Diffusion Coefficients," *Ind. Engng. Chem.*, Vol. 58, pp. 18-27.

- Gnielinski, V., 1976, "New Correlations for Heat and Mass Transfer in Turbulent Pipe and Channel Flow," *Int. Chem. Eng.*, Vol. 16, pp. 359-368.
- Hijikata, K., Himeno, N., and Nakabeppu, O., 1989, "Condensation of a Binary Mixture of Vapors in a Vertical Tube," *Trans. JSME*, Ser. B, Vol. 55, pp. 3813-3189 [in Japanese].
- Honda, H., Nozu, Sh., Matsuoka, Y., Aoyama, T., and Nakata, H., 1989, "Condensation of Refrigerants R11 and R113 in the Annuli of Horizontal Double-Tube Condensation With an Enhanced Inner Tube," *Experimental Thermal and Fluid Science*, Vol. 2, pp. 173-182.
- JSME, 1982, *JSME Data Book; Thermophysical Properties of Fluids*, Tokyo.
- Kawano, Sh., 1990, "Condensation of Binary Mixture in Vertical Condensers," *Proc. of the 2nd Int. Symp. on Condensers and Condensation*, pp. 49-58.
- Kays, W. M., and Perkins, H. C., 1985, "Forced Convection, Internal Flows in Ducts," in *Handbook of Heat Transfer Fundamentals*, W. M. Rohsenow, J. P. Hartnett, and E. N. Ganic, eds., McGraw-Hill, pp. 71-7.180.
- Kinney, R. B., and Sparrow, E. M., 1970, "Turbulent Flow, Heat Transfer, and Mass Transfer in a Tube With Surface Suction," *ASME JOURNAL OF HEAT TRANSFER*, Vol. 92, pp. 117-125.
- Koyama, S., Miyara, A., Takamatsu, H., and Fujii, T., 1990, "Condensation Heat Transfer of Binary Refrigerant Mixtures of R-22 and R-1124 Inside a Horizontal Tube With Internal Spiral Grooves," *Int. J. Refrigeration*, Vol. 13, pp. 256-263.
- Lockhart, R. W., and Martinelli, R. C., 1949, "Proposed Correlation of Data for Isothermal Two-Phase, Two-Component Flow in Pipes," *Chem. Engng. Prog.*, Vol. 45, pp. 39-48.
- Mochizuki, S., Yagi, Y., Tadano, R., and Yang, W.-J., 1984, "Convective Filmwise Condensation of Nonazeotropic Binary Mixtures in a Vertical Tube," *ASME JOURNAL OF HEAT TRANSFER*, Vol. 106, pp. 531-538.
- Mochizuki, S., Inoue, T., and Tominaga, M., 1988, "Condensation of Non-azeotropic Binary Mixtures in a Horizontal Tube," *Trans. JSME*, Ser. B, Vol. 54, pp. 1796-1801 [in Japanese].
- Nusselt, W., 1916, "Die Oberflächencondensation des Wasserdampfes," *Z. Ver. Dt. Ing.*, Vol. 60, pp. 541-546, pp. 569-575.
- Petukhov, B. S., 1970, "Heat Transfer and Friction in Turbulent Pipe Flow With Variable Physical Properties," in: *Advances in Heat Transfer*, J. P. Hartnett and T. F. Irvine, eds., pp. 504-564, Academic Press, New York.
- Reid, R. C., Prausnitz, J. M., and Sherwood, T. K., 1977, *The Properties of Gases and Liquids*, 3rd ed., McGraw-Hill, New York.
- Rose, J. W., 1980, "Approximate Equations for Forced-Convection Condensation in the Presence of a Non-condensing Gas on a Flat Plate and Horizontal Cylinder," *Int. J. Heat Mass Transfer*, Vol. 23, pp. 539-546.
- Shizuya, M., Itoh, M., and Hijikata, K., 1990, "Condensation of Nonazeotropic Binary Refrigerant Mixtures Including R22 as a More Volatile Component Inside a Horizontal Tube," *Proc. 2nd Int. Symp. on Condensers and Condensation*, pp. 27-38.
- Taitel, Y., and Dukler, A. E., 1976, "A Model for Predicting Flow Regime Transitions in Horizontal and Near Horizontal Gas-Liquid Flow," *AIChE J.*, Vol. 22, pp. 47-55.
- Wallis, G. B., 1968, "Use of the Reynolds Flux Concept for Analysing One-Dimensional Two-Phase Flow," *Int. J. Heat Mass Transfer*, Vol. 11, pp. 445-458.
- Wallis, G. B., 1970, discussion in Kinney and Sparrow (1970).
- Wilke, C. R., 1950, "A Viscosity Equation for Gas Mixtures," *J. Chem. Phys.*, Vol. 18, pp. 517-519.

Surface Roughness and Its Effects on the Heat Transfer Mechanism in Spray Cooling

M. R. Pais

L. C. Chow

Department of Mechanical Engineering,
University of Kentucky,
Lexington, KY 40506

E. T. Mahefkey

Aero Propulsion and Power Laboratory,
Wright Research and Development Center,
Wright-Patterson Air Force Base, OH 45433

In the spray cooling of a heated surface, variations in the surface texture influence the flow field, altering the maximum liquid film thickness, the bubble diameter, vapor entrapment, bubble departure characteristics, and the ability to transfer heat. A new method for determining and designating the surface texture is proposed, and the effects of surface roughness on evaporation/nucleation in the spray cooling flow field studied. A one-dimensional Fourier analysis is applied to determine experimentally the surface profile of a surface polished with emery paper covering a spectrum of grit sizes between 0.3 to 22 μm . Heat transfer measurements for liquid flow rates between 1 to 5 l/h and air flow rates between 0.1 to 0.4 l/s are presented. Maximum heat fluxes of 1200 W/cm² for the 0.3 μm surface at very low superheats were obtained.

Introduction

Current heat transfer enhancement research has been directed toward phase-change processes. Such processes take advantage of the fact that a pure substance will absorb or release heat during phase change at a fixed temperature. The exchange of this latent heat is feasible at low degrees of superheat, and depending on the substance, the magnitude can be far greater than the corresponding sensible heat exchange for the same temperature difference.

In the conventional methods of forced convective and radiative heat transfer, high heat fluxes can be achieved. However, such modes entail excessively high surface temperatures, which could be detrimental to the system. Modern computer technology is making possible the manufacture of microminaturized circuits of ever-increasing density. Such compactness has also resulted in an increase in the heat dissipation density. Similar advances in jet engines, rocket engine nozzles, and the nuclear industry are increasing demands on low-superheat, high-heat-flux technology. The coolant used in this study is water for simplicity of method. However, the need to perform experiments with highly wetting dielectric fluids for cooling of microelectronics is recognized.

Spray cooling (Choi and Yao, 1987; Goldstein et al., 1967; Pais et al., 1989b) in particular has proven to be far more efficient than the conventional pool boiling method of heat removal (Cole, 1974; Berenson, 1962; Kurihara and Myers, 1960; Webb, 1981). This is partially because the hydrodynamic instabilities inherent in pool boiling in the region of the critical heat flux (CHF) are precluded by the deposition of only a thin film of liquid (Parizhskiy, 1972; Kopchikov et al., 1969) on the surface in spray cooling. The objective of this work is to study the effect of surface roughness on heat transfer under conditions of spray cooling.

Figure 1 illustrates the physics of evaporation/boiling taking place within a thin film of liquid deposited on a hot surface by droplet impingement assisted by an external gas stagnation flow field. If the film is ultra-thin (of the order of a micron or less in the case of water), then the heat can be conducted through the liquid to the surface, where the liquid will evaporate directly into the ambient. From thermodynamics, at a specified temperature, a pure liquid can exist in equilibrium

contact with its vapor at but one pressure, its vapor pressure. If by some means the vapor pressure is reduced in the immediate vicinity of the surface, then the phase change temperature will also decrease. In the case of water, for a 30 percent decrease in vapor pressure, the phase-change temperature is reduced by 10 percent (Mark's, 1978).

An air/droplet impingement flow field on the surface produced by an air atomizing nozzle is illustrated in Fig. 1. The air jet on impinging the surface forms a stagnation point flow field. The drops do not follow the air streamlines close to the surface but follow straight paths due to their relatively higher inertia. These drops impinge on the hot surface to form flat disks, whose thickness is much smaller than the diameter of the drop (Jussim, 1988). Simultaneously, the stagnation flow field spreads the droplet/disks further, through shear forces, to form a thin film on the surface. Any vapor that emanates from the hot surface due to evaporation is instantly swept away. Hence, the effect of the stagnation flow field is to enhance evaporation even further, by clearing away the vapor and reducing the partial vapor pressure in the immediate vicinity of the liquid surface. Thus, the possibility of phase change, at or below 100°C, i.e., with "negative" superheats (based on 100°C at 1 atm system pressure) exists.

Concurrently, if the superheat is sufficient, nucleation will occur at the solid-liquid interface, the radius above which a bubble will survive and grow being given by (Defay et al., 1966),

$$r_m'' = \frac{2\sigma v'' T_s}{\Gamma(T_w - T_s)} \quad (1)$$

In the case of nucleate boiling, roughness plays a governing role in the enhancement of heat removal. Primarily, the cavities created by the roughness elements serve as regions of vapor germination and entrapment (see Fig. 1). When a growing bubble penetrates through the liquid film into the ambient and bursts, liquid flows in to take the place formerly occupied by the vapor. The geometry of the cavity and wettability of the surface, determine whether vapor will be trapped in the cavity (Bankoff, 1958). If the trapped vapor bubble has a large radius of curvature then the degree of superheat required for nucleation is reduced. This not only enhances heat removal in the form of latent heat, but also maintains surface temperatures near saturation conditions, the degree of superheat being a function of the roughness spacing λ (Griffith and Wallis, 1960). Lack of this facility will require a higher surface temperature

Contributed by the Heat Transfer Division for publication in the JOURNAL OF HEAT TRANSFER. Manuscript received by the Heat Transfer Division August 1990; revision received July 25, 1991. Keywords: Boiling, Phase-Change Phenomena, Sprays/Droplets.

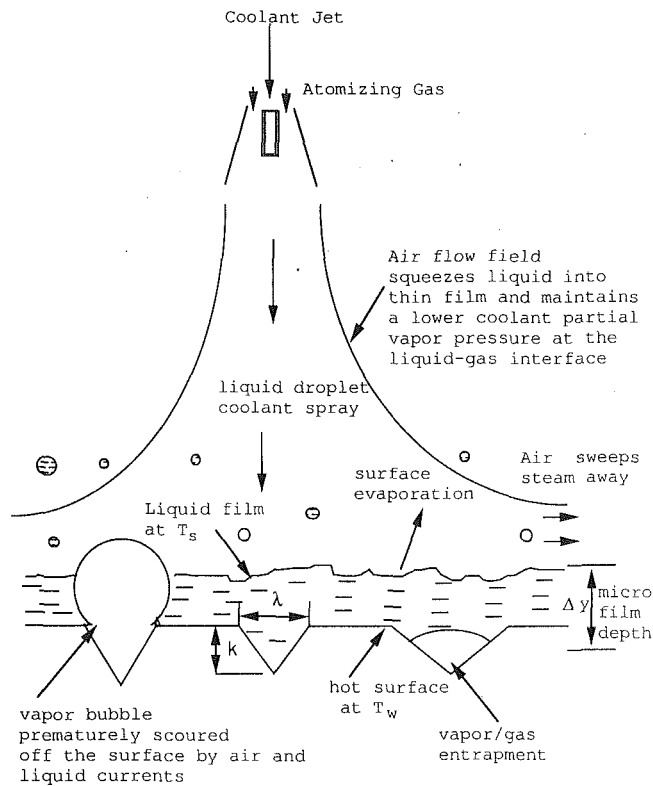


Fig. 1 Spray dynamics

for nucleation. Secondly, the heat flux is also increased due to the increase in surface area subtended by the roughness elements (see Fig. 2). Here, the smaller elements act as nucleation sites, and provide a sizable increase in area, as compared to the larger undulation of the overall surface, over which the smaller elements are distributed.

The density of nucleation sites and heat transfer depends on the density and distribution of the roughness elements, i.e., primarily on λ , the space between the roughness elements (Pais and Singh, 1988; Webb, 1981). Consider nucleation on a rough wall; as the density of the nucleation sites increases, at first, the heat flux increases as would be expected. However, as the nucleation sites get closer, the growth of bubbles created by neighboring sites will cause the bubbles to combine to form large vapor films with dry vapor stems and hot spots (Dhir and Tung, 1988; Mesler, 1976; Hospeti and Mesler, 1969), which are detrimental in the CHF region. Hence, there may exist a roughness configuration that produces the maximum heat flux at the lowest superheat, the spacing in this being far more than that for a densely packed surface.

When a bubble forms, a thin microlayer of liquid that lies between vapor and the hot surface (Cooper and Merry, 1973) governs the rate of evaporation into the bubble, and in the case of water, takes between 50 μ s and 2 ms to disappear (Yu and Mesler, 1977). The bubble grows further by evaporation through its walls, heat being conducted from the hot surface through the surrounding liquid. This latter process (≥ 10 ms) is considerably slower than direct evaporation of the microlayer. Consequently, heat removal can be further enhanced if the microlayer can be continuously maintained. This is realized if the bubble is removed the instant its microlayer evaporates, making available the nucleation site for a new bubble to form on a fresh microlayer (Mesler, 1976).

In spray cooling, the thermal boundary layer is limited to the thickness of the liquid film. The bubble on emerging from the cavity and growing above the liquid film, see Fig. 1, will be exposed (within the liquid film and vapor above) to temperature gradients and the forces of the external flow field. The bubble temperature, being higher, will induce its walls to evaporate into the ambient. Second, the temperature gradients will make it unstable (Faneuff et al., 1958; Hsu, 1962). Third, the external droplet/ambient flow field may also assist in the early departure/breakup of the bubble. Thus, the bubble breaks up before reaching its minimum radius required by the cavity size; i.e., the superheat required, as given by Eq. (1), is lower (Griffith and Wallis, 1960).

Roughness Definition

The classical definition of roughness strives to describe surface irregularities quantitatively and qualitatively in a number of ways (Mark's, 1978): (a) the roughness-height index value, (b) waviness, (c) lay. Current numerical and experimental methods utilize a variety of geometry forms (pyramids, grooves, sand grains) in simulating roughness. Owing to the large number of parameters describing such forms, the precise measurement and definition of irregularly shaped surfaces is further complicated. Hence, there is a need for improved methods of determining, designating, and controlling the surface texture. Texture can be qualitatively described by its coarseness, which is related to the spatial repetition period of the local structure. If the surface is composed of a combination of a number of elementary surfaces superimposed on one another, see Fig. 2, then a one-dimensional Fourier analysis can be applied. Several studies (Lendaris and Stanley, 1970; Oppenheim and Schafer, 1975; Pais, 1987; Rosenfeld, 1962) have considered textural analysis in terms of the Fourier spectrum of a region.

Fourier Analysis

A surface array is considered to be a linear array of N altitude samples, see Fig. 2, described by the function $f(x)$ over the surface coordinates ($-L < x < L$). The coefficients of the one-

Nomenclature

a, b = Fourier coefficients
 A = surface area
 d = diameter of drop
 D = apparent diameter of drop
 f = surface profile function
 H = complex Fourier coefficients
 k = roughness height
 K = thermal conductivity
 L = half signal interval
 n = Fourier frequency index
 N = total number of samples
 p = pressure

q = heat flux
 r = radius
 T = temperature
 w = uncertainty
 X, Y = Cartesian coordinates
 Γ = latent heat of vaporization
 Δ = difference
 λ = roughness spacing
 ν = specific volume
 σ = surface tension
 Φ = angle of contact

Superscript

" = vapor phase

Subscripts

Co = constantan
 Cu = copper
 m = minimum equilibrium bubble radius
 q = heat flux
 s = saturation
 $Surf$ = surface
 T = temperature
 w = wall

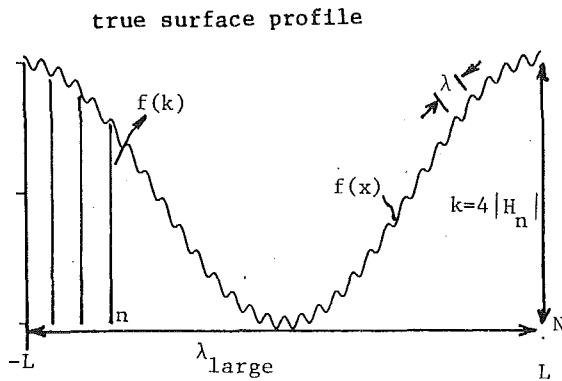


Fig. 2 Surface line profile

dimensional Fourier transform, $H(n)$ are the complex Fourier coefficients that specify the amplitude of the basis functions (Lighthill, 1962; Andrews, 1970). The surface can then be written in the Fourier series representation as (Pais and Singh, 1988),

$$f(x) = a_0 + \sum_{n=1}^{N/2-1} \left\{ a_n \cos \frac{n\pi x}{L} + b_n \sin \frac{n\pi x}{L} \right\} \quad (2)$$

$$H(n) = (a_n + ib_n)/2 \quad (2a)$$

The parameter n that belongs to sets of functions of the form given in Eq. (2) is interpreted as the number of complete cycles generated by a sinusoidal function per length $2L$. Fourier series in this sense can be used for analyzing oscillations or waveforms periodic in space, or on a restricted interval (Lighthill, 1962; Oppenheim and Schaffer, 1975).

When experimental studies have to be performed on rough surfaces, difficulties arise in fabricating a surface that conform to the rough surface profile. To circumvent this problem typically a smooth profile is calculated by averaging a number of the rough cross sections. The roughness is incorporated into the model by superimposing roughness elements of varying geometries and size. Fourier analysis extracts the characteristic elements of the surface to give a spectrum of elements of fixed geometry and spacing, which can be selectively applied to an equivalent smooth profile taking the local flow field into consideration.

To specify the size of a roughness pattern, the typical dimensions of k and λ are used. The dimension k can be represented by double the amplitude of a sinusoidal function (equivalent to the total peak-to-valley distance). The width/spacing, $\lambda_n = 2L/n$, is given by the inverse of the frequency of the function; see Fig. 2. The surface is described using N points in the physical plane, and $N/2$ points in the Fourier domain. Depending on the superheat, wetting characteristics, and flow field, cavities of certain geometry and size will play a predominant role. By selectively choosing the k and λ values of cavities that determine the flow field, and discarding the other k and λ description as ineffectual and redundant, a further reduction in the data can be attained (Pais, 1987). Hence, even though the whole surface is described by $N/2$ (k, λ) points in Fourier domain, only a few such points are necessary to describe the surface with respect to its heat transfer characteristics. The Fourier analysis is implemented using a fast Fourier transform (FFT) algorithm (Andrews, 1970).

Application of Fourier analysis to define such surface profiles provides a twofold advantage:

(a) the large amount of discrete surface coordinate data is described using mathematical relations that are simple and require far less memory, allowing a sizable data reduction (Pais, 1987; Pratt, 1978); and

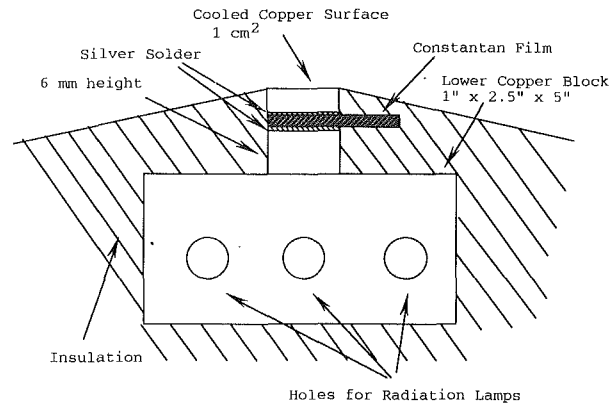


Fig. 3 Temperature measurement setup

(b) the amplitude and frequency of the sinusoidal functions are analogous to the properties of the classical definition of roughness.

Three surface roughnesses were studied. The surface was polished successively with polishing abrasive paper and lapping compound of size 22, 14, and $0.3 \mu\text{m}$, respectively. Owing to the bulkiness of the heater block (see Experimental Description), sample film surfaces were prepared, care being taken to expose these samples to the same heat treatment conditions imposed on the experimental surface. The surfaces were polished only in one direction, given it a definite "lay" (Mark's, 1978). Next surface coordinates were obtained using a diamond tip profilometer with a resolution of $0.1 \mu\text{m}$. The surface was mounted on a vibration-free table and scanned in a direction perpendicular to the "lay," to obtain a number of profiles, which were digitized. Fourier analysis were performed on these surface data.

Experimental Description

Owing to the large thermal gradients required to drive large heat fluxes through any surface ($> 1500 \text{ W/cm}^2$), care must be taken in the design of the apparatus so as to arrive at temperatures within the body that maintain the physical and chemical integrity of the system.

With reference to Fig. 3, high-power (40 W/cm) tungsten-quartz tubular heat lamps are inserted into cylindrical chambers within the lower cuboid copper heater block of size $25 \text{ mm} \times 64 \text{ mm} \times 127 \text{ mm}$. This system, i.e., the tungsten filament, which can be viewed as a line element radiative heat source (temperature = 2200°C , $0.5 \leq \lambda \leq 4.5 \mu\text{m}$), enclosed within a cylinder closed at its ends, constitutes a black body. Thus, all the radiative energy is absorbed into the copper block. This heat is then conducted through the pyramidal construction to the surface to be cooled. The design is such as to arrive at a uniform temperature on the surface to be cooled. These radiation lamps have a fast thermal response (99 percent rated power within 3 s), can withstand high temperatures by virtue of their sealed quartz envelope, and provide a high radiative heat flux. Depending on the heat flux required, a multiple number of these lamps can be used in this setup.

The temperature controller, as shown in Fig. 4, monitors the temperature of the cooled surface, maintaining it at some preset value by sending a control signal to the phase-angle SCR power supply, which in turn regulates the power to the quartz lamps by varying the phase angle on each a-c cycle proportional to the control signal. In the event of an overshoot in the temperature of the surface, an alarm disconnects the power to the heaters via relays. The power to the lamps along with the temperatures are continuously indicated by the panel meters and recorded by the data acquisition system. All process parameters are displayed and stored on the PC.

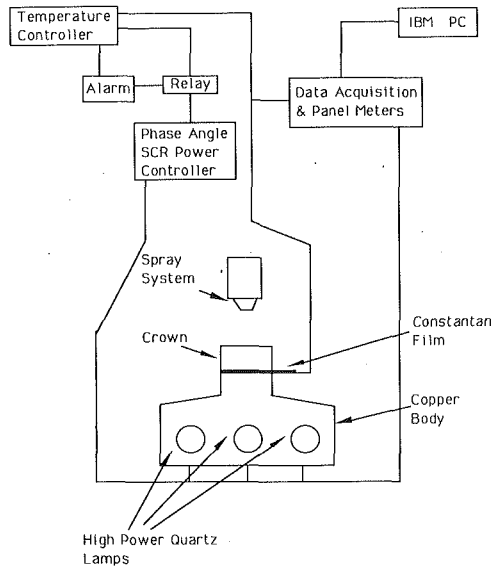


Fig. 4 Experimental schematic

The heat source consists of two parts, namely, the lower cuboid copper body, with inserted radiation lamps, and the 1 cm² circular crown (11 mm diameter × 8 mm height) or cooled surface (shown in Fig. 3) from which heat removal is desired. The whole assembly (excluding the surface exposed to the spray) is insulated in high-temperature insulation to keep heat losses to a minimum. By measuring the temperature difference across a known distance in a section of the crown where the isotherms have flat profiles, the heat flux can be determined using Fourier's law of heat conduction.

At a desired heat flux of 1000 W/cm², in a copper body of uniform cross section, the temperature gradient is 25.4°C/mm. This requires that the size of the thermocouple be of the order of 40 μm for a temperature measurement resolution to be within 1°C. Temperature measurement using such fine thermocouples is not recommended at such high temperatures, being more susceptible to standard wire errors (ASTM, 1974), corrosion, and failure. Secondly, an uncertainty analysis,

$$\frac{w_q}{q} = \sqrt{\left[\frac{w_x}{\Delta x}\right]^2 + \left[\frac{w_T}{\Delta t}\right]^2} \quad (3)$$

implies that the prediction of the heat flux is also dependent on the accurate measurement of the distance between the two thermocouples, Δx. Ideally, this is a parameter in the heat flux equation, which should be minimized for maximum temperature reduction within the system.

An alternative method of temperature measurement would be to use a thin film of Constantan (127 μm thick in this case, selected because with copper it composes a thermocouple), interleaved between a copper film on the top (which constitutes the cooled surface shown in Fig. 3), and the heated copper block at the bottom, located in a region of the crown 6 mm above the lower copper block where flat isotherms are predicted. Constantan has a low thermal conductivity (21.12 W/m·K); thus the thinner the film, the lower the temperature rise across it. Second, the film thickness measurement, Δx, when accurately determined (127 ± 12 μm), further reduces the uncertainty in the heat flux prediction.

The thermocouple junction cannot be assumed to be isothermal, as a heat flux exists across the solder layer (50–70 μm thick). Hence, a simple copper-constantan thermocouple calibration is invalidated. Therefore, copper-silver and silver-constantan calibrations were obtained and the corrected temperatures used in the calculation of the heat flux. Knowl-

Table 1 Experimental flow-field parameters

Case	Water flow rate, l/h	Drop size range, μm	Average velocity, m/s	Air Pressure /flow rate psig, l/s
1	5.1	14–23	15–50	60/0.32
2	5.1	18–26	15–31	40/0.25
3	5.1	21–28	9–22	20/0.16
4	2.6	15–22	8–45	40/0.25
5	1.4	7–14	9–47	75/0.38
6	1.4	8–14	9–44	60/0.32
7	1.4	9–15	10–38	40/0.25
8	1.4	11–15	7–28	20/0.16

edge of the heat flux allows evaluation of surface temperature by extrapolation.

$$T_{\text{surf}} = T_{\text{Co}} - q \frac{\Delta x_{\text{Cu}}}{K_{\text{Cu}} A} \quad (4)$$

Spray System. Details of the coolant supply unit are provided by Pais et al. (1989a, 1989b). An air atomizing nozzle was used to generate homogeneous droplet sprays over small areas (approximately 15 mm diameter). A thin (<0.5 mm) annular liquid stream of distilled, deionized water is aspirated or injected into the path of an accelerating jet of air (minimum jet diameter = 0.7 mm). Through surface shear forces, the air jet atomizes the liquid into small droplets (ranging in size from 7 μm to 28 μm depending on liquid and air flow rates), and imparts momentum to them (7–50 m/s; see Table 1). The compressed air to drive the nozzle is supplied at 584 kPa with a relative humidity of nearly 100 percent. A regulating valve is used to reduce the pressure of the moist air; as a result, the exit relative humidity of air is found from calculations to be less than 30 percent.

Droplet Size and Velocity Measurement. Using a single-component phase-Doppler particle analyzer, droplet size and velocity distributions were obtained over the surface for a fixed set of air and water flow rates. Table 1 provides the flow field parameters for eight different cases used in the experiments presented later.

Experimental Results

A fixed set of experiments was conducted with the objective of studying the effect of surface roughness, liquid coolant flow rate, atomizing air flow rate, and sensible heat content of the liquid on the heat transfer rate at surface temperatures below the Leidenfrost point. All comparisons are in the form of heat flux versus the surface temperature.

Initially experiments were performed to study the convective heat transfer contribution, solely due to the air jet. At a surface temperature of 100°C the heat flux was 17 W/cm², negligibly small compared with the spray cooling heat flux.

Before each experiment the test surface was burnished with the polishing abrasive, then swabbed with hydrochloric acid, and finally washed with deionized distilled water. This cleaning procedure was followed to remove any oxide that is formed when the surface jumps into the Leidenfrost region. Freshly distilled, deionized water was used as the coolant in all experiments. Experiments were performed with the spray nozzle approximately 23 mm above the surface. In such a position, the whole surface received the spray evenly, the liquid impinging on the surface before being swept away by the air flow. The liquid and air flow rates were monitored at preset rates throughout each experiment.

Experiments were begun at room temperature and ramped up continuously until Leidenfrost conditions were reached. The heaters were then switched off and the recorded data analyzed. The power was ramped up slowly enough to ensure that the measurements are quasi-steady. Heating up and cooling down cycles were performed up to and prior to the CHF region. The

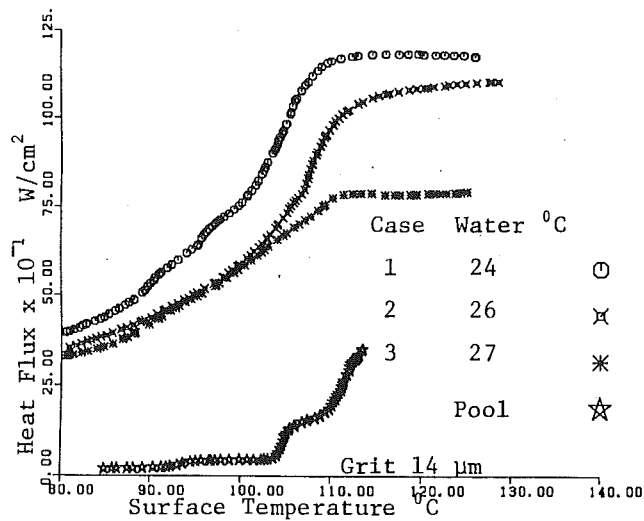


Fig. 5 Effect of air flow rate, 14 μm grit

hysteresis noted was minimal, indicating a negligible effect of any existing transient conditions. The surface was cleaned again for the next run. An immediate rerun or cooling cycle data is not taken, as after the temperature jump to Leidenfrost conditions, a thin layer of oxide forms on the surface, changing the surface properties. A copper surface was selected because of its high thermal conductivity and wettability with water, an important parameter in thin-film evaporation and boiling.

Table 1 provides the parameters of the flow field for eight different cases of liquid and gas flow rates. A number of experiments were performed to check for repeatability, occurrence, and value of the critical heat flux (CHF). The experiments are repeatable in heat flux within $\pm 50 \text{ W/cm}^2$ and $\pm 2^\circ\text{C}$ in surface temperature. However, determination of the CHF point exactly is beyond the means of this heater-block system. The copper block system has a thermal capacity of approximately $850 \text{ J/}^\circ\text{C}$, which means, in the CHF region, where heat flux rates are of the same magnitude or higher, it takes approximately a second for every degree drop. However, the surface temperature fluctuates at a much higher rate, and hence, if the surface flow condition changes to an adverse vapor film boiling situation, then the heat flux will drop, which exacerbates the problem further, driving the surface temperature even higher, this having a runaway effect. At the lower coolant flow rates the control of the flow was within $\pm 0.3 \text{ l/h}$.

Figure 5 illustrates the effect of the increase of air flow rate on the heat removal capabilities for a surface prepared using $14\text{-}\mu\text{m}$ grit polish. As the air flow rate is increased, for the same liquid flow rate of 5.1 l/hr , a thinner liquid film is expected on the surface. This is true because, first, the droplets are smaller in diameter and have higher velocities, which on impinging on the surface will flatten to thinner disks. Second, the stagnation flow field due to the air has increasing ability not only to squeeze the film thinner, but also to sweep away the evaporating vapor, creating a lower partial vapor pressure on the surface of the liquid. Below 100°C , subcooled liquid forced convection and evaporation play an important part. The droplets impact with higher velocities as the air flow rate increases (see Table 1). Hence, the instantaneous local heat transfer coefficient in the region of impact is higher, leading to an overall higher heat transfer rate as evidenced from Fig. 5. This is evidenced by measuring the slope of the profile in the region where temperatures are less than 100°C . The rate of change of heat flux with temperature changes from 13.5 to $21 \text{ W/cm}^2 \cdot ^\circ\text{C}$ going from cases 3 to 1, Table 1. At about

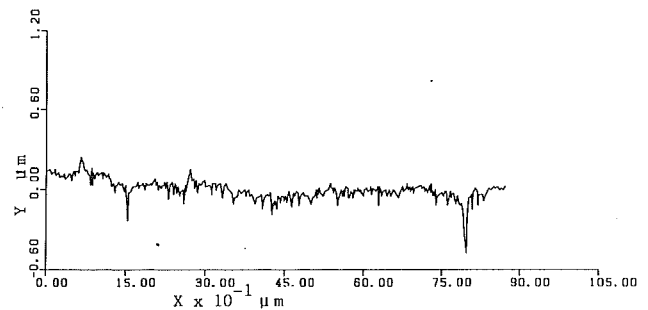


Fig. 6(a) 14 μm grit surface

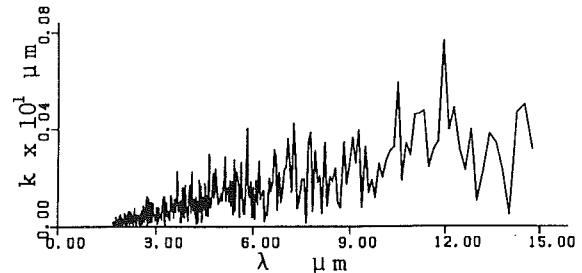


Fig. 6(b) Roughness description

102°C , the profile makes a positive turn, the slopes almost doubling to 20 , 43 , and $48 \text{ W/cm}^2 \cdot ^\circ\text{C}$ from cases 3 to 1, respectively. This is due to the onset of nucleation, which greatly augments the process. Past 110°C , for cases 1 and 3, and 113°C for case 2, the surface begins to dry out sporadically, this being due to a dearth of liquid. At this juncture, the profile shows a sudden downturn, leveling off rapidly with a comparatively insignificant slope. The maximum heat removal capabilities are observed in this region, removing 1180 , 1110 , and 780 W/cm^2 for cases 1 to 3, respectively. For further increase in temperature, the liquid film becomes highly unsteady, jumping to the Leidenfrost/dryout region instantaneously.

The surface profile prepared using polishing paper of grit size less than $14 \mu\text{m}$ is shown in Fig. 6(a), and its Fourier spectrum is shown in Fig. 6(b). The maximum roughness protuberance occurring on a 0.9 mm scan is $k \cong 0.35 \mu\text{m}$. Hence, with the assistance of the air flow field, the film thickness can be of the order of $1 \mu\text{m}$. If only conduction through such film of water is considered as the means of heat transport, it is noted that if such superheats are imposed on the surface, the liquid film can substantially support the heat flux measured.

Also presented in Fig. 5 are test data for the surface submerged in a shallow pool of water. The study was performed to determine the superheat for the onset of nucleation and conditions were not extended into the CHF region. The profile clearly indicates the onset of nucleation at a temperature of $\approx 105^\circ\text{C}$. From Eq. (1), this relates to $\lambda \cong 12 \mu\text{m}$, or from Fig. 6, $k \approx 0.008 \mu\text{m}$, the predominant element on the surface.

Figure 7 illustrates the effect of the increase of air flow rate on the heat removal capabilities for a constant liquid flow rate of 5.1 l/h . The flow conditions are similar to those in Fig. 5; however, the surface in this case is prepared using a coarser $22 \mu\text{m}$ grit polish. As the air flow rate is increased, for the same liquid flow rate of 5.1 l/h , a thinner liquid film is expected on the surface as was explained earlier for the case of Fig. 5. Prior to 100°C , due to the subcooled liquid used, forced convection and evaporation play an important part as described for Fig. 5. At approximately 107°C , the profile shows a sudden downturn, leveling off rapidly with a comparatively small slope. The maximum heat removal capabilities in this region are 1050 , 930 , and 850 W/cm^2 for cases 1–3, Table 1, respectively. A profile of a section of the surface using polishing paper of grit

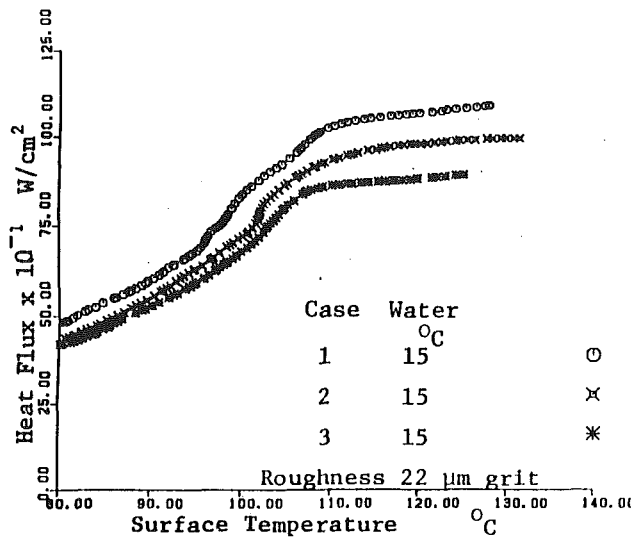


Fig. 7 Effect of air flow rate, 22 μm grit

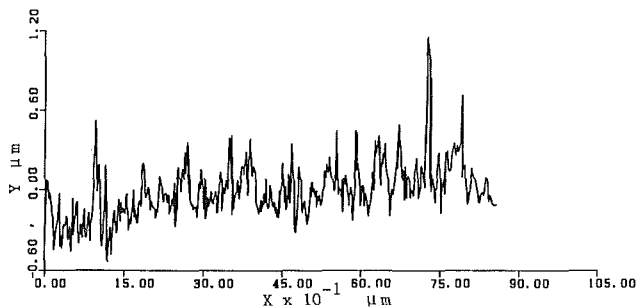


Fig. 8(a) 22 μm grit surface

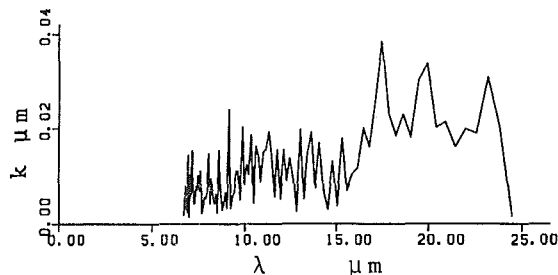


Fig. 8(b) Roughness description

size less than 22 μm is shown in Fig. 8(a), and its Fourier spectrum is shown in Fig. 8(b). The rms roughness value is 1.2 μm .

From Fig. 9(a), we note that the average value of liquid film thickness Δy will be greater than 1.2 μm . Thicker liquid films will tend to impede vapor escape, and dampen out droplet impingement. The higher roughness, when compared to Fig. 6, implies a thicker film, which leads to: (a) later bubble breakup/departure and impeding of vapor escape, (b) increased resistance to heat flux via evaporation on film surface and within bubble, (c) dampening of droplet impingement. It follows that the maximum heat flux for this roughness, at the higher air flow rates, will be lower than for the 14 μm grit surface.

Figure 10 illustrates the effect of increasing air flow rate for a far lower liquid flow rate of 1.4 l/h. The surface in this case was prepared with a 14 μm grit polish. The droplet sizes decrease and their velocity increases, the liquid film thinning concurrently in cases 8, 7, 6, and 5, respectively. The higher

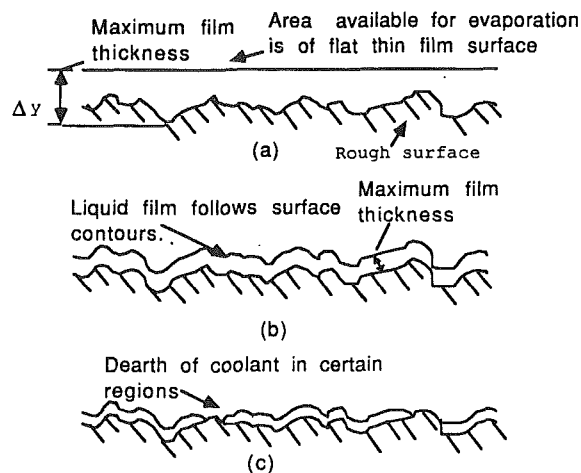


Fig. 9(a, b, c) Surface evaporation dynamics

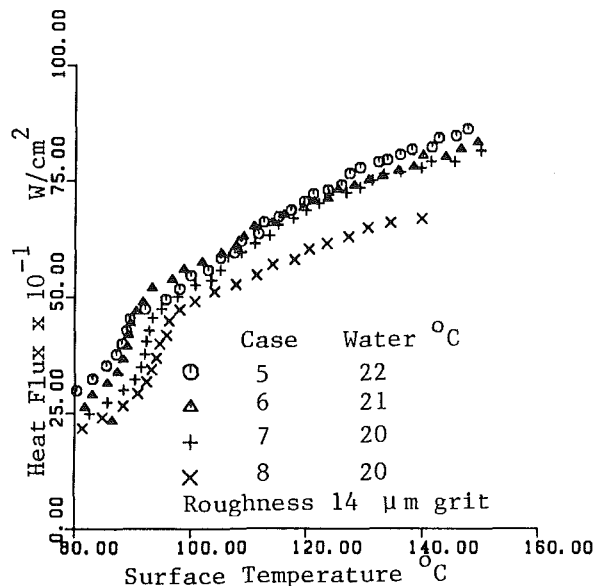


Fig. 10 Effect of air flow rate at a coolant flow rate of 1 l/hr

air flow rates are noted to initiate evaporation and consequently an augmentation in heat flux at lower temperatures. The slope in the region between 85 and 95 $^{\circ}\text{C}$ lies in the range of 25 to 45 $\text{W}/\text{cm}^2 \cdot ^{\circ}\text{C}$, the higher air flow rates/thinner liquid films producing the greater change. For temperatures greater than 100 $^{\circ}\text{C}$, the surface indicates a dearth in liquid and the slope drops to 5 $\text{W}/\text{cm}^2 \cdot ^{\circ}\text{C}$ for all cases. Because of the lower liquid flow rate, the heat flux is limited to around 600 W/cm^2 at 110 $^{\circ}\text{C}$. The steam generation rate in this case is not as profuse as the case described in Fig. 5. Hence, the film is more stable at higher temperatures, blow-off of the liquid film not being obvious.

Figure 11 illustrates the effect of the change of liquid flow rate on the heat flux. In this case the air flow rate is held constant and the surface was prepared using 22 μm grit polish (see Fig. 8a, b). From Table 1, for cases 7, 4, and 2, the droplet size increases with increasing liquid flow rate. Below 100 $^{\circ}\text{C}$ the predominant mode of heat removal is by evaporation. The maximum slope increases from 25 to 35 $\text{W}/\text{cm}^2 \cdot ^{\circ}\text{C}$, when the liquid flow rate increases from 1 to 5.1 l/h. On drying out of the surface, the slope again drops to about 5 $\text{W}/\text{cm}^2 \cdot ^{\circ}\text{C}$, for cases 4 and 7. In case 2, Table 1, at 102 $^{\circ}\text{C}$ the onset of nucleation is recognized by the steep rise in the heat flux. In cases 4 and 7 no clear distinction is noted between the regions of evaporation and the onset of nucleation. A study of the profile

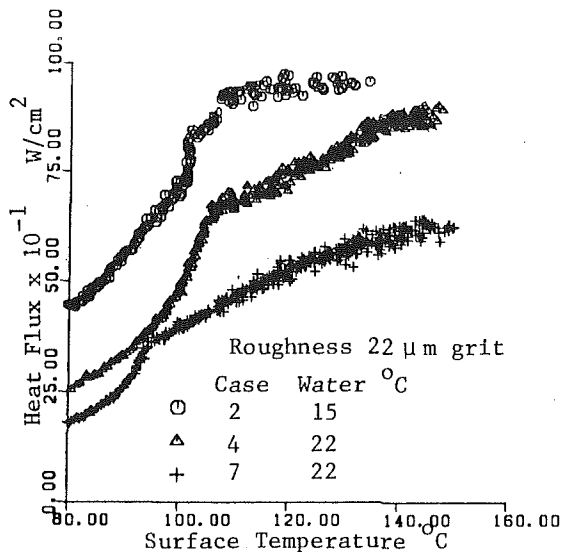


Fig. 11 Effect of coolant flow rate, 22 μm grit

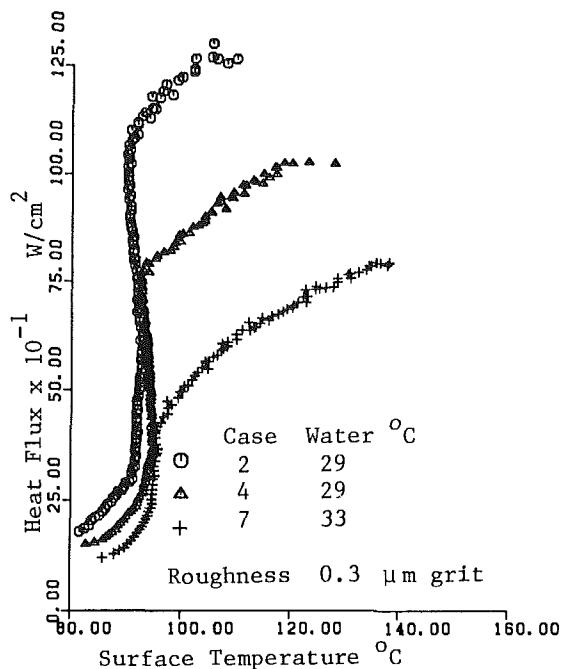


Fig. 12 Effect of coolant flow rate, 0.3 μm grit

of a section of the surface prepared using polishing paper of grit size less than 22 μm , and its Fourier spectrum (Fig. 8a, b) shows that the roughness is distributed over the whole wavelength band. This means that roughness cavities of successively decreasing size (λ) will become active nucleating sites as the superheat given by Eq. (1) is increased. Since the temperature of the surface is increased gradually, increasingly more sites become active, augmenting the heat flux even further, thus giving a gradually increasing slope in the heat flux profile until incipient conditions for dryout are reached.

Figure 12 illustrates the effect of coolant flow rate on the heat flux, for a surface lapped with 0.3 μm abrasive. Figure 13(a, b) show the profile of the surface and the Fourier spectrum, respectively. The maximum protuberance on a 1000 μm scan (Fig. 13a) is approximately 0.1 μm , which means the liquid film thickness will be of the same order of magnitude. The heat flux profile follows a steep slope at temperatures well below saturation, rising rapidly, and assuming at higher heat fluxes a negative slope. This seemingly impossible trend can

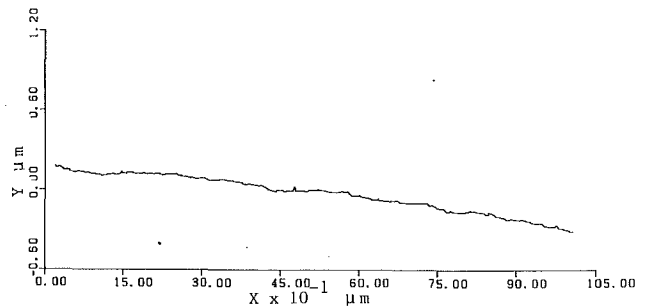


Fig. 13(a) 0.3 μ surface

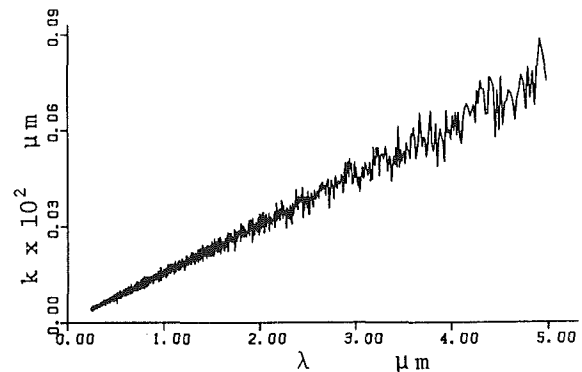


Fig. 13(b) Roughness description

be explained with reference to Figs. 1 and 9(a, b, c). Because of the ultrathin nature of the liquid film, the ability of the heat to be transported by conduction through the film and be evaporated at the surface is easily verified. The evaporation at temperatures below 100°C is possible because of the existence of the secondary air flow field, which reduces the partial vapor pressure, thus reducing the saturation temperature. Initially, the liquid film can be imagined to be a flat film on the surface of which evaporation is taking place. Now, as the heat flux increases by evaporation, the film thickness decreases. This means that the temperature gradient across the liquid film increases, augmenting the heat transport further, which manifests itself as an increase in slope of the profile. Eventually, the film thickness is such that the liquid surface can be conceived to begin to follow the surface profile, Fig. 9(b). At this juncture the actual area of the curvilinear liquid surface has increased (as opposed to the flat surface), which enhances the heat flux even further. However, the heat flux prediction is based on the plan surface area, which leads to forecasting a higher heat flux (Pais, 1987), and it follows, on extrapolation using Eq. (4), yields a lower surface temperature. Consequently, the profile begins to assume a negative slope. The Fourier analysis indicates a surface with uniformly increasing cavity sizes of $\lambda \leq 5 \mu\text{m}$, the k values being less than 0.001 μm . This implies the superheat required for nucleation would be greater than 6.5°C. However, if the liquid film thickness is of the same order of magnitude as the roughness, then the emerging bubbles will be scoured off the surface before reaching the minimum radius given by Eq. (1). This would imply that nucleation at superheats less than 6.5°C is feasible on this surface. For temperatures greater than 100°C the profile assumes an almost flat profile. Maximum heat fluxes of 1250, 1000, and 600 W/cm^2 were obtained at 100°C for cases 2, 4, and 7, respectively.

Figure 14 contains results for conditions similar to those presented in Fig. 12, with the exception that the liquid is preheated to about 90°C. In all experiments atomization of the liquid is brought about by unheated compressed air exiting into the ambient. Hence, when hot water is introduced into

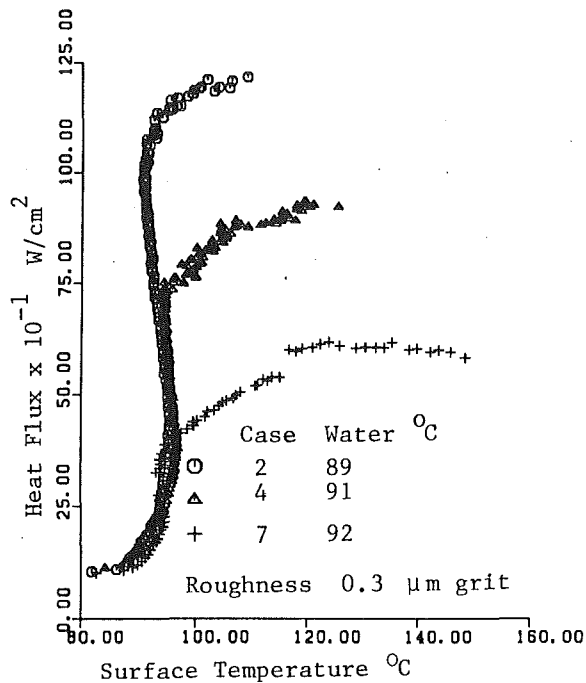


Fig. 14 Heat flux at higher coolant temperatures

the nozzle, flash evaporation will occur, cooling the liquid droplets. Temperature measurements presented are taken before the liquid enters the nozzle. The study shows that the initial heat flux is much lower in the subcooled region compared to Fig. 12; however, in the higher heat flux domain the trend and maximum heat fluxes are similar for the higher liquid flow rates. This is expected, since the latent heat contribution to the heat flux is much higher than that of the sensible heat content in the case of water. For the lower flow rate, the small droplet sizes and their higher temperatures will cause them to flash evaporate within the air flow field, causing a deficiency of liquid on the surface and premature dryout.

The trend of the heat flux with surface temperature followed in Figs. 13 and 14 have important advantages. Primarily, the steep vertical climb of the heat flux within a 4°C temperature band indicates the stability of the heat removal process in maintaining the temperature of a system stable within narrow limits for large excursions in heat generation. Secondly, as stated earlier, the hysteresis in this case is negligible as long as the temperature is maintained below conditions of dryout.

Figure 15 examines the effect of roughness on the heat removal capabilities. As the roughness decreases, the maximum heat flux removed increases. The surfaces polished with 22 and 14 μm abrasive have similar trends, though the latter yields higher dissipation. However, there exists a definite difference between the 0.3 μm abrasive finished surface and the other two rougher surfaces. Not only is the heat flux higher, but the superheat is very low and, depending on the region, even negative. This is in direct contrast to the trends observed in pool boiling (Cole, 1974).

Uncertainty Analysis

The heat flux is calculated by using Fourier's law of heat conduction across the constant film to give

$$q = k_{Co} \frac{\Delta T_{Co}}{\Delta x_{Co}} \quad (5)$$

Here, q is a function of ΔT and Δx . Then the uncertainty (elemental propagation of errors being taken into account) in the value of q obtained using measurements of ΔT and Δx is given by

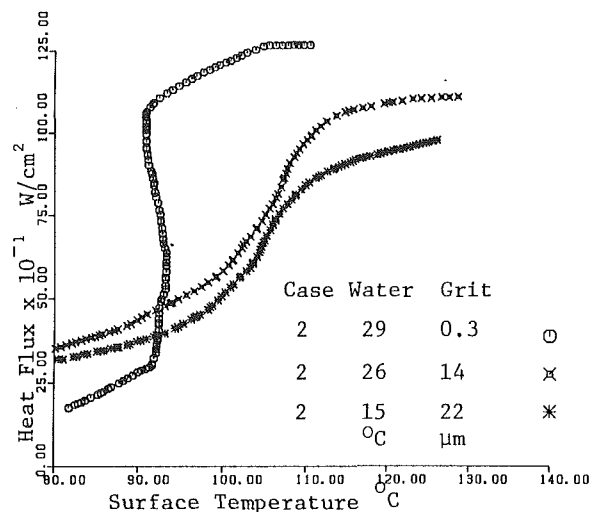


Fig. 15 Effect of roughness on heat flux

$$w_q = \pm \sqrt{\left(\frac{K}{\Delta x} w_T\right)^2 + \left(\frac{K \Delta T}{\Delta x^2} w_x\right)^2} \quad (6)$$

where w_T and w_x are the uncertainties in the measurement of the temperature across and the thickness of the constant film and w_q is the uncertainty in the heat flux. When the uncertainty is represented as a ratio of

$$w'_q = 100 w_q/q \quad (7)$$

and an uncertainty analysis is performed using Eqs. (6) and (7) over the presented data, it is observed that $w'_q \leq 10$ percent. The uncertainty in the surface temperature is $w_{Tsurf} \leq 1.6$ percent.

Conclusions

Fourier analysis was applied to three rough surfaces prepared using polishing grit within the size range of 0.3 to 22 μm. A roughness k versus wavelength λ spectrum was calculated for each of the surfaces. The ability of the surface to dissipate heat under conditions of spray cooling using air-atomized nozzles was studied. Heat flux rates were obtained for three different rough surfaces, for liquid flow rates of 1 to 5.1 l/h and air flow rates of 0.1 to 0.4 l/s. The heat flux increases with increase in liquid flow rate and air flow rate. For roughness greater than 1 μm, nucleation plays a major role in the heat transfer. However, for films of the order of 0.1 μm, heat is conducted through the film and evaporated on the surface, yielding very high heat fluxes of the order of 1200 W/cm² at very low superheats. Spray cooling an ultrathin liquid film on a flat surface enhances heat removal from the surface by evaporation, nucleation being enhanced by early bubble departure.

The Fourier analysis indicates a distribution of roughness elements on the surface, which covers a spectrum of λ values. However, no roughness element λ is noted to be predominant. Hence, the temperature of incipience of nucleation is noted to change as the different roughness elements become active.

Further analysis of the roughness size and film thickness determination is underway to arrive at a better understanding of the phenomenon.

Acknowledgments

This work is supported by the Air Force Aero Propulsion and Power Laboratory through Contract No. F33615-87-C-2777. Mr. Micheal Morgan is the technical monitor. The PDPA system was obtained through a grant provided by NSF.

References

- Andrews, H. C., 1970, *Computer Techniques in Image Processing*, Academic Press, New York.
- ASTM, 1974, "Manual on the Use of Thermocouples in Temperature Measurement," ASTM Special Publication.
- Bankoff, S. G., 1958, "Entrapment of Gas in the Spreading of a Liquid Over a Rough Surface," *AIChE J.*, Vol. XX, pp. 24-26.
- Berenson, P. J., 1962, "Experiments on Pool-Boiling Heat Transfer," *Int. J. Heat Mass Transfer*, Vol. 5, pp. 985-999.
- Choi, K. J., and Yao, S. C., 1987, "Mechanisms of Film Boiling Heat Transfer of Normally Impacting Spray," *Int. J. Heat Transfer*, Vol. 30, pp. 311-318.
- Cole, R., 1974, "Boiling Nucleation," *Advances in Heat Transfer*, Vol. 10, p. 85.
- Cooper, M. G., and Merry, J. M. D., 1973, "A General Expression for the Rate of Evaporation of a Layer of Liquid on a Solid Body," *Int. J. Heat Mass Transfer*, Vol. 16, pp. 1811-1815.
- Defay, R., Prigogine, I., Bellemans, A., and Everett, D. H., 1966, *Surface Tension and Adsorption*, Wiley, p. 342.
- Dhir, V. K., and Tung, V. X., 1988, "A Thermal Model for Fully Developed Nucleate Boiling of Saturated Liquids," presented at the ASME Winter Annual Meeting, Chicago, IL.
- Faneuff, C. E., McLean, E. A., and Scherrer, V. E., 1958, "Some Aspects of Surface Boiling," *Journal of Appl. Phys.*, Vol. 29, No. 1, pp. 80-84.
- Goldstein, M. E., Yang, Wen-Jei, and Clark, J. A., 1967, "Momentum and Heat Transfer in Laminar Flow of Gas With Liquid-Droplet Suspension over a Circular Cylinder," *ASME JOURNAL OF HEAT TRANSFER*, Vol. 89, pp. 185-194.
- Griffith, P., and Wallis, J. D., 1960, "The Role of Surface Conditions in Nucleate Boiling," *Chem. Engg. Progr. Symp. Ser.*, Vol. 56, No. 30, pp. 49-63.
- Hospeti, N. B., and Mesler, R. B., 1969, "Vaporization at the Base of Bubbles of Different Shape During Nucleate Boiling of Water," *AIChE J.*, Vol. 15, pp. 214-219.
- Hsu, Y. Y., 1962, "On the Size Range of Active Nucleation Cavities on a Heating Surface," *ASME JOURNAL OF HEAT TRANSFER*, Vol. 84, pp. 207-216.
- Jussim, E., 1988, *Stopping Time: The Photographs of Harold Edgerton*, Harry N. Abrams, Inc., New York.
- Kopchikov, I. A., Voronin, G. I., Kolach, T. A., Labuntsov, D. A., and Lebedev, P. D., 1969, "Liquid Boiling in a Thin Film," *Int. J. Heat Mass Transfer*, Vol. 12, pp. 791-796.
- Kurihara, H. M., and Myers, J. E., 1960, "The Effects of Superheat and Surface Roughness on Boiling Coefficients," *AIChE J.*, Vol. 6, pp. 83-91.
- Lendaris, G. G., and Stanley, G. L., 1970, "Diffraction Pattern Sampling for Automatic Pattern Recognition," *Proc. IEEE*, Vol. 58, pp. 198-216.
- Lighthill, M. J., 1962, *Fourier Analysis and Generalized Functions*, Cambridge Univ. Press, United Kingdom.
- Marks' Standard Handbook for Mechanical Engineers*, 1978, Chap. 4 and 13, 8th ed., McGraw-Hill.
- Mesler, R., 1976, "A Mechanism Supported by Extensive Experimental Evidence to Explain High Heat Fluxes Observed During Nucleate Boiling," *AIChE J.*, Vol. 22, No. 2, pp. 246-252.
- Oppenheim, A. V., and Schaffer, R. W., 1975, *Digital Signal Processing*, Prentice Hall, New Jersey.
- Pais, M. R., 1987, "Determination of the Local Heat Transfer Characteristics on Glaze Ice Accretion on a Cylinder and a NACA 0012 Airfoil," PhD Dissertation, University of Kentucky.
- Pais, M. R., and Singh, S. N., 1988, "A Fourier Analysis Approach for Surface Definition and the Effect of Roughness on the Local Convective Heat-Transfer Coefficient as Related to Ice Accretion, Paper No. AIAA-88-0117.
- Pais, M. R., Chow, L. C., and Mahefkey, E. T., 1989a, "Rotating Jet Impingement Cooling," Paper No. AIAA-89-175.
- Pais, M. R., Tilton, D., Chow, L. C., and Mahefkey, E. T., 1989b, "High Heat Flux Low Superheat Evaporative Spray Cooling," Paper No. AIAA-89-0241.
- Parizhskiy, O. V., 1972, "Study of Boiling Heat Transfer With a Falling Film of Refrigerant," *Heat Transfer—Soviet Research*, Vol. 4, pp. 43-47.
- Pratt, W. K., 1978, *Digital Image Processing*, Wiley, New York.
- Rosenfeld, A., 1962, "Automatic Recognition of Basic Terrain Types From Aerial Photographs," *Photogrammic Engineering*, Vol. 28, No. 1.
- Webb, R. L., 1981, "The Evolution of Enhanced Surface Geometries for Nucleate Boiling," *Heat Transfer Engg.*, Vol. 2, No. 3-4.
- Yu, C. L., and Mesler, R. B., 1977, "A Study of Nucleate Boiling Near the Peak Heat Flux Through Measurement of the Transient Temperature," *Int. J. Heat Mass Transfer*, Vol. 20, pp. 827-840.

Thermal Analysis of Droplet Spray Evaporation From a Heated Solid Surface

K.-K. Tio

Department of Applied Mechanics and
Engineering Sciences,
University of California, San Diego,
La Jolla, CA 92093-0411

S. S. Sadhal

Department of Mechanical Engineering,
University of Southern California,
Los Angeles, CA 90089-1453

This paper deals with the heat transfer aspects of droplet spray evaporation from a heated solid surface. The analysis is restricted to the low superheat regime, in which the impinging droplets stick onto the solid without bubble nucleations. In this limit of approximation, the heat flow is quasi-steady and conduction dominated. The difficulty arising from droplet thermal interactions is overcome with an approximate model of an evaporating droplet surrounded by a uniform surface heat flux. The size of the droplet changes with time, but the effect of the surrounding droplets, which are treated as a continuum producing the uniform surface flux, is taken into consideration in an average sense. In addition, the analysis also incorporates the effects of droplet contact angle, droplet concentration, and solid conductivity. A transcendental equation has been derived and solved by using the Newton-Raphson method to obtain the Nusselt number.

1 Introduction

It has been well established that cooling of hot surfaces by liquid droplets is an effective process since large heat fluxes are involved. Consequently, there are numerous industrial applications of spray cooling of surfaces; examples include spray cooling of hot metals in the steel industries, cooling of turbine blades, emergency spray cooling of reactors in the nuclear power industries, etc. These industrial applications have in turn generated considerable interest in the study of droplet spray on heated solid surfaces. Bonacina et al. (1979), Grissom and Wierum (1981), and Rizza (1981) have conducted a study of droplet spray in the low superheat regime. Wachters et al. (1966) and Hoogendoorn and den Hond (1974) carried out experimental studies covering the film boiling region. Other studies in the film boiling region include experimental and theoretical studies by Chandra and Avedisian (1988) and Avedisian and Koplik (1987). Zhang and Gogos (1991) gave a thorough theoretical analysis of a droplet evaporating near a solid surface. An experimental study covering the nucleate and film boiling regimes was conducted by Yao and Choi (1987). Toda (1972, 1974) carried out an experimental/theoretical study of droplet spray in all the three regimes of superheat. Recently, a review article was published by Bolle and Moureau (1982). In connection with evaporation of translating droplets, Ayyaswamy (1989) gave an extensive review, particularly with regard to combustion.

In this paper, we investigate the heat transfer from a heated solid surface to sprays of droplets impinging on the surface. In general, sprays have a spectrum of size distribution. However, to make the problem analytically tractable, it is assumed that the sprays consist of droplets of the same size. In addition, the Weber number of the droplets is sufficiently low that the droplets do not disintegrate when they hit the solid surface. Instead, after arriving at the surface, they stay there until the evaporation is complete. Our analysis is restricted to the low superheat regime, and bubble nucleations within the droplets are ruled out. Furthermore, we confine our attention only to the stage when the droplets are evaporating on the heated surface. We also assume that the gaseous region close to the solid surface and the evaporating droplets is filled with the vapor of the droplet liquid.

The model employed in the heat transfer analysis consists of droplets in the form of a spherical cap evaporating on the surface of a semi-infinite solid (see Fig. 1). The droplet contact angle is assumed to remain constant as the droplets evaporate. While this may somewhat limit the results, it is necessary to make this assumption because the general problem of varying contact angles is exceedingly complicated. In the low superheat regime considered here, the heat flow is conduction dominated, and may also be regarded as quasi-steady since the time scale of heat diffusion is much shorter than that of evaporation. This is owing to the very small Jakob number for liquids such as water. In the present case of small ΔT , we have $Ja = (c_p \Delta T / \lambda) \ll 1$. Natural convection can also be neglected because the Grashof number is less than 10. Thus, the added effect of natural convection is weak. Furthermore, the conduction Nusselt number is very high, as the analysis shows, and in comparison convective effects can be neglected. At the solid-liquid interface, perfect thermal contact is assumed, and the usual conditions of continuity of temperature and heat flux across the interface hold. Since the conductivity of vapor is much lower than that of solid or liquid, it is reasonable to assume that heat diffusion across the solid-vapor or liquid-vapor interface is negligible. Thus, the solid-vapor interface is assumed to be impervious to heat flow, and all the heat crossing the solid-liquid interface diffuses toward the liquid-vapor inter-

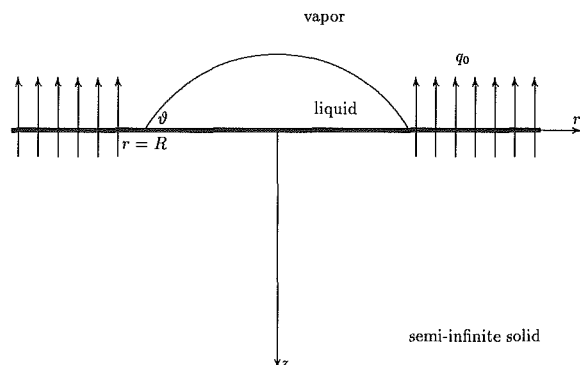


Fig. 1 A lens-shaped droplet evaporating on the surface of a semi-infinite solid; the uniform surface heat flux, q_0 , outside its interface with the solid is a macroscopic approximation of the effects of the surrounding droplets.

Contributed by the Heat Transfer Division and presented at the National Heat Transfer Conference and Exposition, Minneapolis, Minnesota, July 28-31, 1991. Manuscript received by the Heat Transfer Division January 14, 1991; revision received July 15, 1991. Keywords: Conduction, Evaporation, Multiphase Flows.

face, where it is taken up as the latent heat of evaporation. Saturation temperature will be assumed for the liquid-vapor interface; this assumption is quite reasonable in view of the results of Plesset (1952) and Plesset and Prosperetti (1976), which state that the temperature of an evaporating liquid surface can be approximated with that of the surrounding vapor. It should be noted that the assumption of an isothermal liquid-vapor interface effectively decouples the transport processes in the vapor phase from the remaining system.

As mentioned earlier, the dry region of the surface is assumed to be impervious to heat flow. However, in the calculations of the heat transfer to a reference droplet, we approximate the entire set of droplets on the solid surface surrounding it as a continuum producing a uniform heat flux. This uniform flux is an unknown quantity to be determined by coupling it with the heat flow through the reference droplet. This approximate boundary condition emulates the behavior of droplets that may choose any location on the solid surface with equal probability. Thus, in a time-averaged sense, it is quite reasonable to consider a total effect in the form of a uniform flux. The validity is, however, restricted to the case of low fractions of wetting. For high wetting fractions, the truly random problem involves the near-field interactions between discrete droplets. The major difficulty with that problem is the calculations of the temperature distribution for a large set of arbitrarily placed droplets. In addition, the probability function for the spatial distribution of droplets on a surface is, in general, not available.

Of main interest in this study is the calculation of heat transfer from the solid to the droplets and the corresponding time-averaged heat transfer coefficient, h . In dimensionless form, it is given by the Nusselt number, Nu , defined by

$$Nu \equiv \frac{hR_0}{k_l} \equiv \frac{q_0R_0}{k_l\Delta T} \quad (1.1)$$

In Eq. (1.1) above, q_0 is the average heat flux at the solid surface, k_l the thermal conductivity of the liquid, R_0 the initial base radius of the droplets, and ΔT the difference between the average temperature of the entire solid surface and the temperature of the liquid-vapor interface.

2 Problem Formulation

We first consider a droplet evaporating on the heated solid surface. The overall energy balance can be written as

$$\frac{q_0 t_0}{N} = Q, \quad (2.1)$$

where t_0 is the lifetime of the droplet, N is the number of evaporation sites per unit area of the solid surface, and Q is the total energy conducted from the solid into the droplet during its lifetime. In Eq. (2.1), q_0 and N are time-averaged quantities. Here, it is assumed that the number of evaporation sites per unit area remains constant. This assumption is implied by Eq. (2.1), which, in principle, states that as soon as a droplet evaporates completely, another one arrives to take its place in the vicinity. Since all the energy conducted into the droplet is utilized to evaporate all the liquid,

$$Q = \lambda \rho_l V_0, \quad (2.2)$$

where V_0 is the initial volume of the droplet, ρ_l is the density of the droplet liquid, and λ is the latent heat of evaporation. For a droplet with a constant contact angle ϑ ,

$$V_0 = \frac{\pi}{3} R_0^3 F(\vartheta), \quad (2.3)$$

where

$$F(\vartheta) = \frac{(1 - \cos \vartheta)^2 (2 + \cos \vartheta)}{\sin^3 \vartheta}, \quad (2.4)$$

and R_0 is the initial base radius of the droplet (see Fig. 1). Equation (2.1) now becomes

$$q_0 t_0 = \frac{\pi}{3} \lambda \rho_l N R_0^3 F(\vartheta). \quad (2.5)$$

To derive the Nusselt number from Eq. (2.5), we first need to calculate t_0 , which is dependent on q_0 and ΔT . Thus, we have to solve the heat transfer problem associated with a droplet evaporating on the surface of the solid (see Fig. 1). Since the heat flow is conduction dominated and quasi-steady, the temperature distributions in the solid and liquid, T_s and T_l , satisfy Laplace's equations:

$$\nabla^2 T_s = 0, \quad (2.6)$$

$$\nabla^2 T_l = 0. \quad (2.7)$$

At the liquid-vapor interface, the temperature is equal to that of the surrounding vapor, i.e.,

$$T_l = T_v. \quad (2.8)$$

Nomenclature

\mathcal{A}, \mathcal{B} = integral expressions in Eqs. (3.16) and (3.17)	\dot{q} = heat flux at solid-liquid interface	β = defined in Eq. (4.9)
\mathcal{C} = defined in Eq. (3.22)	\dot{Q} = rate of heat flow into one droplet	ζ = defined in Eq. (B.4)
c_p = specific heat of droplet liquid	Q = total heat flow into one droplet	η_0 = defined in Eq. (3.5)
F = defined in Eq. (2.4)	R, R_0 = droplet base radius, initial base radius	ϑ = contact angle
h = heat transfer coefficient	t = time	κ = time-averaged wetted fraction of solid surface
Ja = Jakob number, Eq. (4.13)	t^* = dimensionless time, Eq. (4.14)	λ = latent heat of evaporation
k = thermal conductivity	t_0 = lifetime of a droplet	μ = liquid-to-solid conductivity ratio
\mathcal{L}, \mathcal{S} = coefficients of eigenfunction expansions, Eqs. (3.8) and (3.9)	T = temperature distribution	ρ = density
N = number of evaporation sites per unit area	T_0 = average solid surface temperature	Subscripts
Nu = Nusselt number, Eq. (1.1)	T_v = vapor temperature	l = liquid
$Nu^{(n)}$ = coefficients in the asymptotic expansion for Nu , Eq. (4.1)	$\Delta T = T_0 - T_v$	s = solid
q_0 = average surface heat flux	V_0 = initial volume of a droplet	Coordinate Systems
	x = distance away from contact line into solid	(r, ϕ, z) = cylindrical coordinates
	α = thermal diffusivity	(ξ, η, ϕ) = toroidal coordinates
		h_ξ, h_η, h_ϕ = metric coefficients, Eqs. (3.3) and (3.4)

At the solid-liquid interface,

$$T_s = T_l, \quad (2.9)$$

$$k_s \frac{\partial T_s}{\partial z} = k_l \frac{\partial T_l}{\partial z}, \quad (2.10)$$

where k_s and k_l are the solid and liquid conductivities, respectively. For the region of the solid surface surrounding the droplet, we prescribe the boundary condition of constant flux:

$$k_s \frac{\partial T_s}{\partial z} = q_0. \quad (2.11)$$

Deep inside the solid, i.e., $z \rightarrow \infty$,

$$T_s = T_0 + \frac{q_0 z}{k_s}. \quad (2.12)$$

Effectively, Eq. (2.12) states that there is a uniform flux of q_0 in the far-field region of the solid. Also, it can be easily seen that T_0 is the average temperature of the entire solid surface. The choice of the boundary condition of Eq. (2.11), however, needs some elaboration. Since we are dealing with a system of multiple droplets evaporating on the solid surface, their thermal interactions must, in general, be taken into account when we analyze the heat transfer problem. Tio and Sadhal (1991) have set up a model of identical droplets arranged in regular arrays, and carried out the analysis of droplet interactions for a wide range of droplet concentrations. Their results show that for water droplets evaporating on most metals, droplet interactions through the solid cannot, in general, be ignored, except for vanishing droplet concentrations. However, that analytical method cannot be implemented here since we are dealing with droplets in random distributions. The random case is much more complex and demands solutions to a different combination of highly mixed boundary value problems. In fact, for cases of nondilute concentrations, analytical methods are yet to be developed to deal with the thermal interactions of droplets distributed randomly. When the droplet under consideration is evaporating, so are its neighboring droplets at various stages of evaporation, and heat is continuously flowing from the solid into those droplets. In effect, the reference droplet sees a continual heat flow leaving the solid. Thus, it is reasonable to replace the surrounding droplets and their effect on the droplet under consideration with the boundary condition in Eq. (2.11). Here, q_0 is the heat flux leaving the solid, and thus flowing into the droplets, averaged over its entire surface and time [see Eq. (2.1)].

Our problem, now, is to find the solution to Eqs. (2.6)–(2.12), from which the lifetime of the droplet, t_0 , will be calculated. Then, the Nusselt number will be calculated using Eq. (2.5). These will be carried out in the following section.

3 Solution

The exact solution to Eqs. (2.6)–(2.12) can be found by using the toroidal coordinates (ξ, η, ϕ) , which are related to the cylindrical coordinates (r, ϕ, z) in Fig. 1 by the formulas (Lebedev, 1972)

$$r = \frac{R \sinh \xi}{\cosh \xi - \cos \eta}, \quad (3.1)$$

$$z = \frac{R \sin \eta}{\cosh \xi - \cos \eta}, \quad (3.2)$$

where $0 \leq \xi < \infty$, $0 \leq \eta < 2\pi$. The metric coefficients are given by

$$h_\xi = h_\eta = \frac{R}{\cosh \xi - \cos \eta}, \quad (3.3)$$

$$h_\phi = \frac{R \sinh \xi}{\cosh \xi - \cos \eta}. \quad (3.4)$$

In the toroidal coordinate system, the solid surface not wetted

by the droplet corresponds to $\eta = 0$, while the wetted region is identified by $\eta = \pi$. The edge of the droplet corresponds to $\xi = \infty$, and for the z axis $\xi = 0$. The liquid-vapor interface is given by $\eta = \eta_0$, where

$$\eta_0 = \pi + \vartheta. \quad (3.5)$$

In Appendix A, the temperature distributions in the droplet and solid are found to be

$$\frac{T_l - T_0}{\Delta T} = -1 + (2 \cosh \xi - 2 \cos \eta)^{1/2} \times \int_0^\infty \mathfrak{L}(\tau) \sinh(\eta_0 - \eta) \tau P_{i\tau-1/2}(\cosh \xi) d\tau, \quad (3.6)$$

$$\frac{T_s - T_0}{\Delta T} = \frac{q_0 z}{k_s \Delta T} - (2 \cosh \xi - 2 \cos \eta)^{1/2} \int_0^\infty \mathfrak{S}(\tau) \cosh \eta \tau P_{i\tau-1/2}(\cosh \xi) d\tau, \quad (3.7)$$

where $P_{i\tau-1/2}$ is the Legendre function of the first kind of complex degree, $\Delta T = T_0 - T_v$, and

$$\mathfrak{L}(\tau) = \frac{\left[\sinh \pi \tau + \frac{2q_0 R}{k_s \Delta T} \tau \cosh \pi \tau \right] \operatorname{sech}^2 \pi \tau}{[\tanh \pi \tau \tanh \vartheta \tau + \mu] \cosh \vartheta \tau}, \quad (3.8)$$

$$\mathfrak{S}(\tau) = \frac{\left[\mu - \frac{2q_0 R}{k_s \Delta T} \tau \tanh \vartheta \tau \right] \operatorname{sech}^2 \pi \tau}{[\tanh \pi \tau \tanh \vartheta \tau + \mu]}, \quad (3.9)$$

$$\mu = \frac{k_l}{k_s}. \quad (3.10)$$

The heat flux at the solid-liquid interface is

$$\dot{q} = -k_s \left[\frac{1}{h_\eta} \frac{\partial T_s}{\partial \eta} \right]_{\eta=\pi} = q_0 + \frac{k_s \Delta T}{2R} (2 \cosh \xi + 2)^{3/2} \times \int_0^\infty \tau \mathfrak{S}(\tau) \sinh \pi \tau P_{i\tau-1/2}(\cosh \xi) d\tau. \quad (3.11)$$

Integrating \dot{q} over the entire wetted area then yields the rate of heat flow conducted into the droplet:

$$\dot{Q} = 2\pi \int_0^\infty \dot{q} [h_\phi h_\xi]_{\eta=\pi} d\xi = \pi R^2 q_0 + 4\pi R k_s \Delta T \times \int_0^\infty \tau \mathfrak{S}(\tau) \sinh \pi \tau \int_0^\infty \frac{\sinh \xi P_{i\tau-1/2}(\cosh \xi)}{(2 \cosh \xi + 2)^{1/2}} d\xi d\tau. \quad (3.12)$$

The inner integral in Eq. (3.12) is the zeroth-order Mehler-Fock transform of the function $(2 \cosh \xi + 2)^{-1/2}$, and is found in the textbook of Sneddon (1972) as $(1/\tau \sinh \pi \tau)$. Thus,

$$\dot{Q} = \pi R^2 q_0 + 4\pi R k_s \Delta T \int_0^\infty \mathfrak{S}(\tau) d\tau. \quad (3.13)$$

Having determined \dot{Q} , we can now calculate the volume rate of evaporation, which is equal to $\dot{Q}/\lambda \rho_l$. Furthermore, the volume of the droplet and its base area are related by the formula in Eq. (2.3). Thus,

$$\pi F(\vartheta) R^2 \frac{dR}{dt} = -\frac{\dot{Q}}{\lambda \rho_l}. \quad (3.14)$$

Substituting Eq. (3.13) into Eq. (3.14) and rearranging, we obtain

$$-\lambda \rho_l F(\vartheta) R \frac{dR}{dt} = q_0 (1 - 8\mathfrak{B}) R + 4G k_s \Delta T, \quad (3.15)$$

where

$$\mathcal{Q}(\mu, \vartheta) = \int_0^\infty \frac{\mu \operatorname{sech}^2 \pi \tau}{[\tanh \pi \tau \tanh \vartheta \tau + \mu]} d\tau, \quad (3.16)$$

$$\mathcal{B}(\mu, \vartheta) = \int_0^\infty \frac{\tau \tanh \vartheta \tau \operatorname{sech}^2 \pi \tau}{[\tanh \pi \tau \tanh \vartheta \tau + \mu]} d\tau. \quad (3.17)$$

From Eq. (3.15), we obtain

$$t = \lambda \rho \mu F(\vartheta) \int_R^{R_0} \frac{\bar{R}}{q_0(1-8\mathcal{B})\bar{R} + 4\mathcal{Q}\kappa_s \Delta T} d\bar{R} = \frac{\lambda \rho \mu R_0 F(\vartheta)}{q_0(1-8\mathcal{B})} \times \left[1 - \frac{R}{R_0} - \frac{4\mathcal{Q}}{(1-8\mathcal{B})\mu \text{Nu}} \ln \left(\frac{1 + (1-8\mathcal{B})\mu \text{Nu}/4\mathcal{Q}}{1 + (R/R_0)(1-8\mathcal{B})\mu \text{Nu}/4\mathcal{Q}} \right) \right]. \quad (3.18)$$

When $t = t_0$, $R = 0$; it follows from Eq. (3.18) that the lifetime of the droplet is given by

$$t_0 = \frac{\lambda \rho \mu R_0 F(\vartheta)}{q_0(1-8\mathcal{B})} \left[1 - \frac{4\mathcal{Q}}{(1-8\mathcal{B})\mu \text{Nu}} \ln \left(1 + \frac{(1-8\mathcal{B})\mu \text{Nu}}{4\mathcal{Q}} \right) \right]. \quad (3.19)$$

With t_0 found, we can now proceed to derive an equation for the Nusselt number Nu . Substituting Eq. (3.19) into Eq. (2.5), we obtain

$$1 - \frac{4\mathcal{Q}}{(1-8\mathcal{B})\mu \text{Nu}} \ln \left(1 + \frac{(1-8\mathcal{B})\mu \text{Nu}}{4\mathcal{Q}} \right) = \frac{\pi R_0^2 N}{3} (1-8\mathcal{B}). \quad (3.20)$$

In Appendix B, it is shown that the initial base area of the droplet is approximately twice the area averaged over t_0 , i.e., $\pi R_0^2 \approx 2\pi \bar{R}^2$. Noting that the time-averaged wetted fraction of the solid surface, κ , is equal to $\pi \bar{R}^2 N$, Eq. (3.20) can be rewritten as

$$\ln(1 + \mathcal{C}\text{Nu}) = \left[1 - \frac{2}{3}(1-8\mathcal{B})\kappa \right] \mathcal{C}\text{Nu}, \quad (3.21)$$

where

$$\mathcal{C}(\mu, \vartheta) = \frac{(1-8\mathcal{B})\mu}{4\mathcal{Q}}. \quad (3.22)$$

4 Results and Discussion

The objective of this paper is to evaluate the Nusselt number as a function of the wetted fraction of the heated solid surface. We are also interested in the effect of droplet contact angle and solid conductivity on heat transfer. First, we evaluate the two integrals in Eqs. (3.16) and (3.17) using Simpson's rule.

In Tables 1 and 2, we tabulate the two integrals \mathcal{Q} and \mathcal{B} , respectively, as functions of contact angle and conductivity ratio. For a given κ , the Nusselt number is then calculated from Eq. (3.21) using the Newton-Raphson method with a tolerance of 1.0×10^{-7} .

However, before we present the numerical results for the Nusselt number, it is worthwhile to discuss the behavior of Nu for small values of κ and μ . From Eq. (3.21), it is seen that $\text{Nu} = 0$ when $\kappa = 0$. Thus, for small κ , we may expand the Nusselt number as

$$\text{Nu} \sim \text{Nu}^{(1)}\kappa + \text{Nu}^{(2)}\kappa^2 + \dots \quad (4.1)$$

Substituting Eq. (4.1) into Eq. (3.21), we obtain

$$\text{Nu}^{(1)} = \frac{16\mathcal{Q}}{3\mu}, \quad (4.2)$$

$$\text{Nu}^{(2)} = \frac{128\mathcal{Q}}{27\mu} (1-8\mathcal{B}). \quad (4.3)$$

Thus,

$$\text{Nu} \sim \frac{16\mathcal{Q}}{3\mu} \kappa + \frac{128\mathcal{Q}}{27\mu} (1-8\mathcal{B})\kappa^2 + \mathcal{O}(\kappa^3). \quad (4.4)$$

Inspection of Eqs. (3.9) and (3.17) reveals that the integral \mathcal{B} is associated with the thermal effects of the surrounding droplets on a reference droplet. Effectively, Eq. (4.4) indicates that the Nusselt number consists of a leading term proportional to κ and other higher-order terms. The leading-order term simply states that the average surface heat flux q_0 increases as the population density of the droplets increases. This leading term is, however, augmented by the effects of droplet thermal interactions, yielding the total surface heat flux. We can proceed further to examine the behavior of Nu for small values of μ . When $\mu \rightarrow 0$, the dominant contributions to the integral in Eq. (3.16) take place near $\tau = 0$, and we can replace $\tanh \vartheta \tau$ with $(\vartheta/\pi)\tanh \pi \tau$. Then, the resulting integral can be integrated exactly to give the leading approximation as

$$\mathcal{Q} \sim \frac{1}{2} \left(\frac{\pi\mu}{\vartheta} \right)^{1/2} + \mathcal{O} \left(\frac{\pi\mu}{\vartheta} \right). \quad (4.5)$$

Similarly, we obtain

$$\mathcal{B} \sim \frac{1}{8} - \frac{1}{2\pi} \left(\frac{\pi\mu}{\vartheta} \right)^{1/2} + \mathcal{O} \left(\frac{\pi\mu}{\vartheta} \right), \quad (4.6)$$

where $1/8$ is the exact value of \mathcal{B} when $\mu = 0$. Then, Eq. (4.4) reduces to

$$\text{Nu} \sim \frac{8\kappa}{3\mu} \left(\frac{\pi\mu}{\vartheta} \right)^{1/2} \left[1 + \frac{32}{9\pi} \left(\frac{\pi\mu}{\vartheta} \right)^{1/2} \kappa + \dots \right]. \quad (4.7)$$

Table 1 The coefficient \mathcal{Q} as a function of ϑ and μ

	$\vartheta = \pi/12$	$\vartheta = \pi/6$	$\vartheta = \pi/4$	$\vartheta = \pi/3$	$\vartheta = \pi/2$
$\mu = 0.001$	0.04980	0.03621	0.02995	0.02614	0.02156
$\mu = 0.002$	0.06777	0.04983	0.04142	0.03627	0.03003
$\mu = 0.004$	0.09084	0.06782	0.05677	0.04993	0.04158
$\mu = 0.006$	0.10686	0.08068	0.06790	0.05992	0.05010
$\mu = 0.008$	0.11932	0.09093	0.07686	0.06801	0.05707
$\mu = 0.010$	0.12958	0.09953	0.08444	0.07490	0.06305
$\mu = 0.020$	0.16409	0.12974	0.11165	0.09992	0.08509
$\mu = 0.040$	0.20052	0.16433	0.14400	0.13039	0.11273
$\mu = 0.060$	0.22129	0.18568	0.16474	0.15040	0.13144
$\mu = 0.080$	0.23524	0.20086	0.17992	0.16530	0.14569
$\mu = 0.100$	0.24541	0.21243	0.19177	0.17712	0.15721
$\mu = 0.200$	0.27236	0.24580	0.22749	0.21381	0.19436
$\mu = 0.400$	0.29150	0.27273	0.25852	0.24728	0.23052
$\mu = 0.600$	0.29931	0.28482	0.27330	0.26391	0.24948
$\mu = 0.800$	0.30358	0.29178	0.28211	0.27406	0.26147
$\mu = 1.000$	0.30628	0.29632	0.28800	0.28096	0.26980

Table 2 The coefficient \mathcal{B} as a function of β and μ

	$\vartheta = \pi/12$	$\vartheta = \pi/6$	$\vartheta = \pi/4$	$\vartheta = \pi/3$	$\vartheta = \pi/2$
$\mu = 0.001$	0.10874	0.11326	0.11532	0.11657	0.11806
$\mu = 0.002$	0.10266	0.10873	0.11153	0.11323	0.11528
$\mu = 0.004$	0.09468	0.10264	0.10639	0.10868	0.11146
$\mu = 0.006$	0.08901	0.09821	0.10261	0.10531	0.10861
$\mu = 0.008$	0.08453	0.09464	0.09953	0.10256	0.10626
$\mu = 0.010$	0.08078	0.09161	0.09689	0.10019	0.10422
$\mu = 0.020$	0.06782	0.08070	0.08726	0.09142	0.09660
$\mu = 0.040$	0.05345	0.06770	0.07537	0.08039	0.08675
$\mu = 0.060$	0.04489	0.05936	0.06749	0.07291	0.07989
$\mu = 0.080$	0.03898	0.05327	0.06157	0.06720	0.07455
$\mu = 0.100$	0.03458	0.04853	0.05687	0.06260	0.07016
$\mu = 0.200$	0.02247	0.03435	0.04214	0.04778	0.05552
$\mu = 0.400$	0.01344	0.02225	0.02862	0.03349	0.04049
$\mu = 0.600$	0.00963	0.01659	0.02189	0.02608	0.03226
$\mu = 0.800$	0.00752	0.01326	0.01779	0.02144	0.02692
$\mu = 1.000$	0.00616	0.01105	0.01500	0.01823	0.02315

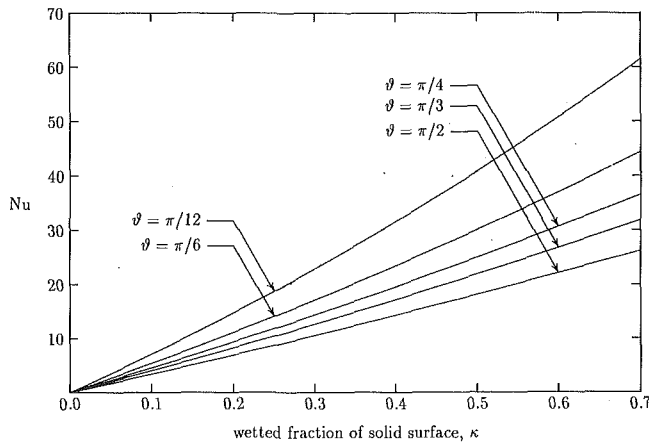


Fig. 2 Nusselt number Nu for a conductivity ratio of $\mu = 0.01$

While we derive Eq. (4.7) by first assuming $\kappa \rightarrow 0$, the same result can also be obtained from Eq. (3.21) without the assumption of small κ . In other words, Eq. (4.7) is valid as long as $(\pi\mu/\vartheta)^{1/2} \rightarrow 0$, even if κ is not small. Thus, we see that in the calculations of heat transfer, droplet interactions can be neglected if $\mu \rightarrow 0$. However, the Nusselt number becomes infinite when $\mu = 0$ since $Nu \sim \mu^{-1/2}$. We will discuss this in greater detail later.

In Fig. 2, the Nusselt number is plotted versus the wetted fraction of the solid surface with ϑ as a parameter and $\mu = 0.01$. It is seen that for a fixed κ , Nu increases as ϑ decreases. This is so because droplets with a smaller contact angle are thinner, resulting in a greater heat transfer rate from the solid. It is also observed that the Nu - κ relationship is almost linear for large contact angles. However, this almost-linear relationship breaks down as the contact angle decreases; it indicates that droplet thermal interactions become significant at that point.

Figure 3 shows the effect of solid conductivity on the Nusselt number. Here, ϑ is chosen to be $\pi/4$. We see that as the solid conductivity increases, so does the heat transfer rate. In particular, when $\mu \rightarrow 0$, the Nusselt number becomes infinite. The reasons are as follows: For a fixed k_l , we see from Eq. (3.7) that the temperature of the solid surface becomes uniform and is equal to T_0 as $\mu \rightarrow 0$. On the other hand, the temperature of the liquid-vapor interface of a droplet remains at T_v . Thus, there exists a temperature discontinuity at the edge of the droplet, resulting in the infinite rate of heat transfer. It can be shown by rigorous mathematical analyses that a temperature discontinuity leads to infinite heat flow across the droplet (Sadhil and Martin, 1977). While the liquid lens has a finite volume, the resistance is theoretically zero when both interfaces have isothermal conditions. This is so because the temperature discontinuity leads to an infinite heat flux at the edge, and this singularity is nonintegrable. Thus, to avoid infinite heat flow rates, we must allow the temperature of the solid surface to vary in such a way that no temperature discontinuity exists at the edge of the droplet. Clearly, this can be achieved only by incorporating the solid into the analysis. In view of these, analyses based on $k_s \gg k_l$ and excluding solid conductivity, which have been quite common, cannot be accepted as rigorous models for wetting situations. From Fig. 3, we also see that the effect of solid conductivity becomes more significant as droplet concentration (or the wetted fraction of the solid surface) increases. However, solid conductivity must still be taken into consideration even if $\kappa \rightarrow 0$ (Sadhil and Plesset, 1979).

In Fig. 4, we plot the Nusselt number versus μ and ϑ as a parameter and $\kappa = 0.5$. Here, we see that the effect of solid conductivity on heat transfer becomes more significant as the contact angle decreases.

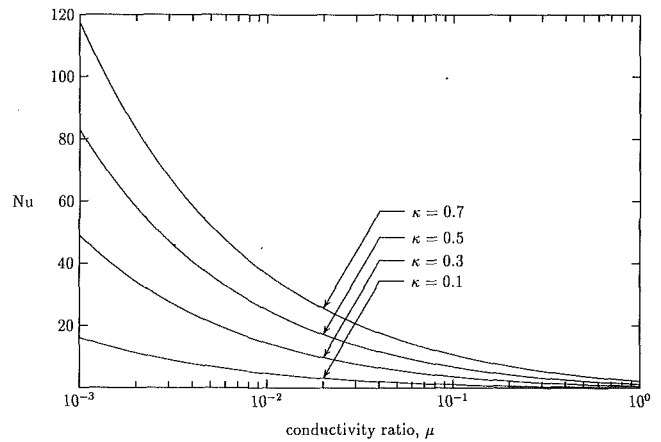


Fig. 3 Nusselt number Nu for droplets of a contact angle of $\vartheta = \pi/4$

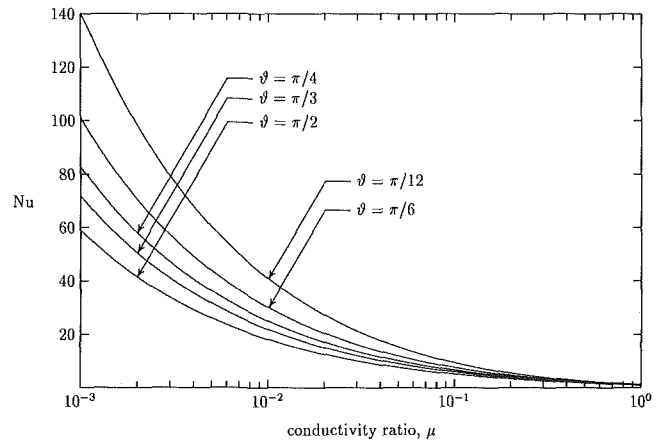


Fig. 4 Nusselt number Nu for the case of $\kappa = 0.5$

As it turns out, the heat transfer rate depends significantly on the solid conductivity, which partly controls the transition in temperature from T_v at the contact line to $T_0 + q_0 z/k_s$ in the solid. It is therefore a matter of interest to understand the behavior of the temperature field in the solid around the contact line region. Since the solid plays a significant role in the heat flow, the fundamentals concerning this behavior need to be analyzed. For this purpose, we examine the temperature field in the solid in the limit of high solid conductivity, i.e., $\mu \rightarrow 0$. To do so, we follow the analysis of Sadhal (1989) for the growing vapor bubble on a solid surface. The development is similar and the final result is nearly the same. Therefore, we leave out the details and give the temperature field only:

$$\frac{T_s(\xi, \eta) - T_0}{\Delta T} \sim \frac{q_0 z}{k_s \Delta T} - \frac{1}{\pi} (2 \cosh \xi - 2 \cos \eta)^{1/2} \times [Q_{-1/2}(\cosh \xi) - Q_{\beta-1/2}(\cosh \xi)], \quad (4.8)$$

where $Q_\nu(\cosh \xi)$ represents the Legendre function of the second kind, and

$$\beta = \left(\frac{\mu}{\pi \vartheta} \right)^{1/2}. \quad (4.9)$$

This result is valid in the entire solid in the asymptotic limit of $\mu \rightarrow 0$. Strictly speaking, the first term on the right-hand side, which is of order $\mu^{1/2}$, should not be included in Eq. (4.8) since it is correct up to $\mathcal{O}(1)$ only. Nevertheless, we retain this term to emphasize that the heat flux is uniform as $z \rightarrow \infty$. Taking further limits toward the contact line ($\xi \rightarrow \infty$), we find that

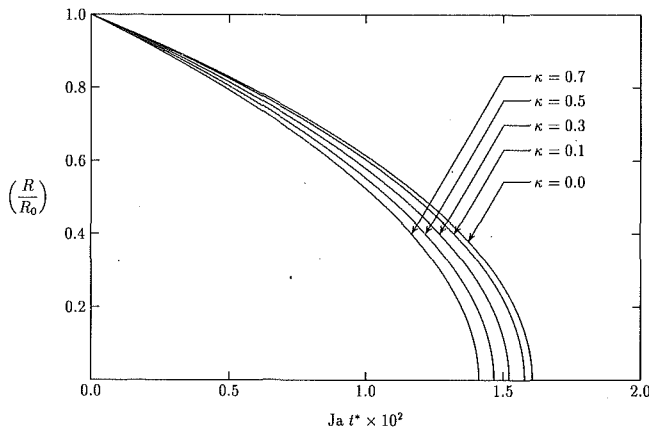


Fig. 5 Variations of droplet radius R with respect to time t for droplets with $\vartheta = \pi/3$ and $\mu = 0.01$

$$T_s(\xi, \eta) \approx \frac{q_0 z}{k_s} + T_v + (T_0 - T_v) \left(\frac{x}{2R} \right)^\beta, \quad (4.10)$$

where x is the distance in a meridian plane directly away from the contact line into the solid. At the contact line, the solid temperature is T_v . It quickly changes to $T_0 + q_0 z/k_s$ at small distances from the contact line. Of interest here is how deep the influence of the contact line temperature penetrates into the solid. To estimate this, we calculate the depth $x_{0.95}$, at which $(x/2R)_\beta$ reaches a value equal to 95 percent. For $\mu = 0.01$ and $\vartheta = \pi/3$, we have

$$x_{0.95} \approx 0.79 R. \quad (4.11)$$

This indicates that for solids with large conductivities, the depth of influence is only as far as the contact radius R . Therefore, the current results are applicable to metallic plates that are at least as thick as the droplet radius. For thinner plates, there will be a significant effect of the thermal conditions at the underside of the plate.

It would be interesting to see how the droplet radius varies as it evaporates. To this end, we make use of the time-versus-radius relation given in Eq. (3.18). In dimensionless form,

$$\text{Ja} t^* = \frac{F(\vartheta)}{(1-8\beta)\text{Nu}} \left[1 - \frac{R}{R_0} - \frac{4\mathcal{Q}}{(1-8\beta)\mu\text{Nu}} \right] \times \ln \left(\frac{1 + (1-8\beta)\mu\text{Nu}/4\mathcal{Q}}{1 + (R/R_0)(1-8\beta)\mu\text{Nu}/4\mathcal{Q}} \right). \quad (4.12)$$

In Eq. (4.12), Ja and t^* are the Jakob number and dimensionless time, respectively:

$$\text{Ja} \equiv \frac{c_p \Delta T}{\lambda}, \quad (4.13)$$

$$t^* = \frac{t \alpha_l}{R_0^2}. \quad (4.14)$$

For the special case of $\kappa = 0$, Eq. (4.12) reduces to

$$\text{Ja} t^* |_{\kappa=0} = \frac{\mu F(\vartheta)}{8\mathcal{Q}} \left[1 - \left(\frac{R}{R_0} \right)^2 \right], \quad (4.15)$$

which does not involve β since droplet interactions are non-existent in the limit of $\kappa = 0$. In Fig. 5, we plot the ratio (R/R_0) versus $\text{Ja} t^*$ for droplets with a contact angle of $\vartheta = \pi/3$ and $\mu = 0.01$. It is seen that the lifetime of a droplet decreases as κ increases. Evidently, this is due to the higher heat flow rate into the droplet resulting from the increase in κ .

In the model for heat transfer calculations, we have made several assumptions. In particular, the temperature field is assumed to be quasi-steady and conduction dominated. The assumption of quasi-steady temperature distribution is justifi-

able in view of the fact that the time scale of evaporation is much larger than that of heat diffusion. Inside the droplets, heat flow may be augmented by liquid motion, which may result from buoyancy effect, surface-tension variations along the liquid-vapor interface, and evaporation-induced flow. However, the contributions to heat transfer by these three types of liquid motion are negligible compared to that of conduction, and, so, can be excluded. A detail discussion on these assumptions has been presented elsewhere (Tio and Sadhal, 1991) and, thus, will not be reproduced here.

5 Conclusion

We have calculated the Nusselt number for droplet spray evaporation from a heated solid surface in the low superheat regime. We have also examined the effect of droplet contact angle, solid conductivity, and droplet concentration on heat transfer.

We have attempted to include droplet thermal interactions in the heat transfer analysis by employing a model of an evaporating droplet surrounded by a uniform/constant surface heat flux. While we give results for wetted area fractions up to $\kappa = 0.7$, the results are rigorously valid only for small κ . The major challenge of truly dealing with droplets in a random spatial distribution and strong close range interactions still remains, although the preliminary studies of this type of random problem have been carried out. The validity of the current model is also limited by the constant contact angle assumption, which is necessary due to the severe complexity of the general problem. Nevertheless, investigations are under way to model the case of varying contact angles.

Acknowledgments

The research reported here was conducted by the authors while the first (K.-K. Tio) was a Ph.D. student in the Department of Mechanical Engineering at the University of Southern California. Support from the National Science Foundation (Grant No. CBT-8351432) is gratefully acknowledged.

References

- Avedisian, C. T., and Koplik, J., 1987, "Leidenfrost Boiling of Methanol Droplets on Hot Porous/Ceramic Surfaces," *International Journal of Heat and Mass Transfer*, Vol. 30, pp. 379-393.
- Ayyaswamy, P. S., 1989, "Combustion Dynamics of Moving Droplets," *Encyclopedia of Environmental Control Technology*, P. N. Cheremisinoff, ed., Gulf Publishing Co., Houston, Vol. 1, pp. 479-532.
- Bolle, L., and Moureau, J. C., 1982, "Spray Cooling of Hot Surfaces," *Multiphase Science and Technology*, G. F. Hewitt et al., eds., Hemisphere, Washington, DC, Vol. 1, pp. 1-97.
- Bonacina, C., Del Giudice, S., and Comini, G., 1979, "Dropwise Evaporation," *ASME JOURNAL OF HEAT TRANSFER*, Vol. 101, pp. 441-446.
- Chandra, S., and Avedisian, C. T., 1988, "The Evaporation and Combustion of Levitated Arrays of Two, Three and Five Droplets on a Hot Surface," *Proceedings, Royal Society of London*, Vol. A349, pp. 261-276.
- Grissom, W. M., and Wierum, F. A., 1981, "Liquid Spray Cooling of a Heated Surface," *International Journal of Heat and Mass Transfer*, Vol. 24, pp. 261-271.
- Hoogendoorn, C. J., and den Hond, R., 1974, "Leidenfrost Temperature and Heat-Transfer Coefficients for Water Sprays Impinging on a Hot Surface," *Proceedings, 5th International Heat Transfer Conference*, JSME, Tokyo, Vol. 4, pp. 135-138.
- Lebedev, N. N., 1972, *Special Functions and Their Applications*, Dover Publications, New York.
- Plesset, M. S., 1952, "Note on the Flow of Vapour Between Liquid Surfaces," *Journal of Chemical Physics*, Vol. 20, pp. 790-793.
- Plesset, M. S., and Prosperetti, A., 1976, "Flow of Vapour in a Liquid Enclosure," *Journal of Fluid Mechanics*, Vol. 78, pp. 433-444.
- Rizza, J. J., 1981, "A Numerical Solution to Dropwise Evaporation," *ASME JOURNAL OF HEAT TRANSFER*, Vol. 103, pp. 501-507.
- Sadhal, S. S., and Martin, W. W., 1977, "Heat Transfer Through Drop Condensate Using Differential Inequalities," *International Journal of Heat and Mass Transfer*, Vol. 20, pp. 1401-1407.
- Sadhal, S. S., and Plesset, M. S., 1979, "Effect of Solid Properties and Contact Angle in Dropwise Condensation and Evaporation," *ASME JOURNAL OF HEAT TRANSFER*, Vol. 101, pp. 48-54.
- Sadhal, S. S., 1989, "Heat Transport to a Slowly Growing Bubble on a Solid

Surface," *Quarterly Journal of Mechanics and Applied Mathematics*, Vol. 42, pp. 477-493.

Sneddon, I. N., 1972, *The Use of Integral Transforms*, McGraw-Hill, New York.

Tio, K.-K., and Sadhal, S. S., 1991, "Dropwise Evaporation: Thermal Analysis of Multidrop Systems," *International Journal of Heat and Mass Transfer*, in press.

Toda, S., 1972, "A Study of Mist Cooling (1st Report: Investigation of Mist Cooling)," *Heat Transfer—Japanese Research*, Vol. 1, No. 3, pp. 39-50.

Toda, S., 1974, "A Study of Mist Cooling (2nd Report: Theory of Mist Cooling and Its Fundamental Experiments)," *Heat Transfer—Japanese Research*, Vol. 3, No. 1, pp. 1-44.

Wachters, L. H. J., Smulders, L., Vermeulen, J. R., and Kleiweg, H. C., 1966, "The Heat Transfer From a Hot Wall to Impinging Mist Droplets in the Spheroidal State," *Chemical Engineering Science*, Vol. 21, pp. 1231-1238.

Yao, S. C., and Choi, K. J., 1987, "Heat Transfer Experiments of Mono-Dispersed Vertically Impacting Sprays," *International Journal of Multiphase Flow*, Vol. 13, pp. 639-648.

Zhang, S., and Gogos, G., 1991, "Film Evaporation of a Spherical Droplet Over a Hot Surface: Fluid Mechanics and Heat/Mass Transfer Analysis," *Journal of Fluid Mechanics*, Vol. 222, pp. 543-563.

APPENDIX A

Under the coordinate transformation given by Eqs. (3.1) and (3.2), Eqs. (2.6) and (2.7) take the form of

$$\frac{\partial}{\partial \xi} \left(\frac{\sinh \xi}{\cosh \xi - \cos \eta} \frac{\partial T_s}{\partial \xi} \right) + \frac{\partial}{\partial \eta} \left(\frac{\sinh \xi}{\cosh \xi - \cos \eta} \frac{\partial T_s}{\partial \eta} \right) = 0, \quad (\text{A.1})$$

where $0 \leq \xi < \infty$, $0 < \eta < \pi$, and

$$\frac{\partial}{\partial \xi} \left(\frac{\sinh \xi}{\cosh \xi - \cos \eta} \frac{\partial T_l}{\partial \xi} \right) + \frac{\partial}{\partial \eta} \left(\frac{\sinh \xi}{\cosh \xi - \cos \eta} \frac{\partial T_l}{\partial \eta} \right) = 0, \quad (\text{A.2})$$

where $0 \leq \xi < \infty$, $\pi < \eta < \eta_0$. The boundary conditions (2.8)-(2.12) are transformed into

$$\eta = \eta_0 : T_l = T_v, \quad (\text{A.3})$$

$$\eta = \pi : T_s = T_l, \quad (\text{A.4})$$

$$k_s \frac{\partial T_s}{\partial \eta} = k_l \frac{\partial T_l}{\partial \eta}, \quad (\text{A.5})$$

$$\eta = 0 : k_s \frac{1}{h_\eta} \frac{\partial T_s}{\partial \eta} = q_0, \quad (\text{A.6})$$

$$(\xi, \eta) = (0, 0) : T_s = T_0 + \frac{q_0 R}{k_s} \frac{\sin \eta}{\cosh \xi - \cos \eta}. \quad (\text{A.7})$$

A convenient form of the solution is (Lebedev, 1972)

$$\frac{T_l - T_0}{T_0 - T_v} = -1 + (2 \cosh \xi - 2 \cos \eta)^{1/2} \times \int_0^\infty \mathcal{L}(\tau) \sinh(\eta_0 - \eta) \tau P_{\tau-1/2}(\cos \xi) d\tau, \quad (\text{A.8})$$

$$\frac{T_s - T_0}{T_0 - T_v} = \frac{q_0 z}{k_s (T_0 - T_v)} - (2 \cosh \xi - 2 \cos \eta)^{1/2} \times \int_0^\infty \mathcal{S}(\tau) \cosh \eta \tau P_{\tau-1/2}(\cos \xi) d\tau, \quad (\text{A.9})$$

where \mathcal{L} and \mathcal{S} are two unknown functions. T_l and T_s as given in Eqs. (A.8) and (A.9) satisfy the boundary conditions (A.3), (A.6), and (A.7). Applying Eq. (A.4), we obtain

$$\int_0^\infty [\mathcal{L}(\tau) \sinh \vartheta \tau + \mathcal{S}(\tau) \cosh \pi \tau] P_{\tau-1/2}(\cosh \xi) d\tau = \frac{1}{2 (\cosh \xi + 2)^{1/2}}. \quad (\text{A.10})$$

Using the integral expansion of Lebedev (1972),

$$\frac{1}{(2 \cosh \xi - 2 \cos \eta_p)^{1/2}} = \int_0^\infty \frac{\cosh(\pi - \eta_p) \tau}{\cosh \pi \tau} P_{\tau-1/2}(\cosh \xi) d\tau, \quad (\text{A.11})$$

which is valid for $0 < \eta_p < 2\pi$, we conclude from Eq. (A.10) that

$$\sinh \vartheta \tau \mathcal{L}(\tau) + \cosh \pi \tau \mathcal{S}(\tau) = \frac{1}{\cosh \pi \tau}. \quad (\text{A.12})$$

On the other hand, application of Eq. (A.5) yields

$$\int_0^\infty \tau [\mu \cosh \vartheta \tau \mathcal{L}(\tau) - \sinh \pi \tau \mathcal{S}(\tau)] P_{\tau-1/2}(\cosh \xi) d\tau = \frac{2q_0 R}{k_s (T_0 - T_v)} \frac{1}{(2 \cosh \xi + 2)^{3/2}}. \quad (\text{A.13})$$

Making use of Eq. (A.11), we conclude from Eq. (A.13) that

$$\mu \cosh \vartheta \tau \mathcal{L}(\tau) - \sinh \pi \tau \mathcal{S}(\tau) = \frac{2q_0 R}{k_s (T_0 - T_v)} \frac{\tau}{\cosh \pi \tau}. \quad (\text{A.14})$$

Equations (A.12) and (A.14) then yield the functions \mathcal{L} and \mathcal{S} as given in Eqs. (3.8) and (3.9).

APPENDIX B

The time-averaged base area of a droplet is

$$\overline{\pi R^2} = \frac{1}{t_0} \int_0^{t_0} \pi R^2 dt. \quad (\text{B.1})$$

Substitution of Eq. (3.15) into Eq. (B.1) yields

$$\overline{\pi R^2} = \frac{\pi \lambda \rho_l F(\vartheta)}{t_0} \int_0^{R_0} \frac{R^3}{q_0 (1 - 8\mathcal{B})R + 4\mathcal{Q}k_s \Delta T} dR. \quad (\text{B.2})$$

Integrating Eq. (B.2) and then making use of formula (3.19), we obtain

$$\frac{\overline{\pi R^2}}{\pi R_0^2} = \frac{1}{\zeta^2} + \left(\frac{1}{3} - \frac{1}{2\zeta} \right) \left[1 - \frac{1}{\zeta} \ln(1 + \zeta) \right]^{-1}, \quad (\text{B.3})$$

where

$$\zeta = \frac{(1 - 8\mathcal{B})\mu \text{Nu}}{4\mathcal{Q}}. \quad (\text{B.4})$$

Since the expression for ζ , Eq. (B.4), contains the initial radius R_0 , we can, in principle, solve Eq. (B.3) for $\overline{\pi R^2}$ in terms of πR_0^2 . However, this is impractical. Instead, we will first estimate the magnitude of ζ . For small μ , $\mathcal{Q} \sim (\pi\mu/\vartheta)^{1/2}/2$, $(1 - 8\mathcal{B}) \sim 4(\pi\mu/\vartheta)^{1/2}/\pi$, and $\mu \text{Nu} \sim 8\kappa (\pi\mu/\vartheta)^{1/2}/3$. Thus, $\zeta \ll 1$, and we can expand the right-hand side of Eq. (B.3) asymptotically in terms of ζ . This results in

$$\frac{\overline{\pi R^2}}{\pi R_0^2} \sim \frac{1}{2} + \mathcal{O}(\zeta). \quad (\text{B.5})$$

Thickness-Dependent Radiative Properties of Y-Ba-Cu-O Thin Films

P. E. Phelan¹
Assoc. Mem. ASME

G. Chen

C. L. Tien

A. Martin Berlin Professor.
Fellow ASME.

Department of Mechanical Engineering,
University of California,
Berkeley, CA 94720

Some applications of high-temperature superconductors where their radiative behavior is important, such as bolometers, optically triggered switches and gates, and space-cooled electronics, require the superconductor to be in the form of a very thin film whose radiative properties cannot be adequately represented by a semi-infinite analysis. Two properties of particular importance are the film absorptance and the combined film/substrate absorptance, which are crucial to the operation of many devices. Here, calculations of the spectral, normal-incidence absorptance of superconducting-state Y-Ba-Cu-O films on MgO substrates suggest that a decrease in the film thickness often leads to an increase in both the film and the film/substrate absorptance. Furthermore, both can exhibit a maximum at some optimal value of film thickness. Room-temperature experiments verify the qualitative features of the spectral film/substrate absorptance, indicating the assumption that the film is a smooth, continuous slab with a refractive index equal to that of well-aligned bulk Y-Ba-Cu-O is valid, at least in the normal state and for films as thin as 35 nm.

Introduction

The initial applications of high-temperature superconductors (HTSC) are likely to be in the form of electronic devices constructed from thin films. Superconducting bolometers fabricated from HTSC will enable more sensitive far-infrared radiation detection at liquid-nitrogen temperature than is currently achievable, and will therefore be one of the first major applications of HTSC (Richards et al., 1989). Other applications include superconducting radiation shielding (Zeller, 1990), which will improve the effectiveness of cryogenic insulation, an optically triggered opening switch capable of supporting large electrical currents (Francavilla et al., 1989), a rapid logic gate that operates in a manner similar to the opening switch (Wautelet, 1987), and possibly various hybrid electronic circuits consisting of both superconducting and semiconducting elements.

The operation of some devices, such as bolometers, radiation shields, and space-based electronics, depends significantly on thermal radiation. Radiation absorption is crucial to the operation of superconducting bolometers and optically triggered switches and logic gates. Superconducting radiation shielding is attractive because of the nearly perfect reflectance exhibited by relatively thick, well-aligned superconductors in the far-infrared. Furthermore, space-based 77-K electronics can conceivably be cooled solely through radiation to the space environment.

Previous analyses of the thermal radiative properties of Y-Ba-Cu-O films (Phelan et al., 1990, 1991) concentrated exclusively on relatively thick films where the substrate beneath the film and the film thickness have little or no effect on the radiative properties. This approach is justified for films of thicknesses much greater than the radiation penetration depth. In the applications mentioned above, however, and perhaps in other electronic devices that require their total volume to be minimized, very thin films are employed. The sensitivity of a bolometer increases as its heat capacity is reduced; a decrease in the film thickness, thereby reducing the film volume, lowers

the heat capacity of the device. Similar reasoning applies to the optically triggered switch and logic gate, which rely on the temperature increase in the film due to the incident optical signal to change from a superconducting to a nonsuperconducting state. The "semi-infinite" analysis must fail in these situations.

Relatively few studies concerning the thickness-dependent radiative properties of thin-film HTSC have been performed. Bozovic et al. (1987) examined the room-temperature reflectance, ρ , and film/substrate transmittance, τ , of Y-Ba-Cu-O films on SrTiO₃ substrates as functions of wavelength, λ . Their samples ranged from 90 to 1000 nm in thickness. Their measured transmittance through the film and substrate, as expected, increased as the film thickness, d , decreased, and the reflectance increased with increasing d , in agreement with the results presented here. They did not, however, discuss the role d plays with regard to radiative behavior, nor was the film absorptance mentioned, along with any possible substrate effects. Furthermore, the substrate thickness was unspecified.

More recently, Flik et al. (1990) examined the dependence of the normal-state film emittance on the film thickness. Their study focused on the deposition process of a thin-film superconductor, and thus they were concerned with temperatures near 1000 K. Their calculations indicated that the film thickness has a great effect on the emittance for film thicknesses less than about 300 nm. In this study, however, the emittance and structure of the films were not directly measured or observed, and the calculations were carried out only for sputtering temperatures.

Further investigation of the thickness-dependent radiative properties of thin-film HTSC is in order, especially the superconducting-state radiative behavior. An especially important property is the spectral, normal-incidence film absorptance α , which is a property essential to many thermal analyses of thin-film devices. In this paper the results of an analytical and experimental investigation of the radiative properties of thin-film Y-Ba-Cu-O are reported. The films are sufficiently thin so that both their thickness and the substrate material must be taken into account. Both α and the spectral, normal-incidence combined film/substrate absorptance α_c are calculated for various temperatures in the superconducting state, using the electromagnetic relations appropriate for two adjacent,

¹Present address: Tokyo Institute of Technology, Department of Mechanical Engineering Science, 2-12-1 Ohokayama, Meguro-ku, Tokyo 152 Japan.

Contributed by the Heat Transfer Division and presented at the 3rd ASME/JSME Joint Thermal Engineering Conference, Reno, Nevada, March 17-22, 1991. Manuscript received by the Heat Transfer Division November 30, 1990; revision received July 1, 1991. Keywords: Cryogenics, Radiation.

continuous slabs bordered by semi-infinite media. The superconducting-state radiative properties are calculated using an approximate form (Phelan et al., 1991) of the Mattis–Bardeen theory (Mattis and Bardeen, 1958). It is determined that a decrease in d usually brings about an increase in α until some optimum d is reached, after which α decreases with decreasing d . This result cannot be predicted from the approximate geometric optics relations, which neglect interference effects. The validity of employing a thin-film optics analysis in conjunction with bulk refractive indices is qualitatively verified, at least in the normal state and for films thicker than 35 nm, by comparing normal-state, room-temperature analytical results with experimental data.

Analytical Model

The radiative behavior of the film/substrate system can be calculated using the electromagnetic theory relations for a system composed of two adjacent, continuous slabs bordered by semi-infinite media on each side. The incident radiation is assumed to be normal to the plane of the thin film. The complex amplitudes of the reflected and transmitted electric fields, along with the amplitudes of the electric fields inside the film and the substrate, are derived by the matrix method given by Heavens (1965). The combined film/substrate absorptance α_c is calculated by subtracting the sum of the reflectance, ρ , and transmittance through the rear of the substrate, τ , from one. Formulae for ρ and τ are given by Heavens (1965). The authors, however, could not locate an explicit expression for the film absorptance α , and thus an appropriate expression had to be derived.

The film absorptance is calculated in a manner completely analogous to the calculation of the combined film/substrate absorptance. That is, α is given by

$$\alpha = 1 - \rho - \tau_f \quad (1)$$

where τ_f is the transmittance through the film and into the substrate. The quantity τ_f is determined from the ratio of the amplitude of the time-averaged Poynting vector at the film/substrate interface, to the amplitude of the incident Poynting vector:

$$\tau_f = \frac{1}{n_o} \operatorname{Re} \left\{ \left[\left(\frac{E_f^+}{E_o^+} \right) \exp \left(\frac{i\omega d N_f}{c} \right) + \left(\frac{E_f^-}{E_o^+} \right) \exp \left(-\frac{i\omega d N_f}{c} \right) \right] \cdot N_f^* \left[\left(\frac{E_f^+}{E_o^+} \right)^* \exp \left(-\frac{i\omega d N_f^*}{c} \right) - \left(\frac{E_f^-}{E_o^+} \right)^* \exp \left(+\frac{i\omega d N_f^*}{c} \right) \right] \right\} \quad (2)$$

where n_o is the real part of the complex refractive index of the

incident medium, i is $\sqrt{-1}$, c the speed of light in vacuum, $\omega = 2\pi c/\lambda$ the angular frequency of the incident electric field in vacuum, $N_f = n_f + \kappa_f i$ the complex refractive index of the film, and E_f^+ , E_f^- , and E_o^+ the complex electric field amplitudes, at the first interface between the incident semi-infinite medium and the film, traveling in the positive direction inside the film, in the negative direction inside the film, and in the positive direction in the incident medium, respectively. The quantities E_f^+ , E_f^- , and E_o^+ are equal to E_1^+ , E_1^- , and E_o^+ , respectively, given by Heavens (1965), along with the stated positive and negative directions. Equation (2) assumes $\exp(-i\omega t)$ dependence on time t . The electric field amplitudes are functions of d , N_f , λ , the substrate thickness d_s , and the refractive indices of the incident and transmitted semi-infinite media and of the substrate. An asterisk (*) denotes the complex conjugate, and “Re” represents the real part.

Refractive Indices. The refractive indices of the film, substrate, incident medium, and the transmitted region behind the substrate are all required for calculating α and α_c . Here, both the incident semi-infinite region and the semi-infinite region behind the substrate are assumed to be vacuum. This is appropriate especially for the bolometer application, where it is desired to isolate the bolometer thermally to maximize its temperature response (Newhouse, 1964).

For the Y–Ba–Cu–O film in its superconducting state, the refractive index N_f , appropriate for an incident electric field vector parallel to the ab plane, is determined from approximate fits (Phelan et al., 1991) to the Mattis–Bardeen (MB) theory of the superconducting-state electrical conductivity (Mattis and Bardeen, 1958). A complete discussion of the applicability of the MB theory to high-temperature superconductors is given by Phelan et al. (1991). The MB theory was demonstrated to predict reasonably the near-normal reflectance of an epitaxial Y–Ba–Cu–O film over the entire superconducting temperature range, and for wavelengths longer than about 10 μm . Furthermore, the error engendered by using the approximate expressions for the MB theory was shown to be less than 0.2 percent when calculating the normal-incidence reflectance (Phelan et al., 1991).

The MB theory should be applicable provided the film thickness is larger than the superconducting coherence length, which for Y–Ba–Cu–O is approximately 2 nm (Cava et al., 1987). Three inputs are required: the energy gap parameter A , the critical temperature T_c , and the direct-current electrical resistivity r_{dc} . The energy gap parameter A is taken to be 3.52, the value obtained from the weak-coupling form of the Bardeen–Cooper–Schrieffer (BCS) theory, and the critical temperature is assumed to be 91 K, which is typical for high-quality Y–Ba–

Nomenclature

A = energy gap parameter	α = spectral, normal-incidence film absorptance = $1 - \rho - \tau_f$	τ_f = spectral, normal-incidence transmittance through the film and into the substrate
c = speed of light in vacuum = $2.998 \times 10^8 \text{ m s}^{-1}$	α_c = spectral, normal-incidence combined film/substrate absorptance = $1 - \rho - \tau$	ω = radiation angular frequency in vacuum, rad s^{-1}
d = film thickness, nm	δ = electromagnetic power penetration depth in the film, m	Subscripts
E = electric field vector, V m^{-1}	κ = imaginary part of the complex refractive index	c = combined film and substrate
i = $\sqrt{-1}$	λ = radiation wavelength in vacuum, μm	f = film
n = real part of the complex refractive index	λ_g = radiation wavelength corresponding to the energy gap, μm	o = incident medium
N = complex refractive index = $n + \kappa i$	ρ = specular, spectral, normal-incidence reflectance	s = substrate
N_e = electron number density, m^{-3}	τ = spectral, normal-incidence transmittance through the back of the substrate	Superscripts
r_{dc} = direct-current electrical resistivity, Ωm		$+$ = positive direction
Re = real part		$-$ = negative direction
T = temperature, K		$*$ = complex conjugate
T_c = critical temperature, K		

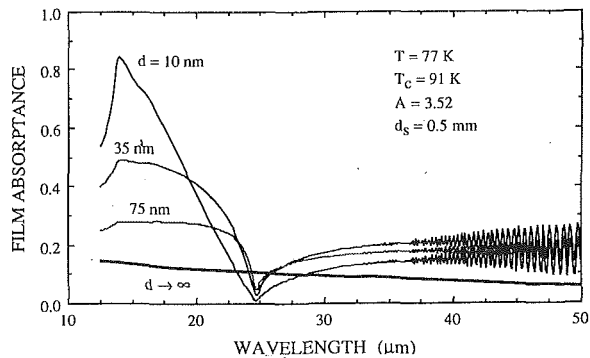


Fig. 1 Calculated normal-incidence film absorptance of superconducting Y-Ba-Cu-O on an MgO substrate, as a function of irradiation wavelength

Cu-O films. As discussed by Phelan et al. (1991), A is not known precisely for high-temperature superconductors. Later in this report, the results of further calculations performed for $A = 7.0$ are described.

The normal-state electrical resistivity is assumed to obey the function

$$r_{dc} = (2.87 \times 10^{-8})T \quad (3)$$

where r_{dc} is in [Ω -m] and the temperature, T , is in [K]. Equation (3) is assumed to apply for all Y-Ba-Cu-O films, regardless of the film thickness. Its value at room temperature corresponds to an average from several studies (Phelan et al., 1990), and extrapolation of r_{dc} down to zero at 0 K has been noted in at least one study of Y-Ba-Cu-O films (Roas et al., 1988). Equation (3) is meant to serve as an approximate function that generally represents epitaxial Y-Ba-Cu-O thin films.

For small film thicknesses comparable to the electron mean free path, r_{dc} becomes a function of d . The estimated electron mean free path for the temperatures considered here is less than 10 nm (Phelan et al., 1991), so Eq. (3) should be most accurate for films thicker than this. The normal-state electrical conductivity required by the Mattis-Bardeen theory is assumed to be the inverse of the electrical resistivity, and so a change in r_{dc} will affect the value of the predicted refractive index. In this study, however, any influence of the film thickness on r_{dc} is neglected.

For the Y-Ba-Cu-O film in its normal state, the room-temperature Drude theory reported in a previous study (Phelan et al., 1990) is employed. The Drude theory was demonstrated to describe accurately the far-infrared, normal-state, normal-incidence reflectance of Y-Ba-Cu-O single crystals and epitaxial films. The necessary input parameters, the electrical resistivity r_{dc} and electron number density N_e , are taken to be the average room-temperature values given earlier (Phelan et al., 1990): $r_{dc} = 8.6 \times 10^{-6}$ Ω -m and $N_e = 7.4 \times 10^{27}$ m^{-3} . Although this value of r_{dc} is assumed to hold for films of all thicknesses, again it may become inaccurate for very thin films where r_{dc} becomes a function of film thickness.

The refractive index of the MgO substrate, $N_s = n_s + \kappa_s i$, is conveniently given by Lorentz-type oscillator fits to reflectance data (Jasperse et al., 1966). They measured the reflectance of single-crystal MgO samples over the spectral region $12.5 \mu m \leq \lambda \leq 50 \mu m$, and for temperatures ranging from 8 K to 1950 K. Values of the oscillator formula coefficients at the desired temperatures are determined by interpolating between the temperatures reported by Jasperse et al. (1966).

Superconducting-State Calculations

Both the absorptance of the film, and that of the film/substrate combination, are of interest. In general, it is desired to maximize the absorptance in order to increase sensitivity. In applications where a fast response is required, such as in

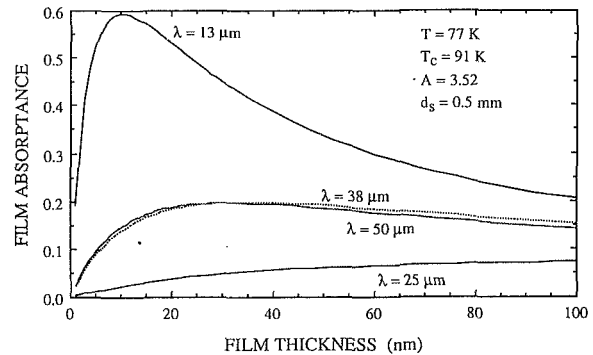


Fig. 2 Calculated normal-incidence film absorptance of a varying-thickness, superconducting Y-Ba-Cu-O film on an MgO substrate

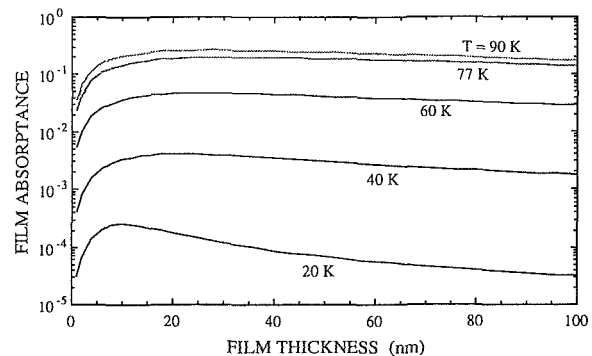


Fig. 3 Calculated normal-incidence film absorptance of a varying thickness, superconducting Y-Ba-Cu-O film on an MgO substrate. The calculation parameters are $T = 77$ K, $T_c = 91$ K, $A = 3.52$, $\lambda = 50 \mu m$, and $d_s = 0.5$ mm.

optically triggered switches and gates, and very fast bolometers, the *film* absorptance is more crucial than the combined film/substrate absorptance. This is due to the fact that it takes much less time to heat up and cool down the film, i.e., the thermal time scale of the film is short compared to the thermal time scale of the film/substrate combination. For this simple type of configuration, the film/substrate thermal time scale is estimated to be on the order of 1 ms (Forrester et al., 1988), whereas that of the film itself is on the order of 1 ns (Flik et al., 1990). At least one design, however, has been proposed that may significantly decrease the film/substrate thermal time scale (Hu and Richards, 1989).

In this section, the results of calculations of both α and α_c are presented. The Y-Ba-Cu-O film is in the superconducting state. The parameters varied in the calculations include irradiation wavelength, film thickness, and temperature.

Film Absorptance. The calculated normal-incidence film absorptance, as a function of wavelength, is given in Fig. 1. The film temperature is 77 K, and the film thickness is varied between 10 nm and infinity, i.e., a semi-infinite medium. The predominant structures in the spectra, namely the peak at $\lambda \approx 14 \mu m$, the minimum at $\lambda \approx 25 \mu m$, and the interference fringes occurring for $\lambda > 35 \mu m$, are due in large part to the radiative properties of the MgO substrate. The peak at $\lambda \approx 14 \mu m$ comes about because of a local maximum in the reflectance at the film/substrate interface (giving a greater film absorptance) resulting from the relative magnitudes of N_f and N_s at that wavelength. Around $\lambda = 25 \mu m$, both the real and the imaginary parts of N_s are much higher than at shorter or longer wavelengths, and actually reach values slightly greater than those of N_f . Since N_f and N_s are of the same magnitude, here little reflectance occurs at the film/substrate interface, leading to the observed decreased film absorptance. Finally, the interference fringes appearing at long wavelengths result

from wave interference within the substrate. For long wavelengths, the substrate penetration depth $\delta_s \equiv \lambda/(4\pi\kappa_s)$ becomes the same order as the substrate thickness d_s , making it possible for interference fringes to appear. The spacing of the observed peaks occurs for changes in the parameter $n_s d_s/\lambda$ of 0.5, as expected for substrate wave interference.

The absorptance of the semi-infinite Y-Ba-Cu-O medium, on the other hand, shows no particular structures and decreases smoothly with increasing wavelength. This is to be expected since the wavelength corresponding to the energy gap, λ_g , which at 77 K is about 69 μm , is not within the calculated spectrum, and therefore no features related to the energy gap are present.

Figure 2 presents the calculated film absorptance, as a function of film thickness, at $T = 77$ K and for several representative wavelengths. The film absorptance is a strong function of d , especially for $\lambda = 13$ μm . The $\lambda = 13$ μm , $\lambda = 38$ μm , and $\lambda = 50$ μm curves display a maximum in the film absorptance. The magnitudes of the peaks, for each given wavelength, are determined to large extent by the substrate refractive index, as discussed for Fig. 1. The $\lambda = 25$ μm curve has no peak since at that wavelength the film absorptance is relatively independent of film thickness (Fig. 1).

The effect of varying temperature on the film absorptance is given in Fig. 3. The calculations are performed for $\lambda = 50$ μm and for temperatures ranging from 20 K to 90 K. Absorptance peaks occur for all temperatures. The drastic decrease in film absorptance with temperature occurs primarily because of the changes in N_f , and to a much lesser extent on the changes in N_s . The absorptance of the superconducting film, for wavelengths longer than λ_g , comes about only because of the presence of normal-state electrons. For wavelengths shorter than λ_g , both the superconducting Cooper pairs and the normal-state electrons contribute to the absorption process. Thus, the reason the calculated absorptance at 20 K and 40 K is much lower than at higher temperatures is that the wavelength, 50 μm , is longer than λ_g , which is about 46 μm for $T = 40$ K, and 45 μm for $T = 20$ K. In comparison, λ_g is about 52 μm for 60 K, 69 μm for 77 K, and 236 μm for 90 K.

Varying the substrate thickness has little effect on the magnitude of the film absorptance. Provided the penetration depth in the substrate is sufficiently longer than the substrate thickness, changing the substrate thickness introduces interference characteristics in the absorptance curve, but otherwise does not significantly increase or decrease the film absorptance. For cases where the substrate penetration depth is less than the substrate thickness, changing the substrate thickness has almost no effect on the film absorptance.

The most striking features of Figs. 2 and 3 are the maxima observed in the film absorptance versus film thickness curves. This has been noted before (Armaly and Tien, 1970), and is not surprising since the films are very thin compared to the irradiation wavelengths. Earlier calculations (Born and Wolf, 1980) indicated that when the optical thickness, defined as $n_f d$, is less than a quarter wavelength, the reflectance tends to decrease with decreasing d , while on the other hand the transmittance through the film and into the substrate tends to increase with decreasing d . The film absorptance is $1 - \rho - \tau_f$, and hence it should be maximum at some optimum value of film thickness. The two figures show that this is indeed what occurs. Thus, in any application where it is desired to maximize the film absorptance, the film thickness should be chosen as near to the optimum value as possible.

The absorptance maximum is due to interference. If the approximate geometric optics relations, which neglect interference and are based on intensity superposition, are used to calculate the thickness-dependent reflectance of a thin film, a reflectance that *increases* with decreasing film thickness results. On the other hand, the film transmittance increases with decreasing film thickness even if interference is not considered. In short, calculations of the film absorptance for films whose

optical thickness is less than a quarter wavelength require the complete thin-film electromagnetic relations. The approximate geometric optics formulae are inadequate in such cases.

For the parameters used in these calculations, the maximum absorptance occurs for film thicknesses between 10 and 35 nm. Earlier studies have indicated that the superconducting properties of very thin Y-Ba-Cu-O films can be degraded (Venkatesan et al., 1989; Xi et al., 1989). One study (Venkatesan et al., 1989) reported that both T_c and the critical current density of pulsed-laser-deposited Y-Ba-Cu-O films on SrTiO₃ substrates deteriorated rapidly for $d < 30$ nm, and that a 5-nm-thick film exhibited metallic, but not superconducting, features. Similar behavior was observed in another investigation (Xi et al., 1989), in which Y-Ba-Cu-O films were deposited on both SrTiO₃ and MgO substrates by inverted cylindrical magnetron sputtering. They found that superconductivity could be observed in films as thin as 3 nm (SrTiO₃ substrates) and 6 nm (MgO substrates), although with diminished T_c . A recent study (Streiffer et al., 1991) stated that in general, T_c decreases and the width of the resistance transition increases for $d \leq 10$ nm. Thus, a more detailed theory of the thickness-dependent radiative properties would need to take into account the effects of film thickness on superconducting behavior.

Another important aspect is that the minimum film thickness for which the film can be assumed to be a perfect, continuous slab is not known. An earlier study on evaporated metal films suggested that the minimum film thickness for which the theory was applicable was about 20 nm (Sennett and Scott, 1950). Below this thickness, the radiative properties and behavior of the films were calculated by assuming the films to consist of an aggregated structure, where small spheres of the metal are randomly distributed in a dielectric matrix (Sennett and Scott, 1950). A similar procedure can perhaps be applied to Y-Ba-Cu-O films, but experimental data on the structure and radiative behavior of very thin Y-Ba-Cu-O films are first necessary to establish such a theory. Some room-temperature data are given later in this report, but the accuracy of the experiments was not sufficient for such a detailed examination.

The qualitative features of Figs. 1–3, and especially of the peaks in Figs. 2 and 3, are relatively independent of the input parameters A and T_c of the MB theory. For example, A was taken to be 7.0 rather than 3.52, and T_c was chosen to be 80 K instead of 91 K. These changes yielded almost no perceptible difference in the 77 K, $\lambda = 13$ μm α curve of Fig. 2, and only slightly increased the other curves. A change in the temperature function for r_{dc} (Eq. (3)), however, can shift the maxima in Fig. 2 to substantially different optimum film thicknesses; a lower value of r_{dc} pushes the maxima toward smaller film thicknesses. Thus, at present it is difficult to predict in general the optimum film thickness for maximum absorptance without performing these calculations using appropriate values of the input parameters A , T_c , r_{dc} , and N_s .

Figures 1–3 suggest that fast-response high- T_c superconducting bolometers need not suffer from the nearly perfect reflectance exhibited by relatively *thick* superconducting films and single crystals. Finite-thickness films can have absorptances much higher than semi-infinite media. The result is that an uncoated Y-Ba-Cu-O film, which has a relatively low heat capacity, may be competitive with a Y-Ba-Cu-O film coated with an optical absorber, which adds its heat capacity to that of the superconducting film and thus slows its response and decreases the voltage output.

A previous investigation of low-temperature superconducting bolometers (Clarke et al., 1977) examined bolometers in which the absorbing film (in this case not the superconducting film) was located *behind* the substrate, that is, the incident radiation struck the substrate first. Following this lead, some calculations were performed where the locations of the film and substrate were reversed. The results indicate that for long

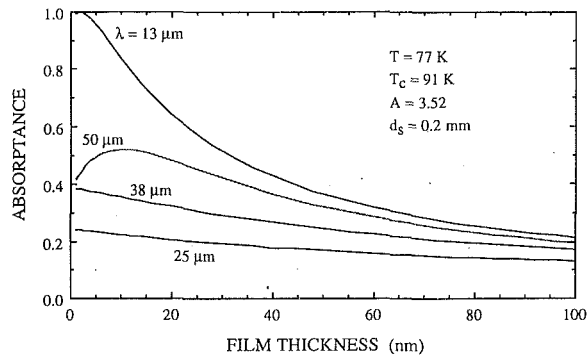


Fig. 4 Calculated normal-incidence combined film/substrate absorptance of a varying-thickness, superconducting Y-Ba-Cu-O film on an MgO substrate

wavelengths where δ_s is the same order as d_s , the magnitude of the peak α can be slightly less or slightly more than when the film is in front of the substrate, but that the optimum film thickness does not change. For short wavelengths where δ_s is much less than d_s , as expected the film absorptance is very low.

A few calculations were also performed for short-wavelength irradiation that is more representative of laser wavelengths, which would probably be used in the optically triggered switch and gate applications. For the HeNe wavelength of $0.63 \mu\text{m}$, the refractive index of Y-Ba-Cu-O is approximately $N_f = 1.8 + 0.3i$ (Schlesinger et al., 1987; Wang et al., 1987; Kamaras et al., 1989), is relatively independent of temperature (Kamaras et al., 1989), and thus applies for both the superconducting and normal states. For MgO, the refractive index is approximately $N_s = 1.7 + (1.7 \times 10^{-6})i$ (Bohren and Huffman, 1983), and is also independent of temperature (Touloukian and DeWitt, 1972). The calculated results, however, at this wavelength, using these values of N_s and N_f , and taking the substrate thickness to be 0.5 mm , revealed no maximum in the film absorptance for values of d down to $d = 1 \text{ nm}$. The film absorptance increased as the film thickness increased, suggesting that for short wavelengths the optimum film thickness has to be chosen considering both the film heat capacity and its absorptance. Similar results were obtained for $\lambda = 1.06 \mu\text{m}$, and for the situation discussed above where the film is placed behind the substrate.

Film/Substrate Absorptance. Figure 4 shows the combined film/substrate absorptance as a function of film thickness, for a fixed substrate thickness of 0.2 mm . Peaks in the absorptance curve appear for $\lambda = 13 \mu\text{m}$ and $\lambda = 50 \mu\text{m}$, whereas for the other two curves α_c decreases as d increases. The absorptance peak occurs for $\lambda = 50 \mu\text{m}$ because the penetration depth in the substrate, δ_s , is about 0.5 mm and is much longer than at other wavelengths, thus allowing sufficient transmittance to yield a peak in α_c , as per the above discussion of the maximum film absorptance. The observed peak for $\lambda = 13 \mu\text{m}$ at $d = 2 \text{ nm}$, however, cannot be due to this mechanism, since here δ_s is only about $33 \mu\text{m}$. For this wavelength, the reflectance exhibits a local minimum at $d = 2 \text{ nm}$, leading to the peak in α . The physical mechanism behind this peak is not clear.

Increasing the substrate thickness can increase the combined film/substrate absorptance, provided δ_s is the same order as d_s . Similar to the film absorptance results, in this situation interference ripples are also introduced into the absorptance curves, but no distinct maxima can be seen.

Finally, placing the film behind the substrate can lead to results very different from those when the film is in front of the substrate, as indicated in Fig. 5. A maximum is again seen for $\lambda = 50 \mu\text{m}$, and is somewhat higher than before. The $\lambda = 13 \mu\text{m}$ and $\lambda = 25 \mu\text{m}$ absorptances are nearly independent of film thickness. More striking, however, is that the trend

displayed by the $\lambda = 38 \mu\text{m}$ curve is the opposite of that in Fig. 4: α_c increases with increasing d . Except for $\lambda = 13 \mu\text{m}$, the maximum α_c is greater when the film is behind the substrate. This characteristic suggests that for applications where it is desired to maximize the combined film/substrate absorptance, it is beneficial to place the substrate between the film and the incident radiation.

Room-Temperature Experiments

A short series of room-temperature reflectance and transmittance experiments, from which the film/substrate absorptance can be determined, was carried out in order to investigate the validity of the present theoretical approach. The tests were conducted to determine whether thin-film optics, meaning the electromagnetic theory of Eqs. (1) and (2), which assumes the film and substrate to be two perfect, continuous slabs, are applicable to Y-Ba-Cu-O films. Furthermore, it was desired to test the validity of applying the refractive index of relatively thick, epitaxial, and nontransparent Y-Ba-Cu-O films or single crystals, to the very thin films examined here. Due to some experimental difficulties, the number of samples was limited to only two films, and thus the experimental results are not conclusive. Still, a comparison between the experimental data and the theoretical results is useful, and is presented below.

Samples. The experiments were performed on two Y-Ba-Cu-O thin films deposited on $1 \text{ cm} \times 1 \text{ cm} \times 0.5\text{-mm}$ -thick single-crystal MgO substrates. The film thicknesses were 35 nm and 75 nm , with a measurement error of $\pm 5 \text{ nm}$. The *in situ* deposition was carried out by laser evaporation deposition, and the substrate was maintained at an approximate temperature of 920 K . The films were *not* deposited in-house—they were supplied through the courtesy of Professor H.S. Kwok and his student, Q. Y. Ying, at SUNY Buffalo. Full details of the deposition procedure are given elsewhere (Kwok et al., 1988; Ying et al., 1989). The films appeared shiny and black, with the thinner film being noticeably more transparent than the thicker film. The critical temperatures of both films were greater than 80 K .

A mechanical profilometer scan of one of the films revealed the surface to be relatively smooth. The surface features were generally much less than $1 \mu\text{m}$ in size. For the wavelengths considered here ($\lambda \geq 2 \mu\text{m}$), the amount of diffuse reflection should be small.

Apparatus. A Nicolet 740 Fourier Transform Infrared (FTIR) spectrometer was employed for measuring the near-normal specular reflectance and the normal transmittance. The results reported here were taken at a resolution of 4 cm^{-1} . The transmittance measurements required no special accessory other than that already supplied with the spectrometer. On the other hand, for the reflectance measurements, a mirror accessory purchased from Harrick Scientific Corporation of Ossining, NY, was utilized. The approximate incidence angle was 11 deg from normal.

Procedure. The transmittance measurements were conducted employing typical FTIR procedure. The width of the optical beam was less than 7 mm . The incidence angle was approximately zero degrees. The transmittance measurements were performed twice for each sample: once with the mid-infrared beam splitter and detector in place, which were used for $2 \mu\text{m} \leq \lambda \leq 25 \mu\text{m}$, and once with the far-infrared beam splitter and detector, which allowed measurement for $16 \mu\text{m} \leq \lambda \leq 200 \mu\text{m}$. In the overlapping region from $16 \mu\text{m}$ to $25 \mu\text{m}$, the two spectra were averaged to give a single curve from $2 \mu\text{m}$ to $200 \mu\text{m}$, with possible small kinks in the curve appearing at $\lambda = 16 \mu\text{m}$ and $\lambda = 25 \mu\text{m}$. The difference between the two sets of data in the overlapping region was less than 10 percent.

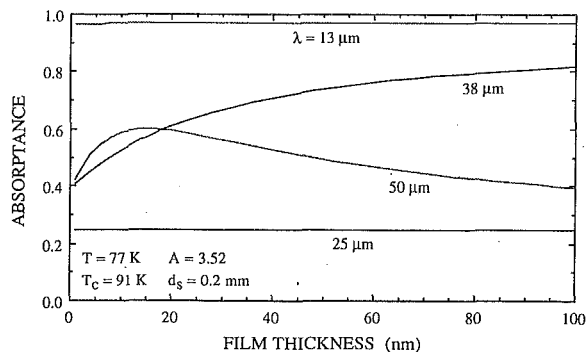


Fig. 5 Calculated normal-incidence combined film/substrate absorptance of a varying-thickness, superconducting Y-Ba-Cu-O film on an MgO substrate, in which the film is located *behind* the substrate

The reflectance measurements were slightly more difficult and more susceptible to error, and thus a total of four spectra were recorded for each sample: two in the mid-infrared, and two in the far-infrared. The two mid-infrared spectra were averaged to give a single mid-infrared curve; the same procedure was applied to the far-infrared spectra. As was the case for the transmittance data, the resulting average curves were again averaged in the overlapping wavelength region between the mid- and far-infrared, and again the difference between the two sets of data was less than 10 percent.

A reflectance measurement was initiated by measuring the spectrum of a 1 cm² aluminized-glass mirror, which has an estimated reflectance of about 97 percent. After this initial measurement, the mirror was replaced by the sample, which was mounted directly on the dark plastic mirror holder. The reflectance of the mirror holder itself was less than the instrument resolution. The reported reflectance is the spectrum obtained from the sample divided by that from the mirror, multiplied by 0.97.

Calibration. Reflectance measurements on blank single-crystal MgO substrates were compared with other single-crystal data found by Touloukian and DeWitt (1972). In the following, all given percentages represent relative differences. For $2 \mu\text{m} \leq \lambda \leq 15 \mu\text{m}$, the measurements agreed within a few percent; for $15 \mu\text{m} < \lambda \leq 25 \mu\text{m}$, they agreed within about 10 percent, and for longer wavelengths the present measurements lay at most about 20 percent below the former measurements. Generally, the present measurements are lower than those reported earlier. The repeatability of the data was within five percent.

Transmittance measurements on a blank, single-crystal MgO substrate were also compared with previous results in Touloukian and DeWitt (1972) and with a calculated transmittance, assuming no interference effects, of a 0.5-mm-thick MgO slab bordered on both sides by vacuum. For the calculation, the refractive index of the MgO substrate, $N_s = n_s + \kappa_s i$, was determined from a two-oscillator fit to reflectance data (Jasperse et al., 1966). The transmittance measured here was substantially less than that reported previously for $\lambda \leq 10 \mu\text{m}$, but the sample thickness differed (0.5 mm versus 0.3 mm). The comparison with the calculated transmittance, for $\lambda > 10 \mu\text{m}$, was much more satisfactory, except for a small spectral region near $\lambda = 15 \mu\text{m}$, where the calculated transmittance was nearly zero, and the measured transmittance was about 5 percent.

Reflectance Data. The measured reflectance spectra are presented in Fig. 6, along with the results of calculations in which N_f is determined from normal-state Drude theory, and N_s from Lorentz-type oscillator formulae. Since the calculated results are limited to the spectral region $12.5 \mu\text{m} \leq \lambda \leq 50 \mu\text{m}$, only these wavelengths are presented on the graph. The calculations assume the film and substrate are surrounded by

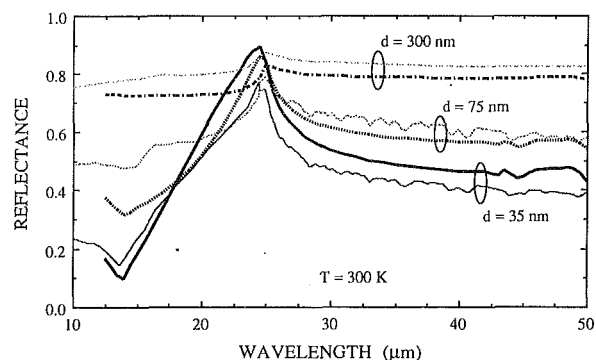


Fig. 6 Measured and calculated room-temperature near-normal specular reflectance of normal-state Y-Ba-Cu-O films on MgO substrates. The thicker curves are the calculated results, while the thinner curves are the experimental results.

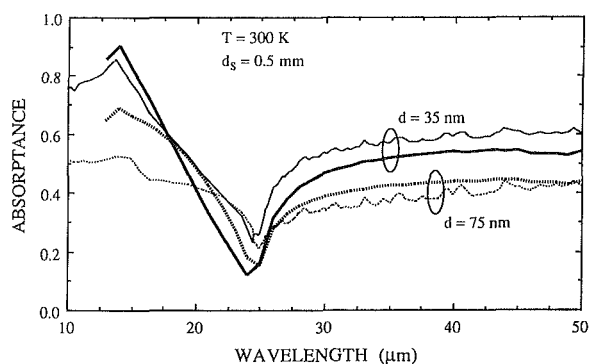


Fig. 7 Measured and calculated room-temperature normal-incidence film/substrate absorptance of normal-state Y-Ba-Cu-O films on MgO substrates. The thicker curves are the calculated results, while the thinner curves are the experimental results.

vacuum. For comparison, the reflectance data of another study (Kamba et al., 1989) are also shown. Their sample was a 300-nm-thick Y-Ba-Cu-O film deposited on an MgO substrate by pulsed laser sputtering. The influence of the film thickness is substantial over the entire spectrum, except near the sharp peak at $\lambda \approx 25 \mu\text{m}$, where the curves converge. This same behavior can also be observed in the curves of Fig. 1. The calculated results consistently lie below the measurements (except near $\lambda \approx 25 \mu\text{m}$), suggesting that the value of r_{dc} used here, $r_{dc} = 8.6 \times 10^{-6} \Omega\text{-m}$, may be somewhat higher than the actual resistivity. Figure 5 indicates that, for this range of film thicknesses, the film reflectance increases with increasing film thickness.

Film/Substrate Absorptance. Figure 7 shows a direct comparison between the measured and calculated normal-incidence film/substrate absorptance. The experimental absorptance is determined by subtracting the sum of the reflectance and the transmittance (not shown) from one. The largest discrepancy between theory and experiment occurs for the 75-nm curves at the absorptance peak near $\lambda = 15 \mu\text{m}$, and is thought to result from experimental error, where perhaps a surface feature of the 75-nm film caused significant diffuse scattering at short wavelengths. Figure 6 also shows a large discrepancy between the calculated and experimental curves for $d = 75 \text{ nm}$ at this wavelength. Otherwise, the qualitative agreement between theory and experiment generally validates the analytical approach of the two-film electromagnetic relations, coupled with the normal-state Drude model, at least for films as thin as 35 nm. This suggests that assuming the film and substrate to be continuous slabs, and the use of bulk refractive indices, is justified in the above low-temperature calculations, at least for film thicknesses as small as 35 nm.

Conclusions

Theoretical calculations of the spectral, normal-incidence absorptance of superconducting Y-Ba-Cu-O films suggest that, for smooth, continuous films, the film absorptance is maximum at an optimum value of film thickness, which for superconducting Y-Ba-Cu-O on an MgO substrate is generally less than 35 nm. The appearance of a peak in the film absorptance is a general result that should apply to all films, and not only to the superconducting films considered here. A maximum in the combined film/substrate absorption can also exist. As a result, in fast bolometer applications, it may be competitive to absorb the incident radiation directly by the Y-Ba-Cu-O film, as opposed to employing a radiation absorber and thus slowing the response of the bolometer. On the other hand, for slower bolometers, which rely on the combined film/substrate absorptance, it is beneficial to place the substrate between the incident radiation and the superconducting film, since comparative calculations indicate that generally the combined film/substrate absorptance is increased for this geometry, as compared to when the incident radiation strikes the film before the substrate.

Room-temperature reflectance and transmittance measurements of Y-Ba-Cu-O films on MgO substrates were performed in an attempt to validate the assumption that the film and substrate are smooth, continuous slabs whose radiative behavior can be calculated by thin-film optics and bulk refractive indices. A comparison between the calculated and measured film/substrate absorptance suggests that the assumption is qualitatively verified, at least for films as thin as 35 nm.

A general correlation relating the film and substrate refractive indices, the irradiation wavelength, and the film and substrate thicknesses to the peak absorptance would be useful for the design of thin-film devices in which it is desired to maximize the radiation absorption. Such a correlation, however, cannot be used with confidence until experiments determine the minimum film thickness for which the film can be considered a smooth, continuous slab, and for which a bulk refractive index is applicable. Thus, careful experiments are required in which the structure and thickness of films less than 35 nm thick are accurately correlated with their radiative properties.

Acknowledgments

The authors express their sincere appreciation to Professor H. S. Kwok and Q. Y. Ying of SUNY Buffalo, who provided the films for our study; to D. Chin of UC Berkeley who measured the film thicknesses; and to A. Majumdar of Arizona State University for his general assistance. G. Chen also gratefully acknowledges the financial support of the K. C. Wong Education Foundation in Hong Kong.

References

Armaly, B. F., and Tien, C. L., 1970, "Emissivities of Thin Metallic Films at Cryogenic Temperatures," presented at the 4th International Heat Transfer Conference, Versailles, France.

Bohren, C. F., and Huffman, D. R., 1983, *Absorption and Scattering of Light by Small Particles*, Wiley, New York, p. 269.

Born, M., and Wolf, E., 1980, *Principles of Optics*, 6th ed., Pergamon Press, New York, pp. 628-632.

Bozovic, I., Kirillov, D., Kapitulnik, A., Char, K., Hahn, M. R., Beasley, M. R., Geballe, T. H., Kim, Y. H., and Heeger, A. J., 1987, "Optical Measurements on Oriented Thin YBa₂Cu₃O_{7-δ} Films: Lack of Evidence for Excitonic Superconductivity," *Physical Review Letters*, Vol. 59, pp. 2219-2221.

Cava, R. J., Batlogg, B., vanDover, R. B., Murphy, D. W., Sunshine, S., Siegrist, T., Remeika, J. P., Rietman, E. A., Zahurak, S., and Espinosa, G. P., 1987, "Bulk Superconductivity at 91 K in Single-Phase Oxygen-Deficient Perovskite Ba₂YCu₃O_{9-δ}," *Physical Review Letters*, Vol. 58, pp. 1676-1679.

Clarke, J., Hoffer, G. I., Richards, P. L., and Yeh, N.H., 1977, "Superconductive Bolometers for Submillimeter Wavelengths," *Journal of Applied Physics*, Vol. 48, pp. 4865-4879.

Flik, M. I., Choi, B. I., Anderson, A. C., and Westerheim, A. C., 1990, "Thermal Analysis and Control for Sputtering Deposition of High-T_c Superconducting Films," *Thermal Phenomena in Materials Processing—1990*, P. J. Bishop et al., eds., ASME HTD-Vol. 146, pp. 73-82.

Flik, M. I., Phelan, P. E., and Tien, C. L., 1990, "Thermal Model for the Bolometric Response of High-T_c Superconducting Films to Optical Pulses," *Cryogenics*, Vol. 30, pp. 1118-1128.

Forrester, M. G., Gottlieb, M., Gavaler, J. R., and Braginski, A. I., 1988, "Optical Response of Epitaxial Films of YBa₂Cu₃O_{7-x}," *Applied Physics Letters*, Vol. 53, pp. 1332-1334.

Francavilla, T. L., Nelson, H. H., Baronavski, A. P., Wolf, S. A., Gubser, D. U., and Hein, R. A., 1989, "Further Studies of a Laser Quenched Superconducting Opening Switch," *IEEE Transactions on Magnetics*, Vol. 25, p. 1996-1999.

Heavens, O. S., 1965, *Optical Properties of Thin Solid Films*, Dover, New York, pp. 46-95.

Hu, Q., and Richards, P. L., 1989, "Design Analysis of a High T_c Superconducting Microbolometer," *Applied Physics Letters*, Vol. 55, pp. 2444-2446.

Jasperse, J. R., Kahan, A., Plendl, J. N., and Mitra, S. S., 1966, "Temperature Dependence of Infrared Dispersion in Ionic Crystals LiF and MgO," *Physical Review*, Vol. 146, pp. 526-542.

Kamaras, K., Herr, S. L., Porter, C. D., Tanner, D. B., Etemad, S., and Chan, S. W., 1989, "Optical Excitations in Thin Film YBa₂Cu₃O₇," *Progress in High Temperature Superconductivity*, Vol. 17, L. H. Bennett, Y. Flom, and G. C. Vezzoli, eds., World Scientific Publishing Company, Singapore, pp. 347-363.

Kamba, S., Petzelt, J., Zelezny, V., Pechen, E. V., Krasnosvobodtsev, S. I., and Gorshunov, B. P., 1989, "Infrared Reflectance of Anisotropic (110) YBCO Epitaxial Film," *Solid State Communications*, Vol. 70, pp. 547-551.

Kwok, H. S., Mattocks, P., Shi, L., Wang, X. W., Witanachchi, S., Ying, Q. Y., Zheng, J. P., and Shaw, D. T., 1988, "Laser Evaporation Deposition of Superconducting and Dielectric Thin Films," *Applied Physics Letters*, Vol. 52, pp. 1825-1827.

Mattis, D. C., and Bardeen, J., 1958, "Theory of the Anomalous Skin Effect in Normal and Superconducting Metals," *Physical Review*, Vol. 111, pp. 412-417.

Newhouse, V. L., 1964, *Applied Superconductivity*, Wiley, New York, pp. 248-253.

Phelan, P. E., Flik, M. I., and Tien, C. L., 1990, "Normal-State Radiative Properties of Thin-Film High-Temperature Superconductors," *Advances in Cryogenic Engineering*, Vol. 36A, pp. 479-486.

Phelan, P. E., Flik, M. I., and Tien, C. L., 1991, "Radiative Properties of Superconducting Y-Ba-Cu-O Thin Films," *ASME JOURNAL OF HEAT TRANSFER*, Vol. 113, pp. 487-493.

Richards, P. L., Clarke, J., Leoni, R., Lerch, Ph., Verghese, S., Beasley, M. R., Geballe, T. H., Hammond, R. H., Rosenthal, P., and Spielman, S. R., 1989, "Feasibility of the High T_c Superconducting Bolometer," *Applied Physics Letters*, Vol. 54, pp. 283-285.

Roas, B., Schultz, L., and Endres, G., 1988, "Epitaxial Growth of YBa₂Cu₃O_{7-x} Thin Films by a Laser Evaporation Process," *Applied Physics Letters*, Vol. 53, pp. 1557-1559.

Schlesinger, Z., Collins, R. T., Kaiser, D. L., and Holtzberg, F., 1987, "Superconducting Energy Gap and Normal-State Reflectivity of Single Crystal Y-Ba-Cu-O," *Physical Review Letters*, Vol. 59, pp. 1958-1961.

Sennett, R. S., and Scott, G. D., 1950, "The Structure of Evaporated Metal Films and Their Optical Properties," *Journal of the Optical Society of America*, Vol. 40, pp. 203-211.

Streiffner, S. K., Lairson, B. M., Eom, C. B., Clemens, B. M., Geballe, T. H., and Bravman, J. C., 1991, "Microstructure of Ultrathin Films of YBa₂Cu₃O_{7-δ} on MgO," *Physical Review B*, Vol. 43, pp. 13007-13018.

Touloukian, Y. S., and DeWitt, D. P., 1972, *Thermophysical Properties of Matter*, Vol. 8, IFI/Plenum, New York, pp. 301-327.

Venkatesan, T., Wu, X. D., Dutta, B., Inam, A., Hegde, M. S., Hwang, D. M., Chang, C. C., Nazar, L., and Wilkens, B., 1989, "High-Temperature Superconductivity in Ultrathin Films of Y₁Ba₂Cu₃O_{7-x}," *Applied Physics Letters*, Vol. 54, pp. 581-583.

Wang, X. L., Nanba, T., Ikezawa, M., Hayashi, S., and Komatsu, H., 1987, "Optical Reflectivity of Single Crystals of YBa₂Cu₃O_{7-δ} and ErBa₂Cu₃O_{7-δ}," *Japanese Journal of Applied Physics*, Vol. 26, pp. L2023-L2025.

Wautelet, M., 1987, "The Principle of a Gate Obtained by Laser Irradiation of a Thin Superconductor Film," *Journal of Physics D: Applied Physics*, Vol. 20, pp. 1318-1319.

Xi, X. X., Geerk, J., Linker, G., Li, Q., and Meyer, O., 1989, "Preparation and Superconducting Properties of Ultrathin YBa₂Cu₃O_{7-δ} Films," *Applied Physics Letters*, Vol. 54, pp. 2367-2369.

Ying, Q. Y., Kim, H. S., Shaw, D. T., and Kwok, H. S., 1989, "Nature of in Situ Superconducting Film Formation," *Applied Physics Letters*, Vol. 55, pp. 1041-1043.

Zeller, A. F., 1990, "High T_c Superconductors as Thermal Radiation Shields," *Cryogenics*, Vol. 30, pp. 545-546.

Transient Radiation Properties of a Subgrid Scale Eddy

J. P. Gore

J. H. Jang

Thermal Sciences and Propulsion Center,
School of Mechanical Engineering,
Purdue University,
West Lafayette, IN 47907-1003

Analysis of transient radiative cooling of a strongly radiating turbulent diffusion flame is described. The specific objective is to study the possibility of including realistic radiative cooling effects in transient simulations of turbulent reacting flows. The laminar flamelet concept is used to estimate all scalar properties other than temperature and density. These are obtained from transient evolutions for total enthalpy in conjunction with the state relationships. The equation is numerically solved in the mixture fraction-time space. Results show a flame structure involving a relatively cold soot layer on the fuel-rich side consistent with recent experimental data.

Introduction

Transient simulations of turbulent reacting flows have generally neglected the effects of radiation heat transfer (Ghoniem and Krishnan, 1988; Givi and Jou, 1988; Rehm et al., 1989). Recently, Baum et al. (1990) studied transient combustion in a turbulent eddy with radiation accounted for as a fixed loss in the heat of combustion. These authors found that radiative heat loss can interact significantly with turbulent mixing and reaction. For strongly radiating flames, where up to 60 percent of the heat of reaction may be lost by radiation, a more detailed treatment of the radiation heat transfer is needed.

The range of length and time scales needed to resolve practical turbulent flows and chemical reactions is well below the resolution limit of any direct numerical simulation with existing and anticipated advances in computers (Baum et al., 1990). Consideration of radiative heat transfer makes the problem even worse by introducing additional time and length scales. Motivated by this observation, a recent approach to the simulation of turbulent reacting flows involves numerical computations of the largest scales in conjunction with semi-analytical subgrid scale models for the treatment of heat release at the smallest scales.

Consistent with this philosophy, the present model assumes that three-dimensional computations of the largest scales that define the local scalar dissipation rates and radiation field while accounting for the effects of heat release and radiation heat loss are in progress. The results of these calculations define the local instantaneous environment in which the small-scale combustion and radiation processes are to be studied. In the present work, it is further assumed that a small-scale solution to the evolution of a conserved scalar variable is available using any one of the techniques described in many recent papers (Baum et al., 1986; Peters and Williams, 1988; Cetegen and Sirignano, 1988). It is noted that the treatment of radiative heat transfer is not included in all of these semi-analytical solutions to the evolution of the conserved scalar.

The objective of the present work is to study the evolution of the total enthalpy of a strongly radiating stretched diffusion flame. Coupled solutions of the conservation of momentum, mass, species, and soot concentrations together with the conservation of energy are not attempted here. Instead, approximate but plausible information concerning the velocity field (in the form of scalar dissipation rates), gas species concentrations, and soot volume fractions is specified. In particular, it is assumed that the scalar dissipation rates are small, leading

to the fast chemical reaction limit and the application of the laminar flamelet concept for gaseous species and soot volume fractions. For these specifications, the results of the present work define the temperature distribution that is consistent with conservation of energy. As discussed later, the results also reveal interesting features of the structure of strongly radiating diffusion flames.

Following Baum et al. (1986), a coordinate frame moving with the large-scale fluid motion is selected for the small scale analysis. A calculation of the transient mixture fraction (fraction of local mass that originated in the fuel stream) evolution is assumed to be in progress. As before (Baum et al., 1990), attention is focused in the vicinity of the fuel oxidizer interface because it is here that the temperature is highest and significant heat release and radiative heat transfer can occur. The present treatment of the radiative heat loss is independent of the specific large-scale model of a specific mixture fraction model for the subgrid scale. It is only required that the scalar dissipation rate, the local mixture fraction field, and the local radiation field incident on the eddy under consideration be known. For simplicity, it is further assumed that the fuel-oxidizer combination is such that the radiative processes are dominated by soot particles and that the gas phase radiation is negligible. Consistent with this approximation, acetylene and air are selected as the reactant combination.

In the following, the evolution equation for the enthalpy (chemical and sensible) is written. The equation is then transformed into mixture fraction-time space. The radiative source term for the subgrid scale eddy is then discussed. The resulting equation for the evolution of enthalpy is solved using a numerical method. Results for four different scalar dissipation rates, two different large-scale radiation fields, and fixed initial conditions are considered as representatives from a large number of combinations studied.

Model Formulation

Following Baum et al. (1990), the combustion and radiation processes viewed on the subgrid scale involve: the molecular mixing of fuel and oxidizer and consequent reaction releasing heat and species which lead to radiation heat losses; a large-scale radiation field from which energy can be absorbed by the species; and a mechanism whereby the local mixing and chemical reaction is affected by the heat release and radiation heat loss processes. In the present, attention is focused on the calculation of the radiative heat losses for a prescribed large-scale radiation field. The effects of heat release and radiative heat loss on mixing are discussed elsewhere (Baum et al., 1990). The equation for the conservation of energy in its total enthalpy form can be written as:

Contributed by the Heat Transfer Division for publication in the JOURNAL OF HEAT TRANSFER. Manuscript received by the Heat Transfer Division April 15, 1991; revision received September 6, 1991. Keywords: Combustion, Fire/Flames, Radiation Interactions.

$$\rho \left(\frac{\partial H}{\partial t} + V \cdot \nabla H \right) = \nabla \cdot (\rho D \nabla H) + Q_R \quad (1)$$

Note that the enthalpy H includes both the chemical and the sensible energy of the mixture:

$$H = \sum_{i=1}^N Y_i \left(h_{fi}^0 + \int_{T_o}^T C_{p,i} dT \right) \quad (2)$$

The symbols used in Eqs. (1) and (2) are defined in the nomenclature. The kinetic and potential energy changes and viscous dissipation have been neglected. D is a diffusivity assumed to be the same for all gaseous species and enthalpy in the present. D is a function of temperature and therefore of the enthalpy.

Direct simulation of turbulent combustion and radiation requires that Eq. (1) be solved with equations of conservation of mass, momentum, and species simultaneously. In particular, the density, the velocity, and the radiative source term depend on the solution to these additional equations, which are coupled with the enthalpy equation and also involve strong nonlinearities. In the present study, we focus attention on Eq. (1) to study the effects of radiative transfer on the evolution and distribution of enthalpy. The information needed from the solution of the other equations is provided via plausible simplifications mostly obtained from experimental data as discussed later in the article.

In order to simplify Eq. (1), a conservation equation for the mixture fraction (Eq. (3)) is utilized:

$$\rho \left(\frac{\partial Z}{\partial t} + V \cdot \nabla Z \right) = \nabla \cdot (\rho D \nabla Z) \quad (3)$$

Following Bilger (1976) and Peters (1983), Eq. (1) is transformed into a coordinate frame defined by the mixture fraction and an orthogonal pair of axes in the constant mixture fraction plane. Peters (1983) has argued that the gradients in a direction normal to the constant mixture fraction plane are much larger than those within the plane (also see Williams, 1985). Following this argument, the equation for the conservation of enthalpy can be reduced to:

$$\rho \left(\frac{\partial H}{\partial \tau} - D (\nabla Z)^2 \frac{\partial^2 H}{\partial Z^2} \right) = Q_R \quad (4)$$

It should be noted that a recent numerical study (Ashurst and Williams, 1990) has shown that in certain regions of the flame gradients along the constant mixture fraction plane may not be negligible. Also, the validity of Peters' (1983) argument has never been directly tested for strongly radiating flames. Particularly, the influence of soot transport and radiative heat loss on gradients along the constant mixture fraction plane has

not been studied in the past. The boundary conditions for Eq. (4) are:

$$\begin{aligned} H &= 0; & Z &= 0 \\ H &= h_{ff}^0; & Z &= 1.0 \end{aligned} \quad (5)$$

In the present treatment, the appropriate initial conditions for Eq. (4) are given by:

$$H = Zh_{ff}^0 - X_{RC} Q_{chem}; \quad \tau = 0; \quad 0 \leq Z \leq 1.0 \quad (6)$$

where Q_{chem} is the chemical energy released during the combustion process, defined as:

$$Q_{chem} = \sum Y_i h_{fi}^0 |_{Products} - Zh_{ff}^0 \quad (7)$$

It is noted that Q_{chem} is a function of mixture fraction Z and is 0 for $Z=0$ and 1. X_{RC} is an initial radiative heat loss fraction. Although the choice of specific value of X_{RC} is rather arbitrary, various values between 0 and 0.6 were studied. The steady-state solution was found to be independent of the particular choice of X_{RC} . Hence, results for only one value of X_{RC} are presented. In the context of combining this procedure with an overall simulation, the insensitivity to the initial conditions can be exploited.

The physical content of Eq. (4) is that the rate at which the total enthalpy of a small volume of the subgrid scale material changes is determined by a balance between the radiative heat loss/gain term on the right-hand side of Eq. (4) and the diffusion term involving the scalar dissipation rate $X = 2D(\nabla Z)^2$ on the left-hand side. The boundary conditions at $Z=0$ and 1 combined with the diffusion flux (determined by the scalar dissipation rate and the second derivative of the H - Z relationship) contain the effects of mixing and chemical reaction. In the absence of the diffusion flux, Eq. (4) degenerates to a first-order equation describing the transient radiative cooling of the well-mixed exhaust gases.

Equation (3) is coupled with the enthalpy equation (Eq. (4)) via the density, the mass diffusivity, and the modification of the volumetric expansion velocity caused by the radiative heat loss. Baum et al. (1990) have introduced a generalized Cole-Hopf transform to define a modified mixture fraction involving weighting by the density and the diffusivity (similar to the Howarth-Dorodnitsyn transform of compressible boundary layer theory). The only nonlinearity left in the modified mixture fraction equation is due to the dependence of the velocity potential on volumetric expansion. Baum et al. (1990) have described an approximate method for the treatment of this nonlinearity. The mixture fraction equation may be solved in a coupled manner or through simplifying assumptions such as those of Baum et al. (1990). Irrespective of the technique used to solve Eq. (3), the information needed from this solution, for the present study of the radiative cooling process, involves the distribution of mixture fraction and its gradient.

Nomenclature

a_λ = monochromatic absorption coefficient
 C = function of soot refractive index
 C_o = constant in soot emission and absorption terms
 C_p = specific heat
 c = speed of light
 D = diffusivity
 $e_{\lambda b}$ = black body emissive power
 f_v = soot volume fraction
 H = enthalpy (sum of local chemical and sensible energy of a gas mixture)

h = Planck constant
 h_{fi}^0 = heat of formation of i
 k_B = Boltzmann constant
 N = total number of species in the gaseous mixture
 P = pressure
 Q_{abs} = energy absorbed
 Q_R = radiative source term
 $Q_{emitted}$ = emitted energy
 Q_{chem} = chemical energy release
 R = universal gas constant
 T = temperature
 T_o = reference temperature
 t = time

V = velocity vector
 W = molecular weight of a gaseous mixture
 X = scalar dissipation rate = $2D(\nabla Z)^2$
 X_R = radiative heat loss fraction
 X_{RC} = initial condition for radiative heat loss fraction
 Y_i = mass fraction of gaseous species i
 Z = mixture fraction
 λ = wavelength
 ρ = density
 τ = time

Note that the transients in enthalpy caused by the transients in mixture fraction are included in the second term of the left-hand side of Eq. (4) while independent transients in enthalpy are included in the first term of the left-hand side. The problem now is reduced to the solution of Eq. (4) with the prescribed initial conditions.

The calculation of volumetric radiative heat loss/gain term, the state relationships for gas species concentrations, the distribution of soot volume fractions, and the specification of scalar dissipation rate X are described in the following. Then the solutions of Eq. (4) are presented and discussed.

Radiative Source Term. The radiative source term can be expressed as the energy absorbed minus the energy emitted by a small local participating volume. The energy absorbed must be calculated from the large-scale radiation field by integrating the flux over the surface of the small volume. The energy emitted depends on the temperature and absorption coefficient of the material in the small volume.

The emission of the present case is dominated by radiation from soot particles. The radiative source term is a nonlinear function of both composition and total enthalpy. Neglecting self absorption, since the volume under consideration is a small part of a subgrid scale eddy, the emitted energy can be written as:

$$Q_{\text{emitted}} = 4 \int_0^{\infty} a_{\lambda} e_{\lambda b} d\lambda \quad (8)$$

where $e_{\lambda b}$ at wavelength λ is given as:

$$e_{\lambda b} = \frac{2\pi hc^2}{\lambda^5 (\exp(hc/\lambda k_B T) - 1)} \quad (9)$$

Within the Rayleigh approximation for soot particles combined with the experimental observation that the refractive indices of soot are relatively invariant, the absorption coefficient can be expressed as:

$$a_{\lambda} = C f_v / \lambda \quad (10)$$

where C is a constant depending on the refractive indices of soot. There is considerable discussion in the literature concerning the appropriateness of the Rayleigh approximation for soot and concerning the variations in the refractive indices (see for example, Sivathanu and Faeth, 1990, and their references).

Next, the substitution $hc/\lambda k_B T = y$ is made into Eqs. (9) and (10) and these equations are substituted into Eq. (8) to obtain:

$$Q_{\text{emitted}} = \frac{8\pi Chc^2}{(hc/k_B)^5 f_v T^5} \int_0^{\infty} \frac{y^4}{(e^y - 1)} dy \quad (11)$$

The integral in Eq. (11) is the fourth-order Riemann zeta function and has a value of 24.8863. This constant is combined with the other constants in Eq. (11) assuming the refractive indices for acetylene soot given by Dalzell and Sarofim (1969) and an expression for the emission heat loss is obtained as:

$$Q_{\text{emitted}} = C_o f_v T^5 \quad (12)$$

where C_o is a constant given by:

$$C_o = \frac{8\pi Chc^2}{(hc/k_B)^5} \int_0^{\infty} \frac{y^4}{(e^y - 1)} dy = 2.77 \times 10^{-7} \text{ kW/m}^3 \text{K}^5 \quad (13)$$

Naturally f_v , the volume fraction of soot for the small radiating volume, must be known in order to calculate the radiative source term. The specification of f_v is discussed later in the article.

Specification of Absorbed Energy. The energy absorption by the participating volume is calculated as the local absorption coefficient multiplied by a mean radiative heat flux on the surface of the volume that is determined by the large-scale radiation field. In the small-scale calculation, the large-scale

radiation heat flux serves as a parameter. The large-scale radiation flux is specified in the form of an equivalent radiation temperature T_{abs} of a non-gray field that radiates with the spectral properties of soot particles. Steps similar to those shown above lead to:

$$Q_{\text{absorbed}} = C_o f_v T_{\text{abs}}^5 \quad (14)$$

The above simplified treatment of the absorbed energy is utilized in the following only for completeness. In a complete simulation, the incident energy flux would have directional dependence and a more complicated spectral distribution. It is noted that self-absorption within the small-scale eddy is neglected in the present calculations but could be included in extensions of the present analysis.

As discussed above, the present treatment of the radiative history is independent of a specific radiation model and Eqs. (12) and (14) are written only as an example. Other models of the radiation process can be incorporated as well but are not expected to alter the conclusions of the present study.

Specification of Gas Species Concentrations. Concentrations of gas species are needed in the solution of Eq. (4) for calculating the temperature and the density. The solution of Eq. (4) strongly depends on the temperature as prescribed by Eq. (12). The temperature of the mixture depends on the species concentrations and the enthalpy (see Eq. (2)). The density of the mixture is calculated using the ideal gas law at constant pressure:

$$\rho = PW/RT \quad (15)$$

W is the molecular weight of the mixture, which is a function of the species concentrations.

Bilger (1977) observed that concentrations of major gas species could be related to a single conserved scalar, such as the mixture fraction, for diffusion flames away from the point of extinction. The correlations of major gas species concentrations with mixture fractions were also observed to be independent of the scalar dissipation rate. The accuracy of this method has generated some discussion in the recent literature (Bilger, 1988; Effelsberg and Peters, 1988; Mauss et al., 1990). However, its effectiveness for radiation calculations has been demonstrated (Faeth et al., 1989).

For strongly radiating flames, the species concentrations may be independent of the scalar dissipation rate but may depend on the state of radiative cooling since the change in temperature will affect reaction rates. Measurements of species concentrations as a function of radiative cooling are not presently available. Details of the reaction steps and kinetic constants for the present reactant combination are also not well known. In order to keep the present problem tractable, the concentrations of major gas species are obtained from the state relationships reported by Gore and Faeth (1988). It is noted that measurements from two laminar flames and three different positions in each flame were observed approximately to collapse on one curve supporting the present simplification for a range of scalar dissipation rates not approaching the extinction limit. The two flames considered by Gore and Faeth (1988) had similar radiative heat loss.

Specification of Soot Volume Fractions. Prediction of soot volume fractions in laminar diffusion flames has remained a challenging problem (Kent and Honnery, 1990; Kennedy et al., 1990). In particular, the effects of temperature are not treated by recent models. As a result, discrepancies of a factor of two are observed between measurements and predictions of soot volume fractions in laminar flames (Kennedy et al., 1990). Kennedy et al. (1990) use a high activation energy Arrhenius kinetic scheme for soot growth rates while another recent study shows that the net soot formation rates depend more strongly

on composition than on temperature (see Fig. 8 of Kent and Honnery, 1990). Kent and Honnery (1990) expect a relatively high growth rate at temperatures below 1400 K based on their experimental map of net soot growth rate while Glassman (1988) has emphasized that 1400 K is a threshold temperature below which spot inception does not occur. It is possible that soot inception may occur only at temperatures above 1400 K, but growth may continue at lower temperatures. This continues to be an active area of research.

A recent study by Dasch and Heffelfinger (1991) has confirmed earlier findings (Gore and Faeth, 1986, 1988) that the bulk of the spot particles in turbulent jet flames occur in thin layers representing a narrow mixture fraction range. The reactions involving soot particles are frozen elsewhere due to chemical kinetic limitations resulting in passive mixing on the leaner and richer side of the narrow soot layer. Gore and Faeth (1988) found that, for laminar flames, the position of the soot layer showed some scatter in the mixture fraction space due to hydrodynamic effects, thermophoresis, and lack of molecular diffusivity of the particles. Recent simultaneous measurements of soot volume fractions, temperatures, and CO₂ concentrations (Sivathanu and Gore, 1991) have shown that these effects also appear in turbulent jet flames at moderate Reynolds numbers.

Based on these considerations, two representative distributions of soot volume fractions labeled SOOT-1 and SOOT-2 in the first of three parts of Fig. 1 were considered. The range of these two distributions covers most of the scatter in the soot volume fraction measurements of Gore and Faeth (1988). Based on their measurements, the distribution labeled SOOT-1 is appropriate for locations near the base of the flame where the convective velocity field carries the soot particles toward the fuel-rich regions (away from the flame sheet) and SOOT-2 is appropriate for regions where the convective velocities carry soot particles toward the fuel lean regions (towards the flame sheet).

It is noted that the soot distributions shown in Fig. 1 result from a balance between formation, oxidation, convection, and thermophoresis of soot particles. The present calculations utilize these (experimentally observed) distributions to estimate the local temperature based on an energy balance between chemical reaction, convection, diffusion and radiation.

Specification of Scalar Dissipation Rates. The specification of the scalar dissipation rate X is one of the most important problems in turbulent combustion (see, for example, Williams, 1975; Peters, 1983; Sirignano, 1987; Haworth et al., 1988; Ashurst and Williams, 1990). A variety of prescriptions for estimating X have been suggested by these authors. Sirignano (1987) derived a conservation equation for X and suggested a procedure for obtaining an approximate solution. Haworth et al. (1988) related X to the mean square fluctuation of mixture fraction, g , and the ratio of the dissipation rate of turbulence kinetic energy, ϵ , and the turbulent kinetic energy, k , obtained from an uncoupled k - ϵ - g model. Mauss et al. (1990) created a stochastic simulation of X using a log normal PDF based on measurements in turbulent jets and flames (Effelsberg and Peters, 1988; Long and Yip, 1988). Baum et al. (1990) and Ashurst and Williams (1990) propose methods of obtaining the transient distributions of Z at the subgrid scale using a vortex model for the large scale flow field.

In the present work, X is treated as a parameter independent of Z and T as a first step. This assumption implies that the changes in D with composition and total enthalpy balance the variation in $(\nabla Z)^2$. Results for four cases in the range $X = 0.25$ – 2.0 s^{-1} are shown. Mauss et al. (1990) have noted that stable hydrocarbon flames can exist for values of X less than 7.0 s^{-1} . For values greater than 7.0 s^{-1} , the flamelets first become unstable and then are extinguished. It is noted that the state relationships for gas species and distributions of soot volume

fractions utilize in the present study are not valid for X nearing the extinction limit. Therefore, the maximum value of X considered in the following is limited to 2.0 s^{-1} . It is noted that since flames in all possible combustion applications have scalar dissipation rates between 0 and 7 s^{-1} , the present range is relevant to many. Particularly, the results are of relevance to unwanted fires and furnace flames. Chemical kinetic effects must be treated simultaneously with the energy equation for higher scalar dissipation rates.

Other prescriptions of X including measurements from laminar flames in counterflow, coflow jet and porous wall configurations were considered in a separate study (Gore and Jang, 1991). This study included the effects of changes in $(\nabla Z)^2$ and diffusivity D with Z and temperature. The results showed that although X varied with Z and T , the conclusions of the present study are independent of the prescription of X used in the simulation.

Specification of Initial Conditions. The initial conditions for soot volume fractions were identical to the distributions shown in the first part of Fig. 1. Two cases labeled SOOT-1 and SOOT-2 were considered. The initial concentrations of gaseous species were identical to the state relationships given by Gore and Faeth (1988) and remained unchanged throughout the simulation.

The initial conditions for the total enthalpy are specified in the form of a radiative heat loss during fast reactions fraction X_{RC} . As discussed above, several values of X_{RC} between 0 and 0.6 were examined. The steady-state results have been verified to be independent of the initial condition. Therefore, results corresponding to $X_{RC} = 0.3$ are presented in this article.

The second part of Fig. 1 shows the initial conditions for the enthalpy H normalized by the heat of formation of the fuel as a function of Z calculated using Eq. (6) with $X_{RC} = 0.3$. For adiabatic combustion, the initial profile of H normalized by the heat of formation of fuel would be a straight line from 0 to 1. The initial heat loss shifts the curve down from the

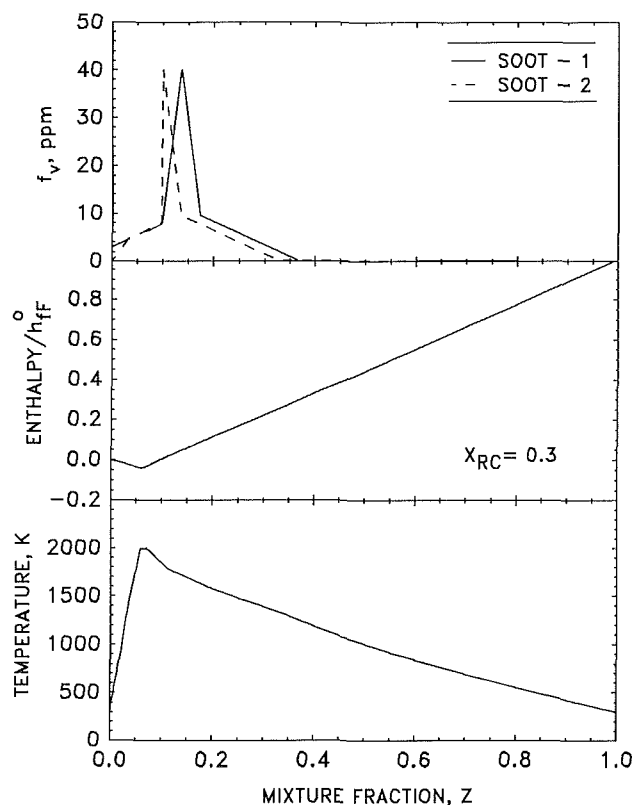


Fig. 1 Soot volume fraction distributions, initial conditions for total enthalpy, and corresponding temperatures

straight line due to radiative heat loss. As the mixture fraction is increased, the departure from the straight line decreases and finally the boundary value of $H=1$ at $Z=1$ is attained. The temperatures calculated based on these enthalpy values and the state relationships for gaseous species of Gore and Faeth (1988) are shown in the third part of Fig. 1. The profile shows that the peak temperature (approximately 2000 K) is about 600 K lower than the adiabatic flame temperature. The temperature profile also shows that effects of uniform heat loss from all mixture fractions and no special features are observed at the mixture fractions corresponding to the soot layer.

Numerical Method

Due to the strong nonlinearity of Eq. (4), a fourth-order Runge-Kutta integration is undertaken. At each step, in the Runge-Kutta procedure, the second term of the left-hand side of Eq. (4) is evaluated using a fully implicit central difference formula. The mixture fraction space is divided using a dense grid near the flame sheet and the soot layer and a coarse grid elsewhere. A total of 100 grid points are considered. An approximate time step is found using the solution of the conservation of energy equation for a solid sphere in the low Biot number limit with a radiative source term and comparing the results with the readily available analytical solution. The results are found to be independent of the time step within 0.5 percent and independent of the mixture fraction grid within 1 percent.

Summary of the Cases Presented

The choice of the initial radiative heat loss fraction X_{RC} did not alter the results as discussed above, hence $X_{RC}=0.3$ was used for all the cases presented in the following. The remaining two parameters: (1) the scalar dissipation rate X , and (2) the equivalent temperature T_{abs} of the large-scale radiation field, were varied to cover the relevant range. Table 1 summarizes the eight cases resulting from the choice of four scalar dissipation rates and two absorption temperatures. Scalar dissipation rates in the range $X=0.25-2\text{ s}^{-1}$ increasing a factor of 2 with each case are studied with $T_{abs}=800\text{ K}$ in cases 1-4. For these four cases, results for each of the two soot distributions shown in Fig. 1 are considered. In cases 5-8, identical scalar dissipation rates are studied for $T_{abs}=1400\text{ K}$. As seen from the results, the latter choice of T_{abs} represents a strong incident radiation field, which may exist only in few parts of large luminous flames.

Results and Discussion

The steady-state behavior of enthalpy, temperature, and the radiative heat loss fraction, which is related to the enthalpy and the mixture fraction as

$$X_R = (Zh_{FF}^0 - H) / Q_{Chem}, \quad (16)$$

is discussed first. It is noted that X_{RC} defined in Eq. (6) is simply the initial value of X_R defined above.

Effect of Scalar Dissipation Rate. The first part of Fig. 2 shows the steady-state enthalpy plotted as a function of mixture fraction for cases 1-4 with the soot distribution SOOT-1. It is noted that the steady-state enthalpy profiles show progressive departure from the adiabatic condition as the scalar dissipation rate is decreased. This departure is most pronounced in regions near the soot layer around a mixture fraction of 0.1. As a scalar dissipation rate is increased, the mixing rates become relatively fast compared to the radiative heat loss rate and the radiative cooling in steady state is decreased due to the limited time available.

The second part of Fig. 2 shows the steady-state temperatures for the four cases plotted as a function of mixture fraction.

Table 1 Summary of cases presented

Case	X_{RC}	$2D(\nabla Z)^2, \text{ s}^{-1}$	$T_{abs}, \text{ K}$
1	0.3	0.25	800
2	0.3	0.5	800
3	0.3	1.0	800
4	0.3	2.0	800
5	0.3	0.25	1400
6	0.3	0.5	1400
7	0.3	1.0	1400
8	0.3	2.0	1400

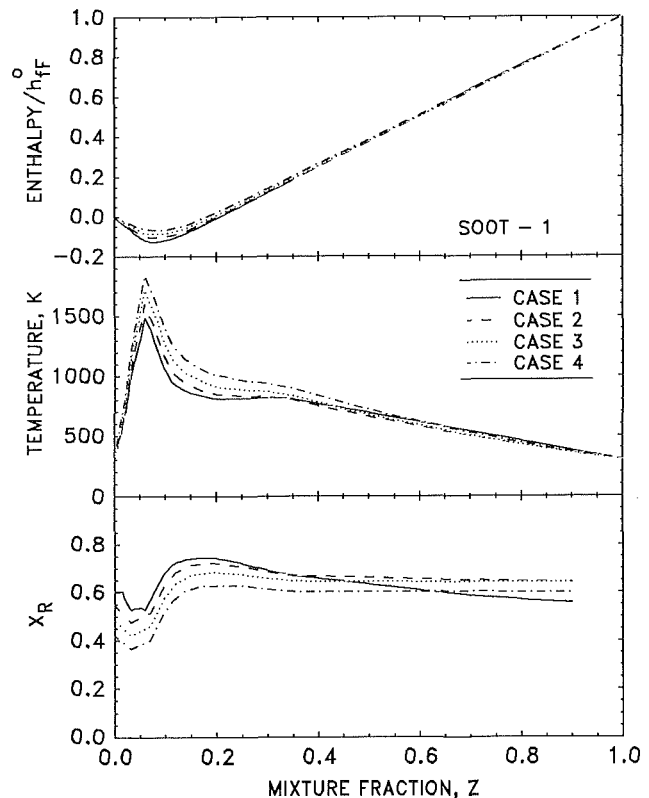


Fig. 2 Steady-state solution for total enthalpy, temperature and radiative heat loss fractions for $X=0.25, 0.5, 1.0,$ and 2.0 s^{-1} and $T_{abs}=800\text{ K}$ and SOOT-1 distribution

These profiles represent the state relationships for temperature. It is noted that the temperature profiles for all cases show that the soot layer acts as a sink of enthalpy due to its ability to lose energy by radiation. The strong radiative heat loss leads to an inflection point in the temperature profiles. The regions involving the highest soot concentrations have relatively low temperature and radiate energy received by diffusion mainly from the flame sheet on the fuel lean side. The energy transfer from the fuel lean side to the soot layer must be supported by a steep temperature gradient. This flame structure is unique to strongly radiating flames.

A plausible picture of the flame structure involves oxidation of CO, H₂, and possibly some soot particles in the flame sheet by OH radicals and O atoms leading to the release of chemical energy, part of which is transported to the soot layer by diffusion. The equilibrium temperature of the soot layer is determined by a balance between the energy diffusion and the radiative heat loss. It appears that for high concentrations of soot, the low temperature at equilibrium implies small contributions of exothermic reactions within the layer. The small temperature gradient on the fuel-rich side also implies low diffusion losses from the soot layer.

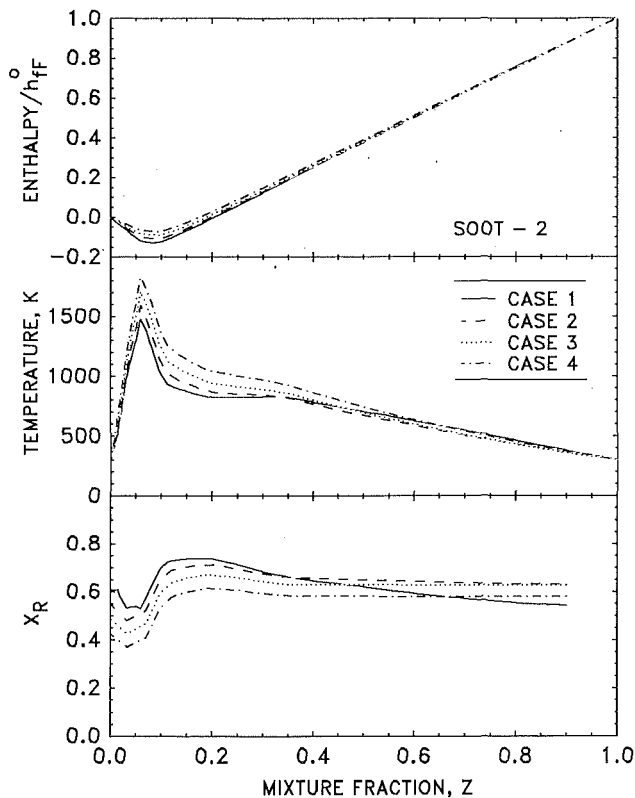


Fig. 3 Steady-state solution for total enthalpy, temperature and radiative heat loss fractions for $X=0.25, 0.5, 1.0,$ and 2.0 s^{-1} and $T_{\text{amb}}=800 \text{ K}$ and SOOT-2 distribution

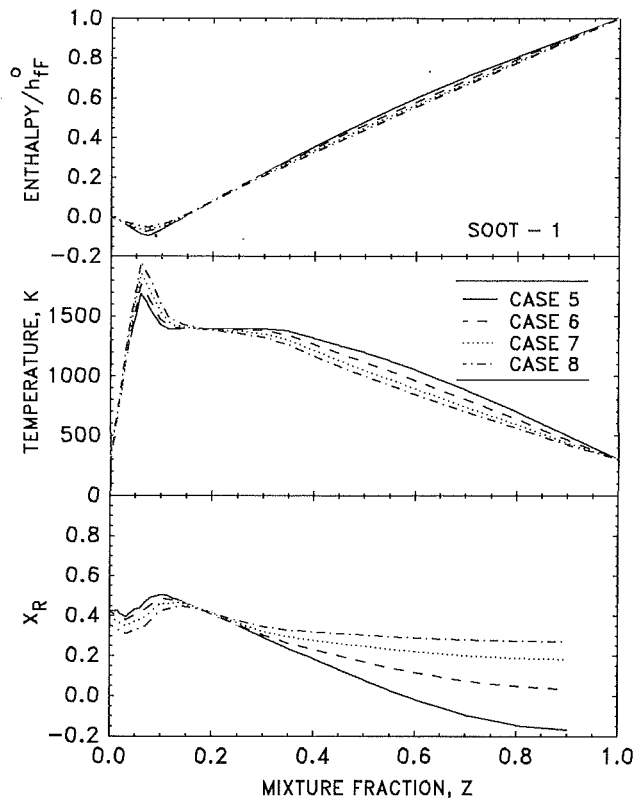


Fig. 4 Steady-state solution for total enthalpy, temperature and radiative heat loss fractions for $X=0.25, 0.5, 1.0,$ and 2.0 s^{-1} and $T_{\text{amb}}=1400 \text{ K}$ and SOOT-1 distribution

The low temperature of the soot layer has been experimentally observed in independent laboratories in flames burning a variety of fuels (Best et al., 1991: ethylene; Kent and Honnery, 1990: ethylene; Sivathanu and Faeth, 1990: ethylene, acetylene, propylene; Sivathanu et al., 1991: acetylene; Sivathanu and Gore, 1991: acetylene; and Gore et al., 1991: toluene). Sivathanu et al. (1991) and Sivathanu and Gore (1991) have considered several possible reasons for these experimental observations and found that radiative cooling of the soot layer is the only plausible reason for its low temperature. Simultaneous measurements of CO_2 concentrations, soot volume fractions and temperature showed that extinguished flamelets are not the cause of large amounts of cold soot in a range of turbulent diffusion flames representative of the present scalar dissipation rates (Sivathanu and Gore, 1991).

The temperature for the highest scalar dissipation rate are high near the flame sheet and then decrease near the soot layer. Both the flame sheet and the soot layer temperatures for this scalar dissipation rate are higher than those for lower scalar dissipation rates. On the fuel-rich and the fuel-lean sides, the effects of scalar dissipation rate on the temperature profiles appear to be small. This is expected from an inspection of Eq. (4). Since at steady state, $\partial H/\partial \tau=0$, if the radiative heat loss Q_R becomes negligible, then Eq. (4) reduces to $d^2H/dZ^2=0$, which has a linear solution independent of the scalar dissipation rate. The temperatures (near the soot layer and the flame sheet) at a scalar dissipation rate of 0.25 s^{-1} are approximately 100 K lower than those at 0.5 s^{-1} . As the scalar dissipation rate is increased to 1 s^{-1} , the temperatures increase by approximately another 100 K. Finally for the highest scalar dissipation rate (2 s^{-1}), the temperatures at the stoichiometric point and the soot layer are approximately 400 K higher than these seen for the lowest scalar dissipation rate.

A result of practical importance for direct numerical simulations of the conservation of energy equation is that the

departure from a universal (within 100 K) state relationship for temperatures occurs only in regions near the soot layer and the flame sheet ($0.04 < Z < 0.35$). Thus more than half of the mixture fraction space can be treated using a universal state relationship for temperature.

The third part of Fig. 2 shows the steady-state predictions of X_R for the four cases considered here plotted as a function of Z . Predictions for both lower and higher scalar dissipation rate show that X_R is remarkably constant with Z for a range of mixture fractions on the fuel-rich and fuel-lean sides. This is because the total enthalpy in these regions is a unique function of mixture fraction in the zeroth order. Near the soot layer, the radiative heat loss fraction increases significantly, exceeding 70 percent for the case involving the lowest scalar dissipation rate. The overall radiative heat loss fraction (weighted average over the mixture fraction space) predicted by the analysis is in reasonable agreement with the measurements of X_R for low scalar dissipation rate flames.

Effect of Soot State Relationships. As discussed previously, there is some scatter in the measurements of soot volume fractions plotted in the mixture fraction space. In order to evaluate the effects of this scatter on the present results, the calculations for Cases 1-4 were repeated with the soot state relationship labeled SOOT-2.

The variation of the total enthalpy, the temperature, and the radiative heat loss fraction calculated using SOOT-2 are plotted in Fig. 3. Qualitatively, all of the findings reported above for the state relationship SOOT-1 are observed in the present case as well. The temperatures reach relatively low values near the soot layer and show a peak on the fuel-lean side corresponding to the flame sheet. The radiative heat loss fractions show small variations from those shown in Fig. 2. Therefore, it can be concluded that the scatter in the soot volume fraction data of Gore and Faeth (1988) does not affect the present results.

Effect of Incident Radiation Field. Total enthalpy, temperatures, and radiative heat loss fractions for cases 5–8, which represent an incident radiation field with $T_{\text{abs}} = 1400$ K, plotted as a function of mixture fraction, are shown in Fig. 4. As an example, the state relationships labeled SOOT-1 were used for these calculations.

The variation of enthalpy shown in first part of Fig. 4 shows the effect of lower net radiative heat loss for all mixture fractions. In fact, at the lowest scalar dissipation rates, enthalpy at relatively rich mixture fractions is higher than its adiabatic value.

The temperatures at all mixture fractions are higher than those shown in Fig. 2 for all values of X . The differences in temperature for the two absorption temperatures are most pronounced in the soot layer where the radiative exchange process is the most dominant. When T_{abs} is 1400 K, the soot layer temperature reaches this value and attains equilibrium. The temperatures of the flame sheet increase by approximately 150 K while those of the soot layer increase by between 300–600 K from those shown in Fig. 2. Therefore, the heat loss from the flame sheet to the soot layer decreases. The temperatures on the fuel-rich side increase considerably from those shown in Fig. 2. This is a result of increased absorption by the soot layer and subsequent diffusion to the fuel rich side. For the lowest scalar dissipation rates, the fuel-rich side gains energy from the incident radiation field, leading to super-adiabatic conditions.

The radiative loss fractions for Cases 5–8 are shown in the third part of Fig. 4. As a result of the lower net loss, the radiative loss fraction near the soot layer reaches approximately 50 percent (as compared to 70 percent in Fig. 2) for these cases. The radiative heat loss fractions are relatively independent of the scalar dissipation rate near the soot layer and then decrease on the fuel rich side. For the lowest scalar dissipation rate, the radiative loss fraction takes a negative value beyond the mixture fraction of approximately 0.6, reaching -0.2 at a mixture fraction of 0.8. As there are no absorbing species considered in the calculations at these mixture fractions, the negative X_R is a result of diffusion of energy from the 1400 K soot layer into the fuel-rich portion. The chemical energy release corresponding to these mixture fractions is relatively small, requiring only a small amount of excess enthalpy to yield X_R profile shown in Fig. 4. The overall X_R from Fig. 4 is much lower than typical measurements of global radiative heat loss fractions for acetylene/air flames. This indicates that flamelets with both weak and strong incident radiation fields must exist in turbulent flames.

In practical flames, strong incident radiation fields are possible only at few positions. It is noted that the flame structure at such positions is affected by the incident radiation field and shows distinct features from those observed in case of the relatively weak incident field seen earlier.

The transient evolution of the temperature profile is studied in Fig. 5 to gain an understanding of the time scales associated with radiative cooling. Case 2 ($X = 0.5 \text{ s}^{-1}$) is selected as a representative case for this study. The first part of Fig. 5 shows the initial conditions and temperature profiles at 1 and 5 ms and at steady state. It is seen that as a result of the fast radiative cooling process for 5 ms, the temperature of the soot layer at Z_2 is within 150 K of the steady-state value. As a result of the high gradient between the flame sheet at Z_1 and the soot layer, the temperature at the flame sheet also decreases to within 100 K of its equilibrium value during the initial 5 ms. The temperature profile on the fuel-rich side develops much more slowly due to the inverse gradient during the early time steps between the soot layer and the fuel rich side. The steady state for the fuel-rich side is attained to within 1 K only after 1 s. However, this is an artifact of the present selection of the initial conditions.

The second part of Fig. 5 shows the radiant cooling process

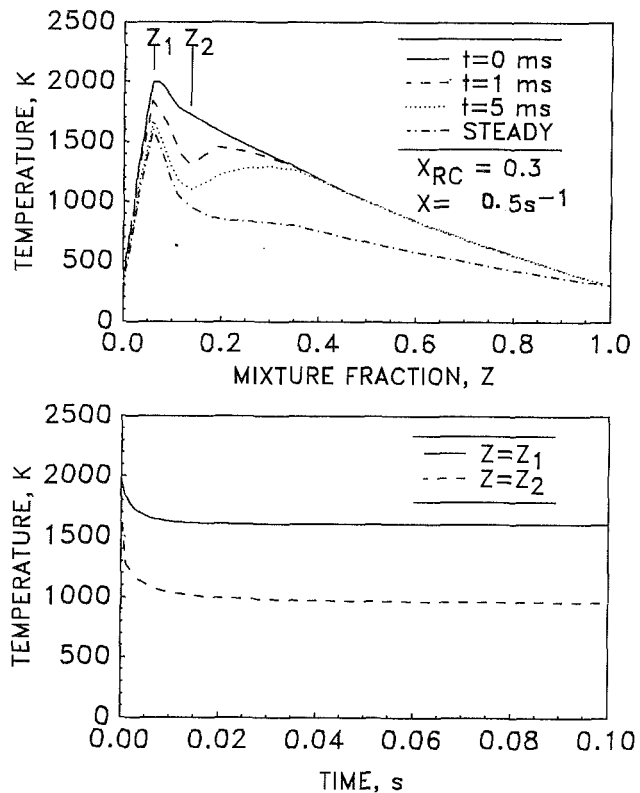


Fig. 5 Transient evolution of temperature for $X = 0.5 \text{ s}^{-1}$, $T_{\text{abs}} = 800$ K, and SOOT-1 distribution

for the flame sheet (Z_1) and the soot layer (Z_2) as a function of time. The flame sheet and the soot layer cool rapidly to their steady-state values. The soot layer cools by radiative heat loss and the flame sheet cools both by radiation and diffusion of energy into the radiating soot layer. The temperature of the flame sheet reaches to within 10 K of the equilibrium value within 10 ms and that of the soot layer is within 10 K of its equilibrium value in 20 ms. These estimates are the characteristic radiative cooling times for the case shown in Fig. 5.

Discussion Regarding Soot Formation and Transport

In the present study, experimentally observed distributions of gas species concentrations and soot volume fractions were combined with a transient energy equation to obtain a solution for the temperature distribution as a function of mixture fraction. Reasonable values for scalar dissipation rates and incident radiation fields were studied as discussed above. The strong incident field ($T_{\text{abs}} = 1400$ K) may occur only in certain regions of the flame and linkage of the soot growth and oxidation to its presence is too restrictive. For a relatively weak incident radiation field, the solution has shown that the soot layer must be at relatively low 800–1300 K temperatures. As discussed before, low temperatures of the soot layer have been recently observed in emission-absorption experiments by a number of researchers. Previous studies (for example, Gore and Faeth, 1986, 1988) did not involve simultaneous measurements of emission and absorption by the flames. The resulting emission spectra are biased toward high temperatures of the small quantities of soot particles passing through the flame sheet. All the color temperature measurements techniques also bias the results toward higher temperatures.

Based on extensive studies, Glassman (1988) has stressed that a threshold temperature of 1400 K must exist for inception while Kent and Honnery (1990) have found that net growth in the volume fraction of soot may occur at temperatures lower than this threshold value.

The present solutions give the temperatures at which a prescribed soot layer must exist in order to satisfy the conservation of energy and cannot directly reveal any information about the kinetics and steps in the soot inception and growth process. Particularly, the present results should not be interpreted as showing that soot inception occurs at the relatively low equilibrium temperatures of the soot layer. However, a successful soot formation and transport model must be compatible with the results of conservation of energy equation discussed above and with the experimentally observed low temperatures of the soot layer. Such a model does not exist at the present time.

One possibility is that, in certain regions of the flame, soot inception occurs at relatively high temperatures (at or above the threshold temperature for inception) on the fuel-lean side of the soot layer and the particles are then transported to the soot layer due to lack of molecular diffusivity and effects of thermophoresis. During this transport process and at the soot layer the volume fraction of the particles may increase by possible low-temperature growth processes observed by Kent and Honnery (1990). In regions of the flame where the soot particles are not transported away from the flame sheet but toward it, the soot layer and the newly formed particles oxidize and continue to radiate. When the balance between the heat release in the flame sheet by CO, soot, and H₂ oxidation cannot sustain the radiative heat loss, the temperature drops and soot formation as well as oxidation processes cease leading to the emission of soot through the flame. Correspondence between the emission of unburnt soot and CO observed by several investigators (see Koyle et al., 1991, and their references) may also be related to the process described above. It should be noted that other plausible mechanisms involved in the soot and CO emission processes have also been proposed (Puri and Santoro, 1991).

The soot transport and radiative heat loss processes described above weaken the assumption that gradients normal to the constant mixture fraction plane dominate the energy balance. If this assumption is relaxed, the radiative heat loss by the soot layer would be supported by diffusion from the CO, H₂, and soot oxidation layer and convection of energy from locations at the same mixture fraction but much lower soot concentration. Further study of these possibilities is needed for improving the understanding of strongly radiating flames.

Conclusions

The present analysis has shown that, for strongly radiating flames, the radiative heat loss fraction depends on the local mixture fraction. The mixture fractions corresponding to the soot layer have higher and those on the fuel-lean and fuel-rich side have lower radiative heat loss fractions.

The analysis has revealed a range of mixture fractions in which the temperature state relationships vary with scalar dissipation rates ($0.04 < Z < 0.35$). Outside this range, a universal (within 100 K) state relationship for temperature can be used in direct numerical simulations leading to savings in computer costs.

A unique flame structure involving an inflection point in the temperature profile near the soot layer was observed for strongly radiating flames. This is caused by the transfer of energy to the soot layer by diffusion from both sides balancing the high radiative heat loss. The existence of this structure is sufficient to explain recent experimental observation of large quantities of cold soot in strongly radiating flames.

It should be noted that the low temperature of the soot layer does not imply that soot inception occurs at low temperatures. The local volume fraction of soot is determined by a balance between the convective transport, thermophoresis, and formation and oxidation rates. A successful model of all these soot processes must comply with the requirements of conser-

vation of energy revealed in the present study and the experimentally observed low soot temperatures.

Possible modifications of the flame structure introduced by gradients along the constant mixture fraction plane need further study.

Acknowledgments

This work was completed while the authors were members of the Mechanical Engineering Department at the University of Maryland. Many useful discussions with Dr. Howard Baum of the National Institute of Standards and Technology are gratefully acknowledged. This study is supported by the National Science Foundation under Grant No. CTS-8914520 with Dr. Garris, Gosink, and Grosshandler serving as NSF scientific officers.

References

- Ashurst, W. T., and Williams, F. A., 1990, "Vortex Modification of Diffusion Flames," *Twenty-Third Symposium (International) on Combustion*, The Combustion Institute, Pittsburgh, PA, pp. 543-550.
- Baum, H. R., Rehm, R. G., and Corely, D. M., 1986, "Time-Dependent Simulation of Small Scale Turbulent Mixing and Reaction," *Twenty-First Symposium (International) on Combustion*, The Combustion Institute, Pittsburgh, PA, pp. 1263-1270.
- Baum, H. R., Rehm, R. G., and Gore, J. P., 1990, "Transient Combustion in a Turbulent Eddy," *Twenty-Third Symposium (International) on Combustion*, The Combustion Institute, Pittsburgh, PA, pp. 715-722.
- Best, P. E., Chien, P., L., Carangelo, R. M., Solomon, P. R., Danchak, M., and Ilovoco, I., 1991, "Tomographic Reconstruction of FT-IR Emission and Transmission Spectra in a Sooting Laminar Diffusion Flame: Species Concentrations and Temperatures," *Comb. Flame*, Vol. 85, pp. 309-318.
- Bilger, R. W., 1976, "The Structure of Diffusion Flames," *Combust. Sci. Tech.*, Vol. 13, pp. 155-170.
- Bilger, R. W., 1977, "Reaction Rates in Diffusion Flames," *Comb. Flame*, Vol. 30, pp. 277-284.
- Bilger, R. W., 1988, "The Structure of Turbulent Nonpremixed Flames," *Twenty-Second Symposium (International) on Combustion*, The Combustion Institute, Pittsburgh, PA, pp. 475-488.
- Cetegen, B. M., and Sirignano, W. A., 1988, "Study of Molecular Mixing and a Finite Rate Chemical Reaction in a Mixing Layer," *Twenty-Second Symposium (International) on Combustion*, The Combustion Institute, Pittsburgh, PA, pp. 489-494.
- Dalzell, W. H., and Sarofim, A. T., 1969, "Optical Constants of Soot and Their Application to Heat Flux Calculations," *ASME JOURNAL OF HEAT TRANSFER*, Vol. 91, pp. 100-104.
- Dasch, C. J., and Heffelfinger, D. M., 1991, "Planar Imaging of Soot Formation in Turbulent Ethylene Diffusion Flames: Fluctuations and Integral Scales," *Comb. Flame*, Vol. 85, pp. 389-402.
- Effelsberg, E., and Peters, N., 1988, "Scalar Dissipation Rates in Turbulent Jets and Jet Diffusion Flames," *Twenty-Second Symposium (International) on Combustion*, The Combustion Institute, Pittsburgh, PA, pp. 693-700.
- Faeth, G. M., Gore, J. P., Chuech, S. G., and Jeng, S. M., 1989, "Radiation From Turbulent Diffusion Flames," *Ann. Rev. Numerical Fluid Mech. and Heat Trans.*, C. L. Tien and T. C. Chawla, eds., Hemisphere, New York, pp. 1-38.
- Ghoniem, A. F., and Krishnan, A., 1988, "Origin and Manifestation of Flow-Combustion Interactions in a Premixed Shear Layer," *Twenty-Second Symposium (International) on Combustion*, The Combustion Institute, Pittsburgh, PA, pp. 665-675.
- Givi, P., and Jou, W. H., 1988, "Direct Numerical Simulations of a Two-Dimensional Reacting, Spatially Developing Mixing Layer by a Spectral-Element Method," *Twenty-Second Symposium (International) on Combustion*, The Combustion Institute, Pittsburgh, PA, pp. 635-643.
- Glassman, I., 1988, "Soot Formation in Combustion Processes," *Twenty-Second Symposium (International) on Combustion*, The Combustion Institute, Pittsburgh, PA, pp. 295-311.
- Gore, J. P., and Faeth, G. M., 1986, "Structure and Spectral Radiation Properties of Turbulent Ethylene/Air Diffusion Flames," *Twenty-First Symposium (International) on Combustion*, The Combustion Institute, Pittsburgh, PA, pp. 1521-1531.
- Gore, J. P., and Faeth, G. M., 1988, "Structure and Spectral Radiation Properties of Turbulent Acetylene/Air Diffusion Flames," *ASME JOURNAL OF HEAT TRANSFER*, Vol. 110, pp. 173-181.
- Gore, J. P., and Jang, J. H., 1991, "An Application of the Conservation of Energy Equation to Stretched Laminar Flamelets," in preparation.
- Gore, J. P., Klassen, M., Hamins, A., and Kashiwagi, T., 1991, "Effects of Fuel Properties on Burning Rates and Radiation Properties of Pool Flames," *Third International Symposium on Fire Safety Science*, Edinburgh, Scotland, in press.

Haworth, D. C., Drake, M. C., and Blint, R. J., 1988, "Stretched Laminar Flamelet Modeling of a Turbulent Jet Diffusion Flame," *Combust. Sci. Tech.*, Vol. 60, pp. 287-318.

Kennedy, I. M., Kollmann, W., and Chen, J. Y., 1990, "A Model for Soot Formation in a Laminar Diffusion Flame," *Comb. Flame*, Vol. 81, pp. 73-85.

Kent, J. H., and Honnery, D. R., 1990, "A Soot Formation Map for a Laminar Ethylene Diffusion Flame," *Comb. Flame*, Vol. 79, pp. 287-298.

Koylu, U. O., Sivathanu, Y. R., and Faeth, G. M., 1991, "Carbon Monoxide and Soot Emissions From Buoyant Turbulent Diffusion Flames," *Third International Symposium on Fire Safety Science*, Edinburgh, Scotland, in press.

Long, M. B., and Yip, B., 1988, "Measurements of Three-Dimensional Concentrations in Turbulent Jets and Flames," *Twenty-Second Symposium (International) on Combustion*, The Combustion Institute, Pittsburgh, PA, pp. 701-709.

Mauss, F., Keller, D., and Peters, N., 1990, "A Lagrangian Simulation of Flamelet Extinction and Re-ignition in Turbulent Jet Diffusion Flames," *Twenty-Third Symposium (International) on Combustion*, The Combustion Institute, Pittsburgh, PA, pp. 00-000.

Peters, N., 1983, "Local Quenching Due to Flame Stretch and Non-premixed Turbulent Combustion," *Combust. Sci. Tech.*, Vol. 30, pp. 1-17.

Peters, N., and Williams, F. A., 1988, "Premixed Combustion in a Vortex," *Twenty-Second Symposium (International) on Combustion*, The Combustion Institute, Pittsburgh, PA, pp. 495-503.

Puri, R., and Santoro, R. J., 1991, "The Role of Soot Particle Formation on the Production of Carbon Monoxide in Fires," *Third International Symposium on Fire Safety Science*, Edinburgh, Scotland, in press.

Rehm, R. G., Baum, H. R., Lozier, D. W., and Aronson, J., 1989, "Diffusion Controlled Reaction in a Vortex Field," *Combust. Sci. Tech.*, Vol. 66, pp. 293-317.

Sirignano, W. A., 1987, "Molecular Mixing in a Turbulent Flow: Some Fundamental Considerations," *Combust. Sci. Tech.*, Vol. 51, pp. 307-322.

Sivathanu, Y. R., and Faeth, G. M., 1990, "Temperature/Soot Volume Fraction Correlations in the Fuel-Rich Region of Buoyant Turbulent Diffusion Flames," *Comb. Flame*, pp. 150-165.

Sivathanu, Y. R., Gore, J. P., and Dolinar, J., 1991, "Transient Scalar Properties of Strongly Radiating Jet Flames," *Combust. Sci. Tech.*, Vol. 76, pp. 45-66.

Sivathanu, Y. R., and Gore, J. P., 1991, "Simultaneous Multiline Emission Absorption Measurements in Optically Thick Turbulent Flames," *Combust. Sci. Tech.*, in press.

Williams, F. A., 1975, "Recent Advances in Theoretical Descriptions of Turbulent Diffusion Flames," *Turbulent Mixing in Nonreactive and Reactive Flows*, S. N. B. Murthy, ed., Plenum, New York, pp. 189-208.

Williams, F. A., 1985, "Crocco Variables for Diffusion Flames," *Recent Advances in Aerospace Sciences*, C. Casci, ed., Plenum, New York, pp. 415-421.

Generalized State-Property Relations for Nonluminous Flame Absorption Coefficients

W. L. Grosshandler¹
Washington State University,
Pullman, WA

E. M. Thurlow
George Washington University,
Washington, DC

The work reported here simplifies computing the local Planck-mean absorption coefficient in nonluminous flames as a function of the mixture fraction and fuel composition. Equilibrium is assumed for fuel/air mixtures up to the point where carbon is predicted to condense, beyond which the gaseous products are assumed to be frozen and to be diluted with cold fuel. The resulting algebraic expressions are suitable for inclusion in any turbulent or laminar diffusion flame model predicated on single-step chemistry. The method accounts for the nongray nature of the gaseous combustion products and their variation in concentration and temperature with mixture fraction, at a computational penalty little more than that for estimating variable fluid properties. Nonluminous flames (in air) of H₂, CO, CH₃OH, CH₄ and lean regions of fuels with the general form C_xH_yO_z can be modeled satisfactorily. The effects of pressure-pathlength and heat loss on the absorption coefficient are addressed.

Introduction

The modeling of turbulent, nonpremixed combustion continues to challenge the ingenuity of fluid mechanics and combustion engineers. The level of sophistication of each aspect of the model reflects the specific answer sought, the expertise of the research team, and the level of computing power available. For large physical systems such as unwanted fires, incinerators, and industrial furnaces, and in high-pressure gas turbines, radiative heat transfer is crucial to operation, so that some means of accounting for it must be present. Bhattacharjee and Grosshandler (1989) have demonstrated that portions of a large confined flame can differ as much as 800 K in temperature when it is modeled with and without radiation, with the resulting effect that centerline velocities change by a third and radiant wall fluxes differ by more than a factor of five.

The laminar flamelet approach of Bilger (1977), which introduces the mixture fraction, f , as a conserved scalar to track the thermodynamic state at each point in the flow, has been used extensively for adiabatic combustion. Jeng and Faeth (1984) combined this technique with the $k-\epsilon-g$ hydrodynamic model and compared their numerical results to the species concentrations measured in a buoyant, turbulent methane flame.

The absorption properties of the mixture enter these types of calculation through the radiative source term, which is equal to the divergence of the radiative flux vector, \mathbf{q}_r , where

$$-\nabla \cdot \mathbf{q}_r = 4\pi a_i i_i - 4\pi a_p i_b \quad (1)$$

The first term accounts for the mean-incident intensity, i_i , which is absorbed in an amount proportional to the value of the mean-incident absorption coefficient, a_i ; the second term is the local energy loss due to emission, with i_b the blackbody intensity, $\sigma T^4/\pi$, and a_p , the Planck-mean absorption coefficient. Gore and Faeth (1986) used the narrow-band radiation model RADCAL (Grosshandler, 1980; based upon the work of Ludwig et al., 1973), with the state variable approach, to model the radiant flux in turbulent ethene/air combustion, and were able to simulate the structure and radiation of the flame.

¹Current address: Building and Fire Research Laboratory, NIST, Gaithersburg, MD.

Contributed by the Heat Transfer Division for publication in the JOURNAL OF HEAT TRANSFER. Manuscript received by the Heat Transfer Division October 24, 1990; revision received July 26, 1991. Keywords: Combustion, Computer Codes, Radiation.

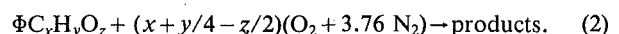
Narrow-band models such as RADCAL are computationally time consuming. Wide-band models provide a significant savings for heat transfer calculations while maintaining much of the versatility of narrow-band models (Edwards, 1976). The use of spectral-mean coefficients reduces the estimation of radiation properties from a field calculation to a local state calculation. Abu-Romia and Tien (1967) calculated values of a_p in the optically thin limit from the spectral line intensity/line spacing ratio for pure CO, CO₂, and H₂O for temperatures between 555 K and 2778 K. Mean coefficients can be relied upon only if much is known about the nature of the radiating system. Grosshandler and Modak (1981) addressed this limitation and were able satisfactorily to mimic narrow-band calculations of total intensity with spectral-mean coefficients for a variety of realistic methane-air combustion environments.

The purpose of this article is to present a simple method for estimating the Planck-mean absorption coefficient, which is based only upon the local properties in the flow field; which is to say, the mixture fraction f . The approach is to estimate the local temperature and composition of an optically thin adiabatic system. The narrow-band model is then used to predict the corresponding absorption coefficient, $a_p(f)$. An empirical relation founded upon the definition of the Planck-mean absorption coefficient for a single vibrational band is derived. Means to account for nonoptically thin and nonadiabatic flames are introduced, and a method to estimate the incident-mean absorption coefficient is suggested.

Hydrogen is discussed first, and then carbon monoxide, since the composition of these flames can be calculated most reliably for all equivalence ratios. Methane flame radiation, minus the contribution from soot, can also be handled. The method is extendable to fuel lean and nonluminous regions of gaseous fuels of the general form C_xH_yO_z. Our lack of understanding of soot formation and an incomplete data base of infrared absorption properties precludes the model from quantitative predictions of the contribution due to unburned fuel and soot.

Basis for Absorption Coefficient

Thermodynamic Considerations. The reaction of a generalized fuel in air can be represented by the following equation:



Φ is the equivalence ratio defined as the stoichiometric air/fuel ratio, AF_1 , divided by the actual air/fuel ratio in the mixture. The products formed depend upon the value of the equivalence ratio, but for fuel lean combustion, the process is usually complete, producing CO_2 and H_2O as the only species of importance to radiative heat transfer. Under adiabatic equilibrium conditions, equivalence ratios greater than one lead to more complex product mixtures. The incomplete products of combustion that contribute significantly to the radiation in rich regions of the flame are carbon monoxide, the fuel, and soot. Other infrared active species such as OH, NO, NO_2 , and fuel fragments are usually present in low enough concentrations to neglect their radiative contributions.

The mixture fraction is related to the mass air/fuel ratio, AF , by $f = (1 + AF)^{-1}$. This parameter varies between zero (pure air) to one (pure fuel), and is conserved even in reacting flows. It is particularly useful in adiabatic, nonpremixed flames in which the characteristic time for chemistry is much shorter than the characteristic time for fluid mixing (large Damköhler number limit), because the complete local thermodynamic state (i.e., the composition and temperature) can be determined directly from the specified value of f . For the purposes of the calculations presented in this article, the modified equivalence ratio, Φ' , is defined as

$$\Phi' \equiv \Phi \cdot (1 + AF_1) / (\Phi + AF_1). \quad (3)$$

The modified equivalence ratio is convenient for radiation calculations because, unlike f , all fuels have a value of unity for Φ' at stoichiometric conditions; and unlike Φ , Φ' is bounded in the fuel rich limit to $\Phi'_{\max} = AF_1 + 1$. Values of Φ'_{\max} range from 35.32 for H_2 to 3.45 for CO.

Computing the Planck-Mean Absorption Coefficient. If one knows the composition and temperature, it is possible to compute the absorption coefficient as a function of Φ' . The program RADCAL (Grosshandler, 1980) has been used for this purpose. It is capable of predicting the spectral intensity, i'_η , along a line-of-sight of length L through nonisothermal mixtures of CO_2 , H_2O , CH_4 , CO, N_2 , O_2 , and soot. For a given temperature, the spectral absorption coefficient, a_η , and transmittance, τ_η , are found. The Planck-mean absorption coefficient is defined as the integral of the spectral absorption coefficient, a_η , at the temperature of interest weighted with the Planck distribution function, i.e.,

$$a_p \equiv \int a_\eta i_{b\eta} / i_b d\eta \quad (4)$$

with $i_{b\eta} = 2C_1\eta^3 / [\exp(C_2\eta/T) - 1]$. C_1 and C_2 are the first and second radiation constants. By numerically integrating Eq. (4)

over wavenumbers between 50 and $10,000 \text{ cm}^{-1}$, the Planck-mean absorption coefficient can be computed. RADCAL has been validated against published experimental measurements of combustion products (Grosshandler, 1980), and is expected to produce a reliable estimate of the actual absorption coefficients under the conditions considered here.

Curve-Fitting the Absorption Coefficient. For a given vibrational band located at η and the gas at some reference temperature T_{ref} , the absorption coefficient is equal to the integrated intensity, α , times the product of the partial pressure of radiating gas, P_i , and the value of $i_{b\eta}$ at the band center. If there is a single vibrational band that dominates the radiative behavior of the gas, then the Planck-mean absorption coefficient can be found from the following expression (e.g., Tien, 1968):

$$a_p(T_{\text{ref}}) = [\alpha(T_{\text{ref}})P_i 2\pi C_1 \eta^3] / \{\sigma T_{\text{ref}}^4 [\exp(C_2\eta/T_{\text{ref}}) - 1]\} \quad (5)$$

The absorption coefficient at other temperatures can be found knowing the dependence of α on temperature. Hence, the value of the absorption coefficient varies with Φ' because the density of the radiating gases changes, and, even for a fixed density, the individual spectral line strengths and line spacings change with temperature (e.g., Penner, 1959).

Combustion gas mixtures generally vary in temperature between 300 K and 2500 K, and have several important vibrational/rotational bands spanning the spectrum from 100 to 8000 cm^{-1} . If some assumptions regarding the spectral and temperature dependence of the absorption coefficient are made, Eq. (5) can be useful as a guide to curve-fit the narrow-band calculated values of a_p empirically. For example, assume: (i) that there exists a single wavenumber, η^* , which dominates the spectrum for a given fuel independent of Φ' , and (ii) that the integrated intensity α varies as some small power of temperature. Then the following relation can be derived for the Planck-mean absorption coefficient at any Φ' in terms of a_1 , its value under adiabatic, stoichiometric conditions:

$$a_p(\Phi') = a_1 B(\Phi') P [T_1/T(\Phi')]^n \times (e^m - 1) / \{\exp[mT_1/T(\Phi')] - 1\} \quad (6)$$

P is the total pressure and B describes how the mole fraction of radiating gases varies with equivalence ratio, making it a function of the specific fuel and the method by which concentration is estimated. $T(\Phi')$ can be approximated either with its equilibrium value or from the relationship between product concentration and the adiabatic temperature in accordance with the usual thin-flame model; viz.,

$$T = T_0 + (T_1 - T_0)P_i/P_1 = T_0 + (T_1 - T_0)B(\Phi'). \quad (7)$$

Nomenclature

a_i, a_p = mean absorption coefficients, incident or Planck, m^{-1}	\mathbf{q}_r = radiative flux vector, W/m^2	Φ', Φ'_{\max} = modified equivalence ratio, maximum value for Φ'
a_{eff}, a_η = absorption coefficients, effective or spectral, m^{-1}	T = temperature, K	Subscripts
AF = air/fuel mass ratio	x = atoms of carbon	0 = 0 pathlength limit, inlet condition
B = function of Φ' defined in Eqs. (6) and (7)	y = atoms of hydrogen	1 = adiabatic, equilibrium, stoichiometric condition ($\Phi = 1$)
C_1, C_2 = first and second radiation constants	z = atoms of oxygen	a = adiabatic
i = intensity, $\text{W}/\text{m}^2/\text{sr}$	α = integrated band intensity, m^{-1}	b = blackbody
L = length, m	β = constant in Eq. (18)	i = incident
m, n = empirical constants in Eq. (6)	η, η^* = wavenumber, effective band center, cm^{-1}	ref = reference
P, P_i = total pressure, or partial pressure of radiating species, atm	σ = Stefan-Boltzmann constant	w = wall
	τ = transmittance	η = spectral quantity
	Φ = fuel/air equivalence ratio	

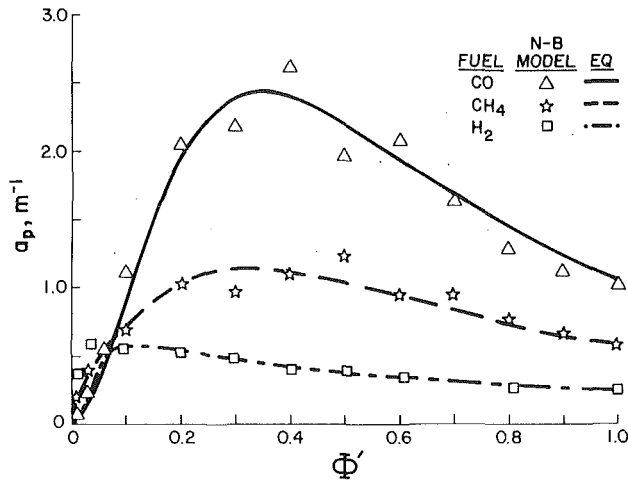


Fig. 1 Planck-mean absorption coefficients for lean combustion of H_2 , CO , and CH_4 in air, as function of Φ' . $PL = 0.0001 \text{ atm}\cdot\text{m}$, $T_0 = 298 \text{ K}$. Symbols, narrow-band calculations with full equilibrium; lines, Eqs. (9a), (10a), and (12).

Equation (5) would suggest that the empirical constant n be of the order of 4, and m , defined as $m \equiv C_2 \eta^* / T_1$, of order unity.

Numerical Results

Hydrogen/Air Diffusion Flames. Equilibrium provides a good approximation to the adiabatic concentration and temperature of hydrogen/air flames (Gore et al., 1987). The absorption coefficient calculated with the narrow-band model and assuming full equilibrium for atmospheric pressure H_2 /air mixtures is plotted with squares in Fig. 1 for fuel lean conditions as a function of Φ' . The equilibrium code STANJAN (Reynolds, 1987) has been used to determine the temperature and concentration. Figure 2 shows the results for rich mixtures, with the modified equivalence ratio normalized so that 0 on the abscissa represents stoichiometric and 1 the pure fuel conditions. The value of a_p varies between about 0.3 and 0.6 m^{-1} , except under the leanest and richest conditions, where a_p drops to zero.

The only significant infrared-active product formed during the lean combustion of hydrogen is water vapor, which simplifies the curve-fitting procedure. From an atom balance, $B(\Phi')$ can be expressed as follows:

$$B(\Phi' \leq 1) = \Phi' / (2.45 + 0.43\Phi') \quad (8a)$$

$$B(\Phi' \geq 1) = 0.0888(35.32 - \Phi') / (2.048 + \Phi') \quad (8b)$$

The squares in Figs. 1 and 2 have been fit to the form of Eq. (6) using Eqs. (8a) and (8b) for B . The following expressions yield a good representation of the Planck-mean absorption coefficient for atmospheric pressure hydrogen/air flames.

$$a_{p,H_2}(\Phi' \leq 1) = 0.047\Phi'(5.7 + \Phi') / (0.12 + \Phi')^2 \quad (9a)$$

$$a_{p,H_2}(\Phi' \geq 1) = 0.0745[(35.32 - \Phi') / (2.048 + \Phi')]^{0.5} / [0.125 + 0.0777(35.32 - \Phi') / (2.048 + \Phi')]^{1.3} \quad (9b)$$

The curve-fitting parameter m was found to be almost zero, which could be interpreted as an indication that the pure vibrational band of water vapor below 500 cm^{-1} dominates the absorption coefficient.

Carbon Monoxide/Air Diffusion Flames. Carbon monoxide/air mixtures produce two species important to the radiative heat transfer, CO and CO_2 . Under lean conditions the reaction is close to complete for laminar and moderately turbulent flames. When the modified equivalence ratio exceeds 2.8, equilibrium predicts that condensed carbon will form, but

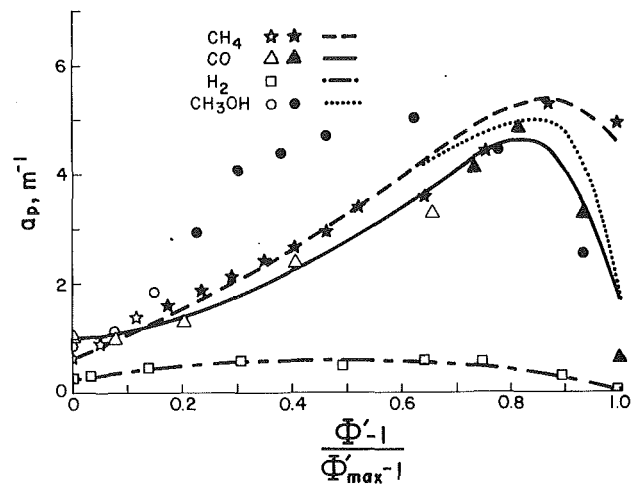


Fig. 2 Planck-mean absorption coefficients of gaseous products for rich combustion of H_2 , CO , CH_4 , and CH_3OH in air, as a function of normalized equivalence ratio. $PL = 0.0001 \text{ atm}\cdot\text{m}$, $T_0 = 298 \text{ K}$. Symbols, narrow-band model with full equilibrium (open) or frozen-dilution (closed); lines, Eqs. (9b), (10b), (14), and (15).

soot is not observed in actual atmospheric flames. A more realistic estimate of the concentration of temperature and gaseous species can be obtained if it is assumed that for $\Phi' \geq 2.8$, the mixture is frozen and that changes in P_i and T occur by simple dilution of the mixture with pure fuel at 298 K.

STANJAN (Reynolds, 1987) has been used to calculate the equilibrium conditions for lean and rich mixtures of CO /air up to $\Phi' = 2.8$, and the frozen-dilution method described above for richer conditions in arriving at the data plotted with triangles in Figs. 1 and 2. Carbon monoxide/air flames are much stronger emitters of radiation than are hydrogen/air flames, with a value of a_p just over 1.0 m^{-1} for stoichiometric conditions. The primary reason is that CO flames contain much less nitrogen than H_2 flames. Secondly, because CO is infrared active, a_p is greater than zero even when $\Phi' = \Phi_{\max}$. The solid triangles in Fig. 1 indicate that for these mixtures, equilibrium predicts that solid carbon should be present, and that the frozen-dilution approximation (without soot) has been incorporated.

An empirical fit of the narrow-band data yields the following equations for the Planck-mean absorption coefficient for atmospheric air/ CO mixtures.

$$a_{p,CO}(\Phi' \leq 1) = 0.0021\Phi' [(7.08 - \Phi') / (0.17 + \Phi')]^{4.1} / \{\exp[0.192(7.08 - \Phi') / (0.17 + \Phi')] - 1\} \quad (10a)$$

$$a_{p,CO}(\Phi' \geq 1) = 0.11[(11.4 + \Phi') / (3.88 - \Phi')]^{3.4} / (11.4 + \Phi') / \{\exp[0.192(11.4 + \Phi') / (3.88 - \Phi')] - 1\} \quad (10b)$$

The solid lines in Figs. 1 and 2 demonstrate reasonable fidelity between Eq. (10) and the narrow-band model. However, a simplistic model based upon a single vibrational band is unable to duplicate the complex behavior of a_p predicted by the sophisticated narrow-band model for values of Φ' between 0.2 and 0.6 due to the nonlinear temperature dependence of the multiple and combination bands of CO_2 .

Lean Regions of $C_xH_yO_z$ /Air Diffusion Flames. The concentrations of H_2O and CO_2 , and to a lesser extent CO , in laminar hydrocarbon flames are close to their equilibrium values under lean conditions (Sivathanu and Faeth, 1990). For the purpose of the radiation calculations here, it will be assumed that equilibrium holds at the local equivalence ratio ($\Phi' \leq 1$) for any combination of C, H, and O in the fuel, and for turbulent flames in general away from extinction conditions. Rather than curve-fitting the calculations of a_p from the

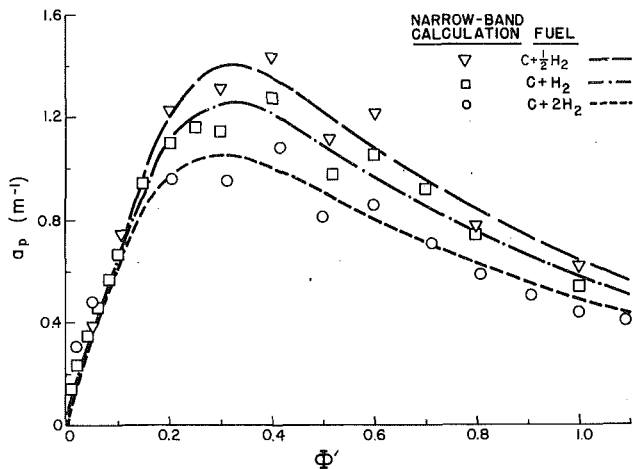


Fig. 3 Planck-mean absorption coefficients for lean combustion of various mixtures of C(s) and H₂ in air, as function of Φ' . Symbols, narrow-band model with full equilibrium; lines, Eq. (12).

narrow-band model of each fuel individually, it is more convenient to express a_p as a combination of the absorption properties of hydrogen and carbon flames.

An empirical equation for lean carbon/air combustion has been reported by Grosshandler and Thurlow (1991) as follows:

$$a_{p,C}(\Phi' \leq 1) = 3.1\Phi' / \{ (0.164 + \Phi')^{4.4} [\exp(1.34/(0.164 + \Phi')) - 1] \} \quad (11)$$

Inspection of the narrow-band calculations for methane ($x=1$, $y=4$, $z=0$) reveals that the absorption coefficient is about midway between the values for pure carbon and pure hydrogen at the same value of Φ' . Therefore, the following mixing rule is suggested for a general hydrocarbon (no fuel oxygen) under lean, atmospheric conditions:

$$a_{p,C_xH_y}(\Phi' \leq 1) = (4x a_{p,C} + y a_{p,H_2}) / (4x + y) \quad (12)$$

Equation (12) is plotted in Fig. 3 for three different C/H ratios, and can be compared to the narrow-band calculations based upon equilibrium concentrations from a fuel composed of mixtures of C(s) and H₂. The C/H ratios shown duplicate ethyne, ethene, and methane. By choosing carbon and hydrogen as the fuel, the variations in enthalpy of formation of different hydrocarbons are ignored. This can affect the adiabatic flame temperature somewhat, but the major features of the absorption coefficient are retained and the generality afforded by a single equation for all C/H ratios justifies the approximation. For the important case of methane, whether or not the correct enthalpy of formation is used has little effect, as can be seen by comparing the data for CH₄ in Fig. 1 with the narrow-band data of C(s) + 2H₂ in Fig. 3.

When oxygen atoms are present in the parent fuel ($z \geq 1$), the effect is to concentrate the radiating species since less air, and thus, less N₂, is present for a given value of Φ' . Through a bit of algebraic manipulation, the narrow-band calculations for lean methanol, ethanol, propanol, and acetone can be empirically fit by modifying Eq. (12) as follows:

$$a_{p,C_xH_yO_z}(\Phi' \leq 1) = \{ 1 + z[(19.04x + (4.76 + \Phi')y) / (19.04x + (4.76 + \Phi')y + 2\Phi' - 9.52) - 1] \} a_{p,C_xH_y}(\Phi') \quad (13)$$

Figure 4 compares Eq. (13) to the narrow-band calculations for four singly oxygenated fuels. The appropriate enthalpy of formation for the liquid fuels has been used in the STANJAN equilibrium calculations.

Rich Regions of Methane/Air and Methanol/Air Diffusion Flames. Full equilibrium is not a good model for methane flames when $\Phi' \geq 1.25$ based upon numerous studies, which

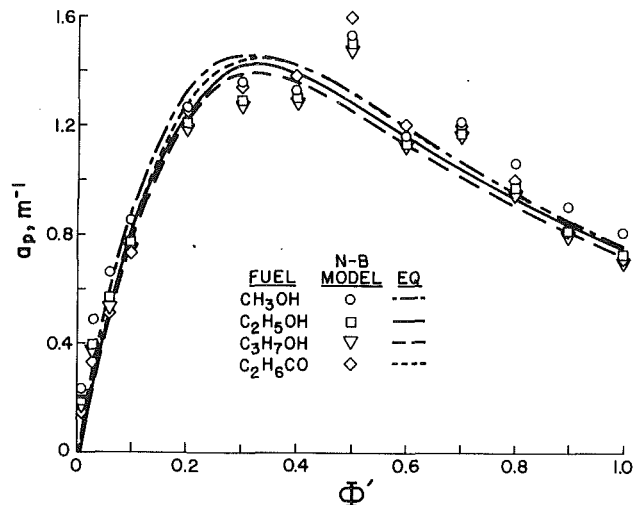


Fig. 4 Planck-mean absorption coefficients for lean combustion of alcohols and acetone in air, as function of Φ' . Symbols, narrow-band model with full equilibrium; lines, Eq. (13).

have shown that actual CO₂ and H₂O levels are greater than equilibrium and CO concentrations are much below what equilibrium would predict. Jeng and Faeth (1984) have plotted state relations for the major products of reaction in a methane/air flame. Bilger and Stärner (1983) have developed a model for the composition of methane/air flames based upon a constrained equilibrium approach, which approximates the absolute concentrations of CO₂, CO, H₂O, CH₄, and hydrocarbon intermediates (as C₂H₄).

Equilibrium predicts that soot should form when the modified equivalence ratio exceeds 3.0. While a small amount of soot is common in a methane flame, the nonluminous radiation is a major contributor to the total radiant flux. The radiating gases for rich methane/air mixtures have been approximated in the present article by equilibrium up to the first evidence of soot ($\Phi' \approx 3$), and then by frozen-dilution as described in the case of rich CO oxidation for Φ' between 3 and its maximum value, 18.16. While the adiabatic temperature and absolute concentration of CO are overpredicted relative to the constrained model of Stärner and Bilger, the effect on the absorption coefficient is not large.

Figure 2 contains the data from the narrow-band calculations of a_{p,CH_4} for rich, atmospheric pressure methane/air mixtures, and which are approximated with the following empirical expression:

$$a_{p,CH_4}(\Phi' \geq 1) = 2.1(2.4 + \Phi')[(22.6 + \Phi') / (23.4 - \Phi')^{2.2} / \{ (22.6 + \Phi') [\exp(0.4(22.6 + \Phi') / (23.4 - \Phi')) - 1] \}] \quad (14)$$

The filled-in stars indicate that the nonluminous radiating mixture has been approximated using the frozen-dilution assumption.

Methanol does not form soot (even though condensed carbon is thermodynamically favored when $\Phi' \geq 5.2$), making it easier to model than methane in one respect. When using the frozen-dilution approach, though, one is faced with evaluating the contribution of CH₃OH, itself, to the absorption coefficient. While the infrared spectrum of methanol is well known, quantitative narrow-band models have not been developed. The major infrared bands of methanol lie between 2.7 and 9.7 μm , and their integrated strength is related to the mass involved with the vibrational and rotational motion of the molecule. Carbon monoxide has a molecular weight 88 percent that of methanol and strong band at 4.67 μm . As a rough approximation, a lower bound on the absorption properties of CH₃OH has been found by treating the unburned fuel as if it behaved as CO.

The circles in Fig. 2 are data from the narrow-band model, with the closed symbols indicating that the methanol contribution to a_p is estimated as CO and using the frozen-dilution scheme. Interestingly, for reduced equivalence ratios up to 0.7, the methanol combustion produces higher values of a_p than either the methane or carbon monoxide flames plotted in Fig. 2. This cannot be attributed to the way in which the absorption properties of CH₃OH are computed because the fuel concentration is relatively low and the approximations involved should lead to an underestimation. An empirical mixing rule for methanol is proposed that treats $a_{p,\text{CH}_3\text{OH}}$ as behaving like methane combustion for stoichiometric conditions and like carbon monoxide for the pure fuel case, viz.,

$$a_{p,\text{CH}_3\text{OH}}(\Phi' \geq 1) = a_{p,\text{CH}_4}(\Phi') + [(\Phi' - 1)/(\Phi'_{\text{max}} - 1)]^3 [a_{p,\text{CO}}(\Phi') - a_{p,\text{CH}_4}(\Phi')]. \quad (15)$$

This equation is plotted as a dotted line in Fig. 2.

Extension to Rich Regions of Other Diffusion Flames. These are three major difficulties associated with the extension of the current technique to the rich combustion of multiple-carbon fuels: (i) serious deviations of gaseous species concentrations from local equilibrium, (ii) the presence of a significant soot concentration, and (iii) the lack of narrow-band models for the fuel species. Becker (1974) circumvented all three difficulties when modeling a turbulent propane/air diffusion flame by ignoring the radiation from soot and the parent fuel. He computed the composition of the products by assuming equilibrium for slightly rich mixtures, no CO₂ once the equivalence ratio exceeded 2, and neither CO₂ nor H₂O beyond a rich limit. This technique for estimating composition can be shown to be about equivalent to the equilibrium/frozen-dilution method used in the present study.

Bilger and Stärner (1983) applied their partial equilibrium model to a propane/air flame as well. The CO, CO₂, H₂O, and hydrocarbon concentrations are predicted reasonably well (when compared to full equilibrium), but neither soot nor radiation from the flame have been included. Sivathanu and Faeth (1990) reviewed the extensive work from their own laboratory on state relationships for the major radiating products in methane and ethene flames, as well as the data of others on laminar propane (Tsuji and Yamaoka, 1968) and heptane (Abdel-Khalik et al., 1974; Kent and Williams, 1975) flames. Faeth's method is very promising for determining the gaseous radiating species, but a satisfactory technique for dealing with soot, which may dominate the radiation, is not yet available. Grosshandler and Thurlow (1991) discuss a crude approximation to estimate the soot levels in a general hydrocarbon flame, and estimated that the Planck-mean absorption coefficient from the condensed carbon could exceed the contribution from the gaseous species by over a factor of fifty.

There are preliminary data to suggest that a mass-weighted absorption coefficient of methane may provide a useful approximation to gaseous higher hydrocarbons (Hamdan and Grosshandler, 1985), and this is the technique used in the previous study by Grosshandler and Thurlow (1991). Lacking narrow-band models for oxygenated fuels, the following expression, based upon the number of bonds in the molecule, n , is also a possibility for approximating the absorption coefficient of the pure fuel:

$$a_{p,\text{C}_x\text{H}_y\text{O}_z}(\Phi' \geq 1) \approx a_{p,\text{CH}_4}(\Phi') + [(\Phi' - 1)/(\Phi'_{\text{max}} - 1)]^3 [a_{p,\text{CO}}(\Phi') - (1 + z - n/4)a_{p,\text{CH}_4}(\Phi')] \quad (16)$$

Grosshandler (1991) used a similar approach for rich regions of ethanol, propanol, and acetone diffusion flames.

Pressure and Pathlength Corrections. Because combustion gases are highly nongray, the value of a_p calculated varies with

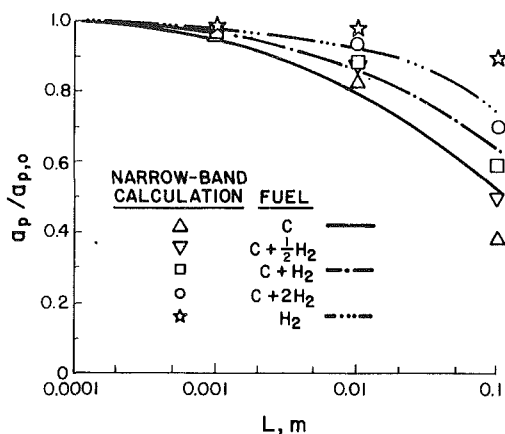


Fig. 5 Relative Planck-mean absorption coefficients for stoichiometric combustion of mixtures of C(s) and H₂ in air at one atmosphere, as function of pathlength over which calculation is performed. Reference length is 0.0001 m. Symbols, narrow-band model; lines, Eq. (18).

the choice of the pathlength. The expressions for the Planck-mean absorption coefficient presented above are valid strictly speaking only when the element length is equal to 10⁻⁴ m and the total pressure is 1 atm. In most cases such a small element size is inconvenient or incompatible with the flow field being modeled. Under those circumstances the Planck-mean absorption coefficient should be replaced by an effective absorption coefficient, a_{eff} , found from the Planck-mean transmittance; that is,

$$a_{\text{eff}} \equiv - \left\{ \ln \left[\pi \int i_{b,\eta} \exp(-a_{\eta}L) d\eta / (\sigma T^4) \right] \right\} / L. \quad (17)$$

In the optically thin limit, a_{eff} found from Eq. (17) is identical to a_p . Figure 5 is a plot of the Planck-mean absorption coefficient versus pathlength, normalized by $a_{p,0}$, the value computed for a pathlength of 10⁻⁴ m. The results shown apply to stoichiometric conditions, and vary with Φ' and the carbon fraction. The effect of increasing pathlength is to decrease the Planck-mean absorption coefficient significantly. Hydrogen is less sensitive to variations in pathlength because its products of combustion are closer to the absolute optically thin limit. Fuels with a higher carbon fraction are more sensitive.

A number of calculations were also performed with the total pressure varied between 1.0 and 50 atm. The following empirical equation relates the absorption coefficient at any total pressure and pathlength to its value at 1 atm and 0.0001 m, $a_{p,0}$:

$$a_{\text{eff}}(P, L) = a_{p,0} P (10^4 PL)^\beta, \quad (18)$$

with $\beta \equiv -0.28 (a_{p,0} PL)^{1/2}$.

The effective absorption coefficient is plotted in Fig. 5 for carbon, hydrogen, and model ethene with the total pressure fixed at one atmosphere. The agreement is satisfactory as long as the pathlength is below 0.01 m, suggesting that care be taken for calculations involving individual elements greater than 0.01 m in length.

Correcting for Heat Loss. Since the purpose of computing the radiation source term is to account for heat loss from the flame, it is necessary to estimate the effect of temperature change on the value of a_p calculated. Assuming the effects of temperature are confined to the exponential and fourth-power terms in Eq. (5), the following equation can be used to adjust for nonadiabatic behavior:

$$a_p(T) = a_p(T_a) (T_a/T)^4 [\exp(T_1/T_a) - 1] / [\exp(T_1/T) - 1] \quad (19)$$

T_a and T_1 are the adiabatic temperatures at the local and stoichiometric equivalence ratios, respectively.

The accuracy of Eq. (19) varies somewhat with the equiv-

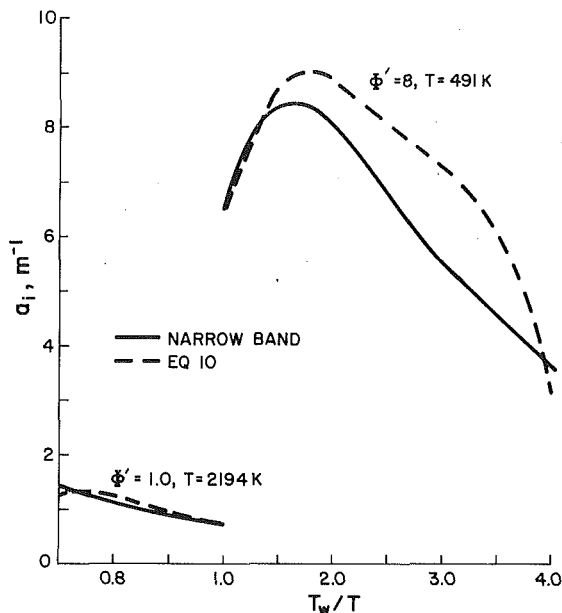


Fig. 6 Incident-mean absorption coefficient for products of ethanol combustion under stoichiometric ($\Phi' = 1$) and rich ($\Phi' = 8$) conditions, as a function of the temperature of incident radiation. Solid line, narrow-band calculation; dashed line, Eq. (20).

alence ratio and carbon fraction, but for temperatures within a few hundred degrees of the adiabatic condition, the equation can be expected to track absolute variations within 20 percent of the narrow-band model.

Incident-Mean Absorption Coefficient. The Planck-mean absorption coefficient (or more properly, a_{eff}) is used to determine the local radiative flux leaving any portion of the flame volume. To estimate the amount of radiative energy absorbed from a gray, isothermal boundary, the incident-mean absorption coefficient, a_i , needs to be used. As a first approximation to adjust for the two temperatures that are involved in such a calculation, Cess and Mighdoll (1967) suggest that the Planck-mean can be used if it is evaluated at the wall temperature and then multiplied by the ratio of the wall and local temperatures; i.e.,

$$a_i(T_w, T) = a_p(T_w)(T_w/T) \quad (20)$$

The accuracy of this approach has been tested for ethanol flames (approximated as $\text{CO} + \text{CH}_4$ in accordance with Eq. (16)) (Grosshandler, 1991) with a variety of wall temperatures and equivalence ratios by using RADCAL to integrate numerically a_η weighted with the Planck function at T_w . Equation (20) was found to model the general trend of the narrow-band calculations, but discrepancies of over 30 percent were not uncommon. Best agreement occurs for $0.5 \leq T_w/T \leq 1.2$. Figure 6 gives two examples, one representing the stoichiometric region subjected to a subadiabatic wall, and the other the cooler fuel-rich region exposed to a hotter wall. In both cases the wall is black and the gas volume is optically thin.

If the incident intensity emanates from a highly nongray source, such as from a different region in the flame, a_i can change dramatically. For example, if the radiation from a 0.10-m-thick stoichiometric region of an ethanol flame at 1964 K is incident upon a volume of gas with Φ' of 8 and $T = 491$ K, then the narrow-band model predicts that a_i is 22 m^{-1} , as compared to 6.5 m^{-1} found when the radiating layer is only 0.0001 m thick. Equation (20), which assumes the source is gray at 1964 K, predicts a value of only 3.2 m^{-1} for a_i . The Planck-mean would better approximate a_i than Eq. (20) in this case since it is equal 6.5 m^{-1} .

Summary

The absorption coefficient has been calculated for air/ H_2 , CO , CH_4 , CH_3OH , and $\text{C}_2\text{H}_5\text{OH}$ mixtures as a function of the modified equivalence ratio. For these lightly sooting fuels, as well as for lean regions of general hydrocarbon fuels, the nongray gaseous radiation plays a significant role in the energy transport. The algebraic expressions developed in Eqs. (9)–(15) are proposed for the effective absorption coefficient (equivalent to the Planck-mean under optically thin conditions), which eliminate the need for time-consuming spectral band calculations. This is an important consideration when choosing a radiation model for simulating nonpremixed turbulent combustion, making the approach compatible with generalized state relationships and the conserved scalar technique.

Under fuel-lean conditions the more complex fuels behave similarly, with a_p reaching a maximum between 1.3 and 1.4 m^{-1} for $\Phi' \approx 0.4$ and between 0.7 and 0.8 m^{-1} under stoichiometric conditions. Carbon monoxide combustion products emit more strongly and methane products less strongly, and hydrogen the least with $a_{p,\text{H}_2}(\Phi' = 1) = 0.28 \text{ m}^{-1}$. The absorption coefficient is predicted to be much larger in very fuel-rich regions of the flame, reaching a maximum close to 5 m^{-1} for CO and CH_4 .

The results of this study can be applied to the nonluminous region of any $\text{C}_x\text{H}_y\text{O}_z$ non-premixed flame as long as limitations of the analysis are kept in mind. Accuracy is highest when equilibrium defines the local thermodynamic state ($\Phi' \leq 1.1$ for fuels other than H_2 and CO) and when the computational cells are kept below 0.01 m in length. The problem of estimating the influx of radiation from the surrounding volume remains since a_i is inherently not a local property, but for optically thin flames or those with gray boundaries dominated by a single temperature, the algebraic expressions presented here apply.

References

- Abdel-Khalik, S. I., Tamaru, T., and El-Wakil, M. M., 1974, "A Chromatographic and Interferometric Study of the Diffusion Flame Around a Simulated Fuel Drop," *Fifteenth Symposium (International) on Combustion*, The Combustion Institute, pp. 389–399.
- Abu-Romia, M. M., and Tien, C. L., 1967, "Appropriate Mean Absorption Coefficients for Infrared Radiation of Gases," *ASME JOURNAL OF HEAT TRANSFER*, Vol. 89, pp. 321–327.
- Becker, H. A., 1974, "Effects of Concentration Fluctuations in Turbulent Diffusion Flames," *Fifteenth Symposium (International) on Combustion*, The Combustion Institute, pp. 601–615.
- Bhattacharjee, S., and Grosshandler, W. L., 1989, "Effect of Radiative Heat Transfer on Combustion Chamber Flows," *Comb. Flame*, Vol. 77, pp. 347–358.
- Bilger, R. W., 1977, "Reaction Rates in Diffusion Flames," *Comb. Flame*, Vol. 30, pp. 277–284.
- Bilger, R. W., and Stärner, H., 1983, "A Simple Model for Carbon Monoxide in Laminar and Turbulent Hydrocarbon Diffusion Flames," *Comb. Flame*, Vol. 51, pp. 155–176.
- Cess, R. D., and Mighdoll, P., 1967, *Int. J. Heat Mass Transfer*, Vol. 10, p. 1291.
- Edwards, D. K., 1976, "Molecular Gas Band Radiation," in: *Advances in Heat Transfer*, Vol. 12, T. F. Irvine, Jr., and J. P. Hartnett, eds., Academic Press, New York, pp. 116–195.
- Gore, J. P., and Faeth, G. M., 1986, "Structure and Spectral Radiation Properties of Turbulent Ethylene/Air Diffusion Flames," *Twenty-first Symposium (International) on Combustion*, The Combustion Institute, pp. 1521–1531.
- Gore, J. P., Jeng, S.-M., and Faeth, G. M., 1987, "Spectral and Total Radiative Properties of Turbulent Hydrogen/Air Diffusion Flames," *ASME JOURNAL OF HEAT TRANSFER*, Vol. 109, pp. 165–171.
- Grosshandler, W. L., 1980, "Radiative Heat Transfer in Nonhomogeneous Gases: A Simplified Approach," *Int. J. Heat Mass Transfer*, Vol. 23, pp. 1447–1459.
- Grosshandler, W. L., and Modak, A. T., 1981, "Radiation From Nonhomogeneous Combustion Products," *Eighteenth Symposium (International) on Combustion*, The Combustion Institute, pp. 689–699.
- Grosshandler, W. L., 1991, "Model Absorption Coefficients for Oxygenated and Lightly Sooting Fuels," presented at the ASME National Heat Transfer Conference, Minneapolis, MN, July.
- Grosshandler, W. L., and Thurlow, E. M., 1991, "Generalized State-Property

Relations for Hydrocarbon Flame Planck-mean Absorption Coefficients," *Proceedings of the ASME/JSME Joint Thermal Engineering Joint Conference*, Vol. 5, pp. 13-21.

Hamdan, M., and Grosshandler, W. L., 1985, "Transmittance Through Non-isothermal Combustion Gas Mixtures," ASME HTD-Vol. 45, National Heat Transfer Conference, Denver, August.

Jeng, S.-M., and Faeth, G. M., 1984, "Species Concentrations and Turbulence Properties in Buoyant Methane Diffusion Flames," *ASME JOURNAL OF HEAT TRANSFER*, Vol. 106, pp. 721-727.

Kent, J. H., and Williams, F. A., 1975, "Extension of Laminar Diffusion Flames for Liquid Fuels," *Fifteenth Symposium (International) on Combustion*, The Combustion Institute, pp. 315-325.

Ludwig, C. B., Malkmus, W., Reardon, J. E., and Thomson, J. A., 1973,

Handbook of Infrared Radiation From Combustion Gases, NASA SP-3080.

Penner, S. S., 1959, *Quantitative Molecular Spectroscopy and Gas Emissivities*, Addison-Wesley, Reading, MA.

Reynolds, W. C., 1987, "STANJAN: Chemical Equilibrium Solver," Vol. 3.90, Stanford University, CA.

Sivathanu, Y. R., and Faeth, G. M., 1990, "Generalized State Relationships for Scalar Properties in Nonpremixed Hydrocarbon/Air Flames," *Combustion and Flame*, Vol. 82, pp. 211-230.

Tien, C. L., 1968, "Thermal Radiation Properties of Gases," in: *Advances in Heat Transfer*, Vol. 5, T. F. Irvine, Jr., and J. P. Hartnett, eds., Academic Press, NY, pp. 254-324.

Tsuji, H., and Yamaoka, I., 1968, *Twelfth Symposium (International) on Combustion*, The Combustion Institute, p. 997.

Radiation, Conduction, and Convection From a Sphere in an Absorbing, Emitting, Gray Medium

P. D. Jones

Department of Mechanical Engineering,
Auburn University,
Auburn, AL 36849-5341

Y. Bayazitoglu

Mechanical Engineering and
Materials Science Department,
Rice University,
Houston, TX 77251

Combined mode heat transfer is solved for an emitting, reflecting sphere in low Peclet number motion through a gray, nonscattering, absorbing, emitting, and conducting infinite medium. The coupled formulation of the energy and radiative transfer equations is solved numerically. The radiative transfer equation is expressed in a unique spatial/directional coordinate system, whose object is to exploit the axisymmetry of the problem. The radiation intensity field is solved using the discrete ordinates method. Results are presented in terms of the Planck and Peclet numbers, and serve as a combined radiation/convection analog to the well-known Nusselt number result for a radiatively nonparticipating medium.

Introduction

Although heat transfer by conduction and convection from a sphere in motion through an infinite medium has been extensively addressed in the literature, the case in which the medium is also radiatively participating has received little attention. In such a medium, the combined modes of heat transfer give rise to temperature profiles distinct from those resulting from either radiation or convection alone. It is necessary to perform a combined mode heat transfer analysis in such cases; it is not accurate simply to add together heat flux correlations taken from independent analyses of either mode.

In nonradiating problems, heat transfer correlations are derived by considering the sphere to be the inner surface of a spherical annulus, where the outer surface is expanded to infinity. In the case of the decoupled momentum and energy equations, and a known velocity field, the energy analysis in this annulus reduces to solution of a second-order differential equation. In the present radiatively participating case an infinite spherical annulus is likewise addressed, although the analysis is considerably more involved. Radiation heat transfer terms in the energy equation are governed by the continuous radiation intensity, which is the solution of the radiative transfer equation. In the present problem it is necessary to solve a coupled formulation for temperature (energy) and radiation intensity in the thermal boundary layer around the sphere. The results of the present analysis, either in graphic or correlation equation form, express heat transfer between a spherical body in motion through a radiatively participating, gray, continuous medium, developed in a manner analogous to the widely used correlations for the special case of a radiatively nonparticipating medium.

The radiation part of the present problem is the most difficult, and hence is the focus of our analysis. Spherically symmetric (no flow) heat transfer by radiation alone in a spherical annulus has been solved by a variety of methods. Ryhming (1966) and Viskanta and Crosbie (1967) presented coupled temperature and intensity solutions by applying an exponential integral solution for the radiative transfer, outlined by Kuznetsov in a 1951 Russian language paper. Viskanta and Merriam (1968) included conduction in the medium in a similar analysis. Bayazitoglu and Suryanarayana (1989) developed closed-form solutions to the pure radiation problem using the spherical harmonics method. Tsai et al. (1989) addressed the

radiative transfer for an assumed temperature profile using the discrete ordinates method. These analyses are all one-dimensional in that there is only radial variation in the temperature, leading to spatial radial symmetry. The variation of intensity with direction may be expressed in a single angular coordinate, as these problems are directionally radially symmetric as well. The present problem, flow over a sphere, is spatially two-dimensional and axisymmetric. The resulting radiative transfer expression must involve two angular coordinates. Therefore, none of the previous solutions for radiative transfer in a spherical annulus apply directly to the present problem.

We have applied the discrete ordinates method to solution of the radiative transfer equation. This is a differential method, which may be integrated easily into the computational grid for the conduction/convection side of the problem. Recalling that radiation intensity is a quantity varying spatially (in two dimensions) and directionally (in two dimensions), the discrete ordinates method may be described as a finite difference representation of the problem (in four dimensions), where the spatial grid is chosen to suit the problem, and the directional grid is chosen to satisfy a quadrature. The mathematics of the discrete ordinates method are treated in several texts, such as Lewis and Miller (1984). Application to radiation heat transfer problems is discussed in a series of papers by Fiveland (1984, 1987, 1988) and Truelove (1987, 1988), among others, who have addressed radiation problems in up to three spatial dimensions in Cartesian media. In Cartesian media, the radiative transfer equation contains only spatial derivatives. However, curvilinear media involve directional derivatives as well.

The discrete ordinates method has been used to solve the radiation part of coupled energy and radiative transfer equation formulations by several authors in Cartesian as well as curvilinear media. Kumar et al. (1988) showed a formulation for combined radiation and convection in flow between infinite parallel plates. Yucel and Williams (1987) and Jamaluddin and Smith (1988) studied combined radiation and conduction in cylindrical media. Jones and Bayazitoglu (1990a) addressed the problem of a sphere in an infinite medium with no convection. In the present problem, coupled energy/radiation analysis using the discrete ordinates method is extended to spherical media with axial (directionally two-dimensional) rather than radial (one-dimensional) symmetry.

Analysis

The geometry of the problem is illustrated in Fig. 1 as an axisymmetric slice of a spherical annulus. Assuming steady

Contributed by the Heat Transfer Division for publication in the JOURNAL OF HEAT TRANSFER. Manuscript received by the Heat Transfer Division August 1990; revision received July 1, 1991. Keywords: Radiation, Radiation Interactions, Sprays/Droplets.

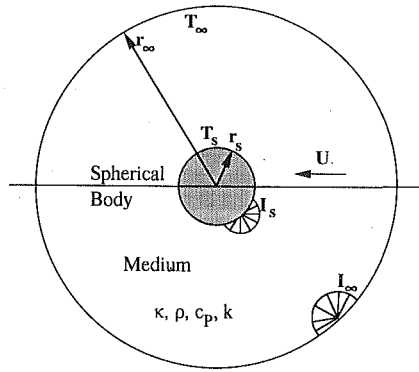


Fig. 1 Spherical body in motion through a gray, absorbing, emitting, conducting medium

state, constant properties, an index of refraction of unity, and Kirchoff's law, the energy equation may be written:

$$\rho c_p \mathbf{V} \cdot \nabla T - k \nabla^2 T + 4\kappa \sigma_b T^4 - \kappa \int_{4\pi} I d\Omega = 0 \quad (1)$$

where the radiation intensity I is integrated over the directional element of solid angle, $d\Omega$. We assume that the medium is gray, so that κ is a spectrally averaged absorption coefficient. The velocity field is assumed to be known. Equation (1) may be written in scalar form in r and ϕ in the usual way.

We assume that the medium is nonscattering. A principal application for this analysis is to express the interphase heat transfer term in gas/particle flows. In such flows, the principal scattering mode is scattering from the particles or droplets themselves. The present problem represents only a single particle, surrounded by the continuous medium in pure (non-particle-laden) form. Although it may be possible for very small particles nearby to effect significant scattering, we neglect this for the sake of clarity. The present analysis could be extended to include scattering in a straightforward manner, as, for instance, in Kim and Lee (1988). The present analysis might be regarded as an inner, single-particle problem, where the outer, multiparticle problem would involve both interparticle scattering and the inner problem heat transfer results. The radiative transfer equation may thus be written:

$$\frac{dI}{ds} + \kappa I = \kappa \frac{\sigma_b}{\pi} T^4 \quad (2)$$

where the radiation intensity I and the differential path length ds are functions of both spatial variables and the two angular variables necessary to define the direction.

The unique spatial/directional coordinate system used in this problem is illustrated in Fig. 2. The spatial point is defined by r and ϕ , where ϕ lies in an axisymmetric plane defined by the polar axis (the azimuthal angle). In spherically symmetric problems, the commonly used coordinate system is an efficient coordinate system as spherical symmetric implies independence from the azimuthal angle.

In the present problem, flow over the sphere violates spherical symmetry, leading instead to axisymmetry. We choose a spatial/directional coordinate system for this axisymmetric problem (Fig. 2), which allows us to represent directions that lie in the plane of axisymmetry (and in parallel planes) using one scalar variable, as opposed to a combination of the polar and azimuthal angles necessary with the more commonly used coordinate system. The present coordinate system is explained as follows: The polar axis is normal to the plane of axisymmetry (\mathbf{n} in Fig. 2), and the polar angle, α , is the angle away from the polar axis ($\alpha = \pi/2$ lies in the plane of axisymmetry). The azimuthal angle, γ , represents rotation about the polar axis (parallel to the plane of symmetry), using the radial direction as a starting point.

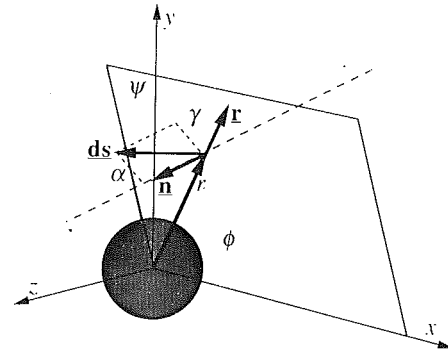


Fig. 2 Spatial/directional coordinate system for use in spatially spherical, axisymmetric geometries

(\mathbf{n} in Fig. 2), and the polar angle, α , is the angle away from the polar axis ($\alpha = \pi/2$ lies in the plane of axisymmetry). The azimuthal angle, γ , represents rotation about the polar axis (parallel to the plane of symmetry), using the radial direction as a starting point.

The intensity pathlength derivative for the spatial/directional coordinate system is derived by Jones (1990) for the coordinate system of Fig. 2:

$$\begin{aligned} \frac{dI}{ds} = & \frac{1}{r^2} \sin \alpha \cos \gamma \frac{\partial}{\partial r} (I r^2) + \frac{\sin \alpha \sin \gamma}{r \sin \phi} \frac{\partial}{\partial \phi} (I \sin \phi) \\ & + \frac{1}{r} \left(\cos \gamma + \frac{\sin \gamma}{\tan \phi} \right) \frac{\partial}{\partial \alpha} (I \cos \alpha) - \frac{\sin \alpha}{r} \frac{\partial}{\partial \gamma} (I \sin \gamma) \quad (3) \end{aligned}$$

Energy equation temperature boundary conditions include the temperatures on the sphere's surface and at the far field boundary:

$$T(r_s, \phi) = T_s \quad (4a)$$

$$T(r_\infty, \phi) = T_\infty \quad (4b)$$

as well as leading and trailing edge conditions:

$$\frac{\partial T}{\partial \phi}(r, 0) = 0 \quad (5a)$$

$$\frac{\partial T}{\partial \phi}(r, \pi) = 0 \quad (5b)$$

The radiative transfer equation is first order, requiring only one intensity boundary condition in each variable. However, the known boundary conditions apply to divided ranges of direction. Thus, for diffuse emission and reflection from an opaque, gray sphere, we write:

$$\begin{aligned} I(r_s, \phi, \alpha, \gamma_{\text{out}}) \\ = \epsilon_s \frac{\sigma_b}{\pi} T_s^4 + (1 - \epsilon_s) \frac{1}{\pi} \left[\int_{\pi/2}^{3\pi/2} \int_0^\pi I(r_s, \phi, \alpha, \gamma_{\text{in}}) \sin^2 \alpha \cos \gamma d\alpha d\gamma \right] \quad (6a) \end{aligned}$$

where γ_{out} on the left side denotes that the boundary condition is given only for those directions facing away from the sphere's surface, and the integration range for γ on the right side includes only those directions facing toward the surface. For directions toward the sphere, we assume a black, diffuse, far field boundary condition:

$$I(r_\infty, \phi, \alpha, \gamma_{\text{in}}) = \frac{\sigma_b}{\pi} T_\infty^4 \quad (6b)$$

Leading and trailing edge boundary conditions also apply to the radiation intensity:

$$\frac{\partial I}{\partial \phi}(r, 0, \alpha, \gamma) = 0; 0 \leq \gamma \leq \pi \quad (7a)$$

$$\frac{\partial I}{\partial \phi}(r, \pi, \alpha, \gamma) = 0; \pi < \gamma \leq 2\pi \quad (7b)$$

where the spatial location of the boundary condition is again divided by directional range. The problem is symmetric across the plane of axisymmetry, so for the directional polar angle we have:

$$\frac{\partial I}{\partial \alpha}\left(r, \phi, \frac{\pi}{2}, \gamma\right) = 0 \quad (8)$$

The radiation intensity is continuous through a 2π rotation of γ . Parallel to the plane of axisymmetry plane we have:

$$I(r, \phi, \alpha, 0) = I(r, \phi, \alpha, 2\pi) \quad (9)$$

While the spatial grid for numerical solution is chosen to suit the problem, the directional grid is chosen as a specific set of directions (ordinates) and their associated integration weights. In the present two-dimensional quadrature, each ordinate is specified by a pair (α_l, γ_m) , where $1 \leq l \leq L$ and $1 \leq m \leq M$, and we follow the suggestion of Abu-Shumays (1977) by letting $w_{l,m} = w_l w_m$. Fiveland (1987) noted that numerical stability is enhanced if the weights for each coordinate are equal. Thus, we allow $w_l = w_L$ for all l , and likewise $w_m = w_M$. In the present problem, we choose an unconstrained distribution of γ (rotation parallel to the plane of axisymmetry), $\gamma_m = (m-1/2)\Delta\gamma$, where $\Delta\gamma = 2\pi/M$. The weight w_m is then solved from the γ component of the first (flux) moment of area, integrated over an octant of the directional unit sphere, $\Omega = 4\pi$:

$$\int_0^{\pi/2} \cos \gamma d\gamma = \sum_{m=1}^{M/4} \cos \gamma_m w_m \quad (10a)$$

The weight w_l is solved from the zeroth moment over an octant:

$$\int_0^{\pi/2} \int_0^{\pi/2} \sin \alpha d\alpha d\gamma = \frac{\pi}{2} = \sum_{m=1}^{M/4} \sum_{l=1}^L w_l w_m \quad (10b)$$

We choose an even cosine distribution for the α_l 's, thus favoring directions near the plane of axisymmetry. Thus $\alpha_l = (L+1/2-l)[\Delta(\cos \alpha)]$, and the complete first moment of area integrated over an octant:

$$\int_0^{\pi/2} \int_0^{\pi/2} \sin^2 \alpha \cos \gamma d\alpha d\gamma = \frac{\pi}{4} = \sum_{m=1}^{M/4} \sum_{l=1}^L \sin \alpha_l \cos \gamma_m w_l w_m \quad (10c)$$

serves to define $\Delta(\cos \alpha)$. Table 1 shows the α ordinates corresponding to a quadrature of fourth order in α (note that for the axisymmetric problem, only the half range $0 \leq \alpha \leq \pi/2$ need be considered).

For ultimate solution, the overall numerical scheme is to estimate temperature, solve the radiative transfer equation for the temperature estimate, and use the resulting intensity to solve the energy equation with the T^4 term linearized about the temperature estimate. The temperature solution is then com-

Table 1 Ordinate for a quadrature of fourth order in the direction angle out of the axisymmetric plane ($\alpha = \pi/2$ lies in the axisymmetric plane)

l	α_l	w_l
1	0.47139	0.25
2	0.88099	0.25
3	1.17902	0.25
4	1.44317	0.25

pared to the temperature estimate, a new estimate formed by overrelaxing the estimation error, and the loop is repeated until convergence is achieved. The energy equation is multiplied by an element of volume, $2\pi r^2 \sin \phi d\phi dr$, and integrated between $r_{j-1/2}$ and $r_{j+1/2}$, and between $\phi_{k-1/2}$ and $\phi_{k+1/2}$, to reach the final form of the finite difference equation. A variable grid is used in r to provide very fine spacing near the sphere's surface and expand to very large values for the outer boundary. A uniform grid is used in the ϕ direction. The energy equation is block tridiagonal and could be solved with a block matrix version of the Thomas algorithm; however, since iteration is already required for the linearized terms, the more rapid, iterative solution method of alternating direction implicit (ADI, see Anderson et al., 1984) is used to solve the energy equation in the r and ϕ directions. For convergence to within 0.1 percent, about 25 iterations are required for combined mode (neither radiation or convection dominated) or convection-dominated cases. Radiation-dominated cases require many more iterations, but no instance of solution divergence is found.

The radiative transfer equation is multiplied by an element of volume and solid angle, $2\pi r^2 \sin \phi d\phi dr \sin \alpha d\alpha d\gamma$, and integrated over Δr , $\Delta\phi$, and the solid angle element. Partial derivatives are formulated over the computational cells by assuming linear forms by the intensity in each cell over each variable.

The conservative form of the intensity pathlength derivative, Eq. (3), is used to promote numerical stability. However, in this form, it arises that $dI/ds \neq 0$ for constant I in a direct discretization (Lewis and Miller, 1984). The discretized equation is brought back into balance ($dI/ds = 0$ for constant I) by altering the difference coefficients for the angular terms, as described in Jones and Bayazitoglu (1990b).

The radiative transfer equation is solved for the current temperature estimate using nested marching algorithms in the explicitly bound variables r , ϕ , and α . In γ , continuity provides only an implicit boundary condition. Hence, the r , ϕ , and α dependencies are solved for an assumed γ distribution, followed by iterations to solve the correct γ dependence. Due to the large number of intensity values over the four-dimensional range, convergence is judged by convergence of the radiation heat flux in two dimensions. Generally three to four cycles are sufficient, using the intensity values from the previous temperature iteration to start the process.

The steep temperature gradients near the sphere surface dictate a fairly fine radial grid for accurate temperature profile representation. A non-uniform radial grid of 72 points produces the results reported here. Coarser grids usually result in underprediction of heat flux from the sphere surface, although if heat flux alone is of interest (as opposed to temperature profile), smaller radial grids are often found to give acceptable results. This general criterion applied to judge grid fineness is agreement within 1 percent with the heat flux computed in the special cases reported by Viskanta and Crosbie (1967) and by Tsai et al. (1989) (no flow, finite spherical annulus, radiation only). A polar angular quadrature of four points (in the half range $0 \leq \alpha \leq \pi/2$) and a uniform azimuthal grid of 16 points (in the range $0 \leq \gamma \leq 2\pi$; hence four by four or 16 ordinates in each octant) is found to be the coarsest grid conforming to 1 percent agreement with the test cases. Coarser grids lead both to overprediction of heat flux and numerical instability. Ray effects are mitigated in this problem by temperature field smoothing due to conduction/convection.

Results and Discussion

The controlling parameters of the solution are illustrated by nondimensional forms of the energy and radiative transfer equations. Using the radiative transfer equation to substitute dI/ds for the radiation terms, we write:

$$\begin{aligned}
& \frac{1}{\text{Pl}} \int_0^{2\pi} \int_0^\pi \frac{1}{\zeta^2} \sin \alpha \cos \gamma \frac{\partial}{\partial \zeta} (\zeta^2 \Phi) \sin \alpha \, d\alpha \, d\gamma \\
& + \frac{1}{\text{Pl}} \int_0^{2\pi} \int_0^\pi \frac{\sin \alpha \sin \gamma}{\zeta \sin \phi} \frac{\partial}{\partial \phi} (\sin \phi \Phi) \sin \alpha \, d\alpha \, d\gamma \\
& + \frac{1}{\text{Pl}} \int_0^{2\pi} \int_0^\pi \frac{1}{\zeta} \left(\cos \gamma + \frac{\sin \gamma}{\tan \phi} \right) \frac{\partial}{\partial \alpha} (\cos \alpha \Phi) \sin \alpha \, d\alpha \, d\gamma \\
& - \frac{1}{\text{Pl}} \int_0^{2\pi} \int_0^\pi \frac{\sin \alpha}{\zeta} \frac{\partial}{\partial \gamma} (\sin \gamma \Phi) \sin \alpha \, d\alpha \, d\gamma \\
& - \left[\frac{1}{\zeta^2} \frac{\partial}{\partial \zeta} \left(\zeta^2 \frac{\partial \Theta}{\partial \zeta} \right) + \frac{1}{\zeta^2 \sin \phi} \frac{\partial}{\partial \phi} \left(\sin \phi \frac{\partial \Theta}{\partial \phi} \right) \right] \\
& + \frac{\text{Pe}}{2} \left[\left(\frac{v_r}{U} \right) \frac{\partial \Theta}{\partial \zeta} + \frac{1}{\zeta} \left(\frac{v_\phi}{U} \right) \frac{\partial \Theta}{\partial \phi} \right] = 0 \quad (11)
\end{aligned}$$

where $\Theta = T/T_s$, $\Phi = I/4\sigma_b T_s^4$, and $\zeta = r/r_s$. The first group of four terms in Eq. (11) is the radiation part of the energy equation, the second group is the conduction part, and the third group is the advection part. The radiation part is governed by the Planck number, $\text{Pl} = k/(4r_s \sigma_b T_s^3)$, and the advection part by the Peclet number, $\text{Pe} = (2U r_s \rho c_p)/k$. The Planck number results instead of the more familiar Stark number ($N = \text{Pl} \, \kappa r_s$) because the medium radial coordinate, r , is nondimensionalized by the sphere radius, r_s , rather than by the absorption coefficient, κ . The radiative transfer equation is written:

$$\begin{aligned}
& \frac{1}{\zeta^2} \sin \alpha \cos \gamma \frac{\partial}{\partial \zeta} (\zeta^2 \Phi) + \frac{\sin \alpha \sin \gamma}{\zeta \sin \phi} \frac{\partial}{\partial \phi} (\sin \phi \Phi) \\
& + \frac{1}{\zeta} \left(\cos \gamma + \frac{\sin \gamma}{\tan \phi} \right) \frac{\partial}{\partial \alpha} (\cos \alpha \Phi) - \frac{\sin \alpha}{\zeta} \frac{\partial}{\partial \gamma} (\sin \gamma \Phi) \\
& + \Phi(\kappa r_s) = \frac{1}{4\pi} (\kappa r_s) \Theta^4 \quad (12)
\end{aligned}$$

to illustrate the governing parameter κr_s ; the importance of ϵ_s is indicated by the boundary conditions. Note that κr_s is the nondimensionalized radius of the sphere rather than any physically meaningful optical thickness, as the region inside r_s is not part of the medium. Further, due to the nonlinear influence of Θ upon Φ , the temperature ratio T_s/T_∞ is also a governing parameter. Summarizing, the important parameters in this problem are Pl , Pe , κr_s , ϵ_s , and T_s/T_∞ . The rather large number of controlling parameters, as compared to conduction/convection without radiation, is a result of the combined mode nature of the problem. In pure radiation, for instance, it may be possible to nondimensionalize heat flux in such a way as to remove κr_s from the parameter list. However, with combined modes, this is not justifiable.

Figure 3 shows the nondimensionalized heat flux leaving the surface of a black sphere hotter than the surrounding medium for a variety of Pl and T_s/T_∞ , as a function of κr_s , for $\text{Pe} = 0$. The results are nondimensionalized by the factor $[\sigma_b(T_s^4 - T_\infty^4) + k(T_s - T_\infty)/2r_s]$ in order to be bounded over the entire range from radiation-dominated to conduction-dominated cases (In viewing Fig. 3 from the point of determining the increase in heat flux calculated by considering a conduction-dominated case to which radiation effects have been added, the nondimensionalizing basis must be kept in mind.) Note that in the $\text{Pe} = 0$ case, the problem is spatially one dimensional. For high Pl , the result is dominated by conduction, and approximates the familiar result $\text{Nu} = 2$. As κr_s increases, radiation begins to have an effect. At low Pl , a radiation-dominated case, the pure radiation result of $q/\sigma_b(T_s^4 - T_\infty^4)$ versus κr_s is nearly recovered. At $\text{Pl} = 1$, clearly a combined mode case, variation with T_s/T_∞ is more apparent due to dependence of each heat transfer mode on a different order of T . It is interesting to note the finite outer-annular radius, which must be employed computation-

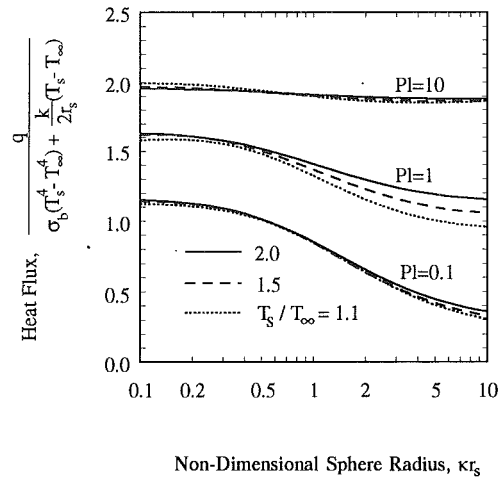


Fig. 3 Combined radiation and conduction heat flux from a hot, black sphere in an infinite medium

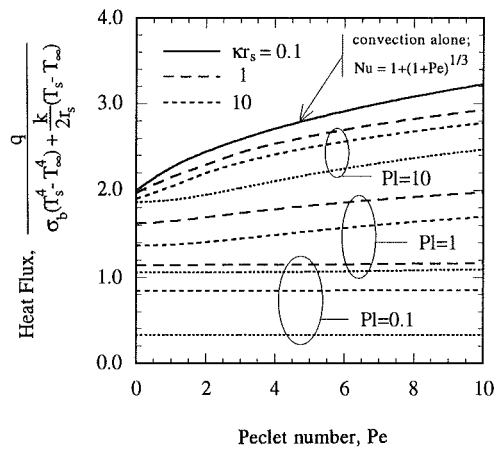


Fig. 4 Combined radiation and convection heat flux from a hot, black sphere in an infinite medium at low Peclet numbers, for $T_s/T_\infty = 1.5$

ally to approach infinite medium heat flux results. Figure 3 was computed using $r_\infty/r_s = 200$, which gives results within 0.5 percent of the infinite medium results in conduction-dominated cases. In combined mode and radiation dominated cases it was possible to achieve similar accuracy with much smaller computational domains. For $\text{Pl} = 1$, $r_\infty/r_s = 100$ was sufficient, while for $\text{Pl} = 0.1$, only $r_\infty/r_s = 50$ was necessary.

The energy equation is decoupled from the momentum equation in this problem, and so, in $\text{Pe} \neq 0$ cases, any descriptive velocity field may be used. We have used the velocity field of Stokes flow in the following results (see Panton, 1984):

$$v_r = -\frac{U}{2} \cos \phi \left[\left(\frac{r_s}{r} \right)^3 - 3 \left(\frac{r_s}{r} \right) + 2 \right] \quad (13a)$$

$$v_\phi = \frac{U}{4} \sin \phi \left[-\left(\frac{r_s}{r} \right)^3 - 3 \left(\frac{r_s}{r} \right) + 4 \right] \quad (13b)$$

This velocity field is valid for Reynolds numbers less than one. However, for slightly higher Reynolds numbers, the deviation of the velocity field from Eqs. (13) due to separation in the wake has only a minor effect on heat transfer.

Figure 4 shows the effect of low Peclet numbers on combined radiation and convection heat flux from the surface of a hot, black sphere in a gray, nonscattering infinite medium. The indicated heat flux is a mean, integrated over the sphere and normalized by the surface area. The results in Fig. 4 were computed using a spatial angular grid of nine points, which

was found to give results within 1 percent of results for a 19-point grid. Also shown is the convection-only result $Nu = 1 + (1 + Pe)^{1/3}$, which is valid up to a Peclet number of about 10. Note that as with the radiation/conduction results, inclusion of radiation effects results in a higher overall heat flux, but a lower nondimensional heat flux due to the effect of the nondimensionalizing factor. At high Planck numbers the heat flux is dominated by conduction and convection, and variation with Pe is similar to variation for convection alone. At low Pl, the radiation terms in Eq. (11) dominate the conduction and convection, and Pe does not have an effect. Presumably, at higher Pe, outside the range of Stokes flow, low Pl cases will show greater variation with Pe. Although the objective of this study has focused on low Pe flow, the formulation given is general, and results for higher Pe could easily be developed.

Acknowledgments

This paper is based in part on work partially supported by the Texas Advanced Technology Program, under grant No. 003604-008.

References

- Abu-Shumays, I. K., 1977, "Compatible Product Angular Quadrature for Neutron Transport in x - y Geometry," *Nuclear Science and Engineering*, Vol. 64, pp. 299-316.
- Anderson, D. A., Tannehill, J. C., and Pletcher, R. H., 1984, *Computational Fluid Mechanics and Heat Transfer*, Hemisphere Publishing Corp., New York.
- Bayazitoglu, Y., and Suryanarayana, P. V. R., 1989, "Transient Radiative Heat Transfer From a Sphere Surrounded by a Participating Medium," *ASME JOURNAL OF HEAT TRANSFER*, Vol. 111, pp. 713-718.
- Fiveland, W. A., 1984, "Discrete Ordinates Solutions of the Radiative Transport Equation for Rectangular Enclosures," *ASME JOURNAL OF HEAT TRANSFER*, Vol. 106, pp. 699-706.
- Fiveland, W. A., 1987, "Discrete Ordinate Methods for Radiative Heat Transfer in Isotropically and Anisotropically Scattering Media," *ASME JOURNAL OF HEAT TRANSFER*, Vol. 109, pp. 809-812.
- Fiveland, W. A., 1988, "Three Dimensional Radiative Heat Transfer Solutions by the Discrete Ordinates Method," *Journal of Thermophysics and Heat Transfer*, Vol. 2, pp. 309-316.
- Jamaluddin, A. S., and Smith, P. J., 1988, "Discrete Ordinates Solution of Radiative Transfer Equation in Non-axisymmetric Cylindrical Enclosures," *Proceedings of the 1988 National Heat Transfer Conference*, Vol. 1, HTD-Vol. 96, H. R. Jacobs, ed., pp. 227-232.
- Jones, P. D., 1990, "Radiation and Convection Heat Transfer in Particle-Laden Fluid Flow," Ph.D. Thesis, Rice University, Houston, TX.
- Jones, P. D., and Bayazitoglu, Y., 1990a, "Combined Radiation and Conduction From a Sphere in a Participating Medium," *Heat Transfer 1990, Proceedings of the Ninth International Heat Transfer Conference*, Vol. 6, G. Hetsroni, ed., Hemisphere Publishing Corp., Washington, DC, pp. 397-402.
- Jones, P. D., and Bayazitoglu, Y., 1990b, "Combined Radiation, Conduction, and Convection From a Sphere in an Infinite Medium," *Radiation Heat Transfer*, ASME HTD-Vol. 154, S. T. Thynell and J. R. Mahan, eds., pp. 9-17.
- Kim, T. K., and Lee, H., 1988, "Effect of Anisotropic Scattering on Radiative Heat Transfer in Two-Dimensional Rectangular Enclosures," *International Journal of Heat and Mass Transfer*, Vol. 31, pp. 1711-1721.
- Kumar, S., Majumdar, A., and Tien, C. L., 1988, "The Differential Discrete Ordinate Method for Solutions of the Equation of Radiative Transfer," *Proceedings of the 1988 National Heat Transfer Conference*, H. R. Jacobs, ed., ASME, New York, pp. 179-186.
- Lewis, E. E., and Miller, W. J., Jr., 1984, *Computational Methods of Neutron Transport*, Wiley, New York.
- Panton, R. L., 1984, *Incompressible Flow*, Wiley, New York.
- Ryhming, I. L., 1966, "Radiative Transfer Between Two Concentric Spheres Separated by an Absorbing and Emitting Gas," *International Journal of Heat and Mass Transfer*, Vol. 9, pp. 315-324.
- Truelove, J. S., 1987, "Discrete Ordinate Solutions for the Radiation Transport Equation," *ASME JOURNAL OF HEAT TRANSFER*, Vol. 109, pp. 1048-1051.
- Truelove, J. S., 1988, "Three Dimensional Radiation in Absorbing, Emitting, Scattering Media Using the Discrete Ordinates Approximation," *Journal of Quantitative Spectroscopy and Radiative Transfer*, Vol. 39, pp. 27-31.
- Tsai, J. R., Ozisik, M. N., and Santarelli, F., 1989, "Radiation in Spherical Symmetry With Anisotropic Scattering and Variable Properties," *Journal of Quantitative Spectroscopy and Radiative Transfer*, Vol. 42, pp. 187-199.
- Viskanta, R., and Crosbie, A. L., 1967, "Radiative Transfer Through a Spherical Shell of an Absorbing Emitting Gray Medium," *Journal of Quantitative Spectroscopy and Radiative Transfer*, Vol. 7, pp. 871-889.
- Viskanta, R., and Merriam, R. L., 1968, "Heat Transfer by Combined Conduction and Radiation Between Concentric Spheres Separated by Radiating Medium," *ASME JOURNAL OF HEAT TRANSFER*, Vol. 90, pp. 248-256.
- Yucel, A., and Williams, M. L., 1987, "Heat Transfer by Combined Conduction and Radiation in Axisymmetric Enclosures," *Journal of Thermophysics and Heat Transfer*, Vol. 1, pp. 301-306.

M. I. Flik

B. I. Choi

Department of Mechanical Engineering.

A. C. Anderson

Lincoln Laboratory.

A. C. Westerheim

Lincoln Laboratory and Department of
Materials Science and Engineering.

Massachusetts Institute of Technology,
Cambridge, MA 02139

Thermal Analysis and Control for Sputtering Deposition of High- T_c Superconducting Films

For the preparation of high-quality films of high- T_c superconductors (HTSC) on crystalline substrates, it is necessary to control the substrate temperature accurately during deposition. This study shows that thermal radiation heat transfer in the deposition chamber governs the substrate temperature. The application of thin-film optics yields the emittance of the substrate holder-substrate-film composite as a function of the thickness of the growing film. In a single-target off-axis sputtering system, the substrate temperature is measured during film deposition using a novel method for the attachment of a thermocouple to the substrate front surface. For constant heater power, the measurements show a decrease of the substrate temperature, in agreement with the theoretical prediction. Based on the substrate emittance variation determined in this work, a pyrometric in-situ temperature measurement technique can be developed.

1 Introduction

The discovery of superconductivity above 90 K in the compound $\text{YBa}_2\text{Cu}_3\text{O}_{7-\delta}$ has opened the door for new applications in microwave electronics and in semiconductor-superconductor hybrid devices. For the first time superconductivity occurs at temperatures where semiconductor devices perform well. These promising applications will require the deposition of high-quality superconducting thin films on semiconductor substrates.

Films deposited onto unheated room-temperature substrates require an annealing process to become superconducting. Films are annealed in an oxygen environment at a temperature of about 900°C. This annealing process raises several difficulties. First, high temperatures are not compatible with integrated-circuit technology (Van Duzer, 1988). In addition, chemical reaction and interdiffusion between film and substrate degrade the superconducting properties. Finally, a difference in the thermal expansion coefficients of film and substrate may cause microcracks. This problem becomes worse with larger differences between processing and operating temperatures.

In-situ growth without an annealing process is the most feasible solution for these problems. In this procedure, films are deposited on a heated substrate and cooled in an oxygen environment. Laser ablation and sputtering deposition processes have yielded the best films of high- T_c superconductors (Murphy et al., 1988). A critical parameter in the in-situ growth process is the temperature of the substrate (Li et al., 1988). It influences film orientation, stoichiometry, and crystallinity. Since the temperature drop across the deposited film is small, the substrate temperature is equal to the film temperature. Previous work showed that the substrate temperature must be kept between $650^\circ\text{C} \leq T \leq 800^\circ\text{C}$ to ensure good film quality (Norton et al., 1989; Ramesh et al., 1991; Westerheim et al., 1991a). As it is very difficult to measure the substrate temperature directly during deposition, the temperature of the substrate holder is usually reported. This temperature can be up to 150 K higher than the substrate temperature (Inam et al., 1988). It is the purpose of this study to predict and measure the substrate temperature during the deposition process. Par-

ticular attention is paid to the substrate emittance change caused by the film growth.

The substrate temperature can be determined by analyzing the heat transfer between the substrate and the other parts of the deposition chamber. Nevis and Tisone (1974) calculated the silicon wafer temperature in sputtering and sputter-etching systems based on thermal radiation heat transfer. Their results showed that the wafer temperature depends significantly on the surface emittance. They did not analyze the change of emittance during film growth. Thornton and Lamb (1984) investigated substrate heating rates by sputtering, but they did not extend their study to predict the film temperature. Recently Vassenden et al. (1991) investigated the substrate temperature change with a simplified heat balance between the substrate and the oven.

This study shows that the substrate temperature can be calculated with radiative heat transfer analysis during the sputtering deposition process. Thin-film optics is employed to determine the change of substrate emittance with film thickness. The typical thickness of the film is $1\ \mu\text{m}$, which is of the order of magnitude of the wavelength in the near-infrared. Interference is expected to influence the radiative properties of the film as it grows. This study shows that the emittance depends on the optical properties of the substrate, substrate holder, and film. To verify the theoretical predictions, the substrate temperature is measured in a single-target off-axis RF sputtering system during deposition. A miniature thermocouple is attached to the substrate by a novel method. The comparison between theoretical and experimental results shows good agreement. While allowing the verification of the theory developed in the present study, this temperature measurement technique is not practical in processing.

The results of this study remove one of the major obstacles for the fabrication of high-quality films of high- T_c superconductors. The prediction of the substrate temperature permits the optimization of the thermal design of sputtering systems. This work provides the theoretical basis required for the development of a time-variant heating procedure to keep the substrate temperature constant during deposition, and of in-situ pyrometric substrate temperature measurement techniques.

2 Heat Transfer Modes in a Sputtering Chamber

A schematic of the sputtering system used for the study is shown in Fig. 1. A general description of sputtering systems

Contributed by the Heat Transfer Division and presented at the ASME Winter Annual Meeting, Dallas, Texas, November 25-30, 1990. Manuscript received by the Heat Transfer Division September 24, 1990; revision received July 1, 1991. Keywords: High-Temperature Phenomena, Materials Processing and Manufacturing Processes, Radiation.

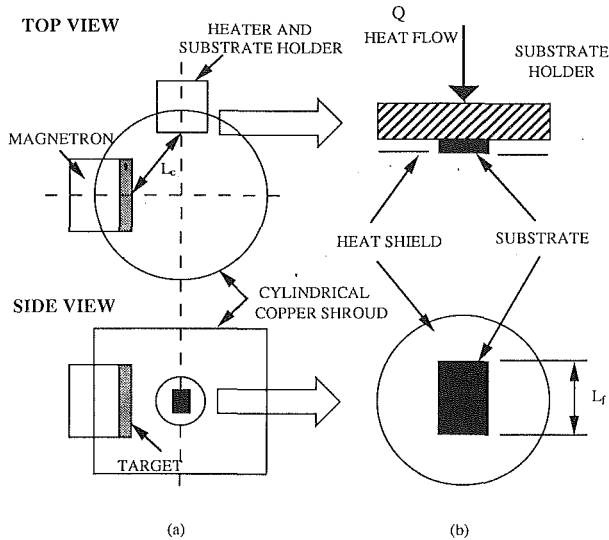


Fig. 1 Schematic of a sputtering system for high- T_c superconducting films: (a) top and side view of the target, substrate, and copper shroud; (b) detail of the substrate and the heat shield

is given by Vossen and Kern (1978). In the off-axis configuration, the target and substrate faces are oriented perpendicularly to avoid the resputtering associated with negative oxygen ions generated at the target. The copper shroud is the ground of the electric circuit and is regarded as an enclosure in the analysis of radiation heat transfer. All of the parts shown in Fig. 1 are placed in a vacuum chamber. The chamber pressure is maintained at 18.6 Pa (13.3 Pa Ar, 5.3 Pa O₂).

Radiation is expected to be the main heat transfer mode in the low-pressure environment of a deposition chamber. It has

not been previously reported, however, how much thermal conduction and convection contribute to the total heat exchange, and how these contributions change with the operating conditions. Considering the temperature jump between a wall and a gas at low pressures using an expression given by Devienne (1965), the ratio of the gas conduction heat flux to the radiation heat flux, N , is given by

$$N = \frac{k(T_S - T_E)/[L_c(1 + CKn)]}{\epsilon\sigma T_S^4 - \alpha\sigma T_E^4} \quad (1)$$

where T_S and T_E are substrate and enclosure temperature, respectively, Kn is the Knudsen number, $Kn = l/L_c$, C is a constant, σ is the Stefan-Boltzmann constant, ϵ and α are the substrate emittance and absorptance, respectively. The target temperature is equal to that of the enclosure. The length scale for conduction, L_c , is the distance between the target and the substrate. In the sputtering system of Fig. 1, L_c is approximately 5 cm. The gas thermal conductivity, k , depends on the mixture composition and temperature, not on pressure.

The conductivity of the argon-oxygen mixture was given by Bird et al. (1960),

$$k = \sum_{i=1}^2 \frac{x_i k_i}{\sum_{j=1}^2 x_j \frac{1}{\sqrt{8}} \left(1 + \frac{M_j}{M_i}\right)^{-1/2} \left[1 + \left(\frac{\rho \bar{v} l}{M_j}\right)^{1/2} \left(\frac{M_j}{M_i}\right)^{1/4}\right]^2} \quad (2)$$

where x is the mole fraction and the subscripts 1 and 2 refer to argon and oxygen, respectively. The thermal conductivity for each gas is found using the kinetic theory relation (Rohsenow and Choi, 1961)

$$k = \frac{1}{3} \rho c_v \bar{v} l \quad (3)$$

Nomenclature

A = area, m ²	L_f = characteristic length for free convection, m	β = volumetric thermal expansion coefficient, K ⁻¹
c_p = specific heat at constant pressure, J kg ⁻¹ K ⁻¹	M = molecular weight, kg kmol ⁻¹	δ = complex phase angle, rad
c_v = specific heat at constant volume, J kg ⁻¹ K ⁻¹	n = real part of refractive index	ϵ = emittance
C = constant, Eq. (1)	\bar{n} = complex refractive index = $n + ik$	κ = imaginary part of refractive index
d = thickness, m	N = ratio of gas conduction heat flux to radiation heat flux	λ = wavelength in vacuum, m
dG_E = spectral radiation heat flux arriving at enclosure, W m ⁻²	O = ratio of gas convection heat flux to radiation heat flux	ρ = mass density, kg m ⁻³
dG_S = spectral radiation heat flux arriving at substrate, W m ⁻²	P = RF magnetron power, W	σ = Stefan-Boltzmann constant = 5.67×10^{-8} W m ⁻² K ⁻⁴
dJ_E = spectral radiation heat flux leaving enclosure, W m ⁻²	q = heat flux, W m ⁻²	τ = transmittance
dJ_S = spectral radiation heat flux leaving substrate, W m ⁻²	Q = heat flow = qA , W	Ω = thermal resistance, K W ⁻¹
D_g = gold film dot diameter, m	r = Fresnel coefficient of reflection	
e_b = blackbody spectral emissive power, W m ⁻³	R = normal reflectance	Subscripts
E_R = average energy required to produce one ion, J	R_a = reflectivity of film at vacuum-film interface	a = interface between vacuum and film
E_I = ionization potential, J	R_b = reflectivity of film at film-substrate interface	b = interface between film and substrate
F = view factor	R_c = reflectivity at substrate-substrate holder interface	c = interface between substrate and substrate holder
g = gravitational acceleration = 9.81 m s ⁻²	t = Fresnel coefficient of transmission and time, s	E = enclosure
$i = (-1)^{1/2}$	T = thermodynamic temperature, K	F = film
k = thermal conductivity, W m ⁻¹ K ⁻¹	\bar{v} = average molecular speed, m s ⁻¹	h = high-temperature property
Kn = Knudsen number = l/L_c	V = velocity of gas, m s ⁻¹	H = substrate holder
l = mean free path, m	x = mole fraction	HS = heat shield
L_c = characteristic length for conduction, m	α = absorptance	P = plasma
		S = substrate
		T = target
		0 = vacuum
		1 = argon
		2 = oxygen

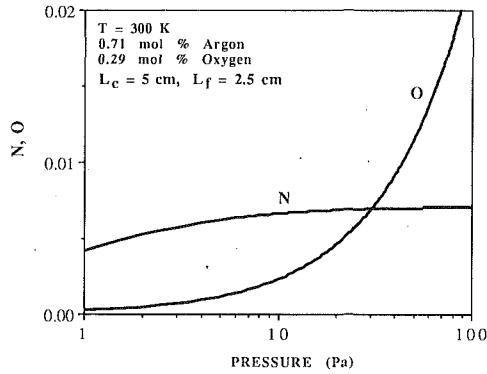


Fig. 2 Comparison between conduction, convection, and radiation heat transfer in a sputtering chamber

where \bar{v} is the average molecular speed and l is the mean free path.

If the Knudsen number Kn is of the order of unity, then the conduction heat transfer is reduced due to the temperature discontinuity at the wall. For the pressure range from 100 Pa to 1 Pa, Kn varies from 0.0014 to 0.14. Figure 2 shows the result of Eq. (1), for $\epsilon = 0.7$, $\alpha = 0.3$, and $C = 5.08$ (Devienne, 1965). In the entire pressure range, thermal conduction heat transfer is less than 1 percent of the radiation heat transfer. The decrease of N toward lower pressures results from the increasing mean free path, leading to an increasing Knudsen number.

The ratio of the gas convection heat flux to the radiation heat flux, O , is given by

$$O = \frac{\rho c_p V (T_S - T_E)}{\epsilon \sigma T_S^4 - \alpha \sigma T_E^4} \quad (4)$$

The characteristic velocity V for free convection is scaled as (Kays and Crawford, 1980)

$$V \sim \sqrt{g \beta L_f (T_S - T_E)} \quad (5)$$

where β denotes the volumetric thermal expansion coefficient. The length scale for free convection L_f is the height of the substrate. For the sputtering system under consideration, $L_f = 2.5$ cm. Figure 2 indicates that unlike N , O shows a strong dependence on pressure because of density changes, and increases rapidly around 100 Pa. The contribution of convective heat transfer cannot be neglected above 100 Pa.

As shown in Fig. 2, both conduction and convection contributions in the ordinary pressure range of a high- T_c superconductor sputtering system are negligible compared to radiation. The present study considers only radiation heat transfer.

3 Radiative Heat Exchange in a Sputtering System

Flik and Tien (1990) applied general enclosure theory to estimate the radiative heat exchange in a sputtering system. In the present study an approximate relation is derived considering the chamber geometry. Since the view factor from the target to the substrate holder is 0.02 and that from the substrate holder to the target is 0.13, the radiative energy exchange between substrate holder and target is neglected. There is no radiation heat exchange between the target and the enclosure, since both are approximately at the same temperature.

The radiation heat transfer between substrate and enclosure is given by

$$dJ_S = \epsilon_S(\lambda) e_b(T_S, \lambda) d\lambda + [1 - \alpha_S(\lambda)] dG_S \quad (6)$$

$$dG_S = F_{S-E} dJ_E \quad (7)$$

$$dJ_E = \epsilon_E(\lambda) e_b(T_E, \lambda) d\lambda + [1 - \alpha_E(\lambda)] dG_E \quad (8)$$

$$dG_E = F_{E-S} dJ_S + F_{E-E} dJ_E \quad (9)$$

where ϵ and α are hemispherical emittance and absorptance, respectively, dJ is the spectral radiative heat flux leaving a surface, and dG the spectral radiative heat flux arriving at a surface. The subscript S denotes the substrate and E denotes the copper shroud. In the sputtering system under consideration, $A_S/A_E = 0.002$, and in the limit $A_S/A_E \rightarrow 0$, the view factors become $F_{E-S} = 0$, $F_{E-E} = 1$, where $F_{S-E} = 1$ is used. For this limiting case, Eq. (6) can be expressed as

$$dJ_S = \epsilon_S(\lambda) e_b(T_S, \lambda) d\lambda + [1 - \alpha_S(\lambda)] \frac{\epsilon_E(\lambda)}{\alpha_E(\lambda)} e_b(T_E, \lambda) d\lambda \quad (10)$$

The copper shroud surface can be regarded as spectrally diffuse, and Kirchhoff's law applies in the form $\epsilon_E(\lambda) = \alpha_E(\lambda)$. The net heat flux from the substrate is

$$q_S = \int (dJ_S - dG_S) = \epsilon_S \sigma T_S^4 - \alpha_S \sigma T_E^4 \quad (11)$$

Equation (11) accounts for the fact that the radiation emitted by the substrate has a different spectral distribution from that incident on the substrate. This equation signifies that the substrate is located inside an enclosure that acts as a blackbody since its area is very large compared to the substrate area.

The substrate holder can either be of the same size as the substrate, or larger than it. The first case is preferable, because it prevents substrate temperature changes due to heat flux diversion between the substrate and the portion of the substrate holder not covered by the substrate. In this section, radiation heat exchange in the sputtering system is analyzed for the substrate. This applies directly to the first case. In the second case, the additional radiation heat exchange from the remaining substrate holder surface must be analyzed. This is done in section 6 for the present experimental configuration. This separate treatment of radiative exchange for the substrate and the remaining area of the substrate holder is possible if the total substrate holder area is small compared to the enclosure area. In the present experiment, $A_H/A_E = 0.01$, which satisfies this criterion.

In order for Eq. (11) to be valid, the gases in the chamber must not interfere with the radiative heat exchange. Oxygen is normally inactive in the infrared and its absorption is significant only when the pressure is extremely high (Crawford et al., 1949). As argon is a monatomic molecule, it has no rotational-vibrational absorption. Its excited metastable state has a potential of 11.5 eV, which is equivalent to the energy of a photon with 0.1 μm wavelength, in the ultraviolet region. The molecular gases in the vacuum chamber have no influence on the radiative heat exchange.

The substrate is heated by a heater during the film deposition process. In addition to the thermal power from the heater there are other mechanisms delivering thermal energy to the film: heat of condensation, sputtered atom kinetic energy, plasma radiation, ion neutralization and reflection at the target (Thornton and Lamb, 1984). The magnitude of each contribution depends significantly on the system configuration (Class and Hieronymi, 1982) and the operating conditions. Thornton (1978) showed that all of them can be of the same order of magnitude. Previous investigations focused on sputtering systems for metal-film coating. In this case, the substrate faces the target directly and experiences the bombardment of particles with high kinetic energy. Due to the off-axis geometry of the present system, the substrate is placed outside the region of direct collisions. The energy flux associated with the sputtered atoms and negative ions is neglected in the present study.

The plasma is locally confined near the target by a magnetic field. Thus the plasma can be regarded as a thin sheet having the same view factor as the target. The plasma radiation heat flux, Q_p , was estimated by Thornton (1978) as

$$Q_p = \frac{E_R - E_I}{2E_R} P F_{T-H} \quad (12)$$

where E_I is the ionization potential, E_R the average energy required to produce one ion, F_{T-H} the view factor from the target to the substrate holder, and P the RF magnetron power. Approximately one-half of the additional energy above the ionization potential must be radiated away. For argon, E_R is 26.4 eV (Christophorou, 1971) and E_I is 15.75 eV (Chapman, 1980). For the present system, P is 125 W and F_{T-H} is 0.0203. This equation yields $Q_D = 0.51$ W, which is two orders of magnitude less than the heat flow from the heater (18.9 W). Thus, the plasma heat flux can be neglected.

4 Emittance of Film-Substrate-Substrate Holder Composite

4.1 Thin-Film Optics. Single crystals of the superconductor compound $YBa_2Cu_3O_{7-\delta}$ are optically anisotropic and the optical properties for incidence normal to the c axis of the crystal unit cell are much less well known than for incidence parallel to the c axis. Although Eq. (11) requires the hemispherical emittance, in this work ϵ_S is calculated as the normal emittance along the c axis, because high-quality films possess an orientation of the c axis normal to the plane of the film. Schlesinger et al. (1990) investigated the optical properties of $YBa_2Cu_3O_7$ single crystals at 100 K for different crystal axes. If the hemispherical emissivity of the $YBa_2Cu_3O_7$ compound is calculated based on the data given by Schlesinger et al. (1990), the hemispherical emissivity is 25 percent larger than the normal emissivity. Although the difference between the hemispherical emissivity and the normal emissivity of the $YBa_2Cu_3O_6$ compound cannot be calculated due to the lack of optical constants, the difference for the $YBa_2Cu_3O_7$ compound provides an estimation of the difference for the $YBa_2Cu_3O_6$ compound.

Since the substrate emits at a temperature of approximately 1000 K, the wavelength of maximum spectral emissive power is around $3 \mu\text{m}$. Since this is the order of the film thickness, interference effects must be considered. From thin-film optics (Born and Wolf, 1980), the normal reflectivity of the film for incidence from vacuum is

$$R_a = \left| \frac{r_a + r_b e^{2i\delta_F}}{1 + r_a r_b e^{2i\delta_F}} \right|^2 \quad (13)$$

and for incidence from the substrate

$$R_b = \left| \frac{r_b + r_a e^{2i\delta_F}}{1 + r_a r_b e^{2i\delta_F}} \right|^2 \quad (14)$$

The transmissivity of the film is

$$\tau_F = \frac{n_S}{n_0} \left| \frac{t_a t_b e^{i\delta_F}}{1 + r_a r_b e^{2i\delta_F}} \right|^2 \quad (15)$$

where n_0 , n_S are the real parts of the refractive index of a vacuum and the substrate, respectively, and r_a , t_a and r_b , t_b are the Fresnel coefficients at the vacuum-film interface and the film-substrate interface,

$$r_a = \frac{\bar{n}_0 - \bar{n}_F}{\bar{n}_0 + \bar{n}_F} \quad (16)$$

$$t_a = \frac{2\bar{n}_0}{\bar{n}_0 + \bar{n}_F} \quad (17)$$

$$r_b = \frac{\bar{n}_F - \bar{n}_S}{\bar{n}_F + \bar{n}_S} \quad (18)$$

$$t_b = \frac{2\bar{n}_F}{\bar{n}_F + \bar{n}_S} \quad (19)$$

where \bar{n}_0 , \bar{n}_F , and \bar{n}_S are the complex refractive indices of vacuum, the film, and the substrate, respectively. The complex phase angle is given by

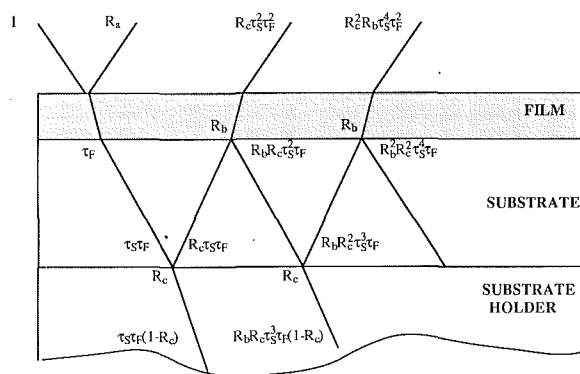


Fig. 3 Multiple reflections within the film-substrate-substrate holder composite

$$\delta_F = \frac{2\pi}{\lambda} \bar{n}_F d_F \quad (20)$$

Due to interference and absorption, the reflectance depends on the film thickness, d_F .

The substrate thickness is $1200 \mu\text{m}$, which is three orders of magnitude larger than the wavelength. In the case of $d_S \gg \lambda$, the spacing of fringes due to substrate interference is given by (Bohren and Huffman, 1983)

$$\frac{\Delta\lambda}{\lambda} \sim \frac{\lambda}{2n_S d_S} \quad (21)$$

At a wavelength of $3 \mu\text{m}$, $\Delta\lambda/\lambda \sim 10^{-3}$, which yields high-frequency oscillations of the emittance, $\epsilon(\lambda)$, with wavelength. Since the determination of the total normal emittance requires the integration of $\epsilon(\lambda)$ over $d\lambda$, substrate interference effects do not influence the results, because the integration extends over a wavelength interval much larger than $\Delta\lambda$. Only the absorption of radiation in the substrate is considered. The substrate material $SrTiO_3$ is absorbing for wavelengths greater than $3 \mu\text{m}$. Referring to Fig. 3, the sum of all reflected individual beam intensities gives the reflectance R of the film-substrate-substrate holder composite,

$$R = R_a + \frac{R_c \tau_S^2 \tau_F^2}{1 - R_c \tau_S^2 R_b} \quad (22)$$

$$\tau_S = \exp\left(-\frac{4\pi\kappa_S d_S}{\lambda}\right) \quad (23)$$

$$R_c = \left| \frac{\bar{n}_H - \bar{n}_S}{\bar{n}_H + \bar{n}_S} \right|^2 \quad (24)$$

Since the substrate holder is opaque, the normal emittance for a given wavelength is $\epsilon(\lambda) = 1 - R(\lambda)$. The total normal emittance and absorptance are

$$\epsilon_S = \frac{\int_0^\infty \epsilon(\lambda) e_b(T_S, \lambda) d\lambda}{\sigma T_S^4} \quad (25)$$

$$\alpha_S = \frac{\int_0^\infty \epsilon(\lambda) e_b(T_E, \lambda) d\lambda}{\sigma T_E^4} \quad (26)$$

Equations (25) and (26) are based on Kirchhoff's law, $\epsilon(\lambda) = \alpha(\lambda)$, which is valid because the normal emittance $\epsilon(\lambda)$ is a directional spectral property. For each film thickness, iterations are required to calculate the substrate temperature T_S for a given heat flux q_S and a given value of T_E .

4.2 Optical Constants. The stoichiometry of the growing

Table 1 Room-temperature optical constants of film, substrate, and substrate holder

Wavelength	YBa ₂ Cu ₃ O ₆		SrTiO ₃		Steel	
	n	κ	n	κ	n	κ
1.0	2.234	.544	2.316	.000	2.960	4.439
2.0	2.495	.693	2.268	.000	4.135	7.095
3.0	2.625	.445	2.231	.000	5.200	9.610
4.0	2.616	.435	2.184	.001	6.067	11.860
5.0	2.607	.425	2.122	.003	7.000	14.060
6.0	2.598	.415	2.026	.004	7.830	15.810
7.0	2.589	.405	1.921	.007	8.755	17.850
8.0	2.579	.395	1.790	.012	9.530	20.060
9.0	2.570	.385	1.623	.020	10.510	21.770
10.0	2.561	.375	1.404	.033	11.440	23.540
11.0	2.552	.366	1.093	.060	12.270	25.260
12.0	2.543	.356	.547	.171	13.060	26.900
13.0	2.534	.346	.146	.929	13.960	28.600
14.0	2.525	.336	.137	1.503	15.260	30.410
15.0	2.516	.326	.166	2.039	16.390	31.740
16.0	2.506	.316	.250	2.661	17.320	33.150
17.0	2.497	.306	.532	3.588	18.300	34.550
18.0	2.488	.296	2.481	5.190	19.280	35.950
19.0	2.479	.286	4.149	1.546	20.260	37.350
20.0	2.470	.276	2.579	.689	21.240	38.750
21.0	2.460	.266	1.519	.651	22.220	40.150
22.0	2.452	.256	.664	1.134	23.200	41.550
23.0	2.442	.247	.383	1.767	24.180	42.950
24.0	2.433	.237	.298	2.220	25.160	44.350
25.0	2.424	.227	.265	2.579	26.140	45.750
26.0	2.415	.217	.250	2.888	27.120	47.150
27.0	2.405	.207	.246	3.167	28.100	48.550

film in the chamber depends on the deposition conditions such as the oxygen partial pressure and the substrate temperature. At temperatures above 400°C and at low oxygen pressures, YBa₂Cu₃O_{7-δ} becomes depleted of oxygen. For a processing temperature of about 700°C and an oxygen partial pressure of 5.3 Pa, the growing film is close to the tetragonal phase (YBa₂Cu₃O₆). The tetragonal phase is transformed into the superconducting orthorhombic phase (YBa₂Cu₃O₇) during a cooling process in an oxygen environment. These two phases have very different optical properties. The optical properties of the YBa₂Cu₃O₆ film are extracted from the measurements by Kircher et al. (1989) and Thomsen et al. (1988). The imaginary part of the dielectric function and the reflectance reported by Kircher et al. (1989) determine the optical constants in the wavelength range 1 μm ≤ λ ≤ 3 μm. The real part of the refractive index is linearly extrapolated up to λ = 27 μm based on the values at λ = 2.5 μm and λ = 3.0 μm. Using the extrapolated real part of the refractive index and the reflectance measured by Thomsen et al. (1988) at λ = 17 μm, the values of the imaginary part of the refractive index for wavelengths 3 μm ≤ λ ≤ 16 μm and 18 μm ≤ λ ≤ 27 μm are interpolated and extrapolated linearly from those at λ = 2.5 μm and λ = 17 μm, respectively.

The optical properties of SrTiO₃ at room temperature in the infrared were reported by Spitzer et al. (1962). The properties for the wavelength range 1 μm ≤ λ ≤ 5 μm were given in more detail by Herzberger and Salzberg (1962). Stainless steel SS316 is used as the substrate holder material. The optical properties of SS316 are obtained from those of a similar composition reported by Sasovskaya et al. (1969). Since Fe, Ni, and Co are all transition metals, no great error is expected in this approximation. Table 1 summarizes the room-temperature optical constants of the film, substrate and substrate holder materials. Since the values of the complex refractive index for all materials are calculated from reflectivity data, the predicted radiative properties are believed to be accurate.

In what follows, estimates are provided for the error caused by employing the room-temperature optical constants of Table 1 in the emittance calculations for high temperature. The optical properties of both the SrTiO₃ substrate and the YBa₂Cu₃O₆ film at high temperatures have not been previously investigated. The high-temperature properties can be estimated from those of the metal oxides MgO, Al₂O₃, and ZrO₂. The normal total emissivities of the oxides are 0.8 at 300 K and 0.4 at 1000 K (Touloukian and De Witt, 1972). The decrease of the emissivity is caused mainly by the increase of the imaginary part of the refractive index. When the temperature changes from room temperature to 1000 K, the electrical conductivity

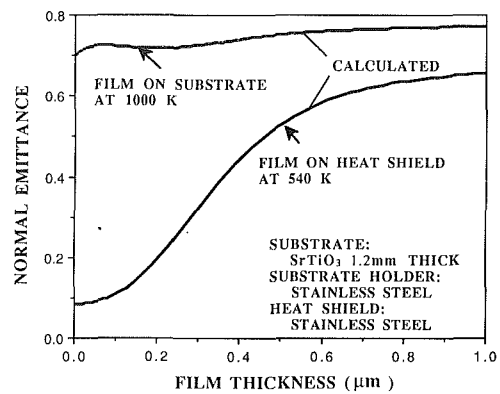


Fig. 4 Calculated normal emittance of YBa₂Cu₃O₆ film as a function of the film thickness on the substrate and the heat shield

of the oxides increases by several orders of magnitude (Linz, 1953), which is related to the increase of the free-electron number density. Assuming that the real part of the refractive index is temperature independent and that the spectral emittance at high temperature, ε_h, is 50 percent of that at 300 K, i.e., ε_h = 0.5ε, the high-temperature imaginary part of the refractive index, κ_h, is calculated by

$$\frac{4n_h}{(n_h + 1)^2 + \kappa_h^2} = 0.5 \frac{4n}{(n + 1)^2 + \kappa^2} \quad (27)$$

where *n* and *κ* are room-temperature real and imaginary part of the refractive index, respectively. Assuming *n_h* = *n*, Eq. (27) gives

$$\kappa_h = [(n + 1)^2 + 2\kappa^2]^{1/2}. \quad (28)$$

From Eq. (28) the high-temperature imaginary part of the refractive index of the YBa₂Cu₃O₆ film is 3.7 and that of the SrTiO₃ substrate is 3.2 at the wavelength λ = 3 μm. It appears that the error caused by using room-temperature optical constants for SrTiO₂ and YBa₂Cu₃O₆ could be substantial. There is a need for high-temperature optical constants of these crystals.

The radiative properties of stainless steel have a much weaker dependence on temperature than those of metal oxides. The normal total emissivity of stainless steel is 0.15 at 300 K and 0.19 at 700 K (Siegel and Howell, 1981). Since a change in temperature shifts the wavelength where the maximum of the spectral emissive power occurs, the total emissivity can change with temperature even for temperature-independent optical constants if they depend on wavelength. But the total emissivity change caused by this effect is small for stainless steel, and the optical constants of stainless steel are assumed to be temperature independent from 300 K to 1000 K.

For better thermal contact between the substrate and the substrate holder, a silver paste layer of about 100 μm thickness is used. This results in significant uncertainty of the substrate holder optical properties. Silver paste is composed of silver powder, acrylic resin, and butyl acetate, and its optical properties are not known. Moreover, the thickness of the paste is nonuniform. Therefore, the optical properties of stainless steel are used in the present study. Since SrTiO₃ is transparent for wavelengths λ < 4 μm, the substrate holder has an influence in this region. If the optical properties of silver are used, the reflectivity of the substrate holder-substrate-film composite is 0.97 at the wavelength λ = 3 μm and zero film thickness, compared to 0.70 if the stainless steel properties are used. Despite this substantial difference in the reflectivity with small film thickness, the general dependence of reflectance on the film thickness is the same.

4.3 Emittance. Figure 4 shows the calculated normal emittances of the substrate holder-substrate-film composite and heat shield-film composite as a function of YBa₂Cu₃O₆

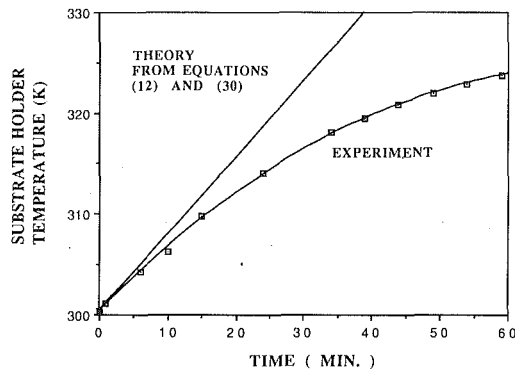


Fig. 5 Temperature rise of the substrate holder due to the plasma effects

film thickness. The film deposited on the heat shield is amorphous and its optical properties are not equal to those of the crystalline films. Since the optical properties of amorphous $\text{YBa}_2\text{Cu}_3\text{O}_6$ films are not available at present, they are assumed to be the same as the crystalline film properties. The variation of ϵ with d_F is due to both interference and absorption effects. The penetration depth in $\text{YBa}_2\text{Cu}_3\text{O}_6$ is about $0.5 \mu\text{m}$ at a wavelength of $3 \mu\text{m}$, yielding a transparent film during growth. As the real part of the refractive index of the $\text{YBa}_2\text{Cu}_3\text{O}_6$ film is close to that of the substrate at wavelengths around $3 \mu\text{m}$, the emittance of the film on the substrate does not change very strongly with the film thickness. However, the film on the heat shield shows a dramatic change of the emittance.

5 Experiments

The temperature measurements for this study are performed in the single-target magnetron sputtering system shown in Fig. 1. The target is a polycrystalline disk of $\text{YBa}_2\text{Cu}_3\text{O}_{7-\delta}$, 76.2 mm in diameter and 4.8 mm thick. The magnetron source is a US-gun modified to operate at high pressure. The RF power is 125 W at 13.56 MHz.

The heater uses a quartz halogen lamp enclosed by a water-cooled copper reflector. The substrate holder is a 57-mm-dia SS316 disk roughened and oxidized on the side facing the lamp and polished on the substrate side. A 0.5 mm SS316 heat shield, gold-plated on the side facing the holder, is used to minimize radiation losses. The heat shield has a rectangular hole slightly larger than the substrate to accommodate the substrate. The heat shield is separated from the substrate holder by stainless steel washers.

A $1.27 \times 2.54 \text{ cm}^2$ SrTiO_3 substrate is attached to the substrate holder using silver paste. Although this method is widely used in thin-film work, the thermal resistance of the bond is unknown and in this work the substrate temperature was measured using a novel technique. A $25.4 \mu\text{m}$ Platinel II pair of thermocouple wires is bonded ultrasonically to a $1\text{-}\mu\text{m}$ -thick, 1-mm-dia thin-film gold dot, evaporated on the substrate (Westerheim et al., 1991b). These wires are very fragile and $127 \mu\text{m}$ chromel-alumel extension wires are used to connect them to a feedthrough in the vacuum system walls. An alumina block thermally anchored to the heat shield is used to connect the thermocouple wires. The temperature of this block is measured by another chromel-alumel thermocouple. This is necessary to compensate for the electromotive force difference between the Platinel II and chromel-alumel thermocouples.

To minimize RF interference, all thermocouple wire pairs are kept parallel and close together using double-bored-alumina beads. RF filters with 60 dB RF suppression were used to decrease RF interference further. The temperature of the copper shroud at the point facing the target is 351 K and that at the point facing the substrate is 348 K. Both temperatures change less than 1 K during deposition. Before the film dep-

osition starts, the substrate was maintained at a temperature of 992 K by the heater. Thermocouple readings were recorded every minute during the 7 hour deposition process.

The gold film might disturb the original temperature field in the substrate, because gold has a low emittance. If the surface of the substrate covered by the gold film is assumed to be adiabatic, the heat flux entering the substrate under the gold dot must be diverted laterally. The diversion of the heat flux is assumed to affect the temperature of the substrate surface within a distance D_g from the center of the gold dot, where D_g is the diameter of the gold dot. The maximum temperature difference between the gold film and the undisturbed substrate surface, ΔT_{max} , can be estimated by

$$q_S \frac{\pi D_g^2}{4} = (\pi D_g d_S) k_S \frac{\Delta T_{\text{max}}}{D_g} \quad (29)$$

where k_S is the thermal conductivity of the substrate. Touloukian et al. (1970) reported the thermal conductivity of SrTiO_3 at 808.2 K as $4.73 \text{ W m}^{-1} \text{ K}^{-1}$. With $q_S = 4 \times 10^4 \text{ W m}^{-2}$, the maximum temperature difference is $\Delta T_{\text{max}} \sim 1.8 \text{ K}$.

To measure the heat flow incident onto the substrate due to all of the mechanisms discussed in section 2, a separate experiment is performed. The temperature of the substrate holder is measured as a function of time. For this experiment the heat shield is not installed and the heater is off. Under these conditions, the heat flow Q_p is calculated using the equation

$$Q_p = Mc_p \frac{dT}{dt} \quad (30)$$

where M denotes the mass of the substrate holder. This equation does not account for the heat flux from the substrate holder by radiation and is only valid for low temperatures. The rate of temperature decrease due to conduction loss through the supports of the substrate holder was observed experimentally to be extremely slow. From this observation, the conduction loss is believed to be negligible.

The heat flow from the heater, Q , is obtained in a similar way. Equation (30) and the measured rate of temperature rise give the heat flow when the holder is at room temperature. The radiative heat flow from the substrate holder to the copper reflector must be subtracted in order to find the net heat flow at the operating temperature. The total hemispherical emissivity of copper at room temperature changes from 0.04 to 0.09 depending on the surface conditions (Touloukian and Ho, 1970). The mean value of 0.07 is used and the heat flow from the heater, Q , is found to be 18.9 W. This value is only 10 percent of the electric power to the heater, 184 W.

6 Comparison of Theory and Experiment

Figure 5 shows the temperature rise for the substrate holder when the plasma is turned on and the heater is off. Since the radiation heat flux can be neglected at low temperatures, initially the holder temperature increases linearly with time. As the temperature increases, the radiation heat flow from the holder becomes significant and the temperature increases nonlinearly. Therefore Eq. (30) can be used only at the initial stage of the temperature rise. From Eq. (30) and the curve in Fig. 5, Q_p is 0.44–0.47 W. This value is quite close to the result obtained from Eq. (12) (0.51 W), and can be neglected compared to the heat flow from the heater (18.9 W). Due to the off-axis geometry, Q_p is small compared to the heat flow from the heater.

As the film emittance depends significantly on the optical properties of the film and those of the material beneath the film, the emittances of the films deposited on the substrate and the heat shield are quite different, as shown in Fig. 4. The emittance of $\text{YBa}_2\text{Cu}_3\text{O}_6$ deposited on the substrate changes much less with film thickness than that of the film on the heat shield. The total heat flow from the heater, Q , flows in part

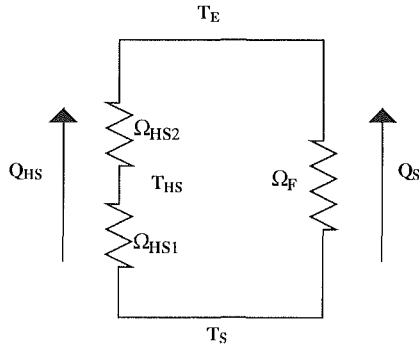
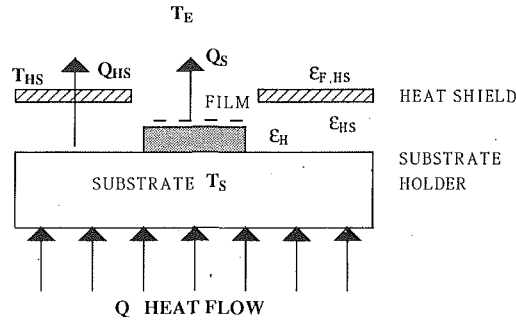


Fig. 6 Heat flow paths through the film and the heat shield

through the film, Q_S , and in part through the heat shield, Q_{HS} , $Q = Q_S + Q_{HS}$. Because the surface emittance of the heat shield increases significantly with film thickness, more heat flows through the heat shield as the film grows. With a constant heat flow from the heater, the power delivered to the substrate decreases with increasing film thickness. Referring to Fig. 6, the heat flow through the substrate is calculated as

$$Q_S = \frac{\Omega_{HS1} + \Omega_{HS2}}{\Omega_{HS1} + \Omega_{HS2} + \Omega_F} Q \quad (31)$$

where Ω is the thermal resistance for each flow path. Since the conduction resistances of the heat shield and substrate are much smaller than the radiative resistances, only the radiative resistances are considered. The resistance across the heat shield is composed of two resistances in serial connection: the resistance between the substrate holder and heat shield, Ω_{HS1} , and the resistance between the heat shield and the enclosure, Ω_{HS2} . The magnitude of the resistance between the heat shield and the enclosure, Ω_{HS2} , changes with the film thickness due to variation of the shield emittance as shown in Fig. 4. The thermal resistances are calculated as

$$\Omega_F = \frac{1}{\epsilon_F \sigma (T_S^2 + T_E^2) (T_S + T_E) A_S} \quad (32)$$

$$\Omega_{HS1} = \frac{\frac{1}{\epsilon_H} + \frac{1}{\epsilon_{HS}} - 1}{\sigma (T_H^2 + T_{HS}^2) (T_H + T_{HS}) A_{HS}} \quad (33)$$

$$\Omega_{HS2} = \frac{1}{\epsilon_{FHS} \sigma (T_{HS}^2 + T_E^2) (T_{HS} + T_E) A_{HS}} \quad (34)$$

where ϵ_F and ϵ_{FHS} are the emissivities of the substrate and the heat shield surface facing the enclosure, respectively.

Depending on the thermal coupling between the substrate and the substrate holder, the thermal contact resistance can be large and result in a temperature drop of up to 150 K (Inam et al., 1988). Since the temperature difference between the substrate and the substrate holder is less than 9 K in the present system, Eq. (32) neglects the thermal contact resistance of the substrate holder-substrate interface. The heat shield temper-

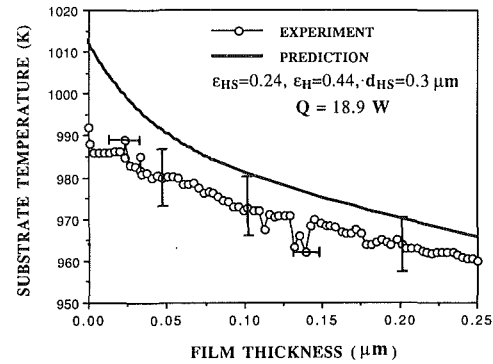


Fig. 7 Comparison of the experimental data with predicted results

ature, T_{HS} , is monitored during film deposition and remains within ± 5 K of 540 K. Since the substrate holder temperature, T_H , is only 9 K higher than the substrate temperature, T_S , it is set equal to T_S in the calculation.

The emissivities of the holder, ϵ_H , and the heat shield surface facing the holder, ϵ_{HS} , are measured at room temperature with a Digilab FTS-60A Fourier-transform infrared spectrometer. These values are found to be $\epsilon_H = 0.44$ and $\epsilon_{HS} = 0.24$. From the Hagen-Rubens result, the emissivity of metals increases linearly with temperature. However, the variation for both gold and stainless steel is small at temperatures from 300 K to 1000 K (Siegel and Howell, 1981). Polished gold has a constant emissivity of 0.02 at temperatures from 300 K to 1400 K. The emissivity of stainless steel has a weak dependence on temperature for both polished and oxidized surfaces. Since the substrate bonding procedure requires the holder to be heated up to 520°C in air, the surface oxidizes. The emissivity of oxidized and sand-blasted stainless steel is 0.85 at temperatures from 300 K to 700 K.

Equations (31)–(34) describe the heat flow through the substrate and the heat shield for the same temperature difference $T_S - T_E$. The substrate temperature decrease is caused by the heat flow redistribution between the substrate and the remaining substrate holder area during the deposition process. For given total heat flow, Q , an iterative procedure is required to calculate T_S with Eq. (11) because ϵ_S and Ω_F are also dependent on T_S through Eqs. (25) and (32), respectively.

The predicted substrate temperature during the deposition process is compared with experimental data in Fig. 7. The total heat flow is constant at 18.9 W and the emissivities of the surfaces where the film is not deposited are assumed to be constant as indicated in the figure. This temperature measurement is the first in-situ measurement of the substrate temperature during high- T_c superconductor film deposition. The measured data are estimated to be accurate within ± 7 K. The film thickness is measured after deposition by a profilometer with an accuracy of 0.01 μm . Assuming the deposition rate is constant, the film thickness is calculated from the total thickness and the elapsed time after starting the deposition. Since the same heat shield was used in a previous run, a film is already deposited on the surface facing the target. Its thickness, d_{HS} , is estimated to be 0.3 μm . This initial film thickness is incorporated in the prediction.

Figure 7 shows that if the film thickness is larger than 0.025 μm , the predicted results are consistently higher than those of the experiment by about 8 K. In this region, the experimental data confirm very well the temperature decrease predicted by the theory. The constant temperature shift is believed to be caused by an overestimation of the heat flow into the substrate holder and by the use of room-temperature optical constants. For film thicknesses below 0.025 μm , the data do not follow the theory. Incipient films form islands and coalesce at a certain point during deposition (Norton et al.,

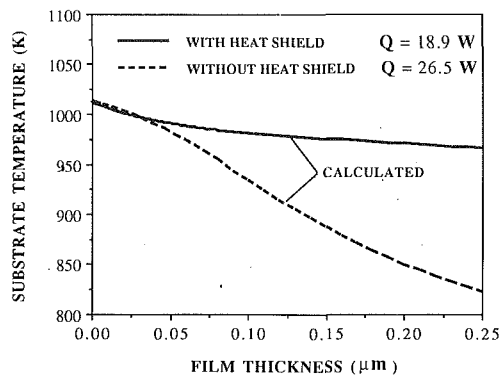


Fig. 8 Comparison of the calculated substrate temperature with heat shield and without heat shield

1989). It is not appropriate to describe an incipient film by a smooth, continuous film on which thin-film optics is based.

The parameters yielding the greatest uncertainty in the prediction of the substrate temperature are the high-temperature optical properties and the heat flow into the substrate holder, Q . The high-temperature optical constants of the film and the substrate are calculated from Eq. (28) and those of the stainless-steel substrate holder are assumed to be temperature independent. If the high-temperature optical constants are used for the prediction, the predicted substrate temperature becomes higher by 130 K at zero film thickness and the substrate temperature drops 20 K when the film is 0.25 μm thick. To estimate the error in the heat flow due to uncertainty in the emissivity of copper, the heat flow is calculated using copper emissivities of 0.04 and 0.09, resulting in heat flows of 14.2 W and 27.2 W, respectively. The greater heat flow increases the predicted temperature of Fig. 7 by 95 K and the smaller heat flow decreases the temperature by 70 K. Although the uncertainties in the high-temperature optical properties and the heat flow can change the predicted substrate temperature, the mechanism of the substrate temperature drop due to the emittance change resulting from the film growth remains the same.

The substrate temperature is calculated for the case without a heat shield to illustrate the effectiveness of a heat shield. The heat flow Q is calculated theoretically as the value that gives the same initial temperature of the substrate as in the case with a heat shield. Figure 8 shows that without a heat shield the substrate temperature decreases dramatically with film thickness. The heat shield is very effective in reducing the variation of the substrate temperature. In the current system, the substrate cannot be heated to 1000 K without a heat shield because of a limit on the heater power.

7 Concluding Remarks

This work presents the basic mechanisms for substrate temperature change during high- T_c superconducting film deposition. The film emittance changes during film growth due to both interference and absorption effects. In the single-target sputtering system investigated in the present study, the decrease of the substrate temperature is also caused by heat flow redistribution between the substrate and the remaining substrate holder area.

There are two ways to keep the film temperature constant. One is to use highly reflective materials for the heat shield. In this case the temperature change is induced by the emittance change of the film on the substrate itself. The temperature change due to this mechanism is 10 K for 0.25 μm film growth and 25 K for 1 μm film growth. The other method is to reduce the emittance change of the heat shield by depositing film material on it beforehand. Both of these methods are based on reducing the heat flux redistribution between the substrate and the heat shield. Since the dependence of the substrate

temperature on the film thickness can be determined with the methods presented in this study, it is now possible to control the substrate temperature more effectively by adjusting the heater power.

A noncontact temperature measurement technique such as pyrometry appears to be promising for measuring the substrate temperature, but has to account for the emittance change. If a reliable technique is developed, then a feedback control system can maintain the substrate temperature at the optimum level by adjusting the heater power.

The present study also raises fundamental research problems. It is assumed that the film is coherent even for a very small film thickness and that such a very thin film can be described by the optical constants determined from much thicker samples. But it is known from semiconductor processing that incipient films form islands and coalesce at a certain point during deposition. Therefore, it is necessary to measure the emittance of a film-substrate-substrate holder composite for varying film thickness. It is also assumed that the growing film is perfectly smooth. Quantitative studies of film topography are needed. A quantitative study is also needed for the hemispherical emittance of the optically anisotropic film. The exact oxygen stoichiometry of the growing film must be determined and the Y-Ba-Cu-O superconductor optical properties should be measured for a continuous variation of the oxygen content from the tetragonal ($\text{YBa}_2\text{Cu}_3\text{O}_6$) to the orthorhombic phase ($\text{YBa}_2\text{Cu}_3\text{O}_7$).

Acknowledgments

M.I.F. acknowledges the support of the Lynde and Harry Bradley Foundation through a Career Development Chair. The authors benefited from discussions with Professor E. G. Cravalho and Dr. D. A. Rudman, Dr. R. L. Sandstrom, D. K. Chin, and Dr. P. E. Phelan. The technical assistance of J. M. King is acknowledged. This work was conducted under the auspices of the Consortium for Superconducting Electronics with support from the Defense Advanced Research Projects Agency, contract No. MDA972-90-C-0021.

References

- Bird, R. B., Stewart, W. E., and Lightfoot, E. N., 1960, *Transport Phenomena*, Wiley, New York, p. 258.
- Bohren, C. F., and Huffman, D. R., 1983, *Absorption and Scattering of Light by Small Particles*, Wiley, New York, p. 38.
- Born, M., and Wolf, E., 1980, *Principles of Optics*, 6th ed., Pergamon Press, Oxford, United Kingdom, pp. 627-632.
- Chapman, B., 1980, *Glow Discharge Processes*, Wiley, New York, p. 30.
- Class, W., and Hieronymi, R., 1982, "The Measurement and Sources of Substrate Heat Flux Encountered With Magnetron Sputtering," *Solid State Technology*, Vol. 25, No. 12, pp. 55-61.
- Crawford, M. F., Welsh, H. L., and Locke, J. L., 1949, "Infra-red Absorption of Oxygen and Nitrogen Induced by Intermolecular Forces," *Phys. Rev.*, Vol. 75, p. 1607.
- Cristophorou, L. G., 1971, *Atomic and Molecular Radiation Physics*, Wiley, New York, pp 33-35.
- Devienne, F. M., 1965, "Low Density Heat Transfer," *Advances in Heat Transfer*, Vol. 2, J. P. Hartnett and T. F. Irvine, Jr., eds., Academic Press, New York.
- Flik, M. I., and Tien, C. L., 1990, "Thermal Phenomena in High- T_c Thin-Film Superconductors," *Annual Review of Heat Transfer*, Vol. 3, C. L. Tien, ed., Hemisphere, Washington, DC, pp. 115-144.
- Herzberger, M., and Salzberg, C. D., 1962, "Refractive Indices of Infrared Optical Materials and Color Correction of Infrared Lenses," *J. Opt. Soc. Am.*, Vol. 52, pp. 420-427.
- Inam, A., Hegde, M. S., Wu, X. D., Venkatesan, T., England, P., Miceli, P. F., Chase, E. W., Chang, C. C., Tarascon, J. M., and Wachtman, J. B., 1988, "As-Deposited High T_c and J_c Superconducting Thin Films Made at Low Temperatures," *Appl. Phys. Lett.*, Vol. 53, pp. 908-910.
- Kays, W. M., and Crawford, M. E., 1980, *Convective Heat and Mass Transfer*, McGraw-Hill, New York, pp. 324-325.
- Kircher, J., Alouani, M., Garriga, M., Murugaraj, P., Maier, J., Thomsen, C., Cardona, M., Andersen, O. K., and Jepsen, O., 1989, "Anisotropy of the Dielectric Function in $\text{YBa}_2\text{Cu}_3\text{O}_6$," *Phys. Rev. B*, Vol. 40, pp. 7368-7371.
- Li, H. C., Linker, F., Ratzel, R., Smithy, R., and Geerk, J., 1988, "In-Situ Preparation of Y-Ba-Cu-O Superconducting Thin Films by Magnetron Sputtering," *Appl. Phys. Lett.*, Vol. 52, pp. 1098-1100.

- Linz, A., Jr., 1953, "Some Electrical Properties of Strontium Titanate," *Phys. Rev.*, Vol. 91, pp. 753-754.
- Murphy, D. W., Johnson, D. W., Jin, S., and Howard, R. E., 1988, "Processing Techniques for the 93 K Superconductor $\text{Ba}_2\text{YCu}_3\text{O}_7$," *Science*, Vol. 241, pp. 922-930.
- Nevis, B. E., and Tisone, T. C., 1974, "Low-Voltage Triode Sputtering and Backsputtering With Confined Plasma: Part IV. Heat Transfer Characteristics," *J. Vac. Sci. Technol.*, Vol. 11, pp. 1177-1185.
- Norton, M. G., Tietz, L. A., Summerfelt, S. R., and Carter, C. B., 1989, "Observation of the Early Stages of Growth of Superconducting Thin Films by Transmission Electron Microscopy," *Appl. Phys. Lett.*, Vol. 55, pp. 2348-2350.
- Ramesh, R., Inam, A., Hwang, D. M., Sands, T. D., Chang, C. C., and Hart, D. L., 1991, "Surface Roughness Problem in C-Axis Oriented Y-Ba-Cu-O Superconducting Thin Films," *Appl. Phys. Lett.*, Vol. 58, pp. 1557-1559.
- Rohsenow, W. M., and Choi, H., 1961, *Heat, Mass, and Momentum Transfer*, Prentice Hall, Englewood Cliffs, NJ, pp. 486-496.
- Sasovskaya, I. I., Noskov, M. M., and Men'shikov, A. Z., 1969, "Optical and X-Ray Spectra of the Alloy Fe-30% Ni in the F.C.C. and B.C.C. Structural States," *Phys. Metals Metall.*, Vol. 27, No. 2, pp. 272-279.
- Schlesinger, Z., Collins, R. T., Holtzberg, F., Feild, C., Koren, G., and Gupta, A., 1990, "Infrared Studies of the Superconducting Energy Gap and Normal-State Dynamics of the High- T_c Superconductor $\text{YBa}_2\text{Cu}_3\text{O}_7$," *Phys. Rev. B*, Vol. 41, pp. 11237-11259.
- Siegel, R., and Howell, J. R., 1981, *Thermal Radiation Heat Transfer*, 2nd ed., McGraw-Hill, New York, Chap. 5.
- Spitzer, W. G., Miller, R. C., Kleimann, D. A., and Howarth, L. E., 1962, "Far Infrared Dielectric Dispersion in BaTiO_3 , SrTiO_3 , and TiO_2 ," *Phys. Rev.*, Vol. 126, pp. 1710-1721.
- Thomsen, C., Cardona, M., Kress, W., Liu, R., Genzel, L., Bauer, M., Schönherr, E., and Schröder, U., 1988, "Raman and Infrared Studies of the Oxygen Deficient Semiconducting Phase of the Superconducting Cuprate Perovskites," *Solid State Comm.*, Vol. 65, pp. 1139-1144.
- Thornton, J. A., 1978, "Substrate Heating in Cylindrical Magnetron Sputtering Sources," *Thin Solid Films*, Vol. 54, pp. 23-31.
- Thornton, J. A., and Lamb, J. L., 1984, "Substrate Heating Rates for Planar and Cylindrical-Post Magnetron Sputtering Sources," *Thin Solid Films*, Vol. 119, pp. 87-95.
- Touloukian, Y. S., and Ho, C. Y., 1970, *Thermophysical Properties of Matter*, Vol. 7, IFI/Plenum, New York, p. 137.
- Touloukian, Y. S., Powell, R. W., Ho, C. Y., and Klemens, P. G., 1970, *Thermophysical Properties of Matter*, Vol. 2, IFI/Plenum, New York, pp. 303-306.
- Touloukian, Y. S., and De Witt, D. P., 1972, *Thermophysical Properties of Matter*, Vol. 8, IFI/Plenum, New York, pp. 142, 291, 526.
- Van Duzer, T., 1988, "Superconductor-Semiconductor Hybrid Devices, Circuits and Systems," *Cryogenics*, Vol. 28, pp. 527-531.
- Vassenden, F., Linker, G., and Geerk, J., 1991, "Growth Direction Control in YBCO Thin Films," *Physica C*, Vol. 175, pp. 566-572.
- Vossen, J. L., and Kern, W., 1978, *Thin Film Processes*, Academic Press, Orlando, FL, Part II.
- Westerheim, A. C., Yu-Jahnes, L. S., and Anderson, A. C., 1991a, "Off-Axis Magnetron Sputtering of YBCO Films: the Influence of Atomic Oxygen," *IEEE Transactions on Magnetics*, Vol. 27, pp. 1001-1005.
- Westerheim, A. C., Anderson, A. C., and Cima, M. J., 1991b, "Substrate Temperature Measurements Using Ultrasonically Bonded Platine II Thermocouples," submitted to *Rev. Sci. Inst.*

Thermal Analysis of Electron-Beam Absorption in Low-Temperature Superconducting Films

M. I. Flik

Assistant Professor.
Mem. ASME

K. E. Goodson

Research Assistant.
Student Mem. ASME

Department of Mechanical Engineering,
Massachusetts Institute of Technology,
Cambridge, MA 02139

The absorption of an electron beam in a superconducting microbridge reduces its critical current, the maximum d-c electric current it can carry without resistance. A two-dimensional heat conduction analysis determines numerically the temperature field in the film caused by electron-beam heating, considering the nonlinear thermal boundary resistance between film and substrate. The method of Intrinsic Thermal Stability yields the critical current for this temperature field. The critical current predictions agree with experimental data from low-temperature scanning electron microscopy (LTSEM) with superconducting lead microbridges. The method developed in this study permits the quantitative prediction of LTSEM experiments, enhancing the value of this technique for the local characterization of superconducting films.

Introduction

Low temperature scanning electron microscopy (LTSEM) is a high-resolution technique for determining the spatial variation of properties in a sample at low temperatures (Huebener, 1988). A highly focused electron beam is scanned across the surface of the sample while a response signal is recorded simultaneously. The spatially dependent response provides information about sample properties such as chemical microstructure or surface inhomogeneity. One of the most useful applications of LTSEM is the characterization of superconducting films. The critical current of a superconducting microbridge is the maximum dc electric current it can carry without resistance. The absorption of the electron beam results in a temperature field that decreases the critical current of the microbridge. If a bias current is maintained in the microbridge that exceeds the reduced critical current, a voltage signal is measured along the microbridge.

In the past, LTSEM was applied to superconducting films in a qualitative manner. There is a need for a quantitative prediction of the critical current reduction resulting from the electron-beam absorption. Thermal analysis provides the theory to interpret LTSEM results quantitatively and determines the spatial extent of the temperature field that governs the resolution of LTSEM. The thermal interaction between superconducting devices, such as Josephson junctions, and semiconducting devices dictates a packing limit for the design of hybrid electronic circuitry (Flik and Hijikata, 1990). The experimental technique of LTSEM can be coupled with thermal analysis to investigate this limit. In the case of electron-beam pulses shorter than the time required to achieve thermal equilibrium, the comparison of thermal analysis with experimental data can assess the possibility of a nonequilibrium voltage response. Flik et al. (1990) applied this method to the case of laser-pulse absorption in high-temperature superconducting films.

Skocpol et al. (1974) studied the effect of Joule heating on current-voltage curves along a superconducting microbridge using a one-dimensional thermal model. Clem and Huebener (1980) determined the temperature field in a low-temperature superconducting microbridge resulting from the absorption of an LTSEM electron beam considering the finite width of the microbridge. Pavlicek et al. (1984) investigated the effect of

modulating the beam power on the spatial resolution of the LTSEM technique using a one-dimensional thermal model. Flik and Tien (1990b) applied the criterion of Intrinsic Thermal Stability (Flik and Tien, 1990a) to the LTSEM experimental data of Stoehr et al. (1978) assuming an approximate point-symmetric temperature field.

This study predicts the temperature field and the reduced critical current in a superconducting microbridge resulting from electron-beam absorption. All of the aforementioned studies assumed a temperature-independent film thermal conductivity and a linear dependence of the heat flux from the film into the substrate on the film temperature. This work is the first thermal analysis of the absorption of an electron beam in a superconducting microbridge to investigate the importance of the variable thermal conductivity of the film, the nonlinear dependence of the heat flux between the film and substrate on the film temperature, and the influence of the beam-focus location. The theory of Intrinsic Thermal Stability is modified to account for the nonuniform distribution of the critical current in the microbridge cross section due to magnetic self-field effects. The critical current predictions are compared to experimental data of Stoehr et al. (1978) for a superconducting lead microbridge at 4.2 K on a sapphire substrate.

Electron-Beam Heat Source

Oatley (1972) and Wells (1974) gave summaries of the theory for the absorption of an electron beam in matter. Gross and Koyanagi (1985) showed that the spatial structure of the perturbation state of a lead superconducting film resulting from the absorption of an electron beam can be determined using the heat conduction equation. This section develops the distribution of heating power in the film used to model the absorption of the electron beam.

In electron-stopping theory applied to planar films, the electron fractional transmission $\eta(z)$ is the fraction of electrons incident on the surface of the film that pass through the plane parallel to the film surface at a depth z into the film. The electron mean energy $E_m(z)$ is the average energy of electrons transmitted through this plane. The electron mean range z_e is the depth into the film at which the quantity $E_m(z)$ is reduced to a value negligible compared to the electron initial energy, E_0 . The mean energy, mean range, and fractional transmission of electrons with initial energies E_0 from 5 to 20 keV were measured by Cosslett and Thomas (1964a, 1964b) for aluminum, copper, silver, and gold films. The product of mass

Contributed by the Heat Transfer Division and presented at the 3rd ASME/JSME Joint Thermal Engineering Conference, Reno, Nevada, March 17-22, 1991. Manuscript received by the Heat Transfer Division January 3, 1991; revision received June 30, 1991. Keywords: Conduction, Cryogenics, Radiation Interactions.

density and electron mean range, ρz_e , varies slowly with atomic number Z for constant E_0 (Oatley, 1972). In the present analysis, the mean range of electrons in lead ($Z=82$) is determined using the correlation provided by Cosslett and Thomas (1964b) for gold films ($Z=79$):

$$\rho z_e = 1.1 \times 10^{-4} E_0^{3/2}, \quad (1)$$

where E_0 is in keV and ρz_e is in kg m^{-2} . This correlation is assumed to be accurate for the initial energies of $E_0=2, 3, 5, 10, 20,$ and 30 keV used by Stoehr et al. (1978). Their microbridges were $1.1 \mu\text{m}$ in thickness. Using $11,340 \text{ kg m}^{-3}$ for the density of lead, Eq. (1) yields electron mean ranges less than the film thickness for each value of E_0 except 30 keV, for which the electron mean range is $1.6 \mu\text{m}$. For electron initial energies E_0 between 2 and 20 keV, the entire electron beam energy is absorbed within the film.

In the case of electrons with 30 keV initial energy, a portion of the electron-beam power is deposited in the substrate. The ratio of the electron-beam power absorbed within the substrate P_s to the total electron-beam power P for a film of thickness d is

$$\frac{P_s}{P} = \frac{E_m(z=d)}{E_0} \eta(z=d). \quad (2)$$

Cosslett and Thomas (1964a) correlated the electron fractional transmission to experimental data for values of E_0 from 15 to 25 keV, $\eta(z) = \exp(-19,000 \rho z Z^{1/2}/E_0^2)$, where E_0 is in keV, and ρz is in kg m^{-2} . Cosslett and Thomas (1964b) showed that the electron mean energy at a depth z into the film satisfies $E_m(z) = E_0 (1 - z/z_e)^{1/2}$. Using these relations with $z=d=1.1 \mu\text{m}$ and $z_e=1.6 \mu\text{m}$ for 30 keV electrons and evaluating Eq. (2) yields $P_s=0.05 P$. This fraction is neglected in the present analysis, allowing the use of a heat source entirely contained in the film to model the absorption of the electron-beam energy in the experiments of Stoehr et al. (1978).

The experiments of Stoehr et al. (1978) involved electron mean ranges that varied from $0.03 \mu\text{m}$ to $1.6 \mu\text{m}$ when calculated using Eq. (1). This indicates that the spatial extent of the heated volume was highly dependent on E_0 . These experiments and later work (Stoehr and Huebener, 1979) showed that the variation of E_0 has a negligible effect on the critical current. This suggests that the points in the microbridge with a temperature dependent on E_0 were confined to a region with dimensions small compared to the microbridge width. This is confirmed in the present analysis by the comparison of temperature profiles in the microbridge determined using heat sources of varying size. In each case the maximum electron beam power in the experiments of Stoehr et al. (1978), $P=3 \text{ mW}$, is uniformly distributed in a cylinder bounded by

the top and bottom surfaces of the film. Cylinders with radii equal to the mean ranges of 2 keV and 30 keV electrons in lead are used for comparison. The variation by more than 2 percent in temperature between the two analyses is confined to a radius around the beam focus of $1.6 \mu\text{m}$. This dimension is small compared to the microbridge width of $100 \mu\text{m}$ in the experiments of Stoehr et al. (1978). In the present analysis, the beam power is assumed to be deposited uniformly in the film within a cylinder of radius $0.87 \mu\text{m}$, which is the mean range of 20 keV electrons. Depending on the value of E_0 , the actual film temperature within a radius of $1.6 \mu\text{m}$ of the beam focus in the experiments of Stoehr et al. (1978) may have differed significantly from the temperature predicted in the present analysis. This error is not important for the calculation of the critical current because for all but the lowest beam powers it occurs at temperatures greater than the critical temperature of lead, $T_c=7.2 \text{ K}$, the superconducting transition temperature. Regions of the film with temperature greater than 7.2 K do not contribute to the critical current of the film.

Film-Substrate Thermal Boundary Resistance

At low temperatures, the major obstacle to the flow of heat out of the film is the thermal boundary resistance between the film and substrate. Anderson (1981) reviewed the previous work on the low-temperature solid-solid thermal boundary resistance problem. Little (1959) developed the acoustic mismatch theory to predict the finite temperature drop measured at the interface of two solids at low temperatures. Acoustic mismatch theory predicts the rate of phonon transmission between two solids that have isotropic speeds of sound and share a smooth interface at which displacement and stress are continuous. Each solid is modeled as a Debye gas with phonons characteristic of a distinct temperature incident on the interface. If the temperature of each solid is much lower than its Debye temperature, Little (1959) found that the phonon heat flux q'' is

$$q'' = \kappa(T^4 - T_0^4) \quad (3)$$

where T and T_0 are the temperatures of the two solids and κ is a constant calculated from the velocities of longitudinal and transverse phonons in both solids and their mass densities (Anderson, 1981). Cheeke et al. (1976) tabulated parameters required for the calculation of κ for most interfaces. Acoustic mismatch theory is appropriate for the case of a metal film on a dielectric substrate because phonon transmission is the dominant mode of heat transfer. The value of κ used in the present analysis for the lead-sapphire interface, $\kappa=73 \text{ W m}^{-2}\text{K}^{-4}$, was calculated by Cheeke et al. (1973) using

Nomenclature

A = area of film cross section, m^2	k_{eff} = effective thermal conductivity along film, $\text{W m}^{-1}\text{K}^{-1}$	
c = average sound velocity, m s^{-1}	k_B = Boltzmann constant = $1.38062 \times 10^{-23} \text{ J K}^{-1}$	v_e = Fermi velocity, m s^{-1}
d = film thickness, m	m = electron rest mass = $9.10956 \times 10^{-31} \text{ kg}$	w = microbridge half-width, m
E_0 = initial electron energy, keV	P = electron-beam power, W	x = coordinate across microbridge width, m
E_m = mean energy of transmitted electrons, keV	P_s = electron-beam power absorbed in substrate, W	x_f = beam focus location, m
h = heat transfer coefficient, $\text{W m}^{-2}\text{K}^{-1}$	q'' = heat flux from film to substrate, W m^{-2}	y = coordinate along microbridge, parallel to current flow, m
h_P = Planck's constant = $6.62620 \times 10^{-34} \text{ J s}$	r = distance from beam focus, m	Z = atomic number
I_c = microbridge critical current, A	r_e = radius of cylinder directly heated by electron beam, m	z = coordinate normal to film, m
I_{c0} = microbridge critical current at temperature T_0 , A	T = film temperature, K	z_e = electron mean range, m
J_c = local microbridge critical current density, A m^{-2}	T_0 = bath temperature, K	η = fraction of electrons transmitted
k = thermal conductivity, $\text{W m}^{-1}\text{K}^{-1}$	T_c = superconducting film critical temperature, K	K_0 = modified Bessel function of the second kind of order zero
		κ = constant, Eq. (3), $\text{W m}^{-2}\text{K}^{-4}$
		ρ = mass density, kg m^{-3}

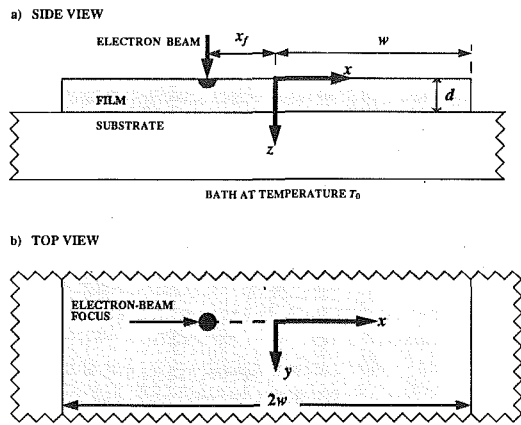


Fig. 1 Schematic of the absorption of an electron beam in a superconducting microbridge: (a) side view; (b) top view

a value of the Poisson ratio of 0.33 in both materials. Although Swartz and Pohl (1989) calculated $\kappa = 133 \text{ W m}^{-2}\text{K}^{-4}$ for a lead-sapphire interface using the actual Poisson ratios of the materials, the heat flux calculated using $\kappa = 73 \text{ W m}^{-2}\text{K}^{-4}$ is in better agreement with the experimental data of Cheeke et al. (1973) for lead films on sapphire.

The acoustic mismatch theory assumes that the interface between the two solids is smooth. This assumption is incorrect if the average phonon wavelength is comparable to or smaller than the characteristic dimension of roughness at the interface (Majumdar, 1991). At low temperatures the average phonon wavelength is of the order of $h_p c / k_B T$, where c is the speed of sound, h_p is Planck's constant, and k_B is the Boltzmann constant. This expression yields an average wavelength in lead at 4.2 K which is less than 3 percent of the thickness of the vapor-deposited films used by Stoehr et al. (1978), indicating that diffuse transmission might have affected the boundary resistance. The diffuse mismatch theory (Swartz and Pohl, 1989) predicts only a 6 percent increase in the thermal boundary resistance for lead-sapphire interfaces due to diffuse transmission compared to the value predicted by the acoustic mismatch theory. The effect of diffuse transmission on the accuracy of the acoustic mismatch theory is neglected in the present analysis.

Thermal Model and Numerical Analysis

Figure 1 illustrates the absorption of an electron beam in a thin-film microbridge of thickness d , 0.1 to 2 μm , and width $2w$, 10 to 500 μm , which has been deposited on a dielectric substrate. The bottom of the substrate is in contact with flowing liquid helium or nitrogen at the temperature T_0 , and the top and the edges of the microbridge are exposed to a vacuum (Huebener, 1984). The electrons enter the microbridge at the focus of the electron beam that is 10 nm in diameter.

In the temperature range of the present analysis, 4.2 to 20 K, the thermal conductivity of the film material, lead, is highly dependent on temperature. Thermal conduction in metals is dominated by the motion of electrons and is limited by the scattering of electrons on defects and phonons. The rate of scattering of an electron on defects is independent of temperature and the rate of scattering of an electron on phonons increases with temperature. The thermal conductivity of a metallic superconductor such as lead is reduced in the superconducting state because superconducting electrons do not transport entropy. The thermal conductivity of superconducting lead is approximated by the following two polynomial functions fitted to experimental data given by Powell et al. (1966):

$$k(T) = 1352.7 - 407.57 T + 38.894 T^2, \quad (4)$$

$$4.2 \leq T < 7.2,$$

and

$$k(T) = 40244 T^{-2} - 3946.0 T^{-1} + 199.36 - 2.1698 T, \quad (5)$$

$$7.2 \leq T \leq 20,$$

where T is in K and k is in $\text{W m}^{-1}\text{K}^{-1}$.

If the mean free path of electrons in a metal film is of the order of or larger than the film thickness, the effective thermal conductivity along the film is less than that of a bulk sample. In a normal metal, the electron mean free path Λ is related to the thermal conductivity by (Kittel, 1986) $\Lambda = 3kmv_e / (\pi^2 k_B^2 n T)$, where v_e is the Fermi velocity of the electrons, m is the electron rest mass, and n is the electron number density. At 7.2 K, the properties of lead are $k = 412 \text{ W m}^{-1}\text{K}^{-1}$, $v_e = 0.50 \times 10^6 \text{ m s}^{-1}$, and $n = 1.3 \times 10^{29} \text{ m}^{-3}$, yielding $\Lambda = 0.32 \mu\text{m}$, which is of the order of the film thickness, 1.1 μm . For $\Lambda < d$, the effective conductivity along the film is approximately (Flik and Tien, 1990c) $k_{\text{eff}} = (1 - 2\Lambda / (3\pi d)) k$, yielding $k_{\text{eff}} = 0.94 k$ for the 1.1 μm film with $\Lambda = 0.32 \mu\text{m}$. This size effect is neglected in the present analysis because of its small estimated magnitude.

The scanning speed of an electron beam is typically 0.1 m s^{-1} (Huebener, 1984). Steady thermal analysis in the frame of reference of the moving electron beam has been shown to be appropriate for the experiments of Stoehr et al. (1978) by Flik and Tien (1990b) due to the large thermal diffusivity of lead at 4.2 K, 0.19 $\text{m}^2 \text{ s}^{-1}$, and the small scanning velocity. This approach is confirmed by consideration of the thermal relaxation time of 2 μs measured in pulsed electron beam experiments by Stoehr et al. (1978). The scanning beam traveled 0.2 μm in this time, which is small compared to the film thickness, $d = 1.1 \mu\text{m}$, the smallest dimension of the microbridge.

The top and sides of the microbridge are insulated by vacuum space and a radiation shield, yielding adiabatic boundary conditions at these surfaces. The energy from the electron beam travels through the film, across the film-substrate interface, through the substrate, and across the substrate-bath interface before it is absorbed by the flowing liquid helium. The thermal boundary resistance at the substrate-bath interface is neglected. Because of the nonlinear film-substrate boundary resistance and the variable thermal conductivity of both sapphire and lead at low temperatures, the relative importance of the remaining thermal resistances is highly dependent on temperature.

The substrate is modeled as isothermal at the bath temperature because of its low thermal resistance relative to the lead-sapphire boundary resistance. The error incurred by this assumption for a film temperature T is estimated by solving the steady, constant conductivity, two-dimensional heat equation in the substrate using separation of variables. The substrate is 1 mm thick (Stoehr et al., 1978) and 10 mm wide. The top of the slab is adiabatic except for the portion covered by the film, where the heat flux is approximated using Eq. (3) with T as the film temperature and T_0 as the bath temperature. The edges and bottom of the substrate are at the bath temperature. Using the minimum conductivity of sapphire between 4.2 K and 20 K, the largest temperature difference between the top and bottom surfaces of the substrate is found to be less than 10 percent of the total temperature difference between the film and the bath for film temperatures less than 20 K. For larger film temperatures the neglect of the thermal resistance of the substrate results in a significant underprediction of the film temperature.

Using Eq. (3), the temperature-dependent conductance h between the film and substrate is $h = \kappa(T^4 - T_0^4) / (T - T_0)$. Using this expression for h and Eqs. (4) and (5) for k , the Biot number $\text{Bi} = hd/k$ for conduction normal to the film is less than 0.01 for film temperatures less than 21 K. Therefore,

temperature gradients in the film in the z direction are neglected, resulting in a two-dimensional analysis of heat conduction in the film. The two-dimensional energy equations in the film are

$$\frac{\partial}{\partial x} \left(k \frac{\partial T}{\partial x} \right) + \frac{\partial}{\partial y} \left(k \frac{\partial T}{\partial y} \right) - \frac{\kappa}{d} (T^4 - T_0^4) + \frac{P}{\pi d (r_e)^2} = 0; \quad (6)$$

$$(x_f - x)^2 + y^2 \leq (r_e)^2$$

and

$$\frac{\partial}{\partial x} \left(k \frac{\partial T}{\partial x} \right) + \frac{\partial}{\partial y} \left(k \frac{\partial T}{\partial y} \right) - \frac{\kappa}{d} (T^4 - T_0^4) = 0; \quad (7)$$

$$(x_f - x)^2 + y^2 > (r_e)^2,$$

where r_e is the radius of a cylinder of uniform power absorption in the film centered around the line normal to the film surface through the point $(x = x_f, y = 0)$, which is set at the mean range of 20 keV electrons in lead, $r_e = 0.87 \mu\text{m}$. The boundary conditions are

$$\frac{\partial T}{\partial x} = 0 \text{ for } x = -w \text{ and } x = w \quad (8)$$

and

$$T \rightarrow T_0 \text{ for } y \rightarrow +\infty \text{ and } y \rightarrow -\infty. \quad (9)$$

The governing equations are solved numerically using the central difference technique described by Patankar (1980). The energy balance is verified globally in the microbridge and locally at each grid element by independent computational routines. The repeatability of the solution for different initial temperature distributions is verified. For the case of very narrow microbridges the numerical solution matches an independently computed solution of the one-dimensional heat transfer problem. If the film-substrate heat flux given by Eq. (3) is linearized to $q'' = 4\kappa T_0^3 (T - T_0)$, the computed solution for very wide microbridges approaches the point-symmetric closed-form solution of Flik and Tien (1990b),

$$T(r) = T_0 + \frac{P}{2\pi k d} K_0 \left[\frac{r}{\sqrt{k d / 4\kappa T_0^3}} \right], \quad (10)$$

where r is the distance from the beam focus and K_0 is the modified Bessel function of the second kind of order zero.

Microbridge Critical Current

The critical current of a microbridge decreases with increasing temperature and is reduced to zero at the critical temperature of the superconductor, T_c . Flik and Tien (1990a) computed the critical current of a microbridge in the presence of a temperature field. If J_c is the local critical current density at a point in the microbridge resulting from the temperature T at that point, the critical current of a cross section is

$$I_c = \int_A J_c dA, \quad (11)$$

where dA is an area element in the bridge cross section A normal to the direction of current flow. The critical current of the entire bridge is the minimum of the critical currents of all cross sections. Flik and Tien (1990b) determined the critical current of the microbridge by assuming a uniform distribution of critical current density in an isothermal bridge. This approach neglects the complex interaction of geometry and magnetic field in planar superconducting microbridges, which results in a nonuniform distribution of critical current density (Edwards and Newhouse, 1962). The present work considers the nonuniform distribution of critical current.

The dependence of J_c on temperature for a type-I superconducting film like lead deposited on a cylinder is (Newhouse, 1964)

$$\frac{J_c(T)}{J_c(T_0)} = \frac{\left[1 - \left(\frac{T}{T_c} \right)^2 \right]^{3/2} \left[1 + \left(\frac{T}{T_c} \right)^2 \right]^{1/2}}{\left[1 - \left(\frac{T_0}{T_c} \right)^2 \right]^{3/2} \left[1 + \left(\frac{T_0}{T_c} \right)^2 \right]^{1/2}}. \quad (12)$$

where $J_c(T_0)$ is the critical density of the film when it is isothermal at T_0 . Although Eq. (12) predicts the temperature dependence of the uniform critical current density of a film deposited on a microbridge, it is assumed in the present analysis to predict the temperature dependence of the local critical current density of a planar microbridge in terms of the local value of $J_c(T_0)$. The variation of $J_c(T_0)$ with x in a planar microbridge is determined using the relation of Newhouse (1964) for the supercurrent density $J(x)$ at a position x in the cross section of an isothermal microbridge,

$$J(x) = \frac{I}{2\pi d [w^2 - x^2]^{1/2}}, \quad (13)$$

where I is the bias current and w is the half-width of the microbridge. Equation (12) is valid for films of thickness much larger than London penetration depth. The London penetration depth characterizes the exponential decay of magnetic field strength from the edge of a superconductor into its interior in the case of an externally applied magnetic field. Equation (13) is valid for microbridges that are much wider than they are thick, yet have thickness much larger than London penetration depth. These criteria are satisfied by the lead microbridges used by Stoehr et al. (1978), which had a width $2w$ of $100 \mu\text{m}$, a thickness d of $1.1 \mu\text{m}$, and a London penetration depth of $0.051 \mu\text{m}$.

In the present analysis, the local critical current density at a point in the film is assumed to depend only on the x coordinate and the temperature at that point, $J_c = J_c(T, x)$. Equation (13), with I_{c0} substituted for I and $J_c(T_0, x)$ substituted for $J_c(x)$, is assumed to give the distribution of local critical current density in the bridge when it is isothermal at temperature T_0 . The critical current I_{c0} of the unirradiated microbridge, which was isothermal at the bath temperature, was measured to be $I_{c0} = 0.869 \text{ A}$ by Stoehr et al. (1978). Equation (12), with $J_c(T_0, x)$ substituted for $J_c(T_0)$ and $J_c(T, x)$ substituted for $J_c(T)$, is assumed to determine the local critical current density in the microbridge as a function of the local temperature T and the local critical current density at that point at the bath temperature. The effects of geometry and temperature on the local critical current density are assumed to be independent.

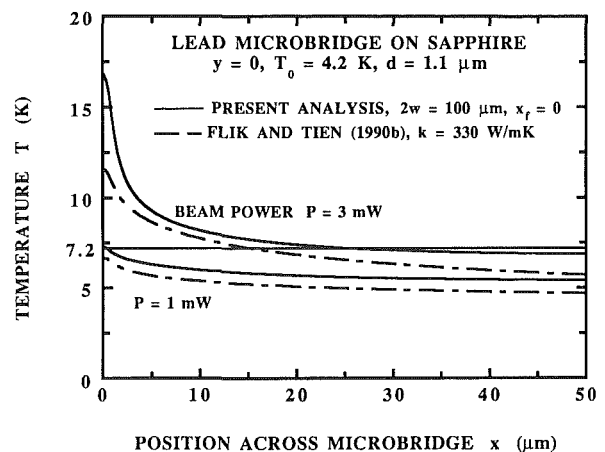


Fig. 2 Comparison of the present analysis with the closed-form solution of Flik and Tien (1990b)

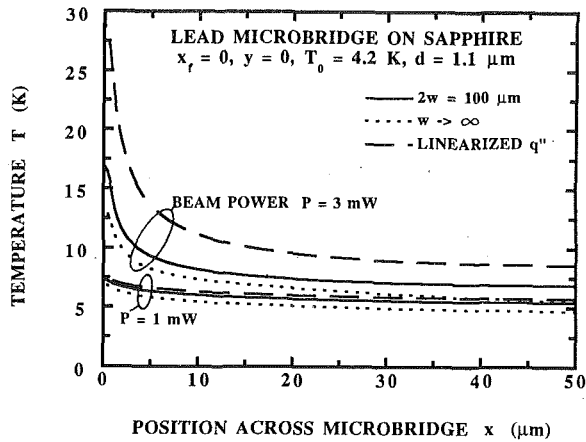


Fig. 3 Influence of the assumptions of infinite microbridge width and linearized film-substrate heat flux

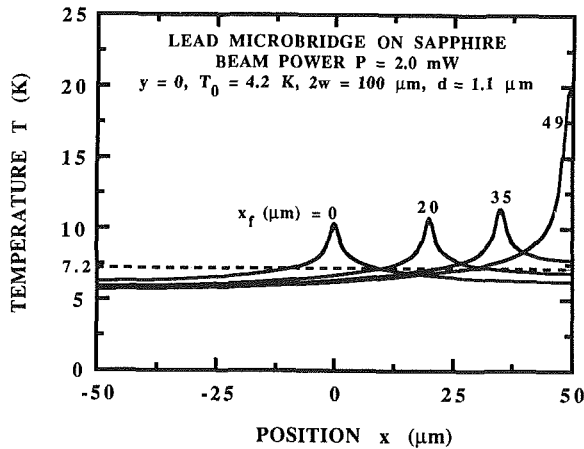


Fig. 4 Temperature profiles across the microbridge for different electron-beam focus locations

Equations (11), (12), and (13) are combined with the temperature-field solution from the thermal analysis, $T(P, x_f; x, y)$, to compute the critical current in each cross section of the microbridge. The critical current of cross section y during the absorption of an electron beam of power P , which is focused on the microbridge at the coordinates $(x = x_f, y = 0)$, is given by

$$I_c(P, x_f, y) = \int_{-w}^w \frac{I_{c0}}{2\pi[w^2 - x^2]^{1/2}} \times \frac{\left[1 - \left(\frac{T(P, x_f; x, y)}{T_c}\right)^2\right]^{3/2} \left[1 + \left(\frac{T(P, x_f; x, y)}{T_c}\right)^2\right]^{1/2}}{\left[1 - \left(\frac{T_0}{T_c}\right)^2\right]^{3/2} \left[1 + \left(\frac{T_0}{T_c}\right)^2\right]^{1/2}} dx. \quad (14)$$

Equation (14) assumes that, in the presence of the electron beam, the current in the film redistributes itself such that it makes the best use of the available current density distribution, which is different from that given by Eq. (13) due to the temperature field. A voltage along the bridge appears only if the bridge current exceeds I_c given by Eq. (14) for some y .

The temperature along lines of constant x peaks at the cross section directly under the beam focus, $y = 0$. This cross section limits the critical current of the entire bridge. For given bridge dimensions and film and substrate materials, the overall microbridge critical current I_c depends on the beam power P and beam focus location x_f . Stoehr et al. (1978) measured the crit-

ical current as a function of the power of the electron beam, which scanned the entire width of the microbridge. The present analysis shows that for different beam powers the maximum reduction of the microbridge critical current occurred at different locations of the beam focus. Equation (14) predicts the critical current in cross section y resulting from the absorption of a beam of power P at the beam focus location x_f . To predict the experimental results obtained using a scanning beam, it is necessary to determine the critical current in the cross section $y = 0$ for all beam focus locations at each beam power. The minimum value of I_c for all beam focus locations at each beam power predicts the critical current measured by Stoehr et al. (1978) at that beam power,

$$I_c(P) = \text{MIN}[I_c(P, x_f, y = 0)], \quad 0 \leq x_f \leq w. \quad (15)$$

Results and Discussion

The microbridge cross section whose critical current is most reduced by the electron beam is located at $y = 0$. Since temperature differences in the z direction in the film are neglected, temperature profiles in this cross section are presented in Figs. 2-4 with respect to the x coordinate only. Figure 2 compares temperature profiles obtained in the present analysis to those obtained using the theory of Flick and Tien (1990b), which was derived for a microbridge of infinite width with a temperature-independent thermal conductivity. In addition, the heat flux between the film and substrate was linearized to the form

$$q'' = 4\kappa T_0^3(T - T_0). \quad (16)$$

The thermal conductivity of lead at 4.2 K, $330 \text{ W m}^{-1} \text{ K}^{-1}$, and a heat absorption cylinder of radius $0.87 \mu\text{m}$ are used in evaluating the closed-form solution. The critical temperature of lead, $T_c = 7.2 \text{ K}$, is shown in Fig. 2 to indicate the importance of the error in temperature of the closed-form solution for the calculation of the critical current.

Since the closed-form solution applies to microbridges of infinite width it underpredicts the temperature field in a microbridge of finite width. The importance of this effect increases with an increase in the ratio of the film thermal healing length, $(kd/h)^{1/2}$, to the distance from the beam focus to the nearest microbridge edge. Using $330 \text{ W m}^{-1} \text{ K}^{-1}$ for k and $2.1 \times 10^4 \text{ W m}^{-2} \text{ K}^{-1}$ for h yields a linearized thermal healing length of $130 \mu\text{m}$, which is larger than the microbridge half-width of $50 \mu\text{m}$. The linearization of Eq. (3) given by Eq. (16) is appropriate only for film temperatures T such that $(T - T_0)/T_0 \ll 1$. If this condition is not satisfied, Eq. (16) underpredicts the flow of heat into the substrate.

The good performance of the closed-form solution results from two compensating assumptions, whose relative importance is shown in Fig. 3. The solid curves indicate the exact solution of the present analysis. The other curves indicate solutions of the present analysis either for bridges of infinite width or for microbridges with linearized heat flux. Both assumptions are justified at the beam power of 1 mW. At 3 mW the linearization is the worst simplification, resulting in an error in temperature of more than 50 percent at $x = 4.3 \mu\text{m}$. The error due to the heat flux linearization increases more rapidly with beam power than the error due to the infinite microbridge width assumption.

The effect of neglecting the temperature dependence of the thermal conductivity of lead is also investigated. If the thermal conductivity of lead is assumed to be constant at its value at 4.2 K, $330 \text{ W m}^{-1} \text{ K}^{-1}$, the temperature is underpredicted near the beam focus. This is because the film thermal conductivity given by Eqs. (4) and (5) is actually much lower than $330 \text{ W m}^{-1} \text{ K}^{-1}$ in the regions with higher temperature.

Figure 4 shows the effect of varying the beam focus location on the temperature profiles for a single beam power. The maximum temperature of the film and the spatial extent of

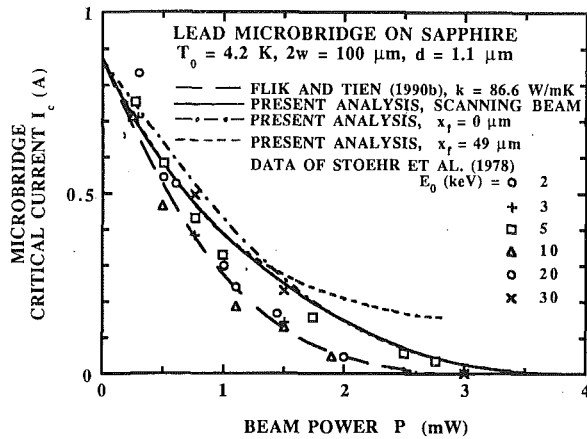


Fig. 5 Comparison of theory with experimental data for the dependence of the critical current on the beam power

the portion of the film with temperature above the critical temperature T_c are highly dependent on the beam focus location. While the maximum temperature increases as the beam focus location approaches the adiabatic edge of the microbridge, the width of the portion of the film above the critical temperature reaches a maximum for a beam focus location in the interior of the microbridge. The beam focus location has a strong influence on the microbridge critical current because the critical current density distribution in the bridge cross section given by Eq. (13) peaks at the bridge edges.

Figure 5 compares the present solution for the critical current as a function of the beam power to the closed-form solution of Flik and Tien (1990b) and to the experimental data of Stoehr et al. (1978). The closed-form solution of Flik and Tien (1990b) was calculated using a thermal conductivity of lead of $86.6 \text{ W m}^{-1} \text{ K}^{-1}$. The theory of Flik and Tien (1990b) is in agreement with the experimental data. This is due in part to the competing effects of the assumptions of linearized film-substrate heat flux and infinite microbridge width. This theory cannot be expected to predict other data as well, in particular for the cases of very narrow films and large values of $(T - T_0)/T_0$.

Stoehr et al. (1978) varied both the electron beam voltage and the electron beam current to control the beam power. The electron initial energy E_0 , which increases linearly with the beam voltage, is of negligible importance to the measured critical current. For low beam powers, a beam focused near the edge of the microbridge ($x_f = 49 \mu\text{m}$) has the greatest effect on the critical current, the density of which is assumed to be greatest near the microbridge edges. In contrast, an electron beam focused at the center of the microbridge ($x_f = 0 \mu\text{m}$) requires less power to make the entire width of the microbridge normal than a beam focused at the edge. The electron beam is scanned across the entire width of the microbridge, and each beam focus location determines at some beam power the microbridge critical current. The solid curve for the scanning beam is the minimum envelope of curves relating critical current to beam power for all beam focus locations. Figure 6 shows this minimum envelope for three values of the microbridge width $2w$. The ordinate of this graph is the ratio of the microbridge critical current to the critical current of the unirradiated microbridge, I_c/I_{c0} . The normalized critical current increases for a given beam power with increasing microbridge width. The beam power at which the critical current in the microbridge is reduced to zero increases with increasing microbridge width.

Figure 7 shows temperature profiles in planes parallel to the flow of current and normal to the film surface. For each beam focus location x_f the temperature profile is given for the plane

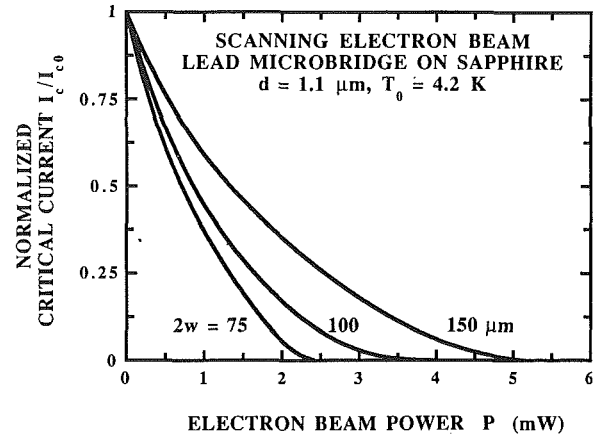


Fig. 6 Dependence of the critical current on the beam power for three microbridge widths

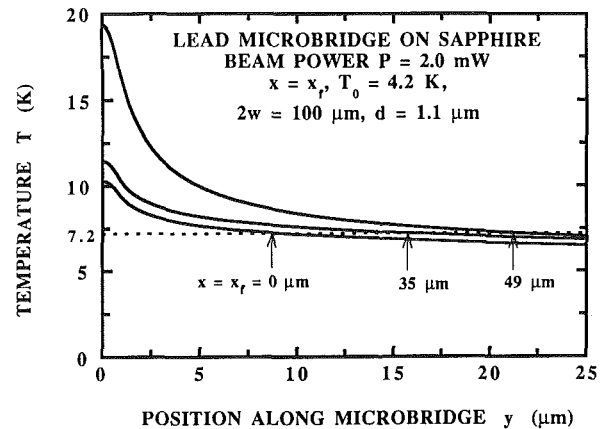


Fig. 7 Longitudinal temperature profiles for different beam focus locations

parallel to the flow of electric current that contains the line $x = x_f, z = 0$. The arrows show for each beam focus location the value of y at which the temperature is equal to the critical temperature. This figure indicates that the longitudinal extent of the normally resistive region in the microbridge increases as the beam focus approaches the microbridge edge. This helps to explain the shape of the voltage response obtained by Stoehr et al. (1978) due to scanning the electron beam across the microbridge width at constant power with a constant bias current in the microbridge. The greater longitudinal extent of the normal region, along with the maxima in the critical current density distribution at the microbridge edges, resulted in the peaks in voltage response when the beam was focused near the microbridge edges.

Concluding Remarks

If the characteristic dimension of the film volume directly heated by the electron beam is much smaller than the width of the microbridge, the variation of the distribution of heating intensity within that volume has little effect on the microbridge critical current. Thermal analysis of a microbridge of width of the order of or smaller than its linearized thermal healing length, $(kd/h)^{1/2}$, must consider the finite microbridge width. A linearization of the heat flux from the film to the substrate is appropriate if the temperature T in the film satisfies $(T - T_0)/T_0 \ll 1$, where T_0 is the substrate temperature. The error due to this linearization increases rapidly with the power of the electron beam.

The voltage response in a superconducting microbridge is determined by the beam power and focus location and the bias

current in the microbridge. The present thermal analysis becomes appropriate for investigation of the voltage response if Joule heating is incorporated into the energy balance and the potential for normal-zone thermal propagation is considered. Prediction of the voltage response requires experimental data for the resistivity in the microbridge as a function of its temperature and bias current.

The theory in the present analysis for the prediction of critical currents in low-temperature superconducting microbridges is an idealization of the complex interaction of electrical current, magnetic field, and temperature with the microbridge geometry. A theory for the case of epitaxial high-temperature superconducting microbridges must consider the anisotropy of those materials and the effects of flux creep and grain boundaries. There is a need for simple, yet accurate models that describe the behavior of supercurrent in specific geometries with temperature fields. The agreement of the predicted critical current with experimental data in the present work shows that the method of Intrinsic Thermal Stability has promise for the prediction of the critical current of high-temperature superconductors in the presence of thermal disturbances.

Acknowledgments

The authors thank Professor J. L. Smith of the Massachusetts Institute of Technology for his commentary and criticism. M.I.F. acknowledges the support of the Lynde and Harry Bradley Foundation through a Career Development Chair and K.E.G. the support of the Office of Naval Research through an academic fellowship.

References

- Anderson, A. C., 1981, "The Kapitza Thermal Boundary Resistance Between Two Solids," in: *Non-Equilibrium Superconductivity, Phonons, and Kapitza Boundaries*, K. E. Gray, ed., Plenum Press, New York, pp. 1-30.
- Cheeke, J. D. N., Hebral, B., and Martinon, C., 1973, "Transfert de Chaleur entre Deux Solides en Dessous de 100 K," *J. Phys. (Paris)*, Vol. 34, pp. 257-272.
- Cheeke, J. D. N., Ettinger, H., and Hebral, B., 1976, "Analysis of Heat Transfer Between Solids at Low Temperatures," *Can. J. Phys.*, Vol. 54, pp. 1749-1765.
- Clem, J. C., and Huebener, R. P., 1980, "Applications of Low-Temperature Scanning Electron Microscopy to Superconductors," *J. Appl. Phys.*, Vol. 51, pp. 2764-2773.
- Cosslett, V. E., and Thomas, R. N., 1964a, "Multiple Scattering of 5-30 keV Electrons in Evaporated Metal Films: I. Total Transmission and Angular Distribution," *Br. J. Appl. Phys.*, Vol. 15, pp. 883-907.
- Cosslett, V. E., and Thomas, R. N., 1964b, "Multiple Scattering of 5-30 keV Electrons in Evaporated Metal Films: II. Range-Energy Relations," *Br. J. Appl. Phys.*, Vol. 15, pp. 1283-1300.
- Edwards, H. H., and Newhouse, V. L., 1962, "Superconducting Film Geometry with Strong Critical Current Asymmetry," *J. Appl. Phys.*, Vol. 33, pp. 868-874.
- Flik, M. I., and Hijikata, K., 1990, "Approximate Thermal Packaging Limit for Hybrid Superconductor-Semiconductor Electronic Circuits," *Heat Transfer 1990*, G. Hetsroni, ed., Hemisphere, New York, Vol. 2, pp. 319-324.
- Flik, M. I., Phelan, P. E., and Tien, C. L., 1990, "Thermal Model for the Bolometric Response of High- T_c Superconducting Films to Optical Pulses," *Cryogenics*, Vol. 30, pp. 1118-1128.
- Flik, M. I., and Tien, C. L., 1990a, "Intrinsic Thermal Stability of Anisotropic Thin-Film Superconductors," *ASME JOURNAL OF HEAT TRANSFER*, Vol. 112, pp. 10-15.
- Flik, M. I., and Tien, C. L., 1990b, "Intrinsic Thermal Stability for Scanning Electron Microscopy of Thin-Film Superconductors," *J. Appl. Phys.*, Vol. 67, pp. 362-370.
- Flik, M. I., and Tien, C. L., 1990c, "Size Effect on the Thermal Conductivity of High- T_c Thin-Film Superconductors," *ASME JOURNAL OF HEAT TRANSFER*, Vol. 112, pp. 872-881.
- Gross, R., and Koyanagi, M., 1985, "Effect of Electron-Beam Irradiation on Superconducting Films," *J. Low Temp. Phys.*, Vol. 60, pp. 277-295.
- Huebener, R. P., 1984, "Applications of Scanning Electron Microscopy," *Rep. Prog. Phys.*, Vol. 47, pp. 175-220.
- Huebener, R. P., 1988, "Scanning Electron Microscopy at Very Low Temperatures," in: *Advances in Electronics and Electron Physics*, P. W. Hawkes, ed., Academic Press, New York, Vol. 70, pp. 1-79.
- Kittel, C., 1986, *Introduction to Solid State Physics*, Wiley, New York, p. 150.
- Little, W. A., 1959, "The Transport of Heat Between Dissimilar Solids at Low Temperatures," *Can. J. Phys.*, Vol. 37, pp. 334-349.
- Majumdar, A., 1991, "Effect of Interfacial Roughness on Phonon Radiative Heat Conduction," *Proceedings of the ASME/JSME Thermal Engineering Joint Conference*, Reno, NV, Vol. 4, pp. 99-110.
- Newhouse, V. L., 1964, *Applied Superconductivity*, Wiley, New York, pp. 109-112, 122-126.
- Oatley, C. W., 1972, *The Scanning Electron Microscope, Part 1: The Instrument*, Cambridge University Press, Cambridge, United Kingdom, pp. 134-167.
- Patankar, S. V., 1980, *Numerical Heat Transfer and Fluid Flow*, Hemisphere, New York, pp. 41-77.
- Pavlicek, H., Freytag, L., Seyfert, H., and Huebener, R. P., 1984, "Resolution Limit Due to Thermal Effects in Low-Temperature Scanning Electron Microscopy," *J. Low Temp. Phys.*, Vol. 56, pp. 237-257.
- Powell, R. W., Ho, C. Y., and Liley, P. E., 1966, *Thermal Conductivity of Selected Materials*, Part 2, U.S. Government Printing Office, Washington, pp. 19, 175-181.
- Skocpol, W. J., Beasley, M. R., and Tinkham, M., 1974, "Self-Heating Hotspots in Superconducting Thin-Film Microbridges," *J. Appl. Phys.*, Vol. 45, pp. 4054-4066.
- Stoehr, P. L., Noto, K., and Huebener, R. P., 1978, "Superconducting Microbridges Under Irradiation With an Electron Beam," *J. Phys. (Paris)*, Coll. C6, Suppl. 8, Vol. 39, pp. C6/527-528.
- Stoehr, P. L., and Huebener, R. P., 1979, "Two-Dimensional Imaging of the Resistive Voltage Changes in a Superconductor Caused by Irradiation With an Electron Beam," *J. Low Temp. Phys.*, Vol. 37, pp. 277-287.
- Swartz, E. T., and Pohl, R. O., 1989, "Thermal Boundary Resistance," *Rev. Mod. Phys.*, Vol. 61, pp. 605-668.
- Wells, O. C., 1974, *Scanning Electron Microscopy*, McGraw-Hill, New York, pp. 37-68.

Moving Front Fixing in Thin Film Laser Annealing

C. P. Grigoropoulos

Department of Mechanical Engineering,
University of California,
Berkeley, CA 94720

W. E. Dutcher, Jr.¹

Department of Mechanical Engineering,
University of Washington,
Seattle, WA 98195

The process of laser melting and recrystallization of thin silicon films, which are deposited on amorphous substrates, is capable of improving the semiconductor electrical and crystalline properties. The process is controlled by the intensity of the laser beam, the material translation speed, and the thermal and radiative properties of the semiconductor layer and the encapsulating structure. Accurate theoretical modeling of the associated phase change process is essential for optimal material processing. This paper presents a numerical model implementing a front-fixing approach and body-fitted curvilinear grids to analyze the heat transfer and the induced crystallization rates in thin film laser annealing. The results are compared to experimental data and reasonable agreement is obtained. Further improvements depend upon knowledge of thin film thermal and optical properties.

I Introduction

Thin film heat treatment is of growing importance to current microchip technology because it enables the fabrication of novel electronic devices. The use of light sources to melt and recrystallize thin semiconductor layers has been investigated. Laser melting and recrystallization are effected by sweeping a radiative source across a polycrystalline layer that has been deposited on a bulk amorphous substrate or an oxidized wafer. The induced crystal grain size increase results in improvement of the electrical transport properties that significantly enhances the value of the material as an active component in electronic devices (Celler, 1983).

Single crystal, thin film material has been produced in isolated lithographically patterned areas, usually of 20 by 100 μm size. Electronic devices fabricated in this recrystallized material have shown good performance and reliability. However, consistent control of the crystal growth orientation is not yet possible, and the strong tendency toward supercooling and rapid solidification may cause numerous defects (Geis et al., 1986). The benefits of modifying the temperature field have been shown by Biegelsen et al. (1981), Stultz and Gibbons (1981), and Kawamura et al. (1982). These investigators shaped the heating laser source profile to obtain concave solidification trailing edge boundaries, curved inward, into the liquid pool. Production of single-crystal thin silicon strips of up to 50 μm width and of several centimeters in length, was reported using this technique. It is evident that in order to improve laser recrystallization it is necessary to analyze the heat transfer and the induced phase-change transformations.

Current numerical models of thin-film laser annealing include simulations of silicon film melting by laser line heat sources of infinite width (Kubota et al., 1986); approximate methods (Waechter et al., 1986); and three-dimensional simulations (Grigoropoulos et al., 1991a). These models use the enthalpy formulation (Atthey, 1974; Shamsundar and Sparrow, 1975, 1977). The enthalpy method circumvents the need for satisfying the exact energy balance conditions across the phase-change boundary. The position of the moving phase-change boundary does not appear in the calculations and it is not a direct part, but rather an implicit derivative of the so-

lution. Upon melting, the silicon thermal conductivity increases by a factor of three (Appendix B), while the absorbed energy is decreased by a factor of two. The treatment of these property changes in an enthalpy change of phase scheme using fixed rectangular grids is not straightforward. On the other hand, the use of Kirchoff's transformation as by Kubota et al. (1986) cannot completely eliminate the temperature dependence of the material thermal properties, since the silicon thermal diffusivity remains a strong function of temperature.

Control of the phase boundary shape and the induced crystallization rates is essential. To achieve that, it is necessary to apply accurate numerical models that capture the motion of a distinct isothermal phase boundary and solve the exact system of field equations and interfacial boundary conditions. Locating the position of the phase boundary can either be done by tracking its motion in time or by fixing it with a suitable choice of spatial coordinates (Crank, 1987). Front-fixing is accomplished by mapping the solid and the liquid phases into fixed rectangular domains. Direct transformations, such as the transformation in radial coordinates for arbitrarily shaped regions (Saitoh, 1978), can be used for this purpose.

The present work uses boundary-fitted curvilinear coordinate systems that are generated by the solution of an elliptic system of partial differential equations (Thompson et al., 1977a, 1977b; Thames et al., 1977). The resulting finite difference conductive heat transfer equations in the solid and the liquid regions are solved separately in their respective transformed, fixed domains. Phase boundary advancement is then determined by the energy balance across the solid-liquid interface. The computational results are compared to a set of experimental data (Grigoropoulos et al., 1991a).

II Computational Analysis

A sketch of the basic structure to be modeled is shown in Figure 1. A polysilicon film of thickness d_{si} is deposited on a fused silica substrate of thickness d_{ss} and encapsulated by a SiO_2 layer of thickness d_{enc} . A multiline laser beam of Gaussian intensity distribution passes through the transparent substrate and is partially absorbed by the silicon layer. Heat is lost from the upper and lower surfaces of the structure by convection and radiation. Matsushima and Viskanta (1990) examined coupled radiative transfer and heat convection in silicon crystal growth from the melt using a vertical Bridgman method. This is a large-scale system, with small temperature differences and resulting temperature gradients. In the structure examined in the present study, the typical length scale representing the size

¹Present address: Boeing Commercial Airplane Group, Advanced Projects, Seattle, WA 98124-2207.

Contributed by the Heat Transfer Division and presented at the 3rd ASME/JSM E Joint Thermal Engineering Conference, Reno, Nevada, March 17-22, 1991. Manuscript received by the Heat Transfer Division November 19, 1990; revision received July 1, 1991. Keywords: Laser Processing, Materials Processing and Manufacturing Processes, Moving Boundaries.

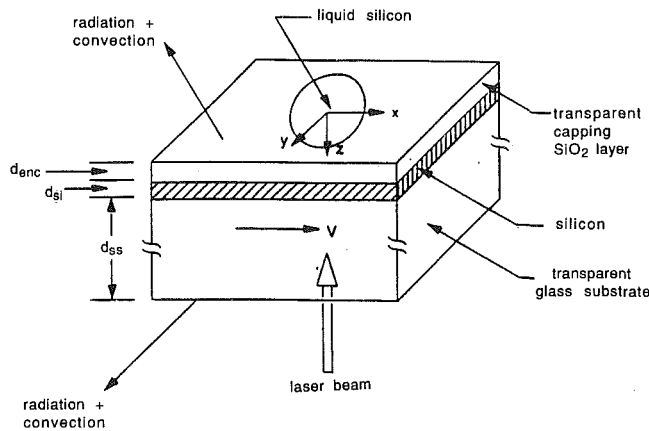


Fig. 1 Sketch of a silicon layer of thickness $d_{si} = 0.5 \mu\text{m}$, deposited on a glass substrate of thickness $d_{ss} = 0.5 \text{ mm}$, and encapsulated by a glass layer of thickness $d_{enc} = 0.5 \mu\text{m}$

of the heat affected zone in the solid material, $H = 1 \text{ mm}$. Estimate of the conduction-radiation parameter (Viskanta and Anderson, 1975), $N_{R-C} = \sigma T_m^3 / (k/H)$ yields a value of about 0.01 in the solid silicon region. Liquid silicon has a high extinction coefficient, and is opaque to radiation, with an absorption coefficient of the order of 10^8 m^{-1} for wavelengths close to $1 \mu\text{m}$. Conduction is therefore the dominant mode of heat transfer. The complete equation of radiative transport in participating media need not be solved, unless the detailed radiation distribution is desired, possibly for the purpose of comparison with in-situ process diagnostics.

II.1 Formulation. Both the silicon film and the encapsulating layer are thin, each having a thickness of $0.5 \mu\text{m}$. The heat transfer in these layers can, therefore, be represented by the heat conduction equation integrated across the respective layer thickness. The heat transfer in the silicon layer is

$$\rho_{si}(T_{si})c_{p,si}(T_{si})\left(\frac{\partial T_{si}}{\partial t} + V\frac{\partial T_{si}}{\partial x}\right) = \frac{\partial}{\partial x}\left(k_{si}(T_{si})\frac{\partial T_{si}}{\partial x}\right) + \frac{\partial}{\partial y}\left(k_{si}(T_{si})\frac{\partial T_{si}}{\partial y}\right) + \frac{1}{d_{si}}[Q_{ab}(x, y, T_{si}) - Q_{rad,si}(T_{si})]$$

Nomenclature

a_n = linear coefficient of temperature dependence of the real part of the silicon refractive index
 c_p = specific heat
 d_{enc} = encapsulating layer thickness
 d_{si} = semiconductor layer thickness
 d_{ss} = substrate thickness
 e = percent error
 F = function indicating the phase boundary position
 h = convective heat transfer coefficient
 H = length scale
 \mathbf{i} = unit vector in the x direction
 J = Jacobian of the grid transformation
 \mathbf{j} = unit vector in the y direction
 \hat{j} = imaginary unit
 k = thermal conductivity
 k^{ext} = extinction coefficient
 k_{si}^o = extinction coefficient of silicon at 300 K
 L = latent heat of fusion
 M = number of grid points in the ξ direction
 N = number of grid points in the η direction

$$+ \frac{1}{d_{si}}\left(k_{si}(T_{si})\frac{\partial T_{si}}{\partial z}\Big|_{z=d_{enc}+d_{si}} - k_{si}(T_{si})\frac{\partial T_{si}}{\partial z}\Big|_{z=d_{enc}}\right) \quad (1)$$

In the encapsulating layer the heat transfer is given by

$$\rho_{enc}(T_{enc})c_{p,enc}(T_{enc})\left(\frac{\partial T_{enc}}{\partial t} + V\frac{\partial T_{enc}}{\partial x}\right) = \frac{\partial}{\partial x}\left(k_{enc}(T_{enc})\frac{\partial T_{enc}}{\partial x}\right) + \frac{\partial}{\partial y}\left(k_{enc}(T_{enc})\frac{\partial T_{enc}}{\partial y}\right) - \frac{Q_{rad,enc}}{d_{enc}} - \frac{1}{d_{enc}}\left[h_{top}(T_{enc} - T_{\infty}) - k_{enc}(T_{enc})\frac{\partial T_{enc}}{\partial z}\Big|_{z=d_{enc}}\right] \quad (2)$$

The heat conduction equation in the substrate is

$$\rho_{ss}(T_{ss})c_{p,ss}(T_{ss})\left(\frac{\partial T_{ss}}{\partial t} + V\frac{\partial T_{ss}}{\partial x}\right) = \frac{\partial}{\partial x}\left(k_{ss}(T_{ss})\frac{\partial T_{ss}}{\partial x}\right) + \frac{\partial}{\partial y}\left(k_{ss}(T_{ss})\frac{\partial T_{ss}}{\partial y}\right) + \frac{\partial}{\partial z}\left(k_{ss}(T_{ss})\frac{\partial T_{ss}}{\partial z}\right) \quad (3)$$

The laser beam energy that passes through the transparent substrate and is absorbed by the silicon layer is given by

$$Q_{ab}(x, y, T_{si}) = \sum_{i=1}^{n_w} [1 - R_{\lambda_i}(T_{si}) - \tau_{\lambda_i}(T_{si})] Q_{\lambda_i}^{ext}(x, y) \quad (4)$$

The radiative heat flux balance and the thin film reflectivity and transmissivity, R_{λ_i} and τ_{λ_i} , are calculated (Grigoropoulos et al., 1991a) using thin film optics, which take into account wave interference effects (Born and Wolf, 1970; Knittl, 1976; Heavens, 1955). The material optical properties used in these calculations are given in Appendix B. When liquid, the silicon film is opaque and its reflectivity is $R_{\lambda,b,l} = 0.527$. The absorption penetration depth is about 10 nm for visible wavelengths in the spectral range of the annealing laser beam. The solid silicon density varies slightly with temperature (3 percent change from the ambient temperature, $T_{\infty} = 300 \text{ K}$, to the melting temperature, $T_m = 1685 \text{ K}$). This density change does affect the optical properties and is included in the analysis. The melted silicon film exhibits a metallic behavior, and the change in the silicon density from the solid phase to the liquid phase does not affect the light absorption in the semiconductor.

The laser beam intensity distribution is assumed to be Gaussian and circular;

$$Q_{\lambda i}^{\text{ext}}(x, y) = Q_{\lambda i}^0 \exp\left(-\frac{x^2 + y^2}{w_{\lambda i}^2}\right) \quad (5)$$

The laser beam parameters, $w_{\lambda i}$, and the power fractions corresponding to the $n_w = 6$ laser line centers were measured as described by Grigoropoulos et al. (1991a). The emission losses are estimated in a simple manner, by considering an isothermal structure irradiated from above and below, with a blackbody source at conditions of thermal equilibrium. The local energy flux and the light absorption through the stratified structure are given by the time-averaged Poynting vector. The light absorption in the encapsulating layer, the polysilicon film, and the substrate is evaluated by considering the incident radiation as coherent and unpolarized, following Planck's intensity distribution. Using Kirchhoff's law, the total hemispherical emissivities $\epsilon_{\text{enc}}^{\pm}$, $\epsilon_{\text{si}}^{\pm}$, and $\epsilon_{\text{ss}}^{\pm}$ are obtained by integrating, first with respect to direction and then over the wavelength spectrum. The + and - superscripts indicate losses through the upper structure surface and the bottom substrate surface, correspondingly. The radiative loss from the silicon layer is

$$Q_{\text{rad,si}} = \sigma(\epsilon_{\text{si}}^+ + \epsilon_{\text{si}}^-)(T_{\text{si}}^4 - T_{\infty}^4) \quad (6)$$

For the encapsulating layer, ϵ_{enc}^- is negligible,

$$Q_{\text{rad,enc}} = \sigma\epsilon_{\text{enc}}^+(T_{\text{enc}}^4 - T_{\infty}^4) \quad (7)$$

Similarly, the radiative loss from the substrate surface, through the encapsulating layer, $\epsilon_{\text{ss}}^+ \cong 0$

$$Q_{\text{rad,ss}} = \sigma\epsilon_{\text{ss}}^-(T_{\text{ss}}^4 - T_{\infty}^4) \quad (8)$$

Perfect thermal contact and continuity of the heat flux across the interfaces between layers are assumed throughout the calculations. The solid and liquid silicon regions are separated by a sharp interface, described by the equation

$$F(x, y, t) = 0 \quad (9)$$

The phase boundary is isothermal:

$$T_{\text{si,s}}(x, y, t) = T_{\text{si,l}}(x, y, t) = T_m, \quad \text{at } F(x, y, t) = 0 \quad (10)$$

The energy balance across the silicon phase change interface is:

$$k_{\text{si,s}}(T_{\text{si,s}}) \frac{\partial T_{\text{si,s}}}{\partial n} - k_{\text{si,l}}(T_{\text{si,l}}) \frac{\partial T_{\text{si,l}}}{\partial n} = \rho_{\text{si,s}}(T_m) L_{\text{si}} \cdot (v_n - \mathbf{V}_i \cdot \mathbf{n}) \quad \text{at } F(x, y, t) = 0. \quad (11)$$

In the above equation, v_n is the local speed of the phase boundary in the normal direction to the phase change boundary, \mathbf{n} , pointing into the solid region.

The boundary condition at the bottom substrate surface is

$$-k_{\text{ss}}(T_{\text{ss}}) \frac{\partial T_{\text{ss}}}{\partial z} \Big|_{z=z_{\text{bot}}} = h_{\text{bot}}[T_{\text{ss}}(x, y, z_{\text{bot}}) - T_{\infty}] + \epsilon_{\text{ss}}^- \sigma[\tau_{\text{ss}}(x, y, z_{\text{bot}})^4 - T_{\infty}^4] \quad (12)$$

where $z_{\text{bot}} = d_{\text{enc}} + d_{\text{si}} + d_{\text{ss}}$. The boundary condition at the top surface has been included in the integrated equation for the encapsulating layer, Eq. (2). The coefficients h_{top} and h_{bot} that appear in Eqs. (2) and (12) are estimated using expressions for free convection from horizontal surfaces. It is unlikely that these estimates are accurate, in view of the time scale of the problem, and the highly localized temperature distribution. Simple order of magnitude arguments and computational results show that the convective losses are a small fraction of the absorbed energy in the area of interest. Far away from the laser beam center, the temperature $T \rightarrow T_{\infty}$.

The heat transfer is solved in a transformed computational domain. The transformation required is from the Cartesian (x, y, z) system to a curvilinear system, $(\xi(x, y), \eta(x, y), z)$, where the z coordinate remains unaffected. The curvilinear coordinates $(\xi(x, y), \eta(x, y))$, are solutions of the Poisson type, elliptic system of partial differential equations with exponentially varying grid control functions $P(\xi, \eta)$, and $Q(\xi, \eta)$ (Thompson et al., 1977a, 1977b, 1985). Equation (1) for the heat transfer in the silicon layer becomes in the transformed domain:

$$\rho_{\text{si}} c_{p,\text{si}} \left[\frac{\partial T}{\partial t} - \frac{1}{J} (y_{\eta} T_{\xi} - y_{\xi} T_{\eta}) \times \left(\frac{\partial x}{\partial t} - V \right) - \frac{1}{J} (x_{\xi} T_{\eta} - x_{\eta} T_{\xi}) \left(\frac{\partial y}{\partial t} \right) \right] = \frac{1}{J^2} [\alpha(k_{\text{si}} T_{\xi})_{\xi} - \beta(k_{\text{si}} T_{\eta})_{\xi} - \beta(k_{\text{si}} T_{\xi})_{\eta} + \gamma(k_{\text{si}} T_{\eta})_{\eta}]$$

Nomenclature (cont.)

s	= phase boundary position
Ste	= Stefan number
t	= time
T	= temperature
T_m	= silicon melting temperature = 1685 K
T_{∞}	= ambient temperature
V	= material translation speed
v_n	= velocity of the phase boundary in the normal to the interface direction
$w_{\lambda b}$	= distance from the laser beam center to the point when the irradiance intensity of the blue ($\lambda = 488$ nm) component of the laser beam drops to $1/e$ of its peak value
$w_{\lambda i}$	= distance from the laser beam center to the point where the irradiance of the λi wavelength component of the laser beam drops to $1/e$ of its peak value
x	= coordinate in the scanning direction
y	= coordinate in the transverse direction
z	= coordinate normal to the sample surface
$\alpha, \beta, \gamma, \mu, \nu$	= grid geometry coefficients
α_s	= solid silicon thermal diffusivity

α_l	= liquid silicon thermal diffusivity
ϵ	= emissivity
η	= curvilinear coordinate
λ	= wavelength
λ_i	= wavelength of laser line center ($i = 1, \dots, n_w$)
λ_b	= blue ($\lambda = 488$ nm) laser light wavelength
ξ	= curvilinear coordinate
ρ	= density
σ	= Stefan-Boltzmann constant
τ	= transmissivity

Subscripts

bot	= bottom substrate surface
enc	= encapsulating layer
l	= liquid region
s	= solid region
si	= silicon layer
ss	= substrate
top	= top structure surface

Accents

\sim	= nondimensional variable
--------	---------------------------

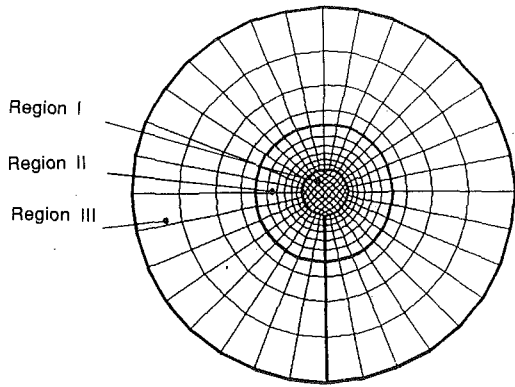


Fig. 2 Composite curvilinear finite difference grid

$$+ k_{si}(\mu T_{\eta} + \nu T_{\xi}) + \frac{1}{d_{si}}(Q_{ab} - Q_{rad,si}) + \frac{1}{d_{si}} \left(k_{si} \frac{\partial T}{\partial z} \Big|_{z=d_{enc}+d_{si}} - k_{si} \frac{\partial T}{\partial z} \Big|_{z=d_{enc}} \right) \quad (13)$$

In the above equation, the temperature dependence of ρ_{si} , $c_{p,si}$, and k_{si} is not explicitly shown. The "grid speed" terms $\partial x/\partial t$, $\partial y/\partial t$ are evaluated at constant (ξ, η) , to yield the motion of the transformed mesh points on the physical (x, y) plane. Similar expressions are obtained for the heat transfer in the encapsulating layer and the substrate. The grid geometric parameters are given below:

$$J = x_{\xi}y_{\eta} - x_{\eta}y_{\xi} \\ \alpha = x_{\eta}^2 + y_{\eta}^2, \quad \beta = x_{\xi}x_{\eta} + y_{\xi}y_{\eta}, \quad \gamma = x_{\xi}^2 + y_{\xi}^2 \\ \mu = (y_{\xi}Dx - x_{\xi}Dy)/J, \quad \nu = (x_{\eta}Dy - y_{\eta}Dx)/J \\ Dx = \alpha y_{\xi\xi} - 2\beta x_{\xi\eta} + \gamma \xi_{\eta\eta}, \quad Dy = \alpha y_{\xi\xi} - 2\beta y_{\xi\xi} + \gamma y_{\eta\eta} \quad (14)$$

II.2 Numerical Implementation. The finite difference grid used in the solution of the laser annealing problem is composed of nonuniformly spaced in the z -direction layers of the three-region curvilinear mesh, shown in Fig. 2. Region I is fit to the liquid silicon. Region II, which is doubly connected, has a circular outer boundary with a radius equal to five times that of the average radius of Region I. Region III, also doubly connected, is radial with uniform angular spacing and non-uniform spacing radially. The outer radius is taken to be 20 times the laser beam radius, $w_{\lambda b}$, to provide a sufficiently large computational domain.

The curvilinear coordinates (ξ, η) are generated in regions I and II by solving an elliptic partial differential equation system. The solution utilizes a fully nested multigrid algorithm (Hackbush, 1985; McCormick, 1987) in the internal region I and a Gauss Seidel iteration method in the external doubly connected region II. To allow for consistent spacing of the coordinate lines when using the control functions P and Q , and avoid numerical problems, the regions are normalized by the average phase boundary radius. Region III is created algebraically by extending the coordinate lines in the radial direction. The nonuniform radial spacing is provided by linearly increasing distance between gridpoints.

The transformed rectangular domains were discretized using uniform increments, $\Delta\xi = 1/M$, $\Delta\eta = 1/N$. The finite difference representations of the spatial derivatives of the transformed equations are based on a centered nine-point computational molecule. Second-order accurate, central difference expressions are used to evaluate the geometric parameters J , α , β , γ , μ , and ν as well as the spatial, first-order partials of temperature T_{ξ} and T_{η} . The second-order derivative terms $(kT_{\xi})_{\xi}$, $(kT_{\eta})_{\xi}$, $(kT_{\xi})_{\eta}$, and $(kT_{\eta})_{\eta}$ are evaluated as shown by Thompson et al. (1985), by combining forward and back-

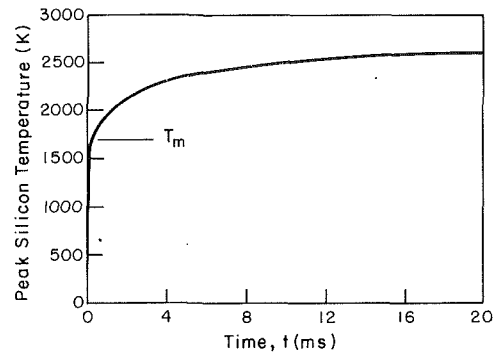


Fig. 3 Predicted peak silicon layer temperature history: laser beam power $P_T = 1.8$ W, $1/e$ irradiance radius $w_{\lambda b} = 40$ μ m, and material translation speed $V = 2$ mm/s

ward finite difference expressions. The resulting expressions maintain the nine-point computational molecule and reduce to the second and mixed derivative finite difference approximations for the constant thermal conductivity case. The spatial derivatives in the z direction and the convective boundary conditions at the lower and upper surfaces are treated using a thermal resistance approach. The grid speed terms, $\partial x/\partial t$ and $\partial y/\partial t$, are evaluated using second-order accurate, backward finite difference approximations. The time derivative of temperature is approximated with a first-order accurate, forward difference.

Special treatment is required in applying the discretized field equations at the computational nodes that define the inner region I in the encapsulating layer and the substrate and that also belong to region II. The corner nodes of region I are handled by defining a local (ξ, η) coordinate system (Thompson et al., 1985). The thermal gradients across the phase-change boundary, $\partial T_{si,s}/\partial n$ and $\partial T_{si,l}/\partial n$, Eq. (11), are evaluated by using second-order accurate, forward and backward finite difference expressions, correspondingly.

Explicit, finite difference expressions for the transient heat conduction equation are thus derived. The nonlinear radiative loss terms are evaluated at the previous time step. A local stability criterion is determined numerically and used to obtain the allowable time step. The initial condition is that at zero time the structure is isothermal, at the ambient temperature, T_{∞} . An enthalpy scheme on a fixed nonuniform orthogonal grid is used to begin the solution. After a short time, the moving grid scheme is applied. Bilinear interpolation is used to obtain the temperature fields on the curvilinear grid and define an initial phase-change boundary. The front-fixing algorithm consists of the following steps:

- (i) Determine the temperature field in the solid and liquid silicon regions at the new time.
- (ii) Obtain the new temperature field in the encapsulating layer and the substrate.
- (iii) Based on the new silicon layer temperatures, calculate the displacement of the phase boundary nodes using the energy balance equation.
- (iv) Generate the new boundary-fitted grids and repeat the process.

The accuracy of the algorithm was evaluated by comparing numerical results versus known analytical solutions for one-dimensional phase change problems with cylindrical symmetry (Appendix A).

II.3 Results. Computations were carried out for a range of parameters corresponding to experimental data provided by Grigoropoulos et al. (1991a). It was assumed that the laser beam is suddenly turned on and focused on the moving silicon layer.

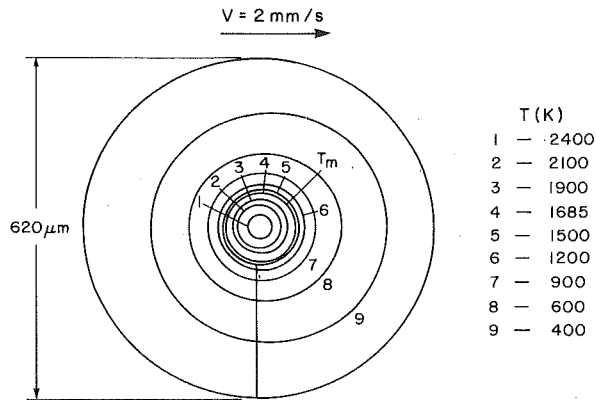


Fig. 4(a) Predicted temperature distribution in the silicon layer at $t = 20$ ms, for the laser beam parameters and material translation speed of Fig. 3

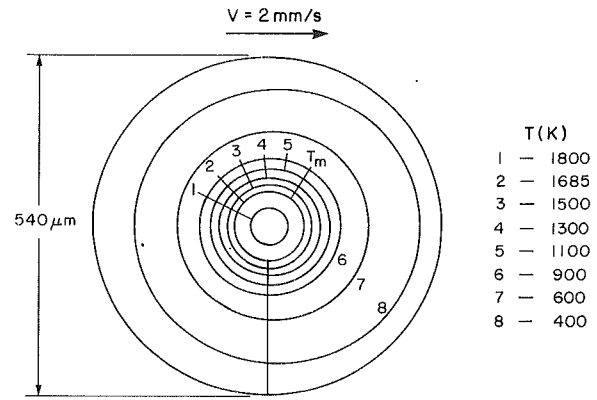


Fig. 5(a) Predicted temperature distribution in the silicon layer, for $P_T = 1.8$ W, $V = 2$ mm/s, and $w_{\lambda b} = 70$ μ m, at $t = 20$ ms

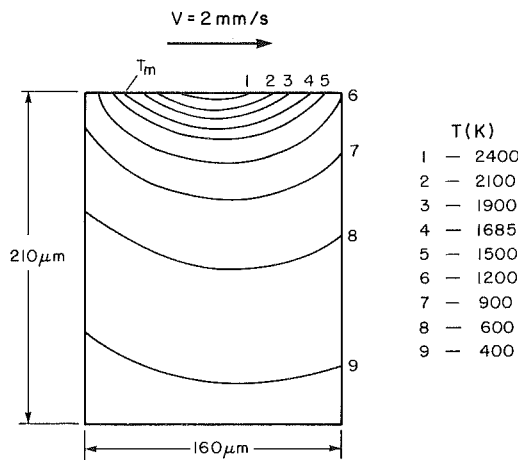


Fig. 4(b) Predicted temperature distribution of a x - z cross section through the glass substrate that corresponds to Fig. 4(a)

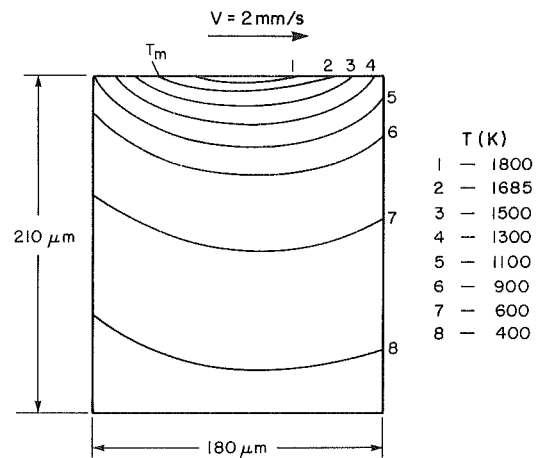


Fig. 5(b) Predicted temperature distribution on a x - z cross section through the glass substrate that corresponds to Fig. 5(a)

Figure 3 shows the predicted peak silicon layer temperature as a function of time for a laser beam of total power, $P_T = 1.8$ W and $1/e$ intensity radius, $w_{\lambda b} = 40$ μ m. Over 260,000 time steps were necessary to reach the final time, $t = 20$ ms, at which a quasi-static temperature distribution, fixed with respect to the laser beam, is established. Figure 4(a) is a contour plot of the induced temperature fields in the silicon layer. Figure 4(b) shows the corresponding temperature distribution in the glass substrate on the x - z cross section through the axis of the laser beam. It can be seen that the molten pool is almost circular and that the isotherm migration in the silicon layer and the substrate due to the translation of the structure is relatively small. Figures 5(a) and 5(b) show the temperature fields in the silicon layer and in the substrate, for a laser beam radius $w_{\lambda b} = 70$ μ m. The peak temperature in the silicon layer drops to about 1950 K. Figure 6 shows the effect of increasing the material translation speed, V , on the temperature field distribution in the silicon layer. For $V = 20$ mm/s, the peak temperature in the silicon layer, at a time $t = 20$ ms, is about 2400 K.

It is also evident that for this set of parameters, the predicted maximum temperature in the silicon layer and the glass substrate exceeds the softening point of glass, which is about 1880 K. No critical temperatures and corresponding latent heats of fusion are defined for amorphous glass, but discontinuities in the glass specific heat upon rapid transformation may occur (McLellan and Shand, 1984). In the absence of specific data, these changes are neglected in the analysis, which considers phase transformation only in the silicon layer. Table 1 compares experimental and computational values of the average

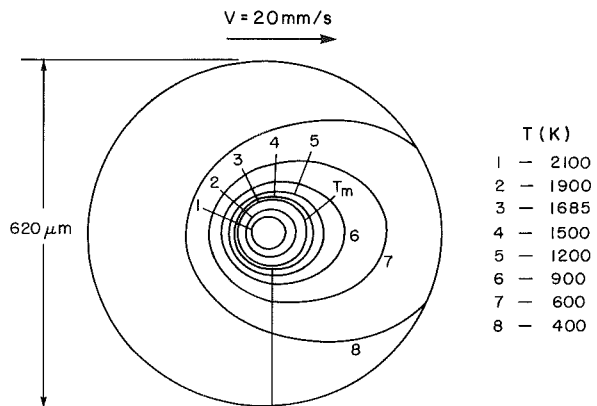


Fig. 6 Predicted temperature distribution in the silicon layer, for $P_T = 1.8$ W, $w_{\lambda b} = 40$ μ m, and $V = 20$ mm/s, at $t = 20$ ms

molten spot diameter for a laser beam total power $P_T = 1.8$ W and material translation speed, $V = 2$ mm/s at a time, $t = 20$ ms.

In the experiments, the laser beam total power was controlled within 5 percent, and the laser beam size, $w_{\lambda b}$, was measured with an average estimated accuracy of 7 percent. The results for $w_{\lambda b} = 40$ μ m show that the front fixing model overpredicts the molten pool size, in contrast to the underprediction of the enthalpy code. The computational results indicate a pool reduction with increasing beam diameter, in contrast to the trend of slight increase recorded by the experiments. Solidification of laser-melted silicon films is a complex phenomenon, with

Table 1 Comparison between the experimental results, the enthalpy-based calculations, and these computations

$w_{\lambda b}$, μm	Molten Spot Diameter, μm		
	Experiment	Enthalpy scheme	Present computations
40	108	89	122
50	118	107	120
60	120	106	116
70	126	102	110

partial melting observed at low incident laser power densities (Grigoropoulos et al., 1988, 1991a). For a laser beam total power $P_T = 1.8$ W, partial melting begins at $w_{\lambda b} = 80$ μm , with an increasing solid phase fraction in coexistence with the liquid phase. This phenomenon cannot be captured by the present numerical scheme, which assumes that the molten zone contains only the uniformly liquid phase. The difference between the experimental data and the numerical results may also be attributed to deviations of the thermal conductivity of the polycrystalline silicon film and the bulk silicon thermal conductivity (Tai et al., 1988). At large laser beam diameters, an increased part of laser light absorption occurs in the solid silicon. The high-temperature thin polycrystalline film properties may deviate from the bulk properties for single-crystal silicon that were used in these calculations, and must be studied in detail. An experimental method was developed by Grigoropoulos et al. (1991b) to obtain spatially resolved surface reflectivity measurements during thin film annealing. These quantitative experimental results demonstrated the need for extensive studies of the thin film radiative properties.

III Conclusions

A three-dimensional, transient computational model was constructed for the analysis of laser melting of thin silicon films on glass substrates. The numerical model implements a front-fixing approach using body-fitted curvilinear grids. The mesh is generated by the solution of a system of elliptic partial differential equations. The model accuracy was tested and verified versus analytical solutions for a phase-change problem with cylindrical symmetry. The computational results for the laser annealing process were compared to a set of experimental data and reasonable agreement was obtained. The front fixing method complements the enthalpy-based approach, when attention is focused on the details of the thermal gradient distribution across the moving phase boundary. Algorithm improvements include implementation of curvilinear meshes that are naturally adapted to the temperature field distribution. The major computational constraint results from the time step requirement imposed by stability.

Acknowledgments

Support by the National Science Foundation under Grants MSM-8708757 and CTS-8918389-9096253 is gratefully acknowledged. The authors appreciate the comments on this work by Dr. Gerald A. Domoto and Professor Ralph A. Seban.

References

Atthey, D. R., 1974, "A Finite Difference Scheme for Melting Problems," *J. Inst. Math Applics.*, Vol. 13, pp. 353-365.

Biegelsen, D. K., Johnson, N. M., Bartelink, D. J., and Moyer, M. D., 1981, "Laser Induced Crystal Growth of Silicon Islands on Amorphous Substrates," *Proceedings, Materials Research Society*, J. F. Gibbons et al., eds., North-Holland, New York, Vol. 1, pp. 487-494.

Born, M., and Wolf, E., 1970, *Principles of Optics*, 6th ed., Pergamon, Exeter, United Kingdom, pp. 55-60, 611-624.

Carlsaw, H. S., and Jaeger, J. C., 1959, *Conduction of Heat in Solids*, 2nd ed., Oxford University Press, Oxford, United Kingdom, pp. 295-296.

Celler, G. K., 1983, "Laser Crystallization of Thin Silicon Films on Amorphous Insulating Substrates," *J. Crystal Growth*, Vol. 63, pp. 429-444.

Crank, J., 1987, *Free and Moving Boundary Problems*, Oxford University Press, New York, pp. 192-199.

Geis, M. W., Smith, H. I., and Chen, C. K., 1986, "Characterization and Entrainment of Subboundaries and Defect Trails in Zone Melting-Recrystallized Silicon Films," *J. Appl. Phys.*, Vol. 60, No. 3, pp. 1152-1160.

Grigoropoulos, C. P., Buckholz, R. H., and Domoto, G. A., 1988, "An Experimental Study on Laser Annealing of Thin Silicon Layers," *ASME JOURNAL OF HEAT TRANSFER*, Vol. 110, pp. 416-423.

Grigoropoulos, C. P., Dutcher, W. E., Jr., and Emery, A. F., 1991a, "Experimental and Computational Analysis of Laser Melting of Thin Silicon Films," *ASME JOURNAL OF HEAT TRANSFER*, Vol. 113, pp. 21-29.

Grigoropoulos, C. P., Dutcher, W. E., Jr., and Barclay, K. E., 1991b, "Radiative Phenomena in CW Laser Annealing," *ASME JOURNAL OF HEAT TRANSFER*, Vol. 113, pp. 657-662.

Hackbush, W., 1985, *Multi-Grid Methods and Applications*, Springer-Verlag, Berlin, Germany.

Heavens, O. S., 1955, *Optical Properties of Thin Solid Films*, Butterworths, London, United Kingdom, pp. 69-80.

Jellison, G. E., Jr., 1984, "Optical and Electrical Properties of Pulsed Laser-Annealed Silicon," in: *Semiconductors and Semimetals*, Vol. 23, R. F. Wood, C. W. White, and R. T. Young, eds., Academic Press, Orlando, FL, pp. 95-164.

Jellison, G. E., Jr., and Burke, H. H., 1986, "The Temperature Dependence of the Refractive Index of Silicon at Elevated Temperatures at Several Laser Wavelengths," *J. Appl. Phys.*, Vol. 60, No. 2, pp. 841-843.

Kawamura, S., Sakurai, J., Nakano, M., and Takagi, M., 1982, "Recrystallization of Silicon on Amorphous Substrates by Doughnut-Shaped CW Ar Laser Beams," *Appl. Phys. Lett.*, Vol. 40, No. 5, pp. 394-395.

Knittl, Z., 1976, *Optics of Thin Films*, Wiley, Prague, Czechoslovakia, pp. 240-282.

Kubota, K., Hunt, C. E., and Frey, J., 1986, "Thermal Profiles During Recrystallization of Silicon on Insulator With Scanning Incoherent Light Line Sources," *Appl. Phys. Lett.*, Vol. 46, No. 12, pp. 1153-1155.

Matsushima, H., and Viskanta, R., 1990, "Effects of Internal Radiative Transfer on Natural Convection and Heat Transfer in a Vertical Crystal Growth Configuration," *Int. J. Heat Mass Transfer*, Vol. 33, No. 4, pp. 1957-1968.

McCormick, S. F., 1987, *Multigrid Methods*, SIAM Frontiers in Applied Mathematics, Philadelphia, PA.

McLellan, G. W., and Shand, E. B., 1984, *Glass Engineering Handbook*, McGraw-Hill, New York, pp. 2; 8-10.

Palik, E. D., 1985, *Handbook of Optical Constants of Solids*, Academic Press, Orlando, FL, pp. 547-569; 749-763.

Saitoh, T., 1978, "Numerical Method for Multi-dimensional Freezing Problems in Arbitrary Domains," *ASME JOURNAL OF HEAT TRANSFER*, Vol. 100, pp. 294-299.

Shamsundar, N., and Sparrow, E. M., 1975, "Analysis of Multidimensional Phase Change via the Enthalpy Method," *ASME JOURNAL OF HEAT TRANSFER*, Vol. 97, pp. 333-340.

Shamsundar, N., and Sparrow, E. M., 1977, "Effect of Density Change on Multidimensional Phase Change," *ASME JOURNAL OF HEAT TRANSFER*, Vol. 99, pp. 551-557.

Shvarev, K. M., Baum, B. A., and Gel'd, P. V., 1975, "Optical Properties of Liquid Silicon," *Sov. Phys. Solid State*, Vol. 16, No. 11, pp. 2111-2112.

Stultz, T. J., and Gibbons, J. F., 1981, "The Use of Beam Shaping to Achieve Large-Grain CW Laser-Recrystallized Polysilicon on Amorphous Substrates," *Appl. Phys. Lett.*, Vol. 39, No. 6, pp. 498-500.

Tai, Y. C., Mastrangelo, C. H., and Muller, R. S., 1988, "Thermal Conductivity of Heavily Doped Low-Pressure Chemical Vapor Deposited Polycrystalline Silicon Films," *J. Appl. Phys.*, Vol. 63, No. 5, pp. 1442-1447.

Thames, F. C., Thompson, J. F., Mastin, C. W., and Walker, R. L., 1977, "Numerical Solutions for Viscous and Potential Flow About Arbitrary Two-Dimensional Bodies Using Body-Fitted Coordinate Systems," *J. Comp. Phys.*, Vol. 24, pp. 245-273.

Thompson, J. F., Thames, F. C., and Mastin, C. W., 1977a, "Boundary-Fitted Curvilinear Coordinate Systems for Solution of Partial Differential Equations on Fields Containing Any Number of Arbitrary Two-Dimensional Bodies," NASA Report CR-2729.

Thompson, J. F., Thames, F. C., and Mastin, C. W., 1977b, "TOMCAT—A Code for Numerical Generation of Boundary-Fitted Curvilinear Coordinate Systems on Fields Containing Any Number of Arbitrary Two-Dimensional Bodies," *J. Comp. Phys.*, Vol. 24, pp. 274-302.

Thompson, J. F., Warsi, Z. U. A., and Mastin, C. W., 1985, *Numerical Grid Generation*, North-Holland, New York, pp. 122-129, 140-155.

Touloukian, Y. S., 1970, *Thermophysical Properties of Matter, Thermal Conductivity*, IFI-Plenum, New York.

Viskanta, R., and Anderson, E. E., 1975, "Heat Transfer in Semitransparent Materials," *Advances in Heat Transfer*, Vol. 11, pp. 317-440.

Waechter, D., Schvan, P., Thomas, R. E., and Tarr, N. G., 1986, "Modeling of Heat Flow in Multilayer CW Laser-Annealed Structures," *J. Appl. Phys.*, Vol. 59, No. 10, pp. 3371-3374.

APPENDIX A

Validation of the Numerical Algorithm

The front-fixing algorithm for the analysis of phase change

Table A1 Comparison of boundary position using a 9 × 9 inner grid with Ste = 0.1; $\bar{q} = 10$, $k_l/k_s = 3$

\bar{t}	\bar{s}_{an}	\bar{s}_{num}	ϵ_{min}	ϵ_{max}	ϵ_{avg}
.70000	1.131436	1.133376	0.39	1.57	0.79
.97100	1.332573	1.335433	0.50	1.90	0.98
1.38100	1.589198	1.593582	0.49	1.94	1.05
1.97900	1.902411	1.909128	0.42	1.88	1.08
2.84299	2.280184	2.290278	0.34	1.79	1.10
3.84299	2.651042	2.664909	0.26	1.71	1.13
4.84301	2.976046	2.993487	0.20	1.64	1.14
5.84304	3.268896	3.289786	0.15	1.59	1.16
7.38305	3.674512	3.700650	0.08	1.61	1.18
9.38308	4.142423	4.175100	0.00	1.68	1.19
11.38312	4.562602	4.600953	0.05	1.73	1.21

Table A2 Comparison of boundary position using a 17 × 17 inner grid with Ste = 0.1; $\bar{q} = 10$, $k_l/k_s = 3$

\bar{t}	\bar{s}_{an}	\bar{s}_{num}	ϵ_{min}	ϵ_{max}	ϵ_{avg}
.60000	1.047057	1.046788	0.00	0.31	0.12
.70000	1.131436	1.130213	0.00	0.42	0.16
.86500	1.257734	1.256000	0.00	0.50	0.18
1.06499	1.395582	1.393490	0.01	0.53	0.19
1.32399	1.556054	1.553759	0.00	0.54	0.20
1.63399	1.728650	1.726366	0.00	0.53	0.19
2.03399	1.928662	1.926659	0.00	0.51	0.19
2.52400	2.148456	2.147035	0.00	0.47	0.19
3.11000	2.384857	2.384319	0.04	0.43	0.20
3.80400	2.637559	2.638187	0.00	0.38	0.20
4.62199	2.907344	2.909412	0.01	0.37	0.22
5.55799	3.188164	3.191874	0.02	0.41	0.24
6.55801	3.463123	3.468529	0.04	0.45	0.25
7.55803	3.717802	3.724826	0.01	0.48	0.26
8.55806	3.956120	3.964680	0.00	0.51	0.28
9.55808	4.180875	4.190897	0.01	0.54	0.29
10.5581	4.394194	4.405563	0.00	0.56	0.30
11.5581	4.597540	4.610283	0.01	0.57	0.31

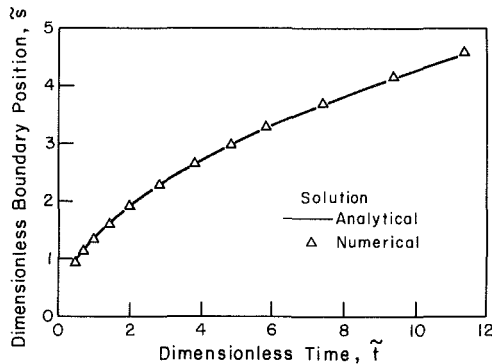


Fig. A1 Plot of phase boundary position \bar{s} as a function of time, \bar{t} for Ste = 0.1, $\bar{q} = 10$, $k_l/k_s = 3$; a 9 × 9 finite difference grid was used in the inner region

in two dimensions was validated by comparing the numerical result to a known analytical solution. The sole exact solution that is available for this purpose describes freezing by a line heat sink in an infinite medium with cylindrical symmetry (Carslaw and Jaeger, 1959). For a heat sink of strength q , in a medium of constant density at an initial temperature $T_\infty > T_m$, the nondimensional heat sink strength, \bar{q} , is

$$\bar{q} = \frac{q}{4\pi k_s (T_\infty - T_m)} \quad (A1)$$

and the Stefan number

$$Ste = \frac{c_{p,s} (T_\infty - T_m)}{L} \quad (A2)$$

The comparison between the analytical solution and the numerical solution that was obtained using a 9 × 9 inner grid, for Ste = 0.1, $\bar{q} = 10$, and $k_l/k_s = 3$ is shown in Table A1. It can be seen that the maximum error is less than 2 percent. For the same set of parameters, Table A2 compares the analytical solution with the numerical solution that was obtained on a 17 × 17 inner grid. The increased number of time steps is the result of the reduction of the maximum time step allowable. The maximum error is decreased, to less than 0.6 percent. Figure A1 shows the dimensionless phase boundary location, as a function of the dimensionless time, for the 9 × 9 inner computational grid.

APPENDIX B

Material Properties Used in the Calculations

B.1 Optical Properties. The real part of the silicon refractive index is a linear function of temperature between approximately 300 and 1000 K (Jellison and Burke, 1986; Jellison, 1984).

$$n_{si}(\lambda, T) = n_{si}^0(\lambda) + a_n(\lambda) (T - 300) \quad (B1)$$

The coefficient $a_n(\lambda)$ is a fifth-order polynomial of the wavelength λ . The extinction coefficient, k_{si}^{ext} , is given by the following expression:

$$k_{si}^{ext}(\lambda, T) = k_{si}^0(\lambda) \exp(T - 273/430) \quad (B2)$$

The liquid refractive index at the blue ($\lambda_b = 488$ nm) wavelength has been measured by Shvarev et al. (1975):

$$\hat{n}_l = 2.2 + \hat{f}4.4 \quad (B3)$$

The glass substrate and the encapsulating layer are transparent in the visible region where the annealing laser source operates, but absorbing in the infrared and ultraviolet ranges that contribute to thermal emission. These layers were assumed to have a common complex refractive index, independent of temperature, but a function of wavelength, taken from Palik (1985).

B.2 Thermal Properties. The silicon thermal conductivity varies with temperature (Touloukian, 1970):

$$k_{si,s}(T) = 2.99 \times 10^4 / (T - 99) \text{ (W/m/K)} \quad (B4)$$

The liquid silicon thermal conductivity $k_{si,l} = 67$ W/m/K. The solid silicon volumetric specific heat is:

$$\rho_{si,s}(T) c_{p,si,s}(T) = 1.4743 \times 10^6 + \frac{0.17066 \times 10^6}{300} \frac{J}{m^3K} \quad (B5)$$

The glass volumetric specific heat, $\rho_{enc}(T) c_{p,enc}(T) = \rho_{ss}(T) c_{p,ss}(T) = 2.64 \times 10^6$ J/m³K and the thermal conductivity $k_{enc}(T) = k_{ss} = 1.4$ W/m/K.

The latent heat of fusion $L = 1.4 \times 10^6$ J/kg.

This section contains shorter technical papers. These shorter papers will be subjected to the same review process as that for full papers.

A Solution for the Parallel-Flow Regenerator

F. E. Romie¹

Introduction

Regenerators are characterized by the thermal capacitance of their matrices, which supply or accept heat from two fluids, a and b , that enter at different but constant temperatures and flow, alternately, through the same flow passages for time periods t_a and t_b . For parallel-flow regenerators the fluids flow through the passages in the same direction. Steady-state periodic operation is attained after a sufficient number of alternating periods following start-up.

The purpose of this note is to give a solution for the thermal effectiveness and the fluid and matrix temperatures for the parallel-flow regenerator operating under steady-state periodic conditions. The solution is restricted to equal fluid capacitance rates, $(wc)_a = (wc)_b = wc$, and equal conductances, $(hA)_a = (hA)_b = hA$, for transfer of heat between the fluids and the matrix. Thus, for heat transfer, the fluids are differentiated only by their inlet temperatures and flow periods, which, in general, are different. The convention is adopted that the subscript a is assigned such that t_a/t_b does not exceed unity.

Hausen (1983), using a different mathematical approach, finds the solution under the additional constraint that $t_a/t_b = 1$. He shows, as is true of the recuperator, that a regenerator operating with parallel flow has a thermal effectiveness less than would be obtained with counterflow. Baclic and Heggs (1986) treat the parallel-flow regenerator with $\Lambda \equiv hA/wc \rightarrow \infty$. At the limit the local difference between the fluid and matrix temperatures is zero and in this extreme case the thermal effectiveness can be unity over certain ranges of other parameters.

A solution without the restrictions of equal capacitance rates and conductances can be obtained using the methods employed by Romie and Baclic (1988) for the asymmetric counterflow regenerator. However, the parallel-flow regenerator finds little or no application in technology and the main motivation for this note is the simplicity of the solution presented.

The Differential Equations

The regenerator analyzed is defined by the following idealizations: (1) The capacitance rates, wc , thermal conductances, hA , and matrix thermal capacitance, WC , are uniform and

constant. (2) No heat is conducted in the matrix material in the direction of fluid flow. (3) No resistance is offered by the matrix material to heat flow in the direction normal to fluid flow. (4) The thermal capacitances at the contained fluids are negligibly small compared to the thermal capacitance of the containing matrix. This latter idealization means, in effect, that the fluids must be gases and that transit times for gas particles to flow through the matrix must be negligibly small compared to the flow periods. (Operating conditions for which this fourth idealization is not required are described at the end of this note.)

With these idealizations, energy balances give two equations applicable during period a :

$$\frac{\partial \tau_a}{\partial (\Lambda_a y)} = T_a - \tau_a = -\frac{\partial T_a}{\partial (\Pi_a x)} \quad (1)$$

The two equations applicable during period b are:

$$\frac{\partial \tau_b}{\partial (\Lambda_b y)} = T_b - \tau_b = -\frac{\partial T_b}{\partial (\Pi_b x)} \quad (2)$$

In these equations, x is the fractional completion of a period ($x = t/t_a$ during period a and $x = t/t_b$ during period b) and y is the fractional distance through the matrix of flow length L , $\Lambda_a = (hA)_a/(wc)_a$, $\Lambda_b = (hA)_b/(wc)_b$, $\Pi_a = (hA)_a t_a/WC$ and $\Pi_b = (hA)_b t_b/WC$. Due to the restrictive conditions mentioned above, $\Lambda_a = \Lambda_b = \Lambda$ and $\Pi_a/\Pi_b = t_a/t_b$. The equations are linear and no loss of generality is incurred by using inlet gas temperatures of 0 and 1 for τ_a and τ_b . T_a and T_b are matrix temperatures during periods a and b .

Functions Used

The Anzelius-Schumann functions, $F_0(u, v)$ and $G_0(u, v)$ (Romie, 1987) are used to express the sought solution. The functions satisfy two equations,

$$\frac{\partial G_0(u, v)}{\partial v} = F_0 - G_0 = \frac{\partial F_0(u, v)}{\partial u} \quad (3)$$

with $F_0(0, v) = 1$ and $G_0(u, 0) = 0$. An integral used in this note is

$$\int_0^u G_0(z, v) dz = -F_1(u, v) + v \quad (4)$$

Numerical values of the required functions can be found by evaluating three functions:

$$G_{-1}(u, v) = \exp(-u-v) I_0(2\sqrt{uv}) \quad (5)$$

$$F_{-1}(u, v) = \exp(-u-v) (u/v)^{1/2} I_1(2\sqrt{uv}) \quad (6)$$

$$G_0(u, v) = \exp(-u-v) \sum_{r=0}^{\infty} \left(\frac{v}{u}\right)^{(r+1)/2} I_{r+1}(2\sqrt{uv}) \quad (7)$$

Using these functions gives

$$F_0(u, v) = G_0(u, v) + G_{-1}(u, v) \quad (8)$$

¹ Palos Verdes Estates, CA 90274.

Contributed by the Heat Transfer Division of the THE AMERICAN SOCIETY OF MECHANICAL ENGINEERS. Manuscript received by the Heat Transfer Division November 1990; revision received July 29, 1991. Keywords: Heat Exchangers, Thermal Energy Storage, Transient and Unsteady Heat Transfer.

$$F_1(u, v) = (v - u)G_0(u, v) + v(G_{-1} + F_{-1}) \quad (9)$$

I_r is the modified Bessel function of the first kind, r th order, and u and v are positive.

Solution of Equations

Consider a gas at unity temperature flowing through the matrix also at unity temperature. At time zero the gas entrance temperature is stepped to zero. The matrix and gas temperature responses to this excitation are

$$T_n = \dot{F}_0(\Pi_n t / t_n, \Lambda y) \quad (10)$$

$$\tau_n = G_0(\Pi_n t / t_n, \Lambda y) \quad (11)$$

In these equations the subscript n is either a or b and t can have any positive value. The negative of the excitation produces the negative of these responses.

The inlet gas temperature excitation for the regenerator is a periodic rectangular wave of unit height with a trough duration Π_a and peak duration Π_b . The steady-state periodic solutions during period a at time $\Pi_a x$ are found by summing the responses to all excitations preceding the time $\Pi_a x$.

$$\tau_a(x, y) = \sum_{m=0}^{\infty} (G_0(\Pi_a x + m(\Pi_a + \Pi_b), \Lambda y) - G_0(\Pi_a x + \Pi_b + m(\Pi_a + \Pi_b), \Lambda y)) \quad (12)$$

$$T_a(x, y) = \sum_{m=0}^{\infty} (F_0(\Pi_a x + m(\Pi_a + \Pi_b), \Lambda y) - F_0(\Pi_a x + \Pi_b + m(\Pi_a + \Pi_b), \Lambda y)) \quad (13)$$

For initial matrix and gas temperature zero a unit step increase of inlet gas temperature produces the responses,

$$T_n = 1 - F_0(\Pi_n t / t_n, \Lambda y) \quad (14)$$

$$\tau_n = 1 - G_0(\Pi_n t / t_n, \Lambda y) \quad (15)$$

Summing responses to all excitations preceding the time $\Pi_b x$ gives the temperatures during period b .

$$\tau_b(x, y) = 1 - \sum_{m=0}^{\infty} (G_0(\Pi_b x + m(\Pi_a + \Pi_b), \Lambda y) - G_0(\Pi_b x + \Pi_a + m(\Pi_a + \Pi_b), \Lambda y)) \quad (16)$$

$$T_b(x, y) = 1 - \sum_{m=0}^{\infty} (F_0(\Pi_b x + m(\Pi_a + \Pi_b), \Lambda y) - F_0(\Pi_b x + \Pi_a + m(\Pi_a + \Pi_b), \Lambda y)) \quad (17)$$

These solutions satisfy Eqs. (1) and (2) and the conditions $\tau_a(x, 0) = 0$ during period a and $\tau_b(x, 0) = 1$ during period b . Also the matrix temperature distribution at the end of a period is the matrix temperature distribution at the beginning of the succeeding period; $T_a(1, y) = T_b(0, y)$ and $T_b(1, y) = T_a(0, y)$. Note that the start-up transient can be obtained using the preceding method of solution.

With adoption of the convention regarding assignment of the subscript a and the use of 0 and 1 for inlet gas temperatures, the thermal effectiveness, ϵ , is the time-mean temperature of the gas leaving the matrix during period a .

$$\epsilon = \int_0^1 \tau_a(x, 1) dx \quad (18)$$

Using Eqs. (4) and (12) for the integration gives

$$\epsilon = \frac{1}{\Pi_a} \sum_{m=0}^{\infty} (F_1(m(\Pi_a + \Pi_b), \Lambda) - F_1(\Pi_a + m(\Pi_a + \Pi_b), \Lambda) - F_1(\Pi_b + m(\Pi_a + \Pi_b), \Lambda) + F_1((m+1)(\Pi_a + \Pi_b), \Lambda)) \quad (19)$$

The magnitudes of the change in enthalpy of the mass of gas that passes through the matrix during a flow period and the net heat transferred between the gas and matrix during the period are equal and necessarily the same for both periods.

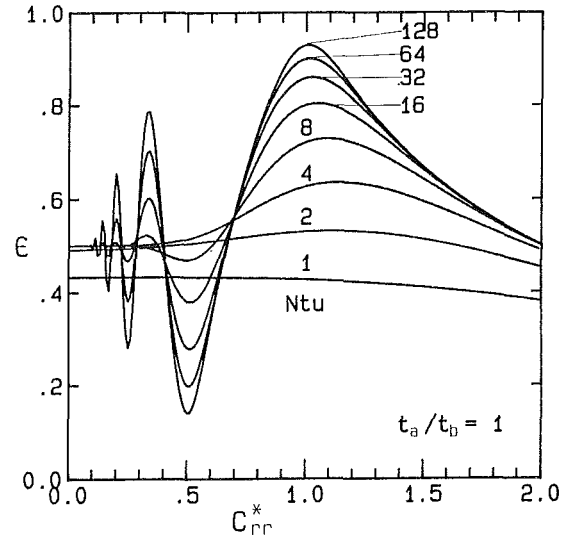


Fig. 1 Thermal effectiveness with $t_a/t_b = 1$

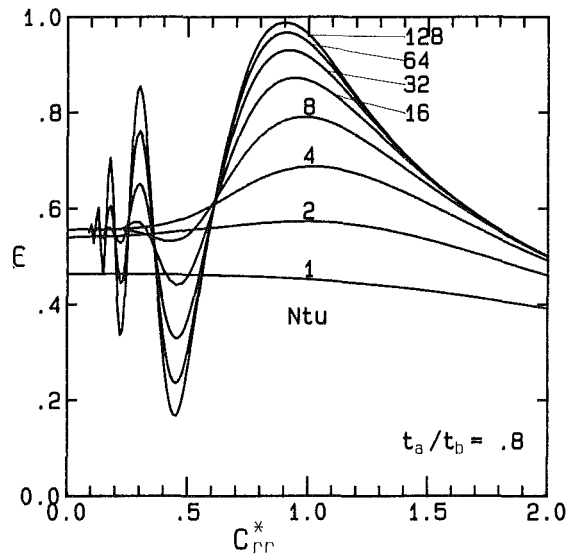


Fig. 2 Thermal effectiveness with $t_a/t_b = 0.8$

The net heat, Q , transferred during a period is

$$Q = \epsilon(wct)_a(\tau_{hin} - \tau_{cin}) \quad (20)$$

in which τ_{hin} and τ_{cin} are the actual hot and cold inlet temperatures.

Results and Discussion

Figures 1 and 2 give the thermal effectiveness for, respectively, $t_a/t_b = 1$ and 0.8. The abscissa is $C_{rr}^* = \Pi_a/\Lambda_a$ and the parameter differentiating the curves is $Ntu = \Lambda_a/(1 + \Pi_a/\Pi_b)$. For the restrictions of this note, $C_{rr}^* = wct_a/WC$ and $Ntu = \Lambda/(1 + t_a/t_b)$. The thermal effectiveness given in Fig. 1 ($t_a/t_b = 1$) is in agreement with the results presented by Hausen. The figures show that the effectiveness can either increase or decrease with increasing Ntu depending on the value of C_{rr}^* . For large Ntu the peaks in Fig. 1 occur at $C_{rr}^* = 1, 1/3, 1/5, \dots$. The peak magnitudes decrease rapidly as C_{rr}^* becomes small. At the limit, $C_{rr}^* = 0$, the effectiveness, as noted by Hausen, is given by the expression for the effectiveness of the parallel-flow recuperator; $\epsilon = (1 - \exp(-Ntu(1 + C_{rr}^*)))/(1 + C_{rr}^*)$. Here $C_{rr}^* = \Pi_a\Lambda_b/(\Pi_b\Lambda_a)$ and, for this note, equals t_a/t_b . For both counterflow and parallel-flow regenerators the

Table 1 Comparison of parallel-flow, ϵ_p , and counterflow, ϵ_c , effectiveness at $C_{rr}^* = 1$

Ntu	$t_a/t_b = 1$		$t_a/t_b = 0.8$	
	ϵ_p	ϵ_c	ϵ_p	ϵ_c
1	0.427	0.466	0.452	0.486
2	0.531	0.601	0.573	0.630
4	0.628	0.709	0.688	0.744
8	0.722	0.790	0.790	0.828
16	0.801	0.850	0.867	0.886
32	0.859	0.893	0.916	0.924
64	0.900	0.925	0.945	0.949
128	0.929	0.946	0.963	0.965

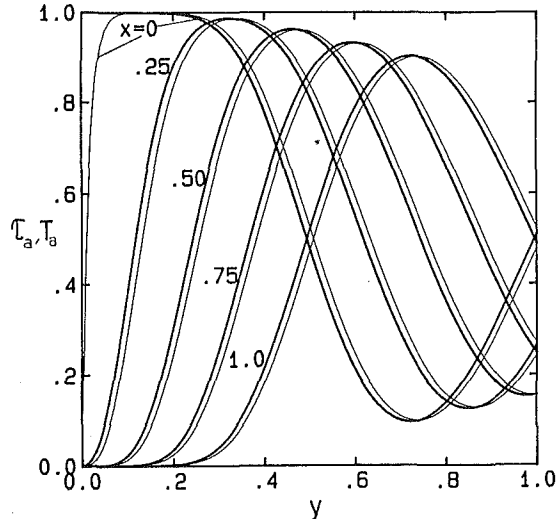


Fig. 3 Gas (thin lines) and matrix temperature distributions during period a with $Ntu = 32$, $C_{rr}^* = 0.5$, and $t_a/t_b = 1$

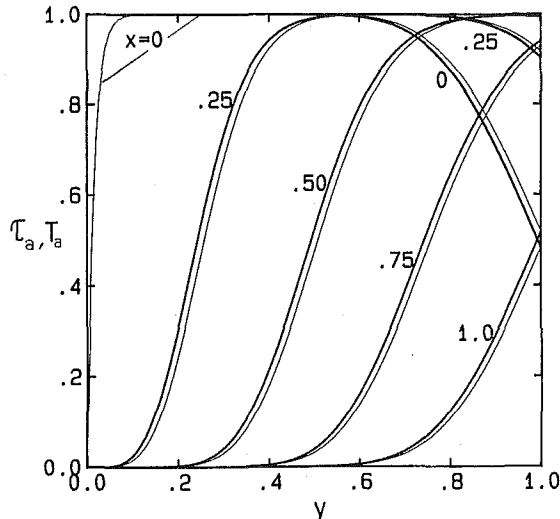


Fig. 4 Gas (thin lines) and matrix temperature distributions during period a with $Ntu = 32$, $C_{rr}^* = 1.0$, and $t_a/t_b = 1$

product ϵC_{rr}^* is the capacitance utilization (Romie, 1979), which cannot exceed unity. Thus for $C_{rr}^* > 1$ the effectiveness cannot exceed $1/C_{rr}^*$.

Table 1 gives a comparison of the thermal effectiveness of parallel-flow and counterflow regenerators at $C_{rr}^* = 1$. The effectiveness of the counterflow regenerator increases monotonically with decreasing C_{rr}^* and becomes equal to the effectiveness of the counterflow recuperator at $C_{rr}^* = 0$ ($\epsilon_c = Ntu / (1 + Ntu)$ at $C_{rr}^* = 0$ if $t_a/t_b = 1$). As indicated above, for $C_{rr}^* > 1$ the effectiveness of both types of regenerator is asymptotic to the curve $\epsilon = 1/C_{rr}^*$.

Figures 3 and 4 show matrix and gas temperature distributions for $Ntu = 32$ and $t_a/t_b = 1$ at five times during period a . Figure 3 is for $C_{rr}^* = 0.5$, which corresponds to the approximate minimum effectiveness for $Ntu = 32$. Figure 4 is for $C_{rr}^* = 1$, which corresponds to the maximum effectiveness. Note that Figs. 3 and 4 give the temperature of the exiting ($y = 1$) gas at five times during period a .

The supply of gas a or gas b to the regenerator is controlled by a two-position valve. Similarly the gas leaving the regenerator is controlled by a valve that diverts the gas to an a or b gas duct. If, following operation of the upstream valve, the operation of the downstream valve is delayed by the time it takes the newly admitted gas to replace the resident gas, then (ideally) no mixing of the two gases will occur. (The inlet gas pressures are assumed to be equal and mixing in the plenums and flow passages is assumed not to occur.) With this delay it can be shown that the fourth idealization is not required and therefore the fluids need not be restricted to gases. No valve operation mode that avoids mixing of the admitted gas and resident gas is available to the counterflow regenerator.

References

- Bacic, B. S., and Heggs, P. J., 1986, "Unidirectional Thermal Regenerator With Vanishing Transfer Potential in Both Periods," *Zeitschrift für Angewandte Mathematik und Mechanik*, Vol. 66, pp. 356-360.
- Hausen, H., 1983, *Heat Transfer in Counterflow, Parallel Flow and Cross Flow*, McGraw-Hill, New York, pp. 381-391.
- Romie, F. E., 1979, "Periodic Thermal Storage: the Regenerator," *ASME JOURNAL OF HEAT TRANSFER*, Vol. 101, pp. 726-731.
- Romie, F. E., 1987, "Two Functions Used in the Analysis of Crossflow Exchangers, Regenerators, and Related Equipment," *ASME JOURNAL OF HEAT TRANSFER*, Vol. 109, pp. 518-521.
- Romie, F. E., and Bacic, B. S., 1988, "Methods for Rapid Calculation of the Operation of Asymmetric Counterflow Regenerators," *ASME JOURNAL OF HEAT TRANSFER*, Vol. 110, pp. 785-788.

Vortex Generator Induced Heat Transfer Augmentation Past a Rib in a Heated Duct Air Flow

T. A. Myrum,¹ S. Acharya,¹ S. Inamdar,¹ and A. Mehrotra¹

Nomenclature

- c_p = constant-pressure specific heat of air
- d = diameter of the cylindrical vortex generator
- D_h = hydraulic diameter = 10.2 cm
- h = rib height
- $h(x)$ = local heat transfer coefficient = $q_c(x) / (T_w(x) - T_b(x))$
- k = air thermal conductivity at $(T_{b,in} + T_b(L_I)) / 2$
- $k(x)$ = air thermal conductivity at $(T_w(x) + T_b(x)) / 2$
- L = downstream displacement of the rod from the rib
- L_I = length over which the average Nusselt number is computed
- \dot{m} = mass flow rate
- $Nu(x)$ = local Nusselt number = $h(x)D_h/k(x)$
- \bar{Nu} = average Nusselt number = $(D_h/k) \int_0^{L_I} q_c(x) dx / \int_0^{L_I} (T_w(x) - T_b(x)) dx$

¹Mechanical Engineering Department, Louisiana State University, Baton Rouge, LA 70803.

Contributed by the Heat Transfer Division of the AMERICAN SOCIETY OF MECHANICAL ENGINEERS. Manuscript received by the Heat Transfer Division December 3, 1990; revision received July 1, 1991. Keywords: Augmentation and Enhancement, Flow Separation, Forced Convection.

Table 1 Comparison of parallel-flow, ϵ_p , and counterflow, ϵ_c , effectiveness at $C_{rr}^* = 1$

Ntu	$t_a/t_b = 1$		$t_a/t_b = 0.8$	
	ϵ_p	ϵ_c	ϵ_p	ϵ_c
1	0.427	0.466	0.452	0.486
2	0.531	0.601	0.573	0.630
4	0.628	0.709	0.688	0.744
8	0.722	0.790	0.790	0.828
16	0.801	0.850	0.867	0.886
32	0.859	0.893	0.916	0.924
64	0.900	0.925	0.945	0.949
128	0.929	0.946	0.963	0.965

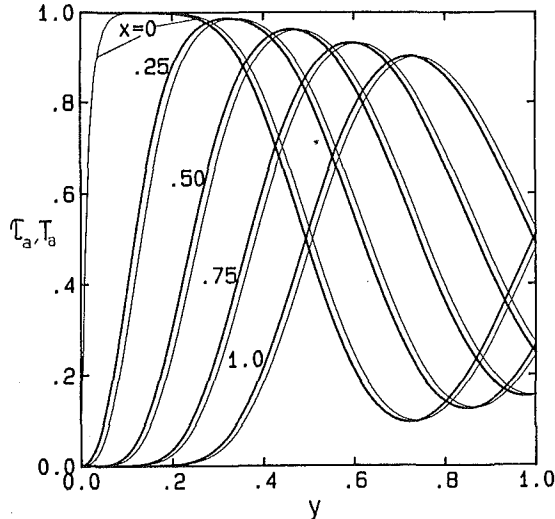


Fig. 3 Gas (thin lines) and matrix temperature distributions during period a with $Ntu = 32$, $C_{rr}^* = 0.5$, and $t_a/t_b = 1$

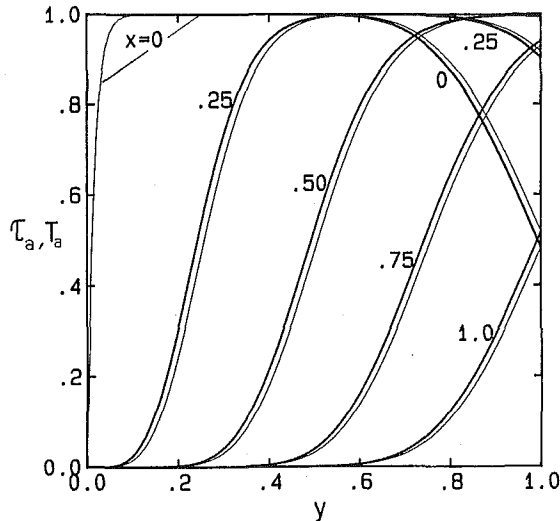


Fig. 4 Gas (thin lines) and matrix temperature distributions during period a with $Ntu = 32$, $C_{rr}^* = 1.0$, and $t_a/t_b = 1$

product ϵC_{rr}^* is the capacitance utilization (Romie, 1979), which cannot exceed unity. Thus for $C_{rr}^* > 1$ the effectiveness cannot exceed $1/C_{rr}^*$.

Table 1 gives a comparison of the thermal effectiveness of parallel-flow and counterflow regenerators at $C_{rr}^* = 1$. The effectiveness of the counterflow regenerator increases monotonically with decreasing C_{rr}^* and becomes equal to the effectiveness of the counterflow recuperator at $C_{rr}^* = 0$ ($\epsilon_c = Ntu / (1 + Ntu)$ at $C_{rr}^* = 0$ if $t_a/t_b = 1$). As indicated above, for $C_{rr}^* > 1$ the effectiveness of both types of regenerator is asymptotic to the curve $\epsilon = 1/C_{rr}^*$.

Figures 3 and 4 show matrix and gas temperature distributions for $Ntu = 32$ and $t_a/t_b = 1$ at five times during period a . Figure 3 is for $C_{rr}^* = 0.5$, which corresponds to the approximate minimum effectiveness for $Ntu = 32$. Figure 4 is for $C_{rr}^* = 1$, which corresponds to the maximum effectiveness. Note that Figs. 3 and 4 give the temperature of the exiting ($y = 1$) gas at five times during period a .

The supply of gas a or gas b to the regenerator is controlled by a two-position valve. Similarly the gas leaving the regenerator is controlled by a valve that diverts the gas to an a or b gas duct. If, following operation of the upstream valve, the operation of the downstream valve is delayed by the time it takes the newly admitted gas to replace the resident gas, then (ideally) no mixing of the two gases will occur. (The inlet gas pressures are assumed to be equal and mixing in the plenums and flow passages is assumed not to occur.) With this delay it can be shown that the fourth idealization is not required and therefore the fluids need not be restricted to gases. No valve operation mode that avoids mixing of the admitted gas and resident gas is available to the counterflow regenerator.

References

- Bacic, B. S., and Heggs, P. J., 1986, "Unidirectional Thermal Regenerator With Vanishing Transfer Potential in Both Periods," *Zeitschrift für Angewandte Mathematik und Mechanik*, Vol. 66, pp. 356-360.
- Hausen, H., 1983, *Heat Transfer in Counterflow, Parallel Flow and Cross Flow*, McGraw-Hill, New York, pp. 381-391.
- Romie, F. E., 1979, "Periodic Thermal Storage: the Regenerator," *ASME JOURNAL OF HEAT TRANSFER*, Vol. 101, pp. 726-731.
- Romie, F. E., 1987, "Two Functions Used in the Analysis of Crossflow Exchangers, Regenerators, and Related Equipment," *ASME JOURNAL OF HEAT TRANSFER*, Vol. 109, pp. 518-521.
- Romie, F. E., and Bacic, B. S., 1988, "Methods for Rapid Calculation of the Operation of Asymmetric Counterflow Regenerators," *ASME JOURNAL OF HEAT TRANSFER*, Vol. 110, pp. 785-788.

Vortex Generator Induced Heat Transfer Augmentation Past a Rib in a Heated Duct Air Flow

T. A. Myrum,¹ S. Acharya,¹ S. Inamdar,¹ and A. Mehrotra¹

Nomenclature

- c_p = constant-pressure specific heat of air
- d = diameter of the cylindrical vortex generator
- D_h = hydraulic diameter = 10.2 cm
- h = rib height
- $h(x)$ = local heat transfer coefficient = $q_c(x) / (T_w(x) - T_b(x))$
- k = air thermal conductivity at $(T_{b,in} + T_b(L_I)) / 2$
- $k(x)$ = air thermal conductivity at $(T_w(x) + T_b(x)) / 2$
- L = downstream displacement of the rod from the rib
- L_I = length over which the average Nusselt number is computed
- \dot{m} = mass flow rate
- $Nu(x)$ = local Nusselt number = $h(x)D_h/k(x)$
- \bar{Nu} = average Nusselt number = $(D_h/k) \int_0^{L_I} q_c(x) dx / \int_0^{L_I} (T_w(x) - T_b(x)) dx$

¹Mechanical Engineering Department, Louisiana State University, Baton Rouge, LA 70803.

Contributed by the Heat Transfer Division of the AMERICAN SOCIETY OF MECHANICAL ENGINEERS. Manuscript received by the Heat Transfer Division December 3, 1990; revision received July 1, 1991. Keywords: Augmentation and Enhancement, Flow Separation, Forced Convection.

$q_c(x)$ = convective heat flux corrected for radiation and conduction losses

Re = Reynolds number = UD_h/ν

s = rod-rib spacing

$T_b(x)$ = local bulk temperature = $(w/\dot{m}c_p) \int_0^x q_c(x') dx' +$

$T_{b,in}$

$T_{b,in}$ = measured inlet bulk temperature

$T_w(x)$ = local shim temperature

U = average duct velocity

w = channel width = 30 cm

x = streamwise (axial) coordinate

ν = kinematic viscosity at $(T_{b,in} + T_b(L_I))/2$

Introduction

The present investigation represents the initial phase of a comprehensive experimental program designed to study the potential for increasing the heat transfer per unit pressure drop in a ribbed duct by positioning vortex generators at key locations in the flow. In particular, the present investigation consists of a rib positioned at the inlet to a rectangular test section with uniform heating at its bottom wall. Local and average Nusselt number results are obtained for a circular rod positioned either immediately above or just downstream of the rib. Of particular interest are the effects of the dimensionless rod-rib spacing, s/h , the dimensionless rod diameter, d/h , and the Reynolds number on the local and average Nusselt numbers. Pressure measurements have been omitted because, owing to the small pressure drop across a single rod-rib configuration, the uncertainty is significant (as large as ± 100 percent at a Reynolds number of 3300).

To these authors' knowledge, no studies dealing with the present rod-rib configuration are reported in the open literature. Relevant studies are those for reattaching shear layers behind backward-facing steps, for which Bradshaw (1975), Eaton and Johnston (1981), Aung and Watkins (1979), and Aung (1983) provide comprehensive reviews. The studies of Sparrow and Tao (1983, 1984) and McEntire and Webb (1990) are representative of local heat (mass) transfer studies for separated flows past multiple ribs and two-dimensional protruding heat sources, respectively.

As for the effect of circular rods on the heat transfer (mass transfer) from smooth surfaces, the studies of Thomas (1965, 1966), Watson and Thomas (1967), and Karniadakis et al. (1988) showed that for laminar flow, circular wires placed above a smooth horizontal surface resulted in increased heat transfer (mass transfer). This was attributed to a premature transition to turbulent flow conditions.

The Experiments

The experiments were conducted in an insulated, asymmetrically heated test section (101.6 cm long \times 30 cm wide \times 6.10 cm high), which was located after a 40 hydraulic diameter long flow-development section. A constant heat flux boundary condition at the bottom wall of the test section was simulated by dissipating d-c current in a 0.025-mm-thick stainless steel shim.

Chromel-constantan thermocouples (0.076 mm dia) spot welded to the underside of the shim at 15 mm intervals along the centerline were used to measure the local shim temperatures. Thermocouples positioned at off-centerline locations confirmed that the spanwise temperature variation was less than 4 percent of the minimum shim-to-bulk fluid temperature difference. The maximum effect of the heating current on the measured thermocouple voltage was less than 12 μ V (0.2°C), which is within the uncertainty of the temperature measurement.

The rib, made from cold-drawn steel, had a square profile and was 6.35 mm on a side. It spanned the entire test section width and was positioned with its upstream face flush with the leading edge of the shim.

To minimize buoyancy effects, the power supplied to the shim was set to give $Gr_H/(Re_H)^2 < 0.10$, where Gr_H and Re_H are the Grashof and Reynolds numbers, respectively. Both Gr_H and Re_H were based on the duct height, and Gr_H is based on the maximum shim-to-inlet temperature difference.

The local Nusselt number distribution for the heated wall of the test section was determined from the local convective heat flux, $q_c(x)$, and the measured shim temperatures (see Nomenclature). The determination of $q_c(x)$ involved subtracting conduction and radiation heat losses from the local electric heat flux generation, $q_{elec}(x)$, which was verified to be uniform (i.e., less than a 2 percent variation) over the shim surface.

Conduction losses through the bounding walls of the test section were determined at three different axial locations from a finite-difference solution of the two-dimensional (y - z plane) heat conduction between the inner bounding surfaces of the test section and the outer surface of the wooden box surrounding the insulation. It was found that for a given Reynolds number, a single conduction correction factor could be used for the entire test-section length. The conduction heat flux through the walls ranged from 5.40 percent ($Re \approx 24,000$) to 17 percent ($Re \approx 3,300$) of q_{elec} . Axial conduction effects were accounted for by using a finite difference solution for the conduction in the x - y plane and included the stainless steel shim, the plexiglass sheet, to which the shim was attached, and the insulation. Local radiation losses were estimated using $\epsilon = 0.17$ for the shim and $\epsilon = 0.9$ for the plexiglass top wall and side walls. The radiation loss ranged from 5 percent ($Re \approx 24,000$) to 18 percent ($Re \approx 3300$) of q_{elec} .

Experimental Results

Uncertainty and Preliminary Results. Experimental uncertainties were computed using the method of Kline and McClintock (1953). Typically, the uncertainties in the local and average Nusselt numbers were ± 4.5 percent, ± 5.5 percent, and ± 10 percent for $Re \approx 24,000$, 5000, and 3300, respectively. Reproducibility measurements revealed that for $Re \approx 3300$, 5000, and 24,000, the local and average Nusselt numbers could be reproduced to within ± 10 , ± 5 , and ± 5 percent, respectively. The uncertainty in the Reynolds number was ± 3.5 percent (the flow rate was measured using ASME orifice plates).

To test the experimental apparatus and the methods used to account for the heat conduction and radiation losses, a set of data runs was performed for a smooth duct (i.e., no rib or rod). For Reynolds numbers between 3100 and 24,000, it was found that the average Nusselt number for the entire test-section length was within ± 12 percent of that predicted by the correlation of Gnielinski (1976). This is well within the ± 20 percent uncertainty associated with the Gnielinski correlation.

Effect of Rod-Rib Spacing—Local Results. Figure 1 shows that the local Nusselt number distributions for the "rib-only" case and the "rod-rib" cases for all of the s/h values at each Reynolds number have the same general shape. That is, the Nusselt number initially increases in the recirculation region, peaks near the reattachment point, and decays in the redevelopment region.

The increase in Nusselt number toward the rib from its local minimum is believed to be the result of a counterrotating vortex located immediately behind the rib. Sparrow and Tao (1983) observed a similar effect for mass transfer in a multiple-ribbed duct. They documented the presence of the counterrotating vortex using flow visualizations. Baughn et al. (1984) also observed an initial decrease in the local Nusselt number for flows past an abrupt circular channel expansion. They, too,

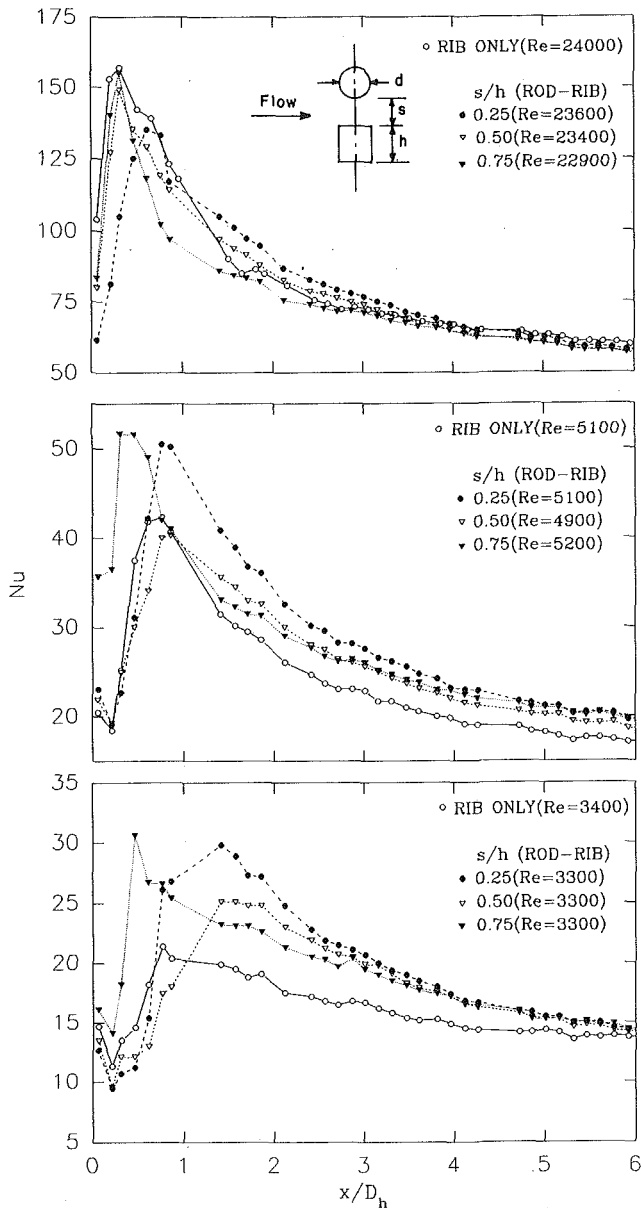


Fig. 1 Effect of rod-rib spacing on the local Nusselt number, $d/h = 0.5$; the x values are measured from the downstream face of the rib

rationalized that the decrease was due to a counterrotating vortex. The absence of the initial decrease for $Re \approx 24,000$ is believed to be caused by a shrinking of the counterrotating vortex at the higher Reynolds number and therefore its presence cannot be detected by the present thermocouple distribution.

Inspection of the "rib-only" results shows that the location of the maximum Nusselt number, hereafter to be loosely referred to as the "reattachment point," for $Re \approx 3300$ and 5000 occurs downstream of that for $Re \approx 24,000$. The flow is fully turbulent for $Re \approx 24,000$, and the much greater "reattachment length" at $Re \approx 3300$ and 5000 would seem to indicate a transitional flow at these Reynolds numbers. It is well known that the reattachment length is much larger in the laminar-transitional regimes (Aung, 1983).

A comparison between the "rod-rib" results and the "rib-only" result in Fig. 1 shows that at the lowest flow rate, the presence of the rod results in considerable Nusselt number enhancement up to about four hydraulic diameters. It is also seen that for $s/h = 0.25$ and 0.5 the "reattachment point" is downstream of that for the "rib-only" case, whereas for s/h

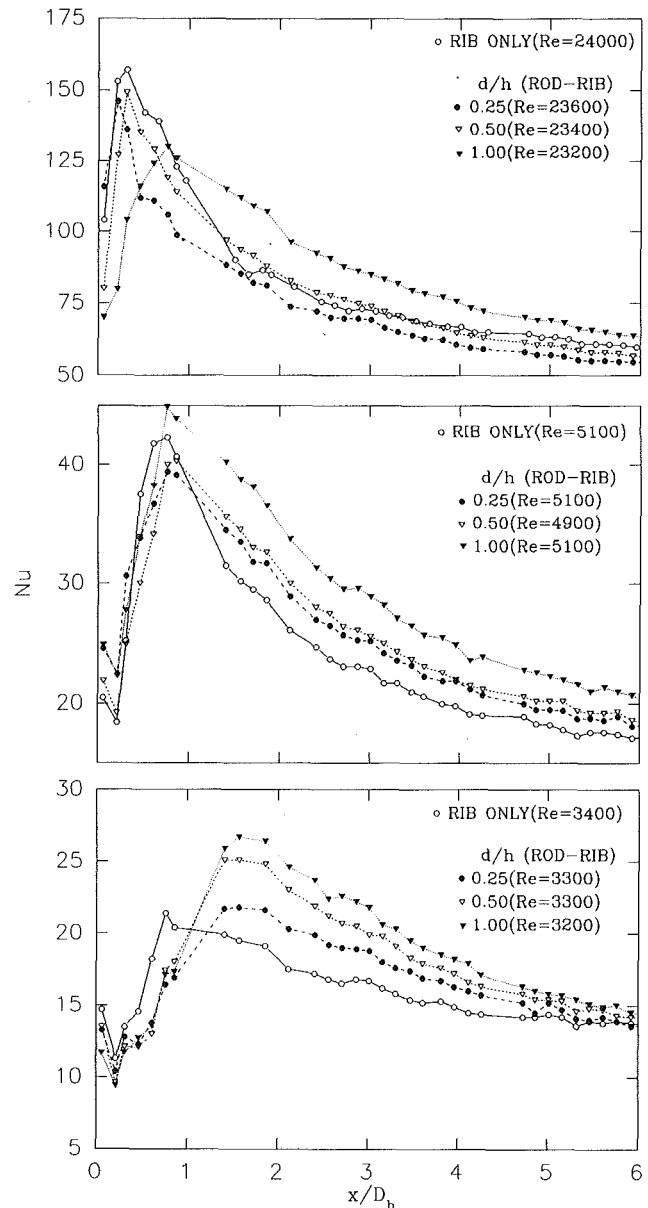


Fig. 2 Effect of rod diameter on the local Nusselt number, $s/h = 0.5$

$= 0.75$, the "reattachment location" is upstream of that for the "rib-only" case.

The above-described behavior can be explained intuitively as follows: At the lowest Reynolds number considered, $Re \approx 3300$, the flow is either in the transitional or in the low-turbulence Reynolds number regime, and the introduction of a vortex generator promotes turbulence, which, in turn, is likely to enhance heat transfer. For $s/h = 0.25$, the vortex generator is in close proximity to the rib, and the shift downstream of the "reattachment" could well be due to the rod-rib acting like a single element. For $s/h = 0.75$, the rod is vertically displaced by a sufficient distance, and acts as a separate entity. Consequently, the reattachment length is much shorter, and in fact, is less than the "rib-only" case. This reduction is either due to the downward deflection of the flow by the rod or due to the interaction of the vortex street behind the rod and the shear layer behind the rib.

For the medium flow rate ($Re \approx 5000$), the general behavior is similar to that at $Re \approx 3300$. The increase in Reynolds number results in decreased "reattachment lengths" for all of the s/h values. The degree of rod-induced enhancement is observed to be less than at the lowest flow rate.

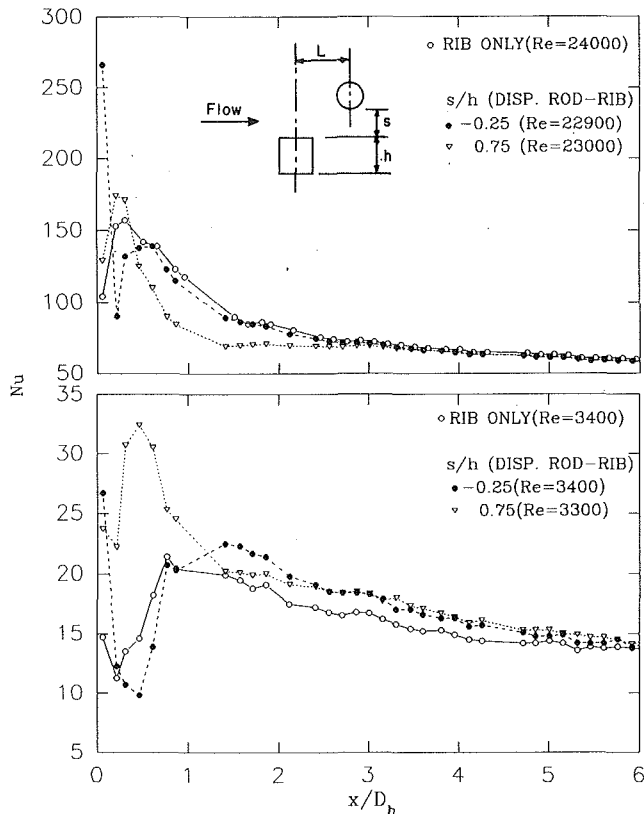


Fig. 3 Effect of rod-rib spacing on the local Nusselt number for a downstream rod, $L/h = 1.75$, $d/h = 0.5$

In contrast to the results for $Re \approx 3300$ and 5000 , the results for $Re \approx 24,000$ show that the presence of the rod, at whatever spacing, causes a slight reduction in the peak Nusselt number. It is also seen that the “reattachment lengths” for $s/h = 0.50$ and 0.75 are nearly identical to each other and to that for the “rib-only” case. On the other hand, reattachment for $s/h = 0.25$ occurs downstream of that for the “rib-only” case.

At $Re \approx 24,000$, the flow is fully turbulent, and the vortex generator does not enhance the turbulence levels or the heat transfer, as it apparently does at the lower Reynolds numbers. The decrease in Nusselt number due to the rib can perhaps be explained by the retardation in local velocity due to the frictional loss associated with the rod.

Effect of Rod Diameter—Local Results. Figure 2 displays the effect of the rod diameter for a fixed rod-rib spacing, $s/h = 0.5$. At the lowest Reynolds number, the reattachment location is shifted downstream relative to the “rib-only” case due to the spacing effect, but the rod diameter has no effect on the reattachment location. Note, however, that the Nusselt numbers increase with increasing rod diameter.

With increasing rod diameter, it is believed that turbulence promotion is enhanced. This belief is supported by earlier studies of flow past a single rod (Tritton, 1960) where the vortex shedding frequency is observed to increase with rod Reynolds number. Higher vortex shedding frequencies are expected to lead to greater unsteadiness and turbulence. This effect promotes higher values of the local heat transfer maximum, and Nu increases with increasing d/h .

At the medium flow rate, for the two smallest diameters, the results appear to be virtually identical, with the peak values lying below that for the “rib-only” case. This is probably due to the reduction in velocities caused by the vortex generator. Beyond reattachment, however, the “rod-rib” results lie above those for the “rib-only” case. The results for the largest diameter are observed to lie above the rest of the results.

Re	L/h	d/h	s/h	$\overline{Nu}/\overline{Nu}_{rib}$	
3,300+	0	0.25	0.25	1.1	
			0.50	1.0	
			0.75	1.1	
	0	0.50	0.25	1.2	
			0.50	1.1	
			0.75	1.2	
	0	1.0	0.50	1.1	
			1.0	1.3	
			1.5	1.3	
	1.75	0.50	-0.25	1.1	
			0.75	1.2	
	5,000+	0	0.25	0.25	1.10
0.50				1.05	
0.75				1.12	
0		0.50	0.25	1.15	
			0.50	1.05	
			0.75	1.13	
0		1.0	0.50	1.17	
			1.0	1.18	
			1.5	1.05	
24,000++		0	0.25	0.25	0.92
				0.50	0.91
				0.75	0.91
	0	0.50	0.25	0.95	
			0.50	0.97	
			0.75	0.90	
0	1.0	0.50	1.01		
		1.0	0.92		
		1.5	0.94		
1.75	0.50	-0.25	0.98		
		0.75	0.82		

* Average includes the rib

+ Average over first four hydraulic diameters

++ Average over first two hydraulic diameters

No diameter effect is observed for the two smallest diameters at $Re \approx 24,000$. However, contrary to the results at the lower Re values, the peak for the largest diameter lies below those for the lower diameters and the “rib-only” case, and the “reattachment point” lies downstream of the other “reattachment points.” It is speculated that the behavior for $d/h = 1.0$ is the result of a reduction in the local velocities due to the frictional loss associated with the increased rod size.

Results for the Displaced Rod—Local Results. Figure 3 examines the effect of s/h for a rod located downstream of the rib. For $s/h = -0.25$, which corresponds to the rod centerline being at the same height as the rib, the Nusselt number has two local peaks, with the first peak being immediately below the rod. It is seen that the magnitude of this peak is considerably higher than the corresponding peaks for the “rib-only” and the $s/h = 0.75$ cases. Since the centerline of the rod for $s/h = -0.25$ corresponds to the top of the rib, it is speculated here that the flow, as it comes off the rib, is deflected by the rod in two directions: downward into the heated shim and upward and around the top of the rod. The first large peak is caused by the premature reattachment of the flow due to the downward deflection of the flow by the rod. With increasing x/D_h , it is seen that the Nusselt number drops off rapidly to a minimum value, which is below the minimum “rib-only” value.

Beyond the minimum point, the Nusselt number recovers and attains a secondary peak which lies above the “rib-only” peak. It is believed that the second peak corresponds to a second reattachment point. The second reattachment point is believed to be caused by the reattachment of the flow that moves over the top of the rod.

For $s/h = 0.75$, the rod is placed above the plane of the

rib, and there is only a single reattachment as in the earlier cases of $L/h = 0$. Beyond reattachment, the Nu curve lies above the other two curves until about $x/D_h = 1.3$ (20 rib heights).

At the highest flow rate, the Nusselt number for $s/h = -0.25$ displays the same behavior that it did at the lowest flow rate, with an initial maximum below the rod, subsequent minimum, and secondary maximum. After the secondary maximum point, the $s/h = -0.25$ results merge with the "rib-only" results.

Average Nusselt Results. Average Nusselt numbers, \overline{Nu} , are presented in Table 1. They have been normalized by \overline{Nu} for the rib. Since the rod effect is confined to the first four hydraulic diameters for $Re \approx 3300$ and 5000 and to the first two hydraulic diameters for $Re \approx 24,000$, in order to obtain a more accurate picture of the effect of the rod on the heat transfer, the average results were obtained by averaging over the first four hydraulic diameters for the two lowest flow rates and over the first two hydraulic diameters for the highest flow rate.

The table shows that the maximum enhancement in \overline{Nu} due to the rod is 30 percent. This occurs at the minimum flow rate, maximum diameter, and spacings of 1.0 and 1.5 rib heights. It is also seen that enhancements of 20 percent are quite common at the lowest flow rate, while enhancements ranging from 15 to 18 percent occur at the medium flow rate. At $Re \approx 24,000$, the effect of the rod degrades heat transfer relative to the "rib-only" case, with this degradation being between 6 and 18 percent. The results for $s/h = 0.75$ and $d/h = 0.5$ show that moving the rod downstream decreases the \overline{Nu} by 8 percent at the highest flow rate, and has no effect on \overline{Nu} for the lowest flow rate.

Acknowledgments

This work was supported by contracts from Gas Research Institute (GRI-5090-260-1961) and NSF (CBT-8800736). Their support is gratefully acknowledged.

References

- Aung, W., and Watkins, C. B., 1979, "Heat Transfer Mechanisms in Separated Forced Convection," in: *Turbulent Forced Convection in Channels and Bundles—Theory and Applications to Heat Exchanges and Nuclear Reactors*, S. Kakac and D. B. Spalding, eds., Hemisphere Publishing Corporation, Washington, DC, pp. 233–256.
- Aung, W., 1983, "Separated Forced Convection," *Proceedings of the ASME-JSME Thermal Engineering Joint Conference*, Vol. 2, pp. 499–516.
- Baughn, J. W., Hoffman, M. A., Takahashi, R. K., and Launder, B. E., 1984, "Local Heat Transfer Downstream of an Abrupt Expansion in a Circular Cylinder With Constant Wall Heat Flux," *ASME JOURNAL OF HEAT TRANSFER*, Vol. 106, pp. 789–796.
- Bradshaw, P., 1975, "Review—Complex Turbulent Flows," *ASME Journal of Fluids Engineering*, Vol. 97, pp. 146–154.
- Eaton, J. K., and Johnston, J. P., 1981, "A Review of Research on Subsonic Turbulent Flow Reattachment," *AIAA J.*, Vol. 19, pp. 1093–1100.
- Gnielinski, V., 1976, "New Equations for Heat and Mass Transfer in Turbulent Pipe and Channel Flow," *Int. J. Chem. Eng.*, Vol. 16, pp. 353–368.
- Karniadakis, G. E., Mikic, B. B., and Patera, A. T., 1988, "Minimum-Dissipation Transport Enhancement by Flow Destabilization: Reynolds Analogy Revisited," *J. Fluid Mech.*, Vol. 192, pp. 365–391.
- Kline, S. J., and McClintock, F. A., 1953, "Estimating Uncertainty in Single-Sample Experiments," *Mechanical Engineering*, Vol. 75, pp. 3–8.
- McEntire, A. B., and Webb, B. W., 1990, "Local Forced Convective Heat Transfer From Protruding and Flush Mounted Two-Dimensional Discrete Heat Sources," *Int. J. Heat Mass Transfer*, Vol. 33, pp. 1521–1533.
- Sparrow, E. M., and Tao, W. Q., 1983, "Enhanced Heat Transfer in a Flat Rectangular Duct With Streamwise-Periodic Disturbances at One Principal Wall," *ASME JOURNAL OF HEAT TRANSFER*, Vol. 105, pp. 851–861.
- Sparrow, E. M., and Tao, W. Q., 1984, "Symmetric vs. Asymmetric Periodic Disturbances at the Walls of a Heated Flow Passage," *Int. J. Heat Mass Transfer*, Vol. 27, pp. 2133–2144.
- Thomas, D. G., 1965, "Forced Convection Mass Transfer: Part II. Effect of Wires Located Near the Edge of the Laminar Boundary Layer on the Rate of Forced Convection From a Flat Plate," *AICHE J.*, Vol. 11, pp. 848–852.
- Thomas, D. G., 1966, "Forced Convection Mass Transfer: Part III. Increased Mass Transfer From a Flat Plate Caused by the Wake from Cylinders Located Near the Edge of the Boundary Layer," *AICHE J.*, Vol. 12, pp. 124–130.

Tritton, D. J., 1960, "Experiments on the Flow Past a Circular Cylinder at Low Reynolds Number," *J. Fluid Mechanics*, Vol. 6, No. 4, pp. 547–558.

Watson, J. S., and Thomas, D. G., 1967, "Forced Convection Mass Transfer: Part IV. Increased Mass Transfer in an Aqueous Medium Caused by Detached Turbulence Promoters in a Rectangular Channel," *AICHE J.*, Vol. 13, pp. 676–677.

Heat Transfer From a Square Source to an Impinging Liquid Jet Confined by an Annular Wall

D. L. Besserman,¹ F. P. Incropera,² and S. Ramadhyani²

Nomenclature

- A_r = area ratio = $\pi(1.9d)^2/L^2$
 d = internal nozzle (jet) diameter
 D_c = diameter of confining (annular) wall
 D_{eff} = effective diameter of square heater = $(\sqrt{2}L + L)/2$
 \bar{h} = average heat transfer coefficient
 k_f = fluid thermal conductivity
 L = width of square heater
 L^* = average radial extent of wall jet
 $Nu_{D_{\text{eff}}}$ = average Nusselt number = $\bar{h}D_{\text{eff}}/k_f$
 Nu_L = average Nusselt number = $\bar{h}L/k_f$
 Pr = Prandtl number
 q = convection heat transfer rate (power dissipation)
 R = radius of round heater
 Re_d = Reynolds number = $u_m d/\nu$
 Re_{L^*} = Reynolds number = $u_m L^*/\nu$
 S = separation from jet exit to impingement surface
 T_o = upstream fluid (jet) temperature
 \bar{T}_s = average surface temperature
 u_m = mean exit velocity of jet
 ν = kinematic viscosity

Introduction

Steady advances in manufacturing technologies related to very large-scale integrated circuit (VLSI) chips are sustaining significant increases in circuit densities. With an attendant increase in power dissipation, related heat fluxes are approaching 5×10^5 W/m², and within this decade, fluxes in excess of 2×10^6 W/m² are anticipated. Dissipation of such fluxes will require a liquid coolant, as well as an effective means of coolant delivery, such as jet impingement. For a scheme in which the jet is separated from the chip by conducting plates (Yamamoto et al., 1987), water may be used as the coolant, but if jet-to-chip contact is desired, a dielectric fluorocarbon must be used (Incropera, 1990).

In high-speed computing and data processing systems, it is desirable to space chips closely in an aligned, planar array for which cooling to each chip may be independently effected by a single circular jet. Manifolding for such an arrangement is likely to involve a concentric discharge tube, which redirects

¹Pratt and Whitney, Hartford, CT 06033.

²Purdue University, W. Lafayette, IN 47907.

Contributed by the Heat Transfer Division of the AMERICAN SOCIETY OF MECHANICAL ENGINEERS. Manuscript received by the Heat Transfer Division October 4, 1990; revision received July 20, 1991. Keywords: Electronic Equipment, Forced Convection, Jets.

rib, and there is only a single reattachment as in the earlier cases of $L/h = 0$. Beyond reattachment, the Nu curve lies above the other two curves until about $x/D_h = 1.3$ (20 rib heights).

At the highest flow rate, the Nusselt number for $s/h = -0.25$ displays the same behavior that it did at the lowest flow rate, with an initial maximum below the rod, subsequent minimum, and secondary maximum. After the secondary maximum point, the $s/h = -0.25$ results merge with the "rib-only" results.

Average Nusselt Results. Average Nusselt numbers, \overline{Nu} , are presented in Table 1. They have been normalized by \overline{Nu} for the rib. Since the rod effect is confined to the first four hydraulic diameters for $Re \approx 3300$ and 5000 and to the first two hydraulic diameters for $Re \approx 24,000$, in order to obtain a more accurate picture of the effect of the rod on the heat transfer, the average results were obtained by averaging over the first four hydraulic diameters for the two lowest flow rates and over the first two hydraulic diameters for the highest flow rate.

The table shows that the maximum enhancement in \overline{Nu} due to the rod is 30 percent. This occurs at the minimum flow rate, maximum diameter, and spacings of 1.0 and 1.5 rib heights. It is also seen that enhancements of 20 percent are quite common at the lowest flow rate, while enhancements ranging from 15 to 18 percent occur at the medium flow rate. At $Re \approx 24,000$, the effect of the rod degrades heat transfer relative to the "rib-only" case, with this degradation being between 6 and 18 percent. The results for $s/h = 0.75$ and $d/h = 0.5$ show that moving the rod downstream decreases the \overline{Nu} by 8 percent at the highest flow rate, and has no effect on \overline{Nu} for the lowest flow rate.

Acknowledgments

This work was supported by contracts from Gas Research Institute (GRI-5090-260-1961) and NSF (CBT-8800736). Their support is gratefully acknowledged.

References

- Aung, W., and Watkins, C. B., 1979, "Heat Transfer Mechanisms in Separated Forced Convection," in: *Turbulent Forced Convection in Channels and Bundles—Theory and Applications to Heat Exchanges and Nuclear Reactors*, S. Kakac and D. B. Spalding, eds., Hemisphere Publishing Corporation, Washington, DC, pp. 233–256.
- Aung, W., 1983, "Separated Forced Convection," *Proceedings of the ASME-JSME Thermal Engineering Joint Conference*, Vol. 2, pp. 499–516.
- Baughn, J. W., Hoffman, M. A., Takahashi, R. K., and Launder, B. E., 1984, "Local Heat Transfer Downstream of an Abrupt Expansion in a Circular Cylinder With Constant Wall Heat Flux," *ASME JOURNAL OF HEAT TRANSFER*, Vol. 106, pp. 789–796.
- Bradshaw, P., 1975, "Review—Complex Turbulent Flows," *ASME Journal of Fluids Engineering*, Vol. 97, pp. 146–154.
- Eaton, J. K., and Johnston, J. P., 1981, "A Review of Research on Subsonic Turbulent Flow Reattachment," *AIAA J.*, Vol. 19, pp. 1093–1100.
- Gnielinski, V., 1976, "New Equations for Heat and Mass Transfer in Turbulent Pipe and Channel Flow," *Int. J. Chem. Eng.*, Vol. 16, pp. 353–368.
- Karniadakis, G. E., Mikic, B. B., and Patera, A. T., 1988, "Minimum-Dissipation Transport Enhancement by Flow Destabilization: Reynolds Analogy Revisited," *J. Fluid Mech.*, Vol. 192, pp. 365–391.
- Kline, S. J., and McClintock, F. A., 1953, "Estimating Uncertainty in Single-Sample Experiments," *Mechanical Engineering*, Vol. 75, pp. 3–8.
- McEntire, A. B., and Webb, B. W., 1990, "Local Forced Convective Heat Transfer From Protruding and Flush Mounted Two-Dimensional Discrete Heat Sources," *Int. J. Heat Mass Transfer*, Vol. 33, pp. 1521–1533.
- Sparrow, E. M., and Tao, W. Q., 1983, "Enhanced Heat Transfer in a Flat Rectangular Duct With Streamwise-Periodic Disturbances at One Principal Wall," *ASME JOURNAL OF HEAT TRANSFER*, Vol. 105, pp. 851–861.
- Sparrow, E. M., and Tao, W. Q., 1984, "Symmetric vs. Asymmetric Periodic Disturbances at the Walls of a Heated Flow Passage," *Int. J. Heat Mass Transfer*, Vol. 27, pp. 2133–2144.
- Thomas, D. G., 1965, "Forced Convection Mass Transfer: Part II. Effect of Wires Located Near the Edge of the Laminar Boundary Layer on the Rate of Forced Convection From a Flat Plate," *AICHE J.*, Vol. 11, pp. 848–852.
- Thomas, D. G., 1966, "Forced Convection Mass Transfer: Part III. Increased Mass Transfer From a Flat Plate Caused by the Wake from Cylinders Located Near the Edge of the Boundary Layer," *AICHE J.*, Vol. 12, pp. 124–130.

Tritton, D. J., 1960, "Experiments on the Flow Past a Circular Cylinder at Low Reynolds Number," *J. Fluid Mechanics*, Vol. 6, No. 4, pp. 547–558.

Watson, J. S., and Thomas, D. G., 1967, "Forced Convection Mass Transfer: Part IV. Increased Mass Transfer in an Aqueous Medium Caused by Detached Turbulence Promoters in a Rectangular Channel," *AICHE J.*, Vol. 13, pp. 676–677.

Heat Transfer From a Square Source to an Impinging Liquid Jet Confined by an Annular Wall

D. L. Besserman,¹ F. P. Incropera,² and S. Ramadhyani²

Nomenclature

- A_r = area ratio = $\pi(1.9d)^2/L^2$
 d = internal nozzle (jet) diameter
 D_c = diameter of confining (annular) wall
 D_{eff} = effective diameter of square heater = $(\sqrt{2}L + L)/2$
 \bar{h} = average heat transfer coefficient
 k_f = fluid thermal conductivity
 L = width of square heater
 L^* = average radial extent of wall jet
 $\overline{Nu}_{D_{\text{eff}}}$ = average Nusselt number = $\bar{h}D_{\text{eff}}/k_f$
 \overline{Nu}_L = average Nusselt number = $\bar{h}L/k_f$
 Pr = Prandtl number
 q = convection heat transfer rate (power dissipation)
 R = radius of round heater
 Re_d = Reynolds number = $u_m d/\nu$
 Re_{L^*} = Reynolds number = $u_m L^*/\nu$
 S = separation from jet exit to impingement surface
 T_o = upstream fluid (jet) temperature
 \bar{T}_s = average surface temperature
 u_m = mean exit velocity of jet
 ν = kinematic viscosity

Introduction

Steady advances in manufacturing technologies related to very large-scale integrated circuit (VLSI) chips are sustaining significant increases in circuit densities. With an attendant increase in power dissipation, related heat fluxes are approaching 5×10^5 W/m², and within this decade, fluxes in excess of 2×10^6 W/m² are anticipated. Dissipation of such fluxes will require a liquid coolant, as well as an effective means of coolant delivery, such as jet impingement. For a scheme in which the jet is separated from the chip by conducting plates (Yamamoto et al., 1987), water may be used as the coolant, but if jet-to-chip contact is desired, a dielectric fluorocarbon must be used (Incropera, 1990).

In high-speed computing and data processing systems, it is desirable to space chips closely in an aligned, planar array for which cooling to each chip may be independently effected by a single circular jet. Manifolding for such an arrangement is likely to involve a concentric discharge tube, which redirects

¹Pratt and Whitney, Hartford, CT 06033.

²Purdue University, W. Lafayette, IN 47907.

Contributed by the Heat Transfer Division of the AMERICAN SOCIETY OF MECHANICAL ENGINEERS. Manuscript received by the Heat Transfer Division October 4, 1990; revision received July 20, 1991. Keywords: Electronic Equipment, Forced Convection, Jets.

the spent coolant 180 deg following impingement on a chip and routes it through an annular passage in counterflow with the jet. Although recent studies have experimentally addressed single- and two-phase convection heat transfer from a chiplike heater to an impinging circular jet (Stevens and Webb, 1989; Nonn et al., 1989; Womac et al., 1990), they were performed under conditions for which motion of the spent fluid did not influence heat transfer. Experiments involving heat transfer from a discrete source to a circular jet with annular collection of the spent fluid have been performed (Sparrow et al., 1987; Besserman et al., 1991), but in both cases the source was a circular disk, coaxial with the jet.

The objective of this study has been to consider experimentally impingement cooling of a chiplike source by a liquid, circular jet under conditions for which single-phase convection heat transfer from the source may be influenced by annular collection of the spent fluid. The experiments were performed with water and for operating conditions that are consistent with chip cooling requirements.

Experimental Procedures

The test cell used for the experiments is shown schematically in Fig. 1. Water exits a tubular nozzle of inside diameter d , traverses a distance S from the nozzle exit to a square heater of width L on a side, and is discharged in counterflow through an annular gap having an outer (confinement) diameter of D_c . Two jet nozzles, having diameters of $d = 4.42$ mm and 9.27 mm, with corresponding wall thicknesses of 0.91 mm and 1.74 mm, respectively, were tested, and dimensionless nozzle exit to heater separation distances were varied over the range $1 \leq S/d \leq 5$. With a fixed tube length of 190 mm, the dimensionless tube development length exceeded 20, insuring near fully developed conditions for turbulent flow at the nozzle exit. The width of the heat source (a square copper block bonded to a chromium alloy resistance heater) was fixed at $L = 12.7$ mm, which is representative of today's VLSI chips, while diameters of $D_c = 22.23$ mm and 38.10 mm were considered for the lexan substrate in which the heater was flush mounted. Corresponding dimensionless length scales were in the ranges $1.37 \leq L/d \leq 2.87$ and $2.40 \leq D_c/d \leq 8.62$. Conduction losses through the substrate and heater module were negligible (<2 percent), permitting the assumption that all of the power dissipated by the heater was transferred by convection to the jet.

Seven 0.076 mm (3 mil) copper-constantan thermocouples were routed through small channels machined in the copper block and soldered flush with the surface to insure an accurate measure of the surface temperature (Fig. 1). Calibration of the thermocouples indicated consistency to within 0.1 °C, and all readings were used to obtain an area-weighted-average surface temperature, \bar{T}_s . To calculate \bar{T}_s , the heater surface was subdivided into three zones (identified by the concentric squares in Fig. 1). The average temperature of each zone was determined by an arithmetic averaging of the temperatures registered by the associated thermocouples. The three zone-average temperatures were then combined into an area-weighted average. With the heat source fabricated from copper, temperature variations along the surface were small ($\leq 2^\circ\text{C}$), rendering the assumption of an isothermal surface condition appropriate for evaluating the average convection coefficient.

From additional measurements of the upstream fluid temperature T_o and the power dissipation q , the average convection coefficient, $\bar{h} = q/L^2(\bar{T}_s - T_o)$, was determined and a corresponding Nusselt number, based on either the heater width or an effective diameter, was computed. The heater power was adjusted to maintain a temperature difference of $(\bar{T}_s - T_o) \approx 10^\circ\text{C}$ for each operating condition, providing a corresponding temperature rise of the coolant that was less than 0.1 °C. Hence, mixing between the impinging jet and the return flow had a negligible effect on the jet temperature T_o . The

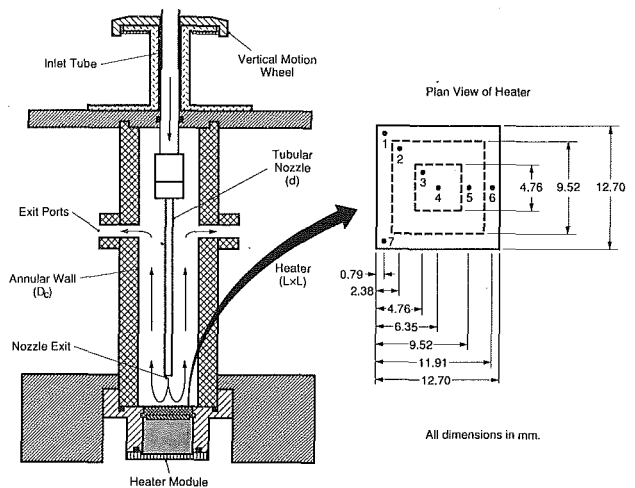


Fig. 1 Schematic of annular jet impingement geometry and plan view of square heater with thermocouple placement (dimensions in mm)

flow loop used to supply the test cell with water is described elsewhere (Besserman, 1989). Flow rates were varied from 0.26 to 11.36 liter/min, providing Reynolds numbers in the range $1000 \leq Re_d \leq 40,000$. All properties were evaluated at the film temperature, $(\bar{T}_s + T_o)/2$, and maximum uncertainties in \bar{Nu} and Re_d were estimated to be ± 6.3 and ± 2.8 percent, respectively.

Results

To assess effects of the confining annular wall and the nozzle-to-heater separation distance, results are presented in terms of the dimensionless parameters Re_d and $\bar{Nu}_{D_{eff}}$. From hydrodynamic considerations, it is appropriate to base the Reynolds number on the exit velocity of the jet and a characteristic length corresponding to the nozzle diameter. The characteristic length for the Nusselt number should provide some measure of thermal boundary layer development on the heater, and since the width L does not account for different radial distances from the stagnation point to the edges of the heater, the effective diameter, $D_{eff} = (\sqrt{2}L + L)/2$, may be the more appropriate choice. Although the experiments of this study were restricted to water ($Pr \approx 7$), a Prandtl number exponent of 0.4 has been found to correlate data obtained over a range of Prandtl numbers for unconfined jets impinging on a square heater (Womac, 1989).

Results are shown in Fig. 2, and for the smaller nozzle diameter (Fig. 2a), the effects of nozzle spacing (S/d) and the confining wall ($5.0 \leq D_c/d \leq 8.6$) are small to negligible. This behavior suggests that the nozzle-to-heater spacing is less than the length of the potential core of the jet over the full range of S/d (Hrycak et al., 1970), thereby precluding decay of the centerline velocity due to mixing of the jet with its ambient. For $d = 9.27$ mm and $D_c/d = 2.4$ (Fig. 2b), however, the jet is more closely constrained by the annular wall and the Nusselt number is more strongly influenced by S/d . The existence of a maximum at $S/d \approx 3$ may be due to a strong influence of the confining wall on jet hydrodynamic development. Tighter confinement brings the impinging jet and the counterflow into closer proximity, thereby enhancing turbulence production in the adjoining mixing zone and reducing the length of the potential core. For $S/d = 3$, impingement may still occur within the potential core, thereby preserving the centerline velocity, while enhancing heat transfer due to increased turbulence in the mixing zone. For $S/d = 5$, however, impingement may occur beyond the potential core, and the attendant decay in the centerline velocity may reduce heat transfer by more than the increase associated with enhanced mixing. With decreasing d , however, shear interactions between the jet and the opposing

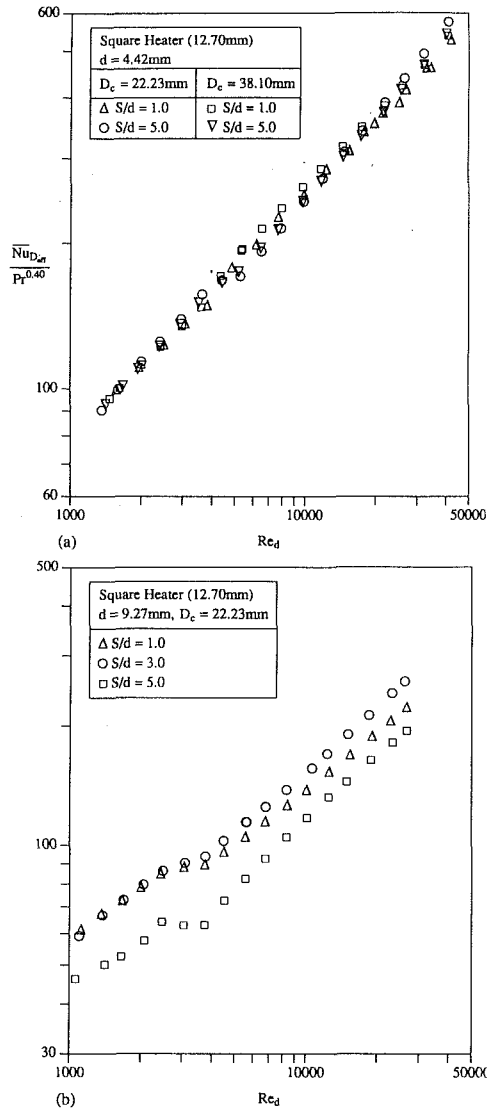


Fig. 2 Effect of Reynolds number and separation distance on the average Nusselt number for different nozzle and confinement diameters: (a) $d = 4.42$ mm and (b) $d = 9.27$ mm

annular flow diminish, and for $d = 4.42$ mm (Fig. 2a) there is no longer an effect of the confining wall.

Another distinguishing feature of the data for $d = 9.27$ mm (Fig. 2b) is that, in the range $2500 \leq Re_d \leq 4000$, $\overline{Nu}_{D_{eff}} / Pr^{0.4}$ ceases to increase monotonically with increasing Re_d . In this Reynolds number range, the length of the jet's potential core is known to decrease sharply with increasing Re_d (Hrycak et al., 1970), thereby reducing the transverse extent of the potential core impinging on the heated surface. The effect is apparently manifested more strongly with increasing nozzle diameter and, according to the results of Fig. 2(b), with increasing S/d .

While limited data preclude development of a correlation that accounts for the effect of the confining wall, it is of interest to determine the extent to which results of this study agree with a correlation previously developed for a circular, submerged jet impinging on a square heater without annular collection of the spent fluid (Womac, 1989). The correlation is based on an area-weighted superposition of component correlations for the impingement and wall jet regions of the flow, which, respectively, are of the form

$$\frac{\overline{Nu}_d}{Pr^{0.4}} = C_1 Re_d^{m_1} \quad (1)$$

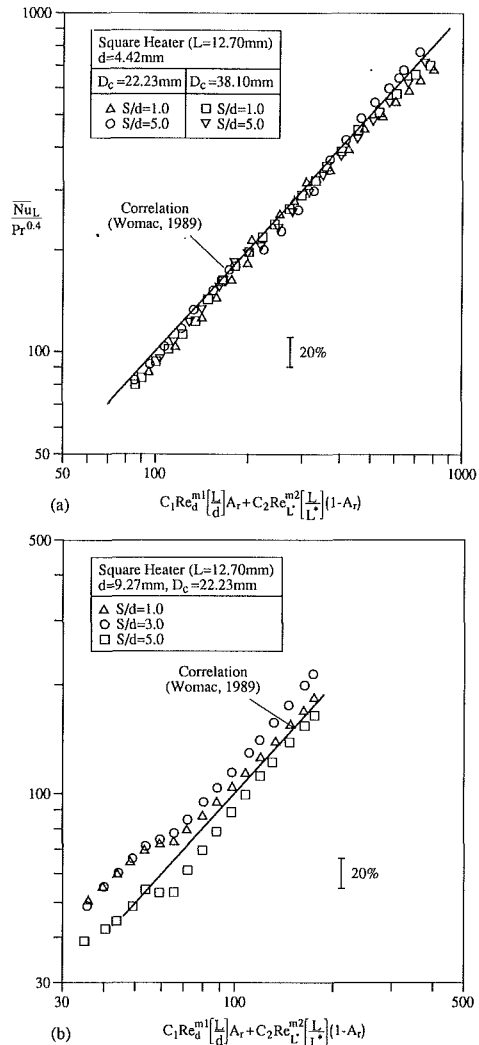


Fig. 3 Correlation of heat transfer data for: (a) $d = 4.42$ mm ($D_c/d = 5.03, 8.62$) and (b) $d = 9.27$ mm ($D_c/d = 2.41$)

and

$$\frac{\overline{Nu}_L}{Pr^{0.4}} = C_2 Re_L^{m_2} \quad (2)$$

Equation (1) is based on a stagnation point correlation for which $m_1 = 0.5$ (Ma and Bergles, 1988); while Eq. (2) applies for turbulent flow in the wall jet region (Gardon and Akfirat, 1965), for which an appropriate value of the exponent is $m_2 = 0.8$. The characteristic length L^* is the average radial extent of the wall jet region on the heater surface, which may be expressed as

$$L^* = \frac{\left(\frac{\sqrt{2}}{2} L - 1.9d\right) + \left(\frac{L}{2} - 1.9d\right)}{2} \quad (3)$$

where $1.9d$ is the approximate radial extent of the impingement region (Gardon and Cobonpue, 1961). Superimposition of Eqs. (1) and (2) results in the desired correlation:

$$\frac{\overline{Nu}_L}{Pr^{0.40}} = C_1 Re_d^{0.5} \left(\frac{L}{d}\right)^{A_r} + C_2 Re_L^{0.8} \left(\frac{L}{L^*}\right)^{(1-A_r)} \quad (4)$$

where A_r is the ratio of the heater surface associated with the impingement zone, $A_r = \pi(1.9d)^2 / L^2$. Values of $C_1 = 0.785$ and $C_2 = 0.0257$ have been recommended by Womac (1989), with the proviso that values of $A_r = 1.0$ and $C_2 = 0$ be prescribed if $A_r > 1$ or $L^* < 0$.

Data of this study are compared with Eq. (4) in Fig. 3. For the smaller nozzle and annular confinements corresponding to $D_c/d = 5.03$ and 8.62 , the agreement is excellent, as differences between the correlation and the data are within 5 percent over the entire range of conditions. For the larger nozzle diameter and tighter confinement (Fig. 3b), heat transfer is influenced by the confining wall and agreement between the data and the correlation is less satisfactory. Nevertheless, although the correlation does not account for the influence of S/d , it falls within the range of the data and for turbulent jets agrees with the data to within ± 20 percent. Underprediction of the data for $S/d = 3$ suggests that, for the larger nozzle diameter, confinement enhances heat transfer relative to results for an unconfined jet.

Although meaningful comparisons with the round heater results of Besserman et al. (1991) are limited by differences in heater shapes and sizes, it is useful to note that similarities do exist with respect to the applicability of Eq. (4). If the radial extent of the wall jet region is expressed as $L^* = R - 1.9d$ for the round heater, Eq. (4) successfully collapses the data for large confinement-to-nozzle diameter ratios (D_c/d), but is less satisfactory for smaller values of D_c/d . This trend is consistent with the results of Fig. 3, suggesting that, irrespective of the shape of the heater, the data may be correlated by separately accounting for conditions in the stagnation and wall-jet regions, if the influence of the confining wall is negligible. A more detailed comparison of round and square heater results is provided by Besserman (1989).

Acknowledgments

Support of this work by the National Science Foundation under Grant No. CBT-8611840 is gratefully acknowledged.

References

- Besserman, D. L., 1989, "Axisymmetric Liquid Jet Impingement Heat Transfer With Annular Collection of the Spent Fluid," M.S. Thesis, Purdue University, W. Lafayette, IN.
- Besserman, D. L., Incropera, F. P., and Ramadhyani, S., 1991, "Experimental Study of Heat Transfer From a Circular Source to a Circular Liquid Jet With Annular Collection of the Spent Fluid," *Experimental Heat Transfer*, Vol. 4, pp. 41–58.
- Gardon, R., and Cobonpue, J., 1961, "Heat Transfer Between a Flat Plate and Jets of Air Impinging on It," *Proc. Second Int. Heat Transfer Conf.*, pp. 454–460.
- Gardon, R., and Akfirat, J. C., 1965, "The Role of Turbulence in Determining the Heat Transfer Characteristics of Impinging Jets," *Int. J. Heat Mass Transfer*, Vol. 8, pp. 1261–1272.
- Hrycak, P., Lee, D. T., Gauntner, J. W., and Livingood, J. N. B., 1970, "Experimental Flow Characteristics of a Single Turbulent Jet Impinging on a Flat Plate," NASA TN D-5690.
- Incropera, F. P., 1990, "Liquid Immersion Cooling of Electronic Components," *Heat Transfer in Electronic and Microelectronic Components*, A. E. Bergles, ed., Hemisphere Publishing Corp., Washington, DC, pp. 407–444.
- Ma, C. F., and Bergles, A. E., 1983, "Boiling Jet Impingement Cooling of Simulated Microelectronic Chips," *Heat Transfer in Electronic Equipment*, S. Oktay and A. Bar-Cohen, eds., ASME, New York, pp. 5–12.
- Nonn, T., Dagan, Z., and Jiji, L. M., 1989, "Jet Impingement Flow Boiling of a Mixture of FC-72 and FC-87 Liquids on a Simulated Electronic Chip," *Heat Transfer in Electronics*, ASME HTD-Vol. 111, pp. 121–128.
- Sparrow, E. M., Xu, Z. X., and Azevedo, L. F. A., 1987, "Heat (Mass) Transfer for Circular Jet Impingement on a Confined Disk With Annular Collection of the Spent Air," *ASME JOURNAL OF HEAT TRANSFER*, Vol. 109, pp. 329–335.
- Stevens, J., and Webb, B. W., 1989, "Local Heat Transfer Coefficients Under an Axisymmetric, Single-Phase Liquid Jet," *Heat Transfer in Electronics*, ASME HTD-Vol. 111, pp. 113–119.
- Womac, D. J., 1989, "Single Phase Axisymmetric Liquid Jet Impingement Cooling of Discrete Heat Sources," M.S. Thesis, Purdue University, W. Lafayette, IN.
- Womac, D. J., Aharoni, G., Ramadhyani, S., and Incropera, F. P., 1990, "Single Phase Liquid Jet Impingement Cooling of Small Heat Sources," *Heat Transfer—1990*, Proceedings International Heat Transfer Conference, Hemisphere Publishing Corp., Washington, DC, Vol. 4, pp. 149–154.
- Yamamoto, H., Udagawa, Y., and Suzuki, M., 1987, "Cooling System for FACOM M-780 Large Scale Computer," *Cooling Technology for Electronic Equipment*, W. Aung, ed., Hemisphere Publishing Corp., Washington, DC, pp. 701–714.

Surface Factors Influencing Burnout on Flat Heaters

J. M. Ramilison,^{1,2} P. Sadasivan,¹ and J. H. Lienhard¹

Nomenclature

- A, B, C, D = constants in the correlation
 g = acceleration due to gravity
 h_{fg} = latent heat of vaporization
 q_{\max} = the peak, or *burnout*, heat flux
 $q_{\max,Z}$ = the peak heat flux predicted by Zuber (Eq. (4))
 r = rms surface roughness of a heater surface
 Z = the characteristic burnout heat flux that arises in the hydrodynamic theory; defined in Eq. (2)
 β_r = retreating contact angle
 λ_d = Helmholtz unstable wavelength
 ρ_f, ρ_g = saturated liquid and vapor densities, respectively
 σ = surface tension between a liquid and its vapor

Introduction

Ever since Kutateladze (1951) and Zuber (1958) proposed hydrodynamic descriptions of the burnout heat flux, q_{\max} , confusion has marked the scope of their agreed-upon equation. The problem stems from Kutateladze's original correlation. The sequence proceeds as follows:

Kutateladze based the famous q_{\max} correlation on data for *cylinders*, not flat plates. That expression was

$$q_{\max} = 0.131 Z \quad (1)$$

where Z is a characteristic heat flux,

$$Z = \rho_g^{1/2} h_{fg} [\sigma (\rho_f - \rho_g)]^{1/4} \quad (2)$$

The size range of the cylinder data Kutateladze used was fairly wide, and the correlation showed fair scatter.

Later, Zuber derived a peak heat flux prediction without reference to any geometrical conditions. He got

$$0.12 Z \leq q_{\max} \leq 0.157 Z \quad (3)$$

Zuber also showed that for certain assumptions about wavelengths, Eq. (3) reduced to

$$q_{\max} = (\pi/24) Z \quad (4)$$

which is numerically the same as Kutateladze's correlation.³

The mischief in all of this is that Zuber's sketches and other aspects of his derivation suggested that he was deriving an expression applicable to a flat heater. In fact, Zuber operated under the premise—later disproved by many investigators—that the geometry did not affect burnout. His comparison of his prediction with Kutateladze's correlation did not reflect a lack of care. It reflected the conviction that geometry did not matter.

So for many years, workers in the field have viewed Zuber's equation as representing the flat-plate geometry. Finally, Lienhard and Dhir (1973) suggested a derivation of q_{\max} that was specific to a flat, horizontal heater. They obtained

¹Heat Transfer/Phase Change Laboratory, Mechanical Engineering Department, University of Houston, Houston, TX 77204-4792.

²Presently Associate Professor, Saga University, Dept. of Mechanical Engineering, 1, Honjo-Machi, Saga 840, Japan.

³In the remainder of the paper, we will denote the peak heat flux given by Eq. (4) by $q_{\max,Z}$.

Contributed by the Heat Transfer Division of the THE AMERICAN SOCIETY OF MECHANICAL ENGINEERS. Manuscript received by the Heat Transfer Division March 19, 1991; revision June 30, 1991. Keywords: Boiling, Phase-Charge Phenomena.

Data of this study are compared with Eq. (4) in Fig. 3. For the smaller nozzle and annular confinements corresponding to $D_c/d = 5.03$ and 8.62 , the agreement is excellent, as differences between the correlation and the data are within 5 percent over the entire range of conditions. For the larger nozzle diameter and tighter confinement (Fig. 3b), heat transfer is influenced by the confining wall and agreement between the data and the correlation is less satisfactory. Nevertheless, although the correlation does not account for the influence of S/d , it falls within the range of the data and for turbulent jets agrees with the data to within ± 20 percent. Underprediction of the data for $S/d = 3$ suggests that, for the larger nozzle diameter, confinement enhances heat transfer relative to results for an unconfined jet.

Although meaningful comparisons with the round heater results of Besserman et al. (1991) are limited by differences in heater shapes and sizes, it is useful to note that similarities do exist with respect to the applicability of Eq. (4). If the radial extent of the wall jet region is expressed as $L^* = R - 1.9d$ for the round heater, Eq. (4) successfully collapses the data for large confinement-to-nozzle diameter ratios (D_c/d), but is less satisfactory for smaller values of D_c/d . This trend is consistent with the results of Fig. 3, suggesting that, irrespective of the shape of the heater, the data may be correlated by separately accounting for conditions in the stagnation and wall-jet regions, if the influence of the confining wall is negligible. A more detailed comparison of round and square heater results is provided by Besserman (1989).

Acknowledgments

Support of this work by the National Science Foundation under Grant No. CBT-8611840 is gratefully acknowledged.

References

- Besserman, D. L., 1989, "Axisymmetric Liquid Jet Impingement Heat Transfer With Annular Collection of the Spent Fluid," M.S. Thesis, Purdue University, W. Lafayette, IN.
- Besserman, D. L., Incropera, F. P., and Ramadhyani, S., 1991, "Experimental Study of Heat Transfer From a Circular Source to a Circular Liquid Jet With Annular Collection of the Spent Fluid," *Experimental Heat Transfer*, Vol. 4, pp. 41–58.
- Gardon, R., and Cobonpue, J., 1961, "Heat Transfer Between a Flat Plate and Jets of Air Impinging on It," *Proc. Second Int. Heat Transfer Conf.*, pp. 454–460.
- Gardon, R., and Akfirat, J. C., 1965, "The Role of Turbulence in Determining the Heat Transfer Characteristics of Impinging Jets," *Int. J. Heat Mass Transfer*, Vol. 8, pp. 1261–1272.
- Hrycak, P., Lee, D. T., Gauntner, J. W., and Livingood, J. N. B., 1970, "Experimental Flow Characteristics of a Single Turbulent Jet Impinging on a Flat Plate," NASA TN D-5690.
- Incropera, F. P., 1990, "Liquid Immersion Cooling of Electronic Components," *Heat Transfer in Electronic and Microelectronic Components*, A. E. Bergles, ed., Hemisphere Publishing Corp., Washington, DC, pp. 407–444.
- Ma, C. F., and Bergles, A. E., 1983, "Boiling Jet Impingement Cooling of Simulated Microelectronic Chips," *Heat Transfer in Electronic Equipment*, S. Oktay and A. Bar-Cohen, eds., ASME, New York, pp. 5–12.
- Nonn, T., Dagan, Z., and Jiji, L. M., 1989, "Jet Impingement Flow Boiling of a Mixture of FC-72 and FC-87 Liquids on a Simulated Electronic Chip," *Heat Transfer in Electronics*, ASME HTD-Vol. 111, pp. 121–128.
- Sparrow, E. M., Xu, Z. X., and Azevedo, L. F. A., 1987, "Heat (Mass) Transfer for Circular Jet Impingement on a Confined Disk With Annular Collection of the Spent Air," *ASME JOURNAL OF HEAT TRANSFER*, Vol. 109, pp. 329–335.
- Stevens, J., and Webb, B. W., 1989, "Local Heat Transfer Coefficients Under an Axisymmetric, Single-Phase Liquid Jet," *Heat Transfer in Electronics*, ASME HTD-Vol. 111, pp. 113–119.
- Womac, D. J., 1989, "Single Phase Axisymmetric Liquid Jet Impingement Cooling of Discrete Heat Sources," M.S. Thesis, Purdue University, W. Lafayette, IN.
- Womac, D. J., Aharoni, G., Ramadhyani, S., and Incropera, F. P., 1990, "Single Phase Liquid Jet Impingement Cooling of Small Heat Sources," *Heat Transfer—1990*, Proceedings International Heat Transfer Conference, Hemisphere Publishing Corp., Washington, DC, Vol. 4, pp. 149–154.
- Yamamoto, H., Udagawa, Y., and Suzuki, M., 1987, "Cooling System for FACOM M-780 Large Scale Computer," *Cooling Technology for Electronic Equipment*, W. Aung, ed., Hemisphere Publishing Corp., Washington, DC, pp. 701–714.

Surface Factors Influencing Burnout on Flat Heaters

J. M. Ramilison,^{1,2} P. Sadasivan,¹ and J. H. Lienhard¹

Nomenclature

- A, B, C, D = constants in the correlation
 g = acceleration due to gravity
 h_{fg} = latent heat of vaporization
 q_{\max} = the peak, or *burnout*, heat flux
 $q_{\max,Z}$ = the peak heat flux predicted by Zuber (Eq. (4))
 r = rms surface roughness of a heater surface
 Z = the characteristic burnout heat flux that arises in the hydrodynamic theory; defined in Eq. (2)
 β_r = retreating contact angle
 λ_d = Helmholtz unstable wavelength
 ρ_f, ρ_g = saturated liquid and vapor densities, respectively
 σ = surface tension between a liquid and its vapor

Introduction

Ever since Kutateladze (1951) and Zuber (1958) proposed hydrodynamic descriptions of the burnout heat flux, q_{\max} , confusion has marked the scope of their agreed-upon equation. The problem stems from Kutateladze's original correlation. The sequence proceeds as follows:

Kutateladze based the famous q_{\max} correlation on data for *cylinders*, not flat plates. That expression was

$$q_{\max} = 0.131 Z \quad (1)$$

where Z is a characteristic heat flux,

$$Z = \rho_g^{1/2} h_{fg} [\sigma (\rho_f - \rho_g)]^{1/4} \quad (2)$$

The size range of the cylinder data Kutateladze used was fairly wide, and the correlation showed fair scatter.

Later, Zuber derived a peak heat flux prediction without reference to any geometrical conditions. He got

$$0.12 Z \leq q_{\max} \leq 0.157 Z \quad (3)$$

Zuber also showed that for certain assumptions about wavelengths, Eq. (3) reduced to

$$q_{\max} = (\pi/24) Z \quad (4)$$

which is numerically the same as Kutateladze's correlation.³

The mischief in all of this is that Zuber's sketches and other aspects of his derivation suggested that he was deriving an expression applicable to a flat heater. In fact, Zuber operated under the premise—later disproved by many investigators—that the geometry did not affect burnout. His comparison of his prediction with Kutateladze's correlation did not reflect a lack of care. It reflected the conviction that geometry did not matter.

So for many years, workers in the field have viewed Zuber's equation as representing the flat-plate geometry. Finally, Lienhard and Dhir (1973) suggested a derivation of q_{\max} that was specific to a flat, horizontal heater. They obtained

¹Heat Transfer/Phase Change Laboratory, Mechanical Engineering Department, University of Houston, Houston, TX 77204-4792.

²Presently Associate Professor, Saga University, Dept. of Mechanical Engineering, 1, Honjo-Machi, Saga 840, Japan.

³In the remainder of the paper, we will denote the peak heat flux given by Eq. (4) by $q_{\max,Z}$.

Contributed by the Heat Transfer Division of the THE AMERICAN SOCIETY OF MECHANICAL ENGINEERS. Manuscript received by the Heat Transfer Division March 19, 1991; revision June 30, 1991. Keywords: Boiling, Phase-Charge Phenomena.

$$q_{\max} = 0.149 Z \quad (5)$$

This result compared favorably to all the available data—data provided by a number of observers for fairly similar surfaces.

Lienhard et al. (1973) also noted that only one vapor jet can exist on a small heater. Thus the gross heat removal cannot change, and q_{\max} must decrease with the inverse area of the heater when the heater is small.

Recently, other premises behind the hydrodynamic theory have crumbled as well. Most importantly, we have found that q_{\max} is not as weakly influenced by surface variables as we had once thought. Berenson's flat-plate figures showed a surface roughness dependence of ± 10 percent. But these were average values. His tables showed that the actual variation with both roughness and other aspects of the heater surface was ± 20 percent.

Bui and Dhir (1984) have more recently shown much greater variations of q_{\max} in another geometry: a vertical flat heater. Ramilison (1985) provided q_{\max} data for a horizontal flat heater that showed up to ± 15 percent variation over a fairly narrow range of heater surface conditions.

Therefore, as we look more closely, surface conditions become more important than we once thought. The objective of this paper is to take into account, as best we are able, the influence of the condition of the heater surface in recreating a correlation of q_{\max} for horizontal heaters.

An Inventory of Existing Data

We have located five sources of usable flat horizontal heater q_{\max} data. By usable, we mean the following things:

- The geometry must be such that side currents do not have access to the boiling process. The heater must have vertical side walls surrounding it. Lienhard and Keeling (1970) showed that absence of sidewalls can strongly enhance, or reduce, q_{\max} as a result of induced convective effects.
- The heater should have a characteristic dimension greater than twice the Helmholtz wavelength, λ_d , for the liquid used in the experiment. For heaters smaller than this value, we have already noted that q_{\max} decreases with heater area.
- The heater must be one for which either we know the receding contact angle, β_r , or we know enough about the heater to reconstruct it within reasonable bounds. The heater must also be one for which we know something about the surface finish—enough to make a reasonable estimate of what the rms roughness, r , was.

Based on the above criteria, we used data from the following sources: Berenson (1960), Lienhard and Dhir (1973), Ramilison (1985), Rajab and Winterton (1990),⁴ and Reguillot (1990). Figure 1 shows the peak heat fluxes obtained from these sources. In each case, the peak heat flux has been normalized with respect to the corresponding value predicted by Zuber, Eq. (4). The peak heat flux clearly varies considerably from one case to another. This could be a reflection of the variation in surface characteristics from one experiment to another.

A quantification of surface characteristics with regard to boiling requires an accurate knowledge of the liquid behavior on a given solid surface. One can talk about smooth (or rough) and wetted (or nonwetted) surfaces only in connection with a given liquid–solid combination. For a given method of surface preparation, the relative variations of rms roughness probably describe the boiling surface characteristics. Similarly, the contact angle is also a characteristic of the boiling surface combination. In this study, we estimated the surface characteristics—surface roughness and contact angle—for each

⁴Rajab and Winterton (1990) provide two values of q_{\max} : one for water, and one for Freon-113. We have used only the Freon-113 data point for our present study. The value of D/λ_d was smaller than 2.0 for water, and hence was not used.

case, and sought to correlate the normalized peak heat flux with these parameters.

Estimating Surface Roughnesses

Typically our sources did not report measured values of the heater surface roughness. However, they all provide descriptions of the mechanical processes used to prepare the surface. These processes ranged from mirror finishing, using Tuffback A (Berenson, 1960) and alumina (Ramilison, 1985), to polishing with coarse #60 emery paper (Berenson, 1960). Engineering handbooks (Baumeister and Marks, 1966, for example) provide surface roughness ranges for common production processes. Using this information, we have estimated a roughness parameter, r , for each surface. These values have been assigned in such a manner that they represent fairly accurately the trend in roughness from one surface to another. Our estimates of this parameter range from 2μ for a surface mirror polished with alumina, to about 12μ for a surface finished with #60 emery paper. These are listed in Table 1.

Estimating Contact Angles

In the transition from nucleate boiling to the critical heat flux condition, the liquid front recedes from the heater surface. Therefore the receding contact angle, β_r , is the relevant parameter that we must consider. With the exception of Ramilison (1985), the sources of data do not report measurements of β_r . Rajab and Winterton (1990) measured contact angles in their experiments, but their measurement procedure could only have yielded an equilibrium value, rather than the receding angle. Surfaces typically used in boiling experiments are far from being an "ideal surface," and exhibit considerable contact angle hysteresis. Therefore, consideration of the advancing or equilibrium contact angle in a critical heat flux situation is incorrect.

For cases where receding contact angle data were not directly available, we either measured the angles on close reproductions of surfaces originally employed in the experiments, or estimated them. We measured contact angles for water and methanol on copper surfaces, and for Freon-113 on stainless steel. Receding contact angles were measured using a conventional tilting plate method. The criteria used to estimate β_r for other cases include the following facts, based on our previous experience in measuring β_r :

1 For a given liquid-heater material combination, (a) a smoother surface finish decreases the contact angle, and (b) oxidizing the surface results in an almost perfectly wetting situation, $\beta_r \approx 0$.

2 For a given liquid, a metal and its alloys exhibit the same contact angle.

3 For organic liquids (low surface tension), teflon-coating the surface leads to a minor reduction in the contact angle.

The values of the receding contact angle in this study range from 0 deg for *n*-pentane on oxidized copper to about 40 deg for water on copper. The complete set of β_r values is listed in Table 1.

Discussion

Using the estimated values of r and β_r , we attempted a correlation of the form

$$q_{\max}/q_{\max,Z} = A(\pi - \beta_r)^B (r)^{(C+D\beta_r)} \quad (6)$$

where β_r is expressed in radians. We used the term $(\pi - \beta_r)$ in the correlation to ensure the physical requirement that the peak heat flux must tend to zero for the case of $\beta_r = \pi$, the perfectly nonwetting case. Correlation yielded the following equation:

$$q_{\max}/q_{\max,Z} = 0.0336(\pi - \beta_r)^{3.0} (r)^{0.125} \quad (7)$$

The original correlation yielded an extremely small value for the constant D . Therefore we revised the values of A , B , and

Table 1 Previously published flat-plate burnout data

Ramilison (1985)					
q/q _z	rms	β _r (deg)	surface characteristics	liquid/heater surface	q/q _z eq. 7
1.19	5	8	Teflon-coated	acetone/Teflon	1.12
1.09	12	15	polished with #80	acetone/copper	1.10
0.92	2	13	mirror polish with 0.05μ alumina	"	0.91
1.20	5	8	Teflon-coated	Freon-113/Teflon	1.12
1.12	12	13	polished with #80	"	1.14
0.99	2	10	mirror polish with 0.05μ alumina	"	0.96
1.25	5	8	Teflon-coated	n-pentane/teflon	1.11
1.06	12	15	polished with #80	n-pentane/copper	1.10
0.92	2	10	mirror polish with 0.05μ alumina	"	0.96

Lienhard and Dhir (1973)					
q/q _z	rms	β _r (deg)	surface characteristics	liquid/heater surface	q/q _z eq. 7
1.18	10	15	polished with #220	acetone/Copper	1.07
1.22	10	15	"	"	1.07
1.14	10	15	"	"	1.07
1.07	10	15	"	"	1.07
1.21	10	17	"	benzene/Copper	1.03
1.05	10	17	"	"	1.03
1.07	10	17	"	"	1.03
0.94	10	17	"	methanol/Copper	1.03
1.02	10	17	"	"	1.03
1.04	10	17	"	"	1.03
1.01	10	17	"	"	1.03
1.01	10	17	"	"	1.03
1.00	10	17	"	"	1.03
0.70	10	40	"	water/Copper	0.65
0.72	10	40	"	"	0.65
0.66	10	40	"	"	0.65
0.67	10	40	"	"	0.65
0.62	10	40	"	"	0.65
0.59	10	40	"	"	0.65

Berenson (1960)					
q/q _z	rms	β _r (deg)	surface characteristics	liquid/heater surface	q/q _z eq. 7
1.10	4	8	mirror-finished; Tufback 600A; cleaned	n-pentane-Copper	1.08
1.05	4	8	mirror-finished; Tufback 600A; cleaned	"	1.08
1.18	9	10	lapped - one direction; #280; cleaned	"	1.16
1.20	11	10	Ditto; #120; cleaned	"	1.18
1.20	11	10	lapped circular; #120; cleaned	"	1.18
1.20	8	10	rubbed one direction; #320; cleaned	"	1.14
1.23	11	10	lapped circular; #120; cleaned	"	1.18
1.24	11	10	Ditto; #120; cleaned	"	1.18
1.33	11	0	lapped one direction; #120; oxidized	"	1.41
1.27	11	0	lapped circular; #120; oxidized	"	1.41
1.29	11	0	lapped circular; #120; oxidized	"	1.41
1.30	9	0	lapped one direction; #280; oxidized	"	1.37
1.32	9	0	lapped one direction; #280; oxidized	"	1.37
1.34	11	0	lapped one direction; #120; oxidized	"	1.41
1.38	11	0	lapped one direction; #120; oxidized	"	1.41
1.34	12	0	lapped one direction; #60; oxidized	"	1.42
0.98	4	10	mirror finished; Tufback A; cleaned	n-pentane/Inconel	1.04
0.95	4	10	mirror finished; Tufback A; cleaned	"	1.04
1.06	11	15	lapped circular; #160; cleaned	"	1.08
1.06	11	15	lapped circular; #160; cleaned	"	1.08
1.07	11	15	lapped circular; #160; cleaned	"	1.08
1.03	4	10	mirror finished; Tufback A; cleaned	n-pentane/Nickel	1.04
1.24	11	15	lapped circular; #160; cleaned	"	1.08

Other data					
q/q _z	rms	β _r (deg)	surface characteristics	liquid/heater surface	q/q _z eq. 7
1.14	8	13	polished with #320 (Rajab and Winterton, 1990)	Freon-113/aluminum	1.06
1.00	5	15	stainless steel foil (Regullot, 1990)	Freon-113/Stainless steel	0.98

C after setting D equal to zero. Equation (7) correlates all the data used within ± 6 percent. Figure 2 shows the corrected normalized peak heat flux, q_{max}/q_{max,Z} for the various cases.

$$q_{max}/q_{max,Z}$$

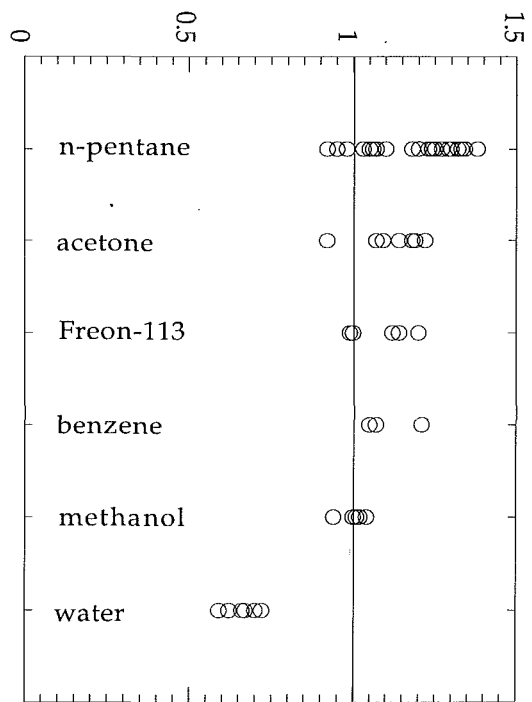


Fig. 1 Variation of the peak heat flux for different liquids

$$q_{max}/q_{max,Z,corrected}$$

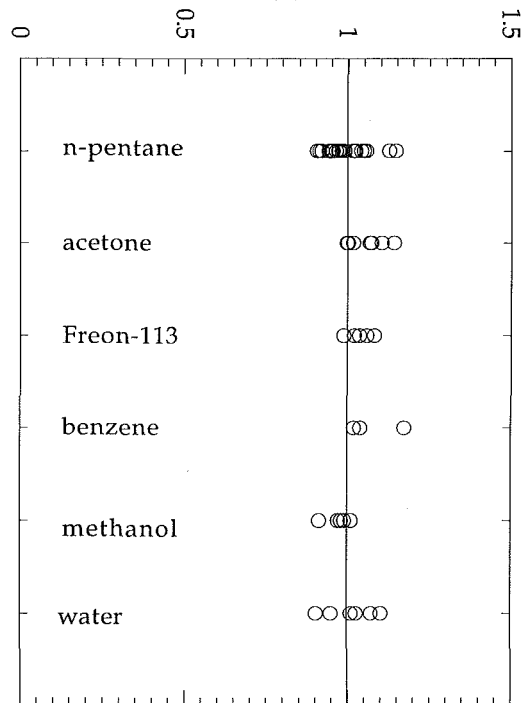


Fig. 2 Peak heat flux corrected to account for surface effects (Eq. (7))

It is clear that the surface-to-surface variation in the peak heat flux seen in Fig. 1 is fairly well accounted for by the combined influence of the receding contact angle, and to a lesser extent the surface roughness.

It is not surprising to see that the influence of β_r on the peak heat flux is greater than that of surface roughness. Close to burnout, the vapor escape pattern on the heater surface is in the form of thin vapor channels on the heater surface, formed

as the result of the coalescence of vapor bubbles generated at a few adjacent nucleation sites. The manner in which these vapor channels adhere to the heater surface is dictated by the liquid–solid contact angle. Surface roughness, on the other hand, is important mainly in the lower portion of the nucleate boiling curve, where individual nucleation sites are not shadowed by neighboring sites, and little interaction occurs between these sites. However, after individual bubbles begin to coalesce, the influence of surface roughness should abate.

Concluding Remarks

No doubt, other observers might adjust some of our estimates of r and β_r up or down. In this sense, Eq. (7) must be regarded as a first rough cut at identifying the influence of these often neglected variables. It is unlikely that any such adjustment could change the overall form of Eq. (7) drastically. What Eq. (7) and Fig. 2 do show, fairly unequivocally, is that these surface characteristics *cannot be* neglected.

It is our hope that future peak heat flux studies will turn to creating more accurate correlations of heater surface influences, and to creating physical models to describe these influences.

References

- Baumeister, T., and Marks, L. S., eds., 1966, *Standard Handbook for Mechanical Engineers*, 7th ed., McGraw-Hill, New York.
- Berenson, P. J., 1960, "Transition Boiling From a Horizontal Surface," D.Sc. Thesis, Massachusetts Institute of Technology, Cambridge, MA.
- Bui, T. D., and Dhir, V. K., 1984, "Transition Boiling Heat Transfer on a Vertical Surface, presented at the ASME National Heat Transfer Conference, Niagara Falls, NY.
- Kutateladze, S. S., 1951, *Hydrodynamic Theory of Changes in the Boiling Process Under Free Convection Conditions*, p. 529.
- Lienhard, J. H., and Dhir, V. K., 1973, "Hydrodynamic Prediction of Peak Pool-Boiling Heat Fluxes From Finite Bodies," *ASME JOURNAL OF HEAT TRANSFER*, Vol. 95, pp. 152–158.
- Lienhard, J. H., Dhir, V. K., and Riherd, D. M., 1973, "Peak Pool Boiling Heat Flux Measurements on Finite Horizontal Flat Plates," *ASME JOURNAL OF HEAT TRANSFER*, Vol. 95, p. 477.
- Lienhard, J. H., and Keeling, K. B., 1970, "An Induced Convection Effect Upon the Peak Heat Flux," *ASME JOURNAL OF HEAT TRANSFER*, Vol. 92, pp. 1–5.
- Rajab, I., and Winterton, R. H. S., 1990, "The Two Transition Boiling Curves and Liquid–Solid Contact on a Horizontal Surface," *Int. J. Heat Fluid Flow*, Vol. 11, pp. 149–153.
- Ramilison, J. M., 1985, "Transition Boiling Heat Transfer and the Film Transition Regime," Ph.D. Dissertation, Dept. of Mechanical Engineering, University of Houston, TX.
- Reguillot, F., 1990, "Boiling on Flat Resistance Heaters," M.S. Thesis, Dept. of Mechanical Engineering, University of Houston, TX.
- Zuber, N., 1958, "On the Stability of Boiling Heat Transfer," *Trans. ASME*, Vol. 80, p. 711.

On the Pulse Boiling Frequency in Thermosyphons

J. F. Liu¹ and J. C. Y. Wang²

Nomenclature

- a = thermal diffusivity
 c_1 = constant
 d = diameter, m, in Eq. (9)
 h_{fg} = latent heat of vaporization
 P = pressure

- q = heat flux, kW/m², in Eq. (9)
 r = radius, variable
 R = tube radius
 r_n = bubble radius
 R' = ideal gas constant
 T = temperature
 ΔT = superheat
 ν = frequency, 1/min, in Eq. (9)
 λ = thermal conductivity
 σ = surface tension
 τ = time or period

Subscripts

- b = at site b in Fig. 2
 c = condenser
 s = saturation state
 v = vapor

Introduction

The unsteady periodic boiling phenomenon, pulse boiling, appearing in the evaporator of thermosyphons has been mentioned and investigated by many researchers. The heat transfer coefficient in evaporators was predicted according to different considerations of flow patterns. For instance, Shiraishi et al. (1981) proposed a method based on a combination flow pattern: the nucleate boiling in a liquid pool and the evaporation from a falling condensate film. Liu et al. (1986) only considered a pure pulse boiling flow pattern, and Xin et al. (1987) focused on the flow pattern of the continuous boiling process without pulse phenomenon. Besides, the forming conditions of pulse boiling were also described differently. Xin et al. (1987) also reported that pulse boiling cannot occur in a carbon-steel/water heat pipe; Ma et al. (1987), however, observed this phenomenon in a carbon-steel/water thermosyphon. Nearly all researchers mentioned that this phenomenon indeed exists in glass/water thermosyphons. Although the influential factors have been discussed qualitatively, the quantitative analysis has yet to be conducted.

This study focuses on the pulse boiling frequency as a criterion for the determination of flow patterns, and attempts are made to predict the frequency both experimentally and theoretically.

Experiment and Observation

As test samples, several thermosyphons are made of glass pipes with diameters of 14, 20, and 30 mm and the same length of 1.25 m. One of the experimental elements consists of a carbon-steel evaporator and glass condenser, which are connected smoothly at the adiabatic section. The common feature of the setup is shown in Fig. 1(a). The evaporator was electrically heated, while the condenser was cooled by a water jacket made of glass. The heat input and output were measured, and also checked with the data of the cooling side. Seven copper-constantan thermocouples were pasted on the outside surface for every test sample. In the middle part of the sample, the adiabatic section was formed by covering with a thick insulation material. The temperature taken from the adiabatic section is reasonably considered as the temperature inside the thermosyphon.

The temperature fluctuation against time of the adiabatic section is shown in Fig. 1(b). It can be seen that every fluctuation is an approximate wave shape with a certain frequency. This may be explained as follows: when pulse boiling occurs, an upward superheated vapor–liquid column sweeps over the adiabatic surface and raises its temperature to the wave peak. Subsequently, as the boiling phenomenon ends, the liquid pool calms down, and then the temperature falls to the wave valley. The amplitude of every wave is inversely proportional to its frequency.

¹Harbin Institute of Technology, Harbin, People's Republic of China.

²Concordia University, Montreal, Canada.

Contributed by the Heat Transfer Division of the AMERICAN SOCIETY OF MECHANICAL ENGINEERS. Manuscript received by the Heat Transfer Division April 1, 1991; revision received August 1991. Keywords: Boiling, Heat Pipes and Thermosyphons, Phase-Change Phenomena.

as the result of the coalescence of vapor bubbles generated at a few adjacent nucleation sites. The manner in which these vapor channels adhere to the heater surface is dictated by the liquid–solid contact angle. Surface roughness, on the other hand, is important mainly in the lower portion of the nucleate boiling curve, where individual nucleation sites are not shadowed by neighboring sites, and little interaction occurs between these sites. However, after individual bubbles begin to coalesce, the influence of surface roughness should abate.

Concluding Remarks

No doubt, other observers might adjust some of our estimates of r and β_r up or down. In this sense, Eq. (7) must be regarded as a first rough cut at identifying the influence of these often neglected variables. It is unlikely that any such adjustment could change the overall form of Eq. (7) drastically. What Eq. (7) and Fig. 2 do show, fairly unequivocally, is that these surface characteristics *cannot be* neglected.

It is our hope that future peak heat flux studies will turn to creating more accurate correlations of heater surface influences, and to creating physical models to describe these influences.

References

- Baumeister, T., and Marks, L. S., eds., 1966, *Standard Handbook for Mechanical Engineers*, 7th ed., McGraw-Hill, New York.
- Berenson, P. J., 1960, "Transition Boiling From a Horizontal Surface," D.Sc. Thesis, Massachusetts Institute of Technology, Cambridge, MA.
- Bui, T. D., and Dhir, V. K., 1984, "Transition Boiling Heat Transfer on a Vertical Surface, presented at the ASME National Heat Transfer Conference, Niagara Falls, NY.
- Kutateladze, S. S., 1951, *Hydrodynamic Theory of Changes in the Boiling Process Under Free Convection Conditions*, p. 529.
- Lienhard, J. H., and Dhir, V. K., 1973, "Hydrodynamic Prediction of Peak Pool-Boiling Heat Fluxes From Finite Bodies," *ASME JOURNAL OF HEAT TRANSFER*, Vol. 95, pp. 152–158.
- Lienhard, J. H., Dhir, V. K., and Riherd, D. M., 1973, "Peak Pool Boiling Heat Flux Measurements on Finite Horizontal Flat Plates," *ASME JOURNAL OF HEAT TRANSFER*, Vol. 95, p. 477.
- Lienhard, J. H., and Keeling, K. B., 1970, "An Induced Convection Effect Upon the Peak Heat Flux," *ASME JOURNAL OF HEAT TRANSFER*, Vol. 92, pp. 1–5.
- Rajab, I., and Winterton, R. H. S., 1990, "The Two Transition Boiling Curves and Liquid–Solid Contact on a Horizontal Surface," *Int. J. Heat Fluid Flow*, Vol. 11, pp. 149–153.
- Ramilison, J. M., 1985, "Transition Boiling Heat Transfer and the Film Transition Regime," Ph.D. Dissertation, Dept. of Mechanical Engineering, University of Houston, TX.
- Reguillot, F., 1990, "Boiling on Flat Resistance Heaters," M.S. Thesis, Dept. of Mechanical Engineering, University of Houston, TX.
- Zuber, N., 1958, "On the Stability of Boiling Heat Transfer," *Trans. ASME*, Vol. 80, p. 711.

On the Pulse Boiling Frequency in Thermosyphons

J. F. Liu¹ and J. C. Y. Wang²

Nomenclature

- a = thermal diffusivity
 c_1 = constant
 d = diameter, m, in Eq. (9)
 h_{fg} = latent heat of vaporization
 P = pressure

- q = heat flux, kW/m², in Eq. (9)
 r = radius, variable
 R = tube radius
 r_n = bubble radius
 R' = ideal gas constant
 T = temperature
 ΔT = superheat
 ν = frequency, 1/min, in Eq. (9)
 λ = thermal conductivity
 σ = surface tension
 τ = time or period

Subscripts

- b = at site b in Fig. 2
 c = condenser
 s = saturation state
 v = vapor

Introduction

The unsteady periodic boiling phenomenon, pulse boiling, appearing in the evaporator of thermosyphons has been mentioned and investigated by many researchers. The heat transfer coefficient in evaporators was predicted according to different considerations of flow patterns. For instance, Shiraishi et al. (1981) proposed a method based on a combination flow pattern: the nucleate boiling in a liquid pool and the evaporation from a falling condensate film. Liu et al. (1986) only considered a pure pulse boiling flow pattern, and Xin et al. (1987) focused on the flow pattern of the continuous boiling process without pulse phenomenon. Besides, the forming conditions of pulse boiling were also described differently. Xin et al. (1987) also reported that pulse boiling cannot occur in a carbon-steel/water heat pipe; Ma et al. (1987), however, observed this phenomenon in a carbon-steel/water thermosyphon. Nearly all researchers mentioned that this phenomenon indeed exists in glass/water thermosyphons. Although the influential factors have been discussed qualitatively, the quantitative analysis has yet to be conducted.

This study focuses on the pulse boiling frequency as a criterion for the determination of flow patterns, and attempts are made to predict the frequency both experimentally and theoretically.

Experiment and Observation

As test samples, several thermosyphons are made of glass pipes with diameters of 14, 20, and 30 mm and the same length of 1.25 m. One of the experimental elements consists of a carbon-steel evaporator and glass condenser, which are connected smoothly at the adiabatic section. The common feature of the setup is shown in Fig. 1(a). The evaporator was electrically heated, while the condenser was cooled by a water jacket made of glass. The heat input and output were measured, and also checked with the data of the cooling side. Seven copper-constantan thermocouples were pasted on the outside surface for every test sample. In the middle part of the sample, the adiabatic section was formed by covering with a thick insulation material. The temperature taken from the adiabatic section is reasonably considered as the temperature inside the thermosyphon.

The temperature fluctuation against time of the adiabatic section is shown in Fig. 1(b). It can be seen that every fluctuation is an approximate wave shape with a certain frequency. This may be explained as follows: when pulse boiling occurs, an upward superheated vapor–liquid column sweeps over the adiabatic surface and raises its temperature to the wave peak. Subsequently, as the boiling phenomenon ends, the liquid pool calms down, and then the temperature falls to the wave valley. The amplitude of every wave is inversely proportional to its frequency.

¹Harbin Institute of Technology, Harbin, People's Republic of China.

²Concordia University, Montreal, Canada.

Contributed by the Heat Transfer Division of the AMERICAN SOCIETY OF MECHANICAL ENGINEERS. Manuscript received by the Heat Transfer Division April 1, 1991; revision received August 1991. Keywords: Boiling, Heat Pipes and Thermosyphons, Phase-Change Phenomena.

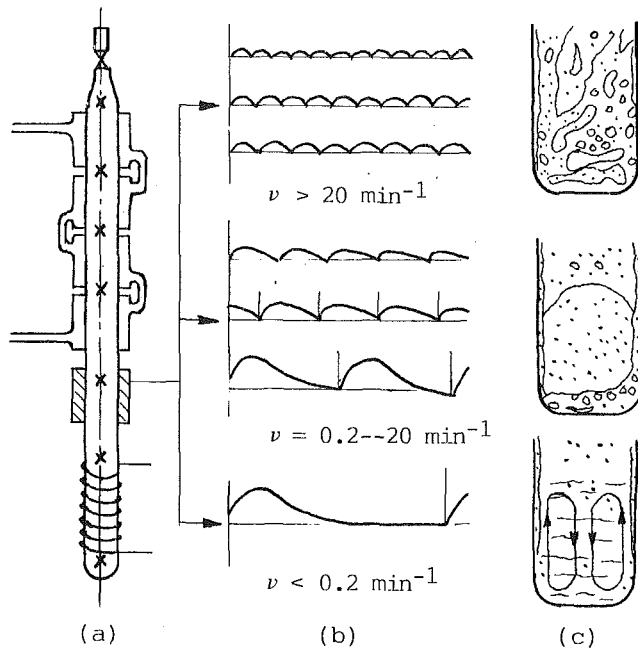


Fig. 1 Setup and some observations

According to the observations, the flow patterns inside the evaporator are closely connected with the frequency of pulse boiling. As frequency increases gradually from zero to a certain value, the flow pattern shifts from one type to another. Hence, fixed values can be proposed to distinguish among flow patterns. When the frequency is less than 0.2/min, the flow pattern can be treated as natural convection in a liquid pool with evaporation from the condensate film, as shown in the lower part of Fig. 1(c). When the frequency exceeds 20/min, pulse boiling occurs so frequently that the flow pattern becomes semicontinuous froth boiling, as shown in the upper part of Fig. 1(c). When the frequency falls in the range between the abovementioned values it belongs to standard pulse boiling, as shown in the middle part of Fig. 1(c).

Theoretical Analysis

The assumptions are as follows: (1) at the beginning of a pulse boiling period, the liquid pool is heated from the saturation temperature and gradually superheated with a constant heat flux at the boundary surface; (2) before the first bubble creation, the liquid pool is motionless and the heating process is treated as a pure transient heat conduction problem.

Similar to the analysis of Hsu (1962), when the liquid pool reaches the superheat required for a bubble formation, the first bubble or pulse boiling starts. As shown in Fig. 2, the dashed line represents the superheat required for bubble formation, while the solid lines denote the superheat of the liquid at different times. The tangent point *A* corresponds to the moment the first bubble is created.

The governing equation of the liquid pool temperature and its boundary conditions are as follows:

$$\frac{dT}{d\tau} = a \left(\frac{d^2T}{dr^2} + \frac{1}{r} \frac{dT}{dr} \right) \quad (\tau > 0, 0 < r < R)$$

$$T(r, 0) = T_o \quad \lambda \frac{dT(R, \tau)}{dr} = q \quad (1)$$

Its solution is given as an infinite series (Carslaw and Jaeger, 1959), namely,

$$\overline{\Delta T} = 2Fo - \frac{1}{4} (1 - r^2) - \sum_{n=1}^{\infty} \left[\frac{2J_o(\mu_n \bar{r})}{\mu_n^2 J_o(\mu_n)} \exp(-\mu_n^2 Fo) \right] \quad (2)$$

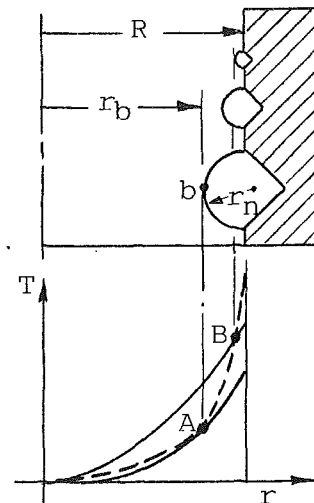


Fig. 2 Incipient boiling model

where

$$\overline{\Delta T} = \Delta T / (qR/\lambda) \quad Fo = \frac{a\tau}{R^2} \quad \bar{r} = \frac{r}{R}$$

Equation (2) can be replaced by the following two regressive equations with a deviation within ± 5 percent:

$$\overline{\Delta T} = (-0.7894 + 0.8101\bar{r} + 16.1616Fo)$$

$$(0 < Fo < 7 \times 10^{-4}) \quad (3)$$

$$\overline{\Delta T} = 1.5r^{5.71} Fo^{0.57} \quad (7 \times 10^{-4} < Fo < 0.21) \quad (4)$$

On the other hand, the superheat equation for bubble formation is derived as follows:

$$T_b - T_s = \frac{R' T_b T_s}{h_{fg}} \ln \left(1 + \frac{2\sigma}{r_n P_s} \right) \quad (5)$$

or

$$T_b - T_s = T_s \left[\frac{1}{1 - \frac{R' T_s}{h_{fg}} \ln \left(1 + \frac{B}{1 - \bar{r}} \right)} - 1 \right] \quad (6)$$

where

$$r_n = \frac{R(1 - \bar{r})}{c_1} \approx R(1 - \bar{r}) \quad (\text{assume } c_1 = 1)$$

$$B = \frac{2\sigma}{P_s R}$$

In Fig. 2, the tangent point *A* can be predicted by equating the slopes of Eq. (3) and Eq. (6), and then the superheat at point *A* is solved:

$$T_b - T_s = T_s \left\{ 1 - \frac{R' T_s}{h_{fg}} \times \ln \left[1 + \frac{2B}{\sqrt{(2+B)^2 - 4(B+1-C) - B}} \right] \right\}^{-1} - T_s \quad (7)$$

where

$$C = \frac{2.47\sigma T_s \lambda}{h_{fg} P_v R^2 q}$$

It should be noted that the practical required superheat at point *A* is much greater than that provided by analytical results. The reasonable explanation is that, as mentioned by Collier (1972), and Davis and Anderson (1966), the first bubble can be created at point *A* only at an idealized heating surface that

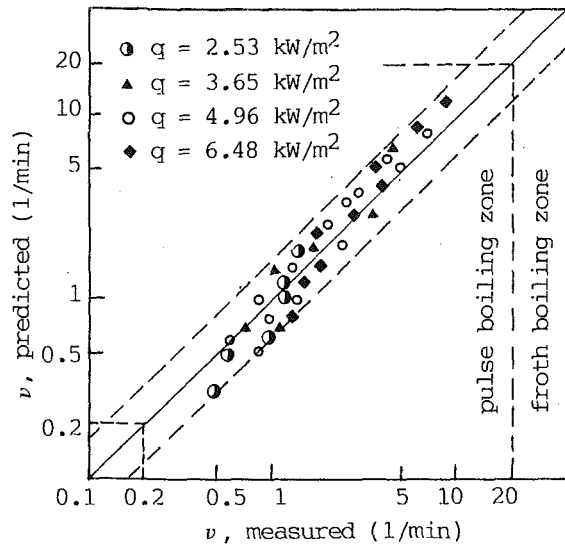


Fig. 3 Comparison of the measured and predicted frequencies

possesses a sufficiently wide range of cavity sizes. In fact, according to the measurement by Davis and Anderson (1966), on a practical heating surface the cavity sizes are generally much smaller than that at point *A*. Hence, the incipient boiling will not start until the superheat of the liquid pool further increases to a certain value corresponding to point *B* (see Fig. 2). By equating Eqs. (4) and (6), the intersection point *B* can be determined and the resultant equation of frequency of pulse boiling may be obtained as follows:

$$\nu = \frac{60a}{R^2} \left\{ \frac{T_s \lambda}{1.57 r^{5.71} R q} \left[\frac{1}{1 - \frac{R' T_s}{h_{fg}} \ln \left(1 + \frac{2\sigma}{P_s R (1 - \bar{r})} \right)} - 1 \right] \right\}^{-1.76} \quad (8)$$

In Eq. (8), the parameter *r* remains unknown at this point. We may assume that *r* is constant for a fixed surface-liquid combination and can be experimentally determined along with Eq. (8).

Regressive Analysis

It can be seen from Eq. (8) that the frequency of pulse boiling is influenced by many factors, i.e., $\nu = f(R', \sigma, a, \lambda, h_{fg}, T_s, P_s, q, R, r)$. The first five variables, *R'*, σ , *a*, λ and *h_{fg}* represent the physical properties, while the variables *T_s*, *P_s*, and *q* are the operating parameters of the thermosyphon, and *r* as well

as *R* reflects the influence of the surface-liquid combination. Since all important physical properties of the working fluid can be considered a function of reduced pressure (*P_s/P_c*), we attempt to use it as a comprehensive effective factor of all physical properties. After step-by-step regressive analysis of experimental data for every variable, the resultant correlation is finally obtained:

$$\nu = C_{sf} (P_s/P_c)^{1.327} q^{1.756} d^{-0.24} \quad (9)$$

where *C_{sf}* is a surface-liquid combination factor, which can be determined experimentally. Several values of *C_{sf}* are recommended as follows:

for glass/water system	0.00316
for carbon-steel/water system	0.0310
for carbon-steel/ethanol system	0.10-0.01

The comparison between experimental data and Eq. (9) for the glass/water system is illustrated in Fig. 3. The deviation is within ± 50 percent, which may be considered acceptable due to the complexity of this phenomenon.

Conclusions

The pulse boiling frequency has been proposed as a criterion to distinguish among the flow patterns appearing in thermosyphons. The analytical and regressive expressions of frequency are derived, in which several important parameters are correlated. Although the studies should be further improved, it is expected that the present results may be used to select and determine the proper heat transfer regime of thermosyphons, and may be helpful for the design and application of thermosyphon elements.

References

- Carlsaw, H. S., and Jaeger, J. C., 1959, *Conduction of Heat in Solids*, 2nd ed., Oxford, p. 203.
- Collier, J. G., 1972, *Convective Boiling and Condensation*, McGraw-Hill, London.
- Davis, E. J., and Anderson, G. H., 1966, "The Incipience of Nucleate Boiling in Forced Convection Flow," *AIChE J.*, Vol. 12, pp. 774-780.
- Hsu, Y. Y., 1962, "On the Size Range of Active Nucleation Cavities on a Heating Surface," *ASME JOURNAL OF HEAT TRANSFER*, Vol. 84, pp. 207-216.
- Liu Xin, Ma Tongze, Wu Xiupi, and Zhao Jiagi, 1986, "Heat Transfer Limit and Correlation of a Two-Phase Closed Thermosyphon," presented at the Sixth Annual Conf. of the Chinese Society of Engineering Thermophysics.
- Ma Yiwei, Liu Jifu, and Feng Yi, 1987, "The Characteristics of Condensation Heat Transfer in Thermosyphon," *Proc. Sixth Int. Heat Pipe Conf.*, Grenoble, pp. 445-450.
- Shiraishi, M., Kikuchi, K., and Yamanishi, T., 1981, "Investigation of Heat Transfer Characteristics of a Two-Phase Closed Thermosyphon," *Advances in Heat Pipe Technology*, Pergamon Press, London, pp. 95-104.
- Xin Mingdao, Chen Gang, and Chen Yuanguo, 1987, "Flow and Heat Transfer in Two-Phase Closed Thermosyphons," *Proc. Sixth Int. Heat Pipe Conf.*, Grenoble, pp. 419-423.